NBS SPECIAL PUBLICATION 638

U.S. DEPARTMENT OF COMMERCE / National Bureau of Standards

Laser Induced Damage in Optical Materials: 1981

BOULDER DAMAGE SYMPOSIUM

ASTM

STP 799

NATIONAL BUREAU OF STANDARDS

The National Bureau of Standards[1] was established by an act of Congress on March 3, 1901. The Bureau's overall goal is to strengthen and advance the Nation's science and technology and facilitate their effective application for public benefit. To this end, the Bureau conducts research and provides: (1) a basis for the Nation's physical measurement system, (2) scientific and technological services for industry and government, (3) a technical basis for equity in trade, and (4) technical services to promote public safety. The Bureau's technical work is performed by the National Measurement Laboratory, the National Engineering Laboratory, and the Institute for Computer Sciences and Technology.

THE NATIONAL MEASUREMENT LABORATORY provides the national system of physical and chemical and materials measurement; coordinates the system with measurement systems of other nations and furnishes essential services leading to accurate and uniform physical and chemical measurement throughout the Nation's scientific community, industry, and commerce; conducts materials research leading to improved methods of measurement, standards, and data on the properties of materials needed by industry, commerce, educational institutions, and Government; provides advisory and research services to other Government agencies; develops, produces, and distributes Standard Reference Materials; and provides calibration services. The Laboratory consists of the following centers:

Absolute Physical Quantities[2] — Radiation Research — Chemical Physics — Analytical Chemistry — Materials Science

THE NATIONAL ENGINEERING LABORATORY provides technology and technical services to the public and private sectors to address national needs and to solve national problems; conducts research in engineering and applied science in support of these efforts; builds and maintains competence in the necessary disciplines required to carry out this research and technical service; develops engineering data and measurement capabilities; provides engineering measurement traceability services; develops test methods and proposes engineering standards and code changes; develops and proposes new engineering practices; and develops and improves mechanisms to transfer results of its research to the ultimate user. The Laboratory consists of the following centers:

Applied Mathematics — Electronics and Electrical Engineering[2] — Manufacturing Engineering — Building Technology — Fire Research — Chemical Engineering[2]

THE INSTITUTE FOR COMPUTER SCIENCES AND TECHNOLOGY conducts research and provides scientific and technical services to aid Federal agencies in the selection, acquisition, application, and use of computer technology to improve effectiveness and economy in Government operations in accordance with Public Law 89-306 (40 U.S.C. 759), relevant Executive Orders, and other directives; carries out this mission by managing the Federal Information Processing Standards Program, developing Federal ADP standards guidelines, and managing Federal participation in ADP voluntary standardization activities; provides scientific and technological advisory services and assistance to Federal agencies; and provides the technical foundation for computer-related policies of the Federal Government. The Institute consists of the following centers:

Programming Science and Technology — Computer Systems Engineering.

[1]Headquarters and Laboratories at Gaithersburg, MD, unless otherwise noted; mailing address Washington, DC 20234.
[2]Some divisions within the center are located at Boulder, CO 80303.

Laser Induced Damage In Optical Materials: 1981

Proceedings of a Symposium Sponsored by:
National Bureau of Standards
American Society for Testing and Materials
Office of Naval Research
Department of Energy
Defense Advanced Research Project Agency
Air Force Office of Scientific Research

November 17-18, 1981
NBS, Boulder, Colorado 80303

Edited by:

Harold E. Bennett
Naval Weapons Center
China Lake, California 93555

Arthur H. Guenther
Air Force Weapons Laboratory
Kirtland Air Force Base, New Mexico 87117

David Milam
Lawrence Livermore National Laboratory
Livermore, California 94550

Brian E. Newnam
Los Alamos National Laboratory
Los Alamos, New Mexico 87545

BOULDER DAMAGE SYMPOSIUM

U.S. DEPARTMENT OF COMMERCE, Malcolm Baldrige, Secretary
NATIONAL BUREAU OF STANDARDS, Ernest Ambler, Director

Issued September 1983

Library of Congress Catalog Card Number: 83-600570

National Bureau of Standards Special Publication 638
Natl. Bur. Stand. (U.S.), Spec. Publ. 638, 651 pages (Sept. 1983)
CODEN: XNBSAV

U.S. GOVERNMENT PRINTING OFFICE
WASHINGTON: 1983

For sale by the Superintendent of Documents, U.S. Government Printing Office, Washington, D.C. 20402
Price $12.00
(Add 25 percent for other than U.S. mailing)

Foreword

The Proceedings contain the papers presented at the Thirteenth Symposium on Optical Materials for High Power Lasers held at the National Bureau of Standards (NBS) in Boulder, Colorado, on November 17-18, 1981. The Symposium was jointly sponsored by the National Bureau of Standards, the American Society for Testing and Materials, the Office of Naval Research, the Defense Advanced Research Projects Agency, the Department of Energy, and the Air Force Office of Scientific Research. The Symposium was attended by approximately 200 scientists from the United States, the United Kingdom, Japan, France, West Germany, the Peoples Republic of China, Sweden, and the USSR. It was divided into sessions devoted to the following topics: Materials and Measurements, Mirrors and Surfaces, Thin Films, and finally Fundamental Mechanisms. The Symposium Co-Chairmen were Dr. Harold E. Bennett of the Naval Weapons Center, Dr. Arthur H. Guenther of the Air Force Weapons Laboratory, Dr. David Milam of the Lawrence Livermore National Laboratory, and Dr. Brian E. Newnam of the Los Alamos National Laboratory. They also served as editors of this report. Dr. Alexander J. Glass of KMS Fusion acts as Conference Treasurer with Aaron A. Sanders of the National Bureau of Standards as the Conference Coordinator.

The editors assume full responsibility for the summary, conclusions, and recommendations contained in the report, and for the summaries of discussion found at the end of each paper. The manuscripts of the papers presented at the Symposium have been prepared by the designated authors, and questions pertaining to their content should be addressed to those authors. The interested reader is referred to the bibliography at the end of the summary article for general references to the literature of laser damage studies. The Fourteenth Annual Symposium on this topic will be held in Boulder, Colorado, from November 15-17, 1982. A concerted effort will be made to ensure closer liaison between the practitioners of high peak power and the high average power community.

The principal topics to be considered as contributed papers in 1982 do not differ drastically from those enumerated above. We expect to hear more about improved scaling relations as a function of pulse duration, area, and wavelength, and to see a continuing transfer of information from research activities to industrial practice. New sources at shorter wavelengths continue to be developed, and a corresponding shift in emphasis to short wavelength and repetitively-pulsed damage problems is anticipated. Fabrication and test procedures will continue to be developed, particularly in the diamond-turned optics and thin-film areas.

The purpose of these symposia is to exchange information about optical materials for high power lasers. The editors will welcome comment and criticism from all interested readers relevant to this purpose, and particularly relative to our plans for the Fourteenth Annual Symposium.

H. E. Bennett, A. H. Guenther,
D. Milam, and B. E. Newnam,
Co-Chairmen

Disclaimer

Certain papers contributed to this publication have been prepared by other than NBS authors. These papers have not been reviewed or edited by NBS; therefore, the National Bureau of Standards accepts no responsibility for comments or recommendations contained therein.

Certain commercial equipment, instruments, and materials are identified in this publication in order to explain the experimental procedure adequately. Such identification in no way implies approval, recommendation, or endorsement by the National Bureau of Standards, nor does it imply that the equipment, instruments, or materials identified are necessarily the best available for the purpose.

CONTENTS

SYMPOSIUM WELCOME

Harold E. Bennett
Naval Weapons Center
China Lake, California 93555

Welcome to the Thirteenth Annual Symposium on Optical Materials for High Power Lasers, familiarly known as the Boulder Damage Symposium. To the uninitiated the expression "Boulder Damage" connotes the damage one can do with boulders, hence the more descriptive official name "Optical Materials for High Power Lasers." In some cases, however, the two ideas may not be too far apart. Figure 1 shows a 10-cm or 4-inch diameter laser doubler for the Livermore National Laboratory Argus laser after it was radiated by mistake with a 500-joule pulse rather than a 50-joule pulse. The results are similar to those which would have been observed if it had been hit by a boulder, and are clear evidence to those of us who are used to examining small damage sites under a microscope that laser damage phenomena do indeed scale.

Pictures like this are the spectacular part of our business, but we are only successful when nothing happens to the optical components during laser irradiation. To meet this goal, a wide number of unspectacular and usually unrelated specialties must be employed. Surface physics, multilayer film technology, materials technology, optical design, crystal growth, metallurgy, optical finishing technology, infrared and restrahlen spectroscopy, solid state physics and chemistry, and laser technology are a few examples of the wide range of fields which have been applied to produce the fairly spectacular advances in laser damage threshold which have been achieved over the past decade or so. Our subject is clearly at the boundaries between conventional fields of science rather than in the mainstream of any one of them, and anyone who expects our work to be mainly running lasers and blowing up samples is simply naive.

In another sense, however, we are establishing a new field of optics. Several years ago at this symposium Major Harry Winsor, now at the Air Force Office of Scientific Research, pointed this out and suggested the name "power optics" in analogy with the handling of electrical power which at low frequencies has long been a part of electrical engineering. Previous to the advent of high powered lasers the field of optics was almost entirely concerned with what might be called signal optics, the handling of small signals, maximizing signal-to-noise ratio, etc. Radio and microwave technology is the analogous specialty in the field of electrical engineering. This symposium was set up to attack the problem of power optics and has always been the primary forum for advances in this new field of optics. It is now in its 13th year, and, although the hope was once expressed that all the power optics problems would be solved by now, I see no more evidence that will occur than that the field of power engineering at electrical frequencies will disappear.

Through the years the number of papers given at this symposium and the number of people attending it have both grown, as seen in figure 2. This year we will have 63 papers presented, the most ever, and about the maximum which can be given in a two-day meeting without going to double sessions. The meeting has also become international in scope, and we would like to warmly welcome the participants from overseas who are with us now. In addition to the Japanese and the many countries in Western Europe which are represented, we have a delegation from the Soviet Union with us today and also one from mainland China. We welcome you and are happy to prove again that science has no national boundaries.

A lot of basic information has been reported at this conference over the years, and even the old timers are having difficulty remembering where it is in the Proceedings. We therefore all owe a special debt of gratitude to the Air Force Weapons Laboratory Library which has now assembled an index

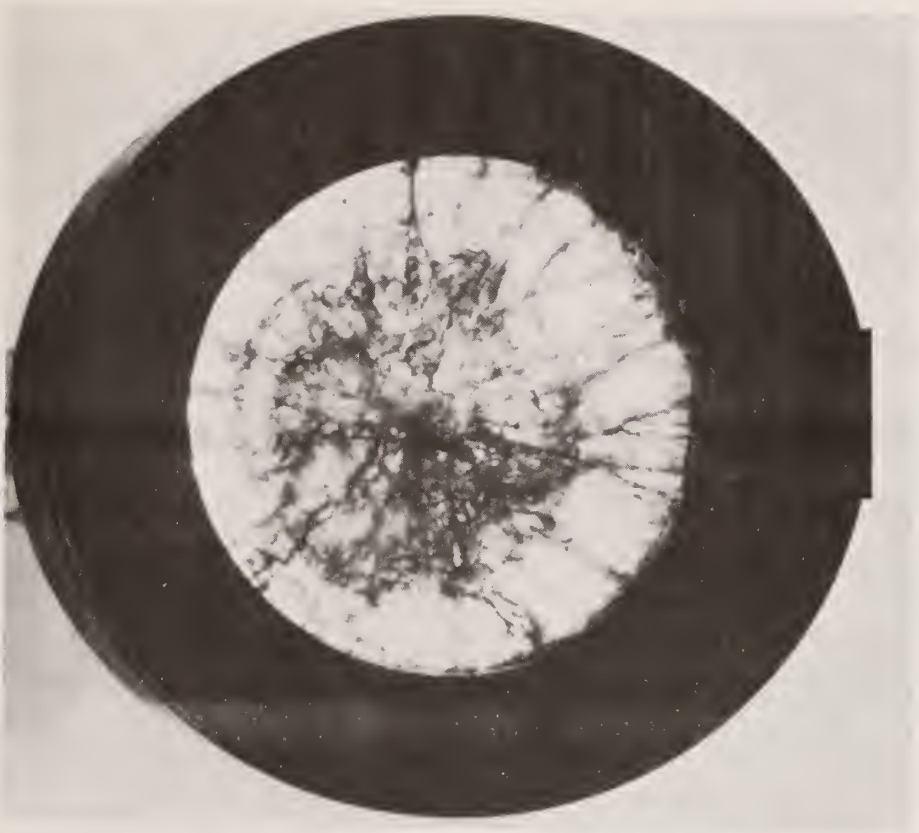

FIGURE 1. Component damage in the Argus Laser

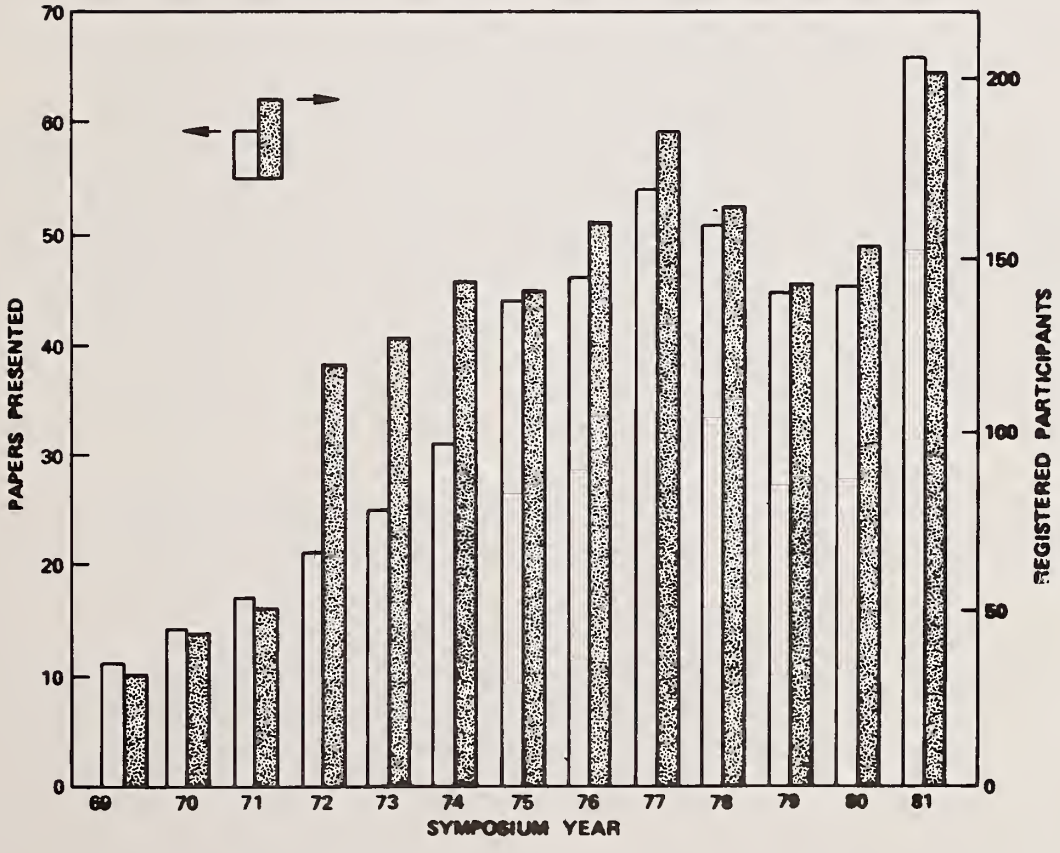

FIGURE 2. A history of the Boulder Damage Symposium

of the Symposia proceedings for the last 10 years. It includes listings by author, co-author, title, subject and key words as well as a compilation of all the published abstracts for the first 10 years. The index will be distributed to all participants of this meeting and also to those who attended the Tenth Annual Meeting but are not present today. A second index is planned by the Library to cover the following five years. It is expected to be equal in size to the initial ten-year index, which indicates how interest in the subject of power optics has grown.

A word about our poster papers. There are 22 poster papers presented on each day. Authors are to be at their poster boards during the morning poster break and again during the afternoon break. To help the audience, a rapporteur will report at the end of each morning's session on the poster papers for that day. The afternoon break is then available for members of the audience to see those papers they missed during the morning break. We are proud of the contribution our poster papers make to the symposium and are encouraged that authors often request that their papers be given as posters rather than as an oral presentation.

We are pleased to report a new addition to our management team. Dave Milam from Lawrence Livermore National Laboratory has joined Art Guenther, Brian Newnam, and myself as a full fledged member of the Steering Committee for the Symposium. Alex Glass, who with Art Guenther was responsible for initiating this Symposium and whose name is a household word to participants in the field, will remain as Treasurer of the organization. Aaron Sanders of the National Bureau of Standards in Boulder has taken the responsibility for developing funding for the symposium and will also coordinate the Bureau's support for its activities. We welcome him to the team.

Special thanks are due to Susie A. Rivera, Aaron's secretary, for acting as a focal point for the Symposium Proceedings and for handling many of the innumerable details which make the symposium possible. Thanks are also due to the others at the registration desk and especially to Pat Whited, Art Guenther's secretary, for her efficient help in making the symposium run smoothly.

Let me conclude by thanking our professional sponsor, the American Society for Testing and Materials, and our financial sponsors, the National Bureau of Standards, the Air Force Office of Scientific Research, the Office of Naval Research, the Department of Energy through both Livermore and Los Alamos National Laboratories, and the Defense Advanced Research Projects Agency for making this meeting possible. They and we hope that you will find the next two days both pleasant and valuable to your work in power optics.

ASTM Welcome

John A. Detrio
University of Dayton
Dayton, Ohio 45469

Welcome to the Thirteenth Annual Boulder Damage Symposium. Maintaining the quality and high standards of technical excellence and the timely presentation of new results is indeed a difficult challenge to the participants and one that Art Guenther, Alex Glass, Hal Bennett, Brian Newnam, and Dave Milam have faced, and they have met the challenge successfully. In spite of the maturity of the laser damage field, this conference continues to provide an effective international forum for the interchange of data and ideas on laser induced damage.

There was talk a few years ago that interest was waning, the laser damage issues were dead or at least put to rest, and that not much new would be uncovered. This first midlife crisis occurred after about the seventh year. If the folk wisdom concerning changes in life directions every seven years is correct, then our second passage is fast approaching.

As with individuals whose character is strengthened by adjusting and successfully making these passages, this conference has changed its character in an evolutionary way over the years and should successfully take up the future challenges. Where will these challenges lie? Where will the pursuit of fundamental questions of laser interactions lead? No one knows for certain, but just as certainly there are still unresolved questions and issues which are being uncovered as shorter laser wavelengths are used, as pulse durations are shortened, and as power levels increase.

Many practical issues have already been identified but not solved. Multiple irradiation damage effects, the influence of contamination and its control, improved surface preparation, coating deposition, and cleaning are examples of important but seemingly mundane issues. The study of these problems will provide new insights and lead to improved components and lasers and to a better understanding of materials and laser interactions.

The experimental efforts will stimulate theoretical analysis and improvements in diagnostics. Many improvements in materials purification and analysis have benefited from, or been driven by, the needs of lasers and designers or by the desire to increase the laser damage resistance of optical components.

As long as the Boulder Damage Symposium serves the international community of scientists concerned with laser damage, the American Society for Testing and Materials will continue to support these meetings.

Last year I challenged the attendees to consider working on Laser Damage Standards. This year I have emphasized a different challenge, but one consistent with the second role that ASTM fulfills - to share knowledge and to stimulate the pursuit of knowledge.

On behalf of ASTM, WELCOME TO THE THIRTEENTH ANNUAL BOULDER DAMAGE SYMPOSIUM.

Laser Induced Damage in Optical Materials

Thirteenth ASTM Symposium

November 17-18, 1981

The Thirteenth Annual Symposium on Optical Materials for High Power Lasers (Boulder Damage Symposium) was held at the National Bureau of Standards in Boulder, Colorado, November 17-18, 1981. The Symposium was held under the auspices of ASTM Committee F-1, Subcommittee on Laser Standards, with the joint sponsorship of NBS, the Defense Advanced Research Project Agency, the Department of Energy, The Office of Naval Research, and the Air Force Office of Scientific Research. Approximately 200 scientists attended the Symposium, including representatives of the United Kingdom, France, Japan, West Germany, the Peoples Republic of China, Sweden, and the USSR. The Symposium was divided into sessions concerning Materials and Measurements, Mirrors and Surfaces, Thin Films, and finally Fundamental Mechanisms. As in previous years, the emphasis of the papers presented at the Symposium was directed toward new frontiers and new developments. Particular emphasis was given to materials for high power apparatus. The wavelength range of prime interest was from 10.6 μm to the uv region. Highlights included surface characterization, thin film-substrate boundaries, and advances in fundamental laser-matter threshold interactions and mechanisms. The scaling of damage thresholds with pulse duration, focal area, and wavelength was discussed in detail. Harold E. Bennett of the Naval Weapons Center, Arthur H. Guenther of the Air Force Weapons Laboratory, David Milam of the Lawrence Livermore National Laboratory, and Brian E. Newnam of the Los Alamos National Laboratory were co-chairmen of the Symposium. The Fourteenth Annual Symposium is scheduled for November 15-17, 1982,at the National Bureau of Standards, Boulder, Colorado.

Key words: laser damage; laser interaction; optical components; optical fabrication; optical materials and properties; thin film coatings.

1.0 Introduction

The Thirteenth Annual Symposium on Optical Materials for High Power Lasers (Boulder Damage Symposium) was held, as in previous years, at the National Bureau of Standards in Boulder, Colorado, November 17-18, 1981. The Symposium was held under the auspices of the ASTM Committee F-1, Subcommittee on Laser Standards, with the joint sponsorship of NBS, the Defense Advanced Research Projects Agency, the Department of Energy, the Office of Naval Research, and the Air Force Office of Scientific Research. Working sessions of the Committee F-1 Subcommittee on Lasers were held on Monday, November 16. Approximately 200 scientists attended the Symposium, including representatives of the United Kingdom, France, Japan, West Germany, the Peoples Republic of China, Sweden, and the USSR. The Symposium was divided into sessions concerning Materials and Measurements, Mirrors and Surfaces, Thin Films and finally Fundamental Mechanisms. In all, over 60 technical presentations were made. Harold E. Bennett of the Naval Weapons Center, Arthur H. Guenther of the Air Force Weapons Laboratory, Dave Milam of the Lawrence Livermore National Laboratory and Brian E. Newnam of the Los Alamos National Laboratory, were co-chairmen of the Symposium. Alexander J. Glass of KMS Fusion, is Conference Treasurer and Aaron A. Sanders of the National Bureau of Standards acts as Conference Coordinator.

The purpose of these symposia is to exchange information about optical materials for high power lasers. The authors will welcome comments and criticism from all interested readers relevant to this purpose and particularly relative to our plans for the Fourteenth Annual Symposium, scheduled for November 15-17, 1982, at the National Bureau of Standards, Boulder, Colorado.

2.0 Principal Conclusions

There was considerable diversity in papers at this year's symposium. Nowhere was this more apparent than in the area of materials for high-power transmitting optics. At one extreme was the report of a survey and assessment of 23 potential window materials for a specific laser, namely iodine at 1.3 μm. Many candidates exhibit acceptable absorption levels in the 10^{-4} cm^{-1} range. From this highly focused study, one proceeded to development on new classes of glass materials such as the fluorides of heavy metals useful for multi-spectral applications. Besides the demonstration of acceptable absorption levels in the infrared, they possess improved mechanical properties, at least when compared to chalcogenide materials. Another major technical achievement was the production of single-phase polycrystalline CVD ZnS which is colorless and exhibits reduced scatter and absorption. However, the most enthusiastic attention was given to a report on the development of polymeric optical elements, which, because of improved process control, exhibited damage levels greater than some frequently used glasses. This development portends potentially great cost savings in the fabrication of high-power elements.

It was not unexpected that in the press of evolving applications and new high-power lasers that several papers dealt with the short-wavelength response of materials, particularly when the irradiation is rep-rated. The subject of an accumulation of damage under such repeated exposure was given due attention and should be most useful in practical system applications. It was noted that depending upon the material class e.g., alkali halide crystals versus fused silica, that the accumulation effect was not similar and could be impurity dominated, a non-linear response, or even avalanche breakdown. Of course, the irradiation levels where damage can be observed to accumulate are well below the single-pulse damage level. In some cases, our understanding of the damage mechanism is proceeding from studies on more "perfect" materials such as intrinsic silicon.

While the research for new materials proceeds, we continue to realize improvements in the utility of several workhorse standards through new processes such as annealing by heat treatment, baking, and preconditioning. In some cases, e.g., alkali halides, the pulsed laser induced damage threshold was raised by an impressive factor of five.

As materials improve, so must instrumentation and measuring techniques. The most critical property in transparent optics is the absorption level. Usually this means resorting to calorimetry, a somewhat slow measurement method. As materials become better, there becomes a need to determine the uniformity of critical properties and even to identify potential, damage sensitive areas. Thus we were grateful to see several advances along these lines by developments in photo-acoustics, calorimetry, and their correlation with damage experiments. Some of these advances are also allowing us to separate surface and bulk absorption. To these instrumental advances is added improved accuracy in determining basic properties such as the thermo-optic coefficient necessary to perform system design or comparative assessments of different candidate materials.

To the above developments on characterization and instrumentation, several novel methods were reported useful during the fabrication of a high-power optical element such as during the deposition of high reflectivity coatings. These new techniques are, in fact, leading to direct improvements in fabricating high-performance elements, both in determining their sensitivity to polarization effects, higher reflectivity (CAPS), and lower scatter where a sensitivity in measuring the scattered light level to 10 ppb/sr was reported.

The cavity-attenuated phase-shift (CAPS) method has been applied to the mid-IR (2.6 - 4.2 μm) to measure 99.20 ± 0.50 percent reflectance. Mode matching between active modes of the laser and

longitudinal cavity modes gave problems resulting in greater uncertainty. The CAPS method has been demonstrated to measure 1-R to within 25 ppm at 633 nm and thus appears to allow calculation of ultrahigh reflectances > 99.99 percent.

In the deposition area, a rotating-analyzer ellipsometer was installed in situ to measure thickness with high precision for production of an 84° phase retardance coating. Such a device can provide refractive index, packing density, and perhaps stoichiometry versus deposition conditions.

In the area of mirrors and surfaces, continued attention was given to improvements in metal mirror surface finishing, corrosion resistance, etc., such as by surface alloying, etc. For transparent elements improved surfaces and damage resistance were reported through improved polishing with soft abrasives and heat treatment, as well as by the use of a deuterium environment to reduce the amount of OH^- in fused silica which has a deleterious effect on optical performance at ~2.75 μm.

Since surfaces are the barrier to the environment, they must withstand environmental attacks in a manner so as not to degrade system performance. Several papers dealt with this area of concern, most notably adsorption of absorbing species e.g., H_2O, at the HF laser operating wavelength. In another vein, an interesting technique for keeping optical elements clean by an electrostatic fence was also heard. Other papers in this area dealt with certifying our understanding of the employment of these elements under a variety of conditions such as non-normal incidence or at cryogenic temperatures. It is gratifying to note that the physical understanding of these cases is well in hand. On the other hand, the thermo-elastic response of surfaces to repeated irradiation is not sufficiently complete. However, in some cases, the long-term behavior can be quite adequately handled by modeling, as if a cw laser were employed at a power level comparable to the average power in a train of pulses. But when all else fails, one must remove the heat and a novel method using porous metallic substrates and heat pipes was reported by workers in the Soviet Union.

Just as in the case of the previous categories of optical materials, thin films were subjected to pulsed, short-wavelength lasers, to repeated pulses, and to adverse environments, such as the chemical species present in excimer lasers. A rapidly growing data base of the utility of various candidate film materials is being generated, principally at the various laser fusion laboratories where the trumpet is ever loudly blaring, "to shorter wavelengths, to shorter wavelengths....."

State-of-the-art assessments of performance are being accomplished, much as was the case for infrared lasers when they were more in vogue. This time, however, we have benefited from our past efforts and much earlier in their development, we see films fabricated for this new wavelength region improved in their performance by design considerations such as the use of under- and overcoats or through nonquarterwave designs. To go with the expected materials such as MgF_2 and SiO_2, new candidates such as Sc_2O_3 are finding favor in the search for UV-quality materials. From these studies, it was determined that several coatings vendors, using electron-gun deposition, now produce HR and AR coatings for 248 nm that consistently exceed 6 J/cm^2 for single-shot, 20-ns pulses. Halfwave overcoats and barrier layers appear necessary to reach this high level of damage resistance. Reflectors for 248 nm using Sc_2O_3/MgF_2 have exhibited increased damage resistance (2.5X greater) when overcoated with a HW-thick film of MgF_2. Similarly, as used in an AR configuration on fused silica, a HW barrier layer of SiO_2 raises the threshold by 50 percent. The physical reason for these improvements has not as yet been established.

Repetition rates between 1 and 35 pps do not influence damage resistance of oxide reflectors for 248 nm. Failure in multiple-shot irradiaton of oxide coatings is apparently prompt with 90 percent of the failures occurring within four shots under 2 pps/248 nm exposure. Most test sites on UV

reflectors damage promptly or survive at least 1000 shots, apparently independent of the fluence level.

Concentration on promising film materials, e.g., Al_2O_3 and Sc_2O_3, has resulted in higher thresholds consistently between 3 to 4 J/cm^2 for 10-ns, 35-pps irradiation. Using the new definition of damage threshold as the maximum fluence for which no test site damages under multiple-shot irradiation will provide necessarily conservative and useful data for laser designers. Additionally, thresholds determined with this definition may well be independent of laser spot size. Application of the principle of suppression of the peak, standing-wave electric field in the top high-index layers substantially increased the damage resistance for multilayer reflectors of Sc_2O_3/MgF_2 at 248 nm. An average increase in threshold of 50 percent was realized with one pair of optimized non-QW layers on the top, but no further advantage was realized with two pairs.

Useful information on environmental degradation of films in the infrared was reported. Factors studied included cleaning solvents, sunlight, humidity, and nominally corrosive gases.

The issue of characterization of thin films is even more important than for bulk optical materials and surfaces because of the greater complexity and interplay between properties and performance e.g., thickness, homogeneity, structure variations, and the like. Thus, considerable attention was given to film analysis and the correlation of structure, design, and performance. This type of analysis coupled with damage testing leads to novel solutions such as gradient-index surfaces. It was shown that guided-wave techniques can be used to measure index of refraction and thickness of a thick film (~1 μm thick) to ± 0.001 percent and 0.3 percent, respectively, while ellipsometry seems to be a very sensitive method for measuring film nonuniformities such as in absorption and/or reflectance. A variation in Δ of 0.1° signifies 0.01 percent in film nonuniformity, while a variation in Ψ of 0.1° signifies a differential reflectance of 0.001. Mirrors can also be scanned for mapping.

As regards film performance, the secondary minima on either side of the principal reflectance maxima can reveal deviations in 1) overall thickness of layers, 2) which films are absorbing and by how much. It is then possible to calculate the principal reflectance maximum if the film thicknesses are all correct and volume absorption limits the reflectance.

In the case of gradient-index surfaces, Sol-gel coatings on fused silica are, on the average, three to four times more damage resistant than titania/silica AR coatings deposited on large-diameter optics and 40 percent more damage resistant than optimized 4-layer Ta_2O_5/SiO_2 e-gun-produced AR coatings on small-diameter optics. However, their fragile nature and cleaning difficulties must be considered in their application. Reflectance in the samples tested was nonuniform over the surface from approximately 0.13 percent to 2 percent.

There was the usual range of damage tests, from specific optical elements such as anti-reflection coated $LiNbO_3$ where site-selective damage as a function of coating vendor was measured to reviews of the damage resistance of e-beam deposited Ta_2O_5/SiO_2 anti-reflection coatings. In this latter study, the purpose was to maximize the damage resistance by varying the deposition process and material finish. Bowl-feed polished fused silica (BK-7) substrates resulted in 85 percent higher AR-coating (Ta_2O_5/SiO_2 with HW SiO_2 barrier layer) damage thresholds than those on conventionally-polished substrates. The threshold did not correlate with film reflectance or net macrostress or film absorption (unless over 10^4 ppm). Baking at 400° C substantially reduced film absorption and net stress (from compression to tension), but only a modest increase in threshold was obtained.

There was continued emphasis this year on new materials and new processes, particularly in the preparation of amorphous films, with much attention given to diamond-like and amorphous carbon films,

as well as silicon coatings.

Co-evaporation of SiO_2 with ZrO_2 produced a high-index film of greatly reduced crystallinity. It is expected that this will lead to greater damage resistance, as was reported last year for films of TiO_2.

Absorption of silicon films alloyed with hydrogen showed a reduction in absorption to 3 cm^{-1} at 2.7 μm. Film composition of $Si_{1-x}H_x$ was continuously variable during rf-diode sputtering, with the optimum value of x being 0.12. On the other hand, sputtered films of Si tended to exhibit lower absorption and higher damage resistance than evaporated films by a factor between 2 and 3X.

In the case of carbon films, the optical properties of hydrogenated amorphous carbon (a-C:H) films deposited in an rf-excited, hydrocarbon plasma could be methodically varied by changing the kinetic energy with which the ions hit the substrate surface. By increasing the ratio of negative bias voltage to gas pressure (U_b/p), the refractive index increases, and the absorption edge shifts to longer wavelengths. In another vein, ion-beam deposition of diamond-like carbon coatings on CaF_2 only produced very adherent films when carbon ions were implanted first within the upper 600 Å of the window surface. Optical absorption of 150 cm^{-1} at 3.8 μm is still quite high, limiting them at present to low-power applications. Finally, the rf-plasma decomposition of an alkane gas to produce carbon ions for deposition on CaF_2 yielded films of unsatisfactory adhesion. Only by reducing the deposition rate and interrupting the coating process over a 45-minute run could 700 to 1000 Å-thick films be produced. Fracture strength of CaF_2 bars was only slightly increased by the addition of such coatings. It is obvious that additional emphasis will be placed on silicon/carbon film technology. This emphasis is being generated by the promise of environmentally durable, damage resistant, high-index coatings. The deposition mechanics of producing high quality, uniform, laser absorption films of good adhesion over large areas is still in its infancy compared to other competing film materials.

Much of the interest in the area of fundamental mechanisms in laser-induced damage centered on describing the impurity-dominated damage process in real, as opposed to ideal, optical materials. The role of these defects was considered, not only as initiators in pulsed laser irradiation, but as the major contribution to the absorption in cw-laser exposures. In one analytical study, it was concluded that if defects are closer than 10X their diameter, they cannot be treated independently. This consideration of defect separation is critical to the greater question of spot-size scaling, particularly for anything but the smallest (typically < 5μm) beam diameters. For very small diameter exposures, the response is probably governed by purely thermal considerations, providing one takes into account the appropriate geometry of the interaction.

There was, as well, a good number of papers dealing with nonlinear interaction processes such as multiphoton absorption and self focusing, particularly in the case of semiconductors, which are more amenable to analysis than purely dielectric materials. Key to many studies is the question of the generation of free carriers and their growth under intense, coherent illumination. From this approach, any spot-size dependence, self-focusing, or other material response can be analyzed. One interesting result was the suggestion that while the conduction electron energy may increase under intense illumination, the energy of valence electrons would remain at low-field values; i.e., there is an intensity dependence in the effective bandgap, even to the point where three-photon processes would dominate those of two photon. One practical proposal from other work indicated that nonlinear refraction in doubling crystals can reduce conversion efficiency as the result of an induced phase mismatch, while another paper suggested that nonlinear refraction as manifested in self-focusing could be employed as a limiter to prevent damage.

Several papers also catalogued nonlinear, refractive coefficients in several glasses, crystals, and semiconductor materials. It was shown that absorption by excited free carriers can be a major source of error in determining nonlinear absorption coefficients.

The meeting concluded with a discussion of microwave absorption in optical materials and the role electronegative gases play in controlling gas breakdown levels in various mixtures. All in all, the meeting was most successful with the largest number of papers, to date, included in the conference proceedings.

3.0 Summary of Papers

The subject matters of the Thirteenth Annual Symposium covered four, broad areas of interest to the high-power laser community: (1) Materials and Measurements, (2) Materials and Surfaces, (3) Thin Films, and finally, (4) Fundamental Mechanisms. These conference proceedings are organized accordingly. In this section, a concise summary of each paper is provided. Closely related papers are discussed together, whenever possible. The interested reader is referred to the complete manuscript of any paper for further details. Our intention here is to provide the reader with an overview of the Symposium and to identify the topics of current interest, the authors, and their organizations. To highlight this year's presented papers, each topical area is discussed with a brief statement of the underlying problems and the status of understanding within the area of interest.

3.1 Materials and Measurements

The principal factor governing the performance of transparent, optical materials for high-power or high-energy applications concerns, in the large, their level of absorption of radiant energy. Thus, there is a continual search for highly transparent, environmentally stable, optical materials which exhibit low absorption. To this search for new materials, one must also address new procedures for the generation of these materials while maintaining low absorption, such as the growth of crystals, melting of glasses, or deposition of thin films. A necessary adjunct to the development of new materials is the concurrent development of measuring techniques to rapidly and accurately determine the absolute absorption or monitor its radiation. As such, instrumentation plays a major role in the development of new materials.

To start this summary, we will first address the subject of new materials. The variety at this year's Symposium was most interesting. Surveys of materials specific to certain lasers were addressed, as well as the development of a new class of multispectral glasses. The subject which drew most interest concerned the potential of polymers as materials for high-power applications.

Transparent polymer optical materials could have excellent utility for solid-state dye cells, bleachable filters, and for Q-switching lasers, but they presently have rather low damage thresholds. K. Dyumaev, A. Manenkov, A. Maslyukov, G. Matyushin, V. Nechitailo, and A. Prokhorov of the Lebedev Physics Institute have studied transparent polymers in an effort to increase their damage threshold. Not suprisingly, they found that laser damage was usually due to absorption by impurities. Finer filtering of the original monomers, in some cases, resulted in a 30-fold increase in damage threshold. Modification of the visco-elastic properties to decrease the forced elasticity limit so that it is lower than the cleavage fracture limit was found to increase the number of pulses before damage occurred at a given power level. Introduction of low molecular weight additives also increased the damage threshold by deactivating excited electron states during irradiation.

Laser rate calorimetry was used by N. Fernelius, D. Dempsey, D. O'Quinn and M. Gangl of the University of Dayton Research Institute and W. Knecht of the Wright-Patterson Air Force Base to screen

additional materials for use with iodine lasers operating at 1.315 μm. The effective optical-absorption coefficients for 23 candidate materials were reported. Most were in the 10^{-4} cm^{-1} range.

Initial characterization tests on multispectral-grade, chemically vapor-deposited ZnS were reported by C. Willingham, C. Klein, and J. Pappis of Raytheon Company. Extrinsic absorption and light scattering of this colorless material have been greatly reduced as compared with standard-grade, dark-orange, milky-appearing material. This material is now commercially available. It is unfortunate that company proprietary considerations made it impossible for these authors to publish a full manuscript describing their work.

A collaborative study by M. Drexhage, B. Bendow, O. El-Bayoumi, R. Brown, and P. Banerjee of the Rome Air Development Center, T. Loretz of Galileo Electro-Optics Corporation, C. Moynihan of the Rensselaer Polytechnic Institute and J. Shaffer, P. Temple, and H. Bennett of the Naval Weapons Center determined that heavy-metal fluoride glasses offer the possibility of (1) reduced absorption and broad regions of transparency in the infrared region, and (2) improved mechanical properties as compared with chalcogenide infrared glasses.

Much of the interest in the fluoride glasses has been focused on possible fiber optics applications, but other applications include laser windows, IR domes, low dispersion, infrared refractive elements, and laser hosts. First investigated were the fluorozirconate glasses which contain ZrF_4 as a primary constituent, BaF_2 as a secondary constituent, and various metal fluorides as additional constituents. Subsequently, the fluorohafnate glasses, in which HfF_4 replaces ZrF_4 as the primary constituent, were investigated. Most recently, other glasses, some based on ThF_4 and BaF_2, have been investigated. One of these glasses, BZnYbT, has an absorption in the 3-5 μm range which is about two orders of magnitude lower than that of the fluorozirconate glass ZBT. A minimum loss coefficient of $2 \times 10^{-8} cm^{-1}$ is predicted if scattering losses comparable to those of fused silica can be achieved and if impurity absorption can be reduced adequately. Glasses containing Yb present a sharp, absorption peak near 1-μm wavelength. Glasses have recently been synthesized in which the Yb is replaced by Y, eliminating this 1μm absorption while maintaining the infrared transparency.

Another class of papers in materials and measurements concerned, as might be expected, material resistance to high power lasers. Considerable emphasis was placed on laser damage experiments in the ultraviolet region. In addition, we saw, for the first time, studies relative to the accumulation of damage in transparent materials as a function of repeated exposures, an area of obvious input for rep-rated systems. An area which also received attention in the materials area concerned the improvement of materials by additional treatment such as baking, operating at cryogenic temperatures, or conditioning by pre-exposure with low-energy laser pulses. Orientation of crystals or the related subject of polarization sensitivity of the damage threshold was treated as well.

In a very interesting research effort, the optical damage threshold, nonlinear transmission, and doubling efficiency of $LiIO_3$ were reported by W. Williams, M. Soileau, E. Van Stryland, and A. Smirl of North Texas State University. Forty-five and 145-psec pulses at 0.53 μm and 1.06 μm wavelengths were used in the study. The damage thresholds were found to depend on wavelength, crystal orientation, and number of times the sample had been irradiated. The doubling efficiency decreased markedly with increasing irradiance beyond a critical value, probably from the onset of optical parametric down-conversion. Both reversible and irreversible changes in the complex index of refraction were observed.

Damage by ultraviolet laser pulses was studied by B. Gorshkov, A. Epifanov, A. Manenkov, and A. Panov of the Lebedev Physical Institute of the USSR Academy of Sciences. They measured laser damage thresholds for 14 different optical materials at 0.266 μm. For most alkali-halide crystals,

damage appeared to be caused by direct photo-ionization of impurities. In sapphire, damage most likely was due to self-focusing, while for fused quartz, LiF, and CaF_2, the damage appeared to be caused by electron avalanche ionization.

To confirm that the damage to the fused quartz was caused by electron avalanche, they irradiated a sample simultaneously with 0.266-μm and 1.06-μm pulses and monitored the photoconductivity and thus the number of free electrons in the generated material. Addition of the UV pulses reduced the damage threshold at 1.06 μm by liberating electrons to start the avalanche. Thus, the observation confirmed that the damage was due to electron avalanche.

A new instrument for measuring laser damage threshold over a range of visible and ultraviolet wavelengths was reported by C. Marrs, W. Faith, J. Dancy, and J. Porteus of the Naval Weapons Center. The heart of the damage facility is a flashlamp pumped, dye laser which produces 500-ns, 0.18 J pulses at 492 nm. The pulse-to-pulse energy stability is ±3 percent, and the focused, spatial profiles were flat-topped Gaussians with $1/e^2$ widths of 270 μm. A continuous range of wavelengths could be produced with this instrument, but only measurements at 492 nm were reported. Multilayer dielectric films having reflectances in excess of 0.99 were tested. Selective damage was the failure mode observed, and no correlation with reflectance was found. Metal mirror damage was also measured, and a comparison was made with calculated slip and melt thresholds.

Repeated pulses can damage glass with pulse energies considerably below that required for damage with a single pulse. This effect was investigated in detail by E. Maldutis, S. Balickas, and R. Kraujalis of the Academy of Science of Lithuanian SSR. They irradiated K-8 glass with 17-ns laser pulses at a wavelength of 1.06 μm and 0.53 μm. A study of the number of pulses required to cause bulk damage versus relative pulse energy showed that the glass damage had to be caused by a gradual degradation accumulation rather than by the statistical nature of laser-induced, electron avalanche. The accumulated damage was observed to produce changes in the absorption coefficient of the glass in the 1000-100 cm^{-1} range.

They concluded that damage with the 1.06-μm wavelength light was caused by a thermo-avalanche initiated by absorbing inhomogeneities and that damage with the 0.53-μm light was caused by two photon generation of free electrons, absorption of light by the free carriers, and the development of an electron avalanche.

A novel interpretation of laser damage kinetics in the picosecond pulse regime was presented by R. Walser, M. Becker, and D. Sheng of the University of Texas at Austin. They suggested that laser damage can be viewed as a non-equilibrium phase transition involving the nucleation of embryonic clusters to near-liquid-phase charge densities. In this view, the incident photons are absorbed resonantly by surface plasmons, i.e., collective electronic oscillations associated with these clusters. This view suggests that clusters will occur even though there are no submicroscopic collections of inpurities. Such unobservable impurity collections have been proposed as a mechanism to explain the laser damage kinetics in various experimental studies of picosecond laser damage. The new, theoretical explanation proposed in this paper could be quite significant in extending our understanding of laser damage phenomena, but critical experiments to test the suggested hypothesis need to be devised and carried out.

J. Franck from the Naval Weapons Center and M. Soileau from North Texas State University have verified that the bulk laser damage threshold of both NaCl and KCl single-crystal samples can be increased by annealing the crystals at temperatures as high as 1° C below the melting temperature, followed by rapid cooling. Increases in damage threshold as high as 4.6X were observed. These results are in agreement with those previously reported by Manenkov at an earlier meeting in this

symposia series.

A method for raising the bulk damage threshold of KDP was given by J. Swain, S. Stokowski, D. Milam, and F. Rainer, all of Lawrence Livermore National Laboratory. The median damage threshold for ~ 100 untreated KDP crystals subjected to 1-ns, 1064-nm, pulsed-laser irradiation was 7 J/cm^2 for a 2.5 mm diameter spot. Preliminary, subthreshold laser irradiation raised the average threshold value to 11 J/cm^2. Extended baking (several days) at temperatures up to 165° C did not, by itself, consistently raise the threshold, but when combined with subthreshold laser irradiation, raised the median damage threshold by over a factor of two relative to the unbaked thresholds. Increases from 1.5 to 5 times were observed in individual samples. As the pulse duration increased, the threshold increased, but not as rapidly as the square root of the pulse length.

Absorption can take place not only within the bulk of an optical material but at their surfaces as well. In fact, the surface contribution to the total absorption is not insignificant, nor would one expect it to be, since the surface furnishes the barrier to the outside world and must withstand all the environmental attacks. Thus, it is not surprising that considerable attention at this Symposium was given to the measurement of the surface absorption and its relationship to the total absorption exhibited by a component. These measurements require highly sensitive instrumentation, usually calorimetry. A closely related problem concerns changes in surfaces or within the bulk of materials as a function of laser properties such as rep rate, intensity, wavelength, etc. In many cases, properties such as the thermo-optic coefficient are a property of import along with others necessary to analyze the thermal response of optical elements. To this end, several papers dealt with accurate measurements of the response of optical materials to laser exposure.

N. Fernelius at the University of Dayton Research Institute used photoacoustic absorption measurements to determine the ratio of surface-to-bulk absorption in uncoated sapphire and zinc selenide. The sapphire samples were irradiated by a 1.319-μm beam, chopped at frequencies of 50, 100, 500, and 1000 Hz. Photoacoustic signals were recorded with an electret microphone and a lock-in analyzer. At each chopping frequency, he adjusted the lock-in phase to give zero-quadrature signal, and recorded the amplitude and phase. Similar experiments were done at 10.6 μm on zinc selenide, and the total absorption of both samples was measured by laser calorimetry. When the data were compared to four photoacoustic theories, the Rosenczwaig-Gersho theory, as modified to account for surface absorption, was found to be in closest agreement with the experimental results. The theory indicated that 1.319-μm surface absorption β_S and bulk absorption β_B of 0.78-cm-thick sapphire samples were $7.3 \times 10^{-6} \leq \beta_S \leq 1.4 \times 10^{-5}$ and $7.1 \times 10^{-4}\ cm^{-1} \leq \beta_B \leq 7.3 \times 10^{-4}\ cm^{-1}$. For the 0.79-cm-thick zinc selenide sample, the 10.6-μm absorptions were $\beta_S = 1.0 \times 10^{-4}$ and $\beta_B = 4.1 \times 10^{-3}\ cm^{-1}$ respectively.

The work of Fernelius continues to emphasize some difficulties with practical usage of photoacoustic absorption measurement. The technique is usually unable to perform stand-alone, absolute measurements of absorption, and even relative quantities such as the ratio of surface-to-bulk absorption must be obtained by comparing data to a body of theory that is still evolving.

The temperature dependent absorption in copper at wavelengths of 0.647, 1.08, and 10.6 μm was reported by R. Quimby, M. Bass, and L. Liou of the Center for Laser Studies, University of Southern California, using laser rate calorimetry. Measurements were made from 20° C to 1000° C. The linear dependence of absorption on temperature predicted by the Drude theory was verified experimentally for copper at wavelengths of 10.6 μm and 1.08 μm. At 0.647 μm it was stronger than predicted, perhaps because of the onset of interband transitions. After thermal cycling, a permanent increase in absorption at 1.08 μm and 0.647 μm was observed which could be correlated with a change in microstructure of the sample. No change was observed at 10.6 μm.

In another paper from the University of Southern California by S. Wu, M. Bass, and J. Stone, pulsed CO_2 laser calorimetery was used to study the absorption at 10.6-μm wavelength of pure KCl and NaCl crystals. At a low intensity (~250 Mw/cm^2) a 50 percent increase in absorption occurred. It was reversible in the sense that below that intensity level the lower absorption level was observed. No additional changes in absorption occurred (as the intensity was raised) until at a high intensity (~ 2-4 GW/cm^2) an irreversible change in absorption occurred. This intensity was 1/3 to 1/2 that required for single-shot damage, and coincided with the threshold for multiple-shot damage, here called the fatigue laser damage threshold. Below this threshold no change occurred, even after 1800 pulses. Above it, fatigue damage, which was similar in morphology to single pulse breakdown, occurred. Studies of the focal volume dependence of the fatigue damage phenomena suggested that microscopic inclusions or defects were responsible for the observed damage.

In yet another paper from the group at the Institute for Laser Studies, N. Koumvakalis, C. Lee, and M. Bass discussed the use of repetitively pulsed calorimetry to evaluate mechanically-polished and diamond-turned copper mirrors exposed to laser irradiation at 1.0 μm. The absorption increased with temperature approximately as predicted by the Drude model. When laser damage occurred as a result of repetitive pulsing, the absorption increased dramatically. There was no difference in the increase in absorption with temperature for multi-shot and single-shot damage tests performed with the same beam radius. The increase in absorption was reversible until damage occurred. The data suggest that the observed change in absorption of these copper mirrors is caused by temperature changes induced by laser irradiation.

The change in index of refraction with temperature, dn/dT, for eleven materials at 0.63, 1.15, 1.315, and 3.39 μm was reported by R. Harris and M. Gangl of the University of Dayton Research Institute. The measurements were made in the 25-100° C range using an interferometric technique. The lowest value of dn/dT was observed for Kigre Q-98 glass, which also had a very low absorption coefficient at 1.3 μm as measured by laser rate calorimetry. A significant, systematic error may result in dn/dT values, using the author's technique, if the order of interference is incorrect. It is not clear whether or not such an error exists or was evaluated in this report.

Finally, we come to the subject of measurement instrumentation, and this year, several new, interesting, diagnostic techniques and measuring concepts were presented. They ranged from polarization sensitive calorimetry to scattering measurements as indicators of material quality, to monitors useful during the deposition of thin films. Finally, a novel concept which offers great promise for the accurate determination of high reflectance was heard.

Calorimetric absorption coefficient measurements must deal with both bulk absorption in the material and absorption at the two surfaces. P. Miles of the Raytheon Company showed that if the sample is in the form of a 60^o prism (for materials with index of refraction less than 1.75) or a truncated, 40^o prism for higher indices, and use is made of polarization and prism orientation, a series of simultaneous equations can be obtained from which both surface and volume absorption can be extracted.

B. Tirri of the Perkin Elmer Corporation emphasized that certain applications of multilayer dielectric reflectors, such as phase retarders, require highly-exact layer thicknesses. To produce such coatings, it is necessary to utilize a very accurate monitor during the deposition process. One such device described by him is the rotating-analyzer ellipsometer, which provides refractive-index information, as well. A design featuring minicomputer-generated values of the ellipsometric parameters ψ and Δ and integrated with a large, vacuum-deposition chamber was described. Various coatings, including an 84° phase retardance coating comprising a four-layer design of $ZnSe/ThF_4$, were

used to illustrate the capabilities of the ellipsometer. A precision in the fabrication of the four-layer coating of ±0.007° and a thickness resolution of ~10Å with information generated every 2 s was demonstrated. Such a device should also provide valuable information on the effects of various deposition parameters on such properties as packing density and stoichiometry.

Successful demonstration of the cavity-attenuated phase-shift (CAPS) technique for high-reflectance measurements in the mid-infrared (2.6 - 4.2 μm) was reported by M. Kwok, J. Herbelin, R. Ueunten, and G. Segal from the Aerospace Corporation. Dielectric reflectors on silicon substrates were prepared for 2.911 μm, at which wavelength the atmospheric water absorption has a minimum. A reflectance of 99.20 ± 0.50 percent was measured. The larger uncertainty, as compared to similar, visible-wavelength measurements with the CAPS technique, was attributed to the fewer number of longitudinal modes available from IR gas lasers, thus not filling the cavity with a sufficient number of modes to approach the limit.

An instrument for measuring light scatter from high-reflectance surfaces such as laser gyro mirrors was reported by W. Stowell of RLG Laboratory and F. Orazio, Jr., and R. Silva of VTI, Inc. The data was plotted three dimensionally using an elaborate computer system to show the point to point variation as the 0.5 mm diam spot was moved over the surface to be tested. Sensitivity to scattered light was quoted as 10 ppb/sr.

3.2 Mirrors and Surfaces

Mirrors have become favorite components in many high-energy and high-power laser systems. Here the problems of the bulk indepth response of the element are no longer a major concern. However, the problems of surface quality become even more important in these reflecting elements. Thus, one sees continued attention to developing techniques for improving surface finish and the protection of surfaces from the environment. The obvious advantage that mirrors offer is heat removal by the substrate, primarily high-conductivity metals, in most applications. This year, all the aforementioned aspects were covered to various degrees and were indicative of a continuous attention to this important area.

Obviously, in any meeting on optical materials for high-power lasers, one is concerned with their response and utility under high-intensity radiation. Thus, as usual, several papers dealt with the damage to materials as a function of laser exposure. The mirror area did not escape this attention, and papers dealing with laser damage to this class of optical elements were heard. Inasmuch as the absorption of radiant energy is to be minimized at all costs, in the case of mirrors this dictates the requirement for the development of very high reflectivity; and, in at least one case, the development of instrumentation for measuring reflectivity has led to improvement in mirror quality.

Ultra-high reflectance mirrors are essential for low-gain oscillators, e.g., the free-electron laser, and for systems with high cw power loading. The measurement and, thereby, the production of mirrors with reflectance greater than 99.5 percent is very difficult with standard spectrophotometers having typical accuracies of ±0.5 percent. Addressing this need, J. Herbelin and J. McKay at the Aerospace Corporation developed a cavity-attenuated phase-shift (CAPS) method capable of less than 0.01 percent accuracy, which was previously described in Appl. Opt. 19, 144 (1980). At this year's symposium, the authors demonstrated the use of this technique to produce mirrors with reflectances of 99.975 ± 0.005 percent for 874 nm. Their four-step procedure consisted of 1) use of low-scatter quartz substrates with rms roughness ≤10Å, 2) cleaning the substrates to minimize scattering losses, followed by careful isolation from environmental contamination, 3) deposition of a low-scatter dielectric coating by a capable, commercial vendor, and 4) the measurement of the resultant mirror

reflectivity.

The key to their success was the ability of the CAPS technique to measure the scattering and other losses of the substrates and dielectric coatings in steps 2 and 4. This method also allowed them to quantitatively select a cleaning technique to minimize scattering from the substrate. They determined that the resultant losses in the reflectors amounted to 0.0025 percent each for substrate and coating scatter, and 0.010 percent each for coating absorption and transmission.

Damage levels as a function of angle of incidence for copper, stainless steel, molybdenum, and aluminum surfaces have been measured using a short pulse, (1.7 ns), CO_2 laser with a maximum fluence of 50 J/cm^2 by J. Figueira, S. Thomas, and R. Harrison of the Los Alamos National Laboratory. Angles of incidence between 0° and 85° were tested. Angular results were in good agreement with predictions from the Fresnel equations, particularly the $\cos^{-2}$ dependence of s-polarization damage threshold. For example, the damage threshold of stainless steel increased from 0.6 J/cm^2 at normal incidence to 24 J/cm^2 at 80° incidence, a factor of 40. Fatigue tests were also run by measuring the decrease in focused brightness from the mirror at 10.6-μm wavelength as a function of number of times the mirror was irradiated. No heat build-up between pulses occurred since the pulse repetition rate was about one pulse every 20 sec. The data from both diamond-turned and conventionally polished copper fit the expression $N=10^{7(1-F/F_o)}$ where F/F_o is the ratio of the flux level for each of the multiple pulses (F) to the single shot damage flux level F_o and N is the number of pulses required to reduce the mirror reflectance to 90 percent of its initial value. If N = 100 shots, then the laser flux level must be not more than 71 percent of single-shot damage levels; if N = 1000 shots, not more than 57 percent of single-shot damage levels. The decrease in brightness after multiple pulses was correlated to a roughening of the copper surface.

At the shorter infrared wavelength of 3.8 μm, D. Decker and J. Porteus of the Naval Weapons Center also verified that the change in damage threshold with angle of incidence predicted by Fresnel's equations for uncoated metal surfaces does indeed hold in practice. The theoretical prediction that the melt threshold for p-polarized light at 45° angle of incidence should be the same as for normal incidence was verified to within 3 percent, and the prediction that the s-polarized light melt threshold at 45° should be twice that for normal incidence was verified to within 5 percent. It should be pointed out that at the 1975 Damage Symposium Goldstein, Bua, and Horrigan experimentally verified the Fresnel equations' predictions at 1.06 μm. These predictions are for uncoated metals only. Multilayer dielectric coatings are another and much more complicated situation.

Besides the obvious desirability of polishing and finishing surfaces to high quality, it is sometimes possible to improve surfaces through nonmechanical processes, and several papers were presented which dealt with the effects of such treatments for improving surface quality. Surfaces can always be modified, in some cases undesirably such as by increased absorption through adsorbed contamination. These latter cases must not only be understood but procedures for desorption must be developed particularly if they are deleterious such as by their being absorptive at the operating laser wavelength. This is not only a fundamental problem but it is also of a very practical concern in most operational situations.

A survey was given by C. Draper of the Western Electric Company and S. Bernasek of Princeton University of surface alloying techniques for improving the erosion and wear properties, corrosion resistance, electrical, magnetic, and optical properties of surfaces through laser, electron- and ion-beam processing. Au-Ni, Cu-Zr, Cr-Cu, Cu-Mo, and Au-Ru systems were considered in detail. It was suggested that surface modification using directed energy sources should be a fertile field for improving laser mirror surfaces. The conference organizers agree.

S. Bilibin, V. Egorov, A. Katsnelson, V. Kovalev, N. Kolesova, Yu. Sidorov, N. Tkachenko, and F. Faizullov at the Lebedev Physical Institute of the USSR Academy of Sciences studied surface damage resistance of KCl windows when irradiated by a pulsed CO_2 laser. Surface-damage thresholds were found to be related to the depth to which the crystal structure was damaged during grinding. They found that smaller grain sizes used for grinding abrasive before the final polishing produced a shallower depth of crystal destruction and a higher surface-optical-breakdown threshold. Surface breakdown appeared to be initiated by water absorption at the surface. Proper choice of grinding compound produced windows with surface-breakdown thresholds at least as great as their bulk damage thresholds. Pulsed, surface-damage thresholds for amorphous materials such as fused silica are not sensitive to sub-surface microfracture, as shown by Guenther and co-workers at a previous symposium.

H. Vora, R. Anderson, and R. Stokes at the Honeywell Corporate Techology Center have been investigating the use of soft abrasives to optically polish materials, without introducing surface damage. Two techniques, float polishing and mechano-chemical, were investigated. Both techniques were developed in Japan, and the physics of the polishing process is somewhat obscure. Both processes, however, were successfully used to yield sharp Kikuchi patterns on silicon, indicating that virtually no surface damage was produced in the polishing process. The laser damage threshold of these surfaces should thus be significantly higher than conventionally polished surfaces. Sapphire, gallium arsenide, and silicon nitride were also polished using these novel techniques. High polishing pressures, up to 0.7 kg/cm^2 were used, and $CaCO_3$, MgO, $BaCO_3$ and Fe_2O_3 or Fe_3O_4 were used as polishing "abrasives." No residual Fe was found embedded in the surface after polishing using Auger and XPS analysis. These novel, polishing techniques could be very important for laser surfaces and deserve further study, and certainly damage testing.

Flame production, fused silica contains a significant amount of OH^-, which absorbs at a wavelength of 2.75 μm (fundamental) and at its first overtone band at 1.38 μm. It was shown by B. Kumar, N. Fernelius, and J. Detrio that this absorption can be eliminated by producing the silica in a water-free plasma arc, but at an increase in cost of over an order of magnitude. Alternately, it can be eliminated in optical fibers by heating the fiber in deuterium at temperatures over 200° C. The deuterium takes the place of hydrogen, moving the overtone band to a wavelength of 1.85 μm, an important change if the material is to be used with an iodine laser operating at 1.3 μm. It was further shown that this technique also works for Suprasil II window samples. The absorption at 1.3 μm in a 6-mm-thick sample heated to 900° C and 150 psi for 104 hours dropped by a factor of 5, to 5 x 10^{-4} cm^{-1}. No subsequent increase in absorption was observed when this sample was stored at room temperature over a period of six months.

J. Porteus, and W. Faith of the Naval Weapons Center and S. Allen of the University of Southern California used a pulsed laser to desorb surface contaminants which were detected using a quadrapole mass analyzer. It was shown that this technique is particularly useful for detecting H_2O and OH^- since an HF/DF laser which operates in the infrared water band can be used. The technique is nondestructive and can detect as little as 0.02 molecules/nm^2. Illuminated areas ranged from 121 μm to 522 μm in diameter. At the smallest spot size, considerable variation was found for adsorbed water with position. This result is in agreement with other data on the distribution of water on surfaces and may be associated with microcracks and other surface defects which can act as initiation sites for laser damage. Laser desorption analysis may thus be an attractive, nondestructive, laser-surface characterization technique.

Mirrors exhibit damage primarily as a result of thermal distortion which usually arises from absorption of incident radiation. As such, heat removal is a concern in the manufacture of high-power

mirrors. Additionally, the dimensional stability, or the response of mirrors as a function of temperature fluctuation, is also of concern. In the case of mirror applications in pulsed laser situations, then thermo-mechanical response becomes an important consideration, as in the thermo-elastic response of metal substrates.

The design and use of an electrostatic system to keep dust off of mirrors used in high power laser systems was discussed by S. Hoenig of the University of Arizona. Units have been built which use a needle-screen principle with a 25-mm needle-to-needle spacing and a 35-mm needle-to-screen distance. A voltage of -17 kV applied to the grounded screen results in an intense, corona discharge which creates an "electric wind" to repel dust particles. Particles 80-100 μm in size were not repelled, but smaller size particles were. In one test, reduction of dust particles by approximately 10 percent was noted when the precipitator was used. Dust was not only repelled but also removed, apparently by agglomeration induced as a result of the electrical charging.

D. Decker and V. Hodgkin from the Naval Weapons Center considered that if metal mirrors can be operated at cryogenic temperatures, their absorption should decrease, their thermal conductivity should increase, and thus their laser damage threshold should improve. Their preliminary experimental data verified these predictions. Drude-like behavior was observed for both diamond-turned and evaporated silver down to 80° K in the infrared. As a result, at cryogenic temperatures a bare metal mirror can exhibit the same absorption as a can a multilayer dielectric coated mirror at room temperature. They report that the reflectance of multilayers, on the other hand, is insensitive to temperature. This conjecture bears experimental verification. The pulsed laser damage threshold for silver or silver coated mirrors can be increased by a factor of 1.5 by cooling them to cryogenic temperatures.

The stringent figure tolerances required for laser mirrors used in the visible and ultraviolet require high dimensional stability in the mirror material used. Ultralow-expansion glasses such as Zerodur and ULE quartz have the best dimensional stability at room temperature of any known optical material. However, J. Shaffer, J. Bennett, and H. Bennett of the Naval Weapons Center have shown that when heated to temperatures above 200° C, Zerodur can suffer a permanent figure change. On the other hand, ULE shows no similar effect. A quick, simple, interferometric technique for checking the low thermal coefficient of expansion of these low-expansion coefficient materials was also reported.

In a paper presented by title only, V. Apollonov, S. Chyotkin, V. Khomich, and A. Prokhorov of the P. N. Lebedev Institute of the USSR discussed the thermo-elastic behavior of materials subjected to high repetition rate, laser pulses. The quasi-cw nature of the interaction loading of solid-state surfaces was employed to evaluate allowable, elastic-surface distortion, plastic flow in the target material, as well as fatigue distributions and ultimately melting of the surface by recourse to computed temperature and stress fields. This area has many consequences for material processing applications and high-energy laser mirrors.

Frequently it is necessary to employ cooled mirrors for high-energy laser optics. The use of heat pipes employing liquid materials, coupled with porous structures featuring low coefficients of thermal expansion materials was the subject of a paper by V. Apollonov, P. Bystrov, S. Chyotkin, V. Goncharov, V. Khomich, and A. Prokhorov of the Lebedev Institute in Moscow, USSR. A comprehensive analysis of the thermal behavior, in particular, the deformation characteristics of various substrate materials employing powder or porous structures, was investigated in conjunction with possible dielectric or liquid metal, heat conduction fluids. It was concluded that use of porous heat exchangers for laser mirrors, coupled with the use of liquid metal cooling, opened up the possibility of developing low distortion, high quality mirrors with concurrent high damage thresholds. The

parametric analysis reported allows one to establish in each case (governed by metals selection) the optimum porous structure parameters to most efficiently remove thermal loads from reflector surfaces and thus minimize distortion. The fluids evaluated included water, alcohol, kerosene, silicon, dauterm, and sodium-potassium. The use of porous substrates for high energy laser mirrors is an interesting concept and should receive further study.

3.3 Thin Films

Inasmuch as thin-film coatings are easily the most damage-sensitive general class of optical materials, and due to the fact that thin films, from deposition, to structure, physical properties, and finally, damage resistance, present a very complex road to travel, they usually receive the most attention at this symposium. This year was no exception.

Just like the attention given this year to the response of bulk materials to short wavelength and repetitive irradiation, several papers were given on the response of thin films under these conditions. Presentations relative to the degradation of dielectric films, now the barrier to the environment, were heard. These papers ranged from degradation due to chemical reactions taking place with intermediates in excimer lasers, to damaging responses of coatings to intense, pulsed-laser radiation. As is usually the case, the effects of the environment on the performance of thin films were covered, as well as the proposal of several design tricks to ameliorate the damage sensitivity of thin-film coatings.

In support of the current interest on the part of the Department of Energy in short-wavelength lasers for inertial confinement fusion, ultraviolet laser damage facilities at the Lawrence Livermore and Los Alamos National Laboratories have been quite active for the past two years. Most of the testing has been with conventional, rare-gas halide excimer lasers, most generally at the KrF wavelength of 248 nm. This year, F. Rainer, D. Milam, and W. Lowdermilk of Lawrence Livermore Laboratory reported on their survey of the damage resistance of over 100, multilayer dielectric coatings for use at 248 nm, primarily in the form of high reflectors and antireflection coatings. Test samples supplied by commercial vendors were compared with those produced under research conditions. All samples were irradiated once per test site with temporally multilobed, 20-ns pulses and with an irregularly shaped beam whose most intense portion provided a somewhat uniform area of diameter 100 μm. An average of seven shots was required to establish the damage threshold which, under Nomarski microscopy, appeared as microscopic pits usually separated by a few microns. The micropit spacing on the best samples was considerably larger, about 100 μm, comparable to the width of the most intense part of the laser beam.

As a reference point, 20 commercial, high reflectors had a mean threshold of 1.8 J/cm^2, which, remarkably, was exceeded by a similar number of AR coatings having a mean value of 3.3 J/cm^2. Research coatings (Sc_2O_3 with MgF_2 or SiO_2) deposited by an electron gun had higher thresholds of 3.1 and 4.2 J/cm^2, respectively, whereas initial attempts with rf sputtering produced low thresholds for the high reflectors at ~ 1 J/cm^2. Even higher thresholds were obtained by use of a half-wave thick MgF_2 or SiO_2 overcoat on the research reflectors (6.3 J/cm^2) and with similar undercoats for the AR coatings (5.4 J/cm^2, mean). A few reflectors when preirradiated with multiple shots (3 to 14) below the single-shot threshold, were observed to be at least or more damage-resistant. Repeated testing after seven months revealed no significant change in thresholds due to aging or handling.

In a directly related paper, the effects of undercoats (barrier layers) and overcoats on the damage thresholds of 248-nm coatings were systematically examined by T. Hart, T. Lichtenstein, and C. Carniglia of the Optical Coating Laboratory, Inc., and F. Rainer of the Lawrence Livermore National

Laboratory. The motivation for this study was the previous experience at 1064 nm where a half-wave (HW) thick silica layer, used as an overcoat for reflectors and as a barrier layer between substrate and AR coating, yielded an average of 50 percent higher thresholds. High reflectors of scandia/magnesium fluoride deposited on BK-7 glass substrates were evaluated with 1) no overcoat, 2) with a HW SiO_2 overcoat, and 3) with a HW MgF_2 overcoat. The laser irradiation conditions were the same as in the preceding paper. Averaged over six parts each, the mean threshold of the SiO_2-overcoated reflectors at 5.7 J/cm^2 doubled that of nonovercoated reflectors at 2.7 J/cm^2. An even higher level, 6.9 J/cm^2, was measured for the MgF_2-overcoated group.

Four-layer designs of AR coatings comprising Sc_2O_3/MgF_2 or Sc_2O_3/SiO_2 were deposited on bowl-feed-polished, Suprasil 2, fused silica substrates. The damage thresholds of these two AR-coated material combinations were essentially the same. With the MgF_2 barrier layer, a small increase in threshold of 14 percent was measured (4.8 J/cm^2) as compared to the same coatings without undercoat (4.2 J/cm^2). However, the SiO_2 undercoat caused a 40 percent increase in threshold to about 4.8 J/cm^2.

Possible explanations given for augmented damage thresholds by use of half-wave undercoats and overcoats have included improved adhesion in the case of AR coatings and mechanical strengthening of the outer layers of the reflectors by stress compensation, at least by the compressive SiO_2 overcoat. However, this argument fails for MgF_2 overcoats which increase the existing, net-tensile stress of the reflector stack. Further work is obviously dictated to determine the operative reason for the demonstrated improvement.

Continued progress in the development of multilayer, dielectric, ultraviolet reflectors for multiple-shot irradiation at 248 nm was described by S. Foltyn, B. Newnam, and L. Jolin of the Los Alamos National Laboratory. The standard test conditions for their damage tests included a 10-ns pulse at 35 pps with a 0.6-mm mean spot-size diameter. By testing ten sites at each fluence, the irradiated area was effectively increased, with each surviving site receiving 1000 shots. At the 1980 Boulder Damage Symposium, they reported damage thresholds averaging 1.5 J/cm^2 with a high of 3.0 J/cm^2 for a ThF_4/cryolite reflector. By concentrating on promising materials, in cooperation with commercial vendors, the average thresholds presented this year fell in the 3 to 4 J/cm^2 range. Highest thresholds were obtained on reflectors having Al_2O_3 or Sc_2O_3 as the high-index component. Some tests were conducted at 2 pps for comparison with the normal 35-pps condition, but the thresholds were essentially the same. Of considerable interest was the number of shots required to damage a given test site. Pulsing at 2 pps, nearly 75 percent of the sites damaged on the first shot and over 90 percent had damaged by the fourth shot. No damage was observed between 25 and 50 shots, and the promptness of damage was independent of the test fluence level.

Of special note is their conservative definition of damage threshold as the maximum fluence at which no damage occurs on any test site. This definition differs from that currently used by other investigators which is the median value between the highest fluence survived by any test site and the lowest fluence that causes damage. Based on an argument involving the density of coating defects, the authors speculated that their measured thresholds should also apply for very large, laser beams. For this case, the slope of the damage probability versus fluence curve would become essentially vertical.

Further success in maximizing 248-nm, reflector damage thresholds was reported by B. Newnam, S. Foltyn, and L. Jolin of the Los Alamos National Laboratory, and C. Carniglia of the Optical Coating Laboratory, Inc. Starting with the most damage-resistant reflector design evaluated in the preceding three papers (MgF_2 overcoated Sc_2O_3/MgF_2), a substantial increase in threshold was achieved by use of nonquarterwave (QW) thicknesses for the top few layers. These designs minimized the peak standing-

wave electric field in the high-index layers, which have proven to be weaker than the low-index components. Although previous damage tests of infrared- and visible-wavelength reflectors fabricated with these designs produced variable results, the authors were motivated to try again at 248 nm because of increasing film absorption near the band edge and an apparently greater density of susceptible defects for uv wavelengths.

Four sets of reflectors in two coating runs of each of four designs (all QW thickness; one modified-pair substitution; two modified-pair substitution; one modified pair plus an extra HW layer of Sc_2O_3) were tested with the same multiple-shot conditions described above employing 8-ns pulses. On the average, the reflectors with one pair of optimized-thickness layers had 50 percent higher thresholds than the all-QW design. Addition of a second pair of optimized, non-QW layers resulted in no further increase in threshold. For this case, the relative field in the low-index overcoat was sufficiently large to initiate damage first. Reflectors with an additional HW thickness of Sc_2O_3 had lower thresholds on the order of 10 percent, consistent with the peak electric-field model.

M. Loudiana, A. Schmid, and J. Dickinson of Washington State University discussed their experimental study of the decomposition of dielectric films in F laser cavities. Films of SiO_2 were subjected to NF_2, obtained from dissociation of N_2F_4, and to XeF_2. Etching did not occur in films of high purity, but in SiO_2 films contaminated by impurities such as carbon, etch rates were comparable to those observed in a similar attack on Si. When SiO_2 films were argon-ion etched in the presence of XeF_2, unpredictably large enhancement of etch yield was observed for ion energies above 300 eV; mass deposition occurred for ion energies below 300 eV. Since few ions in XeF lasers have ion energies exceeding 300 eV, the authors expressed the belief that etching of SiO_2 films would not be a serious limitation to laser operation. A speculative model for the enhanced sputtering was discussed.

S. Amimoto, J. Whittier, A. Whittaker, A. Chase, and R. Hofland, Jr., of the Aerospace Corporation, and M. Bass of the University of Southern California used a pulsed, D_2-F_2 laser to measure large-spot damage thresholds for bare and AR-coated windows of Al_2O_3 and CaF_2, bare polished Cu mirrors, and surfaces of Cu- and CaF_2-bearing carbyne (hard carbon) films. The laser provided 10-20 J pulses with broad spectral bandwidth (3.6 to 4.8 μm) and durations of 0.6 to 0.9 μsec. Bare Cu had the highest threshold at 48 J/cm^2. Damage thresholds of some AR-coated windows were equal to exit-surface thresholds of the bare windows, i.e., 21-27 J/cm^2. The absorption coefficient of the carbon film was 600 cm^{-1} at 0.6 μm. A value was not reported at the DF laser wavelengths. The carbon films had abrasion resistance less than that of fused silica and adhesion strengths ranging from 57 to 652 Kg/cm^2. Isolated, carbon-bearing sites in the carbyne films damaged at 10-25 J/cm^2.

J. Porteus, P. Archibald, J. Bethke, J. Dancy, W. Faith, J. Franck, and P. Temple of the Naval Weapons Center investigated the influence of cleaning, exposure to sunlight, humidity, and HF-gas environments on the optical properties and laser damage thresholds of Mo and Si mirrors bearing dielectric overcoats and on ZnSe and CaF_2 windows bearing dielectric, antireflective coatings. Six samples of each type were sequentially subjected to the several treatments and evaluated after each treatment. A control sample received no treatment but was put through each evaluation. Damage thresholds were measured with 3.8 μm, 100-ns pulses, focused to a spot 63 μm in diameter at e^{-2} in intensity. Damage data were reduced by an algorithm which excluded some site-selective damage thought to be related to isolated defects, and defined "uniform-coating" thresholds based on observation of erosion, flow or coating perforation. The treatments generally produced only small variations in measurable optical properties (absorptance, scattering, transmission, and reflection). The exception was ultrasonic cleaning which produced visible deterioration and measurable changes in all parameters. The observed variations in optical properties seldom correlated with observed changes in

uniform-coating thresholds. Over the set of 28 samples, 1) cleaning or exposure to sunlight either reduced uniform thresholds or left them unaffected. 2) Exposure to humidity increased thresholds of mirrors and decreased thresholds of the windows, and 3) exposure to HF gas usually increased thresholds, although this increase was not sustained in two out of three follow-up tests conducted two months after HF exposure.

It should be pointed out that applications of these results to predict effects on optical elements in large beams may not be possible since damage in large beams is dominated by site-selective damage which was excluded from this study.

An understanding of the sensitivity of thin films from start to finish requires the concurrent development of techniques for measuring requisite optical qualites, whether it be refractive index, figure error, birefringence, or whatever. Thus, it was gratifying to see several papers address the film characterization question. Just as one continually looks for new processes in the fabrication of bulk optical materials, there is always a search for new methods to prepare novel, thin-film coatings. The minor revolution created by the suggested use of gradient-index materials for a wide variety of applications has not escaped the thin-film community. Thus, we now see this latter class of coatings being evaluated for its utility under adverse, laser environments.

The utility and accuracy of the guided-wave technique to measure the refractive index and thickness of dielectric films used in high-power laser optics was reported by A. Feldman and E. Farabaugh of the National Bureau of Standards. The authors were motivated by the potential for high accuracy (1 part in 10^4) of the index reported by previous investigators. A single-layer, 1.1 μm-thick film containing a mixture of 90 mol percent MgO and 10 mol percent SiO_2 was produced by coevaporation with two separate e-guns onto a fused silica substrate. Such a relatively thick film was required for sustainance of the guided modes. Use of SiO_2 with the MgO was necessary for stress compensation since a pure MgO film exhibited considerable crazing at this thickness.

Light from three, visible, argon-ion laser lines was coupled into the film by a prism. From the positions of the mode-coupling angles, the index and thickness were calculated with accuracy of ±0.001 and ±0.3 percent, respectively. A large birefringence of 0.006 was attributed to internal stresses, e.g., $n_0 = 1.692$ and $n_e = 1.698$ at 488 nm. The measured values of refractive index agreed to within 0.005 with a volume additivity model for mixed films based on the Drude model.

The need for nearly-diffraction-limited laser systems leads to very severe requirements for the wavefront error tolerance per mirror in a typical laser optical train. For example, a cumulative, optical figure error of λ/14 rms at the operating wavelength causes a decrease of 20 percent in the on-axis intensity at the focal plane. Obviously, the error tolerance for a single mirror of a many-element system would therefore be much less than λ/14. As previously described by H. Bennett and D. Burge of the Naval Weapons Center at last year's Symposium, the effective optical figure of a multilayer, dielectric mirror is determined not only by the geometrical perfection of the optical surface but also by the uniformity of the multilayer coating. As an example, a 2 percent film thickness nonuniformity for a mirror designed for 3.8 μm corresponds to a visible-equivalent of λ/8. This year, these same authors addressed the need for a sensitive technique to measure the apparent optical figure error caused by coating nonuniformity. After evaluating several possibilities, they determined that, by far, ellipsometry appears to be the most sensitive. To avoid ambiguities, measurements should be performed at the wavelength at which the mirror will be employed. The ellipsometric parameter Δ was found to be very sensitive to variations in film thickness, but insensitive to film absorption. The converse holds for the parameter Ψ. For example, for a representative, infrared, high-reflectance, multilayer coating, a measurable change in Δ of 0.1 percent corresponds to film thickness nonuniformities of less than 0.01 percent, and a measurable

change in Ψ of 0.1 percent corresponds to a change in peak reflectance of 0.001.

In an additional paper concerning imperfections in multilayer-dielectric, high reflectors, H. Bennett and D. Burge evaluated the secondary minima on either side of the primary reflectance maximum as indicators of film thickness nonuniformity and film absorption. A decrease in the primary reflectance maximum caused by thickness errors of a few percent or moderate film absorption is smaller than the accuracy limitations of most spectrophotometers. However, their calculations indicated that the positions and depths of the secondary reflectance minima are very sensitive indicators. First, the wavelengths at which the adjacent minima occur depend directly on the thickness of a quarterwave stack. Secondly, absorption in either or both high- or low-index film components produces a predictable and measurable decrease in these minima. If the thicknesses are correct, and if volume absorption in the film materials is the main source of decreased reflectance, they found excellent correlation between the measured peak reflectance and that calculated from the depths of the secondary minima. However, errors in film thickness or significant interface absorption complicate this simple picture, prompting the authors to recommend direct measurement of the peak reflectance.

To transcend the current, damage-resistance limitations of multilayer dielectric antireflection coatings produced by physical vapor deposition, W. Lowdermilk of the Lawrence Livermore National Laboratory and S. Mukherjee of Battelle Columbus Laboratories discussed a single-layer, gradient-index AR coating deposited by the sol-gel process. In contrast to similar, graded-index surfaces produced on phase-separable glasses, the sol-gel films can be deposited on glass of any composition or other substrate materials. Their sol-gel process involves dipping fused-silica substrates into an inorganic solution of tetramethoxysilane, trimethylborate, and sodium methylate with ethanol and methanol. Transparent gel films form by polymerization when the substrate is withdrawn and exposed to atmospheric moisture. After several cycles of dipping and drying, the desired, quarter-wave thickness at 1064 nm can be obtained. Heating in a furnace to 350 to 500° C produces the desired microporous structure, and a leachable phase then can be removed with an acified NH_4F solution.

The reflectance of surfaces coated by sol-gel films was as low as 0.13 percent at 1064 nm, but substantial variation (up to 2 percent) was observed over a given surface. Scattering losses were expected to be of the order of 0.1 percent. Laser damage thresholds, measured with single-shot-per-site, 1-ns pulses at 1064 nm, averaged at 21 J/cm^2. This high level of damage resistance is three to four times greater than production titania/silica AR coatings and 40 percent greater than that of optimized Ta_2O_5/SiO_2 AR coatings on fused silica (bowl-feed polished) produced in research coaters. Drawbacks of sol-gel coatings include their fragile nature and difficulty in cleaning the optical components to which they are applied when held in fixed mounts.

Besides the novel deposition processes being addressed, there is an indication of continued improvement in more classical schemes such as electron- or ion-beam evaporation, all types of assisted sputtering, etc. The continued attention to these workhorses of the thin-film industry primarily concerns modifications of the resultant thin-film structure through variations in the deposition process. The samples of thin films so generated are then tested under appropriate laser conditions. Of course, many of these process modifications are dictated by the type of substrate upon which the films are to be deposited, thus one may see gross differences in the design and structure of films deposited on metal mirrors, glass or crystalline media.

S. Seitel, J. Franck, C. Marrs, J. Dancy, and W. Faith of the Naval Weapons Center, and G. Williams of Crystal Technology, Inc. used a 1064-nm, 9.5 ns-pulse width laser, focused to a spot size of 52 μm (e^{-2} in intensity) to perform two types of damage tests on "stock" and "new process" antireflection films on $LiNbO_3$ crystals. Tests of the first type determined "uniform-coating"

thresholds (based on observation of erosion, flow, etching, plasma formation, or film perforation), the purpose being to determine the potential threshold that could be achieved if coating defects were eliminated. Damages determined (by three criteria) to be site-selective, i.e., due to isolated defects, were not considered in determination of uniform-coating thresholds. To address site-selective damage, the authors then irradiated many sites to determine the probability of damage at fluences below uniform thresholds. The uniform-threshold measurements indicated that existing stock Al_2O_3 and SiO_2 films had developmental potential exceeding that of new-process Al_2O_3 which, in turn, had potential exceeding that of new-process SiO_2. However, the stock SiO_2 and new-process Al_2O_3 films were found to have high probability for site-selective damage at low fluences, which suggested that their high ranking in uniform-threshold testing would not correlate to their performance in actual, laser usage. The authors reported general correlation between results of large-spot performance tests and small-spot measurements of the probability of low-fluence, site-selective damage.

Maximization of the damage resistance of four-layer AR coatings of Ta_2O_5/SiO_2 (deposited by electron-gun evaporation) was the object of an extensive parametric study by D. Milam, F. Rainer, W. Lowdermilk, and J. Swain of Lawrence Livermore National Laboratory, and C. Carniglia and T. Hart of the Optical Coating Laboratory, Inc. First, they determined the influence of deposition parameters on laser damage threshold at 1064 nm. From a series of 18 different coating conditions (repeated twice) the optimum conditions for the tantala layers were 175° C substrate temperature, 1.0×10^{-4} torr oxygen pressure and 1.5Å/s deposition rate. Deposition at high rate (5 Å/s) and low oxygen pressure (0.5×10^{-4} torr) produced highly absorptive films with low thresholds. The one-on-one damage tests were conducted with 1-ns pulses.

Using these optimized coating parameters, they then varied the substrates (BK-7 glass and Suprasil 2 fused silica) and polishing process (conventional and bowl-feed) and determined that AR coatings on bowl-feed-polished fused silica had the highest thresholds (14.9 J/cm^2, mean value) and those on conventionally polished, BK-7 glass had the lowest values (6.5 J/cm^2, mean value). Further, damage resistance did not correlate with film reflectance (0.01 to 0.18 percent) or net stress in the films, and correlation with film absorption was observed only for values greater than 10^4 ppm. Baking the films for four hours at 400°C substantially reduced film absorption, reduced the magnitude and sign of net film stress (from compressive to tensile), and yielded a moderate increase in damage threshold for most samples.

At the 1979 Damage Symposium, W. Pawlewicz and coworkers at Battelle Pacific Research Laboratory reported that TiO_2 films produced by rf-sputtering demonstrated increased laser damage resistance with decreasing grain size, and furthermore, that amorphous films had the highest thresholds. This year E. Farabaugh, D. Sanders, M. Wilke, S. Hurwitz, and W. Haller of the National Bureau of Standards at Washington, DC, described an alternate technique for obtaining amorphous films using electron-gun deposition. By coevaporating a small fraction of SiO_2 along with ZrO_2, the high-index film of interest, a marked reduction in crystallinity was attained. It was apparent that addition of SiO_2 inhibited the grain growth normally exhibited by pure ZrO_2 films. With the mixture of 75% ZrO_2/25% SiO_2 (19 mol %) deposited on substrates at 325° C, no crystalline structure was observed using either X-ray diffraction or scanning-electron microscopy. The authors now hope to determine if these and other similarly co-deposited films also have increased damage resistance.

A coating development which continues to attract considerable attention concerns amorphous carbon coatings. They are thought to exhibit desirable characteristics as an environmental barrier against abrasion or chemical attack. This is probably the most exciting aspect of new coating development. We are just at the beginning of our understanding of these classes of films, their stabilization, etc.

Until this year, the moderately high, infrared absorption of Si films, ranging from 20 to 80 cm^{-1} at 2.7 μm, seriously limited the cw power handling capability of optics compromising this coating material. By use of rf-diode sputtering, W. Pawlewicz and P. Martin of Battelle Pacific Northwest Laboratory demonstrated that the alloying of Si with H during coating deposition substantially reduced the absorption coefficient. Although absorption of $Si_{1-x}H_x$ films decreased exponentially at each of the ir laser wavelengths of 1.06, 1.315, and 2.7 μm as x was varied from 0 to 0.4, the lowest absorption attained was 3 cm^{-1} at 2.7 μm with x = 0.12. While this is comparable to the 1 to 2 cm^{-1} absorption coefficients typical of other high-index film materials, such as ZnS and ZnSe, Si films have additional, desirable, physical properties. These include nonhygroscopicity, glassy structure, hardness, and a useful, high-refractive index. Although alloying with H was observed to monotonically decrease the refractive index, values of n above 3.0 were obtained for $x < 0.2$. The authors attributed the reduced absorption to band-gap state removal as H completes dangling bonds associated with incomplete, Si-tetrahedral sites and decreased numbers of defect states to which transitions can occur from the valence band. By sputtering from a pure Si source and alternately introducing H_2 and O_2 gases, along with Ar gas, into the reaction chamber, multilayer reflectors of $Si_{1-x}H_x/SiO_2$ were fabricated for iodine, HF and DF lasers.

Sputtered-silicon films tend to have water content, lower absorption, and a higher, laser-damage threshold than evaporated silicon coatings. It was shown by T. Donovan, E. Ashley, J. Franck, and J. Porteus of the Naval Weapons Center that by adding a stainless-steel grid mounted 0.5 inches below the substrate and charged at -100 V, the morphology of the silicon film deposited from a dc magnetron source is dramatically improved as compared to that produced by dc magnetron sputtering alone. Island structure is nearly eliminated, and the large, hydrogen interface contaminant present in both evaporated and dc magnetron sputtered film is nearly absent. Unfortunately, no laser damage measurements were made on these films. Damage measurements were made, however, on both evaporated and rf-diode-sputtered silicon. The rf-sputtered coatings were higher in damage resistance by a factor of between 2 and 3 than the evaporated coatings. Coatings reactively sputtered in hydrogen had lower absorption but also slightly lower (20 percent) damage thresholds than those sputtered in argon alone. The damage thresholds of multilayer Si/SiO_x coatings on molybdenum prepared by evaporation are somewhat lower than multilayers on silicon prepared by sputtering, lending encouragment to futher investigations along the lines suggested in this work.

Further demonstration of the possible use of diamond-like carbon films as both a hard protective and antireflective coating for infrared windows was reported by A. Bubenzer and B. Dischler of the Fraunhofer-Institut für Angewandte Festkörperphysik in Freiburg, West Germany, and A. Nyaiesh of the University of Sussex in England. Their particular interest was hydrogenated amorphous carbon (a-C:H) deposited in an rf excited hydrocarbon plasma. First, they observed that the properties of a-C:H films largely depend on the kinetic energy with which ions hit the substrate surface. As a consequence, they were able to vary the optical properties of the films in a controlled manner by varying the ratio of the negative bias voltage to the gas pressure, U_B/p. As this ratio was increased from 6 to 30 kV/mbar, they observed that: 1) the refractive index varied from 1.86 to 2.24. 2) the short wavelength absorption edge shifted to longer values, and 3) the relative hydrogen content decreased. Further, they were able to deposit single-layer antireflection coatings for 10.6 μm on germanium by adjusting the refractive index to 2.0. However, the coating absorption in each quarter-wave film (1.3-μm thickness) was considerable, ~ 4 percent. In a cw damage test at 600 W/cm^2, an exposure for 1 second caused melting of the germanium substrate by thermal runaway. Apparently, the threshold for coating-limited damage was not reached.

There is presently considerable interest in developing diamond-like carbon coatings to protect optical windows from abrasion and chemical attack. In continuation of their work reported last year, M. Stein and S. Aisenberg of Gulf-Western Applied Science Laboratories, and B. Bendow of the BDM Corporation have specifically addressed the problem of coatings on CaF_2, an important, ir-laser window material. Initial attempts with their ion-beam deposition facility were unsuccessful since the coatings did not adhere well, apparently due to the large coefficient of expansion of CaF_2. Standard techniques such as heating of the substrate and argon-ion bombardment prior to deposition were used, but satisfactory adhesion was only achieved by implanting carbon ions within the upper 600 Å of the window surface. Implantation energies from 2 to 10 kV were used. As measured by a pull test, the bond strength was greater than 6000 kPa. Enhanced abrasion resistance of the coated window was apparent from a falling-sand/light-scattering test. While the optical absorption coefficient of 150 cm^{-1} at 3.8 μm of these films presently makes them suitable only for low-power applications, further improvements are anticipated.

In pursuit of the same goal, T. Moravec of Honeywell Corporate Technology Center reported upon progress in depositing adherent, diamond-like carbon films on CaF_2. Using rf-plasma decomposition of an alkane gas to produce carbon ions, they also encountered difficulties in attaining satisfactory adhesion. Some measure of success was obtained by keeping the deposition process slow enough to allow little heating of the surface. Interrupted deposition over a period of 45 minutes produced 700 - 1000 Å-thick films. As indicated from a four-point bend strength test, the carbon coatings only slightly increased the fracture strength of CaF_2 bars. The absorption coefficients of one sample were 446, 429, and 129 cm^{-1} at 1.3, 2.9, and 3.8 μm, respectively. Continued efforts will hopefully reduce these levels.

3.4 Fundamental Mechanisms

As is the usual case, the Symposium ended on a high interest level through the discussion of fundamental mechanisms whereby the various classes of materials previously discussed fail.

One is continually amazed by both the progress in this area and the new questions raised by the same progress. However, it is clearly becoming evident that in most pulsed-laser damage events, impurity-initiated processes play a dominant role. Continued advances in the theory from this vantage point support the major role of impurities, principally through one's understanding of the observed scaling relations.

From what has been said previously, one would expect considerable attention to be given to the relationships among defects, their density and distribution, and spot-size scaling which primarily address the statistical probability of encountering damage-sensitive impurity sites. One expects that additional attention to the statistical aspects of this fundamental process will be forthcoming.

Laser damage to cooled mirrors usually occurs at localized sites on the mirror and results from coating defects rather than from widespread coating failure. J. Palmer of TRW and H. Bennett of the Naval Weapons Center have examined this question theoretically and have developed a technique for predicting the defect size which will either cause catastrophic coating failure or catastrophic burnthrough of the mirror faceplate as a result of vapor barrier formation at the coolant-faceplate interface. In a companion paper they investigate the separation of defects. They concluded that if defects are closer together than ten times their diameter, they cannot be treated independently and a modification of the single defect theory proposed in the first paper is required. A method for handling the effect of multiple defects was suggested.

A. Stewart and A. Guenther of the Air Force Weapons Laboratory described preliminary results of an experiment in which they measured thresholds of thin films using 6-ns, 1064-nm beams focused to diameters ranging from 8.8 μm to 282 μm. The damage threshold was defined to be the average of the highest fluence that caused no damage and the lowest fluence that caused damage. Using this threshold definition, they found, in agreement with earlier work, that both threshold and the spread in thresholds increased as the spot size decreased. The authors stressed the preliminary nature of the work and discussed a major problem in the study: If increased thresholds for small beams are solely the result of decreased probability of encountering coating defects, it will be necessary to use a very large number of tests in small-beam experiments to equalize for both large and small beams the probability of defect damage. There is an additional conceptual problem. The effective density of defects is known to depend on wavelength, pulse duration, and beam intensity. Therefore, when intensities in small beams are raised above those which induce large-beam damage, different classes of defects may be encountered in the two experiments, and comparison between theory and experiment will be difficult. Finally, two previous experiments, one at the Air Force Weapons Laboratory, showed that the short-pulse, 1064-nm damage response of dielectric films and surfaces is essentially photographic in nature. That is, the surface records in damage a point by point reproduction of those parts of the beam profile which exceed threshold. The graininess of the image is set by the spacing of defects. Such existing data suggest that beams well under 10 μm in diameter would be required to perform experiments that are not limited by the statistics of hitting or missing defects. In fact, other mechanisms may be operative at these ultra-small, spot sizes, such as thermal rather than statistical related scaling.

Besides the attention given to defect-dominated damage, one must also contend with more classical problems such as the intrinsic damage level of solids and their reponse to intense, coherent, optical radiation such as multiphoton absorption processes, and self-focusing, to name but two. This year's Symposium saw several papers address these issues both from an academic and a practical standpoint.

A. Epifanov, S. Garnov, G. Gomelauri, A. Manenkov, and A. Prokhorov of Lebedev Physical Institute have extended the electron avalanche, ionization model for optical material damage by considering the case where no free electrons are present to seed the avalanche. In this case, the probability for material damage depends on the probability of multiphoton absorption releasing a seed electron. This effect was used to account for the peculiar lack of temperature dependence on the damage threshold for sodium chloride at 10.6 μm. The probability of multiphoton absorption, in turn, depends on the volume of material which is irradiated at a sufficiently high intensity. This effect was used to explain the dependence of damage threshold on spot size.

Multiphoton absorption of a free- or quasi-free electron is important for the initiation and maintenance of avalanche ionization in solids for the following reason: The typical electron in the conduction band keeps gaining energy from the incident laser radiation by multiphoton absorption processes until it has enough energy to excite another electron from the valence band to the conduction band. In a paper entitled "Quantum Theory of Multiphoton Free Carrier Absorption at High Intensities in Compound Semiconductors," B. Jensen of Boston University derived general expressions for multiphoton absorption of all orders in polar semiconductors by means of a density-matrix formulation. In her calculation, she took into account the effect of the intense, laser radiation on the electronic wavefunctions by assuming that the latter were described by Houston wavefunctions instead of the usual Kane wavefunctions which are applicable only when the intensity is small. Finally, this author derived expressions for the Joule heating corresponding to the multiphoton absorption by free carriers in compound semiconductors.

A. Vaidyanathan of Universal Energy Systems and A. Guenther of the Air Force Weapons Lab reviewed recent, theoretical work which suggests that the conduction electron energy E_c increases in the presence of intense radiation whereas the energy of valence electrons remains at the low-field value. The predicted end result is an intensity dependence in the effective bandgap. Therefore, in a material where two-photon absorption is allowed, application of a sufficiently intense beam might increase the gap so that two-photon absorption is no longer possible, whence three-photon absorption would predominate over two-photon absorption. They cite one experimental result which indicated absorption at 0.694 μm in GaP initially increased as I^2, but at higher intensities varied as I^3 and ultimately as I^4. The paper discusses potential difficulties in the existing theoretical and experimental work and suggests further work.

As indicated, there are many forms of laser damage besides catastrophic failure which can render the optical element useless in performing its intended function. As such, these noncatastrophic interactions may also lead to limitations on system performance, such as the generation of high-order nonlinearities in the absorption of radiation. Occasionally these same processes can be employed beneficially, such as the use of self-focusing to prevent damage in a variety of situations.

D. Harter and D. Brown of the University of Rochester considered several effects of nonlinear refraction on absorption-free frequency doubling. They show that nonlinear refraction in the doubling crystal can lower conversion efficiency through an induced phase mismatch. Also, beam breakup at the fundamental frequency (and by interference at the harmonic frequency) can be enhanced by the creation of phase-matched weak beams which propagate at a slight angle to the input beam, thereby causing interference fringes. They are, at present, unable to state the actual importance of these effects because evaluation of the equations requires knowledge of the nonlinear susceptibilities of the doubling crystals. Numerous algebraic errors complicate the reading of the paper.

M. Soileau, W. Williams, E. Van Stryland, and S. Brown of North Texas State University demonstrated a power limiter for 40-ps, 1064-nm pulses. The device used two lenses, one to form an initial focus and a second to re-collect the light and focus it through a pinhole. A cell of CS_2 (or other material with a large nonlinear refractive index) was placed at the first focus. When the incident beam power exceeded the critical power for self-focusing in CS_2, induced phase perturbations caused the beam no longer to be properly focused through the pinhole. In CS_2, power was limited to 26 kW. The power limit was varied by using liquids other than CS_2, or mixtures of liquids. A value of n_2 deduced from the critical power for self-focusing in CS_2 was $1.5 \pm 3 \times 10^{-11}$ esu, which is in good agreement with other published values. Unfortunately, the quality of the beam emerging from the limiter at sublimited power levels was not measured.

D. He and G. Fuxi of the Shanghai Institute of Optics and Fine Mechanics reviewed several experimental studies of nonlinear refraction in optical and laser glasses. The nonlinear refractive index n_2 was determined in three experiments which used nanosecond duration pulses: measurements of the critical power for self focusing, self-induced ellipse rotation, and laser-induced birefringence. For all but one, glass, the three measurements of n_2 agreed to within 25 percent. Values of n_2 computed from a model based on electronic polarizability agreed closely with the experimental results. In measurements of the dispersion of n_2, the authors observed n_2 values at 532 nm that were approximately twice as great as those observed at 1064 nm. Thermal blooming, observed with 5-millisecond duration pulses, agreed with a model based on thermal self-focusing. In short-pulse damage experiments, damage thresholds correlated with n_2, but not with the linear refractive index. Unfortunately, the glasses studied were not well identified, and it is difficult to compare these results with other studies of n_2.

Details of the nonlinear absorption and self de-focusing for intense IR irradiation of Ge and Si semiconductors were the subjects of a report by Yu. Danileiko, T. Lebedeva, A. Manenkov, and A.Sidorin of the P. N. Lebedev Institute in Moscow. Using both CO_2 (10.6 μm) and CaF/Er^{3+} (2.76 μm); YAG/Er^{3+} (2.96 μm) lasers, they have shown that the characteristic of the nonequilibrium carriers generated is considerably different for Ge and Si. Thresholds for carrier generation vary from 1 MW/cm^2 for Ge to 5 GW/cm^2 for Si. At high excitation intensities generation of nonequilibrium carriers in Ge is shown to produce nonlinear absorption and self-de-focusing.

Multiphoton absorption of picosecond 1.06-μm pulses in ZnS, ZnSe, CdTe, CdS, and BK-7 glass was investigated by E. Van Stryland, M. Woodall, W. Williams, and M. Soileau of North Texas State University. No nonlinear absorption was found in BK-7 glass and ZnS. Two-photon absorption was dominant in CdTe and three-photon absorption in ZnSe and CdS. The paper points out that absorption by excited free carriers is a major source of error in determining nonlinear absorption coefficients. The numerical process used by the authors for analyzing the experimental data is not described in detail, but a relatively good fit to theory is obtained for the two-photon absorption examples. A poorer fit is found for the three-photon examples, suggesting that the theory in this case is inadequate for high irradiance levels. It is suggested that an avalanche process may be involved in such cases. To obtain reliable results, it is suggested that (1) a wide range of irradiance levels be used, (2) two or more pulse lengths be used, (3) the most reliable, multiphoton absorption data are obtained from the shortest pulselength experiments and the lowest irradiance levels, and (4) photoacoustic detection, which is in a 1:1 correspondence with transmittance data at irradiance levels high enough so that both techniques can be used, may provide a powerful experimental tool for low-level irradiance investigations.

There were several papers of interest at the Symposium which are not easily characterized into our normal categories. This year there were two very interesting but not easily compartmentalized papers. One concerned the improvements in air breakdown that might be evidenced by the introduction of an electronegative gas, while the other paper extended our spectral region of interest to microwaves where the influence of very long wavelength radiation on optical element damage was considered.

M. Sparks, D. King, and D. Mills of Scientific Research Center computed the absorption coefficients of alkali halides for microwave frequencies, $1\ cm^{-1} < \omega < 100\ cm^{-1}$. Previous theories attributed absorption at frequencies slightly below the fundamental restrahlen frequency to two-photon difference processes. Photons were absorbed through annihilation of a phonon and creation of a more energetic phonon. At lower frequencies, where the energy of the incident photons was too small to cause absorption through energy conserving two-photon processes, absorption was attributed to three-phonon processes. The present paper shows that absorption over the stated range of frequencies can be accounted for by invoking two-phonon difference absorption between lifetime broadened phonon modes (described by a Lorentzian distribution), if the calculations also include the temperature dependence of phonon frequencies and of other parameters. The authors obtain a closed-form expression with no adjustable parameters, which gives the magnitude, frequency dependence, and temperature dependence of the microwave absorption coefficient. The calculated values are shown to be in close agreement with experimental results.

H. Volkin of the University of Dayton Research Institute presented detailed calculations of the breakdown thresholds of mixtures of SF_6 and N_2. Mixtures of SF_6 and N_2 are known to have dc-breakdown thresholds higher than that of air or N_2. Volkin's calculations predict a threshold of 2.7×10^9 watts/cm^2 for long-pulse, 10.6 μm irradiation of air at 1 atm pressure and 300° C. The corresponding thresholds for SF_6/Air mixed in the ratio 0.3:0.7 is 1.0×10^{10} watts/cm^2 and for pure SF_6 is 2.9 x

10^{10} watts/cm^2. Within experimental uncertainty, the measured threshold for air breakdown agrees with the calculated value.

The increase in threshold obtained by adding SF_6 to air occurs primarily as the result of competition between ionization and recombination. When breakdown is produced by pulses of long duration ($>10^{-7}$ sec), the total ionization rate is low, and capture of electrons by SF_6 molecules is effective in suppressing the plasma growth. However, the ionization cross section for SF_6 is greater than that of N_2 or O_2. Therefore, when breakdown occurs under intense short pulse ($<10^{-10}$ sec) irradiation, the large rate of ionization dominates over recombination losses, and the presence of SF_6 leads to a reduction of threshold. For pulses 10^{-10} sec in duration, the breakdown threshold is independent of the SF_6 concentration.

4.0 Recommendations

It should be fairly easy to predict where the major, future activity of this conference will lie. While there will be a continuation of the obvious interests characteristic of this meeting such as new materials, new processes, new instrumentation, damage testing, and interaction theory, it is the holes in our understanding that are to be filled in. Those needs that must be addressed in a major way, and the promising areas which must be exploited for their potential in advancing the field of optical materials for high-power lasers will be addressed in this section.

In the area of transparent materials, the continued testing of materials at short wavelengths, preferably under repetitive irradiation, is paramount. Besides the obvious interest in the laser fusion community, we can add laser-isotope separation and several DOD applications. Degradation, lifetime environmental stability and durability information are necessary, as well as means to protect optical elements from adverse environments, e.g., space. An area deserving of increased attention is cleaning and contamination, not only from the external world but from that introduced by the laser itself.

We expect that as we progress into high average power, rep-rated systems that thermal analysis akin to that already developed for the cw case will be applicable. However, we must now augment this understanding with consideration of the thermo-mechanical response, both in isolated elements and fabricated components where real world, system design constraints can be assessed.

One of the most exciting topics discussed at this year's meeting was the proposed use of polymeric materials for high-power laser components. The advances in this area are truly remarkable and illustrate what can be accomplished by the application of sound, scientific methods. We expect considerably more attention to be payed to the potential of this class of materials for the production of low cost, optical elements. However, first we must understand their long term utility by further study of accumulation effects, an area of interest for all classes of optical elements. The other class of materials deserving increased attention will be the semiconductors such as silicon, etc.

Instrumentation both for property measurement and characterization must, as well, be advanced. We saw this year how improved reflectivity measurements (CAPS) could directly lead to improved elements. The CAPS technique should be developed fully to eliminate the existing electronic problems, such as that produced by mirror jitter. Demonstration with pulsed lasers should be pursued so as to increase the number of wavelengths available for testing. Furthermore, the stability problem of the CAPS method as used for mid-IR wavelengths with modematching limitations should be reduced.

The instrumentation, particularly process related, must be more facile, not just more sensitive but more useful, hopefully at a cost commensurate with its utility, e.g., demonstrate an automated, scanning ellipsometer to measure film thickness and reflectance nonuniformities on large mirrors.

Also demonstrate this device on a wide variety of coatings and wavelengths. Show its capabilities to measure in situ properties of growing coatings versus deposition conditions. We should continue to strive for a non-destructive test which truly measures all important aspects relating to the quality of a finished element.

It is expected that the major emphasis relating to surfaces and mirrors will remain improvements in surface finishing. The initial, encouraging results from such diverse, novel techniques as laser annealing and float polishing should be continued to determine the range of applicability, i.e., metal as opposed to dielectric, and scalability to useful sizes. Cosmetic finish is not well enough defined; and new, objective standards, perhaps based upon performance, as well, are needed. Both the standards and new, finishing techniques will have to be evaluated in terms of their resistance to damage, whether it be from high-power lasers or the environment.

The initial improvements noted by post-finishing techniques such as baking or low-level laser irradiation should be continued with the duration of the improvement quantified. Of particular interest is the use of deuterium treatments for improving the damage resistance of fused-silica surfaces.

The use of protective measures such as environmental enclosures, electrostatic shielding surface modification to prevent contamination by adsorbing dust particles should all be pursued. In the end, it may be these controls which could allow high laboratory damage levels to be realized in systems, for example, the immersion of components in beneficial atmospheres, e.g., SF_6 or other electronegative gases. Along the lines of system application it is to be realized that lasers are generally not one-shot devices, and with the continued move towards shorter wavelengths it is to be expected that both relevant theory and tests done under repetitive irradiation will be necessary. Long-term degradation as a function of derating would be most useful.

Continued research on improved heat exchangers is clearly indicated, such as the Soviet proposal on porous substrates as well as operation of these temperature sensitive elements at cryogenic temperatures. Here, as well, improvements in the utility of characterization diagnostics are dictated since we continue to see the important role that surface quality plays in the correlation with damage resistance.

There always seem to be as many recommendations in the thin-film area as there is diversity. The move toward shorter wavelengths requires investigations into the utility of new materials. Overcoats and undercoats for other promising UV materials combinations, e.g., Al_2O_3/SiO_2, should be evaluated. Perhaps even higher thresholds could be obtained. The physical reason for the success of the half-wave low-index film should be determined. In addition, multiple-shot endurance testing of these state-of-the-art, UV excimer coatings should be conducted using sufficiently large spot sizes. Coating techniques which possibly produce lower defect densities than e-gun should be evaluated.

No new material holds greater promise than carbon films, from amorphous to crystalline, from the UV to the IR. However, it is realized that we are only at the beginning in appreciating the processes necessary to vary their structure and properties, let alone deposit them with requisite uniformity over meaningful areas. Adequate damage tests of these carbon films are needed. Surely the adjacent area of hydrogenated silicon and carbon films must be pursued including the appropriateness in their being used as coatings on various types of substrates, be they crystalline, glassy, or metal.

Films have a long way to travel before they can realize their full range of application. New deposition techniques, particularly various ion-sputter processes and molecular beam epitaxy (if we can get someone to dirty up their system) are prime candidates. There is the whole new area of gradient-index films, be they produced in multisource chambers, by leaching, or even through

production of sol-gel coatings. These hold much promise but have not found much use because of questions relating to their fragility, susceptibility to environmental contamination, and, most importantly, the ability to be fabricated with requisite uniformity. Developments in the sol-gel process are needed to obtain increased uniformity of reflectance over the entire surface of a window.

It is hoped that continued "quality" damage testing will proceed but with even more indepth characterization of the films, such as structure, optical properties, and deposition variables. Work along these lines could add measurably to an improved understanding of the defect dominated, damage initiation process for pulsed-laser applications or its contribution in limiting overall absorption levels in films and at the interface between films and the substrate.

No area demands higher priority than the measurement and determination of impurity type, density, size distribution, and structural orientation. If this information could be correlated with process variables and damage testing, one could better appreciate how far one can go in raising the damage threshold of thin films. This assessment will undoubtedly take place through our consideration of heat transfer and other thermal factors such as thermo-mechanical response.

In the meantime, we will continue to look for new materials and processes or fall back on design tricks. Additional wavelengths in the UV (193, 308, 351 nm) and perhaps a few other promising materials, e.g., Al_2O_3/SiO_2, should be tried to see how far non-QW thickness schemes go, while the different slopes of the probability versus fluence curves should be explained since we seem to have had difficulty in establishing a properly focused, comprehensive, well coordinated program to advance thin-film technology, even though most of us realize the tremendous pay-off.

Finally, we come to the most academic subject from which we hope to develop an understanding of the limitations of optical materials for high-power lasers. Historically, various damage mechanisms were assessed in terms of their ability to predict variations in performance in a parametric manner. These scaling assessments will continue to play a major role in developing our understanding, such as spot-size effects to bound the range of the distribution of defects to thermal response considerations. It is expected that in either case a statistical approach will be necessary. As regards the thermal behavior, the variation in available material properties can be assessed in terms of projected improvements and further expanded into the area of damage accumulation to repeated exposures.

Damage tests to establish probability of damage versus laser fluence curves should be conducted for various spot sizes to determine if there is any unique meaning to the "saturation fluence" (minimum fluence for all sites irradiated to damage). Perhaps the intrinsic, coating damage resistance would become apparent under multiple-shot, small-spot tests due to integrating out any probability aspects of damage.

Hopefully other quantifiable indicators such as exo-emission can be extended to pre-catastrophic, damage indicators. Techniques are probably available to make the measurements. What is needed is theoretical explanation of their import.

It seems that rather than attack the problems involved in a theoretical understanding of wide band gap materials from a solid-state standpoint, the community has been addressing the semiconductor problem. It is important not to lose sight of the more complicated problem posed by dielectrics as used in uv, visible, and near-infrared optics.

As we pursue new wavelength regions it is important not to forget what has been previously learned and to account for different conditions that may exist. An example is increased nonlinear behavior near the bandgap. It follows that previously determined scaling relationships will need to be reexamined under the new conditions. Fortunately, we have developed an array of high quality testing facilities and procedures to apply to these problems.

5.0 Acknowledgments

The editors would like to acknowledge the invaluable assistance of Mr. Aaron A. Sanders and the other involved staff members of the National Bureau of Standards in Boulder, Colorado, for their interest, support, and untiring efforts in the professional operation of the Symposium and particularly to Ms. Susie Rivera for her part in the preparation and publication of the Proceedings. The continued success of the Damage Symposium would not have been possible without the enthusiastic support of those named above.

This year the conference co-chairmen and attendees were pleased to have the assistance and presence at the Symposium of Ms. Pat Whited of the Air Force Weapons Laboratory. For primarily technical assistance, we are grateful to an old friend of the Conference, Major Harry Winsor, now of the Air Force Office of Scientific Research and an old friend but relatively new to our conclaves, Dr. Angus MacLeod of the Optical Science Center of the University of Arizona for very effectively serving as rapporteurs for the poster sessions.

Thanks to all!

6.0 References

[1] Glass, A. J.; Guenther, A. H., eds. Damage in laser glass, ASTM Special Technical Publication 469, ASTM, Philadelphia, PA; 1969.

[2] Glass, A. J; Guenther, A. H., eds. Damage in laser materials. Nat. Bur. Stand. (U.S.) Spec. Publ. 341; 1970.

[3] Bloembergen, N. Fundamentals of damage in laser glass, National Materials Advisory Board Publication NMAB-271, National Academy of Sciences; 1970.

[4] Bloembergen, N. High power infrared laser windows, National Materials Advisory Board Publication 356; 1971.

[5] Glass, A. J.; Guenther, A. H., eds. Laser induced damage of optical materials: 1972," Nat. Bur. Stand. (U.S.) Spec. Publ. 372; 1972.

[6] Glass, A. J.; Guenther, A. H., eds. Laser induced damage in optical materials: 1973, Nat. Bur. Stand. (U.S.) Spec. Publ. 387; 1973.

[7] A. J. Glass and A. H. Guenther, "Laser Induced Damage in Optical Materials, 1973: A Conference Report," Aplied Optics 14, 74-88 (1974).

[8] A. J. Glass and A. H. Guenther, Editors, "Laser Induced Damage in Optical Material: 1974," NBS Special Publication 414 (1974).

[9] A. J. Glass and A. H. Guenther, "Laser Induced Damage in Optical Materials: 6th ASTM Symposium," Applied Optics 14, 698-715 (1975).

[10] A. J. Glass and A. H. Guenther, Editors, "Laser Induced Damage in Optical Materials: 1975," NBS Special Publication 435 (1975).

[11] A. J. Glass and A. H. Guenther, "Laser Induced Damage in Optical Materials: 7th ASTM Symposium," Applied Optics 15, No. 6, 1510-1529 (1976).

[12] A. J. Glass and A. H. Guenther, Editors, "Laser Induced Damage in Optical Materials" 1976," NBS Special Publication 462 (1976).

[13] A. J. Glass and A. H. Guenther, "Laser Induced Damage in Optical Materials: 8th ASTM Symposium," Applied Optics 16, No. 5, 1214-1231 (1977).

[14] A. J. Glass and A. H. Guenther, Editors, "Laser Induced Damage in Optical Materials: 1977," NBS Special Publication 509 (1977).

[15] A. J. Glass and A. H. Guenther, "Laser Induced Damage in Optical Materials: 9th ASTM Symposium," Applied Optics 17, No. 15, 2386-2411 (1978).

[16] A. J. Glass and A. H. Guenther, Editors, "Laser Induced Damage in Optical Materials: 1978," NBS Special Publication 541 (1978).

[17] A. J. Glass and A. H. Guenther, Editors, "Laser Induced Damage in Optical Materials; 10th ASTM Symposium," Applied Optics 18, No. 13, 2112-2129 (1979).

[18] H. E. Bennett, A. J. Glass, A. H. Guenther and B. E. Newnam, "Laser Induced Damage in Optical Materials: 1979" NBS Special Publication 568 (1979).

[19] H. E. Bennett, A. J. Glass, A. H. Guenther and B. E. Newnam "Laser Induced Damage in Optical Materials: 11th ASTM Symposium," Applied Optics 19, No. 14, 2375-2397 (1980).

[20] H.E. Bennett, A. J. Glass, A. H. Guenther and B. E. Newnam, "Laser Induced Damage in Optical Materials: 1980" NBS Special Publication 620 (1981).

[21] H. E. Bennett, A. J. Glass, A. H. Guenther and B. E. Newnam "Laser Induced Damage in Optical Materials: 12th ASTM Symposium, "Applied Optics 20 No. 17, 3003-3019 (1981).

Transparent Polymers as a New Class of Optical Materials for Lasers

K. M. Dyumaev, A. A. Manenkov, A. P. Maslyukov,
G. A. Matyushin, V. S. Nechitailo, A. M. Prokhorov

Lebedev Physics Institute, Academy of Sciences
of the USSR, Moscow

Possibilities of using transparent polymer materials for production of different optical elements (active elements with lasing dyes, bleachable Q-switching filters, etc.) for high-power lasers are discussed. Laser damage resistance of various polymers is particularly investigated. The dependences of laser-induced damage threshold on the initial monomer purity, chemical composition and temperature of polymers, frequency and duration of laser pulses, on the focal spot, as well as statistics and morphology of damages, the accumulation effect in damage in a multiple irradition regime, light nonlinear scattering and subthreshold UV-glow have been investigated to elucidate the mechanisms of laser-induced damage in polymers.

Absorbing defects of different kinds have been established to play an initiating role in the damage process. Purification of the initial monomers was found to result in high values of laser damage thresholds of polymers comparable with those for crystals and glasses, although considerable differences are revealed in the polymer damage characteristics compared to other optical materials.

Analysis of these peculiarities is presented and it is concluded that the molecular characteristics of plasticating agents are decisive in the mechanism of microdamage appearance initiated by absorbing defects, and that visco-elastic properties of polymers have a considerable effect on the growth of damages from micro- to macrodimensions.

A theoretical model of laser damage, as well as practical, effective ways of increasing laser damage resistance of polymer materials are discussed.

Key words: absorbing defects; bulk damage; laser-induced damage; polymer materials; surface damage.

1. Introduction

Polymer materials began to be widely used in optical engineering. In this connection, it is interesting to consider the possibilities of their application as optical materials for lasers. In particular, they can be used for producing different elements of routine optics (prisms, waveguides, etc.) and specific laser elements (active elements with lasing dyes, bleachable filters for Q-switching and so on).

From this viewpoint, it is important to investigate laser-damage resistance of polymer materials, which can have great peculiarities due to their specific structure and thermoelastic properties different from those of usual materials (crystals and glasses). In the first works on laser-induced damage to transparent polymer materials (the first paper [1] was published in 1966) their laser-damage resistance was revealed to be essentially lower than that of crystals and glasses.

To elucidate this fact, different damage mechanisms were considered associated with absorbing impurities (a wedging effect of the gases formed due to evaporation of absorbing defects [2], the formation near the defects of highly absorbing products, such as soot, due to chemical transformations at high temperatures [3-6], and the mechanism connected with a multiquantum fracture of "stressed molecular bonds" [7].

However, the question of a dominating mechanism of laser-induced damage to polymers has remained, so far, open to discussion, and the ways of increasing their laser-damage resistance have not been clear.

In the present work, detailed investigations of laser-induced damage to a wide class of transparent polymer materials have been carried out, which cleared up the main characteristics and the mechanism of laser-induced damage to polymers. The dependences of laser-damage resistance on purity of initial monomers, on chemical composition and temperature of polymers, on frequency and duration of laser pulses, and on the size of an irradiated region have been studied, as well as statistics and morphology of damages, effect of accumulation in damage in the multiple irradiation regime, nonlinear light scattering and glow in the visible and near-UV spectrum range.

On the basis of the experimental data obtained, a theoretical model is developed, which explains well enough the observed characteristics, and the ways of increasing laser-damage resistance of polymers are suggested, some of which are attained in practice. In particular, highly laser-damage resistant active elements with lasing dyes, as well as bleachable filters for Q-switching of ruby and neodymium lasers and other optical elements have been created.

2. Experiment

The following transparent polymers were chosen as investigation objects: polystyrene (PS), organic glasses of the methacrylate class, such as polymethylmethacrylate (PMMA), polybutyl-methacrylate (PBMA) and others, their copolymers, and polymers with different plastifying agents (dimethyl phthalate, ethanol, etc.). The degree of optical purity of the polymers was varied with the change in pore size of the filters used for purification of initial monomer compositions.

The Q-switched ruby and neodymium lasers were used in the experiment operating in multi-mode and single-mode regimes with pulse widths of $\tau \simeq 20$ ns, at $\lambda = 0.69$ μm, and $\tau \simeq 10$-40 ns at $\lambda = 1.06$ μm and the second harmonic of the neodymium laser ($\lambda = 0.53$ μm). Laser radiation was focused on the samples by means of lenses with focal lengths F = 18-300 mm, the focal spot-size in this case was $d_k = 5 \cdot 10^{-4} - 10^{-1}$ cm. The samples' temperature varied within a wide range from -55 up to 180°C, which involved all the physical states of polymers.

The laser-damage resistance was determined as a minimum value of the radiation energy density $P_d(N)$, at which the damage sites about 10^{-2} cm in size occur in the polymer bulk after N pulses of irradiation. In the experiments N varied between 1 and 10^4.

Since, in the literature, the question of the influence of inclusions on laser-induced damage to transparent polymers remained open to discussion, we studied a series of characteristics of laser-induced damage, allowing us to draw a well-grounded conclusion on the role of absorbing defects in the damage mechanism.

In one series of experiments, the dependence of damage thresholds of methylmethacrylate (MMA) on optical purity was investigated. It was observed that $P_d(I)$ monotonically increases when using the filters with pores decreasing from 16 to 0.22 μm for monomer purification [8] and (Table 1). It is interesting to note that the increasing of the degree of optical purity gives only a 3.5-fold increase of $P_d(I)$ for PMMA, compared to a more than 30-fold increase of $P_d(I)$ for MMA in wide beams. Besides, a remarkable decrease of damage threshold is observed at the monomer-polymer transformation, while in tightly focused beams such an effect was not observed. It should also be noted that, in wide laser beams, the damage threshold $P_d(I)$ for PMMA is 3.5-12 times less than that of silicate glass K-8, which is one of the most laser-damage-resistant materials. In the tightly focused beams, there thresholds become comparable (they differ by a facter of 2 - 4) [8,9].

These results indicate that the laser breakdown in MMA and PMMA is due to the absorbing inclusions. In tightly focused beams in MMA and PMMA, and in wide beams in MMA, the laser-damaging intensity is high enough and corresponds probably to a "thermal explosion" of the absorbing defects [10], whereas, the effect of considerable lowering of $P_d(I)$, observed in wide beam at MMA transformation to PMMA, proves a change of a damage mechanism. The thermal explosion mechanism in MMA (caused by heating of defects to temperatures above 10^3K) is replaced by a mechanism associated with the triboprocess in PMMA around the inclusions heated to temperatures $\lesssim 10^3$K at considerably lower intensities of incident radiation [11].

Investigations of damage morphology in PMMA also indicate the exchange of damage mechanisms. They have shown that in wide laser beams, and with purification of the initial MMA by filters with the pore sizes of 16-0.45 μm, the damage sites have the form of star-like cracks about 10^{-2} cm in size, randomly scattered in the focal region. In case of inititial MMA purification with the filter with 0.22 μm pores in wide beams, and at any degree of optical purity in tightly focused beams (at increased intensity levels), the damages constitute opaque melts of an ellipsoidal shape ≃ 50 μm in length and ≃ 30 μm in diameter, their occurrance threshold being dependent on the polymer optical purity (Table I).

It should be noted that the formed melts are scattered randomly in the caustic of the focusing lens, and self-focusing filaments are not observed even at levels considerably exceeding the damage thresholds. This indicates that the damage morphology itself cannot be considered as a proof of an intrinsic (not associated with the absorbing defects) damage mechanism.

Similar results were also obtained for other transparent polymer materials. Table 2 presents the damage thresholds in wide and tightly focused beams for a series of polymers.

The dependence of polymer damage thresholds on the size of the irradiated region (fig. 1) also indicates the contribution of inclusions to the damage mechanism of polymer materials [12]. It is seen in figure 1 that $P_d(I)$ decreases more than by a factor of 20 with the increasing of the focal spot diameter from 30 μm to 640 μm.

Investigations of the dependence of damage thresholds on the laser pulse duration in the range of 10-40 ns [8] and on the radiation wavelength (λ = 1.06-0.53 μm) [12], statistics of $P_d(I)$ (its fluctuations from point to point inside a sample) and a strongly pronounced accumulation effect (see below) observed by a nonlinear light scattering and glow in the visible and near-UV range of spectrum [8,9] also confirm the conclusion of a considerable influence of absorbing defects on laser-induced polymer damage.

Thus, an unambiguous conclusion can be made on the basis of the results obtained: the laser-induced damage to the investigated polymers is in all cases connected with the absorbing defects. In the case of wide laser beams, large-size defects ($\gtrsim$ 0.1 μm) participate obviously in a damage process; whereas, for tightly focused beams, the damages arise, as a rule, on small absorbing defects, and the macrodamages are a result of a plasma spreading due to UV-preionization of the surrounding matrix [13], or due to electron heat conduction [9].

A distinctive feature of the polymer materials, compared to other transparent dielectrics (crystals and glasses), is the presence of a strongly pronounced accumulation effect: microdamages and their growth up to macrodimensions at successive laser irradiations are observed at intensities far less (up to 100 times) than $P_d(I)$ [8,9]. This fact was the main obstacle in the way of wide usage of transparent polymers in laser systems.

In order to elucidate the reasons of such a pronounced accumulation effect and the possibilities of its control, a series of experiments were conducted with different polymers (homopolymers, copolymers, and polymers with different plasticizers) in a wide temperature range (-55 + 180°C). As a result, for all the materials studied, a considerable increase in $P_d(N)$ was revealed in the temperature range close to the polymer glass-transition temperature T_g (fig. 2 and Table 3). As the investigations have shown [14], the effect of a transition to a laser-damage resistant state at $T > T_g$ depends considerably on viscous-elastic properties (VEP) of the matrix.

The increasing of $P_d(N)$ due to VEP of the matrix can be attained by introducing plasticizers into a polymer [14-16]. In this case, independent of the atomic composition of polymers with plasticizers (Table 4), or at $T > T_g$ for homopolymers, microdamages (< 10^{-3} cm in size) occur in their bulk at successive laser shots, which slightly increase from pulse to pulse up to $N \gtrsim 10^3$ [14-16]. But, from the practical viewpoint, such microdamages in the matrix do not have a considerable influence on the characteristics of a laser beam propagating through a polymer element and, thus, do not limit the operation of the element in the laser system.

At the same time at $T < T_g$, for the homopolymers and for polymers with the value of the forced elasticity limit σ_{fe}, greater than that of the cleavage fracture parameter σ_{fr}, the microdamages with the size of < 10 μm appeared after a series of shots and grow up to macrosizes of ~ 10^{-2} cm at a considerable rate.

It should be noted that an essential increasing of the number of pulses N_{cr} at a fixed radiation energy density $P_f \leq P_d(I)$ can be attained only by varying VEP to decrease the forced elasticity limit (by introducing plasticizers in essential concentrations) to a level lower than the cleavage fracture limit (Table 4). At the same time, only a slight growth of N_{cr} is observed for polymers with $\sigma_{fe} > \sigma_{fr}$ even after a careful purification (Table 4).

In some cases, however, an essential increasing of laser-damage resistance of polymer materials is observed when introducing low-molecular weight additives in low concentrations, which do not affect markedly the VEP of the matrix. In this case, the levels of the incident radiation intensity, at which microdamages (< 10 μm in size) occur after multiple irradiations and then grow up to microdamages, become dependent on the structure and molecular characteristics of the additives. The experiments have shown that the additives serve as inhibitors of the initiation of microdamages, and introduction of some of them has such a strong influence that, in some cases, it strongly suppresses the accumulation effect in the multishot damage.

Such a considerable increase of laser-damage resistance of polymer materials can be attributed to deactivation of excited electron states by these additives, which occur in the process of microcrack formation in the matrix around the absorbing inclusions [11].

A prethreshold glow in the visible and near-UV range of the spectrum prove the presence of such excited states. The additives considerably increase the level of the incident radiation intensity at which the prethreshold glow is observed [9].

Another typical feature of the polymer materials, compared to other transparent dielectrics, is a higher laser-damage resistance of the polymers' surface in respect to their bulk [8,17]. This remains valid for polymer surfaces obtained by different treatment techniques such as stamping and diamond abrasive polishing. Such an increased surface resistance, compared to bulk, can be attributed to a lower forced elasticity limit of the surface layer.

3. Damage Mechanism

The experimental results obtained suggest the following mechanism of laser-induced damage to polymers [11]. The laser energy absorption by different defects produces the heating of the surrounding matrix, which entails, even at moderate temperatures ($\lesssim 10^3$K), excitation of the electron states capable of absorbing laser radiation in the initially transparent matrix. Such a process involves the triboprocess associated with the crack formation in the polymer or chemical molecular transformation. When the laser radiation intensity exceeds some critical value, determined by thermofluctuation parameters of the polymer breakdown and the laser energy absorption by the electron excited states, the "thermal stability" fails entailing the formation of microdamages in the matrix, as large as < 10 μm, which are filled with the products of polymer breakdown. It should be stressed that, at that stage, strongly absorbing products such as soot do not form [14]. Note that this conclusion is different from that made in [3-5]; that the soot products form on the initial stage of damage and determine the development of polymer breakdown.

A further temperature rise (due to laser intensity increase) or accumulation of the products of the polymer breaking down (at multiple laser pulses with a fixed intensity) gives rise to radical chain-cracking processes with a formation of soot-like products. VEP of the matrix have a considerable influence on this process. Intensive absorption of the laser radiation energy by the soot products leads to a "thermal explosion" with the formation of macrodamages of about 100 μm in size.

A detailed theoretical consideration of this mechanism of laser-induced damage to polymers is presented in [11], where the expressions for the damage thresholds are derived for the case of "short" and "long" radiation pulses, which explain well the observed charactreristics.

Proceeding from the described damage mechanism, the following ways of increasing the laser-damage resistance of polymers can be offered:

1. The change of the viscoelastic properties of the matrix to lower the induced elasticity limit below that of the cleavage fracture. In this case, VEP inhibit the development of microdamages up to macrodimensions. Such a way was considered in [14-16].

2. Introduction into a polymer of low-molecular weight additives or modification of the polymer by inserting definite groups into macromolecules, which are able to deactivate the excited electron states of macromolecules and, therefore, to reduce the laser radiation absorption in the matrix surrounding the defect. The second way is expected to be more promising to obtain polymers with the laser-damage resistance comparable to that of crystals and glasses [18,19].

4. Conclusion

The results of our investigations indicate a decisive role of molecular characteristics of modified additives in the mechanism of microdamage occurrance initiated by the absorbing defects, and prove an essential influence of the viscoelastic properties of polymer materials on the process of microdamage development to macrosizes. The methods of increasing laser-damage resistance to polymer materials, developed on the basis of these concepts and realized for polymers of the methacryl family with low-molecular weight additives, have shown that the transparent polymers, which have already been created, can be competitive for production of different elements of conventional optics (prisms, lenses, etc.), and have definite advantages in preparing such specific laser elements as a solid-state dye cell [18,19], bleachable filters for Q-switch operation of ruby and neodymium lasers.

REFERENCES

[1] Ashkinadze, B. M.; Vladimirov, V. I.; Likhachyov, V. A.; Ryvkin, S. M.; Salmanov, B. M.; and Ydroshetsky, I. D., High Power Laser Induced Damage to Transparent Dielectrics, ZHETF, 50, 1187 (1966).

[2] Barenblatt, G. I.; Vsevolodov, N. N. Mirkin, L. I.; Pelipetsky, N. F.; and Raizer, Yu. P., Laser Induced Damage to Transparent Materials. Appearance of Gas Bubbles and Material Wedging under Gas Pressure, Pis'ma v ZHETF, 5, 87 (1967).

[3] Orlov, A. A. and Ulyakov, P. I., Mechanism of High-Temperature Cell Formation at Laser Induced Damage to Transparent Polymers, Journal of Applied Mechanics and Technical Physics, No 1, 127 (1976).

[4] Butenin, A. V. and Kogan, B. Ya., Mechanism of Transparent Polymer Material Damage Under Multiple Pulsed Laser Irradiation, Kvantovaya Electron, 3, 1136 (1976).

[5] Liberman, M. A. and Tribelski, M. I., The Role of Chemical Reactions in the Laser Induced Damage to Transparent Polymers, ZHETF, 74, 194 (1978).

[6] Kovalyov, A. A.; Makshantsev, B. I.; Pelipetsky, N. F.; Sidorin, Yu. V. and Stonik, O. G., Accumulation Effects and Temporal Dependence of the Optical Breakdown Threshold of Solid Transparent Dielectrics Under Coherent Laser Radiation, Kvantovaja Electronika 7, 1287 (1980).

[7] Agranat, M. B.; Krasyuk, I. K.; Novikov, N. P.; Perminov, V. P.; Yudin, Yu. I. and Yampol'sky, P. A., Laser Induced Damage to Trnasparent Dielectrics, ZHETF, 60, 1748 (1971).

[8] Manenkov, A. A. and Nechitailo, V. S., The Tole of Absorbing Defects in Laser Induced Damage to Transparent Polymers, Kvantovaja Electronika, 7, 616 (1980).

[9] Manenkov, A. A.; Nechitailo, V. S. and Tsaprilov, A. S., Laser Induced Damage to Transparent Polymers in Single-mode Tightly Focused Beams, Izvestiya AN SSSR, Ser.Fizich., 44, 1771 (1980).

[10] Danileiko, Yu. K.; Manenkov, A. A.; Nechitailo, V. S.; Prokhorov, A. M. and Khaimov-Mal'kov, V. Ya., The Role of Absorbing Inclusions in the Mechanism of Laser Induced Damage to Transparent Dielectrics, ZHETF, 63, 1030 (1972).

[11] Manenkov, A. A.; Nechitailo, V. S. and Tsaprilov, A. S., Analysis of Laser Induced Damage to Transparent Polymers in Connection with Their Viscoelastic Properties, Kvantovaya Electronika, 8, 838 (1981).

[12] Aldoshin, M. I.; Manenkov, A. A.; Nechitailo, V. S. and Pogonin, V. I., Frequency and Size Dependences of the Laser Induced Damage Threshold of Transparent Polymers, Journal of Technical Physics, 49, 2498 (1979).

[13] Danielko, Yu. K.; Manenkov, A. A. and Nechitailo, V. S., On the Mechanism of Laser Induced Damage to Transparent Materials Caused by Thermal Explosion of Absorbing Inhomogeneities, Kvantovaya Electronika, 5, 194 (1978).

[14] Dyumaev, K. M.; Manenkov, A. A.; Maslyukov, A. P.; Matyushin, G. A.; Nechitailo, V. S. and Tsaprilov, A. S., Investigation of the Effect of Viscoelastic Properties of the Matrix and Plasticizer Type on the Laser-Damage Resistance of Transparent Polymers, Kvantovaya Electronika, 9, No 4 (1982).

[15] Aldoshin, M. I.; Gerasimov, B. G.; Manenkov, A. A.; Maslyukov, A. P.; Nechitailo, V. S. and Ponomarenko, E. P., Laser Induced Damage to Transparent Polymers Having Different Atomic Compositions, Jurnal Technicheskoi Fiziki, 49, 2496 (1979).

[16] Aldoshin, M. I.; Gerasimov, B. G.; Manenkov, A. A. and Nechitailo, V. S., A Decisive Role of Viscoelastic Properties of Polymers in the Mechanism of Laser Induced Damage, Kvantovaya Electronika, 6, 1866 (1979).

[17] Bebchuk, A. S.; Gromov, D. A. and Nechitailo, V. S., A Measure of the Surface Defectiveness and Optical Strength of Transparent Dielectrics, Kvantovaya Electronika, 3, 1814 (1976).

[18] Gromov, D. A.; Danilov, V. V.; Dyumaev, K. M.; Eryomenko, A. S.; Lan'kova, S. M.; Maxurenki, Yu. T.; Naslyukov, A. P.; Matyushin, G. A.; Nechitailo, V. S. and Stepanov, A. I., Investigation of Active Polymer Elements with Dyes, Proceedings of the 3rd All-Union Conference "Lasers on the Base of Complex Orgniic Compounds and Their Applications, Uzhgorod, 10-12 September 1980, p. 271-272.

[19] Gromov, D. A.; Danilov, V. V.; Dyumaev, K. M.; Eryomenko, A. S.; Lan'kova, S. M.; Maslyukov, A. P.; Matyushin, G. A.; Nechitailo, V. S.; Savel'ev, D. A. and Stepanov, A. I., Efficient Dye Generation in a Polymer Matrix. Proceedings of the X-th Siberian Meeting on Spectroscopy "Inversion Population and Generation in Atom and Molecule Transitions," Tomsk, 16-18 September 1981, p. 294.

TABLE 1. Damage thresholds of MMA and PMMA (relative to the damage threshold of silicate glass K-8) in wide (d_k = 110 μm) and tightly focused (d_k = 4.6 μm) beams at different purification degrees of the initial monomer.

Filter pores size μm	Damage Threshold at d_k = 110 μm		at d_k = 4.6 μm	
	MMA	PMMA	MMA	PMMA
16	0.19	0.08	0.24	0.24
1.6		0.11	0.31	0.31
0.8		0.16	0.38	0.38
0.45		0.21	0.43	0.43
0.22	>6.0	0.28	0.53	0.53

TABLE 2. Damage thresholds of a series of polymer materials (relative to the damage threshold of silicate glass K-8) in wide (d_k = 110 μm) and tightly focused (d_k = 4.6 μm) beams.

Materials	Damage Threshold at d_k = 110 μm	Damage Threshold at d_k = 4.6 μm
Glass K-8	1.0	1.0
PMMA	0.28	0.53
P-izo-BMA	0.16	0.70
PMMA + 20% dimethyl phtalate	0.11	0.39
Modified PMMA	0.59	1.1
PS	0.05	0.06

TABLE 3. Laser-induced damage thresholds $P_d(N)$ (relative to the damage threshold of the glass K-8) at a multiple irradiation for the number of pulses N_{cr} = 200 and at various temperatures. Spot-size diameter d_k = 110 μm.

Polymer	$P_d(I)$ T = 20°C	$P_d(200) \times 10^3$ T = 55°C	$P_d(200) \times 10^3$ T = 20°C	$T_d(N)$, °C	T_g, °C
PMMA	0.08	4	4	120	119
P-izo-BMA	0.13	4	11.2	50	53
P-n-BMA	0.10	5.6	16	20	20
PMMA + 20% DMP	0.08	4	4	65	61
PMMA + 20% DBP	0.09	4	6.4	63	53
PMMA + 20% EA	0.11	8	20.8	60	51

$P_d(I)$ - single shot damage threshold

$T_d(N)$, C - for notation see the text and figure 2

T_g, C - glass transition temperature

DMP - dimethyl phthalate

DBP - dibutyl phthalate

EA - ethyl alcohol

TABLE 4. Laser-damage resistance (in terms of damaging critical number of pulses N_{cr}) of polymer materials in the multiple irradiation regime at a fixed laser intensity corresponding to N_{cr} = 20 for PMMA.

Polymer composition	Atomic composition C	O	H	σ_{fe} (kg/mm^2)	$P_d(I)$	N_{cr}	Type of damage
PMMA initial	100	40	160	12	0.08	20	cracks
purified PMMA (pore size 0.22)	100	40	160	12	0.28	90	"
Copolymer MMA (71%)+ +MMEG (29%)	100	43	162	20	0.14	70	"
PMMA + 20% EA	100	41	182	3.9	0.11	$>10^4$	no damages
P- tret. BMA	100	25	175	11	0.15	40	cracks
P-norm. BMA	100	25	175	1.6	0.10	$>10^3$	melts
PMMEG	100	50	167	8.8	0.14	40	cracks
copolymer MMA(50%) + AA(50%)	100	53	149	9.2	0.42	30	"
copolymer MMA(80%) + DMA(20%)	100	14	186	6.6	0.11	$>10^3$	melts
copolymer MMA(35%) + BMA(65%)	100	30	170	4.5	0.14	$>10^3$	"
PMMA + 30% DBP	100	35	153	2.0	0.11	$>10^3$	"
PS	100	-	100	10	0.05	5	cracks
PS + 30%DBP	100	7	110	0	0.08	$>10^3$	melts

$P_d(I)$ - single shot damage threshold

σ_{fe} - forced elasticity limit

PMMA - polymethyl methacrylate

MMEG - monomethacryl ester of glycol

EA - ethyl alcohol

PBMA - polybutyl methacrylate

AA - acrylic acid

DMA - decyl methacrylate

DBP - dibutyl phthalate

PS - polystyrene

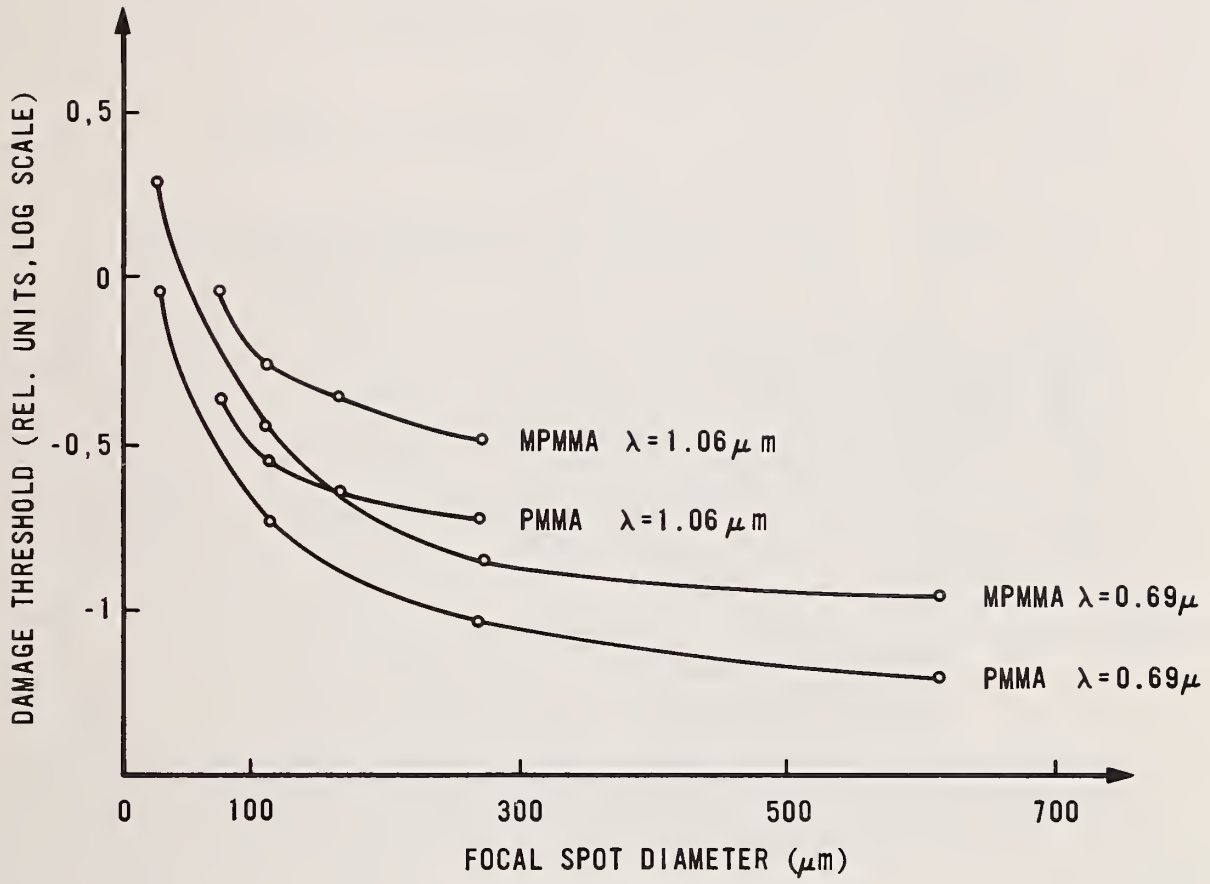

Figure 1. Spot-size dependence of laser damage threshold in polymethyl methacrylate (PMMA) and modified polymethl methacrylate (MPMMA) relative to damage threshold of silicate glass K-8.

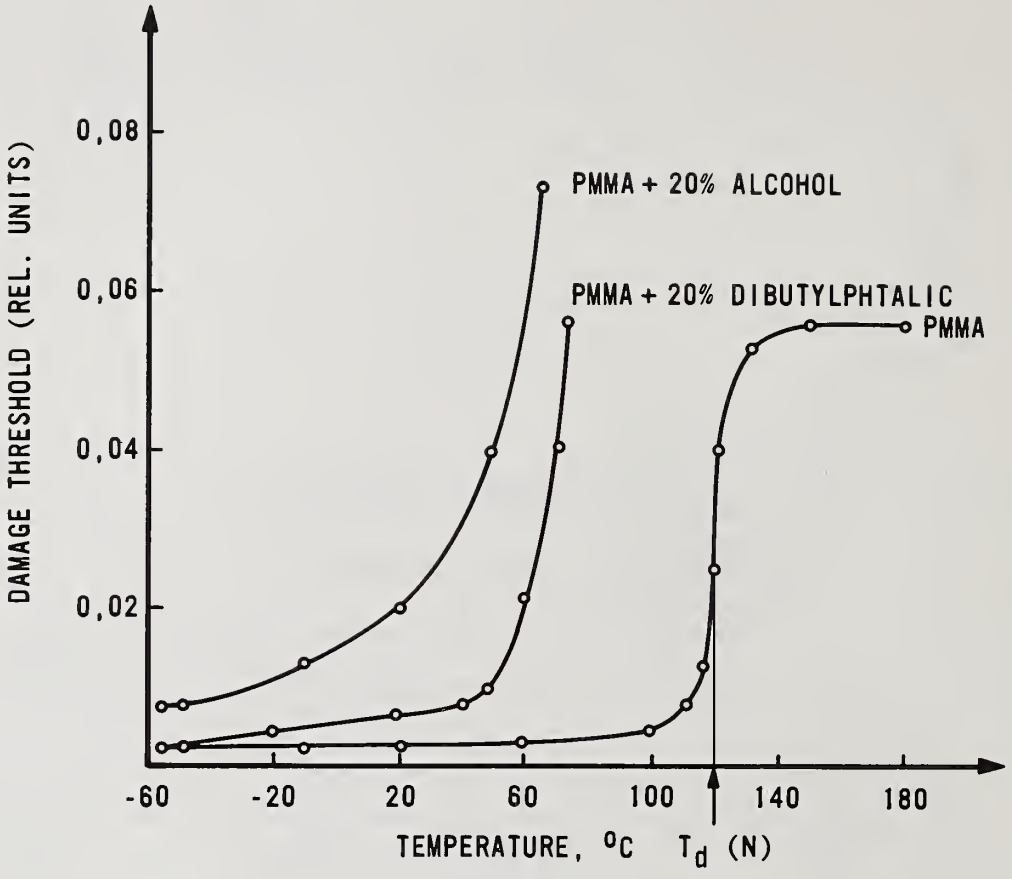

Figure 2. Temperature dependence of laser damage threshold in multishot regime for N_{cr}=200 at wavelength 0.69μm relative to damage threshold of silicate glass K-8.

The damage threshold and pulse length were over 100 GW/cm^2 and 10-30 ns, respectively. No pulsewidth dependence for this material was observed. Laser fluctuations were less than 5 percent in peak power, pulse to pulse. The type of inclusion was not known for the polymer materials tested, but the fact that when the filter size decreased the damage threshold increased shows that inclusions are indeed present in the material. When small spot size damage measurements were made, the large spot size threshold was never observed, however. There must be a scatter in the inclusion sizes in the material. The decrease in damage threshold with increasing frequency the author ascribes to the change in absorption of the inclusion with frequency, not to an intrinsic property of the material itself.

Survey of 1.3 μm Window Materials Continued

Nils C. Fernelius, David V. Dempsey, David B. O'Quinn and Michael E. Gangl

University of Dayton Research Institute
Dayton, Ohio 45469

and

Walter L. Knecht

Air Force Wright-Aeronautical Laboratories
Materials Laboratory
Wright-Patterson Air Force Base, Ohio 45433

The purpose of this work is to screen candidate materials for use in the iodine laser which operates at 1.315 μm. The results presented here are the effective optical absorption coefficient, β_{eff}, measured by laser rate calorimetry using a Quantronix Nd:YAG laser modified to operate at 1.319 μm. Here we extend the measurements reported last year to new materials. These include MgF_2, MgO, Kigre Q-98 phosphate glass, YAG ($Y_3Al_5O_{12}$), water clear ZnS, CdTe, Schott IRG-N6 CaAl silicate, IRG-7 lead silicate, IRG-9 fluorophosphate glasses, and Hughes HBL glass. Spectral transmission scans using a Beckman 5270 and a Perkin-Elmer 180 spectrophotometer are presented for some of the less common materials. We also take this opportunity to report remeasured absorption values for data reported last year.

Key words: As_2S_3; HBL glass; infrared materials; iodine laser; laser calorimetry; $LiYF_4$; MgF_2; MgO; optical absorption coefficients; YAG; $Y_3Al_5O_{12}$; YLF; ZnS.

1. Introduction

The purpose of this work is to screen candidate materials for use in the development of the iodine (I^*) laser which operates at 1.315 μm [1].[1] This wavelength is short enough so that a number of materials, mainly oxides, which were not usable for HF-DF, CO and CO_2 lasers can now be considered. The initial part of this work was reported last year [2]. Here we report properties of additional materials studied.

The optical absorption coefficients given here were obtained using laser rate calorimetry [3,4]. The light source was a Quantronix 114 Nd:YAG laser fitted with special mirrors to operate at 1.319 μm. Except for materials with large OH^- concentrations, this should be an excellent approximation to absorption values at 1.315 μm. There is an absorption band of OH^- at 1.38 μm whose tail may introduce considerable absorption. This problem has been discussed by Wiggens [5] who concluded that the ratio of OH^- absorption coefficients, $\alpha_I/\alpha_{Nd} = 0.925$.

The data reported here are effective optical absorption coefficients, β_{eff}, obtained from the equation

$$\beta_{eff} = \frac{(1-R_b)}{(1+R_b)} \frac{P_A}{P_T} = \frac{2n}{1+n^2} \frac{mC_p}{\ell} \frac{\Delta T}{\Delta t} \frac{1}{P_T} \qquad (1)$$

where P_A is the power absorbed in the sample, P_T is the power transmitted, R_b is the reflection coefficient at the exit face, n is the index of refraction; m is the mass of the sample, C_p is

[1] Numbers in brackets indicate the literature references at the end of the paper.

the heat capacity, ℓ is the sample thickness and $(\Delta T/\Delta t)$ is the sum of the magnitudes of the heat rise and cooling slopes.

$$\beta_{eff} \equiv \beta_B + (1+x)\beta_s/\ell \qquad (2)$$

where β_B is the bulk optical absorption coefficient in cm^{-1} and β_s is the dimensionless surface absorption. Depending upon conditions of the coherence of the irradiating light, x lies between 1 and n. This is discussed in Case 8 of Fernelius and Johnston [6]. So far the only surface-to-bulk absorption studies at 1.3 μm have been performed on single crystal CaF_2 [7] and sapphire [8,9].

The hope of this study was to evaluate the optical absorption of samples as an intrinsic property of the material. Experience has shown that a significant part of the absorption in real world samples is related to the method of sample preparation, to the purity of the window fabricated and to the quality of the surface polish. Thus in the experimental results a discussion of the sample studied is given. A typical discussion includes the name of the manufacturer or vendor, information, if known, about the orientation of noncubic crystals, comments on the appearance of the material and surface condition, and preparation method used.

2. Experimental Results

Here we shall present results on materials studied since Ref. [2]. An occasional spectral trace not included in Ref. [2] will be presented. The calorimetry box was originally designed for operation at 10.6 μm. When it was converted to 1.3 μm use, there were considerable problems due to Rayleigh scattering ($\propto 1/\lambda^4$). A number of baffles were introduced. In the laser calorimetry data reported in Ref. [2], it was discovered that one baffle was heated by front surface reflection from the sample and radiating towards the thermocouple. Thus the values reported in Ref. [2] are high. This was particularly prominent in lower absorbing materials. All β values given here were made since the correction was made. In the summary tabulation we include values for materials covered in Ref. [2] that have been measured. Unfortunately some of the original samples were borrowed and have been returned, some have been damage tested or had a mirror applied to them.

Magnesium difluoride, MgF_2, samples were obtained from two sources. The Harshaw Chemical Company, Solon, Ohio, samples had the faces oriented perpendicular to the c-axis with a standard uv polish. The Optovac, Inc., North Brookfield, MA samples had an optical polish on both faces with the c-axis perpendicular to the face within ±3°. Cross polarization photographs showed considerably more strain in the Optovac samples which may explain why they were more absorbing. A Perkin-Elmer 180 spectral trace is shown in Figure 1. Visible spectral traces showed over 90% transmittance down to 200 nm. Some limitations of MgF_2 in applications are that it is birefringent and has a low susceptibility to thermal shock.

Kigre, Inc., Toledo, Ohio makes a family of laser glasses for uses in various high power laser systems. Among these are several phosphate glasses, Q-88, Q-94, Q-98 and Q-100. We obtained a Q-98 sample cut from the lightly doped end of a boule with about 1% Nd concentration. A Beckman 5270 spectral trace is shown in Figure 2. While there are numerous Nd absorption lines in the visible, the sample appears to be very transparent from 0.95 μm through 1.55 μm. Assuming that the transmission loss is due to back surface reflection, we estimate the index of refraction at 1.3 μm to be about n=1.60. The specific heat C_p was measured to be about 0.611 J/gK. So far this is the lowest absorbing glass we have measured at 1.3 μm. More samples have been ordered where Al replaces Nd in the glass.

Undoped YAG, $Y_3Al_5O_{12}$, samples were purchased from the Airtron Division of Litton Industries, Morris Plains, New Jersey. The samples were 38 mm in diameter and 13.25 mm thick. Since Airtron was accustomed to polishing smaller diameter rods, the surface finish could have been better and presumably the measured β a bit lower. Even so there was no apparent scatter in the temperature versus time traces. Figure 3 shows the uv side of the transmittance taken on a Beckman 5270. Figure 4 shows the IR trace taken on a Perkin-Elmer 180.

One of the major materials developments within the past year is the appearance on the market of water clear ZnS [10]. The water clear material is colorless and it is highly transparent from 0.4-13 μm free of the absorption dip around 6 μm. Raytheon loaned us a Multispectral Grade

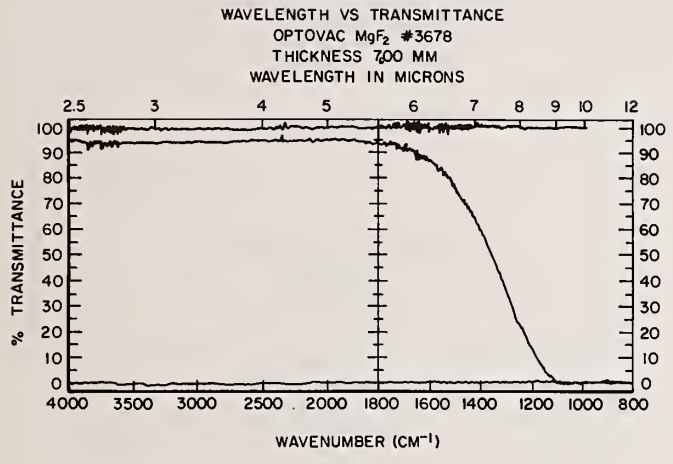

Figure 1. Transmittance versus wavelength for Optovac MgF_2.

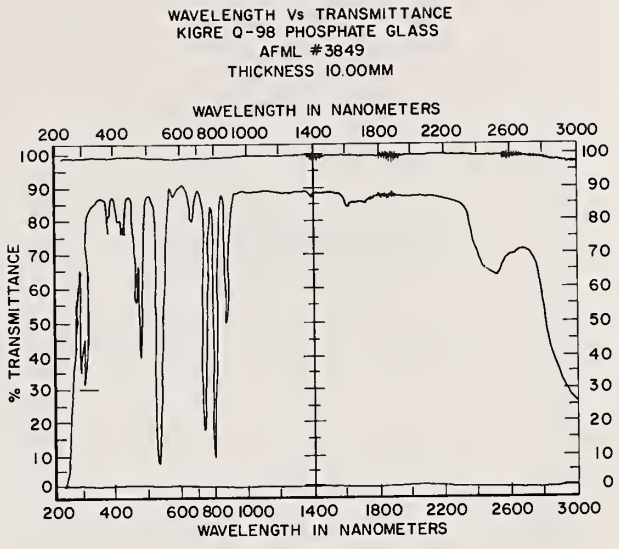

Figure 2. Transmittance versus wavelength for Kigre Q-98 phosphate glass.

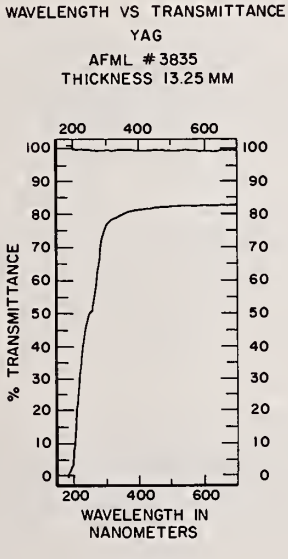

Figure 3. Transmittance versus wavelength for YAG, ($Y_3Al_5O_{12}$).

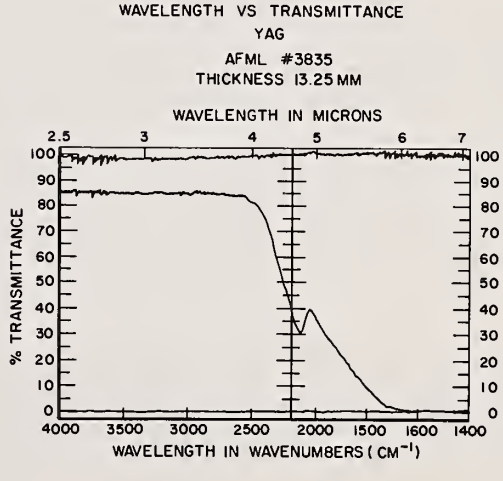

Figure 4. Transmittance versus wavelength for YAG, ($Y_3Al_5O_{12}$).

Raytran® ZnS sample. Figure 5 is a spectral trace of it on the Beckman 5270. Note that the material is highly transparent above 400 nm, whereas the standard Raytran® material, yellowish in color, gradually becomes more transparent through the visible region. Figure 6 shows a Perkin-Elmer 180 trace of the sample. We also measured a CVD Cleartran® sample made at least six months earlier than the Raytheon sample. While the optical properties of water clear ZnS are greatly improved over standard ZnS, this is accompanied by a reduction in flexural strength.

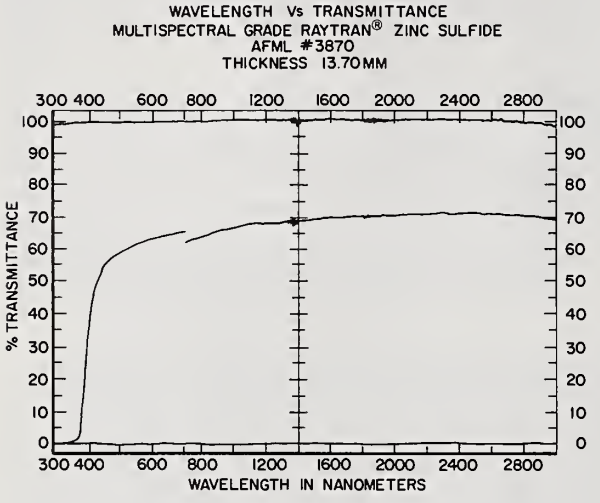

Figure 5. Transmittance versus wavelength for Multispectral Grade Raytran® zinc sulfide.

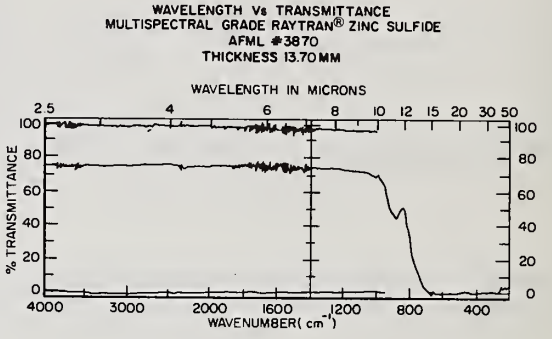

Figure 6. Transmittance versus wavelength for Multispectral Grade Raytran® zinc sulfide.

Some hafnium fluoride glasses were prepared on contract with Hughes, Malibu [11,12]. The composition of the HBL samples is 60% HfF_4, 33% BaF_2 and 7% LaF_3. Presumably the HBLA sample includes some AlF_3. Ice bath calorimetry on one HBL sample yielded a heat capacity, C=0.306 J/gK and on the HBLA sample, C=0.383 J/gK. Perkin-Elmer 180 spectral traces for HBL and HBLA were almost identical. An example is shown in Figure 7. The Beckman 5270 traces were almost flat from 0.3 to 3 μm with about 91% uncorrected transmission.

Schott Optical Glass, Inc., Duryea, PA sells a number of infrared glasses. Here we report measurements made on three types - IRG-N6, IRG-7 and IRG-9. All samples were polished by John Unertle Company, Pittsburgh, PA. Schott IRG-7 is a lead silicate glass. Spectral traces of it are shown in Figures 8 and 9. IRG-9 is a fluorophosphate glass. Its spectral traces are shown in Figures 10 and 11. IRG-N6 is a CaAl silicate glass with spectral traces shown in Figures 12 and 13.

The only commercial source for MgO we could find in North America was Norton Research Corporation, Niagara Falls, Ontario, Canada. We obtained some square single crystal samples whose faces are as cleaved. The samples contained some small scratches and imperfections. We also obtained two disc samples from Adolph Meller Company, Providence, RI who brought blanks at two different times from Norton, then polished them. One was colorless (AFML #3523) and the other had a slight yellow-green tinge (AFML #3524). The latter had a better polish on the faces and yielded the lowest $\beta_{eff} = 6.36 \pm 0.19 \times 10^{-3} cm^{-1}$. Spectral traces of the two samples are shown in Figures 14-17. The as cleaved samples yielded visible traces somewhat between the two shown here and the infrared traces were similar to #3524. We feel that better polished surfaces would yield lower absorption values. MgO is a difficult material to polish due to its hardness. However the properties that make it difficult to polish are very desirable for strength and durability of the finished product.

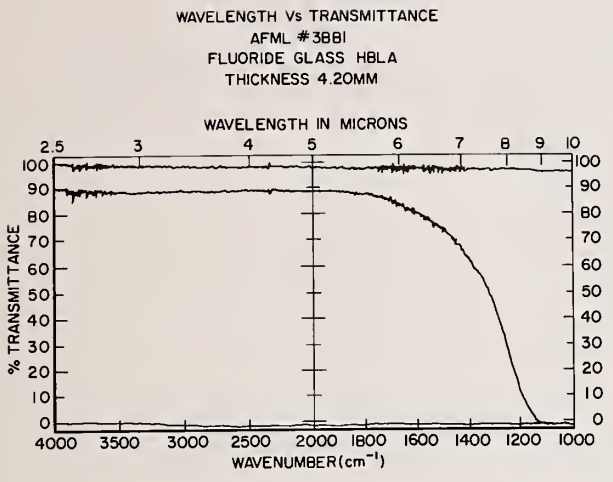

Figure 7. Transmittance versus wavelength for fluoride glass HBLA.

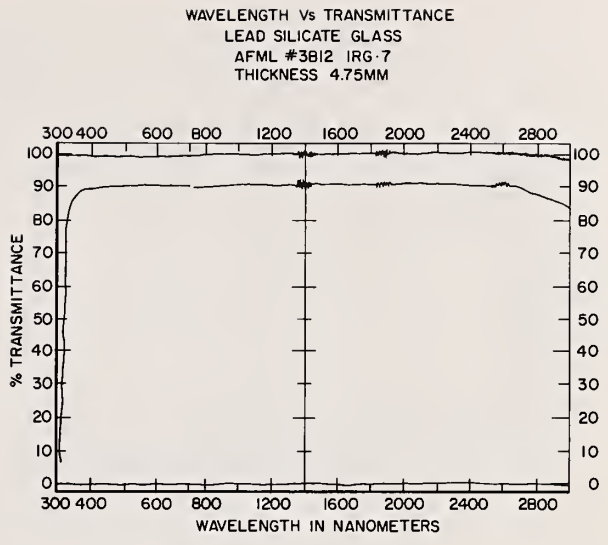

Figure 8. Transmittance versus wavelength for IRG-7 lead silicate glass.

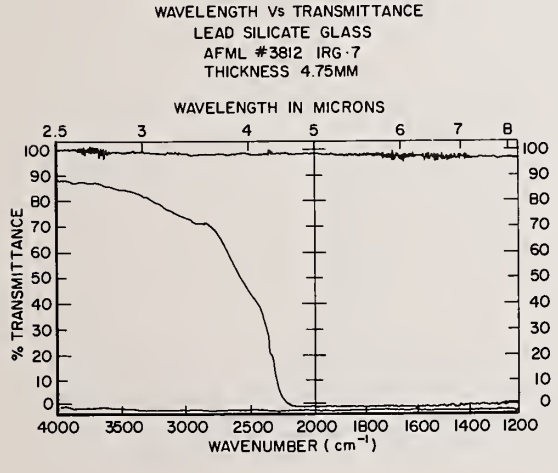

Figure 9. Transmittance versus wavelength for IRG-7 lead silicate glass.

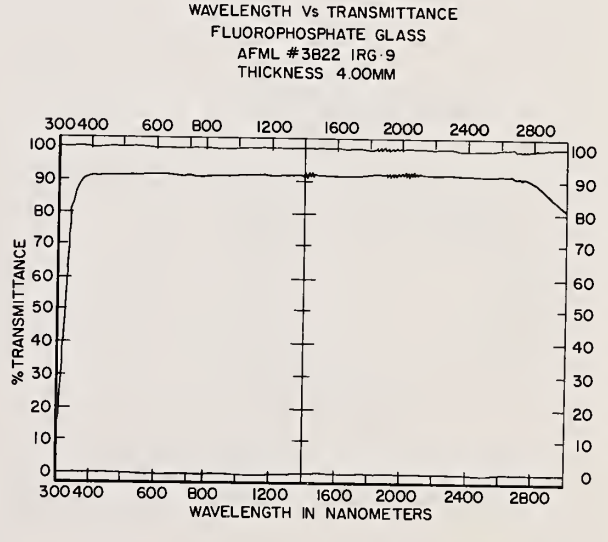

Figure 10. Transmittance versus wavelength for IRG-9 fluorophosphate glass.

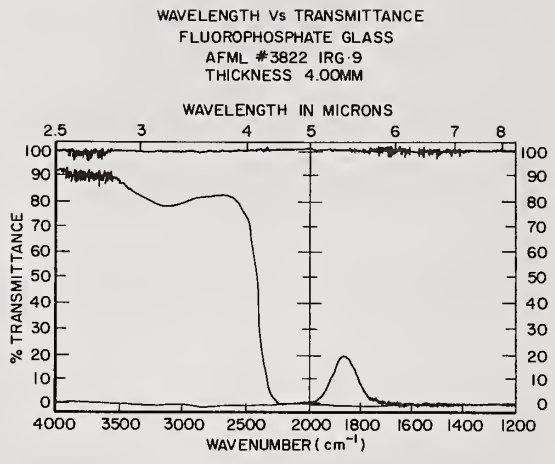

Figure 11. Transmittance versus wavelength for IRG-9 fluorophosphate glass.

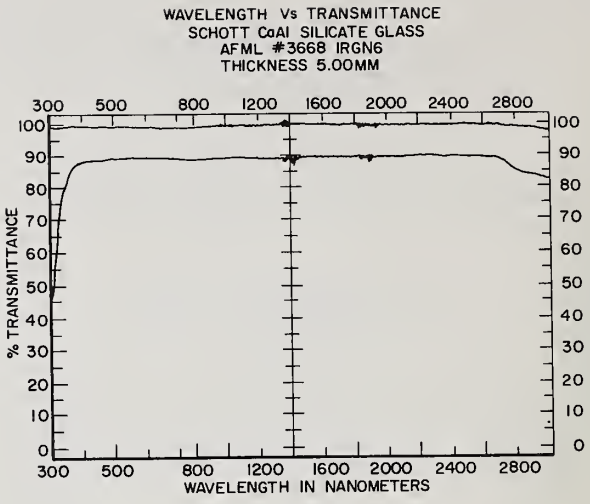

Figure 12. Transmittance versus wavelength for CaAl silicate glass.

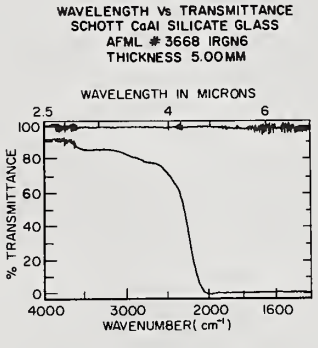

Figure 13. Transmittance versus wavelength for CaAl silicate glass.

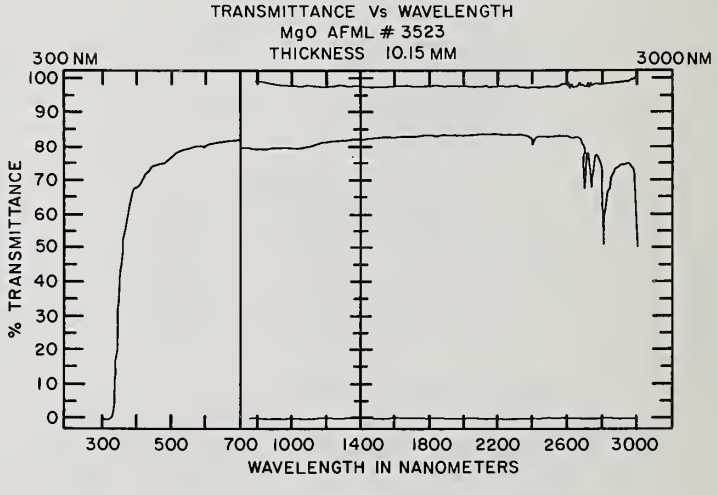

Figure 14. Transmittance versus wavelength for MgO.

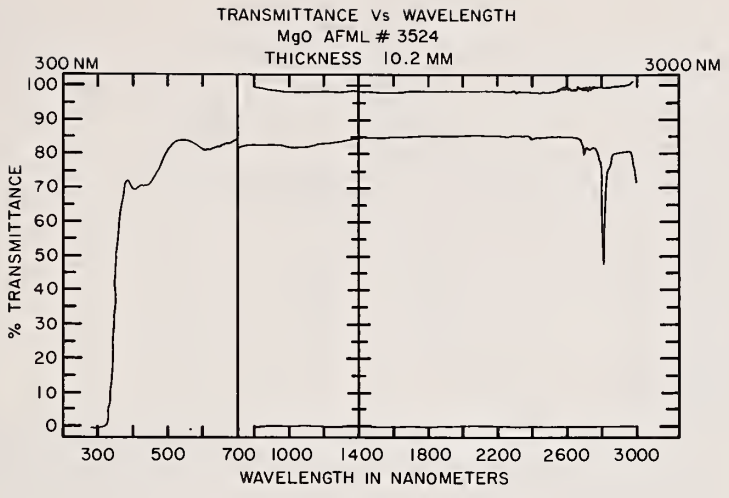

Figure 15. Transmittance versus wavelength for MgO.

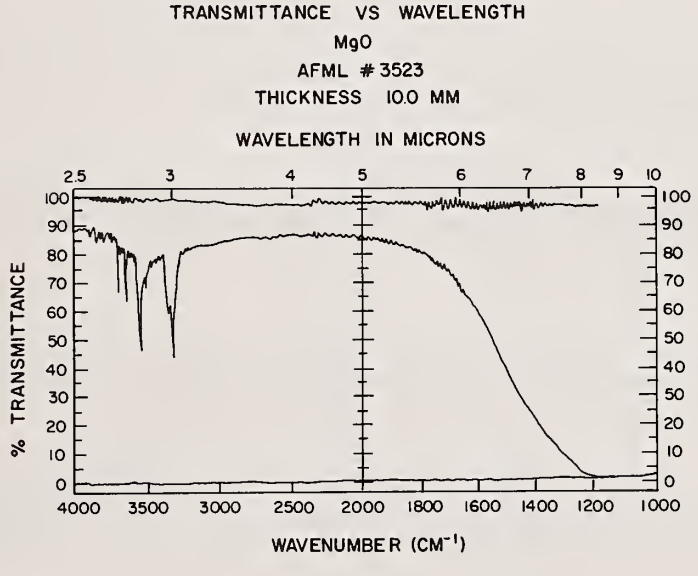

Figure 16. Transmittance versus wavelength for MgO.

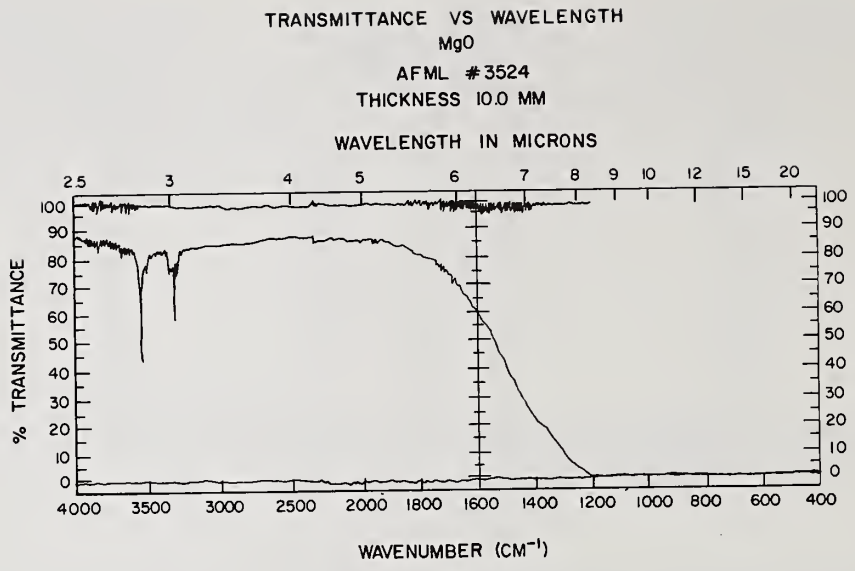

Figure 17. Transmittance versus wavelength for MgO.

A CdTe sample was loaned to us by II-VII, Inc., Saxonburg, PA. Spectral traces of their sample are shown in Figures 18 and 19. While CdTe is too absorbing to be of much use at 1.3 μm, it does have multispectral capability at longer wavelengths.

The remaining samples listed in the summary table were discussed in the previous paper [2]. A uv spectral trace of undoped YLF, $LiYF_4$, which was not in the other paper is shown in Figure 20. Spectral traces of As_2S_3 are shown in Figures 21 and 22. In some cases we were unable to measure the same sample reported in Ref. [2]. The GE 124 (125?) sample was another window ordered at the same time. Different Suprasil II samples were measured.

Table 1 lists materials by order of increasing β_{eff} value measured at 1.319 μm. Also included are the index of refraction, n, at 1.3 μm and the spectral range of high transmission. The materials included are those covered in the text plus remeasurements of samples discussed in Ref. [2].

3. Conclusions

The effective optical absorption coefficient of a number of materials has been measured at 1.319 μm. Spectral traces of a number of these materials are also presented.

This work was supported by the Air Force Wright-Aeronautical Laboratories, Materials Laboratory, Wright-Patterson Air Force Base, Ohio 45433.

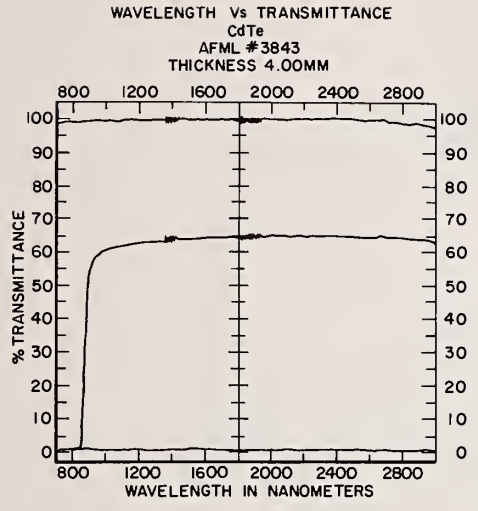

Figure 18. Transmittance versus wavelength for CdTe.

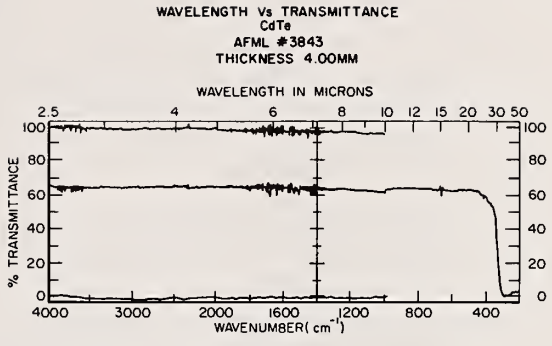

Figure 19. Transmittance versus wavelength for CdTe.

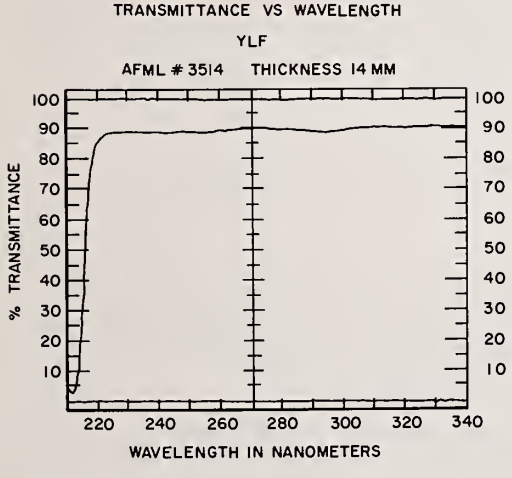

Figure 20. Transmittance versus wavelength for YLF ($LiYF_4$).

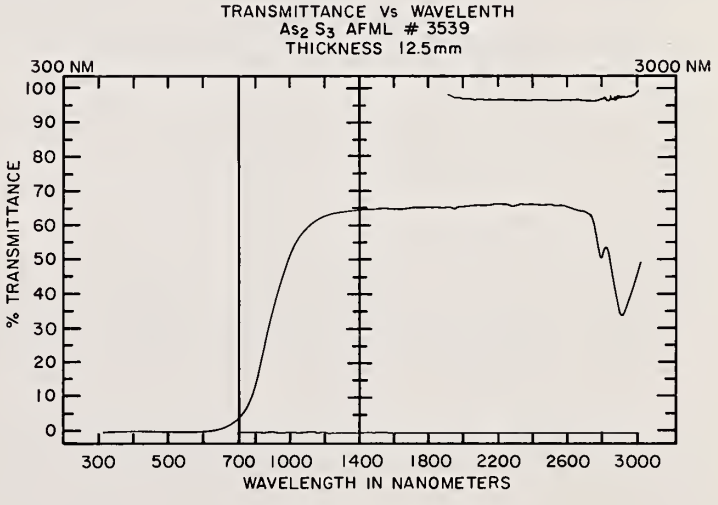

Figure 21. Transmittance versus wavelength for As_2S_3.

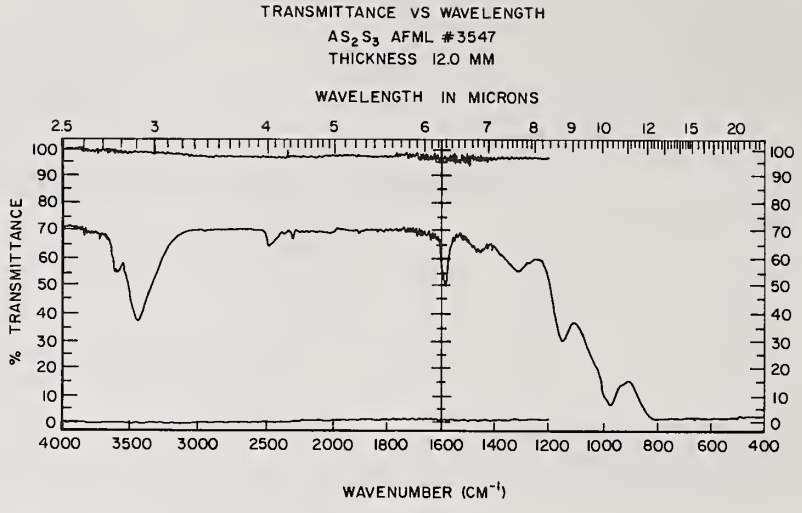

Figure 22. Transmittance versus wavelength for As_2S_3.

References

[1] See for example Hohla, Kristian; Kompa, Karl L. Chapter 12 in Handbook of chemical lasers, R. W. F. Gross; J. F. Bott, ed. New York, NY: John Wiley & Sons; 1976. 667-701.

[2] Fernelius, Nils C.; Dempsey, David V.; Walsh, David A.; O'Quinn, David B.; Knecht, Walter L. Survey of 1.3 μm window materials. Bennett, H. E.; Glass, A. J.; Guenther, A. H.; Newnam, B. E., ed. Proceedings of the twelfth symposium on optical materials for high power lasers; 1980 September 30 - October 1; Boulder, CO. Nat. Bur. Stand. (U.S.) Spec. Publ. 620; 1981 October. 129-143.

[3] Pinnow, D. A.; Rich, T. C. Appl. Opt. 12: 984; 1973.

[4] Hass, M.; Davisson, J. W.; Klein, P. H.; Boyer, L. C. J. Appl. Phys. 45: 3959; 1974.

[5] Wiggens, T. A. Appl. Optics 20: 3481; 1981.

[6] Fernelius, N. C.; Johnston, G. T. Discussion of a theory of analysis of rate calorimetry which includes coating absorption. Glass, A. J.; Guenther, A. H., ed. Proceedings of the 10th annual symposium on optical materials for high power lasers; 1978 September 12-14; Boulder, CO. Nat. Bur. Stand. (U.S.) Spec. Publ. 541; 1978 December. 7-12.

[7] Fernelius, N. C.; Dempsey, D. V.; O'Quinn, D. B. Appl. Surface Sci. 1: 32; 1981; pp. 58-74 in NBS Spec. Publ. 620, Laser induced damage in optical materials: 1980. Edited by H. E. Bennett, A. J. Glass, A. H. Guenther and B. E. Newnam.

[8] Fernelius, N. C. J. Appl. Phys. 52: 6285; 1981 and this volume.

[9] Detrio, John A.; Fernelius, Nils C.; Harris, Richard J.; Walsh, David A. Semiannual Technical Report No. 2, 1981 August. UDR-TR-81-76. 20-22.

[10] Taylor, Raymond L.; Donadio, Robert N. Laser Focus 17(7): 41; 1981 July.

[11] Drexhage, M. G.; Moynihan, C. T.; Saleh, M. Mat. Res. Bull. 15: 213; 1980.

[12] Moynihan, C. T.; Drexhage, M. G.; Bendow, B.; Boulos, M. Saleh; Quinlan, K. P.; Chung, K. H.; Gbogi; E. Mat. Res. Bull. 16: 25; 1981.

Table 1. Summary of 1.319 μm Laser Calorimetry

Material	High Transmission Range in μm	n @ 1.3 μm	$\beta_{slope} \div 10^{-3}cm^{-1}$ @ 1.3 μm
KCl	0.4-15	1.48	
Univ. Utah			0.127
Harshaw			0.183
RAP Rb:KCl			
Hughes			0.268
LiF	0.18?-4.5	1.385	0.133
Harshaw			
NaCl	0.4-13	1.53	0.146
Harshaw single crystal			
CaF_2	0.25-7	1.427	0.176
Harshaw single crystal			
Raytheon			0.201
SiO_2, fused silica	0.2-2.5	1.447	0.190
Suprasil W-1			
T-16 Ultrasil			0.453
T-17 Infrasil			0.489
T-15 Homosil			0.634
T-12 Optosil			0.669
GE 124 (125?)			0.694
T-08 Commercial			0.839
Corning 9740			2.12
Suprasil II			2.92
YLF ($LiYF_4$)	0.22-5	n_e=1.469	0.197
Sanders Assoc.		n_o=1.447	0.199
Al_2O_3, sapphire	0.24-4	n_o=1.7505	
(0001) single crystal			
Premium grade			0.211
Standard grade			0.262
Crystal Systems, Inc.			
MgF_2, single crystal	0.2-6	1.376	
Harshaw			0.307
Optovac			1.10
BaF_2	0.22-9	1.4670	0.335
Optovac			
Q-98 phosphate glass	0.35-2.2	1.60	0.362
Kigre, Inc.			
YAG ($Y_3Al_5O_{12}$)	0.3-4	1.8135	0.655
Litton/Airtron			

Table 1. Summary of 1.319 μm Laser Calorimetry (Concluded)

Material	High Transmission Range in μm	n @ 1.3 μm	$\beta_{slope} \div 10^{-3}cm^{-1}$ @ 1.3 μm
SrF_2, Optovac	0.3-9	1.43	1.00
ZnS Raytheon Multispectral grade	0.4-10	2.289	
Raytran®			1.23
CVD Cleartran®			8.40
Standard Raytran®			25.6
HBL, hafnium fluoride glass Hughes	0.3-6		1.61
Schott IRG-7 Lead silicate glass	0.35-2.8	1.5470	1.67
CORTRAN 9753 $CaO{\cdot}Al_2O_3{\cdot}SiO$ glass	0.6-3.8	1.588	1.90
Schott IRG-9 Lead silicate glass	0.38-2.8	1.4771	2.06
Schott IRG-N6 CaAl silicate glass	0.35-2.6	1.5417	4.65
ZnSe CVD Raytheon	0.65-18	2.44	5.41
MgO	0.4-6	1.7177	
Adolph Meller			6.80
Norton Res. Corp.			8.80
As_2S_3 glass Unique Optical Co.	1-8	2.449	11.9
CdTe II-VI, Inc.	0.9-22	2.78	14.6
CORTRAN 9754 Germinate glass	0.4-4.2	1.644	17.2
Calcium aluminate glass Barr & Stroud			
BS 39B	0.45-4	1.658	220.5
BS 37A	0.4-4	1.649	228.0

Multispectral Chemically Vapor-Deposited ZnS: An Initial Characterization

C. Willingham, C. Klein, and J. Pappis
Research Division, Raytheon Company
Waltham, Massachusetts 02254

ABSTRACT

Standard-grade chemically vapor-deposited (CVD) ZnS has a dark orange, yellow milky appearance and exhibits a substantial amount of scatter in the near infrared, which limits its usefulness at the shorter wavelengths.[1] Recently, we have succeeded in developing a "multispectral" CVD-ZnS material configuration, which is colorless and shows evidence of much improved transmittance throughout the spectral range of interest. In this paper, we report on work that has been carried out in the context of assessing the properties of this material, particularly with regard to (a) Infrared absorption. Thermocouple calorimetry measurements conducted at 1.3, 2.7, and 3.8 μm indicate that multispectral CVD Zns has effective absorption coefficients of 1 x 10^{-3}cm^{-1} or less, thus establishing this material as a credible candidate for chemical-laser window applications. (b) Elastic behavior. Measurements of Young's modulus (87.6 GPa) and Poisson's ratio (0.318) in conjunction with sound-velocity measurements in the longitudinal mode (5.47 km/sec) demonstrate that multispectral CVD ZnS behaves precisely as predicted for a randomly-oriented single-phase polycrystalline aggregate of cubic ZnS. (c) Fracture mechanics. The results of Knoop hardness, flexural strength, and laser-damage experiments will be presented; we will also discuss techniques for improving the fracture toughness.

Key words: chemical vapor deposition; polycrystallinity laser damage tests; multispectral; ZnS.

CIRCUMSTANCES BEYOND THE CONTROL OF THE AUTHORS HAVE PREVENTED THEM FROM SUBMITTING THEIR MANUSCRIPT FOR PUBLICATION IN THIS YEAR'S PROCEEDINGS. WHEN AND IF THE IMPEDIMENTS HAVE BEEN ELIMINATED, THIS PAPER WILL BE PUBLISHED IN A FUTURE PROCEEDINGS. THE AUTHORS AND SYMPOSIUM CO-CHAIRMEN REGRET THAT THIS SITUATION HAS OCCURRED, SINCE THIS CONFERENCE HAS A FIRM POLICY OF REQUIRING THE PUBLICATION OF ALL PRESENTATIONS.

1. C. Klein, B. DiBenedetto, R. Donadio, T. Kohane, and J. Pappis, in Laser-induced damage in optical materials: 1978 (NBS Special Publication 541), p. 86.

In response to a question, Willingham reported that they used a value of 1 x 10^{-3} volume absorption and 1 x 10^{-3} absorption at each surface for this material as an average. At 3.8 μm they have seen half that absorption.

Progress in The Development of Multispectral Glasses Based on The Fluorides of Heavy Metals

M. G. Drexhage, B. Bendow,* O. El-Bayoumi,
R. N. Brown and P. K. Banerjee**
Solid State Sciences Division
Rome Air Development Center
Hanscom AFB, MA 01731

T. Loretz†
Galileo Electro-Optics Corp.
Sturbridge, MA 01741

C. T. Moynihan††
Dept. of Materials Engineering
Rensselaer Polytechnic Institute
Troy, NY 12181

J. J. Shaffer, P. A. Temple, and H. E. Bennett
Michelson Laboratory, Physics Division
Naval Weapons Center, China Lake, CA 93555

Considerable progress has been made recently both in the characterization of existing heavy metal fluoride glasses and in the development of new compositions with extended IR transmission. We here report results of continuing investigations of optical and physical characteristics of fluorozirconate type glasses, including absorption, scattering, and mechanical properties. We also report IR edge measurements of new fluoride glasses based on ThF_4 and BaF_2, which display extended IR transparency and potentially lower minimum absorption compared to fluorozirconates. These developments indicate that heavy metal fluoride glasses are highly promising for a variety of multispectral applications.

Key words: fluoride glasses, multispectral glasses, infrared glasses, infrared materials, infrared absorption

1. Introduction

Multispectral glasses based on the fluorides of heavy metals have attracted considerable attention in recent years as candidate materials for laser windows, IR domes, mid-IR optical

---

*Present address: The BDM Corporation, 1801 Randolph Rd., S.E., Albuquerque, NM 87106.

**IPA Appointee at RADC.

†Research supported by RADC (AFSC) under Contract No. F19628-81-C-0073

††Research supported by RADC (AFSC) under Contract No. F19628-81-K-0010

fibers, low-dispersion optical elements, and laser hosts. For example, the prospective advantages of fluoride glasses for infrared transmission, including ultra-low loss and broad transparency, are illustrated by the projected loss curves in figure 1. The current interest in heavy metal fluoride glasses was sparked by the discovery of fluorozirconate glasses by Lucas, Poulain, and co-workers {1-6}. The glasses generally contain ZrF_4 as the primary constituent, BaF_2 as the secondary constituent, and any of a variety of other metal fluorides as additional constituents. Subsequently, the synthesis of fluorohafnate glasses, in which HfF_4 replaces ZrF_4 as the primary constituent, was reported by Drexhage, Moynihan and co-workers {7,8}. Typical compositions of fluorozirconates and fluorohafnates are indicated in table 1.

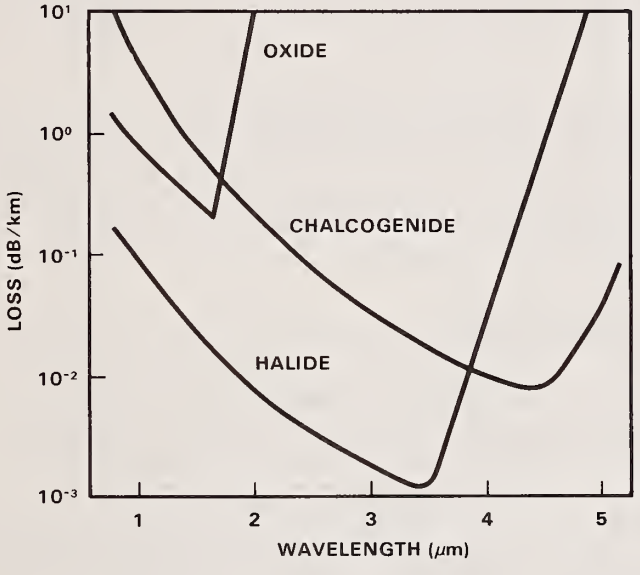

Figure 1. Projected minimum loss of infrared glasses. Long wavelength side of "V" is due to multiphonon absorption and the short-wave side due to Rayleigh scattering. Graph courtesy of T. Manabe, NTT, Japan (private communication).

Currently, a wide body of literature has emerged on these glasses, covering subjects such as processing and preparation {1-7, 9, 10}, IR absorption {8, 11-16}, UV absorption {17} and fluorescence {3, 5, 18}, fundamental vibrational characteristics {19-22}, viscosity {23} and elasticity {24}, dispersive properties {25}, and optical fiber synthesis and properties {23, 26-30}. Additional papers of an overview nature or of broader scope are references {31-36}.

Table 1. Fluoride glass compositions*

	Z	H	B	T	Zn	L	Yb	A
	ZrF_4	HfF_4	BaF_2	ThF_4	ZnF_2	LaF_3	YbF_3	AlF_3
ZBL	60		35			5		
ZBT	58		33	9				
ZBLA	57		36			3		4
HBLA		57	36			3		4
BZnYbT			17.5	30	26.5		26	

*mol%

In addition to fluorozirconate-type glasses, the synthesis of a variety of other heavy metal fluoride glasses has also been reported in the last few years. Examples are glasses reported by Miranday and co-workers {37, 38}, based on combinations of divalent fluorides, such as PbF_2 and/or alkaline earth fluorides, with trivalent metal fluorides such as GaF_3 and FeF_3; and glasses reported by Lucas, Poulain, and co-workers {39-43} which are typically based on ThF_4 and BaF_2, in combination with various divalent fluorides such as ZnF_2 and trivalent fluorides such as rare-earth and transition metal fluorides (a representative composition is indicated in table 1). Some of the latter glasses are of special interest because they appear to possess an extended IR transmission range {39, 42} and increased chemical durability {42} as compared to fluorozirconate-type glasses. However, in contrast to fluorozirconates, only limited reports of fundamental property measurements are available in the literature for these glasses.

In the present work, we report continuing investigations of optical and physical characteristics of fluorozirconate-type glasses. Also, we report selected results of IR absorption edge studies for new fluoride glasses based on ThF_4 and BaF_2, and carry out comparisons between them and fluorozirconates.

2. Studies of Fluorozirconate-type Glasses

Some of the glass properties of interest for IR applications include:

a) refractive index and dispersion
b) scattering
c) infrared absorption edge
d) surface and bulk absorption coefficient at specific laser wavelengths
e) surface finish and stability
f) hardness and strength

We here describe selected results of studies in these areas, conducted on fluorozirconate-type glasses prepared at our laboratories by methods described previously {8,35}.

The IR refractive index of typical fluorozirconate-type glasses, deduced from a combination of visible refractive index data and fundamental IR reflectivity {25} is indicated in figure 2. Depending on composition, the index in the 2-4 μm regime varies from about 1.48 to 1.52, although the accessible range of values may be extended somewhat by selective doping. These relatively low values of index are advantageous for IR transmissive optical elements. Moreover, the glasses possess other potentially desirable attributes, such as low chromatic dispersion and small material dispersion in the IR {25}. The flexibility available for tailoring refractive index is especially important for IR waveguides and gradient-index optics applications.

Total integrated scatter of ZBLA and HBLA was measured at 3.39 μm; data was taken from a number of spots on the samples and averaged to obtain the values indicated in table 2. In certain cases, considerable variations were observed from point to point. The best values measured were in the 10^{-4} range, comparable to those of the lowest scatter IR dome materials such as sapphire. We view these values as very encouraging since they were obtained with a single arbitrary set of samples, without any iterations aimed at optimizing sample quality.

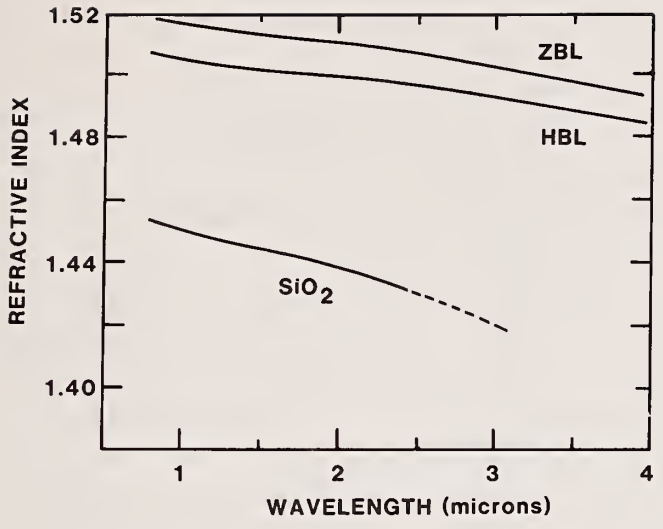

Figure 2. Refractive index vs. wavelength for ZBL, HBL and fused silica (SiO_2)

Table 2. 3.39 μm scattering of fluorozirconates

		BEST	AVERAGE
ZBLA	THIN	3×10^{-4}	1.1×10^{-3}
	THICK	3.2×10^{-3}	6.2×10^{-3}
HBLA	# 107	8×10^{-4}	2.1×10^{-3}
	# 153	1.2×10^{-2}	2.1×10^{-2}

COMPARISON VALUES: $MgF_2 \sim 10^{-2}$, SPINEL PLATES $\sim 10^{-3}$, SPINEL DOMES $\sim 10^{-2}$, SAPPHIRE $\sim 10^{-4}$

Prediction of the ultimate absorption in the ultratransparent regime of glasses requires the assembling of an appropriate data base {44}. Significant progress has been made towards this end, including detailed measurements of the frequency and temperature dependence of IR edge absorption {12,16}, the effects of composition on edge characteristics {13}, reproducibility of edge data {14}, and determination of the relationship between edge behavior and fundamental vibrational characteristics {19-21}. Figure 3 illustrates the type of data currently available, spanning up to five decades in absorption coefficient. Figure 4 typifies the reproductibility of IR edge data which is achievable despite variations in processing conditions. The combined data base from these studies enables extrapolation of existing data to lower absorption levels with a high degree of confidence. An example of such extrapolations will be displayed further on in this paper.

Calorimetric measurements of bulk and/or surface absorption at the DF laser wavelength (3.8 μm) were carried out for representative glasses. Bulk and surface values were deduced for ZBLA using two samples of different length obtained from the same casting. The bulk absorption was $\alpha_B = 8.4 \times 10^{-3}$ cm^{-1} and the surface absorption $\alpha_s = 3 \times 10^{-4}$ per surface. For HBLA, only the total absorption coefficient was measured, yielding $\alpha = 3.97 \times 10^{-3}$ cm^{-1} (assuming the same surface

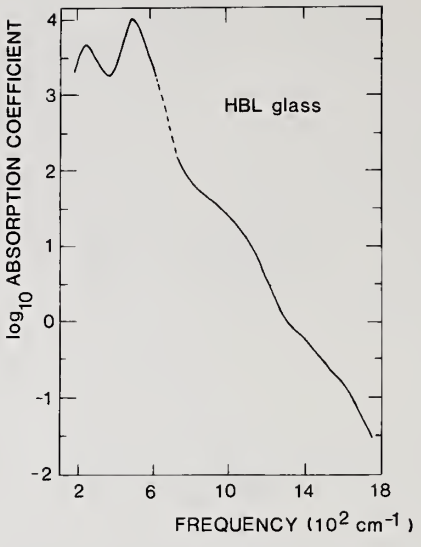

Figure 3. Logarithm of the absorption coefficient vs. frequency for HBL glass. The solid lines are measurements and the dotted lines are extrapolations.

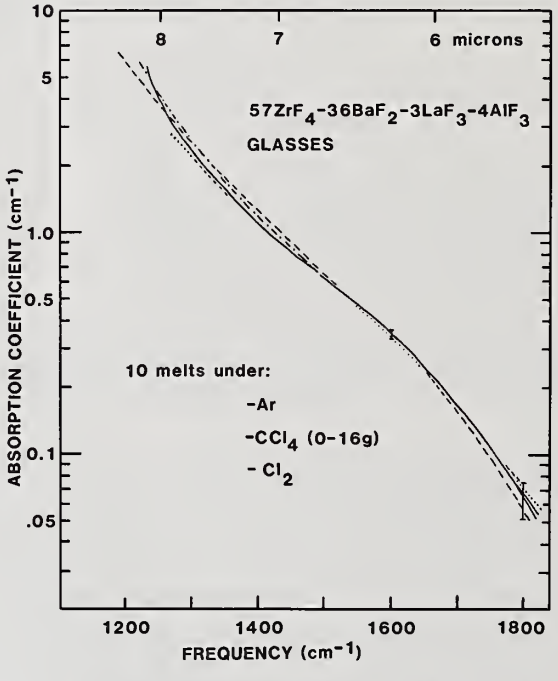

Figure 4. Absorption coefficient vs. frequency for ZBLA glass samples prepared under a variety of atmospheres, including Ar, CCl_4, and Cl_2.

absorption as in ZBLA would imply $\alpha_B = 3.36 \times 10^{-3}$ cm^{-1}). The bulk absorption values are higher than that reported for ZBT glass by Robinson et al. {10}, namely $\alpha = 2 \times 10^{-3}$ cm^{-1}. Despite being orders of magnitude larger than the predicted intrinsic values, the measured values of absorption (especially of surface absorption) are encouraging at this early stage in the development of these glasses. Some related developments which give us optimism are calorimetric measurements, on fluorozirconates containing GdF_3, at visible wavelengths {45} which display $\alpha \sim 1 \times 10^{-4}$ cm^{-1} and a trend toward decreasing absorption at IR wavelengths; and measurements on similar glasses in fiber form by Mitachi et al. {30} which display losses as low as 2-3 $\times 10^{-4}$ cm^{-1} in the vicinity of 3.8

μm. These results demonstrate that low values of absorption in fluoride glasses are achievable, so that refinements in glass processing toward this end are worthy of pursuit. The situation is reminiscent of the early days of silicate fiber optics, when glass absorptions were up in the "stratospheric" 10^{-3} cm^{-1} range. Through extensive and concerted efforts spanning more than a decade, pursued in many laboratories worldwide, the losses in silicate glasses were progressively lowered to near-intrinsic values, $\alpha \sim 2 \times 10^{-7}$ cm^{-1}. Analogous investments in the case of fluoride glasses would be expected to lead to significant decreases in their absorption coefficient as well.

We have prepared optical quality surfaces on fluorozirconate glasses using standard polishing techniques. Use of abrasives such as Al_2O_3, CeO_2, and/or diamond paste in conjunction with both aqueous and nonaqueous slurries such as oils and alcohols, was found to be effective in preparing optically flat surfaces parallel to 30 sec of arc. Precautions were required to avoid any thermal shock, which can induce fracture. We have achieved high quality surface finishes on samples as thin as a tenth of a millimeter, and the surfaces have been observed to remain stable (both visually and in terms of absorptive properties) under laboratory conditions over what is so far time frames of up to a year. One indication of the superior surface quality of the glass is the relatively low surface absorbtance ($\alpha \sim 3 \times 10^{-4}$) measured for ZBLA (see above).

Selected results of mechanical properties measurements are indicated in table 3 and compared with those for other IR materials. The mechanical properties of fluorozirconate-type glasses are seen to be superior to those of chalcogenide glasses and roughly comparable to those of polycrystalline CaF_2. And although silicate glasses are mechanically superior to fluoride glasses they are not, of course, suitable for applications requiring high transparency through the mid-infrared. Depending on the intended application, attempts at toughening fluorozirconate glasses further by ion exchange, compressive cladding, and/or hermetic coating may be worthwhile.

Table 3. Mechanical properties of fluorozirconate-type glasses

MATERIAL	VICKERS HARDNESS (kg/mm^2)	FRACTURE TOUGHNESS (MPa $m^{1/2}$)	FRACTURE STRENGTH (MPa)	THERMAL EXPANSION ($10^{-7}/°C$)
FLUOROZIRCONATE-TYPE	225 - 250	0.25 - 0.27	20	150 - 180
CHALCOGENIDE	100 - 200	0.20	20	240 - 250
FUSED SILICA	~800	0.7 - 0.8	70	5.5
CALCIUM FLUORIDE	175 - 200*	0.35	(40)	~180

*SINGLE CRYSTAL VALUES

3. Extended IR Transparency of Th/Ba Fluoride Glasses

Two interrelated objectives in the search for new fluoride glass compositions are an increase in the IR transparency range and a lowering of the minimum intrinsic absorption coefficient (the value at the bottom of the "V" formed by the IR vibrational edge and the Rayleigh scattering loss curves). Since Rayleigh scattering varies as the inverse fourth power of wavelength, then for constant scattering strength, if the IR edge shifts to longer wavelength, the minimum absorption

coefficient becomes lowered. In practice of course, the scattering strength can depend sensitively on glass composition and structure, and must therefore be determined separately for each particular glass if quantitative predictions of minimum absorption are desired. On the other hand, for rough estimates or comparisons, it may be sufficient to substitute typical values of scattering (such as that of fused silica) for unknown ones.

In this section we examine the potential of alternative fluoride glasses for extending the IR transparency beyond that of fluorozirconates. Specifically, we measured a representative composition denoted BZnYbT (see table 1) of the new glasses based on ThF_4 and BaF_2 {39}. The samples used were obtained courtesy of J. Lucas' group at Univ. de Rennes. The transmission of BZnYbT is illustrated in figure 5, and compared to fluorozirconates and fused silica.

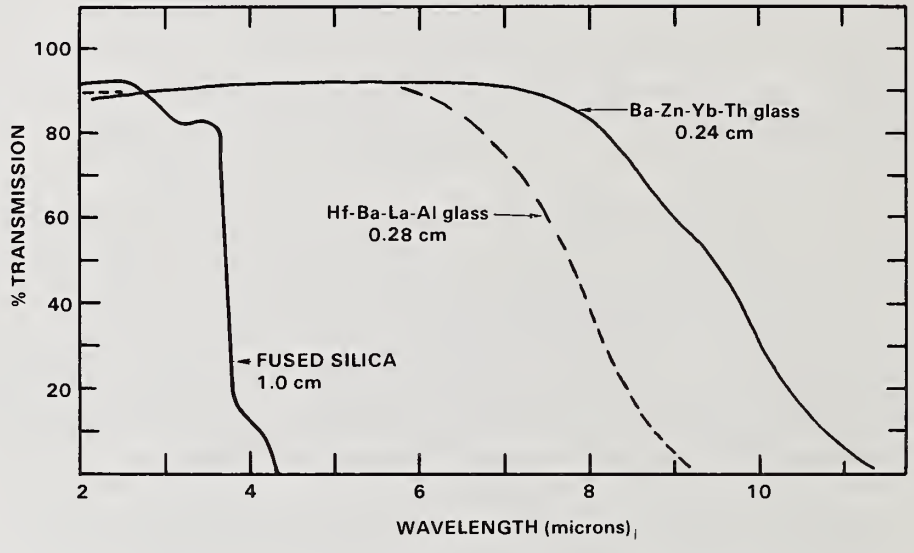

Figure 5. Comparison of transmission vs. wavelength for a fluorozirconate glass (HBLA), a Th/Ba Fluoride glass (BZnYbT), and fused silica.

The results of measurements of the IR absorption edge at several temperatures are indicated in figure 6, and the room temperature spectrum is compared to that of ZBT glass in figure 7. A marked shift to lower frequencies and an increased slope of the IR edge is observed for BZnYbT glass compared to the fluorozirconate glass ZBT. Using measured data as input, we extrapolate the IR edge to lower absorption values by methods described previously {8,12}. Since the Rayleigh scattering strengths are unknown, we employ values for fused silica as a basis for comparison. Note that if the scattering is comparable for both glasses, then for fixed values of frequency BZnYbT possesses, over much of the 3-5 μm range, an absorption which is about two orders of magnitude lower than that of ZBT. Moreover, if its scattering strength is in fact comparable to that of fused silica, then minimum absorptions of less than 10^{-2} dB/km ($\alpha \sim 2 \times 10^{-8}$ cm^{-1}) will be predicted for BZnYbT glass.

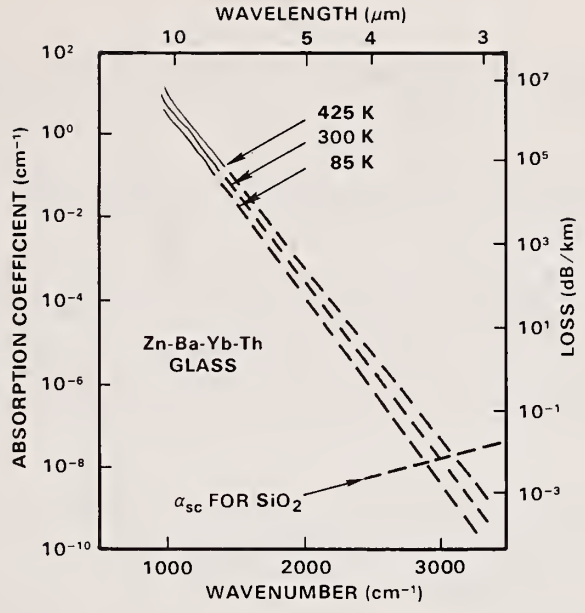

Figure 6. Absorption coefficient vs. wavenumber at selected temperatures for BZnYbT glass. The solid lines are measured, and the broken line continuations are calculated from a multiphonon model. The Rayleigh scattering α_{sc} characteristic of fused silica is indicated for reference purposes.

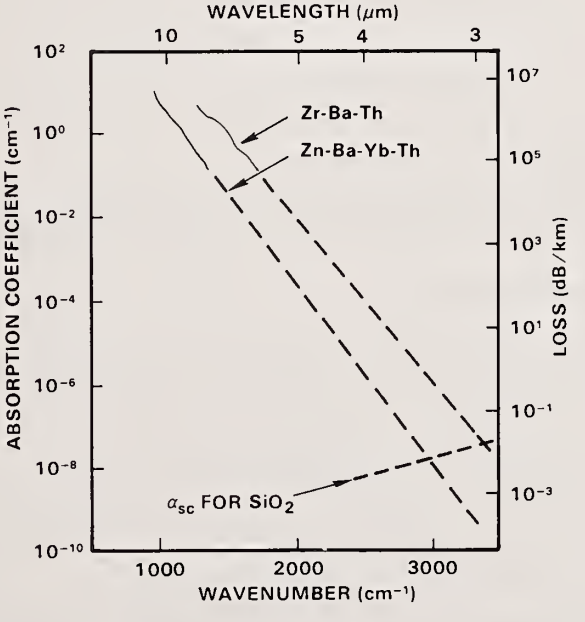

Figure 7. Absorption coefficient vs. wavenumber for ZBT and BZnYbT glasses. Solid lines are measured, and broken line continuations calculated. The Rayleigh scattering of fused silica is indicated for reference purposes.

Glasses containing Yb possess a sharp absorption peak in the vicinity of 1 μm. We have recently synthesized analogous glasses to BZnYbT in which the YbF_3 is replaced entirely by YF_3. Such glasses maintain the advantages of transparency from mid-IR to near-UV inherent to fluorozirconates, while also extending the IR transparency in the manner described above.

4. Concluding Remarks

Substantial progress has been made in determining the fundamental properties of fluorozirconate-type glasses. For the most part, the available data on absorption coefficient, scattering, refractive index, and mechanical strength suggest that these glasses are highly promising candidates for a variety of IR and multispectral applications.

The synthesis of new fluoride glasses with extended IR transparency is a significant development. In addition to their extended transparency range, such glasses offer prospects for lower absorption minima in the mid-IR. The compositional flexibility which has been demonstrated to date will hopefully lead to the synthesis of fluoride glasses with even greater IR transparencies in the future.

The authors gratefully acknowledge the contributions of P. Archibald of NWC, who performed the scattering measurements; J. Mecholsky of Sandia National Laboratories, who performed the hardness and strength measurements; and H. G. Lipson of RADC who performed certain of the IR edge measurements. We also thank Professor J. Lucas and his co-workers at Univ. de Rennes for supplying the samples of BZnYbT glass, and for technical discussions.

5. References

{1} Poulain, M., Chanthanasinh, M., and Lucas, J. New Fluoride Glasses, Mat. Res. Bull. 12, 151-6 (1977).

{2} Poulain, M., and Lucas, J. A New Class of Materials: Fluoride Glasses Made with ZrF_4, Verres Refract. 32, 505-13 (1978).

{3} Lucas, J., Chanthanasinh, M., Poulain, M., Brun, P., and Weber, M. J., Preparation and Optical Properties of Nd Fluorozirconate Glasses, J. Non-Cryst. Solids 27, 273-83 (1978).

{4} Lecoq, A., Poulain, M., and Lucas, J. La Fluorozirconate Glasses, J. Non-Cryst. Solids 34, 101-10 (1979).

{5} Aliaga, N., Fonteneau, G., and Lucas, J. Synthesis and Spectroscopic Study of Mixed Fluoride Glasses Based on Zr, Ba and U, Ann. Chim. Fr. 3, 51-8 (1978).

{6} Matecki, M., Poulain, M., Poulain, M., and Lucas, J. New ZrF_4 Glasses Not Containing a Modifying Element, Mat. Res. Bull. 13, 1039-46 (1978).

{7} Drexhage, M. G., Moynihan, C. T., and Saleh Boulos, M. Infrared Transmitting Glasses Based on HfF_4, Mat. Res. Bull. 15, 213-18 (1980).

{8} Drexhage, M. G., Bendow, B., Lipson, H. G., and Moynihan, C.T. IR Absorption in Highly Transparent Glasses Based on HfF_4, in Laser Induced Damage in Optical Materials, 1980 (USGPO, 1981).

{9} Robinson, M., Pastor, R. C., Turk, R. R., Braunstein, M., and Braunstein, R. IR Transparent Glasses Derived from the Fluorides of Zr, Th, and Ba, Mat. Res. Bull. 15, 735-42 (1980).

{10} Robinson, M., Pastor, R. C., Turk, R. R., Devor, D. P., Braunstein, M., and Braunstein, R. Infrared Transparent Glasses Derived from Hafnium Fluoride, Proc. SPIE 266, 78-83 (1981).

{11} Lipson, H. G., Bendow, B., and Drexhage, M. G. Multiphonon Absorption in IR Glasses Based on ZrF_4 and HfF_4, in Basic Optical Properties of Materials, A. Feldman, Ed. (USGPO, Washington, D.C., 1980), NBS Spec. Pub. #574.

{12} Bendow, B., Drexhage, M. G., and Lipson, H. G. IR Absorption in Highly Transparent Fluorozirconate Glass, J. Appl. Phys. 52, 1460-1 (1981).

{13} Moynihan, C. T., Drexhage, M. G., Bendow, B., Saleh Boulos, M., Quinlan, K. P., Chung, K. H., and Gbogi, E. Composition Dependence of IR Edge Absorption in ZrF_4 and HfF_4 Based Glasses, Mat. Res. Bull. 16, 25 (1981).

{14} Drexhage, M. G., Moynihan, C. T., Bendow, B., Gbogi, E., Chung, K. H. and Boulos, M. Influence of Processing Conditions on IR Edge Absorption in Fluorohafnate and Fluorozirconate Glasses, Mat. Res. Bull 16, 943-7 (1981).

{15} Gbogi, E., Chung, K. H., Moynihan, C. T., and Drexhage, M. G. Surface and Bulk-OH Absorption in ZrF_4 and Hf_4-Based Glasses, J.Am. Ceram. Soc. 64, C51-53 (1981).

{16} Bendow, B., Drexhage, M. G., Lipson, H. G., Banerjee, P. K., Goltman, J., Mitra, S.S., and Moynihan, C.T. Infrared Absorption of Fluorozirconate Glass in the 200-1800 cm^{-1} Frequency Regime, Appl. Opt. 20, 2875-2877 (1981).

{17} Brown, R. N., Bendow, B., Drexhage, M. G., and Moynihan, C.T. UV Absorption Edge Studies of Fluorozirconate and Fluorohafnate Glasses, Appl. Opt. (1981, in press).

{18} Corre, O., Poulain, M., Lucas, J., and Boujalt, H. Analyse par Spectrométrie de Fluorescence X d'eléments Traces dans les Verres au Tétrafluorue de Zirconium, Verres Réfract. 34, 764-70 (1980).

{19} Bendow, B., Drexhage, M. G., Banerjee, P. K., Goltman, J., Mitra, S. S. and Moynihan, C. T. Vibrational Spectra of Fluorohafnate Glass, Sol. State Commun. 37, 485-9 (1981).

{20} Banerjee, P. K., Goltman, J., Mitra, S. S., Bendow, B., Drexhage, M. G., and Moynihan,C.T. Polarized Raman Scattering Studies of Fluorozirconate and Fluorohafnate Glasses, J. de Physique, Suppl. (1982, in press).

{21} Bendow, B., Banerjee, P. K., Drexhage, M. G., Goltman, J., Mitra, S. S., and Moynihan, C. T. Comparative Study of Vibrational Characteristics of Fluorozirconate and Fluorohafnate Glasses, J.Am. Ceram. Soc. (1982, in press).

{22} Almeida, R. M., and Mackenzie, J. D., Vibrational Spectra and Structure of Fluorozirconate Glasses, J. Chem. Phys. 74, 5954-61 (1981).

{23} Drexhage, M. G., Bendow, B., Loretz, T. J., Mansfield, J., and Moynihan, C. T. Preparation of Multicomponent Fluoride Glass Fibers by the Single Crucible Technique, in Technical Digest, 3rd International Conference on Integrated Optics and Optical Fiber Communication, p. 32-3 (Opt. Soc. Am., Washington, D.C., 1981).

{24} Brassington, M. P., Hailing, T., Miller, A. J., and Saunders, G. A. Elastic Constants of a Fluorozirconate Glass, Mats. Res. Bull. 16, 613-21 (1981).

{25} Bendow, B., Brown, R. N., Drexhage, M. G., Loretz, T. J., and Kirk, R. L. Material Dispersion of Fluorozirconate-type Glasses, Appl. Opt. 20, 3688-90 (1981).

{26} Takahashi, S., Shibata, S., Kanamori, T., Mitachi, S. and Manabe, T. New Fluoride Glasses for IR Transmission, in Physics of Fiber Optics, Bendow, B., and Mitra, S. S. eds. (Am. Cer. Soc., Columbus, Ohio, 1981), pp. 74-83.

{27} Ginther, R. J., and Tran, D. C. Fluoride Glasses for IR Transmitting Fibers, in Tech. Digest, op cit, Ref. 23, pp. 32-3.

{28} Mitachi, S. and Manabe, T. Fluoride Glass Fiber for IR Transmission, Jap. Journal Appl. Phys. 19L, 313-4 (1980).

{29} Mitachi, S., Shibata, S., and Manabe, T. Teflon FEP-Clad Fluoride Glass Fiber, Elec. Lett. 17 128-9 (1981).

{30} Mitachi, S., Miyashita, T. and Kanamori, T. Fluoride-Glass-Cladded Optical Fibres for Mid--Infrared Ray Transmission, Elec. Lett. 17, 591-2 (1981).

{31} Drexhage, M. G., Bendow, B. and Moynihan, C. T. IR-Transmitting Fluoride Glasses, Laser Focus 15, 62-68 (1980).

{32} Baldwin, C. M., Almeida, R. M., and Mackenzie, J. D. Halide Glasses, J. Non-Cryst. Solids 43, 309-44 (1981).

{33} Gannon, J. R., Optical Fibre Materials for Operating Wavelengths Longer than 2μm, J. Non-Cryst. Solids 42, 239-46 (1981).

{34} Gannon, J. R., Materials for Mid-Infrared Waveguides, Proc. SPIE 2a66, 62-68 (1981).

{35} Drexhage, M. G., Moynihan, C. T., Saleh, Boulos, M., and Quinlan, K.P. Fluoride Glasses for Visible to Mid-IR Guided Wave Optics, in Physics of Fiber Optics, Bendow, B. and Mitra, S. S., eds. (Am. Ceram. Soc., Columbus, OH, 1981), pp. 57-73.

{36} Bendow, B. and Drexhage, M. Prospective Vitreous Materials for Infrared Fiber Optics, Proc. SPIE 266, 16-21 (1981).

{37} Miranday, J. P., Jacoboni, D. and DePape, R. New Glasses Formed from the Fluorides of Transition Metal Elements, Rev. Chim. Miner. 16, 277-82 (1979).

{38} Miranday, J. P., Jacoboni, D. and DePape, R. New Transition Metal Fluoride Glasses Isolated in the PbF_2-$M_t^{II}F_2$-$M^{III}F_3$ Systems. J. Non-Cryst. Solids 43, 393-401 (1981).

{39} Fonteneau, G., Lahaie, F. and Lucas, J. Une Nouvelle Famille de Verres Fluores Transmetteurs dans L'Infrarouge: Fluorures Vitreaux dans les Systems ThF_4-BaF_2, Mat. Res. Bull. 15, 1143-7 (1980).

{40} Fonteneau, G., Slim, H., Lahaie, F. and Lucas, J. Neauveaux Verres Fluores Transmitteurs dans L'Infrarouge dans les systems LnF_3-BaF_2-ZnF_2, Mat. Res. Bull. 15, 1425-32 (1980).

{41} Lucas, J., Slim, H. and Fonteneau, G. New Fluoride Glasses Based on 4f and 5f Elements, J. Non-Cryst. Solids (1981, in press).

{42} Poulain, M., Poulain, M., and Matecki, M. Verres Fluores a Large Bande de Transmission Optique at a Haute Resistance Chemique, Mats. Res. Bull. 16, 666 (1981).

{43} Matecki, M. Poulain, M., and Poulain, M. Etude des Fluores dans les Quaternaires ZnF_2-ThF_4-AlF_3-MF_2, Mat. Res. Bull. 16, 749-57 (1981).

{44} Bendow, B. Multiphonon Infrared Absorption in the Highly Transparent Frequency Regime of Solids, Solid State Physics 33, 249-316 (1978).

{45} Poignant, H., Le Mellot, J., Bayon, J. F. Fluoride Glasses for Infrared Optical Fibers, Elec. Lett. 17, 295-6 (1981).

{46} Shultz, P. Vapor Deposition Process Capabilities for Optical Waveguide Fabrication, in Physics of Fiber Optics, Bendow, B., and Mitra, S. S., Editors, (Am. Ceram. Soc., Columbus, OH, 1981), pp. 3-7.

The question was raised as to whether the intrinsic absorption of any material has been reached. Bendow replied that in fused silicon fibers the Japanese have reached intrinsic values in the infrared, i.e., 10^{-6} to 10^{-7} cm^{-1} at a wavelength of one micrometer. However, it cost several million dollars. The fluoride glasses are not there yet.

Optical Damage, Nonlinear Transmission, and Doubling Efficiency in $LiIO_3$

E. W. Van Stryland, William E. Williams,
M. J. Soileau, and A. L. Smirl

Center for Applied Quantum Electronics
North Texas State University
Denton, Texas 76203

Laser-induced damage thresholds of single crystal $LiIO_3$ have been studied using picosecond pulses at 1.06 μm and 0.53 μm. These thresholds depend on wavelength, crystal orientation, and on the number of times the sample has been irradiated. In addition, the doubling efficiency at high irradiance levels was observed to be a decreasing function of irradiance beyond a critical value. We present evidence to show that this results from the onset of optical parametric down conversion. In separate nonlinear transmission studies, reversible nonlinear transmission of 1.06 μm light was measured, and in self-diffraction experiments, both reversible and irreversible optically-induced complex index of refraction changes at 0.53 μm were observed.

Key words: $LiIO_3$, laser induced damage, second harmonic generation, transient gratings, nonlinear absorption.

1. Introduction

Is it well known that the large nonlinear coefficient of lithium iodate ($LiIO_3$) makes it an attractive candidate for applications where second harmonic generation is required [1]. Consequently, we have begun a study of the laser-induced damage (LID) thresholds of this material and of the mechanisms that limit its second harmonic conversion efficiency. Here, we report the results of five separate but related experiments in this area. (1) In the first of these (Sec. 2), we measure the laser-induced damage thresholds of single crystal $LiIO_3$ using picosecond pulses at 1.06 μm and 0.53 μm. We find that the LID thresholds vary with wavelength, pulsewidth, crystal orientation, and the number of times that the sample is irradiated. Specifically, we observe that the sample is more easily damaged when green (0.53 μm) light is present and that the damage is initiated by some nonlinear absorption process, which is more efficient at 0.53 μm. The sample also damages more easily with repeated irradiations at both wavelengths. We thus obtain a single shot and a multishot threshold. (2) Next (Sec. 3), we determine the dependence of the second-harmonic conversion efficiency of 1.06 μm radiation to 0.53 μm radiation on incident irradiance. We find that the efficiency initially increases with excitation level to a maximum at approximately 50% and then decreases. This decrease is consistent with one of three mechanisms: (a) any absorption processes of the second harmonic or nonlinear absorption of the fundamental, (b) a nonlinear refractive index change that destroys the exact phase-matching conditions, or (c) the onset of parametric down conversion. In an effort to identify the mechanism limiting the conversion efficiency and to identify the nonlinear mechanism responsible for the onset of damage, we perform three related studies. (3) We first measure (Sec. 4)

the nonlinear transmission of $LiIO_3$ at both 0.53 μm and 1.06 μm (under non-phase-matched conditions). We observe multiphoton absorption of the 1.06 μm radiation (the order appears to be greater than four) at irradiances well above the multishot threshold for damage. No nonlinear absorption at 0.53 μm is resolved up to the multishot damage threshold for green light. The onset of the observed nonlinear absorption of the fundamental occurs at too high an irradiance to account for the observed decrease in the conversion efficiency. (4) Although no nonlinear absorption or index changes are observed at 0.53 μm in the transmission studies just described, both reversible and irreversible changes in the complex refractive index are observed at 0.53 μm by using a more sensitive background-free two-pulse self-diffraction technique (Sec. 5). (5) Finally (Sec. 6), we measure the dependence of the spatial beam profile of the second harmonic on the fundamental irradiance. From the distortion in the 0.53 μm beam profile for large irradiances we conclude that down conversion is responsible for the decrease in conversion efficiency with increasing irradiance.

2. Damage Thresholds

The initial experimental arrangement to be used in damage and conversion efficiency experiments is shown in figure 1. The laser source was a passively mode-locked 1.06 μm Nd:YAG laser that produced Gaussian spatial mode pulses of temporal width externally variable between 40 and 200 psec (FWHM). Details of the experimental apparatus are given in Ref. [2] included in these proceedings. The laser beam traversed the $LiIO_3$ with a uniform beam radius of 440 μm (all spot sizes are quoted as the half width at the e^{-2} point in irradiance). When 0.53 μm light was required, a second doubling crystal (KD*P) was inserted prior to the sample. The collimated 0.53 μm beam had a spatial width of 310 μm in the $LiIO_3$. In this case, residual 1.06 μm light was removed with polarizers and 1.06 μm blocking filters.

The laser-induced damage thresholds (LIDT) for $LiIO_3$ were measured at 1.06 μm and 0.53 μm for various crystal orientations and pulsewidths. Both the single shot or 1 on 1 thresholds (i.e., each site irradiated only once) and multiple shot or N on 1 thresholds (i.e., each site irradiated many times with irradiance levels well below the single-shot damage threshold) were measured. The onset of damage was determined by observing both increased scattering of coaxial HeNe light and by observing other visible sample changes with a long working distance microscope. In $LiIO_3$, both damage signitures occurred simultaneously. The LIDT is defined as that fluence or irradiance which produces visible damage with 50% probability as determined by the method of Porteus et al. [3]. The experimental uncertainties in the LIDT measurements are indicated by the dotted lines in Tables I and II, and they include the relative uncertainty as determined in ref. 3, absolute energy calibration error and the uncertainty in the spot size measurements.

The results of the damage measurements using 1.06 μm light are presented in Table I. The LIDT was measured for 45 psec and 120 psec (FWHM) pulses with a spot size of 0.44 mm. Both the fluence and the corresponding irradiance threshold are shown. The single shot (1 on 1) LIDT fluence for front surface damage to the sample was approximately 1.3 J/cm^2 for both pulsewidths. For a beam radius that is constant throughout the sample, one would expect normally to see rear surface damage at lower fluence levels than front surface damage since the field at the exit surface should be approximately 30% greater than at the front surface for transparent samples. However, in this case (as we shall discuss in Sec. 4), depletion of the beam by nonlinear processes reduced the fluence at the rear surface by as much as a factor of 8 for input irradiance near the LIDT levels. As expected, the surface damage thresholds were independent of crystal orientation (i.e., whether or not the crystal was phasematched).

Because single shot damage first occured on the sample front surface, the single shot bulk damage threshold could not be determined. However, approximately 20% of the shots at a fluence of 1.3 J/cm^2 resulted in bulk damage just below the front surface. From these measurements, we estimate a lower limit for the bulk, single shot, damage threshold to be 1.3 J/cm^2.

Table I also contains the results of the multiple shot or N on 1 measurements for 1.06 μm light for both phase-matched and non-phase-matched conditions. For the non-phase-matched (NPM in Table I) configuration, the $LiIO_3$ crystal was rotated about the laser beam propagation axis to an orientation 90° from the phase-matched orientation. In this configuration, no 0.53 μm light was visible. Each site was irradiated at levels far below the single shot threshold and slowly increased until damage was observed. Multiple shot damage was always initiated in the bulk, and the thresholds were determined to be substantially below the lower limit of 1.3 J/cm^2 found for the 1 on 1 experiments. Maximum lowering of the LIDT was achieved after approximately 50 irradiations at 0.2 J/cm^2. Notice that the N on 1 thresholds are considerably lower for the crystal oriented to produce second harmonic light. The 1.06 μm to 0.53 μm conversion efficiency (see Sec. 3) was of the order of 50% for the input irradiance that produced breakdown. These results suggest that the green light may be responsible for damage under phase-matched conditions. To confirm this suggestion, we measured the multiple-shot LIDT for 0.53 μm radiation. For these measurements, a KD*P second-harmonic crystal was inserted following the Nd:YAG laser, and all residual 1.06 μm light was removed, as described above. Indeed, the results (presented in Table II) indicate that when 0.53 μm radiation is present, it is primarily responsible for initiating damage. Because of the role of the green light in determining the LIDT when the crystal is phase matched, we investigate the dependence of the second harmonic conversion efficiency on irradiance in the next section.

In addition, the lowered threshold for multishot irradiation is indicative of the formation of microscopic defects that eventually absorb enough energy to cause crystal fracture (what we observe as LID). This may be similar to the irreversible absorption changes seen in NaCl at 1.06 μm (Wu *et al.* these proceedings) [4] or to a charge migration or photorefractive effect reported in other materials such as $BaTiO_3$ [5]. We conclude that these defects must be produced by a non linear process since no amount of irradiation at very low intensities causes a lowering of the damage threshold. Also the defects appear to be more efficiently produced by 0.53 μm light as shown by the much lower multishot threshold at this wavelength. To investigate this supposition, we have also monitored the transmission of both 1.06 μm light and 0.53 μm light (no 1.06 μm light present) as a function of the incident irradiance (Sec. 4). Similar multiple shot damage threshold changes have been observed previously at 0.69 μm [6].

3. Doubling Efficiency in $LiIO_3$

In the determination of the damage thresholds at 1.06 μm with the crystal in the angle phase matched orientation, we also monitored both the transmission at 1.06 μm and the harmonic conversion efficiency (i.e. energy at 0.53 μm divided by incident 1.06 μm energy). Figure 2 shows both the transmission and conversion efficiency as a function of input 1.06 μm irradiance for 40 psec (FWHM) pulses. Each data point is the average of 5 laser firings. The five data points at the highest irradiance were taken after damage was observed. The efficiency increases rapidly at low irradiance, reaches a maximum at ~3 GW/cm^2, corresponding to an efficiency of 50%, and then decreases for higher incident irradiance levels (although the second harmonic energy continues to increase slowly). An identical experiment was performed using ~140 psec (FWHM) pulses that reproduced the data of figure 2

up to 3 GW/cm^2 where the sample damaged. Physical mechanisms that produce a theoretical fit to such a turnover in efficiency include nonlinear absorption of the second harmonic, [7,8] nonlinear refractive index changes that result in loss of phase matching at high irradiance levels, [7,8] and parametric down conversion of the 0.53 μm light [9,10]. To distinguish the contributions of these separate mechanisms, we performed three related measurements, to be described below.

4. Nonlinear Transmission Measurements

The transmission of the $LiIO_3$ at 1.06 μm was measured with the sample oriented such that no second harmonic was produced. This data for 45 psec pulses is shown in figure 3 as a plot of the inverse third power of the transmission versus the cube of the incident irradiance. The data is plotted in this manner to investigate whether four photon absorption might explain the results. Neglecting the Gaussian transverse structure of the beam, four photon absorption should yield a straight line on such a graph [2]. Integrals over the Gaussian spatial and temporal profiles tend to make the line curve downward as explained in ref. 2 of these proceedings. The curvature is upward indicating that the nonlinearity is of an order higher than four. We cannot account for the order of the nonlinearity even when the absorption caused by the subsequent photogenerated carriers is included. It is important that we emphasize that the data points are single laser firings and only a few shots were taken because the sample damaged more easily after each shot. The highest irradiance data point was taken first and the irradiance decreased with each subsequent shot. A final data point was taken at an increased irradiance to observe any possible hysteresis; none was observed for this small number of laser firings. Note also that several sites had to be irradiated to obtain the data shown, since many sites damaged on the first shot. All the data shown were obtained at irradiance levels near to or above the multishot damage threshold. (The single shot surface threshold is 27 GW/cm^2). This transmission data was taken with a 1.06 μm spike filter in front of the detectors. The possibility of conversion of the 1.06 μm light to other frequencies is not excluded although no visible light was observed.

The transmission of the $LiIO_3$ was also measured at 0.53 μm for both a phase-matched and non-phase-matched geometry. When great care was taken to eliminate all of the residual 1.06 μm light, no nonlinear transmission of the 0.53 μm light was observed up to the multishot damage threshold. These measurements determine an upper limit for the two-photon absorption coefficient at 0.53 μm of 0.03 cm/GW [11]. We were unable to obtain transmission at irradiances significantly above the multishot threshold as was done with 1.06 μm light, since our source of 0.53 μm radiation was not sufficiently intense. Whenever the crystal was in the phase-matched orientation and any residual 1.06 μm was allowed to strike the sample along with the 0.53 μm light, it was amplified depleting the 0.53 μm beam - a clear indication of parametric down conversion [9].

We also studied the spatial profile of the transmitted beams in the far field at both 0.53 μm and 1.06 μm as a function of incident irradiance at the same wavelength. These measurements were performed in the non-phase matched configuration. In this geometry, we could easily distinguish a half-wave distortion in the beam profile caused by self-focusing or defocusing. For a 0.5 cm-thick sample, this means that we should be able to detect a change in index on the order of 10^{-4}. No detectable distortion was observed up to the multishot damage thresholds.

From these two types of nonlinear transmission measurements, we conclude that any induced change in either the absorption coefficient or index of refraction is far too small to account for the turn over in the diffraction efficiency as displayed in figure 2.

5. Irradiance Dependent Complex Refractive Index Changes

The sensitivity of the nonlinear transmission measurements discussed in the previous section was limited by the large background signal present. That is, we were attempting to measure a very small change in a large signal. In this section, we describe the use of a more sensitive background-free self-diffraction technique to measure both transient and permanent optically-induced changes in the complex index of refraction at 0.53 μm. We emphasize that no such change was observed at this wavelength in the preceeding experiments. In this technique, a single picosecond pulse at 0.53 μm was divided into two parts by a beamsplitter. These two pulses were then recombined so that they were temporally and spatially coincident in the $LiIO_3$ at an angle $\theta = 1.2°$. The interference of these two pump pulses spatially modulates the electric field which may cause a periodic change in the complex index of refraction of the sample. If such an irradiance dependence is present, each pump beam will be self-diffracted by this laser-induced grating into two first orders at $\pm\theta$. One first order for each pump beam will be scattered into the direction of the other pump, and one will be diffracted in a background-free direction (which we label $-\theta$). There is no signal at $-\theta$ unless a grating is produced by the pump pulses.

The self-diffraction efficiencies as a function of irradiance are shown in figure 4 by the crosses. The crystal was oriented so the 0.53 μm beams were incident near the phase-matched condition for down conversion. The irradiances recorded in figure 4 are for one of two equally intense pump beam. Following these measurements, we subsequently blocked one pump beam while continuing to measure the diffraction efficiency of the other pump. The results are the solid dots in figure 4. Clearly, a parmanent component to the grating has been produced that continues to diffract light when the modulation of the intensity has been removed. As expected, the diffraction efficiency of the permanent grating is independent of pump irradiance. This grating was not erased by irradiating with a single beam as occurs with photorefractive materials such as $BaTiO_3$ [5].

In figure 5, we present measurements similar to those of figure 4 except that the crystal has been rotated 78° about the bisector of the angle between the two pump beams, away from the phase-matched orientation. Here the energy in one of the pump beams has been reduced by a factor of six with respect to the other pump. The irradiance quoted in figure 5 is for the strong pump beam. Notice that the measured self-diffraction efficiencies are larger for this orientation and that no permanent grating was observed, even with equally intense pump beams. This dependence of the self-diffracted signal on sample orientation is emphasized in figure 6. Here, the diffraction efficiency is shown as a function of the angle the sample is rotated away from phase-match, as described above.

For this sample thickness (~5 mm) and this grating spacing (~ 25 μm), we are in the Bragg grating regime. That is, the gratings produced here cannot be considered thin, and the measured self-diffracted signal at $-\theta$ violates the Bragg condition. This makes quantitative analysis of the results of figure 4 - figure 6 difficult. Although not all features of this data are understood by the authors at this time, it is clear that we have observed permanent and transient index (or absorption) changes in the sample at 0.53 μm. We emphasize once again that these changes are too small to destroy phase match and account for the saturation and turn down in the diffraction efficiency as shown in figure 2.

6. Phase-Matched Second Harmonic Spatial Profiles

Having shown that laser-induced absorptive and index changes (both at 0.53 μm and 1.06 μm) are small, we suspect that the eventual decrease in the diffraction efficiency with increasing 1.06 μm irradiance is caused by down conversion. In this section, we show that this is indeed so.

In these experiments, we monitored the spatial profile of the second harmonic produced by phase matching the $LiIO_3$ crystal as a function of incident fundamantal irradiance. At low incident 1.06 μm irradiance, the profile at 0.53 μm is a smooth Guassian as shown in figure 7. As the 1.06 μm irradiance is increased past the efficiency maximum (as shown in figure 2), the profile is distorted as shown in figure 8. That is, the second harmonic is skewed to one side. This can be understood by recalling that $LiIO_3$ possesses a large walk-off angle (4°) between the fundamental and second harmonic when phase matched. For a fundamental beam radius of 0.44 mm (half width at the e^{-2} point in irradiance) and a crystal length of 5 mm, the two beams (fundamental and second harmonic) will be separated by 0.33 mm at the exit surface. This separation is of the order of the 1.06 μm beam radius. Down-conversion would be expected to be important only in regions where the fundamental and second harmonic beams overlap and where both irradiances are large, i.e., near the rear of the crystal. This would produce a lopsided spatial distribution of second harmonic light, as shown in figure 8. We would expect then that by rotating the crystal 180° about the incident beam direction that both the walk-off direction and the distortion would be inverted. That this is the case can be seen in figure 9. From these results, we conclude that parametric down conversion is primarily responsible for limiting the harmonic conversion efficiency [9,10].

7. Conclusions

Laser-induced damage thresholds in $LiIO_3$ have been determined for two pulsewidths (45 and 145 psec), for two wavelengths (0.53 and 1.06 μm), and for phase-matched and non-phase-matched crystal orientations. Multiple shot thresholds were lower than single-shot thresholds for all pulsewidths, crystal orientations and wavelengths studied. In addition, the multiple shot LID thresholds were lower at 0.53 μm than at 1.06 μm, indicating that the laser-induced threshold is lowered by cummulative defects produced by absorption of the 0.53 μm radiation. Self-diffraction experiments confirmed the presence of both reversible and irreversible changes in the material refractive index prior to damage, even though no nonlinear absorption was resolvable at 0.53 μm for the maximum irradiances available from our system. Higher order nonlinear absorption was, however, observed for 1.06 μm light. We emphasize that this absorption was only observed for 1.06 μm irradiances well above those available at 0.53 μm. Finally, for picosecond optical pulses, the second harmonic conversion efficiency was shown to be limited by optical parametric down conversion - not by nonlinear absorption, index changes that destroy phase matching, or by laser-induced damage.

The authors gratefully acknowledge the support of the Office of Naval Research, The Robert A. Welch Foundation, and the North Texas State Faculty Research Fund. We also thank T. Nowicki and Interactive Radiation Inc. for supplying the $LiIO_3$ crystals used in these experiments.

8. References

[1] F. R. Nash, J. G. Bergman, G. D. Boyd, and E. H. Turner, J. of Appl. Physics, 40, 5201, 1969.

[2] E. W. Van Stryland, M. A. Woodall, W. E. Williams, and M. J. Soileau, Proceedings of the 1981 Symposium on Laser Induced Damage, Boulder, Colorado, Nov. 1981.

[3] J. O. Porteus, J. L. Jerniga, and W. N. Faith, NBS Spec. Pub. 509, 507 1977).

[4] S.-T. Wu, M. Bass, and J. P. Stone, Proceedings of the 1981 Symposium on Laser Induced Damage, Boulder, Colorado, November 1981.

[5] Jack Feinberg, D. Heiuman, A. R. Tanguay, and R. W. Hellwarth, J. Appl. Phys. 51, 1297 (1980).

[6] G. Nath, H. Mehmanesch, and M. Bsaager, Appl. Phys. Lett. 17, 286 (1970).

[7] Christine A. Schwartz, Jean-Louis Oduar, and Edmond M. Batifol, IEEE J. Quantum Elec. QE-11, 616, 1975.

[8] V. G. Dimitriev and V. A. Konovolov, Sov. J. Quantum Elec. 9, 300, 1979.

[9] J. A. Armstrong, N. Bloembergen, J. Ducuing, and P. S. Pershan, Phys. Rev. 127, 1918 (1962).

[10] R. Stephen Craxton, IEEE, J. Quantum Elec., QE-17, 1771, 1981.

[11] N. M. Bitzurius, V. I. Bredikhin, and V. N. Genkin, Sov. J. Quantum. Elec. 8, 1377, 1978.

Figure Captions

Figure 1. Second harmonic conversion efficiency x's as a function of irradiance, and 1.06 μm transmission •'s as a function of irradiance.

Figure 2. Inverse cube of the transmission versus the cube of the incident 1.06 μm irradiance.

Figure 3. Diffraction efficiency in a light by light scattering experiment versus the irradiance of the of the pump beam as explained in section 5. Crosses indicate data taken with irradiance increasing. Dots indicate one beam blocked and irradiance decreasing.

Figure 4. Diffraction efficiency in a light by light scattering experiment versus incident irradiance of the strong pump beam with the crystal rotated 90° about the beam axis from the arrangement used to obtain the data of figure 4.

Figure 5. Diffraction efficiency versus the angle about the beam direction as described in section 5. Both pump beams were equally intense for this measurement.

Figure 6. Two-dimensional spatial beam profile of the second harmonic produced in $LiIO_3$ at low irradiance.

Figure 7. Two-dimensional spatial beam profile of the second harmonic produced in $LiIO_3$ at high irradiance.

Figure 8. Two-dimensional spatial beam profile of the second harmonic produced in $LiIO_3$ at high irradiance. The crystal has been rotated 180° about the beam axis from the position used in figure 8 as described in section 6.

TABLE I

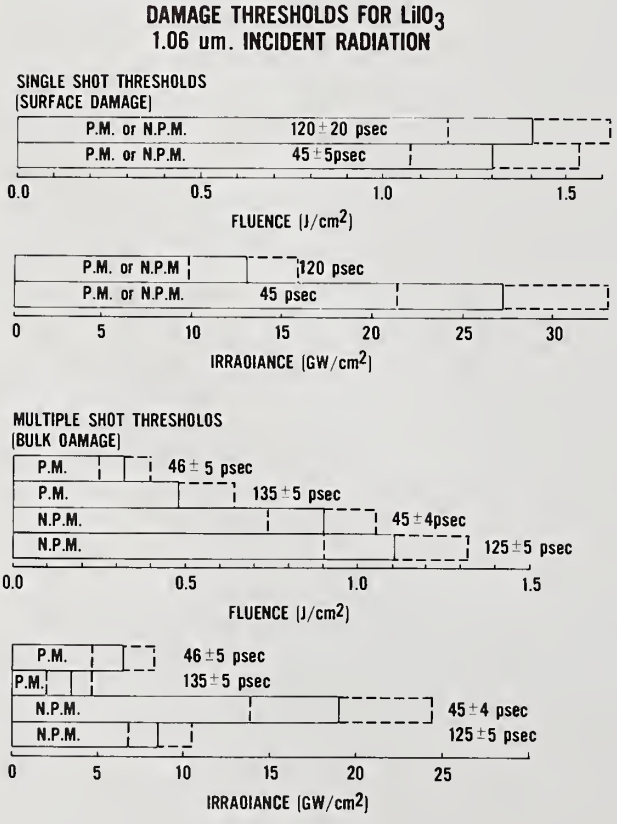

TABLE II

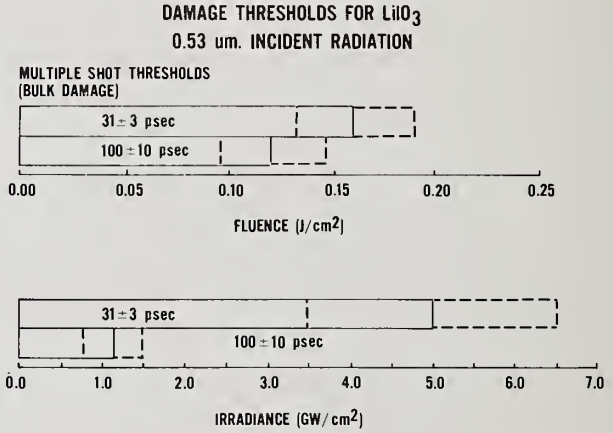

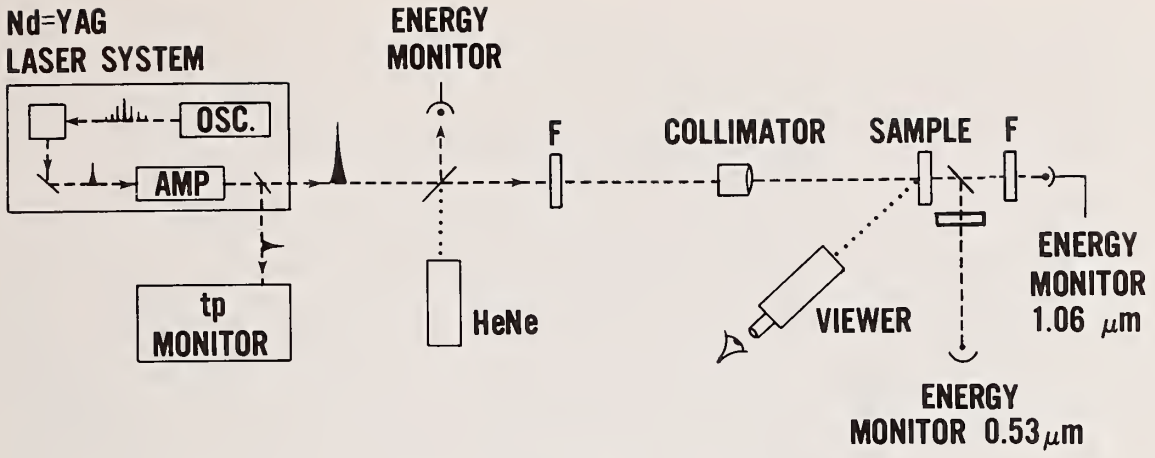

Figure 1

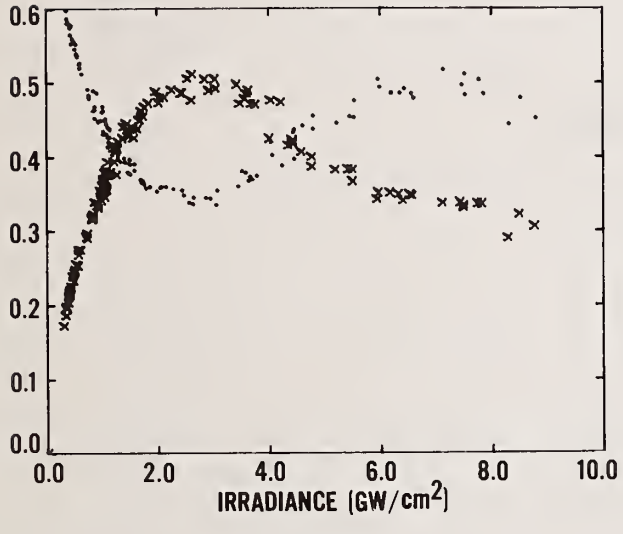

Figure 2

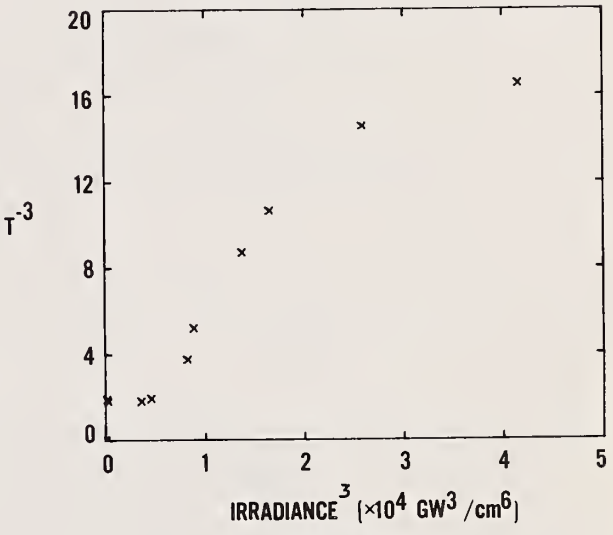

Figure 3

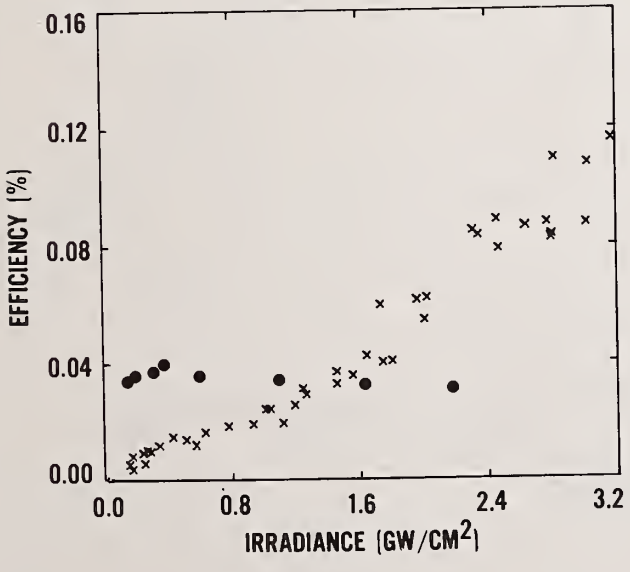

Figure 4

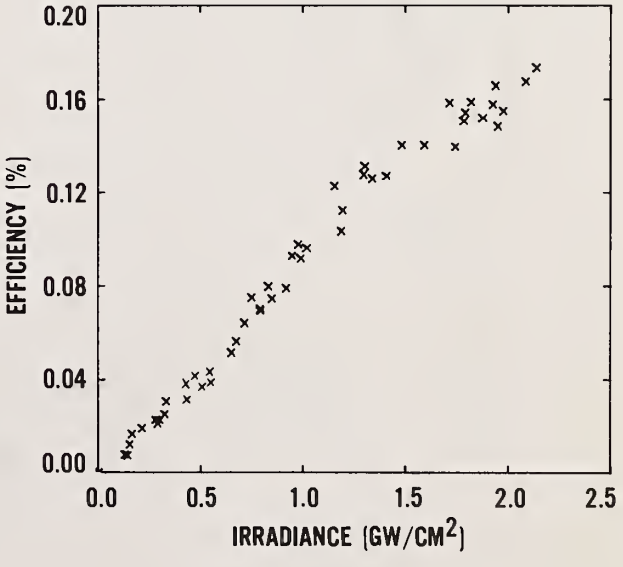

Figure 5

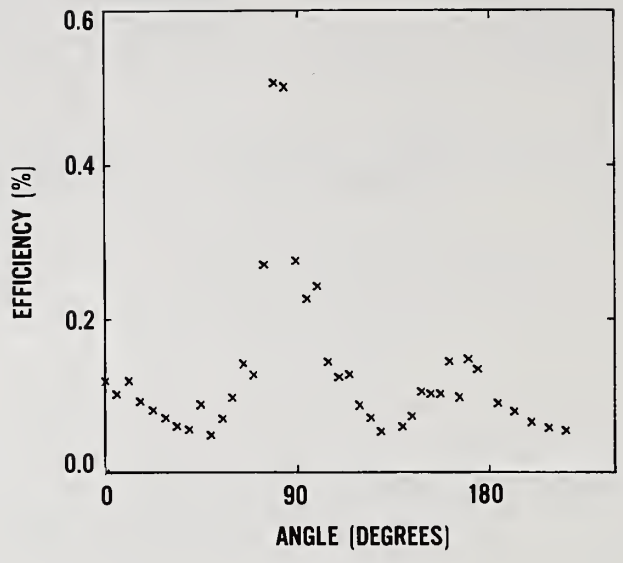

Figure 6

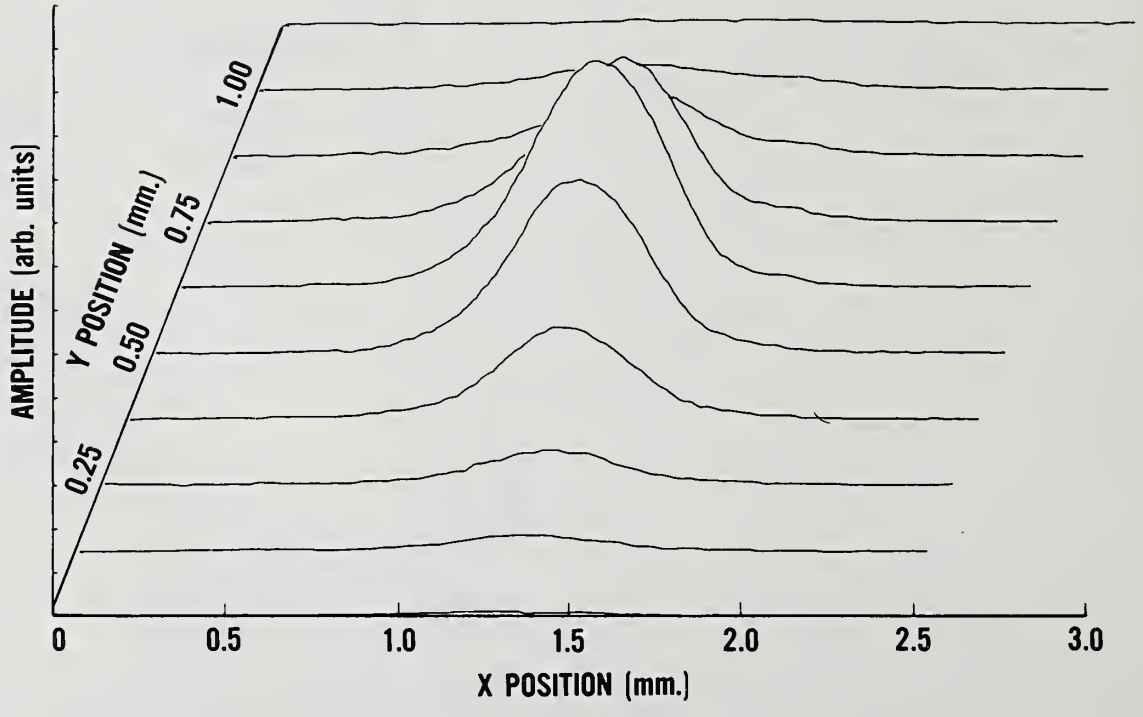

Figure 7

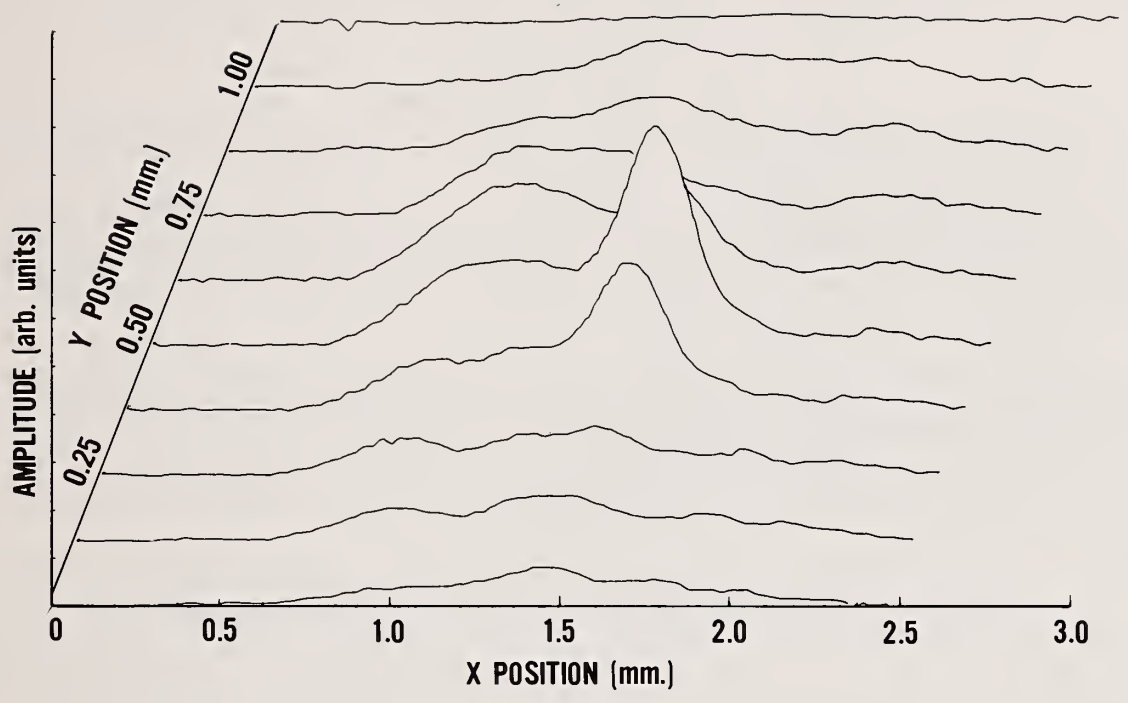

Figure 8

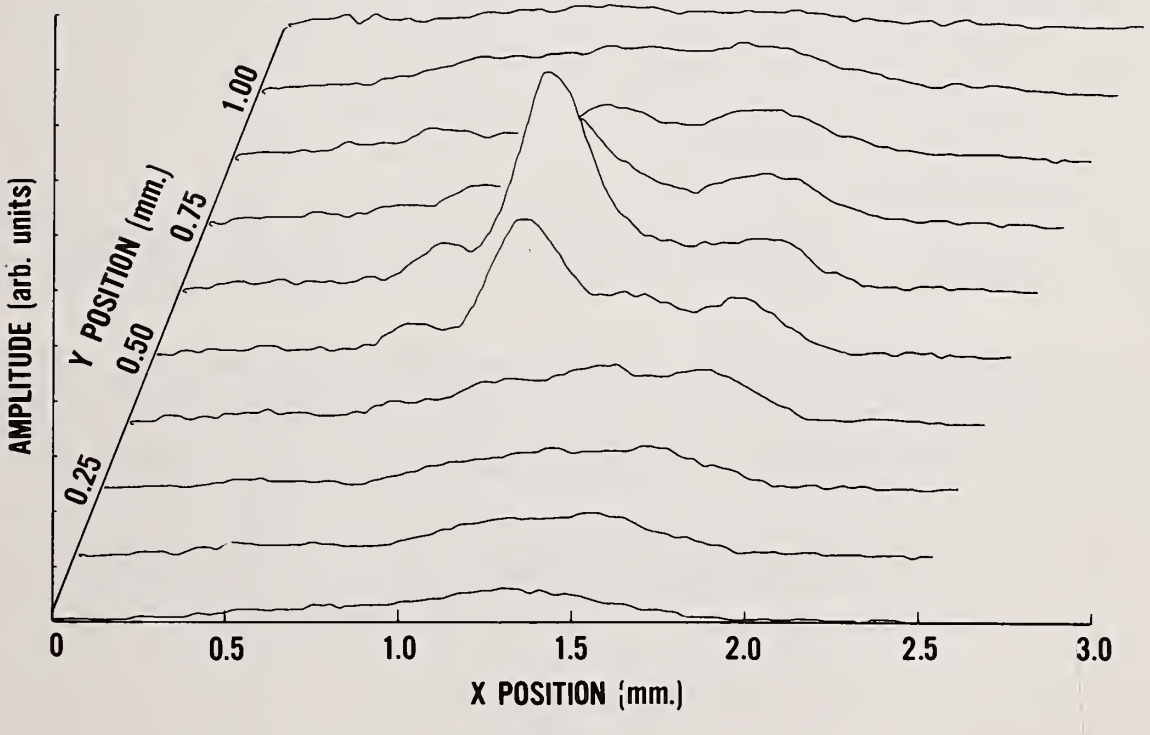

Figure 9

STUDIES OF LASER-PRODUCED DAMAGE TO TRANSPARENT OPTICAL MATERIAL IN THE UV REGION AND IN CROSSED UV-IR BEAMS

B. G. Gorshkov, A. S. Epifanov, A. A. Manenkov, and A. A. Panov

Lebedev Physical Institute of the USSR Academy of Sciences, Moscow, USSR

The values of the damage thresholds of some alkali halide crystals, sapphire and fused quartz at λ = 0.266 μm are presented.

The role of electron avalanche in the damage of real wide-gap dielectrics in the UV region is discussed.

Some peculiarities of the interaction of intense UV radiation with dielectrics (nonlinear absorption, photoionization of impurities, self-focusing and others) are considered.

Experiments on laser damage induced by two synchronous, crossed laser beams with different frequencies (λ_1 = 1.06 μm and λ_2 = 0.266 μm) are described. This method makes it possible to establish the influence of "seeding" electrons on the development of laser-produced damage, as well as to determine if the damage mechanisms are similar at different frequencies.

In order to record directly and estimate concentrations of the free carriers excited by UV laser radiation, d.c. photoconductivity experiments have been carried out.

Key words: crossed laser beams; d.c. photoconductivity; electron avalanche; frequency dependence of damage thresholds; "seeding" electrons; UV laser-produced damage.

1. Introduction

So far, a fairly complete theory of laser-produced damage of transparent dielectrics due to impact ionization (electron avalanche) has been developed. This theory describes the process over a wide frequency range, from DC to the UV region [1-3]. The role of electron avalanche in the damage of real optical materials (especially alkali-halides) has been experimentally investigated in detail [4-5] at wavelengths from 10.6 μm to 0.53 μm. For shorter wavelengths, particularly in the UV region, there have been only limited investigations of laser-produced damage, and the experimental data available are rather scanty [7-8]. The investigation of damage in this region is, however, of great importance, as the theory of impact ionization predicts the existence of essential peculiarities in the frequency dependence of damage thresholds [3]. In this connection, we investigated the damage process in a variety of optical materials at the fourth harmonic wavelength (λ = 0.266 μm) of the neodymium laser.

We have studied damage due to the simultaneous action of two laser beams with λ_2 = 1.06 μm and λ_2 = 0.266 μm, respectively, coincident in the interaction region. This two-beam experiment is of interest for both the investigation of the role of "seeding" electrons in the development of laser-produced damage and the elucidation of the nature of damage mechanisms at different frequencies.

In the first version of the two-beam experiment, one of the crossed beams (in our case, the λ_2 = 0.266 μm beam) having a relatively low intensity, is used for generation of the seeding electrons, and the other for the damage of a sample. In the latter case, when the intensities of both beams are close to damage levels, one can investigate the influence of each beam on the damage threshold and, thus, determine if the damage mechanisms are the same at different frequencies.

We have also carried out d.c. photoconductivity experiments to record directly and estimate concentrations of free carriers excited by UV laser radiation.

2. Damage of wide-gap dielectrics by UV laser radiation at λ = 0.266 μm

A Q-switched YAG:Nd^{3+} laser, operating in the single longitudinal and single transverse mode with output energy of 0.5J was used in our experiments.

A two-step frequency doubling of 1.06 μm radiation using KDP and DKDP nonlinear crystals was used to produce fourth harmonic radiation at λ = 0.266 μm. A spatial filter with a 300 μm pinhole was used to obtain a spatially homogeneous UV output beam. The pulse width of this beam was 8 ns.

We paid particular attention to correct measurements of the laser radiation intensities. The radiation was focused into a sample by a CaF_2 lens with a focal length of 11 mm. The diameter of the lens caustic was measured by a razor blade scanning technique, as described in reference 4, and was found to be 3.0 μm at the 1/e level of the beam axis intensity. The radiation focusing depth in the sample was ~ 1.5 mm.

The materials investigated were NACl, KCl, KBr, CAI, KI, RbCl, CsBr, NaF, LiF, which had been examined earlier at other frequencies [4], as well as other materials widely used in UV optics: Al_2O_3, CaF_2, KDP, and fused silica.

Appearance of damage in a sample was determined by observation of residual destruction in an optical microscope and of plasma formation in the lens focus, and by the scattering of He-Ne probe laser radiation. The latter method appeared to be preferable, as the plasma radiation was strongly masked by an intense, visible luminescence, observed in almost all the crystals, and arising from impurities.

The experiments have shown that considerable variations of the damage threshold are observed in alkali-halide crystals from sample to sample, and in the same sample, from point to point, both in the UV and at lower frequencies [4]. For example, for a hundred NaCl samples, grown under different conditions, the damage thresholds varied in our experiments from 2×10^9 to 4.5×10^{10} W/cm^2. In this case, thermal treatment [4] gave rise to an increase of the optical strength by a factor of 5, indicating the influence of defects on the laser-produced damage to such samples.

The damage thresholds measured are given in table 1, together with the data obtained earlier [4,10] at the wavelengths of λ = 1.06 μm (caustic diameter d_c = 4.6 μm, and pulse width τ = 10 ns) and λ = 0.69 μm (d_c = 3.6 μm, τ = 10 ns). The table presents the data on the most optically resistant samples among those investigated. Note that variations in threshold were not seen in some materials (sapphire, fused quartz), while in others, for example in LiF, they amount to the factor of 25. Investigation of the morphology of residual damage has shown that in the majority of crystals, one finds a series of "point defects" randomly located in the focal region. In some materials, the damage morphology is different. In fused quartz, and in the best samples of LiF and CaF_2, one finds a series of spindle-shaped melts, and in sapphire, long and thin filaments, whose transverse size does not exceed 1 μm.

Analyzing the experimental data, it is necessary to take into consideration some features of the interaction of intense UV radiation with dielectrics:

1. In many crystals, the linear absorption coefficient α is rather large at λ = 0.266 μm (for example, for KCl d = 0.01-0.1 cm^{-1}).

2. The nonlinear absorption coefficients associated with two-photon processes can be considerable. Thus, the two-photon absorption coefficient measured at λ = 0.266 μm [12] amounted to about 1 cm/GW for the majority of alkali-halide crystals.

3. Intrinsic two-photon absorption and photoionization of impurities produce free carriers which serve as an additional absorption source.

4. All the absorption sources mentioned can affect the damage process both directly and indirectly, due to the amplitude and phase distortions of a laser beam. For instance, thermal self-focusing or self-defocusing, due to free carriers [13], can play an important role.

5. The process of laser-produced damage can be affected also by F-centers and other defects arising under an intense UV irradiation. In our experiments, the concentration of F-centers in KCl crystals exceeded 10^{16} cm^{-3} (estimated from light absorption). The linear absorption coefficient at λ = 0.266 μm did not exceed ~ 0.1 cm^{-1} for the samples investigated, and therefore, linear absorption can be neglected if the optical path length to focus in the bulk is minimized. Using the data of [12], one can expect the nonlinear absorption coefficient for NaCl and KCl to be of the order of 0.1 cm^{-1} at the measured damage thresholds.

We have investigated the dependence of the sample transmission on the incident intensity of the UV beam focused into the bulk of KCl and KBr crystals and did not detect nonlinear absorption up to the damage threshold intensities. This indicates that the two-photon absorption coefficient β does not exceed 1 cm/GW.

To determine the influence of the nonlinear effects mentioned on the field transverse distribution in the lens caustic, which is important for measuring the damage threshold intensities, we have carried out the following experiments. The radiation was focused on the output surface of the KCl sample (fig. 1). The second lens formed an image of the output surface on a fluorescent screen. A 300-fold magnified image of the minimum caustic cross section of the focusing lens was thus displayed. The luminescent spot diameter was measured as a function of the power of radiation passing through the sample. The experiment showed that there are no noticeable changes in the lens caustic diameter up to the damage intensities. This, and the above results on the evaluation of nonlinear absorption, shows that the values of the damage threshold intensities, measured without due regard for nonlinear effects, appear to be reasonably correct.

The results obtained enable us to draw the following conclusions:

1. Profound variations of the damage thresholds, damage morphology, and the influence of thermal treatment on the sample optical strength, allow us to conclude that, for the majority of alkali-halide crystals (NaCl, KCl and others) and crystalline quartz, damage threshold are determined by the influence of impurities and defects, even for the best, most resistant samples. This is not surprising, since under the radiation of UV quanta, direct photoionization of the impurities in crystals is a probable process.

2. The filament-like damage in sapphire crystals (Al_2O_3) evidently indicates the presence of self-focusing. This fact, as well as the absence of self-focusing at longer wavelengths, with the use of short focal length lenses [10] indicates either a considerable dispersion of the nonlinear, refractive index n_2, or an important role of thermal self-focusing in the UV region. Direct experiments on the investigation of the dispersion of n_2 are not found in the literature. Thus, the question of the role of Kerr-type self-focusing is open. The thermal self-focusing, due to a considerable nonlinear absorption in the UV region, can lead to a strong beam narrowing compared to the linear absorption case, which is known [14] to result in a relatively weak beam compression.

3. The damage threshold of fused quartz at λ = 0.266 μm is lower by a factor of 15 than that at λ = 0.69 μm. This decrease can be explained by the avalanche ionization theory [3], since the condition $h\Omega/I>0.5$ apparently holds for the UV quanta.

We have investigated the temperature dependence of the fused quartz damage threshold and established that, in the range from 300° to 700°K, the threshold intensity at λ = 0.266 μm decreases from 40 to 23 GW/cm^2. Such a behavior is in qualitative agreement with that predicted by the theory of avalanche ionization [2,3].

4. For LiF and CaF_2, which have been the widest band gaps among the crystals investigated, the damage thresholds at λ = 0.266 μm are close to those measured at 1.06 μm and 0.069 μm. Such a frequency independence of threshold as well as a rather high optical resistance of the best samples of these crystals, could be explained by the avalanche ionization mechanism, since it does not contradict the theory at $h\Omega/I$ = 0.3 to 0.4 [3]. However, investigation of the temperature dependence of the damage threshold, which, along with the frequency dependence, is a criterion of the mechanism [2], indicated that, with the temperature increasing from 300° to 700°K, only a slight decrease of the optical strength is observed (by 20%); whereas, according to the avalanche ionization theory, a two-fold reduction of the threshold is expected. This could be due to a shortage of seeding electrons [15].

The experimental results presented show that the best materials for high-power UV optics are LiF and CaF_2 crystals. It should be borne in mind, however, impurities and defects in these crystals may considerably decrease the threshold of laser-oroduced damage. As for sapphire and fused quartz, which are frequently used in the UV optics, even the purest samples of these materials have noticeably lower damage thresholds.

3. Photoconductivity measurements with UV irradiation

To investigate photoconductivity, we used samples of alkali-halide crystals with natural cleavages and typical dimensions of 3x3x20 mm^3. Thin platinum plates 2x8 mm^2 in size were employed as electrodes. The platinum work function exceeds the energy of the YAG:Nd^{3+}-laser fourth harmonic quantum and, therefore, the use of platinum is required to avoid stray effects in the study of dielectric photoconductivity at high radiation frequencies. The absence of stray effects due to electrode illumination was demonstrated in an experiment in which a scattering plate was placed in the path of the laser beam, and no signal amplification was observed when the scattered radiation reached the electrode. To avoid surface photoconductivity contributions, the sample surfaces were placed outside the electric field. A diagram of the electric part of experimental setup is shown in figure 2. A high-voltage generator G produces, simultaneously with the ignition of the laser flashlamps, an electric pulse of amplitude up to 12 KV and 2 ms duration. The voltage on capacitor C_o reaches its maximum at the moment of the giant pulse laser generation. This is attained by adjusting the values of resistance, R_1 and R_o, and capacitance C_o.

A sample photoconductivity signal extracted from resistor R_L arrives at the oscilloscope with the input capacitance C_{in} and input resistance R_{in}. Hence, $R_L \ll R_{in}$ and $R_L \cdot C_{in} \gg t_L$, where t_L is the laser pulse duration (in dielectrics, the recombination time $\tau_r < t_L$). The signal has a short rise time and exponential decay time $R_L \cdot C_{in}$. The signal amplitude is given by

$$U = \frac{V \ t_L}{R \ C_{in}} \tag{1}$$

where R is the sample resistance during the laser pulse, and V is the voltage on the sample.

The conductivity σ is determined by the relationship

$$\sigma = \frac{t}{Ra\ell} \tag{2}$$

where t is the distance between the electrodes, and a and ℓ are the width and length of the electrodes, respectively.

From the known photoconductivity, one can evaluate the concentration of the nonequilibrium carriers

$$N = \frac{\sigma \ m^*}{e^2 \tau_c} \tag{3}$$

where m* is the effective mass of carriers, e is the electron charge, and τ_c is the characteristic time between the electron-photon collisions.

It is easy to show that, in the case of partial irradiation of a sample, the voltage on R_L is determined by the relation

$$U = K \frac{V \ t_L}{R \ C_{in}} \tag{4}$$

where K is the interelectrode filling factor for laser radiation

$$K = \frac{b^2}{at} \tag{5}$$

Here, b^2 is the laser beam cross section.

In the case $R_L C_{in} << t_L$, the photoconductivity signal is similar in shape to the laser pulse, and its amplitude is

$$U = \frac{VR_L}{R} \tag{6}$$

(this formula is, of course, valid at $U << V$).

4. Damage to optical materials in crossed laser beams

As we noted above, important information on the nature of the processes causing laser damage can be provided by the investigation of the material's optical resistance under two synchronous, crossed laser beams with different frequencies. The use of the crossed beams method makes it possible to establish whether there is a sufficient number of initial electrons in the crystal to initiate the process of impact avalanche ionization, as well as to determine if the damage mechanisms are similar at the different frequencies.

In this work, we carried out crossed beams experiments to investigate laser damage in a number of optical materials, under combined irradiation by the fundamental and fourth harmonic beams of a YAG:Nd^{3+} laser (λ_1 = 1.06 μm and λ_2 = 0.266 μm) respectively. The experimental setup is shown in figure 3. Two beams from the YAG:Nd^{3+} laser at the fundamental frequency and the fourth harmonic were spatially coicident in the orthogonal configuration. Beam characteristics have been described in Section 2.

To combine the beams in the lens' focal region, the microscope with axes directed along the two beams were used. Due to the visible luminescence of the samples investigated, under 0.266 μm radiation, the caustic of the lens focusing the radiation at λ_2 was seen through one of the microscopes. The fundamental beam was visualized by means of an electro-optic image converter. The accuracy of the coincidence of the beams corresponded to the optical microscope resolution (~ 1 μm).

The beam power was smoothly varied by changing the pump energy of the laser amplifiers and by an electro-optic attenuator.

Damage to crystals of NaCl, KCl, LiF, CaF_2 and fused silica was investigated. DC photoconductivity measurements, as described in Section 3, were carried out to detect laser-induced generation of nonequilibrium carriers and to evaluate their concentration.

In order for laser damage to occur, there must be a sufficient number of seeding electrons in the sample to initiate impact avalanche ionization. As is known [1], the damage threshold due to avalanche ionization does not significantly depend on the electron initial concentration n_0, if $n_0V > 1$, where V is the volume of the interaction region. Under this condition, the artificial injection of excessive carriers, which can be produced by photoionization in the crystal under auxiliary UV radiation, does not affect the breakdown threshold. However, with $n_0V < 1$, UV-irradiation of the sample exerts considerable influence on the threshold of damage, if the avalanche ionization is a dominating damage mehcanism.

Based on these conclusions, we investigated laser-produced damage in the most resistant samples of NaCl and CaF_2 by the crossed-beam method. The avalanche mechanism of damage at the wavelength λ_1 = 1.06 μm was previously determined to be possible in the materials [4].

Subjecting these samples to laser radiation with λ_2 = 0.266 μm at an intensity I below the damage threshold, we have detected the d.c. photoconductivity in NaCl which indicates generation of non-equilibrium carriers in concentrations from 10^{13} to 10^{14} cm^{-3} at I = 10^7 to $10^8 W/cm^2$. It was established that such a generation of carriers by UV irradiation does not change the damage threshold observed at λ_1 = 1.06 μm.

As was pointed out, this fact does not contradict the concepts of the avalanche mechanism of breakdown. Assuming that this mechanism is present in the samples investigated, we may conclude that a high-enough, initial concentration of electrons is available in the conduction band of the samples, which is probably formed due to impurity photoionization by the 1.06 μm radiation. This conclusion is evidently valid for damage processes at the shorter wavelengths (λ < 1 μm) also. The question of the presence of a sufficient initial concentration at longer wavelengths remains open to investigation.

The dependence of the damage threshold on the radiation frequency is one of the most important characteristics for elucidating the mechanism of laser-produced damage. It is necessary, however, for an unambiguous interpretation of this dependence, that the damage mechanism be the same at different frequencies. As we noted above, the experiments with crossed beams enable us to resolve this issue. Indeed, if a sample is subjected simultaneously to irradiation with two laser beams with frequencies Ω_1, Ω_2, and intensities I_1, I_2, then, in case of the same damage mechanism at both frequencies, the following relationship should evidently hold

$$I_1/I_{10} + I_2/I_{20} = 1 \qquad (7)$$

where I_{10} and I_{20} are the damage threshold at frequencies Ω_1 and Ω_2, respectively, without the second beam action.

In two-beam experiments, we investigated laser damage in NaCl, CaF_2, LiF crystals and fused quartz under simultaneous irradiation by 1.06 μm and 0.266 μm beams.

In the experiment, we recorded the dependence of the damage threshold at λ_1 = 1.06 μm on the intensity of radiation at the wavelength λ_2 = 0.266 μm.

The results for the NaCl and SiO_2 samples are shown in figure 4. It is seen that, in NaCl (similar results were obtained for LiF and CaF_2), the damage mechanisms at λ_1 and λ_2 are different. The damage threshold at λ_2 is apparently associated with the absorbing inclusions, whereas, at λ_1 there are reasons to assume the electron avalanche breakdown mechanism [4]. Consideration of the morphology of residual damage (which is a spindle-shaped melt at λ_1, and a series of randomly located points at λ_2) leads to the same conclusion.

The most interesting results have been obtained for the fused quartz samples. A marked decrease in the damage threshold at one of the frequencies, in the presence of reduction at the other frequency, shows that the damage mechanism is the same at both frequencies. The frequency and temperature dependences of the damage thresholds for such samples [1,4] indicate that this mechanism is associated with electron avalanche.

Note that some deviation of the observed dependence of I_1 on I_2 from that predicted by relationship eq (7) is easily attributed to the lack of spatial coincidence of the beams. Diffusion of the carriers from the interaction region may also contribute to such a behavior.

REFERENCES

[1] Epifanov, A. S., JETP, 67, 1805 (1974).

[2] Epifanov, A. S., Manenkov, A. A., and Prokhorov, A. M., JETP, 70, 728 (1976).

[3] Gorshkov, B. G., Epifanov, A. S., and Manenkov, A. A., JETP 76, 617 (1979).

[4] Gorshkov, B. G., Danileiko, Yu. K., Epifanov, A. S., Lobachev, V. A., Manenkov, A. A. and Sidorin, A. V., JETP, 72, 1171 (1977).

[5] Manenkov, A. A., NBS Special Publication, 509, pp 455-464, Washington, DC (1977).

[6] Gomelauri, G. V., and Manankov, A. A., Kvantovaya Electronica 6, 45 (1979).

[7] Aleshkevich, V. A., Akhmanov, S. A., Zhdenov, B. V., Kovrigin, A. I., Kuznetsov, V. I., and Sukhorukov, A. P., JTP, 46, 1693 (1976).

[8] Zverev, G. M., Mikhailova, G. N., Pashkov, V. A., and Solov'eva, N. M., JETP, 53, 1849 (1967).

[9] Danileiko, Yu. K., Manenkov, A. A., and Nechitailo, V. S., Kvantovaya Electronika, 1, 604 (1974).

[10] Gorshkov, B. G., Dissertation, Lebedev Physics Institute, (unpublished) (1977).

[11] Fridkin, V. M., Popov, B. N., and Verknovskaya, K. A., FTT, 20, 1263 (1978).

[12] Liu, P., Smith, W. Lee, Lotem, H., Bechtel, J. H., and Bloembergen, N., Phys. Rev. B17, 4620 (1978).

[13] Danileiko, Yu. K., Epifanov, A. S., Lebedeva, T. P., Manenkov, A. A., Milyaev, V. A., and Sidorin, A. V., Proceedings of the USSR Academy of Sciences, 232, 1296 (1977).

[14] Aleshkevich, V. A., Akhmanov, S. A., Zhdanov, B. V., and Sukhorukov, A. M., Kvantovaya Electronika, 2, 1179 (1975).

[15] Gomelauri, G. V., Epifanov, A. S., Manenkov, A. A., and Prokhorov, A. M., JETP 79, 9355 (1980).

Table 1.

LASER DAMAGE THRESHOLDS, Gw/cm^2

MATERIAL / WAVELENGTH, μm	NaCl	KCl	KBr	CsT	KT	RBCl	CsBr	NaF	LiF	SiO_2 CRYST.	SiO_2 (FUSED)	AL_2O_3	CaF_2	KDP	REF.
1.06	120	70	50	15	22	6	27	140	360	230	400	400	200	—	[4,10]
.69	150	80	58	13	10	7	4	140	360	230	600	400	—	—	[4,10]
.266	45	50	50	5.3	42	7	6	18	240	70	40	18	380	290	THIS PAPER

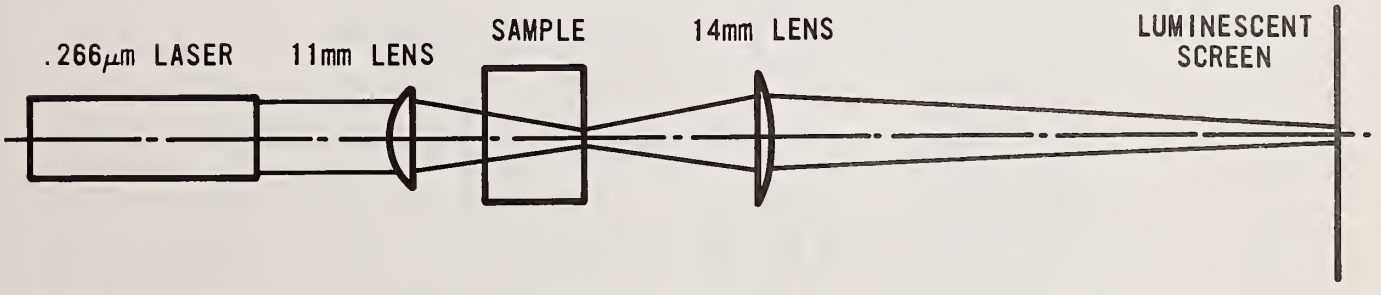

Figure 1. Experimental arrangement for detecting the presence of self-focusing in the laser produced damage process.

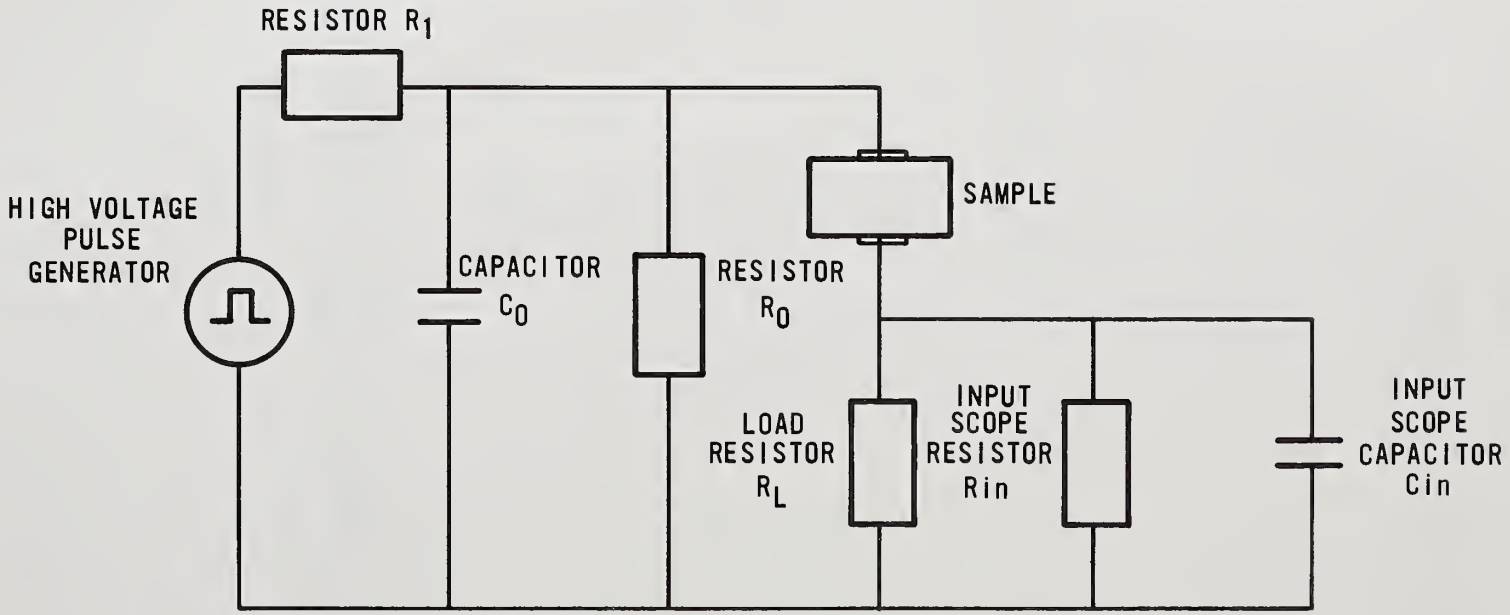

Figure 2. Electric circuit for measuring photoconductivity in dielectrics.

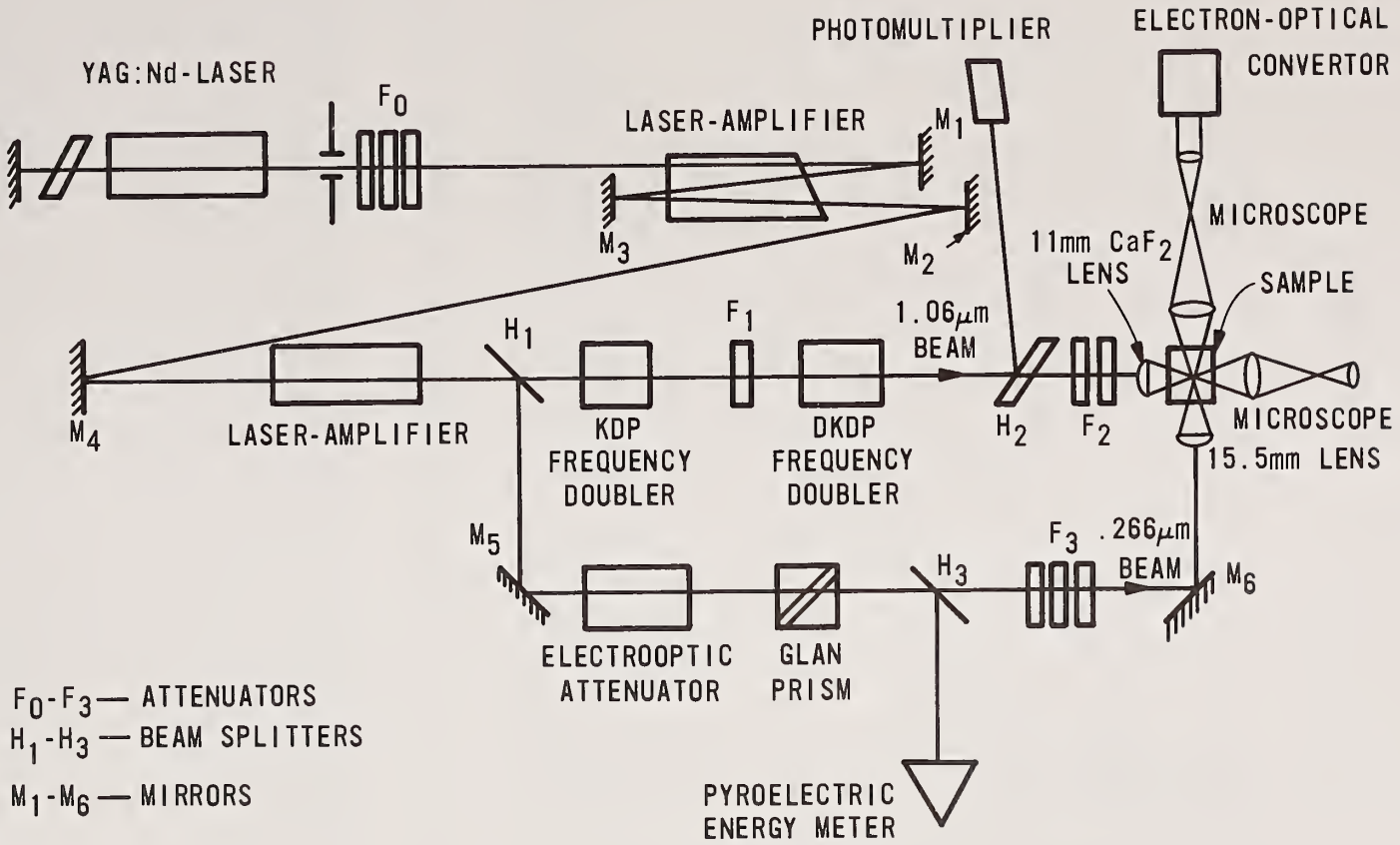

Figure 3. Schematic of apparatus for investigating laser produced damage to dielectrics in two crossed beams with wavelengths 1.06 μm and 0.266 μm.

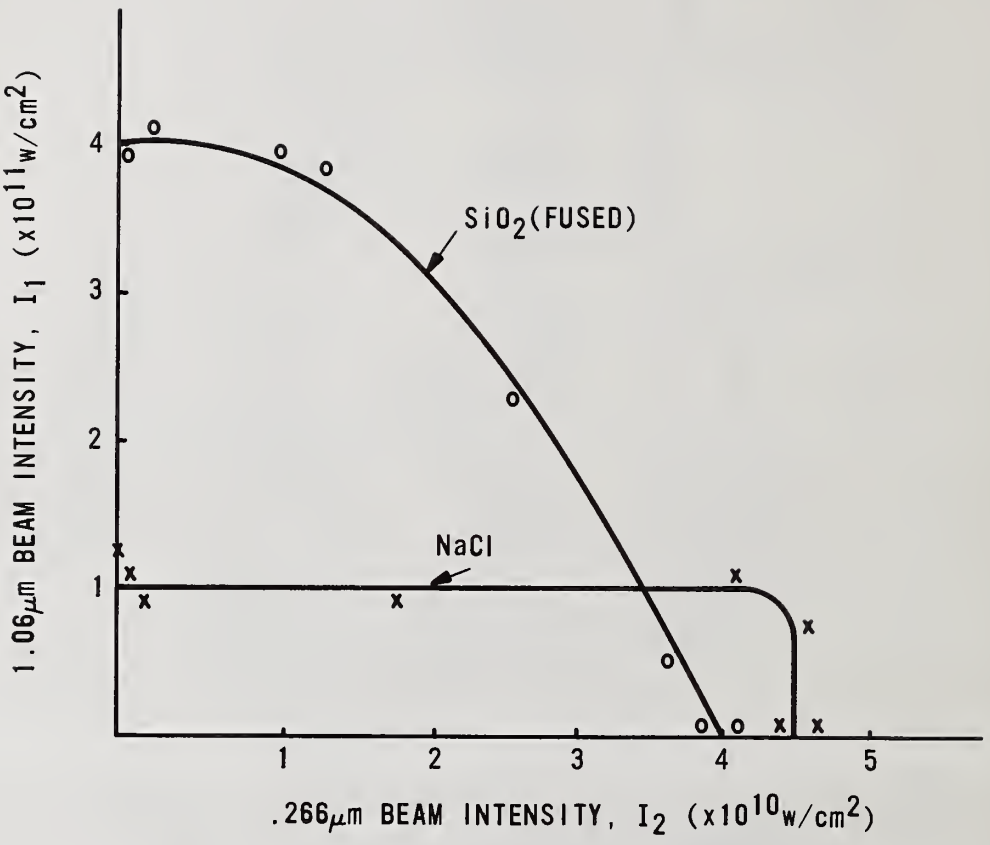

Figure 4. Laser produced damage obtained in a crossed-beam experiment for fused SiO_2 and NaCl crystal: variation damage threshold at 1.06 μm with radiation intensity at 0.266μm.

Laser Damage Measurements at 492 nm Using a Flashlamp-Pumped Dye Laser*

C. D. Marrs, W. N. Faith, J. H. Dancy, and J. O. Porteus

Michelson Laboratory, Physics Division
Naval Weapons Center, China Lake, California 93555

A triaxial flashlamp-pumped dye laser has been developed into a characterizable source for laser damage studies. The temperature of the dye is maintained constant to ±0.2°C via three heat exchangers and flow regulation of the dye, coolant, and refrigerant. Using LD 490 laser dye and maintaining a temperature of 1.1 ± 0.2°C cooler than the temperature of the coolant, the laser produces 0.18 J, 0.5 μsec pulses at 492 nm. The pulse-to-pulse energy stability is ±3%. The spatial profile of the focused beam was measured in orthogonal directions in the plane of damage of the focus lens. The orthogonal profiles were flat-topped Gaussians with $1/e^2$ widths of 270 μm. Laser damage measurements have been performed at 492 nm on high reflectance dielectric mirrors, and no correlation was found between the reflectance or total integrated scatter and the axial fluence at which damage was observed. The damage morphology observed on the dielectric mirrors was dominated by failure of the coatings at defects (selective damage sites). In addition, multithreshold laser damage measurements were performed on polished bulk Mo and on the following diamond-turned metals: bulk Al alloy, bulk Cu, electrodeposited Ag, and electrodeposited Au. Comparisons are made between calculated and experimentally measured slip and melt thresholds.

Key words: damage thresholds; defect damage; diamond-turned mirrors; dielectric mirrors; dye laser; metal mirrors; multithresholds; pulsed laser damage; thin films; visible reflectors.

1. Introduction

With the advent of new pulsed laser sources in the visible and near-ultraviolet, e.g., the HgBr excimer and the free-electron laser, the utility of a single dye laser capable of performing laser damage testing over this spectral region is apparent. In this paper, we describe such a laser and discuss the damage testing performed at 492 nm on high reflectance dielectric mirrors and bare metal mirrors.

2. Experimental Apparatus and Measurements

2.1 Test Specimens

The high reflectance dielectric mirrors were provided by the following commercial vendors and research organizations: Airtron; Coherent, Inc.; Itek Corp.; Optical Coating Laboratories, Inc.; Perkin-Elmer Corp.; and Spectra Physics, Inc. The coatings were comprised of all quarter-wave dielectric stacks. To preclude any possible variations in the coating damage thresholds due to substrate variations in material or roughness, all of the coatings were deposited on 38.6-mm-diameter by 6.4-mm-thick fused silica substrates. The substrates were batch polished at the Naval Weapons Center (NWC) to a roughness of ~ 10 Å rms. Laser damage testing was performed on two coating designs provided by each supplier. Prior to testing, all coatings were characterized via absolute reflectance and total integrated scatter (TIS). The sample within each coating design that possessed the highest reflectance was tested.

The bare metal surfaces that were damage tested are (1) high purity, Al alloy, diamond-turned, (2) electrodeposited Ag on bulk Cu, diamond-turned, (3) electrodeposited Au on bulk Cu, diamond-turned, (4) bulk Cu, diamond-turned, and (5) polished Mo. The 38.6-mm-diameter by 6- to 8-mm-thick metal flats were obtained from the diamond-turning and optical facilities located at NWC. The surfaces were cleaned after preparation with a freon degreaser and ultrasonic rinses in clean acetone. Samples were then blown dry with nitrogen. Just prior to testing, the samples were again blown with nitrogen.

---

*Work supported by the Defense Advanced Research Projects Agency and the Office of Naval Research.

2.2 Dye Laser and Test Facility

The laser source used to perform the damage testing was a Phase-R Corp. Model 2100B dye laser. The laser is a triaxial flashlamp configuration, as shown in figure 1. Modifications of the laser were performed by Phase-R Corp. and NWC to produce a pulse-to-pulse energy stability of ±3%. Figure 1 also shows the dye flow system that was developed to maintain thermal stability of the dye solution and coolant. Three heat exchangers — two which involve either the dye solution or coolant with the refrigerant and one which involves the dye solution and the coolant — are used. The final exchanger is located close to the laser head to provide thermal stability to the dye solution/coolant temperature differential. Regulation of the temperatures and flows of the dye solution, coolant, and refrigerant allows maintenance of a temperature differential of -1.1 ± 0.2°C between the dye solution and coolant; the minus sign denotes that the dye solution is cooler than the coolant. This temperature differential is necessary to maintain the spatial quality of the laser beam. To help facilitate the maintenance of the temperature differential, methanol is used for the dye solvent and coolant. LD 490 laser dye was used to produce radiation in the 480- to 500-nm spectral region. Three Brewster-cut intercavity prisms are employed to produce polarized laser radiation at 492 nm with a line width of ~ 0.3 nm. Under the conditions stated above, the laser produces 0.18 J pulses in 0.5 μsec. The temporal profile of the laser is shown in figure 2.

Figure 3 shows the experimental arrangement used to perform the laser damage testing of the dielectric and metal mirrors. As shown in figure 3, the pulse energy is limited by bulk attenuators. The pulse energy is monitored by a fast photodiode whose output is calibrated to a calorimetric standard detector. The 488-nm laser line from an argon-ion laser is coaxial with the dye laser beam and is used to align the optics in the dye laser. It also allows alignment of the optics train which takes the dye laser beam to the focus lens and onto the test specimen. A focused helium-neon laser beam is used in conjunction with the cross hairs of the observation telescope and the focused argon-ion laser beam to maintain a ±7-μm focus on the sample surface.

In situ beam scans of the focused laser beam are performed by replacing the test specimen with a pinhole/detector combination. Scans are measured in orthogonal directions using a 15-μm pinhole. The spatial profiles of the focused beam are shown in figures 4 and 5. The orthogonal profiles are flat-topped Gaussians, flat to within ±10% over a diameter of ~ 80 μm. The full widths at $1/e^2$ of the spatial profiles are 270 μm.

Damage profiles were measured by the same single-pulse-per-site (1-on-1) multithreshold techniques described in previous work [1-3][1]. Light emission, selective damage (dielectric mirrors), and pit formation (metals) are observed on-line, while other damage features are subsequently identified using a Nomarski microscope. The thresholds measured on the dielectric mirrors were the lowest energy densities that produced observable damage, i.e., selective damage. All of the damage thresholds presented here correspond to the energy density on-axis of the spatial profile of the focused beam. Throughout the remainder of this paper, this energy density will be referred to as the axial fluence.

3. Results and Discussion

3.1 Dielectric Mirrors

Some examples of uniform coating failure observed on a TiO_2/SiO_2 stack are shown by Nomarski micrographs in figure 6. Here, uniform damage is defined as damage which occurs uniformly over the area of the incident beam, and the spatial distribution of damage is determined by the laser beam intensity. The damage shown in figure 6(a), (b), and (c) represents an axial fluence of 367, 63, and 87 J/cm^2, respectively. Figures 6(b) and (c) are from different halves of the coating sample, thus showing the nonuniformity in the laser damage resistance of the coating. The nonuniformity may be due to variation in individual layer thickness. This order of magnitude of nonuniformity was observed on every set of comparable reflectors.

Though uniform damage was observed on all of the dielectric mirrors, the type of damage that dominated the damage morphology in this study, and thus limits coating performance, occurs at a much lower fluence. The initial or first-observed film damage typically occupies off-axis regions within the focal spot area; this is referred to as selective damage, or damage which is spatially selected by defects or inhomogeneities in the coating. Normarski micrographs of selective damage are shown for an Al_2O_3/Na_3AlF_6 stack in figure 7. Figure 7(a) and (b) represent an axial fluence of 38 and 30 J/cm^2, respectively. Recall that the dimension of the flat-top region of the spatial profile is ~ 80 μm (see figs. 4 and 5) as compared to the ~ 50 μm overall dimension of the damage region seen in figure 7(a). Even though the fluence over ~ 80 μm of the spatial profile is essentially constant, the laser damage occurs at selected sites on the coating with an average spacing and diameter of 9 and 3.5 μm, respectively. This contrasts to the damage shown in figure 7(b), where the average

[1]Numbers in brackets indicate the literature references at the end of the paper.

spacing is 42 μm and the average diameter of the selective damage sites, excluding the crater, is 17 μm. Figures 7(a) and (b) are representative of the variation in the selective damage observed from different areas of a given coating sample at nearly the same axial fluence. The disparity in the spacing and diameter of the selective damage sites suggests a variation in the distribution and possibly the character of the defects or inhomogeneities in the coating. The specific characteristics and causes of the selective damage sites are unknown and beyond the scope of this paper. An investigation of selective damage mechanisms is planned.

Since the damage morphology was dominated by selective damage, the minimum fluence at which selective damage was observed is given as the figure of merit for the coatings tested in this study. A summary of the reflectance, TIS, and laser testing on the dielectric mirrors is shown in table 1, where the coatings are listed in order of decreasing reflectance.

Table 1. Laser tests on dielectric mirrors at 492 nm

Sample	Reflectance	TIS	Minimum axial fluence for selective damage, J/cm^2
1	0.9981	3.09×10^{-4}[a]	34.8
2	0.9972	9.59×10^{-3}	37.3
3	0.9971	8.65×10^{-4}	29.7
4	0.9970	1.80×10^{-3}	150.1
5	0.9964	1.28×10^{-3}	17.2
6	0.9964	6.65×10^{-4}[a]	77.5
7	0.9955	3.11×10^{-4}	14.9
8	0.9955	2.82×10^{-4}	65.9
9	0.9952	5.27×10^{-4}	29.6
10	0.9943	5.27×10^{-4}	192.8
11	0.9942	2.79×10^{-4}	71.7
12	0.9920	1.55×10^{-3}	58.5

[a]TIS measurements indicated for samples 1 and 6 were made on companion samples whose reflectances were 0.9979 and 0.9963, respectively.

Examination of the data in table 1 shows that all the mirrors possessed a 99+ reflectance, varying by 0.61% from high to low; however, the selective damage minimum varied from 14.9 to 192.8 J/cm^2, a factor of 12.9. Table 1 also shows a variation of 34.4 for the TIS. No correlation between the optical characteristics, reflectance and TIS, and the fluence producing damage was found for these tests. This was the general observation of Foltyn and Newnam in their testing of ultraviolet coatings [4]. They also found that failure at selected sites on the coating dominated the damage morphology of the ultraviolet coatings, in agreement with what was found in this study. The subject of selective damage mechanisms merits more intensive research to improve coatings to their intrinsic limit of laser damage resistance.

3.2 Metal Mirrors

Figures 8 through 12 show the damage profiles of the five metals tested. A cursory examination of the profiles shows the same general ordering of thresholds that are observed on profiles generated at infrared wavelengths [1-3]. More specifically, slip is observed first for all the metals, while melting and craters are observed at the highest fluences. Upon comparison of the damage profiles, certain features are apparent. Polished Mo (fig. 12) was found to have a higher slip threshold than any of the diamond-turned metals. Surface disorder introduced by polishing is often greater than the surface disorder introduced by diamond machining [1]. The increased surface disorder is associated with an increase in the number of dislocations, i.e., cold working of the surface. This in turn tends to inhibit slip and thus raise the slip threshold. The damage profile of Au (fig. 10) shows that Au possesses a very low slip threshold compared to the other metals. A possible explanation lies in the model given by Musal [5] for computing the plastic yield threshold (slip).

A brief description of Musal's model will be given here. For a more comprehensive treatment, see ref. [5] and the references therein. The mechanical stresses and strains induced at the surface of a metal under pulsed-laser irradiation are directly related to the transient surface temperature rise caused by the fraction of the incident laser radiation that is absorbed [5]. Thermal expansion of the metal, resulting from this temperature rise, causes distortion (strain) in the near-surface region and thus induces stress parallel to the surface. If this induced stress exceeds the yield stress of the metal, irreversible plastic strain, which is manifested as a surface roughness, will occur. Musal has modeled the surface yield temperature

$$\Delta T_y = \frac{(1 - \nu)Y}{\alpha E} \quad , \tag{1}$$

where ν is Poisson's ratio, Y is the yield stress, α is the coefficient of thermal expansion, and E is Young's modulus of the metal, in an idealized case of the stress increasing linearly with strain [5].

Table 2 shows computed ΔT_y values for the five metals, along with other metal properties. Note that Au has the lowest ΔT_y, based on a yield stress of 1000 psi [6]. Musal also modeled the pulse fluence, F_y, at which the plastic yield threshold (slip) is reached as

$$F_y = \frac{5}{4}\left(\frac{2\sqrt{2}}{3}\right)^{3/2} \frac{\pi^{\frac{1}{2}}(\kappa\rho C)^{\frac{1}{2}}t^{\frac{1}{2}}}{2(1 - R)} \Delta T_y \quad , \tag{2}$$

where t is the pulse width [5]. This equation and analysis are based on the assumption that 1 - R is equal to the absorptance, a good approximation for a good bare metal surface, and the material properties of the metal are independent of temperature, which may be justified for small temperature changes. In addition, the assumption is made in first order that the laser temporal pulse shape (fig. 2) can be approximated as parabolic. Table 3 compares the measured slip thresholds to the slip threshold calculated from eq (2).

Table 2. Metal properties[a]

Metal	$\alpha \times 10^6$, $°K^{-1}$	ν	E x 10^{-6}, psi	Y x 10^3, psi	$(\kappa\rho C)^{\frac{1}{2}}$, $\frac{w\text{-}s^{\frac{1}{2}}}{cm^2 °K}$	R,[b] @492 nm	ΔT_y, °K	T_m,[c] °K
Al	23.1	0.34	10.0	3	2.40	0.918	10[e]	933
Ag	19.2	0.37	10.5	8[d]	3.15	0.963	25[e]	1234
Au	14.2	0.42	11.2	Nil	2.81	0.378	3.6[f]	1336
Cu	16.7	0.345	17.9	5.2	3.70	0.466	11[e]	1356
Mo	5.0	0.32	45.0	80[d]	1.88	0.578	242[e]	2890

Note:

α - coefficient of thermal expansion
ν - Poisson's ratio
E - Young's modulus
Y - yield stress
κ - thermal conductivity
ρ - density
C - heat capacity
R - reflectance
ΔT_y - surface yield temperature
T_m - melting temperature

[a] After a table in ref. [5], except where noted.
[b] Measured at NWC.
[c] From AIP Handbook.
[d] Marks Std. Handbook for Mechanical Engr. (1967)
[e] Computed using eq (1).
[f] Calculated based on Y ~ 1000 psi [6].

Table 3. Comparison of calculated to measured slip and melt thresholds

Metal	Slip, J/cm²		Melt, J/cm²	
	Calculated	Measured[a]	Calculated	Measured[a]
Al	0.2	3.4	11.7	7.5
Ag	1.53	4.2	51.4	36.7
Au	0.012	0.62	2.9	12.6
Cu	0.057	2.8	4.6	11.6
Mo	0.77	6.4	6.8	24.0

[a] Shown without standard deviations.

Even though the calculated slip threshold does not agree in magnitude with the measured slip threshold, the relative ranking of the thresholds from highest to lowest is intact except for the reverse ordering of Mo and Ag as possessing the highest threshold. Recall that Mo is a polished surface which may cause its slip to be higher than observed on a diamond-machined surface.

A qualitative explanation of the low slip threshold of Au is possible. Au has the lowest yield stress, which is reflected as the lowest surface yield temperature and the highest absorptance (approximated by 1 - R) of all the metals tested. Examination of eq (2) shows that this ordering of values will make the plastic yield threshold a small value for Au. To reiterate, the low slip threshold of Au is possibly a consequence of Au having a low yield stress while at the same time having a high absorptance at 492 nm.

Methods of computing theoretical melt thresholds include an exact solution to the heat flow equation by Sparks and Loh [7] with a temperature-dependent absorptance and finite difference solution [8], which permits greater flexibility in modeling the actual pulse shape and the temperature-dependent material properties. Both methods use temperature-dependent absorptance values, but at 492 nm the temperature dependence of the absorptance, dA/dT, is not known for these metals. Thus, a first-order calculation of the melt thresholds will be performed assuming no temperature-dependent material properties and approximating the laser pulse as a square temporal pulse shape. The solution to the one-dimensional heat flow model under these assumptions is given in refs. [7] and [9]. The fluence required to produce melting is given by

$$F_m = \frac{\pi^{1/2}(\kappa\rho C)^{1/2}t^{1/2}(T_m - T_o)}{2(1 - R)} \qquad (3)$$

where T_m is the melting temperature of the metal and T_o is the initial temperature of the metal [9]. Using the material properties in table 2 and letting T_o = 300°K, table 3 shows the comparison of the measured melt thresholds to the melt thresholds calculated using eq (3). Within the limitations of the calculation, the agreement is as good as can be expected. It is apparent that more precise modeling needs to be performed when some temperature-dependent absorptance values become available in this wavelength region.

4. Conclusions

A dye laser has been described that is a characterizable source for laser damage studies. Laser damage measurements performed at 492 nm on high reflectance dielectric mirrors reveal failure at defect sites (selective damage) as the dominate damage morphology. Values of minimum axial fluence required to produce selective damage were in the range of 14.9 to 192.8 J/cm^2.

Multithreshold measurements at 492 nm were performed on metal mirrors in a spectral region where most metals are no longer good reflectors. Mo exhibited a high slip threshold which is consistent with what has been observed with optically polished surfaces. The slip threshold observed for Au was very low in comparison to the other metals. The explanation proposed is that the low slip threshold is a consequence of Au possessing a very low yield stress and having a high absorptance at 492 nm.

Calculations of the slip and melt thresholds were performed and indicated a need for (1) better modeling techniques for the slip computation and (2) temperature-dependent absorptance values for performing better calculations for the melt thresholds.

5. References

[1] Porteus, J. O.; Decker, D. L.; Grandjean, D. J.; Seitel, S. C.; Faith, W. N. Defect-damage-resistant copper mirrors. Bennett, H. E.; Glass, A. J.; Guenther, A. H.; Newnam, B. E., ed. Proceedings of the 11th annual symposium on optical materials for high power lasers; 1979 October 30-31; Boulder, CO. Nat. Bur. Stand. (U.S.) Spec. Publ. 568; 1980 July. 175-186.

[2] Porteus, J. O.; Decker, D. L.; Jernigan, J. L.; Faith, W. N.; Bass, M. Evaluation of metal mirrors for high power applications by multithreshold damage analysis. IEEE J. Quantum Electron. QE-14; 776-782; 1978.

[3] Porteus, J. O.; Jernigan, J. L.; Faith, W. N. Multithreshold measurement and analysis of pulsed laser damage on optical surfaces. Glass, A. J.; Guenther, A. H., ed. Proceedings of the 9th annual symposium on optical materials for high power lasers; 1977 October 4-6; Boulder, CO. Nat. Bur. Stand. (U.S.) Spec. Publ. 509; 1977 December. 507-515.

[4] Foltyn, S. R.; Newnam, B. E. Multiple-shot laser damage thresholds of ultraviolet reflectors at 248 and 308 nanometers. Bennett, H. E.; Glass, A. J.; Guenther, A. H.; Newnam, B. E., ed. Proceedings of the 12th annual symposium on optical materials for high power lasers; 1980 September 30-October 1; Boulder, CO. Nat. Bur. Stand. (U.S.) Spec. Publ. 620; 1981 October. 265-276.

[5] Musal, H. M., Jr. Electron emission from metal surfaces under pulsed laser irradiation. Proceedings of the international conference on lasers, lasers '80; 1980 December 15-19. 81-91.

[6] Musal, H. M., Jr. Private communication.

[7] Sparks, M.; Loh, E., Jr. Temperature dependence of absorptance in laser damage of metallic mirrors: 1. Melting. J. Opt. Soc. Am. 69; 847-858; 1979.

[8] Gaski, J. D.; Fink, L. C.; Ishimoto, I. Systems improved numerical differencing analyzer. TRW Systems Report 11027-6003-R0-00.

[9] Bennett, H. E. Thermal distortion thresholds for optical trains handling high pulse powers. Glass, A. J.; Guenther; A. H., ed. Proceedings of the 8th annual symposium on optical materials for high power lasers; 1976 July 13-15; Boulder, CO. Nat. Bur. Stand. (U.S.) Spec. Publ. 462; 1976 December. 11-24.

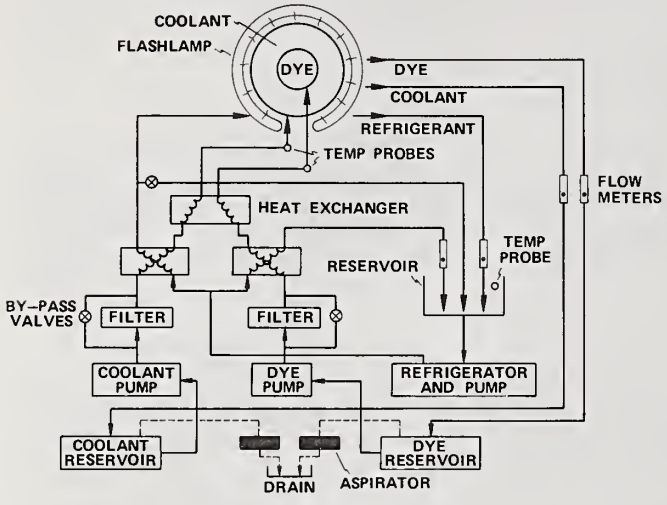

Figure 1. Dye laser flow system. The dye laser is a triaxial flashlamp-pumped configuration using three heat exchangers for temperature control of the dye solution and coolant.

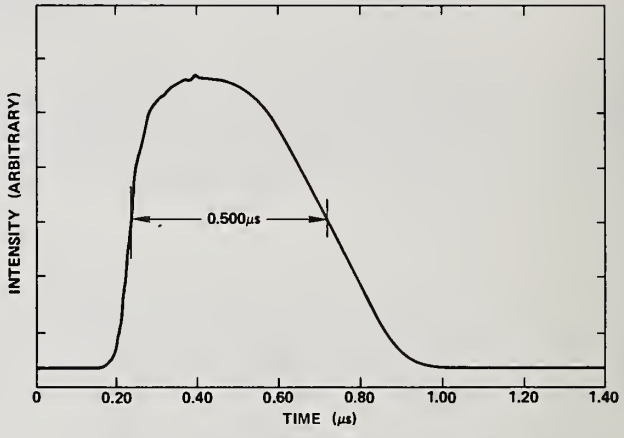

Figure 2. Temporal profile of dye laser.

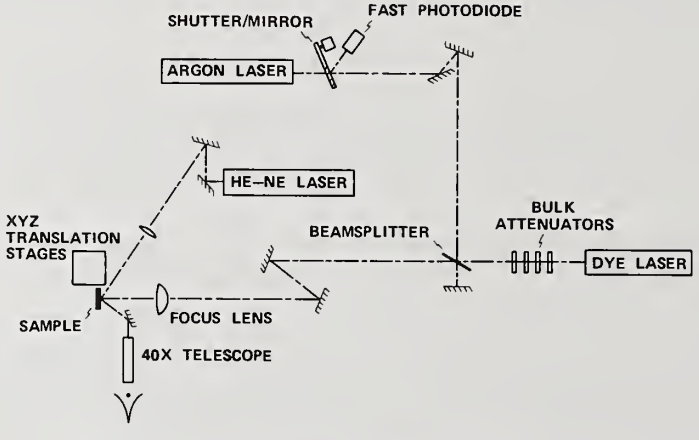

Figure 3. Dye laser damage test facility.

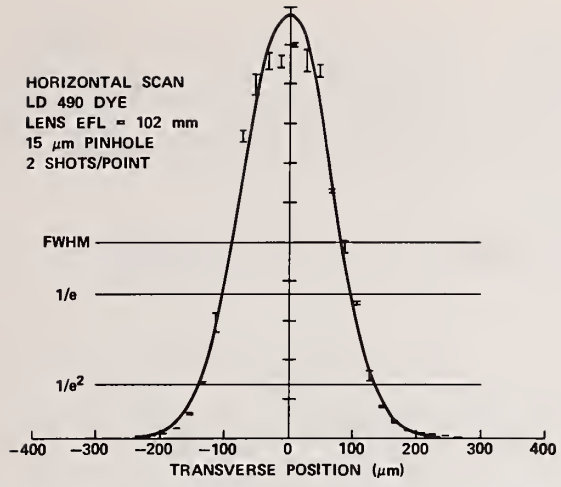

Figure 4. Spatial profile of focused laser beam (horizontal scan). The solid line represents a Gaussian fit at the $1/e^2$ width, 270 μm.

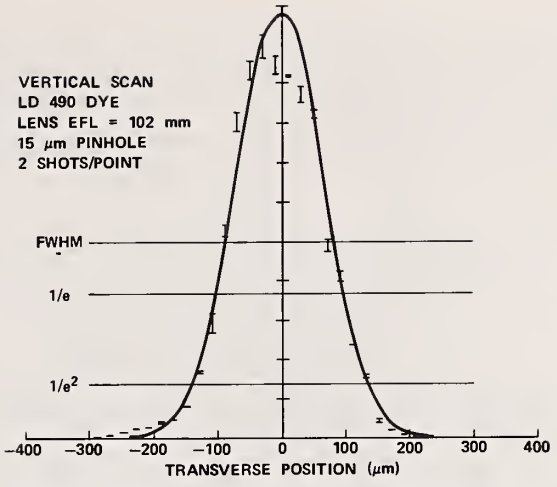

Figure 5. Spatial profile of focused laser beam (vertical scan). The solid line represents a Gaussian fit at the $1/e^2$ width, 270 μm.

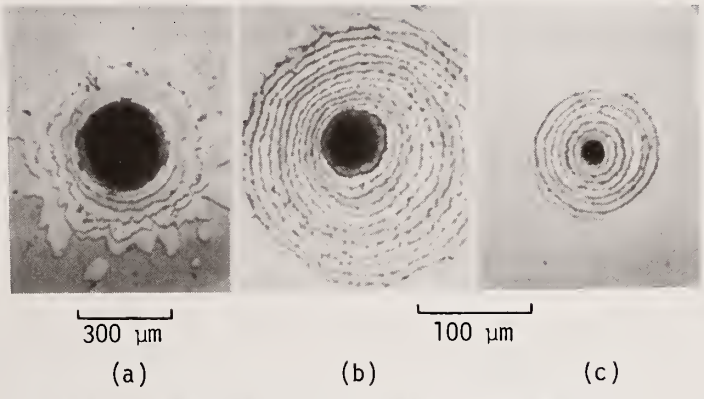

Figure 6. Uniform coating failure observed on a TiO_2/SiO_2 stack: (a) axial fluence of 367 J/cm^2; (b) axial fluence of 63 J/cm^2; (c) axial fluence of 87 J/cm^2.

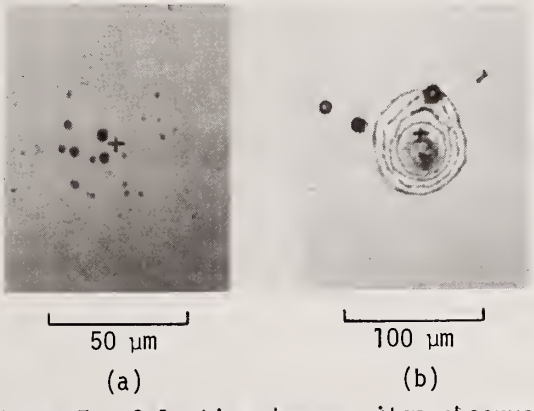

Figure 7. Selective damage sites observed on an Al_2O_3/Na_3AlF_6 stack: (a) axial fluence of 38 J/cm^2; (b) axial fluence of 30 J/cm^2. The cross hairs denote the axis of the spatial profile of the focused beam.

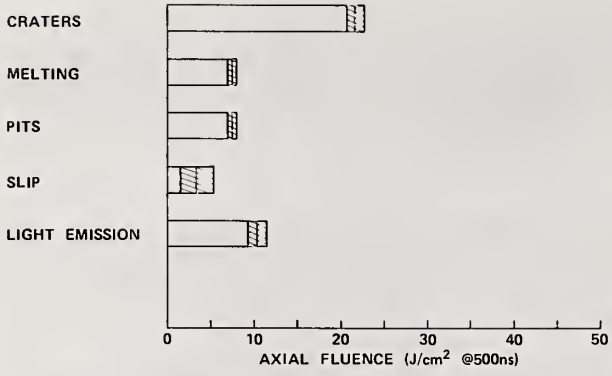

Figure 8. Damage profile of diamond-turned Al alloy at 492 nm.

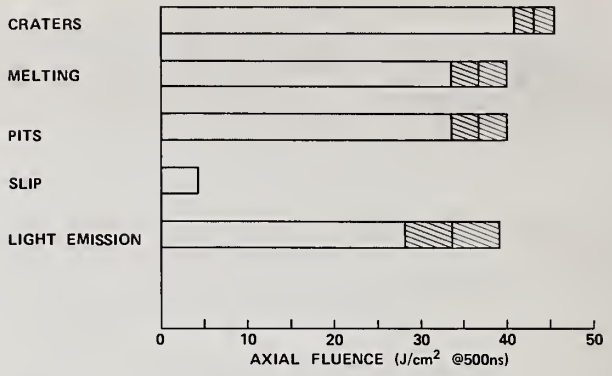

Figure 9. Damage profile of diamond-turned Ag at 492 nm.

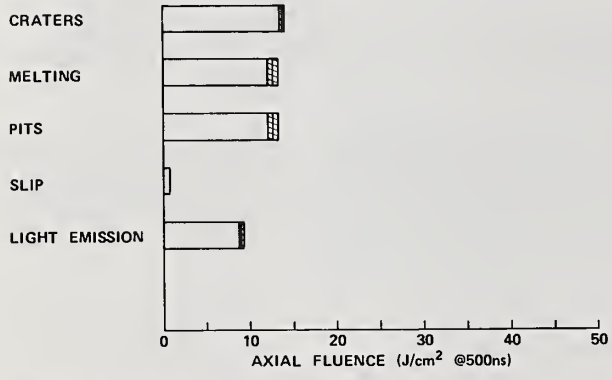

Figure 10. Damage profile of diamond-turned Au at 492 nm.

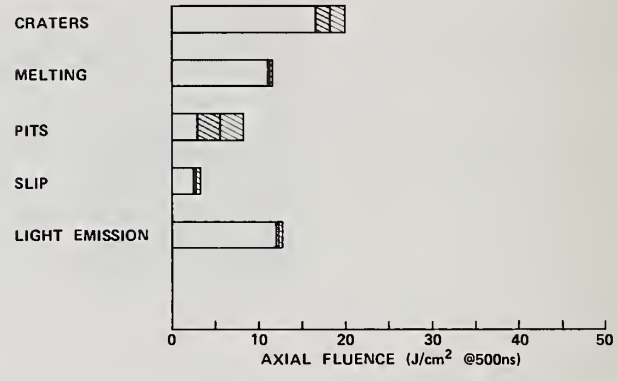

Figure 11. Damage profile of diamond-turned Cu at 492 nm.

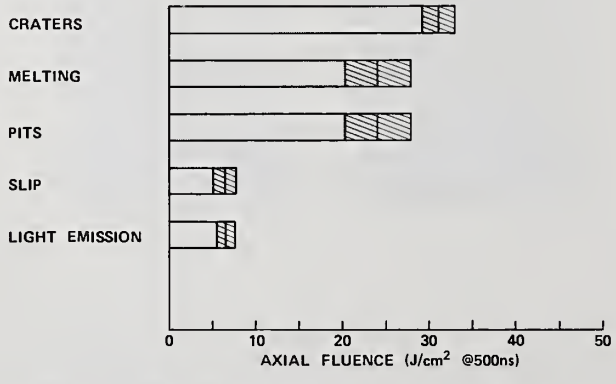

Figure 12. Damage profile of polished Mo at 492 nm.

A question was asked as to whether the authors had made any theoretical predictions as to slip thresholds and whether they agreed with the experimental results. They were also asked whether they had done N on 1 tests or could estimate how low the fluence would have to be before no damage was seen. The authors replied that they had not yet done such measurements but plan to. N on 1 measurements are difficult to do with this system.

Accumulation and Laser Damage in Optical Glasses

E. K. Maldutis, S. K. Balickas, R. K. Kraujalis

Institute of Physics of Academy
of Science of Lithuanian SSR,
Vilnius

Bulk damage of the optical glasses by single and multiple periodic laser pulses of nanosecond duration has been investigated. In the case of multiple irradiation, damage is shown to occur with the energies considerably lower than the damage threshold by a single pulse.

The dependence of the accumulating damage threshold on the number and frequency of the irradiation pulses, the wavelength of laser radiation and the conditions of its focussing into the volume of the sample has been observed.

The bulk damage of glass K-8 induced by a single pulse of radiation with 1.06 μm and 0.53 μm wavelength is shown to be determined by different mechanisms. By employing absorptive-spectral analysis, the degradation of the medium under laser irradiation with intensity ten times lower than damage threshold was observed. The mechanisms of the accumulation and bulk damage are also discussed.

Key words: accumulative damage, glass, optical damage, structural changes.

It is known that optical damage of transparent media limits the power of laser systems. Different mechanisms are proposed for the explanation of laser damage [1-3]. The main mechanism determining bulk damage by the radiation of Q-switched laser is difficult to establish because there exists competition between the mechanisms proposed by different theories. The recently recorded effect of the accumulation of bulk damage induced by Q-switched laser radiation makes it possible to investigate and understand the process of the optical damage in glasses in detail.

Earlier, the change of the coefficient of the scattering of light in the glasses under the prethreshold laser irradiation was observed [4,5]. This was attributed to the existence of microdefects and the overall conclusion that the accumulation of the defects under the prethreshold intensities of radiation causes surface and bulk damage was made. The development of this assumption has taken place in several studies (see, for example, [6]). The degradation of atomic bonds in the surface layers of the glasses induced by multiple periodic laser pulses and some properties of the accumulation were also reported [7,8].

The present report deals with the further investigation of bulk damage by multiple periodic laser irradiation. The bulk damage of glass K-8 at the wavelengths 1.06 μm and 0.53 μm is shown to be determined by different mechanisms. The degradation of this substance under the prethreshold intensity laser irradiation was observed by employing absorptive spectroscopy. Several efforts were made to explain the accumulation and bulk damage.

The radiation of the Nd:YAG laser (λ = 1.06 μm) or its second harmonic (λ = 0.53 μm) was used in the experiment. The laser operated on a single traverse mode and produced 17 nsec. duration 5 mJ energy pulses. The reproducibility of energy in the pulse was not worse than 5% at repetition frequencies up to 50 hz.

The energy of every pulse was measured by photoelectric receiver. Radiation was focused into the volume of the sample by the lens with a focal length F = 12 or 22 mm. The occurrence of damage was registered photoelectrically by the appearance of a spark which followed the damage. The dependence of the number of pulses N, necessary to damage glass K-8 on the relative pulse energy Q/Q_0. (Q_0 - the minimal energy of laser pulse, inducing damage of the sample by the first pulse) is shown in figure 1. The results of 10-20 experimental measurements were averaged to obtain every point. As can be seen in figure 1, the damage of the sample in the case of multiple irradiation is possible with radiation energies considerably lower then Q_0. The decrease of the pulse energy necessary to damage the material at the increase of the number of pulses might be explained by the statistical nature of laser-induced electron avalance [9,10].

Indeed, the probability that damage will be induced by a single irradiation pulse, P_1 decreases with the decrease of the pulse energy. Consequently, the greater (in average) number of pulses is necessary to induce the damage. However, the following facts do not support such an explanation. First of all, if it is assumed that the dependence of N on Q is determined only by the dependence of the probability of damage by a single pulse P_1 on Q and that P_1 does not depend on the number of the irradiation pulses (that is, the parameter of the material remains the same) for the probability that the damage will not be induced by a series of N pulses with certain energy, we get

$$(1 - P_N) = (1 - P_1)^N \qquad (1)$$

where P_N - the probability that the damage will be induced by any of N pulses from the series. However, the experiments have confirmed that the dependence of log $(1 - P_N)$ on N (fig. 2) essentially differs from that given by eq (1). Hence, the conclusion that the difference is due to the increase of the probability P_1 with the increase of N, that is due to the gradual change of the state of the material under laser irradiation. It must be mentioned that for the inhomogeneous material (the probability that the damage will be induced by a single pulse P_1 is different for various areas) logarithm of the probability that the damage will not be induced by a series of N pulses log $(1 - P_N)$ as well as in eq (1) is proportional to N. That is why the experimental curves in figure 2 cannot be explained by the inhomogeneity of the material. Secondly, the comparison of curves 1 and 2 (fig. 1) and also 1 and 3 (fig. 2) demonstrates the dependence of the glass resistance to laser damage by multiple irradiation on the period of pulse repetition T. The number of pulses necessary to induce damage at a certain pulse energy decreases with the decrease of the period of pulse repetition. Such a dependence can hardly be explained only by the statistic nature of the damage. The dependence becomes quite understandable if it is assumed that some changes occur in the material under the prethreshold laser irradiation, the accumulation of which causes the decrease of the resistance to the damage. Then the dependence on the period of pulse repetition can easily be explained by the fact that laser-induced changes are able to relax as well as to accumulate. The comparison of the curves $N = f(Q/Q_0)$, obtained by focussing the radiation into the sample by lenses with different focal length F (curves 1, 4 in fig. 1) demonstrates the dependence of the phenomenon on the conditions of the focussing. This dependence can be explained by the influence of self-pressing of laser beam on the process of damage. The change of energy in the radiation pulse causes a change in the diameter of laser beam due to the self-pressing [11,13]. As a result, the real density of energy in the sample changes more rapidly than the measured input energy. This makes the dependence $N = f(Q/Q_0)$ stronger and the accumulative effect less conspicuous. Since the self-pressing of the beam must be weaker (or absent at all) in the case of sharp focussing of the radiation into the volume of the sample [12,13], the dependence of the curves $N = f(Q/Q_0)$ on the conditions of the focussing of laser beam becomes quite understandable: the sharper the focussing of laser beam into the volume of the sample, the more conspicuous is the accumulative effect. It is also necessary to note the essential difference between the curves $N = f(Q/Q_0)$ for the radiation with λ = 1.06 and 0.53 μm, all other conditions being the same. This must be due to the difference in the mechanisms of absorption of radiations with different wavelengths.

The accumulative effect in the process of damage can hardly be explained by the accumulation of the absorbed energy in the form of heat. Thus, if we assume that all the volume of the caustic absorbs and warms uniformly, the increase of the temperature in the caustic volume will be less than one degree [14] (the glass parameters are taken from [15-17]). On the other hand, the defects of small size ($\leq$ 1 μm) with strong absorption may warm up to the temperature 10^4K [18]. However, because of thermal diffusion and the losses caused by the thermal radiation, the temperature of such small particles after the laser-pulse must decrease with characteristic time less than 1 μs. Thus, during the period between the pulses (not less than 20 ms), the defect must have enough time to cool off. That is why the accumulative effect must be treated as laser-induced accumulation of structural changes. These changes may be the destruction of the interatomic bonds under strong laser irradiation and the accumulation of the number of damaged bonds. When a certain concentration of such microdamages is reached, macroscopic, visible damage may occur. If the damaged bond (before a crack has formed) can restore itself, the process of the accumulation of damaged bonds will depend on the frequency of repetition of laser pulses. This is in full agreement with the results of our experiments. To prove the possibility that laser radiation induced irrevocable changes in the structure of the material, the absorption spectra at the 1000-100 cm^{-1} range was measured before and after the multiple irradiation by laser pulses with the intensity ten times less than damaged threshold. Since the light absorption coefficient in the investigated spectral interval was about 10^3 cm^{-1}, $2 \cdot 10^{-3}$ cm-thick samples were used. The results of the measurements for synthetic waterless quartz are plotted in figure 3. The appearance of the absorption bands in the absorption spectrum, with the maximums at 970 cm^{-1}, 935 cm^{-1}, 885 cm^{-1}, 695 cm^{-1}, and 620 cm^{-1} was recorded after the irradiation.

These bands in the absorption spectrum are shown to be determined by the defects which, in their turn, are caused by the destruction of the interatomic bonds. The aforementioned absorption bands were investigated and identified [19]. Naturally, one can expect that the accumulation of the defects must result in the decrease of the damage threshold.

In order to find out what characterizations of radiation (the density of energy or intensity) determine the damage of the material, the dependence of the energy of the acoustic wave, produced during the damage, on the laser pulse energy was measured. The acoustic signal was registered by the piezoelectric sensing element placed on the surface of the sample and was recorded by the oscillograph. The measurement was carried in such a way that the position of the damage area, with respect to the sensing element, remained unchanged. The time delay of the acoustic signal from laser pulse at the place of the sensing element was about 2 μs which enabled us to avoid the noise produced by the scattered light of the laser. The amplitude of the acoustic signal was proportional to the absorbed energy of laser radiation.

The dependence of the amplitude of the acoustic signal, produced during the damage in glass K-8 by the radiations with wavelengths 1.06 and 0.53 μm on the laser pulse energy are plotted in figure 4. The essential difference noticed in the behavior of the curves testifies to the differences in the damage process for different wavelengths. The points are the results of the experimental measurements, while the solid line is the result of calculation.

If we assume that the damage is preceded by the "darkening"--that is, by the sudden increase of the absorption coefficient--the energy of irradiation after "darkening" is used to develop the breakdown and, at the same time, to produce an acoustic wave.

If the beginning of the "darkening" is defined by a certain threshold energy Q, the energy of the acoustic wave g will be proportional to the part of the irradiation pulse energy $Q-Q_0$ (see fig. 5). Such a dependence is observed experimentally for Q = 1.06 μm. Consequently, the appearance of the damage is defined by the energy of the irradiation.

If the "darkening" occurs at the momemt when the radiation intensity reaches a certain critical value I_0, the dependence of the acoustic signal on the laser pulse energy is

$$q = q_0 \, Q/Q_0 \, [1 + \operatorname{erf} \sqrt{\ln Q/Q_0}\,] \qquad (2)$$

(for Gaussian temporal form of laser pulse), which can be applied to describe the experimental results for 0.53 μm (the solid line in fig. 4). Consequently, the damage threshold for 0.53 μm is determined by the intensity of laser radiation.

It must be mentioned that the temporal form of the pulse does not greatly influence the calculated dependence q = f(Q); the use of non-Gaussian form results in but insignificant pulse corrections. The assumption about the existence of the "darkening" is quite natural, as the blocking of the passing laser beam is observed when the damage occurs. We also noticed the increase of the acoustic signal more than 10^3 times with the appearance of the damage.

The mechanisms of damage which explain the results obtained must be the following: the damage with wavelength 1.06 μm is determined by the thermo-avalanche initiated by the absorbing inhomogeneities. Under the prethreshold heating of the microinhomogeneities, some changes occur in the parameters of the microinhomogeneities as well as in the surrounding medium. As a result, the microinhomogeneity reaches a certain critical size, meaning that the resistance of the medium has decreased and laser radiation can damage the substance.

With 0.53 μm wavelength, damage may be induced by the two photon generation of free electrons (the energy of two photons of radiation with 0.53 μm is higher than the width of the forbidden band for glass K-8) and the ensuing absorption of radiation by free electrons. The decrease of the damage threshold in the case of multiple irradiation may be caused by the gradual accumulation of electrons both in the conduction band and in trop levels, from which they can be freed by one photon during the ensuing irradiation.

This is testified to by the considerably higher deviation of the measured values of N and q (Q being constant) for the wavelength 1.06 μm than in the case of radiation with 0.53 μm wavelength (the difference in the deviation is clear in fig. 4; in fig. 1 the deviation cannot be seen because of the averageing of the results of measurements).

The difference between the curves $N = f(Q/Q_0)$ with 1.06 μm and 0.53 μm can be explained by the accumulation of not only microdamages, but also electrons in the conduction band with the wavelength 0.53 μm.

On the basis of the investigation one may make the following conclusions:

1. The laser damage of glasses induced by multiple laser irradiation is determined not by the statistical nature of optical damage (for instance, by a "happy electron"), but by the accumulating changes of the parameters of the material under irradiation. Statistics, which nevertheless take place in the experiments on damage (the measurement of the damage thresholds or the acoustic signal) are determined by the inhomogeneity of the material.

2. The bulk damage threshold by single and multiple pulses differs. The damage has the quality of accumulation.

3. The degree of radiation induced residual changes in the medium resulting in the damage of the material, depends on the intensity (or the density of energy) of laser radiation, the number of pulses, frequency of the repetition of pulses and radiation wavelength.

4. The damage mechanisms for 1.06 μm and 0.53 μm for glass K-8 differ. It is shown that the damage by a single radiation pulse with the wavelength 1.06 μm occurs when a certain density of energy is achieved, while with 0.53 μm, at a certain intensity of laser radiation.

5. The damage with 1.06 μm wavelength is determined by the thermo-avalanche initiated by the absorbing inhomogeneities. The decrease of the damage threshold in the case of multiple irradiation is caused by the accumulation of changes in the parameters of the microinhomogeneities and the surrounding medium.

6. The damage with wavelength 0.53 μm is determined by the two photon generation of free electrons, the absorption of light by the free carriers, and the development of the electron avalanche. In the case of the prethreshold irradiation, the accumulation of electrons in the trap levels and in the conduction band takes place.

7. The degradation of the quartz glass under the prethreshold laser irradiation has been observed. The changes in the absorption spectra provide information about the break of the chemical bonds between the atoms.

REFERENCES

[1] Danileyko, Yu. K., Manenkov, A. A., Nechitayle, V. S., (Trudy) FIAN, 101:31, (1978)

[2] Bloembergen, N., IEEE QE.10(3):375, (1974).

[3] Proceedings of: a) The Annual Boulder Damage Symposium,
b) Leningrads Nonresonant Interaction of Laser Beam with Condensed Materials Conferences.

[4] Khazov, L. D., Fersman, I. A., Bortnikev, V. Yu., ZhTE-(Journal of Technical Physics). 44(9):2020-2022, (1974).

[5] Danileyko, Yu. K., Manenkov, A. A., Nechitayle, V. S., Quantum Electronics. Z (2):438, (1976).

[6] Artem'yev, V. V., Bonch-Bruyevich, A. M., Memac, Ya. A., Salyadinov, V. S., Letters of the ZhTF (Journal of Technical Physics).

[7] Yeron'ko, S. B., Zharkov, S. N., Ch'mel, A., Solid State Physics, 20(12):3570-3574, (1978).

[8] Balitskas, S. K., Maldutis, E. K., Quantum Electronics 8(4):902, (1981).

[9] Bass, M., Barrett, H. H., IEEE J. Quant. Electr. QE-8.8(3):338, (1972).

[10] Bass, M., Barrett, H. H., Applied Opt. 12(4): 690, (1973).

[11] Zverev, G. M., Maldutis, E. K., Pashkov, B. A., Letters to ZhTF. 9:108, (1969).

[12] Zverev, G. M., Pashkov, B. A., ZhETF. 57:1128, (1969).

[13] Alenkevich, V. A., Akhmanov, S. A., Zhdanov, V. V., Suknorukov, A. P., Quantum Electronics. 2:1179, (1975).

[14] Maldutis, E. K., Reksnis, Yu. Y., Sakalatskas, S. V., Engineering-Physics Journal. 32:1098, (1977).

[15] GOST 13659-68. Optical Colorless Glass, Physical Chemical Properties. Moscow, Publishing House of Standards (1968).

[16] Kolyadin, A. I., Alekseyeva, K. T., Optical Technical Industry 2:43, (1973).

[17] Zkhilionis, A. A., Krauyalis, R. Yu., Maldutis, E. K., Reksnis, Yu. Y., Sakalauskas, S. V., Thesis Reports of the 4th All-Union Conference on Non-Resonant Interactions of Optical Radiation with a Substance, Leningrad, (1978), p. 83.

[18] Danileyko, Yu. K., Manenkov, A. A., Nechitayle, V. S., Quantum Electronics, 5:194, (1978).

[19] Khalilov, V. Kh., Thesis of Reports and Information of the 4th All-Union Conference on the Vitreous State, Leningrad, (1981), pp. 247-248.

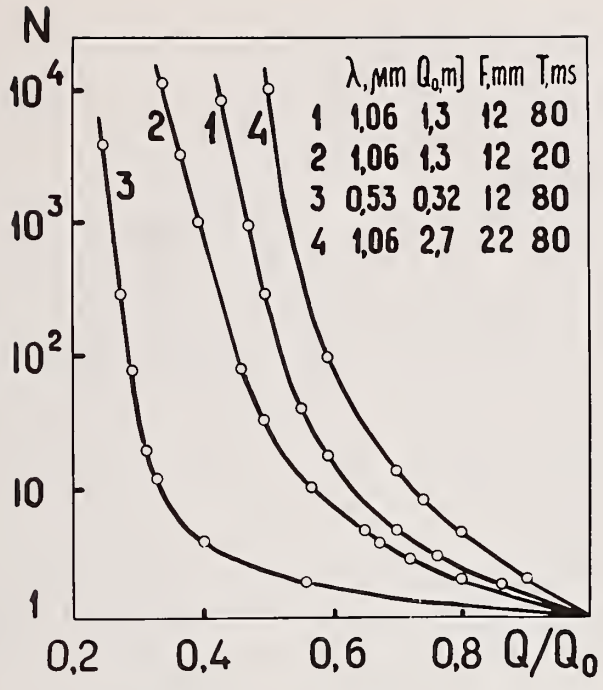

Figure 1. Dependence of the number of laser pulses necessary for the damage on the relative energy in the pulse Q/Q_0 for glass K-8.

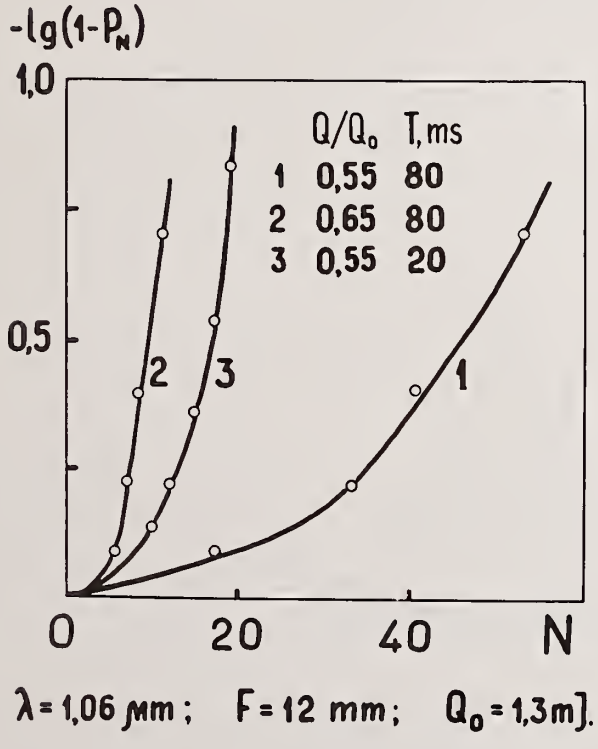

Figure 2. Dependence of the logarithm of the probability that the series of N laser pulses will not damage glass K-8, on the number of pulses in the series.

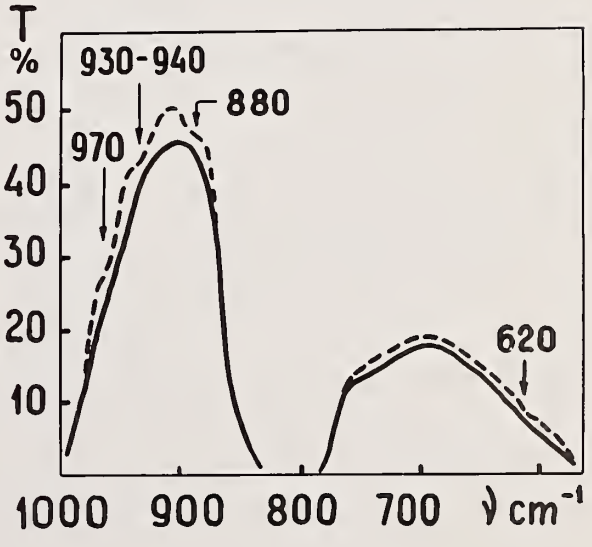

Figure 3. The transmission spectrum of the sample before (a solid line) and after (a dashed line) laser radiation.

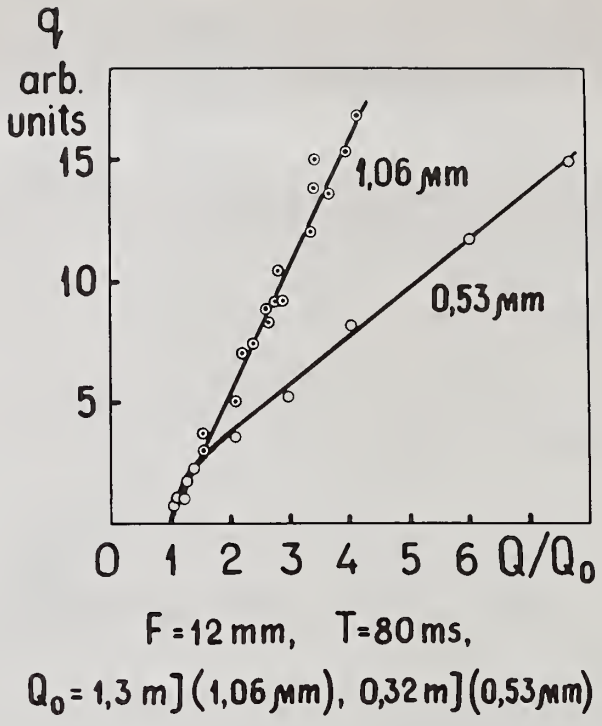

Figure 4. Dependence of an acoustic signal q in glass K-8 on the energy of laser pulse Q.

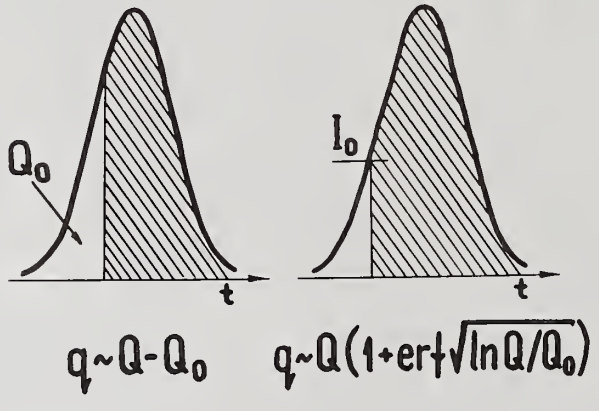

Figure 5. Explanation of the dependence of an acoustic signal Q on the energy of laser pulse Q.

Laser Damage of Crystalline Silicon by Multiple 1.06μm, Picosecond Pulses

R. M. Walser, M. F. Becker and D. Y. Sheng

Electronics Research Center and
Department of Electrical Engineering
The University of Texas at Austin
Austin, Texas 78712

Recent studies [1] have shown that the iso-intensity damage kinetics of crystalline silicon irradiated by picosecond 1.06μm pulses could be fit to the equations of classical nucleation and growth. These results suggested that laser damage be viewed as a non-equilibrium phase transition in which the threshold intensity produced excursions across a first order phase boundary into a metastable region of the material phase diagram.

In the present work we discuss a simplified electronic phase diagram for silicon that we believe is relevant to the picosecond damage experiments. The physics of the metastable region are as yet uncertain, but its presence requires that the statistics of laser damage be determined by the activated nucleation of embryos (charge density fluctuations) to near liquid phase charge densities.

The thermodynamic perspective suggests a new laser damage mechanism in which incident photons are resonantly absorbed by the collective electronic oscillations (surface plasmons) of critical embryos. Evidence supporting this mechanism has been obtained from high resolution SEM studies of the damage morphology showing that a coherent radiative interaction occurred between resonant surface plasmon embryos on adjacent sites just prior to liquid-like phase nucleation. Calculations show that the surface plasmon of a spherical embryo with a near liquid charge density of $\sim 2 \times 10^{22}/cm^3$ is resonantly coupled to the laser photons.

Key words: laser damage; crystalline silicon; picosecond pulses; non-equilibrium phase transition; damage kinetics; damage morphology; damage nuclei; resonant surface plasmons.

1. Introduction

Perhaps the only universally true statement that can be made about laser damage is that it must result from a laser induced non-equilibrium transition across a first order phase boundary in the phase diagram of the damaged material. This observation allows, indeed requires, one to use the thermodynamic formalism of non-equilibrium phase transitions to organize systematic experimental studies aimed at understanding the physics of the critical energy transfer. Yet, there has apparently been no previous attempt to approach the study of laser damage from this thermodynamic perspective. In this paper we describe some initial results of the first such study in which we examined the laser damage of crystalline silicon by picosecond 1.06μm laser pulses.

In section 2, we describe the experimental methods used in the study of laser damage as a non-equilibrium phase transition. In general, three key pieces of information are required: a knowledge of the material phase diagram relevant to the experiments, the region accessed by the laser excitation, and the fluctuations available to the material-laser system in this region. Using the new

experimental techniques outlined in sections 2.1 and 2.2, we indicate how some of the required information can be obtained from the results of our silicon damage experiments. These are discussed in section 3, for the specific case of the damage of silicon by picosecond 1.06μm laser pulses which is nearly the ideal material for this study.

An immediate consequence of this new perspective on laser damage is to emphasize the importance of nucleation phenomena. While the concepts of heterogeneous nucleation are used implicitly in most previous studies of laser damage, e.g., in the search for "critical embryos" for initiating avalanche breakdown; nucleation is usually considered to be dominated by macro-heterogeneities such as macro-cracks, inclusions, etc. Indeed, when present, macro-heterogeneities have profound influence on laser damage. However, when these are eliminated, the non-equilibrium processes leading to laser damage will ultimately always result from the micro-heterogeneous nucleation of a new phase in the same way, for example, that equilibrium melting always results from micro-heterogeneous nucleation. We would also expect that the non-equilibrium nucleation rate will be profoundly influenced by microscopic nucleation catalysts, i.e., impurities on the surface itself, just as the equilibrium processes are.

The formal admission that laser damage is micro-heterogeneously nucleated profoundly alters the present approach to understanding the nature of the critical energy transfer. For example, the experimental results discussed in sections 2.1 and 2.2 indicate that the dominant energy transfer at the damage threshold intensity is to optically resonant surface plasmons of small charge density clusters, i.e., micro-heterogeneously nucleated critical embryos. Without formally admitting the thermodynamic possibility of these charge density clusters, this channel of critical energy transfer could not be accounted for. To our knowledge, this is the first report of such a mechanism in laser damage.

2. Experiments

To study the laser damage of silicon as a non-equilibrium phase transition we conducted two types of experiments with laser intensities near the multiple pulse damage threshold. In the first, described in section 2.1, we determined the kinetics of the iso-intensity damage transformation by using a variation of the "n on one" multiple pulse damage technique. In the second, described in section 2.2, we studied the damage morphology using an experiment that combined "n on one" and "one on n" techniques.

In both experiments the samples of single crystal silicon were prepared from low resistivity 1.5μm or 2.5μm thick epitaxial layers. To obtain the very thin samples used in the transmission experiments, the wafers were masked and electrochemically etched, exposing about 0.5 cm^2 of epitaxial membrane.

The laser pulses were supplied by a passively mode-locked 1.06μm Nd:YAG laser. Single pulses were selected with a FWHM duration of 38 psec and a Gaussian transverse mode. Multiple pulse damage data was taken with the laser operating at a PHF of 5-20 Hz. All of the damage data referred to in this paper was taken using 1.06μm pulses.

Before discussing these experiments we note that all of the data given represents front surface damage. This was always observed with the thick wafers but, even the optically thin 1.5μm membranes always damaged first at the front surface for near threshold intensities.

2.1 Damage Kinetics

These experiments were the first to demonstrate that for multiple iso-intensity pulses, laser damage proceeds by heterogeneous nucleation and growth as reported in more detail elsewhere [1].

The damage kinetics were obtained by continuously monitoring the 633nm transmission of the irradiated spot (fig. 1). The multiple 1.06μm, picosecond pulses were supplied at a 5Hz PRF.

The sample transmission is assumed to be related to the percentage of the irradiated spot area transformed to the final state of damage. The results (fig. 2) show an incubation period, a sigmoidal shape, and have been fit to the Avrami equation for a transformation proceeding by heterogeneous nucleation and growth [1]. These results strongly suggest that near-threshold intensity pulses are inducing non-equilibrium excursions of the system across a phase boundary into a metastable, or unstable, region of the material phase diagram. In the metastable region, heterogeneously assisted fluctuations toward the new phase, must be thermally activated by the most efficient modes of coupling between the laser photons and the fluctuations.

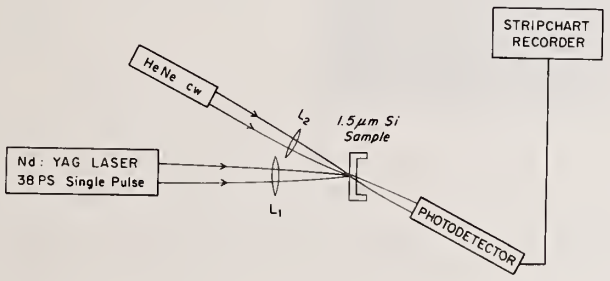

Figure 1. Experimental configuration for measuring isointensity nucleation and growth of laser induced damage.

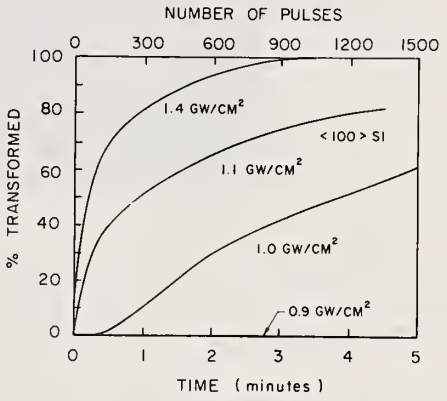

Figure 2. Experimental isointensity damage curves for <100> Si membranes for picosecond pulses at 5Hz prf.

2.2 Damage Morphology

To determine what phase boundary crossing is associated with the damage and to determine the nature of the critical energy transfer, we used the experimental configuration shown in figure 3 to study the evolution of the multiple pulse damage morphology for near threshold intensities. In these

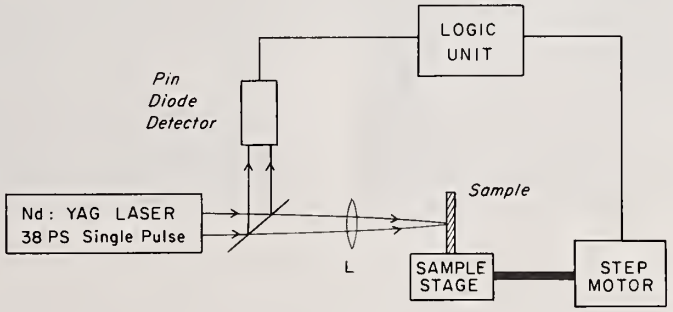

Figure 3. Experimental configuration for performing sequences of 2^N-on-one irradiations for increasing N.

experiments an automatic translation stage counts laser pulses and gives a sequence of spots irradiated with 2^N pulses of constant intensity. A typical sequence of three spots is shown in figure 4.

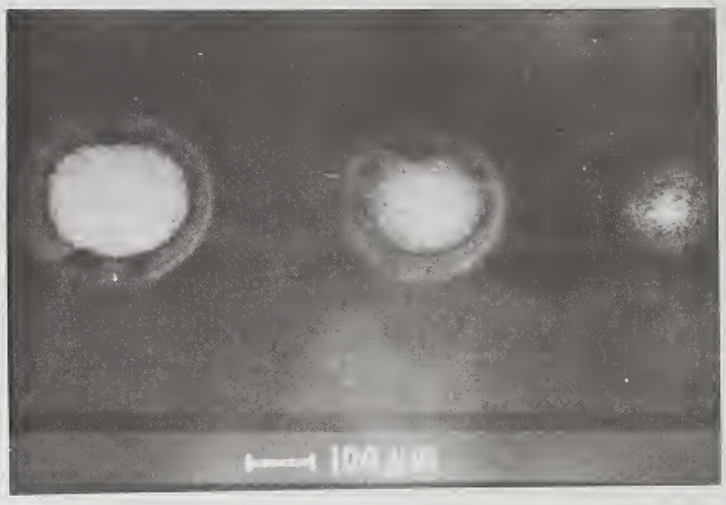

Figure 4. Damage spots from 256, 128 and 64 pulses respectively from left to right.

High resolution SEM micrographs of the damage morphology as a function of intensity and number of pulses were studied to follow the evolution of damage. The SEM micrographs of figures 5-8 illustrate this development. For intensities well below the one shot damage threshold the final damage state was the remarkably coherent, one-dimensional damage grating shown in figure 5. The asymptotic

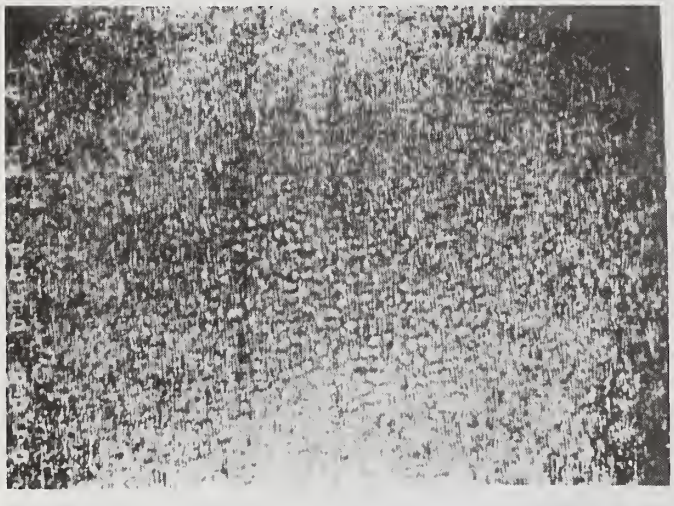

Figure 5. Damage grating on 0.015" thick Si epi wafer produced by 256 pulses at 2 GW/cm^2.

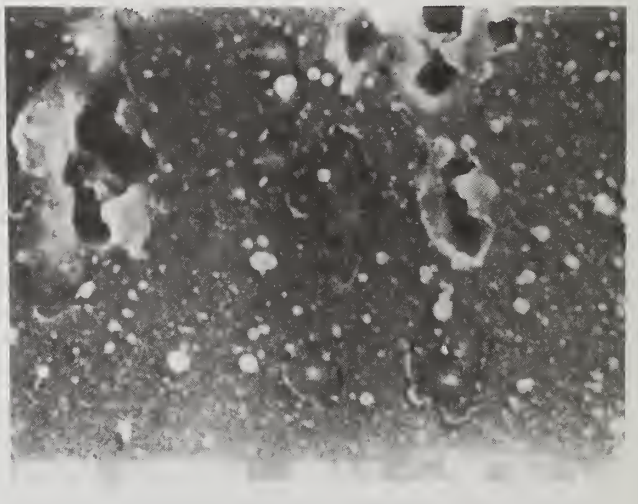

Figure 6. SEM close-up of damage pits at an early stage of damage produced by 8 pulses at 2 GW/cm^2.

approach to damage saturation (100% transformation in fig. 2) corresponds to the emergence of this stationary structure. The damage gratings are generated by linearly polarized light, oriented with the grating lines orthogonal to the optical electric field, and have a grating periodicity equal to the free space laser wavelength. They are commonly observed only in an annular region in damage spots produced by single, more intense pulses. This grating damage is easily understood as resulting from the interference of surface waves launched by linear defects.

Our experiments clearly associate the grating-producing energy transfer with a critical range of intensities in which the grating coherence can be transferred throughout the beam spot. More importantly, the arguments which follow indicate that the defects which produce the symmetry-breaking grating energy transfer are not of extrinsic origin but appear to be induced by intrinsic excitations.

To determine the earliest critical energy transfer we examined SEM micrographs of spots irradiated with only a few pulses with the lowest intensities. By examining many samples we concluded that in the earliest stages of damage small pits are generated by evaporation (fig. 6). These pits invariably show evidence of liquid-vapor instabilities, likely caused by superheating of the liquid-like phase.

Furthermore, in the earliest stages of damage, isolated pits were rarely observed. Invariably, 2-5 pits were simultaneously generated and organized into pit chains perpendicular to the optical electric field. The observation of these pit chains, clearly seen in figures 6-8, suggest that the critical early energy transfer involves a coherent radiative interaction between critical embryos that are the precursors to damage. It is straightforward to understand how an interference grating

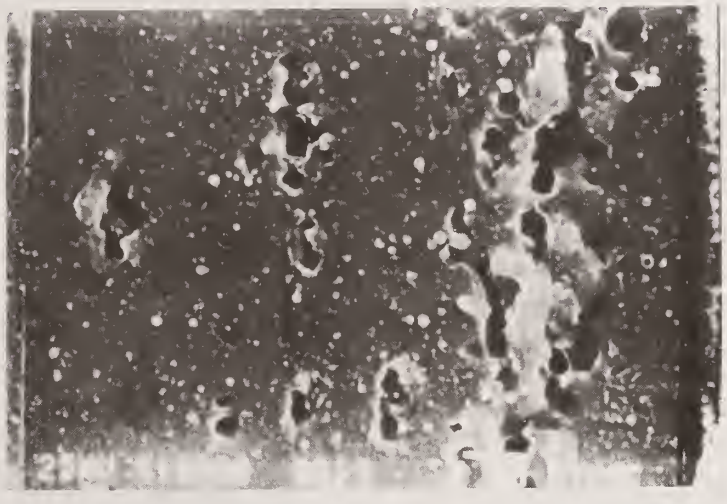

Figure 7. Less magnified view of the same sample as figure 6.

with the period of the free space wavelength can be subsequently generated by scattering from these pit chains (fig. 5). These results indicate that the grating generating defects are of intrinsic, rather than extrinsic origin as previously supposed.

We conclude that the laser damage of crystalline silicon in these experiments is the result of non-equilibrium phase transition in which the localized liquid-like nuclei are thermally activated at the lowest damaging intensities by a cooperative interaction with the laser field.

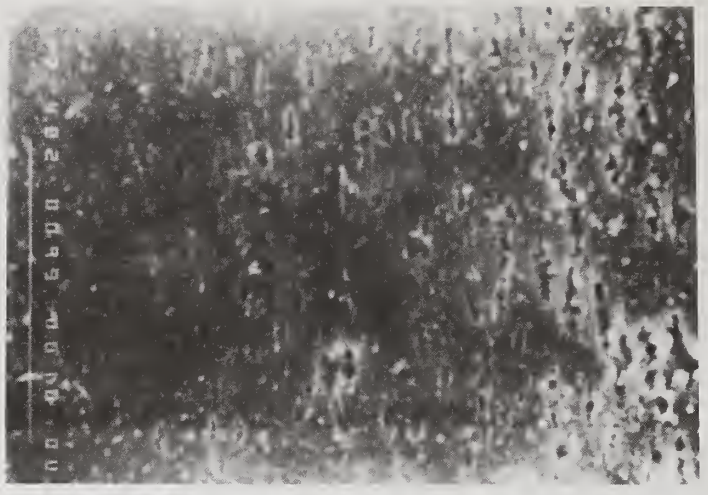

Figure 8. SEM photo of a later stage of damage produced by 128 pulses at 2 GW/cm^2.

3. Discussion of Results

In this section we discuss our interpretation of the experimental results from the perspective of non-equilibrium phase transitions outlined in the introduction. As discussed, we require the material phase diagram containing the relevant phase boundary crossing. For the present experiments we propose the use of the phase diagram of figure 9 which assumes that the energy of the intrinsic silicon system depends on the temperature and the excited one electron density, but is independent of volume changes which should be negligible for the picosecond pulse duration.

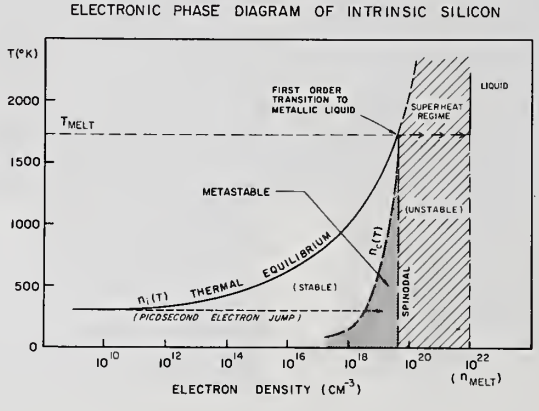

Figure 9. Phase diagram for intrinsic silicon. The various regions are described in the text.

The phase diagram consists of:

A. A stable semiconductor region bounded by the equilibrium equation of state $n_i(T) \simeq \exp(-E_g(T)/2kT)$ and the boundary $n_c(T) \cong \lambda_{TH}^{-3}$ where λ_{TH} is the thermal deBroglie wavelength of the excited electronic charge. At this charge density, statistical electronic correlations commence, and, if accompanied by real interactions, will lead to metastable charge density fluctuations.

B. A metastable region, bounded by $n_c(T)$ and the spinodal density $n_s(T)$, in which the solid phase is metastable to thermally activated nucleation of the liquid phase. In the absence of observable superheating in solids, the metastable region should terminate at T_{melt}.

C. A region inside the spinodal that is unstable to any fluctuations. (Without a specific discussion of the specific electronic interactions for densities greater than $n_c(T)$ we cannot give a more rigorous definition.)

D. The equilibrium liquid phase of metallic electron density.

The SEM data clearly shows that the silicon-picosecond laser pulse experiments access a metastable region in which liquid nuclei are thermally activated. This region must lie between $n_c(T)$ and $n_s(T)$ in figure 9. This implies that in the absence of fluctuations, the energy deposited by the picosecond laser pulse can produce 10^{18}-10^{19} cm^{-3} electronically excited states during the pulse duration without exceeding T_{melt}.

Silicon, with an indirect bandgap of 1.11eV (fig. 10) at 300°K, has a linear absorption coefficient of only 10 cm^{-1} for the 1.06μm picosecond laser pulses. At higher intensities approaching the damage threshold the measured transmission data (fig. 11) was nonlinear indicating the increasing importance of multiphoton absorption. Assuming that the indirect two photon process shown in figure 10 dominated, we obtain a two photon absorption constant β = 52 cm/GW by fitting the data of figure 11.

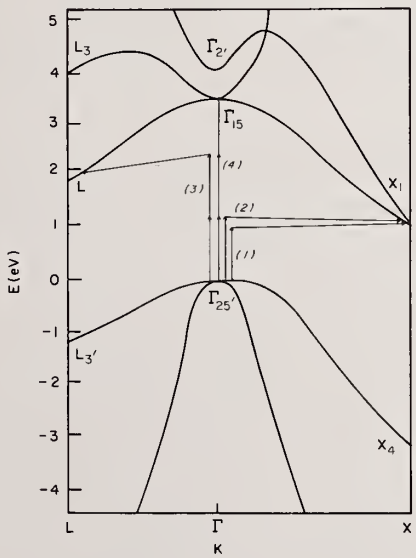

Figure 10. Energy band diagram for silicon showing absorption processes for 1.06μm photons (1.17eV). Processes (1) and (2) are one-photon indirect, (3) is two-photon indirect, and (4) is three-photon absorption.

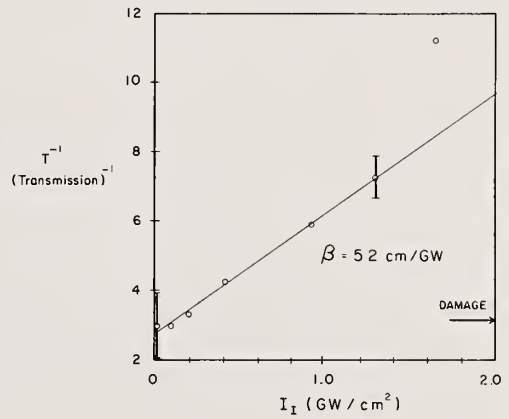

Figure 11. Sample transmission vs. incident intensity for 0.015" thick <100> silicon. Circles are experimental data, and the solid curve is fitted and shows a linear absorption coefficient $\alpha = 10\ cm^{-1}$ and a two-photon absorption coefficient β = 52 cm/GW.

With these data, the excited charge density produced by 38psec, 1.06μm laser pulses with I = 1 GW/cm^2 was computed to be 10^{18}cm^{-3} - 10^{19}cm^{-3}. We assumed that the excess energy $\hbar\omega_0 - E_g \simeq 60$meV is transferred instantaneously to the lattice. The remaining energy E_g was assumed to be transferred by electron-hole Auguer recombination processes [2]. The computed maximum temperature rise during the pulse was negligible (<1°K). Although free carrier absorption was omitted in these calculations, it is not expected to increase n or ΔT significantly. Thus, it appears that the picosecond pulses of threshold intensity do in fact produce nearly isothermal jumps into the metastable region as indicated on the phase diagram (fig. 9).

The preceeding discussion indicates that, in the present case, the scenario of laser damage is as follows. First, during the pulse the laser creates a near-uniform (with suitable corrections for the Gaussian intensity profile) density of $n_c \simeq 10^{19}$ excited states/cm^3 near the band edge with negligible lattice heating. Charge density clusters with $n > n_c^{(T)}$ are then nucleated micro-heterogeneously through fluctuations. These clusters are subsequently thermally activated to the liquid-like phase by transfer of energy from the laser beam to the spatially inhomogeneous electronically excited state. Laser damage results from evaporation or exomission of the locally superheated phase. The crucial unanswered problems are to determine 1) the origin of the micro-heterogeneous nucleated clusters and 2) the nature of the energy transfer to these clusters producing damage.

The question of the origin of the micro-heterogeneities will be discussed in more detail elsewhere [3] and is sidestepped in this paper. We note, however, the improbability of a conventional electron avalanche process in the present case since, for the 1.06μm photons and the typical 10^{-13} sec. electron collision times in silicon, $\omega_0 t \gtrsim 10^2$.

Assuming that micro-heterogeneous nucleated clustering occurs, the thermal activation of "critical" clusters by the laser to damage can be studied by the experiments of sections 2.1 and 2.2. The important result of these experiments was the observation that, at the lowest intensities, damage resulted from coherent radiative energy transfer between critical clusters in a direction orthogonal to the incident optical electrical field. This suggests that the incident field stimulates a self consistent radiative interaction between adjacent charge density cluster oscillations. With clustering, our previous argument against avalanching must be modified to include the possibility of energy transfer to the surface plasmons. Now, energy can be transferred to thermalized excited states if their charge density oscillations have fast radiative decay processes.

While the normally incident light will not couple to the bulk surface plasmons, it strongly couples to the clusters; resonantly to those with a density and geometry such that $\omega_{sp} = \omega_0$. The long electron relaxation (collision) times in silicon insure that the primary decay of these resonantly excited surface plasmons will be partly by a radiative channel. However, for thermal activation to the liquid state, we require a competitively fast carrier relaxation process. The critical embryos that are the precursors to damage must, therefore, be those charge density oscillations activated to densities approaching the liquid phase (fig. 12). At these densities one expects that competitively fast Auger recombination will occur allowing the clusters to be heated to $T \simeq T_{melt}$ during the picosecond pulse. With the collapse of the solid structure there is easy energy transfer to the clusters with near liquid densities, and they should rapidly superheat leading to damage by evaporation or exomission.

If the Auger recombination and surface plasmon radiative decay rates are comparable in the critical embryos, damage at the lowest intensity must necessarily result from the self-selection of favorably oriented, and radiatively coupled, critical cluster nuclei. Non-isotropic, radiative coupling of the surface plasmons must occur in the direction orthogonal to the normally incident optical electric field $\bar{E}_i$ as observed in our experiments.

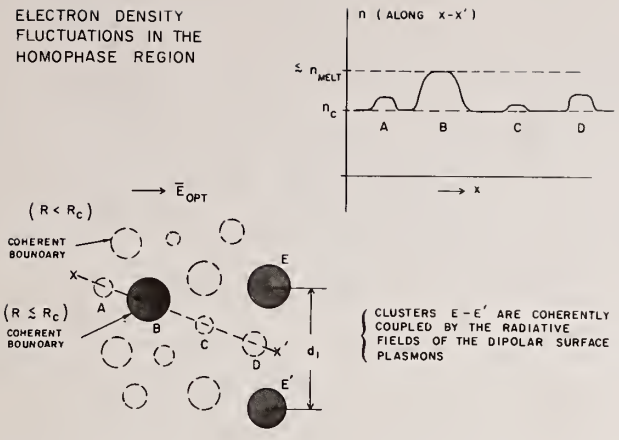

Figure 12. Schematic representation of charge density fluctuations beyond $n_c(T)$.

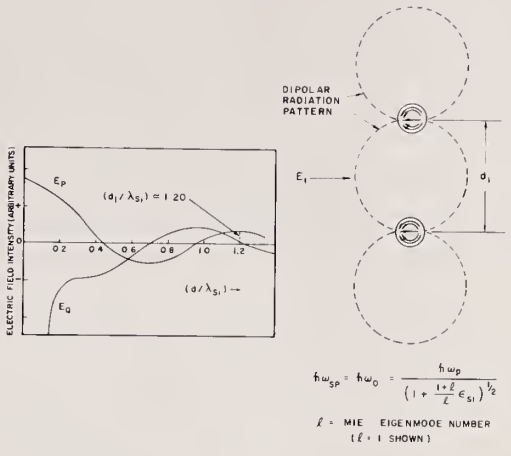

Figure 13. Illustration of the in-phase coupling of the dipole-like radiation patterns of surface plasmon modes on spherical charge clusters. At a critical distance, d_1, the fields reinforce and damage nucleation is preferentially selected.

A crucial requirement of this model is a damage pit spacing in this direction consistent with the self-selection of coherently reinforcing, resonant surface plasmons on critical nuclei as shown in figure 13. If we assume that the resonantly coupled critical nuclei are nearly spherical (low surface to volume energy) and radiatively coupled by dipolar surface plasmons (ℓ = 1 Mie eigenmodes) the resonance condition can be written [4]

$$\omega_0^2 = \omega_{sp}^2 = \frac{\dfrac{n_L^2 q^2}{\epsilon_0}}{1 + \dfrac{1+\ell}{\ell}\epsilon_{si}} \qquad (1)$$

where ℓ the Mie eigenmode number is 1 for the dipolar plasmon. Taking a metallic dielectric function (ϵ_0) for the critical cluster with $n \to n_L$ and $\epsilon_{si} = 11.4\,\epsilon_0$ for the surrounding crystalline matrix, eq. (1) gives a value of $n_L = 2 \times 10^{22}/cm^3$. This is clearly consistent with a near liquid density as required.

An additional requirement is that the 350-380 nm spacing observed between adjacent damage pits (figs. 6-8) correspond to a coherent reinforcement of the incident field by the radiative surface plasmon decay. From the classical theory of radiating dipoles, we have computed the in-phase and quadrature components of the radiative fields (E_p and E_Q respectively in fig. 13) in a direction orthogonal to the incident optical field. This argument was originally made by Willis and Emmony [5] for coherently inferfering avalanche currents generated by 10.6μm radiation in germanium. However, in direct contrast with our result, the experimentally observed radiative coherence length corresponds to 0.7λ indicating that the avalanche current was reinforced by feeding back out-of-phase fields. This point does not seem to have been observed by the authors and appears to indicate that, in their

case, the avalanche is thermally-assisted. The minimum spacing at which the radiative fields will constructively interfere is at a separation of $1.2\lambda_{si}$ or about 375 nm. (A value of 3.4 was used for the refractive index of silicon.) This distance is in good agreement with the previously given experimental values.

It should be emphasized that the relaxation of the excited surface plasmons offers a radiative decay channel essential to interpreting the experiments and not available to one electron excited states in indirect gap semiconductors like silicon. A two level state diagram of the transverse coupling between adjacent damage sites is given in figure 14. This diagram omots the non-radiative decay of the coupled excited states near the band edges by Auger recombination which will lead to rapid local heating of the clusters with near metallic densities.

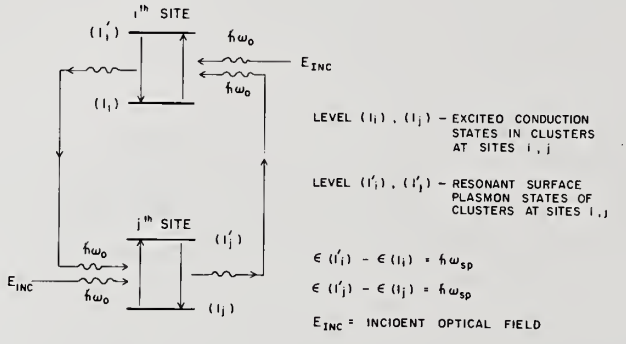

Figure 14. Two level state diagram showing the feedback nature of the site-to-site plasmon coupling described by our model.

4. Conclusions

This study of laser induced damage as a non-equilibrium phase transition has concentrated on modelling the damaged crystalline silicon by 1.06μm picosecond laser pulses. The principal results obtained are:

(1) Multiple picosecond pulse laser damage of silicon is a first order phase transformation which may be accessed by laser induced charge density jumps at intensities less than those required for homogeneous melting.

(2) Multiple pulse damage transformation kinetics indicate that large area damage is a micro-heterogeneously nucleated process. This data suggests that a relevant pulse diagram for silicon contains a metastable region in which charge density clusters can be elevated to or beyond the liquid phase.

(3) The identification of a new, and possibly widespread, laser damage mechanism, in which energy transfer is by resonant surface plasmons on small charge density clusters.

This research was supported by the DoD Joint Services Electronics Program through AFOSR contract F49620-77-C-0101.

5. References

[1] R. M. Walser, M. F. Becker, D. Y. Sheng and J. G. Ambrose, "Heterogeneous Nucleation of Spatially Coherent Damage Structures in Crystalline Silicon with Picosecond 1.06μm and 0.533μm Laser Pulses," Laser and Electron-Beam Solid Interactions and Material Processing; eds. T. J. Gibbons, W. Hess, and T. Sigmon, Elsevier, North-Holland, Inc., 177 (1981); and D. Y. Sheng, R. M. Walser, M. F. Becker and J. G. Ambrose, "Heterogeneous Nucleation of Damage in Crystalline Silicon with Picosecond 1.06μm Laser Pulses," Appl. Phys. Lett. 38, 99, (1981).

[2] D. Y. Sheng, Ph.D. Dissertation, "Heterogeneous Nucleation of Damage Structures in Crystalline Silicon by Picosecond 1.06μm Laser Pulses," University of Texas, December 1981.

[3] R. M. Walser, "The Melting Physics of Group IV Semiconductors," to be published.

[4] F. Fujimoto and K. Komaki, "Plasma Oscillations Excited by a Fast Electron in a Metallic Particle," J. Phys. Soc. Japan 25, 1679 (1968).

[5] L. J. Willis and D. C. Emmony, "Laser Damage in Germanium," Optics and Laser Technology, 222, October 1975.

A Technique for Increasing the Optical Strength of Single-Crystal NaCl and KCl Through Temperature Cycling*

J. B. Franck

Michelson Laboratory, Physics Division
Naval Weapons Center, China Lake, California 93555

M. J. Soileau

Center for Applied Quantum Electronics
North Texas State University, Denton, Texas 76203

This paper relates a technique for increasing the optical strength of NaCl and KCl single-crystal samples. The 1.06-μm pulsed laser damage thresholds were increased by factors as large as 4.6 for some bulk NaCl single crystal, namely the laser grade NaCl purchased from Harshaw Chemical Company. The bulk laser damage breakdown threshold (LDBT) of the crystal was measured prior to and after heat treatment using a Nd:YAG laser operating at 1.06 μm in the TEM_{00} spatial mode with a pulse width of 9 nsec, full width at half maximum. After the LDBT of the untreated sample was measured, it was mounted in a quartz tube and placed in an oven for the heat treatment. The quartz tube was continuously flushed with dry nitrogen gas throughout the heat treatment cycle. The sample was slowly heated to a predetermined annealing temperature: for NaCl, up to 800°C (approximately 1°C below its melting temperature). The sample was maintained at this temperature for a short time and was then removed from the oven to allow rapid cooling. Samples taken to near-melt temperature required repolishing because of surface sublimation, which occurs at elevated temperatures. After repolishing, the bulk LDBT was remeasured and found to be up to 4.6 times greater than the value measured for the untreated crystal. For samples annealed at lower temperatures, bulk and surface LDBT's were studied; for cleaved and polished surfaces, changes in the damage morphology were found.

Key words: annealing; baking; bulk; damage threshold; potassium chloride; single crystal; sodium chloride; surface.

1. Introduction

Recent work has shown that what was previously called intrinsic laser-induced breakdown [1,2][1] is instead caused by material defects [3-6]. It has been shown that the special processing during crystal growth can significantly increase the optical strength of the crystal [3,4,7]. Manenkov [3] has reported that rapid temperature cycling can substantially increase the laser-induced breakdown thresholds of alkali-halide crystals. In this paper, we report an independent confirmation of the results claimed by Manenkov [3] and provide additional details of the treatment used to increase the optical strength of NaCl and KCl. Single-crystal specimens of NaCl and KCl were heated to near-melt temperatures and were rapidly quenched. The laser damage breakdown threshold (LDBT) of these specimens was measured before and after heat treatment, using a pulsed laser (9 nsec, full width at half maximum (FWHM), operating at 1.06 μm). The threshold intensity for laser-induced damage increased by up to a factor of 4.6, depending on the previous history of the samples. A study of lower temperature cycling was performed to see the effect on bulk and surface LDBT's. A change in the damage morphology was found after heat treatment for both cleaved and polished surfaces.

2. Heat Treatment

Samples used in the study were of single-crystal "laser grade" and "spectroscopic grade" NaCl and KCl from Harshaw Chemical Company [8]. The samples were mounted for heat treatment as follows. Samples of two different sizes, either 2.0 x 2.0 x 2.0 cm^3 or 2.5 x 2.5 x 5.1 cm^3, were placed in a quartz tube oven with an internal diameter of approximately 3.6 cm. In some cases, this necessitated

*Work supported by the Office of Naval Research.
[1]Numbers in brackets indicate the literature references at the end of the paper.

the grinding of the corners of the sample to allow insertion into the tube. In such cases, the diagonols were reduced to 3.3 cm. The samples contacted the tube directly. Temperatures were continuously monitored by a thermocouple mounted in a 0.05-cm-wide by 0.5-cm-deep hole drilled into one face of the sample. Specimens were continuously flushed with dry nitrogen gas in order to maintain an inert ambient atmosphere during the heat treatment. A slow flow rate was maintained to reduce heat loss.

In general, specimens were slowly heated and rapidly cooled. A typical heating and quenching cycle can be seen in figure 1. Here the total heating and cooling cycle was about 3.5 hr. Other cycling rates were investigated. In some cases, total cycling rates as high as 40°C/min were used, with positive results. In the 3.5-hr treatment represented by figure 1, the LDBT was found to increase by a factor of 4.6. Comparable increases were found in other cases where the cycling time was on the order of 30 min. The cycling rate was limited by the development of thermal stress, which developed at rates > 30°C/min. In all treated samples, stress zones could be seen using cross polarizers. No stress was found in untreated samples.

Cooling was accomplished by several methods. In one case, the oven was turned off and the sample was allowed to cool to room temperature, requiring about 2 hr. In other cases, the quartz tube was either partially or completely removed from the oven. In a few cases, the sample was quickly removed from the center of the oven and placed in a room-temperature part of the quartz outside the oven and then placed on a 1-kg block of aluminum at room temperature. Such rapid cooling techniques often produce fracturing of the sample.

Cooling rates as low as 7°C/min were investigated. A NaCl sample was cleaved into three pieces, and the LDBT was measured for all three pieces. One of the pieces was kept as a control sample, while the other two were put through the temperature cycle as follows. After the two samples were brought to 796°C at a rate of approximately 14°C/min and held there for 10 min, the oven was turned off and one sample was immediately taken from the oven. That sample reached room temperature within 10 min at a rate of approximately 80°C/min; the other sample required 2 hr at a rate of approximately 10°C/min. The samples were repolished and their LDBT measured. It was found that the slow-quenched sample had an increase in the LDBT of 1.4, while the quick-quenched sample had a LDBT increase of 4.1.

Also studied was the effect of cycling NaCl from room temperature to a maximum temperature of 450°C. This temperature was chosen because it has been shown that annealing at 450°C effectively removes color centers [9]. This is desirable for several reasons. First, for near-melt temperatures, the surfaces of the samples are sublimed, which substantially degrades the surface optical quality. Second, the extreme temperature variation produces thermal stress, which could be greatly reduced by lowering the cooling rates associated with high maximum temperature. The LDBT was measured before and after this lower temperature cycling, and LDBT increases of up to 1.3 were measured in the bulk. In this study, heat rates of 8°C/min and cooling rates of approximately 40°C/min were used, and samples were held at 450°C for approximately 20 min.

The LDBT for front (entrance) surfaces were also compared before and after treatment with the low temperature cycle (450°C max). The LDBT of the cleaved surfaces was increased by as much as a factor of 4, and the damage morphology was influenced by the heat treatment. The front-surface damage morphology for untreated, cleaved NaCl is seen in figure 2. Damage is predominantly in the form of fracturing (from near surface to bulk). Damage on the same sample after treatment is shown in figure 3; LDBT is four times greater. The damage is primarily a plasma-produced pit, with a circular plasma-etched region about the central pit. In figure 4, the damage morphology for polished, untreated NaCl is seen to be a combination of plasma pitting, plasma etching, and fracturing (at or near the surface). Contrasted in figure 5 is the same sample after heat treatment, where the damage is typically a plasma-produced pit surrounded by a plasma-etched disk. The disk can be seen in figure 6. No change in the LDBT was found in the polished samples. Cooling rates of up to 40°C/min were investigated for surface work with up to 80°C/min, used for the bulk. It is possible that there may be some increase in the LDBT for higher cooling rates. The lack of substantial change in the LDBT is an indication that removal of color centers is not associated with the previously referenced annealing process.

Measurements made using newly acquired NaCl and KCl from Harshaw have provided a new insight into the bulk LDBT. These materials were chosen because they have lower metallic-ion contamination. They also have a lower absorption for 10.6-μm radiation, attributed to the lower metallic-ion contamination. Quantitative information on the decreased metallic-ion contamination is unavailable due to proprietary considerations. The new samples were tested and their LDBT was found to be as high as that of conventional samples that have gone through the heat-treatment process. The new samples were put through the treatment process and retested; there was no change in the LDBT.

3. Laser-Induced Damage Measurements

The bulk laser-induced damage threshold of the specimens was measured before and after the heat treatment. The laser used in this work was a Nd:YAG laser operating at 1.06 μm with a pulse width of 9 nsec FWHM. The laser was constrained to operate in the TEM_{00} spatial mode by an intercavity aperture. The laser beam was focused onto the specimen by a 162-mm-focal-length lens used at $f/37$. The beam radius to the $1/e^2$ point in the intensity profile at the lens focus was calculated to be 26 μm using linear Gaussian optics. A more detailed description of this apparatus is given elsewhere [10].

The laser damage threshold was taken to be that power level which produced damage at 50% of the sites irradiated. Each site was irradiated only once, and care was taken to avoid any visible defects in the crystal. We emphasize that only damage sites which exhibited the type failure which had previously been called intrinsic [1,2] were included in the threshold determination. These were sites which failed at the focal plane of the lens, at the peak of the pulse near threshold, and resulted in abrupt truncation of the pulse transmitted through the specimen.

The data from these measurements are summarized in table 1. The power values given are calculated from the measured energy and pulse width. The intensities listed are the peak on-axis intensities calculated using a focal radius of 26 μm, and the electric fields listed are the rms electric fields corresponding to the peak on-axis intensities. The absolute accuracy of the data is estimated to be ±20% in the intensity, and the relative uncertainties in the before and after numbers are given in table 1.

Table 1. Laser-induced damage threshold before and after heat treatment.

P_B is the threshold power defined to be the laser power which produced damage at 50% of the irradiated sites. I_B is the peak on-axis intensity calculated using the linear optics focal radius of 26 μm ($1/e^2$ radius of the intensity). E_B is the rms electric field corresponding to I_B. The relative uncertainties in the thresholds were ±3% before treatment and ±5% after treatment.

	P_B(kW)	$I_B(10^9$ W/cm^2)	$E_B(10^6$ V/cm)
Before heat treatment	68 ± 2	6.5 ± 0.2	1.3 ± .02
After heat treatment	315 ± 16	30.0 ± 1.5	2.7 ± .07

4. Summary and Discussion

The laser-induced damage threshold of single-crystal NaCl can be increased by rapidly cooling a crystal heated to near melt (796°C) at a rate of 40°C/min. The reasons for this improvement are known. Manenkov [3] has speculated that rapid quenching of samples heated to near melting prevents the precipitation of clusters of impurities which may act as initiation sites for electron breakdown. The results reported here for the samples with lower metallic impurity concentration are consistent with Manenkov's explanation. Untreated samples of lower metallic-ion concentrations were found to have a LDBT approximately equal to that of the treated conventional specimens. These samples have shown no change in their LDBT upon heat treatment.

5. References

[1] Bloembergen, N. Laser-induced electric breakdown in solids. IEEE J. Quantum Electron. QE-10; 375-386; 1974.

[2] Smith, W. L. Laser-induced damage in optical materials. Opt. Eng. 17; 489-503; 1978.

[3] Manenkov, A. A. New results on avalanche ionization as a laser damage mechanism in transport solids. Glass, A. J.; Guenther, A. H., ed. Proceedings of the 9th annual symposium on optical materials for high power lasers; 1977 October 4-6; Boulder, CO. Nat. Bur. Stand. (U.S.) Spec. Publ. 509; 1977 December. 455-464.

[4] Soileau, M. J. Frequency and focal volume dependence of laser-induced breakdown in wide band gap insulators. Ph.D. dissertation, University of Southern California, Los Angeles; 1979.

[5] Soileau, M. J.; Bass, M.; Klein, P. H. Frequency and focal volume dependence of laser-induced breakdown in wide band gap insulators. Bennett, H. E.; Glass, A. J.; Guenther, A. H.; Newnam, B. E., ed. Proceedings of the 11th annual symposium on optical materials for high power lasers; 1979 October 30-31; Boulder, CO. Nat. Bur. Stand. (U.S.) Spec. Publ. 568; 1980 July. 497-518.

[6] Van Stryland, E. W.; Soileau, M. J.; Smirl, A. L.; Williams, W. E. Pulse width and focal volume dependence of laser-induced breakdown. Phys. Rev. B 23; 1-8; 1981.

[7] Allen, S. D.; Braunstein, M.; Guiliano, C.; Wang, V. Pulsed CO_2 laser damage studies in RAP grown KCl. Glass, A. J.; Guenther, A. H., ed. Proceedings of the 6th annual symposium on optical materials for high power lasers; 1974 May 22-23; Boulder, CO. Nat. Bur. Stand. (U.S.) Spec. Publ. 414; 1974 December. 66-76.

[8] Harshaw Chemical Co., 6801 Cochran Road, Solon, OH 44139.

[9] Shulman, T. H.; Compton, W. D. Color centers in solids. New York: Macmillan & Co.; 1962.

[10] Soileau, M. J. Mechanism of laser-induced failure in antireflection-coated $LiNbO_3$. Appl. Opt. 20; 1030-1033; 1981.

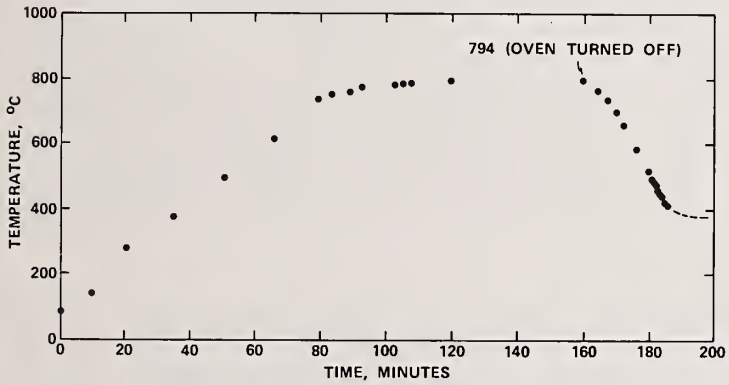

Figure 1. Temperature versus time of single-crystal NaCl. The specimen was heated in a nitrogen atmosphere. It was first brought up to 35°C for 10 min, then taken to 80°C for 187 min, and then heated as shown in the curve above.

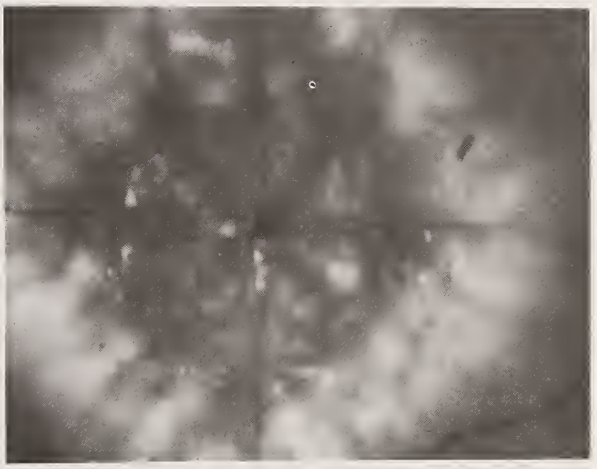

Figure 2. Laser damage at 1.06 μm on an untreated, cleaved NaCl surface.

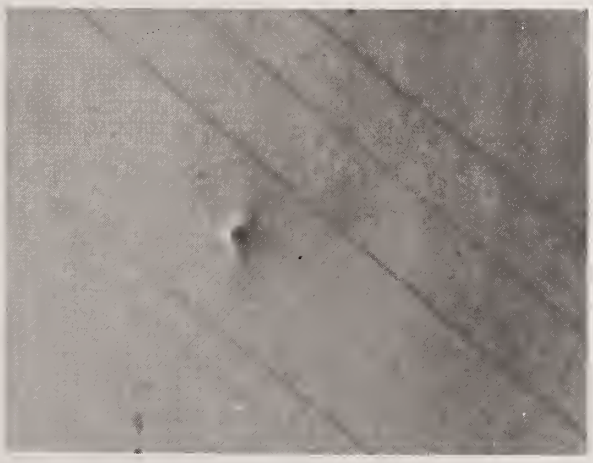

Figure 3. Laser damage at 1.06 μm on same surface shown in figure 2 after heat treatment. Note the marked change in damage morphology.

Figure 4. Laser damage at 1.06 μm on a polished, untreated NaCl surface.

20 μm

Figure 5. Laser damage at 1.06 μm on same surface shown in figure 4 after heat treatment. Note the marked change in damage morphology.

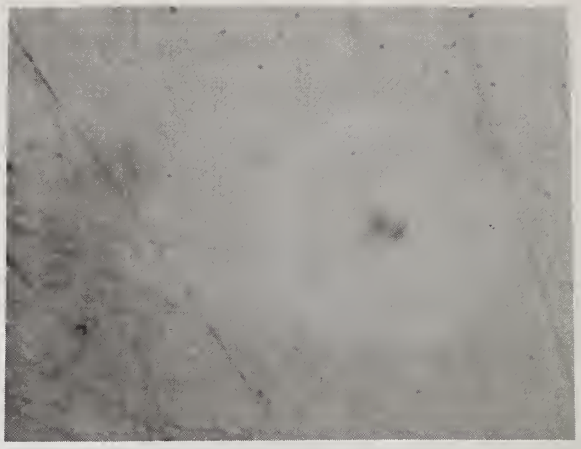

20 μm

Figure 6. Laser damage at 1.06 μm on same surface shown in figure 5 with different contrast to show that the extent of damage is approximately the same size as the untreated sample shown in figure 4.

The author, in response to a question, stated that the thresholds for the low ionic impurity samples were about the same as the thresholds after annealing for the high ionic impurity samples. Plasma was detected visually and also by hearing a loud snap.

Improving the Bulk Laser-Damage Resistance of KDP by Baking and Pulsed Laser Irradiation*

J. E. Swain, S. E. Stokowski, D. Milam and F. Rainer

Lawrence Livermore National Laboratory
P.O. Box 5508
Livermore, California 94550

Isolated bulk damage centers are produced when KDP crystals are irradiated by 1-ns 1064-nm pulses. We have tested about 100 samples and find the median threshold to be 7 J/cm^2 when the samples are irradiated only once at each test volume (1-on-1 tests). The median threshold increased to 11 J/cm^2 when the test volumes were first subjected to subthreshold laser irradiation (n-on-1 tests). We baked several crystals at temperatures from 110 to 165°C and remeasured their thresholds. Baking increased thresholds in some crystals, but did not change thresholds of others. The median threshold of baked crystals ranged from 8 - 10 J/cm^2 depending on the baking temperature. In crystals that had been baked, subthreshold irradiation produced a large change in the bulk damage threshold, and reduced the volume density of damage centers relative to the density observed in unbaked crystals. The data is summarized in the table.

Table Median 1-ns, 1064-nm bulk damage thresholds of KDP crystals tested as received and after baking. All crystals were tested by irradiating each site once (1 on 1 tests), and some sites on some crystals were conditioned by subthreshold shots and then repeatedly irradiated until damage occurred (n on 1 tests).

Baking temperature	Baking time	Median Damage Thresholds, J/cm^2 1 on 1 Tests	n on 1 Tests
unbaked	--	7	11
110°C	4 days	8	14
140°C	1 and 4 days	8	18
165°C	1 and 4 days	10	15

We measured damage thresholds on two KDP samples at pulse durations ranging from 1 nsec to 20 nsec and found they increase more slowly than $\sqrt{\tau}$. Baking and laser-hardening these samples also resulted in increased damage thresholds at all pulse durations.

Key words: bulk laser-damage, damage threshold improvement, potassium dihydrogen phosphate, pulse duration dependence of damage.

*Work performed under the auspices of the U.S. Department of Energy by the Lawrence Livermore National Laboratory under Contract No. W-7405-ENG-48.

1. Introduction

Potassium dihydrogen phosphate (KDP) and its isomorphs are widely used to generate harmonics of laser frequencies and as electro-optic materials. Systems employing these materials range from small commercial lasers and components to large lasers for inertial confinement fusion research. We and others,[1-3] have observed that the usable beam fluence in KDP and its isomorphs is limited by the occurrence of laser-induced bulk damage.

We have recently studied the resistance of KDP crystals to laser-induced damage by 1064-nm, 1-20 nsec pulses. We tested ~ 100 samples from five manufacturers. The bulk damage threshold fluences, shown in figure 1, range from 2 to 18 J/cm^2 at 1-nsec; the median is 7 J/cm^2. In all crystals, damage occurred at isolated centers in the bulk and the volume density of damage points was much greater than that of microscopically visible, pre-existing defects.

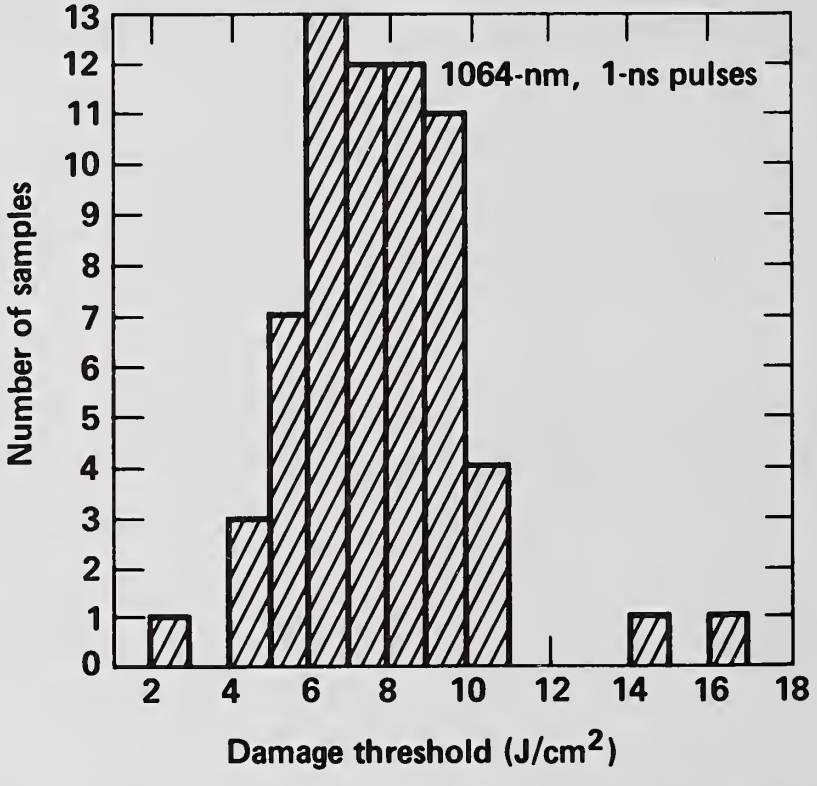

Figure 1. Histograms of the bulk laser-damage threshold fluence of 65 KDP samples from five manufacturers.

Although we have not identified the inclusions responsible for the observed bulk damage, we have observed two interesting and probably related effects -- the bulk damage threshold of KDP crystals can be increased by factors ranging from 1.5 to 5 by irradiating them with laser pulses at fluences below the single-shot threshold or by first baking the crystals and then laser irradiating them.

This paper describes the measurements and results of baking and laser hardening of ~ 30 KDP crystals at 1064-nm and 1-nsec and two KDP crystals at 1064-nm and 1, 3, 6, 9 and 20-nsec.

2. Observing Bulk Damage in KDP

In our measurements we used the laser damage facility at LLNL. A 6-m focal-length lens was used to converge the beam. The sample was placed at a point wher the beam diameter (e^{-2} in intensity) was ~ 2.5 mm. We employed a vidicon camera to record the beam profile, a calorimeter to measure the pulse energy, and a computer to calculate the corresponding peak fluence at the sample positon. An F14A biplanar photodiode and Tektronix 519 oscilloscope were used to determine the pulse duration. Our usual procedures for measuring thresholds was to irradiate several focal volumes once each at progressively higher fluences, until damage was observed. Before and after

each laser shot, we examined the irradiated volume using a collinear HeNe laser beam (~ 1 mm FWHM). The presence of preexisting inclusions or induced damage sites was detected by observing small angle forward scattering in the HeNe beam. The number of damage centers observed in the volume inspected (~ 0.01 cm^3) ranged from 1 to ~ 100. The density of damage sites for fluences two and one-half times the threshold fluences is 10^3 - 10^7 cm^{-3}. In most crystals we tested, the observed volume density of damage centers was > 100 cm^{-3}, and the procedure described above yielded a well-defined threshold fluence. In a few samples, however, site-to-site variations in damage resistance were observed.

3. Laser Hardening

We were concerned that the number and size of damage centers might increase under repeated irradiation and that damage might occur after many sub-threshold laser shots. Because of these concerns, we irradiated several focal volumes with many shots (n-on-1 tests). In general, if damage occurred on the first shot at a given fluence level, neither the size nor the number of damage centers increased upon further irradiation of that focal volume at the same fluence. Also, we never obtained damage by repeated sub-threshold irradiation of a given volume. In fact, we unexpectedly found that repetitive sub-threshold shots hardened the material against damage at fluences higher than the measured single-shot threshold fluence.

To study the effect of sub-threshold irradiation on a particular crystal, we first measured its single-shot threshold as described above. We then applied sub-threshold shots to undamaged focal volumes. Figure 4 demonstrates the increase in damage resistance obtained by low level irradiation of a crystal whose single shot threshold was 3.0 ± 0.3 J/cm^2 at 1064-nm and 1-nsec. We irradiated five volumes, indicated by arrows in figure 2.

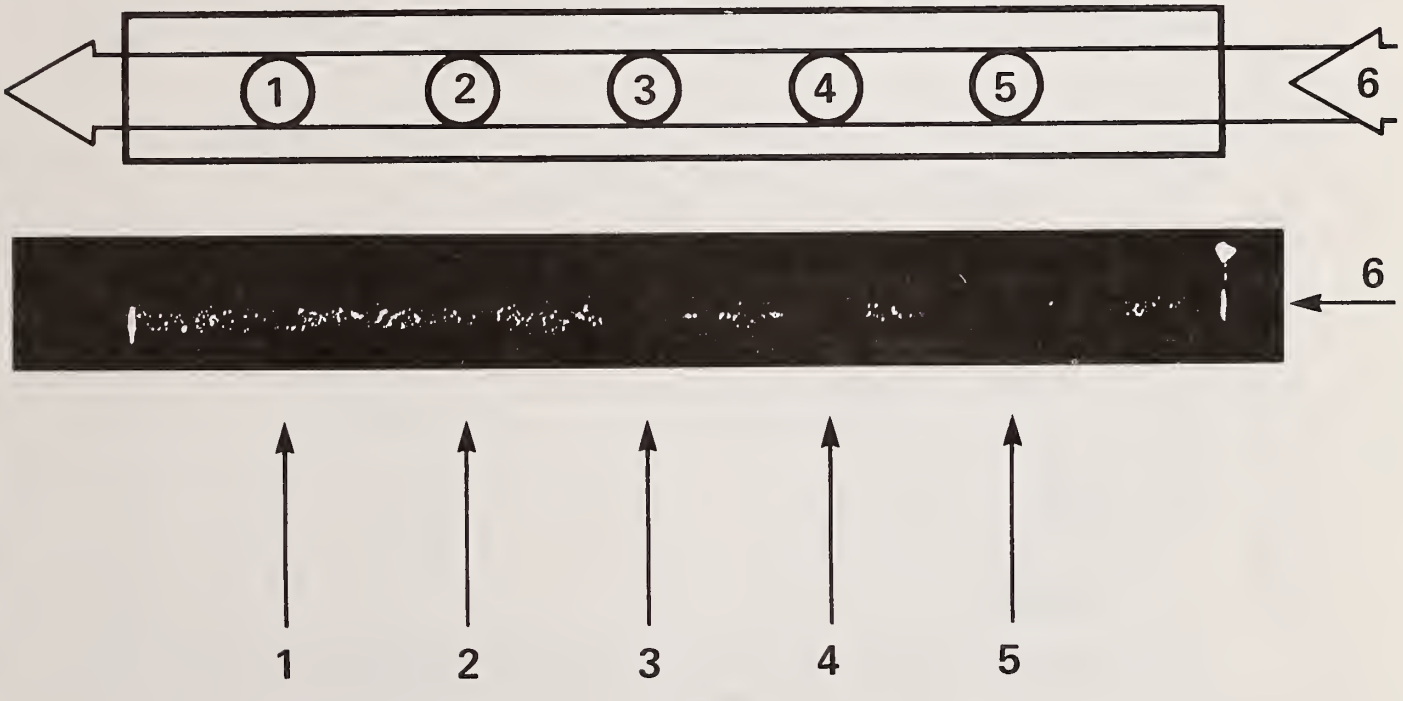

Figure 2. Demonstration of increased damage threshold resulting from pulsed laser irradiation of KDP.

The five volumes were irradiated with laser pulses as follows: volume 1, one shot; volume 2, two shots; volume 3, three shots, etc. The fluences are listed in table 1.

Table 1. Laser-hardening fluence data for the crystal whose damage photo is shown in figure 1.

	Fluence (J/cm^2) at 1064-nm and 1-nsec				
Shot/Volume	1	2	3	4	5
1	1.1±0.1	1.1±0.1	0.67±0.07	1.3±0.1	1.1±0.1
2		2.4±0.2	2.5 ±0.2	2.5±0.2	2.5±0.2
3			3.0 ± .3	2.8±0.3	3.1±0.3
4				3.9±0.4	4.9±0.5
5					5.3±0.5
Tranverse(6)		7.6±0.8 J/cm^2			

The sample was rotated 90°, and a damaging shot was taken across the pretreated volumes. The hardened volumes are clearly visible as gaps in the dense trail of damage sites.

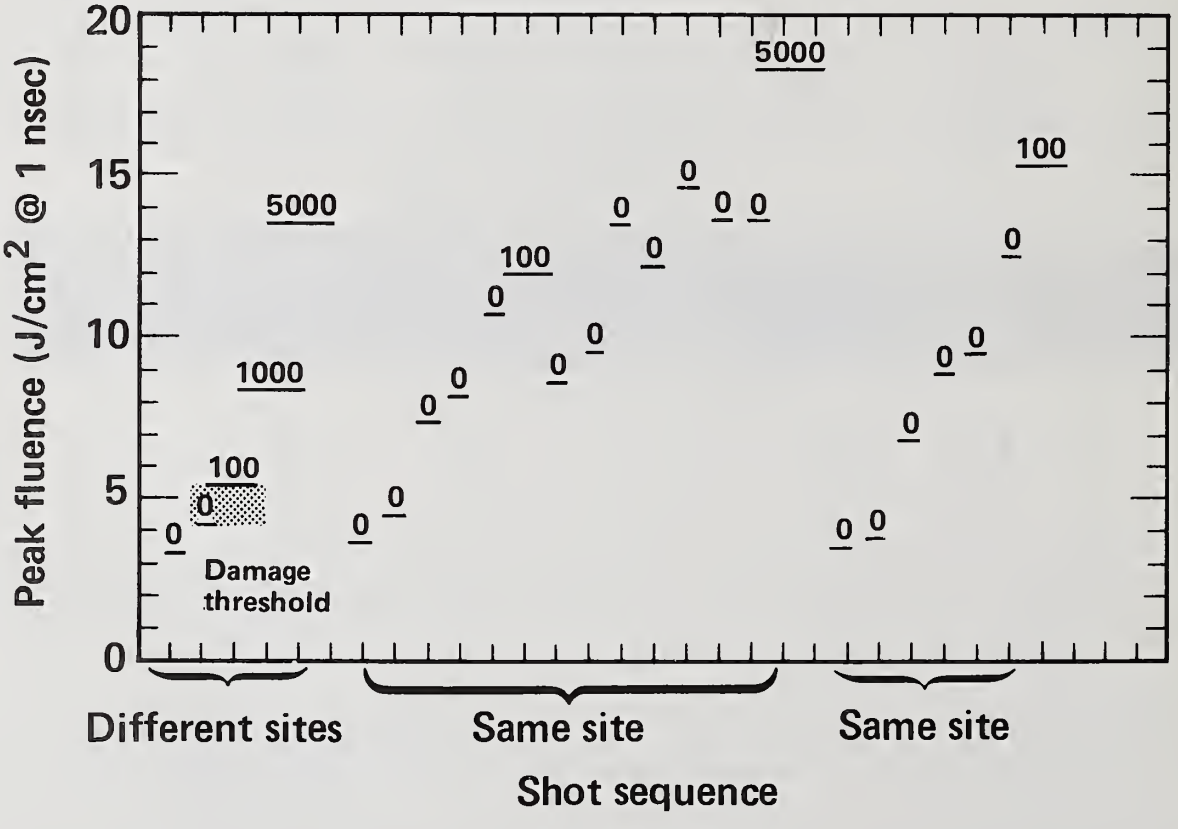

Figure 3. A comparison of 1-on-1 and n-on-1 laser irradiation of KDP, showing the increased damage resistance of multiply-irradiated sites.

In figure 3 we illustrate hardening in a second crystal. Each laser shot is represented by a bar that denotes the fluence level (± 10%) and a numeral giving the number of damage center per cm^3 caused by the shot (one damage center in the observed volume corresponds to approximately 100 cm^{-3}). In single-shot tests, no damage occurred below 4.2 J/cm^2, but damage centers were produced by each shot with fluence exceeding 5.3 J/cm^2. We then irradiated two sites with a sequence of shots beginning at fluences below the single-shot threshold. On the first of these sites, no damage occurred during five shots at fluence levels up to 10.5 J/cm^2. A single damage center was produced at 12 J/cm^2. The focal volume remained unaltered through seven additional shots, and then damaged ($\sim$ 50 centers) at 18 J/cm^2. The second site was undamaged by six shots at fluence levels up to 12.5 J/cm^2. On both sites, the damaging fluence was larger than the single-shot threshold, and when damage occurred the number of damage centers was much lower ($\sim 10^{-1}$) than obtained by single-shot irradiation at comparable fluence. The effect appears to be permanent at room temperature; over a period of a month we observed no degradation in the threshold values of hardened volumes.

In table 2, we give a comparison of single-shot (1-on-1) and laser-hardened (n-on-1) thresholds for 7 crystals from four manufacturers. In KDP samples with single-shot thresholds below the median, 7 J/cm^2 at 1-nsec, laser hardening raised the thresholds to above the median. In a few volumes of a few KDP crystals (e.g. sample 7 of table 2) whose single-shot thresholds were above the median, we were unable to improve the damage threshold by laser hardening. In most volumes of these same crystals, however, laser-hardening was successful in raising the threshold.

Table 2. The effects of laser hardening on unbaked KDP samples

Sample Number	Bulk Damage Threshold (1 nsec, 1064-nm)	
	1 on 1	n on 1
1	2.9 ± 1.0 J/cm^2	9.1 ± 0.9 J/cm^2
2	4.4 ± 0.9	9.0 ± 0.9
		11.1 ± 1.1
		16.1 ± 2.5
3	7.6 ± 1.4	11.4 ± 1.3
		16.1 ± 1.9
4	7.7 ± 0.7	11.8 ± 1.7
		13.2 ± 2.2
5	8.4 ± 0.8	14.2 ± 2.8
6	9.3 ± 1.2	9.2 ± 1.7
7	9.4 ± 0.9	8.9 ± 0.9
		12.7 ± 1.3
		13.9 ± 1.4

4. Combined Baking and Laser-Hardening

To investigate the hypothesis that the laser-hardening effect is thermal, we baked crystals at 110°C, 140°C and 165°C. We determined the damage threshold of these crystals, then laser-hardened and again damage tested them. The maximum baking temperature, 165°C, was chosen to be safely below the 180°C temperature at which KDP undergoes an irreversible transition to a different crystalline state. The transition results in internal fracture and a milky appearance.

The results of the measurements are presented as histograms in figure 4. Damage threshold fluences obtained before the crystals were laser hardened are indicated by open squares, and those obtained after hardening by solid squares. The baking temperatures (± 5°C) are indicated in the upper left hand corner of each histogram. Median values are denoted by an "M".

Figure 4a presents the data of table 3 plus other data. Figure 4b, 4c and 4d are histograms of the damage thresholds of those crystals heated to 110°C, 140°C and 165°C respectively. Included in all of these latter three histograms are thresholds of crystals baked for 24 hours and for 96 hours. Use of different baking times did not produce any obvious difference in the crystals.

Table 3 presents individually the data shown graphically in figures 4b, 4c and 4d. The monotonic increase of the median threshold with baking temperature was the result of slight improvements in some crystals and larger increases in others. For all crystals, laser hardening produced an increase in threshold that was larger than that obtained by baking alone.

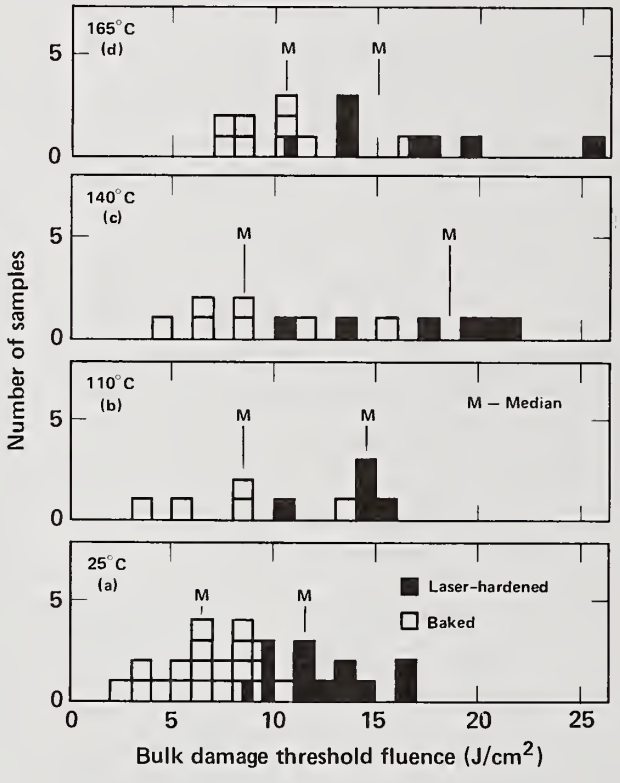

4a

4b

4c

4d

Figure 4. Histograms of the bulk laser-damage threshold of KDP: a) as grown before and after laser-hardening b) baked at 110°C for 24 hours, c) baked at 140°C for 24 and 96 hours and d) baked at 165°C for 24 and 96 hours.

We also observed that baking resulted in fewer damage centers at the same multiple above the single-shot threshold and that the damage centers were smaller.

To see if baking caused any deterioration in harmonic generation, we determined the second harmonic generation parameters of a KDP crystal before and after baking at 165°C for 24 hours; we observed no change.

Table 3. The effects of baking and laser hardening on the bulk damage threshold of KDP.

	Bulk Damage Threshold (J/cm^2 @ 1-ns, 1064-nm)						
Sample Number	Single Shot Threshold	110°C	Laser Hard. 110°C	140°V	Laser Hard. 140°C	165°C	Laser Hard. 165°C
1	3.2±0.3	8.0±1.2	14.4±1.7				
2	3.3±0.5	3.8±0.7	10.9±1.1	4.3±0.4	13.7±1.4	7.6±1.3	10.0±1.3
3	5.0±0.5			7.4±0.7		16.2±1.7	25
4	5.2±0.5	5.9±0.6	15.2±1.6	6.9±0.8	10.8±1.3	8.6±1.0	13.3±2.0
5	6.4±1.3			8.7±0.9	17.2±4.1	10.9±1.6	13.9±1.4
6	6.6±0.7			8.6±1.1	19.3±4.4		
7	6.9±1.0			15.1±2.0	20.4±2.0		
8	6.9±0.7					7.2±0.7	13.2±1.3
9	8.5±1.0					11.3±1.1	17.4±1.7
10	8.5±0.8					8.5±0.9	
11	8.7±0.9	13.0±1.3	14.5±1.6	11.7±1.2	21.3±3.7		
12	9.7±1.0	8.1±0.8	14.3±2.6			10.2±1.0	16.5±1.7
13	10.0±1.0					10.3±1.3	19.9±3.3

Because KDP has a low decomposition temperature, we suspected that the damage threshold might be temperature sensitive. Therefore, we determined the 1-on-1 damage threshold of a KDP crystal at room temperature, 18°C, and at 85°C. The thresholds were 6.9 J/cm^2 and 4.7 J/cm^2, respectively. Extrapolating these two data points indicates decompositon at 220°C, close to the reported decomposition temperature.

5. Pulse Duration Dependence

We tested two KDP samples at 1, 3, 6, 9 and 20-nsec with 1064-nm pulses. One sample (number 2) had an average bulk damage threshold (7.4 J/cm^2) at 1-nsec, while the other (number 1) was below average (3.1 J/cm^2). Each sample was tested at the five pulse durations before baking or laser-hardening, then laser-hardened and retested. They were then baked at 140±5°C for 24 hours and retested. They were laser-hardened and again damage tested. The data from these tests are presented in figure 5, where a $\sqrt{\tau}$ curve is compared to each set of data for reference. The upper error bars indicate the lowest fluence at which damage was observed, and the lower error bars the highest fluence at which no damage was seen. In cases where the "damage" and "no damage" fluences were closer than 10% of the average of the two, the error bars are 10% of the average, which is the system fluence measurement accuracy.

The data for the below average crystal is presented in figure 5a. The scatter in the 1-on-1 data is probably due to nonuniformity in the crystal. In the n-on-1 tests, the scatter can be due to both crystal nonuniformity and variations in the laser-hardening sequence.

In figure 5a, the n-on-1 data, before and after baking are within the range of uncertainty of each other. Although the effect of baking on the 1-on-1 tests is definite, laser-hardening efficiently heats whatever would have damaged in the crystal and little or no further improvement by baking is evident in this crystal.

Figure 5b shows the dependence of threshold on pulse duration, baking and laser-hardening for the average-damage-threshold crystal. Even though the original damage threshold of this crystal is higher than the below average crystal, the final "baked and laser-hardened" data are at nearly the same level.

In the eight sets of data presented in figure 5 a straight line fit would have a slope less than one-half in all cases. Since the data is concerned with just two samples and relatively few determinations on each sample, there are few pulse duration dependence conclusions that can be drawn.

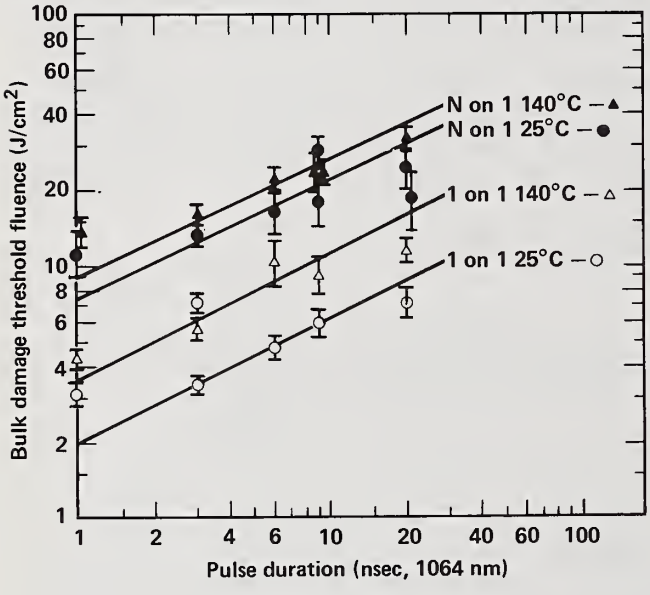

5a

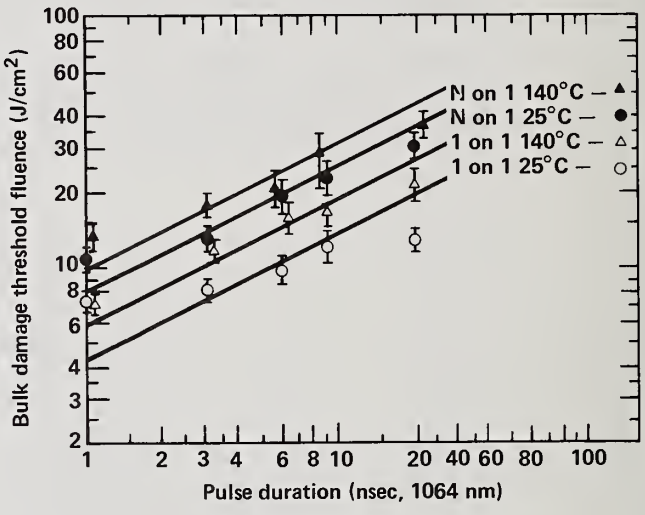

5b

Figure 5. Dependence of the KDP bulk damage threshold fluence on pulse duration: a) sample 1, b) sample 2.

6. Discussion

The demonstration that the bulk damage threshold of KDP can be increased by baking and sub-threshold laser irradiation is unambiguous, but the exact mechanism for the increase is unknown. Bulk damage in KDP at fluence of 2 - 20 J/cm^2 is likely due to extrinsic absorbing inclusions, such as bubbles containing KDP solution, impurities, metallic particles, and misoriented KDP microcrystallites. Unfortunately, the sites at which damage occurs are so small that we have been unable to observe or locate them prior to laser-damage. Identification of the absorbers has, therefore, not been made, and hypotheses about the hardening or baking process, including such mechanisms as changes in structure, chemistry, or valance of impurities, are speculative at best.

7. Conclusions

The bulk damage threshold of KDP can be increased from 1.5 to 5 times its single-shot threshold fluence by a combination of baking and sub-threshold irradiation. The degree of improvement depends upon the individual crystal. From our data, we recommend the following threatment procedure to produce a more damage resistant KDP component:

1) Bake the crystal at 140^{o}C for at least 24 hours (with an ~ 24 hour cool down period to prevent fracture)

2) Initially irradiate the crystal at no more than 3 GW/cm^2 at 1-nsec or .5 GW/cm^2 at 20-nsec.

3) Irradiate with fluence increasing ~ 1.5 GW/cm^2 at 1-nsec or ~ .25 GW/cm^2 at 20-nsec until a fluence just below the operating fluence is reached.

Although the baking temperature and baking duration do not seem to be critical, the initial fluence and the details of the laser-hardening sequence are. Figure 6 illustrates this point. The sequence on site number 1 was disrupted by an unusually large laser output resulting in a jump from 13 J/cm^2 to almost 21 J/cm^2 and one damage center. At the second site an evenly spaced sequence resulted in no damage until almost 36 J/cm^2. Even here, the last two shots in the sequence were separated too widely. Some of the effect seen in this figure may be due to the non-uniformity of the crystal, but in general the details of the laser hardening sequence are important.

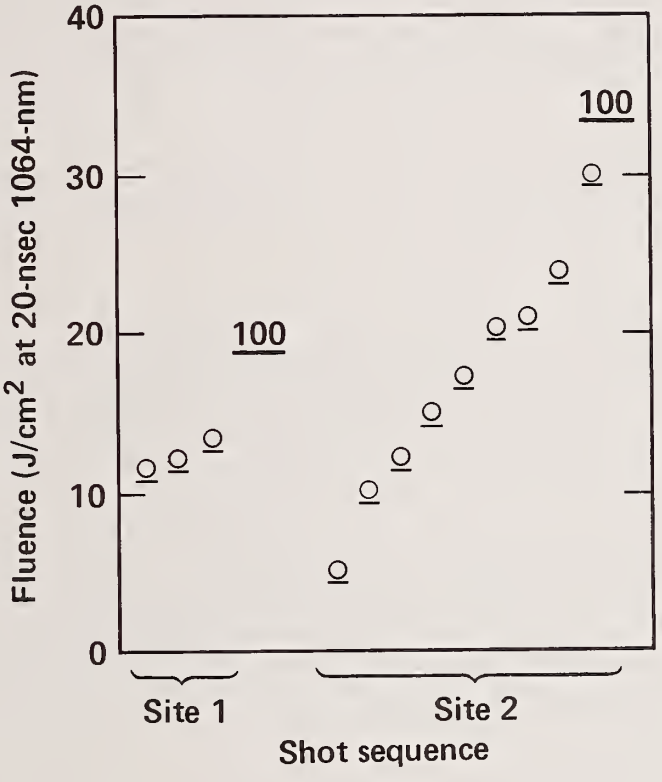

Figure 6. The effect of fluence step size in laser-hardening of a KDP crystal; 1064 nm, 20 nsec.

8. References

[1] Endert, H.; Hattenback, A; and Mello, W. Influence of the real structure of KDP crystals on their optical structure. Sov. J. Quant. Elect. 7: 1516-18; 1977.

[2] Batyreva, I. A.; Bespalov, V. I.; Kiselev, A. M.; and Miller, A. M. Characteristics of laser pulse damage to water-soluble nonlinear crystals. Sov. J. Quant. Elect. 8: 1044-46; 1978.

[3] Wood, R. M. Laser damage in optical materials at 1.06 m. GEC Journal of Science and Technology 45: 109-115; 1979.

In response to a question, the author stated that the surface damage threshold increases along with the bulk threshold as the material is cleaned up. Also, the relative efficiency of laser annealing vs. baking seems to vary from crystal to crystal. The baking or annealing was done by putting the crystal in the oven, raising it to temperature in about two hours, holding it at temperature for 24 hours or so, and then turning the oven off and letting it come down to room temperature. Typically the return to room temperature took about 24 hours. Attempts to characterize the sample microscopically or by using thermographs failed to reveal correlations with damage threshold. There is no change in threshold for at least 30 days after treatment, and the effect appears to be permanent.

Surface-to-Bulk Optical Absorption on Uncoated Sapphire and Zinc Selenide Using Photoacoustic Chopping Frequency Studies

Nils C. Fernelius

University of Dayton Research Institute
Dayton, Ohio 45469

Experimental photoacoustic (PA) signal amplitude and phase angle data were taken on uncoated CVD ZnSe at 10.6 μm and on (0001) oriented single crystal sapphire (Al_2O_3) at 1.3 μm. The data were interpreted using the Rosencwaig-Gersho theory, the McDonald-Wetsel composite-piston model and the Bennett-Forman theory. A modified version of the Rosencwaig-Gersho theory was developed which explicitly incorporates surface absorption. It was also applied to these cases. Comparisons are made with some multithickness sample studies on related materials.

Key words: Al_2O_3; Bennett-Forman theory; CO_2 laser; McDonald-Wetsel theory; Nd:YAG laser; optical absorption coefficient; optoacoustic; photoacoustic; Rosencwaig-Gersho theory; sapphire; surface optical absorption; ZnSe.

1. Introduction

Some previous work [1-3] [1] on the photoacoustic (PA) chopping frequency dependence in zinc selenide was complicated by an antireflective coating on the surface. Thus the experiment was repeated on some uncoated CVD ZnSe samples. Since the PA theories we are comparing were derived for uncoated samples, a better comparison with theory and experiment can be made.

At last year's meeting there was considerable discussion about the amount of surface optical absorption in sapphire (Al_2O_3). Here we present the results of some experiments on (0001) oriented Crystal Systems, Inc. single crystal sapphire.

There are a variety of theories of the photoacoustic signal based on slightly different assumptions. We compare results with the Rosencwaig-Gersho theory [4,5], the Bennett-Forman theory [6], and the McDonald-Wetsel composite-piston model [7]. In a previous analysis it was pointed out that the Rosencwaig-Gersho theory did not consider the surface optical absorption. Here we derive a modified version of the Rosencwaig-Gersho theory which explicitly includes surface absorption. Calculations were made using the four theories for Al_2O_3 and ZnSe and compared with experiment.

2. Experimental Results

All the sapphire data were taken using a Quantronix 114 Nd:YAG laser fitted with special mirrors to operate at 1.319 μm. This approximates the wavelength of the iodine laser at 1.315 μm. The power entering the cell was about 4 W. Laser rate calorimetry was performed on the two sapphire samples which form the entrance and exit windows of the photoacoustic cell. The gas in the cell was air. With the window dimensions used, laser calorimetry measures the quantity [8], $\beta_{eff} = \beta_B + 2\beta_s/\ell$ where β_{eff} is the effective optical absorption coefficient, β_B is the bulk optical absorption in cm^{-1}, β_s is the dimensionless surface absorption, and ℓ is the window thickness. This equation neglects possible exit surface enhanced absorption. This topic has been discussed elsewhere [9]. The average value of the two windows is $\beta_{eff} = 0.745 \times 10^{-3} cm^{-1}$.

The PA data were taken using a Princeton Applied Research (PARC) Model 192 variable frequency light chopper, a GenRad 1961 9601 electret condenser microphone, an Ithaco 167 preamplifier and a PARC 5204 lock in analyzer. As the chopper frequency was varied, the lock in phase was set to yield zero quadrature signal. Then the amplitude and phase setting were recorded. The laser shutter was closed and any signal or quadrature amplitude were recorded at that phase setting, so coherent

[1] Figures in brackets indicate the literature references at the end of this paper.

noise corrections [11] could be made. Further details are given in Reference 11. The PA amplitude versus frequency data could be fit to an expression $S = A f^{-n}$ where f is the chopping frequency. On the first day n = 1.10; on the second, n = 1.07. The phase angle data have considerable noise so that any reading has an error of ±2°-3°. The results are given in Table 1.

Table 1. Experimental Phase Angle Data in Degrees on Sapphire

ϕ	50 Hz	100 Hz	500 Hz	1000 Hz
Run 1	65	58	48	46
Run 2	64.5	57.5	50	49

Similar measurements were made on uncoated CVD ZnSe using a Coherent Radiation Model 40A CO_2 laser operating at 10.6 μm. The estimated power level entering the PA cell was 24 W. Laser calorimetry yielded an average $\beta_{eff} = 2.96 \times 10^{-3} cm^{-1}$. Amplitude data fits yielded n = 1.04. The phase angle changes rapidly from 50 Hz to 150 Hz with a change of about 12° then levels off. More details are given in Reference 12.

3. Theoretical Calculations

All the theoretical programs require the input of thermal parameters for the gas in the PA cell as well as sample parameters. The parameters used for the cell gas were those for N_2 at STP. The values used were the density $\rho_g = 0.00129$ g/cc, the specific heat $C_g = 0.718$ J/gK and thermal conductivity $\kappa_g = 0.000261$ W/cmK. The ambient temperature was taken as 300 K. The values for synthetic sapphire Al_2O_3 are as follows: Density, $\rho_s = 3.98$ g/cc; specific heat, $C_s = 0.75$ J/gK; thermal conductivity, $\kappa_s = 0.230$ W/cmK; coefficient of linear thermal expansion, $\alpha_T = 4.99 \times 10^{-6} K^{-1}$; sample thickness, $\ell_s = 0.78$ cm. The values used for CVD ZnSe were: density, $\rho_s = 5.27$ g/cc; specific heat, $C_s = 0.355$ J/gK; thermal conductivity, $\kappa_s = 0.170$ W/cmK; coefficient of linear expansion, $\alpha_T = 7.80 \times 10^{-6} K^{-1}$; sample thickness, $\ell_s = 0.790$ cm.

The thermal diffusivity of a sample, $\alpha = \kappa/\rho C$. Rosencwaig- Gersho [4,5] define a thermal diffusion length of a sample, $\mu_s \equiv \sqrt{2\alpha_s/\omega} = \sqrt{\kappa_s/(\pi \rho_s C_s f)}$. Some values are shown in Table 2.

Table 2. Thermal and Optical Diffusion Length Values

Material	μ_s in cm		μ_B in cm
	1 Hz	1000 Hz	
sapphire	0.157	0.005	1400
CVD ZnSe	0.170	0.0054	250

Thus for all samples studied here we have the condition $\mu_s < \ell_s$, i.e. a thermally thick solid. The optical absorption length $\mu_B \equiv 1/\beta$. In both cases $\mu_B > \ell_s$ so we are in the optically transparent regime.

3A. Results of Rosencwaig-Gersho Theory Calculations

Calculations were made using a complex number FORTRAN IV program which computes the combination of Eqs. (17) and (21) of Ref. [4] which is quite complicated. In the previous section we saw that we are in the optically transparent and thermally thick regime which is Case 1c of Rosencwaig. Thus the PA signal is proportional to S, where

$$S = -\frac{(1+j)\beta_B}{C_s \rho_s \omega^{3/2}} \qquad (1)$$

where $\omega = 2\pi f$.

For both ZnSe and Al_2O_3, the program yielded PA signals with amplitudes proportional to $f^{-1.5}$ and a phase angle at 45° from 1 Hz to 10 kHz. This agrees with Case 1c but not with experiment.

3B. Derivation of the Rosencwaig-Gersho Theory Modified to Include Surface Absorption

The Rosencwaig-Gersho theory [4,5] does not include the extra surface optical absorption which may be appreciable in the infrared. A derivation which incorporates it into the theory is given here. The derivation follows that presented in pp. 93-103 of Reference [5]. With coherent light there are various theories for enhanced surface absorption at the exit face of a window [9]. In the derivation we shall denote absorption at the entrance face (x=0) as β_{s_1} and at the exit face (x=-ℓ) as β_{s_2}. Thus when one has valid reasons for the amount of enhancement, it can be readily included.

Equation (9.3) of Ref. 11 should now read

$$\frac{\partial^2 \Theta}{\partial x^2} = \frac{1}{\alpha}\frac{\partial \Theta}{\partial t} - A\, e^{\beta x}(1+e^{j\omega t}) - \frac{I_o}{2\kappa}(1+e^{j\omega t})\left[\beta_{s_1}\delta(x)+\beta_{s_2}(1-\beta_{s_1})e^{-\beta\ell}\delta(x+\ell)\right] .$$

Where the Kronecker δ functions have the dimensions of the reciprocal of their arguments, viz. cm^{-1}. With this change, Eq. (9.4) of Ref. 5 should now read

$$A = \frac{\beta(1-\beta_{s_1})I_o\eta}{2\kappa}$$

and thus Eq. (9.10) is

$$E = \frac{\beta(1-\beta_{s_1})I_o}{2\kappa(\beta^2-\sigma^2)}$$

Since the various solutions of Ref. 5, Eq. (9.8) are for various regions within or outside of $-\ell \leq x \leq 0$, the most appropriate place to incorporate these surface absorptions is in the boundary conditions at x=0 and x=-ℓ. The continuity equations for heat flux require that Eq. (9.11c) be modified to

$$\kappa' \frac{\partial \Theta'(0,t)}{\partial x} = \kappa \frac{\partial \Theta(0,t)}{\partial x} - \beta_{s_1} I_o \frac{(1+e^{j\omega t})}{2}$$

and Eq. (9.11d) to

$$\kappa'' \frac{\partial \Theta''(-\ell,t)}{\partial x} = \kappa \frac{\partial \Theta(-\ell,t)}{\partial x} - \beta_{s_2} I_o (1-\beta_{s_1}) e^{-\beta\ell}\frac{(1+e^{j\omega t})}{2}$$

These equations can be solved to yield

$$\Theta_0[(b+1)(g+1)e^{\sigma\ell} - (b-1)(g-1)e^{-\sigma\ell}] = [(r-1)(b+1)e^{\sigma\ell}-(r+1)(b-1)e^{-\sigma\ell}+2(b-r)e^{-\beta\ell}]E$$

$$- \frac{I_0}{2\kappa a(1+j)} \left\{ \beta_{s_1}[(b-1)e^{-\sigma\ell}- (b+1)e^{\sigma\ell}] + 2\beta_{s_2}(1-\beta_{s_1})e^{-\beta\ell} \right\} \qquad (2)$$

Further details of the solution are in Ref. 12. Note if we let $\beta_{s_1} = \beta_{s_2} = 0$, we have Eq. (9.14) of Ref. 5.

In the approximations for Case 1c of Rosencwaig [4,5] we now have

$$S = - \frac{j\sqrt{2}}{\omega(g+1)\sqrt{\kappa_s \rho_s C_s}} \left[\beta_{s_1} + (1-j)\beta(1-\beta_{s_1})\sqrt{\frac{\kappa}{2\omega\rho_s C_s}} \right] \qquad (3)$$

With $\beta_{s_1} = 0$ and remembering that $g \ll 1$, this is the same as Eq. (1).

3C. Results of Calculations Using the Rosencwaig-Gersho Theory Modified to Include Surface Absorption

A complex number FORTRAN IV computer program was written with $\beta_{s_1} = \beta_{s_2} = \beta_s$ which calculates S incorporating the expression for temperature given in Eq. (2).

Experience [1,2,13] has shown that theoretical phase angle values are more sensitive to variation in PA parameters than amplitude values. One problem with experimental phase angles is to determine the zero of the phase angle scale due to phase shifts introduced by amplifiers and other experimental conditions. Often the experimental phase angle should be compared with 360°-Θ calculated. One way to avoid these difficulties is to consider phase angle differences. From the computer calculations the phase angle difference, $\Delta\phi = \phi_{f_1} - \phi_{f_2}$, was obtained where f_1 was 500 and 1000 Hz and f_2 was 50 and 100 Hz. Often the crucial parameter is the surface to bulk optical absorption ratio, $r \equiv \beta_s/\beta_B$ in cm. Figures 1 and 2 exhibit phase angle differences versus r or β_s for sapphire and ZnSe. From these plots one can pick values of r which agree with experiment. Sometimes two values of r agree. Past experience has shown that the smaller value does not yield amplitude plots which agree with experiment. From the sapphire plot (Figure 1) we conclude that r lies between 0.02 and 0.012; from the ZnSe plot (Figure 2), β_s lies between 0.000042 and 0.0425 ($0.00105 \leq r \leq 0.0425$).

Using these values as a guide, amplitude and phase angle plots versus chopping frequency were made. Figures 3 and 4 show the results for sapphire. Straight lines can be drawn through the low frequency and high frequency regions of the plots indicating that the signal amplitude S has the form $S = A f^{-n}$. The frequency at which these two lines intersect can be designated as a crossover frequency, f_c, dividing the two regions. Table 3 lists these values. The experimental values of n=1.10 and n=1.07 are most closely fit by the r=0.02 cm value. Considerations of the angle plots shows that r=0.01 cm seems to fit a bit better. Figures 5 and 6 show similar plots for ZnSe. A similar analysis, given in detail in Reference [2], shows that the experimental values of n=1.04 in the amplitude plots is best fit for r=0.025 cm.

3D. Results of Calculations Using the McDonald-Wetsel Composite-Piston Theory

McDonald-Wetsel [7] extend the Rosencwaig-Gersho theory [4] to include mechanical vibration of the sample. They present three versions of the theory. The complete coupled equations for acoustic wave motion and thermal diffusion are presented and solved numerically. This version they call MW2. Assuming no acoustic wave in the sample, the equations can be solved - Version MW1. Under certain conditions a composite-piston model is shown to be equivalent to MW2. One of these conditions is that of the thermally thick sample we have here. Calculations were made using Eq. 41

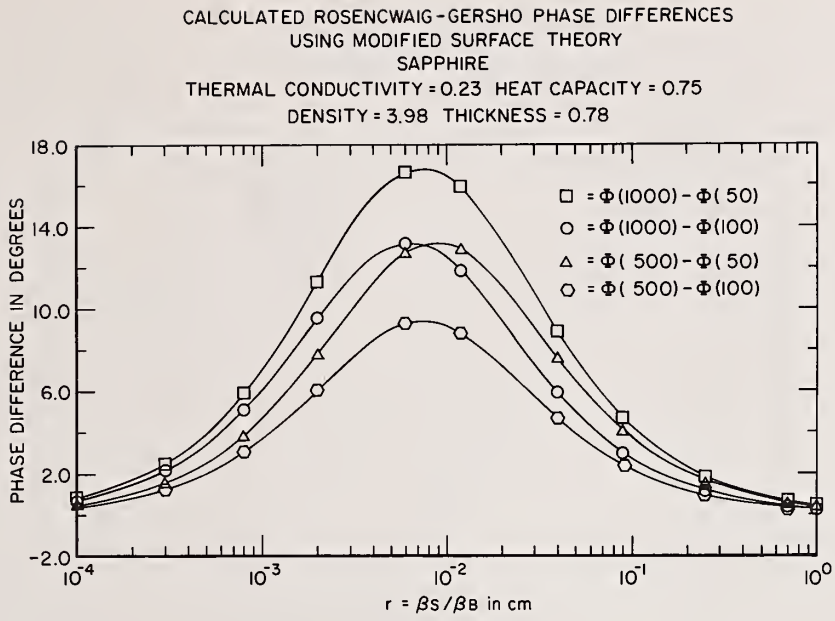

Figure 1. PA phase angle differences versus surface-to-bulk optical absorption ratio. $r \equiv \beta_s/\beta_B$. These were calculated using the Rosencwaig-Gersho theory modified for surface absorption for 0.78 cm thick sapphire.

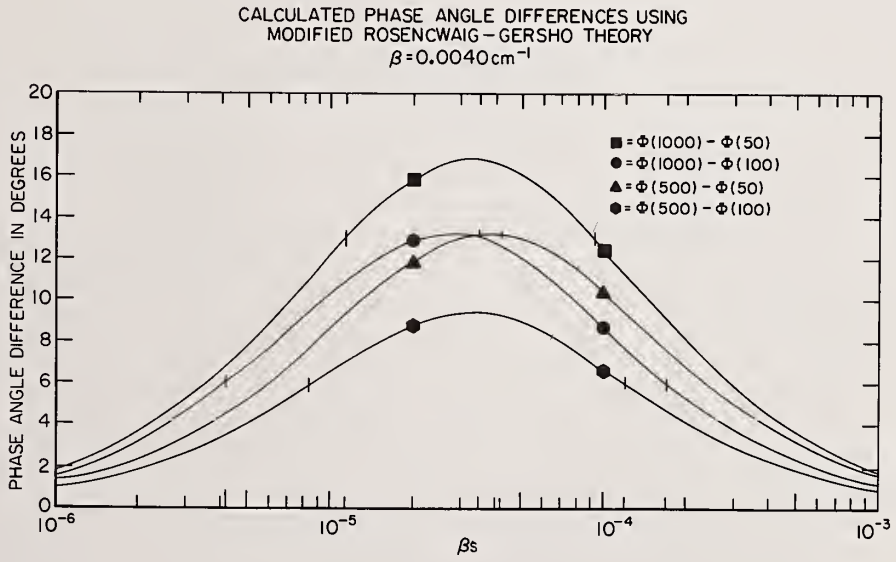

Figure 2. PA phase angle differences versus surface absorption, β_S. These were calculated using the modified Rosencwaig-Gersho theory with β=0.004 cm^{-1}, ℓ=0.79 cm and CVD ZnSe parameter values.

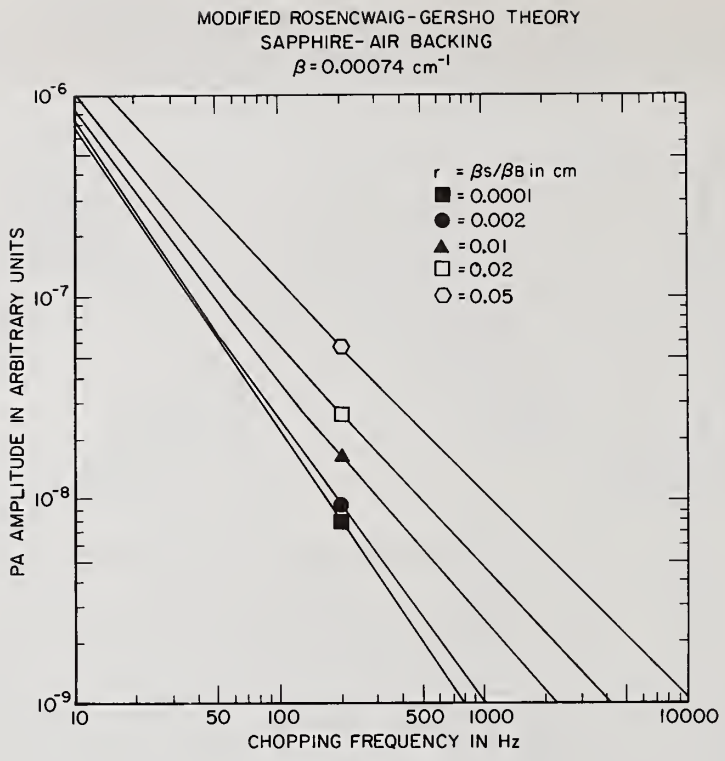

Figure 3. PA signal amplitude for sapphire versus chopping frequency for various values of surface-to-bulk optical absorption ratio, $r=\beta_S/\beta_B$. The amplitudes were calculated using the modified Rosencwaig-Gersho theory.

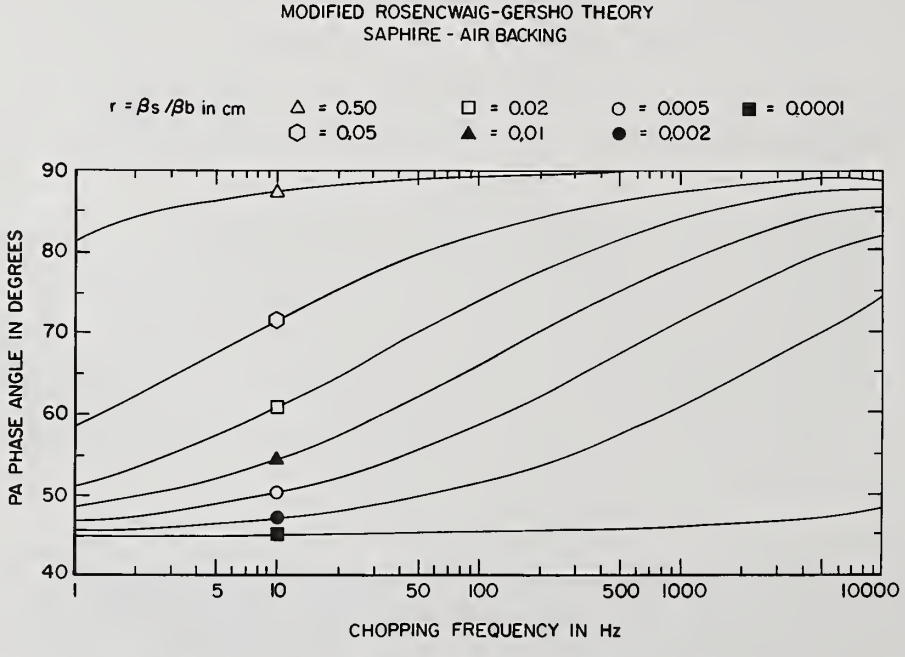

Figure 4. PA signal phase angles for sapphire versus chopping frequency for various values of r. Angles were calculated using the modified Rosencwaig-Gersho theory.

Table 3. Fits of the Modified RG Theory PA Amplitudes for Sapphire to $S=A f^{-n}$

$r = \beta_s/\beta$ in cm	n low f	f_c in Hz	n high f
0.0001	1.50	-	1.50
0.002	1.51	35 ± 15	1.40
0.01	1.37	100 ± 10	1.14
0.02	1.30	85 ± 10	1.08
0.05	1.11	200 ± 50	1.02

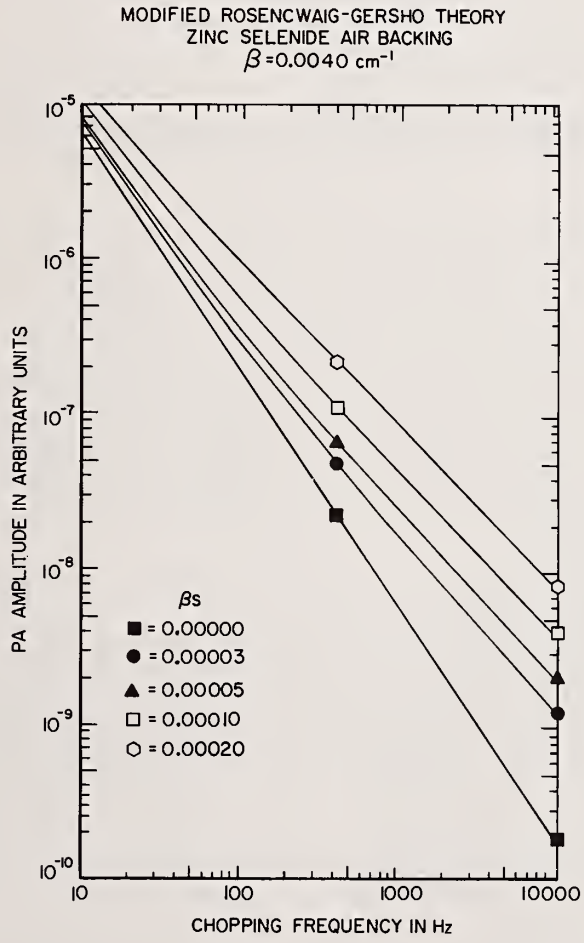

Figure 5. PA signal amplitude for CVD ZnSe versus chopping frequency for various values of surface absorption β_s. The amplitudes were calculated using the modified Rosencwaig-Gersho theory and $\beta=0.0040\ cm^{-1}$.

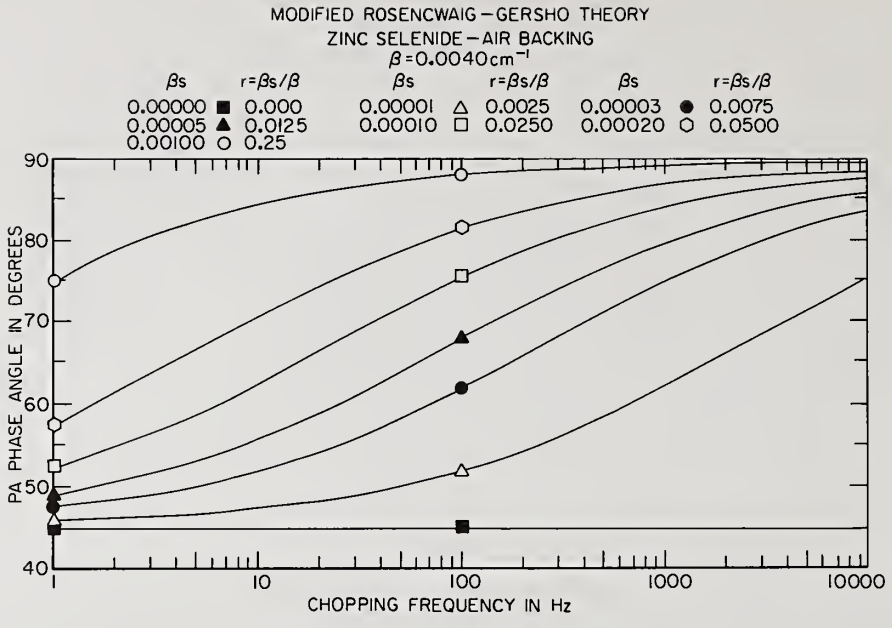

Figure 6. PA signal phase angles for CVD ZnSe versus chopping frequency for various values of r. Angles were calculated using the modified Rosencwaig-Gersho theory.

of Ref. [7]. This can be written as

$$S = -\frac{j}{\omega\rho_s C_s}\left\{\frac{(1-j)}{\sqrt{2\omega}}\frac{\beta}{(1+g)(1+r)} + 3\alpha_T T_o\left(\frac{\rho_g C_g}{\kappa_g}\right)^{\frac{1}{2}}(1-e^{-\beta\ell_s})\right\} \quad (4)$$

When $r<<1$, $g<<1$ and $\alpha_T=0$, we have the R-G results, Case 1c. Calculations using this expression yielded amplitude plots similar to those of R-G. There was considerably more angular variation than R-G but still less than seen experimentally. More details are in Ref. [11] for sapphire and Ref. [12] for ZnSe.

3E. Results of Calculations Using the Bennett-Forman Theory

The Bennett-Forman theory treats a PA cell in which the entrance and exit windows comprise the sample studied. This theory explicitly considers a dimensionless surface absorption designated as β_S as well as a bulk optical absorption, β_B in cm^{-1}. The gas in the cell is treated using linearized hydrodynamic equations. The final results include a thermal and an acoustic term. Bennett states that in the experimentally accessible region the acoustic term is dominant. Our FORTRAN program calculates Eq. (3) in Ref. [6]. Calculations were made verifying that the equation is valid.

In previous work [2] it was noted that all optical absorption information in that equation was contained in a bracket which can be written

$$\beta_B\{r + (1-j)[\kappa_s/2\rho_s C_s]^{\frac{1}{2}}\} \quad (5)$$

where $r\equiv\beta_S/\beta_B$. All phase angle information is contained is contained within the brackets of Eq. (5). The shape of all amplitude plots depends on r and is scaled by the value β_B. As in Section 3C plots of $\Delta\phi$ versus r were made. Figure 7 shows the phase difference plot for sapphire. Figure 8 for ZnSe. Comparing Fig. 7 with experiment, we conclude that r should be between

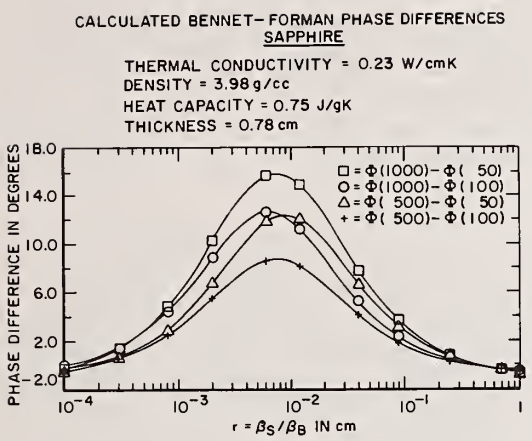

Figure 7. PA phase angle differences for sapphire versus surface-to-bulk optical absorption ratio, $r \equiv \beta_S/\beta_B$. The angles were calculated using the Bennett-Forman theory.

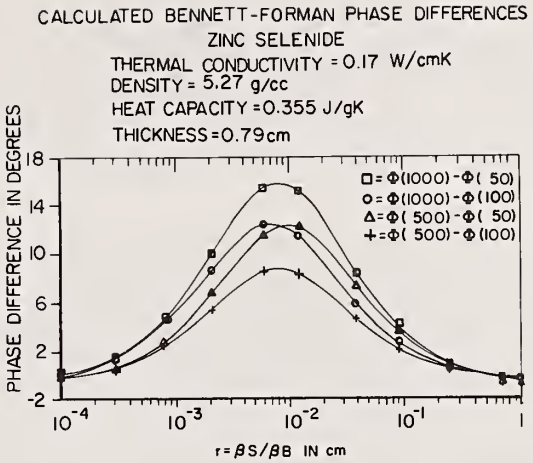

Figure 8. PA phase angle differences for CVD ZnSe versus surface-to-bulk optical absorption ratio r. The angles were calculated using the Bennett-Forman theory.

r=0.009 cm and r=0.025 cm. From the amplitude plots for sapphire, we conclude that r should be between 0.015 and 0.050 cm. The sapphire angle plot is shown in Figure 9. The curves for r= 0.075 cm and r=0.020 cm seem to be more like the experimental plots. More details are given in Ref. [11].

Comparing Fig. 8 with experiment, we conclude that r should lie between 0.019 cm and 0.037 cm for ZnSe. The amplitude plots seem to fit best for r between 0.025 and 0.050 cm. The phase angle plot is shown in Fig. 10. More details are given in Ref. [12].

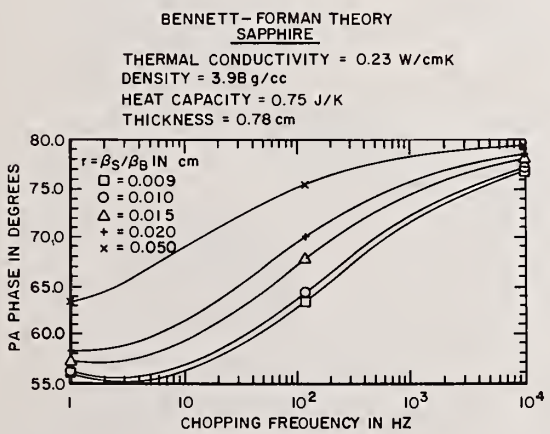

Figure 9. PA phase angles for sapphire versus chopping frequency. The angles were calculated using the Bennett-Forman theory.

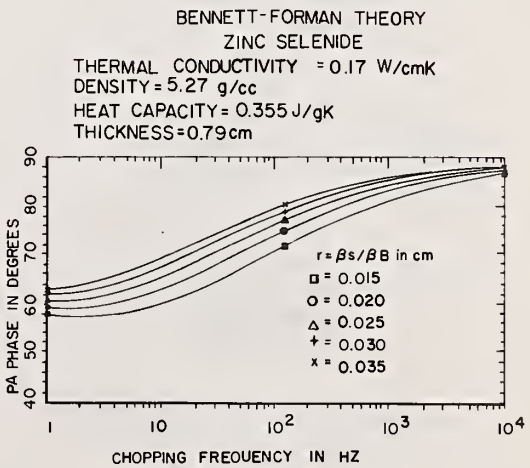

Figure 10. PA phase angles for CVD ZnSe versus chopping frequency. The angles were calculated using the Bennett-Forman theory.

4. Summary and Conclusions

4A. Sapphire, Al_2O_3, Summary

Photoacoustic data were taken at 1.319 μm wavelength and about 4 W power level as a function of chopping frequency on single crystal sapphire, Al_2O_3, windows. Plots of the experimental PA amplitude versus frequency could be fit to a $S=A\,f^{-n}$ dependence with n=1.10 and n=1.07. Somewhat noisy phase angle plots yielded a $\Delta\phi = \phi(1000)-\phi(100) = 12°$ and 8.5° and $\Delta\phi = \phi(500)-\phi(100) = 10°$ and 7.5°. Laser rate calorimetry on these samples yielded an average

$$\beta_{eff} = \beta_B + 2\beta_s/\ell = 0.745\text{x}10^{-3}\text{cm}^{-1}.$$

Theoretical calculations were made using several PA theories and parameters relevant to sapphire. Figure 11 shows PA amplitude versus chopping frequency. It includes the data of two runs corrected for coherent noise [10], plus plots of the various theories normalized to the experimental amplitude at 100 Hz. The Rosencwaig-Gersho theory is the poorest fit with experiment having n=1.50. The McDonald-Wetsel composite-piston model was somewhat better with n=1.48 at the lower frequencies shifting to n=1.25 at 1000 Hz. The Bennett-Forman theory and the Rosencwaig-Gersho theory modified to include surface absorption gave essentially identical results for the same value of $r=\beta_s/\beta_B$. Above 100 Hz, n=1.08 for r=0.02 cm; n=1.14 for r=0.01 cm. Based solely on amplitude considerations r=0.020 looks like the best fit with experiment.

Figure 12 shows experimental data for the phase angle measurements which exhibit considerable noise. Again the results of various theories normalized at 100 Hz are shown. Again the straight Rosencwaig-Gersho theory exhibits the worst fit, the McDonald-Wetsel theory is somewhat better. For the same value of r, the Rosencwaig-Gersho theory modified for surface absorption exhibits a slightly larger angular variation than the Bennett-Forman theory. The value of r=0.01 cm fits Run 1 data better than r=0.02 cm. With the noise factor it is difficult to choose better the two r values.

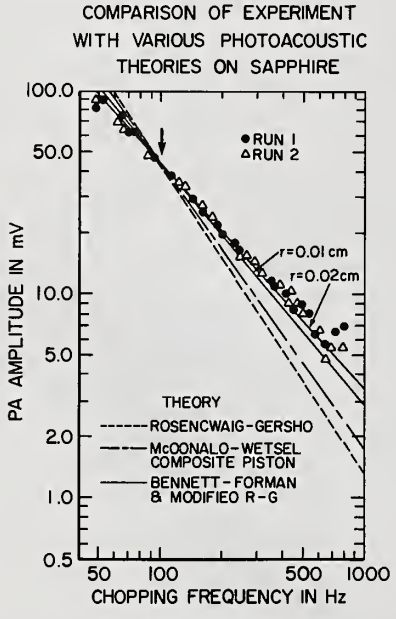

Figure 11. Comparison of experimental PA signal amplitudes for sapphire versus chopping frequency and several theories.

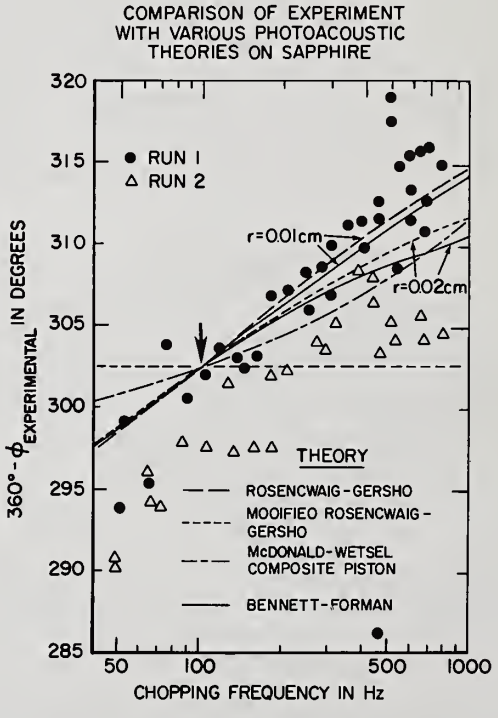

Figure 12. Comparison of experimental PA signal phase angles for sapphire versus chopping frequency and several theories.

Using r=0.020 in $\beta_{eff} = \beta_B + 2\beta_S/\ell = 0.745 \times 10^{-3} cm^{-1}$, we have $(1+2r/\ell) = 1.051$ and thus $\beta_B = 0.709 \times 10^{-3} cm^{-1}$ along with $\beta_S = 0.000014$. Hence for these window dimensions the bulk optical absorption contributes about 95% of the measured β_{eff} from laser calorimetry. Using r=0.010 cm, $\beta_B = 0.726 \times 10^{-3} cm^{-1}$, $\beta_S = 0.0000073$ and β_B is about 97% of the measured β_{eff}.

The only related surface-to-bulk optical absorption study on sapphire is given in Ref. [14] where a multithickness study [15] was made on samples 1, 2, 3, 4 and 5 mm thick. The samples appeared to have a poorer polish than those reported here. It is not certain whether the criteria for accurate values by the multithickness technique were fulfilled. These criteria are that the samples have identical bulk properties, i.e. obtained from the same region of a boule and received identical polishing and cleaning treatments. The results of this gave r=0.26 cm over a factor of ten larger.

4B. CVD ZnSe Summary

Photoacoustic data were taken at 10.6 μm wavelength and about 24 W power level as a function of chopping frequency on uncoated CVD ZnSe windows. PA amplitude plots fit to $S=A f^{-n}$ yielded a dependence of n=1.04. Plots of the phase angle versus frequency yielded $\Delta\phi = \phi(1000)-\phi(50) = \phi(500)-\phi(50) = 13°$ and $\Delta\phi = \phi(1000)-\phi(100) = \phi(500)-\phi(100) = 6°$. Laser rate calorimetry on the samples gave an average $\beta_{eff} = 4.32 \times 10^{-3} cm^{-1}$.

Theoretical calculations were made using several PA theories and parameters relevant to CVD ZnSe. Figure 13 shows PA amplitude versus chopping frequency. Solid points were taken with increasing chopping frequency, hollow ones with decreasing frequency. The Rosencwaig-Gersho theory is the poorest fit with experiment having n=1.50. The McDonald-Wetsel composite-piston was somewhat better with n=1.48 below 100 Hz and n=1.23 above 500 Hz. The surface modified Rosencwaig-Gersho and Bennett-Forman theories gave almost identical amplitude plots for the same r value. The curves for r=0.025 cm and 0.050 cm seemed to fit the amplitudes well with r=0.050 cm being slightly better.

Figure 14 shows phase angle data plus theoretical results normalized at 100 Hz. Again the Rosencwaig-Gersho has the poorest fit while the McDonald-Wetsel composite-piston is considerably better. The modified Rosencwaig-Gersho theory gives slightly larger angular variation than the

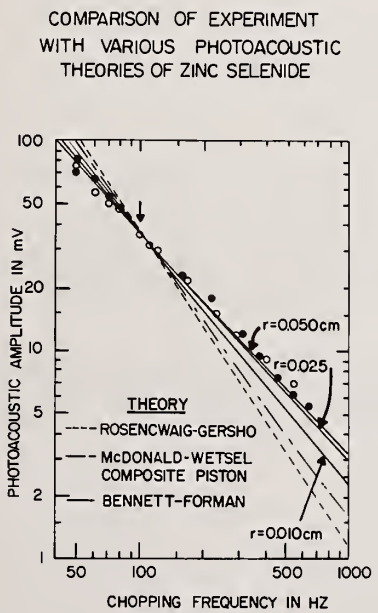

Figure 13. Comparison of experimental PA signal amplitudes for CVD ZnSe versus chopping frequency and several theories.

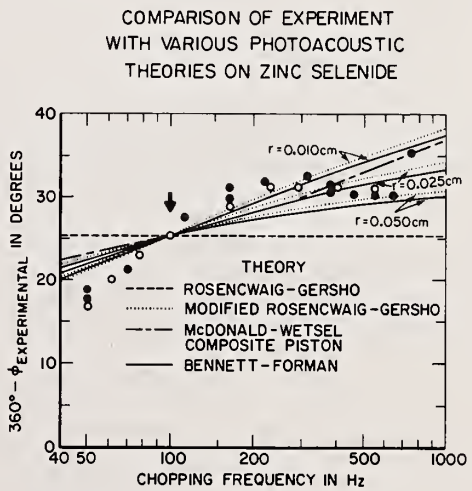

Figure 14. Comparison of experimental PA signal phase angles for CVD ZnSe versus chopping frequency and several theories.

Bennett-Forman theory for the same value of r. These theories give better fit than McDonald-Wetsel for r=0.010 cm, about the same for r=0.025 cm and somewhat worse for r=0.050 cm.

Taking into account both amplitude and phase considerations, r=0.025 cm seems to give the best overall fit. Using r=0.025 cm along with $\beta_{eff} = 4.32 \times 10^{-3} cm^{-1}$, we obtain $(1+2r/\ell) = 1.063$ and thus $\beta_B = 4.06 \times 10^{-3} cm^{-1}$ along with $\beta_s = 0.000102$. Hence for these window dimensions β_B accounts for about 94% of the measured β_{eff}.

A related study on CVD ZnSe using the multithickness technique was done on some samples prepared on a Manufacturing Technology program of the Air Force Materials Laboratory. However the validity criteria for accurate data are fulfilled is unknown for these samples. The MT-11A samples gave r=0.27 cm; the MT-12 samples, 0.21 cm [16]. These values are about an order of magnitude higher than those obtained in this study.

David B. O'Quinn helped in the photoacoustic experiments and he and David V. Dempsey performed the laser rate calorimetry measurements. Jeffrey A. Fox and Douglas M. Chandler helped with the computer programs and plots. This work was supported by the AFWAL Materials Laboratory, Wright-Patterson Air Force Base, Ohio 45433.

References

[1] Fernelius, Nils C. J. Appl. Phys. 51: 1756; 1980.

[2] Fernelius, Nils C. J. Opt. Soc. Am. 70: 480; 1980.

[3] Fernelius, Nils C. Photoacoustic experimental studies on an AR coated laser window and some related theoretical calculations, Calculations using a two-layer Rosencwaig-Gersho photoacoustic spectroscopy theory applied to an anti-reflective coated laser window. Bennett, H. E.; Glass, A. J.; Guenther, A. H.; Newnam, B. E., ed. Proceedings of the 10th anniversary symposium on optical materials for high power lasers; 1979 October 30-31; Boulder, CO. Nat. Bur. Stand. (U.S.) Spec. Publ. 568; 1980 July. 293-300 and 301-311.

[4] Rosencwaig, A.; Gersho, A. J. Appl. Phys. 47: 64; 1976.

[5] Rosencwaig, A. Photoacoustics and photoacoustic spectroscopy. New York: Wiley; 1980.

[6] Bennett, H. S.; Forman, R. A. J. Appl. Phys. 48: 1432; 1977 and references therein.

[7] McDonald, F. A.; Wetsel, G. C. Jr. J. Appl. Phys. 49: 2313; 1978.

[8] Hass, M.; Davisson, J. W.; Klein, P. H.; Boyer, L. L. J. Appl. Phys. 45: 3959; 1974.

[9] Fernelius, N. C.; Johnston, G. T. Discussion of a theory of analysis of rate calorimetry which includes coating absorption. Glass, A. J.; Guenther, A. H., ed. Proceedings of the 10th annual symposium on optical materials for high power lasers; 1978 September 12-14; Boulder, CO. Nat. Bur. Stand. (U.S.) Spec. Publ. 541; 1978 December. 7-12.

[10] Fernelius, N. C.; Walsh, D. A. Photoacoustic spectroscopy studies of thin film coatings on laser windows. Glass, A. J.; Guenther, A. H., ed. Proceedings of the 10th annual symposium on optical materials for high power lasers; 1978 September 12-14; Boulder, CO. Nat. Bur. Stand. (U.S.) Spec. Publ. 541; 1978 December. 43-49.

[11] Fernelius, Nils C. J. Appl. Phys. 52: 6285; 1981.

[12] Fernelius, Nils C.; To appear in Applied Optics.

[13] Roark, J. C.; Palmer, R. A.; Hutchison, J. V. Chem. Phys. Lett. 60: 112; 1978.

[14] Detrio, John A.; Fernelius, Nils C.; Harris, Richard J.; Walsh, David A. Optical characterization of IR transmitting and laser window materials; Semiannual Tech. Rpt. No. 2, September 1981, UDR-TR-81-76. 20-22.

[15] Deutsch, T. F. J. Electronic Materials 4: 663; 1974.

[16] Pappis, J. Private communication.

Are there advantages of one theory over the other for separating bulk and surface absorption? The speaker had not studied that question, but both theories are very messy.

Calorimetric Measurement of Temperature Dependent Absorption in Copper

R. S. Quimby, M. Bass, and L. Liou

Center for Laser Studies
University of Southern California, Los Angeles, Ca 90007

This paper reports the temperature dependence of optical absorption in copper as measured by laser rate calorimetry. It is found that the measured values of the temperature dependence agree well with the predictions of the simple Drude theory for wavelengths of 10.6 μm and 1.08 μm. At 0.647 μm the temperature dependence is stronger, due to the effect of interband transitions. Absolute values of the absorptance are measured to be somewhat higher than predicted by the simple Drude theory, indicating the importance of the anomalous skin effect and possibly other absorption mechanisms. After cycling to a temperature of 200°C or greater, a permanent increase in the room temperature absorptance is observed. This increased absorption is pronounced at 1.08 μm and 0.647 μm, whereas it is not observable at 10.6 μm. The permanent change is correlated with a change in the observed microstructure of the surface.

Key words: copper, absorption, temperature, calorimetry.

1. Introduction

In order to predict the damage threshold for a given metal, it is necessary to know how the absorptance (A) changes with increasing temperature (T). Values of dA/dT are often obtained from the Drude theory by using the experimental variation of dc electrical conductivity with temperature. Because this parameter is of such importance in predicting damage thresholds, it would be useful to have additional experimental verification of the validity of the Drude theory prediction. With this goal in mind, we have made direct measurements of dA/dT in copper using laser calorimetry. The principle result of this study is that the Drude theory does in fact correctly predict the value of dA/dT for wavelengths greater than 1 μm. At shorter wavelengths, interband transitions cause deviations from the Drude theory. In the course of this work several additional interesting effects were observed, including a permanent change upon temperature cycling, and sample-dependent absorption at the shorter wavelengths. These effects will be discussed in more detail in section 5 of this paper.

2. Theory

The first realistic model for the optical properties of metals was presented by Drude early in this century [1]. It is a classical model, in which electrons are subject to two forces: a driving force from the incident oscillating electric field, and a damping force from collisions with impurities or lattice vibrations. The position x of the electron satisfies the classical equation of motion

$$\ddot{x} + \gamma\dot{x} = \frac{eE_o}{m^*} e^{-i\omega t} \qquad (1)$$

where $1/\gamma \equiv \tau$ is the mean time between collisions, m^* is the effective electronic mass, E_o is the magnitude of the incident electric field, and $\omega/2\pi$ is the frequency of the radiation. The dielectric function $\varepsilon(\omega)$ for a metal with free electron concentration N is then easily shown to be

$$\varepsilon(\omega) = 1 - \frac{\omega_p^2}{\omega(\omega + i\gamma)} \tag{2}$$

where the plasma frequency ω_p is given by

$$\omega_p^2 = \frac{4\pi Ne^2}{m^*} \tag{3}$$

The reflectivity for normal incidence is

$$R = \frac{(n-1)^2 + k^2}{(n+1)^2 + k^2} \tag{4}$$

where the complex index of refraction is $\tilde{n} \equiv \varepsilon^{1/2} = n + ik$.

In the visible and IR it is a good approximation that $\omega_p^2 >> \omega^2$, and also that $\omega\tau >> 1$, so equation (4) becomes, after some algebra,

$$R \simeq 1 - \frac{2}{\omega_p \tau} \tag{5}$$

and the absorptance A is

$$A \simeq \frac{2}{\omega_p \tau} \tag{6}$$

The mean collision time τ can be obtained from the measured dc electrical conductivity by means of the relation

$$\sigma = \frac{Ne^2\gamma}{m^*} \tag{7}$$

It is found experimentally that the electrical resistivity $1/\sigma$ is proportional to the absolute temperature for $T > 300^{\circ}K$. Therefore by equation (6) the optical absorptivity A should also be linear with temperature.

Two assumptions which have been made in the preceding discussion should be mentioned. The first is the implicit assumption in equations (6) and (7) that the value of τ is the same for both dc conductivity and IR absorption. Due to a quantum mechanical effect, however, this is not strictly true, the IR value always being smaller than the dc value [2,3]. At room temperature the two τ's differ by about 10%, and the difference becomes smaller with increasing temperature.

The second assumption that has been made is that $\omega\tau >> 1$. To see the effect of this assumption, we keep terms in the expression for A up to order $(\omega\tau)^{-2}$:

$$A \simeq \frac{2}{\omega_p \tau}\left[1 - \frac{1}{8\omega^2\tau^2}\right]$$

Using $\tau_{IR} = 3.2\ 10^{-14}$ s we see that for $\lambda<10$ μm, the correction to A is $\Delta A/A \lesssim 0.01$, and can be neglected.

In addition to the simple Drude absorption, there are other effects which can contribute to optical absorption in metals. One example is the anomalous skin effect, [4-6] which becomes important when the electronic mean free path ℓ is on the order of or greater than the skin depth δ. For Cu at room temperature, $\ell \sim 300$ Å and $\delta \sim 200$ Å, so the anomalous skin effect is in fact important. The contribution to the absorptance arising from the anomalous skin effect is [3]

$$A_s = \frac{3}{4}\ \frac{v_F}{c}\ (1-p) \tag{8}$$

where v_F is the Fermi velocity, c is the speed of light, and p is the fraction of electrons which are specularly reflected at the sample surface. Most experimental results imply diffuse reflection, or p = 0 [3], although for very smooth surfaces p can be close to 1 [6]. Notice that the anomalous skin effect absorption is independent of both wavelength and temperature, so it should not contribute to the temperature dependence dA/dT.

Another possible modification of the Drude theory is the introduction of two distinct types of free carriers, each with a different value of τ [7] . Physically, this could correspond to the distinction between true free carriers in the bulk and carriers in a disordered environment near grain boundaries [7]. Surface roughness can also alter the absorption; generally, surface roughness tends to increase the absorptance, especially at shorter wavelengths.

Finally, there are two intrinsic effects which may be present in a particular metal: interband transitions and electron-electron interactions. In Cu the threshold for interband transitions is about 2 eV, and visible radiation is strongly absorbed. Radiation with a wavelength of 10.6 μm will not be sensitive to the IB transition, though 1.08 μm may be within the range of an IB transition "tail" caused by indirect transitions. Electron-electron interactions give rise to a variation of A with λ, but calculations of this effect show a smaller variation than is actually observed [3].

In giving the numerical value of the expected Drude absorptance A and dA/dT, we must also consider the uncertainty in this predicted value due to uncertainties in the input parameters for the Drude model. In table 1 below, values for the various parameters are given, along with the typical spread in these values obtained from various sources in the literature.

Table 1. Parameters for Drude Theory

Parameter	Value	Error	Units
m/m_c	1.45	0.04	--
$\rho(20^oC)$	1.70	0.05	$10^{-8}\ \Omega$-m
$d\rho/dT$	6.5	1.0	$10^{-11}\ \Omega$-m-$^oC^{-1}$
A_{Drude}	4.56	0.2	10^{-3}
A_s	2.8	0.08	10^{-3}
dA/dT	1.57	0.27	$10^{-5}\ ^oC^{-1}$

3. Experimental Set-up

The experimental procedure used to measure the temperature dependence of absorption in copper was that of laser rate calorimetry. In this well-known technique, the sample of interest is supported by low thermal conductivity supports in a vacuum and is irradiated by a laser beam. The subsequent rise in temperature of the sample is then monitored by a thermocouple attached to the rear of the sample. The absorptivity A is determined by measuring both the rate of temperature increase when the beam is on and the rate of temperature decrease when the beam is off.

In order to measure the absorptance at various temperatures, the sample is mounted in an evacuated quartz tube, which is placed inside a Lindberg tube furnace. The temperature of the Lindberg oven is digitally controlled and can be set to any temperature between 20^{o} and 1000^{o}C. The vacuum system is a "clean" one, with a sorption pump as the roughing pump and a Vac-Ion pump to bring the pressure down to about 10^{-7} torr.

Copper samples were obtained from three sources. China Lake Naval Weapons Center and the INTOP Corporation supplied diamond turned samples of OFHC Cu in the form of 3/8 x 5/8 x 1/8 inch rectangles. The Northrop Corporation supplied mechanically polished samples of the same size and base material. All samples were kept in a vacuum dessicator until they were used in an experiment, in order to keep the surfaces as free as possible from contamination.

4. Results

Absorption measurements were made at three wavelengths: 10.6, 1.08, and 0.647 μm, obtained from a cw CO_2 laser, a cw Nd:$YAlO_3$ laser, and a cw Krypton ion laser, respectively. Irradiation powers were in the range of 1-10 watts cw, and typical temperature excursions were a few degrees C. Figure 1 shows the measured absorptance in one of the China Lake samples as a function of temperature, for λ = 10.6 μm. As expected from the Drude theory, the absorptance rises linearly with temperature, and

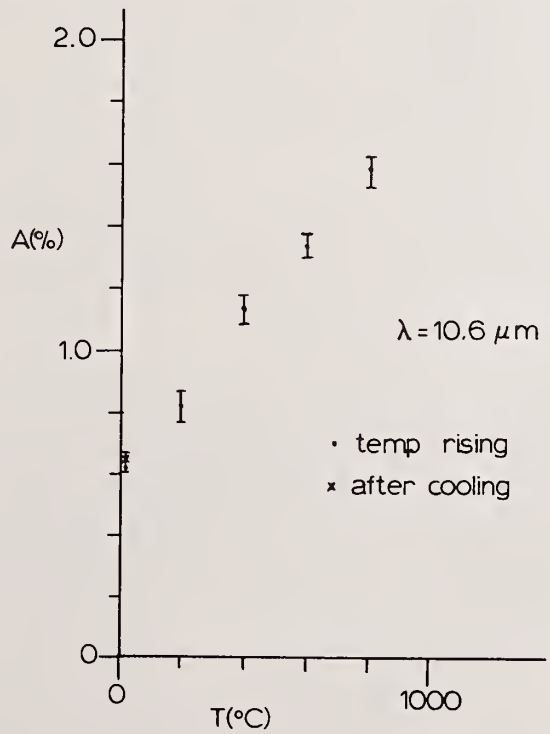

Figure 1. Absorptance A vs. temperature T at λ = 10.6 μm for China Lake diamond turned copper sample.

from the data we can directly determine dA/dT. Note that when the sample was returned to room temperature and the absorption measured again, the value was the same as before within experimental error.

When the oven was set at a particular temperature, absorption measurements were made at each of the three wavelengths, so the temperature history of the sample was the same for any of the wavelengths. Figure 2 shows the absorptance vs. temperature at 1.08 μm for the same sample and conditions as in figure 1. Again the absorptance is linear with temperature, at least for the lower temperatures. Notice, However, that when the sample was returned to room temperature the absorptance was considerably higher than it was at the start of the experiment. There has been a permanent change in the absorptance upon temperature cycling. This change sets in at some temperature above 200°C and causes an increase in absorptance with temperature which is in addition to the normal Drude dA/dT; the resulting plot of A(T) is then no longer linear but has a slight upward curvature. In determining dA/dT from this data we gave a greater weighting to the low temperature data, since this is the temperature region where true Drude-like behavior is most likely to occur.

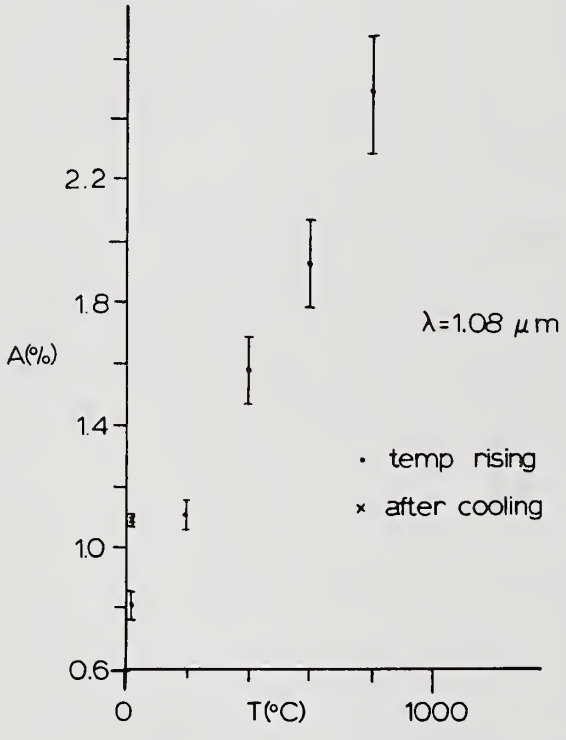

Figure 2. Same as figure 1, with λ = 1.08 μm.

A summary of our absorption results for each of the three wavelengths is given in tables 2 - 4. The room temperature absorption both before and after temperature cycling is given, as well as the value of dA/dT. Meaningful values of dA/dT could not be obtained for the Northrop samples at 1.08 and 0.647 μm due to the presence of an anomalously high initial absorption which decreased as the temperature was increased. The lack of 0.647 μm data for the China Lake samples was due to problems with the Krypton laser.

5. Discussion

The principle result of this study is a confirmation of the validity of the Drude theory in predicting dA/dT. The results in tables 3 and 4 for 1.08 and 10.6 μm are in good agreement with the Drude prediction, which is also given in those tables. In the visible the Drude theory is not

expected to be adequate, and indeed table 2 shows that dA/dT is much larger at 0.647 than in the IR. There are several possible reasons for a larger dA/dT near the onset of interband transition. In copper the most likely possibility is the temperature dependence of unoccupied final states near the Fermi level. The large value of dA/dT which we measure at 0.647 μm is consistent with the results of other workers [7-9].

Table 2. Data for λ = .6471 μm

Sample			Room Temp. Absorptance (%)		
No.	Source	Finish	Initial	After Temp. Cycling	$\frac{dA}{dT}$ (10^{-5} $^{o}C^{-1}$)
1	China Lake	Diamond Turned	---	---	---
2	China Lake	Diamond Turned	---	---	---
3	INTOP	Diamond Turned	---	3.1 ± 0.1	4.0 ± 0.5
4	INTOP	Diamond Turned	2.65 ± 0.10	3.2 ± 0.2	3.7 ± 0.5
5	Northrop	Mechanically Polished	---	---	---
6	Northrop	Mechanically Polished	7.9 ± 0.2	5.0 ± 0.1	---

Table 3. Data for λ = 1.08 μm

Sample			Room Temp. Absorptance (%)		
No.	Source	Finish	Initial	After Temp. Cycling	$\frac{dA}{dT}$ (10^{-5} $^{o}C^{-1}$)
1	China Lake	Diamond Turned	0.81 ± 0.06	1.09 ± 0.05	1.65 ± 0.35
2	China Lake	Diamond Turned	0.87 ± 0.03	1.06 ± 0.10	1.80 ± 0.40
3	INTOP	Diamond Turned	0.65 ± 0.06	0.87 ± 0.04	1.5 ± 0.5
4	INTOP	Diamond Turned	0.63 ± 0.02	1.09 ± 0.06	1.6 ± 0.25
5	Northrop	Mechanically Polished	2.04 ± 0.05	1.21 ± 0.05	---
6	Northrop	Mechanically Polished	1.00 ± 0.09	0.99 ± 0.03	---
Theory	Drude plus surface absorption		0.736 ± 0.03	---	1.57 ± 0.27

Table 4. Data for λ = 10.6 μm

Sample			Room Temp. Absorptance (%)		
No.	Source	Finish	Initial	After Temp. Cycling	$\frac{dA}{dT}$ (10^{-5} $^{o}C^{-1}$)
1	China Lake	Diamond Turned	0.62 + 0.01	0.64 ± 0.04	1.25 ± 0.15
2	China Lake	Diamond Turned	0.61 ± 0.02	0.59 ± 0.05	1.20 ± 0.15
3	INTOP	Diamond Turned	0.58 ± 0.02	0.52 ± 0.03	1.50 ± 0.20
4	INTOP	Diamond Turned	0.61 ± 0.02	0.63 ± 0.02	1.45 ± 0.20
5	Northrop	Mechanically Polished	0.75 ± 0.02	0.60 ± 0.03	1.45 ± 0.15
6	Northrop	Mechanically Polished	0.66 ± 0.04	0.72 ± 0.03	1.42 ± 0.25
Theory	Drude plus surface absorption		0.736 ± 0.03	---	1.57 ± 0.27

The measured absolute absorptance at RT is also close to the Drude prediction although the variation which is seen from sample to sample is, of course, not compatible with the simple Drude theory. The precision of our measurement is such that the differences between samples and between wavelengths indicated in tables 2-4 are real, and not attributable to random measurement error. The absolute accuracy of the calorimetric measurement is less certain, however, and independent calibration experiments indicate that the absolute values reported here may be too low by as much as 30%. It seems, then, that the actual absorption at 10.6 μm is somewhat higher than the simple Drude value of 0.0045. Assuming that electrons are diffusly reflected from the surface, the anomalous skin effect surface absorption contributes approximately 0.0028, which accounts for most of the additional absorption. For most samples, the absorptance at 1.08 μm is somewhat greater than at 10.6 μm. As mentioned in section 2, there are several possible absorption mechanisms which could cause this, including surface roughness, disorder effects, electron-electron interactions, and the tail of the interband transitions. For the INTOP samples, however, the absorptance at 1.08 μm and 10.6 μm is nearly the same, and this absorptance is the lowest value measured on any of the copper samples. If the higher absorption at 1.08 μm in the other samples was due to an "intrinsic" effect such as electron-electron interactions or interband transitions, then the same increased absorption should be seen in the INTOP samples. The fact that the INTOP samples do not show this extra absorption at 1.08 μm implies that "extrinsic" effects such as surface roughness or disorder are responsible for the higher 1.08 μm absorptance seen in the other samples. Additional measurements are presently being made to verify this result, in view of its importance in understanding near IR absorption in copper.

The other major result of this work is the observation of a permanent change in the room temperature absorptance after temperature cycling. This change is quite pronounced at 1.08 μm and 0.647 μm, while it is not observed at 1.06 μm. The effect is also correlated with a change in the

microstructure of the surface, as can be seen in the Nomarski micrographs of figure 3.

500 μm

500 μm

100 μm
Before Heating

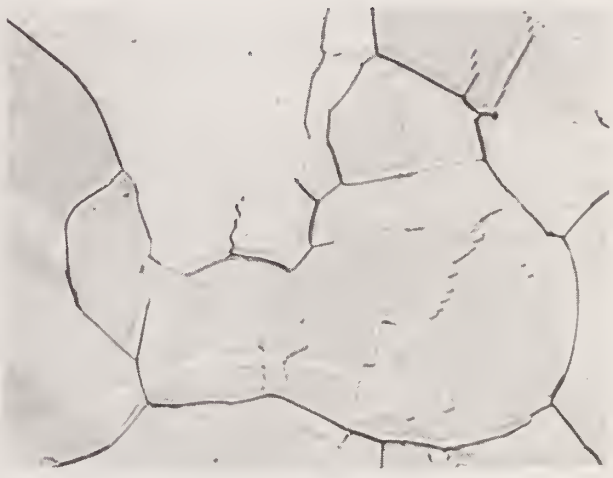

100 μm
After Heating

Figure 3. Nomarski micrographs of China Lake diamond turned Cu sample, showing change in microstructure after heating.

The grain boundaries are more visible after temperature cycling because of a thermal etching process which is shown schematically in figure 4.

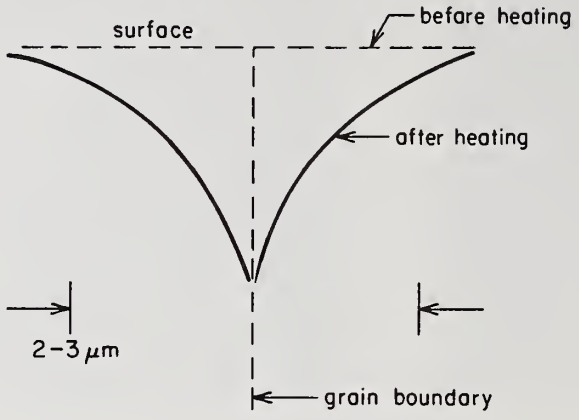

Figure 4. Schematic cross section of copper sample, showing the thermal etching process which occurs at high temperatures.

After heating, channels of average width 2-3 μm are formed along the grain boundaries. Radiation incident on these channels can be absorbed more efficiently than for a flat surface - the radiation is partially "trapped" in the channel. The efficiency of absorption should be less when the wavelength of the light is greater than the dimensions of the channel, a well-known result for the absorption of light by small particles [10]. This is in agreement with our observation that the hysteresis effect is much smaller at 10.6 μm than at 1.08 and 0.647 μm.

6. Conclusions

The applicability of the Drude theory for predicting dA/dT has been verified for copper at 1.08 and 10.6 μm. In the visible dA/dT is significantly higher than the Drude theory prediction. A variation in absolute absorptance has been observed for samples prepared in different ways, and this may have implications for our understanding of basic absorption mechanisms in the near IR. Finally, a permanent increase has been observed in the absorption which is correlated with a change in the observed surface microstructure. These studies are presently being extended to include samples of diamond-turned silver and aluminum.

The authors are grateful to Peter Engstrom of the INTOP Corporation, Abe Klugman of the Northrop Corporation, and Don Decker of China Lake Naval Weapons Center for their helpfulness in supplying the samples used in this work. This work was supported by Selected Research Opportunities, Contract No. N00014-79-C-0896, from the Office of Naval Research.

7. References

[1] Drude, P., Physik Z: 161, 1900.

[2] Holstein, T., Phys. Rev. 96: 535, 1954.

[3] McKay, J. A., Rayne, John A., Phys. Rev. B 13: 673, 1976.

[4] Pippard, A. B., Proc. Roy. Soc. A191: 370, 1947.

[5] Holstein, T., Phys. Rev. 88: 1427; 1952.

[6] Bennett, H. E., Bennett, J. M., Ashley, E. J., Motyka, R. J., Phys. Rev. 165: 755, 1968.

[7] Decker, D. L., Hodgkin, V. A., Laser induced damage in optical materials. Nat. Bur, Stand. Spec. Publ. 620; 1980. 190 p.

[8] Johnson, P. B., Christy, R. W. Phys. Rev. B 11: 1315, 1975.

[9] Roberts, S., Phys. Rev. 118: 1509, 1960.

[10] Van de Hulst, H. C., Light scattering by small particles. New York: Wiley Press; 1957.

Reversible and Irreversible Changes in NaCl and KCl Absorption During Multiple Pulse 10.6 μm Irradiation

S.-T. Wu, M. Bass and J. P. Stone

Center for Laser Studies
University of Southern California, Los Angeles, CA 90007

Repetitively pulsed laser calorimetry was used to detect both reversible and irreversible increases in the 10.6 μm absorption of NaCl and KCl. The irreversible changes are first noted at the same intensity that is found to cause damage after multiple irradiations. Just below this intensity damage is not detected even after ∿1800 pulses. As a result of this work, a redefinition of the fatigue threshold is necessary as it must be distinguished from the breakdown damage threshold studied in earlier research.

Key words: alkali halide absorption; fatigue damage threshold; multipulse laser damage; pulsed laser calorimetry.

1. Introduction

The objective of this research was to study the response of NaCl and KCl to repetitively pulsed 10.6 μm laser irradiation. The technique of pulsed laser calorimetry [1] was used and at low intensity (∿250 MW/cm^2) a reversible increase was observed in the 10.6 μm absorption. This increase occurred over the next 500 - 600 MW/cm^2 and was ∿50% that of the low intensity absorption. This change was entirely reversible. No additional change in the absorption was observed until the intensity was raised to the 2 - 4 GW/cm^2 range. At this level an irreversible increase in absorption was detected. This occurred at intensities ∿1/3 - 1/2 that required to produce single pulse breakdown damage. At the intensity at which the irreversible increase in absorption was first detected, fatigue laser damage or multipulse induced laser damage was observed [2]. Just below this intensity no damage was detected after ∿1800 pulses. It should be noted that the occurrence of fatigue laser damage is similar to single pulse breakdown damage [3]. That is, it is accompanied by a blue white spark and leaves a residual morphology showing a small disrupted volume surrounded by cleavage cracks.

The onset of the irreversible increase in absorption correlates with the first detectable possibility of fatigue laser damage. Since this occurs at intervals less than that required for single pulse breakdown damage, a more practical definition of damage threshold is the intensity at which fatigue damage is observed within a predetermined number of irradiations. If the sample absorption is monitored, an equivalent definition of damage threshold is that intensity at which an irreversible increase in absorption is first noted. Studies of the spot size dependence of the fatigue damage phenomenon and the irreversible increase in absorption sug-

gest that they are both related to the presence of microscopic inclusions or defects. These can interact with the light and form so called microdamages which may then grow upon successive irradiatiions until a breakdown-like macroscopic failure occurs.

2. Experimental Procedures

The experiment is sketched in figure 1 and experimental details are given in references [1, 4, 5]. The TEA CO_2 laser was operated at ∿1 Hz and cooling of the sample between pulses could be detected. Thus the data analysis described in reference [1] was used for this repetitively pulsed laser calorimetric measurement. At each intensity 30 or 50 pulses were used.

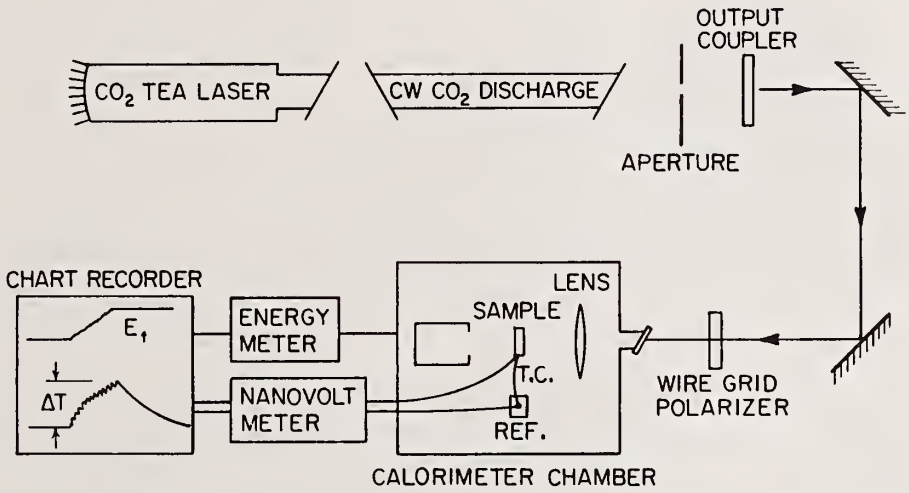

Figure 1 Schematic of the equipment.

The temporal waveform and focused spatial distribution of these pulses are shown in figure 2.

The cw absorption of each sample was measured in a conventional laser calorimetric procedure to obtain an absorption coefficient essentially at zero intensity. During the pulsed irradiations, the intensity was increased until the limit of the particular lens used was reached. Then a shorter focal length lens was installed and the input to the lens lowered to obtain an intensity overlap with the conditions of the first lens. In the range of intensities below that required for an irreversible change in absorption, the lens focal length or, equivalently, the focal volume had no effect on the measured absorption. A focal volume dependence to the irreversible change in absorption and to the occurrence of fatigue damage was observed at high intensities.

A HeNe laser beam coincident with the CO_2 beam was used to try to detect increased scattering in the irradiated volume when irrevesible changes in the absorption occurred. No noticeable change in scattering could be seen before catastrophic failure took place.

(A)

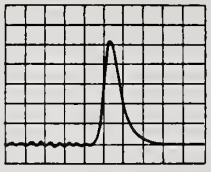

PULSE WIDTH (1/e) = 200 ns

(B)

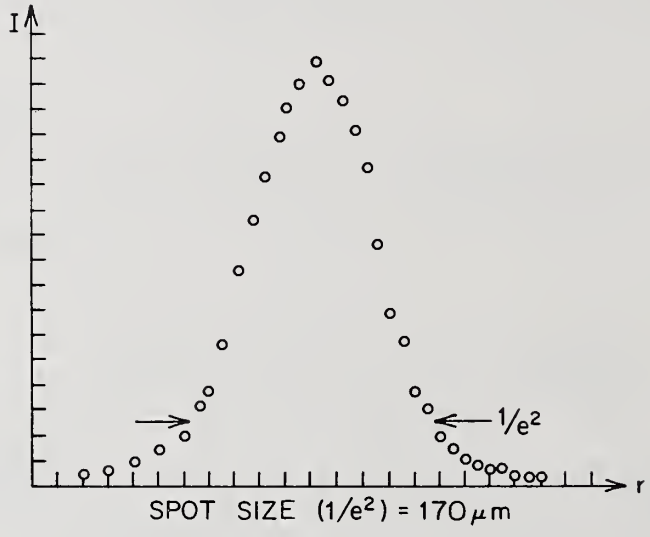

Figure 2. A. Single frequency CO_2 TEA laser temporal waveform.
B. Beam spatial profile when focused to a Gaussian spot of 170 μm in diameter at the $1/e^2$ points in intensity.

3. Results

Figure 3 shows the reversible change in KCl absorption observed between 300 and 700 MW/cm^2 at 10.6 μm. (Throughout this paper the intensity that is given is the aveage intensity in the Gaussian beam.) In this range the absorption increases by almost 50%. The open circles are data points taken with increasing intensity and the X's are data points taken with decreasing intensity. The solid triangle indicates the measured cw absorption of this sample.

Figure 4 shows both reversible and irreversible absorption increases in NaCl. A reversible increase of 40% occurs between ∿200 and 800 MW/cm^2. The absorption then remains constant at the increased value (1.75×10^{-3} cm^{-1}) until ∿5 GW/cm^2 is reached. Then an irreversible increase is detected until, at ∿7 GW/cm^2 multiple irradiation damage occurs. Single shot breakdown-like failure is observed at 10 GW/cm^2 in this crystal as indicated in figure 4.

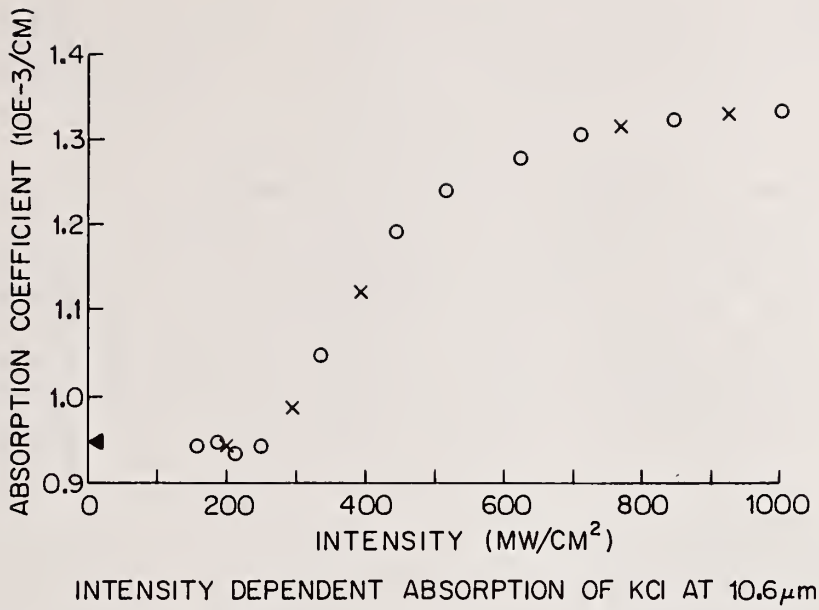

Figure 3. Reversible intensity dependent absorption in KCl. The O's are data points taken with increasing intensity and the X's are data points taken with decreasing intensity in the same site.

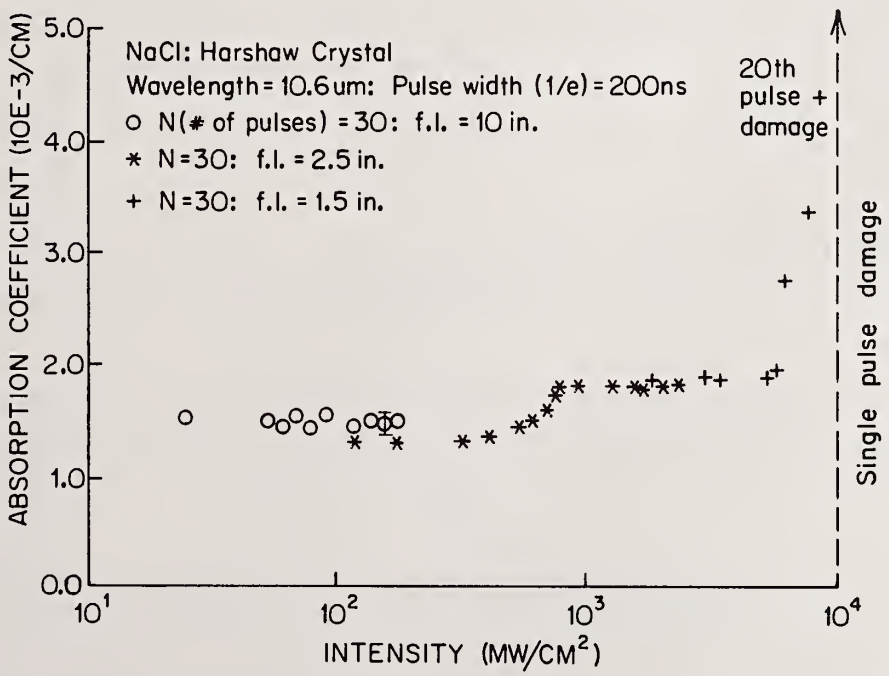

Figure 4. Reversible and irreversible intensity dependent absorption in NaCl.

More evidence for the irreversible nature of the absorption increase at high intensities is shown in figure 5. In this figure, the KCl absorption is shown. The crosses indicate the first sequence in which the intensity was increased until, at 6.4 GW/cm^2 the increase in 4 successive 30 pulse irradiations was from 2×10^{-3} cm^{-1} to 6×10^{-3} cm^{-1}. The intensity was then lowered to 2 GW/cm^2 where the data shows that the increased absorption was retained. The three overlapping open circles show that three successive 30 pulse irradiations at this lower intensity did not result in any additional absorption change. As the intensity was increased from 2 Gw/cm^2 the open circles show that fatigue damage occurred at ∿5.3 GW/cm^2 in a sample which had a single pulse breakdown threshold of ∿7.8 GW/cm^2. Note that when fatigue damage occurred, the test site has been exposed to ∿300 pulses after the first onset of the irreversible change in absorption.

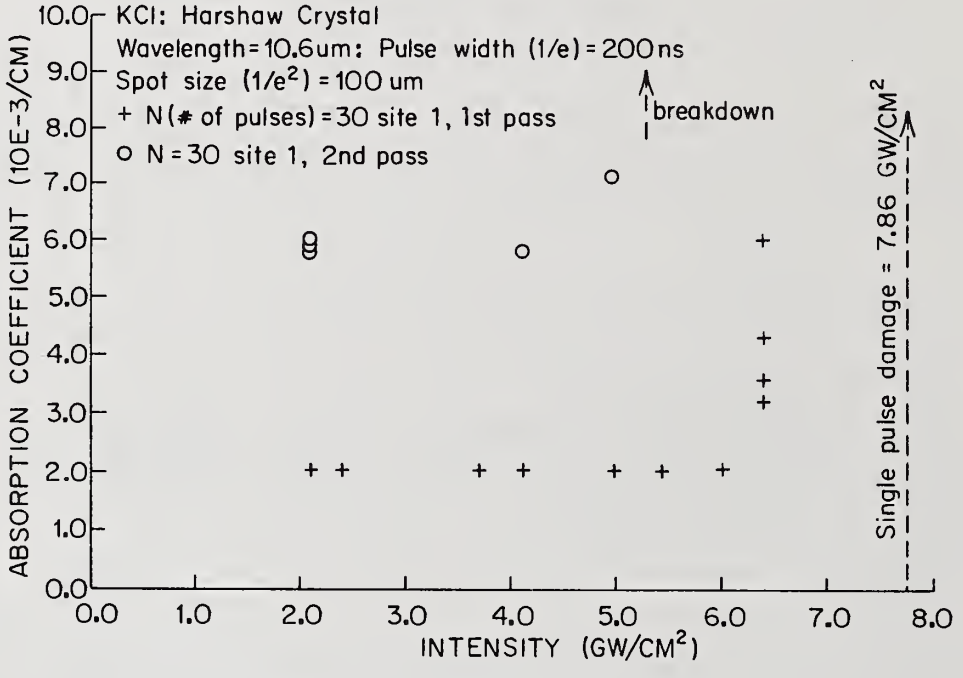

Figure 5. Irreversible intensity dependent absorption in KCl showing the facts that the change is irreversible and that below 4 GW/cm^2 no further increase is detected even though a 3-fold increase was produced at 6.4 GW/cm^2.

Figure 6 shows the effect of focal volume on the observed irreversible increase in absorption in KCl. The increase begins at a lower intensity, I_f, for larger focal volumes and single pulse breakdown failure occurs at lower intensities. The importance of these observations is more clear when figure 6 is compared with figure 7. In figure 7 the number of pulses required to produce fatigue-like failure is plotted versus intensity for the same sample and focal diameters as in figure 6. Below I_f no damage is detected even after as many as 1800 pulses. Above I_f damage occurs after a finite number of pulses which decreases to one at

the single pulse breakdown threshold. Thus, the onset of the irreversible increase in absorption is correlated with the range of intensities which can cause fatigue-like catstrophic failure. The relation to focal beam diameter is discussed further in the next section.

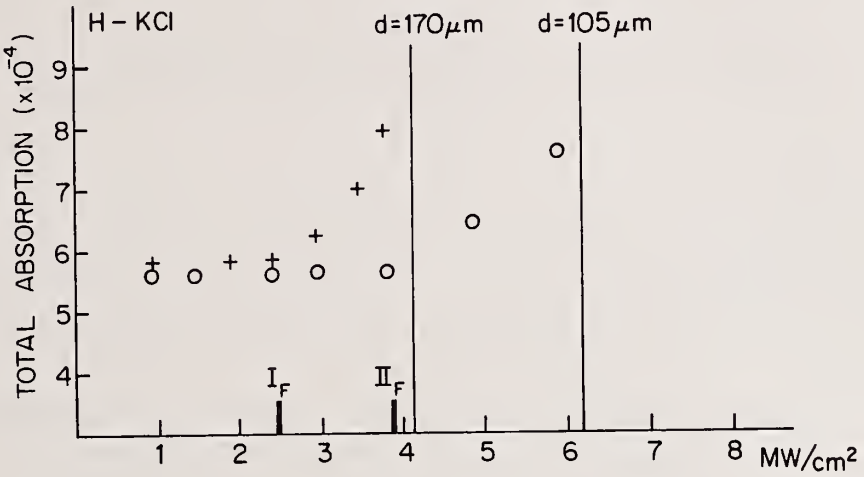

Figure 6. Intensity dependent absorption in KCl for two different focal spot diameters. The single pulse breakdown damage thresholds for each diameter is indicated by the appropriate vertical line.

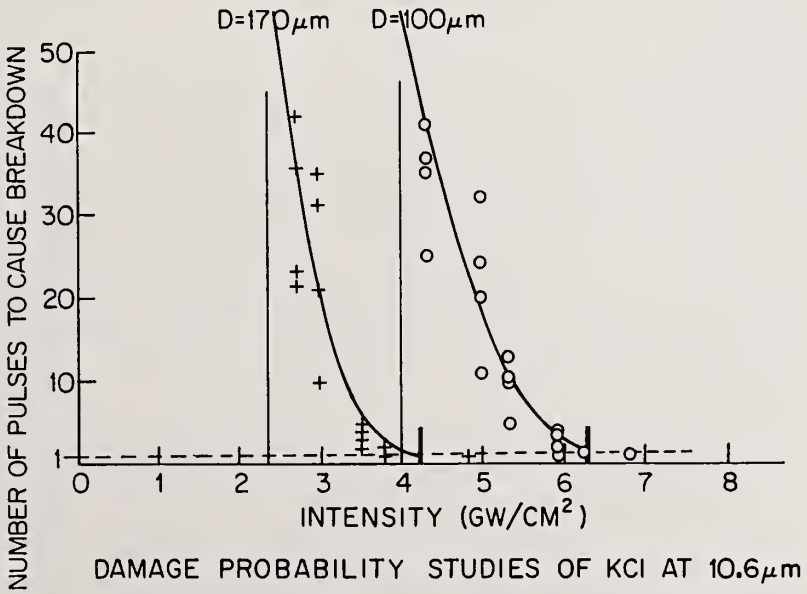

Figure 7. The number of pulses required to produce catastrophic failure as a function of 10.6 μm laser intensity in KCl at two focal spot diameters.

4. Discussion

Mechanisms which can give rise to the reversible increase in absorption seen at intensities below 1 GW/cm^2 in KCl and NaCl are discussed in some detail in reference 5. One clue to the possible mechanism is obtained by noting that the data in figure 3 is fit very well by the function

$$\alpha = \alpha_0 \text{ for } I < I_c$$

$$\alpha = \alpha_0 + A\left[\frac{\pi}{4} + \tan^{-1}[B(I - I_c) - 1]\right] \text{ for } I \geq I_c$$

where α = total absorption at I,
α_0 = total absorption at $I \to 0$,
$A = 1.81 \times 10^{-4}\ cm^{-1}$,
$B = 8.0 \times 10^{-3}\ cm^2/MW$, and
I_c = intensity at which the reversible increase begins, $\sim$250 MW/cm^2 for KCl and NaCl.

Thus, in evaluating the several processes which could give rise to a reversible increase in absorption, one is sought which gives rise to this intensity dependence. To date, we have considered and continue to evaluate such processes as:

1. stepwise resonant absorption in polyatomic impurities in the same manner as it is observed in polyatomic gases in laser chemistry experiments, [6] and
2. optical frequency induced Stark shifts into one photon absorption resonance of impurity bands lying just below the conduction band.

The latter process gives rise to the observed dependence of α on I for a Lorentzian line shape [5). The presence of such impurity bands as needed for these processes was demonstrated in reference [7].

The irreversible absorption increase and the concomittant observation of fatigue-like failure suggests that microscopic inclusions play a role in this process. Since there is some uniform visible light scattering in the materials studied, there is independent evidence for the presence of very small inclusions or defects. As a result the process whereby an irreversible increase in absorption occurs may be as follows: 1) at low intensities microscopic inclusions or defects contribute to the observed absorption but are not altered by their interaction with 10.6 μm laser light 2) at higher intensities, these interactions can cause the inclusions or defects to heat sufficiently to form larger regions of damaged material. (By so doing, the interaction gives rise to an observable increase in absorption.) and 3) when these enlarged microdamages become large enough, a catastrophic failure is formed which resembles single shot breakdown failure. This proposed mechanism is consistent with the initial observation of focal volume dependence described in section 3.

Note that earlier work [8] showed that multiple irradiations at low intensities could increase the resistance of certain KCl and NaCl samples in contrast to the present results. This difference is thought to be caused by the fact that in the earlier work samples of poorer quality were used. These samples had single pulse breakdown thresholds from 1/2 to 1/3 those of the present samples.

It should also be noted that in the present work data for supposedly more pure RAP grown KCl showed smaller reversible increases than for conventionally grown material, higher I_f and higher single pulse breakdown thresholds. This is consistent with the models suggested above in which impurities, inclusions and defects contribute to the intensity dependent absorption processes in KCl and NaCl.

5. Conclusions

Intensity dependent reversible and irreversible 10.6 μm absorption of alkali-halides has been demonstrated. The latter is correlated with multiple pulse irradiation or fatigue failure. As a result is is necessary to redefine the damage threshold as that intensity at which an irreversible increase in absorption is first detected.

This research will continue with studies at shorter wavelengths planned for the alkali-halides and other materials.

This work was supported by NSF Grant No. ENG-7820470. We wish to acknowledge fruitful discussions with Drs. R. T. Swimm, N. Koumvakalis, R. Quimby and L. Merkle and the suggestion by Maj. V. H. Winsor that multiple pulse irradiation damage be called fatigue damage.

6. References

[1] Wu, S.-T.; Bass, M., Nat. Bur. Stand. Spec. Publ. 620; 1981.

[2] Bass, M., Nat. Bur. Stand, Spec. Publ. 341; 1970.

[3] Soileau, M. J.; Bass, M., Appl. Phys. Letters, 35: 370; 1970; Soileau, M. J. Ph.D. Thesis, University of Southern Calfiornia 1979; Manenkov, A. A., Nat. Bur. Stand. Spec. Publ. 509; 1977.

[4] Wu, S.-T.; Bass, M., Appl. Phys. Letters, 39: 948; Dec. 1981.

[5] Wu, S.-T. Ph.D. Thesis, University of Southern California 1981.

[6] Yablonovitch, E.; Bloembergen, N., Physics Today, 23-30; 1978.

[7] Bass, M.; Leung, K. M., IEEE J. of Quant. Electr. 12:

[8] Braunstein, R., Nat. Bur. Stand. Spec. Publ. 620; 1981.

The suggestion was made by Major Harry Winsor of AFOSR that the multi-pulse damage threshold be called the fatigue limit, in consonance with other terminology in Materials Science. The author agreed. In response to another question the author reported that he had looked for scattering sites in his samples prior to irradiation using a HeNe and could not observe any.

Intensity Dependent Absorption and Laser Induced Catastrophic Damage in Diamond Turned and Mechanically Polished Cu Mirrors at 1.06 μm*

N. Koumvakalis, C.-S. Lee and M. Bass

Center for Laser Studies
University of Southern California, Los Angeles, CA 90007

Intensity dependent absorption and multiple pulse induced failure of mechanically polished and diamond turned Cu mirrors were investigated at 1.06 μm. A Q-switched single longitudinal and single transverse mode Nd:YAG laser operating at 10 Hz was the irradiation source in the experiments. Repetitively pulsed calorimetry was used to measure the absorption and to record the onset of the multiple pulse-induced failure at high intensities. The absorptance was found to increase with increasing intensity. The change was compared to that predicted by the Drude model where the increase in absorptance is related to temperature. A spot size dependence of the laser damage intensities was observed which is suggestive of the role of laser induced stresses in the failure process.

Key words: Absorptance; copper; damage; diamond-turned; pulsed calorimetry; stress.

1. Introduction

Metal mirrors, because of their high reflectivity and good thermal conductivity, play an important role in high power pulsed lasers. Under irradiation by high intensity pulsed monochromatic sources intensity dependent absorption mechanisms can be detectable. The most obvious intensity dependent mechanism in metals is caused by the temperature dependence of the absorptance. It has been observed that the absorptance of a metal increases with temperature in a quasi linear fashion. [1-4]. Therefore any temperature variations introduced by changes in the intensity of the incoming laser beam would change the absorption coefficient. What is not known is the magnitude of the effect and how it would compare with other intensity dependent mechanisms, such as multiphoton absorption.

In this paper, we present observations of IDA in metals at 1.06 μm as well as some preliminary theoretical discussions about the IDA mechanisms. In addition, the 1.06 μm laser induced damage intensities of mechanically polished and diamond turned copper mirrors are reported.

2. Experimental

A schematic of our facility is shown in figure 1. The source consists of a Molectron Q-switched Nd:YAG laser equipped with a single axial mode accessory

*Work supported by the Office of Naval Research through the Selected Research Opportunities program, Contract No. N00014-79-C-0896.

and operating at 10 Hz. Excellent beam characterization and pulse reproducibility are crucial to the accuracy of IDA studies. The SAM accessory is capable of producing and maintaining a single axial mode and a Gaussian transverse mode. Beam diagnostics include a fast photodiode for temporal waveform detection and a Reticon diode array to monitor the spatial features.

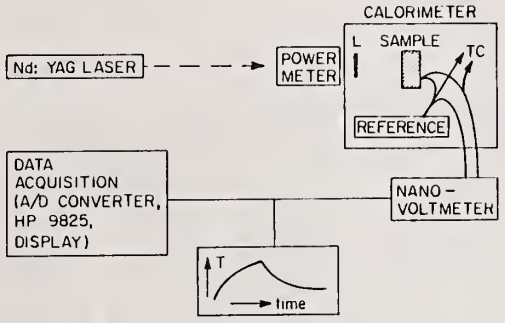

Figure 1. Schematic of experimental apparatus.

Characteristic temporal and spatial profiles are shown in figure 2. The energy was measured with a Laser Precision energy meter before and after each experimental point. If the pulse energy showed fluctuations of more than 5%, the measurement was repeated.

Typical beam parameters were:

Energy	1 - 40 millijoules
Beam profile	Gaussian
Beam radius	100 - 325 μm at the $1/e^2$ level of the intensity
Pulse duration	20, 22 and 28 nsec FWHM

The samples used were OFHC bulk Cu, diamond turned either in the facilities of the NWC in China Lake or by Intop Corp. and mechanically polished by Northrop Corp.

The absorptance was measured calorimetrically. The sample was placed in the calorimetric chamber, shown in figure 1, which was evacuated to 100 millitorr. A 250 mm positive lens, placed in front of the sample at a variable distance permitted the use of different beam spot sizes. The beam energy was changed by using neutral density filters.

A data acquisition system comprised of an HP A/D converter model 59313A, an HP 9825 computer, an HP 1340A display and an HP 59308 timing generator allowed for real time display and fast data analysis.

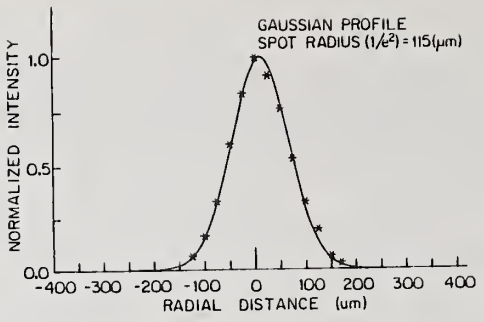

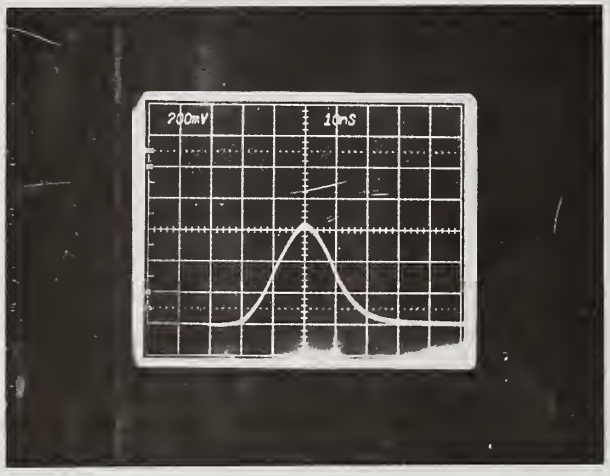

Figure 2. Waveform and spatial profile of 1.06 μm (Nd:YAG) laser pulse.

2. Experimental Technique

In a calorimetric experiment a laser beam of constant intensity is incident on the sample for a certain period of time, energy is absorbed and the temperature rises. At the end of that period, the laser beam is blocked and the sample cools down. Figure 3 shows a classic picture of a calorimetric curve taken from the screen of the display. Plotted is temperature vs. time and from the slopes of the heating and cooling curves, one can calculate the absorptance.

In the present case, a site on the sample's surface was selected for minimal scattering from a HeNe laser beam. This site then was fired at repeatedly with a beam of constant intensity and a temperature vs. time history would be obtained. The absorptance could then be calculated. The same procedure was repeated for several intensities, at the same site, obtaining an absorptance for each intensity. Finally, an intensity level was reached which was high enough to damage the site examined. As soon as damage occurred, the behavior of the heating curve displayed in real time changed dramatically. Heating took place much faster after damage due to the higher absorptance of the damaged material. At the same time, by visually observing the sample, one could see green light emission.

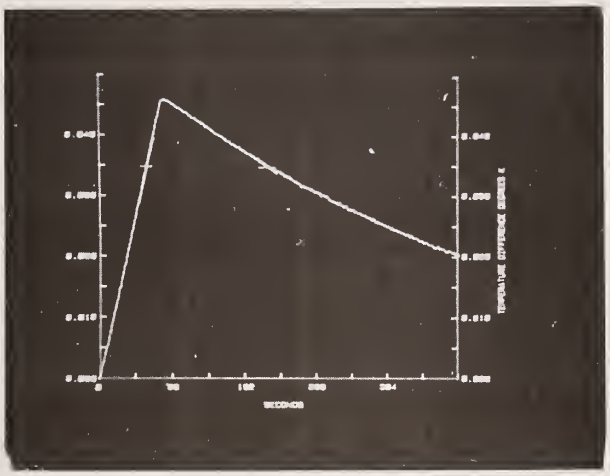

Figure 3. Picture of typical calorimetric curve.

Damage would occur either instantly at the first shot, or after many shots were already fired at the sample. An example of the latter is shown in figure 4. The picture shows the heating part of the calorimetric curve before and after damage. The slope of the heating curve after damage is noticeably steeper.

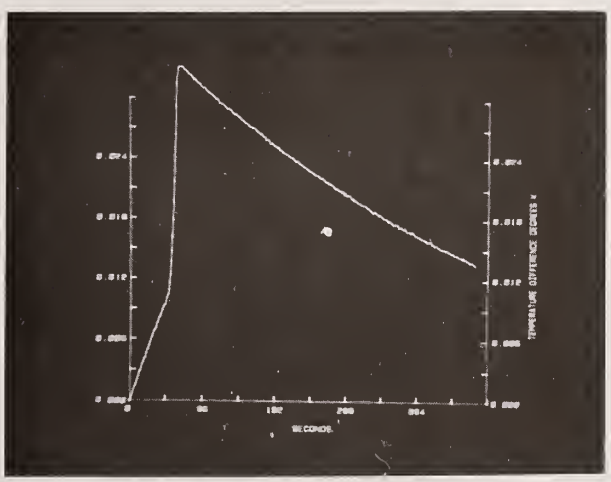

Figure 4. Picture of calorimetric curve before and after damage

After damage occurred, a new site was selected and either irradiated with a beam of the same spot size at damage level intensities to examine fluctuations, or the experiment was repeated with a beam of a different spot size. Finally multi-site experiments were performed, where a different site was chosen for each new intensity until damage occurred. As a final step, the sample was removed from the

calorimeter and the surface examined with a Nomarski microscope. Damage levels quoted here are average intensities for the Gaussian beam distribution on the sample.

3. Results

Figure 5 shows representative absorptance vs. intensity data for the diamond turned sample No. 42 from NWC. The line is a least square fit to the experimental points. The absorptance increases with increasing intensity until damage, indicated by the arrow, occurs.

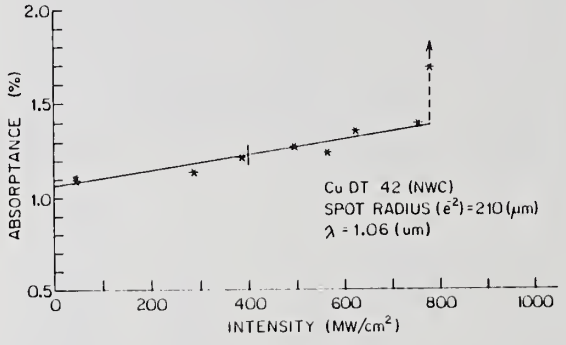

Figure 5. Absorptance vs. intensity plot for Cu DT 42 (NWC). The arrow indicates the damage intensity.

Table I shows the parameters used and the results obtained for the same sample. The values for the absorptance are listed, one at very low intensities and a second at predamage intensities. The damage intensity and damage fluence are given in Mw/cm^2 and J/cm^2 respectively.

Table 1. Parameters and Results for Cu DT 42 (NWC)

r(μm)	t(nsec)	A_0(%)	A_{PD}(%)	I_D(Mw/cm^2)	E_D(J/cm^2)
170	28	1.08 ± 3%	1.25 ± 3%	531 ± 10%	14.5 ± 10%
210	28	1.10 ± 5%	1.40 ± 10%	812 ± 10%	22.7 ± 10%

Typical absorptance vs. intensity data for diamond turned sample 44 from NWC are shown in figures 6 and 7. For each set of data, a different beam spot size was used. The absorptance increases with increasing intensity and the damage intensity seems to be increasing with increasing beam size.

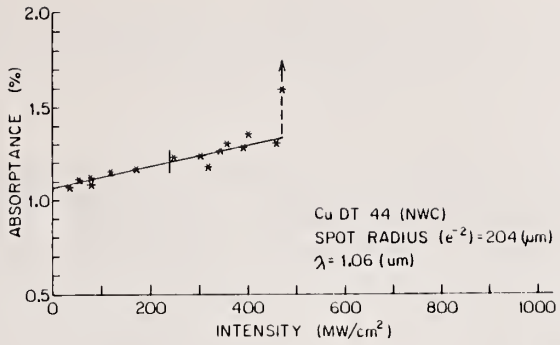

Figure 6. Absorptance vs. intensity plot for Cu DT 44 (NWC). The arrow indicates the damage intensity.

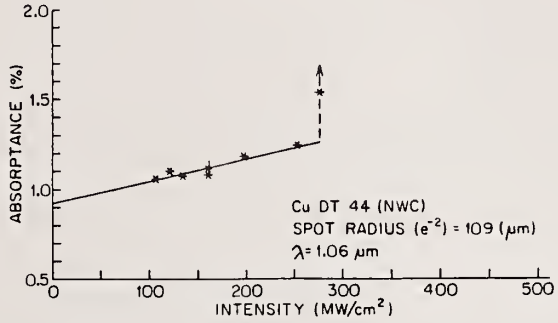

Figure 7. Absorptance vs. intensity plot for Cu DT 44 (NWC). The arrow indicates the damage intensity.

The results are shown in Table 2.

Table 2. Parameters and Results for Cu DT 44 (NWC)

r(μm)	t(nsec)	A_0(%)	A_{PD}(%)	I_D(Mw/cm^2)	E_D(J/cm^2)
109	28	1.07 ± 4%	1.24 ± 4%	240 ± 9%	6.7 ± 9%
				291 ± 9%	8.2 ± 9%
146	28	1.05 ± 4%	1.24 ± 4%	533 ± 7%	15.4 ± 7%
				400 ± 7%	11.2 ± 7%
170	28	1.05 ± 4%	1.22 ± 4%	326 ± 8%	9.1 ± 8%
				299 ± 8%	8.3 ± 8%
204	28	1.07 ± 3%	1.36 ± 3%	503 ± 7%	14.0 ± 7%
				464 ± 7%	13.0 ± 7%
204	28	1.07 ± 4%	1.34 ± 4%	560 ± 9%	15.7 ± 9%
(Multisite)				606 ± 9%	17.0 ± 9%
319	28	1.14 ± 5%	1.52 ± 5%	No damage	No damage
				at 234	at 6.6

The general trend is the one already observed, i.e., the damage intensity is proportional to the beam size. There is no difference in the increase of the absorptance with intensity between the multisite and single site experiments performed with the same beam radius.

Figures 8, 9 and 10 are characteristic absorptance vs. intensity plots for diamond turned sample 46 from NWC, mechanically polished sample 6 from Northrop Corp., and diamond turned sample 7 from INTOP Corp. respectively.

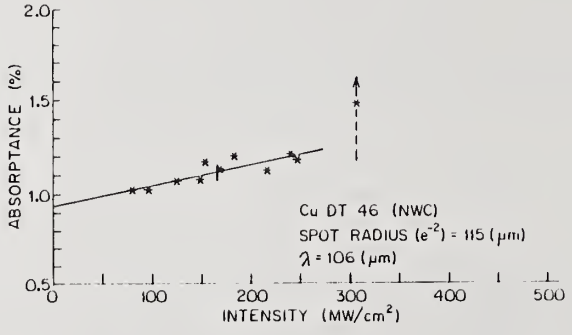

Figure 8. Absorptance vs. intensity plot for Cu DT 46 (NWC). The arrow indicates the damage intensity.

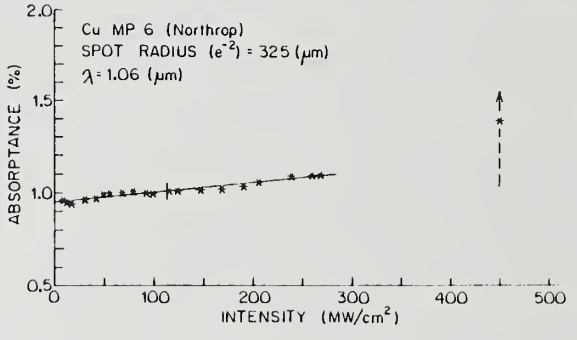

Figure 9. Absorptance vs. intensity plot for Cu MP (Northrop). The arrow indicates the damage intensity.

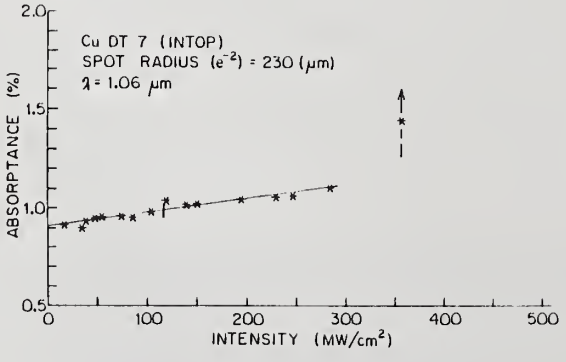

Figure 10. Absorptance vs. intensity plot for Cu DT (INTOP). The arrow indicates the damage intensity.

Tables 3, 4 and 5 present the results. In all samples, the absorptance increases with increasing intensity and the damage threshold increases with increasing beam diameter.

Table 3. Parameters and Results for Cu DT 46 (NWC)

r(μm)	t(nsec)	A_0(%)	A_{PD}(%)	I_D(Mw/cm^2)	E_D(J/cm^2)
100	20	.990 ± 9%	.990 ± 9%	181 ± 10%	2.6 ± 10%
				209 ± 10%	4.2 ± 10%
				216 ± 10%	4.4 ± 10%
115	20	1.00 ± 3%	1.18 ± 3%	322.5 ± 6%	6.5 ± 6%
				246 ± 6%	4.9 ± 6%
				283 ± 6%	5.7 ± 6%

Table 4. Parameters and Results for Cu MP 6 (Northrop)

r(μm)	t(nsec)	A_0(%)	A_{PD}(%)	I_D(Mw/cm^2)	E_D(J/cm^2)
120	22	1.06 ± 3%	1.17 ± 3%	182.5 ± 6%	4.0 ± 6%
				188.4 ± 6%	4.1 ± 6%
325	22	.95 ± 3%	1.09 ± 3%	339 ± 6%	7.4 ± 6%

Table 5. Parameters and Results for Cu DT 7 (INTOP)

r(μm)	t(nsec)	A_0(%)	A_{PD}(%)	I_D(Mw/cm^2)	E_D(J/cm^2)
120	22	1.00 ± 3%	1.15 ± 3%	202 ± 7%	9.2 ± 7%
				218 ± 7%	9.9 ± 7%
				230 ± 7%	10.5 ± 7%
230	22	.96 ± 3%	1.16 ± 3%	285 ± 7%	12.9 ± 7%
				292 ± 7%	13.3 ± 7%
				310 ± 7%	14.1 ± 7%

4. Discussion

As mentioned in the introduction, there is a number of mechanisms which can give rise to intensity dependent processes. One of the most obvious of these is the temperature dependence of the absorptance [1-5]. In order to decide whether the heating of the metal surface by the laser pulse was responsible for the increase of absorptance, a calculation was made of the average temperature excursion resulting from the irradiation at the end of the pulse. In this calculation a one-dimensional heat transfer model was used based on the following assumptions:

1. Short pulse Gaussian beam heating results could be used since the beam dimensions are much larger than the thermal diffusion length ($w >> 2(ktp)^{\frac{1}{2}}$ where w is the beam diameter at $1/e^2$, k is the thermal diffusivity and t_p is the pulse length.)
2. The thermal properties of the metal and the optical absorption were independent of temperature. This assumption allowed a first order calculation of the irradiation induced temperature change.
3. The pulse waveform was rectangular and of duration t_p. Under these conditions one obtains

$$\Delta T_{av} = \frac{2AF}{(\pi k t_p)^{\frac{1}{2}} \rho c}$$

where k is the thermal diffusivity, ρ is the density, C is the specific heat, A is the absorptance and F is the fluence in Joules/cm^2. This change in temperature can be used to calculate a first order approximation to ΔA since $\Delta A = (dA/dT)\Delta T$. The value of $\frac{dA}{dT}$ in Cu calculated from first principles is

$$dA/dT = (1.56 \pm .27) \times 10^{-5} {}^{\circ}C^{-1}$$

Experimental evidence obtained by Quimby et al., [5] gives

$$dA/dT = (1.5 \pm .5) \times 10^{-5} {}^{\circ}C^{-1}$$

for the same copper samples used in this project.

By using the theoretical value, we calculated the absorptance increase due to the temperature increase and compared it to the observed absorptance increase. Table 6 lists the results for every sample. Shown is the slope of the absorptance with respect to fluence.

If the increase of the absorptance with intensity was due to an intensity dependent mechanism other than the one due to temperature, one would expect an experimental value higher than the calculated. For the last three samples, the agreement between theory and experiment is close while for the first two samples the agreement is poor. In almost all cases the calculated value is higher than the experimental value. In the case of the 100 μm radius beam on Cu DT 46, the small size of the beam required irradiation with very low powers which resulted

in rather poor precision. At the present stage, it seems most likely that the intensity dependence of the absorptance is related to irradiation induced temperature changes. The absorptance increase is reversible before damage occurs. This observation means that permanent changes in the surface (i.e., sub-catastrophic laser damage) do not cause the absorptance increase.

Table 6. Comparison between the absorptance increase due to temperature calculated theoretically and the absorptance increase observed experimentally

	r(μm)	$\Delta A/\Delta E$ th. ($x10^{-6}$)	$\Delta A/\Delta E$ exp ($x10^{-6}$)
Cu T 42 (NWC)	170	346	111
	210	378	142
Cu DT 44 (NWC)	109	328	166
	146	333	111
	170	351	196
	204	391	249
	204 (M.S.)	382	205
	319	426	624
Cu DT 46 (NWC)	100	317	0
	115	384	343
Cu MP 6 (Northrop)	120	357	327
	325	350	245
Cu DT 7 (INTOP)	320	361	279
	120	351	375

Figure 11 is a plot of the damage fluence as a function of beam size. For the range of beam sizes examined, the damage intensities increase with increasing beam spot sizes. We believe that stresses developed during the irradiation are responsible for this trend. Previous work [6,7] examined the role of thermal stresses on metal mirrors. However, the range of beam sizes covered in this work is rather limited and a broader range of beam radii is required in order to reach a more thorough understanding of this phenomenon.

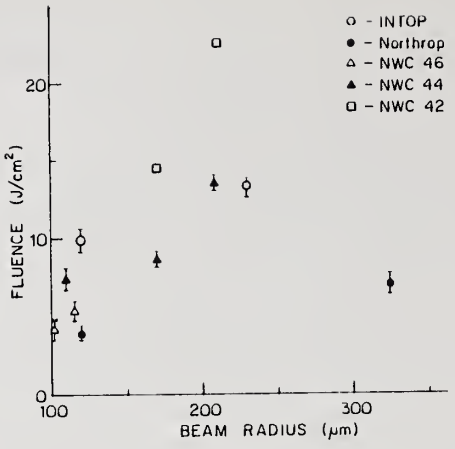

Figure 11. Damage threshold level vs. beam size.

6. Conclusions

Intensity dependent studies on Cu metal mirrors indicates that the observed intensity dependence of the absorptance is related to irradiation induced temperature changes. The measured damage intensities show a correlation to the beam size, with larger beam size corresponding to higher intensities. Continued research is planned including an examination of more mechanically polished and diamond turned samples with a broader range of beam sizes and light wavelengths.

The authors are grateful to D. Decker from the NWC in China Lake, A. Klugman from Northrop Corp., and P. Engstrom from INTOP Corp. for supplying the samples. We want to thank Drs. L. Merkle, R. Quimby and R. Swimm for helpful discussions.

7. References

[1] Roberts, S., Phys. Rev. Ref. Data. 118: 1509; 1959.

[2] Johnson, P. B.; Christy, R. W., Phys. Rev. Ref. Data. B 11: 1315; 1974.

[3] McKay, J. A.; Rayne, J. A., Phys. Rev. Ref. Data. B 13: 673; 1975.

[4] Decker, D. L.; Hodgkin, V. A., Nat. Bur. Stand. Spec. Publ. 620; 1980; 190 p.

[5] Quimby, R. S.; Bass, M.; Liou, L., Calorimetric measurements of temperature-dependent absorption in copper, this conference.

[6[Musal, H. M. Jr., Nat. Bur. Stand. Spec. Publ. 568; 1979; 159 p.

[7] Musal, H. M. Jr., Nat. Bur. Stand. Spec. Publ. 620; 1980; 227 p.

The question was asked what the size of the error bars would be on the values of $\Delta A/\Delta E$ for the experiment. THe author answered that it would be about ±9 percent. The pulse length of the laser used was 22 to 23 ns. The measurements were made in order of increasing laser intensity. However, the curve is reversible, as was demonstrated by going back periodically and checking the low-intensity absorption.

Thermo-Optic Coefficient (∂n/∂T) of 1.3 μm Laser Window Materials

Richard J. Harris and Michael E. Gangl

University of Dayton Research Institute
Dayton, Ohio 45469

The thermo-optic coefficient (∂n/∂T) of several 1.3 μm laser window materials has been measured in the visible and near infrared spectral regions. These materials include CaF_2, Al_2O_3, MgO, MgF_2, YAG, YLF, water clear ZnS, Kigre Q-98 glass, Corning CORTRAN glasses, and LiF. The measurements were made in the temperature range of 25 to 100 degrees C using a laser interferometric technique. The lasers used were HeNe lasers operating at 0.6328 μm, 1.15 μm, and 3.39 μm and a Nd:YAG laser operating at 1.3 μm.

Key words: ∂n/∂T; laser windows; optical properties; thermo-optic.

1. Introduction

The accurate prediction of performance of materials as high power laser windows requires a knowledge of the thermo-optic coefficient. When temperature gradients are introduced in windows thermal expansion, refractive index changes, and stress-optic effects combine to degrade the optical quality of a transmitted beam, causing a decrease in power density in the far field. The calculations of these effects are presented elsewhere [1,2][1] and will not be addressed here.

We have used an interferometric technique to measure the values of ∂n/∂T for CaF_2, Al_2O_3, MgO, MgF_2, YAG, YLF, water clear ZnS, Kigre Q-98 glass, Corning CORTRAN glasses, and LiF. These measurements were made at 0.6328 μm, 1.15 μm, and 3.39 μm using HeNe lasers and at 1.3 μm using a Nd:YAG laser in the temperature range of 25 to 100 degrees C.

2. Experimental Procedure

The experimental setup used is shown schematically in Figure 1. The laser beam is reflected from both the front and back surfaces of the sample and for samples with nearly parallel faces, Fizeau interference fringes are formed at the detector. For non-parallel samples, mirrors M3, M4, and M5 and the beam splitters are used to recombine the two reflected beams at the detector to form the fringes. The lasers used were a Spectra-Physics 155 HeNe at 0.6328 μm, two Spectra-Physics 125 HeNe lasers at 1.15 μm and 3.39 μm, and a Control Laser 510T Nd:YAG laser at 1.3 μm. A Judson J12 indium arsenide detector was used at 3.39 μm, and a Judson J16 germanium detector was used at the other wavelengths. An Ithaco Dynatrac 3 lock-in amplifier was used to amplify the chopped signal from the detectors. The signal from the thermocouple, which was referenced to an ice bath, was amplified with a Keithley 149 milli-microvoltmeter.

The samples are placed in the oven, consisting of a metal box with two light bulbs for heaters, with a thermocouple in intimate contact. The temperature is slowly varied in the oven and the detector signal drives the y axis of the x-y recorder. The x axis is driven by the amplified thermocouple signal, resulting in a sinusoidal plot of reflectance versus temperature. The value of ∂n/∂T is then calculated from Eq. (1) for each pair of fringe maxima or minima, where λ is the wavelength of the laser used, L is the sample thickness, ΔT is the temperature difference between the successive extrama, n is the refractive index of the sample, and α is the linear thermal expansion coefficient. Each set of measurements thus gives a statistically large number of ∂n/∂T values which are then averaged.

$$\partial n/\partial T = \lambda/(2L\Delta T) - n\alpha \qquad (1)$$

[1]Numbers in brackets indicate the literature references at the end of the paper.

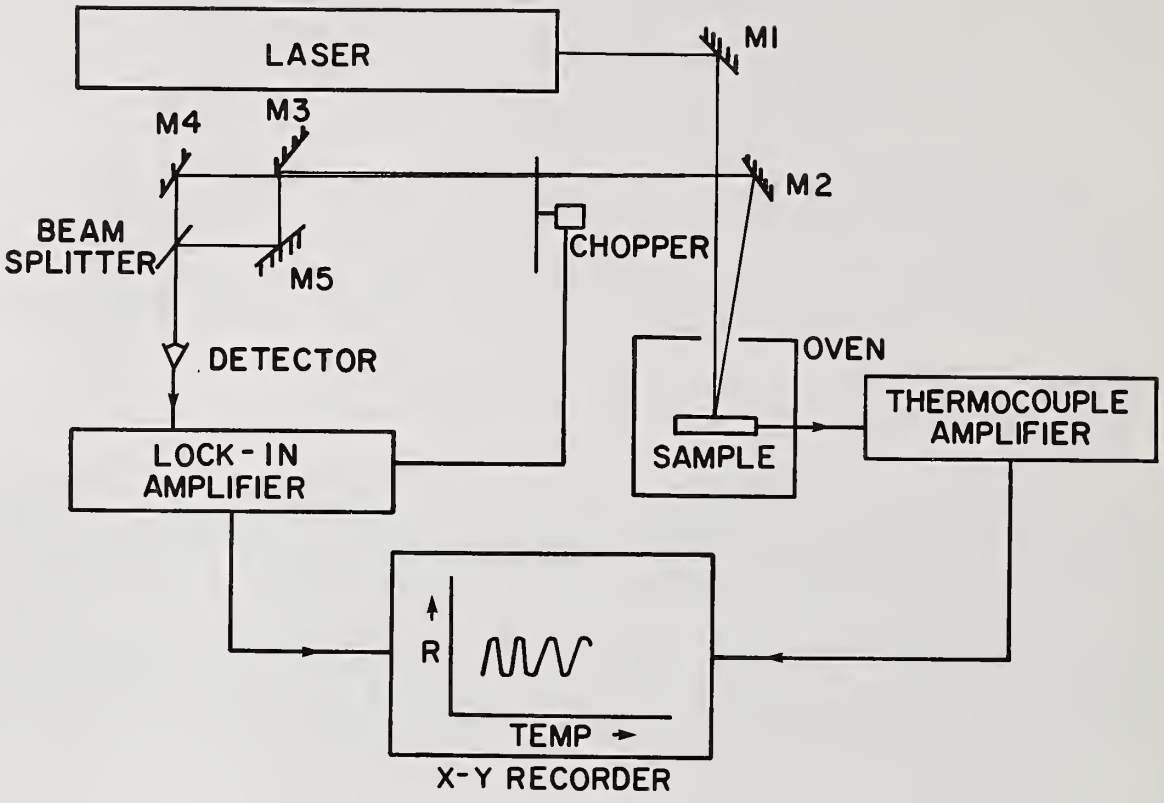

Figure 1. Schematic of experimental setup for ∂n/∂T measurements. The recorder plots interference fringe intensity versus sample temperature from which the change in optical path per unit temperature change is determined. From this and a knowledge of refractive index and expansion coefficient, the value of ∂n/∂T is calculated.

The CaF_2 sample was manufactured by Harshaw and was measured at 0.6328 μm only to serve as a comparison to previous measurements on the same sample [3] and verify the reproducibility of the values obtained. The Al_2O_3 was from Crystal Systems, Inc. and was (0001) orientation, so only the ordinary ray was measured. The MgF_2 was a single crystal sample produced by Optovac, and was also oriented so as to allow only the ordinary ray to be measured. The YAG ($Y_3Al_5O_{12}$) sample was produced by Litton/Airtron. The ZnS was loaned to us by Raytheon and is the new Multispectral Grade Raytran® which is water clear. The Q-98 glass was a phosphate glass lightly doped with Nd and was produced by Kigre, Inc. The CORTRAN glasses were made by Corning and designated 9753 and 9754 by the manufacturer. The LiF was from Harshaw, and the MgO was from Adolph Meller. The YLF ($LiYF_4$) was from Saunders Associates, Inc., and the ordinary ray again was the only one measured.

3. Results and Discussion

The values of ∂n/∂T obtained are given in Table 1. The errors quoted are statistical errors (standard deviations) for the averages calculated in each measurement and represent the precision of the experiment. The accuracy of the values depends largely on the accuracy of the n and α values used in the calculations. The values of these constants used in the calculations

Table 1. Summary of ∂n/∂T Results (10^{-5}/°C)

Material	Wavelength (μm)			
	0.6328	1.15	1.315	3.39
Al_2O_3	0.86±0.41	0.77±0.37	0.75±0.24	0.69±0.12
ZnS	5.84±0.11	4.80±0.78	4.60±1.73	4.15±0.57
Kigre Q-98	0.16±0.38	0.17±0.28	0.18±0.31	*
YAG	0.68±0.37	0.61±0.29	0.99±0.52	0.95±0.51
MgF_2	0.44±0.31	0.42±0.22	0.58±0.43	0.41±0.09
MgF_2		0.44±0.23		
YLF	-0.56±0.23	-0.54±0.23	-0.51±0.26	-0.53±0.12
MgO	1.13±0.46	1.10±0.35	1.15±0.38	1.11±0.24
CaF_2	-1.29±0.20			
LiF	0.66±0.54			
CORTRAN 9753	0.41±0.25			
CORTRAN 9754	0.88±0.43			

* - Kigre Q-98 is opaque at 3.39 μm.

are given in Table 2. Values not shown in Table 1 for some of the materials at longer wavelengths are measurements not yet made with the exception of the 3.39 μm value for Kigre Q-98 glass, which is opaque at that wavelength.

Table 2. Values of Constants Used in Calculating ∂n/∂T

Material	α(10^{-6}/°C)	n at 0.6328 μm	n at 1.15 μm	n at 1.315 μm	n at 3.39 μm
Al_2O_3	7.2	1.77	1.75	1.73	1.73
ZnS	6.9	2.35	2.28	2.28	2.25
Kigre Q-98	8.2	1.55	1.59	1.59	*
YAG	6.9	1.83	1.82	1.82	1.82
MgF_2	10.4	1.38	1.38	1.38	1.38
YLF	13.0	1.48	1.47	1.47	1.47
MgO	10.5	1.74	1.74	1.74	1.74
CaF_2	19.5	1.43			
LiF	35.0	1.39			
CORTRAN 9753	6.2	1.61			
CORTRAN 9754	6.2	1.66			

*Kigre Q-98 glass is opaque at 3.39 μm

The value -1.29×10^{-5}/°C obtained for CaF_2 at 0.6328 μm compares very well with the value obtained several years ago in another experiment done at this laboratory [3] (-1.31×10^{-5}/°C). The reason for making this measurement was to verify the temperature calibration of the thermocouple, which was mounted in a slightly different manner from that used in the former experiment. The values obtained for the water clear ZnS were consistently lower than those listed in Ref. [3] (by an average of 7%). The sample used in Ref. [3] was chemical vapor deposited sample grown by Raytheon about 6 years ago. The lowest $\partial n/\partial T$ values observed were for the Kigre Q-98 glass, which also showed a very low optical absorption as measured by laser rate calorimetry at 1.3 μm [4].

This work was supported by the Air Force Wright-Aeronautical Laboratories, Materials Laboratory, Wright-Patterson Air Force Base, Ohio 45433.

References

[1] Sparks, M. J. Appl. Phys. 42: 5029; 1971.

[2] Sparks, M. J.; Chow, H. C., in Proceedings of the Third Conference on High Power Laser Window Materials (U.S. Government Printing Office, Washington, D.C., 1973), Vol. 3, p. 1087.

[3] Harris, R. J.; Johnston, G. T.; Kepple, G. A.; Krok, P. C.; Mukai, H. Appl. Opt. 16: 436; 1977.

[4] Fernelius, N. C.; Dempsey, D. V.; O'Quinn, D. B.; Gangl, M. E.; Knecht, W. L. in Proceedings of the Thirteenth Boulder Damage Symposium, to be published.

Polarization Sensitive Laser Calorimetry

Perry Miles

Raytheon Company
Missile Systems Division
Bedford, Massachusetts 01730

Techniques used currently to determine bulk and surface laser aborption coefficients of highly transparent materials have drawbacks both inherent and practical that limit their accuracy. Conventional bar calorimetry attempts a two-coefficient characterization of nine separate physical absorption sites. Photo-acoustic techniques require in situ calibration sensitive to sample geometry and material.

This paper proposes a new technique in which a set of conventional ballistic laser calorimetry measurements are made on a single prismatic sample. Systematic changes in the polarization and direction of propagation of the laser beam can lead to an explicit determination of individual surface and bulk absorption coefficients. An equilateral prism sample provides a set of independent measurements sufficient to establish the bulk absorption in each of three internal paths and two absorption components on each of the three surfaces. This geometry can be used, in principle, for materials with refractive indices less than 2; more practically, for indices less than 1.7. For higher indices, a truncated prism is proposed which allows seven independent measures to deduce eight absorption components. An assumption of constant surface anisotropy is proposed to complete the analysis. Design criteria for the prism shape are presented, along with analytical expressions for all relevant absorption experiments, and for the simplest cases of uniform, isotropic high and low index materials.

Background

When a collimated light beam passes through a transparent solid, the average optical intensities inside the entrance and exit surfaces and along the internal paths depend on the Fresnel reflection coefficients at the surfaces. They are found by vector summation of the optical field intensities of the various incident and reflected waves.[1] In conventional laser calorimetry experiments the beam enters and leaves a bar of length L in a direction normal to the end faces (fig. 1). In this case, the surface field reflection coefficient is:

$$r = \frac{n-1}{n+1} \tag{1}$$

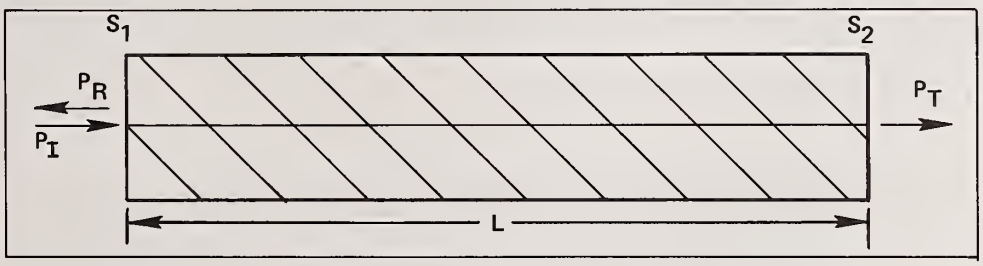

Figure 1. Disposition of Laser Beam and Sample in Conventional Laser Calorimetry

The average power (P_{int}) within the bar is related to the transmitted power P_T by the expression:

$$P_{int} = \frac{1+r^2}{1-r^2} \cdot P_T = \frac{n^2+1}{2n} P_T \tag{2}$$

Phase reversal of the wave reflected at the exit surface and a corresponding phasing at the entrance surface that depends on sample length results in the following power relationships[2]:

Position	Effective Laser Power	
Bulk Path	$\frac{n^2+1}{2n} \cdot P_T$	
Exit Surface	$n \cdot P_T$	
Entrance Surface	$n \cdot P_T$	resonant
	$\frac{n^2+1}{2n} \cdot P_T$	average or incoherent
	$\frac{1}{n} \cdot P_T$	antiresonant

In the usual incoherent case, valid for multiline lasers or for irregular bar surfaces, the total sample heating rate, Q, is given [3] by:

$$Q = \left[\alpha L \frac{n^2+1}{2n} + \beta_{S1} \cdot \frac{n^2+1}{2n} + \beta_{S2} n\right] P_T \quad (\alpha I \ll 1) \tag{3}$$

where α, β_{S1} and β_{S2} are the bulk and surface absorption coefficients, respectively.

The individual factors α and $\left[\beta_{S1} + \beta_{S2} \cdot \frac{2n^2}{n^2+1}\right]$, usually denoted without differentiation as $2\beta_S$, can be estimated from measurements on a series of samples of different lengths on the assumption that both α and $2\beta_S$ remain unchanged from sample to sample. In practice, variation in surface absorption from sample to sample can impose a severe limitation on the accuracy of estimates of the bulk absorption coefficient. In a typical experiment with three sample lengths there are in fact three bulk and six surface sources of heat, none of which is ever derived explicitly. "Long bar"[3] calorimetry and photo-acoustic[4,5] techniques can also be used to separate bulk and surface sources of heating, and in principle, to distinguish between the entrance and exit surfaces although this is rarely, if ever, carried out. The accuracy attainable in long bar calorimetry is compromised if only small samples are available,[2] while quantitative analysis of the sonic signals generated in the photo-acoustic technique depend sensitively on sample, laser beam and transducer geometry, and must be calibrated for each sample assembly.

To overcome these problems we propose a new technique that provides a direct estimate of the bulk absorption of a single sample, together with unambiguous estimates of the absorption of specific surfaces. Furthermore, the measurements can be carried out in a conventional calorimeter with only minor changes in the sample and laser beam geometries.

Prismatic Technique

The new method described in this paper represents an extension of the conventional ballistic technique. It sets out to make use of two facts, first, that at oblique incidence the reflection coefficient of a surface depends on the sense of polarization of the laser beam, and second, that the values of bulk and surface absorptions do not scale equally with that coefficient. To implement this technique the usual rectilinear bar sample is replaced by a prism and the laser beam is arranged to enter and leave the sample at symmetric angles and to execute a simple triangular set of paths within the sample. An equilateral prism (fig. 2) could be used, in principle, for materials with a refractive index less than 2. The relevant Fresnel coefficients for s- and p-polarized waves are:

$$r_s = \frac{n\cos\theta_i - \cos\phi}{n\cos\theta_i + \cos\phi}$$

$$\text{with } \sin\phi = n\sin\theta_i$$

$$r_p = \frac{n\cos\phi - \cos\theta_i}{n\cos\phi + \cos\theta_i}$$

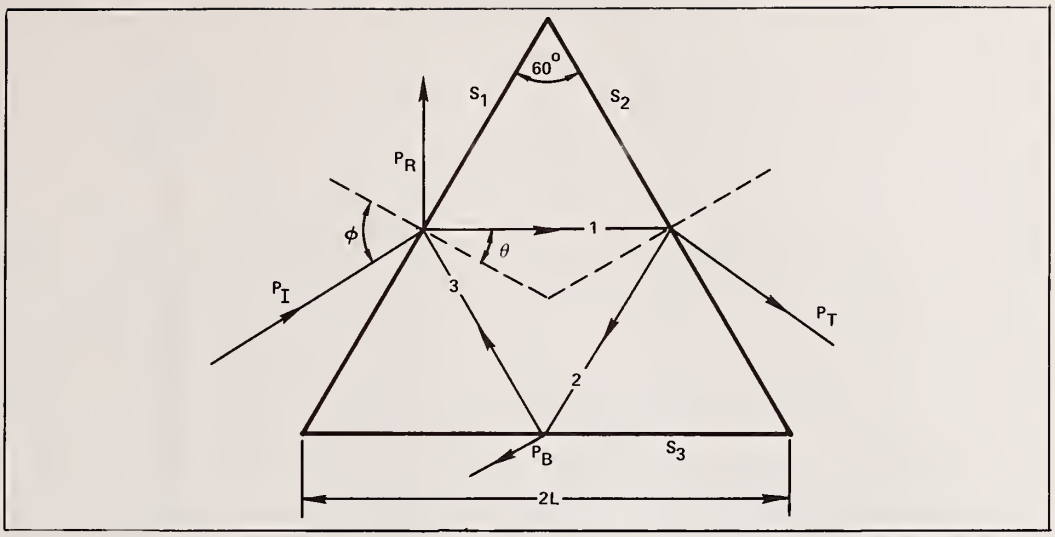

Figure 2. Beam/Sample Disposition for a Material with n ≈ 1.7 - One of Six Symmetrical Prism Arrangements

where θ_i is the internal angle of incidence at the surface. As an example, the corresponding power reflection coefficients r_3^2 and r_p^2 for a material with n=2 are illustrated in fig. 3. The difference between r_s^2 and r_p^2 becomes very large near the polarizing (Brewster's) angle where $(\phi+\theta_i)=90°$, $\tan\theta_i = \frac{1}{n}$. Both reflection coefficients show an extreme dependence on angle beyond the polarizing angle, and for this reason the equilateral prism becomes impractical for materials with an index greater than 1.75. While this geometry is not of wide applicability, therefore, it serves to illustrate the principles involved.

As compared to the bar geometry, there are now three separate surfaces, S_1, S_2, and S_3; and three separate internal paths ① ② and ③ each of length L which must be taken into account. The power P_B escaping from the prism base can be absorbed externally and is of no practical consequence except in its relationship to the effective laser power at surface S_3. As in the simple bar case, the relative values of the various effective laser powers can be calculated from the Fresnel surface reflection coefficients. The difference is that these coefficients now depend on the polarization state of the incident beam and reach extrema for a beam polarized with its E vector parallel to the plane of incidence (E_p) and normal to that plane (E_s). As a result, both the absolute levels and relative distributions of laser absorption in the bulk paths and surfaces will depend on the polarization of the beam. Thus, two linearly independent combinations of absorption coefficients can be deduced from two separate calorimetry experiments for each of the six symmetric positions of the prism. If the surface absorption mechanisms are isotropic, a set of six of these experiments can be chosen to deduce all three surface coefficients β_1, β_2 and β_3 and all three bulk coefficients α_1, α_2 and α_3. For the simplest case of a completely uniform sample, where $\alpha_1 = \alpha_2 = \alpha_3 = \alpha$, and $\beta_1 = \beta_2 = \beta_3 = \beta_s$, only two such measurements are needed.

For a laser beam of s-polarization wherein the E field vectors all lie in the plane of each surface of the sample, the Fresnel reflection coefficient for surfaces S_2 and S_3 is:

$$r_s = \frac{n\cos 30° - \cos\phi}{n\cos 30° + \cos\phi}$$

For the p-polarization, the corresponding coefficient is:

$$r_p = \frac{n\cos\phi - \cos 30°}{n\cos\phi + \cos 30°}\ ,\quad \sin\phi = \frac{n}{2}\ ,\quad n<2$$

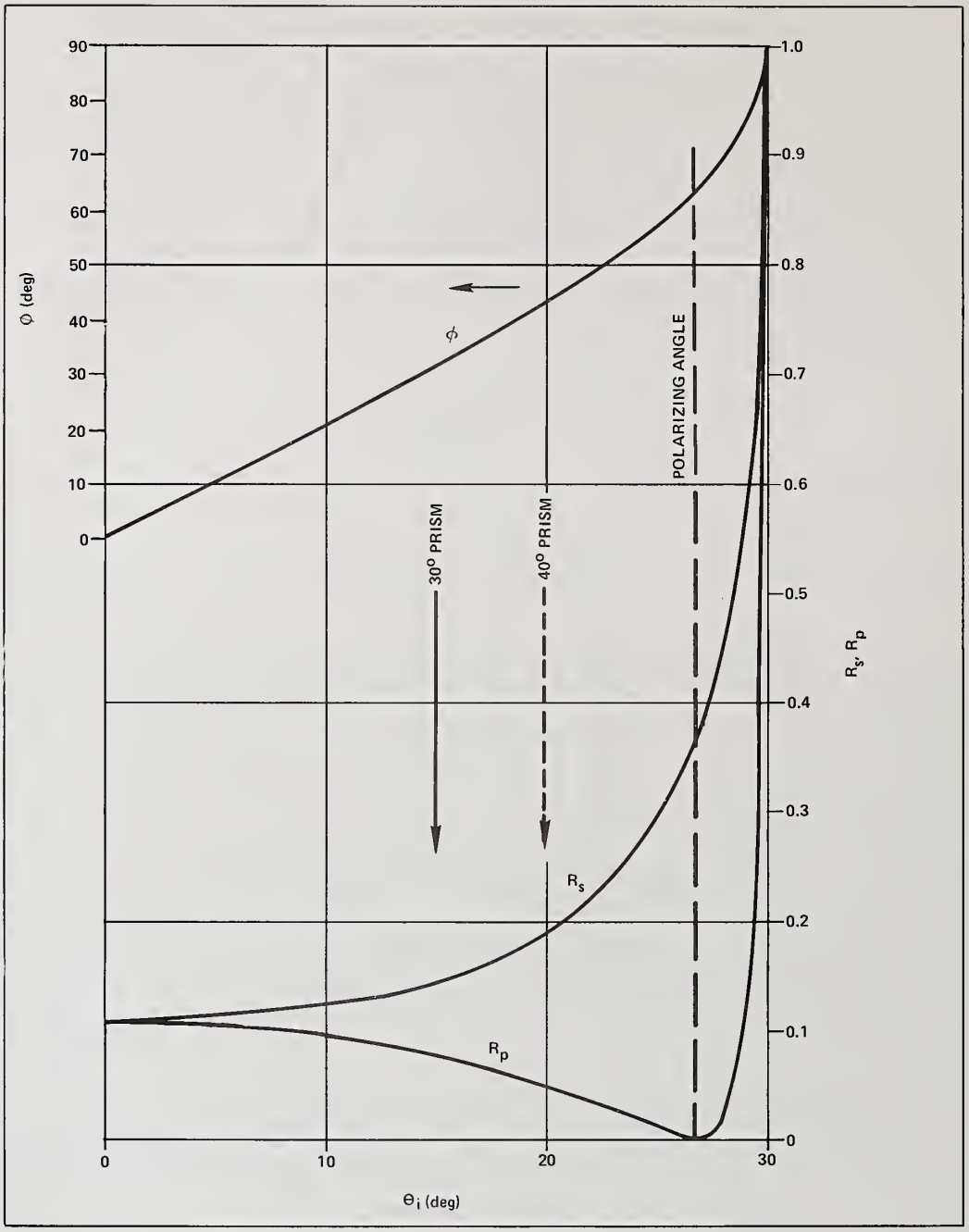

Figure 3. External Refraction Angle and Surface Reflection as a Function of Internal Incidence Angle and Polarization for Material with n $\approx$ 2.0

The effective power fluxes along the three internal paths are:

$$\left.\begin{aligned} P_{1s} &= \frac{1}{1-r_s^2} \cdot P_T \\ P_{2s} &= \frac{r_s^2}{1-r_s^2} \cdot P_T \\ P_{3s} &= \frac{r_s^4}{1-r_s^2} \cdot P_T \end{aligned}\right\} \quad \text{or} \quad \left\{\begin{aligned} P_{1p} &= \frac{1}{1-r_p^2} \cdot P_T \\ P_{2p} &= \frac{r_p^2}{1-r_p^2} \cdot P_T \\ P_{3p} &= \frac{r_p^4}{1-r_p^2} \cdot P_T \end{aligned}\right. \tag{4}$$

The effective powers at the three surfaces are, in s-polarization,

$$\left.\begin{aligned} P_{S2s} &= \sec 30^\circ \frac{(1+r_s)^2}{1-r_s^2} \cdot P_T = n\sec\phi P_T \\ P_{S3s} &= \sec 30^\circ\, r_s^2 \frac{(1+r_s)^2}{1-r_s^2} \cdot P_T \\ P_{S1s} &= \sec 30^\circ \frac{1}{1-r_s^2} \left(1+r_s^4 + \begin{Bmatrix} 2r_s^2 \\ 0 \\ -2r_s^2 \end{Bmatrix}\right) P_T \quad \begin{matrix} \text{--resonant} \\ \text{--average} \\ \text{--antiresonant} \end{matrix} \end{aligned}\right\} \tag{5}$$

For the p-polarization beam, the different constraints on the electric field components lying in and normal to the surfaces result in the effective powers:

$$\left.\begin{aligned} P_{S2p} &= \frac{\sec 30^\circ}{1-r_p^2} (1+r_p+r_p^2) P_T = n\sec\phi P_T\left(\cos^2\phi + \frac{1}{n^4}\sin^2\phi\right) \\ P_{S3p} &= \frac{\sec 30^\circ}{1-r_p^2}\, r_p^2\, (1+r_p+r_p^2) P_T \\ P_{S1p} &= \frac{\sec 30^\circ}{1-r_p^2} \left(1+r_p^4 + \begin{Bmatrix} r_p^2 \\ 0 \\ -r_p^2 \end{Bmatrix}\right) P_T \quad \begin{matrix} \text{--resonant} \\ \text{--average} \\ \text{--antiresonant} \end{matrix} \end{aligned}\right\} \tag{6}$$

The appearance of the sec 30° factor in the effective surface power flux expresses the fact that the absorbing volume at each surface is increased by its inclination to the impinging laser beam.

The total heat deposition, Q, in each case is given by the relationship:

$$\left.\begin{aligned}\frac{Q_s(1-r_s^2)}{P_{Ts}} &= (\alpha_1+r_s^2\alpha_2+r_s^4\alpha_3)L \\ &+\sec 30^\circ\left[(1+r_s^4)\beta_1+(1+r_s)^2\beta_2+r_s^2(1+r_s)^2\beta_3\right]\end{aligned}\right\} \quad (7)$$

or

$$\left.\begin{aligned}\frac{Q_p(1-r_p^2)}{P_{Tp}} &= (\alpha_1+r_p^2\alpha_2+r_p^4\alpha_3)L \\ &+\sec 30^\circ\left[(1+r_p^4)\beta_1+(1+r_p+r_p^2)\beta_2+r_p^2(1+r_p+r_p^2)\beta_3\right] \\ &+\frac{\sec 30^\circ}{4}\left[(1+r_p^4)\Delta\beta_1+(1-r_p)^2\Delta\beta_2+r_p^2(1-r_p)^2\Delta\beta_3\right]\end{aligned}\right\} \quad (8)$$

where we have included the possibility that the surface absorption is anisotropic and can be written as:

$$Q_{surf} \sim \beta E_{11}^2+(\beta+\Delta\beta)E_\perp^2 \quad (9)$$

If such an asymmetry does exist, it is perhaps best established by a separate experiment for each face, wherein the laser beam is realigned to enter and leave the lateral face at normal incidence and to undergo total internal reflection at the basal face under scrutiny (fig. 4). In this latter case, the expressions for the electric fields internal to the basal surface for a unit strength incident field are:[6]

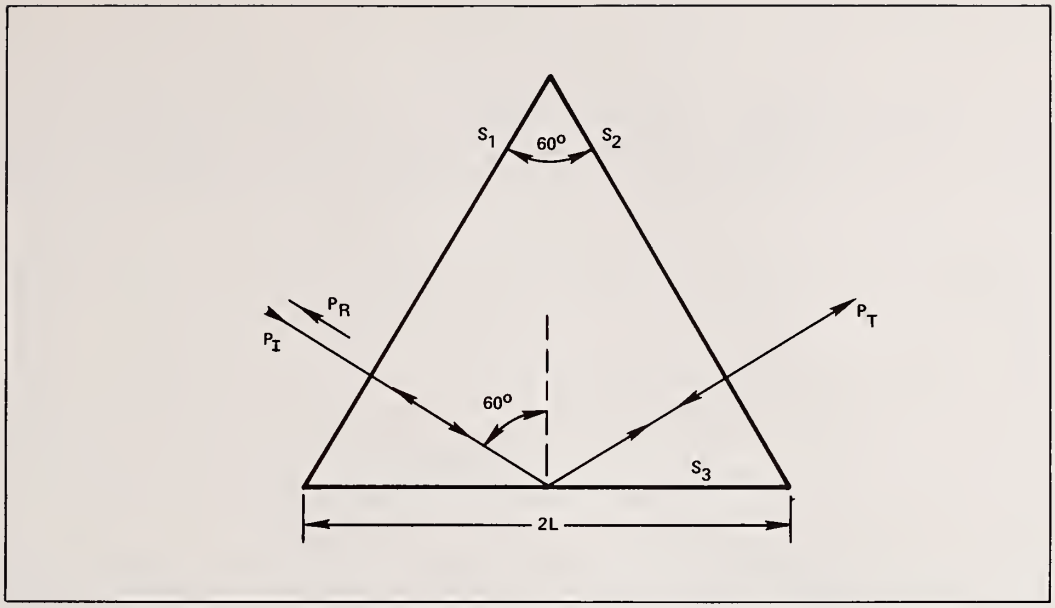

Figure 4. Beam/Sample Disposition for Measurements on Anistropic Surface Absorption

$$\left.\begin{aligned} E_s &= \frac{2n\cos 60°}{(n^2-1)^{1/2}} \\ E_{p\parallel} &= \frac{2n\cos 60°(n^2\sin^2 60°-1)^{1/2}}{(n^2-1)^{1/2}\left[(n^2+1)\sin^2 60°-1\right]^{1/2}} \\ E_{p\perp} &= \frac{2\sin 60°\cos 60°}{(n^2-1)^{1/2}\left[(n^2+1)\sin^2 60°-1\right]^{1/2}} \end{aligned}\right\} \quad (10)$$

The corresponding expressions for sample heating are:

$$\frac{Q_s}{P_{Ts}} \cdot \frac{2n}{n^2+1} = 2\sin 60°.\alpha L+\beta_1+\frac{2n^2}{n^2+1}.\beta_2+\frac{n^2}{n^2-1}\sec 60°.\beta_3 \quad (11)$$

and

$$\frac{Q_p}{P_{Tp}} \cdot \frac{2n}{n^2+1} = 2\sin 60°.\alpha L+\beta_1+\frac{2n^2}{n^2+1}.\beta_2+\sec 60°.\frac{3n^4-4n^2+3}{(3n^2-1)(n^2-1)}\beta_3 \quad (12)$$

$$+\sec 60°\frac{3\Delta\beta_3}{(3n^2-1)(n^2-1)}$$

From these, it follows that

$$\Delta_3 \triangleq \left(\frac{Q_s}{P_{Ts}} - \frac{Q_p}{P_{Tp}}\right) \cdot \frac{2n}{n^2+1} = \frac{6}{(3n^2-1)} \left[\beta_3 - \frac{\Delta\beta_3}{(n^2-1)}\right]$$

or

$$\Delta\beta_3 = (n^2-1)\,\beta_3 - (3n^2-1)\,\frac{\Delta_3}{6} \qquad (13)$$

This value and its two counterparts for surfaces ① and ② can then be substituted in Equation 8. Alternatively, if it is known a priori that the surface absorption is isotropic, this set of measurements could be used to determine β_3 directly, as

$$\beta_3 = \frac{3n^2-1}{6(n^2-1)} \cdot \Delta_3, \text{ etc.} \qquad (14)$$

Finally, before leaving the 60° prism sample geometry, an example can be given for a material with n=1.5, with uniform internal absorption and uniform isotropic surface absorption. In this case,

$$\phi_i = 30° \qquad \phi = 48.59°$$

$$r_s = 0.32523 \qquad r_p = 0.06788$$

with power reflection coefficients

$$R_s = 0.1058 \text{ and } \qquad R_P = 0.0046$$

The relative sample heating factors are given by:

$$\frac{Q_s}{P_{Ts}} = 1.2491\alpha L + 3.8134\beta_s$$

$$\frac{Q_p}{P_{Tp}} = 1.0093\alpha L + 2.4100\beta_s \qquad (15)$$

As expected, the p-beam heating is overwhelmingly dominated by absorption along the primary path and at the entrance and exit surfaces. While these sources are also dominant for the s-beam, the 10 percent surface reflections bring about a 24 percent increase in apparent bulk absorption and a 58 percent increase in apparent surface absorptions, from which the independent αL and β_s factors can be readily deduced.

For materials with refractive index greater than 1.75, the 60° prism is of little use. In its place we propose a truncated prism with an included angle 2θ no greater than 40° in which the laser beam still executes a triangular path but undergoes total internal reflection at the basal surface. Two cases with different power distributions within the sample can be distinguished and are defined as cases A and B of Figure 5. The sample can also be turned end for end to provide four separate beam patterns, each with two possible polarization states of the incident beam, a total of eight configurations. In addition, if necessary, the laser beam can be reoriented to enter and leave the lateral faces at normal incidence (case C).

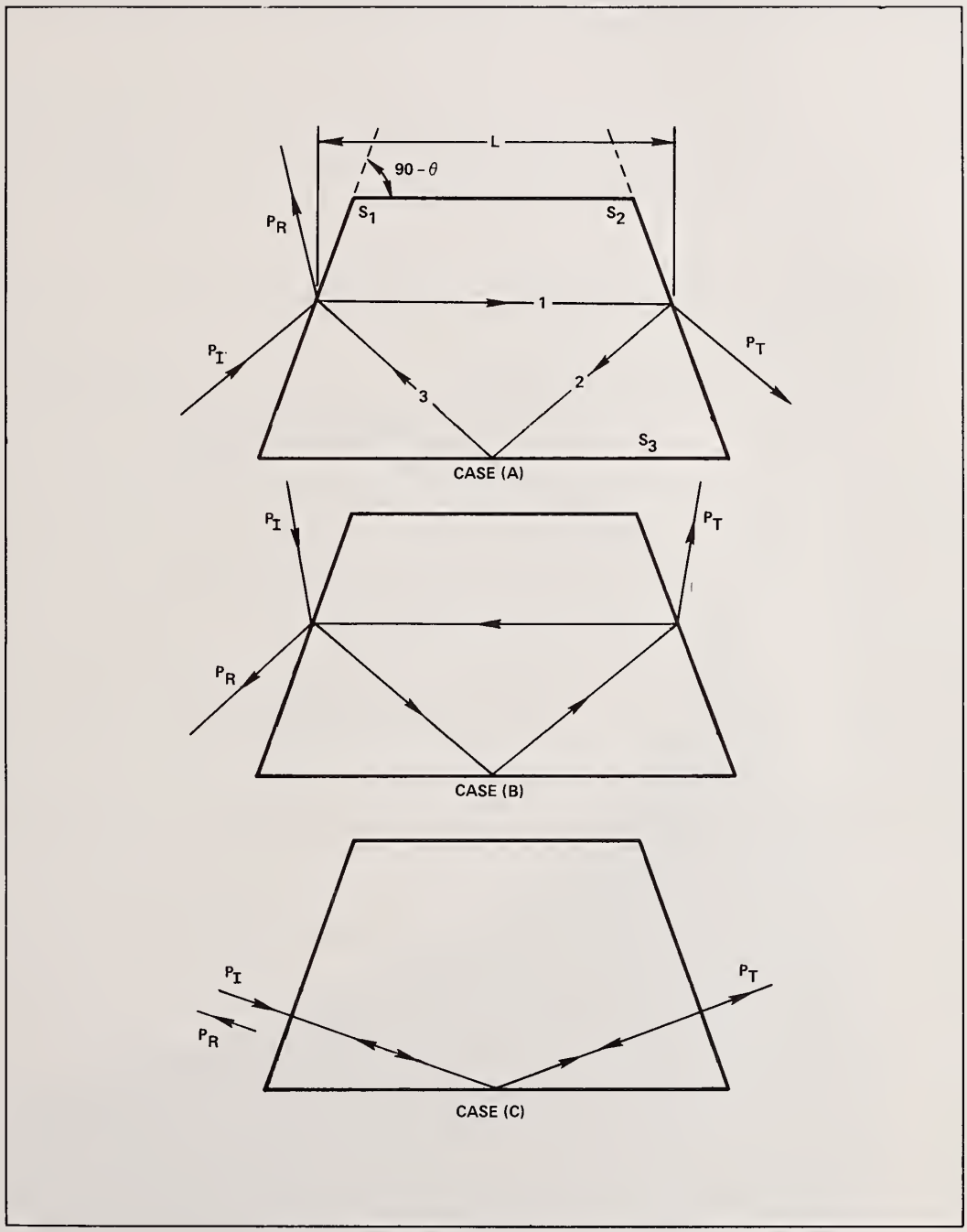

Figure 5. Beam/Sample Disposition for Materials with Refractive Indices Greater than 1.75

The choice of prism angle is limited both by the need to establish total internal reflection at the base, that is $\cos 2\theta < 1/n$, for laser penetration of the lateral surfaces, that is $\sin\theta < 1/n$, and preferably for operation at incidence angles at, or less than the Brewster angle, i.e., $\tan\theta < 1/n$. The resultant design boundaries in the $(2\theta, n)$ plane (fig. 6) show that a $2\theta = 40°$ prism is useful for materials with indices between 1.35 and 2.8. A 30° prism extends this range from 1.2 to 3.8, but at the cost of a reduced discrimination between s and p reflections at the lateral faces (see fig. 2). In principle, a new prism design could be chosen to match the polarization angle for each material, but this has no particular algebraic advantage, and complicates the actual fabrication of prism samples. The only significant changes in the analysis from the equilateral prism are first, that the field strengths at the basal surface follow the TIR formulae and second, since the effective power fluxes along paths ② and ③ are identical, only one average absorption coefficient, α_2, is needed to describe the heat generated therein.

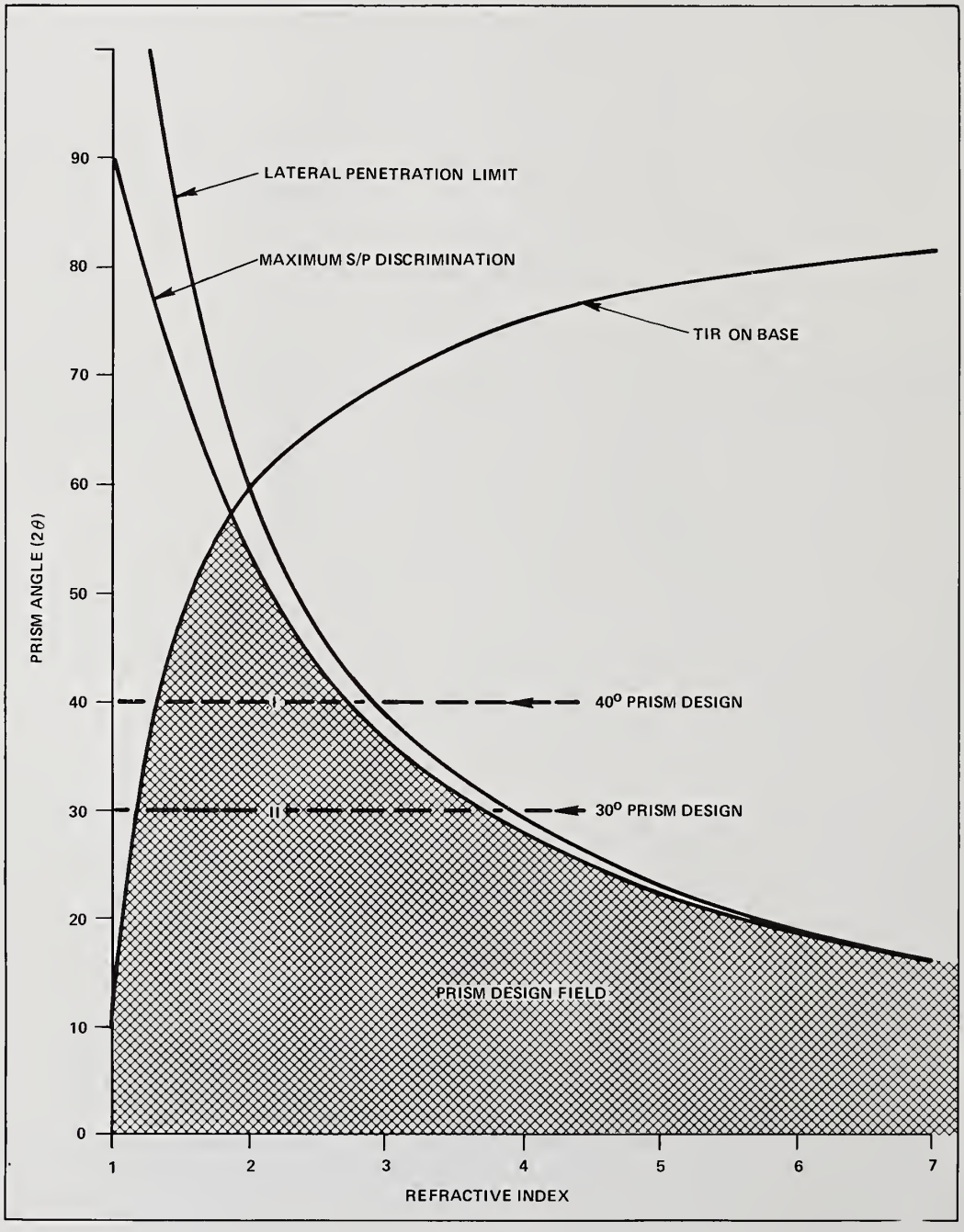

Figure 6. Design Limits for Prismatic Sample Geometries

Thus, by repetition, the sample heating functions for the three cases of Figure 5 are as follows:

Case A

$$\frac{Q_s}{P_{Ts}} \cdot (1-r_s^2) = (\alpha_1+r_s^2\alpha_2\sec 2\theta)\, L+\sec\theta\left[(1+r_s^2)\beta_1+(1+r_s)^2\beta_2\right] + 4r_s^2\sin 2\theta \cdot \frac{n^2}{n^2-1}\ \beta_3 \tag{16}$$

$$\left.\begin{aligned} \frac{Q_p}{P_{Tp}}\ (1-r_p^2) &= (\alpha_1+r_p^2\,\alpha_2\sec 2\theta)\, L+\sec\theta(1+r_p^2)\,\beta_1 \\ &+\sec\theta\ \left[(1+r_p)^2\cos^2\theta+(1-r_p)^2\sin^2\theta\right]\beta_2 \\ &+\frac{4r_p^2\sin 2\theta}{(n^2-1)}\left[\frac{(n^4+1)\cos^2 2\theta-n^2}{(n^2+1)\cos^2 2\theta-1}\right]\cdot\beta_3 \\ &+\sec\theta\sin^2\theta\ \left[(1+r_p^2)\,\Delta\beta_1+(1+r_p)^2\Delta\beta_2\right] \\ &+\frac{4r_p^2\sin 2\theta\cos^2 2\theta}{(n^2-1)\ \left[(n^2+1)\cos^2 2\theta-1\right]}\cdot\Delta\beta_3 \end{aligned}\right\} \tag{17}$$

Case B

$$\frac{Q_s}{P_{Ts}}\ (1-r_s^2) = (\alpha_1 r_s^2+\alpha_2\sec 2\theta)\, L+\sec\theta\left[(1+r_s^2)\beta_1+(1+r_s)^2\beta_2\right] + 4\sin 2\theta\frac{n^2}{n^2-1}\cdot\beta_3 \tag{18}$$

$$\left.\begin{aligned}
\frac{Q_p}{P_{Tp}}\ (1-r_p^2) &= (\alpha_1 r_p^2+\alpha_2 \sec 2\theta)L+\sec\theta(1+r_p^2)\,\beta_1 \\
&+\sec\theta\ \left[(1+r_p)^2\cos^2\theta+(1-r_p)^2\sin^2\theta\right]\,\beta_2 \\
&+\frac{4\sin 2\theta}{(n^2-1)}\ ,\ \left[\frac{(n^4+1)\cos^2 2\theta-n^2\cdot}{(n^2+1)\cos^2 2\theta-1}\right]\cdot\beta_3 \\
&+\sec\theta\sin^2\theta\left[(1+r_p^2)\,\Delta\beta_1+(1+r_p)^2\Delta\beta_2\right] \\
&+\frac{4\sin 2\theta\cos^2 2\theta}{(n^2-1)\ \left[(n^2+1)\cos^2 2\theta-1\right]}\cdot\Delta\beta_3
\end{aligned}\right\} \qquad (19)$$

Case C

$$\frac{Q_s}{P_{Ts}}\cdot\frac{2n}{(n^2+1)} = \alpha_2'\ L\sec\theta+\beta_1+\frac{2n^2}{n^2+1}\ \beta_2 + 4\sin\theta\frac{n^2}{n^2-1}\ \beta_3 \qquad (20)$$

$$\left.\begin{aligned}
\frac{Q_p}{P_{Tp}}\cdot\frac{2n}{(n^2+1)} &= \alpha_2'\ L\sec\theta+\beta_1+\frac{2n^2}{n^2+1}\ \cdot\beta_2 \\
&+\frac{4\sin\theta}{(n^2-1)}\left[\frac{(n^4+1)\cos^2\theta-n^2}{(n^2+1)\cos^2\theta-1}\right]\beta_3 \\
&+\frac{4\sin\theta\cos^2\theta}{(n^2-1)\ \left[(n^2+1)\cos^2\theta-1\right]}\cdot\Delta\beta_3
\end{aligned}\right\} \qquad (21)$$

Again, an appropriate set of these experiments can be carried out to deduce any of the specific absorption factors. For a material with uniform bulk absorption ($\alpha_1=\alpha_2=\alpha$) and isotropic surface absorptions ($\Delta\beta_1=\Delta\beta_2=\Delta\beta_3=0$), the situation is particularly simple. A pair of type C measurements can be used to establish β_3 as

$$\beta_3 = \frac{(n^2+1)\sin 2\theta}{n\left[(n^2+1)\cos^2\theta - 1\right]} \cdot \left[\frac{Q_s}{P_{Ts}}\bigg|_C - \frac{Q_p}{P_{Tp}}\bigg|_C\right] \tag{22}$$

A pair of type A measurements with the sample reversed end for end can be used to establish $(\beta_2-\beta_1)$ as

$$(\beta_2 - \beta_1) = \frac{1-r_s^2}{2r_s\sec\theta}\left[\frac{Q_s}{P_{Ts}}\bigg|_A - \frac{Q_s}{P_{Ts}}\bigg|_{A'}\right] \tag{23}$$

Finally, one of these Type A s-polarization measurements, combined with its p-polarization counterpart, is sufficient to derive α, β_1 and β_2.

In the most elemental case of a uniform material with a uniform and isotropic surface absorption coefficient, β_s, just two type A measurements need to be made. As an example we chose a 40° prism of ZnSe (n=2.403 at 10.6 μm), for which the external angle of incidence is 55.27°, the Fresnel reflection coefficients are r_s = 0.59709, r_p = 0.18592 and the corresponding surface power reflection coefficients are:

$$R_s = 0.3566 \quad \text{and} \quad R_p = 0.0345$$

The resultant heating functions are:

$$\left.\begin{aligned} \frac{Q_s}{P_{Ts}} &= 2.277\alpha L + 6.909\beta_s \\ \text{and} \\ \frac{Q_p}{P_{Tp}} &= 1.083\alpha L + 2.688\beta_s \end{aligned}\right\} \tag{24}$$

In this case, the change in the beam from p- to s-polarization results in an increase in apparent bulk absorption by a factor of 2.10 and an increase of apparent surface absorption by a factor of 2.57, permitting simple and accurate determination of both αL and β_s.

The use of a truncated prism sample has an inherent problem, however, in the most general case of a nonuniform sample with anisotropic surface absorption coefficients. Of the eight possible measurements in the A and B configurations, only six are linearly independent, while the pair of C configuration measurements can be used only to establish a single linear combination of the absorption components of surface S_3. This gives a total of seven independent measures to determine eight unknown coefficients. The indeterminancy must be removed by an assumption, for example, that the same degree of anisotropy exists in all three surfaces, or in particular, that:

$$\frac{\Delta\beta_3}{\beta_3} = \frac{\Delta\beta_1 - \Delta\beta_2}{\beta_1 - \beta_2} \quad \text{- - - - - - - - - -} \tag{25}$$

This last factor can be measured unambiguously by sample reversal end for end. The ambiguity in surface absorption coefficients can be removed, in fact, by a further elaboration of the prism design. This is accomplished by extension of both lateral faces and their termination by two more inclined facets (fig. 7). These facets are set so that a ray entering the prism normal to the base will undergo total internal reflection at the usual entry point on the lateral faces and will strike the new termination facets at normal incidence.

This M-prism profile then allows two additional pairs of C-type calorimetry measurements to be made to establish the linear relationships between β_1 and $\Delta\beta_1$ on the one hand, and β_2 and $\Delta\beta_2$ on the other. Accordingly, all three pairs of C-type measurements, along with any five of the otherwise independent A and B type observations will allow all eight absorption coefficients to be determined.

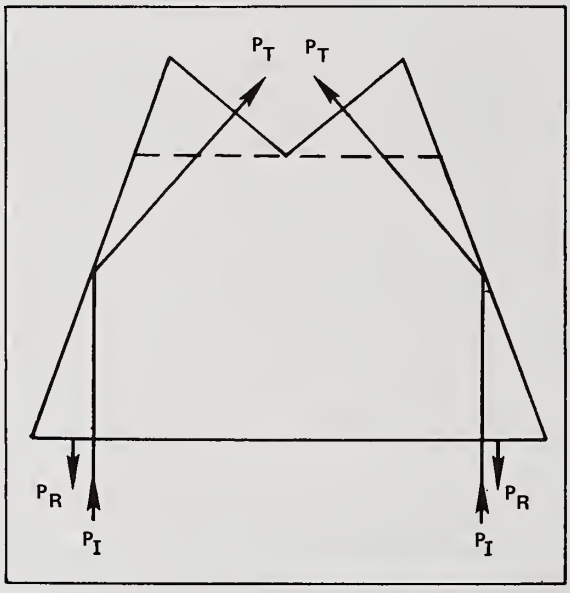

Figure 7. M-Profile Pentagonal Prism Design Showing Laser Beam Geometry for Surface Calorimetry Measurements

Conclusion

The foregoing analysis demonstrates that a simple set of ballistic calorimetry measurements can be made on a prism sample to deduce unambiguously the various absorption coefficients of all the bulk paths and surfaces active in the experiment. While more care in sample preparation and laser beam alignment is necessary than is the case in conventional bar calorimetry, the vagaries of the conventional technique and its analysis are eliminated. This fact should lead to more reliable estimates of bulk absorption coefficients in high transparency materials, and contribute to more careful and perceptive studies of surface absorption and its origins.

Acknowledgement

This research was sponsored by the Air Force Office of Scientific Research (AFSC) United States Air Force under Contract F49620-78-C-0109.

References

[1] M. Born and E. Wolf, "Principles of Optics," MacMillan, NY (1959), pp. 36-50.

[2] P.A. Miles, "Static Profile Calorimetry of Laser Materials," App. Optics 16, 2897 (1977).

[3] H.B. Rosenstock, D.A. Gregory and J.A. Harrington, "Infrared Bulk and Surface Absorption by Nearly Transparent Crystals," App. Optics 15, 2075 (1976).

[4] A. Rosencwaig, "Theoretical Aspects of Photo-Acoustic Spectroscopy," J. App. Phys. 49, 2905 (1978).

[5] A. Hordvik and L. Skolnik, "Photo-Acoustic Measurements of Surface and Bulk Absorption in HF/DF Laser Window Materials," App. Optics 16, 2919 (1977).

[6] N.J. Harrick, "Internal Reflection Spectroscopy," Interscience, NY (1967), pp. 27-30.

Polarization Monitor For Thin Film Depositions*

B. Tirri

Perkin-Elmer Corporation
Wilton, CT 06897

An automatic ellipsometer has been designed, fabricated and integrated into a large vacuum chamber to monitor the deposition of multilayer phase retarders. This technique offers several advantages over conventional monitoring techniques. Precise control of the phase retardance properties of multilayer coatings is possible due to the sensitivity of the ellipsometric parameters Δ and ψ to the changes in film thickness. Phase measurements of several multilayer coating designs deposited using this monitoring technique are presented.

Keywords: Multilayer coding; phase retarders; polarization monitor; ellopsometer.

*Work supported by the Air Force Weapons Lab

Introduction

The performance demands on optical materials used in high power laser systems have led to the development of new processing and analysis techniques. Many of these developments have centered on thin films used in the fabrication of optical coatings. One technique which is becoming increasingly popular is ellipsometry. The high sensitivity and non-destructive nature of ellipsometric measurements make it an ideal technique for studying the formation of and physical properties of thin films. The availability of relatively cheap and fast microcomputers have made is possible to design high precision automatic scanning ellipsometers. One class of automatic photometric ellipsometers, the rotating analyzer ellipsometer (RAE), has been extensively used to study the growth and physical properties of thin films. The high measurement precision inherent in RAE make it possible to examine the effects of various deposition parameters on such properties as packing density and stoichiometry.

RAE may also be used to monitor the deposition of multilayer dielectric coatings. One such coating design, the 90^{o} phase retardance coating used on high energy cone retroflectors, requires precise thickness control to achieve the uniform broadband performance necessary. In this paper a description of an RAE constructed for in situ monitoring and analysis of various types of phase-retardance coatings is presented.

Theoretical Background

The electric field of a TEM wave propagating in the $\hat{K}$ direction may be described by two orthogonal components $\vec{Ep}$ and $\vec{Es}$ referenced to a pair of axes parallel and perpendicular to the plane of incidence of a reflecting surface (fig. 1). The electric field traces out an ellipse whose shape is described by the relative amplitudes of $\vec{Ep}$ and $\vec{Es}$ and the phase difference between them. This is compactly given by the complex parameter χ:

$$\tilde{\chi} \equiv \tilde{Ep}/\tilde{Es} \tag{1}$$

Polarized light, when reflected from a surface, undergoes a change of polarization determined by the optical properties of the surface. This change is given by the ratio of polarization states of the reflected and incident electric field:

$$\tilde{\rho} \equiv \tilde{\chi}_r/\tilde{\chi}_i \tag{2}$$

Using the definition of the Fresnel reflection coefficients,

$$\tilde{E}_{rp} = \tilde{r}_p \tilde{E}_{ip} \qquad \tilde{E}_{rs} = \tilde{r}_s \tilde{E}_{is} \tag{3}$$

this ratio may be written as:

$$\tilde{\rho} = \tilde{r}_p/\tilde{r}_s$$

The complex parameter $\tilde{\rho}$ is conventionally written

$$\tilde{\rho} = \tan\psi \exp(j\Delta) \tag{4}$$

where $\tan\psi = |r_p|/|r_s|$ and $\Delta = \delta p - \delta s$ is the phase difference between the p and s state.

The Fresnel reflection coefficients are related to the optical properties of the surface by:

$$\tilde{r}_p = (\tilde{n}2 \cos\phi 1 - \tilde{n}1 \cos\phi 2)/(\tilde{n}2 \cos\phi 1 + \tilde{n}1 \cos\phi 2)$$
$$\tilde{r}_s = (\tilde{n}1 \cos\phi 1 - \tilde{n}2 \cos\phi 2)/(\tilde{n}1 \cos\phi 1 + \tilde{n}2 \cos\phi 2) \quad (5)$$

$\tilde{n}1$, $\tilde{n}2$ = complex index of refraction for media 1 and 2

$\phi 1$, $\phi 2$ = angle of incidence and angle of refraction.

For a surface covered by one or more films the Fresnel coefficients at each interface may be used to sum up the reflection amplitudes of successive partial waves. An expression is then arrived at for the overall complex amplitude reflection coefficient of the system. By measurement of the incident and reflected polarization states information may be obtained about the thickness and optical constants of the film.

In general, the relationship between $\tilde{\rho}$ and the optical properties of the film is a complex transcendental function:

$$\tilde{\rho} = \tilde{f}(t, n1, n2, n3, \phi, \lambda) \quad (6)$$

This cannot be solved explicitly for the thickness and index of the film. Values must be found by numerically inverting eq. (6).

Polarization Analysis

The polarization state of the electric field in RAE is determined by measuring, with a photometric detector, the periodic variation of flux transmitted by a rotating analyzer (polarizer). The analog output signal of the detector representing the flux variation is Fourier analyzed and used to determine $\tilde{\chi}$ (or $\tilde{\rho}$).

To qunatitatively represent the flux variation, we must calculate the electric field transmitted by the analyzer as it rotates. The electric field incident on the analyzer is resolved into two components $\hat{E}p$ and $\hat{E}s$. Letting θ represent the angle between the transmission axis of the analyzer and the positive $\hat{\rho}$ axis measured counter-clockwise looking in the negative $\hat{k}$ direction the transmitted component of the electric field can be written as:

$$E(\theta) = \cos\theta\{\omega t + \Delta)\}\tilde{\rho} + \sin\theta\{\cos\omega t)\hat{s} \quad (7)$$

To obtain the intensity eq. (7) is squared and time averaged:

$$I(\theta) = Io(1 - \cos 2\psi \cos 2\phi + \sin 2\psi \cos\Delta \sin 2\theta) \quad (8)$$

Io is the average intensity (DC); the second harmonic terms describe the flux variation (AC) as the analyzer is rotated at frequency $\omega' = \theta/t$. The azimuth of the polarization ellipse is determined by the phase of the AC component while the minor/major axis ratio is determined by the AC/DC ratio. The analog detector output is digitized and a discrete Fact Fourier transform performed on the sampled points. The normalized second harmonic Fourier coefficients are used to calculate ψ and Δ:

$$a2 = -\cos 2\psi,\ b2 = \sin 2\psi \cos\Delta \qquad (9)$$

Experimental Details

Figure (2) details the experimental arrangement. The system can be broken up into four modules: an input section consisting of light source and polarizing optics, the vacuum chamber and sample, analyzing section and signal processing and data reduction.

The input section contains the source and optical components necessary to polarize the incident beam. The light source is a Spectra Physics Model 120 HeNe laser operating at 3.39μm and chopped at 800Hz. A beamsplitter is used to couple in a visible HeNe beam for alignment purposes. A quarter wave plate circularly polarizes the linearly polarized output beam of the 3.39μm beam. This minimizes the effects of source polarization on measurement accuracy. A calcite absorption polarizer mounted in a high precision stepping motor driven rotary mount is used to polarize the input beam. The calcite polarizer was chosen for use at 3.39μ due to its high extinction ratio and low wedge angle. A CdS quarter wave plate can be inserted into the optical path after the polarizer. Precision considerations make it necessary to use a quarter wave plate when making measurements on dielectric surfaces ($|\cos\Delta| \approx 1$).

The second moduel consists of the vacuum chamber and sample. The chamber is a 36" oil diffusion pumped system with both resistance heated and electron beam sources. It is equipped with photometric and crystal-controlled monitoring systems. The primary reason for choosing this chamber to do this work was the available locations for entrance and exit windows. The window locations are such that it allows an incident angle of 45°. The sample is located in a precision rotary mount bolted to a rigid platform. Angle of incidence is determined to within 0.05° with this sample holder arrangement. The use of alignment apertures located in the entrance and exit beams allow for accurate repositioning of a sample after it has been removed. The exit and entrance windows are constructed from optical quality stress relieved fused silica.

The analyzing section consists of the rotating analyzer assembly and photometric detector. The analyzer (calcite absorption type) is driven by a 5Hz synchronous motor. They are coupled together by a set of interchangeable timing gears which allow analyzer rotation rates of from ≈3-30Hz. The usual operating frequency is 5Hz. The analyzer is also coupled through a one-to-one gear drive to an optical encoder. The encoder has a two channel output consisting of a zero index pulse and 256 timing pulses/rev. These pulses are used to synchronize the conversion of the analog waveform to a digitized one at equally spaced angular increments. A room temperature PbSe detector is used to sense the modulated (@ 5Hz) and chopped (@ 800Hz) flux transmitted by the analyzer. Chopping at a high frequency is necessary to establish the DC level of flux arriving at the detector.

The signal processing and data reduction sections are used to calculate the Fourier coefficients (or optical constants and thickness if desired) from the analog signal output by the detector. The output signal of the detector is amplified using an AC coupled preamplifier. A low pass filter demodulates the 5Hz analyzer signal from the 800Hz carrier. The 5Hz signal is then digitized using a 12 bit A/D converter in a Hewlett-Packard 1000L computer. The conversion process is initiated by the zero index trigger pulse. The A/D is then triggered by successive pulses from the 256 pulse/rev. channel. The total number of readings is under software control. Averaging over successive cycles increases precision by reducing noise. The A/D converter stores the 12 bit readings in internal memory. A Fast Fourier Transform subroutine then calculates the Fourier coefficients. Additional subroutines are called upon which use previously determined calibration constants and correction factors (see below) to calculate Δ, ψ, and if desired, thickness and index.

Alignment and Calibration

To insure correct angle of incidence, proper positioning of the sample and minimization of systematic errors an alignment and calibration procedure is performed prior to beginning a deposition. The procedure is simple and can be accomplished quickly.

The indicent light beam first must be positioned with respect to the vacuum chamber. The sample, entrance and exit windows are removed. Alignment apertures on the entrance port and opposite wall of the vacuum chamber are used to insure the same beam incidence position from deposition to deposition. The sample is inserted in its rotary mount and adjusted to retroreflect the beam through the entrance aperture. The sample is then rotated 45^{o} and the light beam reflected through two apertures in the exit arm of the system. Proper positioning is achieved when the light beam passes through both exit arm apertures after the 45^{o} rotation.

Each optical component is then sequentially centered in the light beam while maintaining beam position through the alignment apertures. Proper positioning of all components can be verified by examining the waveform of successive cycles of the rotating analyzer. Misalignment of the system will result in a nutation of the light beam on the detector. The output waveform becomes asymmetric. This asymmetry gives rise to a relatively large, first harmonic component in the transformed signal. Large values for harmonics other than the zeroth and second can be traced to various system imperfections. Examination of the total harmonic spectral serves as an excellent check of overall system performance.

System calibration consists in determining the parameters necessary to calculate the optical properties of the system (substrate and film) from the measured Fourier coefficients.

Aspnes and Studnu have detailed a procedure whereby the reference azimuth position of the analyzer and polarizer, the attenuation of the AC component of the detector output signal and the phase shift introduced by the signal processing electronics can be determined. The method is similar to the frequently used residual method and can be incorporated into the existing software and carried out under computer control. One calculates the residuals:

$$r_i(P_i) = 1 - a2_i^2 - b2_i^2 \tag{8}$$

of a series of measurements in the vicinity of the zero azimuth position, Po, using an absorbing substrate for a sample. Linearly polarized light reflected at an oblique angle of incidence remains linearly polarized if it is either parallel or perpendicular to the plane of incidence. In the vicinity of Po the residuals are quadratically related to the polarizer position P:

$$R(P) = c_o + c_1P + c_2P^2 \tag{9}$$

co, c1 and c2 are numerically determined best fit constants. By least squares fitting the residuals $r_i(P_i)$ to a quadratic function of P, Po and z may be determined.

The analyzer zero azimuth position and the phase shift introduced by the signal processing electronics enter additively in the correction of the Fourier coefficients and can be determined as one factor. The polarizer azimuth is set to Po and the analyzer offset, δA, and phase shift measured directly. The offset value is entered into the data reduction program. The corrected values of the Fourier coefficients are related to the measured values by application of the two dimensional rotation matrix:

$$\begin{pmatrix} a2c \\ b2c \end{pmatrix} = \begin{pmatrix} \cos 2\delta A & \sin 2\delta A \\ \sin 2\delta A & \cos 2\delta A \end{pmatrix} \begin{pmatrix} a2m \\ b2m \end{pmatrix}$$

For certain types of measurements it is necessary to use a compensator to achieve the maximum precision in the measured value of Δ. Compensator azimuth offset can be measured in the same manner as δP. The polarizer is set to Po and the measured residuals plotted as a function of C (for $C \approx o$). The compensator relative transmittance and phase shift can next be measured directly using a generalized two measurement technique for rotating analyzer

ellipsometers. This technique has the advantages of two zone averaging in that many of the sources of systematic errors in single zone measurements are eliminated.

The small contribution of cell window birefringence in the measured value of Δ cannot be eliminated in two-zone averaging. The entrance and exit windows can be treated as small retardation wave plates and measured as such. This correction is included in the data reduction program and applied to the measured value of Δ for all measurements.

To successfully use an instrument such as this for monitoring small changes in ψ and Δ it is necessary to have a high degree of measurement precision. The deposition of complex multilayer phase retardance coatings require long term instrument stability. Figure shows the results of measurements of ψ from the average $\bar{\psi}$ has been plotted in histogram form. The spread of readings is within a 0.015^{o} band. This precision is typical of RAEs and is one reason why they are preferred in situations requiring high precision and fast measurement time.

Deposition Monitoring Results

Several types of film systems were deposited while monitoring the phase retardance of the reflected 3.39μm laser beam. The designs are listed in Table I. The two single film designs on Au are the simplest type of phase retardance coating other than a metallic reflector. The maximum (minimum) phase retardance attainable by a single film deposited on Au is determined by the index of the film. The results of the ThF4 deposition are shown in Figure 4. The abscissa represents tine. This may be translated to thickness by assuming a uniform condensation rate (3.6A/sec). This is typically not a good assumption. The measured phase retardance is represented by crosses in the figure. The filled in data and solid lines represent the theoretical Δ using the optical constants indicated ($N_{Au} = 2.91 + 25.2j$, $N_{ThF4} = 1.52$). The failure to match the theoretical curve at all points may be due to several factors: 1) non-uniform condensation rate; 2) variation of index for ThF4 from 1.52; 3) inhomogeneity in index of ThF4 as a function of thickness. These factors are now under investigation.

The results of the single film ZnSe deposition are shown in Figure 5. Here we have plotted phase retardance as a function of film thickness using the same assumptions used in Figure 4. The data is in very good agreement which the phase retardance values predicted for ZnSe ($n = 2.44$). It should be mentioned that the data presented in these figures are a small sampling of the total set (1 data point $\approx$ every two seconds). The thickness resolution for a system like Au-ZnSe is $\approx 10\text{Å}$ for this thickness range.

A four layer 84^{o} monochromatic phase retardance coating was deposited using this monitoring technique. Figure 6 presents the monitoring data in a slightly different format. The abscissa is divided into four parts. Each part is the normalized film thickness for that particular layer. The actual film thickness is given in Table I. This four layer design gives the maximum retardance attainable with four films. The theoretical value measured in-situ agrees to within one degree with values later measured in the laboratory.

We have also used this system to monitor coatings containing up to 25 layers. The results have been similar to those presented for the four layer coating. The instrument is not limited to monitoring thickness. Refractive index may be measured in-situ as a function of deposition parameters (temperature, deposition rate, etc.) the properties such as packing density, homogeneity and stoichiometry, for example, can also be examined.

I would like to acknowledge the support of the Air Force in this work and for permitting me to present our initial results. I would also like to thank Mr. Ronald Wigglesworth for his technical assistance in operating the monitoring system.

TABLE I

Layer No.	Design (Thickness in Full Waves at Design Wavelength)		
1	1	2	3
2	.21 ThF4	.25 ZnSe	.08 ThF4
3			.167 ZnSe
4			.195 ThF4
5			.24 ZnSe

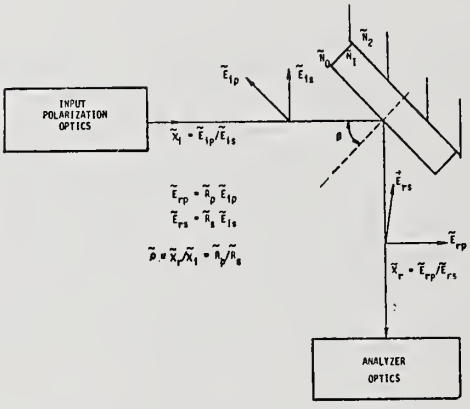

Figure 1: Diagrammatic relationship of electric field, Fresnel reflection coefficients and polarization parameters to film covered surface.

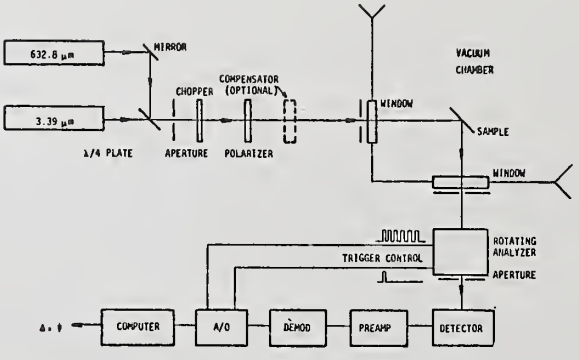

Figure 2: Schematic of rotating analyzer ellipsometer for monitoring phase retardance.

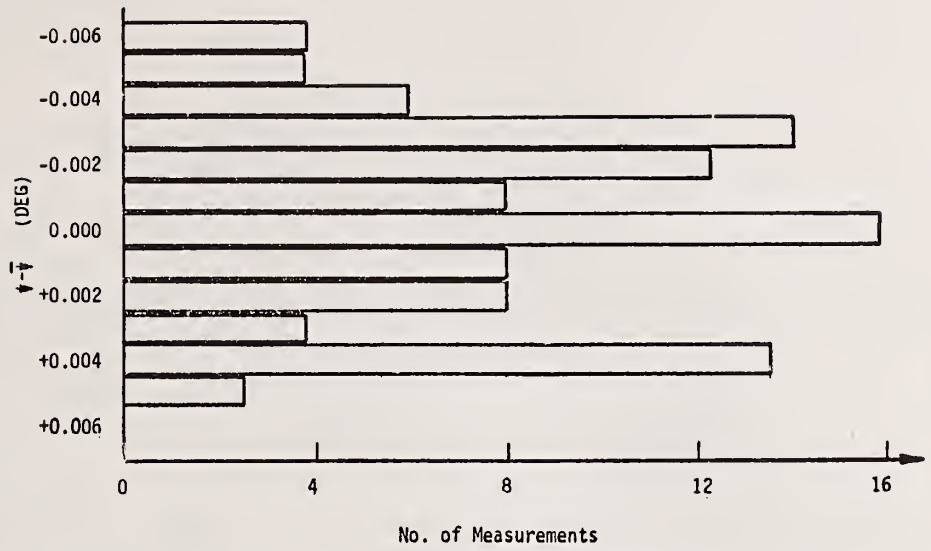

Figure 3: Histogram representing measurements of orthogonal field components over a two hour period.

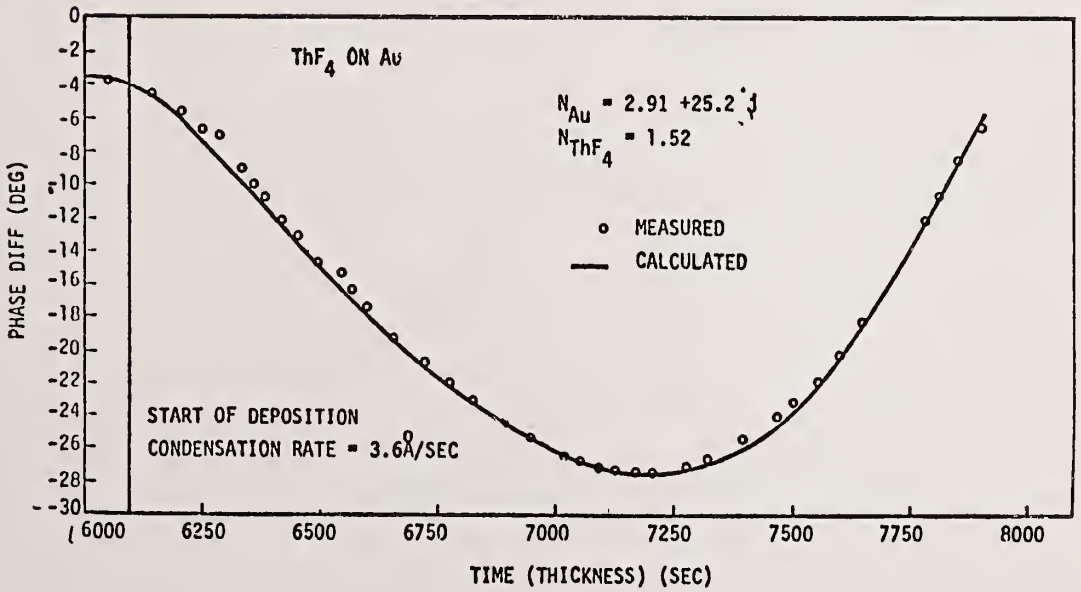

Figure 4: Measured phase retardance of ThF4 on Au as a function of time. Thickness may be equated to time by assuming a uniform condensation rate.

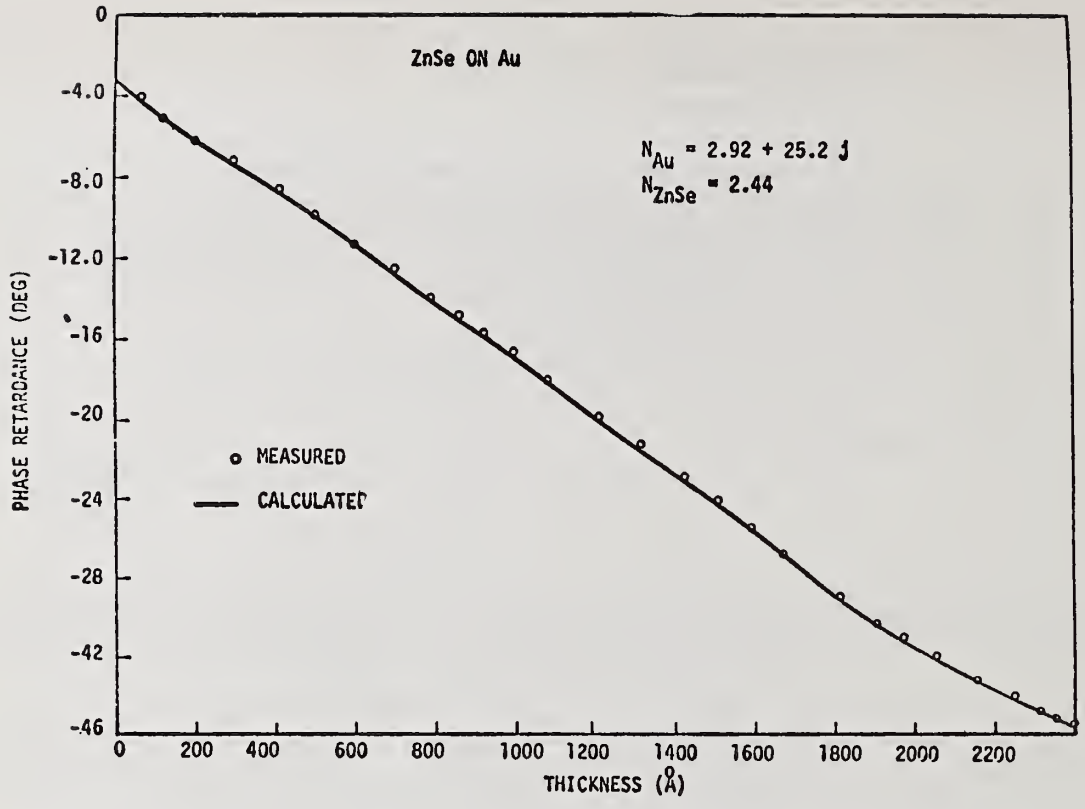

Figure 5: Measured phase retardance of ZnSe on Au as a function of thickness.

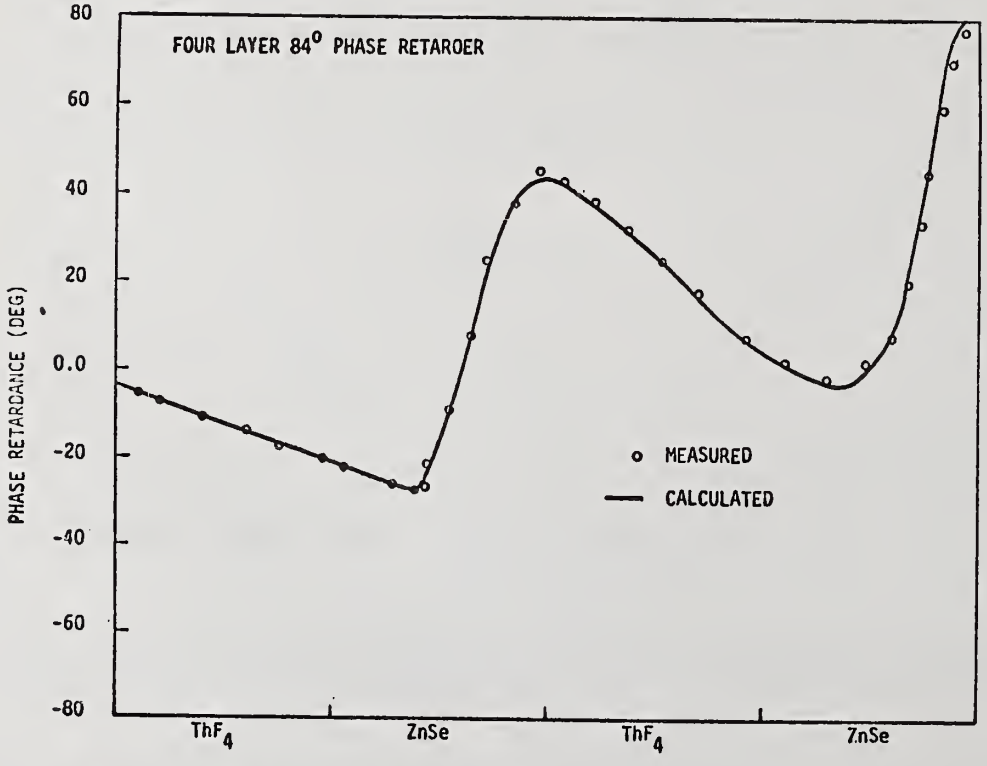

Figure 6: Measured phase retardance in situ during deposition of 4 layer retardance coating.

Cavity Phase Shift Method For High Reflectance Measurements

M. A. Kwok, J. M. Herbelin, R. H. Ueunten and G. I. Segal

The Aerospace Corporation
P.O. Box 92957
Los Angeles, CA 90009

The cavity phase shift method can measure high reflectances on spherical surfaces with good spatial resolution. Successful demonstration at 2.9 microns wavelength is described. A reflectance of 0.9920 ± .0050 has been measured.

Keywords: laser applications; mid-infrared optics; reflectance measurement

1. Introduction

The major objective of this study is a proof-of-principle demonstration of the Cavity Phase Shift method for measuring high reflectances in the mid-infrared wavelength region (2.6 - 4.2 microns). Specifically, these tests have been conducted at HF(or DF) laser wavelengths on appropriate selected large mirrors. The Cavity Phase Shift (CAPS) Method has the capability to evaluate the reflectance, or, because of its high sensitivity, the scattering/absorption losses in these types of optical elements. With good spatial resolution, the CAPS approach is able to provide point-by-point evaluation of a large surface mirror. The spatial uniformity in optical properties of these large elements becomes an increasingly significant issue as sizes grow. The ability of CAPS to monitor spatial and temporal variations, with relative simplicity in setup and instrumentation, permits the method to ultimately be used in a field-operable or in situ situations, such as the study of a flux loaded laser mirror or maintenance of quality control in fabrication of optical coatings.

The approach here has already been used at visible to near infrared (8800°A) wavelengths while supporting work on new chemical lasers.[1] One result is that high quality mirrors at 8742°A were newly developed with use of the method, and were measured to be 0.99975 in reflectance with the same CAPS method.[2]

There are already identified issues in the high energy laser program that only this method can easily address. One current approach in high energy lasers is the use of classical ellipsometry to determine relative reflectances and relative phase shifts in the electric field upon reflection from the mirror at limited spatial resolution.[3] The Aerospace approach differs from all others in that it provides a direct measurement of absolute reflectance at the two possible linear polarizations with the high spatial resolution determined by a cavity mode. Methods devised by others competitive in sensitivity actually detect mirror losses, from which reflectance is deduced.[4,5] These other methods require the movement of crucial mirrors and other elements of the optical train during the measurement; the Aerospace method does not. The other methods appeared constrained to the laboratory environment because of complexity, sophistication or delicateness.

2. Experiment

The CAPS method consists of making the mirror with unknown high reflectance part of an interferometric optical cavity structure of very high Q (fig. 1). As a result of a large number of

multiple passes by radiation off the unknown reflectance, a high sensitivity and great accuracy can be exploited in measuring the unknown reflectance or slight changes in the unknown reflectance. The radiation source is an intensity modulated laser beam passed through the interferometric structure by transverse mode matching. A phase shift in the sine wave modulation of intensity yields a direct measurement of the unknown reflectance. The phase shift is determined by use of a phase sensitive lock-in amplifier to detect the difference between the reference phase without cavity (dotted line, fig. 1) and then the phase shift with cavity (heavy line). Because the method detects a phase difference and not intensity changes, the reference phase apparatus, which consists of four simple mirrors, does not require a crucial alignment and it can be flipped in and out of the path. The unknown high reflectance R_2 is simply related to the phase shift Φ by[1]

$$\tan \Phi = \frac{4\pi fL}{C} \left(\frac{R_1 R_2}{1 - R_1 R_2}\right) \qquad (1)$$

where f is the modulation frequency; L, interferometer length; c, speed of light within the cavity; and R_1, a known previously determined high reflectance. The ability to vary f or L provides techniques for data analysis.

This report describes work extending the CAPS method to the mid-infrared region between 2.7 and 4.0 microns. The high brightness source used is an HF/DF cw laser at the 1 to 5 watt power level on a given lasing transition. In this series the resonator include a 1364 cm radius of curvature mirror and a diffraction grating in littrow position 93 cm apart. The active gain region is a 30 cm wide subsonic flow. The laser beam is passed through a germanium crystal acousto-optic modulator capable of intensity sine wave modulations from DC beyond 1 MHz frequencies. The beam is then mode-matched into a two-mirror optical test cavity. A liquid nitrogen cooled indium antimonide detector receives the phase shifted laser signal. The actual optical layout is shown as a schematic in figure 2.

The test mirrors for this demonstration have transmitting silicon substrates polished to 200 cm radii of curvature at 2.5 cm diameter apertures. The substrates are dielectric-coated in one batch for high reflectances between 2.5 and 3.1 microns. They are anti-reflection coated on the backs. The work has been done with the HF $P_2(8)$ transition, 2.911 microns wavelength. This position was chosen to minimize the effects of atmospheric water vapor absorption prevalent in this region.

3. Results

Demonstration of a reflectance measurement was successfully performed as shown in figure 3. In these measurements, the HF beam has been linearly polarized by the Brewster angle windows. This polarization is preserved in the acousto-optic modulator, which requires linearly polarized radiation for efficient operation. The I_1 beam, the diffracted beam from the modulator, has not been particularly mode-matched into the test cavity. In such a situation, the cavity itself serves as a mode selector since higher order transverse modes have shorter cavity lifetimes, and one adjusts the cavity for longest possible lifetime (i.e. largest observable phase shift.) For reflectances of 0.99 or lower, past studies have shown no great errors. In any case, the observation will provide a lower bound result. Measurements of $\tan \Phi$ at several modulation frequencies were made over several days. Such repeatibility provides an indication of the possible precision of the method. Earlier work[1,2] suggests even better precision figures if the noise

problems discussed below are resolved. A least-squares straight line fit of the data through the origin produces a slope which yields a result of 0.9916 ± .0050 when the reflectances of both mirrors are assumed equal.

Even for the $P_2(8)$ line, a slight correction for water vapor absorption is necessary assuming typical 50% humidity. From recent studies of HF laser line propagation through the atmosphere, the absorption coefficient at $P_2(8)$ has been found to be 4.1×10^{-4} $cm^{-1}(atm\ H_2O).^{-1}$ At 50% humidity for the 72°F room the amount of water vapor present is around 10 torr or 1.3×10^{-2} atm.[6] For a cavity length of 74.3 cm the absorption A is 4×10^{-4} for a single pass within the cavity. For such small absorptions or high transmittances and for reflectances close to unity, this leads to a linear adjustment.

The final estimate of reflectance becomes 0.9920 ± .0050. This value is 0.3% smaller than the quoted manufacturer's reflectance of 0.9952 immediately at fabrication. The manufacturer's measurement was made using a single beam spectrophotometer and a nominal standard gold mirror. The agreement is excellent. The slight discrepancy can be due to coating deteriorations common in this region or dirty coatings since no attempts were made at special cleanings after delivery. The lower bound discrepancy can also be due to slight transverse mode mismatch between the beam and the test cavity as noted above.

The spatial resolution in these demonstration experiments has not been optimized. Conventional empty, passive cavity calculations for the TEM_{oo} transverse mode shows the current spatial resolution to be 3 mm in diameter. This dimension is taken at the e^{-1} point of the hypothetical gaussian intensity profile, within which is contained over 90% of the flux.

The uncertainties depicted in figure 3 represent relatively large uncertainties in phase angle between ±5° and ±10°. Some signals were observed to be noisier than others even after some signal averaging and smoothing by the lock-in amplifier. These fluctuations are attributed to fewer active longitudinal modes available in longer wavelength infrared gas lasers for a given cavity length. These active modes must be matched with the longitudinal modes of the test cavity a sufficient number of times per second. Hitherto, in work at shorter wavelengths, cw gas lasers with wider gain spectral linewidths and cavities with longer lengths from 100-200 cm or more were used[1,2].

TABLE 1. Mode Matching

LASER	λ (MICRONS)	LASER GAIN BANDWIDTH (MHz)	LASER LONGITUDINAL MODES A	100 cm TEST CAVITY LONGITUDINAL MODES B	A-B
He-Ne[1]	.633	1200	3	10	30
Dye[1](CR599)	.874	1.3×10^5	100	1000	10^5
HF(100 cm)	2.9	300	2	2	4
DF(100 cm)	3.9	225	1-2	1-2	1-4

As shown in table 1, the relevant gain linewidth is usually narrower with increasing wavelengths because it corresponds to the Dopper width of the gas laser medium, which is proportional to spectral frequency or inversely proportional to wavelength. Consequently, for a given transverse mode, fewer active or lasing longitudinal modes occur until an infrared gas laser is running virtually single mode for conventional cavity lengths. The number of longitudinal modes available within the passive test cavity with the range of the active laser modes can also be calculated using $\Delta\nu_L = c(2L)^{-1}$. For a fixed 100 cm test cavity, these number of modes will also diminish. The product of laser modes and test cavity modes gives a relative figure for the number of dynamic mode matches per second. The dynamic mode matching on the microsecond time scale allows for no cavity stabilization requirements in this method. The temporal jitter in a cavity is due mainly to small changes in cavity length or mirror movement. Once radiative flux of a particular frequency of a lasing mode is "matched" or "captured" into the test cavity, the flux frequency will follow that of the matched test cavity mode as changes occur due to Doppler shifts at the moving mirrors. The phase measurement is made on the 0.1 second time scale with a large number of integrated, averaged mode matches. In the HF and DF laser regimes, table 1 shows that either cavity lengths must be lengthened or the number of mode coincidences enhanced. Also, we have previously shown that the dithering of the cavity length will significantly stabilize the signal.

4. Conclusions

A high reflectance measurement using the Cavity Phase Shift method has been successfully performed at HF wavelengths. Key improvements to the method for use in the mid-infrared region may include an intracavity chamber for absorption control and a test cavity dither to stabilize mode-matching. The use of the intracavity chamber will also permit studies of propagation or atmospheric attenuation and studies of the gradual degradation of coatings in specified adverse environments. The method appears to be a strong prospect in supporting coating development studies.

This study was made possible by funds from Aerospace Sponsored Research. We thank Dr. Jay Bernard for the information on atmospheric transmission. We also thank Lydia Hammond for manuscript preparation.

5. References

[1] J. M. Herbelin, J. A. McKay, M. A. Kwok, R. H. Ueunten, D. S. Urevig, D. J. Spencer, and D. J. Benard, "Sensitive Measurement of Photon Lifetime and True Reflectances in an Optical Cavity by a Phase Shift Method," Appl. Optics 19, 144 (1980).

[2] J. M. Herbelin and J. A. McKay, "Development of Laser Mirrors of Very High Reflectivity Using the Cavity-Attenuated Phase-Shift (CAPS) Method," Appl. Optics 20 3341 (1981).

[3] Thomas A. Leonard, John Loomis, Kevin G. Harding, and Marion Scott, "Design and Construction of Three Infrared Ellipsometers for Thin-Film Research," Twelfth Annual Symposium on Optical Materials for High Power Lasers, N.B.S., Boulder, Colorado (September 1980).

[4] V. Sanders, High Precision Reflectivity Measurement Technique for Low-Loss Mirrors," Appl. Optics 16 19 (1977).

[5] H. E. Bennett, "Large Optics Coating 8c Evaluation Facility Study, Part 1, Technical Discussion," Naval Weapons Center Report NWC-TP 6177 Final, 11 pp. (August 1980).

[6] Dr. Jay Bernard, private communication.

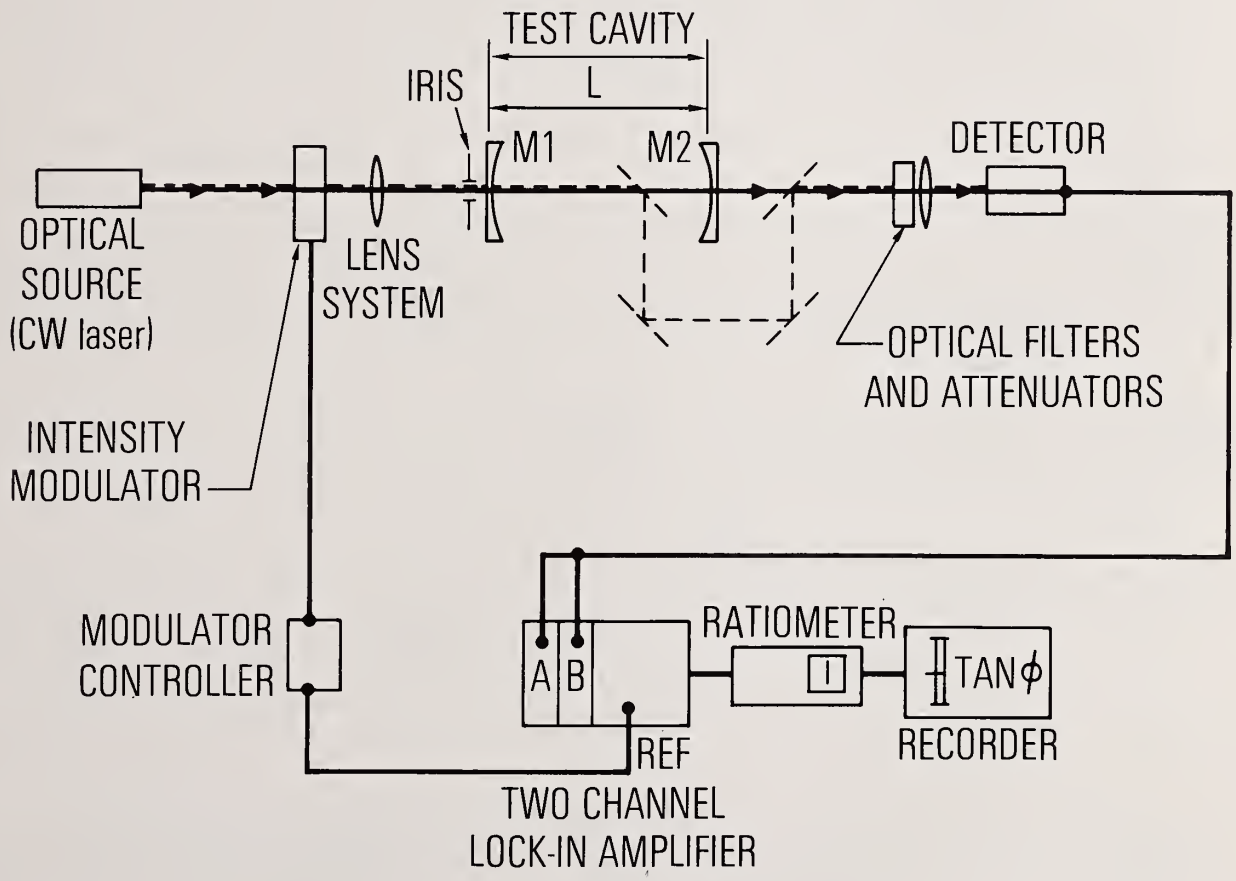

Fig. 1. Schematic of the Cavity Phase Shift (CAPS) Method.

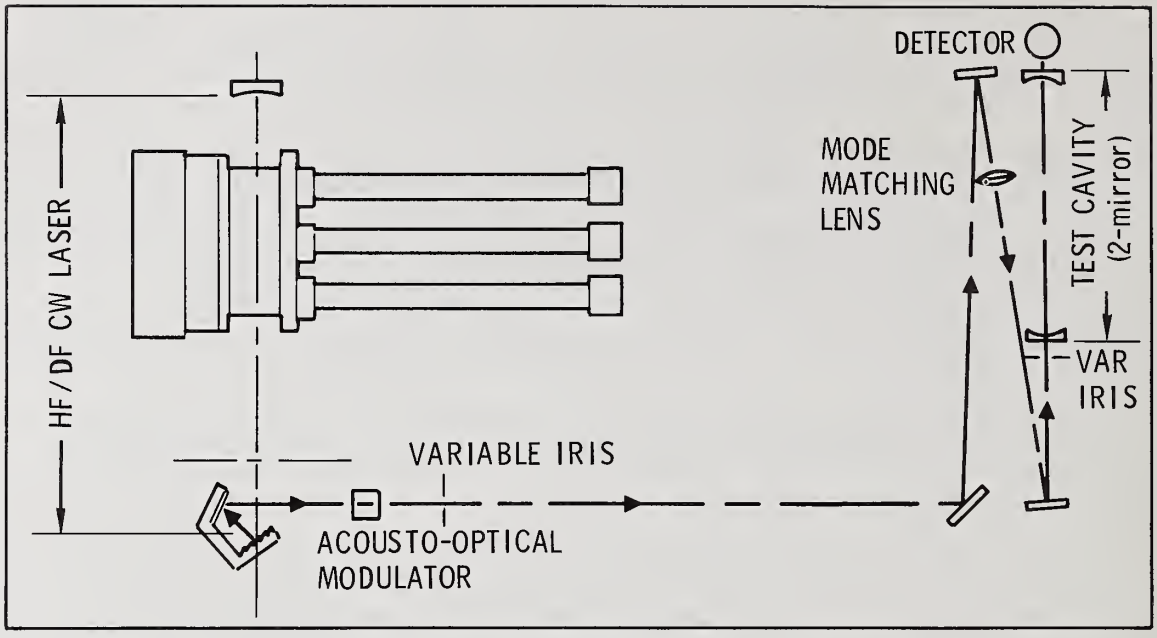

Fig. 2. The optical layout for demonstration of CAPS method at mid-infrared wavelengths.

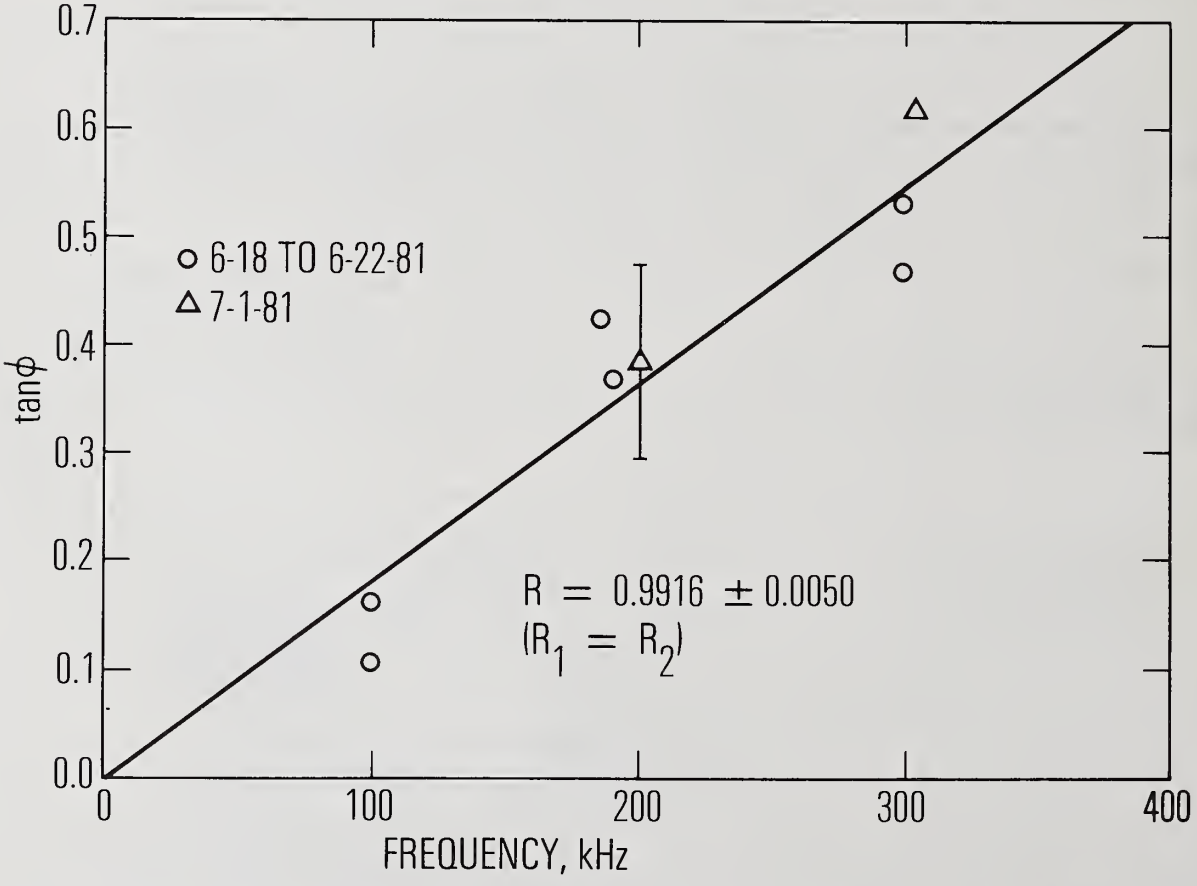

Fig. 3. Plot of tan Φ vs. modulation frequency f for mirrors at 2.911 microns wavelength. The slope of the straight line yields a reflectance measurement.

Instrumentation of a Variable Angle Scatterometer

W. K. Stowell,* F. D. Orazio, Jr.,** R. M. Silva**

Air Force Wright Aeronautical Laboratories

The problem of light scatter from optical surfaces is amplified to a critical level for the optics used in Ring Laser Gyros (RLG). Preparation of these optics is slow, laborious and very expensive. Further, the resulting surfaces are very fragile and extremely difficult to handle without damage. These concerns have led to the development of a scatterometer at the RLG Lab, Wright-Patterson AFB, which can detect light scatter from the so-called "supersmooth" optics used in RLG's without first overcoating with metals. A HeNe laser is used to illuminate a 0.5mm diameter spot on the surface of the test mirror or mirror substrate. The incident angle can be varied to accommodate different mirror designs. The test piece can be maneuvered with five degrees of freedom, four of which are computer controlled to facilitate scanning. Scatter measurements are made with a photomultiplier detection system which has a sensitivity of ten parts per billion per steradian. For these optics the standard process for determining substrate surface quality prior to applying the dielectric coatings is to coat the surface with silver and make a scatter measurement. The silver is then removed by etching and the dielectric coatings are applied. Using the scatterometer we have been able to measure surface scatter without first coating the surface with silver. This equipment has yielded evidence that virtually all the techniques now used to characterize these surfaces damage them, including the technique of coating with silver. Subjecting these optics to vibration, thermal cycling, multiple cleaning steps of almost any type and some classes of shipping containers, all seem to attack the Beilby layer in a way that increases the scatter substantially.

Key words: light scatter; scatter measurement; scatterometer; surface damage; surface quality; surface scatter.

The scatterometer shown in figures 1a and 1b consists of a laser light source, beam steering optics, mirror/substrate mount and positioning stepping motors all mounted on a rotating table. The apparatus resides on a floated table which is enclosed by plexiglass panels. The backside, the side nearest the positioning equipment, is open to a clean room where the optics are cleaned before testing. The measurement instrument is a photomultiplier tube detector modified to perform as a sensitive radiometer. The viewing telescope optics can be seen in the figures.

Figure 2 displays a close-up view of the rotating table upon which the laser, beam steering optics, spatial filter, optics, X, Y and R positioning motors and beam attenuator can be seen.

Figure 3 shows the operator's console, electronics rack and plotter used to control the positioning stepping motors and to record the scatter intensity data.

Figure 4 is a plan view of the measurement arrangement. The Y axis comes out of the figure perpendicular to the sheet at the R-X intersection. When θ_i (angle of incidence) is equal to A (the viewing angle), the resultant readings are Bidirectional Reflectance Distribution Function (BRDF) values directly, in PPM/Sr of the incident beam.

Figure 5 shows the part as viewed from the photometer with the directions of the X-Y, A and R axes drawn in. The beam is positioned so that it intersects the surface under study at the intersection of A and R.

A schematic of the laser and beam conditioning optics is shown in figure 6. The beam splitter sends part of the beam to a power monitor to track laser power fluctuations. Output of the power monitor is fed directly to the computer to normalize each data point so that laser intensity fluctuations are of no consequence to the measurement. As is shown, the beam is collimated with a Rayleigh range of approximately 20cm and a 0.5mm waist so that plane waves are incident on the surface of the part under study.

*RLG Lab, AAAN-T, AFWAL, W-PAFB, OH 45433.
**VTI, Inc., Dayton, OH 45432. This work was performed under Air Force contracts F33615-78-C-1589 and F33615-79-C-1813.

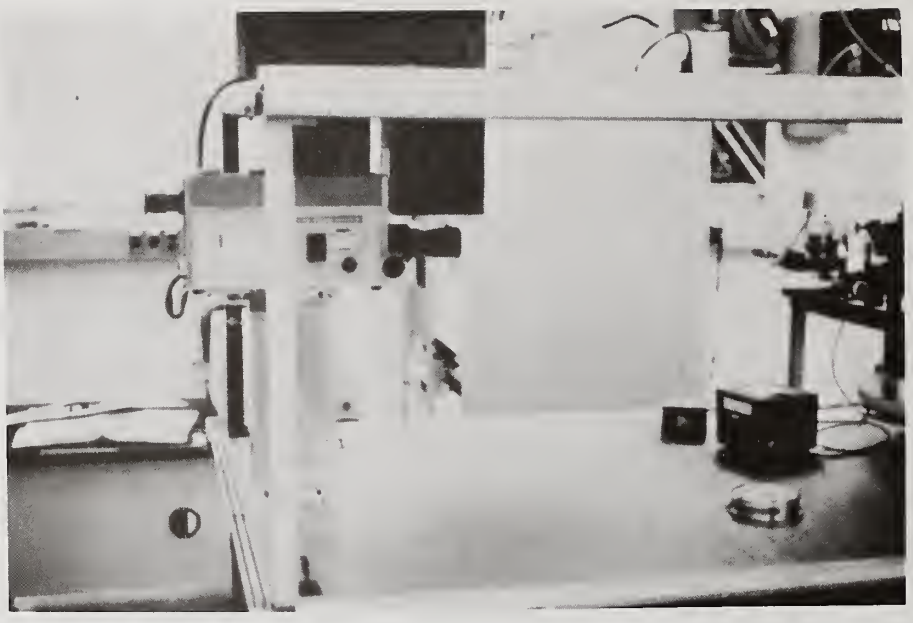

Figure 1a.

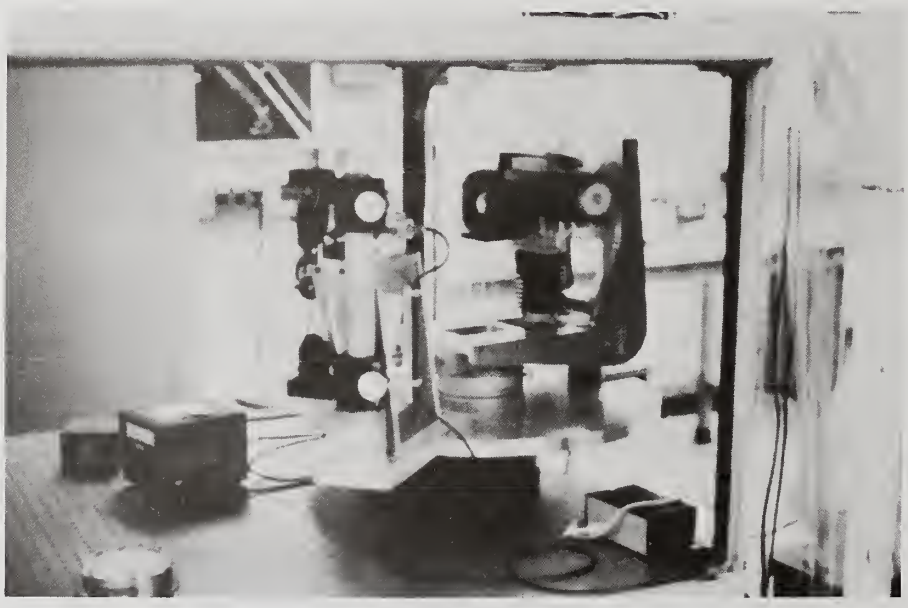

Figure 1b.

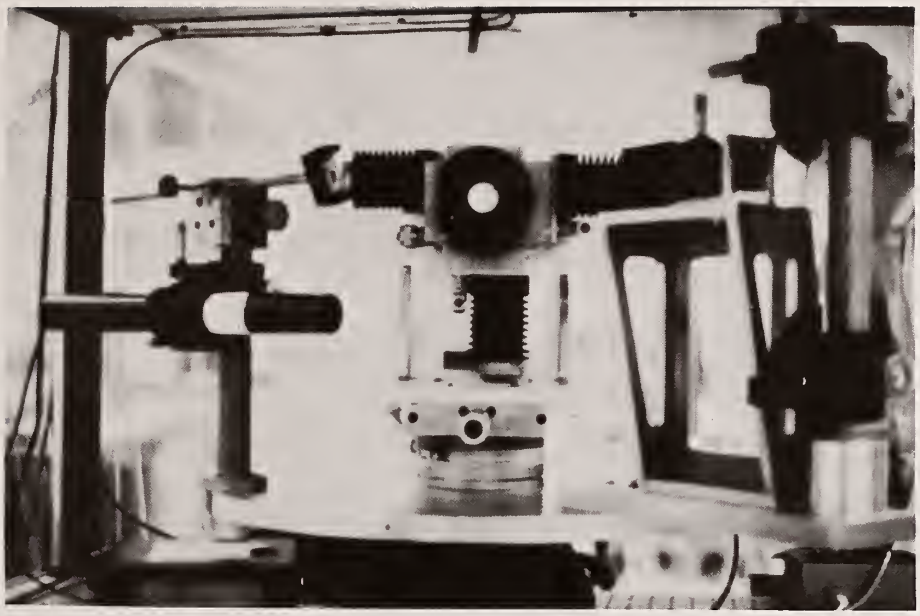

Figure 2.

Figure 3.

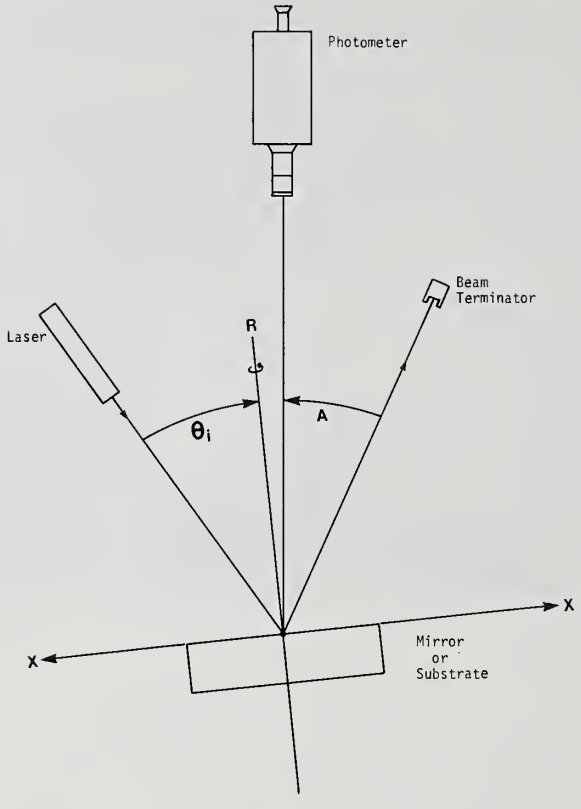

Figure 4.

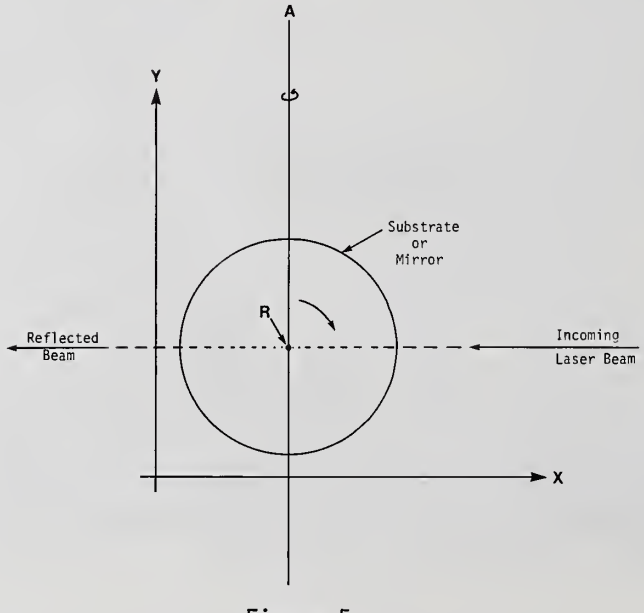

Figure 5.

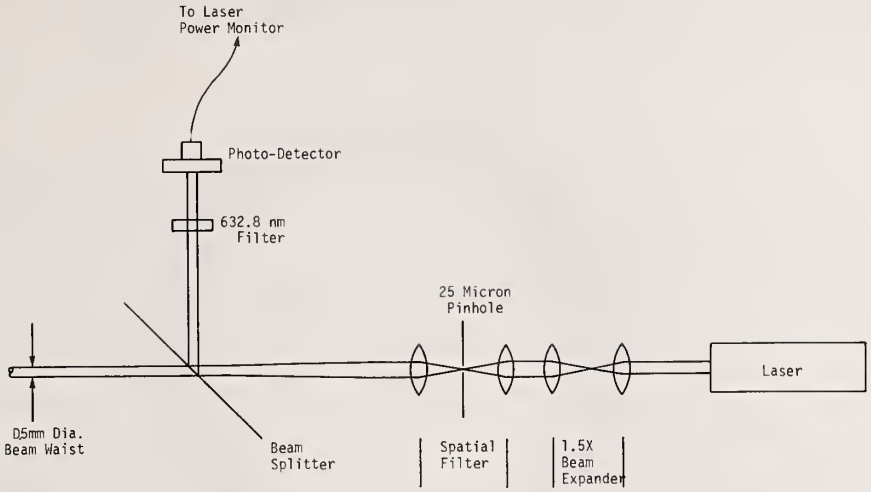

Figure 6.

Figure 7 is a diagram of the detector optics. Of particular note is the aperture mirror which allows precise positioning of the part being measured while eliminating scattered light from other sources.

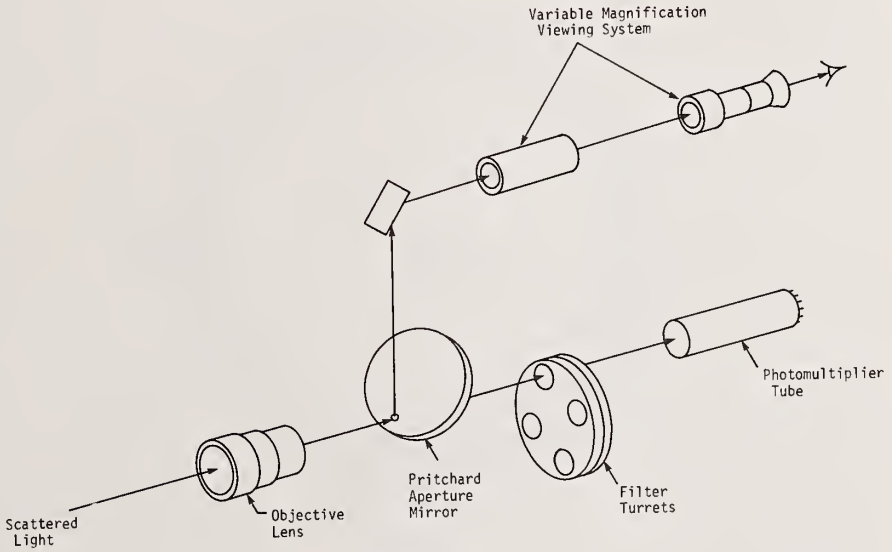

Figure 7.

Figure 8 is a schematic view of the optic being measured as seen through the Photometer/ Radiometer optics of figure 7. The beam is directed at a 30° angle of incidence and measurements are made perpendicular to the optic. In the figure can be seen the beam-optic intersection on the right, the beam in transit through the bulk and exiting at the point on the left, which represents scatter from the backside.

In figure 9, the black aperture spot is shown as it appears in the field of the detector. The black spot is the measurement field of the device, and helps to eliminate almost all scattered light from sources other than the surface of the part under test.

Figure 10 is a display of how the bulk scatter is removed from the measurement. Measurements are made as in the left figure, with the measurement field of figure 9 positioned over the beam-optic intersection point. Scans and rotations are conducted with this configuration. The measurement field is then moved to measure bulk scatter only, as shown on the right, with the beam impact point just outside the measurement field. Many scans are taken in this position, those

readings are averaged by the computer, that single number is divided by 2 (to account for the half space of the measurement in the left drawing) and the resulting number is subtracted from all of the data points stored in the computer.

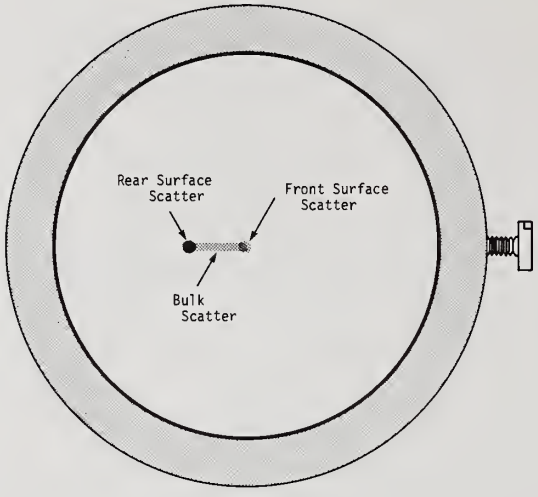

Figure 8.

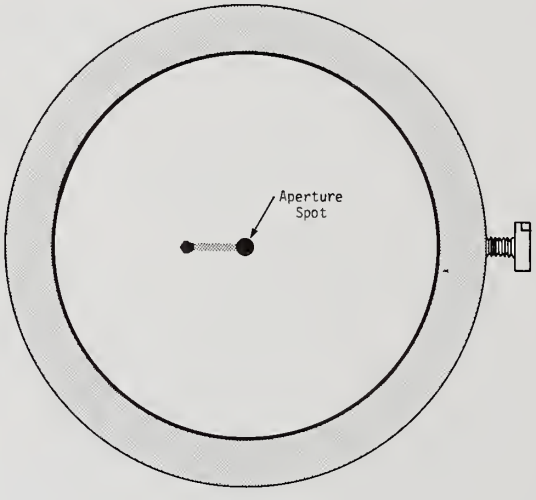

Figure 9.

Figure 11 displays the equipment error summary. The mechanical error is a repeatable positioning error for a part which is removed from the scatterometer, demounted from its holder and then returned to the measurement configuration. The electrical error is due to electrical noise, quantization errors in the A to D converter, and vibration induced electrical error from the laser power monitor, the sensor for which is mounted near the stepping motors. The calibration error is primarily a combination of the error of the Lambertian surface used to calibrate the system plus the ±2% relative error of the photometer.

The limits of each of the computer/stepping motor controlled axes are defined in figure 12. This does not include the manually controlled angle of incidence stage which is capable of 0-85° with resolution to one arc minute.

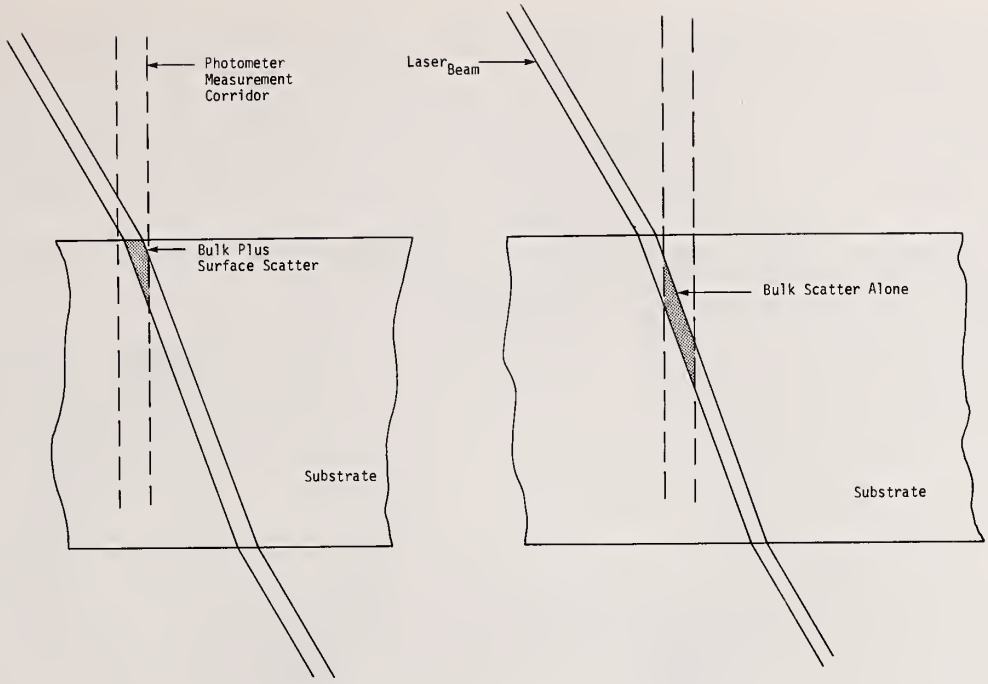

Figure 10.

ERROR SUMMARY

ERROR TYPE	MIRRORS	SUBSTRATES
Mechanical		
Radial (X-Y) Position	±23.3 microns*	±48.1 microns
R-Axis	±3.36 arc min	±3.36 arc min
Angle of Incidence	±2.12 arc min	±2.12 arc min
Electrical	±2.16%*	±4.82%*
Calibration	±3.55%	±3.55%

*Indicates an error derived from an actual measurement.

Figure 11.

TABLE OF AXIS LIMITS

AXIS	INCREMENT SIZE	INCREMENT CONVERSION	RANGE
X	5 Microns	200 Steps/MM	0-5000 Steps (1 inch)
Y	5 Microns	200 Steps/MM	0-5000 Steps (1 inch)
R	1.5 Arc Minutes	40 Steps/Degree	0-14,400 Steps (360°)
A	1 Arc Minute	60 Steps/Degree	1-5200 Steps (86°)

Figure 12.

Figure 13 is a graphic representation of the scanning pattern used to determine a general evaluation of the scatter characteristics of a given part. First, five R-axis scans, or rotations, are completed in the locations shown by the large shaded dots representing the beam diameter, all dimensions are in millimeters. A minimum and maximum R-axis position is chosen by viewing the combination of these five curves which are plotted in position "A" as shown in figure 14. Two area scans (X-Y scans) are now done covering a 3 x 3mm area with the spacing shown by the small arrows (50 microns, or 10 steps). One area scan is done at the minimum R-axis setting, position "B" of figure 14, and one at the maximum R-axis setting, position "C" of figure 14.

Finally, averages are computed for the minimum and maximum area scans, and an overall average. These averages come in two forms, a line average plotted in position "D" of figure 14, and an average BRDF number, which is displayed in the accompanying computer printouts.

Figure 14 shows typical scatter data (runs 1 to 130) for a part named Wax2. This part was cleaned and measured, and gave an overall average BRDF of 0.338 PPM/Sr in the center of this 1.5" diameter part.

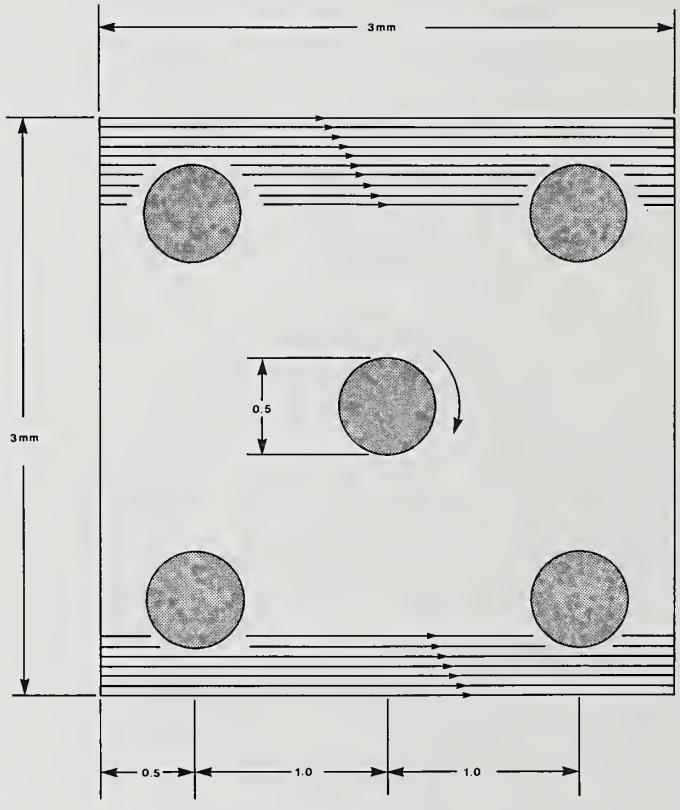

Figure 13.

Figure 15 shows scatter data for the part Wax2, runs 131-260, covering the same area as Figure 14. However, the part was acid dipped - 1 minute - 50% Sol HNO_3, BRDF = 0.338 PPM/Sr. This part was wedged so that it could be polished deeply, hopefully below the fracture zone which is usually caused by grinding the surface for shaping prior to polishing. The part was polished so that nearly 6mm of material was polished away from the center where the above measurements were made.

Polishing so much material away seems to have done one or more of several things: (1) stabilized the Beilby layer, (2) slow polishing left a Beilby layer of different composition and less likely to be attacked by acid.

Recognize this is data on only one 3mm square area near the center of the part. A one minute acid dip usually damages the surface.

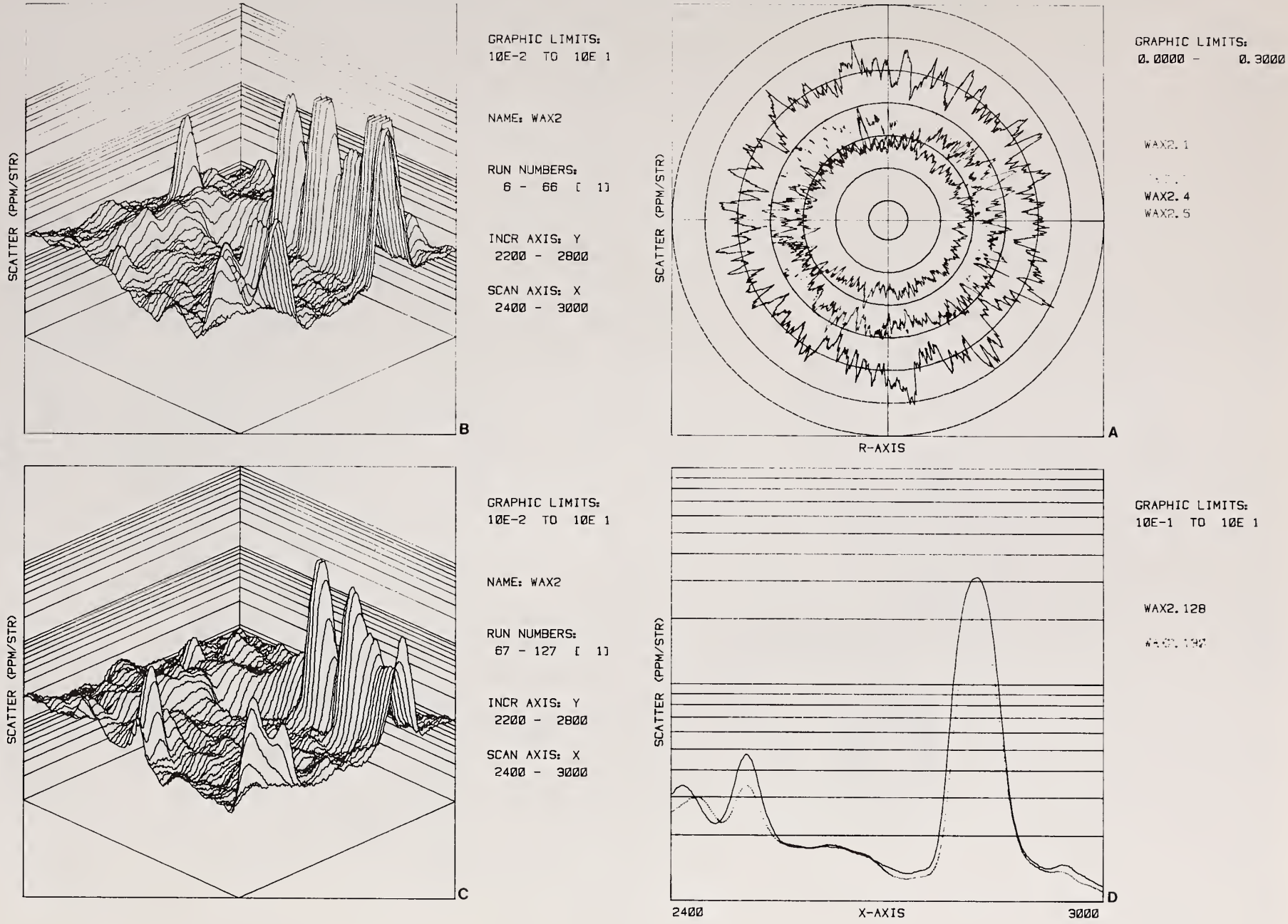
SCATTER (PPM/STR)
B
GRAPHIC LIMITS:
10E-2 TO 10E 1
NAME: WAX2
RUN NUMBERS:
6 - 66 [1]
INCR AXIS: Y
2200 - 2800
SCAN AXIS: X
2400 - 3000
SCATTER (PPM/STR)
R-AXIS
A
GRAPHIC LIMITS:
0.0000 - 0.3000
WAX2.1
WAX2.4
WAX2.5
SCATTER (PPM/STR)
C
GRAPHIC LIMITS:
10E-2 TO 10E 1
NAME: WAX2
RUN NUMBERS:
67 - 127 [1]
INCR AXIS: Y
2200 - 2800
SCAN AXIS: X
2400 - 3000
SCATTER (PPM/STR)
2400
X-AXIS
3000
D
GRAPHIC LIMITS:
10E-1 TO 10E 1
WAX2.128

Figure 14.

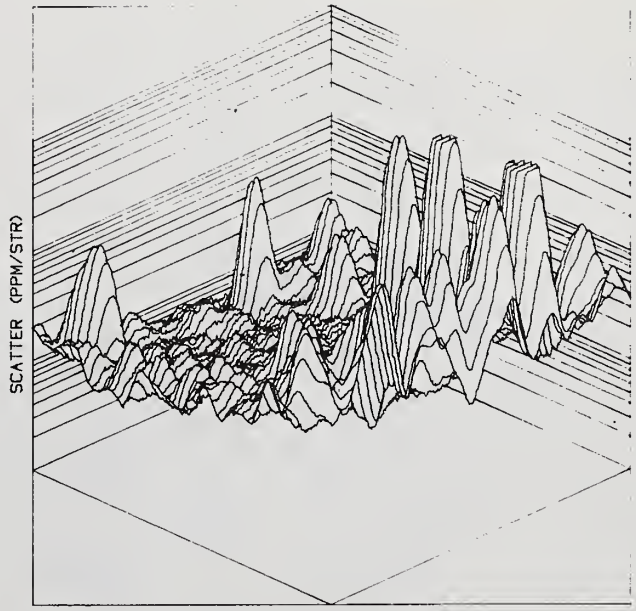

GRAPHIC LIMITS:
10E-2 TO 10E 1

NAME: WAX2

RUN NUMBERS:
136 - 196 [1]

INCR AXIS: Y
2200 - 2800

SCAN AXIS: X
2400 - 3000

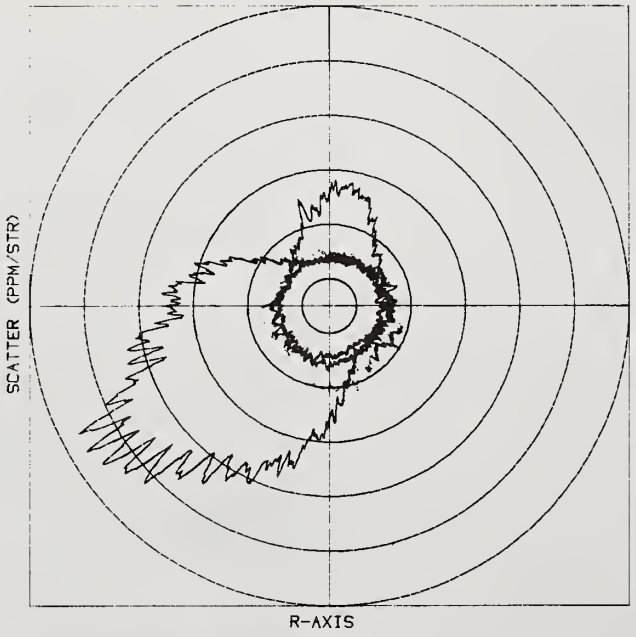

GRAPHIC LIMITS:
0.0000 - 1.0000

WAX2.131

WAX2.134
WAX2.135

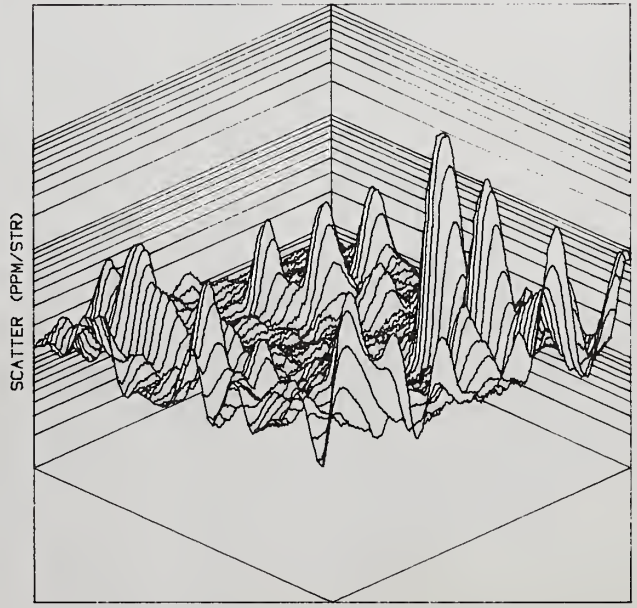

GRAPHIC LIMITS:
10E-2 TO 10E 1

NAME: WAX2

RUN NUMBERS:
197 - 257 [1]

INCR AXIS: Y
2200 - 2800

SCAN AXIS: X
2400 - 3000

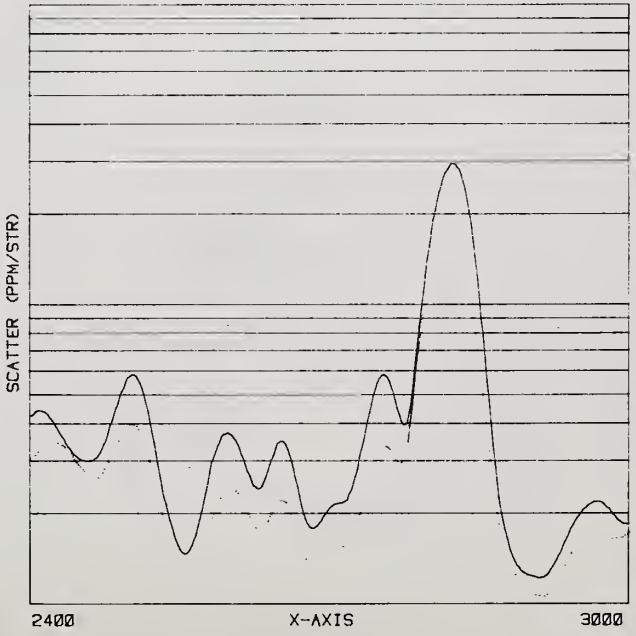

GRAPHIC LIMITS:
10E-1 TO 10E 1

WAX2.258

Figure 15

Figure 16 shows a new area of Wax2, runs 261-321 with average BRDF = 0.229 PPM/Sr. This is an area (3 x 3mm) as close to the ground edge as it was possible to get. Note there is a large identifiable feature close to the right edge of the figure. Figure 16 is before acid attack.

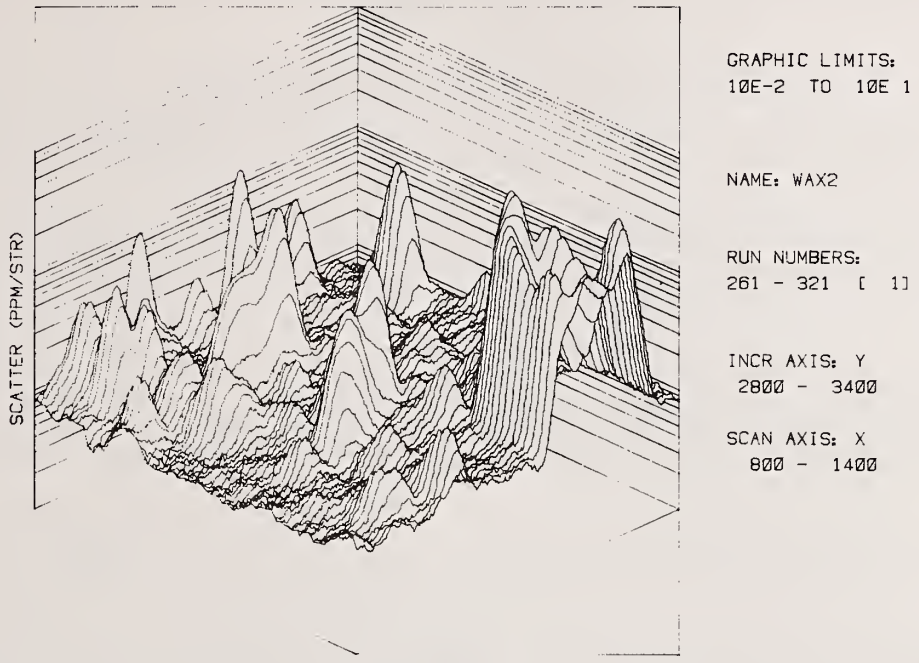

Figure 16.

Figure 17 also shows Wax2, runs 322-382, with an average BRDF = 1.696 PPM/Sr. This is after acid attack. Note the general rise in scatter. Even the large feature has been changed a bit, increasing in scatter magnitude.

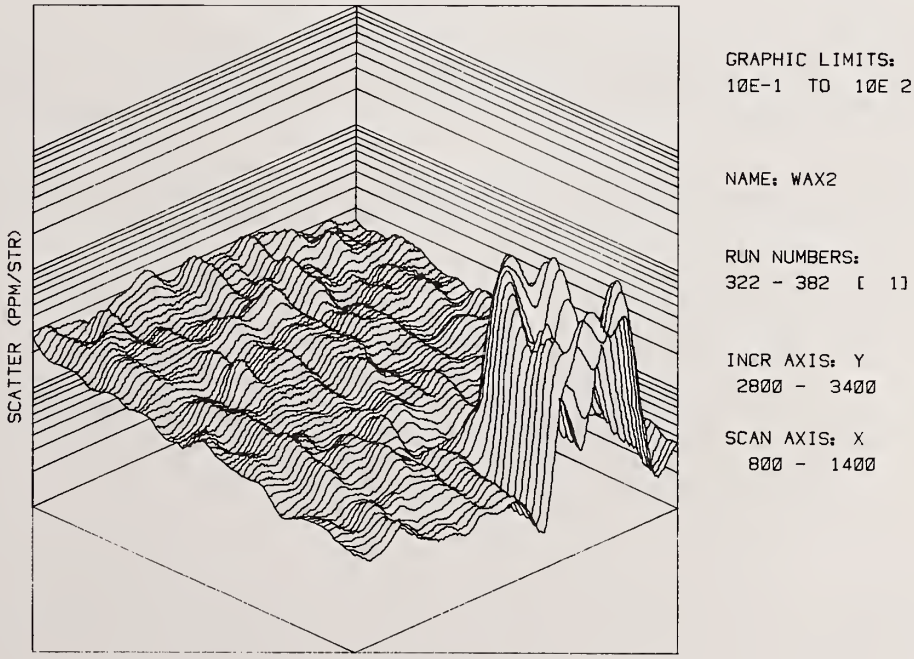

Figure 17.

Figure 18 a and b are contour maps of the scatter terrain shown in figures 16 and 17. In this view of the scatter surface it is equally clear that the scatter has risen after acid attack. This view gives some indication of how the features on the surface causing the scatter have undergone some physical change. The volcano like feature on the bottom edge has gone from a Mt. St. Helens appearance, with an open flank, to a deeper, closed structure with greater total scatter. This is characteristic of the signatures of large irregular pits.

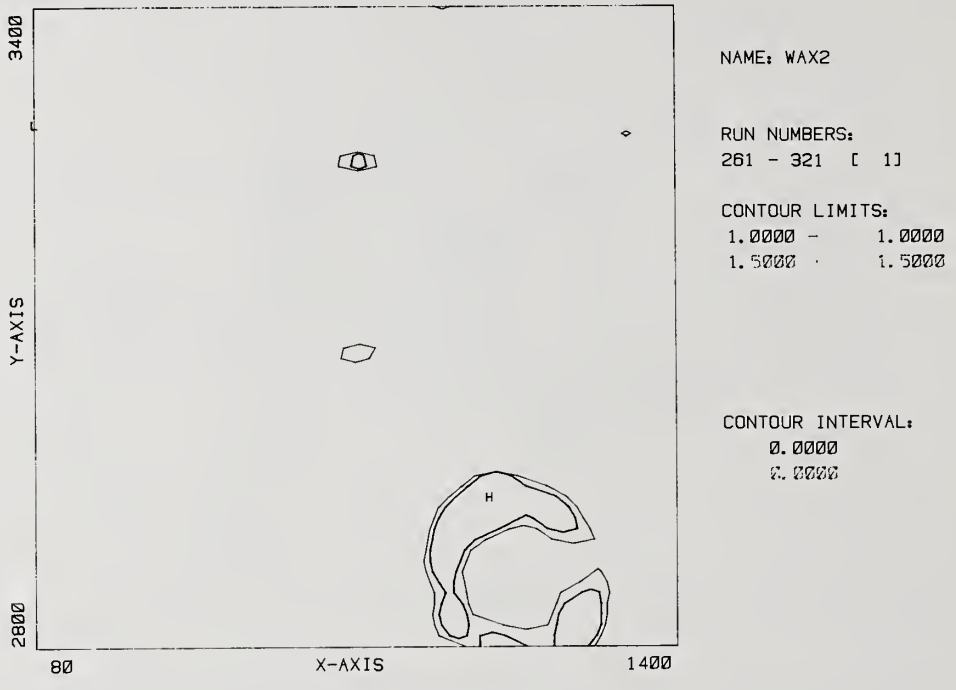

Figure 18a.

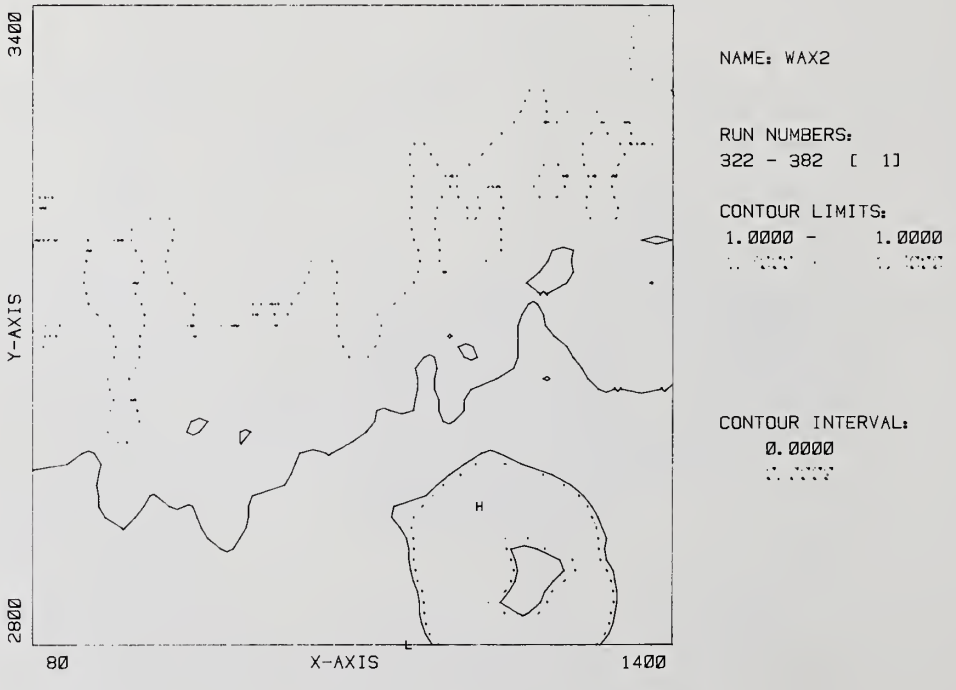

Figure 18b.

Figure 19 shows the best substrate measured to the date of this conference, fused silica, BRDF= 0.029 PPM/Sr. A later BRDF of 0.016 PPM/Sr has been measured on an optic from the same block.

Figure 20 shows four views of the same surface area at different times described below:

A. Scatter plot of clear aperture substrate before silver coating. BRDF min = 0.006, max = 3.524.
B. Plot of first silver coat. BRDF min = 3.221, max = 316.459.
C. Plot of clear aperture substrate after first Ag coat has been etched off with nitric acid. Note scatter increase to BRDF min = 0.009, max = 36.143.
D. Plot of scatter from second Ag coat. Scatter BRDF min = 5.543, max = 417.753. Surface damage from this coat and etch procedure can be seen in comparing A and C or B and D.

Figures 21 and 22 show a superpolished part which was subjected to a slow rise to 400°C (3 hour cycle) and a slow cool back to room temperature. The part was subjected to no other action. Figure 21 is the part before its thermal history and figure 22 is after the thermal cycle. Note the large increase in scatter. The average BRDF for figure 21 is 0.053 PPM/Sr while the average BRDF for figure 22 is 1.884 PPM/Sr.

Figure 23 displays the results of a study of optics from industry in which it was requested that each company supply their best production work considering application in ring laser gyros. Note the wide variation in BRDF's represented among the 19 manufacturers represented here. We only consider the top three manufacturers to have produced optics worthy of consideration for RLG's.

CONCLUSIONS

Using the scatterometer and a Nomarski DIC microscope, we have seen damage to substrates (well polished or "supersmooth" optics) caused by the following:

1. Cleaning procedures such as collodion passes, rubbing or scrubbing the surface with lens tissue soaked with solvents such as alcohol and acetone. The standard alcohol and acetone drag technique did not generate damage, but neither does it yield adequate cleaning of the part. Much caution is called for in cleaning super polished substrates.

2. Solvents such as acids (and aqua regia) and those used for the removal of photo resist have also been found to be destructive, i.e., they raise the measured scatter level of the part.

3. Thermal cycling can cause damage. A super polished part was put in an oven and taken to 400°C and returned to normal over a period of several hours. The result was degradation of the polished surface as manifested by increased scatter.

4. Shipping has caused damage. If the part can rattle around or be rubbed back and forth on even tissue wrappings, it can degrade. Consequently, when VTI ships optics it first paints the surface with a stripable vinyl-like material, a water soluable coating or collodion covered with tape which does not outgas. The authors recommend that any manufacturer of supersmooth optical surfaces use similar practices.

The largest problem remaining with substrates and RLG optics is preserving the surface we can now achieve, i.e., with BRDF's = 0.029 PPM/Sr average, or lower.

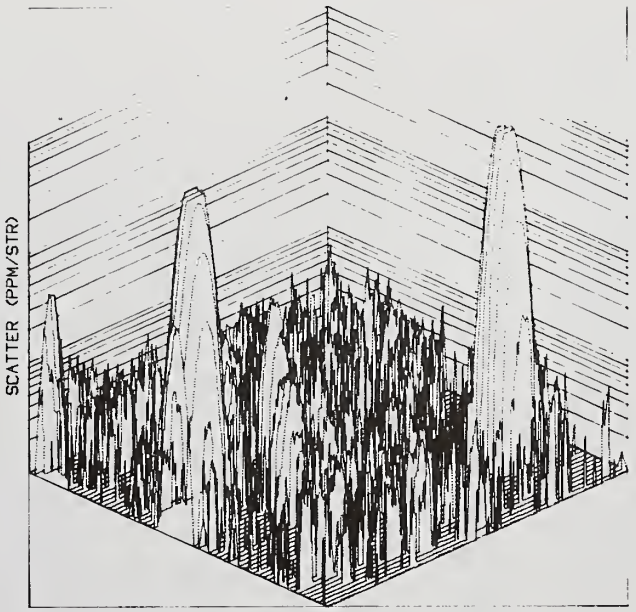

GRAPHIC LIMITS:
10E-3 TO 10E 0

NAME: VT2

RUN NUMBERS:
144 - 204 [1]

INCR AXIS: Y
2200 - 2800

SCAN AXIS: X
2200 - 2800

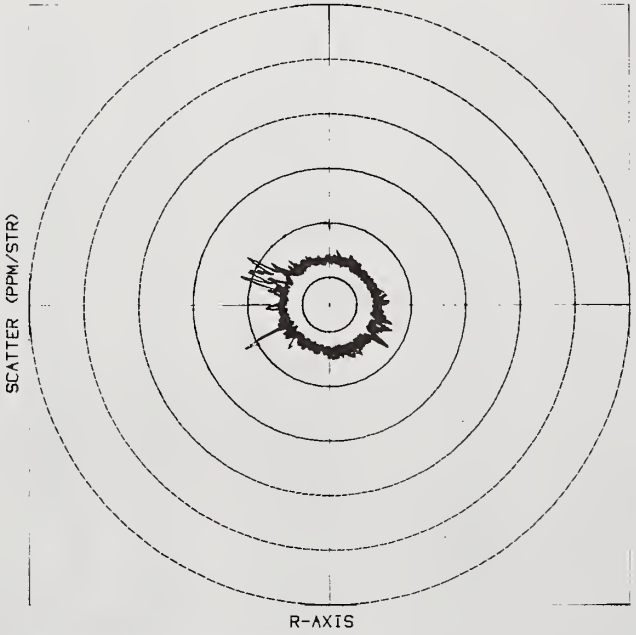

GRAPHIC LIMITS:
0.0000 - 0.5000

VT2.139

VT2.142
VT2.143

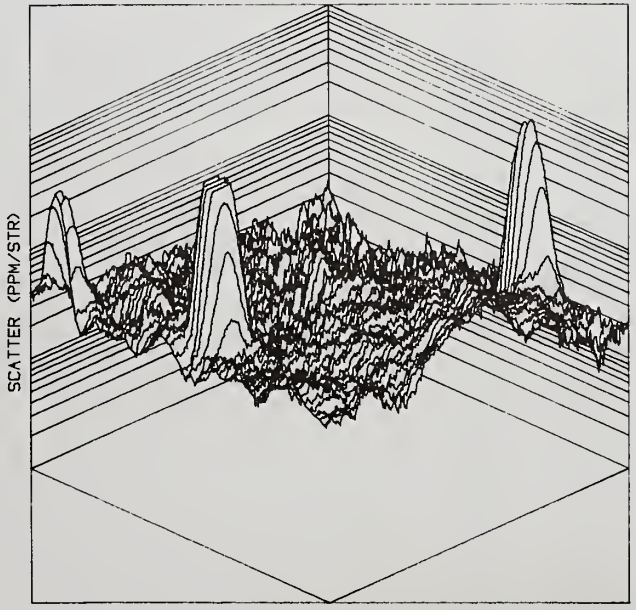

GRAPHIC LIMITS:
10E-3 TO 10E 0

NAME: VT2

RUN NUMBERS:
205 - 265 [1]

INCR AXIS: Y
2200 - 2800

SCAN AXIS: X
2200 - 2800

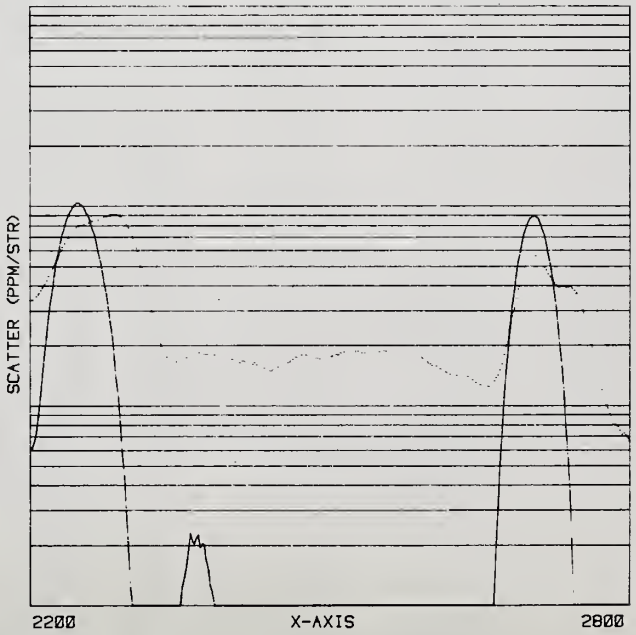

GRAPHIC LIMITS:
10E-3 TO 10E 0

VT2.266

Figure 19.

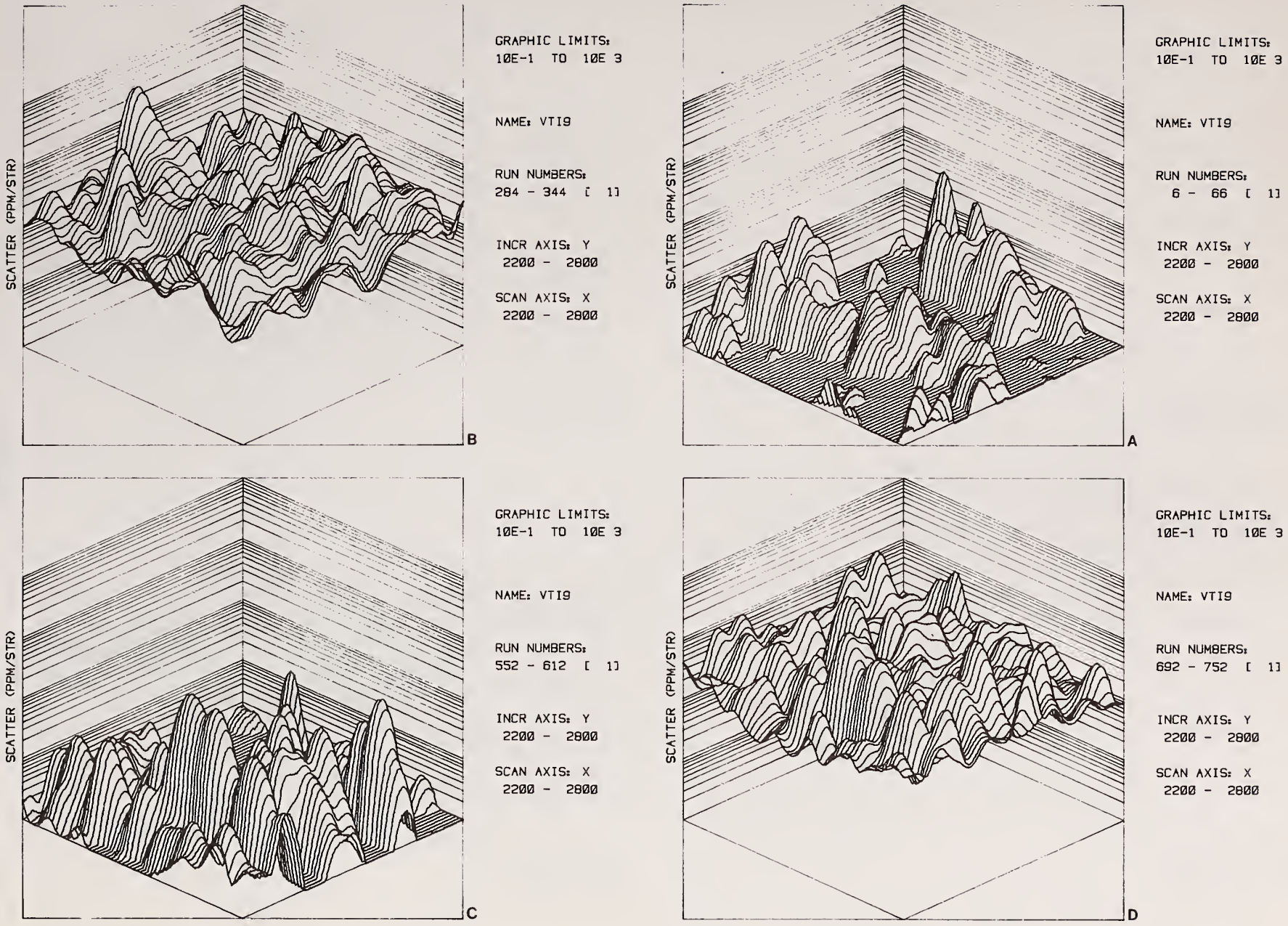
SCATTER (PPM/STR)
GRAPHIC LIMITS:
10E-1 TO 10E 3
NAME: VTI9
RUN NUMBERS:
284 - 344 [1]
INCR AXIS: Y
2200 - 2800
SCAN AXIS: X
2200 - 2800
B
SCATTER (PPM/STR)
GRAPHIC LIMITS:
10E-1 TO 10E 3
NAME: VTI9
RUN NUMBERS:
6 - 66 [1]
INCR AXIS: Y
2200 - 2800
SCAN AXIS: X
2200 - 2800
A
SCATTER (PPM/STR)
GRAPHIC LIMITS:
10E-1 TO 10E 3
NAME: VTI9
RUN NUMBERS:
552 - 612 [1]
INCR AXIS: Y
2200 - 2800
SCAN AXIS: X
2200 - 2800
C
SCATTER (PPM/STR)
GRAPHIC LIMITS:
10E-1 TO 10E 3
NAME: VTI9
RUN NUMBERS:
692 - 752 [1]
INCR AXIS: Y
2200 - 2800
SCAN AXIS: X
2200 - 2800
D

Figure 20

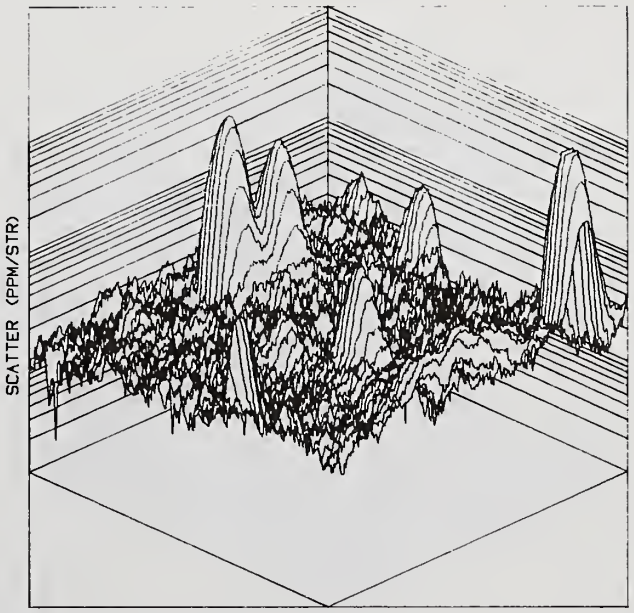

GRAPHIC LIMITS:
10E-3 TO 10E 0

NAME: HSI02

RUN NUMBERS:
6 - 66 [1]

INCR AXIS: Y
2200 - 2800

SCAN AXIS: X
2200 - 2800

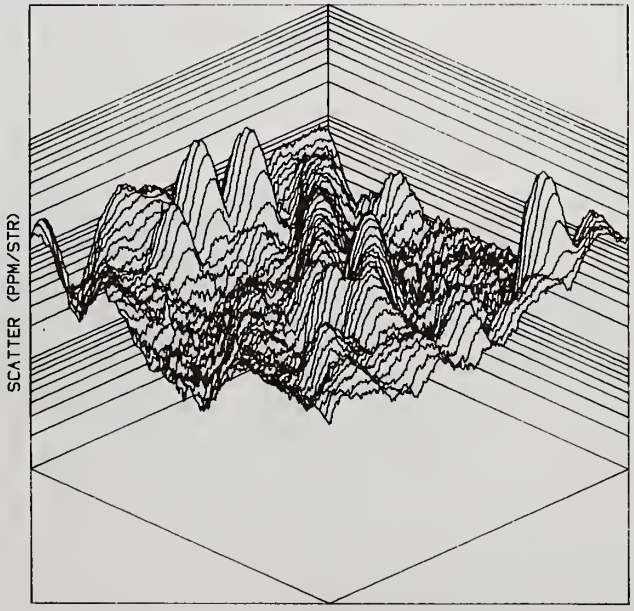

GRAPHIC LIMITS:
10E-3 TO 10E 0

NAME: HSI02

RUN NUMBERS:
67 - 127 [1]

INCR AXIS: Y
2200 - 2800

SCAN AXIS: X
2200 - 2800

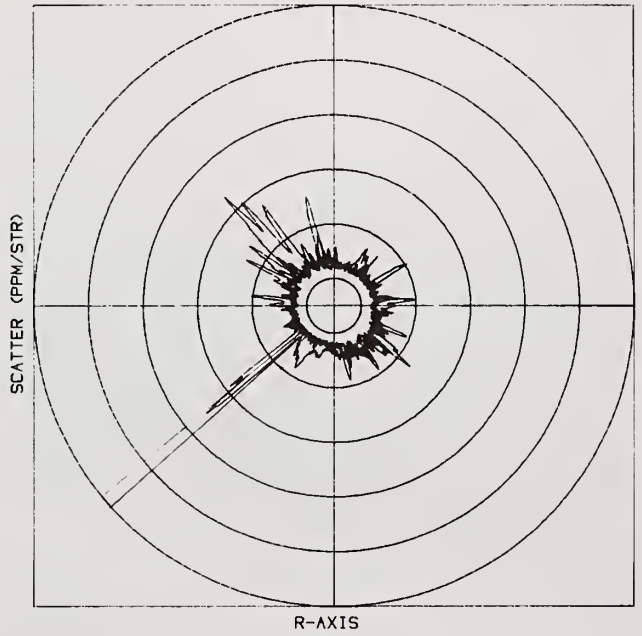

GRAPHIC LIMITS:
0.0000 - 1.0000

HSI02.1

HSI02.4
HSI02.5

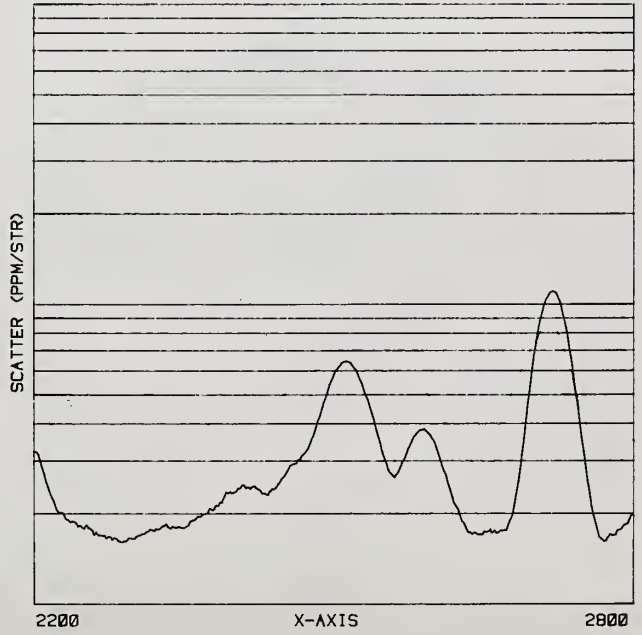

GRAPHIC LIMITS:
10E-2 TO 10E 0

HSI02.136

Figure 21.

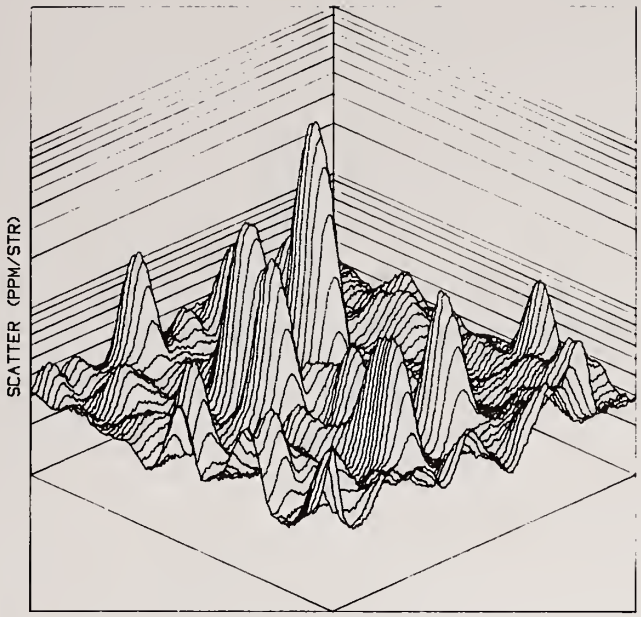

GRAPHIC LIMITS:
10E-1 TO 10E 1

NAME: HSI02

RUN NUMBERS:
144 - 204 [1]

INCR AXIS: Y
2200 - 2800

SCAN AXIS: X
2200 - 2800

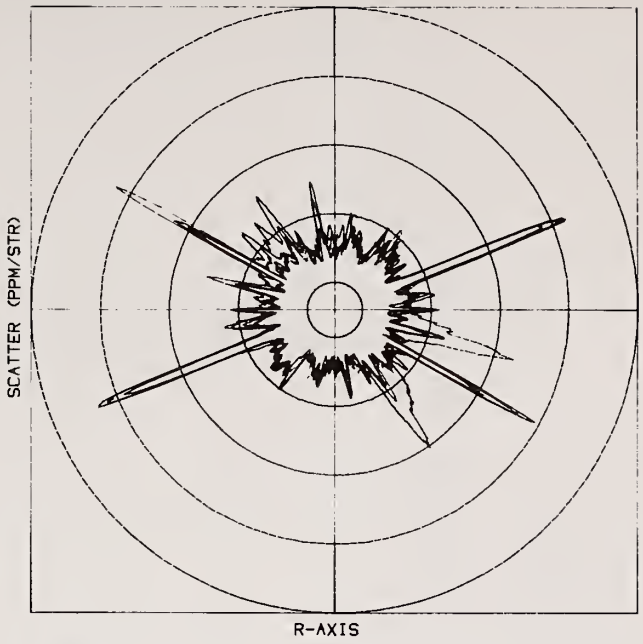

GRAPHIC LIMITS:
0.0000 - 4.0000

HSI02.139

HSI02.142
HSI02.143

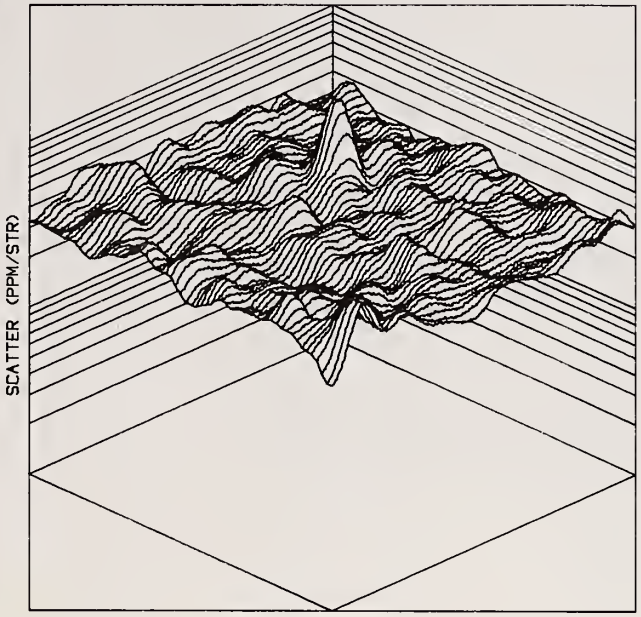

GRAPHIC LIMITS:
10E-1 TO 10E 1

NAME: HSI02

RUN NUMBERS:
205 - 265 [1]

INCR AXIS: Y
2200 - 2800

SCAN AXIS: X
2200 - 2800

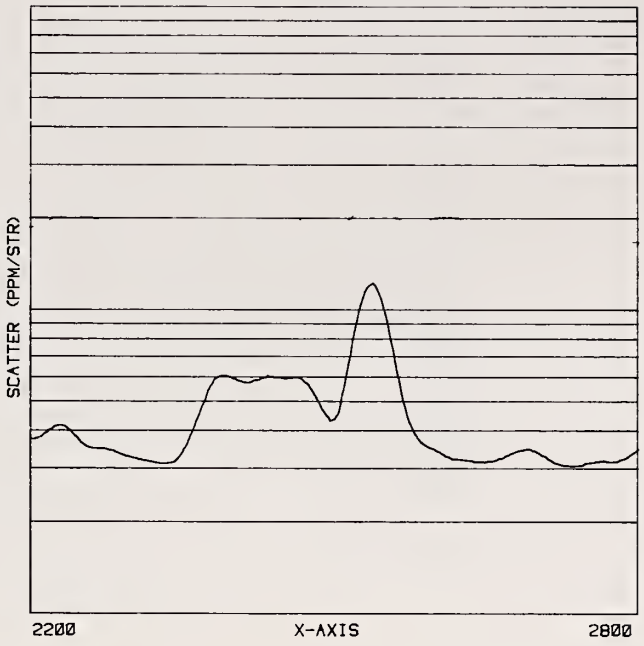

GRAPHIC LIMITS:
10E-1 TO 10E 1

HSI02.266

HSI02.268

Figure 22.

OPTICS FROM INDUSTRY RANKING BY SCATTER FIGURE OF MERIT

POSITION	FIGURE OF MERIT	MFG	POSITION	FIGURE OF MERIT	MFG
1	0.036	A	25	0.521	H
2	0.049	B	26	0.593	I
3	0.074	B	27	0.713	C
4	0.077	A	28(BK-7)	0.748	J
5	0.090	A	29(BK-7)	0.846	J
6	0.091	B	30	0.864	D
7	0.100	B	31	0.954	K
8	0.100	C	32	1.081	L
9	0.141	C	33	1.088	K
10	0.152	B	34(BK-7)	1.150	G
11	0.152	B	35	1.324	L
12	0.177	B	36	1.514	M
13	0.195	B	37*	1.545	N
14	0.199	B	38(BK-7)	1.702	E
15	0.205	B	39	1.751	L
16	0.207	B	40	1.884	O
17	0.216	B	41	2.295	P
18	0.238	B	42	2.387	P
19	0.321	D	43	2.505	B
20	0.382	E	44	2.978	Q
21	0.392	F	45	3.943	R
22	0.398	B	46	4.001	B
23	0.425	B	47	4.954	S
24	0.514	G	48(BK-7)	6.590	Q

*Unknown Material

Figure 23

Development of Laser Mirrors of Very High Reflectivity Using the Cavity-Attenuated Phase-Shift (CAPS) Method

J. M. Herbelin and J. A. McKay
Aerospace Corporation
Aerophysics Laboratory
Los Angeles, CA 90009

It has been possible to obtain mirrors of very high reflectivity by following the simple four-step procedure described herein. The key to success is the ability to measure the scattering and other losses of the substrates and dielectric coatings to ensure that the specifications are being met. These measurements are especially critical in the important cleaning process. The cavity-attenuated phase-shift (CAPS) method is ideally suited for performing these important measurements, permitting us to obtain mirrors with reflectivities of $R = 0.99975 \pm 0.00005$.

Key Words: cavity phase shift method, optical coatings, optics cleaning

1. Introduction

High-power infrared laser systems and shorter wavelength laser systems based upon electronic transitions have created a need for very-high-reflectivity laser mirrors. This requirement arises from the extremely high photon-flux densities associated with these laser devices and the much lower increases in power per transit between mirrors (gain) of the new electronic transition laser systems compared to the infrared laser systems. As a case in point, for the nitrogen fluoride system currently being studied as a potential laser candidate, the gain is so low that mirrors in excess of 99.95% reflectivity are required for an initial lasing demonstration on a laboratory scale.

We are pleased to report that, with the help of several specialist groups in the field, we have been able to produce mirrors with reflectivities of 99.975% (at a wavelength value near 0.87 μm) and that other advances in the state of the art could be achieved if there were a requirement. This accomplishment was possible because we invented a new method for making the critical scattering loss measurements associated with the mirror substrate cleaning process, i.e., the cavity-attenuated phase-shift (CAPS) method.

2. High-Reflectivity Mirror Development Procedure

The procedure that we used to produce the high-reflectivity mirrors consists of four basic steps: (1) the procurement of high-quality quartz substrates from a suitable vendor, (2) the cleaning, measurement, and preparation of these substrates, (3) the coating process by which a low-scatter dielectric coating is applied by a qualified supplier, and (4) the measurement of the resultant mirror reflectivity. Since Steps (1) and (3) are performed by suppliers, only Steps (2) and (4) are necessary for ensuring the desired quality.

2.1 Substrate Procurement

The quartz substrates were obtained from General Optics. These were specified to have an RMS smoothness of $\leq$ 10 Å and be flat and parallel to $\leq \lambda/4$. These substrates had been cleaned by General Optics. To remove the excess grinding material and waxes used in the polishing process, substantially more cleaning was required. Figure 1 is a photograph taken of one of these General Optics quartz substrates before cleaning. A dark-field microscope at 400X magnification was used. Since the field of view is approximately 0.5 mm, the larger particles are approximately 100 μm with the particles ranging to a detection limit of about 10 μm.

2.2 Substrate Cleaning

In our search for a reliable and efficient cleaning procedure, we quickly discovered that each researcher had his own special technique. After some deliberation, we decided to use a "try and see" approach. We started with the special solvent mixture of 1,1,1, trichlorethane and ethanol, which was specially treated to minimize all nonvolatile residues, from Analytical Research Laboratory, Inc. Figure 2 is a photograph of a quartz substrate after being cleaned with this "super solvent." The improvement is obvious. Various cleaning or rubbing techniques were attempted, and microscopic examination followed. We discovered that each technique has its own advantages, and it was difficult to decide which was the most beneficial. It was difficult to correlate the microscope pictures with a quantitative estimate of the scattering. Consequently, we decided to measure the scattering from the surfaces by means of the photon lifetime measurement technique recently developed in this laboratory [1]. Using a modification of this technique we were able to quantitatively measure the scattering and to determine the quickest, easiest, and most reliable technique for cleaning the quartz substrates. The ability to make these quantitative scattering measurements has significantly reduced the labor and equipment costs involved while substantially increasing the reliability of the cleaning procedure.

3. Quartz Substrate Scattering Measurements

This technique is described in detail elsewhere [1]. A brief description is provided here for convenience. An amplitude modulated light beam from a suitable source, usually a laser, is directed through one of the slightly transmitting mirrors into the aligned optical cavity comprised of the mirrors and optics to be measured. The dissipation of the light energy within the cavity is caused by absorption, scattering, or transmission at the surfaces of the cavity mirrors and at other optical components within the resonator. Each loss shortens the effective photon lifetime, which is defined as the characteristic time τ for the photon energy to be dissipated to e^{-1} (or 0.34) of its original value. This photon lifetime is determined from a phase shift in the light-beam intensity that has passed through the optical resonator.

The amplitude modulation, which is required to extract time-dependent lifetime data from a steady-state experiment, is conveniently produced by passing the continuous source beam through a piezo-optical birefringence modulator. A linearly polarized photon beam with a $\sin^2 (2\pi ft + \phi)$ modulation at f = 50 kHz is produced. The resultant phase shift α of the emerging beam is related to the photon lifetime by the simple expression, $\tan(\alpha) = 4 \pi f \tau$. Since this

lifetime corresponds to some number n of round trips that the photons make within the optical resonator $n = c\tau/2L$, where c is the speed of light, and L is the distance between the mirrors, the overall loss of the optical resonator $1 - R$ and, therefore, the product of the reflectivities $R = R_1R_2$ can be obtained from the simple formula $1 - R = 1/(n + 1)$.

With the use of appropriate combinations of different cavity mirrors and other optical components, each of the respective losses and reflectivities can be determined. The most convenient method of measurement is to use a two-phase lock-in amplifier to measure both the $\sin \alpha$ and $\cos \alpha$, which are, in turn, input into a ratiometer to obtain $\tan \alpha$ directly. For large n's (n typically ranges from 200 to 2000), this output signal is directly proportional to the cavity lifetime, affording on-line in-situ measurements.

The two ways that the quartz substrate can be intracavity placed into the optical cavity to minimize reflectance losses, i.e., at Brewster's angle and perpendicular to the cavity axis. At the Brewster's angle, by definition, the reflectance loss for the perpendicular polarized light, which is what is being introduced into the cavity, is theoretically very close to zero. This assumption has been used by other investigators as a means of calibrating their mirror reflectivity measurement methods [2]. However, we quickly discovered that the substrate placed at the perpendicular angle showed considerably less attenuation of the phase shift and, therefore, less loss than when the same substrate was placed at Brewster's angle. Although the reflectance off the surfaces of the substrate at normal angle is much larger, approximately 4%, it is reflected right back at the mirror and therefore does not represent a loss. However, when the substrate is placed at the Brewster's angle, the light which is plane polarized perpendicular to the plane of incidence is reflected out of the cavity while the light polarized parallel to the plane of incidence is not. Consequently, any rotation of the plane of polarization within the cavity, such as through the birefringence of the quartz substrate itself, results in a much higher loss than would have been predicted. Thus, the difference between the two measurements of total loss for these two substrate positions affords a very sensitive measurement of the birefringence of the quartz substrate itself. We were also able to measure the small changes in the birefringences that occur when mechanical stress is applied or removed from the substrate.

By means of the cavity-attenuated phase-shift (CAPS) method, we were able to very quickly establish the best (fastest, easiest, and most repeatable, with the lowest amount of scattering) procedure, which consisted of nothing more than a few light wipes, a few hard wipes, followed by a few more light wipes with ordinary lens paper saturated with the "super solvent."

After cleaning, the substrates were spring loaded into the coating mounting block designed in-house, designed to fit into the commercial coating machines. This block was made from stainless steel that had been specially cleaned to remove all machining oils and greases. It was then preheated to 300°C for 2 hr to remove any residual contamination. The block was not touched by human hands after this. After being loaded with the cleaned substrates, the block was then placed into a special container that formed a vacuum seal. The container was first evacuated and filled with dry filtered nitrogen, then "hand carried" to the supplier for coating. It was returned the same way. Transportation was not trusted to courier services. If dropped, which had happened, the coated substrates could become jammed into the block and could only be removed with the force of a hammer and wood dowel.

Two commercial vendors were investigated to determine the quality of the optical coatings produced. The first of these was CVI, Albuquerque, New Mexico, and the second vendor was Optical Coating Laboratory Incorporated (OCLI). Our criteria were minimum absorption, scattering and transmission losses, and maximum reflectivity. We decided to test the CVI coating quality with a set coated at the 6328-Å wavelength. Using the CAPS method, we measured a reflectivity of R = 99.89, which was surprisingly low. We had expected it to be better, or R = 99.95 based upon a stipulated transmission loss of 100 ppm and an anticipated scattering loss of 400 ppm at 6328 Å. This expectation had been based upon information supplied to us by V. Sanders, Litton Industries. We then examined the reflectivity as a function of the incident angle by means of a three mirror cavity arrangement [1]. We quickly discovered that, at an angle of $\theta = 45$ deg, the reflectivity approached the anticipated higher value. CVI confirmed our suspicions, i.e., that by mistake, the coating had been given a $\theta = 45$ deg maximum reflectivity coating, which is the usual coating for laser gyro mirrors.

We decided to obtain an OCLI coating at the required wavelength of 8742 Å.
The same preparation and handling procedures were again employed, and measurement of the final product yielded a value of R = 99.975. The calculations used to predict the reflectivity of the final product, are:

1. For the coating, $R = 1 - (T + A + S)$, $T \leq 100$ ppm, $A \simeq 30$ to 300 ppm; $S_C \simeq 50$ to 1000 ppm, and $\lambda = 6328$ Å.

2. For the substrate, $S_S \simeq 50$ to 500 ppm.

At $\lambda = 8742$ Å, $S = (6328/8742)^2 \quad (S_C + S_S) = 0.52\ (50 + 50) = 52$ ppm, $A \leq 100$ ppm, $T = 100$ ppm, $R(8742) \geq 0.99975$ or $(1 - R = 0.00025)$.

These calculations include the range of values for transmission T, absorption A, and scattering S losses arising from the coating and the substrate at the helium-neon wavelength (6328 Å) for which the most data are available. Wavelength correction of the anticipated scatter from the coating and measured scatter from the substrate is made and combined with the specified absorption and transmission losses to predict the R = 99.975 reflectivity mirrors, which we indeed obtained.

4. Summary

We found that the use of the cavity-attenuated phase-shift (CAPS) method, in conjunction with simple cleaning practices, results in a simplified procedure for producing very-high-reflectivity mirrors. Our substrate cleaning process is a straightforward procedure. It is reasonable to project that a similar application of this CAPS method to the coating processes itself could permit an order of magnitude improvement over present coating limits. The basic reason is that, unlike other methods, the higher the reflectivity of the mirrors being generated, the more sensitive the phase-shift method becomes. Consequently, there is essentially no limit, other than the materials themselves, in producing extremely high reflectivity mirrors.

This work was supported in part by the Air Force Weapons Laboratory under U.S. Air Force Space Division Contract F04701-80-C-0081.

5. References

[1] J. M. Herbelin, J. A. McKay, M. A. Kwok, R. H. Ueunten, D. S. Urevig, D. J. Spencer, and D. J. Benard, "Sensitive measurement of photon lifetime and true reflectances in an optical cavity by a phase shift method," Appl. Opt. 19, 144 (1980).

[2] V. Sanders, "High-precision reflectivity measurement technique for low-loss laser mirrors," Appl. Opt. 16, 19 (1977).

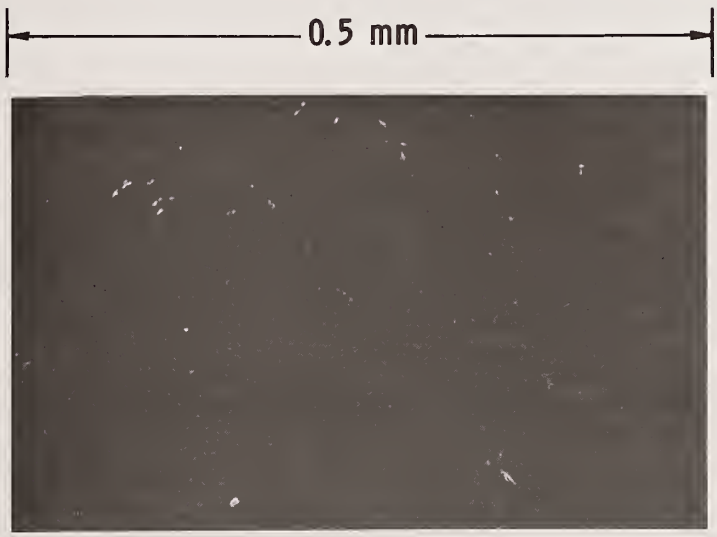

Fig. 1. Photograph of a Quartz Substrate Before Cleaning as Observed Through a Dark-Field Microscope at 400X Magnification. The field of view is 0.5 mm.

Fig. 2. Photograph of a Cleaned Quartz Substrate as Observed Through a Dark-Field Microscope at 400X Magnification. The field of view is 0.5 mm.

The question was asked, "Can you use a white light source?" The author replied that to make the method work well and avoid throughput problems one needs a laser. In the visible range, dye lasers can cover most wavelengths of interest. In the infrared the problem of obtaining a range of wavelengths is more difficult. The sample design may be also important since what is measured is a loss. Loss can occur through absorption, scattering by the sample, or through geometrical optics if the sample is wedge shaped, for example. In answer to another question, the speaker reported that because of the sensitivity of the technique one can do surface mapping of the mirror.

Damage Thresholds to Metal Mirrors by Short-Pulse CO_2 Laser Radiation*

J. F. Figueira, S. J. Thomas and R. F. Harrison

University of California
Los Alamos National Laboratory
Los Alamos, NM 87545

Measurements of damage to metal surfaces induced by intense nanosecond pulses of ir radiation are reported. Single-shot damage thresholds of Cu, stainless steel, molybdenum and aluminum surfaces have been measured for various angles of incidence and the predicted increase in damage thresholds for grazing incidence optical components have been experimentally verified for the first time at 10-μm.

Multiple-shot damage tests have also been performed and practical lifetime curves for Cu mirrors have been established. Scanning electron micrographs of the mirror show the damage mechanism to be the development of a fine scale (1 μm) microstructure on the copper surface.

Key words: CO_2 lasers; grazing incident; laser induced damage; metal mirrors; multiple-shot threshold.

1. Introduction

Metal mirrors have found extensive use in high-power laser systems. In order to maximize system performance an accurate knowledge of the realistic constraints placed on the mirror by damage considerations is necessary. In this paper we report the results of damage testing on metal mirrors by short pulse (1 ns) CO_2 lasers.

In the first section we will describe the results of single-shot damage tests on mirrors at large angles of incidence and show that grazing incidence operation can increase the measured damage thresholds for p-plane radiation by factors of 40. The results are compared to the Fresnel theory and shown to be in good agreement.

In the second section results on multishot damage thresholds for copper mirrors, both polished and diamond turned will be reported and practical lifetime curves based on the observed degradation of optical performance of the mirror will be derived. Scanning electron micrographs of copper mirrors exposed in these multishot damage tests show the development of a regular microstructure which causes a dynamic reduction in the surface reflectivity leading to the observed lifetime effects.

2. Single-Shot Damage Thresholds

When an intense beam of light interacts with a metal surface a fraction of the incident radiation penetrates the metal to a skin depth and is absorbed by the free carriers in the metal. If the absorption is strong enough and the incident radiation intense enough, the absorbed energy can raise the surface temperature to a value in excess of the melting temperature. Thresholds for surface melting have been derived previously for the case of constant surface absorption [1,2] and have shown that for a pulse of intensity $I(W/cm^2)$ and duration $t_p(sec)$,

$$(It_p)_m = \frac{T_m - T_o}{2A_o} \sqrt{\pi KC\, t_p} \qquad (1)$$

where $(It_p)_m$ is the fluence (J/cm^2) required to melt the surface, A_o is the room temperature surface absorption, T_m is the melting temperature for the material (°C), T_o is the ambient temperature (°C), K is the thermal conductivity in $(W/(cm^2 \cdot °C))$, and C is the volumetric specific heat (specific heat x density) in $(W \cdot sec/(cm^3 \cdot °C))$. In general the surface absorp tion is not

independent of the surface temperature and eq. (1) must be generalized by including a temperature dependent surface absorption. This problem has been solved by Sparks and Loh [3,4] by including a linearly temperature-dependent surface absorption.

If the laser beam is chosen to be normal to the metal surface under test, the two components of electric field vector, E_s (field perpendicular to the plane of incidence) and E_p (field in the plane of incidence) are parallel to the metal surface and the absorption experienced by the incident light field is independent of polarization. For the more general case of non-normal incidence, differences in the surface absorption arise for E_s and E_p radiation. Recently Mumola [5] and earlier Goldstein et al. [6] have pointed out that this effect could be used to substantially increase the damage threshold of metal mirrors when used at grazing angles of incidence.

For a metal described by a complex index of refraction $\hat{n}$ where

$$\hat{n} = n + iK$$

the intensity reflection coefficient of a light wave at an angle of incidence Θ is given by [7]

$$R_p = \frac{(n^2+ k^2) \cos^2\Theta - 2n \cos\Theta + 1}{(n^2+ k^2) \cos^2\Theta + 2n \cos\Theta + 1} \tag{2}$$

$$R_s = \frac{(n^2+ k^2) - 2n \cos\Theta + \cos^2\Theta}{(n^2+ k^2) + 2n \cos\Theta + \cos^2\Theta} \tag{3}$$

in the limit where $(n^2+k^2) >> 1$ and where R_p and R_s are the intensity reflection coefficients for radiation polarized parallel and perpendicular to the plane of incidence respectively.

For most metals in the ir $n >> 1$ and $k >> 1$ and eq. (2) and (3) can be further simplified by expanding for the denominator in powers of $2n \cos\Theta/(n^2+k^2)$ to produce,

$$R_p = 1 - \frac{4n}{(n^2+k^2) \cos\Theta} \tag{4}$$

$$R_s = 1 - \frac{4n \cos\Theta}{n^2 + k^2} \tag{5}$$

If we define an angular dependent absorption coefficient $A(\Theta)$ by

$$A(\Theta) = 1 - R(\Theta) \tag{6}$$

then we have from eq. (4) and (5)

$$A_p(\Theta) = A_0/\cos\Theta \tag{7}$$

$$A_s(\Theta) = A_0 \cos\Theta \tag{8}$$

where the normal incidence absorption is given by A_o and

$$A_o = \frac{4n}{n^2 + k^2} \quad . \tag{9}$$

For a metal surface at an angle of incidence Θ to an incoming laser beam, the calculation for the surface damage threshold must be modified in two respects. First, the surface fluence must be reduced from the normal beam fluence I, by the factor cos Θ due to the increased surface area now irradiated by the rotated laser beam. Secondly, the absorption, $A(\Theta)$, must be modified by the complex Fresnel equations above to include electric field components both parallel and perpendicular to the metal surface. If we assume that A_o is not a function of Θ then the expression for the damage threshold for surface melting of eq. (1) can be corrected for non-normal incidence using eq. (7) and (8) and corrected for surface fluence to obtain

$$(It_p)_{m,p} = \frac{(T_m - T_o)}{2A_o} \sqrt{t_p KC} \tag{10}$$

$$(It_p)_{m,s} = \frac{(T_m - T_o)}{2A_o \cos^2\Theta} \sqrt{t_p KC} \tag{11}$$

where p and s refer to parallel and perpendicular polarization of the radiation, I is the beam fluence normal to beam direction (this causes an extra cosΘ to appear on the RHS above). For p-plane polarization, eq. (10), the damage threshold remains constant, independent of incident angle (for large angles the approximations used in deriving eq. (4) and (5) fail and the damage threshold does increase for angles > 80°). For s-plane polarization, eq. (11), the damage fluence increases as $(\cos^2\Theta)^{-1}$ and at large angles (Θ>80°) will show a dramatic increase over the normal incidence value.

In order to experimentally verify these predictions a series of single-shot damage tests were performed in vacuum for three materials, Cu, stainless steel 304, and molybdenum. Cu mirror substrates were 4-inch-diameter copper-plated aluminum-bronze, manufactured for use in the Antares Fusion laser system. The copper plating was .040 inch thick. Several vendors used standard optical fabrication techniques in polishing the test mirrors, while some were finished by single-point diamond turning at the DOE Y-12 facility. Additional samples of copper, molybdenum, and stainless steel 304 mirrors were prepared by standard polishing techniques.

Damage threshold measurements were made using a short pulse (1.7 ns) CO_2 oscillator/amplifier system grating tuned to the 10 P(20) line. A schematic of the damage test setup is shown in figure 1. The sample under test was placed 10 cm inside the focal point of a 1-m focal length lens where the $1/e^2$ spot radius was 1 mm. Peak fluence (J/cm^2) at the sample plane was measured on each shot by the use of a 200-μm-diameter pinhole located in the reference beam at the same distance from an identical lens. By this technique, damage plane fluence was determined on each shot to an accuracy of ± 3%. The maximum fluence available from the laser was 50 J/cm^2 at 1.7 ns with this arrangement. A vacuum chamber with a liquid N_2 cold trap provided a background test environment of less than 100 mtorr. The mirror surfaces were mounted on a rotation stage to allow rotation from Θ = 0° to Θ = 85°. Single-shot damage thresholds were measured by irradiating the test sample at 25 different sites, at a fluence level which produced damage for approximately one half the shots. Samples were not cleaned prior to testing except to blow off dust particles. We have chosen to define the single-shot threshold of damage as that intensity where an observable, permanent change occurs in the surface when examined under 60X magnification with a white light source.

The results of these damage tests for s-plane radiation are shown in figure 2. The value of the damage fluence plotted is the fluence normal to the incident beam. Also shown on the figure are the predicted damage thresholds calculated from eq. (11) normalized to the measured normal incidence damage fluence. In general the agreement between the measured and calculated values is good. In particular the $\cos^2\Theta$ dependence in the damage threshold is well borne out by the experimental data. The largest increase in the damage level measured was that for stainless steel where the threshold increased from 0.6 J/cm^2 to 24 J/cm^2 at an 80° incidence angle.

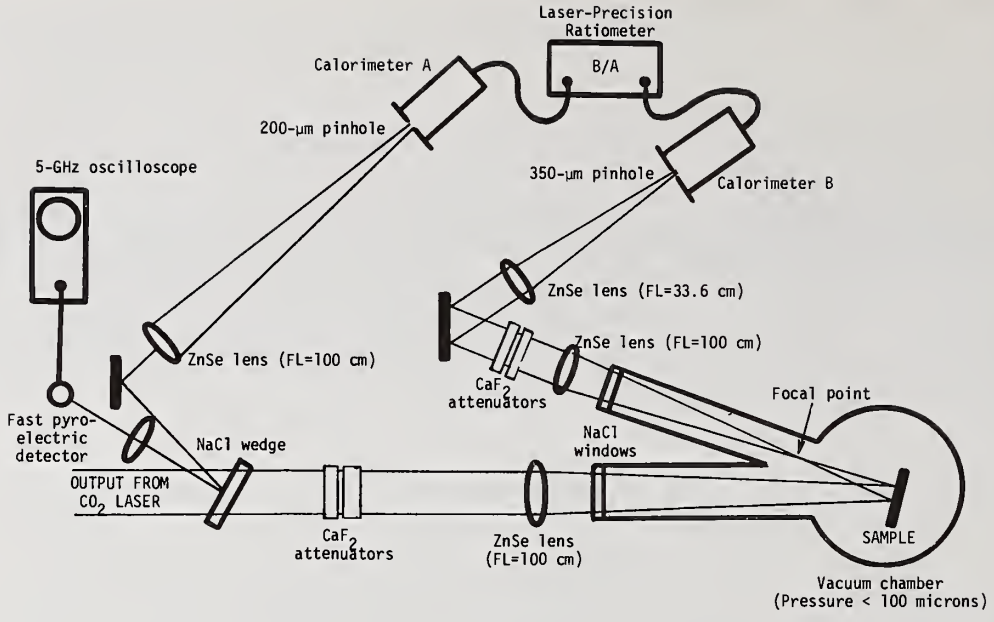

Figure 1. Experimental Apparatus.

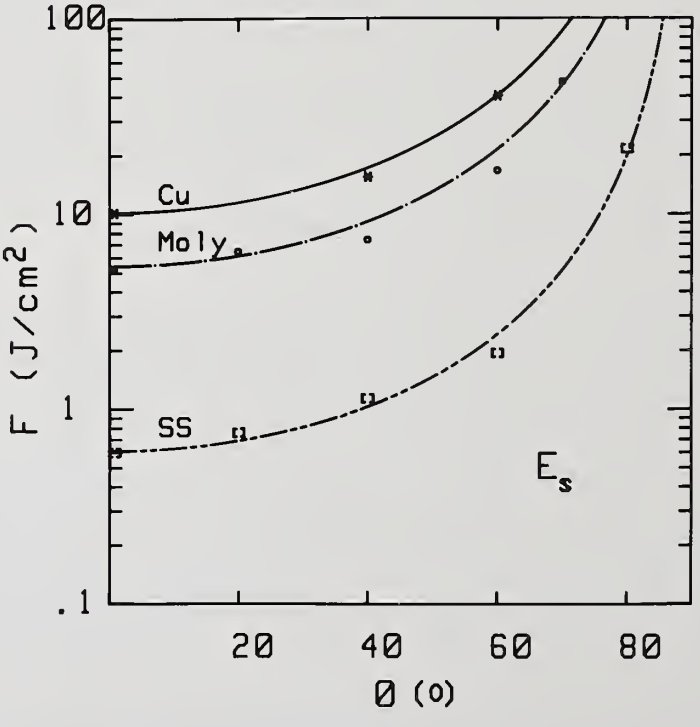

Figure 2. Grazing incidence damage thresholds F, in vacuum for 1.7-ns pulses of 10.6-μm radiation polarized perpendicular to the incident plane (E_S) for various angles of incidence, Θ. Solid curves are calculated from eq. (11). Data for Cu, molybdenum, and stainless steel 304 are shown.

3. Multiple-Shot Damage Thresholds

Single-shot damage thresholds are of interest in determining the physical processes involved in absorption at metal surfaces; however, they do not fully describe the operating constraints faced by a metal mirror when used as an optical element in a high-power laser system. Hence we have chosen to modify the earlier definition of damage by imposing a specific performance criterion on the optical element under test and then measure the element's progressive performance degradation as the surface is repeatedly exposured to a high intensity laser beam. For the performance criterion, we have chosen to measure the peak brightness [8] of the beam reflected from the mirror surface. This is the actual criterion of importance in any high-power/high-brightness laser system and can be directly measured by standard laboratory techniques. An experimental arrangement similar to that described above was employed (see fig. 1). A 10.6-μm laser beam was converged toward a mirror surface in vacuum and the reflected signal was passed through a spatial filter where the peak brightness of the beam was measured on each shot for shot sequences up to 100 shots. For these measurements the mirror was tilted 15° to allow access to the reflected beam. A multiple-shot sequence was acceptable if the maximum brightness variation of the reference beam was less than ± 5% throughout the run. In practice about 50% of the 100-shot damage tests had to be rejected because of this requirement. Pulse repetition frequency was about 0.05 Hz so no appreciable heating of the surface was encountered.

At a fixed fluence level the brightness of the reflected beam was then measured as a function of the number of shots at a fixed location on the mirror surface. For this test both diamond-turned and conventionally polished substrates as described above were used. Figures 3 and 4 show some typical results for Cu mirrors with conventionally polished surfaces (fig. 3) and with diamond-turned surfaces (fig. 4). Beam brightness is plotted vs shot number for several values of incident fluence normalized to the single-shot damage fluence, F_o for the mirror under test. For both the diamond-turned and conventionally polished mirrors the beam brightness decreases with shot number. The rate of brightness degradation is initially fast and then slows as is evident from the slope change after $\sim$ 40 shots. These data show that for operation at one half of the single shot damage level, the mirror lifetime is essentially infinite. For increased values of the irradiating fluence, the brightness of the reflected beam degrades, indicating a trade-off between operating fluence and mirror lifetime. It should be noted that if the laser fluence is decreased to $\sim F_o/100$, the brightness returns to 100%, indicating that the brightness degradation is a dynamic effect at the mirror surface.

With this brightness data, lifetime curves can be constructed. Figure 5 shows such a lifetime curve for Cu mirrors in vacuum where the number of shots required to produce a 10% reduction in beam brightness is plotted as a function of the beam fluence for all of the Cu mirror samples tested. Input fluences have been normalized to the measured single-shot fluence, F_o. The data from all vendors scatter about an exponential trend line. The data can be fit by the function

$$N = 10^{7(1-F/F_o)} \qquad (12)$$

where N is the number of shots at fluence F required to reduce the beam brightness to 0.9 of its starting value, and F_o is the single-shot damage threshold. The prefactor 7 is determined by a least-squares fit to the data. The universality of the trends among polishers suggests that the failure mode is dominated by intrinsic properties of the Cu (e.g., melt levels or vaporization levels) rather than details of the mirror preparation technique. If one defines 10% brightness loss as the maximum acceptable beam degradation, then eq. (12) requires operation at 71% of single-point damage levels for 100 shot-lifetime and operation at 57% of single-point damage levels for 1000-shot lifetime. Note that all lifetime tests to date have been done with no more than 100 shots. The estimates beyond that level are strictly extrapolations.

The systematic change in the optical properties of the copper surface observed in the above tests was correlated to mechanical changes in the micro-detail of the surface by a series of scanning electron micrographs (SEM) taken of the copper surface after exposure to the laser radiation. Samples were placed in the laser test apparatus and then irradiated at 90% of the single-point damage threshold for the surface. The first position on the sample received three shots. The sample was moved to a new location and 10 shots were then taken. The sample was moved again and 20 shots were taken. This sequence was continued at 10-shot intervals up to 100 shots. The entire mirror was then removed and SEMs were taken for each of the tested areas. Figure 6 shows the results of these SEM measurements on a conventionally polished Cu mirror. Note that each picture refers to a different area on the sample. At the three-shot level isolated damage sites appear, caused by surface imperfections remaining from the polishing process. At the ten-shot level a dramatic change occurs in the entire surface structure and long-linear fine-scale structure begins

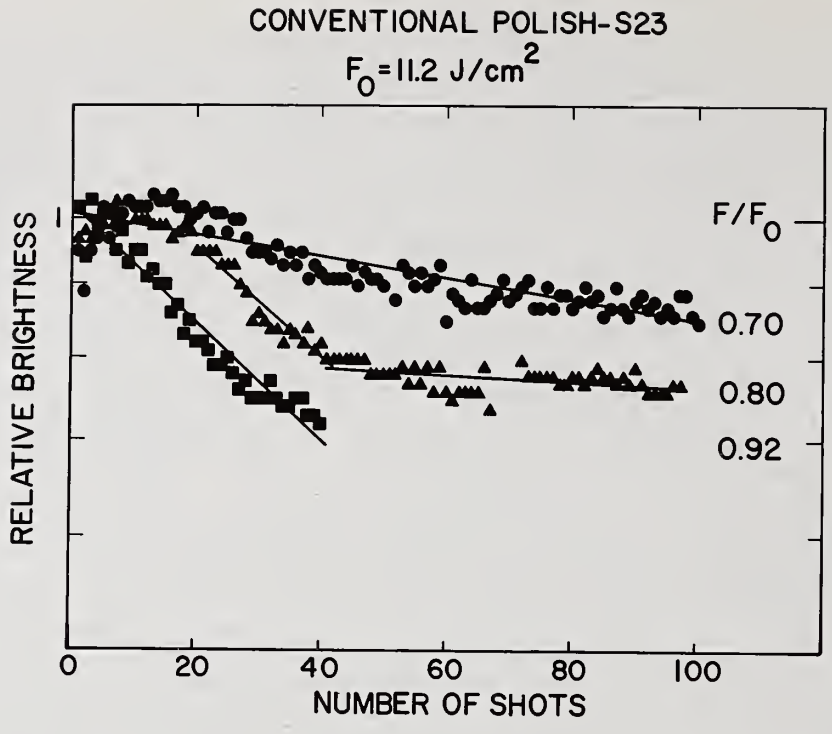

Figure 3. Brightness degradation of a conventionally polished Cu mirror in vacuum at a fixed peak fluence level. Pulse duration 1.7 ns, P(20), 10-μm radiation. Brightness range is from 50% to 100%.

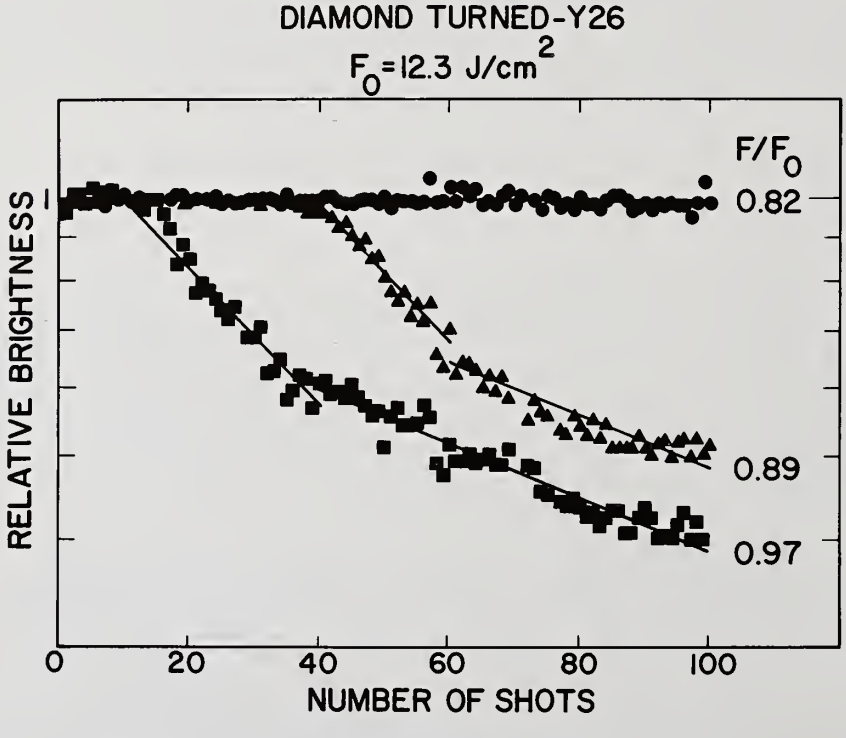

Figure 4. Brightness degradation of single-point diamond-turned Cu mirror in vacuum at a fixed peak fluence level. Pulse duration 1.7-ns, P(20), 10-μm radiation. Brightness range is from 30% to 100%

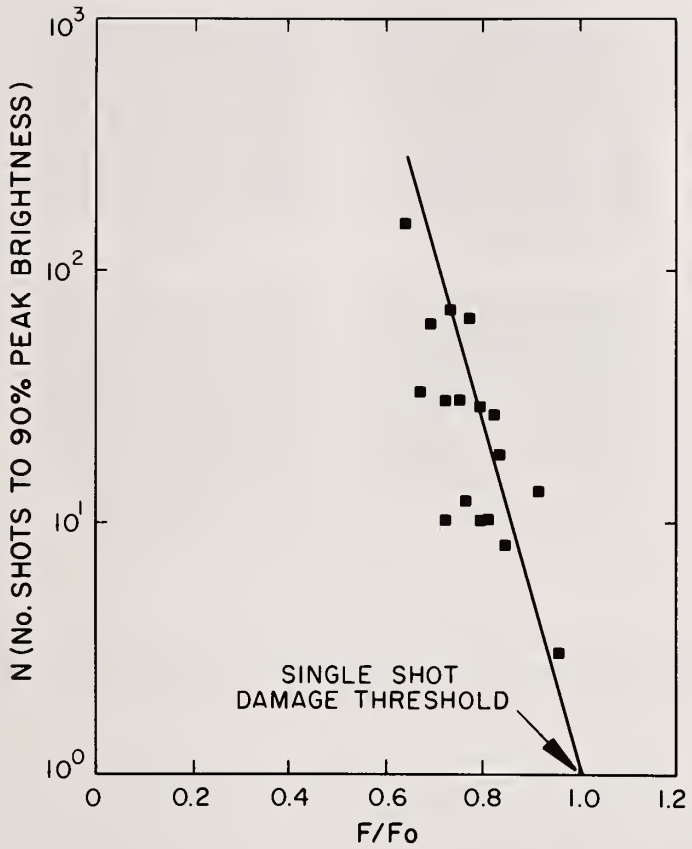

Figure 5. Mirror lifetime for Cu mirrors at various fixed values of the normalized irradiating fluence F/F_0. Lifetime is defined as the number of shots required to reduce the beam brightness to 90% of its initial value. Laser pulse is 1.7 ns at 10.6 μm.

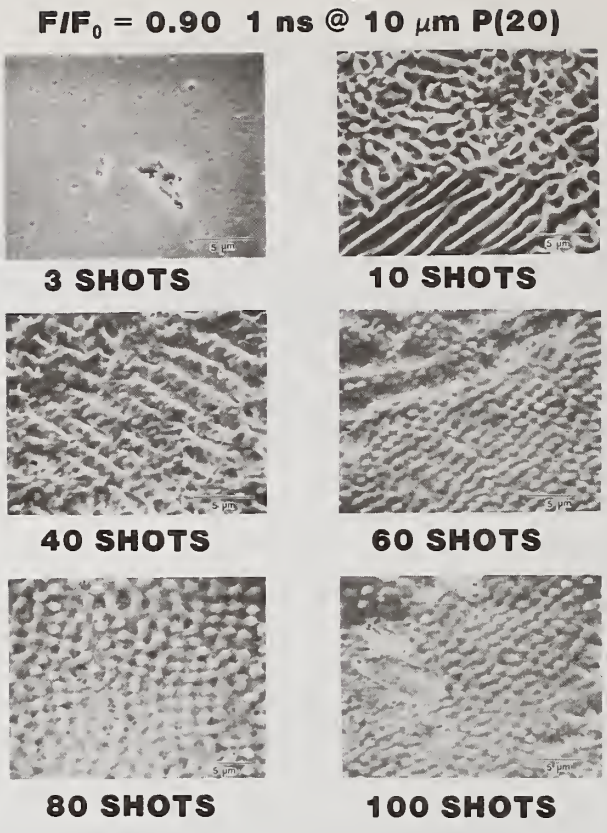

Figure 6. Scanning electron micrographs of polished copper mirrors after irradiation at a fluence level of 90% of the single-point damage level for the number of shots indicated.

to appear. The appearance of these features seems to coincide with the first downward fall in the mirror brightness of figure 3 and figure 4 (e.g., $F/F_0 = 0.8$). As the number of shots increases the linear surface structure begins to breakup into an array of spheres. At the 40 to 60-shot level the conversion to the spherical structure seems complete. This second feature change coincides with the second slope change in the brightness curve of figure 3 and figure 4.

Although the physical mechanism coupling the brightness degradation to the observed surface modifications have not been demonstrated by the present work, some speculations can be attempted. The initiation and growth of the surface structure is similar to processes observed in silicon [9]. Once the structure forms, it may cause a reduction in the threshold for surface plasma formation driven by the incident electric field. This plasma then either absorbs, scatters or refracts the laser radiation causing the observed reduction in the brightness of the reflected beam.

4. Conclusions

In this paper we have described the results of damage tests on metal mirrors with short-pulse CO_2 laser radiation. Single-point damage thresholds were determined for copper, stainless steel, and molybdenum mirrors and dramatic improvements were obtained at grazing incidence for the first time in the ir. The experimental results were compared to model calculations and were found to be in general agreement for radiation polarized parallel to the metal surface.

Lifetime tests of Cu mirrors in vacuum at the 100-shot level have shown consistent results among a variety of manufacturers and manufacturing techniques. Lifetime depends exponentially on the normalized fluence levels at the mirror surface. For 1000-shot lifetimes, operation at $\sim$ 50% of the single-point damage level is required to prevent degradation of the optical quality of the reflected beam.

We have shown that intrinsic alterations of the surface structure of polished copper mirrors take place when the mirrors are exposed to repeated pulses of 10.6 μm radiation at a fluence level below that required for single-shot surface damage. The appearance of this surface structure has been unambiguously correlated to the observed brightness degradation of the surface when used as an optical reflector for ir radiation. The exact mechanism of the induced brightness degradation has not been determined but absorption and/or refraction by a surface plasma appear to be a plausible explanation.

The authors would like to thank Claude R. Phipps, Brian E. Newnam, Peter J. Mumola of Perkin Elmer Corp. and Robert V. Kung of W. J. Schafer Associates for many helpful discussions. The technical assistance of Roberta Shaw is also gratefully acknowledged. This work was performed under the auspices of the U. S. Department of Energy.

References

[1] H. S. Carslaw and J. C. Jaeger. Conduction of Heat in Solids. Clarendon: Oxford Press 1959, 2nd Edition. p. 75.

[2] M. Sparks. Theory of laser heating of solids. JAP 47, 837 (1976).

[3] M. Sparks and E. Loh, Jr. Temperature dependence of absorption in laser damage of metallic mirrors: I. melting. J. Opt. Soc. Am. 69, 847 (1979).

[4] M. Sparks and E. Loh, Jr. Temperature dependence of absorption in laser damage of metallic mirrors: II. vaporization and heating the vapor. J. Opt. Soc. Am. 69, 859 (1979).

[5] P. B. Mumola, J. J. Ewing, W. T. Leland and C. A. Fenstermacher. Advanced CO_2 laser fusion driver concepts. (V. Corkrun, Ed.) Proceedings of the International Conference on Lasers '80, New Orleans, Dec. 1980, in press.

[6] I. Goldstein, D. Bua and F. A. Horrigan. Pulsed laser damage to uncoated metallic reflectors. in Laser Induced Damage in Optical Materials: 1975, NBS Special Publication 435 (1976).

[7] M. Born and E. Wolf. Principles of Optics. New York: Pergamon Press: (5th Edition). p 615-624

[8] The peak brightness of a light beam is a measure of its focusable intensity. Any reduction in beam brightness by an optical element indicates that the beam has been absorbed, scattered, refracted or defracted by the element.

[9] P. A. Temple and M. J. Soileau. Polarization charge model for laser-induced ripple patterns in dielectric materials. IEEE Journal of Quantum Electronics QE-17, 2067 (1981).

In response to a question, the author said that they had not yet done any calculations of why the diameters should be a certain size. The motivation for these experiments was to see if it changed for different materials and it seems to, although there is a change in the fabrication technique also for copper mirrors. There is a slight increase going from polished to diamond-turned copper mirrors. Presumably, the size is related to the recondensation of a surface plasmon. In response to another question, the author said that it was not possible to get unique values of the optical constants n and k from this experiment. It was pointed out that Walser and Becker at the University of Texas have taken similar data on crystalline silicon but in transmission. They found that they could fit the isointensity transformation kinetics of the damage phase to the classical equations for nucleation and growth, which suggests that a first-order phase transition has occurred. The growth phase in such experiments may thus be a result of the vaporization of the material. The damage morphology may then be resonant with the optical electric fields, which take the liquid into vapor phase. The data suggest that first-order transformation growth kinetics apply and even an equilibrium phase transition model gives good results.

Laser Damage to Metal Mirrors at Nonnormal Incidence*

D. L. Decker and J. O. Porteus

Michelson Laboratory, Physics Division
Naval Weapons Center, China Lake, California 93555

Virtually all laser damage experiments have been performed at normal incidence. However, many applications are for nonnormal incidence, and, obviously, it would be appropriate to characterize the surfaces with the intended geometry and polarization.

This paper presents damage threshold data on bare diamond-machined copper at 45-degree angle of incidence at 3.8 μm wavelength. Within experimental uncertainty, the melt threshold for p-polarization is identical to that obtained at normal incidence on the same surface. The threshold for s-polarization is a factor of two larger. The experimental values are compared with theoretical melt threshold calculations and are found to be in reasonable agreement. The polarization dependence is seen to arise from the fundamental infrared optical properties of metals. The relationship between normal incidence and 45-degree incidence thresholds provides a valuable cross-check on the systematic errors in laser damage measurements.

Key words: laser-induced damage; melt threshold; metal mirrors; nonnormal incidence; optical absorptance.

Introduction

Pulsed laser-induced damage to metal mirrors is rather well understood theoretically [1,2].[1] There also exists reasonable agreement between theory and experimental data at normal incidence [2]. Very little has been done at nonnormal incidence, even though many nonnormal applications exist [3]. This paper presents data at 45-degree angle of incidence for p- and s-polarization, together with a theoretical interpretation which can be applied to arbitrary angles of incidence. It is shown that for s-polarization, large increases in damage threshold with increasing angles of incidence occur.

Theory

Pulsed laser damage in pure metals is thermal in origin, provided the pulse length is long compared to the electron relaxation time ($\sim 10^{-14}$ sec). On well-prepared metal surfaces, damage is ordinarily initiated by thermally induced stress, followed by melting as the pulse energy is increased [4]. At slightly higher pulse energies or in the presence of defects or inclusions, vaporization and plasma formation typically occur, resulting in more complicated effects [4]. If the irradiated area is sufficiently large and uniform, heat flow and momentum transfer directions are essentially normal to surface, independent of the incidence angle of laser irradiation.

In figure 1 incident radiation of intensity I_0 with either s- or p-polarization is incident upon a surface. The specularly reflected intensity is $I_0 R_{s(p)}$. R_s and R_p may be simply computed [5]:

$$R_s = \frac{a^2 + b^2 - 2a\cos\theta + \cos^2\theta}{a^2 + b^2 + 2a\cos\theta + \cos^2\theta} \tag{1}$$

$$R_p = R_s \frac{a^2 + b^2 - 2a\sin\theta\tan\theta + \sin^2\theta\tan^2\theta}{a^2 + b^2 + 2a\sin\theta\tan\theta + \sin^2\theta\tan^2\theta}\ , \tag{2}$$

*Work supported by Navy Independent Research funds and by the Air Force Weapons Laboratory.
[1]Numbers in brackets indicate the literature references at the end of the paper.

where

$$a = \frac{n'k'}{n^2}\frac{1}{b} \quad ; \quad b^2 = \frac{-y + (y^2 - 4z)^{\frac{1}{2}}}{2}$$

$$y = \left(\frac{n'}{n}\right)^2 - \left(\frac{k'}{n}\right)^2 - \sin^2\theta \quad ; \quad z = -\left(\frac{n'k'}{n^2}\right)^2$$

If all incident light is either specularly reflected or absorbed, then the absorptances A_s and A_p are just

$$A_s = 1 - R_s \tag{3}$$

and

$$A_p = 1 - R_p \tag{4}$$

For a metal at infrared wavelengths, $k' >> n' >> 1$ so that $A_s << 1$, $A_p << 1$. Figure 2 schematically illustrates the angle of incidence variation for this case. Particularly simple approximations for A_s and A_p can be derived:

$$A_s(\theta) \cong \frac{4n}{k^2}\cos\theta = A(0)\cos\theta \tag{5}$$

$$A_p(\theta) \cong \frac{A(0)}{\cos\theta} \quad ; \quad \theta < 70 \text{ deg} \tag{6}$$

At 45 degrees, the following expression can be obtained either from the above relationships or from an expansion of the Abelès condition, $R_p = R_s^2$,

$$A_s(45) = A(0)/\sqrt{2} \tag{7}$$

$$A_p(45) = \sqrt{2}\,A(0) \tag{8}$$

Figure 3 illustrates the far-field focus of a Gaussian laser beam with an angle of incidence θ of the sample plane to the beam axis. If the ratio of the focal spot size in the oblique plane to the depth of focus is small, the on-axis intensity in the oblique plane is just $I_0\cos\theta$. Laser-induced damage is reached when the energy per unit area absorbed from the laser pulse equals a threshold value. This value will be independent of angle of incidence. Hence,

$$A(\theta)T(\theta)\cos\theta = A(0)T(0) \quad ,$$

where T is the threshold fluence for a damage mechanism, e.g., melting. Therefore, the damage threshold fluence variation with incidence angle is just

$$T(\theta) = \frac{A(0)}{A(\theta)}\frac{T(0)}{\cos\theta} \tag{9}$$

Substituting eqs (5) and (6) in eq (9):

$$T_s(\theta) = \frac{T(0)}{\cos^2\theta} \tag{10}$$

$$T_p(\theta) = T(0) \quad ; \quad \theta < 70 \text{ deg} \tag{11}$$

Beyond an angle of incidence of 70 degrees, $T_p(\theta)$ increases very slowly reaching a value of slightly over 2T(0) at θ = 88 degrees. Table 1 gives computed values of A_s, A_p, T_s, and T_p for selected angles of incidence for copper at 3.8 μm wavelength using eqs (1)-(4),(9).

Table 1. Computed values of A_s, A_p, $T_s(\theta)/T(0)$, and $T_p(\theta)/T(0)$ for copper at 3.8 μm wavelength: n = 1.20, k = 25.0

θ	A_s	A_p	$T_s(\theta)/T(0)$	$T_p(\theta)/T(0)$
0	.0076	.0076	1.00	1.00
30	.0066	.0088	1.33	1.00
45	.0054	.0108	2.00	1.00
60	.0038	.0151	4.00	1.00
70	.0026	.0219	8.55	0.99
80	.0013	.0411	33.7	1.06
88	.0003	.0908	726.0	2.40

At 45 degrees, the theoretical thresholds are

$$T_s(45) = 2T(0) \tag{12}$$

$$T_p(45) = T(0) \tag{13}$$

For pure copper at 3.8 μm and a 100 nsec pulse length, the computed melt threshold (peak on-axis fluence) is 245 J/cm^2 [2]. Hence, the predicted s- and p-thresholds at 45 degrees are

$$T_s(45) = 490 \text{ J/cm}^2$$

$$T_p(45) = 245 \text{ J/cm}^2$$

Experiment

The Naval Weapons Center experimental layout and procedures for laser-induced damage assessment have been previously described [2]. All damage measurements were performed in a vacuum of 0.3 torr (40 Pa). For nonnormal incidence, the sample is tilted appropriately. With the laser output polarized vertically, the sample configuration shown in figure 4 will then yield s-polarized irradiation. The sample is rotated 90 degrees about the axis of the incoming beam to achieve the other polarization. A Lumonics TE HF/DF laser producing 100 nsec pulses was employed. With a 5-in. focal length lens, the $1/e^2$ focal spot diameter was 56 μm. A 1.52-in.-diameter OFHC copper sample was precision diamond single-point machined and analyzed both at normal incidence and at 45 degrees. Figure 5 shows multi-threshold results for this sample at normal incidence. The measured melt threshold of 191 J/cm^2 is somewhat higher than previously reported, but the agreement is well within stated experimental absolute uncertainty of ±10%. In figure 6, very similar results were obtained for p-polarization with a measured melt threshold of 197 J/cm^2. Note that slip thresholds are virtually identical also. The thresholds for s-polarization are shown in figure 7. All thresholds are much larger, melt occurring at 358 J/cm^2, which is in the ratio of 1.9:1 to the normal incidence melt threshold. This ratio is not quite the 2:1 theoretically expected, but is well inside of the experimental uncertainty.

To compare the experimental data just given with the theoretical melt threshold values given in that section, the theoretical values must be corrected for finite spot size effects. The ratio of melt threshold at finite spot radius T_r to that at an infinite radius T_∞ is approximately [2]:

$$\frac{T_r}{T_\infty} \cong \frac{\chi}{\tan^{-1}\chi} \quad , \tag{14}$$

where $\chi = \sqrt{32/\pi}\ \ell/r$, ℓ being the thermal diffusion depth and r the spot radius.

The normal incidence values have been previously corrected by the ratio T_r/T_∞; however, the extended nature of the nonnormal incidence spot must now be taken into account. The focal spot shape for nonnormal incidence is an ellipse with minor axis r and major axis r/cosθ. Correction ratios for T_r/T_∞ and $T_{\sqrt{2}r}/T_\infty$ are given in table 2. The latter ratio of course is appropriate to a spot of diameter equal to the major diameter of the ellipse at 45-degree angle of incidence. An average correction for the ellipse can be obtained from the last column of table 1, the geometric mean.

Table 2. Spot size corrections to melt threshold for Naval Weapons Center TE DF laser damage data for 45-degree angle of incidence

2r(μm)	ℓ(μm)	T_r/T_∞	$T_{\sqrt{2}r}/T_\infty$	$T_{\sqrt{2}r}/T_r$	$\sqrt{T_{\sqrt{2}r}/T_r}$
55.9	9.6	1.32	1.17	0.89	0.94

Table 3 gives the corrected theoretical values as well as the experimental values just given.

Table 3. Theoretical and experimental values of melt thresholds for 100 nsec pulse length, 3.8 μm radiation at normal and 45-degree angles of incidence. Fluence values are given in J/cm^2

	T(0)	$T_s(45)$	$T_p(45)$
Experiment	191	358	197
Theory	245	461	230

Conclusion and Summary

The morphology of the melt damage observed at normal and 45-degree angles of incidence is very similar to that observed on other similar samples at normal incidence [2]. No peculiar morphology was present at nonnormal incidence, as can be seen from an inspection of figures 8-10. The 45-degree angle of incidence damage craters have an aspect ratio on average about 10% less than the expected $\sqrt{2}$:1, presumably as a consequence of asymmetrical heat flow. For the very small crater shown in figure 10, the aspect ratio is only about 3% smaller than expected. This small crater was formed just at threshold and shows no splatter. The most serious discrepancy exists between the measured and computed melt thresholds at normal incidence where the 22% difference lies considerably outside of experimental uncertainty. This has been previously reported and discussed [2]. However, the interrelationships between the measured normal and nonnormal incidence thresholds are excellent. The measured thresholds for s- and p-polarization have a ratio of 1.8:1, about 10% less than expected. The measured melt thresholds for normal incidence and for p-polarization at 45-degree angle of incidence agree within 3%.

Laser damage effects on metals at nonnormal incidence for pulse lengths long enough so that thermal effects dominate are controlled by the variation of optical properties with angle of incidence. In the infrared, where the optical absorptance of metals such as copper, silver, gold, or aluminum is small, the simple relationships between normal and nonnormal incidence absorptance given in this paper permit accurate prediction of nonnormal incidence thresholds which is independent of optical constants. These relationships are particularly useful in providing a check for internal consistency in analyzing laser damage data. The strong increase in the thresholds for s-polarization has laser system design implications and may be a key effect in the design of very high fluence devices.

References

[1] Sparks, M.; Loh, E., Jr. Temperature dependence of absorptance in laser damage of metallic mirrors: one point melting. J. Opt. Soc. Am. 69; 847; 1979.

[2] Porteus, J. O.; Decker, D. L.; Faith, W. N.; Grandjean, D. J.; Seitel, S. C.; Soileau, M. J. Pulsed laser-induced melting of precision diamond-machined Cu, Ag, and Au at infrared wavelengths. IEEE J. Quantum Electron. QE-17; 2078; 1981.

[3] Hayden, J. J.; Liberman, I. Measurements at 10.6 μm of damage threshold in germanium, copper, sodium chloride, and other materials at levels up to 10^{10} W/cm^2. Glass, A. J.; Guenther, A. H., ed. Proceedings of the 8th annual symposium on optical materials for high power lasers; 1976 July 13-15; Boulder, CO. Nat. Bur. Stand. (U.S.) Spec. Publ. 462; 1976 December. 173-180.

[4] Porteus, J. O.; Fountain, C. W.; Jernigan, J. L.; Faith, W. N.; Bennett, H. E. Pulsed-laser stress phenomena on highly reflecting metal and alloy surfaces. Glass, A. J.; Guenther, A. H., ed. Proceedings of the 9th annual symposium on optical materials for high power lasers; 1977 October 4-6; Boulder, CO. Nat. Bur. Stand. (U.S.) Spec. Publ. 509; 1977 December. 204-214.

[5] Tousey, R. On calculating optical constants from reflection coefficients. J. Opt. Soc. Am. 29; 235; 1939.

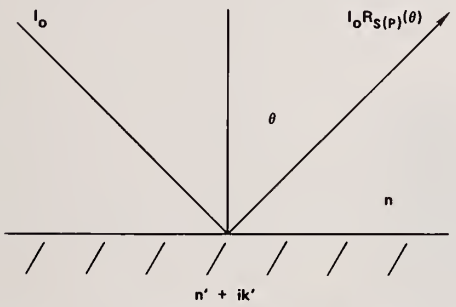

Figure 1. Schematic diagram of radiation of intensity I_0 incident upon a surface. The specularly reflected beam has intensity $I_0 R_{s(p)}$. The reflectance is a function of the angle of incidence, θ, polarization direction, and optical constants of the substrate n' and k', and external media, n.

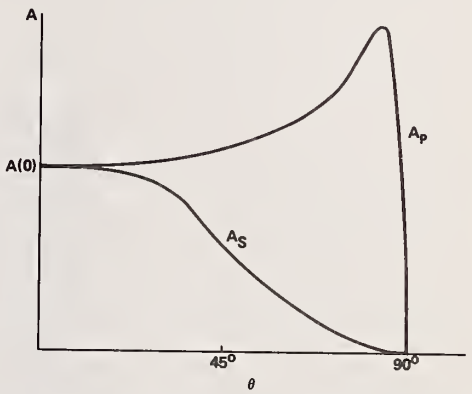

Figure 2. Plot of the angular dependence of the s- and p-absorptance of a metal in the infrared.

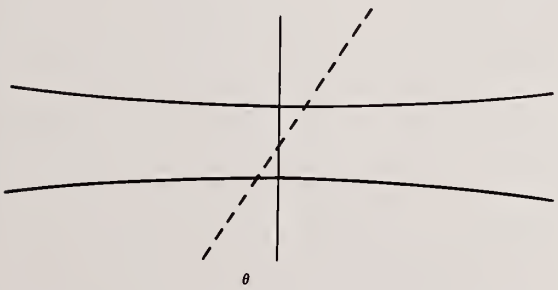

Figure 3. Illustration of the far-field focus of a Gaussian laser beam with a sample surface oriented at angle θ to a plane perpendicular to the beam axis.

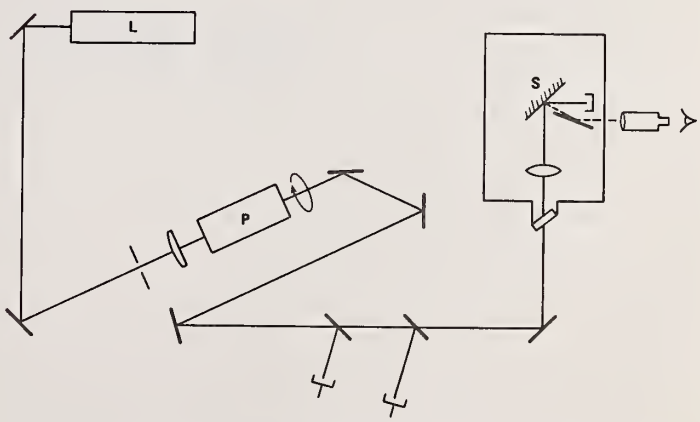

Figure 4. Experimental layout for nonnormal incidence laser-induced damage. With a laser polarization perpendicular to the plane of the drawing, the sample orientation shown will yield s-polarization. To obtain p-polarization, the sample is rotated about the beam axis by 90 degrees.

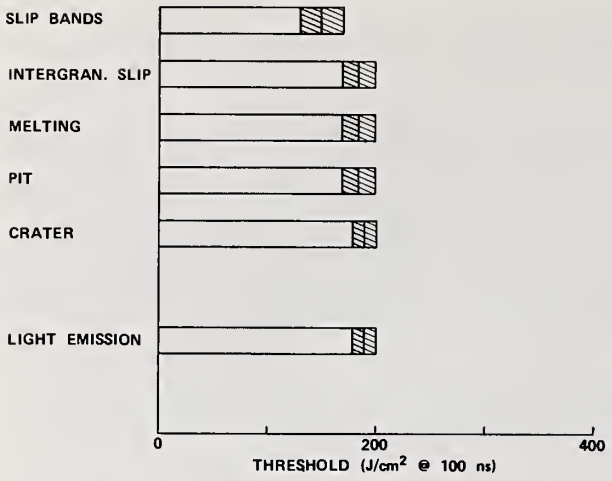

Figure 5. Multithreshold laser damage data for a diamond-machined OFHC copper surface using 100 nsec DF laser pulses. The threshold values plotted are peak on-axis fluences in J/cm^2.

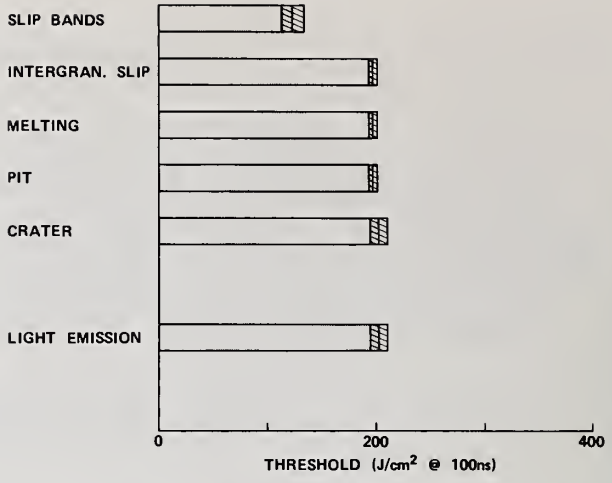

Figure 6. Multithreshold laser damage data for the copper sample shown in Fig. 5, but with an angle of incidence of 45 degrees and for p-polarization.

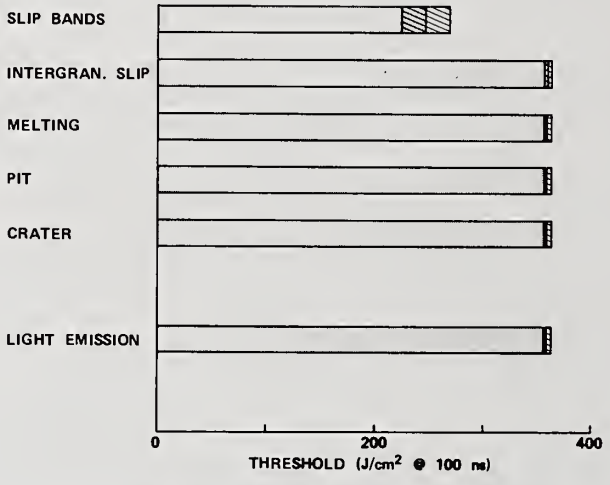

Figure 7. Multithreshold laser damage data for the same copper sample shown in Fig. 6, but with s-polarization.

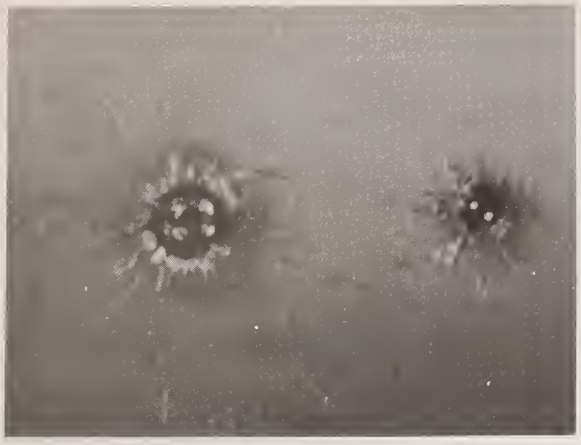

Figure 8. Nomarski micrograph of two damage sites on the diamond-machined OFHC copper sample from which the multithreshold data in Figs. 5-7 were taken. These two sites were damaged at normal incidence. The larger crater is 120 μm in diameter.

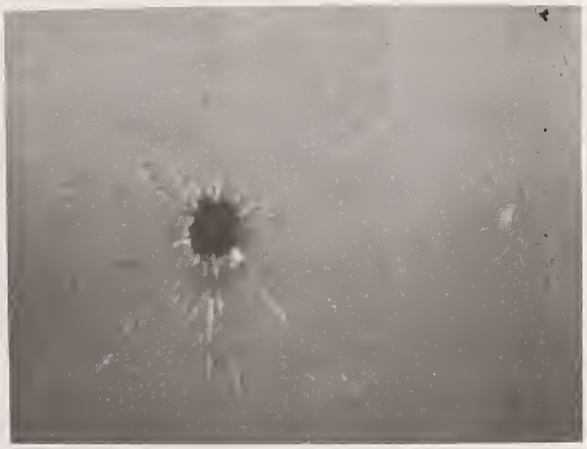

Figure 9. Nomarski micrograph of two damage sites on the same copper sample discussed in Fig. 8, irradiated at 45-degree angle of incidence and with p-polarization. The major axis of the larger crater is about 100 μm.

Figure 10. Higher magnification Nomarski micrograph of the small damage site shown in Fig. 9. This melt crater has a major axis of about 30 μm and was formed just at threshold.

Directed Energy Production of Novel Metallic Surfaces

Clifton W. Draper

Western Electric
Princeton, NJ 08540

and

Steven L. Bernasek

Princeton University, Dept. of Chemistry
Princeton, NJ 08544

Key words: surface alloying; laser beams; metals; surface properties

1. Introduction

Directed energy methods of material modification encompass the use of laser, electron and ion beams. In the case of laser and electron beams compositional changes are introduced by surface alloying, for ion beams both implantation and mixing are used. The laser, electron and pulsed ion beams are also utilized to locally heat near surface regions with the bulk material providing very rapid self-quenching. Metastable microstructures, including metallic glasses, can be routinely produced in this manner. The fact that the chemical or structural transformation is introduced at the material surface, and in many cases constrained to <10,000 Å, has two important consequences for this new field of surface metallurgy. First, the tailoring of surfaces will have to be directed at those material properties which are surface rather than bulk sensitive. Secondly, characterization of these beam introduced chemical and structural changes will require analytical techniques from surface physics.

Those surface modification areas of past and current interest are enumerated in table 1. The literature is rich with examples of the use of directed energy methods to improve material performance. In some instances commercial applications have proved highly successful. For example, in less than a decade ion implantation has all but totally replaced conventional wet chemistry for doping (modifying the electrical properties) in the silicon device industry. Another highly successful application finds lasers and electron beams surface hardening Fe based alloys for a wide range of products including General Motor's power steering gear boxes.

Table 1. Surface sensitive properties that have been modififed in directed energy processing studies

Mechanical -	wear	cavitation
	erosion	fatique life
		microhardness
Chemical -	corrosion (wet & dry)	
	catalysis	
Others -	electrical (semiconductor and superconductor processing)	
	magnetic (glassy Fe-based)	
	optical (decorative)	

At the 1979 Boulder Damage symposium Oron, Svendsen and Sorensen (1) presented results on the improvement in reflectance and damage resistance of Cu following Al implantation and oxidation. Utilizing Rutherford backscattering, they characterized the surface as copper-deficient and Al_2O_3 rich (1, 2). The effects of implantation (3-6) and laser quenching (7) upon atmospheric tarnishing have been investigated. However, with the exception of ref. 1 above and a passing reference to decorative applications in ref. 6, there appears to be little effort toward tailoring metal mirror properties (spectral reflectance, shelf life, shot life) with these directed energy methods.

The point we wish to make here is that, although affecting the optical properties of a metal should be an area rich in applications, there appears to be little, if any, research in this area.

2. Overview

We will very briefly review the concepts of laser, electron and ion beam processing of metals. We will not attempt to enumerate advantages or limitations of one beam technique over the other. In the next section we will examine in detail one specific area - that of surface alloying with laser beams. We will then discuss, with examples, some of the surface physics analytical techniques available for characterizing surface alloys. Finally, we will point out some novel metallic surface alloys which have been produced and briefly summarize and speculate about how these directed energy methods might be used to address metal mirror damage problems.

Figure 1 depicts schematically the various surface alloying beam methods. Laser and electron beam surface alloying are generally accomplished on substrates with predeposited films. The scanning or pulsed beam melts the film and some portion of the underlying substrate. Liquid state diffusion, and in the case of continuous beams diffusion plus convection, promote A-B mixing. The bulk substrate provides an intimate heat sink and recrystallization interface velocities of up to 20 $msec^{-1}$ may occur. In ion implantation solute ions are accelerated to energies between 100-200 KeV and bombarded into the substrate metal. In metals, sputtering limits concentrations to about 20 at. %. Ion beam mixing circumvents the sputtering problem associated with direct solute implantation by predeposition of a thin film structure which is mixed together by ion projectiles. The mixing beam is most often Xe (good ion source and large collision cascade) but A or B ions can be used.

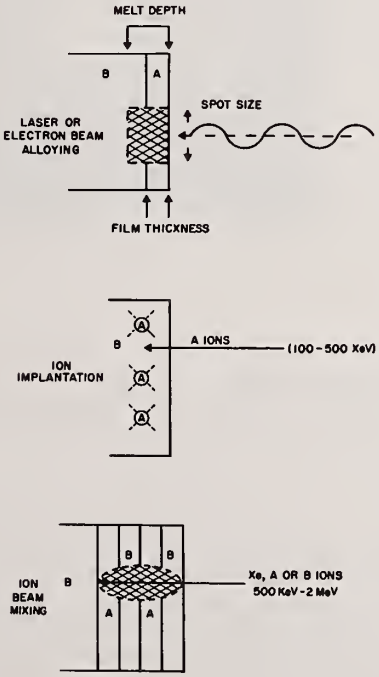

Figure 1. Surface alloying beam methods. Top view - laser or electron beam mixing of film and substrate; middle view - ion implantation of foreign atom into substrate; bottom view - ion beam mixing of predeposited thin films and substrate.

Laser, electron and ion beams can all be operated in either a continuous or pulsed mode. They also have in common the fact that they are point tools requiring a step and repeat motion in order to affect large area coverage. In the application area of surface alloying the laser and electron beam methods are thermodynamically constrained by equilibrium requirements as they apply to the liquid state and phase separation upon resolidifcation. The ion beam methods are solid state processes and in a purely collisional (non diffusion enhanced) regime should be free from any phase diagram limitations. These differences are clearly seen in the RBS, channeling and TEM results (8) on ion implantation and laser pulse melting of Ag in Ni presented in figure 2. Implantation of Ag at 150 KeV at a dose of 10^{17} ions cm^{-2} results in a metastable single phase Ag-Ni surface alloy with a peak concentration of 12 at. %. Q-switched Nd-YAG surface melting of the implanted Ni surface results in Ag precipitation in the liquid state ahead of the resolidification interface. Thus, some of the supersaturation accessible by solid state implantation was lost when the homogeneous solid → liquid transformation allowed the liquid to briefly (<500 nsec) transgress the extensive liquid state miscibility gap (9) for this binary system. At these Ag concentration levels diffusion and nucleation kinetics were competitive with melt time and regrowth transients.

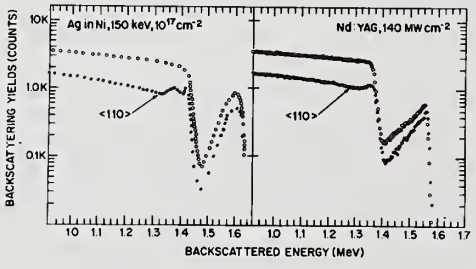

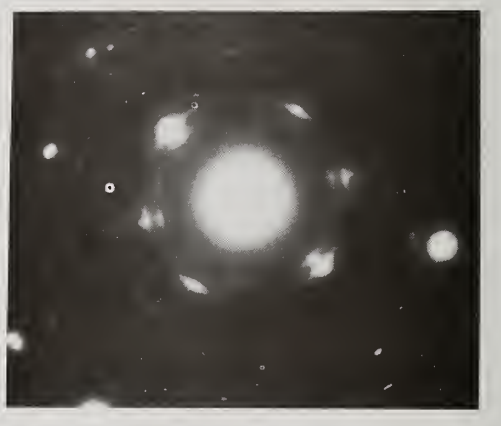

Figure 2. Random (open circles) and channeling (solid circles) Rutherford backscattering spectra for 10^{17} Ag implanted into single crystal Ni before (left view) and after (right view) Q-switched Nd-YAG laser melting. Surface segregation ahead of the resolidification interface is suggested by the Ag backscattering spectra between 1.4 and 1.6 MeV in the right view. Ag precipitate formation is confirmed by the TEM results. The top view is a bright field micrograph with some of the Ag precipitates marked with arrows. The selected area a diffraction pattern shows both single crystal Ni spots and polycrystalline Ag rings.

Those wishing a more detailed treatment of the directed energy methods as applied to materials processing should consult the proceedings of the Materials Research Society (10) or the proceedings of the second international conference on ion beam modification of materials (11).

3. Surface alloying with laser beams

Figure 3 is a schematic representation of a film and substrate combination and an isolated laser event. The many symbols denote the various thermophysical and laser parameters which influence the surface alloying. They will be discussed below. In this schematic the film A has been predeposited (evaporated, sputtered, plated, or painted) which is the most common practice, although codeposition-irradiation (particle or wire injection) is also used. The goal of surface alloying is to controllably incorporate the film element(s) into the substrat B by melting A and some portion of B. Mixing in the liquid state will be followed by a rapid recrystallization. The alloying element(s) will thus be incorporated in the near surface region of the substrate.

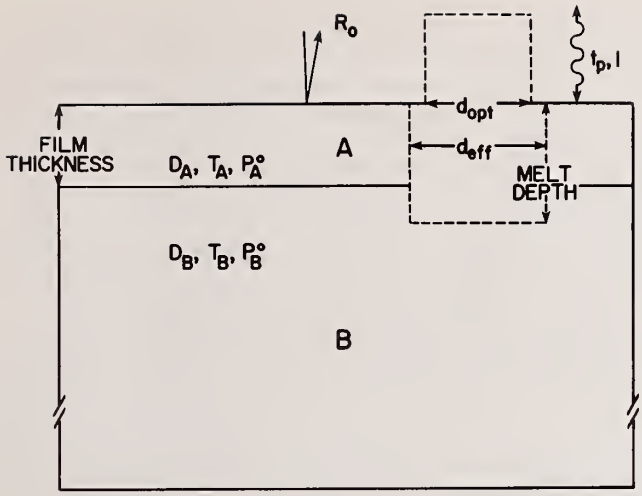

Figure 3. Schematic representation of predeposited thin film and substrate with important thermophysical and processing parameters annotated. D, T and P are respectively the thermal diffusivity, melting point and vapor pressure of the film (A) or substrate (B). R_o is the normal spectral reflectance of the film at the laser wavelength utilized. I, t_p, d_{opt} and d_{eff} are respectively the laser intensity, pulse length, optical spot size and effective spot size.

At this point we want to examine qualitatively the thermodynamic and thermophysical constraints which control the surface alloying. For this purpose it is useful to group the binary A-B systems, which have been experimentally studied, into three categories: i. mutual solid state solubility, ii. limited solid state solubility and iii. liquid state immiscibility. Selected binary phase diagrams are presented in figure 4. Pd-Ni is representative of those systems which exhibit complete mutual solubility across the phase diagram. Single phase solid solutions are of course expected, and have been observed to result following surface alloying. Epitaxial regrowth however is not guaranteed. As has been demonstrated (12) for virgin single crystal Ti and Be, and for surface alloyed Zr-Ti (13), substrates with high temperature allotropes do not necessarily recrystallize epitaxially. In the case of Zr-Ti, X-ray diffraction shows that the alloyed region is polycrystalline hcp single phase with an appropriately expanded lattice to accommodate the substitutional Zr.

Those film-substrate combinations which offer the worst situation thermodynamically are those systems like Ag-Ni, demonstrating liquid state immiscibility. If the film and substrate will not homogenize in the liquid state there is little chance for producing a single phase alloyed region let alone observing epitaxial growth. If i. the film is thin enough ii. the melt temperature high enough, and iii. the time in the melt (at high temperatures) long enough a single phase liquid may result. The extent and shape of the liquid-miscibility gap will dictate whether or not a single phase liquid region is transgressed during the temperature excursion. Even if a homogeneous liquid is produced solute precipitation in the liquid ahead of the resolidification interface may occur. Both the melt time and solute concentration in the liquid are important factors in determining whether second phase nucleation or solute transport will interfere with the solute trapping required to make a metastable solid solution. This has been detailed in reference 14 for the case of Sb implanted Al and then irradiated on various time scales, and for various thin film thicknesses and implantation levels of Ag in Ni surface melted (8) on the same time scale. For a given concentration of Sb implanted into Al only the shorter melt times (50 - 200 nsec) resulted in solid solutions. For a given melt time of ∿500 nsec in Ni only the thin layers/low dose Ag samples form/retain solid solution surface alloys.

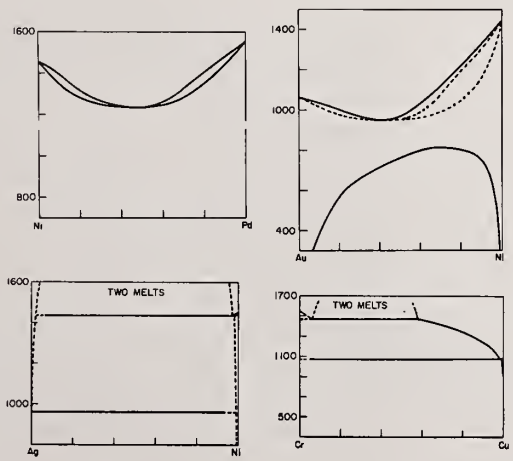

Figure 4. Selected binary phase diagrams.

Referring again to figure 3 it should be obvious that the relative relation between the film thickness and melt depth will most strongly influence the final alloy concentration and profile. Thus, the pulse duration or dwell time and the incident power density of the laser source will be important processing variables. The thermophysical properties included in the schematic may also constrain the surface alloying. Some care needs to be taken to make a judicious choice of A-B combinations in order to avoid large differences in melting points and vapor pressures. It would be futile, for example, to attempt to surface alloy a thin film of low melting point-high vapor pressure Zn onto high melting point Ta or W. The thermal diffusivity can also play a role influencing the thermal diffusion length. This can be particularly important if the film thickness approaches the dimensions of the heat flow. For example in a series of laser alloying experiments (15) on Ni (110) + Au(x) + 200 Å Ni, where X = 500, 1000, 2000 and 5000 Å, it has been found that for a constant laser fluence the melt depth increases significantly with increasing Au thickness. This behavior can be rationalized on the basis of an effective thermal diffusivity which for thin Au is approximately that of Ni, while for thick Au is more closely that of Au, and 5-10 times the value for Ni.

The normal spectral reflectance of the film at the laser wavelength of interest will determine the size of the processing window - that range of incident power densities over which melting without evaporation can be reproducibly achieved. Severely limited and in some instances nonexistent windows occur when very high spectral reflectances lead to orders of magnitude differences between incident and absorbed laser fluences. When operating with incident fluences that high above melting threshold requirements, very small pertubations in local reflectance values can have catastrophic results (16).

4. Surface analysis

In order to appropriately characterize the results of directed energy surface modifications, information must be obtained concerning the overall topography of the surface as well as its microscopic structure and chemical composition. A wide variety of techniques are presently available which can be used to obtain this information. Figure 5 schematically lists a number of these techniques.

Metallographic optical microscopy provides important first order topographical information. When combined with scanning electron microscopy, information about microscopic topographical changes (scratch removal, etch pit annealing, melt zone structure) can be readily obtained. Standard metallographic methods for analyzing grain size and other microstructural aspects of the modified surface are also of use.

Atomic scale surface structure is more appropriately investigated using a number of electron, photon and ion probe techniques. This information is particularly useful in developing an understanding of the mechanisms of surface structrual modification by directed energy methods. For example, low energy electron diffraction (LEED) (17), has been used to monitor the production of laser produced metastable structures on semiconductor surfaces (18). Reflection high energy electron diffraction (RHEED) can be used to obtain information about deeper surface region structure, epitaxial growth conditions, and compound formation in the melt zone (19). Ion channeling studies, low angle x-ray diffraction, and high resolution transmission electron microscopy can also be used to characterize near surface region structural changes TEM is especially useful in investigations of defect production and propagation in laser modified materials (20).

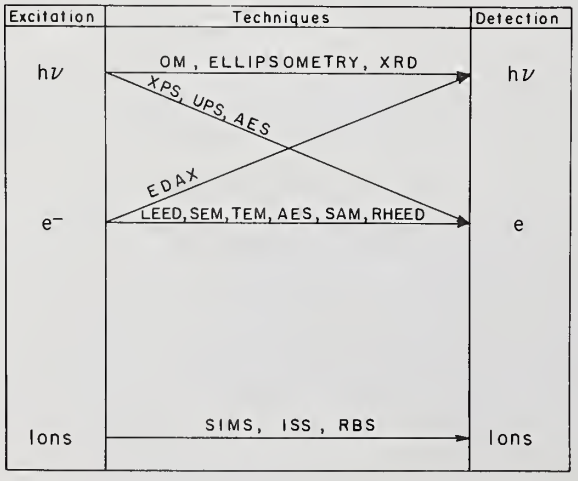

Figure 5. Surface characterization techniques classified by excitation source and detected quantity. OM - optical microscopy, XRD - x-ray diffraction, EDAX - energy dispersive x-ray analysis, LEED - low energy electron diffraction, SEM - scanning electron microscopy, TEM - transmission electron microscopy, AES - Auger electron spectroscopy, SAM - scanning Auger microscopy, RHEED - reflection high energy electron diffraction, SIMS - secondary ion mass spectroscopy, ISS - ion scattering spectroscopy, RBS - Rutherford backscattering. (After ref. [33].)

In addition to laser induced structural changes, it is essential to monitor surface and near surface compositional changes resulting from laser melting and rapid resolidification. Again, the particle probes of surface chemical physics offer a wealth of useful information. Compositional information as a function of depth into the material, which is essential to questions of melt homogeneity and melt-substrate interfacial properties, can be obtained by a number of techniques. Rutherford back-scattering (RBS) (21) gives composition vs. depth information as well as information about the crystallinity of the sampled region. Examples of the use of RBS in laser surface modification studies are included in section 5. So far less extensively used are techniques such as ion profiling using Auger electron spectroscopy (AES) or secondary ion mass spectrometry (SIMS) to determine surface composition (22).

Compositional information parallel to the surface is also very important in understanding the details of laser induced surface modifications. The primary tools here are x-ray dispersive elemental analysis (EDAX), and scanning Auger microscopy (SAM) (23). EDAX has somewhat better lateral resolution but compositional information comes from the first several hundreds of layers of the solid due to the x-ray escape depth. SAM, on the other hand, provides poorer lateral resolution (1-5 μm), but the information is restricted to the first several layers of the solid by the escape depth of the Auger electron. An example of the use of SAM to examine the compositional uniformity of a laser modified ternary (Cu, Al, Fe) alloy is illustrated in Figure 6 (24). The conventionally prepared alloy contains both the BCC Fe-rich precipitates and the FCC Cu-Al matrix. The laser surface melting has caused the near surface region to retain in solution the Fe. The SAM micrographs of figure 6 clearly illustrate this difference.

Figure 6. Scanning Auger, Cu 914 eV elemental maps, before (left view) and after (right view) laser quenching. The dark spots in the unirradiated elemental map correspond to the Fe-rich precipitates, which following resolidification from the melt are retained in solution with the Cu-Al FCC matrix.

5. Novel metallic surface alloys

In this section representative examples have been chosen to demonstrate both the diversity of interest and the potential for new metallurgy offered by laser surface alloying.

5.1 Au-Ni

As the phase diagram in figure 4 shows the Au-Ni system is characterized by a large solid state miscibility gap. Since homogeneous liquids and solids at elevated temperatures are easily produced it is not surprising that even bulk single phase solutions of any concentration are easily produced by the use of conventional quenching methods. Au-Ni surface alloys have been prepared using a number of different laser sources. Figure 7 summarizes Au concentration profiles in Ni resulting from various laser treatments of vapor deposited Au thin films on Ni (25). Due to the longer times in the liquid state associated with the use of relative motion between sample surfaces and continuous laser sources, we have found that surface alloys of low concentration and flat deep profiles result. See the open circles in figure 7. The very high peak power densities associated with the short Q-switched Nd-YAG laser pulses, and the need to operate well above the required absorbed energy densities (because of the high reflectance of Au at 1.06 μm) lead to significant Au loss. Low surface concentrations and sharply sloping concentration gradients that drop to zero in less than 5000 Å result (open circles). Efficient coupling to the surface can be achieved with either the frequency doubled Nd-YAG laser or with the addition of a thin reflectance cap of Ni on the Au for the fundamental laser wavelength. See open squares and solid circles in figure 7. Higher total precious metal concentrations can be achieved by the use of Pd caps instead of Ni (solid squares). The problem of a film thickness dependent thermal diffusivity and therefore melt depth has already been addressed above. In summarizing the Au-Ni work, the point to be made is that a wide range of concentrations and profiles have been shown to be accessible.

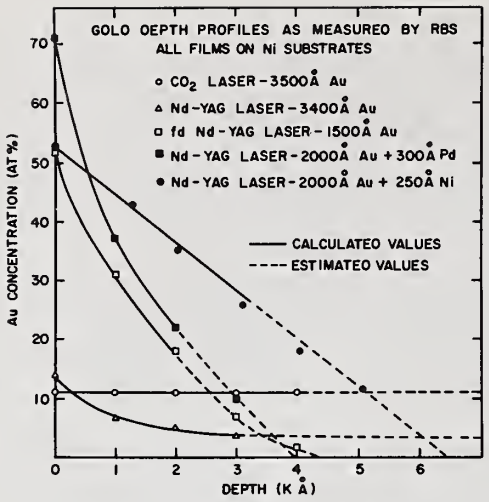

Figure 7. Au depth profiles as determined by RBS for laser mixed Au films on polycrystalline Ni substrates.

5.2 Cu-Zr

Cu is a well known glass former with Zr. Within concentration ranges near eutectic points glass formation is often observed. The backscattering yield data in figure 8 again emphasizes that surface alloy concentrations can be tailored quite easily (13). The Cu surface concentrations as deduced by the Zr step heights at 1.7 MeV are 60, 46, and 32 at. % for 45, 67, and 70 MW cm^{-2} frequency doubled Nd-YAG laser fluences. TEM and selected area XRD on thinned samples confirm the presence of the Cu-Zr glass. The thermal stability of the surface glass was studied by AES in a high vacuum thermal annealing chamber. Figure 9 shows the evolution of the 147eV Auger transitions as a function of annealing temperature. The peak shape change and increase in intensity between 500°C and 600°C is evidence for the recrystallization transformation. Glancing angle XRD confirms the transformation to crystalline $CuZr_2$. This range of temperature is in good agreement with published values for the glass transition. Thus we conclude, that at least for the Cu-Zr system, the continuous transition from crystalline subsurface to glassy surface does not grossly alter the thermal stability of the glass.

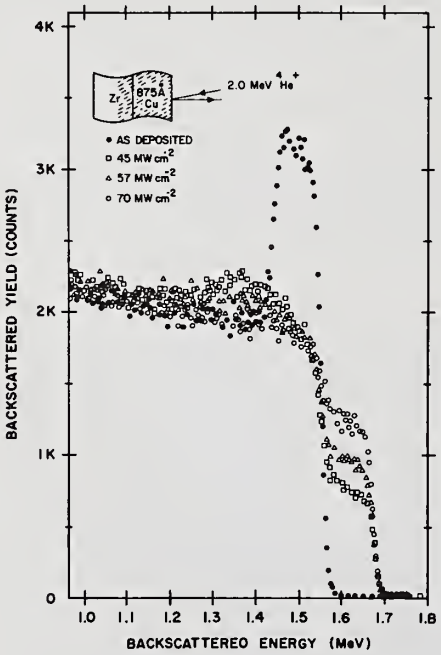

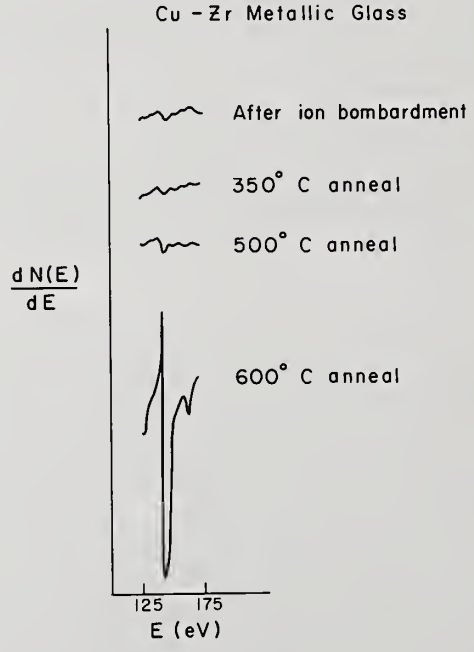

Figure 8. RBS spectra for laser mixed Cu on Zr as a function of laser fluence.

Figure 9. The 147 eV Auger Zr MVV valence state transition as a function of annealing condition for a laser mixed Cu-Zr surface alloy.

5.3 Cr-Cu

The Cr-Cu system is characterized by a phase diagram (see figure 4) with a two melt region at high Cr concentrations and a eutectic at the Cu-rich side with a sharply decreasing temperature. Even the highest quenching rates can produce supersaturation up to only 1.8 at. % in bulk samples. It is reasonable to expect that Cu and Cu alloys with high concentration additions of Cr might exhibit profoundly different surface properties than have been observed to date in conventionally prepared copper alloys.

Figure 10 contains "as deposited" and frequency doubled Q-switched Nd-YAG laser mixed, Rutherford backscattering spectra and Auger electron spectroscopy sputter depth profiles for polycrystalline Cu-2Sn + 700 Å Cr + 500 Å Ni-8V. In the solid circle RBS spectrum the appearance of Sn at the surface kinematic energy following laser mixing clearly shows that the liquid has reached the substrate-Cr interface. The mass and detector resolution for 2 MeV $^4He^+$ for this system are such that elemental depth profiles cannot be extracted. The two sputter depth profiles in figure 11 present results on the Ni, Cr and Cu, with the V and Sn being left out in order to reduce clutter. The sputtering rate was 50 Å min^{-1} calibrated on Ta_2O_5. There is excellent agreement between RBS and AES when comparing the "as deposited" thin film thickesses. Lateral uniformity was checked with both energy dispersive x-ray (EDX) and scanning Auger microscopy (SAM) elemental mapping. No resolvable, lateral gradients were found. Glancing angle XRD confirms that the BCC Cr structure disappears upon laser mixing. Further details on the Cr-Cu system can be found in reference 26.

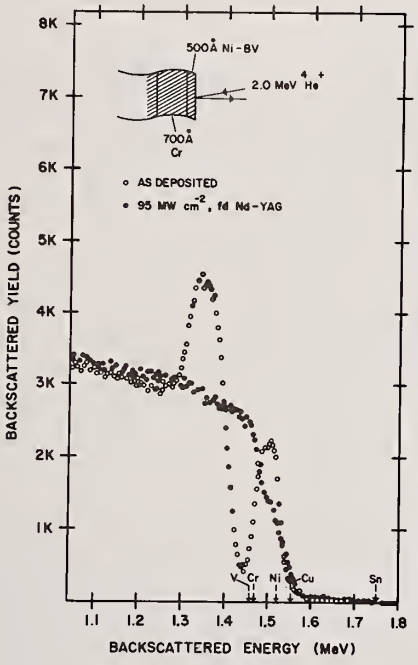

Figure 10. Above-RBS spectra before (open circles) and after (closed circles) laser mixing of Ni and Cr films into a Cu-2SN substrate.

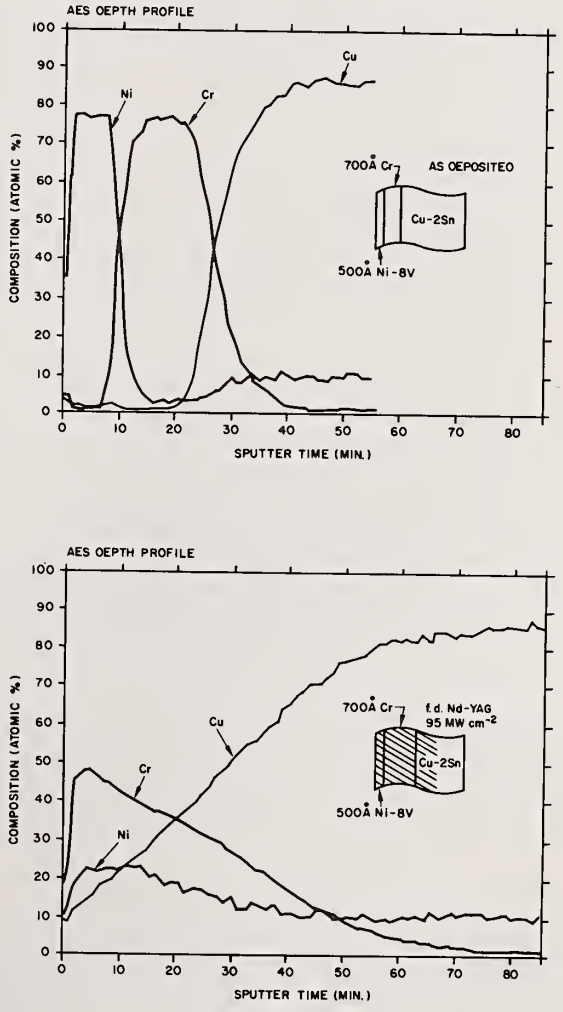

Figure 11. Above right-AES depth profile for as-deposited Ni and Cr films on a Cu-2SN substrate. Right-AES depth profile for laser mixed surface alloy.

5.4 Cu-Mo and Au-Ru

Both the Cu-Mo and Au-Ru systems are characterized by a phase diagram like the Ag-Ni system in figure 4. There is essentially no solid state solubility and very extensive liquid state immiscibility. In the case of Cu-Mo we have magnetron sputter deposited very thin ($\sim$100 Å) Cu films on Mo (100) substrates. Surface alloying with a Q-switched frequency doubled Nd-YAG laser results in epitaxial regrowth of the Mo and incorporation of the Cu on substitutional lattice sites. The formation of the metastable solid solution occurs because for very thin Cu layers the two melt liquid will transgress (at elevated temperatures) into a region where a homogeneous liquid may be formed. Nucleation of the second phase during the cooling cycle will be kinetically sluggish relative to the rapid quenching and the Cu will be trapped at the solid-liquid interface as recrystallization occurs.

The results on the Au-Ru system contrast the Cu-Mo case. Here relatively thick films (1-5000 Å) have been deposited on sputtered polycrystalline Ru substrates. Again the samples were surface melted with Q-switched frequency doubled Nd-YAG radiation. In this case a very small amount of intermixing at the film-substrate interface is observed by RBS. Optical microscopy confirms that the substrate has indeed melted as significant topographical restructuring takes place. Refer again to the Ag-Ni phase diagram in figure 4 and the laser alloying schematic in figure 3. There is no thermodynamic driving force for intermixing in Au-Ru due to the extensive two melt region. Furthermore, the melting point $T_m(Ru) > T_m(Au)$ and the heat of fusion of Ru is rather large. The Ru interface acts as a massive heat sink for the liquid Au above it. The result is that the Au becomes integrally bound to the Ru substrate (better adhesion) and the Au film has been quenched from the liquid (removal of deposition associated defects).

Table 2. Potential applications of directed energy methods in metal mirror damage problem areas

1. Alloying to directly change the optical properties of the base metal.
2. Alloying to change the mechanical properties of the base metal near surface region.
3. Alloying to change the oxidation or corrosion resistance of the base metal.
4. Melting-quenching from the liquid state to remove deposition defects such as porosity or to remove the interface itself.

6. Discussion

We have shown through the use of selected examples in the previous section that laser surface alloying has been used to make precious metal rich surfaces on base metals, Au-Ni; metallic glass surfaces on crystalline metal substrates, Cu-Zr; novel metastable crystalline surfaces on base metals, Cr-Cu and Cu-Mo; and to induce interface mixing without significant dilution, Au-Ru. It is reasonable to ask, "how might one apply this new technology to metal mirror damage threshold and lifetime problems?" Table 2 lists some areas worth consideration.

6.1 Directly change optical properties

What elements intrinsically possess the best radiative properties? What base metals possess those properties best suited for a substrate? If a satisfactory combination can not be produced utilizing conventional film deposition techniques, how might surface alloying be utilized? Molybdenum is a material that has been investigated (27) for high-power laser mirrors. How would the surface alloying of copper into the molybdenum alter its radiative properties?

6.2 Directly change mechanical properties

An ideal metal mirror material would be easy to conventionally machine while at the same time have a finished surface highly resistant to stress damage in the form of slip (28-30). Such a material probably does not exist and one of the most widely utilized metal mirrors, high purity copper, is a rather poor choice from the standpoint of the second criteria (28). Surface alloying by directed energy means has been shown by numerous investigators to be an effective method for altering surface mechanical properties. A large number of implants including Be, W, B, Cr and Al in Cu have been studied under both static and cyclic stress, yet to our knowledge no one is applying this technology in order to directly attempt to increase slip thresholds in Cu or other metal mirror metals.

6.3 Directly change oxidation or corrosion properties

Here too as in 6.2 there has been a sufficiently large number of examples of improvements in material-environment behavior to warrant specific investigations like the work of Oron, et al (1, 2). It may be that "shelf life" or "environmental degradation" are not yet limiting factors because mirrors routinely fail so early that these mechanisms are not yet important. However, it is unreasonable to expect that this situation will continue or that all future high power laser mirror applications will involve clean "field" environments.

6.4 Quenching from the liquid state

Second phase particles, porosity and microscopic topographical defects have all been shown (27, 30) to lead to localized mirror failure in damage threshold studies. The SAM micrographs in figure 5 show that even rather large second phase particles can be homogenized in the liquid and prohibited from nucleating upon cooling because of the very rapid recrystallization. In a paper (16) presented as part of last year's damage symposium it was pointed out that a finely focused Q-switched frequency doubled Nd-YAG laser had been used to repair scratches on mirror surfaces. Figure 12 shows this scratch repair. The surface is electropolished single crystal Mo. The annealing laser pulses are approximately 10 μm in diameter and are melting 2-5000 Å in depth. There has been some published work (31, 32) suggesting that melt quenching can be used to consolidate (eliminate porosity) from thick metal coatings; there have, however, to our knowledge, been no similar reports for bulk substrates. Seitel, et al (30) have used electron beam surface melting of Cu mirrors followed by diamond machining to produce a surface which "pitted least and also had the highest melt threshold" of the group tested. It should be noted that the problem they observed with substrate distortion could probably be overcome with either thicker substrates or shallower melting.

6.5 Summary

We believe that there is sufficient experimental evidence from other fields to suggest that directed energy processing may be advantageously applied to high power laser mirrors in such a manner as to improve their damage resistance. We are currently establishing contacts with other researchers who would be able to measure and compare optical properties and damage thresholds for surface modified samples.

7. References

[1] Oron, M.; Svendsen, L. G.; Sorensen, G. Laser-damage resistant copper surfaces with high reflectivity after oxidation. NBS Spec. Publ. 568, 187 (1980).

[2] Svendsen, L. G. A comparison of the corrosion protection of copper by ion implantation of Al and Cr. Corros. Sci. 20, 63 (1980).

[3] Baumvol, I. J. R. The influence of tin implantation on the oxidation of iron. J. Appl. Phys. 52, 4583 (1981).

[4] Bentini, G. G., et. al. The thermal oxidation of ion-implanted zirconium. Corros. Sci. 20, 27 (1980).

[5] Bennett, M. J.; Dearnaley, G.; Houlton, M. R.; Hanes, R. W. M.; Goode, P. D. and Wilkins, M. A. The influence of surface ion implantation upon the oxidation behavior of a 20% Cr-25% Ni, niobium stablized austenitic stainless steel, in carbon dioxide, at 825°C. Corros. Sci. 20, 73 (1980).

[6] Dearnaley, G. The ion implantation of metals and engineering materials. Trans. IMF 56, 25 (1978).

[7] Draper, C. W. and Sharma, S. P. The effect of laser surface melting on tin modified copper-nickel. Thin Solid Films, 84, 333 (1981).

[8] Buene, L.; Jacobson, D. C.; Nakahara, S.; Poate, J. M.; Draper, C. W. and Hirvonen, J. K. Laser irradiation of Ni: Defect structures and surface alloying. Gibbons, J. F.; Hess, L. D. and Sigmon, T. W., ed. Laser and electron-beam solid interactions and materials processing. New York: Elsevier North-Holland; 1981. 583-590.

[9] Hansen, M. and Anderko, K. Constitution of binary alloys. New York: McGraw-Hill; 1958. 36-37.

[10] Gibbons, J. F.; Hess, L. D. and Sigmon T. W., ed. Laser and electron-beam solid interactions and materials processing. New York: Elsevier North-Holland; 1981. 629 p.

[11] Benenson, B. E.; Kaufmann, E. N.; Miller, G. L. and Scholz, W. N., ed. Ion beam modification of materials. Amsterdam:North-Holland; 1981. 1051 p.

[12] Buene, L.; Kaufmann, E. N.; Preece, C. M. and Draper, C. W. in text of ref. 8 above. 591-597.

[13] Draper, C. W.; den Broeder, F. J. A.; Jacobson, D. C.; Kaufmann, E. N. and Vandenberg, J. M. Studies of laser-alloyed Zr-containing surface layers. Appleton, B.R. and Celler, G. K., ed. Laser and electron beam interactions with solids. New York: Elsevier North-Holland; 1982. in press.

[14] Wampler, W. R.; Follstraedt, D. M. and Peercy P. S. Pulsed laser annealing of aluminum. in text of ref. 8 above. 567-574.

[15] Draper, C.W. Laser surface alloying: the state of the art. Mukherjee, K. and Mazumder, J., ed. Lasers in metallurgy. Warrendale, PA: TMS-AIME; 1981. in press.

[16] Draper, C. W. Regrowth in laser irradiated elemental metals and alloys: surface nonuniformities and coupling phenomena. NBS Spec. Publ. 620, 210 (1981).

[17] Pendry, J. B. Low Energy Electron Diffraction, Academic Press, New York, 1972.

[18] Williams, J. S., Brown, W. L., Celler, G. K., Rozgonyi, G. A., and Sheng, T. T., Characterization of Pulsed Nd-YAG Laser Annealed Arsenic Ion implanted Silicon, J. Appl. Phys. 52, 1038 (1981).

[19] Kennett, H. M. and Lee, A. E. The Initial Oxidation of Molybdenum,I through V. Surf. Sci. 48, 591 (1975).

[20] Fairand, B. P., Wilcox, B. A., Gallagher, W. J. and Williams, P. U. Laser shock-induced microstructural and mechanical property changes in 7075 aluminum, J. Appl. Phys. 43, 3893 (1972).

[21] Feldman, L. C., MeV Ion Scattering for Surface Structure Determination, CRC Critical Reviews in Solid State and Materials Sciences, May 1981, p. 143.

[22] Benninghoven, A. Surface Investigation of Solids by the Statical Method of Secondary Ion Mass Spectroscopy (SIMS) Surface Sci. 35, 427 (1973).

[23] MacDonald, N. C. and Waldrop, J. R. Auger Electron Spectroscopy in the Scanning Electron Microscope: Auger Electron Images, Appl. Phys. Lett. 19, 315 (1971).

[24] Draper, C. W., Sharma, S. P., Yeh, J. L. and Bernasek, S. L. Examination of Elemental Nonuniformities in Laser Surface Melted Ternary Copper Alloys, Surf. and Int. Anal. 2, 179 (1980).

[25] Draper, C. W.; Meyer, L. S.; Buene, L.; Jacobson, D. C. and Poate, J. M. Laser surface alloying of gold films on nickel. Appl. Surf. Sci., 7, 276 (1981).

[26] Draper, C. W.; Jacobson, D. C.; Gibson, J. M.; Poate, J. M.; Vandenberg, J. M. and Cullis, A. G. Laser and ion beam mixing of Cr and Cr + Ni films on Cu. in text of ref. 13.

[27] Bennett, J. M.; Wong, S. M. and Krauss, G., Relation between the optical and metallurgical properties of polished molybdenum mirrors. Appl. Opt. 19, 3562 (1980).

[28] Musal, H. M. Thermomechanical stress degradation of metal mirror surfaces under pulsed laser irradiation. NBS Spec. Publ. 568, 159 (1980).

[29] Porteus, J. O.; Decker, D. L.; Jernigan J. L.; Faith, W. N. and Bass, M. Evaluation of metal mirrors for high power applications by multithreshold damage analysis. IEEE J. Quantum Electron. 14, 776 (1978).

[30] Seitel, S. C.; Porteus, J. O.; Decker, D. L.; Faith, W. N. and Grandjean, D. J. Effect of surface preparation methods on laser-induced pitting of copper mirrors at the 10.6 μm wavelength. IEEE J. Quantum Electron 17, 2072 (1981).

[31] Ayers, J. D.; Schaefer, R. J.; Bogar, F. D. and McCafferty, E. Corrosion behavior of laser consolidated titanium coated steel in sea water. Corrosion, NACE 37, 55 (1981).

[32] Pangborn, R. J. and Beaman D. R., Laser glazing of sprayed metal coatings. J. Appl. Phys. 51, 5992 (1980).

[33] Kane, P. F. and Larrabee, G. B., Editors, Characterization of Solid Surfaces, Plenum Press, New York, (1974).

The question was asked as to the physical surface quality of the resultant laser alloyed surface. The author replied that it is quite good, and a mirror can be made of it. How stable the alloys are to thermal and environmental stresses remains as a research problem. In response to another question, the author pointed out that in their work all the alloys studied so far have been produced by melting. However, at lower laser powers alloying might result from enhanced diffusion of one metal into another. They hope to look at this possibility in future research. It was pointed out that metastable mixtures in silver copper alloys formed by laser annealing in a USC three-year study tended to disappear over a period of months. Were the alloys formed in this study stable? The author replied that the alloys studied appeared to be stable. They had not, however, studied silver copper alloys. The object in developing metastable alloy systems is to make the kinetics so slow that the alloys are effectively stable over an extended period of time. The alloy stability must therefore be studied separately for each system. No general conclusions can be made. Another question addressed the practicality of the method. The author replied that in the laboratory they could make samples 2 1/2" x 2 1/2" in a couple of hours.

The Effect of the Treatment and Ageing on KCl Surface Breakdown Threshold

S. V. Bilibin, V. N. Egorov, A. A. Katsnelson, V. I. Kovalev,
N. S. Kolesova, Yu. S. Sidorov, N. L. Tkachenko, F. S. Faizullov

Lebedev Physical Institute
Academy of Sciences of the USSR

The breakdown thresholds of bare surfaces of KCl windows treated in different ways were measured with a gain-switched-pulse CO_2 laser at 10.6 μm. The studies indicated that grinding abrasive grain size and moisten-cooling liquid determine the destructed layer depth and the breakdown threshold for freshly polished KCl surfaces. The ageing of these samples decreases breakdown thresholds considerably. The high-temperature baking of KCl samples before final polishing increases the surface breakdown threshold up to bulk damage for freshly polished and twice for aged samples as compared with those unbaked.

Key words: Alkali halides; TEA CO_2 laser; KCl; laser damage; grinding grain size; destructed layer depth; baking; surface breakdown.

1. Introduction

It was supposed [1], that TEA CO_2 laser surface breakdown threshold of alkali halides single-crystals depended on the thickness of destructed surface layer under abrasive treatment. Therefore, it was interesting to determine the factors of the surface abrasive treatment which influence the thickness of the destructed layer and surface breakdown threshold. In this work, a series of experiments was conducted on the effect of abrasive grain size, moisten-cooling liquid kind, high temperature baking, and the process of growing old on the optical strength of a KCl polished surface.

2. Test Materials and Experimental Procedure

KCl test specimens were prepared by cleavage on a (100) crystalline plane from a large crystal grown by a Kyropulos, technique in air. Size of samples was 30 x 30 x 10 mm.

All samples were ground with carborundum powder with grain size of 63-50 μm (powder 1) and corund powder with grain size of 20-14 μm (powder 2). A saturated solution of KCl in distilled water, ethanol, or ethylene glycol was used as a liquid component of abrasive suspension.

The final polishing of all samples was done by diamond powder (grain size 1 μm) with ethanol. The surface roughness was measured by profilometer. The thickness of the destruction layer on the cleavage, perpendicular to the polished surface, was measured by microscope. The etching in 25 percent solution of $PbSO_4$ in ethanol for 45 s was used before the microscope investigation.

Standard gain-switch TEA CO_2-laser pulses ($\tau_{0,5}$ = 100 ns), with TEM_{00} mode beam were used. The effective square beam spot on the sample surface was $1.3 \cdot 10^{-4}$ cm^2. The transmitted temporal-pulse termination technique of detecting surface breakdown was used [2]. The measurement accuracy was 25 percent.

3. Results and Discussion

As with all samples, the final polishing was done in the same way. Independent of the previous grinding process, the surface roughness was the same, $R_z \lesssim 0.025$ μm. Since most of the surface layer destruction appears at the grinding stage [3], the structure of the cleavage perpendicular to the polished surface was investigated.

The table shows results of destructed layer depth and surface breakdown threshold measurements for KCl samples treated in different ways. It is easily seen that the samples which were polished after grinding by powder 1 show lower thresholds of surface breakdown than by powder 2. This result correlates with the data of destructed layer depth measurements. These results conclude that the smaller the grinding abrasive grain size before final polishing, the lower the destructed layer depth, and the higher the surface optical breakdown threshold.

As to the liquid phase of grinding suspension, the table shows that a saturated KCl solution in water and ethanol gives the same results, but ethylene glycol is preferred because it gives a lower destructed layer depth. This result is in agreement with Reference 4 which shows that abrasive

destruction of the surface layer is dependent on the suspension liquid phase. In particular, Reference 5 shows that surface treatment ruby crystals with ethylene glycol have a smaller destructed layer depth. To remove the destructed layer, we raised the temperature air atmosphere baking (T = 600 C, t = 12h) of samples which were previously ground by abrasive 2 with ethylene glycol. Figure 1 shows the modification of a destructed layer structure after baking. The density of dislocation decreased and the material structure became homogeneous in bulk near the surface. These samples were then polished by diamond abrasive with ethanol. On the surface of all samples, which were ground with ethylene glycol with and without baking, breakdown thresholds were the same and equal to the bulk damage threshold of KC1 samples under the test. This study has given very significant results. The use of abrasive techniques for polishing IR optical element surfaces, giving minimal destruction layer depth, will raise surface beakdown threshold up to the threshold of bulk damage.

All these breakdown thresholds were measured no later than 24 hours after polishing. But, under real conditions of optical element operation, it should continuously be in contact with real air atmosphere. The absorption of water on the surface of the KC1 should decrease the breakdown threshold in time [6].

It is important to know the value of threshold decrease on the surfaces polished in different ways.

The results of threshold measurements for the samples kept in air atmosphere 6 months are also presented in the table. The destructed layer depths are unchanged, but the breakdown thresholds are considerably diminished. On the samples 1-8, the breakdown threshold is the same independent of the destructed layer depth.

As shown in Reference 6, the surface breakdown threshold is defined by the amount of absorbed water. The equality of thresholds means that the amount of absorbed water is the same on the old surfaces of samples 1-8. The threshold's independence of the destructed layer depth for these samples concludes that the absorption of water takes place not in full depth but in the thinner surface layer. Unfortunately, the depth measurement method does not distinguish this layer, but it is reasonable to assume that on all these surfaces the depth should be no less than the minimum grain size of the grinding abrasive (14-20 μm) (the final polishing only makes the surface smooth).

The depth was determined by the grain size of the polishing abrasive (1 μm) and, therefore, the depth layer and amount of absorbed water on these surfaces are considerably less in cases of baked samples (9-10). This should lead to a notable increase of the breakdown threshold (see table) not only for freshly polished, but for aged samples as well.

References

1. V. I. Kovalev, F. S. Faizullov, Sov J. Quant. Electr., 7, 326 (1977).
2. V. I. Kovalev, V. V. Morosov, F. S. Faizullov., Sov. J. Quant. Electr., 4, 1208 (1975).
3. M. G. Buravleva, I. V. Smushka, Single Crystals and Technology (in Russian), 7, Kharkov, 1972, p. 71.
4. N. Kachalov, Technology of Grinding and Polishing of Sheet Glass (in Russian), Moscow-Leningrad, 1958, p. 132.
5. S. Z. Arushanov, A. S. Bebchuk, D. A. Gromov, V. S. Nechitailo, Physics and Chemistry of Materials Processing (in Russian), N 1, 1978, p. 117.
6. V. I. Kovalev, F. S. Faizullov, Laser Induced Damage in Optical Materials, 1978, N BS Spec. Publ, 541, p. 318.

Table

Destructed layer depths and surface breakdown thresholds for KCl samples after treatment

Sample Number	Treatment Conditions				Freshly Polished		6 Months Later	
	Grinding		Polishing					
	Abrasive Grain Size µm	Liquid Kind	Abrasive Grain Size µm	Liquid Kind	Destructed Layer Depth µm	Breakdown Threshold MW/cm²	Destructed Layer Depth µm	Breakdown Threshold MW/cm²
1	63-50	ethanol	2-1	ethanol	380 ± 50	790	380 ± 50	400
2	63-50	ethanol	2-1	ethanol	380 ± 50	920	310 ± 50	370
3	63-50	KCl saturated solution	2-1	ethanol	420 ± 50	780	-	-
4	20-14	ethanol	2-1	ethanol	-	1100	290 ± 50	350
5	20-14	ethanol	2-1	ethanol	250 ± 50	970	250 ± 50	370
6	20-14	KCl saturated solution	2-1	ethanol	280 ± 50	1250	-	320
7	20-14	ethylene glycol	2-1	ethanol	60 ± 20	1500 x)	60 ± 20	400
8	20-14	ethylene glycol	2-1	ethanol	60 ± 20	1500 x)	60 ± 20	230
9 xx)	20-14	ethylene glycol	2-1	ethanol	1 - 3	1500 x)	1 - 3	720
10 xx)	20-14	ethylene glycol	2-1	ethanol	1 - 3	1500 x)	1 - 3	620

x) surface breakdown threshold equal to bulk damage threshold

xx) baked before polishing

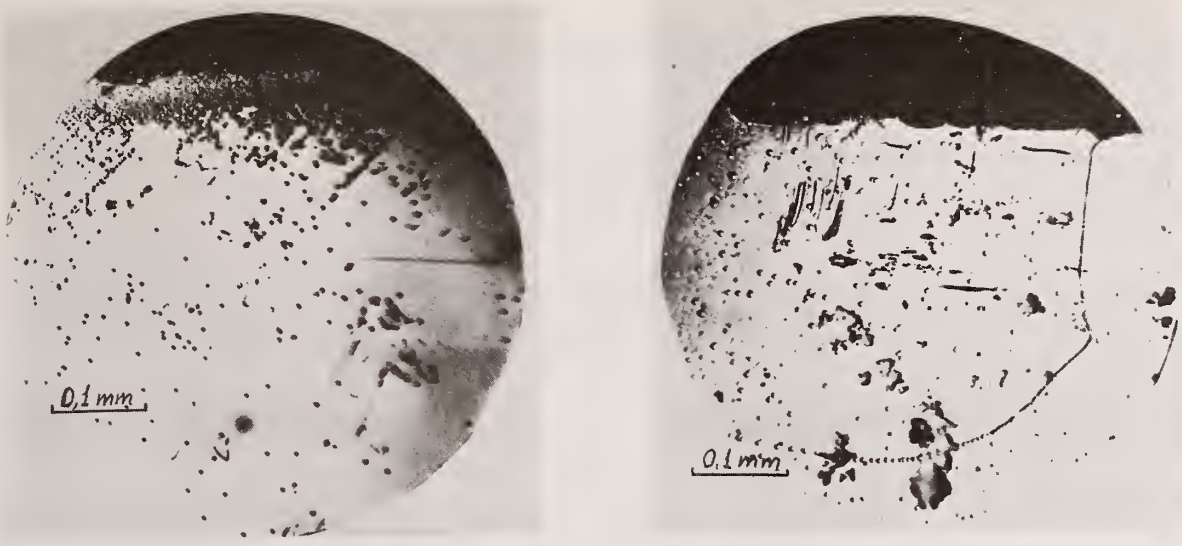

a. b.

Figure 1. Micrographs of single-crystal KCl samples cleaved perpendicular to the treated surface a) Sample 8, unbaked b) Sample 10, baked.

SURFACE FINISHING USING SOFT ABRASIVES*

H. Vora, R. H. Anderson and R. J. Stokes
Honeywell Corporate Technology Center
10701 Lyndale Avenue South
Bloomington, MN 55420

In an effort to produce scratch- and damage-free flat surfaces, two non-conventional polishing techniques, mechano-chemical and float, were recently introduced by Yasunaga et al. and Namba and Tsuwa, respectively. The emphasis in both these techniques is on employing an abrasive whose hardness is less than that of the workpiece. This paper describes the results of our efforts to apply these techniques to tape-cast alumina, hot-pressed Si_3N_4, sapphire and single crystals of silicon and gallium arsenide. Samples of polished materials were observed to be scratch free, and in the case of single crystals, very smooth with a peak-to-peak roughness of $\leq$ 40Å. The polished surfaces have been characterized using several techniques, including reflection high-energy electron diffraction (RHEED), interferometry, profilometry, electron spectroscopy for chemical analysis and Auger electron spectroscopy.

Key words: Float polishing; gallium arsenide; mechano-chemical polishing; sapphire; silicon; silicon nitride; surface characterizations; surface finishing; tape-cast alumina.

1. Introduction

In a variety of applications, particularly those associated with optics and electronics, materials possessing smooth, damage-free, and flat surfaces are required. Such surfaces are difficult to obtain using conventional techniques in which abrasives with hardnesses greater than that of the workpiece are employed. Hard abrasives introduce scratches and a damaged layer, which must be removed by a final treatment. This treatment often consists of chemical polishing in which the material is removed by chemical rather than mechanical means. However, chemical polishing rapidly degrades the flatness of the workpiece and often introduces orange-peel structure on the surface. In order to overcome these problems, two new polishing techniques, mechano-chemical and float, were recently introduced by Yasunaga et al [1][1] and Namba and Tsuwa [2], respectively. The emphasis in both these techniques is on employing an abrasive whose hardness is less than that of the workpiece. Since such an abrasive cannot damage or scratch the workpiece, these techniques can yield damage- and scratch-free surfaces.

Mechano-chemical polishing is performed in a manner similar to the conventional polishing using conventional polishing machines, and it relies on a chemical reaction between the abrasive and the workpiece. A simple way to accomplish this is by applying high pressure of the order of 7×10^4 N/m^2 (10 psi) on the workpiece and performing the mechano-chemical polishing dry. In some cases, chemical reactions can be induced at moderate temperatures, and significant removal rates are observed even when the mechano-chemical polishing is performed wet under nominal pressures.

Figure 1 shows the schematic of the float polishing apparatus described by Namba and Tsuwa [2]. Samples are suspended above a diamond-turned tin lap, apparently by controlling the relative speeds of the lap and the sample holder. In between the tin lap and the surfaces of the samples being polished is a thin layer of slurry, typically containing 2-5 w/o of some soft abrasive. The particles of this soft abrasive continually bombard the surface of the workpiece and thereby remove material from it.

2. Float Polishing

Efforts were made in these on-going programs to float polish hot-pressed Si_3N_4, and single crystals of silicon, gallium arsenide and sapphire. A typical attempt involved polishing three samples $\sim$1 cm x 1 cm in cross section in the case of sapphire and $\sim$2.5 cm x 2.5 cm in cross section in the case of GaAs, Si and Si_3N_4. These samples were mounted on a 10 cm diameter sample holder and polished on a 25 cm diameter lap containing concentratic grooves using a lap rpm of $\sim$100, sample holder rpm in the range of 90-150, and polishing loads in the range 300-3000 gms. Lap materials and soft abrasives used for float polishing are listed in table 1 along with peak-to-peak roughness and flatness achieved by float polishing. Float polished surfaces of silicon and GaAs were analyzed using the electron channeling technique. The electron channeling patterns obtained are shown in figure 2. The presence of sharp Kikuchi lines observed in these patterns are indicative of high surface perfection.

*Research supported by the Materials Division of the Office of Naval Research under contract No. N00014-80-C-0437 and by ERADCOM under contract No. DAAK20-80-C-0267.

1. Figures in brackets indicate the literature references at the end of this paper.

Table 1. Float polishing parameters and some characteristics of float polished surfaces.

Sample	Laps	Abrasives	Peak-to-Peak Roughness	Flatness
Si	PVC, Linen Bakellite	$CaCO_3$ & MgO	40Å	1-3λ*
GaAs	Beeswax	MgO	10Å	1λ
Sapphire	Linen Bakellite	SiO_2	40Å	λ/2
Hot-Pressed Si_3N_4	Linen Bakellite	Fe_2O_3 & Fe_3O_4	200Å	3λ

*λ = 633 nm

3. Mechano-Chemical Polishing

Efforts were made in these programs to mechano-chemically polish tape-cast alumina, hot-pressed silicon nitride and single crystals of silicon of orientation (100) and sapphire of orientation $(10\bar{1}2)$. All these efforts were made on a Strasbaugh polishing machine Model 6Y-1 using a 25 cm diameter lap rotated at speeds in the range 25-50 rpm. Lap materials, polishing pressures and soft abrasives used for mechano-chemical polishing of various materials are listed in table 2.

Table 2. Mechano-chemical polishing parameters

Substrate	Laps	Abrasives	Polishing Pressures
Silicon	PVC, Bakellite	$CaCO_3$, $BaCO_3$, and MgO	100 gm/cm^2
Sapphire	Window Glass	None	700 gm/cm^2
Tape-Cast Al_2O_3	Window Glass	None	700 gm/cm^2
Hot-Pressed Si_3N_4	Bakellite	Fe_2O_3, Fe_3O_4	350 gm/cm^2

Surface profiles of mechano-chemically polished samples of hot-pressed Si_3N_4, tape-cast alumina and single crystals of silicon and sapphire are shown in figure 3. It is seen that mechano-chemical polishing produces much smoother surfaces on single crystals of silicon and sapphire (peak-to-peak roughness of ∿40Å) than on the surfaces of tape-cast alumina (peak-to-peak roughness of ∿2500Å) and hot pressed Si_3N_4 (peak-to-peak roughness of ∿200Å). The ultimate smoothness that can be achieved by mechano-chemical polishing in these polycrystalline materials is limited by the grain size, anisotropy associated with grains of different orientations, and pores and second phases present.

Figure 4 shows the RHEED pattern of a mechano-chemically polished surface of silicon crystal. The presence of well defined Kikuch lines in this pattern indicates that the mechano-chemical polishing introduces very little surface damage.

Surfaces of silicon crystals mechano-chemically polished with $CaCO_3$ and $BaCO_3$ were analyzed using the technique of electron spectroscopy for chemical analysis. No evidence for the presence of calcium or barium on the surfaces of these crystals was obtained in this analysis [3].

Surfacesof hot-pressed Si_3N_4 wet mechano-chemically polished with Fe_2O_3 were analyzed using Auger electron spectroscopy. This analysis indicated that only traces (0.5 atomic percent) of iron is present on these surfaces. Auger spectra of the surfaces exposed by sputter etching the polished surface to a depth of ∿100Å did not show any iron [4].

4. Discussion

This work confirms the feasibility of float polishing silicon, sapphire and GaAs, which was demonstrated earlier by Namba and Tsuwa [2,5], and extends the application of float polishing technique to hot-pressed Si_3N_4. We are also confirming the feasibility of mechano-chemical polishing of sapphire and silicon [1] and extending the application of mechano-chemical polishing technique to tape cast alumina and hot-pressed Si_3N_4.

Most of our observations concerning the mechano-chemical polishing effects in the case of sapphire and silicon are in general agreement with those made by Yasunaga et al [1]. In addition to $CaCO_3$ and $BaCO_3$ abrasives reported by Yasunaga et al., MgO was identified in this work as another suitable soft abrasive for mechano-chemical polishing of silicon.

In the present work, the flatness of both mechano-chemically and float polished surfaces of ~2.5 cm x 2.5 cm in area has fallen in the range of 1-3λ at 633 nm. The main reason for this is that the laps that were used in this work were not very flat. It is believed that the employment of flatter laps would result in flatter surfaces.

Efforts are currently being made to measure removal rates as a function of various mechano-chemical polishing parameters. The data that have been obtained so far indicate that the removal rates are dependent on the surface roughness of the workpiece; the higher the surface roughness, the higher the removal rate. Once the surface of the workpiece becomes smooth, the removal rate reaches a steady value, which varies from material to material and lies in the range of 1-4 μm/hr.

5. Acknowledgements

The authors would like to thank Prof. Y.H. Namba and Mr. J.P. Cummings for many useful discussions and Mr. D.J. Sauve, Jr. for excellent technical support.

References

[1] Yasunaga N., Tarumi N., Obara A., and Imanaka O., in The Science of Ceramic Machining and Surface Finishing II, National Bureau of Standards Special Publication 562, Hockey, B.J., and Rice, R.W., editors, p. 171 (1979).

[2] Namba Y. and Tsuwa H., in Laser Induced Damage in Optical Materials: 1980, National Bureau of Standards Special Publication 620, Bennett, H.E., Glass, A.J., Guenther, A.H., and Newnam, B.E., editors, p. 171 (1981).

[3] Vora H. and Stokes R.J., Office of Naval Research Annual Technical Report No. N00014-80-C-0437-1, (1981).

[4] Vora H., Orent T.W., and Stokes R.J., to be published in the Journal of American Ceramic Society.

[5] Namba Y. and Tsuwa H., Annals of the CIRP 28, 425 (1979).

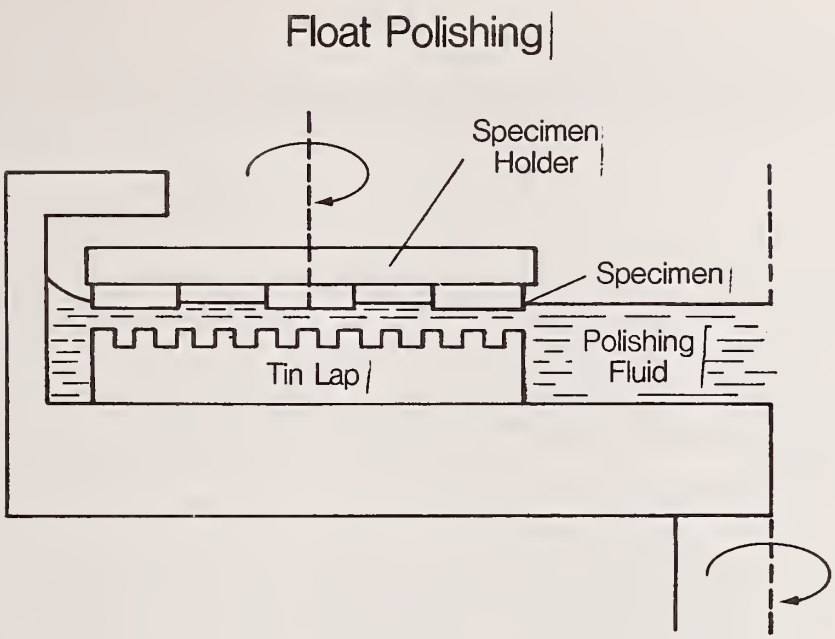

Figure 1. Schematic of the float polishing apparatus.

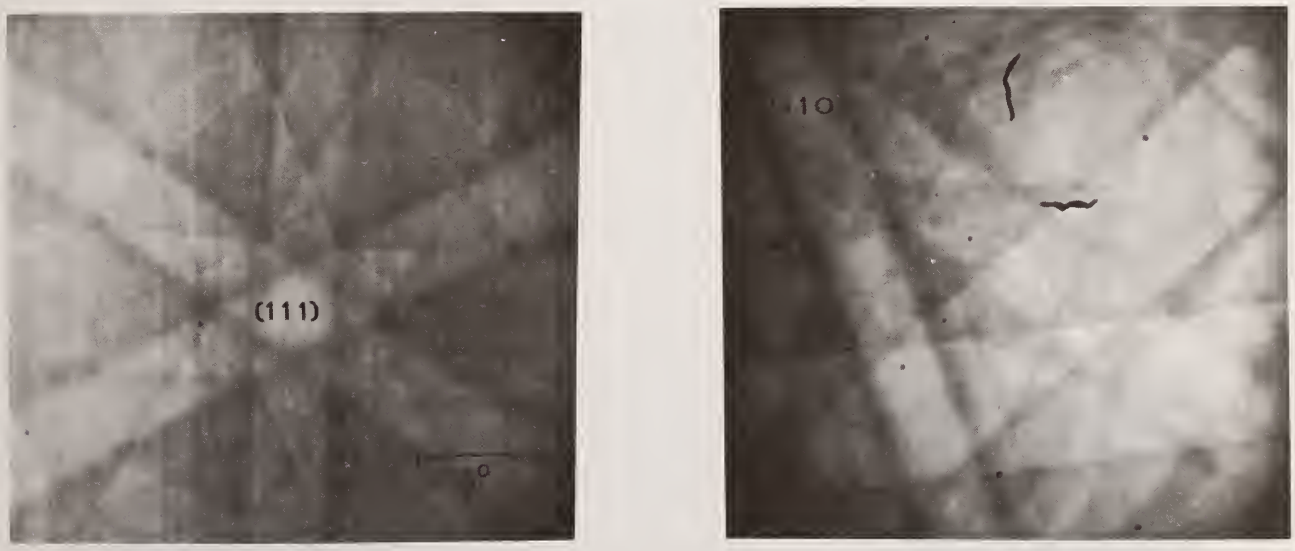

Figure 2. Electron channelling patterns of float polished (a) silicon and (b) gallium arsenide at 22X.

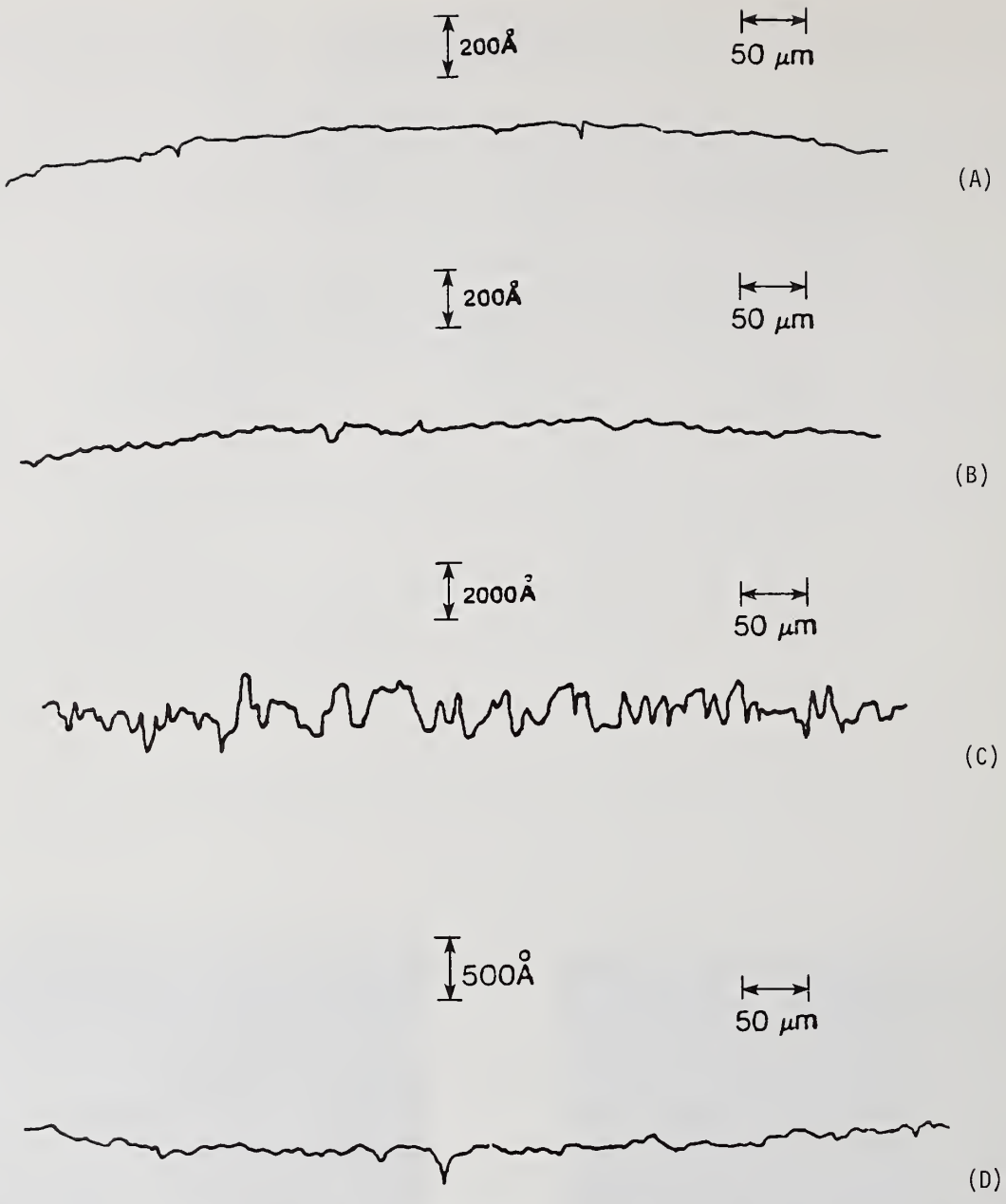

Figure 3. Surface profiles of mechano-chemically polished samples of (A) silicon (B) sapphire (C) tape-cast alumina and (D) hot-pressed Si_3N_4.

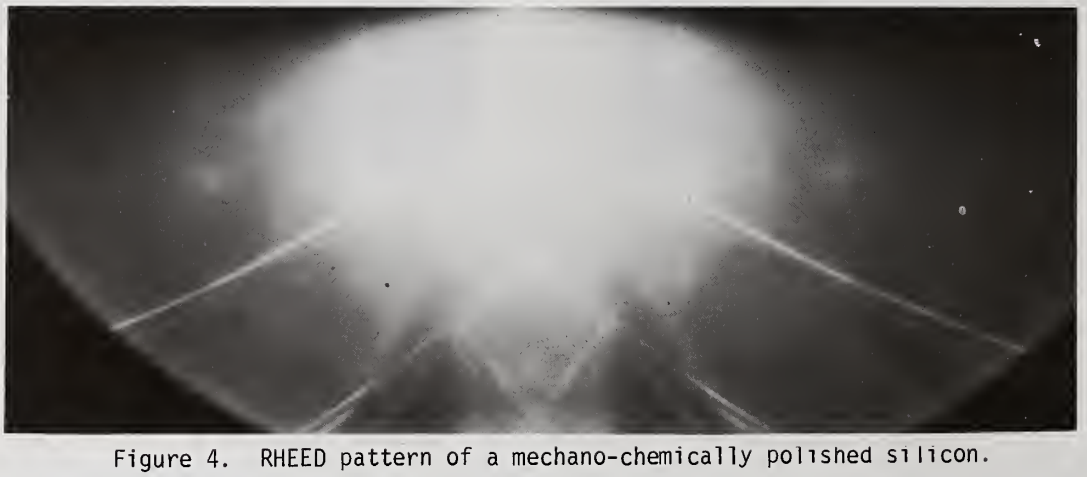

Figure 4. RHEED pattern of a mechano-chemically polished silicon.

It was pointed out that some types of polishing compounds are undesirable because of their absorption. For example, cerium dioxide, which was listed as a polishing compound in the paper, is undesirable if the component is to be used in the ultraviolet. The author agreed.

Effects of Deuterium Treatments on the Optical Properties of Fused Silica

Binod Kumar, Nils C. Fernelius, and John A. Detrio
University of Dayton Research Institute
Dayton, Ohio 45469

Flame produced fused silica, the process used by all American manufacturers, contains a large amount of OH^-. The fundamental OH^- vibration in SiO_2 is at 2.75 μm and its first overtone is at 1.38 μm. Much of the optical absorption at 1.3 μm is due to the wing of the 1.38 μm absorption band. Stone and Burrus[1] described a deuterium treatment given optical fibers to transform the OH^- absorption to OD^- whose fundamental is at 3.72 μm and first overtone at 1.85 μm. Here we describe some related treatments given to Suprasil II window samples. Spectral traces show that the 1.38 μm absorption peak is diminished while a new absorption peak appears at 1.85 μm. Similar changes appear in the spectrum between 2 and 4 μm. 1.3 μm laser rate calorimetry performed before and after treatment on the sample showing the most complete $H \leftrightarrow D$ exchange exhibited a drop in absorption value to about 1/5. Thus we conclude that over 80% of the optical absorption in Suprasil II at 1.3 μm is due to the OH^- molecule. The method offers a way of improving the performance of flame produced fused silica windows used at 1.3 μm.

Key words: fused silica; hydrogen-deuterium exchange treatments; OD^- absorption bands; OH^- absorption bands; 1.3 μm optical absorption; SiO_2.

1. Introduction

Most types of commercially available fused silica are prepared in a natural gas flame which introduces water into the molecular structure. This appears predominately in the form of an OH^- ion. The fundamental OH^- vibration ν_3^1 in SiO_2 is at 2.75 μm. The first overtone $2\nu_3^1$ of this line appears at 1.38 μm; the second, $3\nu_3^1$ is at 0.95 μm. A combination tone, $2\nu_3^1+\nu_1$, where ν_1 is a vibration frequency of SiO_4, occurs at 1.24 μm. The 1.38 and 2.75 μm lines are intense. The wing of the 1.38 μm line contributes an appreciable fraction of the optical absorption measured at 1.3 μm. Thus to obtain low absorbing fused silica at 1.3 μm it is desirable to eliminate or change to another wavelength the absorption band at 1.38 μm. Fused silica produced in a moisture-free plasma arc is free of this absorption band. There is no American manufacturer currently using this process. A German manufacturer charges about twelve times more for plasma arc produced fused silica over flame produced. Thus it would be desirable to investigate treatments of flame produced fused silica to cut down this 1.38 μm absorption.

This water band problem also plagues fabricators of fused silica optical fibers which operate at 1.3 μm. A solution to this problem was presented by J. Stone and C. A. Burrus[1]. The fiber is placed in a deuterium, D_2, atmosphere and heated. Appreciable diffusion of D_2 into silica occurs for temperatures greater than 200°C and 1 atmosphere pressure. The existing OH^- ions are converted to OD^- ions, changing the locations of the absorption bands. $OH^- \rightleftarrows OD^-$ ion exchange was found to be complete in a 110 μm (0.004") diameter fiber in less than 3 minutes at 1000°C and 1 atmosphere.

A two atom harmonic oscillator has vibrational frequencies proportional to $\sqrt{\frac{1}{m_1}+\frac{1}{m_2}}$. Thus the wavelength is proportional to $\sqrt{m_1 m_2/(m_1+m_2)}$. If m_1 = 16, the mass of oxygen, and m_2 = 1 or 2, the masses of a hydrogen or deuterium atom, the ratio of the respective wavelengths is $\sqrt{2x17/1x18}$ = 1.37. The experimental results confirm that the harmonic oscillator is a good approximation.

2. Experimental Results

Since we had a number of Suprasil II window samples which exhibited a large absorption band near 1.38 μm, had cylinders of D_2 gas for the DF laser, and a pressure bomb-furnace apparatus, some

[1] Figures in brackets indicate the literature references at the end of this paper.

preliminary attempts were made to see if the above described process could be scaled to sample dimensions on the order of centimeters. Several samples were treated as described in Table 1. This table also lists the % absorption of the 1.38 μm dip before and after treatment. Figure 1 shows the peak before treatment and afterwards on Sample AFML #3208. Note the peak at 1.38 μm

Table 1. Description of D_2 Treatments

Specimen AFML No.	Deuterium Treatment Condition	Observations	% Abs. at 1.38 μm		$\beta_{slope} \div 10^{-3}$
			Before	After Treatment	@ 1.3μm After Treatment
3191	Treated at 1000°C for 24 hrs. at 1 atm. D_2 pressure. Flow rate of D_2 maintained at 0.5 liter/min.	Specimen crystallized surface. Crystallized surface removed before optical meas. The crystalline phase was melanophlogite.	9	7	2.67
3249	Specimen saturated with D_2 at 100 psi at room temperature for 24 hrs. The reaction chamber was then heated up to 900°C and the temperature was maintained for 8 hrs. D_2 pressure was maintained at 100 psi. Graphite coated to prevent crystallization.	No surface crystallization. Spectra traces made without surface polishing. Polished before calorimetry measurements to remove traces of graphite.	8.8	6	2.38
3227	Specimen saturated with D_2 at 150 psi at room temperature for 60 hrs. The reaction chamber was heated to 900°C and temperature was maintained for 6 hrs. 150 psi. Graphite coated to prevent crystallization.	No surface crystallization. Spectral traces made without surface polishing. Polished before calorimetry measurements to remove traces of graphite.	8.5	6	2.21
3208	Specimen treated at 900°C and 150 psi for 26 hrs.	No surface crystallization. Optical measurements carried out without surface polishing.	8.5	3.2	1.65
3237	Specimen treated at 900°C and 150 psi for 104 hrs.	No surface crystallization. Optical measurements carried out without surface polishing.	-	0.8	0.546

decreases while a peak at 1.85 μm appears. Table 1 also lists the result of laser rate calorimetry at 1.3 μm after treatment on these samples. The first three samples were repolished before measurement since they had graphite coatings before being put in the furnace. Samples 3249 and 3227 were also measured before repolishing and had β_{slopes} of 10.5 and $23.4 \times 10^{-3} cm^{-1}$ indicating evidence of residual amounts of graphite. Samples from this batch of Suprasil II have shown to be reasonably homogeneous. Five other samples were measured while the treatments were made and yielded an average $\beta_{slope} = 2.99 \times 10^{-3} \pm 0.21$ cm^{-1}. Thus the last two treatments did significantly reduce the absorption of the

windows at 1.3 μm. The measured β_{slope} on the most thoroughly treated sample being 18% of the untreated value.

One question we have yet to resolve is the permanence of the treatments. Figure 2 shows a trace of AFML 3227 within a day after the treatment, a run one-month later and a run six months later. There seems to be no change. Further work will have to be done on this problem to check its practicality. For example heat the sample with a high power laser beam while in a moist atmosphere.

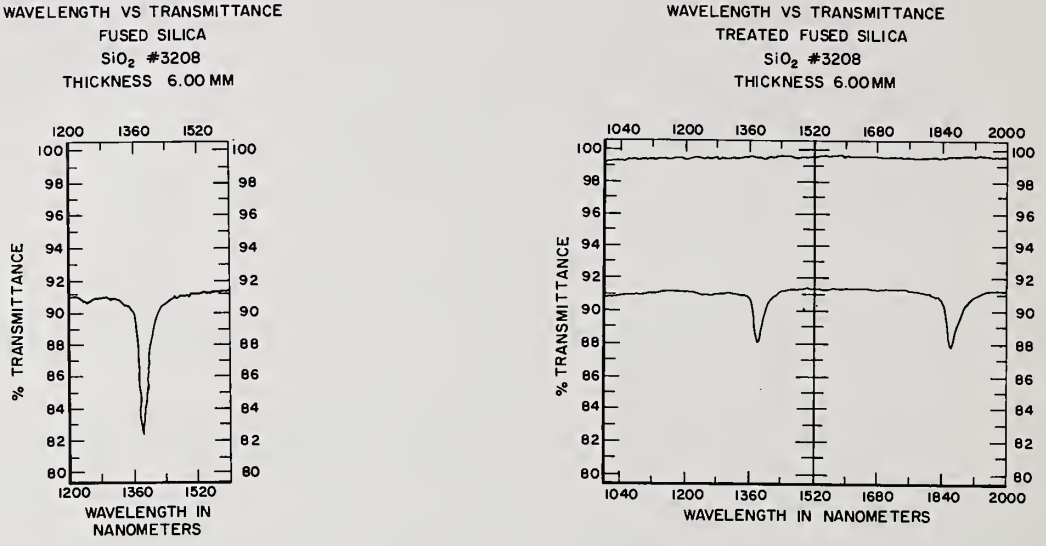

Untreated 6 mm thick fused silica

After treatment

Figure 1. Beckman 5270 spectral traces of AFML #3208 before and after treatment on an expanded scale in the 1.2-1.6 μm region.

As mentioned earlier there are other OH^- absorption bands. The paper by P. Kaiser et al.[2] lists a number of these bands. Table 2 lists the overtones and combinational vibrations in fused silica, the relative loss caused by them and the wavelength at which they occur for OH^- and OD^-. For a material the transmitted divided by the incident intensity, $I/I_0 = e^{-\beta L}$ where β is the optical absorption coefficient. Hence $\log_{10} I/I_0 = -\beta L \log_{10} e$ or

$$\beta = \frac{2.303 \log_{10} I_0/I}{L}$$

From the Radio Amateur's Handbook, $db \equiv 10 \log_{10} \frac{P_o}{P}$, thus

$$\beta \frac{(db)}{km} \times 2.303 \times 10^{-6} = \beta\,(cm^{-1}).$$

An example of $OH^- \rightarrow OD^-$ conversion is shown in Figs. 1 and 3 where the 1.38 μm decreases in intensity with treatment while the 1.85 μm appears and increases in size. Further examples are listed in Table 2 and are shown in Figure 3.

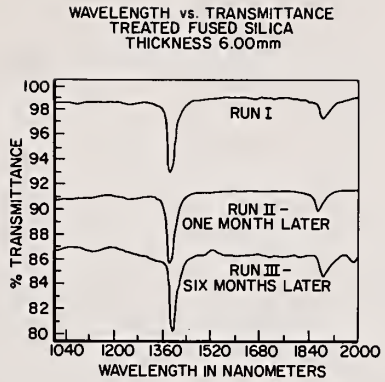

Figure 2. Transmission spectra from specimen #3227 after deuterium treatment, one month later and six months later. Run I vertically displaced upward by 8 percent for clarity. Run III vertically displaced downward by 4 percent.

Table 2. Overtones and Combinational Vibrations of OH^- and OD^- in Fused Silica and Relative Peak Intensities

Frequency	Loss cm^{-1}	Wavelength in μm	
		OH^-	OD^-
$5\nu_3^1$	0.0000138	0.60	
$2\nu_1+4\nu_3^1$	0.00000230	0.64	
$\nu_1+4\nu_3^1$	0.00000921	0.68	
$4\nu_3^1$	0.000161	0.72	
$2\nu_1+3\nu_3$	0.00000921	0.82	
$\nu_1+3\nu_3^1$	0.000207	0.88	
$3\nu_3^1$	0.002303	0.945	1.26
$2\nu_1+2\nu_3^1$	0.0002533	1.13	
$\nu_1+2\nu_3^1$	0.00645	1.24	1.68
$2\nu_3^1$	0.1497	1.38	1.85
$2\nu_1+\nu_3^1$	0.0237	1.90	
$\nu_1+\nu_3^1$	0.5988	2.22	2.95
ν_3^1	23.03	2.72	3.72

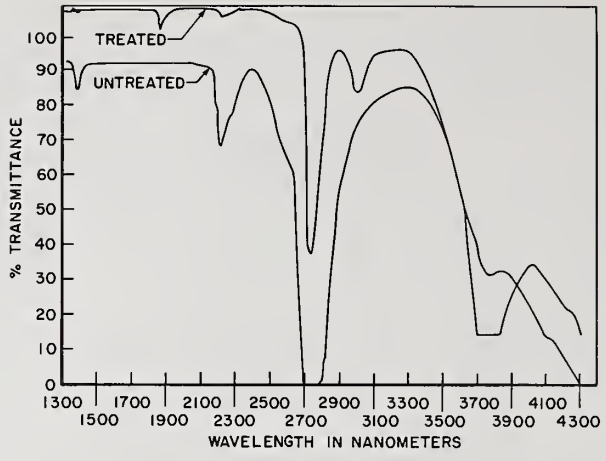

Figure 3. Transmission spectra from untreated and treated fused SiO_2. Spectrum from treated specimen has been displaced 15 percent vertically upward for clarity.

3. Summary

We have shown that OH^- absorption bands in fused silica can be decreased and eliminated by an isotope exchange reaction with deuterium - the so-called deuterium treatment. This treatment does produce additional absorption bands at longer wavelengths (roughly 1.34 longer wavelength) associated with the OD^- ion. From measurements on a thoroughly treated sample, we found that at least 80% of the optical absorption at 1.3 μm in Suprasil II is due to the wing of the 1.38 μm OH^- absorption band. Further work should be done on improving the efficiency of the reaction and to check how stable it is. For example a window passing high power laser beams exposed to a moist atmosphere might reverse the process.

This work was supported by the Air Force Wright-Aeronautical Laboratories, Materials Laboratory, Wright-Patterson Air Force Base, Ohio 45433.

References

[1] Stone, J.; Burrus, C. A. Reduction of the 1.38 μm water peak in optical fibers by deuterium-hydrogen exchange. Bell System Technical Journal 59(8): 1541-1548; 1980 October.

[2] Kaiser, P; Tynes, A. R.; Astle, H. W.; Pearson, A. D.; French, W. G.; Jaeger, R. E.; Cherin, A. H. Spectral losses of unclad vitreous silica and soda-lime-silicate fibers. J. Opt. Soc. Am. 63: 1141; 1973.

The question was asked if the OH^- was introduced by the flame or the atmosphere. The author did not know. Also, a member of the audience stated that they had not seen the absorption at 1.3 μm reported by the authors in fused silica samples they had obtained. Reactive atmosphere processing (RAP) was suggested as the cost effective way to remove it, if it were present.

Laser Desorption Analysis of H_2O and Other Contaminants from Optical Surfaces*

J. O. Porteus and W. N. Faith

Michelson Laboratory, Physics Division
Naval Weapons Center, China Lake, California 93555

Susan D. Allen

Center for Laser Studies
University of Southern California, Los Angeles, California 90007

Contamination at surfaces and interfaces is known to cause lowered damage threshold in high power laser optical components; therefore, it is important to be able to identify and measure the amount of adsorbed species. A technique has been developed for detecting water and other adsorbed molecules on optical surfaces at incident intensities below the damage threshold. A pulsed laser is focused onto the optical surface of interest in a UHV chamber. The laser energy absorbed in the surface layer causes desorption of the contaminants. Detection and identification of the desorbed species are via a quadrupole mass analyzer. As water and other contaminants such as hydrocarbons are strong optical absorbers in the 2.8- to 3.8-μm wavelength region, an HF/DF laser was chosen for the initial investigation. H_2O, OH, and other species have been observed from both coated and uncoated optical surfaces. Surface mapping of adsorbed H_2O with a 121-μm focal spot shows considerable variation with spatial position. This effect may be associated with surface microcracks and other defects which may precipitate laser damage. Possible applications are characterization of laser optical components and laser cleaning of optical surfaces prior to film deposition.

Key words: laser conditioning; laser-induced desorption; optical surfaces; selective damage; surface contamination; surface defects; water desorption.

Introduction

Although laser desorption analysis of optical materials has been occasionally reported [1, 2, 3],[1] application to pulsed laser damage investigations has not been explored. It is known from various studies that water is a common contaminant of optical surfaces and coatings [4, 5, 6, 7]. The tenacity of water or hydroxide ions at elevated temperatures has also been demonstrated [8]. Indirect evidence for a relationship between adsorbed water and pulsed laser damage was presented at this conference three years ago in connection with the N-on-1 (N/1) conditioning of single-layer antireflection coatings at 2.7 μm [9]. After exposure to several nondamaging pulses, the damage threshold of a NaF film was nearly doubled, apparently as a result of water desorption. In other work, it has been speculated that impurity aggregates may be responsible for spatially selective or isolated-spot damage [10, 11]. The ability to detect and characterize these aggregates by laser desorption would greatly enhance our understanding of this serious problem in optical component technology.

The present paper reports results of a preliminary pulsed laser desorption study on various optical materials and representative components, with an emphasis on adsorbed water. Nominal wavelengths used are 2.7 and 3.8 μm, which lie, respectively, inside and outside of the strong optical absorption band corresponding to the O-H molecular stretch frequency. The principal objectives here are to better understand the role of water in laser-induced damage and to explore laser desorption analysis as a possible nondestructive characterization technique.

Experimental Apparatus and Method

The experimental setup used in this work is an adaptation of the pulsed infrared laser damage facility at the Naval Weapons Center (NWC) [12], which has been described several times at this

*Work sponsored by the Office of Naval Research Special Research Opportunities Program and by Navy Independent Research Funding.

[1]Numbers in brackets indicate the literature references at the end of the paper.

conference. The desorption apparatus, which is shown in figure 1, consists basically of a quadrupole mass analyzer (QMA) and a glass collection chamber C', both mounted within the original UHV damage chamber C [13]. The mass analyzer is equipped with an ionizer I to permit detection of desorbed neutral molecules as singly charged positive ions. To minimize inadvertent contamination or desorption, the ionizer filament is obscured from the sample S, thus requiring a desorbed molecule to follow an indirect path P in order to be detected. Maintenance of a low background pressure in C' is critical for adequate sensitivity. This is accomplished by making C' of glass and providing a noninterfering aperture for laser irradiation and desorption. Mounting the samples external to C' provides sample outgassing directly into C during bakeout and permits the convenience of an eight-station carousel. The working pressure in C' is estimated to be in the mid- to low-10^{-10} torr range after outgassing of the QMA and C', while the ion gauge pressure in C is below 1 x 10^{-10} torr.

Desorption is induced by the pulsed laser beam B, which is focused by the 9-in. focal length BaF_2 lens L and admitted through the salt window W. A narrow, low power He-Ne laser beam B' along the axis of B is used for alignment and focus control in conjunction with the 20X filar microscope M. The microscope is also used to observe any laser damage that may occur. Subtle changes in surface texture can be monitored by changes in the appearance of the He-Ne scattering.

The time dependence of the 2.7-μm laser pulse and corresponding mass 18 desorption pulse are shown in figure 2. The sample in this example is Hawshaw-polished CaF_2 which had no special treatment other than the 250°C, 8-hr bakeout. The rise time of the desorption pulse is limited by that of the analyzer. The decay is determined by the time required for the desorbed gas to pump or diffuse from C' to C through interstices around the QMA, W, and S. As shown by the figure, this time is several orders of magnitude longer than the laser pulse.

Since the QMA is calibrated to read partial pressures directly and since the approximate collection volume is known, the peak value of a desorption signal can be used to estimate the corresponding total number of molecules desorbed. This number can then be used to estimate the desorbed average particle fluence, since the focal spot dimensions are known. Resulting desorption fluences are probably correct to within a factor of five in absolute value, while the uncertainty in relative fluences is estimated to be only about 25%. The principal sources of error and uncertainty in absolute fluence values are (1) the collection volume, assumed to be 0.75 ℓ, (2) pumping from the collection chamber, which is neglected here, (3) alteration of molecular species due to cracking and recombination, also neglected, and (4) the distribution of desorption fluence within the approximately Gaussian spatial profile. For present purposes, desorption was arbitrarily taken to be uniformly distributed over the half-maximum area of the essentially Gaussian spatial profile.

Desorption measurements were made with the lens L focused either at the sample surface or 0.5 in. behind the surface. The latter, defocused condition provides a larger and more uniform signal at the expense of spatial resolution. Spot diameters at the maximum/e^2 point of the spatial profiles at 2.7- and 3.8-μm wavelengths were determined from pinhole scans to be 121 and 135 μm, respectively, at focus. Corresponding values in the defocused condition are 380 and 522 μm. Energy densities on-axis were inferred from measured total pulse energies by integration of the spatial profile data.

Desorption Results and Discussion

Mass 18 desorption fluences obtained at 2.7 μm for the polished CaF_2 sample are plotted vs axial energy density in figure 3. Each data point represents a single shot on a fresh site (1/1) in either the focused or defocused condition, as indicated. No flash or permanent damage visible by Nomarski microscopy were detected on any shot represented here, although a change in He-Ne scattering was observed on some shots with the defocused beam. As seen in the figure, the focused data points are much more scattered, suggesting a spatially nonuniform distribution of adsorbate on this scale of resolution. Although considerable data scatter remains even in the defocused case, a nonlinear dependence of desorption fluence on energy density is clearly indicated. The slope which fits this data best is 2.2 on the double logarithmic scale shown here. Unfortunately, direct comparison of this relationship with adsorption theory or measurements [8] is difficult, since the temperature excursions of the surface are not well known. The situation is complicated by the apparent nonuniform adsorbate distribution, since significant localized temperature variations resulting from strong optical absorption in the adsorbate are highly probable.

Figure 4 compares the defocused 2.7-μm data of the preceding figure with corresponding data obtained at 3.8 μm. Although the effect is rather small, the desorption efficiency at 2.7 μm is slightly greater, based on the trend indicated by the solid line. The wavelength dependence is perhaps smaller than one might expect, considering the significantly greater optical absorption of water molecules at 2.7 μm. Repeating these measurements at mass 16 results in the data shown in figure 5. The desorption efficiency is equivalent here at both wavelengths, assuming that the same 2.2 power law applies. Possible sources of mass 16 are either CH_4, which is a measurable background gas in the UHV system, or O. In neither case does the optical absorption depend strongly on the two

wavelengths in question, so that the results in this example are as expected. The mass 16 signal observed here is much too large to be fully accounted for by cracking of H_2O molecules to O^+ ions, the cracking fraction being only a few percent in this case [14].

Smaller amounts of water were obtained from a half-wave- (at 2.7 μm) thick SiO film on a CaF_2 substrate, as indicated in figure 6. Masses 17 and 18, corresponding to OH and H_2O, respectively, were measured at 2.7 μm in the defocused condition. The data scatter is somewhat less than from bare polished CaF_2, suggesting a more uniformly distributed adsorbate. The slope, which is therefore more precisely defined in this case, is 2.6. The mass 18 signal is greater than the mass 17 signal by a factor of three, which agrees very well with the cracking pattern of the H_2O molecule. This indicates that H_2O was desorbed directly in this case. A less likely alternative is that OH^- ions were desorbed and completely recombined with H before entering the ionizer.

The remaining samples and mass numbers explored in this preliminary study are summarized in table 1, together with those discussed above. The values in each case represent the maximum fluence produced by any recorded shot which did not result in damage. Since these values are given without regard to energy density or focus condition, they are only roughly indicative of the amount of adsorbate present. The relative values given for mass 18 are, in fact, consistent with those obtained by a nuclear resonance technique [7] where such data are available. It is noteworthy that only the two mirror samples did not ordinarily produce a water desorption signal. However, water desorption was seen from the enhanced reflection coated mirror in a lightly stained area. Since this sample was cleaned with acetone, the stain is probably a "water spot" resulting from condensation which occurred when the acetone evaporated. No special cleaning was performed on any of the window samples, except for etching of one of the KCl samples.

Table 1. Summary of samples and mass numbers investigated, together with maximum desorption fluences observed. The ThF_4 and SiO films were single layers of half-wave thickness at 2.7 μm and were deposited on CaF_2. The multilayer enhanced reflection (ER) coating was deposited on Mo with ZnS as the top layer. The multilayer antireflection (AR) coating was deposited on bulk ZnSe with ZnSe as the top layer. Both multilayers were optimized for 3.8 μm. The last sample listed is diamond-turned bulk Cu.

Mass number and species / Sample	Maximum molecules/nm² on any shot					
	14 CH_2,N	15 CH_3	16 CH_4,O	17 OH	18 H_2O	19 F
Polished CaF_2	0.2	0.2	0.9	3.0	18.0	0.3
Polished KCl	---	---	---	---	0.2	---
Etched KCl	---	---	---	---	0.6[a]	---
ThF_4 film	---	---	---	0.9	23.0	0.05
SiO film	---	---	---	0.6[a]	0.8[a]	---
$(ZnS/ThF_4)^4$ ER coating	---	---	---	---	< 0.1[b]	---
$ZnSe/ThF_4$ AR coating	---	---	---	---	0.9	---
Diamond-turned Cu	---	---	< 0.02[a]	---	< 0.02[a]	---

[a]Defocused beam
[b]0.3 obtained from stained area

Relationship to Laser Damage

Results of an N/1 desorption study on the CaF_2 sample indicate a definite relationship between water desorption and laser damage at 2.7 μm. This can be demonstrated by two histograms, as shown in figure 7. The dashed line, which pertains to the scale on the right, represents the energy density in each of a sequence of eight shots on a single site. The solid line and left-hand scale show the corresponding cumulative water desorbed in the sequence. The data were taken in the focused condition and averaged over four sites to avoid selective bias. It is apparent from the leveling off of the solid line that most of the desorbable water had been removed after the fifth shot. The energy density of the fifth shot also corresponds to the single-shot (1/1) damage threshold within one standard deviation. This strongly suggests that the 1/1 damage threshold is governed by the amount

of desorbable water. Supporting this hypothesis is the fact that, after desorbing the water gradually, the damage threshold increases dramatically to a level greater than or equal to the minimum indicated. This data clearly tends to confirm our earlier explanation [9] for the N/1 conditioning effect. The data also supports laser desorption analysis as a viable nondestructive characterization tool that is directly related to the 1/1 laser damage threshold when governed by contaminants.

Conclusions

It may be concluded from this work that laser-induced desorption of water from optical surfaces and coatings is a common phenomenon. Window samples with exposed alkaline earth fluoride surfaces are particularly susceptible. The desorption is found to be spatially selective on a scale of 121 μm, particularly on polished CaF_2. Desorption becomes more uniform as the spot size is increased. The dependence on energy density is nonlinear, the desorbed fluence varying approximately as the energy density to the 2.5 power. Water is desorbed somewhat more efficiently at 2.7 than at 3.8 μm, although the difference is not as large as might be expected from the greater optical absorption at 2.7 μm. The N/1 conditioning effect at 2.7 μm reported earlier has been definitely related to water desorption. Also, there appears to be a relationship between the 1/1 damage threshold and the amount of water present. Based on these results, laser desorption analysis shows much promise as a nondestructive test for incipient pulsed laser damage caused by surface contamination. It may also prove useful for surface characterization related to laser cleaning and for detection of microcracks or other defects that act as contamination traps.

The authors wish to express their gratitude to J. B. Franck of NWC for measuring the spatial profiles and for assistance in operating the HF/DF laser. They wish also to thank T. E. Madey of NBS, V. E. Henrich of Yale University, and T. M. Donovan of NWC for helpful discussions.

References

[1] Levine, L. P.; Ready, J. F.; Bernal G., E. Gas desorption produced by a giant pulse laser. J. Appl. Phys. 38; 331-336; 1967.

[2] Winters, H. F.; Kay, E. Gas analysis in films by laser-induced flash evaporation followed by mass spectrometry. J. Appl. Phys. 43; 789-793; 1972.

[3] Temple, P. A.; Burge, D. K.; Bennett, J. M. Optical properties of mirrors prepared by ultra-clean dc sputter deposition. Glass, A. J.; Guenther, A. H., ed. Proceedings of the 8th annual symposium on optical materials for high power lasers; 1976 July 13-15; Boulder, CO. Nat. Bur. Stand. (U.S.) Spec. Publ. 462; 1976 December. 195-202.

[4] Green, A. K.; Bauer, E. Evolution of water from alkali halide single crystals. J. Appl. Phys. 39; 2769-2773; 1968.

[5] Palik, E. D.; Gibson, J. W.; Holm, R. T.; Hass, M.; Braunstein, M; Garcia, B. Infrared characterization of surfaces and coatings by internal-reflection spectroscopy. Appl. Opt. 17; 1776-1785; 1978.

[6] Temple, P. A.; Decker, D. L.; Donovan, T. M.; Bethke, J. W. Measured thin film absorption at the air-film interface, the film bulk, and the film-substrate interface. Glass, A. J.; Guenther, A. H., ed. Proceedings of the 10th annual symposium on optical materials for high power lasers; 1978 September 12-14; Boulder, CO. Nat. Bur. Stand. (U.S.) Spec. Publ. 541; 1978 December. 37-42.

[7] Donovan, T. M.; Ashley, E. J.; Franck, J. B.; Porteus, J. O. Hydrogenated amorphous silicon films: preparation, characterization, absorption, and laser-damage resistance. This proceedings.

[8] Barraclough, P. B.; Hall, P. G. The adsorption of water vapour by lithium fluoride, sodium fluoride and sodium chloride. Surf. Sci. 46; 393-417; 1974; Adsorption of water vapour by calcium fluoride, barium fluoride and lead fluoride. J. Chem. Soc. Faraday Trans. 171; 2266-2276; 1975.

[9] Porteus, J. O.; Donovan, T. M.; Jernigan, J. L.; Faith, W. N. Multithreshold evaluation of 100-nsec pulsed laser damage to coating materials at 2.7- and 3.8-μm wavelengths. Glass, A. J.; Guenther, A. H., ed. Proceedings of the 10th annual symposium on optical materials for high power lasers; 1978 September 12-14; Boulder, CO. Nat. Bur. Stand. (U.S.) Spec. Publ. 541; 1978 December. 202-211.

[10] Seitel, S. C.; Porteus, J. O.; Decker, D. L.; Faith, W. N.; Grandjean, D. J. Effect of surface preparation methods on laser-induced pitting of Cu mirrors at 10.6 μm wavelength. IEEE J. Quantum Electron. 17; 2072-2077; 1981.

[11] Seitel, S. C.; Franck, J. B.; Williams, G. D. Selective and uniform laser-induced failure of antireflection-coated $LiNbO_3$. This proceedings.

[12] Porteus, J. O.; Decker, D. L.; Faith, W. N.; Grandjean, D. J.; Seitel, S. C.; Soileau, M. J. Pulsed laser-induced melting of precision diamond-machined Cu, Ag, and Au at infrared wavelengths. IEEE J. Quantum Electron. 17; 2078-2085; 1981.

[13] Porteus, J. O.; Soileau, M. J.; Bennett, H. E.; Bass, M. Laser damage measurements at CO_2 and DF wavelengths. Glass, A. J.; Guenther, A. H., ed. Proceedings of the 7th annual symposium on optical materials for high power lasers; 1975 July 30-31; Boulder, CO. Nat. Bur. Stand. (U.S.) Spec. Publ. 435; 1976 April. 207-215.

[14] Craig, R. D.; Harden, E. H. The interpretation of mass spectra in vacuum measurement. Vacuum 16; 67-70; 1965.

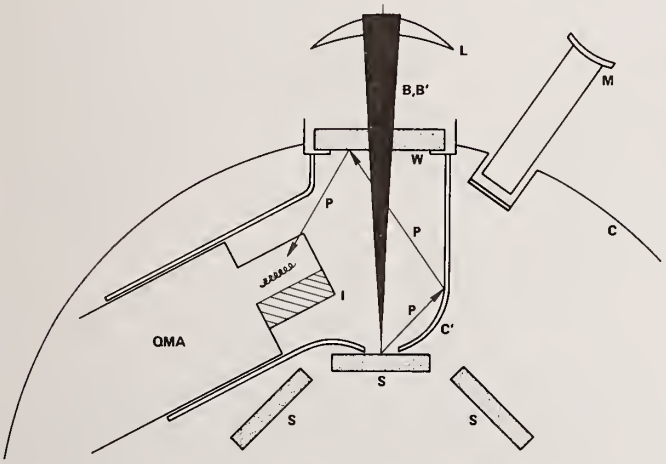

Figure 1. Schematic of laser desorption apparatus used in conjunction with the laser damage facility. The various components are identified and described in the text.

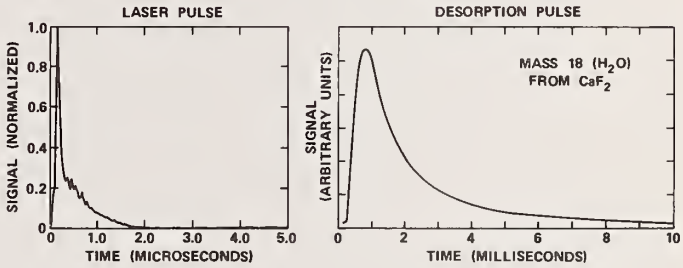

Figure 2. Comparison of 2.7-μm laser pulse and desorption pulse from polished CaF_2. The analyzer was tuned to mass 18, and the laser beam was focused on the sample surface.

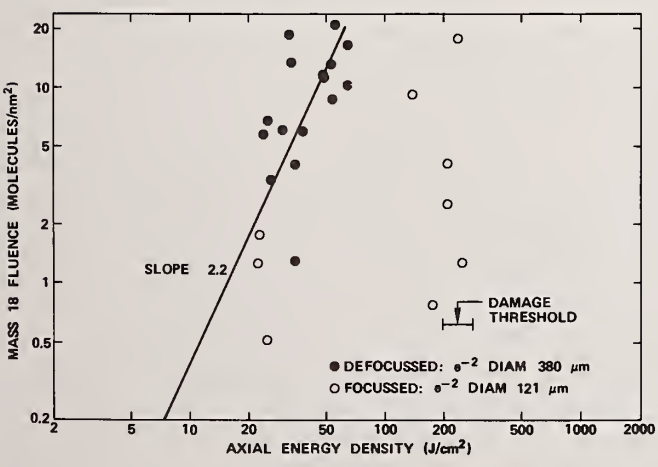

Figure 3. Comparison of mass 18 desorption from polished CaF_2 under different focal conditions. The 1/1 damage threshold corresponding to flash and visible surface damage is indicated, together with its standard deviation. Only 1/1 data where no damage was observed is plotted.

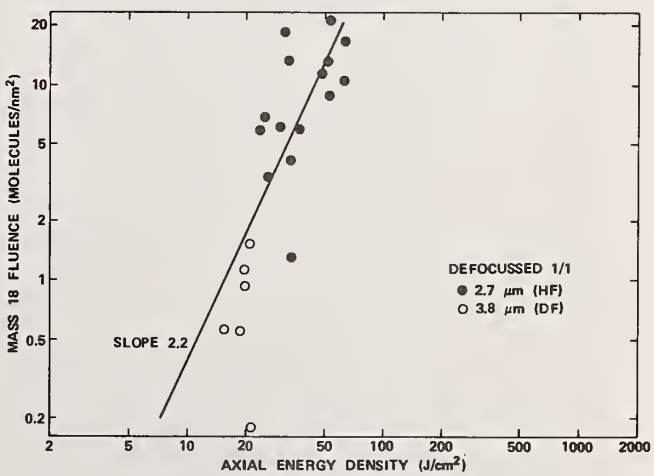

Figure 4. Comparison of 1/1 mass 18 desorption from polished CaF_2 at two wavelengths, using a defocused beam. The solid line with slope 2.2 represents the trend of the 2.7-μm data. No damage was observed with the beam defocused.

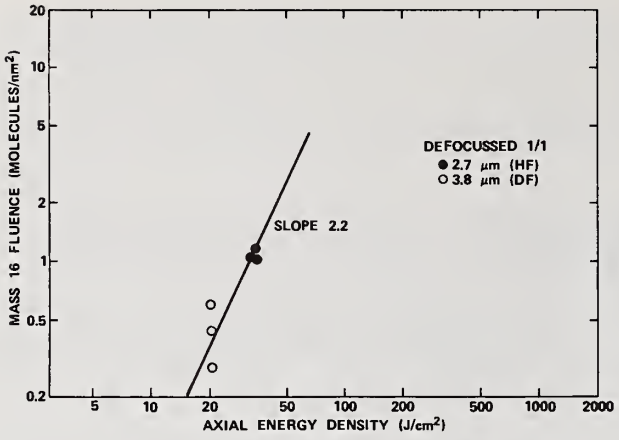

Figure 5. Comparison of 1/1 mass 16 desorption from polished CaF_2 at two wavelengths, using a defocused beam. The solid line is drawn through the 2.7-μm data with the same slope as in the preceding figure.

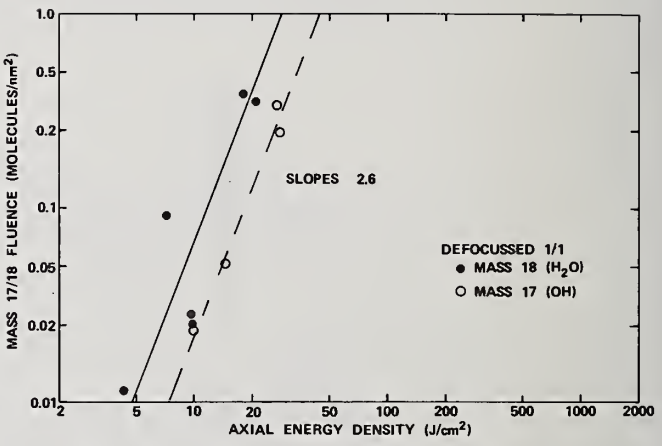

Figure 6. Mass 17 and 18 desorption signals (1/1) from a single-layer SiO film at 2.7 μm, using a defocused beam. The solid (dashed) line represents the trend of the H_2O (OH) data.

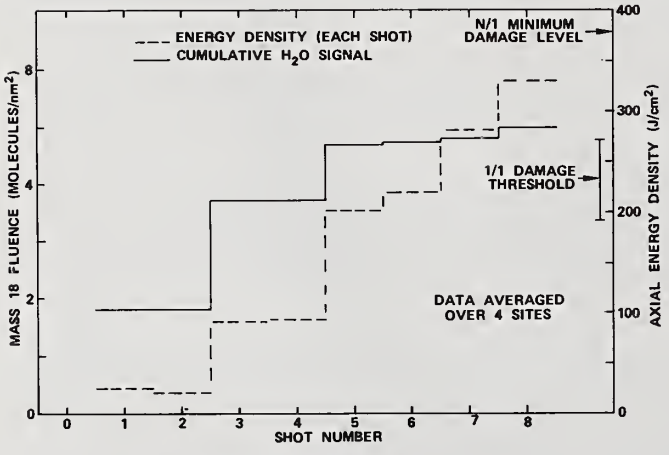

Figure 7. N/1 desorption from polished CaF_2 at 2.7 μm. Cumulative H_2O desorption (solid line) is compared with shot-by-shot energy density (dashed line). The 1/1 damage threshold is also shown for comparison. The N/1 damage level shown is the minimum found in data from many sites and occurred on the second shot.

The suggestion was made to analyze the data using an Arrhenius rate equation model where the log of the signal is plotted versus the reciprocal temperature. A straight line should be obtained, the slope of which would give the activation energy. The question was asked about the fluence of OH^- removed from the surface. The author pointed out that caution must be used since there is OH^- in the ionizer. In answer to another question, the author pointed out that measurements were all done at room temperature, so far. Many interesting measurements remain to be done with this instrument.

Electrostatic Technology for Control of Dust and Hydrocarbon Vapors in High Power Laser Systems

Stuart A. Hoenig, Professor

Department of Electrical Engineering
University of Arizona
Tucson, Arizona 85721

The application of electrostatic techniques has been investigated as a repulsion system to keep dust off mirrors that might be used in high power laser systems. A demonstration unit for a 30 cm mirror was built and shipped to Kirtland Air Force Base, New Mexico as part of the program.

Key words: contamination; dust; electrostatics; lasers; mirrors; telescopes.

1. Introduction

Studies with high power laser systems indicated that the presence of minute amounts of dust on optical components can result in severe damage to the reflecting surface when the laser is turned on. Recognizing that military operations cannot take place in a dust free environment, the United States Air Force supported a study of electrostatic technology as it might be applied to charge dust and "push" it away before it can deposit on an optical surface.

Another facet of the program concerned an examination of how this technology might be applied to larger (8 meter) mirrors in space environments, where the dust may be complicated by other contaminants (e.g., water) desorbed from the structural components or micrometeorites traveling a high velocity with respect to the spacecraft.

The primary objective was the development and testing of a dust repulsion system for a 30 cm mirror. This unit was to be shipped to Kirtland Air Force Base at the end of the on-campus test program.

A secondary objective was the investigation of technology that might be used for optical components in an earth orbiting space vehicle where the size of the elements involved precluded the use of liquid cleaning systems or the simple unit that was developed for the 30 cm mirror. Complicating factors to be aware of in the analysis included the presence of water vapor and/or chemicals desorbed from the vehicle structure and micrometeorites in the orbital environment.

2. Background Development and Parametric Investigation

The original idea for the dust repulsion system was based on earlier work performed under an Environmental Protection Agency contract [1]. In figure 1, an example of a simple repulsion system is shown; figure 2 shows the unit OFF and ON. When the system is ON, the smoke (ammonium chloride), at a flow velocity of some 100 m/min, was pushed backwards.

To adapt a technology of this type for mirror protection, a number of variables and possible designs must be considered. Typical questions were: (a) What is the optimum arrangement, in terms of needle-to-needle spacing, needle-to-screen distance and screen opening dimensions?, and (b) how shall the repulsion system be set up with respect to the mirror in order to achieve the optimum results in terms of dust repulsion, while at the same time remaining entirely out of the optical path?

To settle question a, it was necessary to build and test a number of needle-screen systems since there was no theory that could be used to predict the appropriate parameters. Fortunately, most of this work was performed under a program supported by the United States Army Tank-Automotive Command (TACOM), which had as its objective the development of a dust repulsion system for the turret blower on the M60-A1 main battle tank. The results of this work [2] demonstrated that a 25 mm needle-to-needle spacing and a 35 mm needle-to-screen distance would be most effective for dust repulsion, and these dimensions were chosen for the Air Force system.

The physical phenomena associated with a system of this type are of some interest in that there is an intense corona discharge from the high voltage (-17 kV) needles to the grounded screen as shown in figure 1. This generates a large number of electrons that, in turn, attach to oxygen molecules to produce negative molecular ions. These ions are pushed through the open mesh of the grounded screen

and produce the "electric wind" that helps keep back the dust particles. The ions serve an additional purpose in that they charge incoming dust particles, thereby encouraging their repulsion by the electrostatic field that penetrates the grounded screen. (This is an important factor because the large, 25 mm, screen openings allow the electrostatic field to penetrate and help form a barrier against dust particles with a negative charge.)

Another program in the laboratory concerned an investigation of techniques for keeping dust off astronomical telescope components by charging the dust and forcing it to deposit on an oppositely charged and sticky collector. A separate part of the same program was oriented toward new cleaning systems that might be used on large telescope mirrors without removing them from the mounting system. Both of these investigations were of value to the Air Force study and details are discussed in the following sections. We suggest that while these parallel programs may have had somewhat different objectives there was enough crosstalk between the various studies to permit significant savings of time and money, to the advantage of the overall effort.

3. Experimental Results

Figure 3 shows a schematic drawing of the electrostatic dust repulsion system for the 30 cm mirror. The needle-screen array was designed to provide a significant charging and dust repulsion capability, while at the same time providing a large factor of safety for personnel in the vicinity.

One of the problems occurring in the testing of this new system was the development of experimental techniques to challenge the repulsion unit under conditions that approximated the actual conditions of service. One test of some interest was done in a 1 x 1 x 1 meter fiberglass box, as shown in figure 4. Earlier studies had indicated that an input voltage of -17 kV at 10 mA would provide adequate dust repulsion and these conditions were chosen for the initial experiments.

For the first test, a small quantity of AC Fine dust* was laid in front of the fan outlet inside the test cell. The cell was sealed and the fan was allowed to run for 10 hours. At the end of that time the system was opened and photographs were taken of the glass plate for comparison with earlier photographs taken before the test began.

The test was then repeated with the electrostatic system ON. After about 1 hour of operation a look into the test cell indicated all the dust had disappeared. The cell was opened and it became clear that the electrostatic dust repulsion system had not only kept the dust off the 30 cm glass plate, it had charged the dust and forced it to deposit on the interior walls of the chamber. This result was unexpected, but it implies that the electrostatic system can actually remove dust from an area rather than simply repelling it from a surface.

When the test cell was opened there was a strong ozone odor. It was noted earlier that the intense corona discharge would produce ozone, but this was not expected to be a problem in the proposed Air Force application. There was some evidence of an odor that one of the technicians identified as associated with the plasticizer used for construction of fiberglass tanks and it is suggested the ozone had attacked the interior wall of the test cell. There was also some evidence of a vapor deposit on the Plexiglas windows of the test cell, but not on the 30 cm glass plate suggesting that, here again, the electrostatic system had charged and rejected the material.

In view of the rapid loss of dust when the repulsion system was ON, it was decided to remount the small squirrel cage fan inside the fiberglass box and make provision for periodic injection of dust.

To demonstrate that the dust was actually kept away from the optical surface, a 30 cm glass plate was set up in the mirror mount with the idea that the plate would be photographed before and after the test to qualitatively measure the dust density. For these tests, one-half of the mirror was masked with paper while the other half was exposed to the ambient dust level in the chamber. Figure 5 shows photographs of the glass plate after the power OFF and power ON tests; in both cases the left-hand side of the glass plate was shielded and the right-side was exposed. In the power OFF case there was quite a bit of dust on the exposed side; with the power ON there were some large (80 to 100 micrometer) particles that could not be repelled by the electrostatic field, but there was an almost complete absence of smaller material indicating the unit had operated as expected.

For the next series of tests a medical nebulizer was utilized to generate oil smoke. The oil (UCON, from the Dow Chemical Company) was used because of its high flash point and the knowledge that

*AC Fine is the material normally used for testing air filters. It is a mixture of clay and silica ranging in size from 0.5 to 80 micrometers. The mass median diameter is 8 micrometers.

there is always the danger of accidental sparks that could ignite oil vapors. The resultant oil smoke consisted of very small (e.g., 1 micrometer) particles. Several accidental sparks did occur during the tests, but there was no indication that oil smoke had been ignited so it appears that the choice of the UCON material was appropriate.

The test itself was essentially a repeat of the previous work with dust, but it was found impossible to photograph the oil droplets on the glass plate. The plate was replaced with a 30 cm cardboard disc, painted white, and once again significant deposition was observed with the rejection unit OFF, but very little with the unit ON.

We felt these experiments demonstrated the ability of the system to reject dust and oil vapor in what might be called a "quiet environment." However, there was some interest in studies with significant ambient air movement where the motion of dust and smoke could be more effectively photographed. For these first experiments the system was set up in the laboratory so that dust could be dropped from a modified flour sifter to fall toward the 30 cm mirror.

Figure 6 shows two photographs taken of the test system with dust (AC Fine) falling toward the unit. In the upper photograph, the unit was OFF and the dust fell onto the 30 cm glass plate that simulates the mirror; in the lower photograph, the system was ON and the dust was rejected.

A second series was set up to meet the contract requirement concerning rejection of windborne dust. A small air moving system was used to provide the airflow and an ammonium chloride smoke generator was set up to permit flow visualization. In figure 7, two photographs of the system ON and OFF are shown, at a wind velocity of 300 FPM (91.2 m/min). When the system was ON the smoke was rejected and we feel this may be the limiting wind velocity for a device of this type where there is no possibility of any element in the optical path itself.

The experiments discussed above have demonstrated the qualitative characteristics of the repulsion system, and that the next step would involve more quantitative studies, using a laser dust measurement system designed and constructed by Professor William Wolfe's group in the University Optical Sciences Center.

3.1 Apparatus

The dust monitoring system is shown schematically in figure 8, and in a photograph in figure 9. The optical detector was a model SD-100-41-11-231 integrating photodiode, manufactured by Silicon Detector Corporation of Newbury Park, California; the electrical system is shown schematically in figure 10. The laser was a 2 mW, model 145-01 helium neon unit manufactured by Spectra Physics Incorporated, Mountain View, California; the laser light was chopped mechanically at a rate of 50 Hz.

3.2 Experimental Procedure

For this study, the repulsion system was returned to the 1 x 1 x 1 meter box. The laser light source and the optical detector were set up at the specular angle, but care was taken to insure the detector was off axis and did not "see" the specular reflected light. Personnel from Optical Sciences Center had suggested that the intensity of the scattered light would be the best measure of the build-up of dust on the optical surfaces.

For the initial studies, the electrostatic dust repulsion system was set up inside the 1 x 1 x 1 meter fiberglass box as shown in figure 9 with the idea that the dust injection and circulation system would be used to provide a dust environment. To monitor the dust collected on the "mirror" a plastic petri dish was cleaned, dried, and weighed in a microbalance. The dish was laid on the 30 cm glass plate that simulated the laser mirror; the light from the He/Ne laser was allowed to hit the dish, as shown in figure 9, where some dust had been suspended in the air to show the incident laser beam. This system was successful in that it demonstrated the ability of the detector to receive and measure light scattered by the dust in the dish. However, as the experiment was repeated, it was found that the polycarbonate petri dish acquired a strong, nonhomogeneous electrical charge that interfered with the deposition of a smooth layer of dust.

To solve this problem, a glass microscope slide was substituted for the petri dish and proved quite satisfactory. For each test the slide was cleaned, weighed, exposed to the dust while being illuminated by the laser system, weighed, cleaned and then weighed again to check on the original clean weight. In each case the change in optical scattering was measured just before the slide was removed, and the graph in figure 11 demonstrates the increase in slide weight versus the change in detector signal level.

These data have several interesting aspects. First, the system is quite sensitive, even in its present crude form, and it is interesting to speculate about the potential particle detection

capability without consideration of any variation in scattering with particle size. At present, the smallest division on the curve of figure 11 is 500 micrograms. If one assumes that system improvements would allow detection of a 1% change in scattered light, the effective sensitivity would be 5 micrograms. If it is assumed that this quantity of dust is spread uniformly over the 76 x 25 mm slide, the weight per unit area will be 2.6×10^{-6} kg/m^2. If it is assumed all of the particles are silica spheres 1 micrometer in diameter, weighing 1.6×10^{-15} kg each, there will be a total of 3.1×10^{6} particles or 1.6×10^{9} particles per square meter. If the laser beam is 1/16 inch (1.59 mm) in diameter it will have a cross-sectional area of 2×10^{-6} m^2. If the particle density on the surface is 1.6×10^{9} per square meter, the laser beam will actually detect some 3250 particles. For 10 micrometer particles the number would be proportionately smaller; ideally, only 3.25 particles would be in the laser spot.

Here, it should be emphasized again that the above analysis is highly speculative but it does suggest the laser system offers some potential for detection of dust deposition on optical surfaces. Discussion with personnel in the Optical Sciences Center has indicated that far more sensitive systems, using phase lock technology, have been evaluated and that more data can be provided if necessary.

Returning to figure 11, note that the curve becomes less steep at the 1 mg level. If one assumes, again, that all the particles are 1 micrometer silica spheres there will be some 6.3×10^{8} particles, each having a cross-sectional area of 7.8×10^{-13} m^2, to cover a total area of 4.9×10^{-4} m^2 or about 25% of the 1.9×10^{-3} m^2 available. This may represent the point at which absorption by particle-particle scattering occurs; but, for the moment, all that can be indicated is that the change in slope was repeatedly observed and may represent a phenomenon of some interest deserving further investigation.

This completed the studies of dust deposition with the repulsion system OFF. For the next investigation the dust injection and weighing process was repeated with the repulsion field ON. In this case, no increase in scattering signal was observed, but upon weighing the glass slide it was clear there had been a significant increase in slide weight. At first, this was puzzling; but upon examination of the slide it was clear that some particle agglomeration had occurred and that a number of the large agglomerates had fallen onto the collection slide. The problem here was twofold; in the test box the dust charge circulates around until it either falls out or sticks to the walls of the box. When the electrostatic repeller is ON, there will be agglomeration and some of the agglomerates will inevitably fall on the collecting slide. For this reason, it was decided to move the system out into the laboratory and compare a test slide placed on the center of the 30 cm glass plate with a similar slide that was placed in the same area.

The open air tests in the laboratory were quite successful. In one case, the slide that was exposed to the laboratory environment picked up some 2.06 mg of dust over a 24-hour period, while a similar slide in the protected area gained only 0.11 mg for a net improvement factor of 94.7%. The test was repeated a number of times with very similar results. We suggest that the only possible problem with the repulsion system is dust ingestion as discussed below.

In these experiments, it was interesting to note the electrostatic system had a significant suction capacity since air was pulled through from the back of the repulsion system and forced over the mirror, thereby keeping dust from depositing. This process was quite effective provided the ingested air was free of dust; if dust was present, it was agglomerated by the electrostatic system and fell onto the mirror. If the system is tested in a dusty environment, the back of the repulsion unit should be shielded with plastic to prevent ingestion of ambient dust. The plastic shield does reduce the electrostatic wind to a slight degree, but there is still a very noticeable electrostatic repulsion that keeps ambient dust off the mirror.

It would appear that electrostatic technology offers a simple and effective system for keeping float dust off optical components, without introducing any mechanical components that would block the light or interfere with operations. In this connection, a question was raised about radio frequency noise from the corona system. Tests with a commercial AM-FM receiver indicated there were no detectable signals over the 54-160 kHz AM band and the 88 to 108 MHz FM band. Certainly testing over the military band wavelength will be needed, but it is felt that, at worst, the problem will be no more severe than that observed with conventional spark ignition for internal combustion engines.

4. References

[1] Hoenig, S. A. Use of electrostatically charged fog for control of fugitive dust emissions. Env. Protec. Agency. (U.S.) PB-276 645; 1977 November. 81 p. Available from NTIS.

[2] Hoenig, S. A. Electrostatic dust repulsion. U.S. Army Tank-Automotive Command (U.S.) R&D TR No. 12572; May 1981. 52 p.

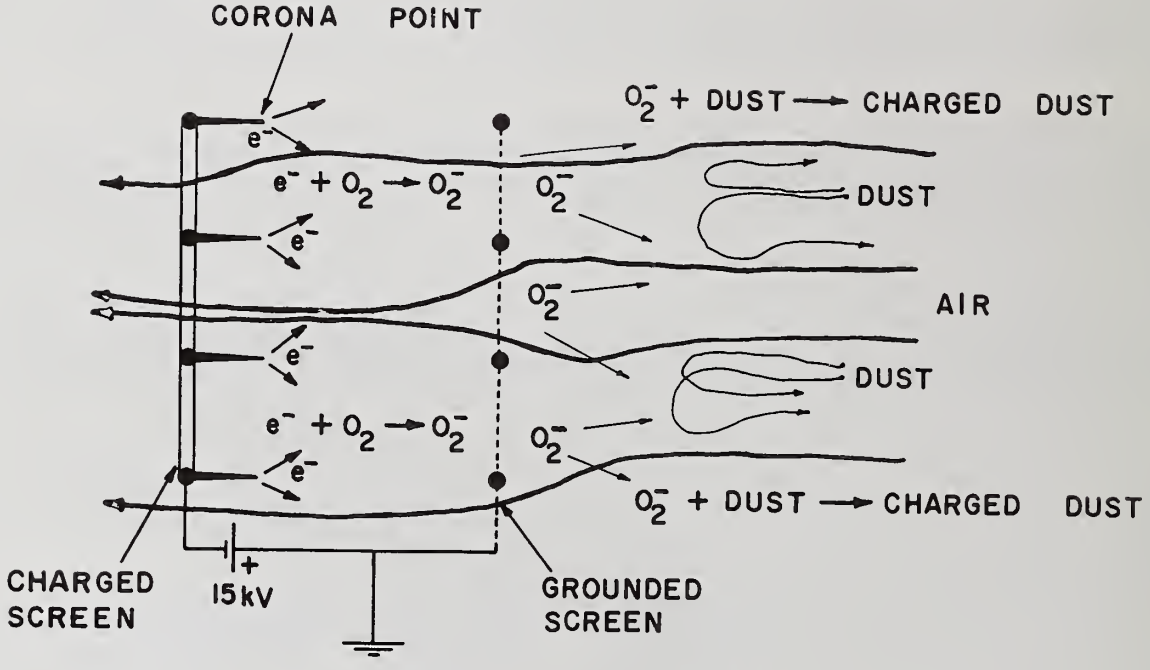

Figure 1. Schematic of electrostatic fence to reject dust and admit air.

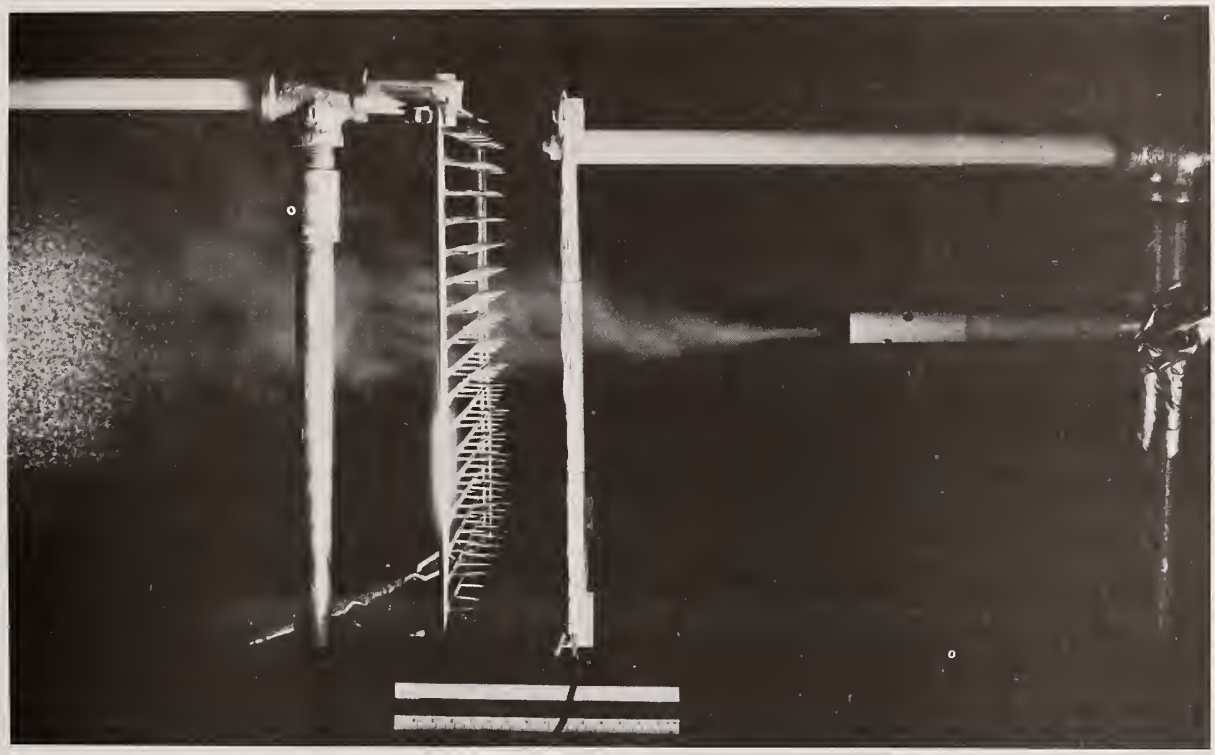

a. OFF

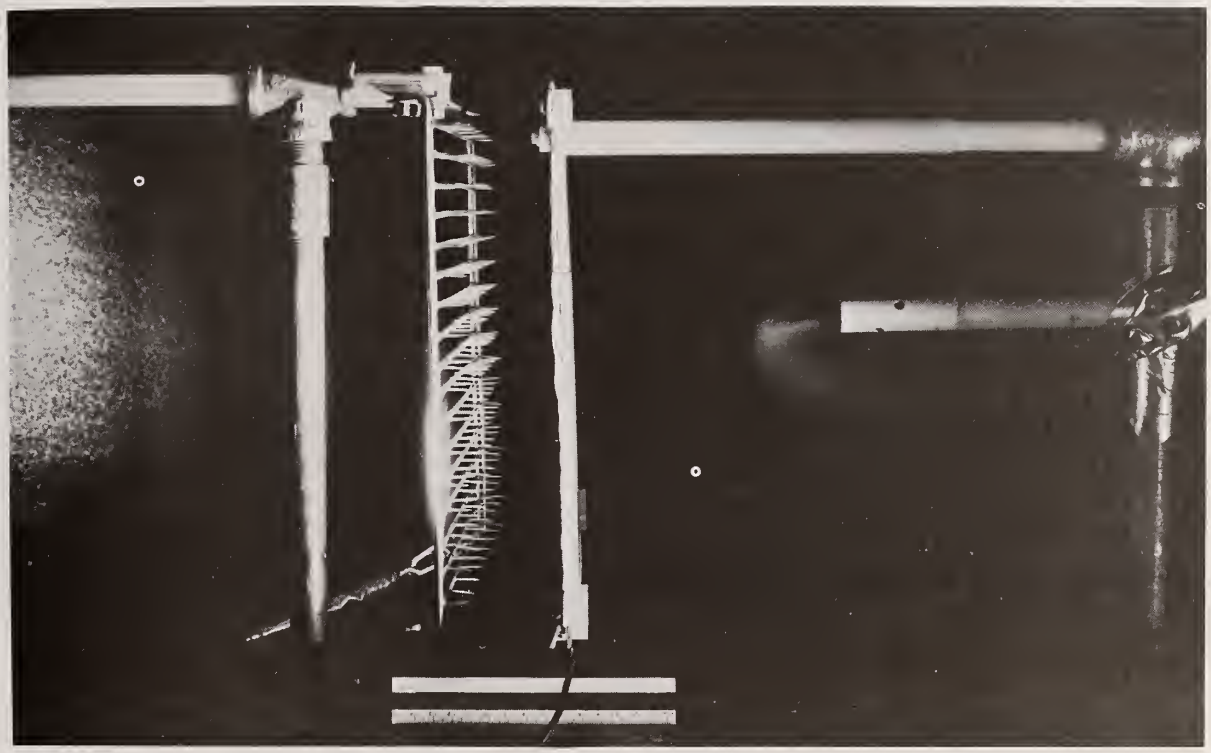

b. ON

Figure 2. Electrostatic fence: a. OFF; b. ON.

a. OFF

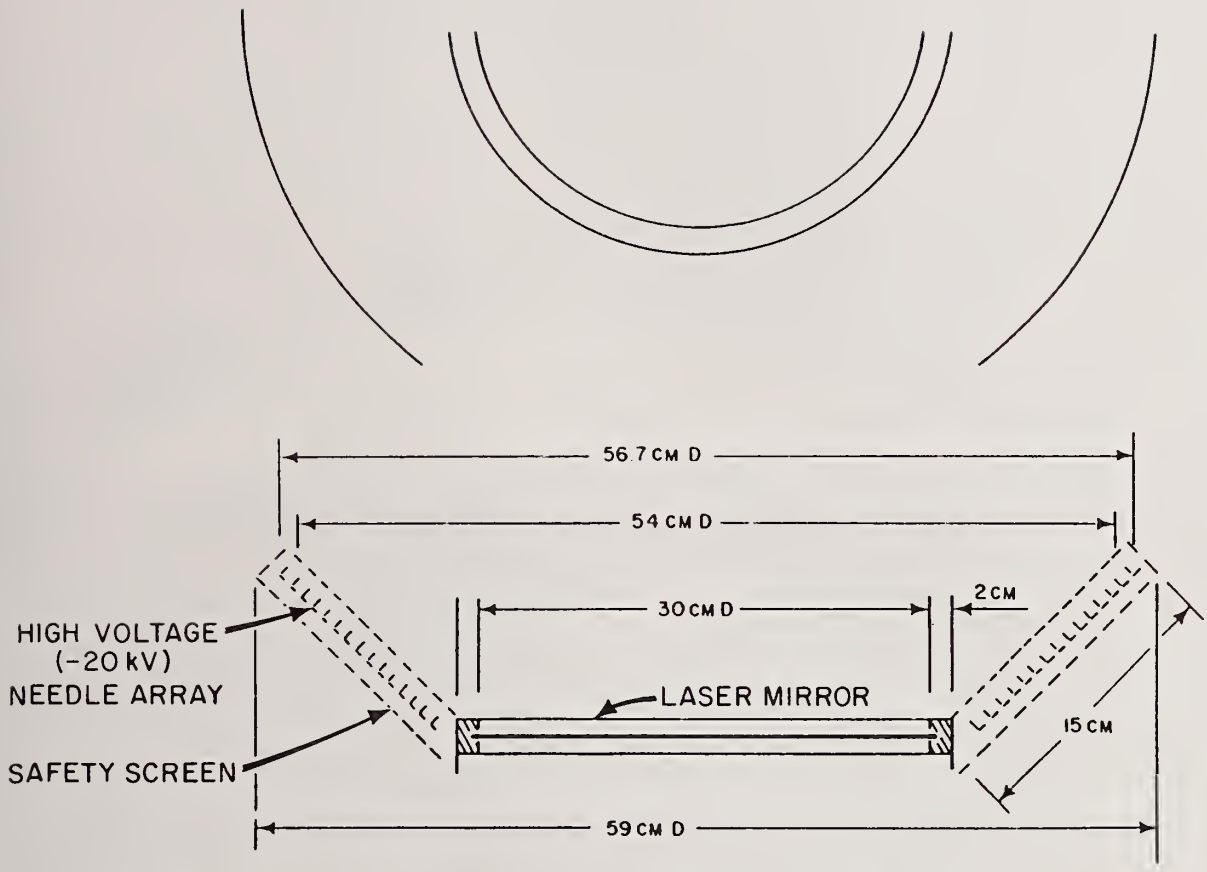

Figure 3. Schematic drawing of electrostatic dust repulsion system for 30 cm mirror.

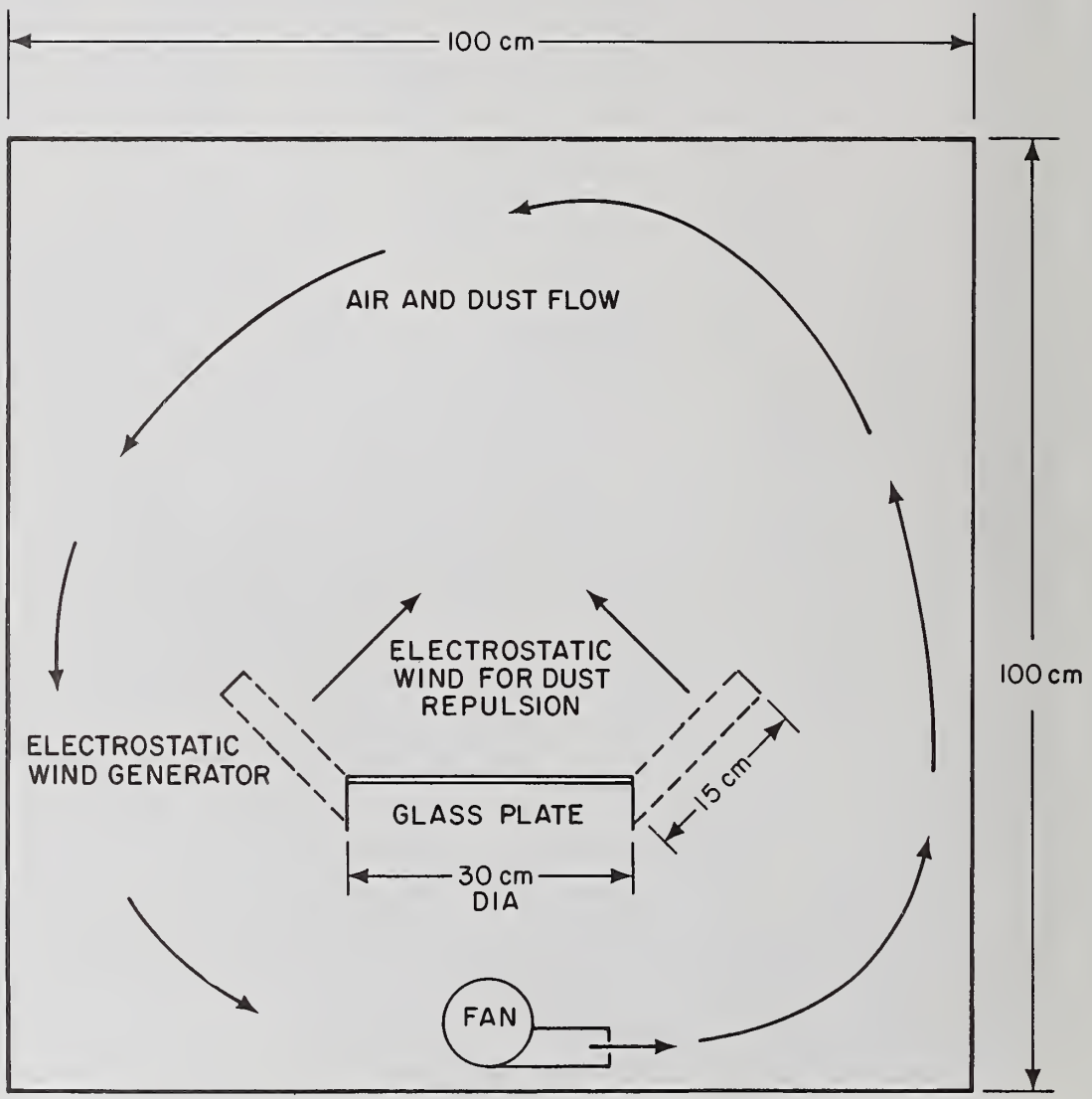

Figure 4. Schematic drawing of electrostatic dust repulsion test facility.

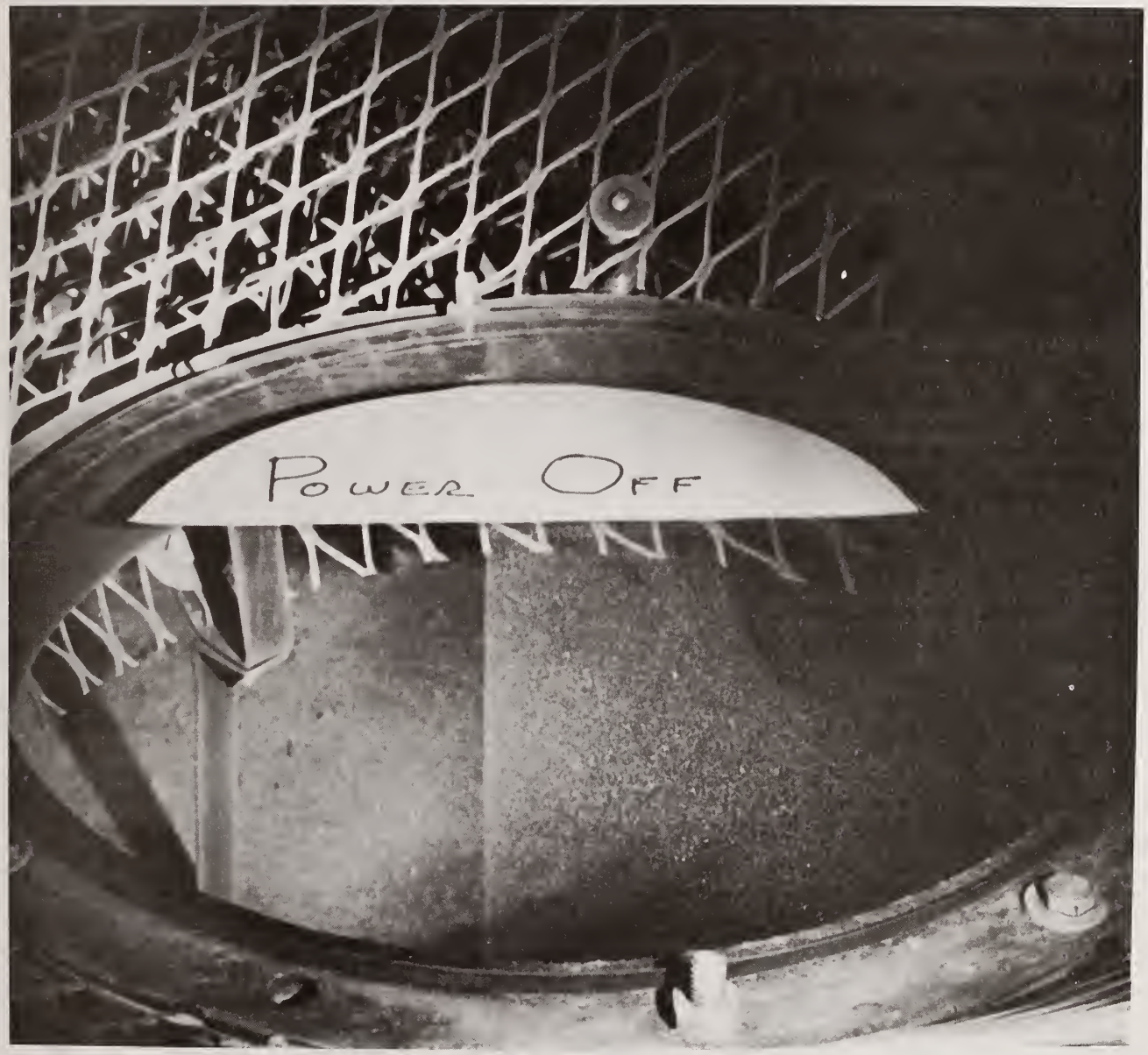

Figure 5A 30 cm Glass Plate After Dust Deposition Test Power Off

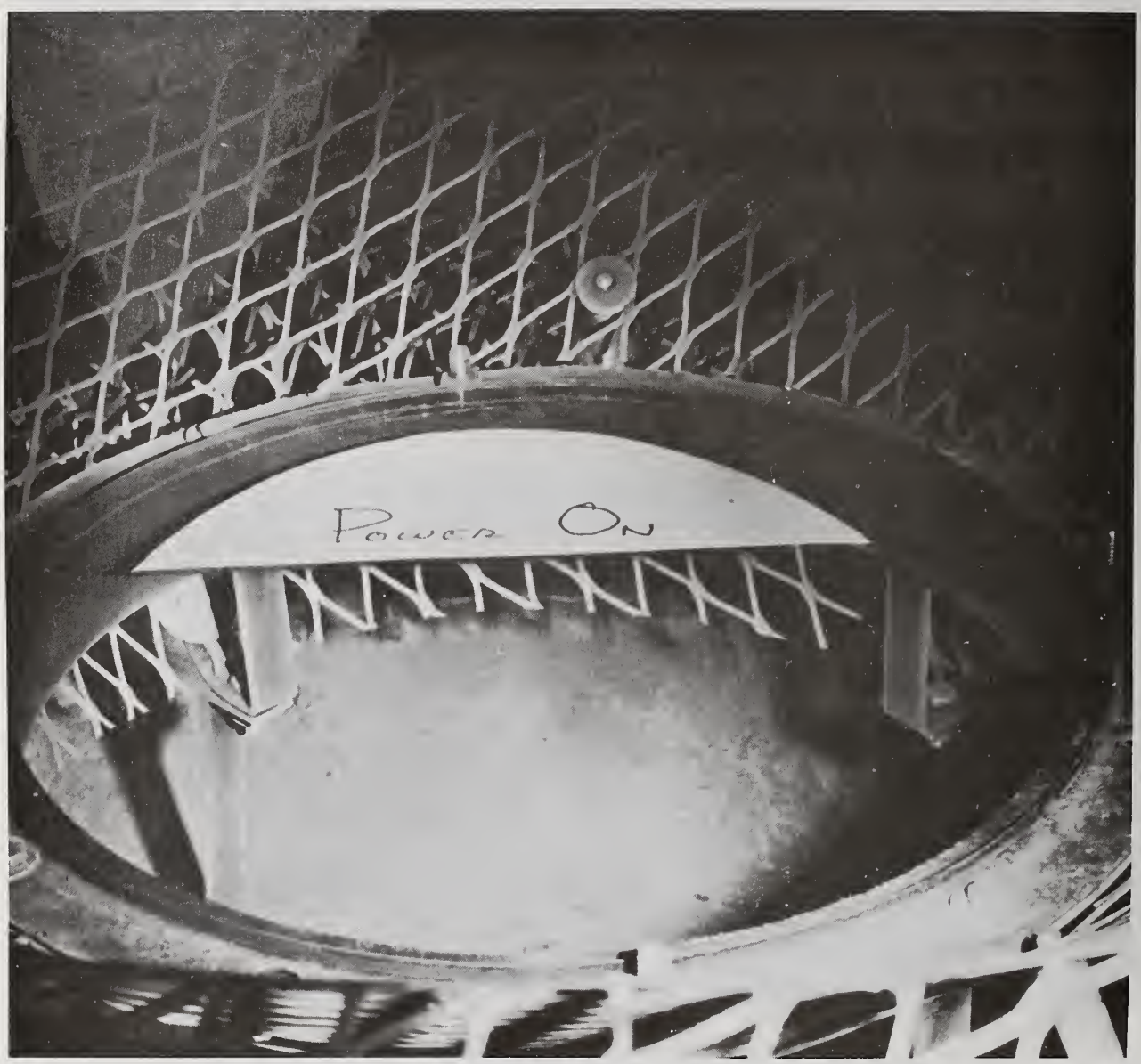

Figure 5B 30 cm Glass Plate After Dust
Deposition Test Power On

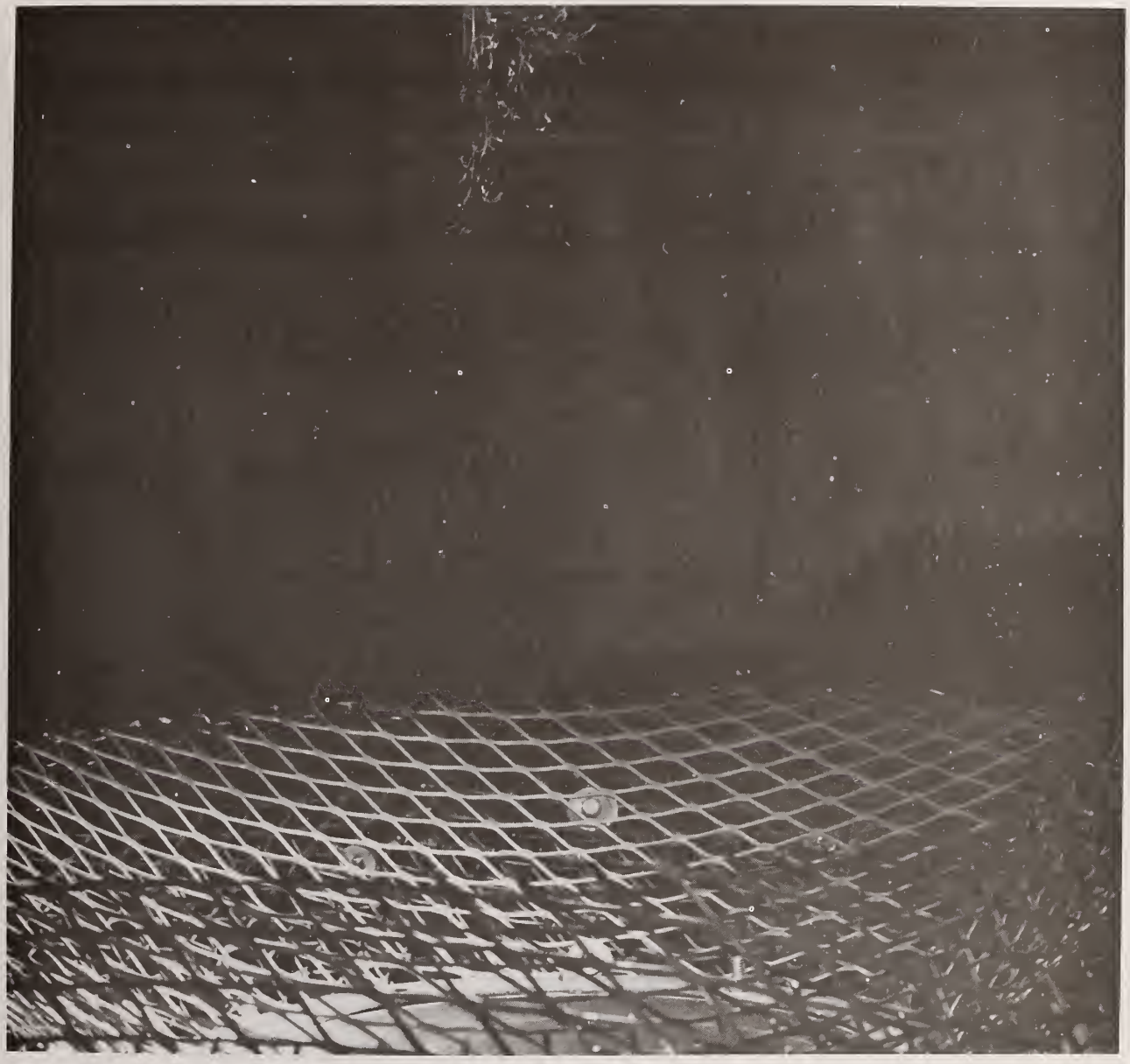

b. ON

Figure 6. Electrostatic repulsion system: a. OFF; b. ON

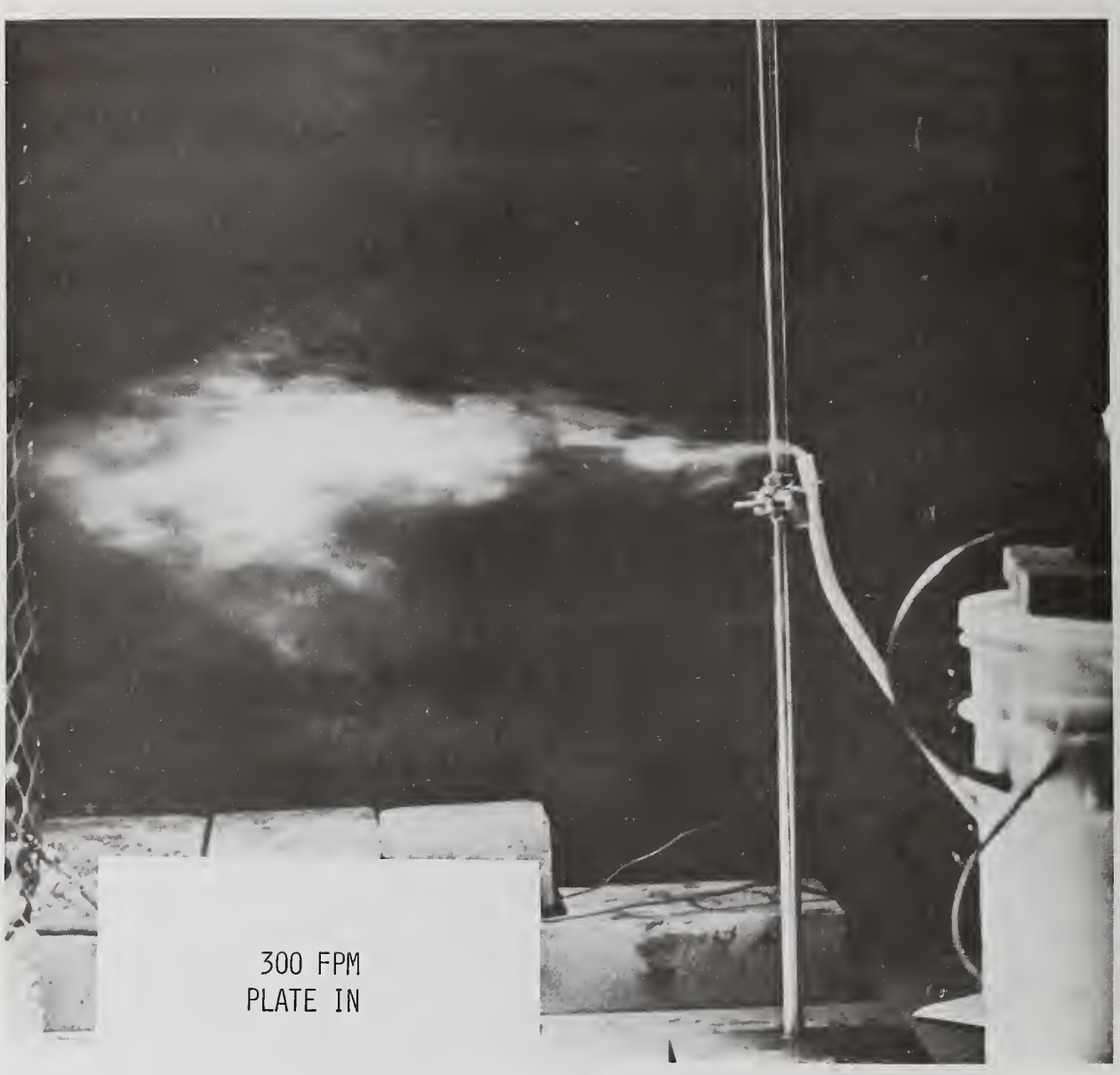

a. OFF

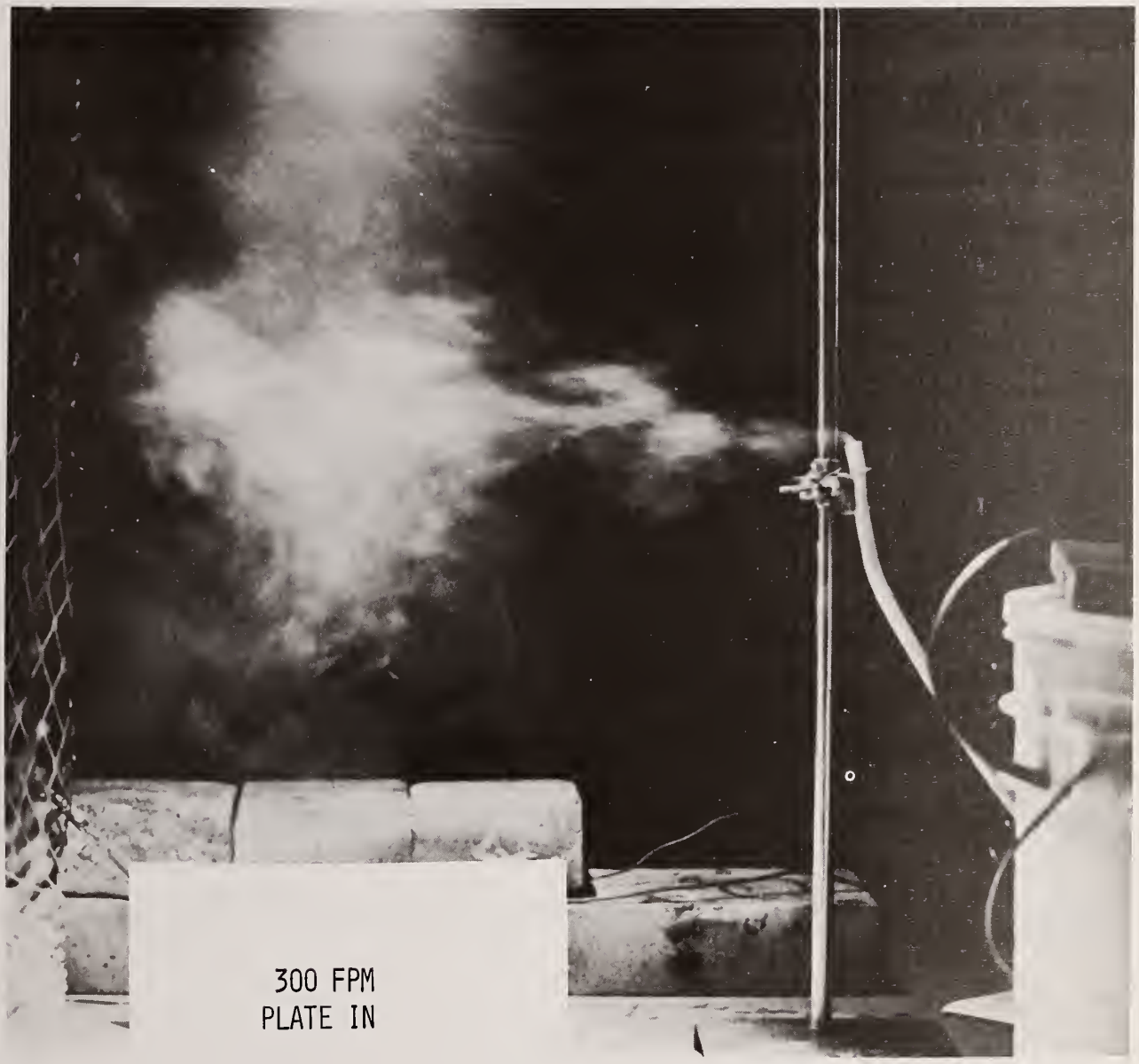

b. ON

Figure 7. Electrostatic repulsion system: a. OFF; b. ON.

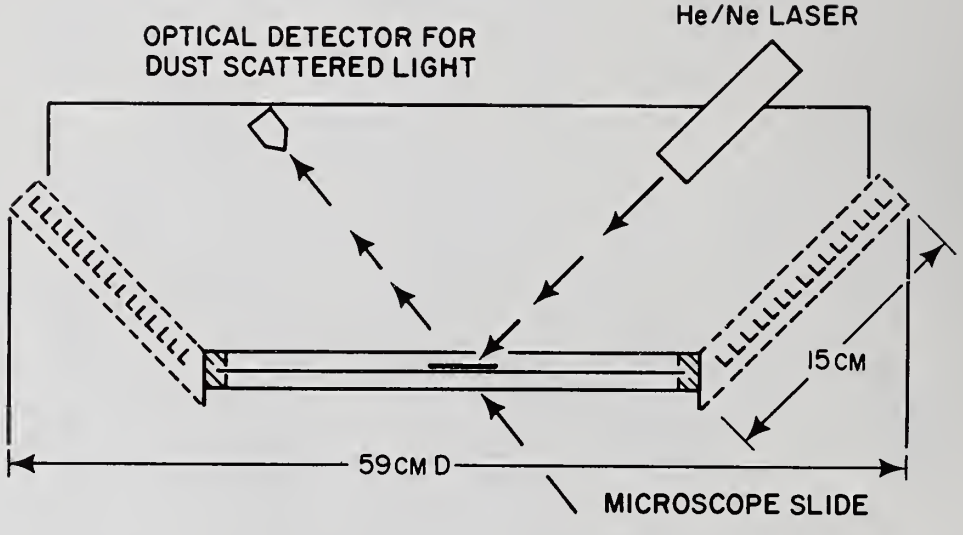

Figure 8. Schematic drawing of electrostatic dust repulsion system for 30 cm mirror with dust monitor.

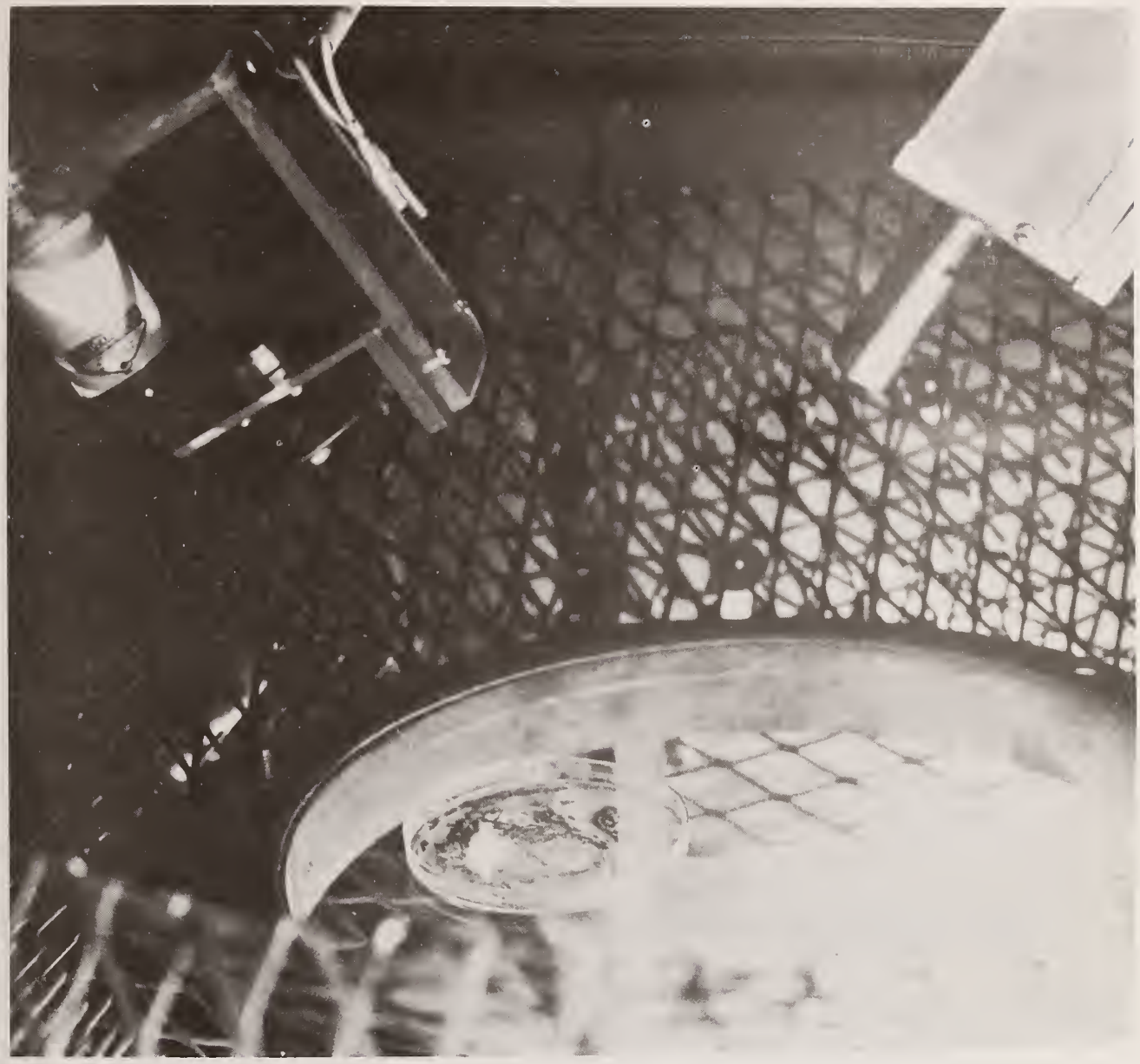

Figure 9. Laser dust monitoring system in action.

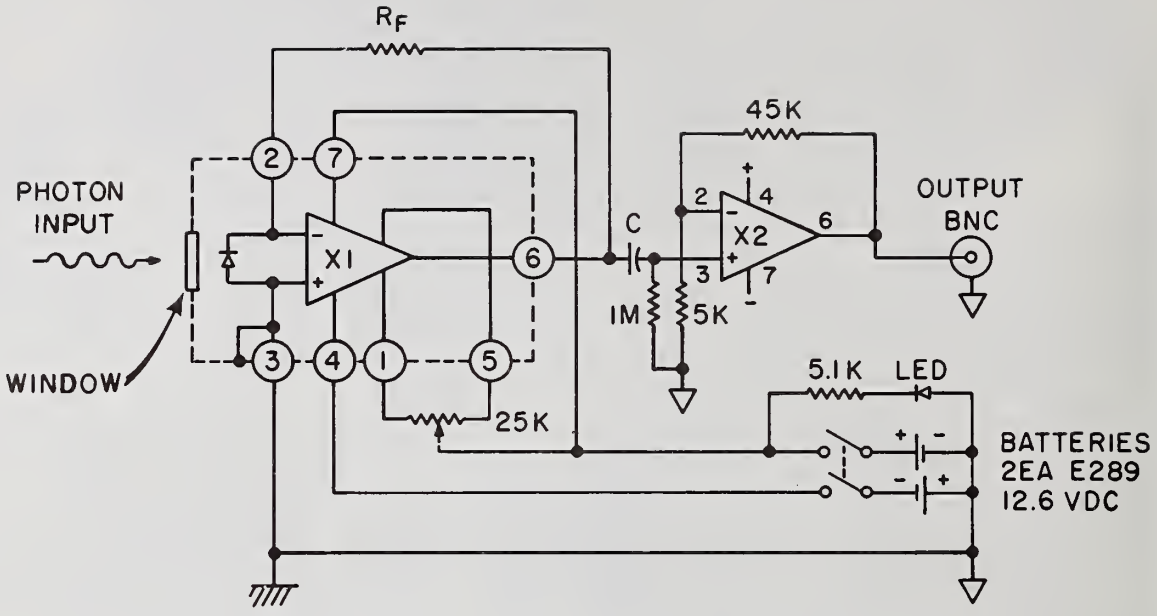

4. C DET. BY CHOPPER FREQ. (IMF FOR 50HZ)
3. X2-TYPE 741
2. X1 = SDC TYPE SD-100-41-11-231
1. SELECT R_F FOR DESIRED OUTPUT (1000M)

NOTE

C-010 SHEET2
SCHEMATIC

Figure 10. Electrical schematic for optical dust detection system.

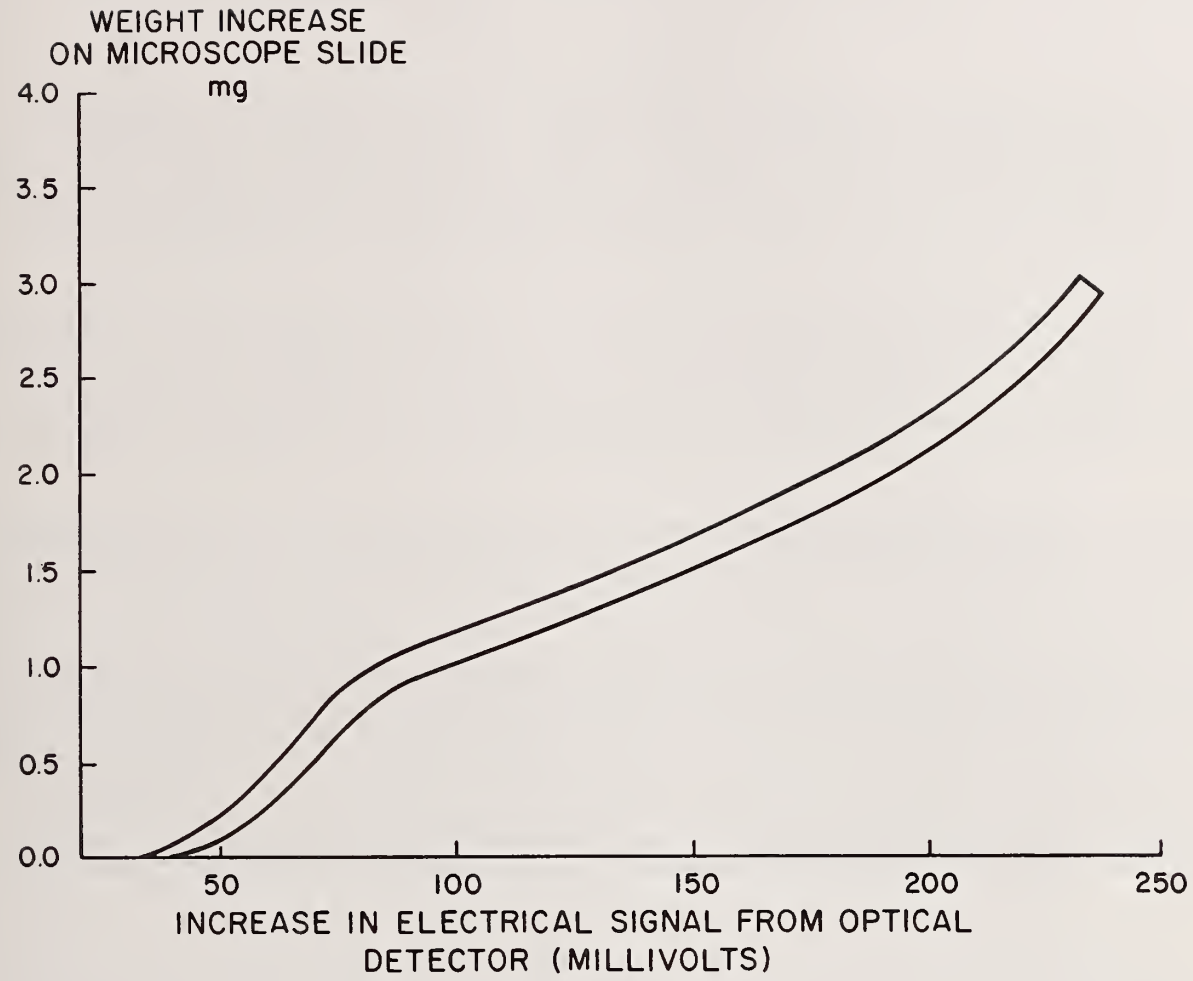

Figure 11. Laboratory data dust build-up vs. scattered light.

The question was asked whether these techniques should work in vacuum as well as in air. The author felt they should work very well in vacuum and could be used to prevent pinholes in thin-film-coated mirrors. The voltages used for the electric fence were 17 kV and 18 mA. The collectors run at 20,000 V, but the short circuit conductivity is very low, 0.3 μA, so there is no danger of shock to personnel.

Laser Mirror Operation at Cryogenic Temperatures*

D. L. Decker and V. A. Hodgkin

Michelson Laboratory, Physics Division
Naval Weapons Center, China Lake, California 93555

It has been suggested many times that operation of laser mirrors at low temperatures could result in significant performance improvements. Specifically for metal mirrors, the advantage perceived is in decreased absorption and increased thermal conductivity. For dielectric-enhanced mirrors, presumably a similar advantage would be present in lowering both the absorption of the initial metal film and perhaps lowering absorption in the dielectric films as well. From an engineering point of view, this proposition is not entirely academic, at least for space applications, where entirely passive methods of cooling could be employed.

This paper presents experimental absorptance vs wavelength and temperature data over the range from 1 to 10 μm and from room temperature to 80°K. Included in this study are silver samples prepared by different techniques including diamond single-point machining. Also included are similar data for a multilayer dielectric mirror. Theoretical interpretation of the performance of both mirror types is made with recommendations for actual use.

Key words: absorption; bare metal surfaces; cryogenic temperatures; dielectric-enhanced mirror; Drude theory; laser mirrors.

Introduction

The decrease in infrared absorption and increase in thermal conductivity of metals as the temperature is lowered is a consequence of the increase in mean-free path of the conduction electrons of the metal as the electron-phonon collision frequency decreases [1].[1] However, to obtain these results, the metal must be very pure and well ordered so that electron collisions with lattice imperfections will be the only limiting effect at very low temperatures. This paper presents data which demonstrate for the first time that useful improvements in performance for practical metal mirror surfaces can be achieved at cryogenic temperatures. Data are presented for evaporated thin film and diamond-machined silver which show optical absorptance in agreement with simple theory at temperatures down to 80°K.

Theory

The Drude theory of free-electron optical absorption has been shown to provide an accurate model of optical behavior of silver and other "good" metals in the infrared [2]. This is true not only at room temperatures but also at both elevated and cryogenic temperatures [3]. The complex dielectric constant $\varepsilon_1 + i\varepsilon_2$ is simply related to the plasma frequency, ω_p, and the electron relaxation time, τ [4]:

$$\varepsilon_1 = 1 - \omega_p^2/(\omega^2 + 1/\tau^2) \tag{1}$$

$$\varepsilon_2 = \omega_p^2/(\omega^2 + 1/\tau^2)\omega\tau \tag{2}$$

The plasma frequency and relaxation time can be related to other macro- and microscopic material parameters (cgs units),

*Work supported by the Defense Advanced Research Projects Agency.
[1]Numbers in brackets indicate the literature references at the end of the paper.

$$\omega_p^2 = 4\pi Ne^2/m^* \tag{3a}$$

$$\tau = m^*\sigma/Ne^2 \quad , \tag{3b}$$

where N is the electron concentration, m^* an effective electron mass, e the electronic charge, and σ the d.c. conductivity. The reflectance is simply given by Fresnel's relationship:

$$R = \left|(\tilde{\varepsilon}^{\frac{1}{2}} - 1)/(\tilde{\varepsilon}^{\frac{1}{2}} + 1)\right|^2 \quad . \tag{4}$$

If $(\omega_p\tau)^2 >> (\omega\tau)^2 >> 1$, which is true for silver, copper, and gold at near- and mid-IR wavelengths, then

$$R \cong 1 - 2/\omega_p\tau \quad . \tag{5}$$

If we assume that all incident light is either specularly reflected or absorbed, the absorptance A is simply 1 - R. The absorptance is then given by the following approximate expression:

$$A \cong 2/\omega_p\tau \quad . \tag{6}$$

The primary temperature dependence of the absorptance arises through the change in relaxation time with temperature. This dependence can be further described from changes in the macroscopic variable, σ, the d.c. conductivity. Figure 1 illustrates schematically the temperature dependence of $1/\sigma$, the electrical resistivity [1]. At temperatures on the order of the Debye temperature, T_D, $1/\sigma \sim T$. At very low temperatures, $1/\sigma \sim T^5$. For impure metals, the high temperature performance is unchanged, but at low temperatures, $T < T_D$, $1/\sigma$ approaches a minimum, "residual" value $1/\sigma_R$. To obtain significant benefit from cooling a metal mirror, the metal must be very pure and well ordered; this allows a small residual resistivity so that departure from linear behavior will occur only at very low temperatures. If we substitute eq (3b) into (6) and assume that $1/\sigma = \rho_0 + \rho_1 T$, the explicit temperature dependence of A is obtained:

$$A(T) = \frac{\omega_p}{2\pi}(\rho_0 + \rho_1 T) \tag{7a}$$

$$= A_0 + A_1 T \tag{7b}$$

$$\cong A_1 T \quad ; \quad T \geqslant T_D/3 \quad . \tag{7c}$$

Table 1 gives values of Debye temperature, Drude theory parameters, and absorptance.

Table 1. Values of the Debye temperature, T_D, the electron relaxation time, τ, the plasma frequency, ω_p, the temperature derivative of the absorptance, A_1, and the absorptance, A, at 300 and 80°K for silver, copper, and aluminum. Values taken from a variety of sources in the open literature.

	T_D(°K)	τ(sec)	ω_p(sec^{-1})	A_1(°K^{-1})	A(300°K)	A(80°K)
Ag	220	3.6×10^{-14}	1.3×10^{-16}	1.5×10^{-5}	4.2×10^{-3}	0.9×10^{-3}
Cu	315	2.7	1.6	1.8	4.5	0.5
Al	396	0.8	2.2	4.2	11.2	2.0

Experiment

The absolute reflectance of precision diamond-machined and evaporated silver as well as a multilayer enhanced reflector tuned for 3.8 μm was determined using equipment previously described [3]. The temperature range examined extended from 80 to 450°K, and measurements were made at 2.7, 3.8, and 10.6 μm wavelength. The precision of these measurements was $\pm 5 \times 10^{-5}$, and the absolute accuracy was $\pm 5 \times 10^{-4}$ at all wavelengths. The quantity 1 - R is plotted in figures 2-4 as an inferred absorptance. Since no scatter correction has been made, the values 1 - R are an upper bound to the true absorptance. In figure 2, data are plotted for a very high quality precision diamond-machined surface of electroplated silver. At room temperature and lower, all data are in agreement within experimental uncertainty with Drude theory predictions. However, the slope of a line fit through the data taken in aggregate at each temperature is somewhat steeper than the Drude theory predicts. At 80°K the value of 1 - R is on the order of 10^{-3} or smaller, a value very similar to that achieved by state-of-the-art multilayer dielectric-enhanced reflectors at room temperature.

Similar results were obtained for evaporated silver deposited on polished silicon, plotted in figure 3. This is a surprising result, since the relatively large disorder present in the evaporated film [5] would be expected to produce a substantial departure from linearity at temperatures not far below room temperature. The measured values of 1 - R at 3.8 μm are considerably larger than expected for reasons unknown. The trend of the data taken in aggregate is again steeper than the Drude theory predictions, and at 80°K, again, values on the order of 10^{-3} are achieved.

The results for a four-pair ZnS/ThF_4 quarter-wave stack on evaporated silver deposited on polished fused quartz are plotted in figure 4. These data are in sharp contrast to the bare silver results and show very little temperature dependence. This stability is considerably different than previously reported on a sample of similar construction and materials upon cycling to elevated temperatures only [6].

Cryogenic Mirror Performance

The primary optical advantage to be gained by cryogenic mirror operation is the substantial reduction in absorption. Nearly an order of magnitude has been obtained by reducing the mirror temperature from 300 to 80°K. For many mirror substrate materials, there is also a substantial increase in thermal conductivity. Table 2 gives values of the ratio of thermal conductivity K at 80°K to that at 300°K for a variety of common or proposed substrate materials [7]. For the metal substrates, the increase is on the order of 1.5. Also advantageous is the increase in elastic moduli that most metals experience upon cooling, resulting in stiffer mirror structures.

Table 2. Ratio of the thermal conductivity at 80°K to that at 300°K for a variety of common mirror substrate materials.

	Ag	Cu	Al	Mo	Si	C(graphite)
$\frac{K_{80°K}}{K_{300°K}}$	1.2	1.6	1.8	1.6	9.3	0.8

Theoretically, both for pulsed and CW laser radiation, substantial increases in laser-induced damage thresholds for metals will occur. However, it is not at all obvious what effect cryogenic operation would have on localized defect-initiated damage [8]. If the mirror absorptance, thermal conductivity, K, and heat capacity, C, are assumed to be constant and not temperature dependent, then for a square pulse of duration τ, the melt threshold fluence, θ_m, is just [9]

$$\theta_m = \frac{(\pi KC)^{1/2}}{2A} (T_m - T_o)\tau^{1/2} \quad , \tag{8}$$

where T_m and T_o are the melting and initial temperatures of the mirror material, respectively. The temperature dependence of the product KC is very small, from 80°K up to the melting point for silver, copper, and gold. The effect of the temperature dependence of A can be approximately taken into account by substituting into eq (8) the average value $(A_o + A_m)/2$, computing the values A_o and A_m using eq (7c). The following expression for the relative melt threshold is obtained from eq (8):

$$\frac{\theta_m(T_1)}{\theta_m(T_o)} = \frac{T_o + T_m}{T_1 + T_m} \quad \frac{T_m - T_1}{T_m - T_o} \quad . \tag{9}$$

This expression is pulse-length independent and for silver yields the result:

$$\frac{\theta_m(80°K)}{\theta_m(300°K)} = 1.16 \times 1.23 = 1.43$$

It can be seen then that the increase in melt threshold arises almost equally from the effects of the lower initial absorption and from the lower initial temperature of the mirror surface. A numerical solution to the one-dimensional heat flow equations with proper boundary conditions for A(T) yields a value of 14% higher than the value obtained above.

Summary

Measurements presented in this paper indicate that upon cooling the absorptance of a multilayer dielectric-enhanced mirror (ZnS/ThF_4) is changed only slightly. Earlier measurements indicated the possibility of larger variation, including irreversible alteration of the sample behavior upon temperature cycling. In either event, little is gained optically by cooling such a mirror. In contrast, cooling a bare metal mirror of silver, copper, or gold from room temperature to 80°K should, theoretically, decrease the absorptance about an order of magnitude. This prediction is verified experimentally for both evaporated thin film and diamond single-point machined silver. The absorptance of silver at 80°K is comparable to the room temperature absorptance of a state-of-the-art dielectric-enhanced reflector. Additional benefit is predicted for mirror performance from an increase in thermal conductivity of the mirror substrate. A theoretical prediction is also made of the increase in pulsed laser melt threshold resulting from cryogenic mirror operation. For a silver mirror, an increase of about 1.5 in the melt threshold would be expected at 80°K compared to room temperature. These improvements in performance may be attractive in the design of high power density laser systems, especially for space application where passive cooling could be employed.

References

[1] Kittel, C. Introduction to solid state physics, 5th ed, chapter 6. New York, NY: John Wiley & Sons; 1976.

[2] Bennett, H. E.; Bennett, J. M. Validity of the Drude theory for silver, gold, and aluminum in the infrared in optical properties and electronic structure of metals and alloys. Abelès, F., ed. North Holland: 1966. 175-188.

[3] Decker, D. L.; Hodgkin, V. A. Wavelength and temperature dependence of the absolute reflectance of metals at visible and infrared wavelengths. Bennett, H. E.; Glass, A. J.; Guenther, A. H.; Newnam, B. E., ed. Proceedings of the 12th annual symposium on optical materials for high power lasers; 1980 September 30-October 1; Boulder, CO. Nat. Bur. Stand. (U.S.) Spec. Publ. 620; 1981 October. 190-200.

[4] Stern, F. Elementary theory of the optical properties of solids in Advances in solid state physics, Vol. 15. Seitz, F.; Turnbull, D., ed. New York, NY: Academic Press; 1963. 344-347.

[5] Théye, M. Investigation of the optical properties of Au by means of thin semitransparent films. Phys. Rev. B 2; 3060; 1970.

[6] Decker, D. L. Temperature and wavelength dependence of the reflectance of multilayer dielectric mirrors for infrared laser applications. Glass, A. J.; Guenther, A. H., ed. Proceedings of the 7th annual symposium on optical materials for high power lasers; 1975 July 29-31; Boulder, CO. Nat. Bur. Stand. (U.S.) Spec. Publ. 435; 1976 April. 230-235.

[7] American Institute of Physics Handbook. New York: McGraw-Hill.

[8] Porteus, J. O.; Decker, D. L.; Faith, W. N.; Grandjean, D. J.; Seitel, S. C.; Soileau, M. J. Pulsed laser-induced melting of precision diamond-machined Cu, Ag, and Au at infrared wavelengths. IEEE J. Quantum Electron. QE-17; 2078; 1981.

[9] Bennett, H. E. Thermal distortion thresholds for optical trains handling high pulse powers. Glass, A. J.; Guenther, A. H., ed. Proceedings of the 8th annual symposium on optical materials for high power lasers; 1976 July 13-15; Boulder, CO. Nat. Bur. Stand. (U.S.) Spec. Publ. 462; 1976 December. 20.

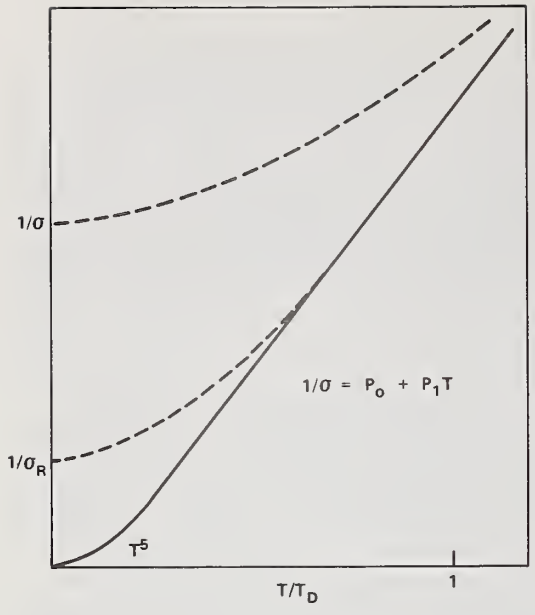

Figure 1. Schematic plot of the electrical resistivity, $1/\sigma$, vs the absolute temperature normalized to the Debye temperature for a metal. For a well-ordered, pure metal in the range above about $T_D/3$, the resistivity is linear with temperature. However, for less well-ordered or impure metals, significant departure from linearity will occur at temperatures ~ T_D, and at lower temperatures an asymptotic "residual" resistivity will be approached. In extreme cases, the residual resistivity will be perhaps only a factor of two smaller than the room temperature value.

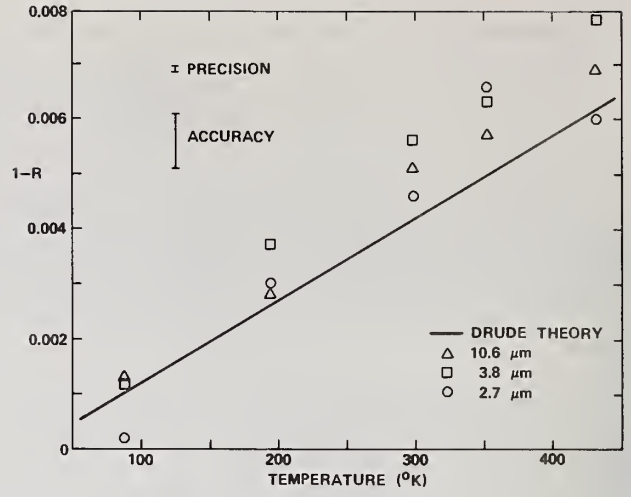

Figure 2. Plot of 1 - R vs absolute temperature for a diamond-machined silver surface at three wavelengths (2.7, 3.8, and 10.6 μm) compared with the Drude theory prediction using nonoptical input parameters.

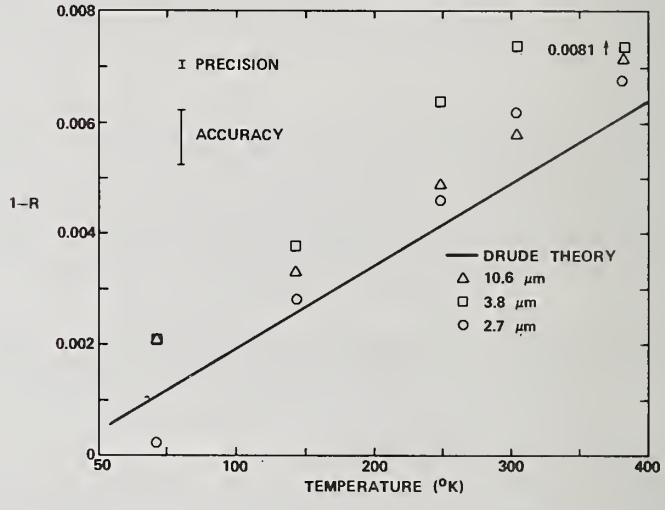

Figure 3. Plot of 1 - R vs absolute temperature for an evaporated thin film of silver deposited on polished single-crystal silicon. Data are shown at three wavelengths (2.7, 3.8, and 10.6 μm) compared with Drude theory predictions using nonoptical input parameters.

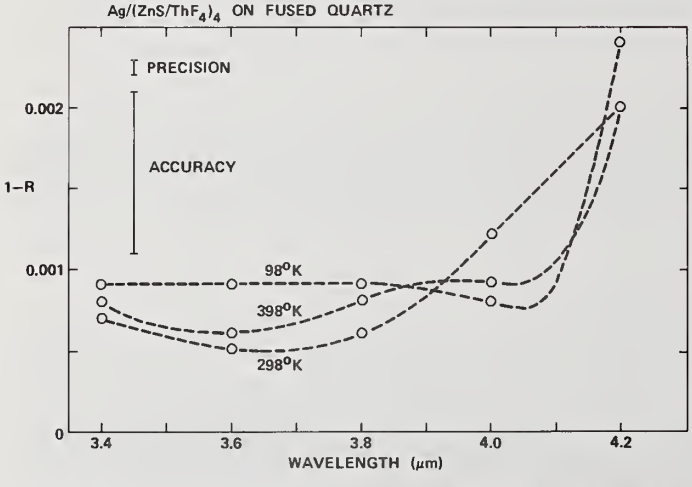

Figure 4. Plot of 1 - R vs wavelength for a multilayer ZnS/ThF_4 dielectric-enhanced silver reflector, tuned for 3.8 μm. Shown are data at three temperatures: 98, 298, and 398°K.

The question was asked of how a complex metal mirror could be cooled to cryogenic temperatures without losing the optical figure. The author suggested that if the mirror were homogeneous it might be possible. If it were a complicated structure, maintaining figure would be much more difficult. Since the reflectance at cryogenic temperatures is so high, active cooling might not be necessary in many cases and the mirror structure might thus be simpler than that required at higher temperatures. The most attractive use of cryogenic mirrors may well be in space applications.

Dimensional Stability of Zerodur and ULE Mirrors Undergoing Thermal Cycling*

J. J. Shaffer, J. M. Bennett, and H. E. Bennett

Michelson Laboratory, Physics Division
Naval Weapons Center, China Lake, California 93555

Zerodur and ULE quartz have been shown to have exceptional dimensional stability over extended time periods and to be insensitive to small temperature variations when they are maintained near room temperature. However, it is not clear what their dimensional stability will be after cycling through a more extended range of temperatures such as might occur during bakeout and film deposition when applying dielectric multilayer high-reflectance coatings. Since mirrors are required to maintain tolerances as severe as λ/100 visible equivalent in some laser applications, the safe limits for temperature cycling are of considerable interest, and a preliminary experiment was performed to investigate this question. During the experiment, a convenient method for interferometrically verifying the thermal expansion coefficient of these low-expansion materials was developed and will be described. In one series of experiments, a 6-inch-diameter Zerodur optical flat of the highest quality having a better than λ/40 average peak-to-valley optical figure was oven heated to a peak temperature and then allowed to cool in air. No permanent change was observed up to a temperature of 200°C, but at 250°C the mirror took a permanent set. After the 300°C cycle, this set increased to λ/5. Under similar conditions, the ULE sample was unaffected; it was then water quenched after heating, a much more severe test. Even at oven temperatures of 350°C, the ULE sample developed no permanent set. These experiments suggest that caution should be employed when heating Zerodur mirrors above 150 to 200°C. There is no comparable restriction on ULE mirrors.

Key words: expansion coefficient; fused quartz; optical figure; thermal distortion; ULE quartz; Zerodur.

Introduction

Figure requirements on mirrors are becoming increasingly severe. Tolerances as small as λ/100 visible equivalent in peak-to-valley figure error are desired for some laser applications. In order to avoid unreasonable requirements on ambient temperature control, low expansion glasses such as ULE, a titanium silicate manufactured by Corning Glass Works, or Zerodur, a quartz ceramic manufactured by Schott, are desirable substrate materials. They have been shown [1][1] to have exceptional dimensional stability over extended time periods and are insensitive to small temperature variations near room temperature. These two materials achieve their low expansion properties by different techniques. ULE is an isotropic, single phase material, a true glass whose low thermal expansivity results from precise control of the composition of constituents. Zerodur is a glass ceramic composed of both vitreous and crystalline phases of quartz. It is approximately 70-75% crystalline by weight [2]. In the high temperature form, quartz crystallites have a mean crystalline diameter of about 500 Å. They also have a negative expansion coefficient. The vitreous quartz has a positive expansion coefficient, so that by adjusting the relative amounts of the crystalline and amorphous phases it is possible, in principle, to drive the expansion coefficient to zero. In practice, the expansion coefficient of the best grade of this material is guaranteed [2] to be $\pm 5 \times 10^{-8}$/°C or less at room temperature. Significantly lower values are often found. It is thus comparable to ULE, which has a typical value of $\pm 3 \times 10^{-8}$/°C at room temperature [3]. These values may be compared to fused silica, which is about 4×10^{-6}/°C at room temperature [4], and was, until the development of these and other low expansion coefficient materials, the best optical substrate material available from an expansion coefficient point of view.

Fused silica has many desirable features as an optical substrate material: it (1) has a thermal behavior which is quite reproducible, (2) can be polished very smooth [5], (3) can in some grades be quite homogeneous and nearly stria-, bubble-, and inclusion-free, and (4) has excellent opto-mechanical and thermo-structural properties. Opticians expect these properties, and it is easy to assume that

* Work partially supported by Navy Independent Research funds.
[1] Numbers in brackets indicate the literature references at the end of the paper.

the lower expansion materials will have similar characteristics. Such an assumption needs to be examined experimentally. This paper discusses two such experiments. One is a simple technique for approximately measuring the thermal coefficient of expansion of these low expansion materials. The second is an investigation of their dimensional stability after thermal cycling such as might occur during a coating process. Thermal shock resistance is also investigated.

Expansion Coefficient

To accurately measure the thermal expansion coefficient of a low expansion material, an elaborate laboratory setup is required [6]. However, an approximate value should be obtainable by producing interference fringes between the test sample, polished optically flat, and a reference flat. The top surface of the test sample is heated and the expansion coefficient inferred from the way the fringes move. The bowing of a simply supported disk-shaped surface of thickness ℓ and radius a is given by [7]

$$w = -\frac{6\alpha(a^2 - \rho^2)}{\ell^3}\int_{-\ell/2}^{\ell/2} T(z,t)z\,dz + \frac{1}{(1-\nu)}\left[(1+\nu)\alpha\int_0^z T\,dz - \frac{\nu\alpha z}{\ell/2}\int_{-\ell/2}^{\ell/2} T\,dz - \frac{3\nu\alpha z^2}{2(\ell/2)^3}\int_{-\ell/2}^{\ell/2} Tz\,dz\right] , \quad (1)$$

where the origin of cylindrical coordinates is at the disk center, the z coordinate is measured normal to the surface, and ρ is the radial coordinate. The temperature T is a function of z and time t, w is the bowing normal to the disk surface caused by nonuniform heating, α is the thermal expansion coefficient, and ν is Poisson's ratio. The first term in eq (1) is the thin shell approximation, and the second term within the square brackets makes it possible to estimate the error involved if the thin shell approximation is used. If the temperature distribution in the disk is independent of ρ and is approximated by a step function in z so that $T = T_0$ for $\gamma/2 \leqslant z \leqslant \ell/2$, and $T = 0$ for $-\ell/2 < z < \gamma/2$, where γ is a running variable, then on the disk axis ($\rho = 0$) the bowing of the disk in the thin shell approximation is given by

$$w = -\frac{6\alpha a^2}{\ell^3}\int_{-\gamma/2}^{\ell/2} T_0\,z\,dz \quad (2)$$

$$= \frac{3}{4}\frac{\alpha a^2}{\ell} T_0\left[1 - \left(\frac{\gamma}{\ell}\right)^2\right] . \quad (3)$$

The bowing initially increases quadratically as the depth which is heated increases and is a maximum when $\gamma = 0$, i.e., when the disk is heated halfway through.

If the surface $z' \equiv z - \ell/2 = 0$ of a semi-infinite solid at temperature $T = 0$ is raised to T_0, the temperature at a depth z' after time t is given by [8]

$$T = T_0\,\mathrm{erfc}\,\frac{z'}{2\sqrt{\kappa t}} , \quad (4)$$

where $\kappa = K/\rho c$ is the diffusivity, K the thermal conductivity, ρ the density, and c the specific heat. Here

$$\mathrm{erfc}\,x \equiv \frac{2}{\sqrt{\pi}}\int_x^\infty e^{-\xi^2} d\xi , \quad (5)$$

which for small x gives [9]

$$\mathrm{erfc}\,x \cong 1 - \frac{2}{\sqrt{\pi}}\left(x - \frac{x^3}{3} + \frac{x^5}{10} + \ldots\right) . \quad (6)$$

Letting $z' = \ell/2$ and $T = T_0/2$, so that the step function in temperature is halfway through the disk, and solving for t using eq (6) gives

$$t = \frac{\ell^2}{\pi\kappa} \quad . \tag{7}$$

Nearly the same result could have been obtained by the approximate technique of letting the diffusion depth $\delta = (\kappa t)^{\frac{1}{2}}$ equal $\ell/2$. Then $t = \ell^2/4\kappa$.

Experimental

The test mount used is shown in figure 1. The sample to be tested, in this case a Zerodur optical flat 14.7 cm diameter and 3.0 cm thick, was mounted on a test plate at the top of the mount. A 10-cm-diameter collimated beam from a Zygo interferometer [10] operating at 0.63 μm wavelength was incident from the left and was deflected vertically to the two flats, which rested on two 3-mm-thick pyrex strips to insulate the assembly from the steel stand. A temperature gradient in the Zerodur flat was produced by first refrigerating it and the master flat at 0°C and then mounting the assembly on the test stand and continuously flooding the top of the Zerodur sample with near-boiling water. A temperature difference of T = 84°C was achieved in this way. A cell was built up of white RTV rubber with a piece of 8-mm i.d. rubber tubing to drain the excess water. A 3-mm-thick disk of pyrex 14 cm in diameter with a 6.4-cm hole was bonded to the RTV rubber to act as a splash guard.

Results

The interference fringes formed during the experiment are shown in figure 2. The finely spaced fringes are caused by the test plate and are to be ignored. The fringe power in the coarsely spaced fringes, which resulted from bowing of the Zerodur flat, was read on a Zygo Automatic Pattern Processor [10] and is shown in figure 3 as a function of time. The power continues to increase slowly after its initial rapid change, probably because the test plate and the rest of the system are beginning to change temperature. The initial change in power with time, however, follows approximately the $(\gamma/\ell)^2$ dependence predicted by eq (3). Only the Zerodur flat should be bending initially and, thus, only it should contribute significantly to this initial change in power. The time at which $\gamma = 0$ and the temperature change has proceeded halfway through the Zerodur flat can be computed from eq (7). At 20°C the thermal diffusivity [2] of Zerodur is 0.8×10^{-6} m/sec^2 so that t = 6.1 min. The power in fringes is then approximately 0.5, which substituted into eq (3) gives the thermal expansion coefficient to be 3×10^{-8}/°C. The value published for this material by Schott [2] is $\alpha \leqslant 5 \times 10^{-8}$/°C, in excellent agreement with the experimental result.

Dimensional Stability

The dimensional stability of both Zerodur and ULE has been shown to be exceptionally good at room temperature [1]. However, the dimensional stability after thermal cycling cannot be inferred from these data and apparently has not been reported in the literature. To investigate this question, Zerodur and ULE flats were oven heated and then quenched, first in air and later in water for the ULE sample. They were then quickly placed in a holder positioned in the beam of the Zygo interferometer so that the optical figure of the blank, hot from the oven, could be measured as a function of time. An index mark was placed on the edge of the blank and aligned with a corresponding mark on the holder so that the sample was in the same position relative to the interferometer for each experiment.

The procedure used was as follows. The oven was allowed to stabilize at each temperature overnight. The flat was then placed in this preheated oven for a minimum of four hours. Significant thermal shock thus occurred when the part was introduced into the oven. Additional schock occurred when it was removed from the oven and mounted in the interferometer holder. The first fringe pattern was photographed as quickly as possible after the sample was mounted. No attempt was made to orient the fringes in any particular manner for this initial test. Additional photographs were taken at varying intervals of time after the oven cycle. At the lowest oven temperature, this time interval was two hours. As the heat was increased, the time interval was also increased.

Results for Zerodur are shown in figures 4 and 5. The same flat was used for these tests as for those on the expansion coefficient. Little change could be seen in the optical figure of this sample, even when it was hot, at oven temperatures of 50°C and 100°C. Some change in figure could be observed initially at 150°C and 200°C, but no permanent figure change occurred. At 250°C a large change in figure occurred when the sample was measured hot, and a residual figure change remained 42 hrs after the initial tests were completed. When the sample was then heated to 300°C, a significant figure change occurred initially, although not as large as the one observed at 250°C, and the residual figure error after cooling increased to about λ/5.

The only piece of ULE available to the Naval Weapons Center Optical Shop at the time these tests were made was a crescent-shaped piece of material about 10-cm long and 3.5-cm wide. This piece was polished flat to $\lambda/10$, except for a 0.5-cm-wide rolled edge. The assumption was made that any changes occurring in the sample would be more obvious in the long dimension, so all photos taken for this series of heat cycles have fringes running the long way of the part.

The first series of heating cycles consisted of soaking the part in a preheated and temperature-stabilized oven for a minimum of 4 hrs. The part was then removed to the interferometer and the fringe pattern photographed as quickly as possible. The part was allowed to normalize for 2 hrs or more and rephotographed. This procedure was then repeated at a higher oven temperature. Results are shown in figure 6. No significant figure change occurred at the lowest oven temperature setting, 100°C, but an initial change did occur at 150°C. At higher temperatures, the magnitude of the initial figure changes tended to increase, although they were not nearly as large as those observed at 250°C and 300°C for the Zerodur sample. In no case was there a permanent change in figure after the sample had cooled to room temperature.

More drastic tests were then applied. The entire series of heat cycles was repeated using an ice water quench of the part after removal from the oven. Since it was not possible to photograph the part during the water quench, only one photograph, which was taken after the part came to room temperature, is shown in figure 6 for each cycle. No permanent figure changes were induced in this part by any of the tests performed on it.

Conclusions

An approximate value for the thermal expansion coefficient, probably accurate to at least a factor of 2, can be obtained for the lowest expansion coefficient materials available by the relatively simple procedure of heating the back surface of an optical flat made from the material and recording the power developed. The expansion coefficient deduced in this way for the Zerodur sample tested agreed very well with the specifications quoted by the manufacturer. This procedure thus provides a simple check on the quality of materials thought to have low expansion coefficients.

The dimensional stability of Zerodur low expansion material is reported to be excellent at room temperature. However, a permanent figure error can be induced in this material by heating it to temperatures above 200°C. If such temperatures are required, for example in coating a mirror made of this material, thermal shock should be avoided, and temperature changes both in bringing the part up to temperature and in lowering the temperature should be made very slowly and very uniformly in area. ULE, on the other hand, appears to be very insensitive to thermal shock and could be used to fabricate optical components used in thermally cycled operations which most opticians would regard as quite unreasonable.

References

[1] Berthold, J. W., III; Jacobs, S. F.; Norton, M. A. Dimensional stability of fused quartz silica, Invar, and several ultralow thermal expansion materials. Appl. Opt. 15; 1898; 1976.

[2] Zerodur data sheet from Schott, Spezial-Glas GMBH, P.O. Box 3833, Rheinallee 143, D-6500 Mainz, West Germany.

[3] ULE Titanium Silicate, Code 7971 data sheet from Corning Glass Works, Corning, NY 14830.

[4] Gray, D. E., ed. American institute of physics handbook, third edition. New York, NY: McGraw-Hill; 1972. 4-138.

[5] Dietz, R. W.; Bennett, J. M. Bowl feed technique for producing supersmooth optical surfaces. Appl. Opt. 5; 881; 1966.

[6] Berthold, J. W., III; Jacobs, S. F. Ultraprecise thermal expansion measurements of seven low expansion materials. Appl. Opt. 15; 2344; 1976.

[7] Boley, B. A.; Weiner, J. H. Theory of thermal stress. New York: John Wiley & Sons; 1960. 279.

[8] Carslaw, H. S.; Jaeger, J. C. Conduction of heat in solids, 2nd ed. London: Oxford University Press; 1959. 60.

[9] *Ibid.* 482.

[10] Manufactured by the Zygo Corporation, Laurel Brook Road, Middlefield, CT 06455.

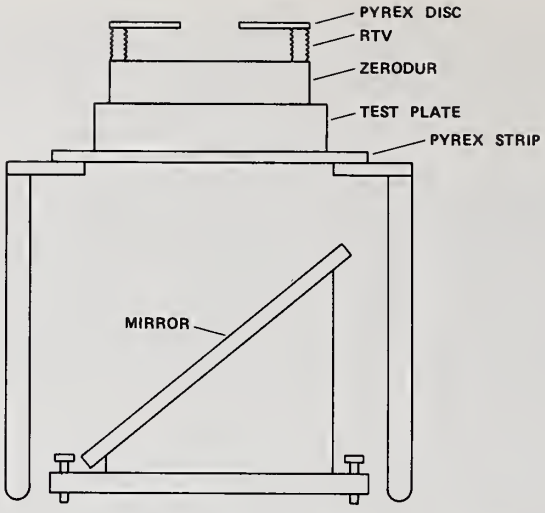

Figure 1. Test mount for measuring coefficient of thermal expansion of Zerodur and other low expansion materials.

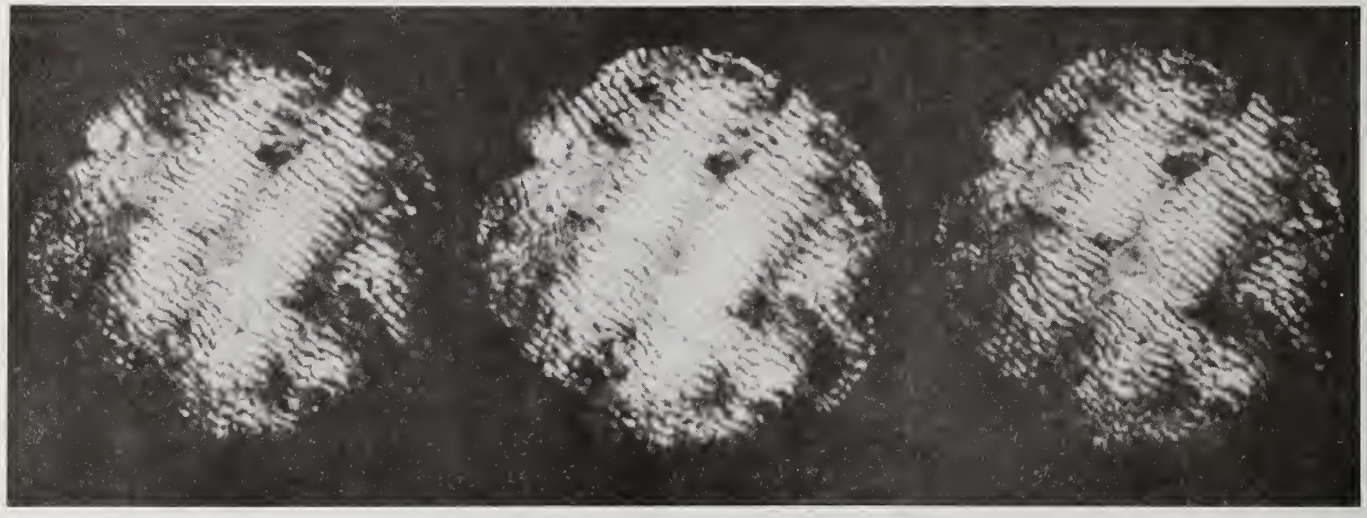

AFTER 1 MINUTE AFTER 2 MINUTES AFTER 3 MINUTES

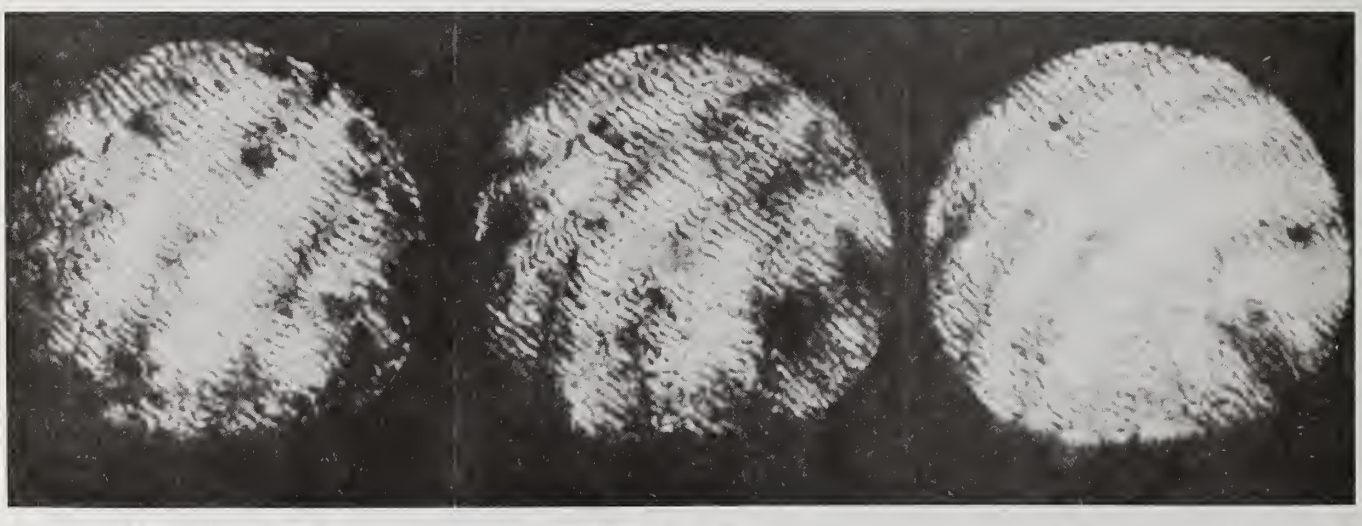

AFTER 4 MINUTES AFTER 8 MINUTES AFTER 12 MINUTES

Figure 2. Interference fringes from which the coefficient of thermal expansion of Zerodur was determined.

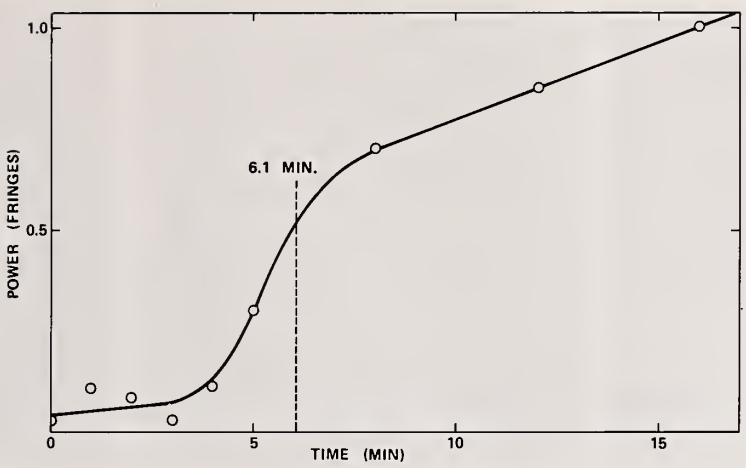

Figure 3. Power in fringes induced by heating the Zerodur flat as a function of time since heating began.

AS SOON AS
POSSIBLE FROM
50°C OVEN

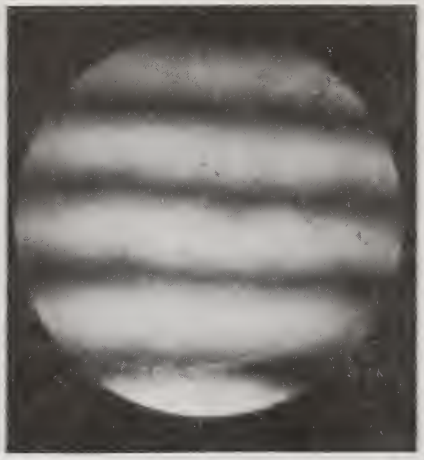

2 HOURS AFTER
50°C OVEN
FRINGES HORIZONTAL

2 HOURS AFTER
50°C OVEN
FRINGES VERTICAL

ASAP
100°C OVEN

3 HOURS AFTER
100°C OVEN
FRINGES HORIZONTAL

3 HOURS AFTER
100°C OVEN
FRINGES VERTICAL

ASAP
150°C OVEN

3 HOURS AFTER
150°C OVEN
FRINGES HORIZONTAL

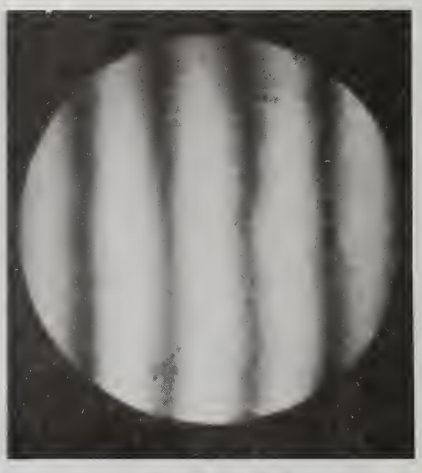

3 HOURS AFTER
150°C OVEN
FRINGES VERTICAL

Figure 4. Interference fringes showing the initial distortion and ultimate optical figure error of a Zerodur flat after thermal cycling to 50°C, 100°C, and 150°C.

ASAP FROM
200°C OVEN

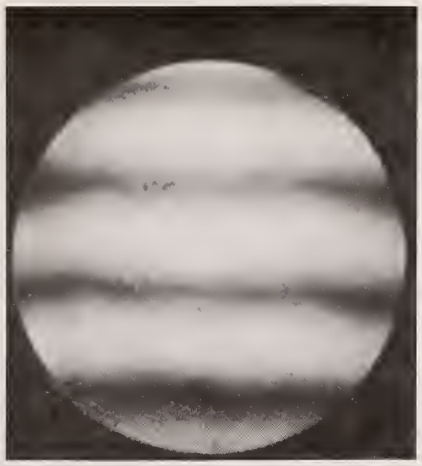

3 HOURS AFTER
200°C OVEN
FRINGES HORIZONTAL

3 HOURS AFTER
200°C OVEN
FRINGES VERTICAL

ASAP FROM
250°C OVEN

42 HOURS AFTER
250°C OVEN
FRINGES HORIZONTAL

42 HOURS AFTER
250°C OVEN
FRINGES VERTICAL

ASAP FROM
300°C OVEN

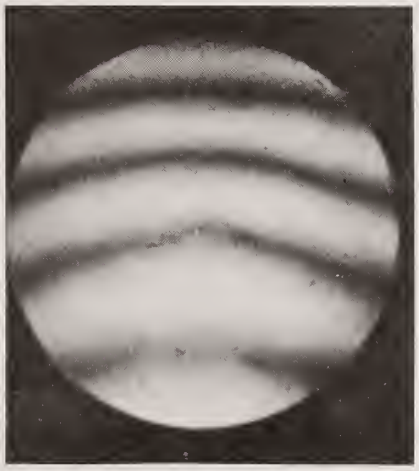

24 HOURS AFTER
300°C OVEN
FRINGES HORIZONTAL

24 HOURS AFTER
300°C OVEN
FRINGES VERTICAL

Figure 5. Same as figure 4 except thermal cycling to 200°C, 250°C, and 300°C. A permanent thermally induced figure error can be observed at 250°C and 300°C.

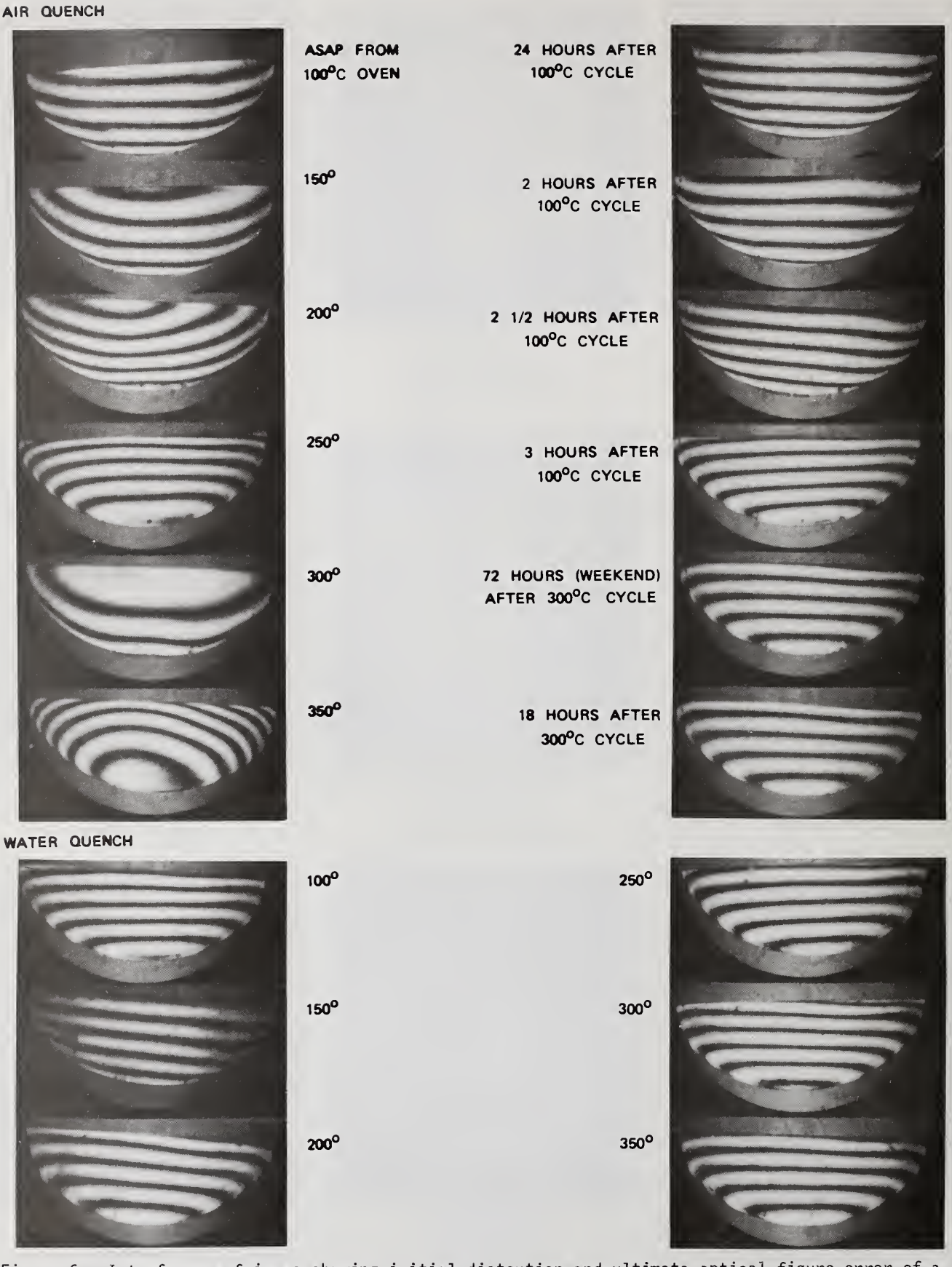

Figure 6. Interference fringes showing initial distortion and ultimate optical figure error of a ULE flat after thermal cycling to various temperatures up to 350°C. Both an air quench and a water quench were used. No ultimate thermally induced figure error can be observed for this material.

Thermo-Elastic Action of the Powerful High Repetition Rate Laser Radiations on the Solid State Surface

V. V. Apollonov, S.A. Chyotkin, V. Yu. Khomich, and A. M. Prokhorov
Lebedev Physical Institute of the USSR Academy of Sciences
Moscow, USSR

The phenomena of the thermoelastic behavior of materials under powerful, high-repetition-rate laser radiation are discussed. An analysis is based on the Duamel integrals for the thermo-stress characteristics which correspond to CW and high-repetition-rate laser irradiations.

Relationships for the upper-level laser intensities which are connected with admissible elastic surface distortion, plastic flow of the material, fatigue distributions, and melting of the surface layer are calculated.

Key words: CW, optical deformation, pulsed, surfaces, thermo-elastic stress.

I. Introduction.

A quasi-static problem of laser radiation action upon the solid-state surface is considered in approaching of incoherence thermoelasticity [1-4]. Nonstationary temperature and stress fields were determined in a stationary thermostress process.

Nowadays, laser systems, generating powerful nonstationary radiation fluxes are widely used in different fields of science and techniques. Therefore, a general conclusion on thermoelastic solid-state behavior, when it is exposed to high-repetition-rate laser radiation, is needed, including high intensity laser optics also.

II. Description of Solid State Thermostresses Produced by Laser Radiation.

Let us consider an isotropic body at the initial moment of time at fixed temperature, when its surface with absorption A is subjeted to an axially symmetrical beam flux. One assumes that the cross-section intensity distribution of laser beam is submitted by Gaussian law: $I(\vec{r}) = I_o \exp(-K_o r^2)$ where $K_o = 2/r^2$, and the energy is absorbed over irradiated surface, since a depth of skin layer is considerably smaller than the temperature field penetration depth for the specific times of the beam intensity charge.

We linearly considered the problem of determination of the temperature field, that is, all thermophysical and mechanical material characteristics are independent of temperature, and energy losses due to radiation and convection are neglected.

If the typical beam size is $r_0 < L$, and the energy input time is $\frac{r_0^2}{a^2} \leqslant t \leqslant \frac{L^2}{a^2}$, then by solving the equation one can use a half-space model. Then, the material heating is described by the equation of thermoconductivity:

$$\frac{\partial T}{\partial t} = a^2 \nabla T \tag{1}$$

under following initial and boundary conditions

$$\frac{\partial T}{\partial z}\Big|_{z=0} = -\frac{I_o A}{\lambda} f(t) \exp(-k_0 r^2)$$

$$T\Big|_{t=0} = 0, \quad \lim_{r,\, z \to \infty} T < M$$

where a^2, λ - are the temperature and theromconductivity coefficients of the body material, respectively, M - is the final value, f(t) - is the normalized time function of laser beam intensity.

By solving the problem with a method of consecutive Hankel and Laplace integral conversion, we have

$$T^* = \frac{1}{2\pi i \sqrt{k_0}} \int_{G-\infty}^{G+\infty} \psi(p) e^{pt}\, dp \int_0^\infty \xi \frac{e^{-\xi/uk_0}}{\gamma} e^{-\gamma z}\, d\xi\, \mu_0(\xi r) \tag{2}$$

where $T^* = \frac{2\lambda\sqrt{K_0}}{I_0 A} T$, p and ξ - are the Laplace and Hankel conversion parameters, $\gamma^2 = \frac{p}{a^2} + \xi^2$, $\psi(p)$ $\psi(p)$ - is the form of Laplace conversion from f(t).

This expression makes it possible to describe a thermal character of the solid state, whose surface is exposed by arbitrary, nonsteady laser irradiations as well as to obtain the solution of incoherence thermoelastic problem in integrated mode.

In general, an analysis of thermoelastic phenomena is based on the equation system of incoherence thermoelasticity [5-7, 10]. If the inequalities are satified

$$\max\left(\frac{\rho a^2}{\lambda'}; \frac{\rho a^2}{\mu}; \sqrt[3]{\frac{\rho^2 a^2}{K_0 E^2}}\right) << \tau >> \sqrt[3]{\frac{\rho^4 c^4 a^2}{\mu^2 \alpha_t^4 (I_0 A)^2}}$$

it is possible to describe an appearing state of the elastic half space basing on quasi-stantionary, theromelastic equations.

$$\mu \nabla^2 \vec{u} + (\lambda' + \mu)\, \text{grad div}\, \vec{u} - (3\lambda' + 2\mu)\, \alpha_t \nabla T = 0 \tag{3}$$

$$\nabla^2 T - \frac{1}{a^2} \frac{\partial T}{\partial t} = 0$$

where λ', μ - are the Lyame coefficient, $\vec{u}$ - is the deformation vector, ρ is the density, α_τ - is the thermal expansion coefficient, E - is the Young's modulus.

Elastic distortions in the solid states are propagated with a sound speed C, therefore, to establish "stationary" stress state, it is necessary for the speed of its estblishment to be considerably higher than that of thermal equilibrium i.e., $\sqrt{a^2\tau} << c\tau$. Furthermore, for the real solid states with finite dimensions, there is a set of natural frequencies of mechanical vibrations. Hence, quasi-stationary conditions also include the fact that frequencies multiple to that of laser pulse movement do not coincide with the natural body frequencies, to avoid a consideration of the resonance phenomena whose analysis is impossible without accounting for $\rho\frac{\partial^2\vec{u}}{\partial t^2}$ in (3).

A general view of the stress tensor components is

$$\hat{\sigma}_{zz} = 2CD\int_0^\infty \xi^2\mu_o(\xi r)\psi(\xi)\left[e^{-\gamma z} - e^{-\xi z}\left(1 + z(\xi-\gamma)\right)\right]d\xi$$

$$\hat{\sigma}_{rr} = 2CD\int_0^\infty \xi\mu_1(\xi r)\,\psi(\xi)\left[\gamma(e^{-\gamma z} - e^{-\xi z}) - \xi z(\xi-\gamma)e^{-\xi z}\right]d\xi \qquad (4)$$

$$\hat{\sigma}_{rr} = 2CD\int_0^\infty \psi(\xi)\left[\mu_o(\xi r)\left[\xi(\xi z-2)(-\gamma)e^{-\xi z} + \xi^2 e^{-\xi z} - \gamma^2 e^{-\gamma z}\right] + \right.$$

$$\left. + \frac{\mu_1(\xi r)}{r}\left[\xi e^{-\gamma z} - \left((\xi-\gamma)(\xi z-2(1-\nu)) + \xi\right)e^{-\xi z}\right]\right]d\xi$$

$$\sigma_{\psi\psi} = 2CD\int_0^\infty \psi(\xi)\left\{\mu_o(\xi r)\left[(\xi^2-\gamma^2)e^{-\gamma z} - 2\nu\xi(\xi-\gamma)e^{-\gamma z}\right] + \frac{\mu_1(\xi r)}{r}\right. \times$$

$$\left.\left[\left((\xi-\gamma)(\xi z-2(1-\nu)) + \xi\right)e^{-\xi z} - \xi e^{-\gamma z}\right]\right\}d\xi$$

where C - is the shear modulus. $\mu_n()$ are the Bessel functions of the order of n,

$$\psi(\xi) = \frac{\xi}{\gamma}e^{-\xi^2/4K_o},\quad D = \frac{\alpha T(1+\nu)}{2(1-\nu)} \times \frac{I_o A a^2}{K_o \lambda p}\psi(p).$$

An equality of the components σ_{zz} and $\sigma_{\psi\psi}$ between themselves, and $\sigma_{zz} = 0$ on the axis OZ is a distinctive feature of the problem (result of cylindrical symmetry).

The above-mentioned expressions describe a nonstationary solid-state character. By analyzing the expressions in eq (4) it is possible to clarify a nature of changing for all half-space points.

The stress state occuring in the solid deforms it, and the greater part of deformations is achieved on irradiated surface. Within a half-space model the value of surface distortion under laser radiation is determined as

$$W^* = \frac{FO}{2\pi i}\int_0^\infty dv \int_{\sigma-i\infty}^{\sigma+i\infty} \frac{dp}{p}\,\psi\left(\frac{p}{t}\right) e^{p-v}\,\mu_o\left(\sqrt{v}\,\delta_r\right)\frac{\sqrt{v}-\sqrt{v+P/FO}}{\sqrt{v+P/FO}} \qquad (5)$$

where $W^* = \frac{\lambda K_o}{(1+v)\alpha_t I_o A} W$, $\delta_t = 2\sqrt{K_o r}$, $FO = 4K_o a^2 t$.

The expression obtained allows us to observe the surface distortions in the process of laser beam activity.

Thus, we fully desribed the character of thermal, thermostress and deformation states appearing in the solid under nonsteady laser irradiations. The following relations between values, characterizing the thermostress state in continuous $\left(\psi(p) = \frac{\ell}{p}\right)$ and any other nonstationary regimes of laser energy input into solid state should be satisfied

$$\sigma_{ik}^{nonst} = \int_0^t f(t-\tau)\,\frac{\partial \sigma_{ik}^{cw}}{\partial \tau}\,d\tau$$

$$W^{nonst} = \int_0^t f(t-\tau)\,\frac{\partial W^{cw}}{\partial \tau}\,d\tau \qquad (6)$$

as a consequence of the type of formula in the form of the Laplace conversion for the thermostress tensor components and thermodeformation vector

$$L_i\left(\sigma_{ik}^{nonst};\ W^{nonst}\right) = p\psi(p)L\left(\sigma_{ik}^{cw},\ W^{cw}\right)$$

where L - is the operation of Laplace conversion.

These relations are similar to that of Duamel integrals known from the thermoconductivity theory. An important aspect of this fact for the values, characterizing the thermostress state is that the time here is not as an independent variable in which a differentiation takes place (say, in theromconductivity equation), but is a parameter that being a result of incoherence on the quasi-stationary problem of thermoelasticity.

Based on the method developed, we compare thermodeformation elastic half-space phenomena under CW, pulsed and power high-repetition-rate laser radiation influence upon the solid-state surface.

III. A Continuous Regime of Laser Radiation Action upon the Solid State Surface

For exposure times of laser radiation satisfying $\frac{r_o^2}{a^2} \leqslant t \leqslant \frac{L^2}{a^2}$, a stationary temperature field may have been settled in the solid state. This process in the center of radiation zone is described by: $T^* = \frac{2}{\sqrt{\pi}} \operatorname{arctg} \sqrt{FO}$

From this expression (see fig. 1) it follows that for the time moments such as FO> 4, a temperature value is 10 percent less and differs from the stationary one. Therefore, we assume that stationary thermal state is settled in the sample material.

The expression for the temperature field in the half-space is

$$T^* = \int_0^\infty \mu_0(\sqrt{v}\,\delta_t)\exp(-\sqrt{v}\,(\delta_z + \sqrt{v}))\,\frac{dv}{\sqrt{v}} \tag{7}$$

where $\delta_z = 2\sqrt{K_o}Z$.

Analyzing the expression, it is evident that temperature field is local, its intensity falls sharply as moving off the center of radiation zone over the surface and into the depth of material (see Figs. 2 and 3). In this case, a half-width of intensity distribution is several times as narrow as that of corresponding temperature profile on irradiated surface. Its maximum value, equal to $T^* = \sqrt{\pi}$, is achieved directly in the center of radiation zone.

In the stationary stress state (P→0) only thermo-stress tensor components σ_{zz} and $\sigma_{\psi\psi}$ are nonzero.

$$\sigma^*_{\psi\psi} = 2(1-v)\int_0^\infty \exp\left(-\sqrt{v}(\delta_z + \sqrt{v})\right)\left[\mu_1(\sqrt{v}\delta_r) - \mu_0(\sqrt{v}\delta_t)\right]\frac{dv}{\sqrt{v}} \tag{8}$$

$$\sigma^*_{rr} = -2(1-v)\int_0^\infty \exp(-\sqrt{v}(\delta_z + \sqrt{v}))\frac{\mu_1(\sqrt{v}\delta_r)}{v\delta_r}\,dv,$$

where $\sigma^*_{ik} = \lambda\sqrt{k_o}(1-v)\,\sigma_{ik}/(I_o A C \alpha_\tau (1+v))$.

a penetration depth σ_{ik} into the sample material turns out to be $\sim r_o$. On the surface a stationary stress field is

$$\sigma^*_{rr} = -\frac{\sqrt{\pi}(1-v)}{2}\,{}_1F_1\left(\frac{1}{2},\,2;\,-\frac{\delta_r^2}{4}\right) \tag{9}$$

$$\sigma^*_{\psi\psi} = \frac{\sqrt{\pi}(1-v)}{2}\left[{}_1F_1\left(\frac{1}{2},\,2;\,-\frac{\delta_r^2}{4}\right) - 2\,{}_1F_1\left(\frac{1}{2},\,1;\,-\frac{\delta_r^2}{4}\right)\right]$$

The thermostress field reaches its maximum in the center of radiation zone: $\sigma^*_{ii} = \frac{\sqrt{\pi}}{2}(1-v)$. An establishment of the stress stationary state is characterized by dependence represented in figure 2:

$$\sigma^*_{ii} = \frac{1+v}{\sqrt{\pi}}\left[\mathrm{FO}\left(\operatorname{arctg}\frac{1}{\sqrt{\mathrm{FO}}} - \frac{1}{\sqrt{\mathrm{FO}}}\right)\frac{1-v}{1+v} \operatorname{arctg}\sqrt{\mathrm{FO}}\right].$$

A value of thermal deformation of reflecting surface in the stationary regime (half-space model) tends to $W^* \approx -\ln(2\sqrt{\mathrm{FO}})$; that is explained by an infinite volume of the effective substance heat region (Fig 3). It is interesting to estimate a growth value of the thermal deformation with long laser beam exposure times (FO >> 1)

$$W^* \approx -\ln(2\sqrt{FO})\,{}_1F_1\left(\frac{3}{2},\ 1;\ -\frac{\delta_r^2}{4}\right) \tag{10}$$

Deformation surface profiles for the different time moments were represented in [1,3].

IV. Pulse Regime of Laser Radiation Action Upon Solid State Surface

We will be interested in interaction times, when $FO_1 = \psi K_o a^r \tau < 1$, that is practically realized in investigation of interaction between pulse laser radiation and substance.

In the case of short radiation times, the penetration depth of the temperature field is proportional to $\sqrt{a^2\tau} \ll r_o$, so the radial heat flows can be neglected and the temperature distribution over the surface repeats the profile of intensity distribution of laser beam.

$$T^* = 2\sqrt{\frac{FO_1}{\pi}}\left[\Theta(t^*)\sqrt{t^*} - \Theta(t^*-1)\sqrt{t^*-1}\right] \tag{11}$$

where $\Theta(t^*)$ - is the Heaviside function τ - is the pulse duration, $T^* = t/\tau$. Its maximum value is reached at the moment of pulse stop in the center of radiation zone and is equal to $T^* = 2\sqrt{\frac{FO_1}{\pi}}$.

The stress tensor components are given by equation (4) with parameter γ^2 represented as P/a^2, because, in the inequality to be satisfied ($FO_1 \ll 1$), a process of heat propagation in the solid state is "quasi-one-dimensional" and the radial heat flows can be neglected.

The maximum values of the components σ_{rr} and $\sigma_{\psi\psi}$ are reached on the surface and are given by: $\sigma^*_{rr} = \sigma^*_{\psi\psi} = -2\sqrt{\frac{FO_1}{\pi}}\, e^{-\delta^2 r/4}$ i.e., the component distribution σ_{ii} over the surface repeats the intensity distribution of laser beams.

A character of behavior of the thermostress tensor components σ_{zz} and σ_{rz} is more complicated. On the surface (z=0) $\sigma_{zz}=0$, then at some distance Z_o, it reaches its maximum and tends to zero. The component value σ_{rz} is equal to zero on the surface (z=0) and on the axis OZ and tends to zero at $r,z \to 00$. Therefore, this component reaches its maximum at Z_o' and r_o'.

Using the parameter Z_o/r_o (if $FO_1 < 1$) and distributing the expressions for σ_{zz} and σ_{rz}, let us estimate α_{rz}^{max} and σ_{zz}^{max} and σ_{zz}^{max} as well as Z_o, Z_o', r_o'. Values Z_o, Z_o', r_o' for σ_{zz}^{max} and σ^{max}_{zz} are determined from $\frac{\partial \sigma_{iz}^{max}}{\partial z} = \frac{\partial \sigma_{rz}^{max}}{\partial z} = 0$ and are equal for σ_{rz}^{max}: $Z_o' = 2\sqrt{a^2\tau}$, $r_o' = \frac{r_o}{2}$ and $Z_o = 0.66 r_o$ for σ_{zz}^{max}. The component values in this case are given by

$$\begin{aligned} \sigma^{*max}_{zz} &= 1.9\ FO_1 \\ \sigma^{*max}_{rz} &= -0.5\ FO_1 \end{aligned} \tag{12}$$

The expression for the thermal-reflecting surface deformation, in case of loading by rectangular pulse, is represented as [11].

$$W^* = -\frac{FO_1}{2}\exp(-\delta_r^2/4) \tag{13}$$

The deformation distribution over the reflecting surface repeats laser beam intensity distribution, and its maximum value is proportional to Fourier number.

IV. The Specific Features of the Solid-State Thermodeformations by Powerful High-Repetition-Rate Laser Radiation.

We have analyzed the phenomena of thermostress solid-state behavior of the powerful, high-repetition rate laser radiation on the basis of correlations of Duamel-type integrals, eq (6). We take time-changing beam flux as a bundle of rectangular pulses with duration τ, period T (frequency $\frac{1}{T}$) and on-off time ratio $SQV = \frac{\tau}{T}$. With this, we assume that $FO_2 = 4K_o a^2 T < 1$.

At the initial time, i.e., value $FO < 1$, a powerful, high-repetition-rate regime of laser radiation action upon the substance has typical features of the pulse regime. Actually, a geometrical essence of eq (6)-type integrals is characterized by a square of the dashes in Figure 4.

For longer times, i.e., when FO>1, temperature and thermal stresses reach their "quasi-stationary" states, there is a constant component of these values, the same as under continuous regime of the energy input with a given intensity $I_o SQV$ (I_o - maximum of stress for the separate pulse). The background of this component, together with laser beam intensity variation, there is a stress and temperature peak approximately the same shape as (accuracy $\lesssim$ SQV) at pulse influence.

For value W a separate "pulse" of the reflecting surface thermodeformation is developed on the background of "stationary" component going to infinity.

In this case an expression for the temperature field is

$$T^* = SQV \int_o^\infty \Theta_o(\sqrt{v}\delta_t)\exp\left(-\sqrt{v}\,(\delta_z + \sqrt{v})\right)\frac{dv}{\sqrt{v}} + \frac{2}{\sqrt{\pi}}\sqrt{FO_2}\, e^{-\delta_r^2/4} \quad x$$

$$x e^{-\delta_z^2/FO_2} \sum_n {}_1\Theta(n+1-t^*)\left[\Phi(t^*-n)\sqrt{t^*-n} - \Phi(t^*-n-SQV)\sqrt{t^*-n-SQV}\right] \tag{14}$$

which is obtained directly from the summarized expression, eq (2) as for the input model of laser pulses

$$f(t) \simeq \psi(p)\,\frac{\left(1-\exp(-p\tau)\right)\left(1-\exp(-p(N-1)T)\right)}{p\left(1-\exp(-pT)\right)}$$

where N - is the number of previous pulses. Directly in the center of radiation zone the temperature is maximum at the moment of pulse stop.

The analysis of the thermostress state shows, that maximum radial and circular stresses are reached in the center of radiation zone and can be represented as:

$$\sigma_{ii}^{rr} = \int_0^t f(t-\tau)\frac{\partial \sigma_{ii}^{cw}}{\partial \tau}d\tau$$

$$\alpha_{ii}^{cw*} = \frac{1+v}{\sqrt{\pi}}\left[FO\left(\operatorname{arctg}\frac{1}{\sqrt{FO}} - \frac{1}{\sqrt{FO}}\right) - \frac{1-v}{1+v}\operatorname{arctg}\sqrt{FO}\right] \tag{15}$$

while reaching "quasi-stational" state, the expression for $\sigma_{ii}^{*RR}(0, 0, FO)$ is considerably simplified

$$\sigma_{ii}^{*RR} = -\frac{\sqrt{\pi}}{2}\left[(1-v)\ SQV + \frac{\psi}{\pi}\sqrt{FO_2}\sum_n \Phi(n+1-t^*)\left(\vartheta(t^*-n)\sqrt{t^*-n} - \Phi(t^*-n-SQV)\sqrt{t^*-n-SQV}\right)\right] \tag{16}$$

and field distribution over the surface for the moment of pulse stop is

$$\sigma_{ii}^{*RR} = SQV\sigma_{ii}^{*(1)} + \sigma_{ii}^{*(2)}$$

$$\sigma_{rr}^{*(1)} = \frac{\sqrt{\pi}}{2}(1-v)\,{}_1F_1\left(\frac{1}{2};\ 2;\ -\frac{\delta_r^2}{}\right) \tag{17}$$

$$\sigma_{\psi\psi}^{*(1)} = \frac{\sqrt{\pi}}{2}(1-v)\left[{}_1F_1\left(\frac{1}{2}\ \ 2;\ -\delta_r^2/4\right) - 2\,{}_1F_1\left(\frac{1}{2};\ 1;\ -\frac{\delta_z^2}{\psi}\right)\right]$$

$$\sigma_{ii}^{*(2)} = -2\sqrt{\frac{FO_1}{\pi}}\exp\left(-\delta_r^2/4\right)$$

In the stationary stress state σ_{rz} and σ_{zz} are equal to zero (a result of the axial symmetry); therefore, their values at power high-repetition-rate action of laser radiation will be the same as the pulse one.

The value of the solid-state surface distortion in powerful, high-repetition-rate regime has stationary and pulse components and are represented as

$$W^* = SQV\ W^{*(1)} + \sum_n \Theta^*n+1-t^*)\ \left[\Theta t^*-n)W^{*(2)}(t^*-n)\right. \tag{18}$$

$$\left.-\Theta(t^*-n-SQV)W^{*(2)}(t^*-n-SQV)\right]$$

where

$$W^{*(1)} = -\frac{FO}{2}\left[e^{-\delta_z^2/4} - \left(\frac{4}{\sqrt{FO}(1+FO)} - \frac{2}{FO}\ln\left(\sqrt{FO} + \sqrt{FO+1}\right)\right){}_1F_1\left(\frac{3}{2};\ 1;\ -\frac{\delta_r^2}{r}\right)\right]$$

$$W^{*(2)} = -\frac{FO_1}{2}\exp\left(-\delta_r^2/4\right)$$

For "quasi-stationary" thermostress state thermodeformation value in the cent of radiation zone is determined as

$$W^* = -SQV \ln(2\sqrt{FO}) - \frac{FO_2}{2} \sum_n \theta(n+1)-t^*)$$
$$x \left[\theta(t^*-n)(t^*-n)-\theta(t^*-n-SQV)(t^*-n-SQV)\right] \quad (19)$$

Thus, we fully described a character of the thermostress state occuring in the elastic half-space under action of CW powerful, high-repition-rate laser radiation. Let us note the following typical features of thermodeformation process which are the consequence of the expressions obtained:

a. The process is local. A characteristic dimension of the field stress localization, temperature and deformation, order of characteristic radiation zone dimension is r_o.

b. At low exposition time of laser radiation in continuous and power, high-repetition-rate regimes, as well as in pulse regime ($FO_1 > 1$), the temperature increasing rate, thermal stresses and deformations are proiportional to I_o laser beam intensity, whereas, at the parameters FO , 3, 4 these values (in continuous and powerful, high-repetition-rate regimes) reach their quasi-stationary level whose value generally is proportion to Io.

c. The expressions obtained make it possible to determine laser beam parameter values Io, A, Ko, t, τ, SQV, which are specified by a stage of elastic material behavior characterized by a total reduction of the initial state of laser beam surface influence. However, in several cases under continuous and power, high-repetition-rate laser radiation thermal optical surface deformation becomes inadmissibly large ($W > \lambda/20$). To take deformation into account is very important for such laser schemes as quasi-optical communication lines, telescopes, stable and nonstable resonators, and focusing systems.

d. A consideration performed allows us to determine the intensity value of laser beam, under which a material transfers into nonelastic region due to stresses, appeared while radiation exceeded its flow limit in continuous and pulse regimes, or fatigue limit of power, high-repetition-rate regime.

The limit stress value $I_{w=\lambda/20}$, $I_{\sigma f}$, I_{tm} under continuous laser radiation action is expressed as

$$I_{tm} = \frac{2\lambda\sqrt{K_o}}{\sqrt{\pi}A}$$

$$I_{\partial f} = \frac{2\lambda\sqrt{K_o}\,\sigma_f}{\sqrt{3\pi}\,AC\alpha_t(1+v)} \quad (20)$$

$$I_w = \lambda/20 = \frac{\lambda K_o \lambda_{laser}}{20(1+v)\alpha_t A \ln(2\sqrt{FO})}$$

In case of physical metal characteristics to be satisfied to

$$\frac{\sigma_f}{(1+\nu)G\alpha_t T_m} < 1 \tag{21}$$

then value $I_{\sigma f} < I_{Tm}$. If laser beam exposition times such as

$$\ln 2\sqrt{FO} > \frac{\sqrt{3\pi K_o}\,\lambda_{laser} G}{20\sigma_f} \tag{22}$$

then $I_w = \lambda/20 < I_{\sigma f}$

Under pulse radiation action the expressions for the limit values of laser beam intensities are

$$I_{tm} = \frac{\sqrt{\pi}\lambda T_m}{2A\sqrt{a^2\tau}}\,; \qquad I_{\sigma f}(\sigma_{rz}) = \frac{\lambda(1-\nu)\sigma_f}{AE\alpha_t\sqrt{K_o a^2\tau}}\,;$$

$$I_{\sigma f}(\sigma_{rr}) = \sqrt{\frac{\pi}{3a^2\tau}}\,\frac{\lambda(1-\nu)\sigma_f}{2AE\alpha_t}\,, \quad I_{\sigma b}(\sigma_{zz}) = \frac{(1-\nu)\lambda\sigma_b}{4AE\alpha_t\sqrt{K_o a^2\tau}}\,; \tag{23}$$

$$I_{\sigma f}(\sigma_{zz}) = \frac{\lambda(1-\nu)\sigma_f}{6.6\ AE\alpha_t\sqrt{K_o a^2\tau}}\,; \quad I_w = \lambda/20 = \frac{\lambda \cdot \lambda_{laser}}{40(1+\nu)A\alpha_t a^2\tau}.$$

With this, it turns out, that $I_{\sigma f}(\sigma_{rz}) > I_{\sigma f}(\sigma_{zz}) > I_{\sigma f}(\sigma_{rr})$ since $I_{\sigma_f}(\sigma_{rz})/I_{\sigma f}(\sigma_{zz}) = 6.6$, and $I_{\sigma f}(\sigma_{zz})/I_{\sigma f}(\sigma_{rr}) > 1/\sqrt{FO_1}$. In case of physical substance characteristics to be satisfied to $\sqrt{3}E\alpha_t T_m/\left((1-\nu)\sigma_f\right) > 1$ (for information $E/\sigma_f \sim 10^3$ to 10^4), the value I_{Tm} exceeds $I_{\sigma f}(\sigma_{rr})$, and for the time such as

$$\tau > \frac{3\lambda^2_{laser}}{400\ \pi a^2}\left[\frac{E}{\sigma_f(1-\nu)^2}\right]^2 \tag{24}$$

$I_{\sigma f} > I_{w=\lambda/20}$ is valid.

Under the action of power, high-repetition-rate laser radiation upon the solid-state surface, the limit intensity values are determined from

$$I_i^{RR} = SQV\ I_i^{cw} + I_i^{IMP} \tag{25}$$

where I_i^{cw} are determined from eq (20) and I_i^{IMP} from eq (23).

As a result of nonstationary, cyclically repeating stress state, the irradiated substance can undergo nonconvertible fatigue changes, if the vibration amplitude of one of the thermostress tensor components 1

σ_{ij} exceeds a fatigue limit $\sigma_f^{(0,1)}$, determined correspondingly for compression or for deflection.

The limit intensity values determined for each of the components σ_{ij} are

$$I_{\sigma_f}(\sigma_{rr}) = \sqrt{\frac{\pi}{FO_1}}\,\frac{\lambda\sqrt{K_o}(1-v)\sigma_f^{(c)}}{AG\alpha_t(1+v)}\,;$$

$$I_{\sigma_f}(\sigma_{zz}) = \frac{\lambda\sqrt{K_o}(1-v)\sigma_f^{(c)}}{2FO_1AG\alpha_t(1+v)}\,;\quad I_{\sigma_f}(\sigma_{rz}) = \frac{2\lambda\sqrt{K_o}(1-v)\sigma_f^{(t)}}{FO_1AG\alpha_t(1+v)} \tag{26}$$

If, at the duration time of the separate laser pulse, the equation is satisfied

$$0 < FO_1 < \frac{1}{4\pi}$$

then the inequality $I_{\sigma_f}^{(c)}(\sigma_{rr}) < I_{\sigma_f}^{(c)}(\sigma_{zz}) < I_{\sigma_f}^{(c)}(\sigma_{rz})$ is valid. If $1/4\pi < FO_1 < 1$, then, $I_{\sigma_f}^{(c)}(\sigma_{zz}) < I_{\sigma_f}^{(c)}(\sigma_{rz}) < I_{\sigma_f}^{(t)}(\sigma_{rt})$.

Since $0_f(0,1) \sim 0.1\,\sigma_f$, then the fatigue distortions of irradiated surface (micro- and macrocrack development, separation of the near-surface layer, structure and phase substance changes) will occur under laser beam intensities by an order of magnitude less than those where the material transfers into nonelastic region [14-17].

One should bear in mind, however, that the results obtained are valid for the ideal surface in vacuum (since the air, a slight pollution of irradiated surface, and the microcracks appearing due to stress concentrations in the granule boundaries, etc.) can resule in gas damage near the surface and, consequently, in the surface destruction under laser radition intensities much less than calculations of (20-26).

V. Conclusion.

The results obtained can estimate a role of thermoelastic damage mechanism in the process of interaction of powerful continuous, pulse and high-repetition-rate laser fluxes with the solid-state surfaces. We generally determined the temperature, stress, and distortion fields. Based on the expressions obtained, we have systematically studied the specific features of thermal and stress states which occured in the solid states under such fluxes of laser radiation. We introduced a system of parameters of the stability for different destruction mechanisms developed under such types of the thermostress states.

VI. Appendix.

The expressions characterizing the thermostress state of the elastic half-space, whose surface is subjected to continuous pulse and high-repetition-rate laser radiation, are represented in this paper as the coordinate and time functions. However, during experimental investigations in laser

radiation interaction with substance, the thermal stresses and deformations are defined by the temperature value.

A relation between the stresses in the center of radiation zone and the temperature during an establishment of the stationary state under continuous laser radiation is

$$\sigma_{ii}^{*cw} = \frac{1+v}{\sqrt{\pi}} \left[tg^2\left(\frac{\sqrt{\pi}}{2}T^*\right)\left(arctg\left(\frac{1}{tg\sqrt{\frac{\pi}{2}}\,T^*}\right) - \frac{1}{tg\left(\frac{\pi}{2}\,T^*\right)}\right) - \frac{\sqrt{\pi}}{2}\,\frac{1-v}{1+v}\,T^*\right] \tag{27}$$

When the termperature T^* tends to its stationary state $\sqrt{\pi}$ expression for σ_{ii}^{*cw} is

$$\sigma_{ii}^{*cw} = -\frac{1-v}{2}\,T^* \tag{28}$$

The expression for thermal deformation value as a function of temperature is

$$W^{*cw} \approx -\ln\left(2tg\frac{\sqrt{\pi}}{2}T^*\right) \tag{29}$$

The specific feature of the stress state developing under pulse influence is that, for the thermostress tensor components σ_{ii} on the surface in the center of radiation zone, the following equality is satisfied

$$\sigma_{ii}^{*IMP} = -T^{*IMP} \tag{30}$$

and for the components σ_{zz}^{max}, σ_{rz}^{max}:

$$\sigma_{zz}^{*max} = 0.5\pi\left(T^{*IMP}\right)^2;\ \sigma_{rz}^{*max} = -0.13\pi^2\left(T^{*IMP}\right)^2 \tag{31}$$

A relation between thermal deformations and temperature is given by

$$W^{*IMP} = -\frac{\pi}{8}\left(T^{*IMP}\right)^2 \tag{32}$$

The symbols for σ_{ii}^{IMP}, σ_{rz}^{IMP}, and σ_{zz}^{IMP} are different because on the surface, in the center of radiation zone, the substance compression is realized, whereas the component at the distance Z_o realizes an extension.

In the case of high-repetition-rate laser radiation action upon the solid state surface, the expressions for $\sigma_{ii}^{*}(T^*)$ and for the moment of pulse stop are

$$\sigma_{ii}^{*RR} = \frac{1}{2}\,(1+v)\sqrt{\pi}\ SQV - T^* \tag{33}$$

The expressions for σ_{rz}^{*max} and σ_{zz}^{*max} are given by

$$\sigma_{zz}^{*RR} = \frac{\pi^2}{2}\left(\frac{T^*}{\sqrt{\pi}} - SQV\right)^2$$

$$\sigma_{rz}^{*RR} = 0.13\pi^2 \left(\frac{T^*}{\sqrt{\pi}} - SQV\right)^2 . \qquad (34)$$

REFERENCES

[1] V .V. Apollonov, E. M. Shefter, "Thermal Effects of Powerful Laser Radiation on the Surface of a Solid." Preprint FIAN SSSR No I05, Moscow, 1974.

[2] V. V. Apollonov, A. I. Barchukov, V. I. Konyukhov, A. M. Prokhorov. Pis'ma ZHETF, t. 15, str. 248, 1972.

[3] A. A. Apollonov, A. I. Barchukov, A. M. Prokhorov. IEEE, J.QE-10, p. 505, 1974.

[4] A. I. Barchukov, Yu.B.Konev. Preprint FIAN, No 158, 1973.

[5] E. Melan, G. Parkus, "Thermal Elastic Stresses Caused by Steady Temperature Fields." Fizmatgis, 1958

[6] G. Parkus, "Irregular Temperature Stresses." Fizmatgis, 1963

[7] Vitold Novatsky, "Problems of Thermoelasticity." Iz-vo AN SSSR, 1962

[8] G. Dech. Rukovodstvo, "Manual on the Practical Application of Laplace Transforms." Fizmatgiz, 1958.

[9] I. S. Pradshtein, I. M. Ryzhik, "Table of Integrals Sums, Series, and Products." Iz-vo Nauka, 1971.

[10] A. D. Kovalenko, "Thermoelasticity." Kiev, 1975.

[11] V. V. Apollonov, F. V. Bunkin, V. Yu.Khomich, S. A. Chyotkin. Pis'ma v ZHETF, v.4, vyp.17, 1978 [1017], "Thermodeformation Method for Changing the Intensity of a Powerful Laser Beam."

[12] F. Lesh, F. Emde, E. Yanke, "Special Functions." Nauka, 1964.

[13] V. I. Krylov, L. T. Shul'gina, "Reference Book on Numerical Intergration." Nauka, 1966.

[14] T. Ekorbi, "Physics and Mechanics of the Failure and Strengths of Solids." M. 1971.

[15] E. G. Kovalenko, V. M. Drpzdpv. M. D. Drozdov, M. D. Tyavlovsky, "Dynamic Strength of Materials."

[16] V. S. Ivanova, "Fatigue Failure of Metals." M. 1963.

[17] V. V. Apollonov, A. I. Barchukov, N. V. Karlov, A. M. Prokhorov, V. Yu.Khomich, E. M. Shefter. "Stability Parameters of Mirror Surfaces of Laser Reflectors." Pis'ma v ZETF, v.1, vyp. II (522), 1975.

[18] V. V. Apollonov, P. I. Bystrov, V. F. Goncharov, A. M. Prokhorov, V.Yu.Khomich, "Prospects for the Use of Porous Structures to Cool Elements of Powerful Optics," Kvantovaya Elektronica, 6 No 123, 1979 (2533).

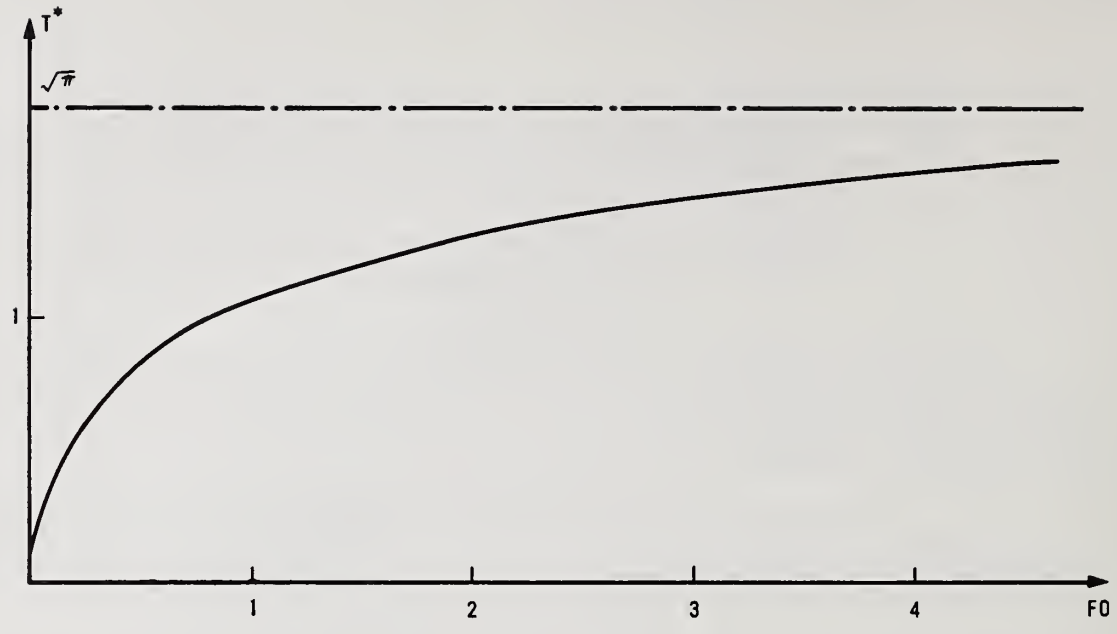

Figure 1. Temperature field on the surface at the point r=0 as a function of Fourier number in CW irradiation regime.

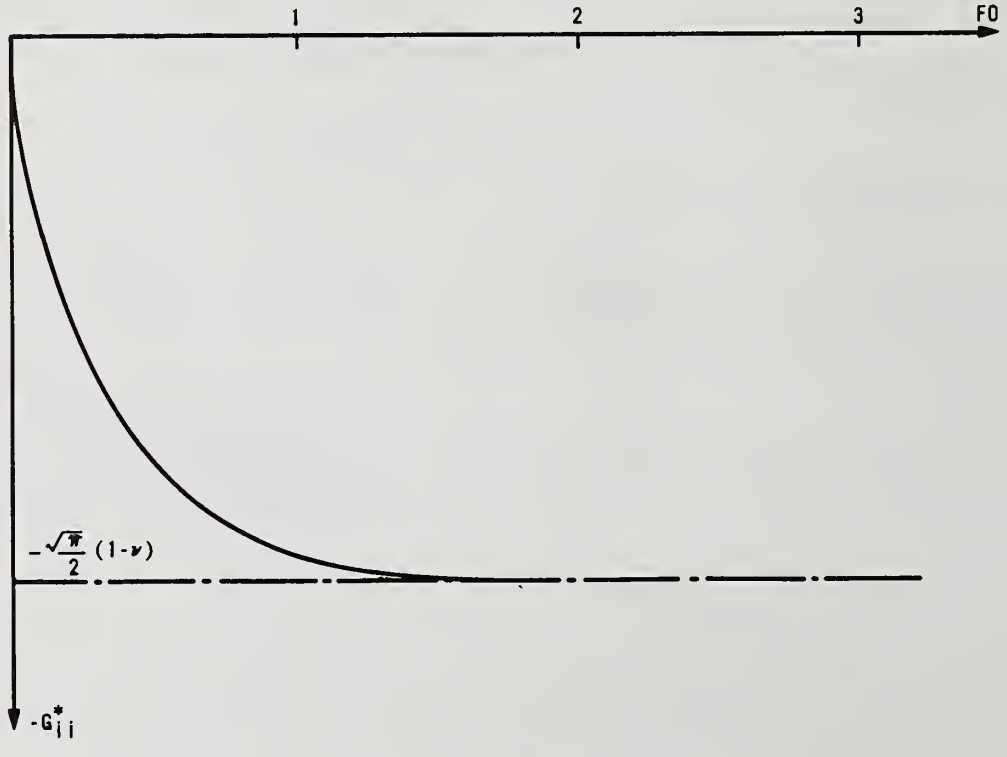

Figure 2. Stresses on the mirror surface at the point r=0 as a function of Fourier number in CW irradiation regime.

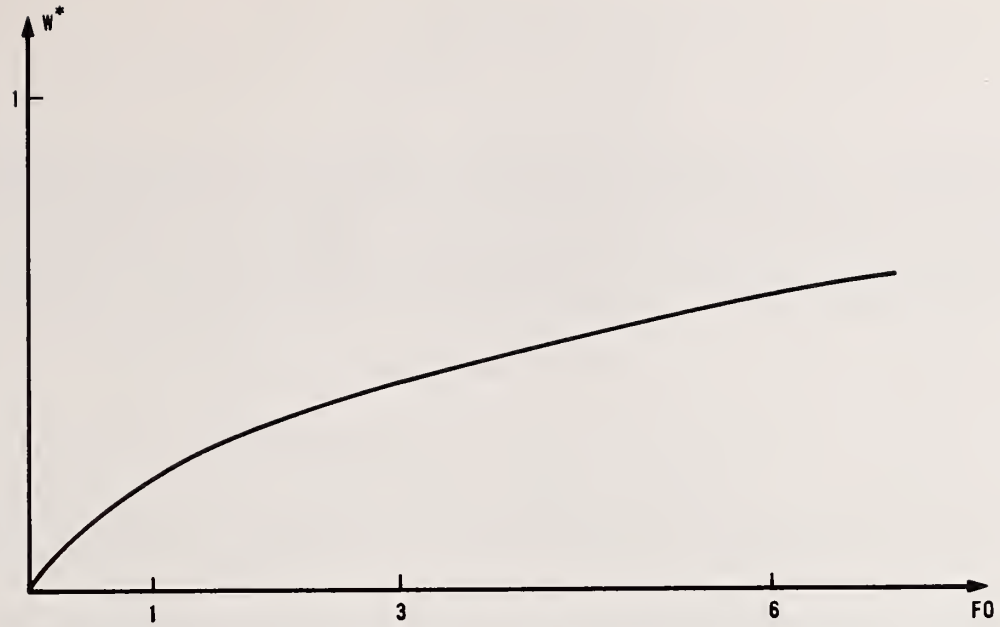

Figure 3. Displacement of mirror surface at the point r=0 as a function of time (Fourier number) in CW irradiation regime.

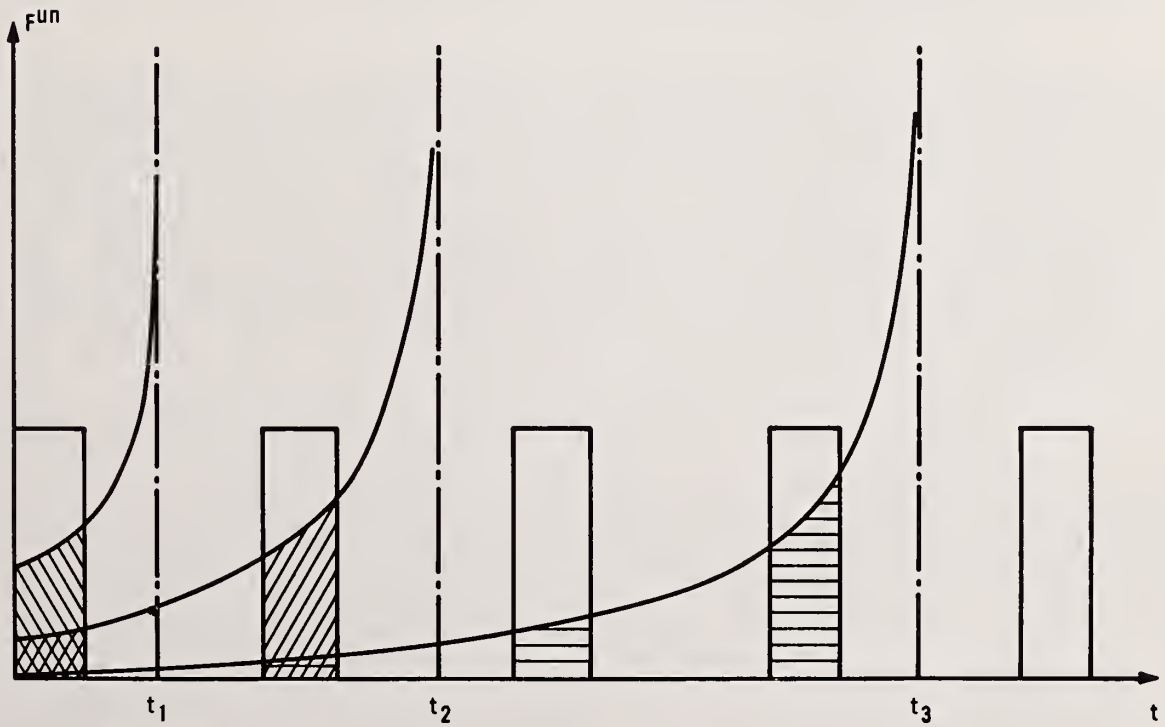

Figure 4. Geometrical interpretation of the Dhuamel integral.

The Promising Use of Some Heat Carriers in High Intensity Laser Optics

V. V. Apollonov, P. I. Bystrov, S. A. Chyotkin, V. G. Goncharov,
V. Yu. Khomich, A. M. Prokhorov

Heat and thermodeformation characteristics of laser mirrors based on powder and felt porous structures cooled by dielectric and liquid metal heat carriers are theoretically investigated. In the case of the heat carriers considered, it is possible to widely vary the regimes of intense heat mass transfer in porous heat exchangers of laser mirrors, whereas use of liquid metal cooling with porous structure fabricated from low coefficient thermal expansion material opens new possibilities in development of especially accurate reflectors with very high optical damage thresholds.

Keywords: high-power mirrors; liquid metal cooling; cooled mirrors; thermal distortion of mirrors.

Papers [1-4] deal with theoretical and experimental investigations of thermophysical processes in the cooling systems of the force optics elements (FOE) based on the porous structure (PS). These papers confirm the methods of intraporous convection cooling being used in the FOE development. The conditions of the intense heat removal process realization are restricted by a temperature interval of the liquid water state used as a heat carrier and by a relatively small value of its heat transfer coefficient.

A number of heat carriers, characterized by a good unity of thermophysical properties used for high intensity laser optics, are investigated in the present paper in order to extend the allowed regimes of the intense heat mass transfer process in the cooling systems and to increase optical damage thresholds (ODT) in FOE. Consideration is given to the dielectric heat carriers with large temperature intervals of liquid state as well as liquid metal with high heat transfer coefficients [6].

In terms of the method suggested in Reference 1, heat and thermodeformation FOE characteristics (Table I) were calculated on the basis of porous powder and felt structures (PPS and PFS), cooled by the heat carriers. An average diameter of the granules (felts) and porosity of the structures used were varied within $20\mu \leq d_s \leq 200\mu$ and $0.1 \leq \Pi_v \leq 0.9$. The variation ranges of heat carrier flow rates obtained as a result of hydraulic calculation of FOE cooling system are listed in Table I. The calculations were carried out assuming the heat carrier pressure differential through the PS reflector was permanent. Maximum temperature of the cooled mirror surface (Table I) was equal to that of the boiling heat carrier [5].

1. Dielectrical Heat Carriers

As the dielectric heat carriers cooled by FOE, a number of liquids whose thermophysical and hydraulic characteristics vary widely were considered (Table I). Figure IA-D represents the results of the family curve calculations of thermodeformation characteristics of the copper PS reflector showing the potential heat carrier possibilities in FOE cooling. Thus, when used in water, deuterium, and silicone the maximum values of thermal fluxes removed from the PPS and PFS FOE surface differ sightly ($\sim$20 to 30%) and are on the level of 4 to 4.5 KW/cm^2 (Fig. IA-C). However, the values of the thermal deformation W_2 corresponding to the thermal fluxes indicated are: for water - 1.5μ, for deuterium and silicone in PFS - 3 to 4μ, and in PPS - 5 to 6μ. When alcohol and kerosene are used as heat carriers, the values of removed thermal fluxes are decreased up to 1.5 and 2 KW/cm^2 in PPS and up to 2 and 4 KW/cm^2 in PFS, respectively. The values of W_2 are then on the level of 1.5μ and 1 to 2μ.

The nature of the curves in Figure IA-D exhibit the specific features of thermo- and mass transfer under convectional PS reflector cooling by the different heat carriers. The output of the closed value of thermal fluxes when used in FOE kerosene, deuterium, and silicone results mainly from the high temperature of the reflecting layer as well as from the different collector systems. The collector systems used in place of deuterium and silicone provide a comparatively high flow rate, which compensates for their low efficiency in the process of intense heat removal. The thermal deformation value of an FOE reflecting surface while using alcohol and water as heat carriers is decreased up to 1.5 to 2μ, which is associated with the relatively low values of their maximum working temperatures. Observed were the comparatively high ODT results from water and alcohol having relatively small values of viscosity and Pr number coefficients (Table I).

In case of high temperature heat carriers (kerosene, deuterium, silicone), the upper and lower curves of thermodeformation characteristics differed, which indicates a degree of stability of realization of the limiting PS cooling regimes.

In real PS, characterized by the average values of the bulk porosity and granule dimensions d_s, each microscopic volume is corresponded with d_s and Π_v -, i.e., we have a situation, when point with $d_s' = d_s + \Delta d_s$ and $\Pi_v' = \Pi_v + \Delta\Pi_v$ is in the upper curve, and with $d_s'' = d_s - d_s$ and $\Pi_v'' = \Pi_v - \Delta\Pi_v$ is in the lower curve which leads to heat removal inhomogeneity in PS and, consequently, decreases FOE reflectors.

Under convection FOE cooling with given structure parameters of the porous layer, high heat transfer intensity independent of constructive features of the collector system is determined by a heat exchange efficiency coefficient in the heat carrier supply zone $A_{eff} = Q_1/\Delta T$: where Q_1- is the high intensity of the removed FOE thermal flux, the cooled surface temperature of the separation layer is the heat carrier boiling temperature; and ΔT - is the difference between the boiling temperature of the heat carrier and its temperature in the porous structure input. A_{eff} is defined as specific density of the removed thermal flux for I C heat carrier warm-up. Based on the model ideas developed in Reference 1, A_{eff} is:

$$A_{eff} = \tilde{\lambda} \sqrt{\frac{SvC}{d_s}} \left(Re_{dr}P\right)^{n/2} \qquad (1)$$

In the semilogarithm coordinate system Figures 2A and 2B show the dependence of $A_{eff} = f(1g\ Re\ d_r)$ upon the heat carrier flow regime.

This dependence characterizes an influence of the structural parameters of porous layer (characteristic dimension d_s and porosity Π_v, providing maximum heat removal) upon the heat exchange intensity and heat carrier flow regime. When $\Pi_v = 0.6$ maximum of A_{eff} reached at PS parameter $d_s = 20\mu$ is listed in Table I. A most value of A_{eff} is realized in PPS if $Lg\ Re\ d_r < I$, then in PFS - if $1g\ Re\ d_r > I$. In case of PPS cooled by water, maximum of $A_{eff} = 14.10^5$ W/M^2°C, whereas in case of kerosene and alcohol A_{eff} falls to $8.3 \cdot 10^5$ and $5.4 \cdot 10^5$, respectively.

2. Liquid-Metal Heat Carriers (LMH)

The optical damage threshold of mirror surfaces [1] performed on the basis of a porous structure can be increased if liquid alkali metals and their alloys are used as heat carriers. A promising use of the liquid-metal heat carriers to cool force optics elements depends on the high coefficient of heat exchange which can be reached in a porous layer due to a good agreement of thermophysical properties of the liquid metals. This makes it possible to reduce the requirements for thermoconductivity of the porous structure materials, which opens the possibility of using the new constructive materials with low thermal expansion coefficient and worsened thermoconductivity in reflectors.

For the purpose of cooling, using laser mirrors of eutectic alloy liquid metals with low fusing temperature (say, Na-K alloy with fusing temperature-II°C) is a question of special interest. In the case of liquid-metal heat carriers, it is possible to carry out the convection reflector cooling at the temperature close to that of the final preparation of the mirror surface.

As an example, Figures 3 and 4 represent the results of calculations of thermodeformation characteristics of the reflector family cooled by eutectic heat carrier Na-K. The porous reflector structures are made from molybdenum and invar felt structures. An average felt diameter and the bulk structure porosity vary within $20\mu < d_s < 200\mu$ and $0.1 < \Pi_v < 0.9$. The curves of Figures 3 and 4 are envelopes of the thermodeformation reflector family characteristics and are plotted considering heat carrier pressure drop in reflector to be constant at the maximum temperature of the cooled surface equal to 100°C [2]. At liquid-metal cooling, this restriction is not decisive (i.e., water cooling). A temperature range for liquid metals can be considerably extended, which increases the removed heat load.

Figure 3 shows that optical surface deformation in the heat carrier removed zone, calculated with consideration of the heat carrier heating in porous layer, greatly exceeds the deformation in supply zone $W_2 >> W_I$. High thermal flux densities for the reflector family considered were in heat carrier supply zone $q_I > 20$ KW/cm^2, and in the removed zone $q_2 = 6.6$ KW/cm^2, then $W_2 = 0.3\mu$. A minimum deformation level in the heat carrier removed zone at the removed flow is 4.2 KW/cm^2 $W_2 = 0.12\mu$, which is considerably lower than the optical damage threshold of CO_2-laser reflectors.

The thermodeformation characteristics of the reflector family represented in Figure 3 show the potential feasibilities of the liquid-metal cooling. A considerable difference of the curves is determined by an influence of heat carrier heating in the porous layer because of relatively low Na-K alloy heat capacity. Therefore, a degree of perfection of the flowing cooling system region is decisive in the development of this kind of reflectors.

Analyzing the calculated results from Figure 4 it is evident that using porous structures from low-thermal expansion coefficient materials (invar fibres) makes it possible at the liquid-metal cooling to considerably decrease (approximately by a factor of 3-4) the thermodeformation mirror surfaces both in the supply zone and in the heat carrier removed zone. In this case, the maximum heat loads removed from the mirror surface, providing 100°C on the level are: $q_I > 20$ KW/cm^2, $q_2 = 3.5$ KW/cm^2 [2].

A thermodeformation characteristic of invar fiber reflector in the range of the minimum optical surface deformation (Fig. 4b) and point W_{min}) is characterized by deformation $W_2 \simeq 0.02\mu$ at the removed thermal flux 2.4 KW/cm^2.

Thermodeformation characteristics of the mirror surface (Figs. 3 and 4), because of lack of reliable data on convection heat exchange of the liquid metals in the porous layer, should be considered as estimated. However, these results show the promising use of liquid metals for cooling the force optics elements based on metal-fiber structures. Using liquid-metal cooling, together with porous structures fabricated from low-thermal expansion coefficient materials, opens new possibilities in development of accurate reflectors with high-optical damage thresholds.

3. Conclusion

It is concluded that for each of the heat carriers considered, it is possible to realize the great values of ODT of the mirror surfaces cooled by FOE as well as the great values of the removed thermal fluxes. From the heat carriers indicated, the regimes of heat mass transfer intensities are widely varied. In addition, the use of LMH, together with PS from the material of low thermal damage coefficient, opens principle possiblities in developing highly accurate ODT reflectors. The obtained families of curves make it possible to establish the optimal parameters of porous structures which remove the necessary heat loads from the reflector surface under allowed mirror surface distortions.

References

1. V. V. Apollonov, P. I., Bystrov, V. F. Goncharov, A. M. Prokhorov, V. Yu. Khomich. Kvantovaya elektron., 6, No I2, 2533-2545 (1979).
2. V. V. Apollonov, A. I. Barchukov, V. I. Borodin, P. I. Bystrov, V. F. Goncharov, et al. Pis'ma v ZHETF, 4, II93 (1978).
3. V. V. Apollonov, A. I. Barchukov, V. I. Borodin, P. I. Bystrov, V. F. Goncharov, et al. Kvantovaya elektron., 5, No 5, II70 (1978).
4. V. V. Apollonov, P. I. Bystrov, V. F. Goncharov, A. M. Prokhorov, V. Yu. Khomich, S. A. Chyotkin, Pis'ma v ZHETF.
5. N. B. Vargaphtik. Spravochnik po teplophizicheskim cvoistvam gasov i zhidkostei. Nauka, M., 1972.
6. V. I. Subbotin, M. Kh. Ibragimov, P. A. Ushakov et al. Hydrodynamica i teploobmen v atomnykh energeticheskikh ustanovkakh (osnovy raschyota). M. Atomizdat, 1975.

Table I

Thermophysical heatcarrier properties.

	T C^o	g/sm-s	$\frac{g}{sm3}$	Cp $\frac{cal}{g \cdot °C}$	$\lambda \cdot 10^{-4}$ $\frac{cal}{sm \cdot g \cdot s}$	Pr	T_{mel} °C	T^W °C	G kg/s	$A_{eff} \cdot 10^{-3}$ $\frac{W}{M° °C}$
Water	100	0.01	1	1	14.3	7	0	100	0.2-4	15
Alcohol	78	0.012	0.8	0.7	4	22	-114	78	0.2-4	8.4
Kerosene	200-302	0.015	0.8	0.5	2.4	27	50	200	02-4	5.6
Silicon	280	0.1	1	0.5	3.3	144	12°C	200	0.5-10	7.2
Dauterm	260	0.044	1.1	0.4	3.2	50	-70	200	0.5-10	5.5
Na-K	780	8.10^{-2}	0.9	0.3	530	0.05	-11°C	100	0.2-4	

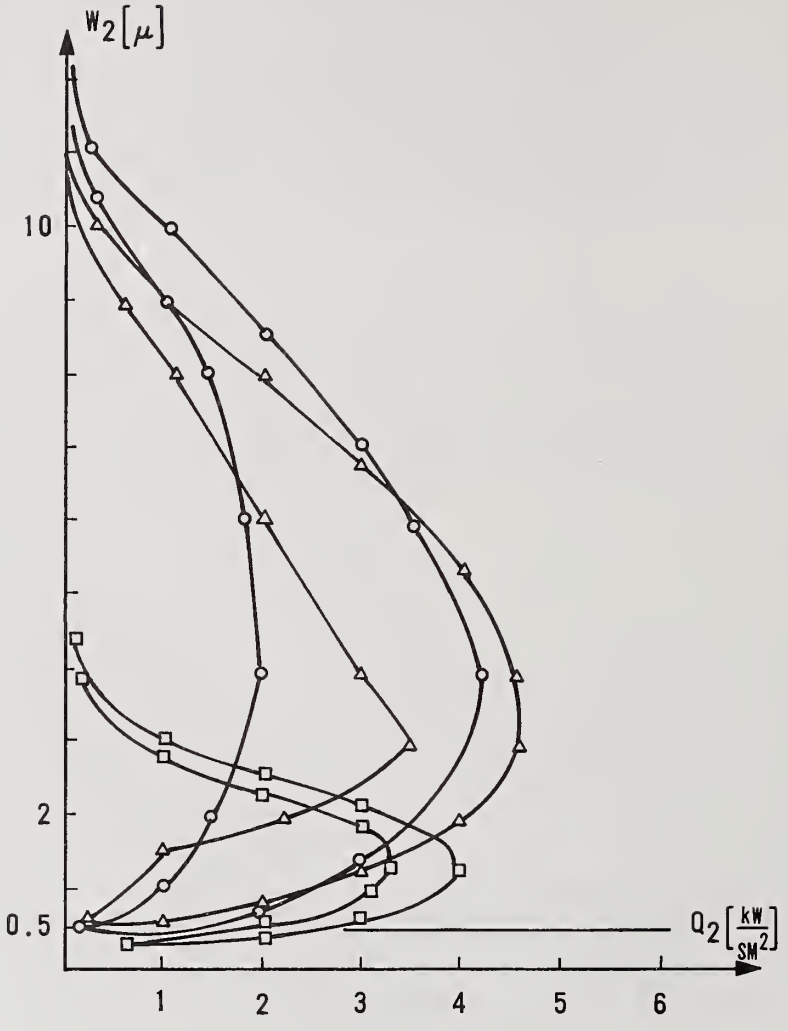

Figure 1A. Thermal deformation for FOE using copper PFS; Δ - dauterm, O - silicon, □ - water.

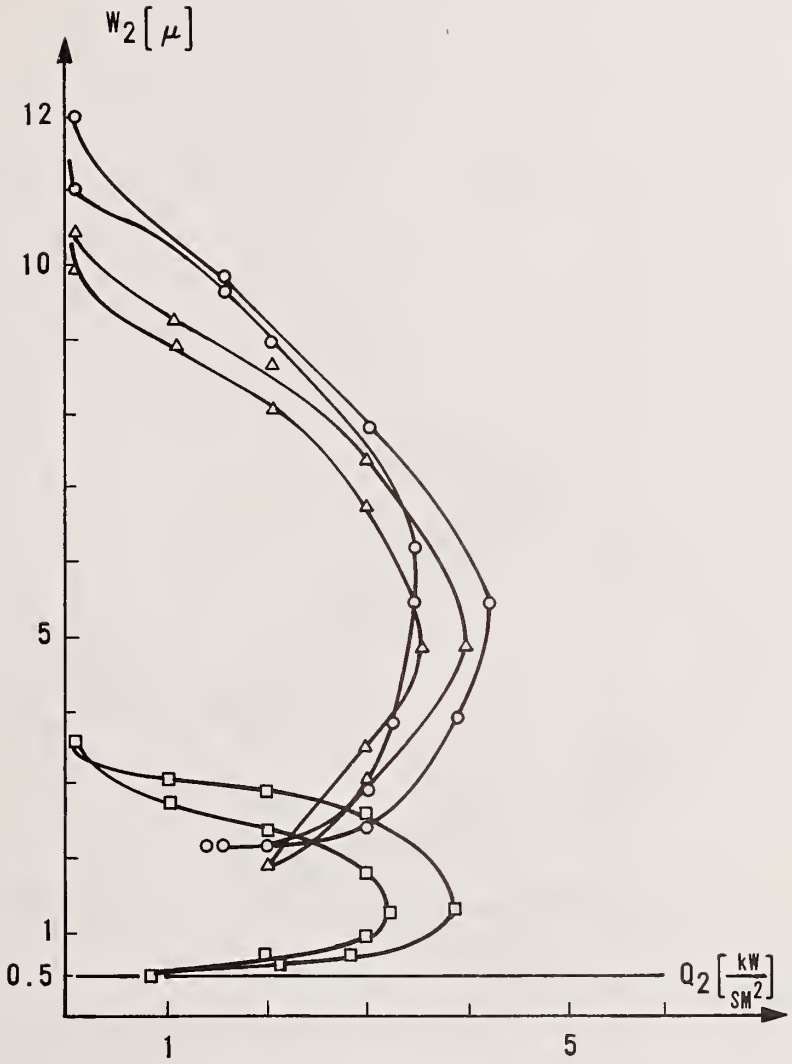

Figure 1B. Thermal deformation for FOE using copper PPS; Δ - dauterm, O - silicon, ◘ - water.

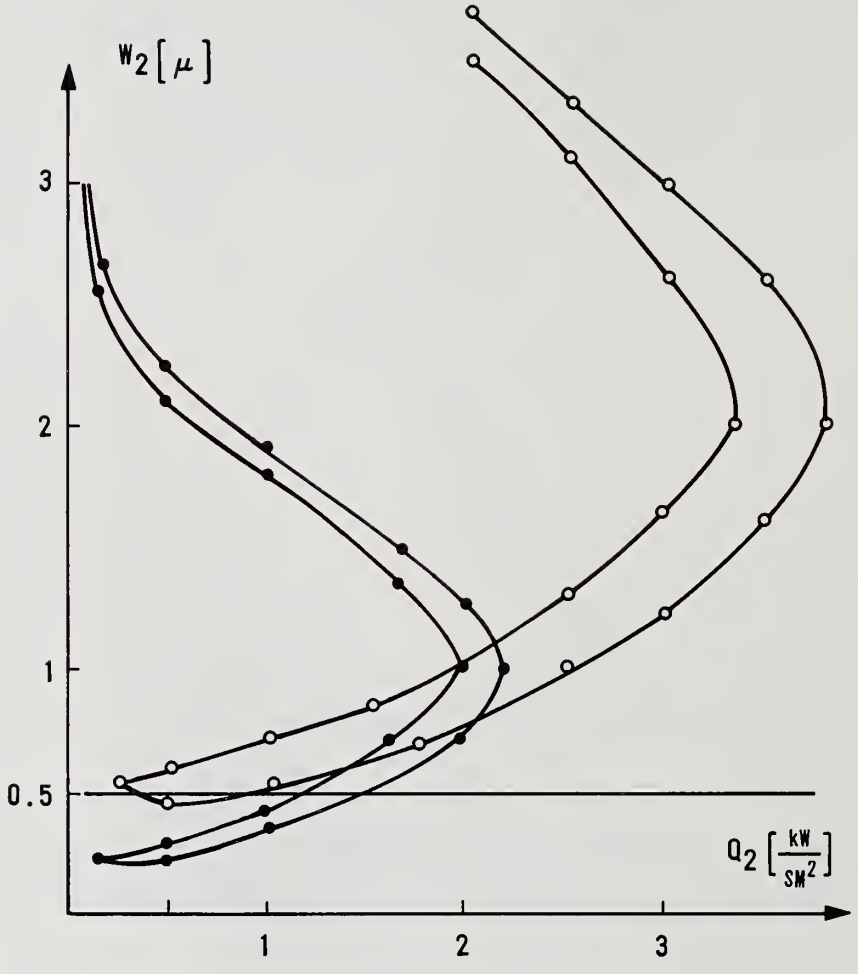

Figure 1C. Thermal deformation for FOE using copper PFS; • - alcohol, O - kerosene.

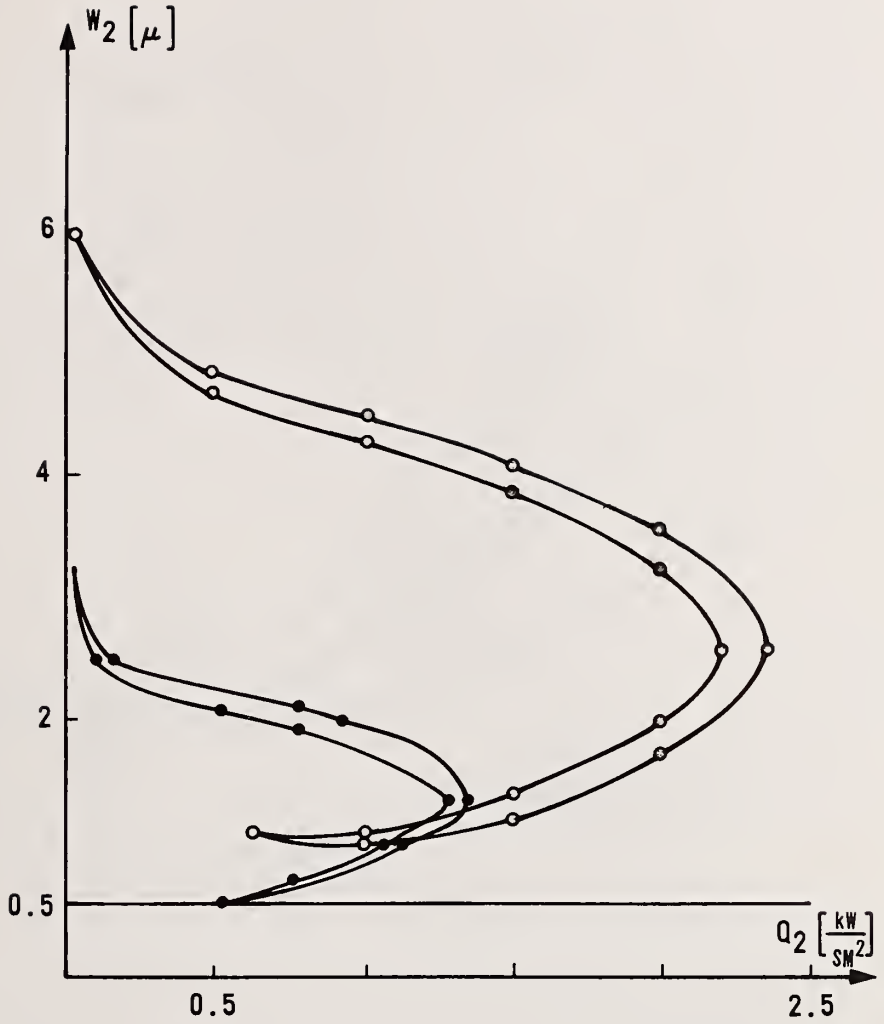

Figure 1D. Thermal deformation for FOE using copper PPS; ● - alcohol, o - kerosene.

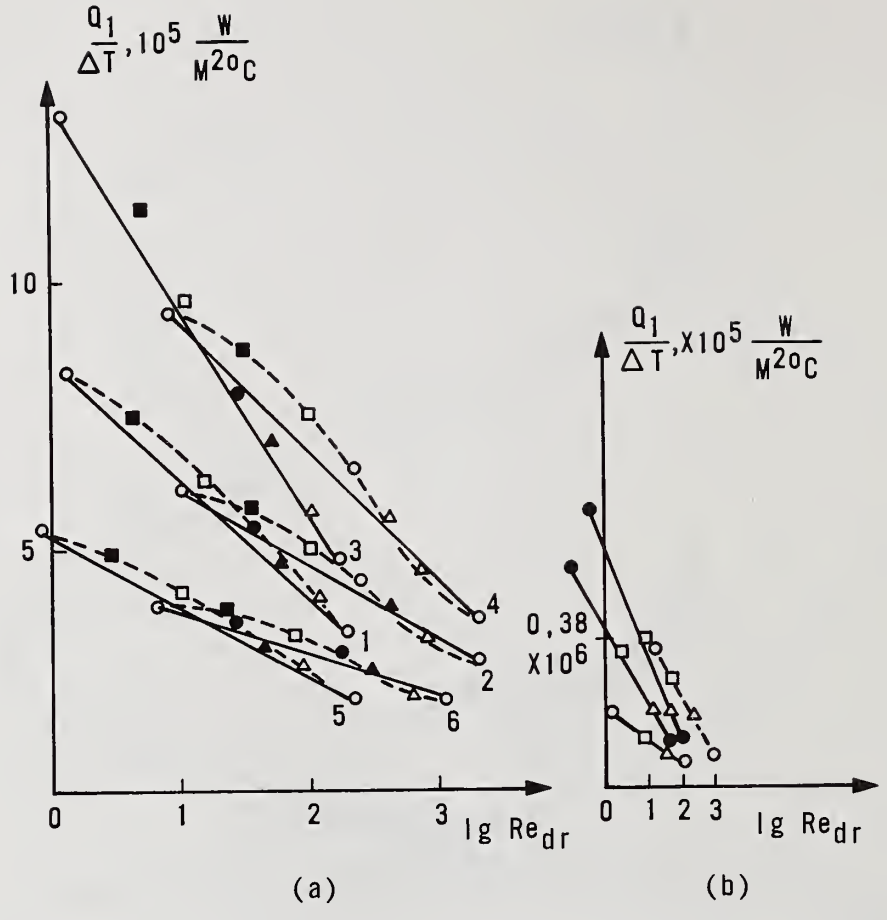

Figure 2. Dependence of the effective heatremoval coefficient cooled by FOE based on copper PPS and PFS vs. hearcarrier flow regime.

a) d_s; O - 20 μ; ■-30 μ; □- 50 μ ● - 75 μ
▲ - 100 μ; Δ - 150 μ; O - 200 μ

b) _____ dauterm; PPS: - black labels

- - - - - - silicon; PPS: - light labels

d_s: O - 20 μ; - 50 μ; Δ - 100 μ; O - 200 μ.

(a)

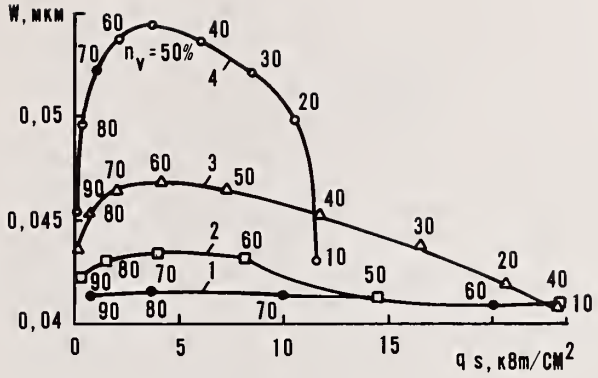

(b)

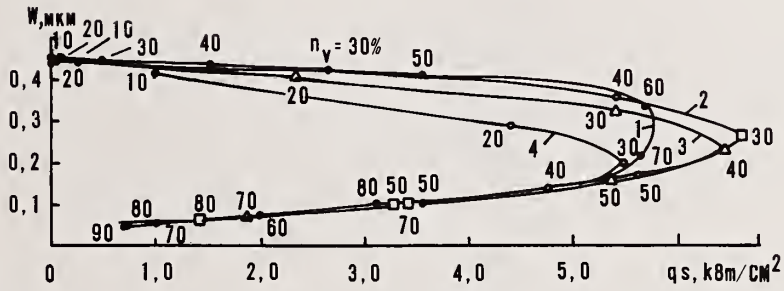

Figure 3. Holograms of thermodeformation FOE characteristics based on Mo PFS cooled by Na-K heatcarrier in the supply (a) and removed (b) zones at d_s = 20 (1), 50 (2), 100 (3), 200 (4) μ.

(a)

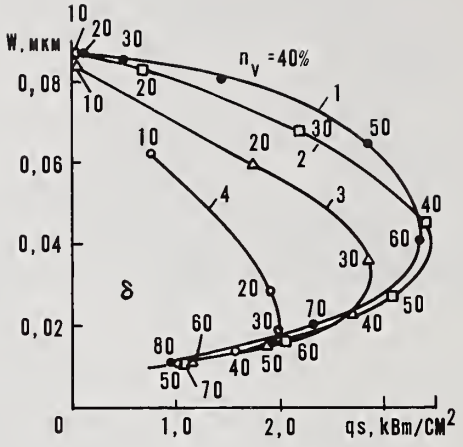

(b)

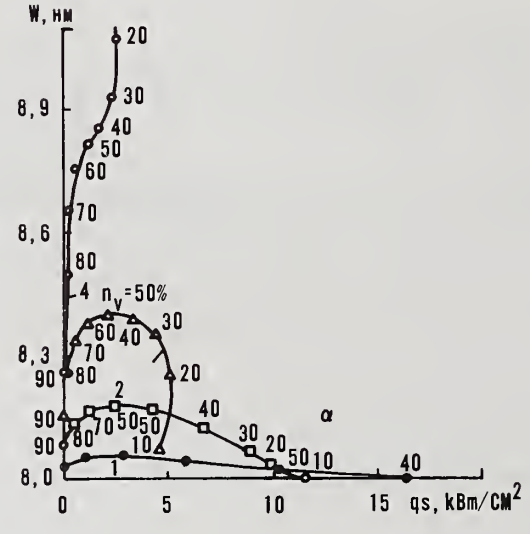

Figure 4. Holograms of thermodeformation FOE characteristics based on invar PFS cooled by Na-K heatcarrier in the supply (a) and removed (b) zones at d_s = 20 (1), 50 (2), 100 (3), 200 (4) μ.

Laser Damage Thresholds of Thin Film Optical Coatings at 248 nm*

F. Rainer, D. Milam and W. H. Lowdermilk

Lawrence Livermore National Laboratory
Livermore, California 94550

We have measured the laser-induced damage thresholds for 248 nm wavelength light of over 100 optical coatings from commercial vendors and research institutions. All samples were irradiated once per damage site with temporally multi-lobed, 20-ns pulses generated by a KrF laser. The survey included high, partial, and dichroic reflectors, anti-reflective coatings, and single layer films. The samples were supplied by ten vendors. The majority of samples tested were high reflectors and antireflective coatings. The highest damage thresholds were 8.5 to 9.4 J/cm^2 respectively. Although these represent extremes of what has been tested so far, several vendors have produced coatings of both types with thresholds which consistently exceed 6 J/cm^2. Repeated irradiations of some sites were made on a few samples. These yielded no degradation in threshold, but in fact some improvement in damage resistance. These same samples also exhibited no change in threshold after being retested seven months later.

Key words: antireflection coatings; damage thresholds; high reflection coatings; KrF lasers; laser damage; optical coatings; thin films.

1. Introduction

Because of the interest in short wavelength lasers for inertial confinement fusion programs, we have in the past year established a facility for laser damage testing at conventional rare-gas-halide laser wavelengths. We have conducted extensive damage tests at the KrF wavelength of 248 nm with 20-ns, p-polarized pulses on high reflection (HR) and antireflection (AR) films supplied by commercial and research institutions. The test results provided a current overview of the damage resistance of commercially available samples, and established possible avenues of approach to improve damage thresholds in research grade samples. Our present goal is to achieve consistent thresholds in both HR and AR coatings exceeding 5 J/cm^2 in commercial samples.

2. Samples Tested

We began our experiments by testing representative samples of commercially available reflective and antireflective coatings purchased for use in the KrF facilities at LLNL. Most of these samples were films that were highly reflective or antireflective in normal incidence beams, but a few were AR and HR films designed for 45^o incidence. The remainder of the samples were partial or multichroic reflectors. Except for some transparent windows with AR films on both surfaces, all samples were tested with the film as the entrance surface of the substrate. Tests on commercially available coatings were later supplemented by tests on a large number of HR, AR and single-layer films fabricated by research vendors for studies of the influence of various coating parameters on damage thresholds. The commercial and research vendors who supplied samples are listed in Table 1.

Table 1. Commercial vendors and research institutions.

Acton Research Corp.	Laser Optics
Airtron Optical & Magnetic Components	Optical Coating Laboratory, Inc.
Battelle Pacific Northwest Laboratory	Optico Glass Fabrication
CVI	Oriel
Design Optics	Spectra-Physics

*Work performed under the auspices of the U.S. Department of Energy by the Lawrence Livermore National Laboratory under Contract No. W-7405-ENG-48.

3. Experiment

3.1 Test Facility

Figure 1 shows a schematic diagram of the damage experiment. The laser consisted of a discharge-pumped KrF oscillator and amplifier with a maximum output energy of 1 J. The circularly apertured output beam passed through a set of polarizers. The first two polarizers were axially rotatable relative to the third to provide a beam which could be attenuated at will with no beam steering. The ensuing p-polarized beam was apertured to 12-mm diameter and focused by a 5-m focal length lens. The separation of the lens and sample was varied to produce at the sample surface, the largest beam with sufficient fluence to cause damage. Diagnostic beams were generated by placing a wedged splitter in the focused beam. The diagnostics included an absorbing-glass calorimeter with a 2.5-mm aperture, a multiple-exposure camera with 1-Z film for beam profiling, and a photo-diode for recording the pulse waveform. A typical temporal profile of the pulse is shown in Fig. 2. The sample, calorimeter aperture and film were all positioned in equivalent planes of the beam.

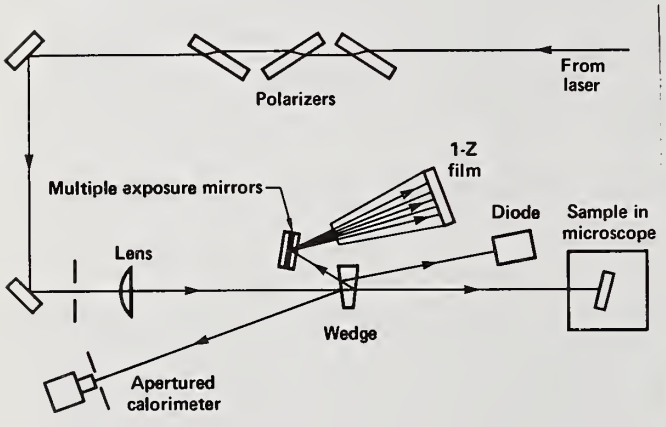

Figure 1. Schematic diagram of the KrF laser damage test facility.

Figure 2. (a) Temporal profile of the laser pulse; (b) spatial cross section of the beam at the damage plane.

3.2 Fluence Measurements

The beam cross section at the sample surface was typically 1.5 mm in diameter, but had an irregular shape as shown in figure 2. In the smallest beams used, the most intense structure was a rectangular spike with dimensions of 150μm x 600μm (FWHM) whose peak provided uniform irradiation over an area with a diameter of 100μm. For each shot, the intensity distribution of the beam was photographically recorded at 6 to 10 incrementally decreasing exposure levels, and the pulse energy was recorded. Data for nine shots were typically recorded on each photographic plate. Computation of peak fluence from these data required a number of steps. 1) For each photographic plate, the maximum photographic densities of the multiple images recorded in one shot were measured by using a densitometer to make 20 to 50 scans across the images. The scans were laterally separated by distances ranging from 28μm to 75μm. 2) The photographic response curve (relative fluence vs. density) of each plate was generated from the set of measured densities. 3) One representative image for each of the nine shots on a plate was scanned using a 100 x 100 point array to generate an unnormalized density record of the beam energy distribution. 4) This record was numerically converted to relative fluence by use of the response curve and then normalized so that the numerical integral agreed with the pulse energy. 5) The peak of the ensuing beam profile was then read as the peak fluence for that shot.

Densitometric recordings of beam photographs usually contain isolated points of high density. In analysis of large smooth beams, such spikes are easily recognized as spurious, and do not much

influence computations of fluence. In analysis of beams known to have complex shapes, it is sometimes difficult to determine whether isolated density spikes are real or spurious. Individual film grains or dust potentially influenced scans made with 28μm-square slits, and caused local density fluctuations. With larger slits, up to 57-μm square, only a few samplings were made in scans across small structures in the beam, and each density value was a spatial average of true local density values. To determine the influence of this uncertainty, we generated, from several plates, two sets of fluence values computed by using the extremes in uncertainty in density measurements. The first used a photographic response curve based on peak measured densities; for the second we used conservatively truncated densities. When a two dimensional raster scan of a beam photograph was interpreted by use of these two response curves, beams of differing shapes were generated, and the normalized peak fluences differed. For the beam size used to generate most of the data reported here, fluences computed by using conservatively truncated densities were 9% to 20% greater than those obtained using peak measured fluences. The average difference was 14%. Therefore, density fluctuations lead to a $\pm$ 5% imprecision (range 9% to 20%), and an absolute uncertainty of about 15%.

For larger beams used to measure a few thresholds, the interpretation of density was less crucial; the mean variation in fluence values obtained from peak measured response curves versus the conservatively truncated response curves usually used was - 3%; the range was - 8% to 1%.

To test the influence of truncating the response curve at the low-density end, we constructed curves by deleting the lowest measured fluence-density datum. Fluences computed from such curves differed by less than 1% from fluences computed with nontruncated curves.

The least contribution to the composite uncertainty was that resulting from uncertainty in energy measurements. Pulse energy was measured with a Scientec absorbing-glass calorimeter which was calibrated by direct comparison with a similar LLNL absorbing-glass calorimeter calibrated to within $\pm$ 1%. The accuracy of routine measurements of KrF pulse energies ranged from 1% to 3%, depending on the magnitude of the energy which determined the signal to noise ratio. We believe the uncertainty was typically $\pm$ 2%.

3.3 Experimental Procedure

Each sample focal area was irradiated only once and examined for damage. Damage was defined to be a permanent alteration of the sample surface that was detectable by examination of the site before and after irradiation. Comparison was done by naked eye and both visually and photographically by either bright or dark field Nomarski microscopy at magnifications ranging from 55 to 1060. In all but the most damage resistant samples the damage consisted of microscopic pits spaced by a few μm. As a set these occupied an area whose shape corresponded to a section through the fluence cross section. The micropit spacing on the best samples, about 100μm, was comparable to the width of the tip of the most intense structure in the beam.

We tested an average of seven sites on each sample. The damage threshold was defined to be the median value of the highest fluence that caused no damage and the lowest fluence that produced damage. The width of this fluence range and the uncertainties in individual fluence values were considered in assigning threshold uncertainty. For 90% of the samples, there was no mixing of damaging and nondamaging fluences that could not be attributed to fluence uncertainty. This, and the close spacing of the pits resulting from damage, indicated that we performed large-spot testing of these samples. In a few low-threshold samples, which had visually apparent large-scale variations in film quality, and in some high-threshold films with low spatial densities of damage susceptible defects, the crossover range between damaging and nondamaging fluences greatly exceeded the uncertainty in individual fluence values. For these samples, we assigned a conservative threshold based on the lowest fluences that caused damage, since the defects responsible for damage at these lower fluences would always be encountered by a larger beam.

4. Test Results

4.1 Highly Reflective Coatings

Figure 3 shows a histogram of the measured laser damage thresholds of 77 HR coatings. The white portions represent samples from commercial vendors. These had, for the most part, already been used in LLNL laser systems so that many were several years old and already damaged. The shaded portions represent various types of research grade samples which were either sputter deposited, e-beam deposited without overcoats or e-beam deposited with overcoats. For certain parameters with the overcoated e-beam deposited samples consistently high thresholds in excess of 6 J/cm^2 were measured. The median damage thresholds and number of samples tested for each category are summarized in table 2.

Table 2. Median laser damage thresholds of thin film coatings at 248 nm, 20 ns

Type	HR Threshold (J/cm^2)	HR Number tested	AR Threshold (J/cm^2)	AR Number tested
Commercial	1.8	20	3.3	19
Research (sputter deposited)	1.0	12	--	--
Research (e-beam deposited) nonovercoated HR, nonundercoated AR	3.1	15	4.2	8
Research (e-beam deposited) overcoated HR, undercoated AR	6.3	30	5.4	16

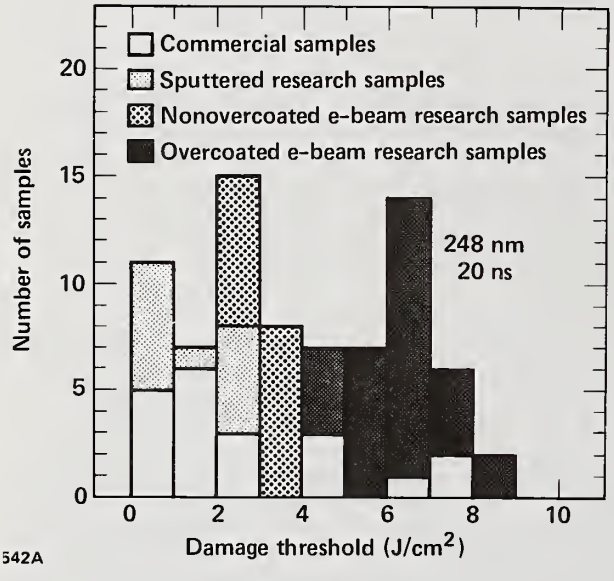

Figure 3. Laser damage thresholds of 77 highly reflective coatings.

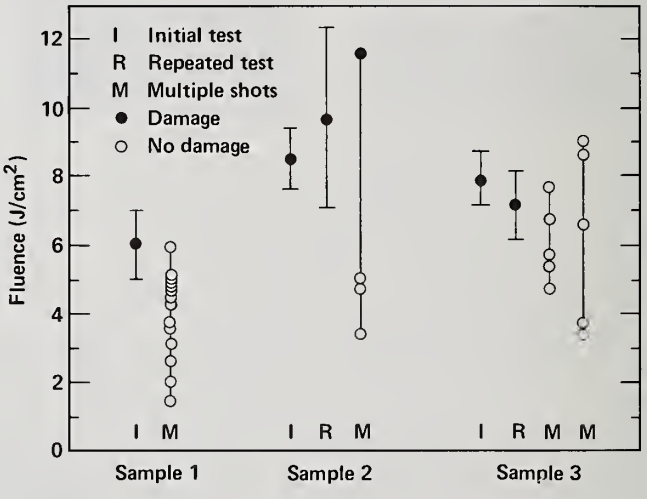

Figure 4. Threshold comparisons after 7 months; multiple irradiations of a single site.

Seven months after the initial tests, we retested some of these latter samples and obtained the same results within experimental error indicating no significant effects due to aging or handling (fig. 4). These tests were typically conducted with only one shot per sample area. To study the effects of multiple irradiations we retested some of these same samples putting from 3 to 14 shots on a site before moving to a new area. The fluence levels per test area ranged from 23% to 114% of the measured single shot threshold. The small size of our beam and shot to shot variation in fluence precluded a more systematic study of the effects of multiple irradiations and sub-threshold laser hardening on damage thresholds. However, for these limited tests there was no indication that multiple irradiations produced damage at or below our measured thresholds.

4.2 Antireflective Coatings

In figure 5 we show a histogram of the damage thresholds of 43 AR films. These data are also summarized in table 2. Unlike coatings tested at 1064 nm and its harmonics, the median thresholds of both commercial AR coatings and research AR coatings without undercoats were higher than median thresholds of corresponding HR films. However, the best sets of HR research samples tested were still superior to the best sets of AR research samples. The latter coatings had damage thresholds up to 6 J/cm^2.

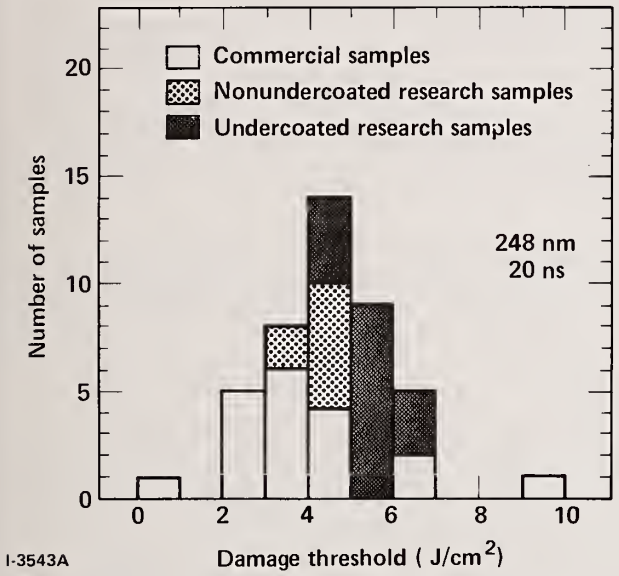

Figure 5. Laser damage thresholds of 43 antireflective coatings.

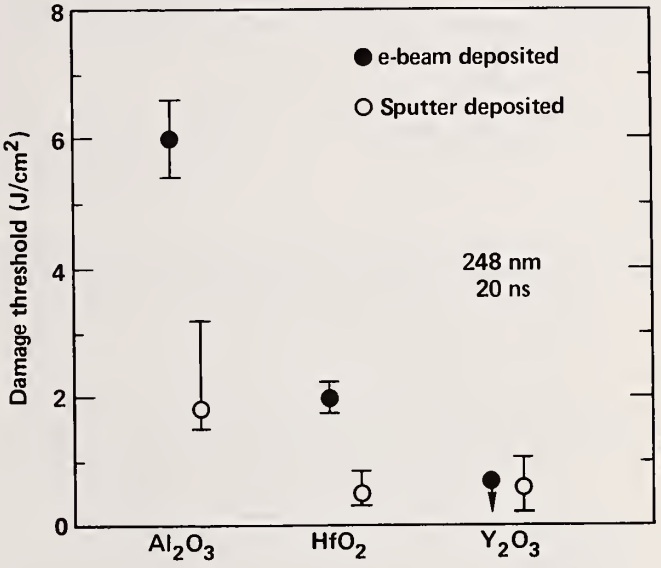

Figure 6. Median laser damage thresholds of single layer films.

4.3 Single Layer Films

We measured thresholds for a few single layer films. Figure 6 shows the median thresholds of films of three materials deposited by e-beam evaporation and by sputtering. In general, the e-beam deposited films had higher thresholds than the comparable sputtered films. High reflectors made with these compositions had damage thresholds that ranked in the same order, but further tests are needed before definitive conclusions can be drawn about the correlation of thresholds for single layer and HR films.

5. Conclusions

We have measured laser damage thresholds of HR and AR films from a variety of commercial and research institutions. Our results have shown the status of currently available coatings and the degree of improvement obtainable by the variation of coating parameters. Thresholds exceeding 6 J/cm^2 at 248 nm with 20-ns pulses were observed for both HR and AR films.

6. Acknowledgements

The authors wish to express their thanks to their colleagues S. Brown, C. Dittmore, J. Goldhar, G. Murphy, J. Odegard, S. Peluso, R. Rapoport and M. Taylor. It was only with their cooperation that this facility was built and maintained and the measurements taken.

Effects of Undercoats and Overcoats on Damage Thresholds of 248 nm Coatings

Trudy Tuttle Hart, Terri L. Lichtenstein, and C. K. Carniglia

Optical Coating Laboratory, Inc.
Santa Rosa, California 95402

and

F. Rainer*

Lawrence Livermore National Laboratory
University of California
Livermore, California 94550

Previous experiments have demonstrated that 1064 nm high reflectors benefit from the addition of halfwave silica overcoats, and that 1064 nm antireflection coatings can be improved by adding halfwave silica undercoats or barrier layers. In each case, a statistical improvement of about 50% has been observed. This paper reports similar results for coatings designed for 248 nm. The high reflectors were scandia/magnesium fluoride quarterwave stacks. Three design variations were tested: with no overcoat, with a halfwave silica overcoat, and with a halfwave magnesium fluoride overcoat. The presence of the overcoat more than doubled the threshold of the reflectors. The highest threshold, 8.5 joules/sq.cm, was measured on a reflector with a magnesium fluoride overcoat. Two material combinations were used for the four-layer antireflection coatings: scandia/silica and scandia/magnesium fluoride. Each of these combinations was coated without a barrier layer, with a silica barrier layer, and with a magnesium fluoride barrier layer. The barrier layer was an undercoat with a halfwave optical thickness. Varying degrees of improvement in thresholds, ranging up to 50%, were found in all cases with barrier layers. The highest thresholds exceeded 6 joules/sq.cm for scandia/silica coatings with silica barrier layers.

Key words: antireflection coating; electric field; laser damage; laser reflector; optical coating; overcoat; undercoat.

1. Introduction

Optical coatings are often the "weak link" in high energy laser systems, usually having lower damage thresholds than uncoated surfaces or bulk optical materials. Therefore it is important to try to find ways of raising the thresholds of the coatings. Many factors have been studied in relation to damage of coatings for fusion laser systems. These include stress, absorption, index of refraction, and electric field distribution within the coatings. However, one simple method of improving the damage resistance of coatings, which has proven to be effective at 1064 nm, is the addition of a low-index layer having a halfwave optical thickness [1-4][1]. The purpose of this paper is to demonstrate that this technique is also effective at 248 nm, the wavelength of the KrF laser.

The additional halfwave layer takes two different forms, depending on the coating type. In the case of a high reflector (HR), where the laser energy is concentrated in the outer part of the coating, the layer is an overcoat, added to the top of a standard quarterwave reflector stack [3,4]. For an antireflection (AR) coating,

* Work performed under the auspices of the U. S. Department of Energy by the Lawrence Livermore National Laboratory under Contract No. W-7405-ENG-48.

[1] Numbers in brackets indicate the literature references at the end of the paper.

where the energy penetrates to the substrate, an undercoat, or barrier layer, is added [1,2,4]. The effect of these layers on 1064 nm coatings has been to raise the damage threshold by approximately 50% for both HR's and AR's.

The reasons for the improvement afforded by the added halfwave layers are not readily apparent. The improvement cannot be attributed to particular properties of the coating material used for the undercoat or overcoat because it is usually one of the component materials already present in the rest of the coating. Because the layer has an optical thickness of a half wavelength, it has no effect on the electric field distribution within the coating. In fact, in the case of the HR, the electric field intensity in the overcoat is actually higher than in the reflector stack itself. At present, the most plausible explanations for the improvement are of a mechanical nature [4]. In the case of the HR, the overcoat adds mechanical strength to the coating, holding it together at laser energies where it could otherwise damage. Similarly, the undercoat is thought to improve the adhesion of the AR coating to the substrate, thus strengthening the interface which has proven to be the weakest point in this type of coating [2].

The present work does not throw additional light on the reasons for the improvement due to the added layers. However, it does confirm that they are just as effective in raising the damage thresholds for 248 nm coatings as they are for 1064 nm coatings.

2. Damage Testing

Laser damage testing was carried out at Lawrence Livermore National Laboratory using 20 ns pulses from a 248 nm KrF laser. The laser beam was focused to provide a uniform, intense beam over a region 100 μm in diameter at the sample surface.

Each site was irradiated with a single laser pulse. Before and after irradiation, the sample was examined visually and using Nomarski microscopy. Any permanent alteration of the surface detected by this inspection was considered to be damage. The damage usually consisted of small micropits spaced 1 - 10 μm apart.

For each shot, the beam intensity distribution and pulse energy were recorded and the peak fluence was computed. The damage threshold was defined to be midway between the lowest fluence which produced damage and the highest fluence which did not produce damage. More complete details of the damage testing procedure may be found elsewhere in these proceedings [5].

3. High Reflectors

The basic high reflectors used for this study consisted of 19 quarterwave layers of scandium oxide and magnesium fluoride, although some 31-layer designs were also tested. The refractive indices for these materials at 248 nm are approximately 2.05 and 1.40, respectively. The scandia was chosen for its high index and low absorption ($k = 0.002$). The absorption in the magnesium fluoride is negligible. The high index ratio of these two materials reduces the number of layers necessary to achieve a high reflectance. The theoretical reflectance of the 19-layer stack is 99.2% and reflectances in excess of 99% were readily achieved in practice. The theoretical maximum reflectance is 99.4% for a sufficient number of quarterwave layers, and is 99.8% for a design optimized for maximum reflectance [6]. The substrate used for the reflectors was Grade A, BK 7 glass. The 19-layer design is illustrated schematically in figure 1, together with the time averaged intensity of the electric field within the coating. The peak electric field intensity occurs at the first scandia/magnesium fluoride interface, and has a value of 0.95 relative to the incident field. The fact that the glass substrate is absorbing at 248 nm is not really important, since the electric field is negligible at this depth. However, enough laser energy penetrates to cause the substrate to fluoresce, thus preventing the observation of the emission of light which usually accompanies laser damage.

Two materials were used for the halfwave overcoats: magnesium fluoride and silicon dioxide. Magnesium fluoride was a natural choice, since it is the low-index material used in the reflector. Silica was used because it has proved successful at 1064 nm. Both materials have low refractive indices ($n = 1.50$ for silica) and low absorption at 248 nm. The E-field profiles for the two designs with overcoats are shown in figures 2 and 3. These figures illustrate that the electric field in the 19-layer scandia/magnesium fluoride stack is unchanged by the addition of either

Figure 1. Time averaged square of the electric field strength for 248 nm radiation incident from the left on a 248 nm scandia/magnesium fluoride quarterwave stack. The arrows indicate the electric field intensities of the incident, reflected, and transmitted waves. The position of the layers is indicated below the field plot. The scandia layers are shaded.

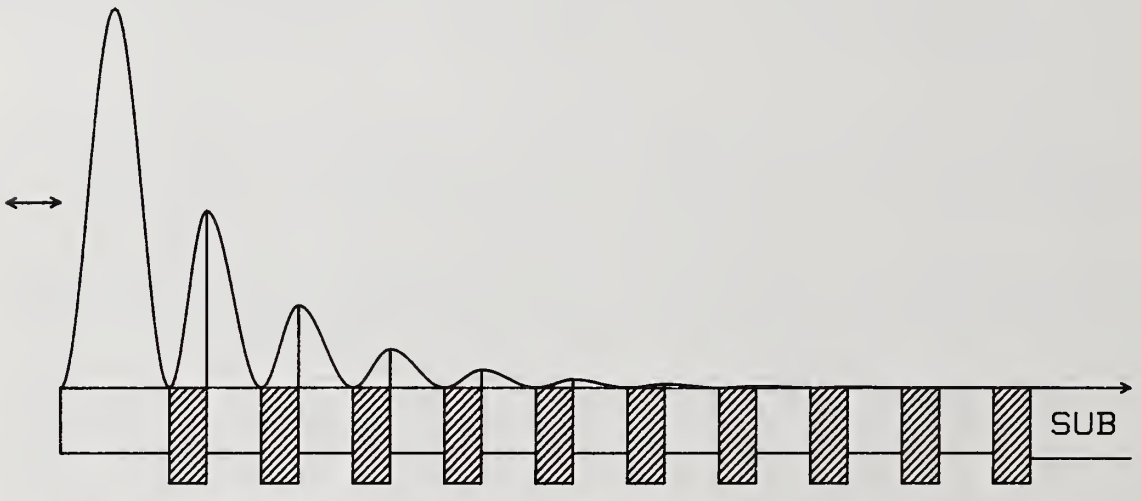

Figure 2. Similar to figure 1 for the scandia/magnesium fluoride reflector with halfwave magnesium fluoride overcoat.

Figure 3. Similar to figure 1 for the scandia/magnesium fluoride reflector with halfwave silica overcoat. The silica layer is dotted.

overcoat. Also, as mentioned earlier, the peak field intensity within the overcoat is much higher than it is within the reflector: 1.78 in the silica overcoat, and 2.04 in the magnesium fluoride overcoat.

A total of 18 HR's were tested as part of this study: six without overcoat, six with silica overcoat, and six with magnesium fluoride overcoat. They were made in three separate runs of six parts each to check for consistency between runs. In a given run, the basic 19-layer reflector was deposited simultaneously on all six parts. Then four parts were covered and the halfwave magnesium fluoride overcoat was added to two of the parts. These two were then covered and the silica overcoat was added to two of the remaining four parts. Thus, the only difference between the reflectors coated in a given run was the overcoat. In one of the runs, a 31-layer reflector was deposited on the parts. Since there was no significant difference between the threshold data for the 31-layer parts and the data for the 19-layer parts, these data have been combined. The results of damage testing these parts are given in table 1. The average threshold for the nonovercoated parts was 2.7 joules/sq.cm, compared with 5.7 joules/sq.cm for the parts with silica overcoats, and 6.9 joules/sq.cm for the parts with magnesium fluoride overcoats. The spread in the observed damage thresholds for each group was small, as demonstrated by the standard deviations given in table 1. These data clearly indicate that the damage threshold is improved by the addition of a low-index halfwave overcoat, the improvement being more than a factor of 2 for the silica overcoat and nearly a factor 2.5 for the magnesium fluoride overcoat.

Table 1. 248 nm, 20 ns Laser Damage Thresholds of Sc_2O_3/MgF_2 HR Films (J/cm^2)

Overcoat Material	Average Threshold[a]	Standard Deviation[a]	Maximum Threshold
None	2.7	0.4	3.2
SiO_2	5.7	0.6	6.5
MgF_2	6.9	1.1	8.5

[a] Average of measurements on 6 parts

3. Antireflection Coatings

Two material combinations were used for the AR coatings: scandia/magnesium fluoride and scandia/silica. A four-layer AR design was used on bowl-feed polished Suprasil II. The designs for each material combination are indicated schematically in figures 4 and 5, together with the E-field plots. It can be seen that the maximum electric field intensity in the scandia layers is 0.66, which is lower than the peak value in the HR's. Thus, from an electric field point of view, one would expect the damage threshold of the AR's to be higher than that observed for the HR's. However, in practice this is seldom the case. The reason is that the interface between the substrate and the first layer of the coating is probably where the damage originates; and this interface is susceptible to the effects of polishing, cleaning, and contamination to a higher degree than the coatings themselves [1,2,4].

Two materials were used for the barrier layer: magnesium fluoride and silica. The electric field profiles for the scandia/silica AR in combination with the two barrier layer materials are shown in figures 6 and 7. Notice that the electric field distribution in the four-layer AR coatings and the field at the substrate interface are unaffected by the presence of the barrier layer. In fact, in the case of the silica layer, from an electric field point of view, the undercoat is just an extension of the substrate. The effect of undercoats on the electric field distribution in scandia/magnesium fluoride AR's is similar to that in the scandia/silica AR's, and the E-field plots are omitted here.

A total of 24 coatings were tested: four each of six designs. The coatings were made in four separate runs. The six coatings made in one run consisted of the scandia/magnesium fluoride AR films deposited on two parts having no barrier layers,

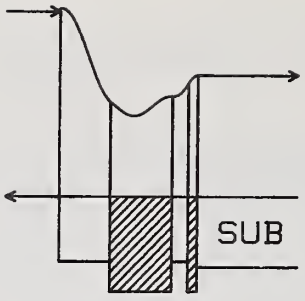

Figure 4. Electric field plot for the scandia/magnesium fluoride AR. Note that figures 4-7 are plotted to the same scale as figures 1-3. In these figures the shading of the layers is the same as for figures 1-3.

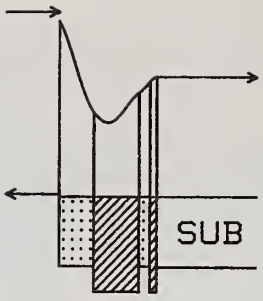

Figure 5. Electric field plot for the scandia/silica AR. See caption for figure 4.

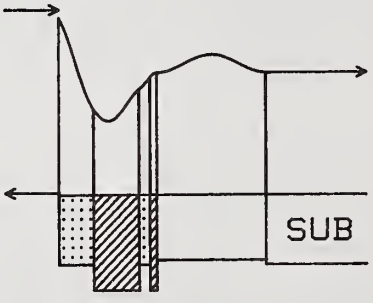

Figure 6. Electric field plot for the scandia/silica AR with halfwave magnesium fluoride undercoat. See caption for figure 4.

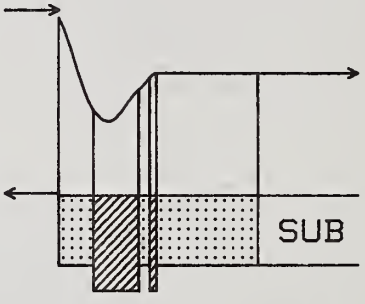

Figure 7. Electric field plot for the scandia/silica AR with halfwave silica undercoat. See caption for figure 4.

two parts with magnesium fluoride barrier layers, and two parts with silica barrier layers. Again, masking was employed to allow the barrier layers to be deposited first on their respective parts and then the AR to be deposited simultaneously on all of the parts. This run was repeated a second time. A similar pair of runs was made for the scandia/silica AR's.

The results of the damage testing are given in table 2. The thresholds for each set of four similar parts have been averaged. The magnesium fluoride barrier layers improve the thresholds of the AR's only slightly, yielding an average improvement of 14%. The silica barrier layer improves the average threshold by 40%. This is a significant improvement and is about the same magnitude as has been observed when using undercoats with 1064 nm coatings.

4. Discussion

In view of the general trend for 1064 nm coatings, it is interesting to consider selected data for scandia/magnesium fluoride AR's and HR's presented in table 3. The particular point to be made is that at 1064 nm, AR's generally have lower thresholds than HR's. On the other hand, at 248 nm the AR without barrier layer has a higher threshold than the HR without overcoat. This fact tends to support the idea that the damage is related to the electric field intensity in the scandia layers. In fact, the ratio of the peak electric field intensities in HR's and AR's is 1.4, which is close to the ratio of the thresholds. This represents one of the few comparisons between thresholds of AR's and HR's which is consistent with E-field theory. On the other hand, this may be only a coincidence, since the overcoat makes a much larger improvement in the HR's than the undercoat does in the AR's. Thus, the overcoated HR's have a higher threshold than the undercoated AR's, contrary to the predictions of the E-field theory. This demonstrates that further work needs to be done before the damage mechanism is fully understood.

Table 2. 248 nm, 20 ns Laser Damage Thresholds of AR Films (J/cm^2)

AR Materials	Undercoat Material	Average[a] Threshold	Standard[a] Deviation	Maximum Threshold
Sc_2O_3/MgF_2	None	4.4	0.3	4.7
Sc_2O_3/MgF_2	MgF_2	4.8	0.6	5.3
Sc_2O_3/MgF_2	SiO_2	5.6	0.4	6.1
Sc_2O_3/SiO_2	None	4.0	0.5	4.6
Sc_2O_3/SiO_2	MgF_2	4.9	0.4	5.4
Sc_2O_3/SiO_2	SiO_2	6.1	0.6	6.7

[a] Average of measurements on 4 parts.

Table 3. 248 nm, 20 ns Laser Damage Thresholds of Sc_2O_3/MgF_2 Coatings (J/cm^2)

Coating Type	Average Threshold
HR/no overcoat	2.7
AR/no undercoat	4.4
AR/SiO_2 undercoat	5.6
HR/MgF_2 overcoat	6.9

5. Conclusions

In conclusion, overcoats make a significant improvement in the threshold of HR's at 248 nm. A magnesium fluoride overcoat gives the largest improvement. Also, barrier layers are effective in raising the threshold of 248 nm AR's. The best results are obtained with the scandia/silica AR with the silica barrier layer.

The authors wish to acknowledge the work of Bill Klapp in preparing the coatings for this study.

6. References

[1] Apfel, J. H., Enemark, E. A., Milam, D., Smith, W. L. and Weber, M. J., Nat. Bur. Stand. (U.S.) Spec. Publ. 509, 255-259; 1977.

[2] Carniglia, C. K., Apfel, J. H., Carrier, G. B. and Milam, D., Nat. Bur. Stand. (U.S.) Spec. Publ. 541, 218-225; 1978.

[3] Carniglia, C. K., Apfel, J. H., Allen, T. H., Tuttle, T. A., Lowdermilk, W. H., Milam, D. and Rainer, F., Nat. Bur. Stand. (U.S.) Spec. Publ. 568, 377-390;1979.

[4] Carniglia, C. K., Thin Solid Films 77, 225-238; 1981.

[5] Rainer, F., Milam, D. and Lowdermilk, W. H., Nat. Bur. Stand.(U.S.) Spec. Publ. (to be published); 1981.

[6] Carniglia, C. K. and Apfel, J. H., J. Opt. Soc. Am. 70, 523-534; 1980.

Laser Damage Results and Analyses for Ultraviolet Reflectors Under Multiple-Shot Irradiation

Stephen R. Foltyn, Brian E. Newnam, and L. John Jolin

University of California, Los Alamos National Laboratory, Los Alamos, NM 87545

In a continuing program intended to evaluate and optimize multi-layer dielectric reflectors for the ultraviolet, additional results are reported.

Standard test conditions at the 248 nm KrF* wavelength are a nominal pulsewidth of 10 ns at a 35 Hz pulse repetition frequency. The 0.6 mm mean spot diam (I_o/e^2) is effectively increased by testing ten sites at each fluence, with each surviving site irradiated for 1000 shots. In this manner, 50 to 100 sites are tested on each reflector. By plotting the fraction of sites which damaged (%) vs laser test fluence (J/cm^2) and employing a linear regression fit to the data, a threshold (0% intercept) and an upper limit (100% intercept) are obtained. Emerging correlations between the slope of the data and physical properties of the coatings are discussed.

We have previously reported damage thresholds averaging 1.5 J/cm^2 with a high of 3.0 J/cm^2 for a ThF_4/Cryolite reflector. Presently, we routinely observe thresholds of 3.0 J/cm^2 up to a high of 5.5 J/cm^2 for oxide films, particularly those employing Al_2O_3 or Sc_2O_3 as the high-index component.

As an initial attempt to ascertain the possible effect of pulse repetition rate, some samples were tested at both 35 pps and 2 pps. Within our experimental uncertainty, no difference in threshold was observed.

Key words: fluoride coatings; KrF* lasers; multiple-shot laser damage; oxide coatings; repetition-rate effect; spotsize effect; ultraviolet reflectors.

1. Introduction

The study of optical damage at excimer laser wavelengths has been the subject of a program at Los Alamos which is now entering its third year. The focus of this effort has been the evaluation and optimization of the multilayer dielectric reflector, necessitated primarily by (a) the inherently low damage resistance of thin film multilayers; and (b) the lack of suitable alternatives for high reflectance in the ultraviolet. It is expected that information obtained in the present work will be useful in future efforts such as the study of AR coatings, halogen-resistant internal coatings, and window materials.

2. Experimental Details

2.1. Test Specimens

With few exceptions, all test coatings were deposited on identical Suprasil 2 substrates of either 38- or 50-mm diameter with a nominal thickness of 10 mm. These were batch-polished by Design Optics. Coating materials (Al_2O_3/SiO_2, Sc_2O_3/MgF_2, or ThF_4/Cryolite) were deposited using conventional thermal or e-beam techniques by a variety of organizations, including: Airtron; Design Optics; Northrop; Optical Coating Laboratories, Inc.; and TecOptics.

2.2. Test Facility

Our test facility has been described in detail elsewhere [1,2]. Table 1 summarizes relevant test conditions.

Table 1. Test Conditions

Laser	Lumonics 861 Multigas Excimer System operating on KrF* (248 nm) at pressure, voltage, and mixture specified by manufacturer.
Pulse Repetition Frequency	35 pps unless otherwise indicated
Pulse Length	10 ns nominal
Mean Spot Size	0.58 mm

Spatial beam profiling was accomplished with a Si-photodiode array (Reticon 256G) having 25 μm element spacing. Measurements were made in both the vertical and horizontal axes of the test plane, and the array was scanned through the entire plane to verify the absence of hot spots. The I_o/e^2 beam size, as indicated in figure 1, was found to be 1.38 mm × 0.24 mm in the focal region of the 25 cm lens which was used for all tests. The shape and spatial smoothness of these profiles are indicative of the cross sectional dimensions and uniformity of the laser discharge. The ~100X diffraction-limited spot size is typical of free-running excimer lasers operating inside stable cavities.

The temporal behavior was monitored with a fast vacuum photodiode (ITT 4014) and a storage oscilloscope. A typical 10 ns pulse is depicted in figure 1.

2.4. Error Analysis

In all tests, peak fluence was determined and monitored by measuring the energy transmitted through a pinhole of well-known diameter. Figure 2 diagrams the error associated with pinhole averaging and indicates other potential sources of error. Also in figure 2 are examples of the kinds of threshold variations that are seen experimentally in these tests. For example, if, for a particular reflector, the damage threshold was measured several times, the results were found to agree to within ±5%. When several samples from the same run were tested, results varied by 10-20%. For this reason, at least three samples from each run were tested, with results quoted as the average for the run. Even so, two seemingly identical runs would yield averaged results which typically differed by 20%, and occasionally by up to 50%. It is apparent, then, that in order to properly evaluate two comparable reflector designs, several optics from each of several runs must be tested for each design.

2.5. Characterization of Damage

Damage to the coatings was observed visually in real time with the aid of a 100X stereo zoom microscope. Disruption invariably began at discrete sites located in or near the intense part of the beam. Initially a few microns in size, these sites grew with continued irradiation, eventually overlapping and evolving into a burn pattern replicating the beam shape. This catastrophic failure generally occurred in less than 100 shots. Observation of damage was facilitated by emission of bright light from the growing sites. Test areas which did not damage were irradiated for 1000 shots. The micrograph of figure 3 depicts a test area after being exposed to fewer than ten shots at high fluence. Eleven individual damage sites are visible--the spots near the center of the beam have grown to 20-30 microns in diameter and are beginning to overlap.

2.6. Test Procedure

During testing, peak laser fluence was continuously monitored by a pinhole/detector combination powered by a 4% reflection from a wedged beamsplitter. This pinhole/detector was initially calibrated against a similar unit in the actual test plane. The laser output was sufficiently stable to allow operator control of peak test fluence via neutral density filters. At each fluence, ten sites were tested; several values were selected between the points at which 0/10 sites damaged and 10/10 sites damaged. A linear regression fit to the data (figure 4) was generally quite good.

Because of similarities between these results and typical plots of threshold/saturation behavior (e.g. laser gain curves), we have chosen to define the threshold as the 0% intercept. This contradicts conventional laser damage notation in which threshold is defined as the midpoint between the highest nondamaging fluence and the lowest damaging fluence--roughly the 50% point on the plots described here. Continuing the analogy, the saturation fluence is the level at the 100% intercept. It should be noted that in past publications, the 100% intercept has been referred to as the upper limit because it was suggestive of maximum potential performance. As explained in following sections, this may not be the case and the term "saturation fluence" will replace "upper limit" in this and future work.

Once threshold was determined, the peak fluence was adjusted to a slightly lower value and the sample was scanned through the beam in what constituted a systematic search for weak areas. In only a very few cases was a downward revision of the threshold necessary. All such cases exhibited a high degree of scatter in the data with correspondingly low coefficients of determination for the fit. In every case, the discrepancy was resolved by additional testing--up to 120 sites/sample--and refitting of the line.

3. Discussion of Results

The test results shown in figure 4 are for two coatings of the same design which were produced by different vendors. Immediately apparent are two differences: the threshold fluence and the

slope of the data. While the threshold is the logical criterion by which laser damage resistance is judged, it is the slope which interests us here.

In an attempt to attach a physical significance to these slopes and to explain observed differences in them, we propose the simple model of a surface which is populated with a uniform distribution of defects, all having the same damage threshold. Let us examine the effect of testing a large number of discrete sites on such a surface with a spatially Gaussian beam. As testing proceeds, the peak test fluence is increased on each succeeding site. When the peak fluence is below the defect threshold no damage is observed. Now, referring to figure 4, when the defect threshold is reached the probability of damage ("Sites Which Damaged") begins to increase from zero. As the peak fluence is further increased, the area within which the threshold fluence is exceeded increases logarithmically with a corresponding increase in damage probability. Eventually, this area becomes sufficiently large that the probability of finding a defect within is one. The associated peak fluence value is the saturation fluence, above which damage of one or more defects is inevitable.

There are several qualitative features of this model which are discussed in following sections. It should be stressed that most of these features await experimental verification and it is for this reason that the quantitative details are omitted here.

3.1. Logarithmic Dependence

As indicated, the probability of damage should increase logarithmically with peak fluence. Upon examination of figure 4, it is evident that the data on the right (dots) exhibits a curvature which is simply averaged out by the linear fit. In figure 5, data from both reflectors are replotted with a logarithmic fit. The error bars correspond to a ±5% uncertainty in both fluence and probability. The segment of the logarithmic curve on the left is effectively a straight line; the quality of the fit in figures 4 and 5 is the same. This is not true for the curve on the right, however, where the logarithmic fit is clearly superior. Since most of our test results have had slopes intermediate between those in figure 4, linear fits have been satisfactory and no corrections to published thresholds are necessary.

3.2. Defect Density

Based upon arguments presented at the beginning of this section, it should be possible to calculate, from knowledge of the saturation and threshold fluences, the average defect density on the surface. For a dense population of defects, the saturation level may be only slightly higher than threshold, resulting in a steep slope. This, for example, is found experimentally with aluminum reflectors. Conversely, if defects are far apart compared to the beam size, very high peak fluence would be necessary to saturate (i.e. produce damage at every site). Numerically, in this simple model, the reflector on the left in figures 4 and 5 has a defect density of 45 mm^{2} whereas the density for the sample with the shallow slope is 7.6 mm^{2}.

3.3. Spotsize Dependence

An argument similar to that of the previous section leads to the conclusion that, for a fixed defect density and threshold, larger spots will produce steeper slopes. An attempt to verify this experimentally by testing the same set of reflectors with a range of spotsizes is planned for the near future.

3.4. Intrinsic Materials Damage

Thus far, the model has allowed only for damage initiated at isolated defects. For sufficiently small spotsize or a tenuous distribution of defects, the fluence required for saturation could easily exceed the level at which intrinsic damage of the coating material begins. In this case, the probability of damage should increase logarithmically up to the intrinsic limit and rise sharply at the limit. It is possible that such a discontinuity exists in some of our results but is unrecognizable because the slopes are already steep.

3.5. Statistics of an Individual Site

While likely that there is a statistical probability of damage associated with each test site, it should be noted that, since each site is irradiated for 1000 shots, the effect is "integrated out" in these tests. Experimental evidence for this is presented in Section 5.

4. Effect of Laser Repetition Rate

One of the intended applications of results generated in this work is the development of optical components for use in devices operating at high repetition rates. As a first step in evaluating possible rep-rate effects, results obtained at 2 pps have been compared to those obtained at our

standard pulse rate of 35 pps. Four 248 nm reflectors (Sc_2O_3/MgF_2) were tested in the normal manner yielding the solid line in figure 6. The same four surfaces were retested at 2 pps resulting in the dashed line of figure 6. The difference in threshold and saturation fluences is well within our ±5% experimental uncertainty leading to the conclusion that there is no effect for 10 ns pulses between 2 pps and 35 pps.

Excimer lasers capable of up to 1000 pps are under development at Los Alamos. As beam time becomes available, these devices will be used to extend this investigation over a much larger range.

5. Number of Shots Required to Produce Damage

During the low rep-rate testing described in the previous section, it became possible to record the shot number on which damage occurred. This had, of course been impossible at 35 pps. Figure 7 contains the resulting data. Of the nearly 300 sites tested on four reflectors, 131 damaged within 50 shots and the rest did not. Nearly 3/4 of these damaged on the first shot, over 90% had damaged by the fourth shot, and one site survived for 24 shots before damaging. No damage was observed after 25 shots. Interestingly, the promptness of damage was independent of fluence level (bar graph, figure 7).

In that such information may eventually prove valuable in understanding the physical nature of the defects on which damage is initiated, we have implemented experimental modifications which will allow the routine compilation of such statistics during future testing.

6. Test Results

Test results for the past two years are summarized in figure 8. On the left are results which were presented in these proceedings last year. By concentrating on promising materials, the average damage threshold has been increased into the 3-4 J/cm^2 range. Optimization of processes and parameters is continuing as well as evaluation of various coating vendors.

7. Conclusions

We have described a laser damage test facility which has been in operation for two years and have presented results of tests which have been performed during this time. We have also described a method of laser damage testing which involves a high data rate and a correspondingly large quantity of gathered information. Initial attempts to understand and unify these data have been discussed.

8. References

(1) Foltyn, S. R.; Newnam, B. E. Multiple-shot laser damage thresholds of ultraviolet reflectors at 248 and 308 nanometers. Nat. Bur. Stand. (U.S.) Spec. Publ. 620; 1980 October, 265 p.

(2) Foltyn, S. R.; Newnam, B. E. Ultraviolet damage resistance of dielectric reflectors under multiple-shot irradiation, IEEE J. Quant. Elect. QE-17 (10); 2092-2098; 1981.

BEAM CHARACTERIZATION

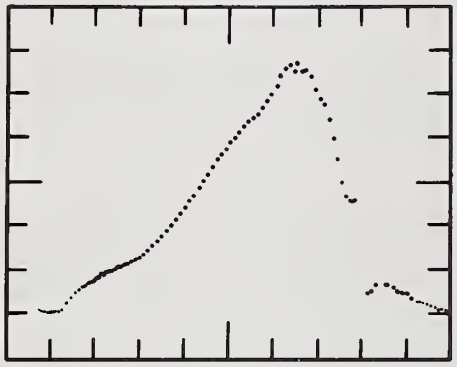

TOP LEFT – HORIZONTAL SPATIAL PROFILE
DIAMETER AT I_0/e^2 = 1.38 mm

BOTTOM LEFT – VERTICAL SPATIAL PROFILE
DIAMETER AT I_0/e^2 = 0.24 mm

MEAN SPOT DIAMETER = 0.58 mm

BELOW – TEMPORAL PROFILE ~ 10 ns
(FWHM)

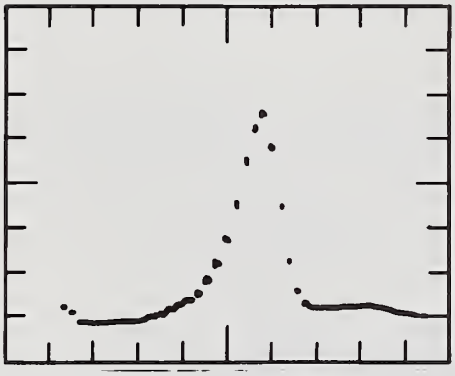

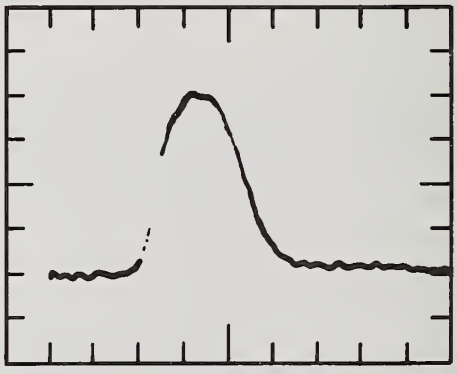

Figure 1. Spatial and temporal beam profiles at 248 nm.

ERROR ANALYSIS

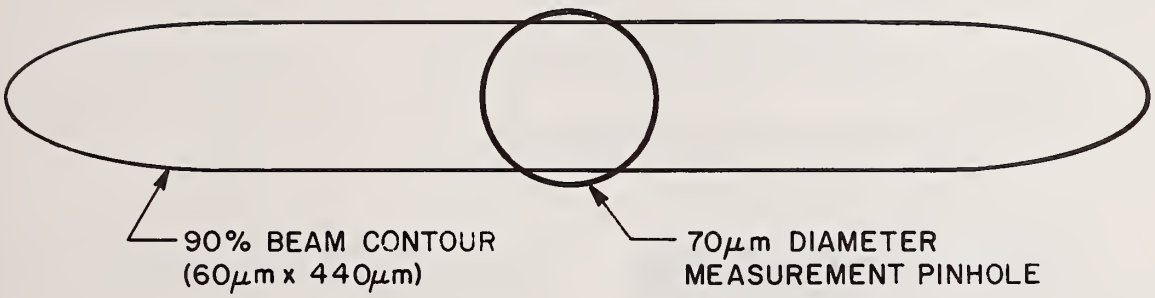

NET EFFECT OF PINHOLE AVERAGING IS ~ 3%

PULSE AMPLITUDE VARIATION IS ± 5% SPECIFIED
± 3% MEASURED

FILTER DENSITY MEASURED *IN SITU* WITH 1% REPEATABILITY

THRESHOLD VARIATIONS

SINGLE SAMPLE (EXPERIMENTAL REPEATABILITY)	5%
INTRA-RUN (SEVERAL SAMPLES IN SAME RUN)	10-20%
INTER-RUN (VARIATION OF AVERAGE FOR EACH RUN)	20-50%

Figure 2. Experimentally observed threshold variations compared to uncertainties in measuring peak fluence.

DAMAGE CHARACTERIZATION

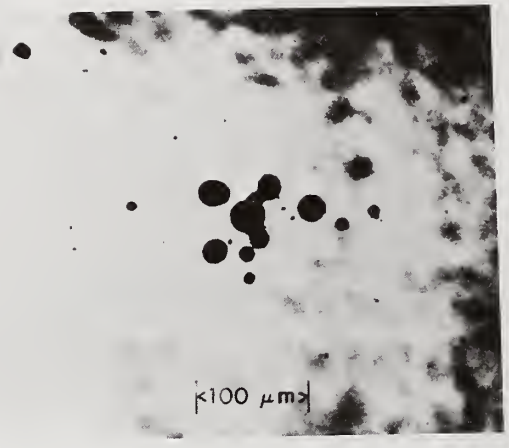

DAMAGE IS INITIATED AT ONE OR MORE SITES LOCATED IN INTENSE PART OF BEAM.

MOST SITES GROW WITH EACH SUCCESSIVE SHOT. CONTINUED IRRADIATION PRODUCES A BURN PATTERN REPLICATING BEAM SHAPE

TEST SITE IS OBSERVED MICROSCOPICALLY DURING IRRADIATION; COATING FLUORESCENCE CONVENIENTLY OUTLINES AREA OF INTEREST. OBSERVATION OF DAMAGE IS FACILITATED BY EMISSION OF BRIGHT LIGHT FROM GROWING SITES.

Figure 3. Characterization of damage. Micrograph taken after 10 shots at a high fluence shows 11 localized damage sites which have grown and are beginning to overlap.

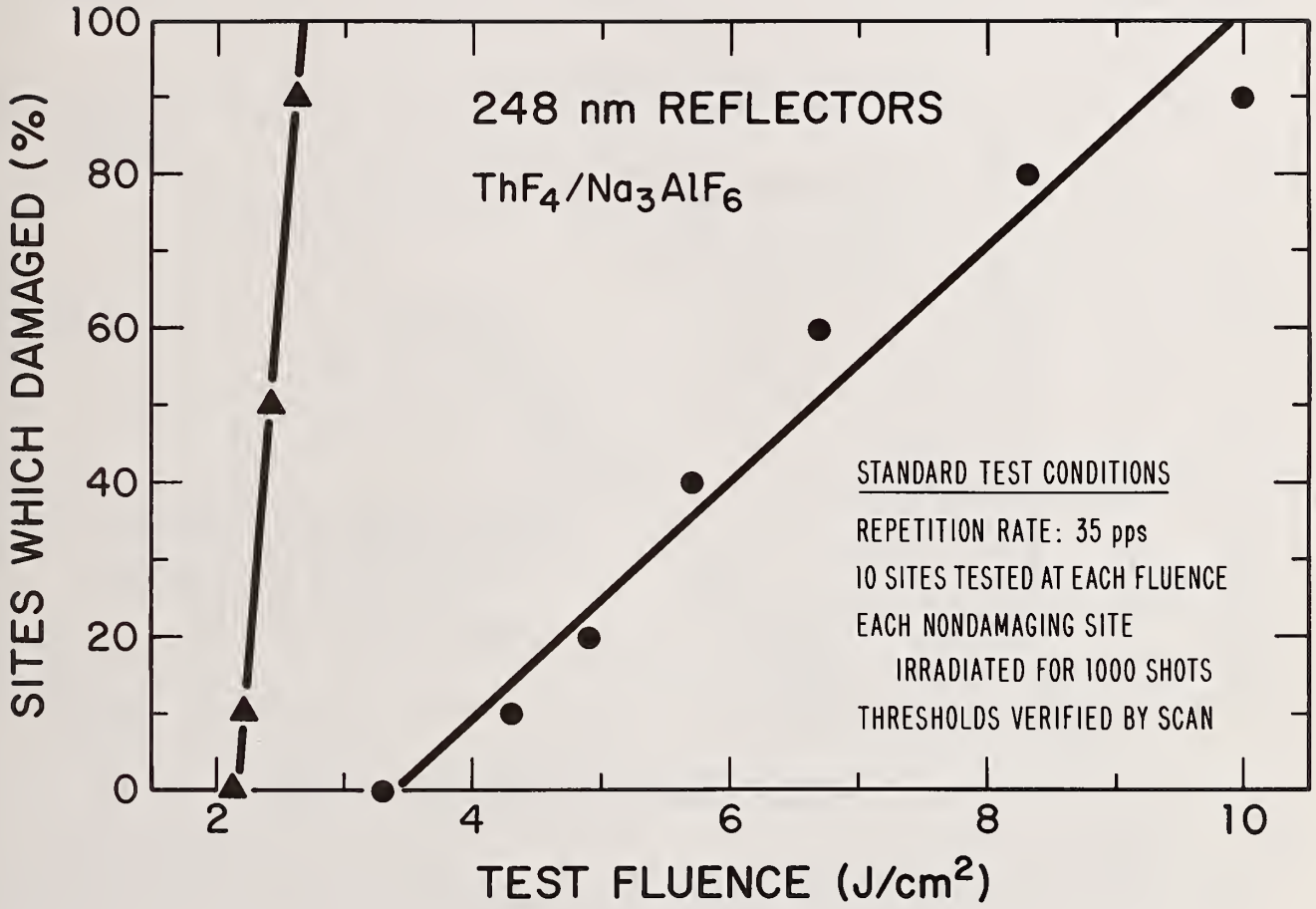

Figure 4. Test results for two reflectors of similar design but produced by different vendors. Threshold is the 0% intercept.

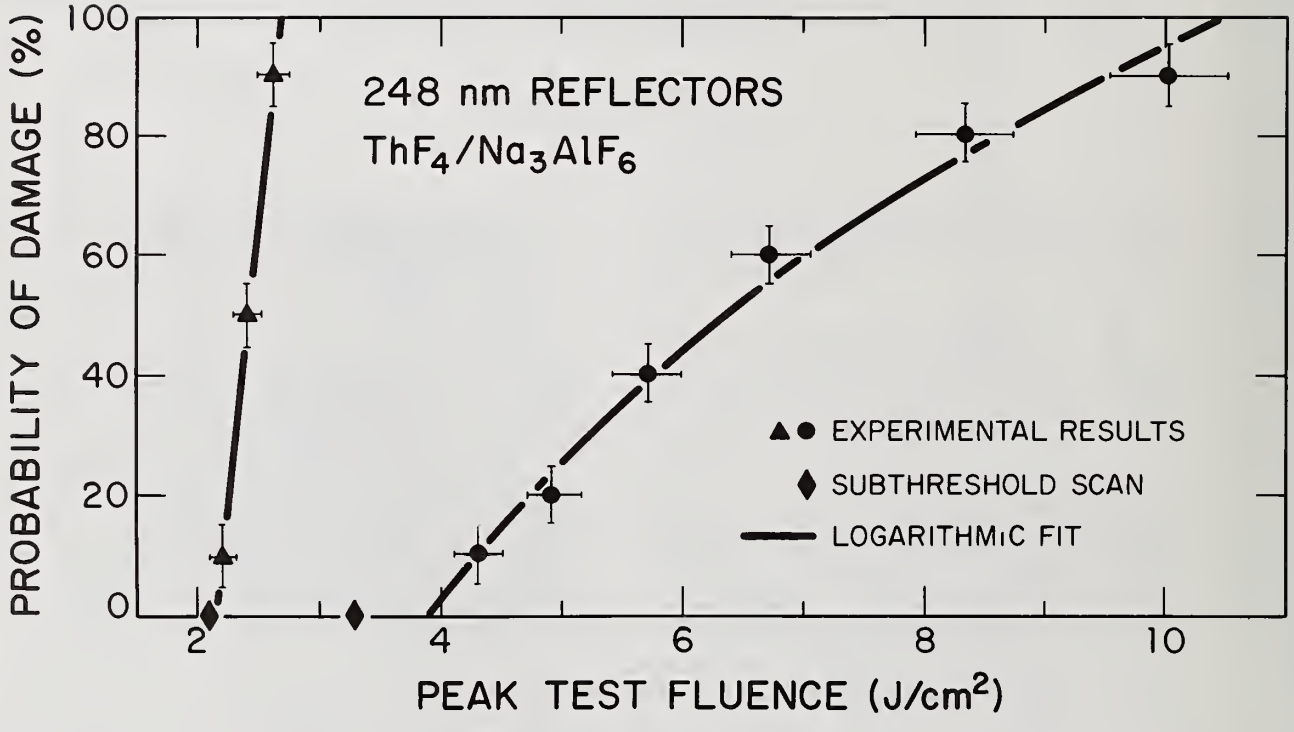

Figure 5. The data of figure 4 replotted with a logarithmic fit as predicted by a simple model. The error bars reflect a ±5% uncertainty in both fluence and probability.

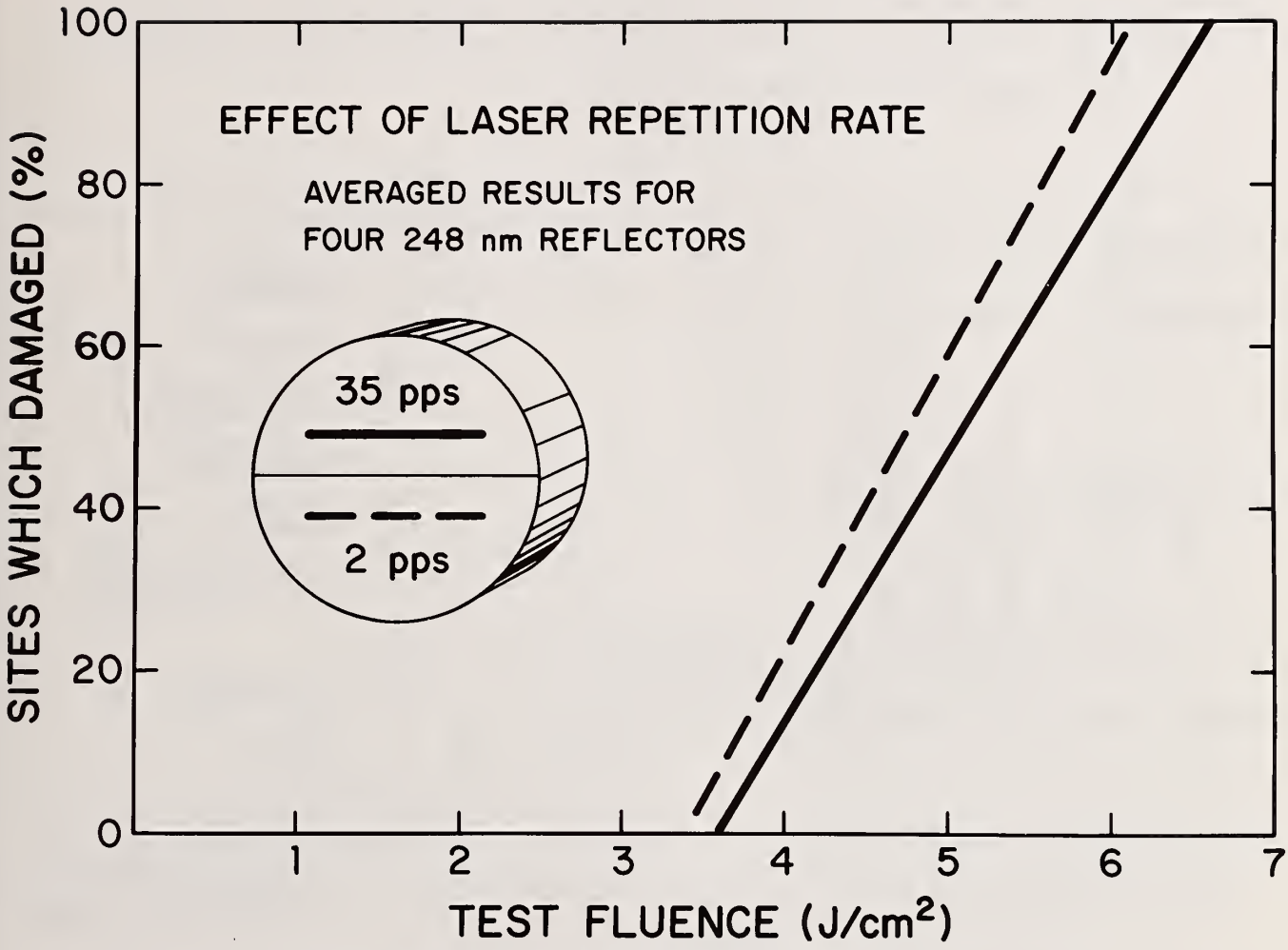

Figure 6. Comparison of test results at 2 pps and 35 pps.

NUMBER OF SHOTS REQUIRED TO PRODUCE DAMAGE

131 SITES EVALUATED AT 2 pps

DAMAGE ON FIRST SHOT	72%
DAMAGE ON SHOTS 2-4	20%
5-10	5%
11-25	3%

NO DAMAGE ON SHOTS 26-50

NO CORRELATION BETWEEN NUMBER OF SHOTS REQUIRED AND FLUENCE LEVEL

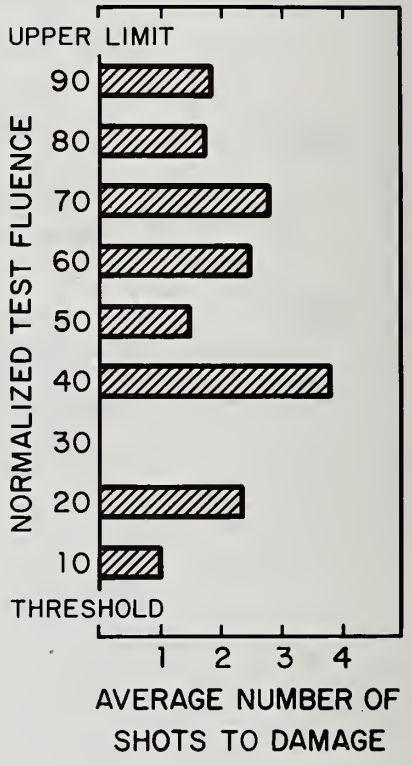

Figure 7. Analysis of the probability of damage vs. number of shots on a single site.

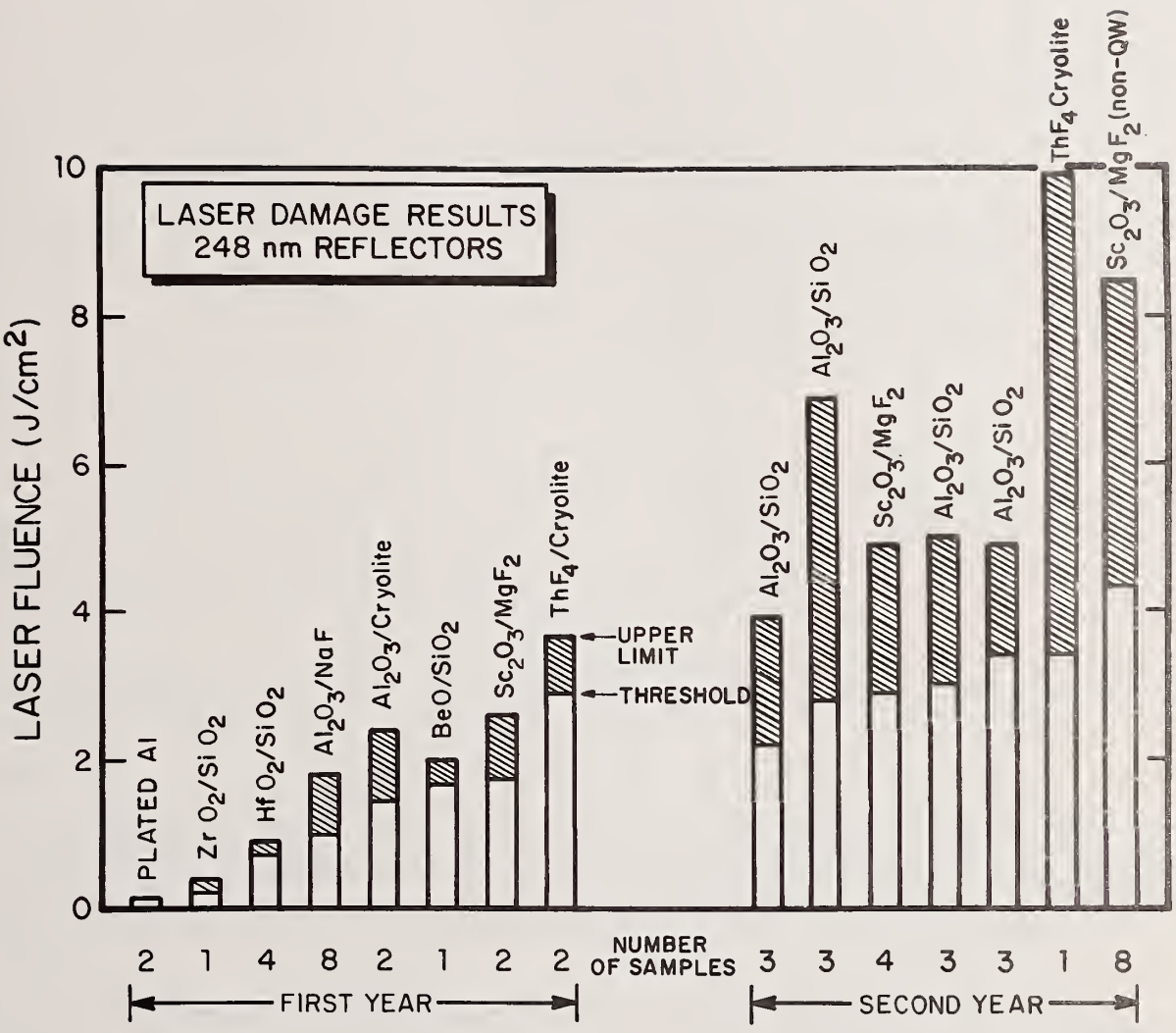

Figure 8. Summary of results for the past two years.

It was suggested that the number of pulses required to produce damage would be expected for a process that has a fixed probability of occurring at any fluence. By looking at these distributions one might get some idea of how uniform the samples are. If the samples are uniform, the distribution should be binomial.

In regard to the fluorescence observed, the speaker reported that there was a fluorescence nm in size which goes way out into the wings of their beam spatial profile. It always occurs, but they have made no attempt to explain it. While the damage sites are growing there is, in addition, very bright emission from the growing areas. The films were deposited by electron beam or thermal evaporation. Vendors were OCLI, Airtron, Design Optics, Tech Optics, and Northrop. The damage sites are sometimes initiated at defects which can be seen on the coating and sometimes on clear areas between defects.

The speaker's conclusion that there is no correlation between the number of shots required for damage and the fluence level was questioned. Could it be due to the nonuniformity of the coating or laser instability? The speaker pointed out that the conclusion is based on four samples of one kind of material and is definitely preliminary.

Multiple-Shot Ultraviolet Laser Damage Resistance of Nonquarterwave Reflector Designs for 248 nm*

Brian E. Newnam, Stephen R. Foltyn, and L. John Jolin

University of California, Los Alamos National Laboratory, Los Alamos, NM 87545

and

C. K. Carniglia

Optical Coating Laboratory, Inc., Santa Rosa, CA 95402

The damage resistance of multilayer dielectric reflectors designed for 248 nm has been substantially increased by use of nonquarterwave (QW) thicknesses for the top few layers. These designs minimize the peak standing-wave electric field in the high-index layers, which have proven to be weaker than the low-index components.

Previous damage tests of infrared- and visible-wavelength reflectors based on these designs have produced variable results. However, at the ultraviolet wavelength of 248 nm, 99% reflectors of Sc_2O_3, MgF_2, and SiO_2 strongly demonstrated the merit of non-QW designs. Four sets of reflectors of each of four designs (all QW thickness; one modified-pair substitution; two modified-pair substitution; one modified pair plus an extra half-wave layer of Sc_2O_3) were tested for damage resistance with a KrF laser operating at 35 pps with a pulsewidth of 8 ns and spot-size diameter of 0.6 mm. Each of 50 sites were irradiated for 1000 shots or until damage occurred.

On the average, the reflectors with one-modified-thickness pair had a 50% higher threshold (10 of 10 sites survived) than the all-quarterwave design. Addition of a second modified-layer pair resulted in no further increase in threshold but the saturation fluence (10 of 10 sites damage) was 110% higher. Reflectors with an additional half-wave of Sc_2O_3 had lower thresholds of the order of 10% as expected. The thresholds correlated best with the peak-field model, whereas the best model correlating the saturation fluences involved the sum of the upper two scandia layer thicknesses.

Key words: Damage thresholds; electric-field suppression; multiple shots; nanosecond pulses; nonquarterwave designs; scandium oxide; standing-wave electric fields; thin films; ultraviolet reflectors.

1. Introduction

In recent years, the anticipated correlation of peak standing-wave (SW) electric field with laser damage of multilayer dielectric reflectors has been under repeated scrutiny [1-7].** Damage studies of various coating designs have been conducted at both Los Alamos and Livermore National Laboratories in cooperation with commercial vendors, primarily Optical Coating Laboratory, Inc. (OCLI). The results of these previous investigations have been variable. Possible reasons for these variations are discussed in Section 6.

Previous correlation of the damage threshold with SW-field patterns for the ultraviolet wavelength of 266 nm [8] provided the motivation for the present study at 248 nm. Here, we examined the use of special reflector designs in which the upper few layers had nonquarterwave (QW) thicknesses. While maintaining high reflectance, this non-QW design modification minimizes the peak SW field in the top high-index layers, which have proven to be weaker than the low-index layer materials. Figure 1 allows a comparison of the field patterns for the standard all-QW reflector and for an optimized suppressed-field design. The latter is obtained in two steps. First, a low-index layer is added to the standard QW stack, but its optimum thickness is such that the electric field at its outer surface exactly equals that at the second H-L interface. Then sufficient thickness of the high-index film is added to obtain a null field at its outer surface, thereby maximizing the reflectance. Additional pairs of layers can be added according to the same principles.

---

* Work performed under the auspices of the U.S. Department of Energy.

** Numbers in brackets indicate the literature references at the end of the paper.

Success of the non-QW design in realizing higher damage thresholds requires that the ratio of the thresholds for the high- and low-index films be substantially greater than unity. Especially for ultraviolet laser wavelengths, suppression of the peak electric field in the high-index layers is expected to be advantageous for at least three reasons: (1) the density of absorbing film defects increases with decreasing wavelength [9], (2) homogeneous absorption increases rapidly near the uv band edge, and (3) multiphoton absorption becomes a probable contributing damage mechanism.

2. Test Specimens

2.1 Reflector Design

Four different 22-layer reflector designs were coated using three materials: scandium oxide (Sc_2O_3), magnesium fluoride (MgF_2), and silicon dioxide (SiO_2). To preclude stress-induced crazing, the initial layers were composed of five pairs of Sc_2O_3/SiO_2 over which six pairs of Sc_2O_3/MgF_2 and a half-wave (HW) thick MgF_2 overcoat were deposited. The four different designs shown in table 1 differed only in the thicknesses of the outer pairs of layers. Design A was the standard all-QW stack. The layer thicknesses of Designs B and D were chosen to minimize the peak SW field in the scandia layers as specified by Gill et al. [4]:

$$\text{Low-index layers:} \quad \sin \theta_{2i-1} = [iN^2-(i-1)]^{-1/2}, \ \theta_{2i-1} > \pi/2 \tag{1}$$

$$\text{High-index layers:} \quad \tan \theta_{2i} = N[i(N^2-1)]^{-1/2}, \ \theta_{2i} < \pi/2 \tag{2}$$

where $0 < i \leq m$ (m being the number of pairs of non-QW layers), $N = n_H/n_L$, and $\theta_i = 2\pi n_i d_i/\lambda$. The subscripts, L and H, refer to the low- and high-index layers and d is the film thickness. Similar expressions have also been derived by Apfel [10]. Design C was the same as B except the top scandia layer was an additional HW thicker. This design was included not to increase damage resistance but to provide insight into the damage mechanism.

Table 1. 248-nm reflector designs

A. Quarterwave stack							
SUB/$(HL')^5$	$(HL)^5H$	LL					
248	248	248					
B. 1 Pair Suppressed E-Field							
SUB/ $(HL')^5$	$(HL)^4H$	L	H	LL			
248	248	377	149	248			
C. 1 Pair Suppressed E-Field with Scandia Half-Wave							
SUB/ $(HL')^5$	$(HL)^4H$	L	H	LL			
248	248	377	645	248			
D. 2 Pairs Suppressed E-Field							
SUB/ $(HL')^5$	$(HL)^3H$	L	H	L	H	LL	
248	248	377	149	404	122	248	

2.2 Reflector Fabrication

Four sets of the above designs were deposited in two essentially identical coating runs, using four suprasil-2 substrates and four BK-7 glass substrates per run. The suprasil substrates (50.8 mm diam) had surface roughness of ~10 Å rms, and the BK-7 substrates (50.8 and 38.1 mm diam) had a low-scatter bowlfeed polish for which 3 - 5 Å rms roughness is typical. The coatings were deposited at a substrate temperature of 150° C for both runs. Flip masking was used so that all of the scandia/silica layers and all QW scandia/MgF_2 layers were common to all parts. Additionally, the 377-L, 149-H layers were common to spindles B, C, and D, and the HW MgF_2 overcoat was common to all parts.

2.3 Spectral Performance

As can be seen in table 2 and figure 2, the spectral performance of the actual reflectors was very close to the theoretical design values. At 248 nm the reflectance generally exceeded 99%. The parts of Design C were about 0.5% lower as expected due to the added absorption in the thick scandia layer. The extinction coefficient k of the Sc_2O_3 was measured to be 0.002 ± 0.005. The k values of MgF_2 and SiO_2 did not exceed zero within this precision.

Table 2. Measured performance of 248-nm reflectors

	Spindle	R_{peak}	R_{248}	λ_o(nm)[a]	λ_{peak}(nm)
A.	Theoretical[b]	0.993	0.993	248	244
	603-1727	0.996	0.992	244	251
	603-1728	0.990	0.989	242	249
B.	Theoretical[b]	0.994	0.994	250	247
	603-1727	0.993	0.989	245	251
	603-1728	0.991	0.991	243	248
C.	Theoretical[b]	0.988	0.988	249	248
	603-1727	0.990	0.982	248	251
	603-1728	0.988	0.988	246	248
D.	Theoretical[b]	0.993	0.993	252	250
	603-1727	0.991	0.990	247	251
	603-1728	0.990	0.990	246	248

[a] The wave number average of the 80% points.

[b] Based on the nondispersive refractive indices of the materials as follows:

		n	k
H:	Sc_2O_3	2.05	0.002
L:	MgF_2	1.40	0.0
L':	SiO_2	1.50	0.0

2.4 Electric-field Distributions

The internal SW electric-field distributions for each reflector design are shown in figure 3. The fields were computed numerically with the assumption of no absorption and are normalized to the incident field E_o^+. The thicknesses, peak fields, and linear absorption in the upper layers are listed in table 3. The first two quantities can be computed from analytical expressions derived previously [4, 10]. The linear absorption was obtained by integration over each layer of thickness t by

$$A = (4\pi nk/\lambda) \int_o^t |E(z)/E_o^+|^2 dz \quad . \tag{3}$$

3. Laser Damage Test Conditions

The experimental arrangement and test procedures have been described previously [11, 12] and in the companion paper in this proceedings by Foltyn et al. [13]. The laser test parameters are given in table 4. In addition to the tests at 35 pps, one of the four sets of reflectors was also tested at 2 pps.

4. Experimental Results

4.1. Irradiation at 35 pps

The results for one of the four sets of reflectors are plotted in figure 4. A least-squares-linear fit to the data is generally quite good and differs only slightly from a logarithmic curve

Table 3. Design and theoretical performances of 248-nm reflectors[a]

Design	A QW Stack	B One Pair Suppressed E-field	C One Pair Suppressed E-field +λ/2 H	D Two Pair Suppressed E-field
Overcoat (MgF_2)				
Thickness[b]	2.0	2.0	2.0	2.0
Peak Field[c]	2.03	2.03	2.03	2.03
Layer 21 (Sc_2O_3)				
Thickness[b]	1.0	0.60	2.60	0.49
Peak Field[c]	0.95	0.62	0.95	0.46
Absorption	0.0030	0.0009	0.0068	0.0005
Layer 20 (MgF_2)				
Thickness[b]	1.0	1.52	1.52	1.63
Peak Field[c]	0.95	1.33	1.33	1.51
Layer 19 (Sc_2O_3)				
Thickness[b]	1.0	1.0	1.0	0.60
Peak Field[c]	0.44	0.62	0.62	0.46
Absorption	0.0014	0.0019	0.0019	0.0006
Layer 18 (MgF_2)				
Thickness[b]	1.0	1.0	1.0	1.52
Peak Field[c]	0.44	0.62	0.62	0.98
Layer 17 (Sc_2O_3)				
Thickness[b]	1.0	1.0	1.0	1.0
Peak Field[c]	0.21	0.29	0.29	0.46
Absorption	0.0006	0.0009	0.0009	0.0014
Total Absorbance	0.0056	0.0045	0.0105	0.0039
Reflectance	0.9935	0.9941	0.9882	0.9940

[a]Based on the refractive indices given in table 2.

[b]Thicknesses are given in terms of quarterwaves at 248-nm.

[c]Peak field is the time average square of the electric field relative to the incident field.

Table 4. Laser test parameters

Wavelength: 248 nm
Pulsewidth: 8 ns (FWHM)
Spot-size Diameter: 0.6 mm, Mean
Repetition Rate: 35 pps, (and 2 pps)
Sites Irradiated: 10 at each of 5 fluence levels
Shots Per Site: 1000

fit which is motivated by a spot-size-dependent damage model [13]. The starred data points on the abscissa indicate the fluence levels for which a slow, 26-mm scan of the laser beam (at 35 pps) produced no additional damage. The damage threshold is defined as the maximum laser fluence at which 0 of 10 test sites damaged. Extrapolation of the linear curve to the 10 of 10 sites damage level determines the "saturation fluence." This latter quantity is the minimum fluence necessary to produce damage of every test site and as discussed earlier [13], is thought to be dependent on the laser spot size. For the data exhibited in figure 4, it is obvious that both the one- and two-pair non-QW designs yielded significantly higher damage thresholds and saturation fluences. On the other hand, the reflector with an additional HW thickness of scandia had nearly the same threshold as the all-QW reflector, and its saturation fluence was only slightly greater than its threshold. Table 5 lists the thresholds for all four sets of reflectors. Not surprisingly, the results for the corresponding reflectors of the different sets reveal only slight differences in magnitudes. In every case but one, the thresholds of the two optimized designs surpassed those of the all-QW reflectors.

Table 5. Experimental damage thresholds (J/cm^2)

Coating Run	Substrate	Coating Design			
		All QW	One Pair Non-QW	Two Pair Non-QW	One Pair Non-QW +HW Sc_2O_3
603-1727	Suprasil 2	3.0,[a] (4.9)[b]	4.4, (6.7)	4.4, (11.5)	2.5, (3.1)
603-1727	BK-7	3.0, (5.6)	5.6, (6.8)	4.7, (10.3)	2.5, (2.9)
603-1728	Suprasil 2	3.0, (5.1)	4.2, (7.2)	4.9, (9.6)	3.0, (3.4)
603-1728	BK-7	2.6, (3.8)	3.4, (6.6)	2.6, (10.0)	2.7, (3.1)

[a] Threshold of damage ≡ maximum fluence at which none of 10 sites irradiated damaged.

[b] Saturation fluence ≡ minimum fluence to damage all 10 of 10 sites irradiated.

The influence of substrate material and/or surface polish was very slight. The mean values for the thresholds and saturation fluences for reflectors on suprasil 2 were about 10% greater than the mean values for reflectors on BK-7 glass. Neither did the results for the two coating runs differ much. Run 1727 yielded reflectors about 10% more damage resistant than Run 1728. While these small differences are considered real, their magnitudes are practically negligible.

As has been demonstrated repeatedly in the last decade of damage research, a result may not be reproducible when retested due to many factors in real materials. Thus, it is the average or trend revealed by repeated tests of a particular design concept or manufacturing procedure that is of most value. We have tried to address this issue in the present work by testing four sets of these reflectors fabricated in two coating runs. From table 5 we computed the average thresholds for each design and present these in table 6. To further clarify the results, we also present the same information in figure 5.

Table 6. Experimental results

Four-set average of four designs of 248-nm reflectors

Design	Threshold J/cm^2	% Change	Saturation Fluence J/cm^2	% Change
All QW	2.9 ± 0.2	--	4.85 ± 0.8	--
One-pair Non-QW	4.4 ± 0.9	+ 50%	6.8 ± 0.3	+ 40%
Two-pairs Non-QW	4.2 ± 1.1	+ 40%	10.4 ± 0.8	+ 110%
One-pair Non-QW + HW Sc_2O_3	2.7 ± 0.1	- 10%	3.1 ± 0.2	- 35%

Clearly the optimized non-QW designs have superior thresholds (higher by 40 to 50%) and saturation fluences (40 to 100% higher). Not unexpectedly, the additional HW scandia thickness resulted in a slightly (significantly) decreased threshold (saturation fluence).

4.2. Irradiation at 2 pps

The test results for the set of reflectors tested at both 2 pps and 35 pps are plotted in figure 6. On the average, the thresholds and saturation fluences for these tests differed by 5% or less. Furthermore, the 2-pps tests allowed us to identify the shot number at which damage occurred. (This was difficult to accurately quantify at 35 pps.) We observed that either a test site damaged within 25 shots or it survived the standard 1000-shot test. Further, for nearly 75% of those sites exhibiting damage, failure occurred on the first shot. This aspect is adequately discussed in the preceding paper by Foltyn et al. [13].

5. Analysis

The experimental results positively reveal the merit of using the suppressed electric-field principle to increase the damage resistance of laser reflectors. It is still conceivable, however, that minimizing the peak field in the scandia layers is serendipitous. That is, there may be another condition that is simultaneously optimized that involves the primary damage mechanism. In this section, we compare our results with the theoretical predictions of various models for laser damage.

First, we can state that the low-index layers of MgF_2 are not the sites of initial breakdown. For each of the four reflector designs, the MgF_2 overcoat thickness was the same, and the peak and average fields were also the same (see table 3). Yet the damage thresholds varied considerably. We considered then, damage models involving initial failure in the scandia layers. (Only for the two-pair non-QW design was initial damage in the MgF_2 indicated, as discussed below.)

The obvious models for damage involve one or more of the following parameters: the peak SW electric field, the average field, absorption, or layer thickness. We have considered ten different possible models. Model 1 is that damage thresholds are inversely proportional to the peak SW electric field. This is consistent with damage via absorption, both linear and nonlinear, and electron avalanche. This dependence between energy linearly absorbed per unit volume and the field squared is given by

$$\varepsilon_a(J/cm^3) = n\alpha|E(z)/E_o^+|^2\varepsilon_o \qquad (4)$$

where $\alpha = 4\pi k/\lambda$ and ε_o is the laser fluence in J/cm^2. Model 2 predicts initial failure at film interfaces having the largest SW field. Possibly, defects could be trapped at these boundaries. Model 3 has damage dependent on the maximum average field in any one layer. This relates to the total absorption within a layer of thickness, t, by the expression

$$|E/E_o^+|^2_{av} = A/n\alpha t \qquad (5)$$

Model 4 involves the average field in the top scandia layer which could be most susceptible to atmospheric contamination.

Model 5 involves the maximum total linear absorption in any one layer, and Models 6 and 7 involve the total absorption in the top scandia layer and upper two scandia layers, respectively. Model 8 involves the sum of the linear absorptions within all the scandia layers.

Model 9 predicts that the threshold will increase with decreasing thickness of the top scandia layer. This is consistent with the number of absorbing defects the laser beam would encounter. Model 10 is the same, except it involves the sum of the thicknesses of the upper two scandia layers, which for the designs tested, were the only ones that were varied.

In figures 7-10 we present graphs of the mean thresholds versus the parameters unique to four of the models. The mean threshold is the average for the four reflectors of identical design and the vertical bars are the standard deviations from these mean values. A linear least-squares-fit is drawn through each plot and the coefficient of determination, r^2, was computed. A value of 1.000 for r^2 would be a perfect fit. Exponential, logarithmic and power curves did not fit the data as well as straight lines.

The four models selected for illustration here had values of r^2 coefficients very close to 1.00. The reader can verify this by examining table 7 where the statistical results for all the models are summarized. Since the mean threshold (no sites damage) for the two-pair non-QW design

Table 7. Statistical analysis of damage models

Model/Hypothesis		Coefficient r^2 for Linear Fit: Thresholds I	Thresholds II	Saturation Fluences I
1.	Peak field	0.71	0.99	0.95
2.	Maximum field at interface	0.35	0.16	0.52
3.	Maximum field average in any one layer	0.65	0.86	0.88
4.	Average field in top Sc_2O_3 layer	0.69	0.93	0.91
5.	Maximum linear absorption in any one layer	0.77	0.84	0.97
6.	Total linear absorption in top Sc_2O_3 layer	0.72	0.99_6[a]	0.98[a]
7.	Total linear absorption in top two Sc_2O_3 layers	0.47	0.87	0.95
8.	Total absorption in stack	0.75	0.69	0.86
9.	Thickness of top Sc_2O_3 layer	0.84	0.86	0.92
10.	Thickness sum of top two Sc_2O_3 layers	0.64	0.71	0.99

[a]Linear fit predicts a threshold of more than 2.0 J/cm^2 at infinite absorption; see text.

Hypothesis I: Initial damage in Sc_2O_3 films.

Hypothesis II: Same as I, except damage initiates in the HW MgF_2 overcoat only for the two-pair non-QW design.

was slightly lower than for the optimized one-pair design (4.15 compared to 4.4 J/cm^2) the linear fits for all ten models initially were poor with $r^2 < 0.90$. An obvious hypothesis is that threshold damage initiated in the MgF_2 overcoat for this design. This is reasonable since the field in the high-index layers can be suppressed to advantage only to the degree that the low-index films have higher damage resistance. With this hypothesis (II), the r^2 coefficients increased markedly for most of the lines drawn through the thresholds. In particular, Models 1 (peak field) and 6 (linear absorption in top scandia layer) provided excellent fits ($r^2 \sim 0.99$) as is apparent in figures 7 and 10.

The very poor correlation of Model 2 (maximum field at a film interface) deserves special mention since it has been previously considered as plausible [5]. Reflectors of Design C with peak field in the interior of the thick scandia layer had thresholds in direct opposition to this model. Apparently film interfaces are not significantly more damage prone than interior material.

For the saturation fluences, a different set of models was most consistent with the data. The best fit was provided by Models 10, 6, and 5 in descending order. Model 10 ($r^2 = 0.99$), predicting higher thresholds for designs with thinner layers, is consistent with failure by beam interaction with a particular class of coating defects. Presumably, the thicker the films, the greater the number of these defects that will be encountered. Walker et al. [9] also reported a similar increase in damage resistance of thinner single-layer films. However, their definition of damage threshold (midway between our threshold and saturation fluence definitions) was the traditional one.

Particular comment is necessary for Model 6 as illustrated in figure 9. Although the linear fits were exceptionally good ($r^2 = 0.99_6$ and 0.98), the projected thresholds for infinite absorption were greater than 2 J/cm^2. This appears to be a nonphysical result since the lines should pass close to the origin.

By use of the slope of the linear fit for the thresholds of figure 7, we computed the mean value of the peak-field threshold for Sc_2O_3 to be 0.36 MV/cm. For the two-pair modified design in which damage is assumed to initiate in the HW MgF_2 overcoat, a mean value of 0.63 MV/cm was computed. The ratio of these field thresholds is 1.76, which is sufficiently large to motivate the present suppressed-field reflector designs.

Summarizing this section, mean threshold data were most consistent with the peak-field Model 1, and the saturation fluence data were most consistent with the top two scandia layer thickness sum of Model 10. The thresholds for two-pair non-QW designs fell markedly below the linear curve fits suggesting initial failure of an MgF_2 layer (presumably the HW overcoat). Finally, the use of all of the models (except Model 2) evaluated here supported the observed trend of increasing thresholds and saturation fluences with decreasing peak and average fields, absorption, and layer thicknesses.

6. Discussion of Past Experience

As mentioned in the introductory section, previous use of the suppressed-field principle has not always correlated well with damage resistance. The Los Alamos group, using 20- to 30-ps pulses at 1064 and 532 nm [1-4] and 20-ns pulses at 266 nm [8] often found a definite correlation. However, Livermore and OCLI researchers using 150-ps and 1-ns pulses at 1064 nm found no firm evidence of the SW-field influence on damage threshold [5-7].

There are several possible explanations for the different observations. First, at the damage threshold fluence, the peak electric field for 20- to 30-ps pulses is much higher than for nanosecond pulses and so field-dependent mechanisms are emphasized. Secondly, whereas the internal SW-field pattern is essentially constant during the picosecond laser pulses, thermal diffusion of deposited energy away from SW peaks can decrease the temperature extremes arising from energy absorbed over nanosecond times. Thirdly, individual defects randomly distributed throughout the films are apparently the first sites to damage. These defects would tend to mask any SW-field threshold correlation. However, for picosecond pulses the density of damageable defects is apparently greatly increased as evidenced by an absence of any spot-size dependence of damage [2]. Thus, the films become essentially uniform in susceptibility to laser damage and the SW fields become manifest. Fourthly, the positive correlation (even for nanosecond tests) with ultraviolet wavelengths is consistent with a uniform density of coating defects argument. The density of susceptible defects increases as the wavelength approaches the absorption edge as reported by Walker et al. [9].

The successful use of suppressed peak fields to increase the damage resistance of 248-nm reflectors is consistent with previous research. Even greater advantage is anticipated at shorter wavelengths.

7. Summary

Application of the principle of suppression of the peak electric field in the top high-index layers has resulted in substantially increased damage resistance for multilayer dielectric reflectors of $Sc_2O_3/MgF_2/SiO_2$ designed for 248 nm. On the average, the reflectors with one pair of optimized-thickness layers had 50% higher thresholds (survival of 10 of 10 sites) than the all-QW design. Addition of a second pair of optimized non-QW layers resulted in no further increase in threshold, but the saturation fluence (damage of 10 of 10 sites) was 110% higher. A model of damage resistance inversely proportional to the electric-field peak in the high-index (scandia) layers provided the best fit to the threshold data. Also, this model was the only one (out of ten) to accurately predict the threshold for the special test reflector incorporating an extra HW thickness in the top scandia layer. The saturation fluences correlated best with the sum of the thicknesses of the upper two scandia layers which is consistent with damage of a special class of film defects.

8. References

[1] Newnam, B. E.; Gill, D. H. Laser damage resistance and standing-wave fields in dielectric coatings. J. Opt. Soc. Am. 66:166; 1976.

[2] Newnam, B. E.; Gill, D. H.; Faulkner, G. Influence of standing-wave fields on the laser damage resistance of dielectric films. Nat. Bur. Stand. (U.S.) Spec. Publ. 435; 1975. 254-271.

[3] Apfel, J. H.; Matteucci, J. S.; Newnam, B. E.; Gill, D. H. The role of electric field strength in laser damage of dielectric multilayers. Nat. Bur. Stand. (U.S.) Spec. Publ. 462; 1976 December. 301-309.

[4] Gill, D. H.; Newnam, B. E; McLeod, J. Use of nonquarter-wave designs to increase the damage resistance of reflectors at 532 and 1064 nanometers. Nat. Bur. Stand. (U.S.) Spec. Publ. 509; 1977 December. 260-270.

[5] Carniglia, C. K.; Apfel, J. H.; Allen, T. H.; Tuttle, T. A.; Lowdermilk, W. H.; Milam, D.; Rainer, F. Recent damage results on silica/titania reflectors at 1 μm. Nat. Bur. Stand. (U.S.) Spec. Publ. 568; 1980 July. 377-390.

[6] Lowdermilk, W. H.; Milam, D.; Rainer, F. Damage to coatings and surfaces by 1.06 μm pulses. Nat. Bur. Stand. (U.S.) Spec. Publ. 568; 1980 July. 391-403.

[7] Lowdermilk, W. H.; Milam, D. Laser-induced surface and coating damage. IEEE. J. Quant. Elect. QE-17 (9) 1888-1903; 1981.

[8] Newnam, B. E.; Gill, D. H. Ultraviolet damage resistance of laser coatings. Nat. Bur. Stand. (U.S.) Spec. Publ. 541; 1978 December. 190-201.

[9] Walker, T. W.; Guenther, A. H.; Fry, C. G.; Nielson, P. Pulsed damage thresholds of fluoride and oxide thin films from 0.26 μm to 1.06 μm. Nat. Bur. Stand. (U.S.) Spec. Publ. 568; 1980 July. 405-416.

[10] Apfel, J. H. Optical coating design with reduced electric field intensity. Appl. Opt. 16 (7) 1880-1885; 1977.

[11] Foltyn, S. R., Newnam, B. E. Multiple-shot laser damage thresholds of ultraviolet reflectors at 248 and 308 nanometers. Nat. Bur. Stand. (U.S.) Spec. Publ. 620; 1981 October. 265-276.

[12] Foltyn, S. R.; Newnam, B. E. Ultraviolet damage resistance of dielectric reflectors under multiple-shot irradiation. IEEE J. Quant. Elect. QE-17 (10) 2092-2098; 1981.

[13] Foltyn, S. R; Newnam, B. E.; Jolin, L. J. Laser damage results and analyses for uv reflectors under multiple-shot irradiation. Nat. Bur. Stand. (U.S.) Spec. Publ. (this volume) 1982.

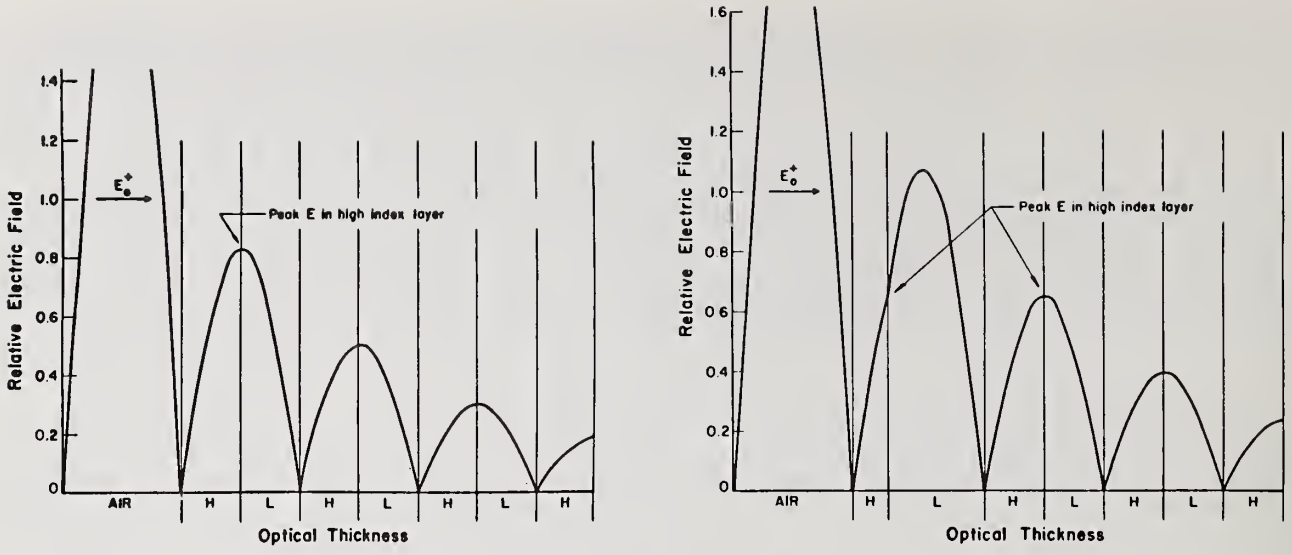

Figure 1. Standing-wave electric-field distribution in two multilayer dielectric reflector designs. E_o^+ is the incident electric field in air. One reflector design (left) uses all QW thicknesses; the other has one pair of non-QW layers optimized for suppression of the peak field in the top H-layer.

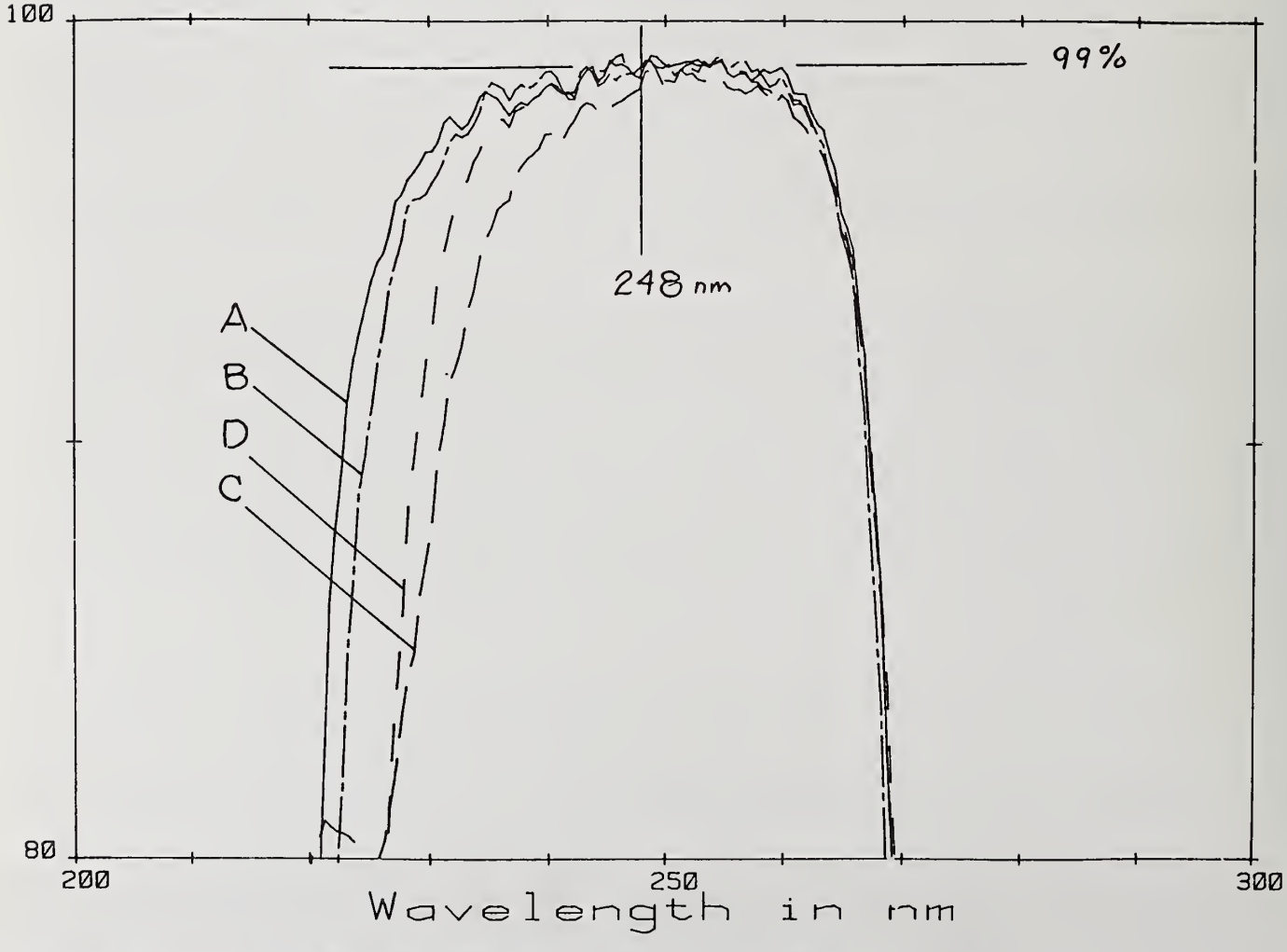

Figure 2. Spectral reflectance (measured) of reflector designs A, B, C, and D.

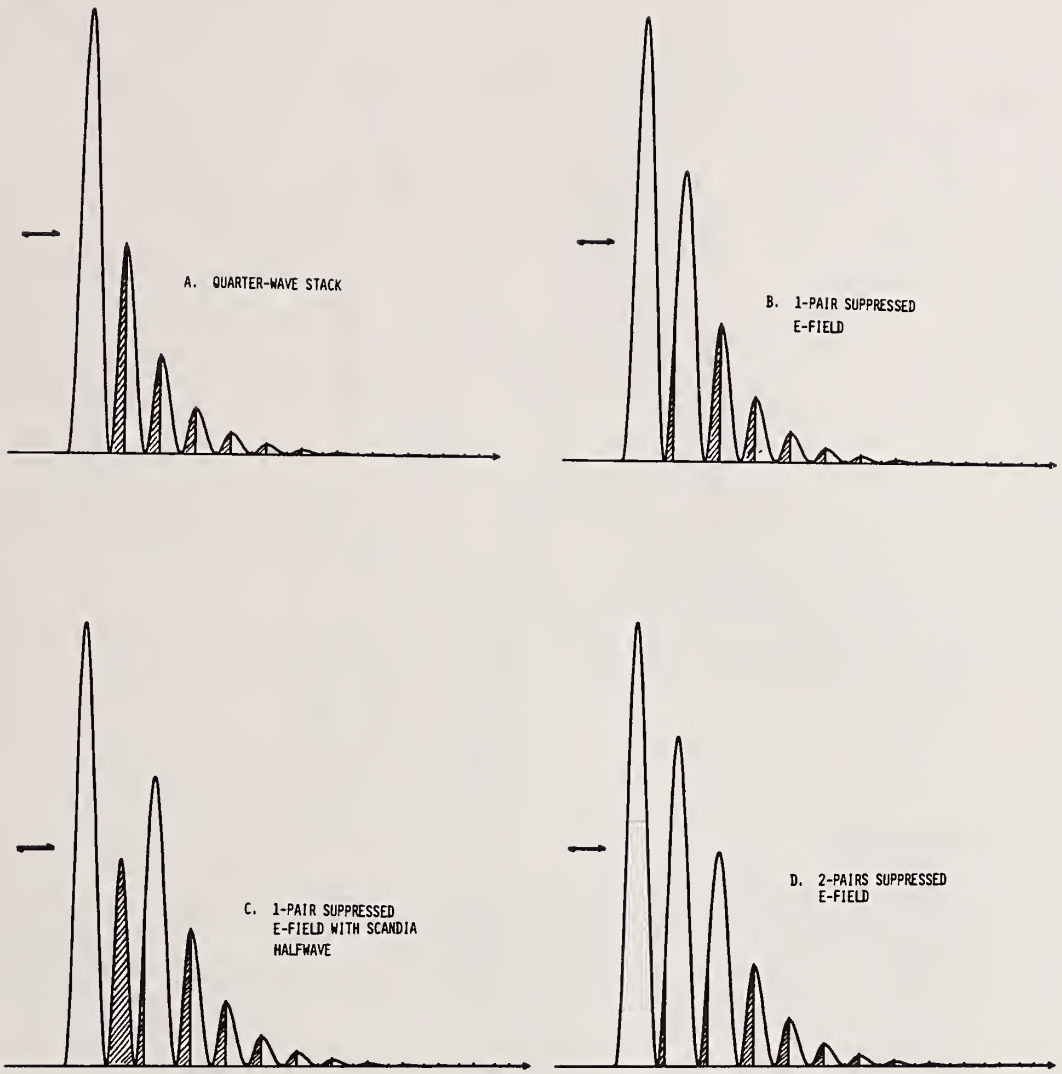

Figure 3. Standing-wave electric field-squared internal to the four reflector designs tested for damage resistance.

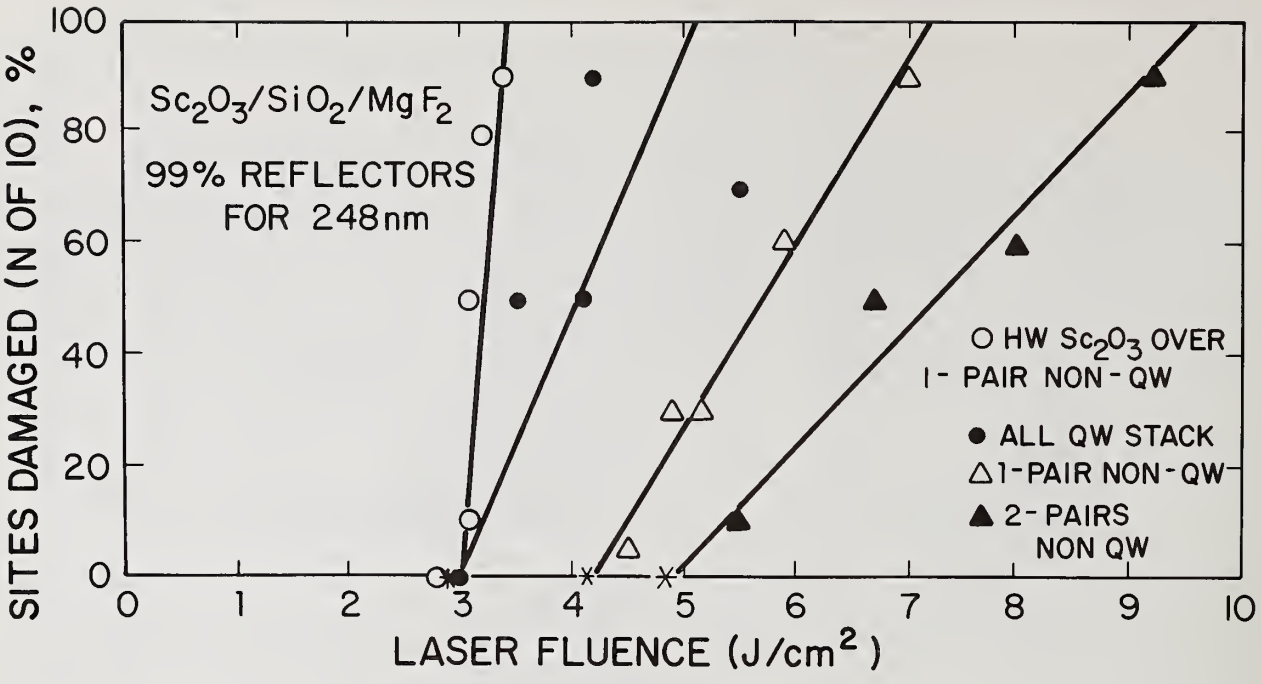

Figure 4. Multiple-shot laser damage test results for one set of reflector designs.

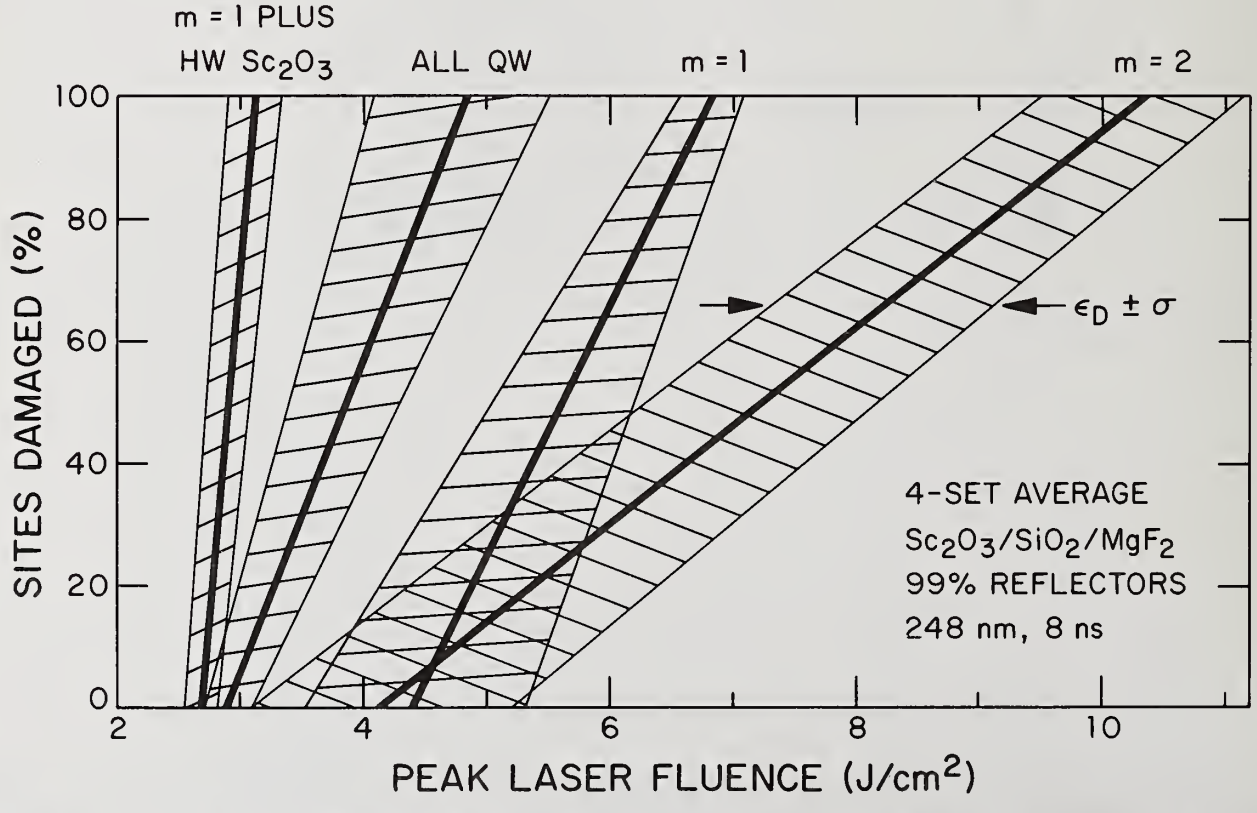

Figure 5. Multiple-shot laser damage test results for four sets of reflector designs. The straight line passes through the mean threshold and saturation fluences; the shaded regions encompass the standard deviations.

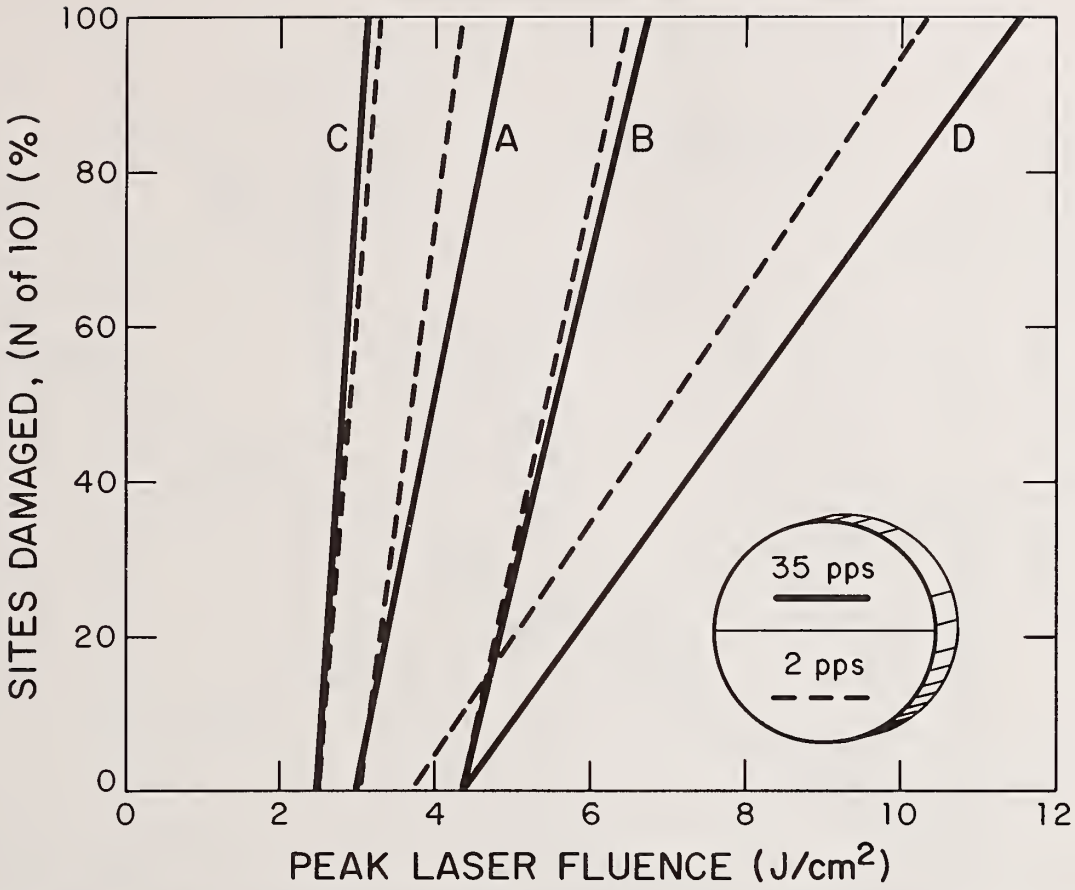

Figure 6. Comparison of multiple-shot damage resistance versus repetition rate for one set of four different reflector designs.

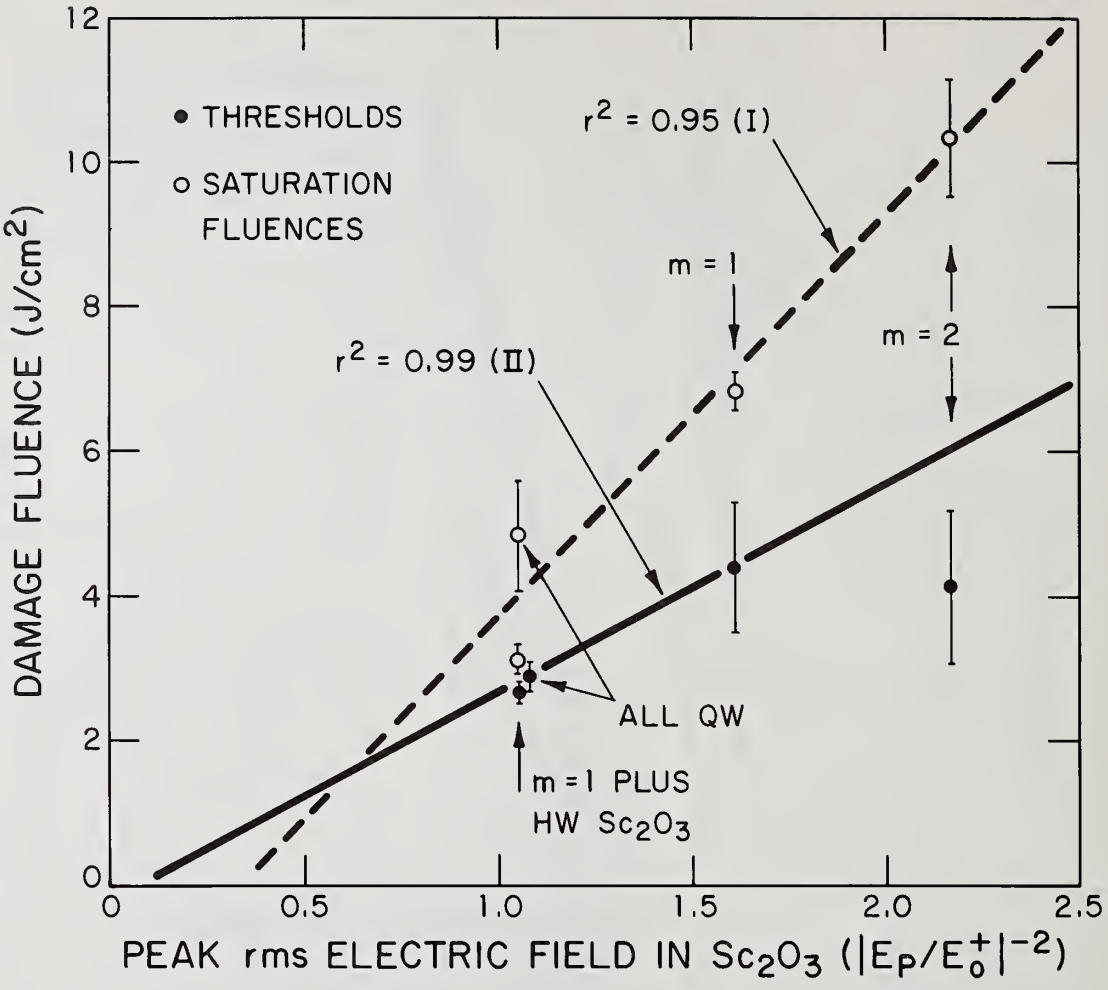

Figure 7. Model 1: Damage fluences versus the inverse of the normalized peak rms electric-field-squared in the scandia layers. Coefficients of determination r^2 indicate the quality of the linear fit to the data according to the hypothesis (I or II) used.

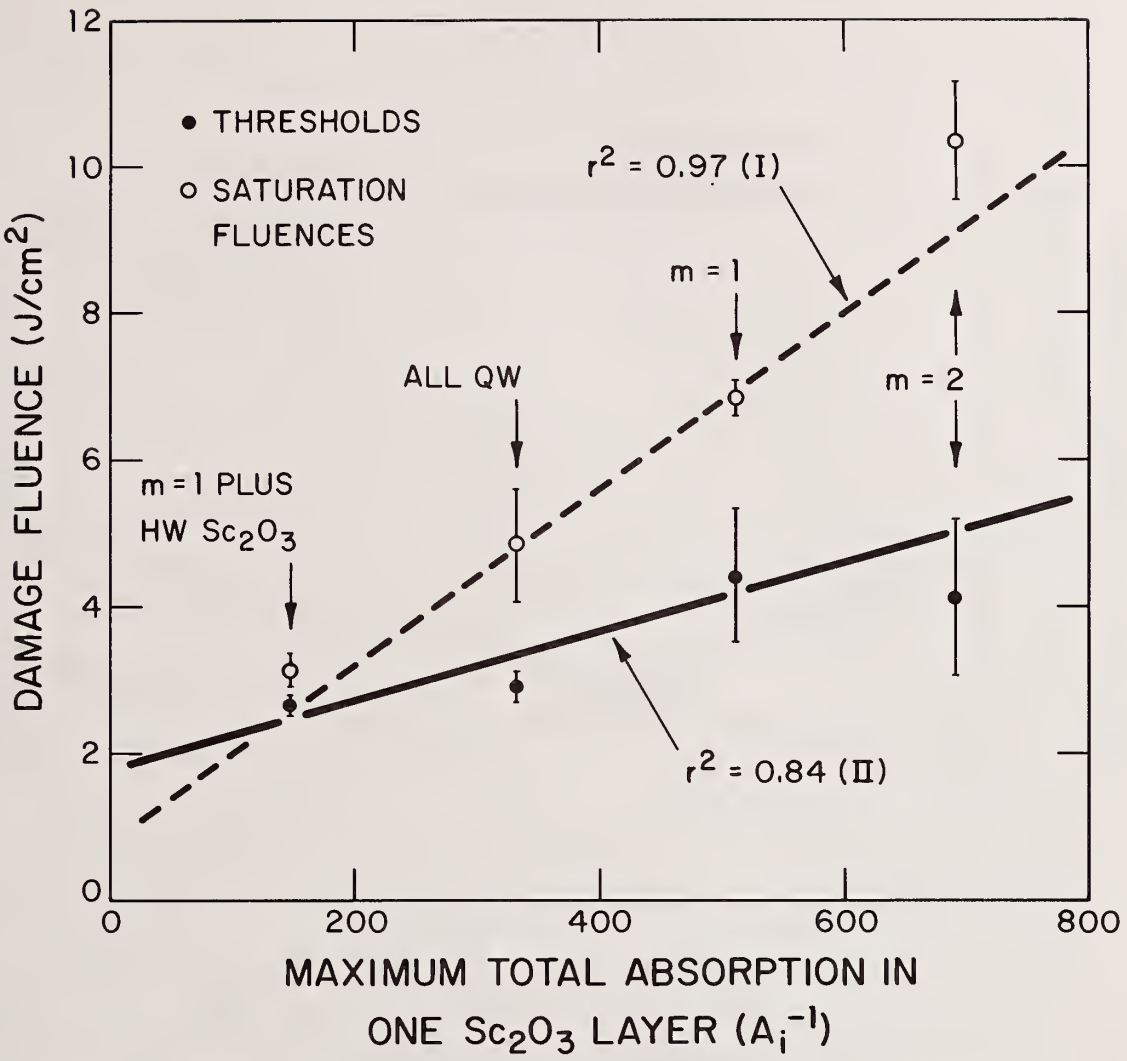

Figure 8. Model 5: Damage fluences versus the inverse of the maximum linear absorption occurring in any single scandia layer.

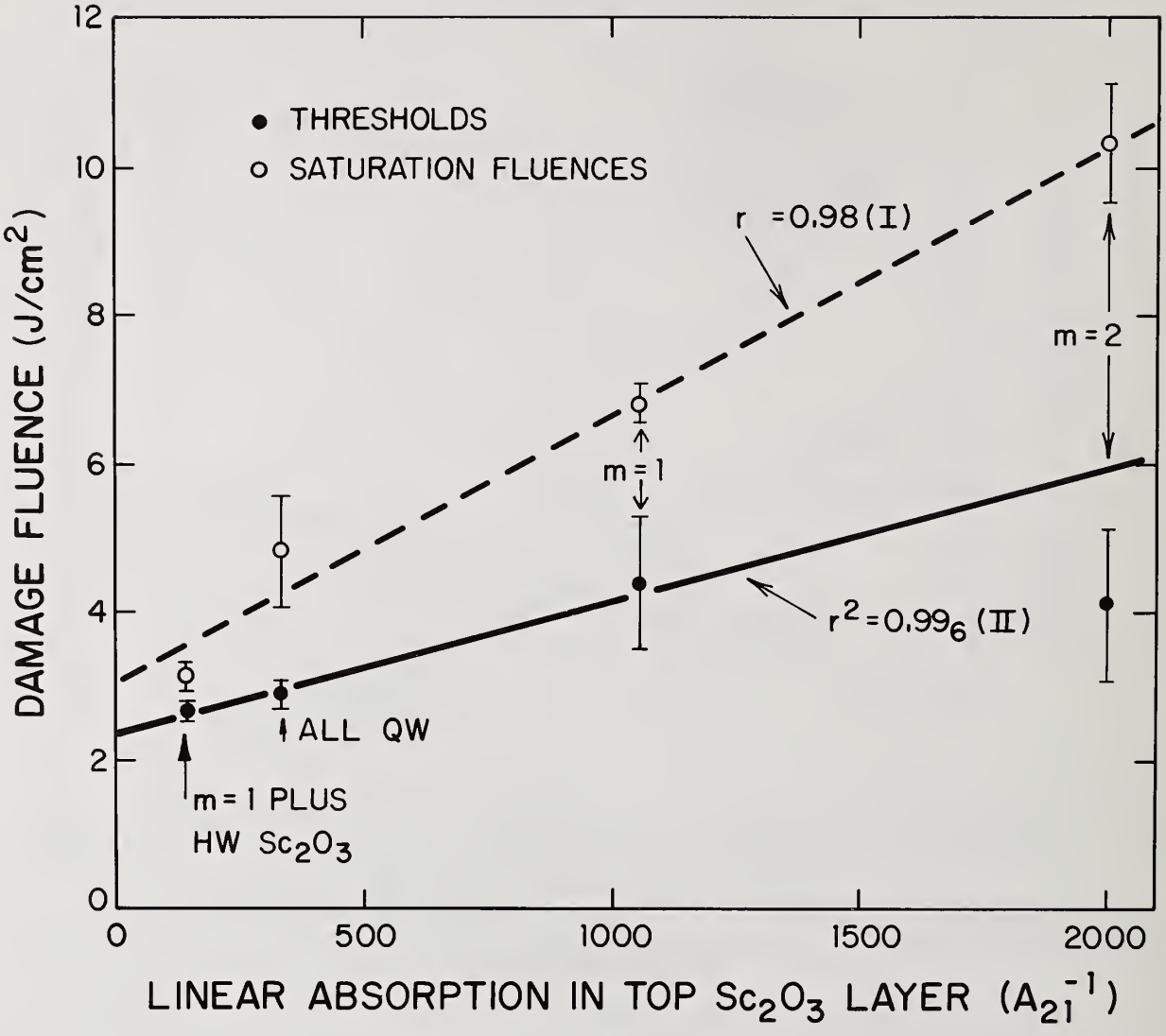

Figure 9. Model 6: Damage fluences versus the inverse of the linear absorption in the top scandia layer.

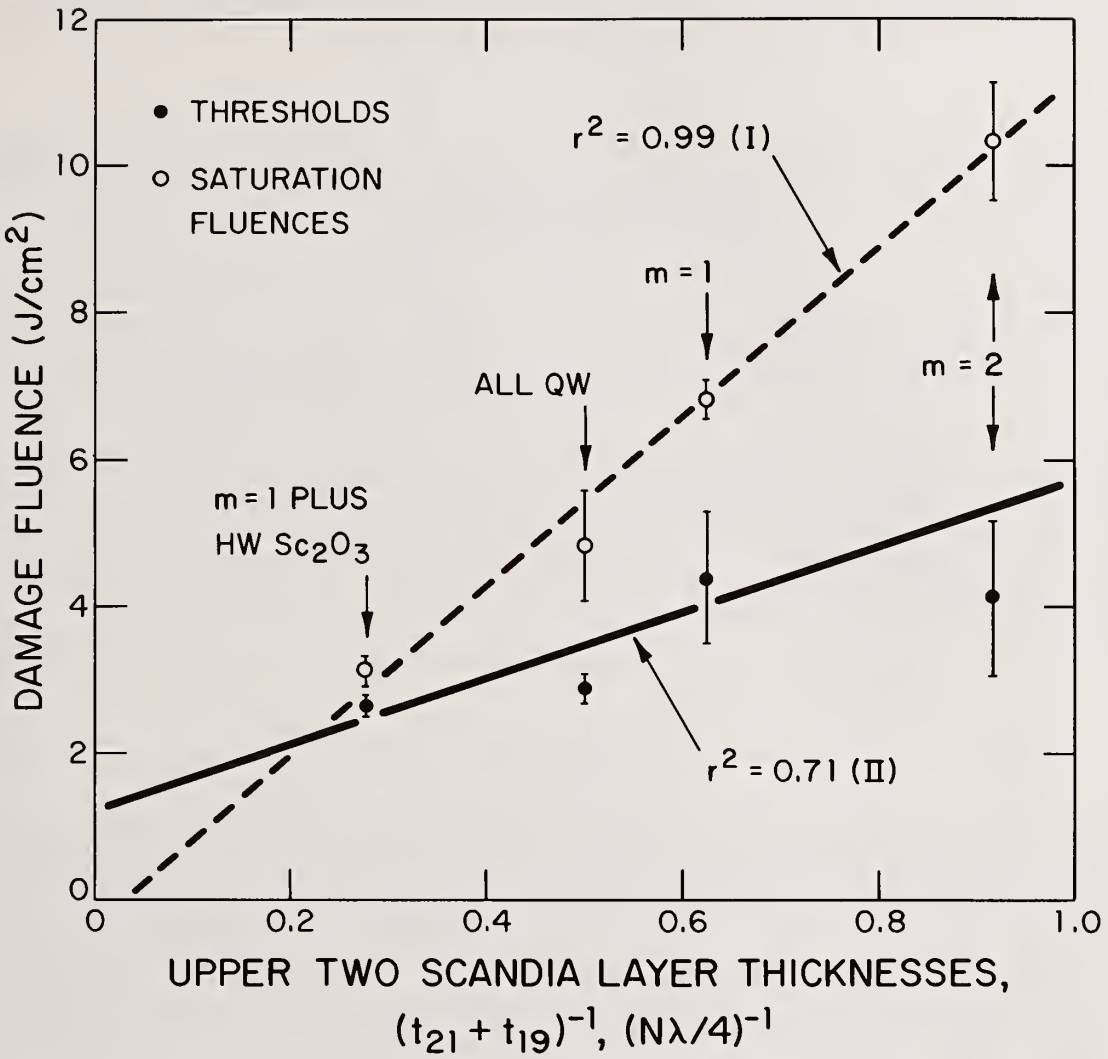

Figure 10. Model 10: Damage fluences versus the inverse of the sum of the thicknesses of the upper two scandia layers.

It was suggested that in addition to absorption and defect density as failure mechanisms one should have substantial contributions from nonlinear absorption. The speaker suggested that the correlation of damage with peak field intensity suggested that it was the small defects which were damaging. The questioner pointed out that it was also an argument for the importance of a nonlinear process.

In response to another question, the speaker reported that no correlation of damage with either substrate composition or polish was observed.

DEGRADATION OF DIELECTRIC FILMS BY XeF EXCIMER INTERMEDIATES

M. Loudiana, A. Schmid and J.T. Dickinson

Physics Department
Washington State University
Pullman, Washington 99164

Many excimer laser designs require optical component surfaces to be in contact with both optical radiation and reactive components of the gain medium. The resulting environmental degradation of coatings on mirrors or windows is analyzed by isolating intermediates from the XeF gain medium and measuring quantitatively corrosive interaction between these species and the dielectric surfaces. Particular attention will be given to SiO_2 films whose reaction with XeF_2 and NF_2 with and without additional stimulation by ions will be surveyed. Temperature effects of the film substrate as well as the importance of synergistic effects for the stability of the SiO_2 coatings will be discussed.

Key words: UV mirrors; excimer lasers; laser material degradation; chemical sputtering

1. Introduction

Chemical survival studies are of great interest in the development of suitable materials for large scale excimer lasers in which optical components are in direct contact with the lasing discharge. This is particularely pertinent to halogen fuelled excimers since many halogen bearing molecules are known to readily engage in reactive ion etching of semiconductor- and dielectric surfaces. Such processes are often refered to as chemical sputtering. UV laser mirrors and AR coatings consist of dielectric films arranged in multilayer stacks. These stacks are topped by what is called the half-wave block which in that position becomes the first mirror or coating part to face chemical radicals impinging from the laser excitation region.

We have started an investigation into the chemical sputtering of a promising half-wave block material, SiO_2, interacting with reactive species from the excitation region of a XeF laser. We were thereby guided by the assumption that i) the XeF laser is electron-beam excited, and ii) the gain medium comprises Xe, Ne and NF_3.

During excitation the F bearing molecule dissociates into the fragments F, NF and NF_2 all of which may also appear in their ionized form. In addition, electron-beam excitation produces large amounts of X-rays, scattered and secondary electrons and lasing photons which all arrive at the optical surfaces together with the chemical species.

We report here results on a set of experiments aimed at categorizing the worst chemical compounds and discharge conditions for SiO_2 film survival. SiO_2 degradation is here understood as decomposition of the film due to reactions between gas phase radicals and film constituents with the subsequent escape of reaction products. Aside from a high density of lattice point defects macroscopic etch features are expected to result from such chemical sputtering. Our experimental approach requires therefore a dynamic mass-spectrometer for identification of volatile reaction products in the gas phase and a scanning electron microscope for

surface evaluation after exposure. Another device concurrently employed in film mass removal measurements from SiO_2 is a standard quartz crystal microbalance.

2. Experimental Technique

A standard UHV system was used as experimental chamber. Pumped on by either a 400 l/sec ion pump or by a 5 W closed-cycle refrigeration cryopump the system operated routinely in the low 10^{-8} Torr range. During the course of these studies aparticular disadvantage of using ion pumps was discovered. In contrast to cryopumps ion pumps tend to "burp" and backstream whenever the gas load contains large amounts of rare gases. Backstreaming H has been identified as cause for serious misinterpretation of early data. Free H readily forms HF when interacting with some fluorinated molecular fragments and thereby compromises etch yields which were at first attributed to other sources. This problem was later eliminated by making cryopumping the standard operational mode.

Sample films were deposited on quartz microbalance substrates by either e-beam evaporation or neutral ion-sputtering. All the film depositions were carried out by the Physical Optics Branch of the Naval Weapons Center, China Lake, CA.. Transport of samples in vacuum-tight contai ners and under positive pressure rare gas ambience assured minimum contamination of films. Storage under similar conditions was to prevent intangible aging effects due to water vapour adsorption or similar "real-life" film-toxins. Film thickness was 100 nm for all samples. Samples were subjected to no further preparations before being exposed to molecular beams of excimer laser constituents.

Once mounted in a standard SLOAN UHV microbalance crystal mount samples could be varied in temperature over a wide range. Up to now, temperature dependencies of etch yields have been studied between room temperature and 100°C. Extension of this temperature range up to 250°C might be of interest in the future. We should caution, however, that over this more limited temperature range problems have already been encountered with film stress-cracking even without any additional chemical attack. We further note that stable films, i.e. those that did not crack, did not exhibit any significant temperature dependencies of etch yield over the 0° to 100°C range.

We report here on gas solid systems involving NF_2 and XeF_2. The latter substance is at room temperature a powder of 3 Torr vapour pressure and is expected to form in XeF excimer laser vessels whenever the gain medium is run at sufficiently high pressure and temperature [1]. XeF_2 deserves particular attention for its well documented capability [2] of etching semiconductor surfaces very efficiently. It has not as widely been applied to films or surfaces of purely ionic compounds such as SiO_2 or other oxides and fluorides.

All reagents were brought into the UHV system through a mechanically pumped foreline and a stainless steel nozzle system, the flow rate through which was regulated by a needle valve. By swinging the sample out of the molecular beam the beam flux could be probed and calibrated by a quadrupole mass spectrometer facing into the beam. In order to prepare NF_2, sufficient current could be passed through the nozzle piece for it to warm up and thermally dissociate N_2F_4. Nozzle temperature of 120°C was found to yield NF_2 with a degree of dissociation reaching the high 90%. N_2F_4 was used as supplied by the vendor. XeF_2 was first purified of byproducts by temperature-cycled cryodestillation. Its molecular flow rate through the nozzle was then controlled by varying the temperature of the heat bath in which the XeF_2 container was immersed. After initial passivation of the chamber this method of control proved entirely sufficient as monitored by the XeF^+ mass peak in the spectrum of the behind-the-sample QMS.

3. Results and Discussion

Irrespective of deposition method we find all 100 nm SiO_2 films quite stable against attack by individual XeF laser constituents. However, if films contain significant amounts of impurities, such as carbon, etching proceeds almost as efficiently as on pure Si surfaces. This was observed for films which had not only common carbon surface contamination but contamination throughout the layer as periodically monitored by Auger spectroscopy.

Low impurity films were not prone to any measurable etching above noise. This outcome changes however dramatically when neutral molecules are acting on the films in conjunction with low energy ions. In figure 1 we show the combined physical and chemical sputtering yield for two representative F bearing etchants and compare this total yield with the purely physical sputtering yield produced by Ar^+. These yields were calculated from raw data assuming a uniform film mass density similar to that of bulk amorphous SiO_2. Data from two different samples of the same evaporation batch are displayed in figure 1. For each etchant the molecular beam species was also used as feed gas for the ion source.

If purely physical knock-on sputtering were the cause for the observed yields in figure 1, a $\sqrt{m}$ -dependence, with m being the ion mass, should obtain. Note that by plotting yield as number of film members removed per incident ion ionization efficiencies for the different gases are already normalized out. The $\sqrt{m}$ -dependence can be invoked to explain N_2F_4 sputtering versus Ar^+ sputtering in the higher ion energy range. But it fails to account for the XeF_2 generated yields. We are therefore led to observe that XeF_2 is not only a practically more potent etchant but that altogether other mechanisms than classical sputtering are taking place during film erosion by XeF_2.

In order to investigate this further, we plot etch-rate data measured as quartz microbalance frequency changes during XeF_2 ion assisted etching. These data are shown in figure 2. As in figure 1, they are plotted against incident ion energy and are independently confirmed by the behind-the-sample QMS monitoring the SiF_3^+ fragmen mass peak. Note that an increased XeF_2 flow rate as expressed by the system pressure units in figure 2 brings about the expected larger XeF^+ ion currents. The very important point of figure 2 is however the characteristic ion energy at which etching cuts off independent of any molecular flow rate. At ion energies below 300 eV we even observe a slight mass deposition instead of any mass removal. Fundamentally similar behaviour was found for ion assisted etching by NF_2 as shown in figure 3. There, however, the ion etching cutoff energy does not appear quite as sharply defined as in the case of XeF_2.

These results are encouraging foremost because of the high cutoff energy at which ion bombardement prompts film decomposition. In e-beam pumped excimer laser systems practically no ions will reach that high a kinetic energy. For those systems ion-assisted thin film damage is not a key mechanism in mirror damage.

Aside from this systems advantage the cutoff energy also helps our understanding of the fundamental chemical sputtering mechanism. Etching of Si surfaces by XeF_2 [3] reveals that XeF_2 dissociates upon arrival at the film surface. We assume that this also happens at oxide surfaces. The dissociated Xe fragment will easily desorb from the surface and is indeed readily observed in the residual gas spectrum. Similarely, the ionization process in the ion gun dissociates XeF_2 and does, provided the newly created ions are not accellerated above 300 eV, lead to virtually indistinguishable etching results from dissociation of XeF_2 at the film surface itself, i.e. no etching at all.

The ion gun does therefore not introduce a chemically new or different species which is responsible for the different etch behaviour below and above 300 eV in figure 2. The same reasoning holds for NF_2 etching as shown in figure 3. This remarkable indifference to the specific type of etchant leads us to conclude that the key issue must lie with an intermediate- or the final reaction product. The final volatilized reaction product from both etching processes has been identified as SiF_4 which leaves a predominantly SiF_3^+ mass peak signature in the residual gas spectrum. On the other hand, no other SiF_x (x 3) species have been detected. Thus, whatever SiF_x surface compound is formed during XeF_2 or NF_2 dissociation, it does not desorb from the surface spontaneously. And it does not do so even at surface temperatures of 100°C. No special effort has been made to accurately determine whether this formation of an intermediate occurs at surface monolayer coverage or at higher coverage. With low energy ions (below 300 eV for XeF_2 and somewhat less for NF_2) incident on the film this formation is enhanced. At what end point this enhanced formation comes to its saturation is not yet clear. Above the critical energy the ion-initiated reaction either allows for SiF_4 formation from among previously prepared SiF_x building blocks or provides already spontaneously formed SiF_4 with sufficient activation energy to desorb. Once etching proceeds the formation of additional intermediate SiF_x is seen to be a linear function of incident molecular beam flux.

This detailed etching model is still incomplete and speculative and requires further experimental work. We will present additional work involving other etchants and films elsewhere. Surface topographic etch studies using the scanning electron microscope will also be presented independently.

4. Acknowledgment

This work was supported by the Office of Naval Research.

References

[1] PRC Corporation, private commun.

[2] Winters, H.F., and Coburn, J.W., Appl.Phys.Lett. 34, 70 (1979)

[3] Tu, Y.Y., Chuang, T.J., and Winters, H.F., Phys.Rev. B23, 823 (1981)

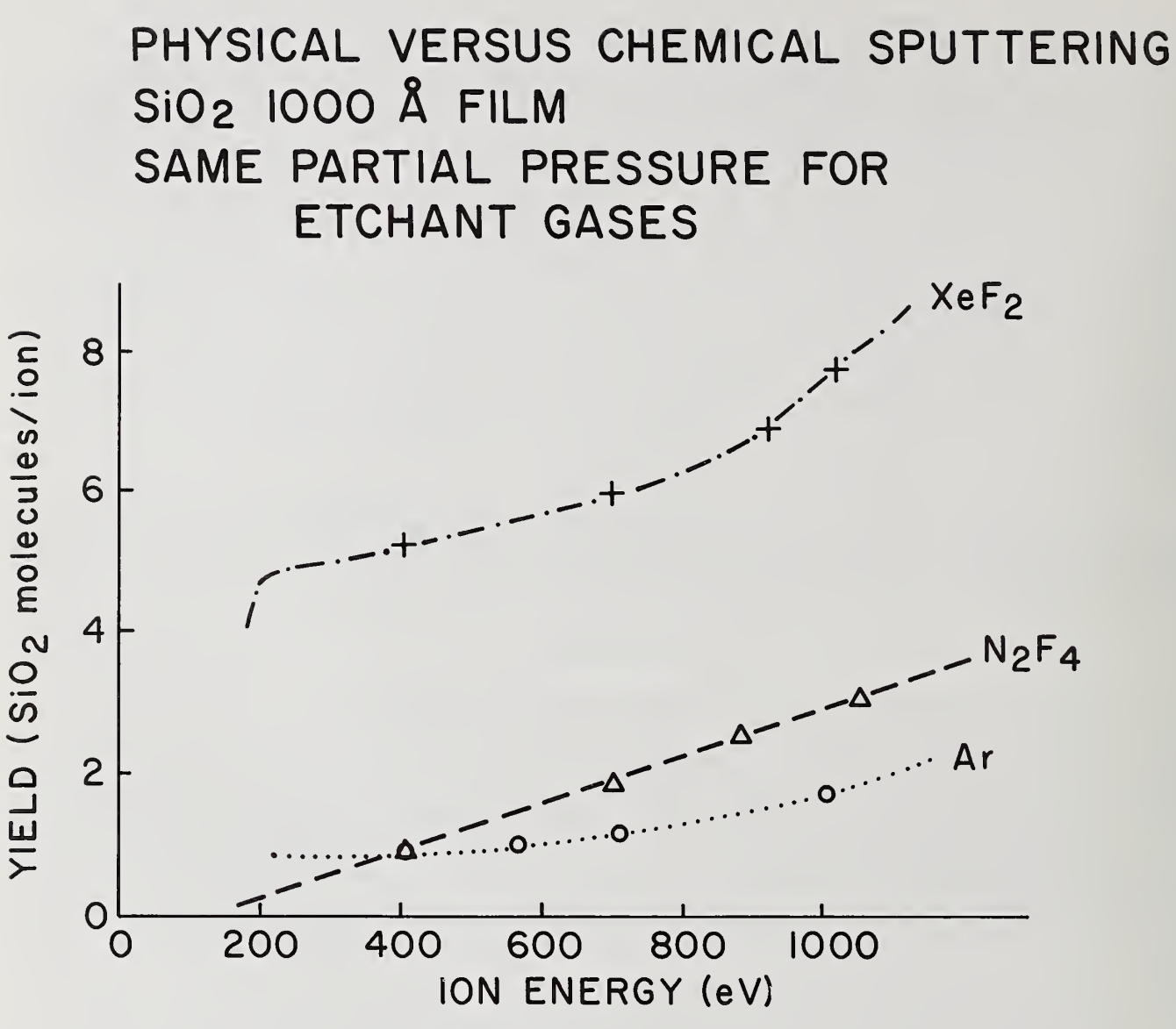

Figure 1. A comparison of ion-assisted etch yields for purely physical sputtering (Ar^+) and physical plus chemical sputtering (XeF_2, N_2F_4).

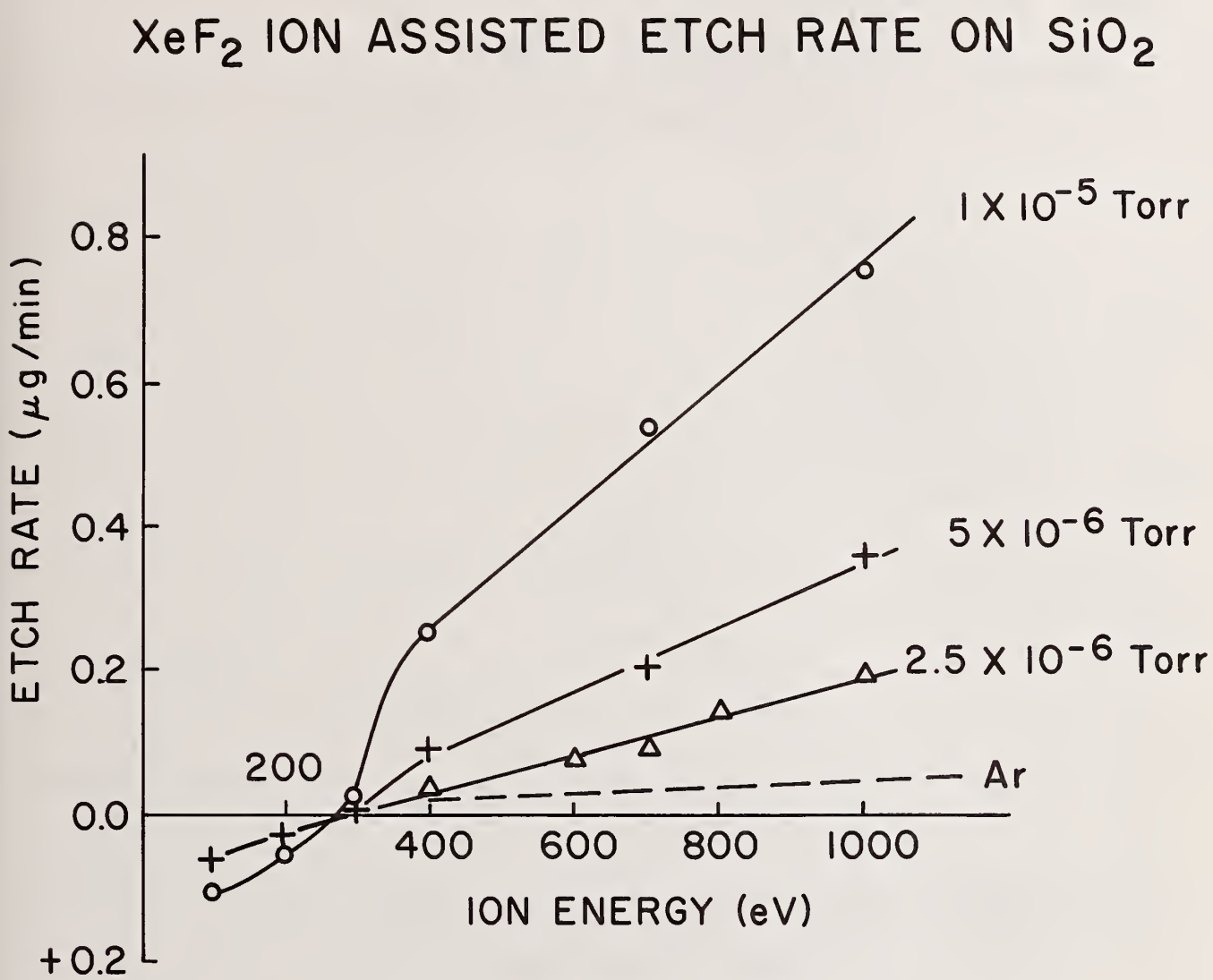

Figure 2. The molecular flow rate- and XeF^+ ion energy dependence of XeF_2 ion assisted etch rate on SiO_2. The physical sputtering rate for Ar^+ shown for comparison was obtained at $5x10^{-6}$ Torr Ar pressure.

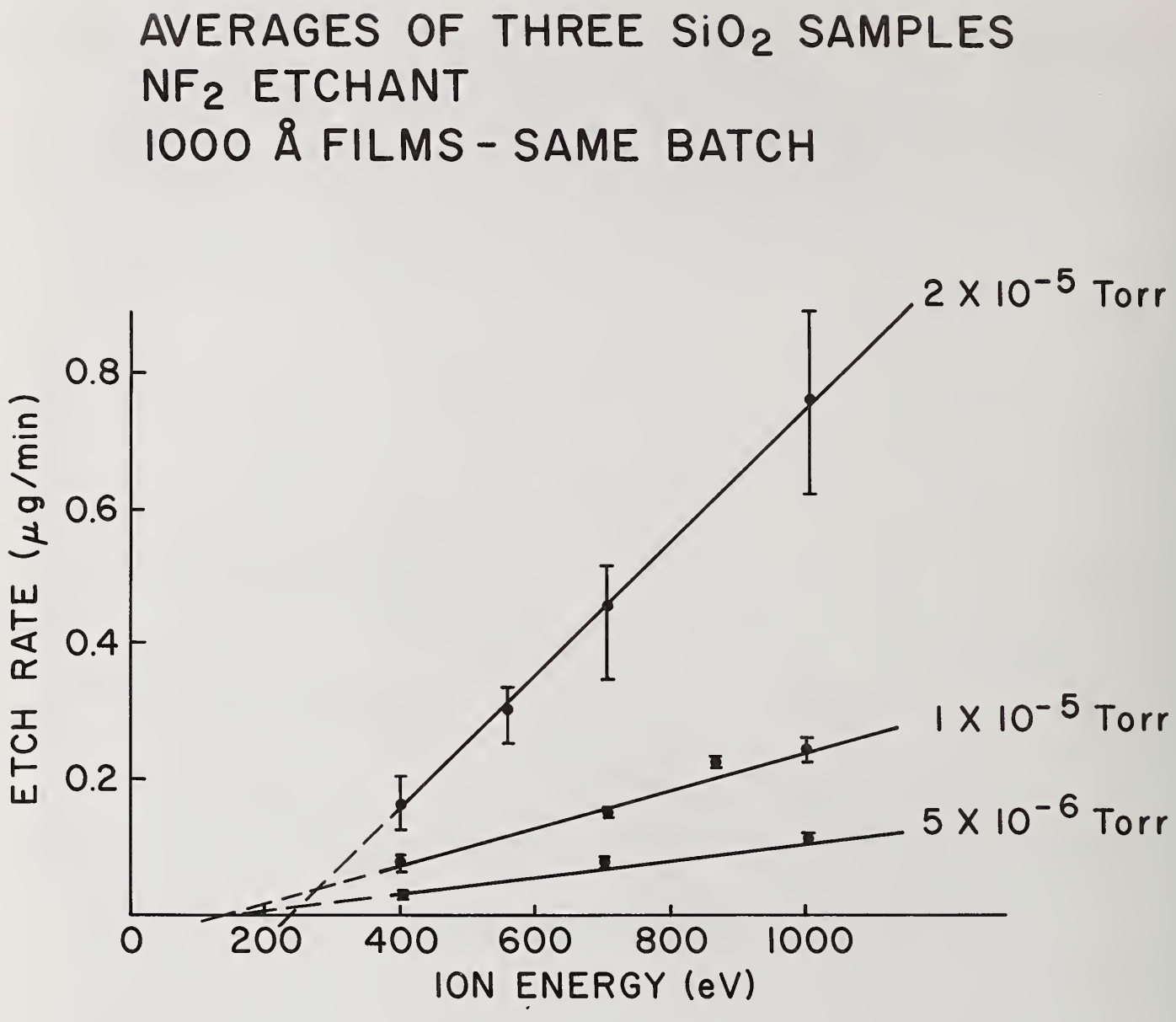

Figure 3. NF_2 ion assisted etch rates averaged over three samples.

A question was raised as to why test silicate optics for applications in XeF excimer lasers rather than fluorid based optics, which are much more resistant to chemical attack by HF. The answer given was that SiO_2 films initially were regarded as a prime candidate for XeF laser optics. They plan to look at fluoride based films later.

Pulsed D_2 - F_2 Chain-Laser Damage To Coated Window and Mirror Components

S. T. Amimoto, J. S. Whittier, A. Whittaker,
A. Chase and R. Hofland, Jr.
The Aerospace Corporation, Los Angeles, CA 90009

M. Bass
USC Center for Laser Studies, Los Angeles, CA 90009

Large-spot laser damage thresholds have been measured for bowl-feed-polished CaF_2 and sapphire windows (bare and antireflection-coated) and for highly-polished copper mirrors (bare and carbyne-coated) at DF chain-laser wavelengths (3.58-4.78μm). The chain reaction between F_2 and D_2 was initiated by a magnetically-confined electron beam, producing DF-laser outputs of 10-20 J in pulses of 0.6 - 0.9 μsec (FWHM) duration. Energy extracted from a transmission-coupled unstable resonator was focussed using a CaF_2 lens. A soft-aperture technique was employed to suppress effects of Fresnel diffraction so that uniform (top-hat) intensity profiles were obtained along the focussing beam. With this laser system, commercially-available antireflection-coated CaF_2 and Al_2O_3 samples were measured to have damage thresholds in the range 21-27 J/cm^2. Significantly larger damage thresholds were found for uncoated, polished samples of Al_2O_3, but damage resistance of uncoated polished CaF_2 was measured to be equal to that of the best antireflection-coated CaF_2 samples. A highly polished copper mirror was found to have the highest damage threshold of all the materials tested (58 J/cm^2). Carbyne films of diamond-like hardness, a type of carbon coating, were applied to polished copper mirrors and bowl-feed-polished CaF_2 surfaces. Such carbyne coatings as were prepared in this work contained numerous carbon-bearing particles that were easily damaged (~10 J/cm^2). However, regions of the irradiated carbyne film that were free of carbon particles withstood high laser fluences (25 J/cm^2), suggesting that improvements in carbyne film preparation would yield attractive protective coatings of high damage resistance at DF wavelengths.

Key Words: carbyne (carbon) coatings; laser windows; laser mirrors; laser damage; DF-chain laser; coating absorption, adhesion strength, acid resistance.

1. Introduction

The performance of optical components can significantly affect the size, weight, and efficiency of high power laser systems. Component failure in pulsed DF chain-reaction lasers presently imposes design limitations on laser gain length and aperture size. Unique challenges associated with component development for DF chain lasers are the laser's broadband spectral output of 3.58-4.78 μm, the requirement for operation in the presence of a corrosive F_2/DF environment, and the need to withstand high impact loadings associated with combustion overpressures of from 6 to 8 atmospheres. Data on the failure of DF laser optical components are restricted primarily to small-energy pulses and, hence, to small spot sizes of the order of hundreds of microns [1,2]. The scaling of these results to large spot sizes of practical importance is known to be unreliable. Damage thresholds of 52 J/cm^2 were recently reported for $ThF(ZnS)_3$-coated mirrors [3] using beam spots up to 1 cm in diameter [4]. Such excellent damage resistance has, however, been observed only in benign (air) environments. Similar coatings on internal mirrors and windows, mounted in repetitively-pulsed systems, have repeatedly failed after several shots at incident fluences of several joules per cm.^{2} Damage was by acid etching and by blowoff induced by laser irradiation.

Coating failure in pulsed chain-laser systems has prompted us to examine the suitability of carbyne coatings as hard protective films on pulsed DF-laser optical components. Carbyne, the carbon form of interest, has been produced at the Aerospace Corporation by means of quench cooling of carbon gas [5,6]. Early studies of carbon films revealed several interesting properties: (1) diamond-like hardness (greater than B_4C); (2) chemical resistance to acids, bases and organic solvents; (3) good adhesion to Cu, Pt, glass, Si, Ge, sapphire, etc.; and (4) low absorption in the 2 to 40 μm range. In view of these different and unique properties, we undertook a brief program to apply carbyne films to candidate DF-laser window and mirror materials for evaluation with regard to (1) adhesion strength, (2) resistance to HF/DF attack, (3) abrasion resistance, (4) optical absorption, and (5) laser damage threshold. During the brief (two-week) study of laser damage resistance, we also measured damage thresholds for selected commercially-available coatings applied to both transparent and reflective optics for purposes of comparison with chaoite film performance. The resulting data show that the best chaoite films have high damage resistance, hardness and resistance to acid attack, and may be attractive for use on pulsed-DF-laser optical components if coatings can be developed that are free of carbon particles.

2. Experimental Technique

A diagram of the laser damage apparatus employed in the present study is illustrated in figure 1. A magnetically-confined electron beam was used to initiate the pulsed chain-reaction DF laser [7]. Mixtures containing 20% F_2- 8% D_2 by volume were irradiated for periods of 0.5 to 1 μsec at current densities of 20A/cm^2 to accomplish laser initiation. Nominal laser energies of 10-20J in 0.6-0.9 μsec (FWHM) pulses were delivered at cavity pressures of 800 torr. Energy was extracted from the gain medium by means of a transmission-coupled half-symmetric unstable resonator and then collimated using a CaF_2 lens of 8-m focal length. Laser windows were uncoated, 1.25-cm-thick CaF_2 crystals that were tilted with respect to the optical axis. A beam splitter at nearly normal incidence to the laser beam diverted about 6% of the total pulse energy into a 9-cm ballistic thermopile. Emission time history of the laser was monitored with a Au:Ge detector. The D_2-F_2 laser spectral output has been measured in a previous study and found to consist of up to 69 lines operating between 3.58 and 4.78 μm [8].

The remaining energy in the pulsed DF-laser beam was focussed by means of a CaF_2 lens of 45-cm focal length. The lens was translated along the direction of the beam to vary the fluence incident upon the optical test sample. A fluence range of 5 to 70 J/cm^2 could be encompassed by this technique. To obtain uniform beam spatial distributions along the focussing beam, an intracavity soft-aperture filter was employed (fig. 1). This filter suppressed effects of Fresnel diffraction during focussing. The spatial distribution of the focussing beam was determined from burn patterns on calibrated witness film (fig. 2). As illustrated in figure 2, a uniform (top-hat) spatial fluence distribution was obtained by use of the soft-aperture filter.

Laser damage measurements were carried out on a variety of transparent and reflective optics in the present work (Table I). Antireflection (AR)-coated windows of Al_2O_3 and CaF_2 were obtained from Laser Power Optics (LPO) and CVI. Coatings on the Al_2O_3 samples were ZnS/ThF_4 and $TiO_2/Al_2O_3/MgF_2$; the AR coating on the CaF_2 sample was PbF_2/ThF_4. Details of the coating designs are available upon request from these vendors [9,10]. Bowl-feed-polished samples of Al_2O_3 and CaF_2 were also tested as a standard against which coated window performance could be assessed. Two mirrors were tested in our study; an uncoated laboratory-grade copper mirror (Spawr) and a carbyne-coated copper mirror. The performance of carbyne-coated CaF_2 windows was also evaluated in our work.

Transparent carbon films for use in the present study were produced by quenching carbon gas on selected substrates, including transparent and reflective optical elements [11]. A schematic diagram of the equipment that was used to produce exploratory carbyne films is shown in figure 3. The sample and a piece of 99.99% pure carbon were located near the center of the coating pressure vessel. The optical sample could be heated to 180° C and was discharge cleaned prior to coating application. The pure carbon source was positioned in a carbon mandrel that was held in the chuck of a spinner mounting. Heating of the spinning carbon target was accomplished by means of a focussed 1.5 kW CO_2 laser beam that entered the chamber through a sodium chloride window. During laser irradiation, the hot carbon rod was surrounded by a cloud of carbon gas that impinged on the surface of the spinning optical sample. The temperature of the solid carbon source was measured by an optical pyrometer of fast response time (~ 0.1 sec). The pyrometer was located, as shown in figure 3, with its line of sight at 30° to the laser beam axis. Careful temperature control of the carbon source was crucial for production of the desired carbyne film. Chamber pressure was measured by a Baratron gauge. Instability in the output of the CO_2 laser led to difficulties in the preparation of uniform, reproducible coatings. In view of the unsophistocated nature of the coating apparatus, it is believed that improvement in the quality and reproducibility of carbyne coatings should be readily achievable.

A total of 50 shots were performed on the ten samples that were available for our laser damage study. Approximately one full day of testing was required to determine the damage threshold of an optical component. During testing, the sample was rotated after each exposure so that a fresh area was irradiated. The large spot sizes used in our study implied that only a few exposures could be performed on each optical sample. Exposure began below 10 J/cm^2 and was increased in steps of 50 to 100% until small-scale and, finally, catastrophic damage was observed. Component damage was determined by post-irradiation inspection with a 10X microscope, using strong illumination.

3. Results and Discussion

Selected properties of carbyne films were briefly examined prior to measurement of damage resistance. Absorption coefficients in the visible were measured to increase from ~ 6 x 10^2 cm^{-1} at 600 nm

to ~ 3 x 10^3 cm^{-1} at 220 nm. Index of refraction averaged about 2.5; one film, however, gave a rather low index value of 1.7. Absorption peaks at 3.1, 5.9, 6.2, 7.3 and 8.5 μm strongly suggested that the present carbyne films were contaminated with pump oil. Contamination was possible since no precautions were taken to prevent backstreaming of pump oil during the carbyne coating process. Because pump oil would be expected to increase absorption in the 3.6-4.8 μm bandpass, its presence in all likelihood would have reduced the DF damage resistance of the carbyne-coated samples that were tested in this work.

An ion microprobe mass analyzer (IMMA) was used to obtain unequivocal identification of carbyne as the film that was produced. Although two different carbon negative ion spectra have been observed using the IMMA, carbon films used in this study gave spectra that stopped at C_4. Unfortunately, the IMMA was incapable of identification of the particular carbyne form that was produced in our work.

Abrasion tests were also performed on the carbyne films. The results revealed that the films were more abrasion resistant than their substrates (Ni, Al, Cu, CaF_2); they were determined to be less resistant than fused quartz. Adhesion strength of the carbyne films was found to vary over the range from 57 to 652 kg/cm^2. The diffusion of vacuum pump oil onto the substrates could have accounted for these low values as well as the wide variation in adhesion strength.

Chemical resistance of the carbyne films was evaluated using concentrated HF acid. The films were unaffected by the acid. Penetration of the films by way of imperfections was observed, however. One continuous film was tested that was not penetrated during the time required for the droplet of acid to evaporate (about 30 minutes).

The laser damage threshold measurements performed during the present study are summarized in Table I. Included in the table are component substrate material, substrate thickness, component coating (when present), coating vendor, type of damage observed, and incident laser fluence at which damage was first detected. For the sapphire substrate case, both the AR coating of $TiO_2/Al_2O_3/MgF_2$ and the bare substrate were found to exhibit high surface-damage thresholds (28-54 J/cm^2). As anticipated, the exit surfaces damaged at thresholds that were well below those of the entrance surface. The damage threshold of the ZnS/ThF_4 AR coating (17 J/cm^2) was found to be the lowest of all the sapphire samples tested.

Damage tests on CaF_2 substrates showed that commercially-available AR coatings have damage resistance equal to that of the uncoated CaF_2 surface (Table I). The carbyne coatings on CaF_2 exhibited damage thresholds that varied over a wide range of fluences (14-25 J/cm^2). The best carbyne film was observed to have a damage resistance equal to the polished CaF_2 surface. On a microscopic scale, the coatings were found to show sample-to-sample variations as well as variations across a given sample. The damage levels could not be correlated with any particular deposition procedure. A micrograph of damage to a carbyne film deposited on CaF_2 and exposed at 23 J/cm^2 incident laser fluence is shown in figure 4. Damage is seen to have occurred preferentially at carbon-bearing spots in the carbyne film. It is likely that these carbon particles absorbed the laser radiation preferentially; the carbyne film in the regions away from the carbon particles showed no degradation at laser fluences large enough to degraded the better commercially-available films. Carbyne coatings of very high damage resistance should be achievable, therefore, if the coatings can be made free of particulated carbon matter.

A limited number of damage tests were performed on reflective optical components (Table I). An oxygen-free, high-conductivity copper mirror of "laboratory grade" surface finish was measured to have

the highest damage threshold of all the component samples that were tested. A micrograph of the laser damage sites on this polished mirror is shown in figure 5. The degree of damage is seen to be quite small considering the high exposure fluence, 58 J/cm^2. The carbyne-coated copper samples were consistently found to fail at low fluences of 9.5 J/cm^2 or less. During the coating of copper samples, one half of each substrate was masked from the hot carbon source. Figure 6a gives clear evidence that particulate carbon contamination occurred on the half of the copper mirror that was thought to have been shielded from the heated carbon source. A method for interception of these carbon particulates must be devised in future coating studies. The irradiation of the carbyne vapor stream by a high-power laser beam would be one technique for interception of particulate material prior to its impingement on a substrate surface. A micrograph, showing laser damage to a carbyne film deposited on half of a polished copper substrate, is shown in figure 6b. Preferential damage at carbon-bearing sites is again seen to be the failure mechanism, as was observed for the case of carbyne coatings on CaF_2 samples. We again speculate that carbyne films on reflective optics would possess high damage resistance in the absence of these particulate carbon sites.

4. Concluding Remarks

Large-spot DF-laser damage thresholds have been investigated for bare substrates, commercially-coated components, and hard carbyne films deposited on transparent and reflective optics. Damage resistance measurements on candidate DF-laser window components have shown that high quality anti-reflection coatings are presently available for CaF_2 and Al_2O_3 substrates. Damage resistance of OFHC polished-copper mirrors has also been found to be excellent at DF chain-laser wavelengths. Unfortunately, the ability of these components to withstand high radiation fluxes in the presence of the hot corrosive gas flows of repetitively-pulsed laser systems is known to be limited. This limitation has motivated us to examine Aerospace carbyne coatings as candidate protective films for pulsed DF optical components. The best carbyne coatings were found to survive high laser fluences of 25 J/cm^2 in our work. However, carbyne films as currently prepared for laser-damage evaluation generally showed numerous particulate carbon sites that were easily damaged. Areas free of these defects were found to possess high laser damage resistance. We recommend, therefore, that improvements in carbyne-coating preparation be pursued which could ultimately lead to the development of practical, damage-resistant films for use in repetitively-pulsed DF laser systems.

5. Acknowledgements

This work was carried out under support of a grant from the Aerospace Sponsored Research Program.

6. References

[1] E. W. Van Stryland, M. Bass, M. J. Soileau, and C. C. Tang, "Pulsed HF/DF Laser Damage in Window Materials", NBS Special Pub. 509, 1977.

[2] T. M. Donavan, J. O. Porteus, S. C. Seitel, P. Kraatz, "Multithreshold HF/DF Pulsed Laser Damage Measurements on Evaporated and Sputtered Silicon Films", NBS Special Pub. 620, 305 , 1980 .

[3] P. Kraatz, "Optical Coatings for 2-6 Microns", Northrop Resh. and Techn. Ctr. Rpt. NRTC78-13R, April 1978.

[4] D. B. Nichols, R. B. Hall and R. A. House, "Large Spot DF Laser Damage of Dielectric-Enhanced Mirrors:, to be published.

[5] A. G. Whittaker, Science 200, 763 (1978).

[6] A. G. Whittaker, Carbon 17, 21 (1979).

[7] S. T. Amimoto, J. S. Whittier, M. L. Lundquist, F. G. Ronkowski, P. J. Ortwerth, R. Hofland, Appl. Phys. Lett. 40, 20 (1982).

[8] S. T. Amimoto, "DF Chain-Laser Spectra", Aerospace Techn. Rpt. TR-81(6404)-1, Oct. 1980.

[9] G. Hahn, CVI Laser, private communciation.

[10] G. H. Sherman, Laser Power Optics, private communication.

[11] A. G. Whittaker, P. L. Kintner, L. S. Nelson, N. Richardson, Rev. Scientific Instr. 48, 632 (1977).

Table 1. DF-Laser-Damage Summary Table

Substrate	Substrate Thickness	Coating (Vendor)	Type of Damage	Fluence (J/cm^2)
Al_2O_3	6.25 mm	None	Isolated spot on exit surface	25
			No entrance damage	≤54
	3.12 mm	$TiO_2/Al_2O_3/MgF_2$ (CVI)	Isolated spot on exit surface coating	28
			Damage to entrance surface coating	38
	3.12 mm	ZnS/ThF_4 (LPO)	Isolated damage on entrance and exit coating	17
CaF_2	5 mm	None	Exit surface and bulk damage at lens focus	21
			Entrance surface and bulk damage at lens focus	27
	5 mm	PbF_2/ThF_4 (LPO)	Exit coating damage	21
			Isolated spot on front	27
	5 mm	Carbyne (Aerospace)	Small spot on entrance coating	14
			No visible damage	25
Cu	-	None (Spawr)	Slight surface damage	58
	-	Carbyne (Aerospace)	Severe coating failure	9.5

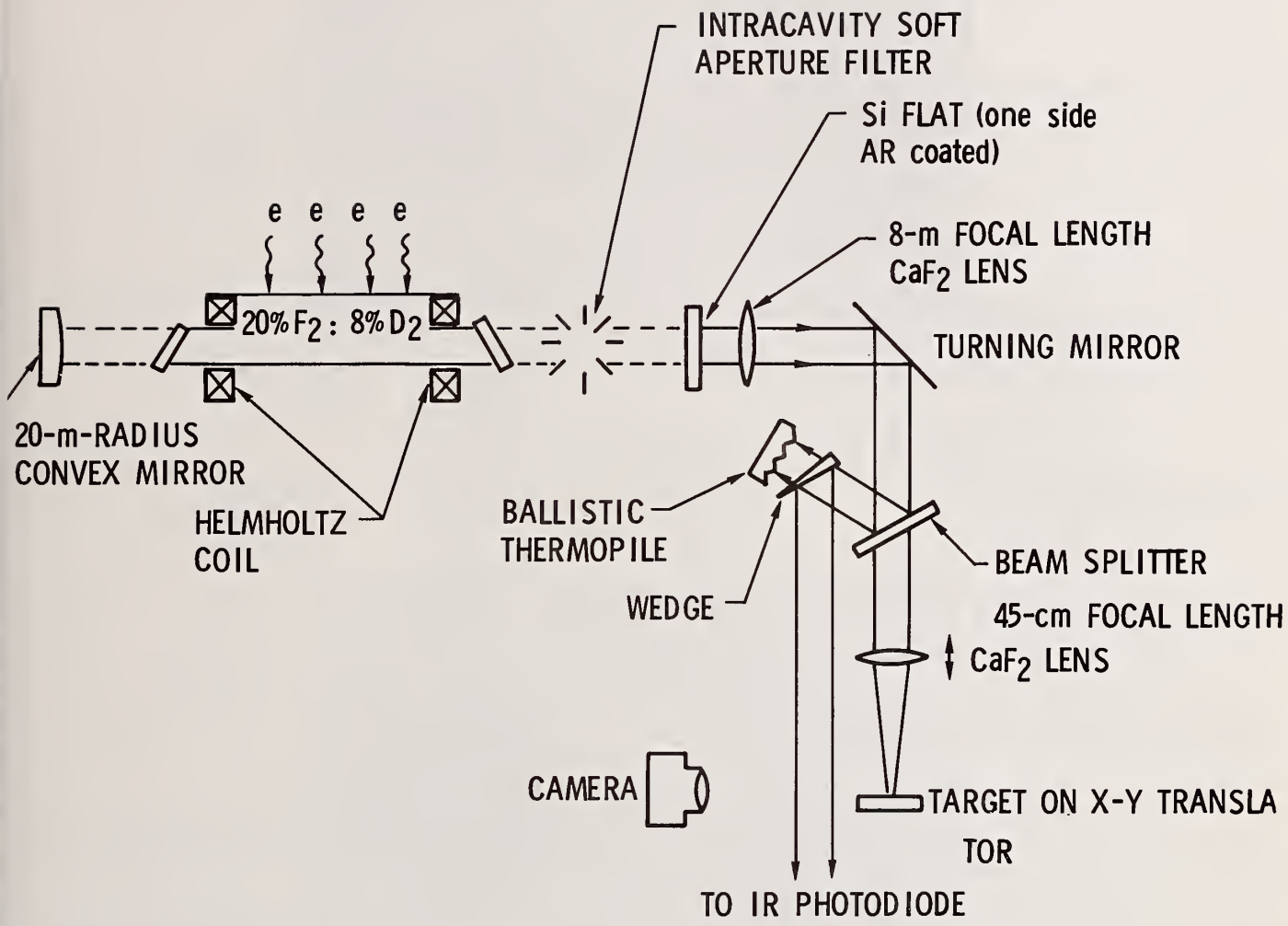

Fig. 1 Laser Damage Apparatus Layout

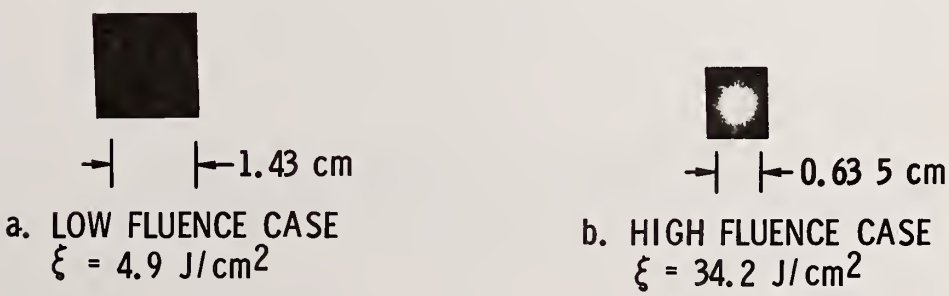

Fig. 2 Calibrated Film Burns Showing Typical DF-Beam Spatial Fluence Distributions

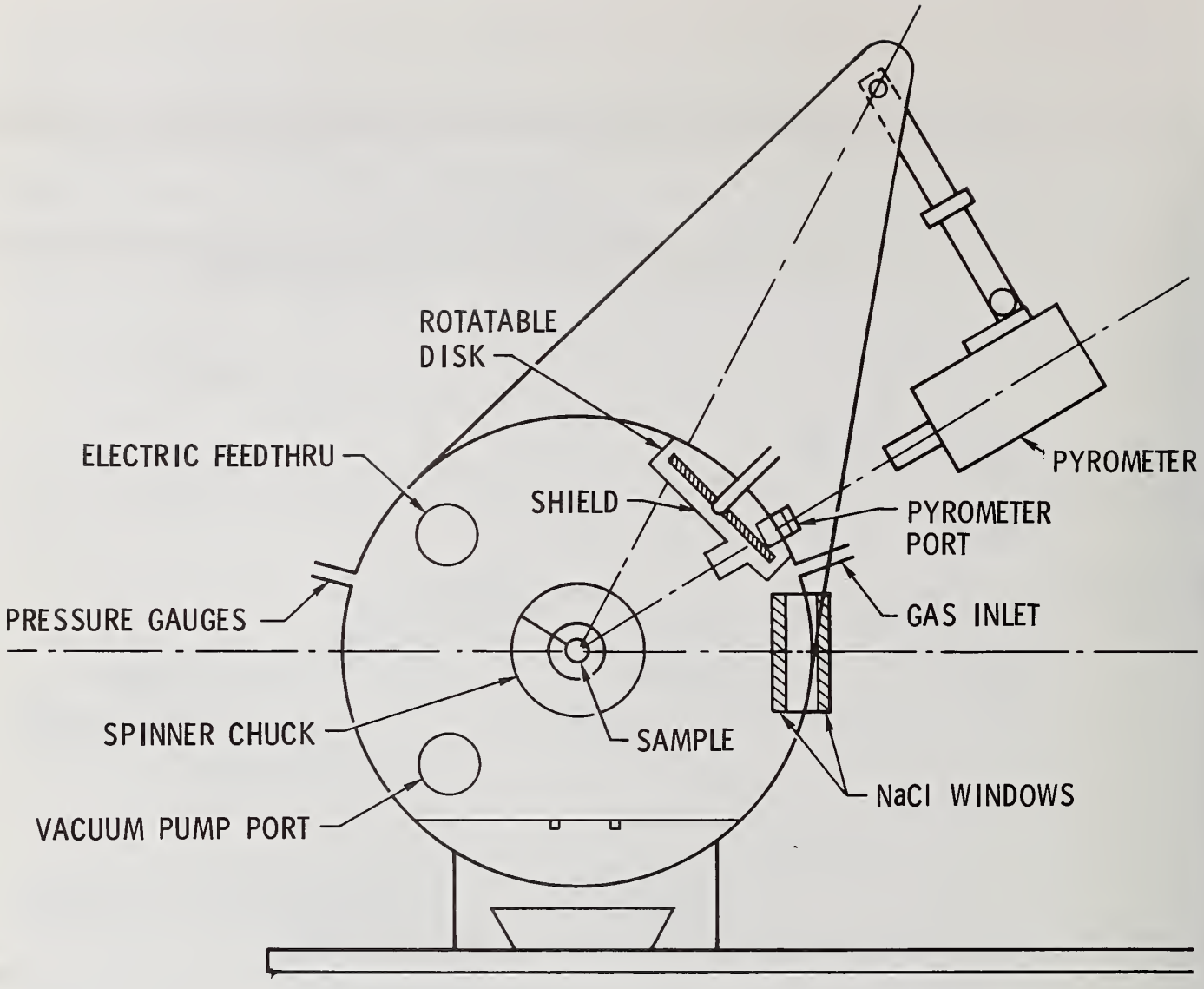

Fig. 3 Diagram of Equipment Used to Apply Carbyne Films to Optical Components

Fig. 4 Carbyne film on CaF_2 irradiated at $23J/cm^2$ showing localized damage at carbon-bearing (black) spots. Magnification is 200:1.

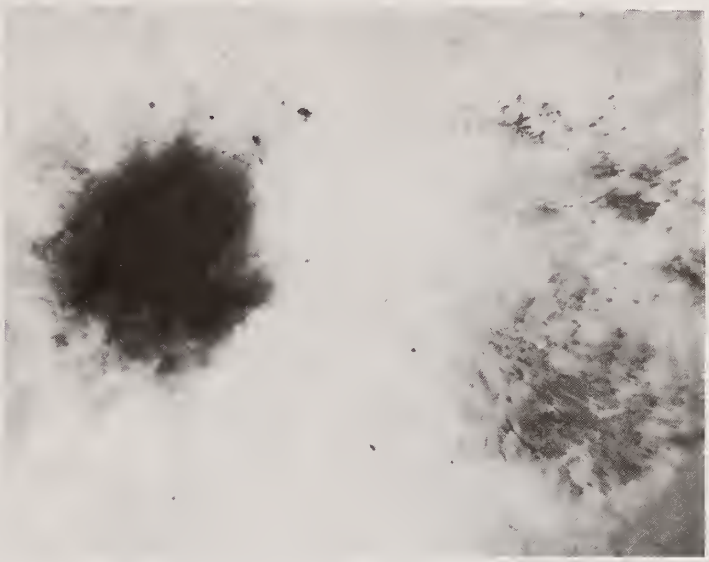

Fig. 5 Micrograph of bare copper (Spawr) mirror showing damage sites at exposure fluence of $58J/cm^2$ and DF-laser pulse duration of 0.5 μsec (FWHM).

a. Masked Mirror Segment
No exposure to laser radiation (magnification = 37.5 x). Carbon particulates have contaminated this copper substrate despite attempts to shield mirror segments from the carbyne effluent.

b. Unmasked Mirror Segment
Lower half unexposed to laser radiation. Upper half exposed to 9.5 J/cm^2 (Magnification = 37.5 x).

Fig. 6 Micrographs of copper mirror showing regions of substrate that were masked and unmasked from the carbyne vapor stream. Localized laser damage to carbyne coating occurs at carbon particulate sites.

Influence of Cleaning Solvents, Sunlight, Humidity, and HF Gas on Pulsed Damage and Optical Characteristics of 3.8-μm Multilayer Coatings*

J. O. Porteus, P. C. Archibald, J. W. Bethke, J. H. Dancy,
W. N. Faith, J. B. Franck, and P. A. Temple

Michelson Laboratory, Physics Division
Naval Weapons Center, China Lake, California 93555

Samples representing state-of-the-art 3.8-μm laser optical components were sequentially exposed to potentially harmful ingredients of an airborne-operating environment and tested for degradation after each exposure. Two enhanced-reflection-coated mirror designs, Mo(substrate)/Ag/ZnS/$(ThF_4/ZnS)^4$ and Si(substrate)/Ag/Si/$(Al_2O_3/Si)^4$, were studied, along with the antireflection-coated window designs, CaF_2(substrate)/PbF_4/ThF_4/PbF_4 and ZnSe(substrate)/ZnSe/ThF_4/ZnSe. Samples were exposed to controlled moderate doses of (1) methanol or acetone applied as cleaning solvents, (2) simulated atmospheric solar radiation at 6-km altitude, (3) 100% humidity ambient, and (4) an ambient containing 10% HF gas. Testing consisted of the following measurements at 3.8 μm: multithreshold pulsed damage profiles, absorptance, scattering, and absolute reflectance/transmission. While cleaning solvents and sunlight generally produce a reduction of thresholds for uniform damage, the influence of humidity and HF is more subtle, resulting in a significant increase in some cases. The windows respond differently than the mirrors, a result that is evidently related to an observed difference in the dominant damage characteristics. Optical characteristics do not correlate well with damage thresholds, suggesting that modification of thermal or other material properties plays a more important role.

Key words: Coating characterization; coating deterioration; damage thresholds; laser optical components; optical maintenance.

1. Introduction

It is well known that high energy laser (HEL) optical components are highly susceptible to deterioration and damage and that this can seriously impair system performance. Accordingly, numerous studies of the destructive influence of HEL radiation have been made on such components. Although most studies have been conducted in a controlled laboratory environment on carefully prepared samples, it is evident that defects, contamination, dirt, and other extrinsic mechanisms play a major role in initiating damage. Operation in the field entails exposure to a much wider variety and to higher levels of destructive ingredients. Here, the components must be extremely durable and maintainable.

The present paper is concerned with the deterioration of optical components for high energy pulsed deuterium fluoride (DF) lasers (3.8-μm wavelength) when exposed to potentially destructive ingredients encountered in an airborne environment. These include cleaning procedures that may contribute directly or synergistically to deterioration, as well as solar radiation, humidity, and corrosive gases in the laser cavity. The objective is to quantify the response to controlled exposures of each of these ingredients in terms of laser damage thresholds and the following optical characteristics: absorption, scattering, and reflectance/transmission. Results are directed toward establishment of maintenance and test procedures that can be transferred to the field.

2. Experimental Procedure

2.1. Samples

Durability tests were performed on the four state-of-the-art sample designs indicated in table 1. These designs were chosen on the basis of projected application, previous laser damage test results [1],[1] availability, and cost. Small-spot laser damage testing of representative window substrate samples from the indicated sources was performed prior to procurement of coated samples to ensure

*Work sponsored by the Air Force Weapons Laboratory.
[1]Numbers in brackets indicate the literature references at the end of the paper.

Table 1. Coated sample designs

Component type	Substrate	Source of substrate material	Polisher	Coating design	Coater
Mirror	Mo	---	NRTC[a]	$Ag/ZnS/(ThF_4/ZnS)^4$	OCLI[b]
Mirror	Si	---	NRTC	$Ag/Si/(Al_2O_3/Si)^4$	NRTC
Window	CaF_2	Optovac[c]	NRTC	$PbF_2/ThF_4/PbF_2$	NRTC
Window	ZnSe	II-VI[d]	II-VI	$ZnSe/ThF_4/ZnSe$	II-VI

[a]Northrop Research and Technology Center
[b]Optical Coating Laboratory, Inc.
[c]Optovac, Inc.
[d]II-VI Incorporated

homogeneity of the substrate material. A bulk optical absorption coefficient of less than $5 \times 10^{-4} cm^{-1}$ was specified for the window substrates. Sample dimensions are 1.52-in. diameter by 0.25-in. thick for the mirrors, and 1.52-in. diameter by 0.404-in. thick for the windows. All optical surfaces are flat to better than 3.8 μm/40, and parallelism is better than 20 arc sec on the window samples, which were polished and coated on both sides. A roughness specification of less than 10 Å rms, as measured by total integrated scatter, was required for the Si substrates, and a goal of 30 Å rms was set for Mo. The scratch and dig specification was 80/40 for the Mo and 40/20 for the remaining samples. Coatings were designed for maximum reflectance/transmission at 3.8 μm with a reflectance goal of > 0.999 on the mirrors and a reflectance/absorption goal of < 0.05% in the windows. In addition, the coatings were required to pass abrasion and humidity tests per specifications of MIL-C-675A and MIL-M-13508C.

Immediately after preparation, the samples were placed in hermetically sealed, light-tight containers manufactured by Spawr Optical Research Co. The container material is of glass-filled polypropylene for minimal outgassing, and the seal is made with a rubber O-ring. Samples are contacted only at the outside edges of the optical surfaces, which are chamfered at 45 degrees. The samples were kept in these containers at all times except during environmental exposure and evaluation.

2.2. Environmental Exposure

2.2.1. Cleaning Procedures

Repeated cleaning which is essential to optical maintenance can in itself contribute to performance degradation. Accordingly, it is appropriate to consider cleaning as a potentially harmful ingredient of the operating environment. Component deterioration and cleaning effectiveness depend on several factors, including scrubbing method, the solvent used, and the particular contaminant to be removed. Some knowledge of the individual influence of these factors is essential to the understanding of deterioration mechanisms and the orderly development of more efficient cleaning procedures. In the present work, attention was focused on degradation introduced by (1) cleaning solvents, including synergistic interactions with the environmental ingredients described below, and (2) scrubbing methods.

The three cleaning procedures that were investigated are summarized in table 2. Procedures A and B were applied to different samples of both mirror designs, which were started into the test series before the windows. Because of the obvious pitting or localized coating delamination produced by the ultrasonic cleaning, particularly on the Mo mirrors, procedure B' was substituted for procedure B on the window samples. Typically, multiple applications (cycles) of a given procedure were applied to a given sample. Only one surface of the window samples was cleaned. Cleaning was applied without deliberate exposure to contaminants, in an attempt to isolate the influences of the specific individual procedures. Since the surfaces were nominally clean at the outset, no specific evaluation of cleaning effectiveness can be made from the investigations reported here.

Table 2. Cleaning procedures

Procedure A
Drape 3 x 5" sheet of Kodak lens tissue across optical surface
Soak tissue with methanol
Drag tissue across the surface
Procedure B
Clean ultrasonically[a] in acetone bath for 2 minutes
Spin-dry sample about sample center
Procedure B'
Spin sample about sample center
Flood with acetone and spin dry

[a]Crest Model 411 ultrasonic cleaner

2.2.2. Solar Radiation

It has been clearly demonstrated that simulated extraatmospheric solar radiation produces rapid degradation in certain conventional coating materials, leading to increased optical absorption and reduced thresholds for laser damage [2]. Extrapolation of these results suggests that the ultraviolet component of atmospheric solar radiation may contribute significantly to degradation, particularly at high altitudes. This effect was investigated in the present study by exposure to simulated solar radiation at 6-km altitude and 45-degree zenith angle.

The source used in a Varian VIX 150 high-pressure xenon arc with integral silver reflector and sapphire window. The radiation is filtered by a Kratos HA60 filter, resulting in the short wavelength spectrum shown in figure 1. The desired solar spectrum is shown for comparison. The filtered source data were derived from manufacturers' specifications. The solar data are based on reported measurements [3] and on clear air standard transmission data [4].

Samples are mounted in a covered 10-station carousel (fig. 2) which rotates at 1 rpm. The 1.5-in.-diameter aperture permits a 5.5 sec maximum exposure for each 60 secs of irradiation time. The source-to-sample distance is adjusted to provide a total spectral power density of 0.27 W/cm^2 as measured by a Tektronix J6502 photometer probe, when corrected for the spectral response of the probe. Based on the relative spectral power densities of wavelengths ranging from 300 to 400 nm (fig. 1), this is equivalent to 2 suns. Light falloff at the edge of the aperture is estimated to be less than 25% of maximum. An upper limit on sample temperature during exposure was obtained from a thermocouple mounted in the carousel enclosure beneath the filter support. The maximum temperature registered was 33°C.

2.2.3. Humidity

To simulate the degrading effects of a hot, humid environment, the samples were placed inside a dessicator cabinet within a temperature-controlled oven, as shown in figure 3. A saturated solution of Na_2SO_4 also located in the dessicator produces a relative humidity of 95% at the set temperature of 50°C (120°F).

2.2.4. HF Laser Gas

Optical components used in a pulsed DF laser cavity are typically subjected to F_2 gas for a brief time prior to firing, and to DF gas until this corrosive by-product can be removed by pumping. While existing laboratory facilities precluded the safe use of F_2, the effect of DF was simulated by exposing the samples to HF gas in the apparatus shown in figure 4. Construction is of corrosion-resistant materials, principally PVC and stainless steel. After loading the samples in chamber C_2, both chambers are evacuated with an oilless roughing pump. C_1 and C_2 are then filled to atmospheric pressure with HF and He, respectively. Opening the valve V_2 permits mixing of the gases in the 10-to-1 volume ratio of C_2 to C_1, which simulates the typical 10% concentration found in a laser cavity. After exposure, N_2 gas is used to purge the HF mixture through a scrubber containing NaOH solution.

2.2.5. Storage

The final ingredient to be evaluated is storage for a period of one year in an airtight cabinet with dessicant material. Unfortunately, time constraints did not permit evaluation of the effects of long periods of storage.

2.3. Evaluation

Initially and following exposure to each of the above environmental ingredients, the samples were evaluated for absorption, scattering, and reflectance/transmission, as well as resistance to pulsed laser damage. All these measurements were made at the 3.8-μm design wavelength. A goal was to identify one more of the above optical characteristics that would provide an independent evaluation of damage resistance, as well as serving as an indicator of optical performance. This would provide a basis for developing a means of evaluating the serviceability of optical components in the field.

Damage measurements were performed on the Naval Weapons Center (NWC) Laser Damage Facility, using a nominal 100-nsec pulse and a 63-μm-diameter focal spot measured at the maximum/e^2 points [5]. In order to provide more information on damage mechanisms and how they are influenced by the operating environment, thresholds for the following damage characteristics were determined independently: erosion or roughening of the surface, flow or melting of the coating, perforation to the substrate, and a visible flash [1]. A profile of uniform damage thresholds and standard deviations was derived at each evaluation from a minimum of 50 one-on-one shots, using a multithreshold technique which has been previously described [6]. Samples were monitored during each shot for flash and selective damage using a 20-power microscope. Detailed damage characterization was performed off line using Nomarski microscopy. Damage that deviates from the mean by more than two standard deviations (1.6 in the case of the Mo-substrate mirrors) is regarded as selective, i.e., related to isolated defects or nonuniformities, and has not been included in the uniform damage evaluations [1]. Sampling of selective sites is generally inadequate to determine the influence of environmental exposure on selective damage levels.

Samples were characterized optically for absorption, backscattering, and transmission or reflectance. Absorptance was measured by laser calorimetry. A rate calorimeter of the Battelle design [7] was used for the mirror samples. The sampling beam makes four passes, yielding a total sampling area of approximately 6 mm^2. Window absorptance was measured with the NWC adiabatic calorimeter [7] using a single beam having a maximum/e^2 diameter of 0.5 mm. Measurements in this case are made at four different points and averaged, yielding an effective sample area of 0.8 mm^2. Front surface backscattering was measured on the NWC Optical Evaluation Facility [8]. The collection angle includes all backscattered radiation falling between the azimuth angles of 2.7 and 80 degrees. A correction is made for backscattering from the rear (exit) surface of the windows, where it is assumed that both surfaces scatter equally. The beam diameter is approximately 2 mm, and results are averaged from 19 individual sites, yielding an effective sampling area of approximately 60 mm^2. Finally, transmission and reflectance were measured with the NWC infrared absolute reflectometer [9], which has a single-beam effective sampling area of approximately 100 mm^2.

2.4. Test Matrix

The program of alternate exposure and evaluation is summarized in table 3, including exposure levels. Due to lack of previous quantitative work, little guidance was available on exposure levels. Within the constraints of an envisioned application, the intent was to use sufficiently high levels to produce a measurable effect, but not a degree of degradation that would preclude further testing. This was essential for the observation of synergistic effects, given the limited opportunity for repeated testing and limited number of samples. As a precaution, the potentially most destructive exposures, e.g., HF exposure, were placed later in the program.

The test and evaluation matrix shown in table 3 requires seven samples of each of the four design types, 28 in all. These were evaluated in three categories, as follows: (1) no cleaning, (2) cleaning A, and (3) cleaning B/B'. As a control on the possible influence of laser damage on the optical evaluations, two samples were run in each category, one with and one without damage testing. Optical evaluations were made in nominally undamaged areas on the damage-tested samples. As a consistency check on the optical measurements, an additional, optical control sample of each type was measured at each evaluation step. Consistency of the damage measurements was controlled with a diamond-turned Au standard sample, and the laser damage measurements were renormalized to this control. The renormalization correction was typically less than 10%.

Because of an unexpected increase in damage thresholds measured immediately following HF exposure, damage measurements on some of the samples were subsequently repeated, but not until two months had elapsed. Meanwhile, the optical evaluation was completed. Although it was not anticipated, time between exposure and evaluation turned out to be important in this case, since deterioration evidently

progresses for some time after HF exposure. Approximately 15 months were required to accomplish the completed elements indicated in table 3.

Table 3. Optical durability

Step \ Sample	Control	No cleaning[a]	No cleaning	A cleaning[a]	A cleaning	B/B' cleaning[a]	B/B' cleaning
Evaluate	●[b]	●	●	●	●	●	●
Clean: 20 cycles				●	●	●	●
Evaluate	●	●	●	●	●	●	●
Solar: 1.5 sunhr.		●	●	●	●	●	●
Evaluate	●	●	●	●	●	●	●
Humidity: 72 hr @95%		●	●	●	●	●	●
Evaluate	●	●	●	●	●	●	●
HF/He: 2 hr.		●	●	●	●	●	●
Evaluate	●	●	●	●	●	●	●
Store: 1 yr.	○[b]	○	○	○	○	○	○
Evaluate	○	○	○	○	○	○	○

[a]Laser damage evaluation on these samples only

[b]Closed (open) circles indicate completed (incompleted) element

3. Test Results

3.1. Laser Damage

Laser damage profiles measured after exposure to each of the various environmental ingredients are presented in figures 5-8. For convenience of discussion, sample types are identified by substrate material, which is underlined at the top of each figure. The lowest level at which damage, either selective or uniform, was observed in each evaluation is indicated by a triangle. Selective damage levels are often well below thresholds for uniform damage (connected circles), particularly on the Mo mirrors, and to a somewhat lesser degree on the Si mirrors. For the windows, uniform damage occurs at two well-defined thresholds: (1) that for erosion and (2) a considerably higher common threshold for visible flash and perforation of the coating. On the ZnSe windows, the threshold for flow (not shown) generally coincides with the flash threshold, while on CaF_2 flow is more closely associated with erosion. On the mirrors, all four of these damage characteristics tend to share a single, common threshold. Occasionally, however, the threshold for perforation lies slightly above that for erosion and flash. Thus, in all cases, the erosion threshold is dominant and provides a basis for describing the environmental test results.

On the windows, erosion thresholds generally tend to be reduced by all environmental ingredients except for HF. Even in this case, subsequent reevaluation of one of the CaF_2 samples showed a significant reduction after two months. Cleaning procedure B' is less harmful than A, as might be expected from the absence of contact scrubbing and the use of a more volatile cleaning fluid. In fact, B' cleaning produced no detectable deterioration in ZnSe. Solar radiation and humidity produce about the same degree of degradation in both window types. Curiously, the uncleaned ZnSe window is largely unaffected, suggesting that cleaning activates this window for subsequent deterioration.

The mirrors respond somewhat differently than the windows, particularly to humidity exposure, after which damage thresholds invariably rise. Comparison of the uncleaned and A-cleaned Si results (fig. 7) suggests an initial deterioration with age, while cleaning and, quite possibly, solar radiation may have little influence. Mo also shows little response to these two ingredients within a rather large uncertainty resulting from considerable variability over the surface. B-cleaning, however, is clearly destructive in a way that suggests a connection with selective laser damage. Further evaluation of the B-cleaned Mo was considered impractical because of the high density of visible pits. The damage response of the Si mirrors to HF exposure is similar to that of the CaF_2 windows, while HF has a less significant effect on the Mo damage thresholds.

3.2. Optical Characteristics

The optical characteristics measured after each exposure are shown in figures 9-12, which correspond, respectively, to figures 5-8. Uniform erosion thresholds are reproduced here for comparison. Data where both optical and laser damage measurements were made on the same sample are connected by heavy solid lines, while the dashed lines connect optical data on samples with no laser damage evaluation. Comparison of the two data sets shows no significant optical degradation resulting from the damage measurements. The star-shaped data points connected by the light solid lines represent the optical control sample in each case (see table 3).

In general, the optical characteristics are far less sensitive to environmental exposure than the damage thresholds, and correlation with damage thresholds is poor, especially on the mirrors. Cleaning ordinarily has little effect, except for the destructive B-procedure, which produces dramatic degradation of all characteristics. Cleaning of the ZnSe windows results in a slight reduction of the absorptance, particularly with B' cleaning, suggesting removal of some contaminant originally present. No consistent changes are associated with solar irradiation. The apparent decrease of absorptance and scattering after solar irradiation of the B-cleaned Si is inconsistent with the decrease in reflectance. This may be a combined result of the difference in sampling area and the nonuniformity of the sample surface. Awareness of this possible problem stimulated the initiation of transmission measurements on the window samples in spite of the difficulty of making such measurements with adequate sensitivity. Humidity exposure increases the absorptance on nearly all samples except the Mo mirrors and increases the scattering of the CaF_2 windows significantly. HF exposure has little optical effect other than to increase the scattering of the Si mirrors.

4. Discussion

The most significant result of this study for large-scale applications is the low level of selective damage commonly observed. Typically, such damage is found well below the lowest excursions of the uniform damage thresholds produced by the exposure levels applied here. Unfortunately, selective damage usually has no well-defined threshold, and actual damage levels may be lower than indicated by the axial fluence, as a result of off-axis occurrence. No reliable technique for a priori evaluation of susceptibility to selective damage has yet been demonstrated, although at least one promising approach has been identified [10]. Such studies require extensive and time-consuming sampling over large areas [11] and are, therefore, incompatible with the scope of the present work.

The essential differences between the damage profiles of the windows and those of the mirrors imply that the respective dominant uniform damage mechanisms are different. This may be attributed to basic differences in the time-averaged field distribution, which typically has a node at the air-film interface of a mirror but is relatively constant in an antireflection coating. The singular predominance of erosion damage on the windows as compared to the mirrors is therefore not surprising. Likewise, environmental ingredients that mainly affect the air-film interface, such as cleaning, have a greater effect on the windows. Another example is humidity exposure, which increases optical absorption at this interface via adsorbed water and thereby reduces the erosion threshold. Evidently, the mirror damage is basically internal, as suggested by its essentially catastrophic nature. Since here the damage threshold increases after humidity exposure, optical absorption is obviously less important than other material properties, e.g., thermal transfer properties. Incidentally, the window threshold for flash and perforation shows a similar response to humidity (figs. 5 and 6) and probably also represents an internal failure mechanism.

The increase in damage thresholds immediately following HF exposure is an unexpected result. The HF apparently associates with water originally present (or remaining from the humidity exposure) to form hydrofluoric acid, which then reacts with the coating. Possible types of reaction processes explaining the observed improvement in damage thresholds are as follows: (1) removal or redistribution of thermally isolated material by etching and (2) chemical alteration resulting in improved optical or thermal properties, e.g., conversion of metal-rich material to metal fluoride. The lack of significant changes in the measured optical properties suggests that the improvement is mainly thermal, rather than optical in nature. However, it is easy to imagine that excessive etching can produce inhomogeneous optical degradation, which may be responsible for the eventual reduction of the damage thresholds observed in most cases. There is some evidence for this in the increased scattering of the Si mirrors. These findings suggest the possibility of using HF exposure as a conditioning treatment; however, some means must be devised for quenching the reaction at the optimum time.

It is apparent from present results that optical characteristics, as measured here, do not provide a reliable indicator of component serviceability in terms of resistance to pulsed laser damage. The lack of correlation between damage and optical properties suggests that thermal properties may play a more important role in uniform environmental degradation. Some form of the newly developed photo-thermal techniques [12] may prove useful in this regard.

5. Summary

A controlled study has been performed on the deterioration of 3.8-μm laser optical components when subjected to various potentially harmful ingredients of an airborne operating environment. Deterioration was monitored by means of multithreshold, pulsed laser damage evaluation combined with measurement of optical characteristics. Selective, i.e., defect-related, damage was generally found to be a more serious limitation than environmental degradation under present conditions. Uniform damage characteristics are much more sensitive to environmental degradation than the optical characteristics investigated here, which do not necessarily correlate with damage thresholds. This suggests that characterization techniques based on thermal properties may be more appropriate for nondestructively evaluating component serviceability in pulsed high-energy laser applications. While cleaning solvents and sunlight tend to reduce damage thresholds, the immediate influence of humidity and HF is less clear, resulting in apparent improvement in some cases. Further exploration of these effects may be useful in providing new approaches to conditioning or refurbishment for improved damage resistance.

The authors wish to acknowledge the assistance of T. W. Humpherys of the Air Force Weapons Laboratory and J. L. Stanford of NWC in specifying and procuring samples. Helpful technical discussions with J. A. Detrio of the University of Dayton Research Institute and T. M. Donovan of NWC are also gratefully acknowledged.

6. References

[1] Porteus, J. O.; Donovan, T. M.; Jernigan, J. L.; Faith, W. N. Multithreshold evaluation of 100-nsec pulsed laser damage to coating materials at 2.7- and 3.8-μm wavelengths. Glass, A. J.; Guenther, A. H., ed. Proceedings of the 10th annual symposium on optical materials for high power lasers; 1978 September 12-14; Boulder, CO. Nat. Bur. Stand. (U.S.) Spec. Publ. 541; 1978 December. 202-211.

[2] Donovan, T. M.; Porteus, J. O.; Seitel, S. C.; Holmes, S. J.; Fogdall, L. B. Performance of reflective Si and oxide coatings for HF lasers. Proceedings of the high power laser optical components topical meeting; 1980 October 2-3; Boulder, CO. (In process)

[3] Thekaekara, M. P. The solar constant and the solar spectrum measured from a research aircraft. National Aeronautics and Space Administration Report TR R-351; 1970 October.

[4] Handbook of geophysics and space environments. Chapter 7. Valley, S. L., ed.; Air Force Cambridge Research Laboratory, Office of Aerospace Research, U.S. Air Force; 1965.

[5] Porteus, J. O.; Decker, D. L.; Faith, W. N.; Grandjean, D. J.; Seitel, S. C.; Soileau, M. J. Pulsed laser-induced melting of precision diamond-machined Cu, Ag, and Au at IR wavelengths. IEEE J. Quantum Electron. QE-17; 2078-2085; 1981 October.

[6] Porteus, J. O.; Jernigan, J. L.; Faith, W. N. Multithreshold measurement and analysis of pulsed laser damage on optical surfaces. Glass, A. J.; Guenther, A. H., ed. Proceedings of the 9th annual symposium on optical materials for high power lasers; 1977 October 4-6; Boulder, CO. Nat. Bur. Stand. (U.S.) Spec. Publ. 509; 1977 December. 507-515.

[7] Temple, P. A. Experimental and theoretical considerations in thin film laser calorimetry. Proceedings of the Society of Photo-Optical Instrumentation Engineers' Los Angeles technical symposium; 1982 January 25-29; Los Angeles, CA. (To be published)

[8] Bennett, H. E.; Soileau, M. J.; Archibald, P. C. Diamond-turned mirrors. Glass, A. J.; Guenther, A. H., ed. Proceedings of the 7th annual symposium on optical materials for high power lasers; 1975 July 30-31; Boulder, CO. Nat. Bur. Stand. (U.S.) Spec. Publ. 435; 1976 April. 49-56.

[9] Bennett, H. E.; Koehler, W. F. Precision measurement of absolute specular reflectance with minimized systematic errors. J. Opt. Soc. Am. 50; 1-6; 1960.

[10] Porteus, J. O.; Faith, W. N.; Allen, S. D. Laser desorption analysis of H_2O and other contaminants from optical surfaces. This proceedings.

[11] Porteus, J. O.; Decker, D. L.; Grandjean, D. J.; Seitel, S. C.; Faith, W. N. Defect-damage-resistant copper mirrors. Bennett, H. E.; Glass, A. J.; Guenther, A. H.; Newnam, B. E., ed. Proceedings of the 11th annual symposium on optical materials for high power lasers; 1979 October 30-31; Boulder, CO. Nat. Bur. Stand. (U.S.) Spec. Publ. 568; 1980 July. 175-186.

[12] Murphy, J. C.; Aamodt, L. C. Optically detected photothermal imaging, Appl. Phys. Lett. 38; 196-198; 1981.

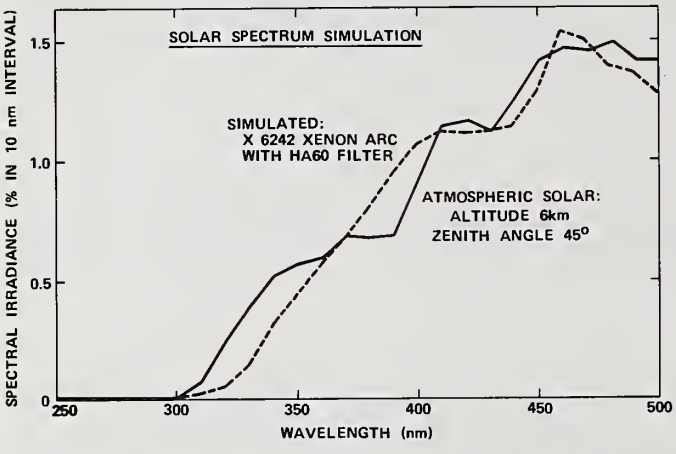

Figure 1. Short-wavelength region of filtered xenon arc spectrum compared with solar spectrum at 6 km, 45-degree zenith angle.

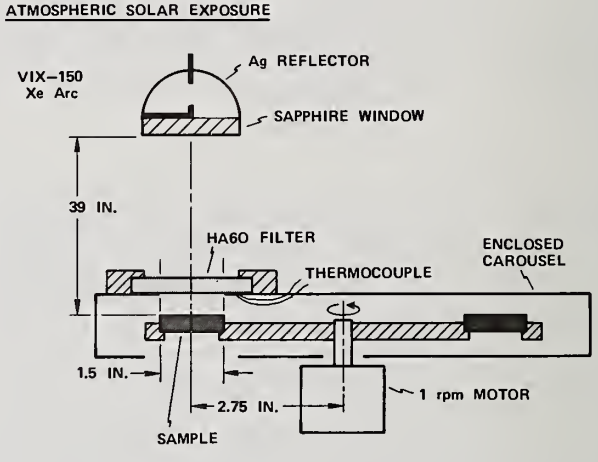

Figure 2. Apparatus for simulated intermittent atmospheric solar irradiation.

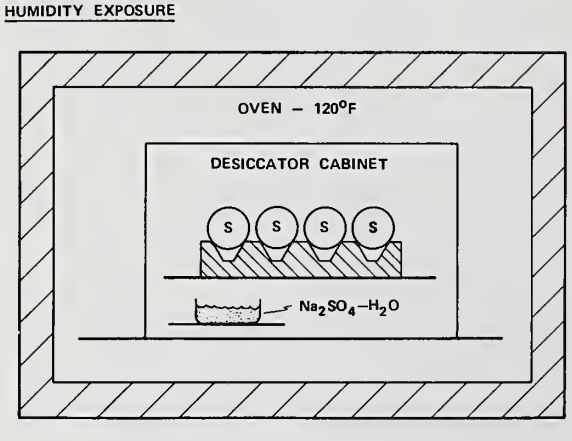

Figure 3. Apparatus for humidity exposure.

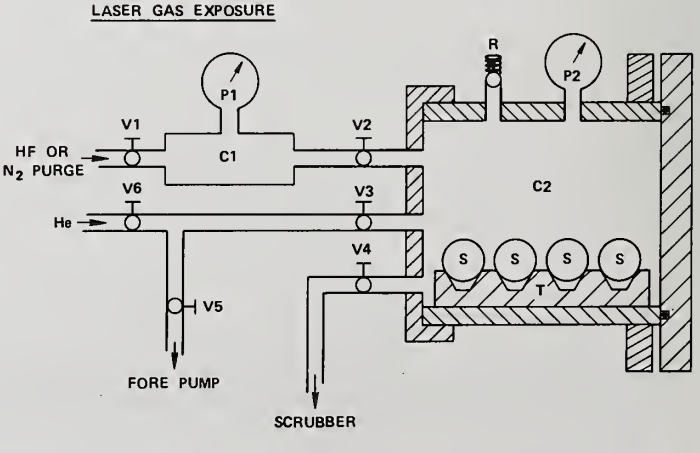

Figure 4. Apparatus for exposure to HF gas.

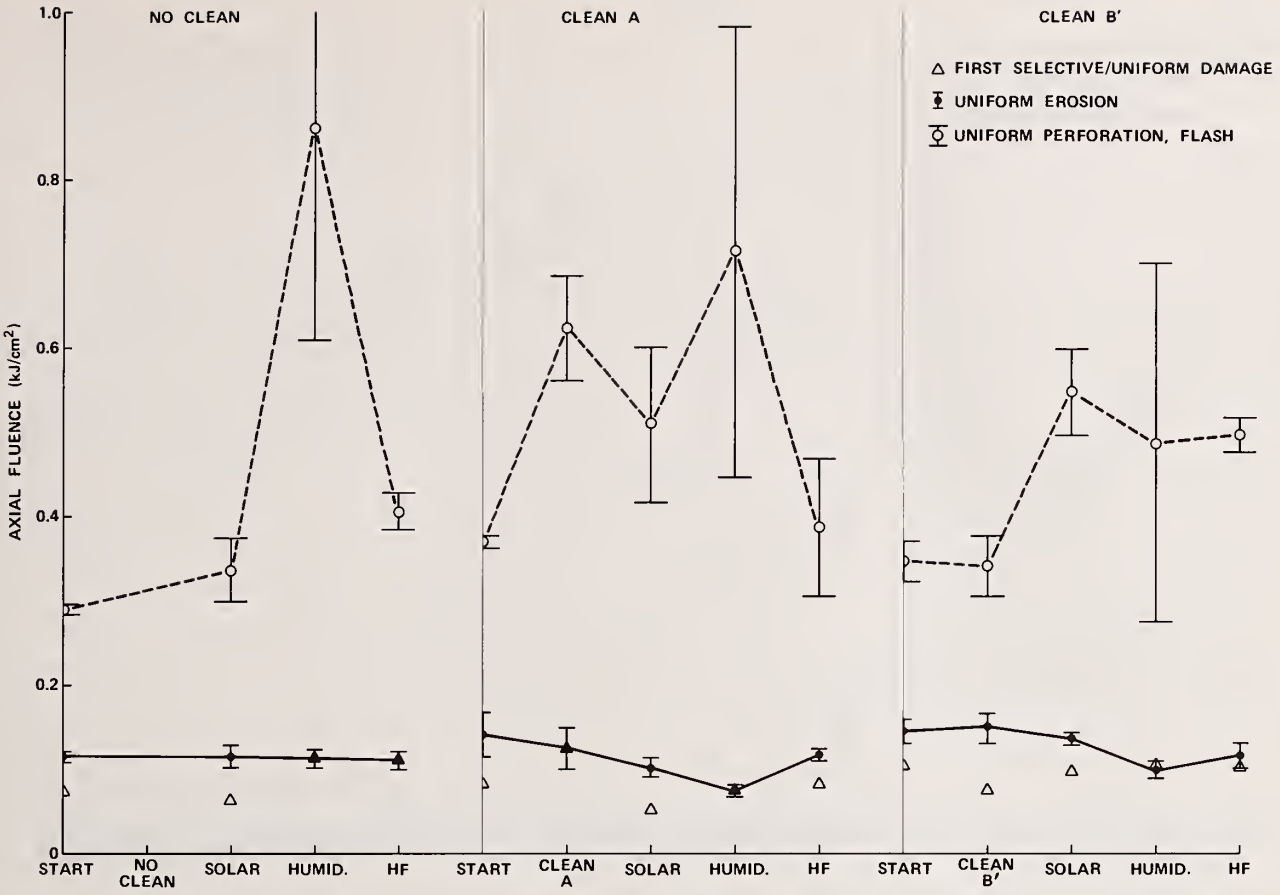

Figure 5. Damage profiles measured on the ZnSe windows after each exposure indicated at the bottom. The three data sets correspond to the three cleaning categories.

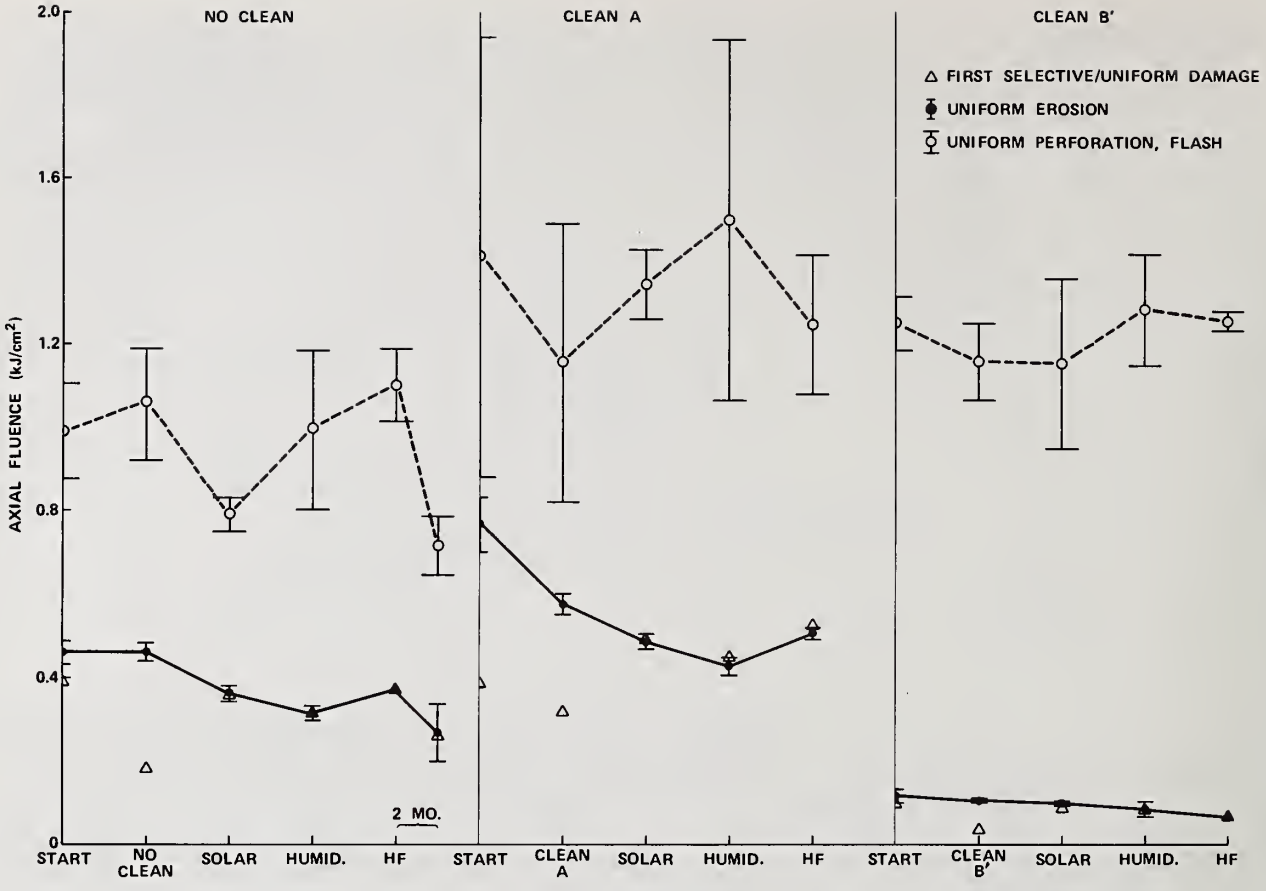

Figure 6. Damage profiles measured on the CaF_2 windows after each exposure indicated. The measurement on the uncleaned sample was repeated two months after HF exposure.

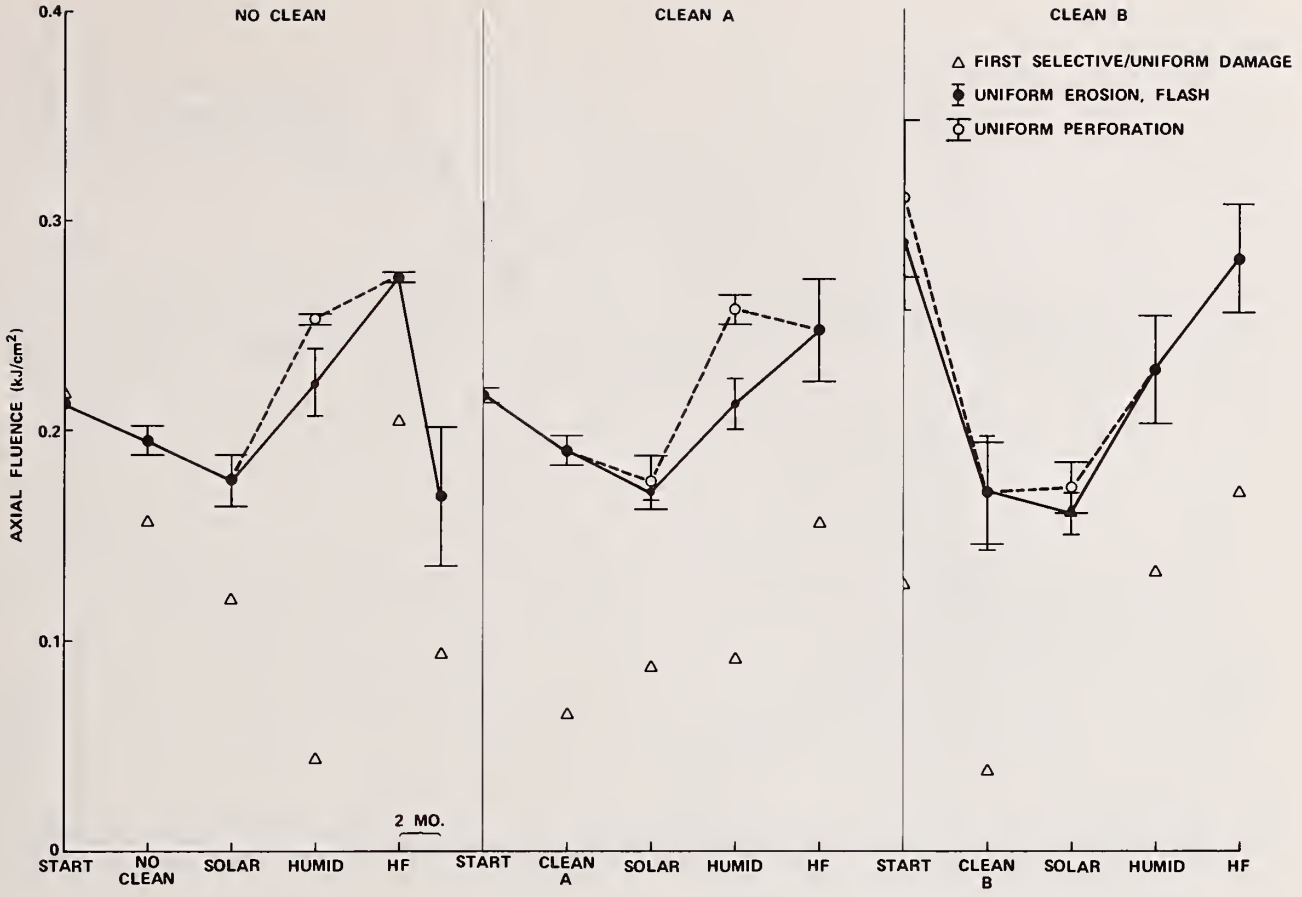

Figure 7. Damage profiles measured on the Si mirrors after each exposure indicated. The measurement in the uncleaned sample was repeated two months after HF exposure.

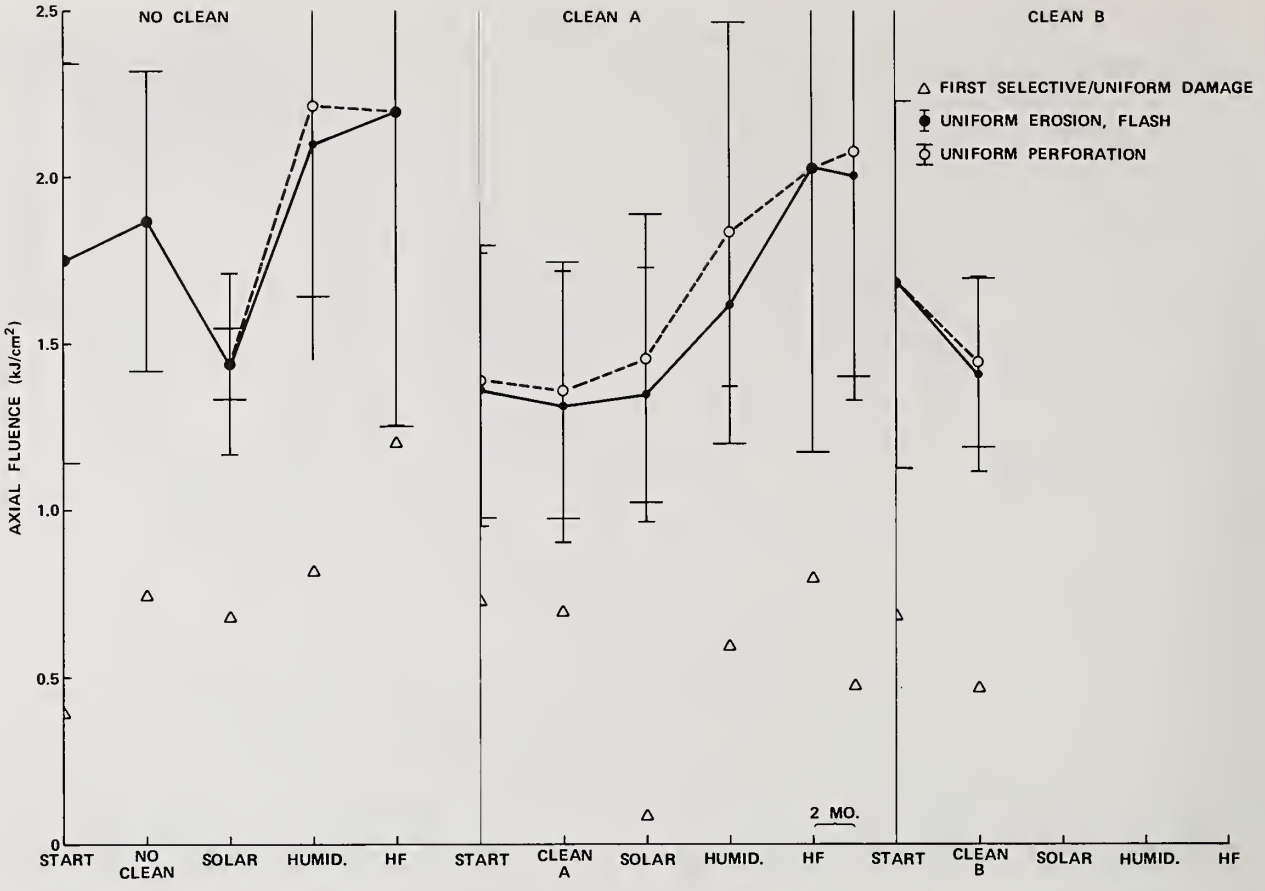

Figure 8. Damage profiles measured on the Mo mirrors after each exposure indicated. The measurement on the A-cleaned sample was repeated two months after HF exposure.

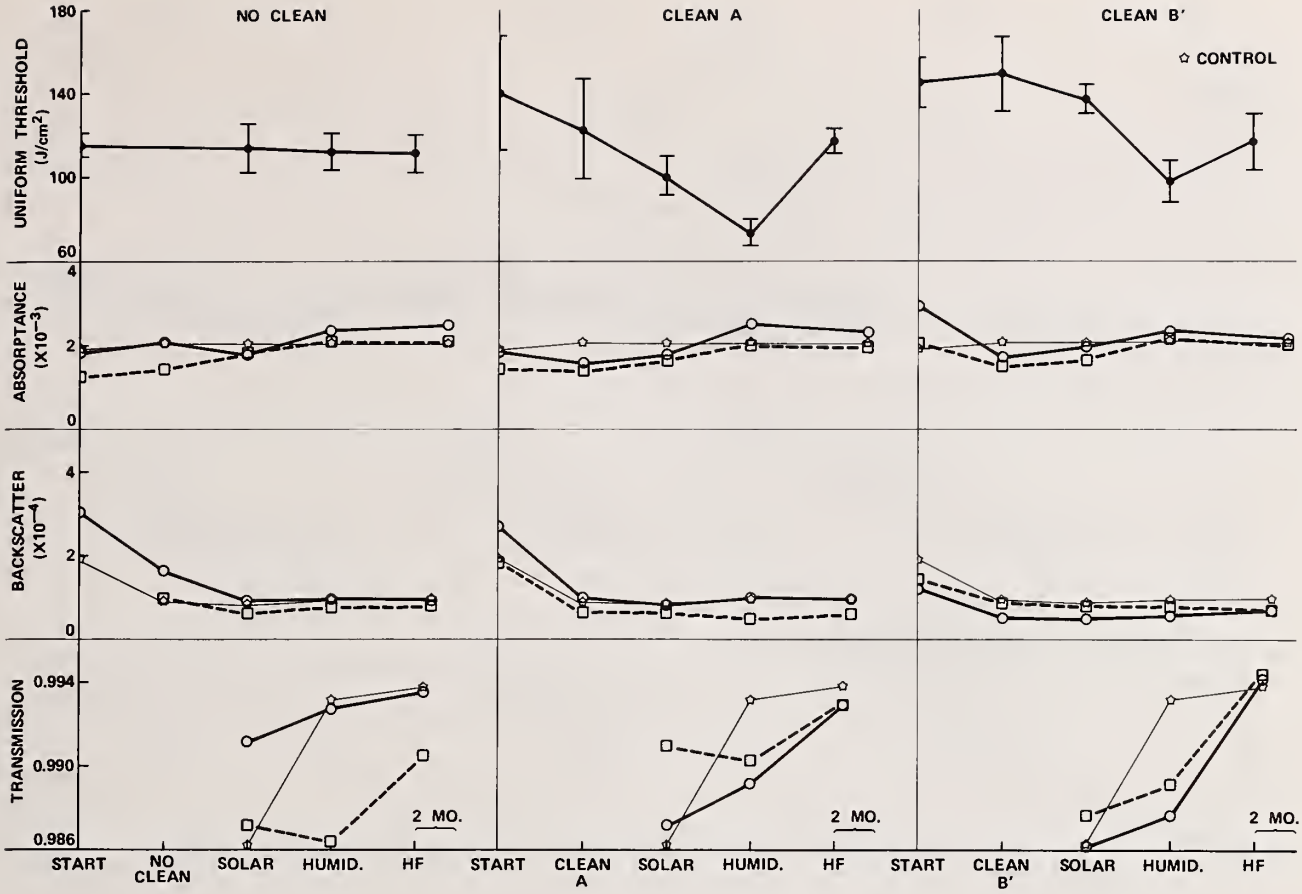

Figure 9. Comparison of optical characteristics with dominant uniform damage thresholds on the ZnSe windows after each exposure indicated. The time elapsed between HF exposure and evaluation is indicated in each case by the position of the last data point with respect to the bracket, whose width represents a two-month period.

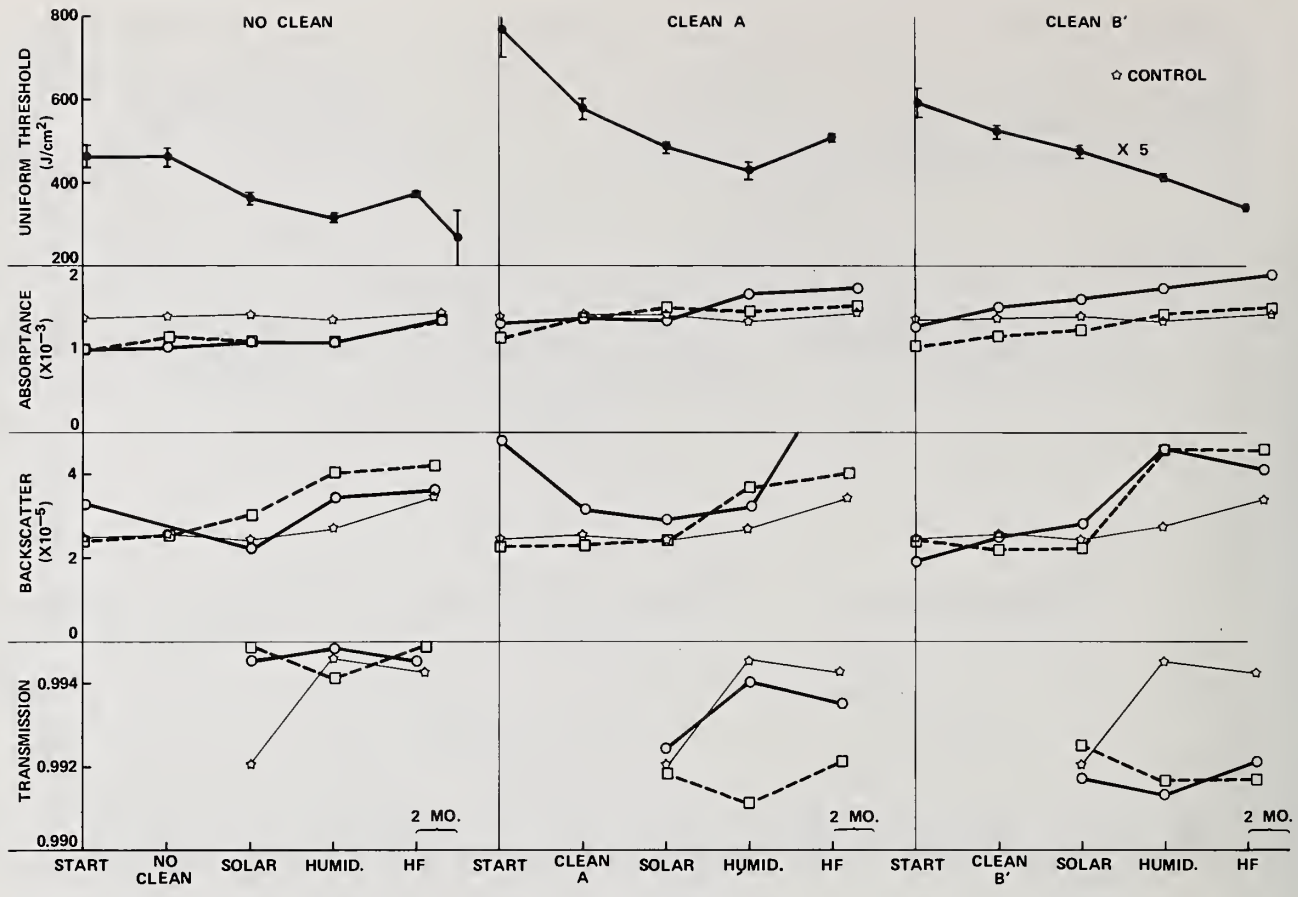

Figure 10. Comparison of optical characteristics with dominant uniform damage thresholds on the CaF_2 windows after each exposure indicated. The two-month bracket has the same significance as in figure 9.

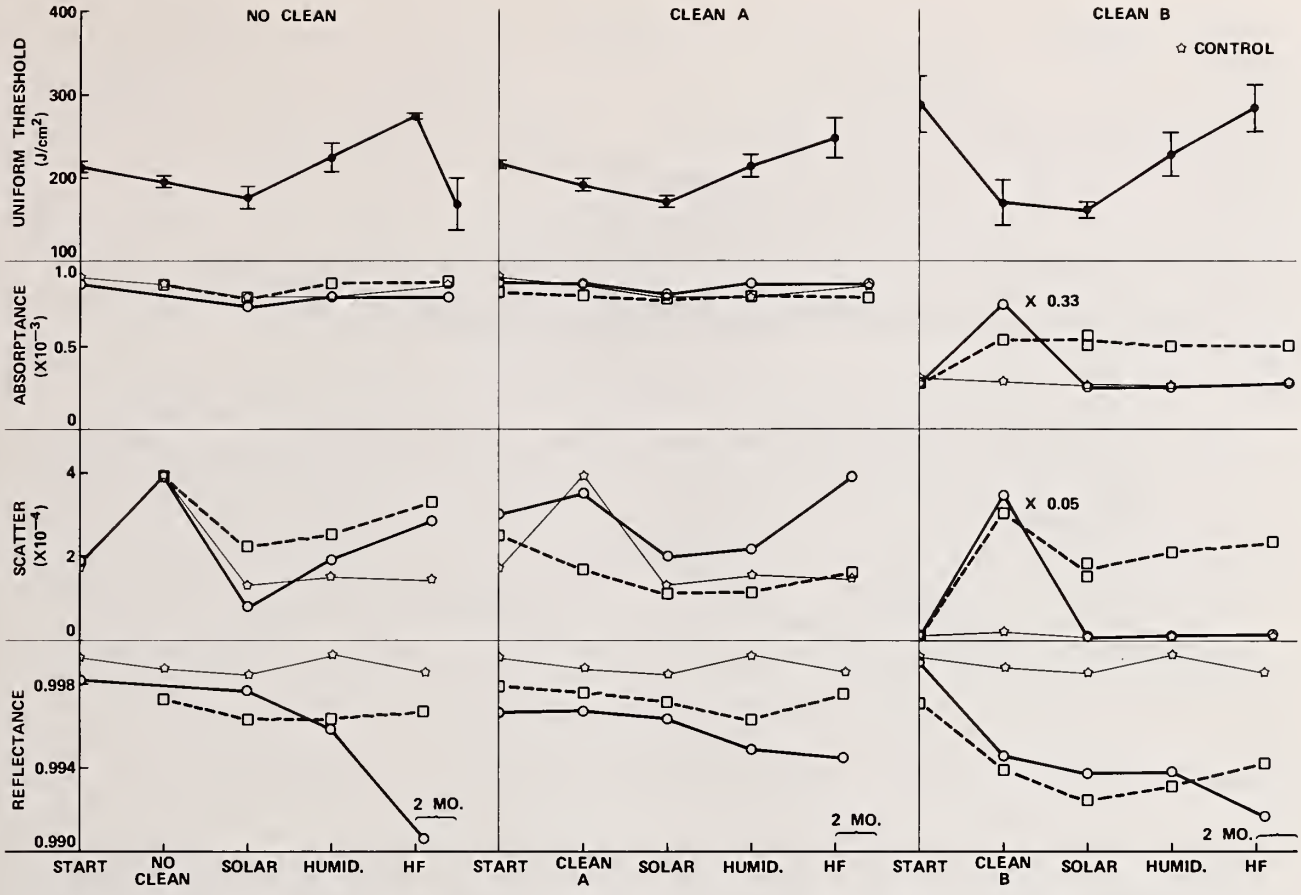

Figure 11. Comparison of the optial characteristics with dominant uniform damage thresholds on the Si mirrors after each exposure indicated. The two-month bracket has the same significance as in figure 9.

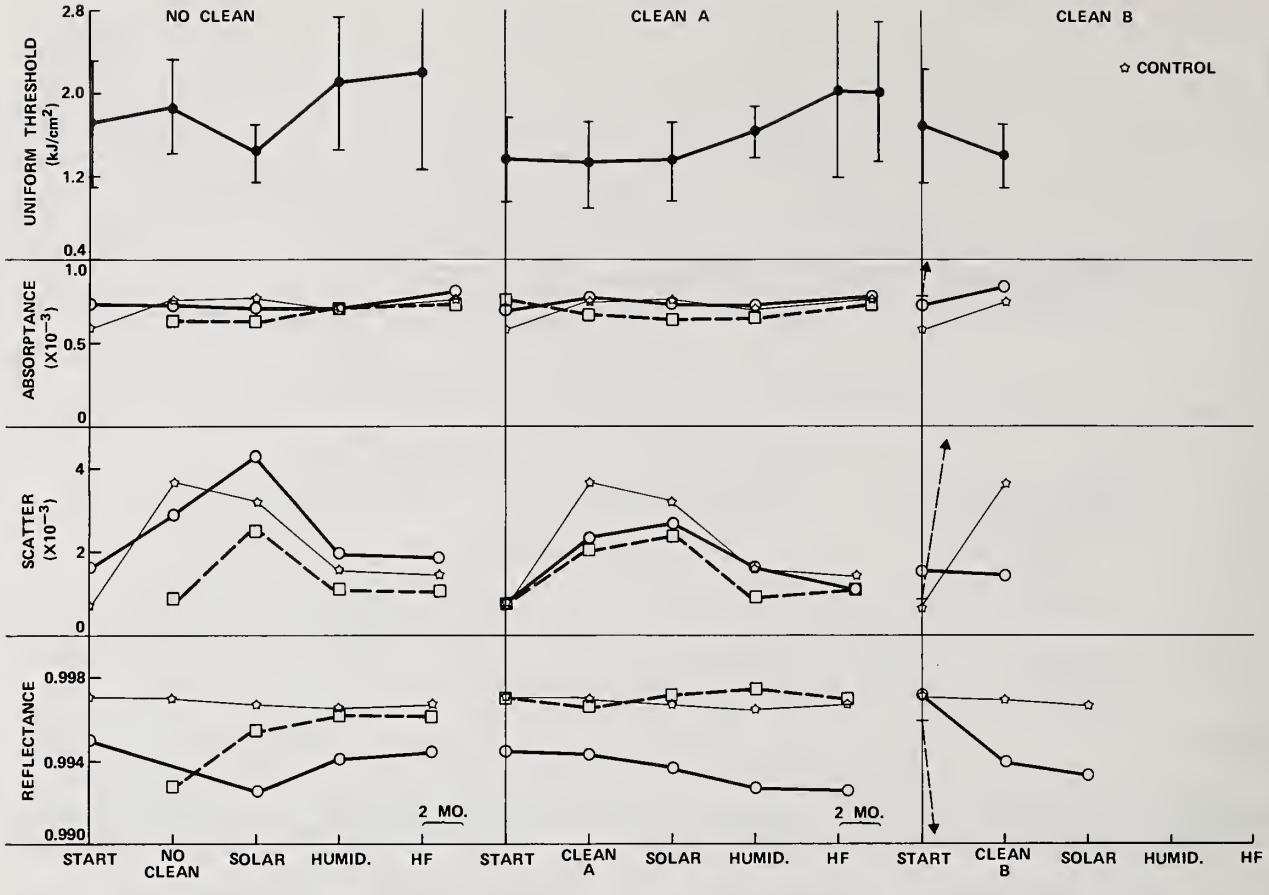

Figure 12. Comparison of optical characteristics with dominant uniform damage thresholds on the Mo mirrors after each exposure indicated. The two-month bracket has the same significance as in figure 9.

Index, Thickness and Birefringence of Thin Films by Guided Waves*

A. Feldman and E. N. Farabaugh
National Bureau of Standards
Washington, D.C. 20234

A guided wave technique has been used to measure the refractive index and thickness of a thin film. The film, which contained approximately 90 mol % MgO and 10 mol % SiO_2 was produced by coevaporation of the two constituents onto a fused silica substrate. Measurements were performed at three visible wavelengths obtained from an argon-ion laser. From the positions of the mode coupling angles, we have calculated the refractive index and thickness of the film. The film was found to have a large birefringence which is attributed to internal stresses. A signature for the birefringence can be observed in the scattered m-line spectrum of the film, in which the order of the TE_0 and TM_0 modes is interchanged as compared to an isotropic film. The optical determination of the film thickness is 1.098 ± 0.003 μm as compared to 1.11 μm measured by a mechanical method. The measured values of refractive index agree well with values calculated on the basis of the Drude model.

Key words: birefringence; coevaporation; guided wave; prism coupler; MgO, SiO_2; refractive index; thickness; thin film.

1. Introduction

The measurement of the guided modes of a thin optical film is an extremely powerful technique for characterizing properties of the film. This technique, which forms the basis of integrated optics, has been utilized for characterizing evaporated dielectric films [1], SiO_2 on Si [2], polymeric films [3,4], and diffused optical waveguides [5]. In particular, the technique has been used to measure film refractive index, thickness, and attenuation. It is the purpose of this paper to bring this method to the attention of the high power laser community.

A recent paper has compared the guided wave method to other methods for measuring the thickness and refractive index of dielectric films on Si substrates [2]. It found that the guided wave method is at least as accurate as other techniques used for measuring refractive index and thickness, but, in addition, the precision in the refractive index determination is significantly better as compared, for example, to ellipsometry. The ultimate accuracy of the technique for determining refractive index has been reported to be one part in 10^4.

The guided wave method has two principal disadvantages: It requires contact with the optical film; it requires relatively thick films for the sustainance of guided modes.

In this paper we report on the measurement of the refractive index and thickness of a mixed film of 90 mol percent MgO, 10 mol percent SiO_2 deposited by coevaporation onto a fused silica substrate. The measurements were performed by the method of Tien, Ulrich and Martin [1]. The estimated error in the refractive index was ± 0.001; the estimated error in the thickness was ± 0.3%. A birefringence of 0.006 was observed in the film, which we attribute to internal stress. A calculation of refractive indices based on the Drude equation and a volume additivity model shows excellent agreement with the measured refractive indices.

* This work supported in part by the Air Force Office of Scientific Research, Air Force Systems Command, USAF, under Grant Nos. AFOSR-ISSA-81-00006 and 82-00001. The U.S. Government is authorized to reproduce and distribute reprints for governmental purposes not withstanding any copyright notation hereon.

2. Thin Film Guided Waves

The treatment of planar guided waves in thin homogeneous dielectric films has been extensively discussed in the literature, and, hence we present here some of the principal conclusions [5].

Figure 1 shows the basic geometry and wave configurations. A uniform dielectric film with negligible loss having a refractive index n_f is deposited on a substrate of refractive index n_s. Air of refractive index n_a is on the opposite side of the film. A necessary condition for the existance of propagating modes within the film is $n_f > n_s$ and $n_f > n_a$. This insures that a ray propagating within a restricted range of angles within the film will be trapped by total internal reflection. The actual modes of propagation are represented by solutions to a set of transcendental equations corresponding to transverse electric (TE) or transverse magnetic (TM) waves. The modes conditions are:

$$2b_1W - 2\tan^{-1}(p_2/b_1) - 2\tan^{-1}(p_o/b_1) = 2\pi m \qquad (1)$$

for TE modes and

$$2b_1W - 2\tan^{-1}(n_f^2p_2/n_a^2b_1) - 2\tan^{-1}(n_f^2p_o/n_s^2b_1) = 2\pi m \qquad (2)$$

for TM modes, where W = thickness, m = order of the mode, p_o = decay constant in substrate, p_2 = decay constant in air, and b_1 = component of propagation constant normal to film surface. Each of the above constants is related to the vacuum wave vector, k, and the ray propagation direction in the film, θ. The problem of solving for the propagation angles of the modes of a thin film with all the material parameters given requires a straightforward solution to eqs (1) and (2) by a numerical procedure such as Newtons method. However, if one is given a set of measured propagation angles and is required to find, say, the index and thickness of the film, one must resort to an iterative trial and error procedure which minimizes the root mean squared deviation of a set of computed angles with respect to the set of measured angles.

3. Thin Film Preparation

The film measured in this work was prepared by coevaporation of MgO and SiO_2 onto a fused silica substrate in a high vacuum deposition chamber equipped with independent electron beam evaporators. The system is described in detail in an accompanying article in these proceedings [6]. Each of the beams was monitored independently by separate quartz crystal monitors that previously had been calibrated for each of the constituents by means of stylus thickness measurements on specially prepared films. The beams were made to impinge onto the substrate which was not heated in order to minimize stresses within the film. The temperature of the substrate during deposition was approximately 50 °C. The relative volume, v_i, for each film component, i, is assumed to be

$$v_i = \frac{T_i}{T_1+T_2} \qquad (3)$$

where i = 1 refers to MgO, i = 2 to SiO_2, and T_i to the monitored thickness of component i. For the particular film reported in this work $v_1 = 0.79$, $v_2 = 0.21$.

4. Experimental Procedure

The experimental arrangement, which is shown in figure 2, is similar to the arrangement given in Tien, Ulrich, and Martin [1] and further elucidated by Ulrich and Torge [7]. The apparatus is based on a design by Sarid, Cressman and Holman [8]. A prism of high refractive index (nominally 1.96) was placed in contact with the thin film. Two steel balls were placed beneath the substrate. By judicious application of a load to the prism, optical coupling could be obtained between the prism and the film just above the steel balls.

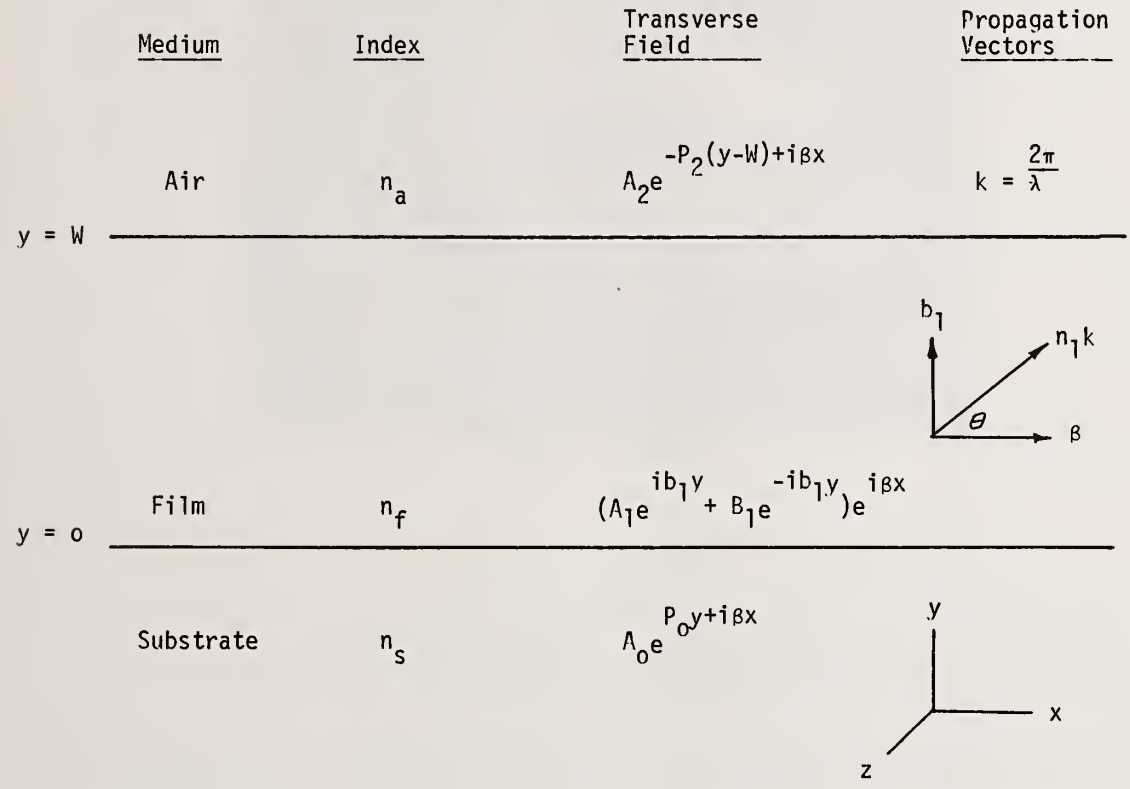

Figure 1. Configuration of fields and propagation in thin film. β = effective propagation constant of guided wave; k = vacuum wave vector; λ = wavelength in vacuum. A_o, A_1, B_1, and A_2 are field amplitudes than are obtained by matching the electromagnetic boundary conditions; see text for definition of other symbols. The notation used is principally that of Ref. [5].

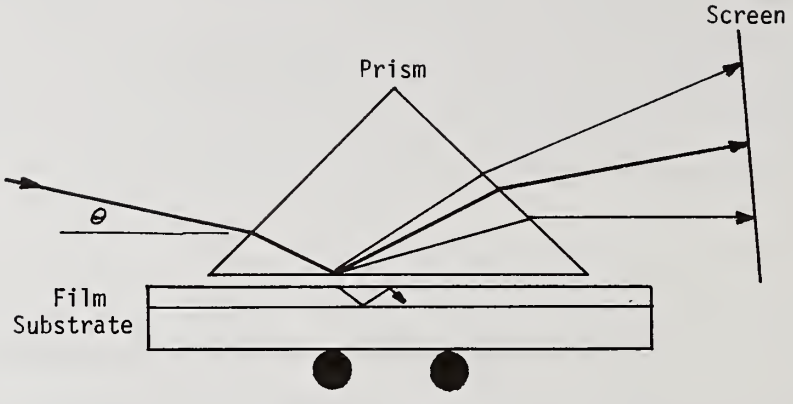

Figure 2. Prism coupler arrangement for observation of m lines.

Radiation from an argon ion laser was made to impinge on the region of optical coupling. The radiation would normally be totally internally reflected at the prism base; however, when the angle of the beam relative to the prism base corresponded to a refracted beam in the film at an angle synchronous to a propagating mode, power would be drawn from the reflected beam and coupled into the film via the evanescent field. Due to optical scatter within the film, the light would couple into all the other allowable film propagation modes. This light would couple back out of the film, into the prism, and could be observed on an observation screen as a series of large streaks. These streaks are called m-lines. A photograph of the m-line spectrum is shown in figure 3. By rotating the prism relative to the incident beam and by altering the state of polarization, we were able to determine the synchronous coupling angles for all the TE and TM modes in the film. The synchronous angles were determined by visual observation of the maximum brightness of the m-lines. The reproducibility of angle readings was several minutes of arc.

5. Results and Discussion

An examination of figure 3 shows seven m-lines visible. The strong intensity of the m-line spectrum suggests that, under the particular deposition conditions employed, a strongly scattering film is obtained. The polarization of the incident beam was set to an intermediate position so that TE and TM m-lines could be photographed simultaneously. With the polarization set in the plane of incidence, we observe only the TM m-lines, whereas, with the polarization set normal to the plane of incidence we observe only the TE m-lines. This indicates weak coupling between the TE and TM modes. The order of the mode lines in the figure, from right to left is, TM_0, TE_0, TM_1 and TE_1 (unresolved), TE_2, TM_2, TE_3 and TM_3. The order of the TM_0 and TE_0 lines is opposite to the order expected for an isotropic film. This strongly suggests that the film is birefringent. Furthermore, the weak coupling between the TE and TM modes suggests that the film is uniaxial with the optic axis normal to the film surface.

We have measured all the mode coupling angles at three wavelengths using an argon-ion

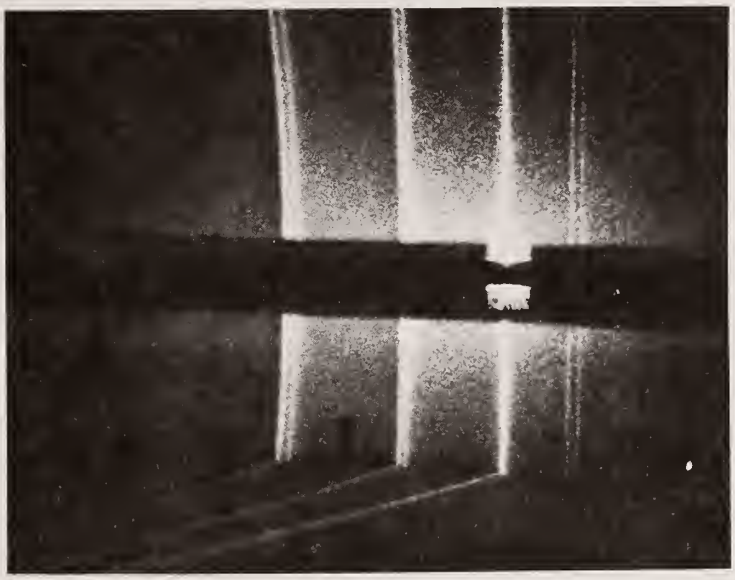

Figure 3. m-line spectrum of mixed MgO (90 mole %), SiO_2 (10 mol %) film. From right to left the lines represent modes TM_0, TE_0, TM_1 and TE_1 (unresolved), TE_2, TM_2, TE_3 and TM_3. The reversed order of TM_0 and TE_0 indicates birefringence. The photograph was taken with the incident polarization set at an intermediate angle to optimize the visibility of all the m lines. The dark horizontal band across the center is the shadow of a mask that blocks out the totally reflected beam and extraneous scattered beams.

laser source. On the basis of the iterative procedure discussed in section 2, we have computed the refractive indices of the mixed MgO-SiO_2 film. Initially the calculation was made under the assumption that the film was isotropic. An examination of the fit residuals showed a systemic deviation of the TE and TM modes from the fit which indicated birefringence in the film. We, therefore, at first fit only the TE modes obtaining a value for n_o and thickness, where n_o is the index of the ordinary ray. Using n_o, we then proceeded to calculate n_e and thickness on the basis of the TM modes, where n_e is the index of the extraordinary ray. Because of the film birefringence, it was necessary to use a modified form of eq (2) that takes into account the angular dependence of the refractive index when the electric field vector does not lie along a principal axis of the indicatrix. Swalen et al. have previously reported on this effect in birefringent polymer films [4].

Table 1 lists the calculated refractive index values of the mixed film. The estimated accuracy of the refractive indices is ± 0.001. Note the consistent dispersion in n_o and n_e. The birefringence, $n_e - n_o = 0.006$ at all wavelengths. This large birefringence is attributed to planar internal strains within the film. We believe this to be the case because efforts to grow a pure MgO film yielded a crazed film that appeared to be torn apart by internal tension. The addition of the SiO_2 stabilized the film forming process.

The optic path through the film normal to the surface has been calculated on the basis of the measured refractive indices and thickness. It is found to agree exactly, within experimental error, to the optic path obtained by a channel spectrum measurement.

The internal strains in the film could be obtained if the elasto-optic coefficient $p_{11}-p_{12}$ were known. Since it is not known, we estimate the strain to be 0.01 by assuming $p_{11}-p_{12}$ to be 0.2, a number typical of optical materials. This corresponds to an estimated stress of 10 Kbar which is in the range of values of thin film stress reported in the literature [9].

Table 1 shows six independently derived values for the thin film thickness. The total range in values is 0.005 μm; the estimated precision is better than ± 0.003 μm. The average value 1.098 μm compares favorably with a stylus thickness measurement of 1.11 μm

It is of interest to compare the measured refractive indices with models based on the indices of the individual constituents. Jacobsson [10,11] has formulated such a composite model based on volume additivity of the individual constituents and based on both the Drude equation and the Lorentz-Lorenz equation. According to the Drude model,

$$n^2 = v_1 n_1^2 + v_2 n_2^2$$

and the Lorentz-Lorenz model

$$n^2 = \frac{\frac{v_1 n_1^2}{n_1^2+2} + \frac{v_2 n_2^2}{n_2^2+2}}{\frac{v_1}{n_1^2+2} + \frac{v_1}{n_2^2+2}}$$

where n_1 is the refractive index of MgO and n_2 is the refractive index of SiO_2. Table 2 summarizes the results of these calculations, which are compared with the averaged experimental values $(n_o+n_e)/2$. Jacobsson [10,11] has pointed out difficiencies in these models. However, agreement of both models with the experimental data is remarkably good. In fact, the index values calculated with the Drude model differ by no more than 0.005 from the experimental values. Clearly, it would be of interest to make the comparison on a number of films having a wide range of compositional proportions. A limited number of such comparisons has been reported in the literature [10,11].

6. Conclusions

The refractive indices and thickness of a mixed film of MgO and SiO_2 produced by coevaporation have been measured by a guided wave method. The accuracy in the refractive index determination was estimated to be ± 0.001; precision in the thickness was better than ± 0.3%. A birefringence of 0.006 was found in the film which was attributed to internal strains. The measured values of refractive index agreed well with values calculated on the basis of a volume additivity models based on both the Lorentz-Lorenz equation and the Drude equation.

All of the results obtained were based on the assumption of a homogeneous film. However, index gradients are known to exist in thin films, and hence, because of the great accuracy of the guided wave method, the method can be used for calculating these gradients. Although the method requires relatively thick films in order to obtain an adequate number of waveguide modes, it is possible to probe the properties of thinner films if they are deposited over thicker films.

We thank Dr. Jerome Swalen of IBM Corporation and Dr. Dickron Merjerian of the Westinghouse Corporation for helpful discussions concerning this work. We thank Dr. Michael I. Bell of NBS

Table 1. Refractive Index and Thickness of Mixed Films
90 mole % MgO, 10 mole % SiO_2

Wavelength (μm)	n_o	n_e		Thickness (μm)
0.5145	1.689			1.097
		1.695		1.100
0.4880	1.692			1.096
		1.698		1.101
0.4579	1.697			1.096
		1.703		1.096
			Avg.	1.098

Table 2. Comparison of Refractive Indices

Wavelength (μm)	MgO[a]	SiO_2[b]	Lorentz-Lorenz Model	Drude Model	Experimental $(n_o+n_e)/2$
0.5145	1.7438	1.4616	1.679	1.688	1.692
0.4880	1.7468	1.4630	1.682	1.691	1.695
0.4579	1.7510	1.4650	1.685	1.695	1.700

[a] R. E. Stephens and I. H. Malitson, J. Res. NBS 49, 249 (1952).

[b] I. H. Malitson, J. Opt. Soc. Am. 55, 1205 (1965).

for providing the specimen holder, Dr. Ted Vorberger for the stylus thickness measurement and Dr. Ludwig Grabner for the channel spectrum.

7. References

[1] Tien, P. K.; Ulrich, R; Martin, R. J. Modes of propagating light waves in thin deposited semiconductor films. Appl. Phys. Letters 14, 291-4 (1969).

[2] Adams, A. C.; Schinke, D. P.; Capio, C. D. An evaluation of the prism coupler for measuring the thickness and refractive index of dielectric films on silicon substrates. J. Electrochem. Soc. 126, 159-43 (1979).

[3] Swalen, J. D.; Tacke, M.; Santo, R.; Fischer. J. Determination of optical constants of polymeric thin films by integrated optical techniques. Opt. Commun. 18, 387-390 (1976).

[4] Swalen, J. D.; Santo, R., Tacke, M. and Fischer, J. Properties of polymeric thin films by integrated optical techniques. IBM J. Res. Dev. 21, 168-75 (1977).

[5] Tien, P. K. Integrated optics and new wave phenomena in optical waveguides. Rev. Mod. Phys. 49, 361-420 (1977).

[6] Farabaugh, E. N.; Sanders, D. M.; Wilke, M. E.; Hurwitz, S.A.; and Haller, W. K. Preparation of thin amorphous films by E-beam evaporation from multiple sources. Proceedings of 13th Annual Symp. on Opt. Mtls for High Power Lasers, Boulder, CO, Nov. 16-20, 1981.

[7] Ulrich, R.; Torge, R. Measurement of thin film parameters with a prism coupler. Appl. Opt. 12, 2901-8 (1973).

[8] Sarid, D.; Cressman, P. J.; Holman, R. L. High efficiency prism coupler for optical waveguides. Appl. Phys. Lett. 33, 514-15 (1978).

[9] Ennos, A. E. Stresses developed in optical film coatings. Appl. Opt. 5, 51 (1966).

[10] Jacobsson, R. The preparation and optical properties of coevaporated homogeneous films and films with controlled gradients in the index of refraction. In Optical Properties of Dielectric Films, edited by N. N. Axelrod (Electrochemical Society, NY. 1968) pp. 169-192.

[11] Jacobsson, R. Inhomogeneous and coevaporated homogeneous films for optical applications. In Physics of Thin Films, Vol. 8, G. Hass, M. H. Francombe and R. W. Hoffman, eds. (Academic Press, New York 1975) pp. 51-98.

The question was asked how an accuracy of 10^{-3} was established for the value of the index of refraction. The speaker replied that the reproducibility of the data, the fit of the data to the experimental angles, the fact that the birefringence at all three angles came out to be the same to one in the third decimal place, and the excellent agreement with the channel spectra established that the precision of the measurements at least was one part in 10^3. He was not willing to equate that to accuracy.

A second question was what in the evidence suggests that the mixed composition coevaporated films are more dense than the MgO or SiO_2 films. The speaker replied that the main evidence was that when the films were prepared by coevaporation with separate monitors it was found that the resultant film thicknesses were much less than the sum of the film thickness of the two monitors.

Sensitive Technique for Measuring Apparent Optical Figure Error Caused by Coating Nonuniformity*

H. E. Bennett and D. K. Burge

Michelson Laboratory, Physics Division
Naval Weapons Center, China Lake, California 93555

If a diffraction-limited wave front is to be produced by an optical train, the requirements on the optical figure of individual mirror components may be very stringent. Peak-to-valley values of $\lambda/8$ visible equivalent are found for some infrared systems, $\lambda/20$ for visible systems, and $\lambda/100$ visible equivalent has been suggested for some ultraviolet systems. These mirrors often have high reflectance multilayer coatings, in which case the optical figure is determined not only by the geometrical perfection of the optical surface but also by the uniformity of the multilayer coating. Although this uniformity can be determined interferometrically or by measuring the secondary structure surrounding the reflectance maxima, the most sensitive technique for determining film nonuniformities appears to be ellipsometry. It should be performed at the wavelength at which the mirror is to be used. Typically, the ellipsometric parameter Δ is found to be very sensitive to variations in film thickness but quite insensitive to absorption in the film; the converse holds for Ψ. For a representative infrared, high reflectance multilayer coating, a measurable change in Δ corresponds to film thickness nonuniformities of less than 0.01%, and a measurable change in Ψ corresponds to a change in peak reflectance of 0.001. An automated ellipsometer could be readily used to scan the surface of even a large mirror. Ellipsometry may thus provide the optimum technique for testing mirror optics for multilayer-film-induced changes in apparent optical figure. It also provides a sensitive technique for measuring the uniformity of reflectance of large, multilayer-coated mirrors.

Key words: ellipsometry; film thickness nonuniformity; multilayer dielectric films; optical figure measurement; wave front distortion.

Introduction

The need for nearly diffraction-limited laser systems leads to very severe requirements for the wave front error tolerance per mirror in a typical laser optical train [1].[1] Peak-to-valley values of $\lambda/8$ visible equivalent are sometimes needed for infrared systems, $\lambda/20$ for visible systems, and $\lambda/100$ visible equivalent has been suggested for some ultraviolet systems [2]. Often these mirrors are coated with multilayer high reflectance films. As was shown in a paper at this meeting last year [3], the effective optical figure is then determined not only by the geometrical perfection of the substrate surface, but also by the uniformity of the multilayer coating used to enhance the reflectance of the mirror. The contribution of the coating to the figure error is composed of two parts: the contribution from (1) variation in physical thickness of the coating across the mirror and (2) differences in phase change on reflection. For metal coatings both these effects are negligible, but for dielectric coatings both may be significant. The individual dielectric films in an infrared multilayer dielectric (MLD) coating stack are thick, typically 4000 - 6000 Å for each film, and there are typically eight to twelve films in a stack. A scale drawing of a representative coating stack for 3.8 μm is shown in figure 1. The four-layer-pair MLD coating in this case is over 50 times as thick as the metal coating alone. A thickness variation of 2% in each coating layer, if cumulative, will cause an equivalent figure error (EFE) in this coating of $\lambda_{vis}/8$, as seen in figure 2, which is repeated from reference 3.

This MLD film effect has been verified experimentally [4]. The results given there point out another aspect of this effect, i.e., measurements to observe the EFE should be made at the wavelength at which the coating is to be used. The phase effect of the MLD coating varies with the wavelength, but, in theory, it would be possible to relate the infrared performance of a coating to measurements made in the visible region. In practice, since all film variables (index, etc.) are not well known [5], the rapid variation of phase in the visible and near-infrared for an intermediate-infrared multilayer coating coupled with the expected uncertainty in film properties make it difficult to rely

*Work partially supported by Navy Independent Research funds.
[1]Numbers in brackets indicate the literature references at the end of the paper.

on visible and near-infrared measurements as a definitive tool for evaluating mirrors for the intermediate infrared. A similar argument may be applied for coatings designed for other wavelengths.

Assuming that the nonuniformity measurement is made at the design wavelength for the film, what are the measurement options available? The most obvious one is to measure the decrease in on-axis intensity in a focused spot at the design wavelength. Such a measurement, if done accurately, will give a good evaluation of the Strehl ratio achieved in a multiple mirror system. Going from a resultant cumulative optical figure error of λ/∞ rms at the operating wavelength to one of $\lambda/14$ rms causes a decrease in on-axis intensity of 20% [6]. Since there usually are many mirrors and other optical elements in an optical train, to achieve a Strehl ratio [1] of unity, which corresponds to a resultant cumulative figure error of $\lambda/14$, each individual mirror must have an allowed figure error which is much less than $\lambda/14$. For example, the typical peak-to-valley tolerance of $\lambda/8$ visible equivalent for infrared mirrors corresponds to a tolerance at a wavelength of 3.8 μm of 0.6/3.8, or approximately $\lambda/50$. The rms mirror figure is approximately $2\sqrt{2}$ less than the average peak-to-valley mirror figure, and the wave front error introduced by a mirror is twice the mirror figure error, so that the wave front error at 3.8 μm introduced by a mirror having an equivalent peak-to-valley figure error in the visible region of $\lambda/8$ would be $(\lambda/50) \div \sqrt{2} \cong \lambda/70$. The decrease in on-axis intensity observed for such a mirror operating singly is too small to be accurately measured. Therefore, although the Strehl ratio or on-axis intensity measurement is a good way to measure overall system performance, it is not a good measurement technique for evaluating individual components.

An alternative technique is to measure mirror figure directly at the operating wavelength. Infrared figure measurements good to perhaps $\lambda/100$ can probably be made using a heterodyne technique [7], but they are difficult and do not separate coating errors from geometrical figure errors caused by polishing errors or dimensional instability in the mirror blank. An auxiliary measurement which tests only the coating errors would thus be most desirable.

We have evaluated two techniques for coating uniformity determination. One, the measurement of the wavelengths of the secondary minima adjacent to the reflectance maximum should be able to detect coating nonuniformities of 1% or less. It is discussed in a companion paper [8]. The second, infrared ellipsometry, which is discussed in this paper, should allow one to detect coating nonuniformities of 0.01% or less on typical MLD stacks. It appears to be the most sensitive technique yet suggested for multilayer film uniformity measurement. The variation in reflectance across the mirror surface can also be detected using this technique. The ellipsometric calculations supporting the above conclusions are discussed in this paper.

Ellipsometric Calculations

To illustrate the sensitivity of ellipsometry to film thickness nonuniformity and absorption, a specific case will be examined in this section. The design considered is a high reflectance multilayer, which may be described as $(ZnS/ThF_4)^3ZnS^*ThF_4^*ZnS^*Ag$, where the asterisk indicates a layer whose thickness is not quarter-wave at the design wavelength (λ). This design is slightly different than the representative coating shown in figure 1, but the resultant reflectance and phase change are very similar. The design wavelength is assumed to be 3.8 μm, and the angle of incidence assumed for the ellipsometric measurements is 60.00 deg. The indices used are $n_{ZnS} = 2.25$, $n_{ThF_4} = 1.51$, and $\hat{n}_{Ag} = 1.2 - i29$. Calculations were made using a slightly modified version of the ellipsometry computer program of McCrackin [9]. The parameters of concern are the ellipsometric observables, Ψ and Δ, which are defined as follows in terms of the polarization properties of the surface:

$$\tan\Psi = r_p/r_s \quad ; \quad \Delta = \Delta_p - \Delta_s \quad ,$$

where r_p and r_s are the amplitude reflection coefficients, and Δ_p and Δ_s are the phase changes on reflection for p- and s-polarized light. These quantities are functions of the indices and thicknesses of all the coating layers (see fig. 3). Since only two quantities are measured, one cannot determine the properties of the individual layers. However, as will be shown, the positional variation of Ψ and Δ provides very sensitive information on film nonuniformity.

For the calculation of the sensitivity of Ψ and Δ to thickness nonuniformity, the same percent thickness error is assumed for all dielectric layers. The sensitivity results are given in Table 1 and are shown graphically in figure 4.

Table 1. Sensitivities of ellipsometric parameters, Ψ and Δ, to film thickness nonuniformity for a representative multilayer at 3.8-μm and 60-deg incidence. Values are given in degrees.

Parameter	Thickness error			
	0	±1%	±2%	±4%
Ψ	44.946	44.954	44.960	44.968
Δ	-113.102	-120.183	-126.619	-138.004
δΨ	---	0.008	0.014	0.022
δΔ	---	-7.081	-13.517	-24.902

The prefix δ indicates the change in Ψ or Δ. The parameter Δ is seen to be about 1000 times more sensitive to thickness variation than is the parameter Ψ. The sensitivity is actually 7 deg/1% film nonuniformity and is linear with nonuniformity to within 15% over the range evaluated (0 - 4% film nonuniformity). A change in Δ or Ψ of 0.1 deg is easily measurable ellipsometrically using present infrared equipment [10], and sensitivities of the order of 0.001 deg have been reported for ellipsometers operating in the visible region [11]. We thus conclude from this calculation that the measurement of Δ is a very sensitive method for measuring film nonuniformity.

The calculation of the sensitivity of Ψ and Δ to absorption in the coating is also of interest. The same absorption coefficient is assumed for all dielectric layers in these calculations. This assumption is simplistic in that absorption coefficients in the two filming materials in actual multilayers seldom coincide. However, the values chosen for the absorption coefficients are representative of those found in real films and thus the calculated trends should be the same in a real case. The results for the absorption sensitivities are given in Table 2 and are shown graphically in figure 5.

Table 2. Sensitivities of ellipsometric parameters, Ψ and Δ, to film absorption for a representative multilayer at 3.8-μm and 60-deg incidence. Values are given in degrees.

Parameter	Absorption coefficient, cm^{-1}		
	0	10	100
Ψ	44.946	44.860	44.083
Δ	-113.102	-113.102	-113.128
δΨ	---	-0.086	-0.863
δΔ	---	0.000	0.026

Here the parameter Ψ is seen to be the sensitive one, about 30 times more than for Δ. The change in Ψ is linear with increasing absorption coefficient over the 0 - 100 cm^{-1} range tested and has a sensitivity of 9×10^{-3} deg/cm^{-1}. A difference of 10 cm^{-1} in the absorption coefficient causes a change in the peak (3.8 μm) reflectance of about 0.001. Since this change corresponds to a change in Ψ of ~ 0.1 deg, it could be useful for finding areas of increased absorption. However, the sensitivity is not nearly as great as the sensitivity of Δ to nonuniformity for the magnitudes of changes of interest.

Conclusion

Of the two measured ellipsometric parameters, one, Δ, is very sensitive to variations in multilayer film thickness but insensitive to changes in reflectance caused by changes in film absorption. The second, Ψ, is sensitive to changes in absorption in a multilayer film and, hence, to changes in multilayer reflectance at the operating wavelength but is insensitive to changes in the thickness of films in the multilayer. In the case of a representative high reflectance infrared multilayer, a readily measurable change in Δ, 0.1 deg, corresponds to a multilayer-film nonuniformity of about 0.01%; δΔ is approximately linear with film nonuniformity over the 0 - 4% nonuniformity range tested. The absorption-related parameter Ψ changed by 0.1 deg for a change of 0.001 in peak reflectance of this representative multilayer. Since peak reflectance values are often specified with an uncertainty of ±0.001, the Ψ measurement provides a useful check on reflectance uniformity across a multilayer coating. It is probably dangerous to rely on it for an absolute measurement of reflectance, however, since it is easy to develop unsuspected systematic errors in ellipsometry which, although not affecting the variation in Ψ and Δ with spatial position, will affect the reliability of the measured values in absolute terms.

We conclude that ellipsometry may provide the optimum technique for testing coated mirror optics for multilayer-film-induced changes in apparent optical figure. It could also be useful in testing reflectance uniformity. These measurements should be performed at the wavelength at which the mirror is to be used. An automated ellipsometer could be readily used to scan the surface of even a large mirror. In view of the difficulty in making such measurements to this accuracy by other techniques in the infrared, a reliable automated scanning infrared ellipsometer is an attractive instrument to consider for multilayer-film evaluation.

References

[1] Bennett, H. E. Thermal distortion thresholds for optical trains handling high pulse powers. Glass, A. J.; Guenther, A. H., ed. Proceedings of the 8th annual symposium on optical materials for high power lasers; 1976 July 13-15; Boulder, CO. Nat. Bur. Stand. (U.S.) Spec. Publ. 462; 1976 December. 11-24.

[2] Bennett, H. E.; and others. Ultraviolet components for high energy applications. China Lake, CA: Naval Weapons Center; 1978. NWC TP 6015, pp. 8-9.

[3] Bennett, H. E.; Burge, D. K. Multilayer thickness uniformities required to meet wave front error tolerances in laser mirrors. Bennett, H. E.; Glass, A. J.; Guenther, A. H.; Newnam, B. E., ed. Proceedings of the 12th annual symposium on optical materials for high power lasers; 1980 September 30-October 1; Boulder, CO. Nat. Bur. Stand. (U.S.) Spec. Publ. 620; 1981 October. 356-368.

[4] Ramsay, J. V.; Ciddor, P. E. Apparent shape of broad band, multilayer reflecting surfaces. Appl. Opt. 6; 2003; 1967.

[5] Knowlden, R. E. Wave front errors produced by multilayer thin film optical coatings. Thesis; University of Arizona; 1981 (unpublished).

[6] Born, M.; Wolf, E. Principles of optics. New York: Pergamon Press; 1959. 467-469.

[7] Wyant, J. C. Use of a white light extended source with a lateral shear interferometer for real time wave front correction systems. Appl. Opt. 14; 2622; 1975.

[8] Bennett, H. E.; Burge, D. K. Limits to the validity of evaluating a quarter-wave, high-reflectance multilayer through analysis of its secondary structure. This proceedings.

[9] McCrackin, F. L. A Fortran program for analysis of ellipsometer measurements. Nat. Bur. Stand. (U.S.) Tech. Note 479; 1969.

[10] Leonard, T. A.; Loomis, J.; Harding, K. G.; Scott, M. Design and construction of three infrared ellipsometers for thin-film research. Bennett, H. E.; Glass, A. J.; Guenther, A. H.; Newnam, B. E., ed. Proceedings of the 12th annual symposium on optical materials for high power lasers; 1980 September 30-October 1; Boulder, CO. Nat. Bur. Stand. (U.S.) Spec. Publ. 620; 1981 October. 345-355.

[11] Jasperson, S. N.; Burge, D. K.; O'Handley, R. C. A modulated ellipsometer for studying thin film optical properties and surface dynamics. Surf. Sci. 37; 548; 1973.

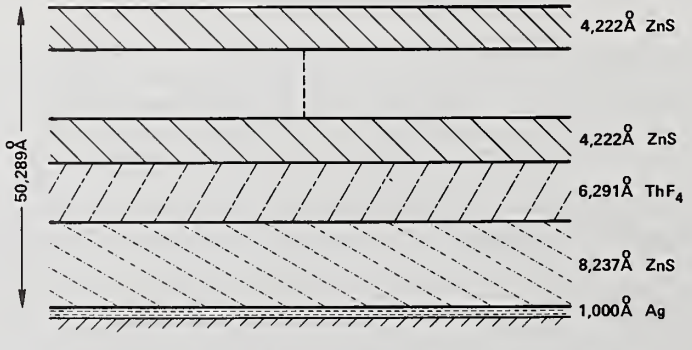

Figure 1. Scale drawing of a $(ZnS/ThF_4)^4ZnS^*Ag$ multilayer film designed for a wavelength of 3.8 μm in the infrared region. Note the thickness of the dielectric layer is 50X that of the metal layer.

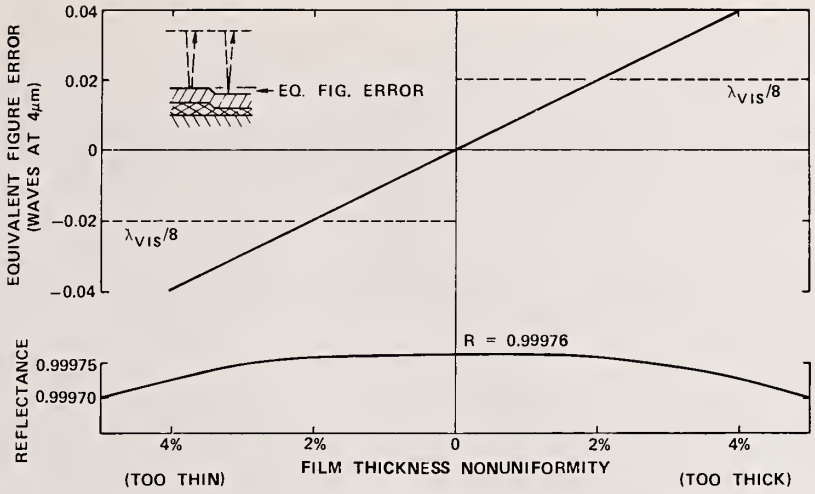

Figure 2. Equivalent figure error in a MLD-coated mirror caused by nonuniform film thickness across the mirror. The multilayer coating design is $(ZnS/ThF_4)^4ZnS^*Ag$, and the design wavelength is 3.8 μm. The dashed lines give the corresponding figure error in visible wavelengths. They would not be the observed figure errors if measurements were made in the visible, however, because of phase shift.

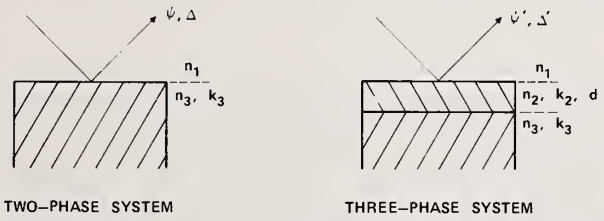

Figure 3. Diagrams indicating that the ellipsometric parameters, Ψ and Δ, are functions of the optical constants of all media making up a reflecting system. Thus for a MLD system, it is not possible to determine the indices and thicknesses of all layers without additional information.

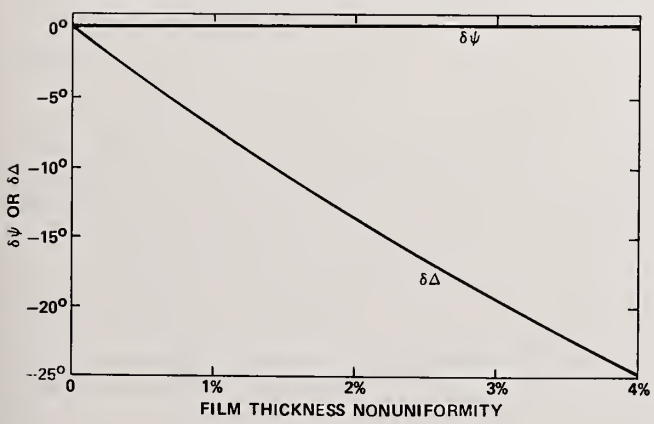

Figure 4. Sensitivities of ellipsometric parameters Ψ and Δ to film thickness nonuniformity for a representative infrared multilayer coating.

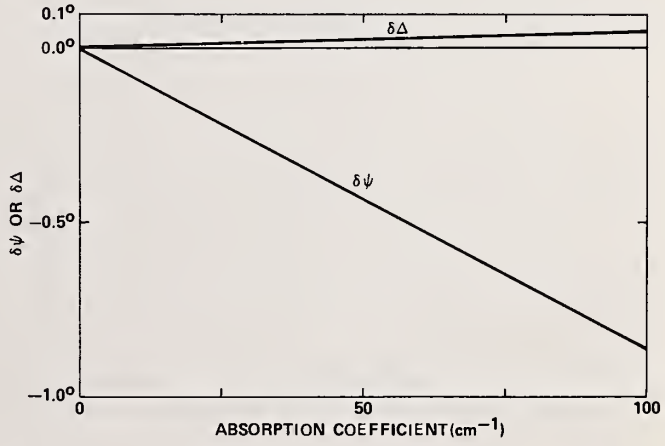

Figure 5. Sensitivities of ellipsometric parameters Ψ and Δ to absorption in the coating layers for a representative infrared multilayer coating. The same absorption coefficient is assumed for all dielectric layers.

Limits to the Validity of Evaluating a Quarter-Wave, High-Reflectance Multilayer Through Analysis of Its Secondary Structure*

H. E. Bennett and D. K. Burge

Michelson Laboratory, Physics Division
Naval Weapons Center, China Lake, California 93555

Information on the perfection of high-reflectance multilayer films can be obtained from a study of the secondary structure surrounding the principal reflectance maximum. The wavelengths at which the adjacent minima occur are a good indication of the correctness of the optical film thicknesses achieved in a quarter-wave multilayer stack. Calculations indicate that the depths of these minima are much more sensitive to absorption in the film layers than is the reflectance at the maximum. If the thicknesses are correct and if volume absorption in the film materials is the main source of decreased reflectance, excellent correlation is found between the measured peak reflectance and that calculated from the depth of the more easily measured secondary reflectance minima. Errors in film thickness or significant interface absorption arising from impurity segregation, surface plasmon excitation, or other sources complicate this simple picture, however, so that the peak reflectance should also be measured directly.

Key words: absorption; high-reflectance coatings; interface absorption; laser components; multilayer film evaluation; nonuniform film thicknesses; reflectance maximum.

Introduction

The on-axis energy which can be focused by an optical train is reduced sharply if the optical train introduces significant wave front distortion into the output wave front. To avoid this loss, an excellent optical figure is required for all components in the system. For infrared laser optics, a mirror tolerance of an eighth-wave or less visible equivalent is not uncommon. Wave front errors can be introduced by multilayer-coated mirrors in two ways. One is a geometric distortion of the surface of the mirror substrate caused either by errors made in polishing the part or by thermal heating. A second type of wave front error is caused by optical thickness nonuniformity in the multilayer coatings themselves [1].[1] Such thickness nonuniformities occur in all multilayer coatings, and their magnitude depends on the care with which the coating was deposited, the deposition technique, the fixturing geometry in the coating chamber, the cleanliness of the substrate, and other factors. For good performance these nonuniformities must be reduced to acceptable levels. For a typical infrared multilayer coating, they should be less than 1 or 2%. A 2% thickness nonuniformity in a typical high-reflectance multilayer coating for a deuterium fluoride (DF) chemical laser operating at a wavelength of 3.8 μm corresponds to a visible equivalent figure error of about one-eighth wave, which may be the total figure error tolerance for the mirror.

In addition to variations in film thickness from point to point on the surface, the entire multilayer may also be too thick or too thin. The decrease in reflectance at the peak wavelength caused by thickness errors of a few percent, however, is negligible [1], and, if the films are uniform in thickness, no wave front error will be introduced. Another problem is the presence of absorption in the films, which may cause the multilayer coating to have too low a reflectance and thus may allow the incident laser beam to thermally distort the mirror structure. Thus both multilayer film reflectance and thickness nonuniformity must be measured. Ellipsometry and other possible measurement techniques are discussed in a companion paper at this symposium. The purpose of this paper is to evaluate one of these techniques, the use of the secondary minima on either side of the primary reflectance maximum in a multilayer high-reflectance coating, to evaluate film thickness nonuniformity and reflectance at the design wavelength. The conclusion drawn is that the secondary minima provide a useful tool for evaluating film thickness errors. The depth of these minima suggests the peak reflectance value, although this technique is not by itself adequate to determine the peak reflectance of the multilayer coating.

*Work partially supported by Navy Independent Research funds.
[1]Numbers in brackets indicate the literature references at the end of the paper.

Coating Calculations

Figure 1 shows the theoretical reflectance as a function of wavelength for a typical four-layer-pair, high-reflectance multilayer designed for an infrared DF laser operating at a wavelength of 3.8 μm. If there is no absorption in the multilayer film (top solid line), the peak reflectance of the multilayer is 0.9997. The two adjacent minima have reflectances of 0.9757 and 0.9774, nearly equal in depth. The decrease in reflectance is only a little over 0.02, so that a sensitive spectrometer is required to see them, but by using an expanded scale they can readily be observed on most good instruments. The first question is the wavelength position of these minima. If the film thicknesses are correct, the minima will be equally spaced in wave numbers about the reflectance maximum and will be separated from it by slightly over 500 cm^{-1}. If the films are uniformly too thick, the minima will both be moved nearly equally to longer wavelengths; if they are too thin, to shorter wavelengths. The apparent variation of thickness (in terms of phase) is dependent not only on the thickness error but also on the phase variation of the coating with wavelength. Explicit expressions for this variation are given by Giacomo [2]. The percentage shift in wave number or wavelength is directly proportional to the percentage error in film thickness. In the case of this multilayer film, a 1% thickness error then corresponds to a wavelength shift of about 0.04 μm, about an order of magnitude larger than the readout accuracy achievable with a conventional infrared prism spectrometer in this region [3]. In view of the difficulty in selecting line centers for this small absorption, however, thickness errors significantly smaller than 1% will be difficult to measure.

The maximum theoretical reflectance for this multilayer pair on silver is 0.9997. There will be some absorption in the multilayers themselves and also at interfaces between the multilayers. The peak reflectance is then given by [4]

$$R = 1 - \left[\frac{\lambda}{2}(\beta_L + \beta_H) + 4A_{HL}\right]\left[1 - \left(\frac{n_L}{n_H}\right)^{2N+1}\right]\frac{1}{n_H^2 - n_L^2} - 4\frac{n_S}{n_H^2}\left(\frac{n_L}{n_H}\right)^{2N}(1 + A_{HS}) - \left(\frac{4\pi\delta}{\lambda}\right)^2 , \qquad (1)$$

where β_L and β_H are the volume absorption coefficients of the low- and high-index films, respectively; n_L and n_H the indices of refraction; N the number of layer pairs (in this case, four); A_{HL} the interface absorption between each high-index film and the low-index film nearer the substrate; A_{HS} the film-substrate interface absorption; λ the wavelength; and δ the rms roughness of the surface. The term $(4\pi\delta/\lambda)^2$ accounts for total integrated scattering (TIS) and may be replaced by a measured TIS value if, as is usual in the infrared, defect scattering is larger than scattering from surface microroughness. The effect of increasing the film bulk absorption coefficient is shown graphically in figure 1. The decrease in reflectance at the peak wavelength, 3.8 μm in this case, is independent of whether the absorption is in the high- or low-index layer, as seen in eq (1). However, the adjacent minima are sensitive to where the absorption occurs. Absorption in the low-index layer depresses the short-wavelength minima more than the long-wavelength minima. Absorption in the high-index layer has the opposite effect. In principle, then, it might be possible if interface absorption can be neglected to determine from measurements of the secondary minima both what the peak reflectance should be and whether the absorption occurs primarily in the high- or low-index layer. In practice, this information cannot be determined unambiguously from the depth of the minima. Although the results are suggestive, other effects can complicate the interpretation, as will be seen.

Figure 2 illustrates one of the complicating effects. The solid line shows the calculated reflectance of the multilayer described in figure 1 when the volume absorption coefficient of thorium fluoride is 10 cm^{-1} and for zinc sulfide is 1 cm^{-1}. The layer thicknesses are all correct, and the short-wavelength minima are slightly deeper than the long-wavelength minima, as in figure 1. The effect is seen more easily in figure 2, because a linear rather than a logarithmic scale is used. In modern coating practice, the multilayer film is monitored during deposition and trimmed to correct for thickness errors in individual films. The dashed line in figure 2 shows the effect on the secondary minima when such trimming has been done. It is assumed that the third-layer pair was 10% too thick. The second-layer pair was then deposited 10% too thin to compensate. There is almost no effect on peak reflectance (the decrease is only one part in 10^5) or in wavelength spread caused by this corrected coating error. However, there is a significant change in the depth of the minima, which would lead one to predict that the ThF_4 film had a higher absorption and the ZnS film a lower absorption than was actually the case.

Another effect which can reduce the reflectance at the short-wavelength minimum relative to that at the long-wavelength minimum is surface plasmon excitation in the silver film caused by substrate or film-induced surface irregularities. Professor Sievers, with whom we have collaborated in studying this phenomena, concludes that surface plasmon excitation has almost no effect on the reflectance maximum [5]. The layer thicknesses are tuned for this wavelength, and consequently the standing wave

electric field in the multilayer does not penetrate to the substrate. At the secondary minima, however, the fields do penetrate to the substrate, and the enhancement of the surface plasmon effect caused by the dielectric layers near the substrate increases the absorption significantly. The effect increases as one goes to shorter wavelengths. Typical predicted values for a plasmon-induced decrease in reflectance of this multilayer design are 0.0003 for the reflectance maximum, 0.012 for the long-wavelength minimum, and 0.030 for the short-wavelength minimum [5].

Experimental and Results

To test the usefulness of the technique for estimating the height of the reflectance maximum from measurements of the reflectance near the secondary minima, an absolute reflectometer [6] believed to be accurate to better than ±0.001 was used. The multilayer film samples were commercially deposited on 1.520-inch-diameter fused quartz optical flats in a single evaporation. The accuracy of the reflectometer was verified by comparing the best fit to the measured reflectance on a very low-scatter, coated silicon sample at discrete wavelengths in the 3.2 - 4.2 μm wavelength range to the absorptance measured using a multiline DF laser and the Naval Weapons Center (NWC) adiabatic calorimeter [7]. The agreement between the best fit to the reflectometer values at 3.8 μm and the calorimetric value was 2 parts in 10^4, which was approximately twice the average deviation of the reflectance points from a smooth curve. The TIS from this Si sample was measured at 3.8 μm using the NWC Optical Evaluation Facility [8] and found to be 6×10^{-5}, so scattered light was not a significant factor in these measurements.

Results for one of the multilayer-coated samples are shown in figure 3. The measured reflectance at 3.8 μm was 0.9982. The calculated value for nonabsorbing films was 0.9997. For films in which $\beta_{ZnS} = 1\ cm^{-1}$ and $\beta_{ThF_4} = 10\ cm^{-1}$ (typical values for these materials in the 3 - 5 μm wavelength region), the calculated reflectance was 0.9990. The minima occurred at 3168 cm^{-1} and 2123 cm^{-1}, respectively, which may be compared to the theoretical values of 3200 cm^{-1} and 2045 cm^{-1} for the above absorbing coating. They were thus, on the average, within about 1% of the theoretical values and averaged within 0.5% of the design wave number, 2632 cm^{-1}. The positions of the minima shift slightly as film absorption increases, and the uncertainty in making the wavelength measurements must also be considered. When these factors are taken into account, the difference between the observed values and those of a coating with perfect layer thicknesses is negligible.

The measured reflectance at the short-wavelength minimum was 0.9365 and at the long-wavelength minimum 0.9631. These values may be compared to the theoretical values for the absorbing coating discussed above. If a linear extrapolation of the reflectance at the minima for various values of the absorption coefficients of ThF_4 and ZnS is made while maintaining the ratio of absorption coefficients of 10:1 as illustrated in figure 4, the observed reflectance minima coincide with absorption coefficient values of about 16 cm^{-1} for ThF_4 and 1.6 cm^{-1} for ZnS. Notice that both minima give approximately the same values for these coefficients. The predicted reflectance for this multilayer at 3.8 μm is then 0.9986, which is only 0.0004 higher than that actually observed. The discrepancy may be easily accounted for by interface absorption, which certainly exists, and by scattered light, which was measured to be approximately 0.0002. The uncertainty in the reflectance measurement itself, however, is of the order of the observed difference.

Although the reflectometer was specially tuned for this experiment and differed by only 0.0002 from calorimetric results, the accuracy normally quoted for reflectance measurements even on this excellent instrument is 2.5 times the magnitude of the difference observed between the theoretically predicted and experimentally measured peak reflectance values. Peak reflectance values on multilayer coatings of this quality are thus very difficult to measure to the required accuracy. On the other hand, the changes in reflectance at the minima are over an order of magnitude larger than those at the design wavelength and are readily measured. There is thus considerable justification for utilizing secondary minima analysis to indicate peak reflectance as well as coating uniformity on high-reflectance multilayer laser coatings.

The sample whose reflectance is shown in figure 3 was only one of eight nearly identical substrates. These samples were mounted at different but equivalent places in the evaporation chamber and were coated simultaneously. Most of the samples were similar in reflectance to the one shown, although the disparity between the short- and long-wavelength secondary minima tended to be less pronounced. Three of the samples which showed the most variation are shown in figure 5. The one represented by the short-dashed curve had the highest peak reflectance of those tested and was higher than 0.999. The averaged reflectances of the secondary minima were higher than for the other samples, and the peak reflectance predicted from figure 4 for this sample would be slightly higher than 0.999. On the other hand, the sample represented by the long-dashed curve had a rather low set of minima. In addition, the long-wavelength minimum was slightly deeper than the short-wavelength minimum and the minima positions were shifted to shorter wavelengths, suggesting that at least some of the layers were somewhat too thin. The deeper long-wavelength minimum may be the result of an anomaly such as that shown in figure 2. If instead it is caused primarily by absorption, it suggests that the ZnS

films in this case have absorption coefficients comparable to those of the ThF_4 films and are about 10 cm^{-1}. The predicted peak reflectance in this case is about 0.998, as can be seen from figure 1. The observed value was 0.997 for this film. An even greater wavelength shift is observed for the multilayer coating represented by the solid line. The long-wavelength minimum for this coating is significantly lower than is the short-wavelength minimum. Although neither of the minima are as deep as those for the coating represented by the long-dashed line, the peak reflectances of the two coatings are almost identical, suggesting that simply averaging the depths of the minima without regard to their wavelength position and depth differences is not adequate to accurately predict peak reflectance.

Conclusions

Significant information about the perfection of high-reflectance multilayer films can be obtained from a study of the secondary structure surrounding the principal reflectance maximum. Both the long- and short-wavelength minima should be measured to obtain reliable data. The wavelengths at which these minima occur are good indicators of the correctness of the optical film thicknesses achieved in a quarter-wave stack. Thickness errors of well under 1% can be measured in this way. The depth of the minima can also be correlated to the peak reflectance of the multilayer stack if the film thicknesses are correct. Although effects such as interface absorption, scattering, surface plasmon excitation, and layer thickness compensation during deposition affect the peak reflectance and the reflectances at the two minima differently, good correlation ($\sim \pm 0.001$ in peak reflectance) was found between theoretical predictions based on depth of minima and experimental results for these accurately deposited films. Since the reflectances at the minima vary at least an order of magnitude more than that at the reflectance peak, requirements on the accuracy of the reflectometer are significantly reduced. A useful estimate of peak reflectance may thus be obtained from secondary minima evaluation. In this study, however, the peak reflectance as measured directly was always less than that predicted from the depth of the minima, and in view of the importance which often attaches to peak reflectance measurement, an additional direct measurement of this quantity is clearly desirable.

References

[1] Bennett, H. E.; Burge, D. K. Multilayer thickness uniformities required to meet wave front error tolerances in laser mirrors. Bennett, H. E.; Glass, A. J.; Guenther, A. H.; Newnam, B. E., ed. Proceedings of the 12th annual symposium on optical materials for high power lasers; 1980 September 30-October 1; Boulder, CO. Nat. Bur. Stand. (U.S.) Spec. Publ. 620; 1981 October. 356-368.

[2] Giacomo, P. Proprietés chromatiques des couches réfléchissantes multi-dielectriques. J. Phys. Rad. 19; 307; 1958.

[3] Bennett, H. E.; Bennett, J. M. Precision measurements in thin film optics in Physics of thin films, Vol. 4. Hass, G.; Thun, R. E., ed. New York: Academic Press; 1967. 53-54.

[4] Bennett, H. E.; Burge, D. K. Simple expressions for predicting the effect of volume and interface absorption and of scattering in high-reflectance or antireflectance multilayer coatings. J. Opt. Soc. Am. 70; 268; 1980.

[5] Sievers, A. Cornell University; private communication; 1981.

[6] Bennett, H. E.; Koehler, W. F. Precision measurement of absolute specular reflectance with minimized systematic errors. J. Opt. Soc. Am. 50; 1; 1960.

[7] Decker, D. L.; Temple, P. A. The design and operation of a precise, high sensitivity adiabatic laser calorimeter for window and mirror material evaluation. Glass, A. J.; Guenther, A. H., ed. Proceedings of the 9th annual symposium on optical materials for high power lasers; 1977 October 4-6; Boulder, CO. Nat. Bur. Stand. (U.S.) Spec. Publ. 509; 1977 December. 281-285.

[8] Bennett, H. E.; Soileau, M. J.; Archibald, P. C. Diamond turned mirrors. Glass, A. J.; Guenther, A. H., ed. Proceedings of the 7th annual symposium on optical materials for high power lasers; 1975 July 29-31; Boulder, CO. Nat. Bur. Stand. (U.S.) Spec. Publ. 435; 1976 April. 49-56.

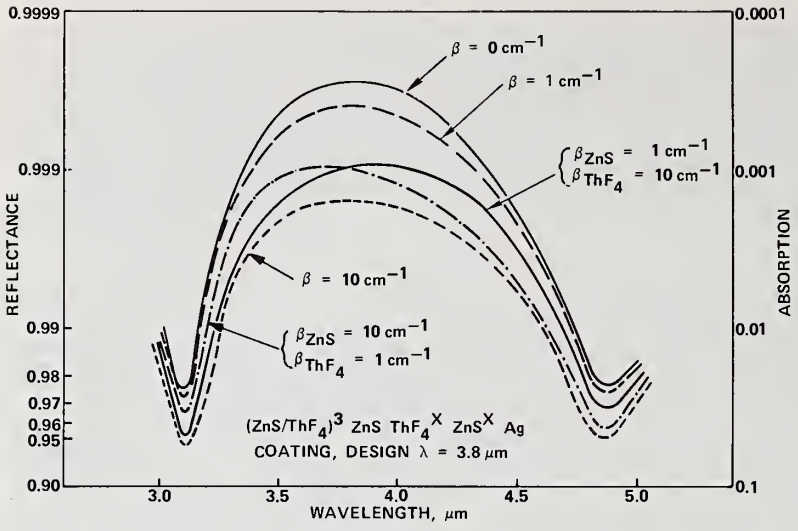

Figure 1. Calculated reflectance of a multilayer dielectric high-reflectance coating having the design $(ZnS/ThF_4)^3$-ZnS $ThF_4^X ZnS^X Ag$, where the x's refer to nonquarter-wave layer thicknesses. The volume absorption coefficients β of the various materials are as indicated. Layer thicknesses are assumed to be correct, and interface absorption is assumed to be negligible.

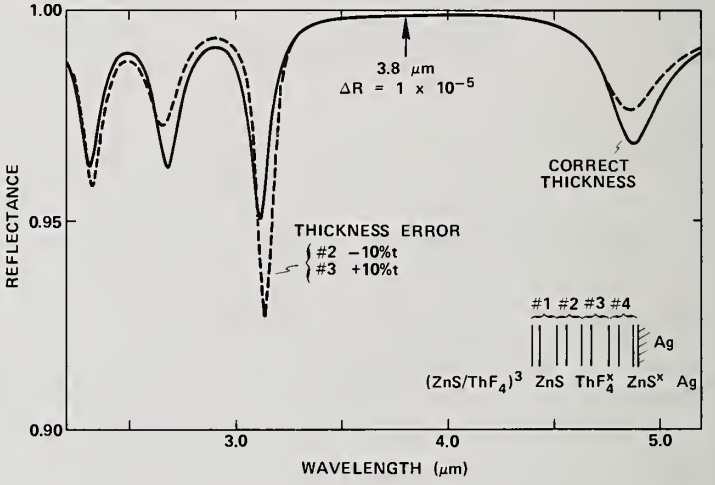

Figure 2. Effect on the secondary minima of an error in layer thickness in the #3 layer pair which was compensated for by a layer change in #2 layer pair. The decrease in peak reflectance caused by this compensated thickness error is negligible, only one part in 10^5, but the change in reflectance at the minima is significant. (After Kyser, NWC)

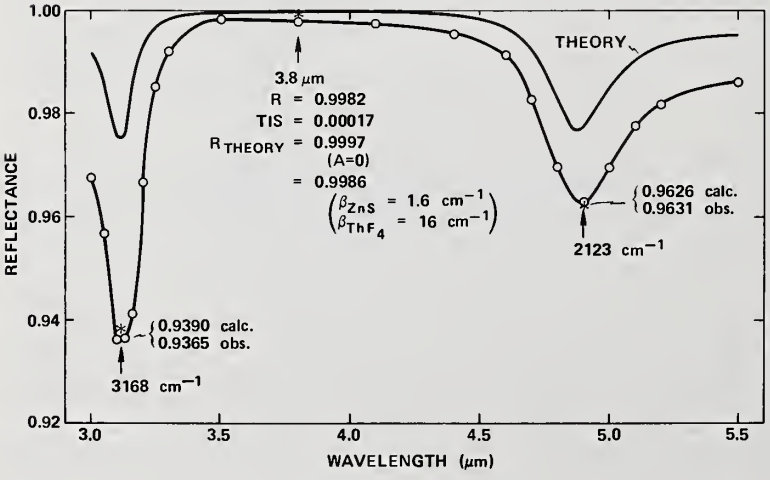

Figure 3. Spectral reflectance of a 3.8 μm multilayer coating on silver. The coating design is as given in the caption for figure 1. The upper curve gives the theoretical reflectance for no absorption in the films. The lower curve gives the measured reflectance. The calculated reflectance at 3.8 μm and at the secondary minima for $\beta_{ZnS} = 1.6$ cm^{-1} and $\beta_{ThF_4} = 16$ cm^{-1} are indicated by *'s. Agreement between these calculated values and the measured values is excellent.

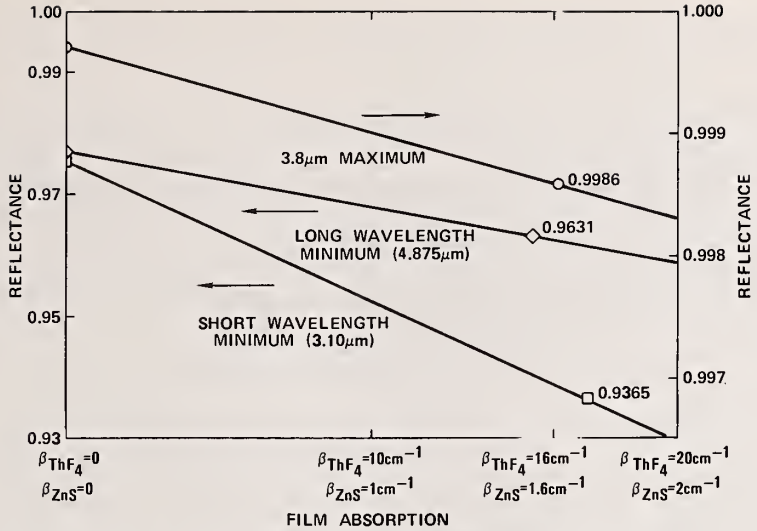

Figure 4. Extrapolation of reflectances at secondary minima for predicting reflectance at the primary maximum. The curves are linear extrapolations of the calculated reflectances at the extrema for various values of the film absorption coefficients β while maintaining the ratio of the β's at 10:1. The labeled points on the curves for the secondary minima are the experimental values for the coating shown in figure 3. These values would then predict the value of 0.9986 at the primary maximum.

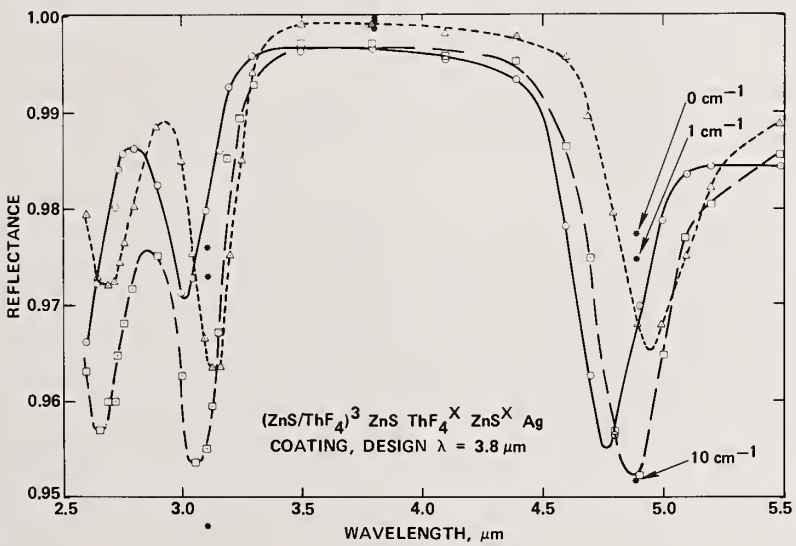

Figure 5. Measured spectral reflectances for three samples of the multilayer coating design studied. The *'s indicate predicted reflectances at the extrema for the labeled values of absorption coefficient. The same coefficient is assumed for both ZnS and ThF_4.

The usefulness of varying the very outside layer or the very inside layer of the multilayer to see its effect was suggested. The author agreed and pointed out that a shift in the depth of the minima did not uniquely identify a change in layer absorption since compensated thickness errors can cause the same effect. Another member of the audience commented that these effects are found in practice as well as theory.

Graded-index Antireflective Coatings for High Power Lasers Deposited by the Sol-Gel Process

W. Howard Lowdermilk*

Lawrence Livermore National Laboratory
P.O. Box 5508, L-465
Livermore, California 94550

and

Shyama P. Mukherjee

BATTELLE
Columbus Laboratories
505 King Avenue
Columbus, Ohio 43201

Gradient-index alkali borosilicate antireflection films for use in lase systems were deposited by the sol-gel process. Laser damage thresholds of these films, measured with 1.07μm, 1-ns pulses, were four times greater than thresholds of widely-used, multilayer, antireflection coatings.

Key words: Antireflection surface, sol-gel process, gradient index.

1. Introduction

Antireflection (AR) coatings are widely used in lasers to reduce reflection losses from surfaces of transmitting optical elements, such as lenses and windows. Typical coatings for high power lasers operating at visible and near-infrared wavelengths consist of two or more layers of materials with different refractive index, such as titania (TiO_2) and silica (SiO_2), which are deposited on the optical surface by physical vapor deposition (PVD). The output power level of the laser is usually limited by laser-induced damage to these coatings. It is, therefore, of practical importance to understand the causes of damage and to develop materials with improved damage resistance.

The morphology of laser damage to PVD coatings suggests that damage occurs initially at the interface between the coating and the substrate,[1] presumably due to a high concentration of absorbing impurities. Consequently, AR surface treatments which modify or eliminate this interface have been examined in recent years.[2] One particularly successful method produces low reflectivity over a broad spectral region by a combination leach and etch procedure. The procedure can be applied to glass of an appropriate composition such that heat treatment will induce phase separation on a microscope scale. The resulting broadband antireflectivity is attributed to the formation of a microporous, high-silica-content layer with graded index of refraction.[3,4] Optical quality glass with this property has been developed and provides reflectivity of 0.1 - 0.2 percent throughout the visible and near-infrared spectrum. In addition, the etched surfaces have median laser damage threshold of 12 J/cm^2 for 1-ns, 1.06-μm laser pulses compared to the median threshold of 5 J/cm^2 for PVD multilayer AR coatings.[5] However, the currently available glass cannot be used for UV wavelength laser pulses due to significant losses from two-photon absorption, solarization and scattering. There are, in addition, special application glasses, such as the Tb-doped phosphate glass (eg. Hoya FR-5) used for Faraday rotators in high power, Nd:glass lasers, which are not amenable to the phase-separation process.

We have developed a process to deposit single-layer, gradient-index AR films on glass of essentially any composition and other substrate materials. Layers of noncrystalline multicomponent inorganic oxide films are deposited by the sol-gel[6-10] process and subsequently phase separated and etched in a manner analogous to the earlier work on bulk phase-separated glass. The sol-gel process consists of polymerization of viscous liquid sol of alkoxysilane with other metal alkoxides or metal salts in alcoholic solutions to form a transparent elastic gel. The residual organic

*Work performed under the auspices of the U.S. Department of Energy by the Lawrence Livermore National Laboratory under Contract No. W-7405-ENG-48.

material is driven off by heating, leaving a microporous structure. The pores can often be eliminated by further heating (without melting) to form a glass-like material.

Use of the sol-gel process to prepare layers of individual and mixed oxides, such as SiO_2, and TiO_2, for various applications, including multilayer reflective and antireflective coatings was extensively reviewed by Schroeder.[10] Recently, Yoldas[11] used the porous nature of the initial film before densification to create a single-layer antireflective film of aluminum oxide on soda-lime glass. The porosity of the film reduced its effective index of refraction to the square root of the substrate's index thus forming a quarter-wave matching layer with minima and maxima of reflectivity at alternate quarter-wave intervals. The deposition of multicomponent borosilicate glass compositions by the sol-gel process was demonstrated by Dislich[7] and more recently by Brinker and Mukherjee.[12]

Our approach[13] for producing gradient-index AR films consists of:

(a) Deposition of multicomponent noncrystalline metal oxide gel films with a leachable phase(s) and appropriate microporosity.

(b) Removing the leachable phase(s) by an appropriate solution causing the pore morphology to change in a controlled way so that a gradient in refractive index develops.

2. Preparation of Films

We studied gel formation of the four compositions shown in table 1 in the Na_2O-SiO_2 and Na_2O-B_2O_3-SiO_2 systems. The first system was chosen to study the phase separation characteristics of gel-derived glasses in relation to the position of their composition in the liquid-liquid immiscibility zone. The miscibility gaps and the nature of microstructures resulting from phase separation of various composite glasses prepared from the molten oxide in the Na_2O-SiO_2 system are well-known.[14,15] The objective was to correlate the microstructures of the gel-derived glasses with those of the glasses obtained from the molten oxides. Composition NS1 lies at the center of the liquid-liquid immiscibility zone and Composition NS2 is near the edge of the immiscibility zone.[15] Glasses in the second system have more flexible and versatile physiochemical properties such as phase-separation behavior, thermal expansion and chemical durability. Moreover, the Corning glass Code 7740 which exhibited gradient-index antireflective surfaces is in this system. Composition of the 7740 glass is also given in table 1.

After some preliminary investigation, the first system was discontinued because it produced more cloudy and translucent films than those developed in the second system. Further investigations were continued with only the second system. The composition NBS2, with lower alkalioxide content, proved to be more stable, and would also presumably have the advantage of greater chemical durability due to its higher silica content.

Table 1. Composition in weight percent of sol-gel coatings and Corning 7740 glass.

	SiO_2	NaO_2	B_2O_3	Al_2O_3
NS1	88	12	--	--
NS2	95	5	--	--
NBS1	80	8	12	--
NBS2	84	4	12	--
7740	81	4	13	2

Two approaches for preparing stable, visibly transparent polymeric solutions in the Na_2O-B_2O_3-SiO_2 system were developed. The two approaches differed primarily in their choice of Na_2O source. In the first approach, the source of Na_2O was a methanolic solution of

sodium methylate; in the second approach the source of Na_2O was an aqueous solution of sodium acetate. Films discussed in this paper were prepared by the first approach.

The coating solution was prepared by mixing tetramethoxysilane with twice its volume of anhydrous ethanol at room temperature. The solution was heated to 40°C and water acidified with 1N HCl was added to partially hydrolyse the tetramethoxysilane. Seven volume percent of acetyl acetene was added and the solution stirred for 1 hour. Boric acid dissolved in anhydrous methanol was then added in sufficient quantity to raise the pH of the solution to four. Sodium methylate dissolved in anhydrous methanol was added and the solution stirred for 15 minutes. This stock solution had a metal oxide content of 0.17 gm/ml. The solution was further diluted with anhydrous ethanol to 0.04 gm/ml metal oxide before deposition of the coatings.

Test films were applied to Pyrex (Corning 7740), BK-7 borosilicate glass and fused silica. The substrates were cleaned[16] by a mild etch for 10 minutes in a one weight percent NaOH solution at 95°C followed by 2 minutes in 1N HCl at 50°C. The substrates were then rinsed with isopropanol and dried overnight at 150°C.

Films were deposited by dipping the substrates in the dilute polymeric solution. Substrates were suspended on a wire, totally immersed in the solution, and then withdrawn vertically at a rate of 5 cm/minute using a variable speed motor. Transparent gel films formed on the substrate when the solution was exposed to atmospheric moisture. We observed that aging the solution affected the transparency of the films. Films deposited 15 minutes after addition of the sodium methylate were somewhat cloudy, while films deposited from solutions aged two hours at room temperature remained transparent.

Thickness of the coatings was built up by multiple dipping. After each dipping, the deposited layer was allowed to dry in air for a minimum of 15 minutes. Substrates have been coated with ten layers without losing transparency. No systemmatic study has been made of the thickness of each layer or the densification of films at different temperatures. However, the thickness of two multi-layer films measured after drying at 150°C indicated that each dipping added a thickness of 325 Å.

The coated substrates were dried overnight in air under an infrared lamp at 80°C. They were then heated in a furnace, with temperature increasing at the rate of 3°C/minute, to various heat-treatment temperatures of 350-500°C.

After heat treatment, samples were leached in a 0.5 weight percent hydrofluoric acid solution or a solution of 0.6 weight percent sodium fluoride in 0.16N nitric acid for various times between 15 seconds and 10 minutes.

3. Film Microstructure

We examined the films with a scanning electron microsope (SEM) before and after etching. Before etching, no microstructure was observed in the films at magnification up to 90,000. However, distinct microstructural features were observed after mild etching. To illustrate the surface morphology, figure 1 shows photographs, at magnification of 90,000, of the etched surface of films heat treated at 350°C for 1.5 hours and 5 hours. These photographs show that increased heat treatment at 350°C coarsens the structure and also promotes sintering. The microstructures of films treated at other temperatures or prepared by other procedures are similar, but show slight differences that become more pronounced with longer heat treatment. Systematic studies are required to confirm and clarify the phenomena, but were outside the scope of this feasibility study. For comparison, the microstructure of Corning 7740 glass after phase separation and etching was examined and found to be qualitatively identical to the film in figure 1a. Surface scattering loss from that surface is typically 0.1 percent.

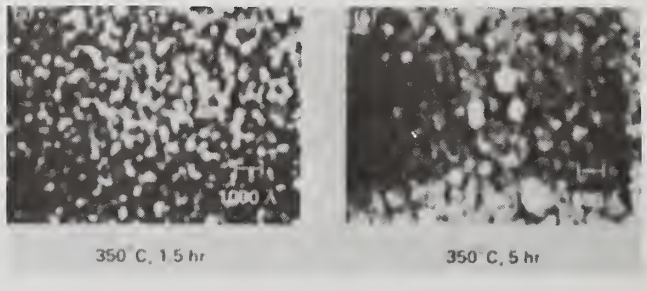

Figure 1. Scanning electron micrographs of films after heat treatment at 350°C for (a) 1.5 hours and (b) 5 hours and etch for 15 seconds in 0.5 percent HF solution. Length of bar is 1000 Å.

4. Reflectance Measurements

Reflectance at 1.06μm wavelength of films with various heat treatments and leaching conditions was measured using a Nd:YAG laser. The results are summarized in table 2. The reflectance values given in the table are the minimum values observed for the surface. Substantial variation over the surface was observed, with reflectance maxima typically of 2 percent.

Table 2. Reflectance of sol-gel films of composition NBS2 after etching in NH_4F/HNO_3 solution at 90°C.

Heat Treatment Temp (C)	Time(hr)	Leaching Time (sec)	Reflectance (percent)
350	1.5	15	0.27
350	5.5	15	0.33
500	1.5	15	0.67
500	5.5	15	0.20
350	1.5	30	0.33
350	5.5	30	0.13
500	1.5	30	0.23
500	5.5	30	0.13

5. Measurements of Damage Threshold

Measurments of laser damage threshold were made with 1-ns, 1.06-μm pulses from a Nd:glass laser. The laser was focused with a lens of 6-m focal length to a spot diameter of 2.5 mm on the surface of the sample. The energy of the pulse was measured by a calorimeter placed behind a 2.5-mm diameter aperture located in a focal plane equivalent to that of the sample surface. The spatial profile of the beam was recorded by a silicon vidicon, and computer analysis was used to determine the peak fluence of the profile with an accuracy of $\pm$ 10 percent.

Sites on the sample surface were irradiated, once each, at increasing fluence level until damage was observed. To detect threshold-level damage, each site was examined with a Nomarski microsope at magnification of 100. Comparison of photographs of the surface taken before and after irradiation allowed small changes in surface morphology to be reliably detected. The surfaces before irradiation were typically free of any defect visible in the Nomarski microscope. When there were visible defects such as pits or dust particles on the surface before irradiation, the damage occurred preferentially, but not exclusively, on those sites.

A typical photograph of a damaged site is shown in figure 2. Damage at fluence levels slightly above threshold consists of isolated pits, typically one micron in diameter, in the center of a 50-μm diameter spot, which is barely visible to the Nomarski microscope. These sites are randomly distributed over the irradiated area with a density of ~ 3-7 cm^{-2}. This morphology suggests that damage is the result of heating particulate impurites with submicron diameter to temperatures sufficient to cause stress fracture of the surrounding glassy material. Avalanche ionization initiated at the damage site by ejection of electrons from the fracture then creates a hot plasma at the surface which causes shallow damage over the surrounding area.

The distribution of damage thresholds measured on the 12 samples tested so far is shown in figure 3. Threshold values given are the midpoint between the lowest fluence which produced damage and the highest fluence which did not produce damage. The difference of these two numbers is twice the uncertainty of the assigned threshold value. This uncertainty, which includes both the experimental error of the measurement and the variation in threshold over the surface, was

typically ± 10 percent of the threshold value for the samples tested. The distribution of damage thresholds measured for a set of commercial, silica/titania PVD antireflection coatings is also given for comparison. The median threshold of the sol-gel coatings is 21 J/cm^2, while the median for the PVD coatings is 5 J/cm^2.

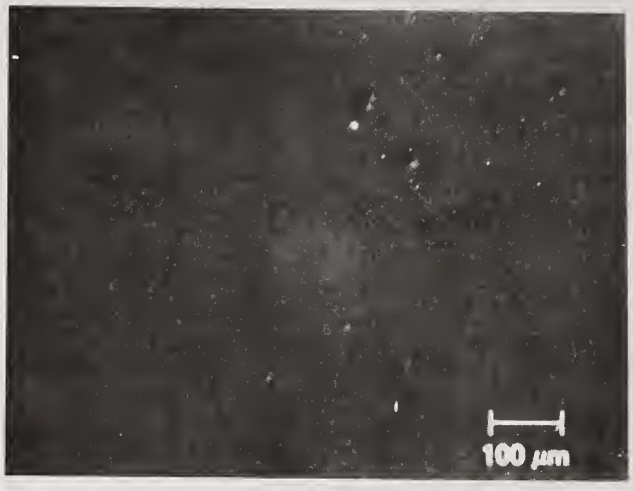

Figure 2. Morphology of surface damage observed with Nomarski microscope. Length of bar is 100μm.

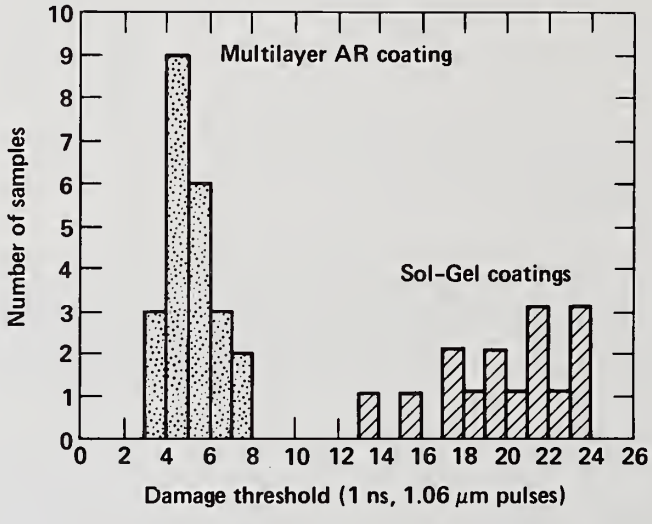

Figure 3. Distribution of damage thresholds for sol-gel coatings and commercial multilayer PVD antireflection coatings. Thresholds were measured with 1-ns, 1.06-μm pulses from a Nd-glass laser.

The higher damage threshold of sol-gel coatings and their ability to be deposited on a wide variety of laser and optical materials are important advantages for many high-power laser applications. The challenge of future development is to produce coatings with uniformly low reflectivity over the entire surface.

One of the authors (W. H. Lowdermilk) wishes to thank N. L. Boling, now with Optical Coating Laboratory, Inc., for introducing him to the potential of sol-gel coatings for applications to laser optics. Damage threshold measurements were made at LLNL by J. E. Swain and reflectance was measured at Battelle-Columbus by G. T. Ruck. The authors wish to acknowledge the laboratory assistance of E. J. Onesto of Battelle-Columbus for the deposition of gel films.

References

1 Lowdermilk, W. H.; Milam D. Laser-induced surface and coating damage. J. Quant. Electron. QE-17: 1888-1903; (1981).

2 Lowdermilk, W. H.; Milam, D.; Rainer, F. Damage to coatings and surfaces by 1.06μm pulses. NBS Special Publ. 568: 391-403; (October, 1979).

3 Minot, M. J. Single-layer gradient refractive index antireflection films effective from 0.35μ to 2.5μ. J. Opt. Soc. Am., 66: 515-519; (1976).

4 Elmer, T. H.; Martin, F. W. Antireflection films produced on alkali borosilicate by chemical treatments. Am. Cer. Soc. Bull. 58: 1092-1097; (1979).

5 Lowdermilk, W. H.; Milam, D. Graded-index antireflection surfaces for high-power laser applications. Appl. Phys. Lett. 36: 891-893; (1980).

6 Schroeder, H. Properties and applications of oxide layers deposited on glass from organic solutions. Opt. Acta. 9: 249-254; (1962).

7 Dislich, H. New routes to multicomponent oxide glasses. Angew. Chem. internal. edit. 10: 363-370; (1971).

8 Mukherjee, S. P.; Zarzycki, J.; Traverese, J. P. A comparative study of "gels" and oxide mixtures as starting materials for nucleation. J. Mat. Sci. 11: 341-355; (1976).

9 Mukherjee, S. P. Sol-gel processes in glass science and technology. J. Non-Cryst Solids 42: 477-488; (1980).

10 Schroeder, H. Oxide layers deposited from organic solutions. Physics of Thin Films, G. Hass and R. E. Thun, eds., (Academic, New York, 1969) Vol. 5., 87-141.

11 Yoldas, B. E. Investigation of porous oxides as an antireflective coating. Appl. Optics 19: 1425-1429; (1980).

12 Brinker, C. J.; Mukherjee, S. P. Comparisons of sol-gel-derived thin films with monoliths in a multicomponent silicate glass system. Thin Solid Films 77: 141-148; (1981).

13 Mukherjee, S. P. Gel-derived single-layer antireflection films with refractive index gradient. Thin Solid Films 81: L89-L90 (1981).

14 Porai-Koshits, E. A.; Averjanov, V. I. Primary and secondary phase separation of sodium silica glasses. J. Non-Cryst. Solids 1: 29-38 (1968).

15 Haller, W.; Blackburn, D. H.; Simmons, J. H. Miscibility gaps -- alkali-silicate binaries -- data and thermo dynamic intrepretation. J. Am. Soc. 57: 120-126 (1974).

16 Tichane, R. M. Cleaning processes for borosilicate glass. Am. Cer. Soc. Bull 42: 441-443 (1963).

"Does the coating exhibit the same characteristics as the Corning process gives in terms of broadband angle insensitivity and wavelength insensitivity?" The speaker replied that these parameters had not yet been measured in any detail. The microstructure obtained by the two processes is similar so that when the new process is finely optimized it should produce a very broadband antireflectivity. For the specific application in which they are interested they only need low reflectivity at particular wavelengths of interest.

A question was asked about the stress properties of the coating. The speaker replied that the coating stayed on the substrate, but he had no further stress information. The question was asked about operation at 500 nm. The speaker felt the coatings should work well. The process should work at any wavelength at which one could make transparent materials. A preliminary look has been made at scattering losses. They are not measureable in the apparatus at Livermore Laboratory. The structures are very thin, less than 0.5 μm thick, so scattering should be negligible.

The fragility of the surfaces and their environmental resistance, i.e., the possibility of the pores filling up with grease and dirt, was questioned. The speaker replied that the coatings themselves are fragile just as the Corning coatings are. They can be cleaned of grease and dirt, but it is difficult. For high power laser operations in a clean room environment there is no problem, but for solar panels, for example, they would probably not be satisfactory. The pores are small enough so that dust does not settle in them. A fingerprint will penetrate the coating. It can be cleaned off if done immediately, otherwise it cannot be cleaned off.

Selective and Uniform Laser-Induced Failure of Antireflection-Coated $LiNbO_3$ Surfaces*

S. C. Seitel, J. B. Franck, C. D. Marrs, J. H. Dancy, W. N. Faith

Michelson Laboratory, Physics Division
Naval Weapons Center, China Lake, California 93555

G. D. Williams

Crystal Technology Incorporated, Palo Alto, California 94303

$LiNbO_3$ surfaces with different antireflection coatings and from different vendors were damaged with 1.06-μm, 9.5-ns full width at half maximum laser pulses. By probing with a laser spot smaller than the separation of isolated surface defects, it was possible to separate uniform damage, which was characteristic of the coating itself, from premature, defect-driven, localized failures. Uniform failure modes were identified and thresholds extracted for each by multithreshold analysis. Frequency of defect damage was determined at several fluences much lower than required for uniform failure. It is likely that defect-driven selective failures reduce the apparent damage threshold of flood-loaded samples. Tentative identification of a selective damage threshold was made and correlated with large-spot, multimode test results. Incorporation of these results into a product-improvement program has resulted in $LiNbO_3$ Q-switches with increased resistance to selective damage.

Key words: antireflection coatings; defect frequency; Fast Waveform Analysis Device; $LiNbO_3$; multithreshold analysis; Short Pulse Laser Damage Facility.

Introduction

In a continuing product-improvement effort, quantitative small-spot laser damage testing at 1.06 μm has been performed on more than 20 antireflection (AR)-coated $LiNbO_3$ surfaces prepared by various methods. In work reported previously [1][1], the vendor [2] was able to modify coating parameters to produce samples with damage resistance improved by an order of magnitude. In that work, the damage threshold for a particular sample was taken as the incident intensity sufficient to alter the appearance of the coating with 50% probability. The values so obtained were strongly affected (lowered) by coating and substrate surface defects such as pits, inclusions, scratches, etc., which were visible on some, but not all, of the samples tested.

The impetus for the work reported in this paper was the perceived need to separate systematically those failures which clearly were defect-related from those which were not. Two benefits were expected. First, by rejecting such "selective" failures, "uniform" damage thresholds could be derived which would predict the performance of an idealized, defect-free sample. Such data is particularly useful when evaluating the potential of new coating designs or materials. Second, information about the nature and density of the defects themselves could be obtained, which would establish the susceptibility to defect-related damage of a particular real coating at the present state of its development and (possibly) suggest improvements in the production process.

In this paper, the uniform failure modes of six different AR-coated $LiNbO_3$ surfaces are described, and the corresponding threshold intensities are given. Criteria used to identify selective failures are discussed, and failure frequencies are presented for several intensities much lower than the uniform thresholds.

Sample Description and Preparation

Six $LiNbO_3$ samples, coated for minimum reflection at 1.06 μm, were tested, as shown in table 1. The nominal substrate dimensions were 9 mm x 9 mm x 25 mm, a standard Q-switch size. The first two columns identify each sample by an arbitrarily assigned reference label and by the supplier, respectively. The AR coatings provided by Crystal Technology were single quarter-wave layers of either SiO_2 or Al_2O_3, as shown in column 3. Two of these represent the currently available stock coatings,

*Work supported by Naval Weapons Center Independent Research funds.
[1]Numbers in brackets indicate the literature references at the end of the paper.

while two were prepared by a new process designed to improve coating uniformity and reduce defect count. The "new process" coatings are so labeled in the last column. The samples from Union Carbide were older crystals for which coating data was not readily available, and so composition and thickness were determined by sputter-etch Auger profiling [3]. The notation in the table indicates that these coatings are incomplete single layers of thorium fluoride containing approximately 25% oxygen. These may or may not be representative of currently available stock.

Table 1. Samples tested

Sample	Supplier	Coating	Type
A-1	Crystal Technology	SiO_2	Stock
A-2	Crystal Technology	Al_2O_3	Stock
A-3	Crystal Technology	Al_2O_3	New process
B-4	Union Carbide	$ThF_{4-x}O_x$	Stock?
B-5	Union Carbide	$ThF_{4-x}O_x$	Stock?
A-6	Crystal Technology	SiO_2	New process

Lithium niobate Q-switches are notorious for attracting dust in an ordinary "clean" laboratory atmosphere [1]. It was necessary to prepare the samples just before testing using a standard procedure. The surface was dusted with a pressurized stream of dry N_2, rinsed with pure isopropyl alcohol, and dried by drag-wiping with a lens tissue. The procedure was repeated until the surface appeared featureless when examined at near-grazing incidence under strong white-light illumination. This preparation method effectively controlled dust accumulation while minimizing the risk of surface scratching.

Experimental Arrangement

Laser damage tests were performed in the Short Pulse Laser Damage Facility, shown schematically in figure 1. The laser source (L1) was a commercial Q-switched Nd:YAG device modified to operate in the TEM_{00} spatial mode. The temporal pulse waveform was nominally Gaussian with a duration of 9.5 ± 0.5 ns full width at half maximum (FWHM). The operating wavelength was 1.06 μm.

Radiation was attenuated to the approximate level desired with precision filters (F) and then fine-tuned with a pair of Glan-laser prisms (P,A) arranged in a rotatable-polarizer/fixed-analyzer configuration. A best-form lens (L) was used to focus the beam on the surface of the test sample. The path length, and thus the spot size, was adjusted by means of a movable mirror M. In this case, the focal spot diameter was 52 ± 2 μm, measured to e^{-2} times the peak intensity. The sample also was illuminated with a coaxial helium-neon visible laser (L2). Subtle surface changes induced by the pulsed 1.06-μm radiation were easily detected as changes in visible scatter by means of a 20X observation microscope focused on the target site.

Radiation incident on the test surface was sampled with a beam splitter (S) and detected with a fast photodiode (D-1), while the transmitted signal was monitored with a second diode (D-2). The detector outputs were analyzed with the Fast Waveform Analysis Device (FWAD). The FWAD is shown in more detail in figure 2. Fast transient digitizers (TWD-1,-2) captured and stored the incident and transmitted waveforms for display and subsequent analysis by the computer (MC). Direct computation yielded pulse peak power, total energy, duration (FWHM), and shape factor. The diodes were calibrated *in situ* by comparing the integrated incident pulse waveform to the total pulse energy as measured with a calibrated Scientech disc calorimeter.

Uniform Damage Measurements

Single-pulse, small-spot, laser-induced failure intensities were determined for each sample by the multithreshold technique developed by Porteus [4]. Approximately 50 separate sites were irradiated, one pulse per site. The axial peak intensities were distributed uniformly over a range including the anticipated failure level. Each site was observed with the 20X microscope during irradiation, and occurrence of light emission (flash) or visible surface change was noted. The sites were then examined with a high-resolution phase contrast microscope to identify and characterize permanent surface changes. Finally, the threshold intensity for each damage type was estimated by maximum likelihood analysis [4].

A few sites failed at intensities which seemed unreasonably low. This damage almost invariably was associated with a pre-existing surface defect, or else was of a massive nature inconsistent with the low incident intensity. Occasionally, pitting occurred well away from the point of maximum intensity in the irradiated region. These selective sites were not felt to be characteristic of the coated surface as a whole and were ignored in the multithreshold analysis. Thus, the thresholds derived are best interpreted as representing the ultimate potential in the absence of defects.

Multithreshold analysis results are contained in table 2. Here a "threshold" value is the maximum likelihood estimate of the single-pulse peak intensity required to cause damage with a probability of 50%. The standard deviations estimate the combined effects of experimental uncertainty and sample surface variability. For these samples, the major contribution comes from gradual variations in surface properties.

Table 2. Uniform damage thresholds.

Sample	Erosion (GW/cm^2)	Flow (GW/cm^2)	Etch (GW/cm^2)	Flash (GW/cm^2)	Perforation (GW/cm^2)
A-1	12 ± 2	12 ± 2	12 ± 2	12 ± 2	12 ± 2
A-2	12 ± 3	12 ± 3	12 ± 3	12 ± 3	12 ± 3
A-3	7.1 ± 0.7	7.1 ± 0.7	7.1 ± 0.7	7.1 ± 0.7	12 ± 4
B-4	5.1 ± 0.9	5.1 ± 0.9	5.1 ± 0.9	5.1 ± 0.9	8.6 ± 0.8
B-5	2.2 ± 0.9	2.6 ± 0.7	2.7 ± 0.6	2.6 ± 0.7	4 ± 1
A-6	2.3 ± 0.4	2.2 ± 0.1	3.9 ± 0.4	3.9 ± 0.4	3.9 ± 0.4

Five failure modes were found to be common to all samples tested, a somewhat surprising result in view of the sample diversity. Figure 3 is a micrograph of a failure site which was exposed well above threshold. Perforation and flow of the coating material clearly are evident. The "etched"-appearing region surrounding the central perforation was only observed in conjunction with light emission and is taken as evidence of surface plasma formation. Not visible in this example, but observed at lower intensities, was a very subtle surface degradation corresponding to a softened state which appeared as a slight roughening. This effect, referred to below as "erosion", was the first (i.e., lowest intensity) observed permanent surface change. Erosion and flow, together, bracket the melting point of the coating. Past experience with $LiNbO_3$ has shown that highly stressed or poorly bonded coatings fail first by cracking or delamination at the interface rather than by melting. Since no evidence for delamination or cracking was observed here, it appears that volume absorption in the coatings, with resultant melting, presently limits performance.

Table 2 lists the samples in order of decreasing flow threshold. Since flow is an easily observed indicator of melting, it often is taken as the sole figure of merit when comparing the relative damage resistance of dielectric-coated surfaces. For these samples, the flow threshold varied by almost a factor of six. Too much emphasis must not be given this conventional ranking, however, since only one sample of each type from Crystal Technology was tested; thus, it was not possible to verify sample-to-sample consistency. In this context, too, it is important to note that Crystal Technology provided virgin samples for this study; whereas, the Union Carbide samples had been used previously as Q-switches and, therefore, had been exposed repeatedly to high-intensity laser radiation over the full aperture. While no observable laser-induced damage existed on the surfaces tested, as verified by 360X microscopic examination, the possibility of submicroscopic damage or multiple-pulse surface preconditioning effects must not be discounted.

Proceeding with these caveats in mind, table 2 shows that the stock SiO_2 (A-1) and Al_2O_3 (A-2) coatings had the highest flow thresholds, about 12 GW/cm^2. Although flow frequently was observed without perforation on both samples, it was not possible to distinguish between the corresponding threshold intensities primarily because of the substantial surface variability. Correlation of failure data with position on the surface revealed a tendency for the Al_2O_3 coating to damage more readily along one edge. This may be due to a gradual change in coating thickness. The data were not sufficient to indicate whether the variation of the SiO_2 coating also was systematic.

The experimental coatings (A-3, A-6) had lower flow thresholds than their stock counterparts. This result, while disappointing, was not unexpected, since optimum deposition parameters are still to be determined for the new process. However, a significant reduction in coating variability was achieved, as indicated by the relatively smaller error bars in the table. This indicates that the experimental coatings are indeed more uniform than the stock coatings.

The nominally identical thorium fluoride samples B-4 and B-5 differed in threshold by about a factor of two. This may be due to unknown differences in prior history, as discussed above. It also may be related to a 30% difference in coating thickness, estimated from the sputtering rate and penetration time.

Selective Damage Measurements

It has long been appreciated that isolated defects play an important role in determining the laser-induced failure threshold of optical surfaces, as evidenced by many papers presented at this conference in previous years. Some recent examples are given [5-7]. Activation of localized, isolated initiation sites has been invoked to explain the apparent decrease in threshold with increasing spot size observed by some [8] (but not all [9]) researchers. A simple "probability of overlap"

model [8] suggests that by exposing many sites with a low-intensity laser spot smaller than the average separation of defects, it is possible to obtain information on defect size and density.

The frequency of premature failure as a function of intensity was evaluated for each sample as follows. The laser intensity was reduced to the desired value, below threshold, and 50 to 100 sites each were exposed to a single pulse. Those which (1) flashed, (2) caused a change in the scattering of the visible beam, or (3) changed appearance in the on-line microscope were further examined at high magnification for association with pre-existing defects. The process was then repeated at a different intensity as often as required to generate the desired curve. This process is an extension of the simple mapping technique reported for diamond-turned Cu mirrors [10].

Four of the samples tested (A-2, B-4, B-5, A-6) exhibited failure rates entirely consistent with a uniform damage mechanism. The data are plotted in figure 4. On the abscissa, incident intensity is measured from the observed flow threshold and is expressed in units of the corresponding standard deviation. By scaling the data in this way, samples with very different thresholds may be compared. The ordinate is the percentage of sites which failed. The solid line is the cumulative normal distribution, which would be the expected result if a normal distribution of coating variations about some mean were the dominant source of measurement uncertainty. The fit to the data is not perfect, presumably because the actual distribution function is skewed, but the essential trend is clear. The damage frequency falls rapidly with decreasing intensity to about 3% at three standard deviations below threshold. For purposes of comparing these samples, the flow threshold is a reasonable measure of coating performance.

In contrast, two samples (A-1, A-3) exhibited very different behavior, as shown in figure 5. Here are plotted the frequencies for only those failures which clearly were associated with pre-existing defects of the types described. At three standard deviations below threshold, both samples had failure rates of about 22%. The general trend in the data (dashed line) suggests that a 3% failure rate would occur at about six or seven standard deviations below threshold. For these samples, the uniform flow threshold alone is not a reliable predictor of overall coating performance.

The essential point demonstrated here is that while a standard small-spot damage threshold measurement can (1) provide valuable insight into uniform failure mechanisms and (2) possibly reveal the potential damage resistance of a coating, it should be supplemented with low-intensity damage frequency measurements when defects are known or suspected to be present. The test intensity should be chosen low enough that the uniform failure rate is small, but not so low that selective events are very rare. The limited data presented here suggest that a test intensity three or four standard deviations below uniform failure is appropriate.

In table 3, the uniform failure level is compared to the damage frequency three standard deviations lower in intensity. The samples are arranged by decreasing flow threshold in the conventional comparison. The first- and third-ranked samples were the ones plagued by defect-driven failures. The last column gives the approximate intensity at which a 3% failure rate was observed (or is expected!). If this were the criterion used to rank the samples, the ordering would be very different. In particular, the top-ranked stock SiO_2 sample A-1 would then be listed last because of its susceptibility to selective failure, while the stock Al_2O_3 sample A-2 would not be affected. The new process coatings A-3 and A-6 would be ranked about equally.

Table 3. Comparison of uniform and selective failure

Sample	Flow threshold[a]	Defect frequency[b]	Selective threshold[a]
A-1	12 ± 2	0.22	$\lesssim$ 0.1
A-2	12 ± 3	0.03	3.0
A-3	7.1 ± 0.7	0.22	2.2
B-4	5.1 ± 0.9	0.03	2.4
B-5	2.6 ± 0.7	0.03	0.5
A-6	2.2 ± 0.1	0.03[c]	1.9[c]

[a] In GW/cm^2
[b] At three standard deviations below flow
[c] Limited data

It is tempting to identify this "selective threshold" as a valid predictor of large-spot damage resistance. Some support for this notion is provided by recent qualification tests performed on Crystal Technology Q-switches [11]. In these large-spot, multimode tests, the stock SiO_2 coatings consistently failed at intensities at least a factor of two lower than did the stock Al_2O_3 coatings. In contrast, the new process Al_2O_3 and SiO_2 coatings failed at essentially the same intensity.

Conclusion

In evaluating new coating designs, it is important to obtain information about the potential performance, as well as about current performance-limiting factors such as isolated surface defects. For the $LiNbO_3$ samples tested here, small-spot laser damage tests were used to separate premature, defect-related, "selective" failures from those which were characteristic of the "uniform" or non-defective portions of the coating. By measuring the frequency of failure at an intensity three standard deviations (or more) below the uniform flow threshold, it was possible to identify and compare those coatings with unusually high defect densities. Three criteria were used to verify the selective nature of a low intensity failure: (1) clear evidence of association with pre-existing surface defects (pits, scratches, etc.); (2) massive damage not consistent with the low intensity; or (3) minor damage occurring well away from the point of maximum intensity. Finally, a tentative identification was made of a "selective threshold" which may prove useful in predicting large-spot damage resistance from small-spot test results.

References

[1] Soileau, M. J. Laser-induced damage in antireflection coatings for $LiNbO_3$ crystals. Bennett, H. E.; Glass, A. J.; Guenther, A. H.; Newnam, B. E., ed. Proceedings of the 12th annual symposium on optical materials for high power lasers; 1980 September 30-October 1; Boulder, CO. Nat. Bur. Stand. (U.S.) Spec. Publ. 620; 1981 October. 300-304.

[2] Crystal Technology, Inc., 1051 E. Meadow Circle, Palo Alto, CA 94303.

[3] Auger measurements were made by A. K. Green, Naval Weapons Center.

[4] Porteus, J. O.; Jernigan, J. L.; Faith, W. N. Multithreshold measurements and analysis of pulsed laser damage on optical surfaces. Glass, A. J.; Guenther, A. H., ed. Proceedings of the 9th annual symposium on optical materials for high power lasers; 1977 October 4-6; Boulder, CO. Nat. Bur. Stand. (U.S.) Spec. Publ. 509; 1977 December. 507-515.

[5] Lowdermilk, W. H.; Milam, D.; Rainer, F. Damage to coatings and surfaces by 1.06 μm pulses. Bennett, H. E.; Glass, A. J.; Guenther, A. H.; Newnam, B. E., ed. Proceedings of the 11th annual symposium on optical materials for high power lasers; 1979 October 30-31; Boulder, CO. Nat. Bur. Stand. (U.S.) Spec. Publ. 568; 1980 July. 391-403.

[6] Walker, T. W.; Guenther, A. H.; Fry, C. G.; Nielson, P. Pulsed damage thresholds of fluoride and oxide thin films from 0.26 μm to 1.06 μm. Op. cit., 405-416.

[7] Carniglia, C. K.; Apfel, J. H.; Allen, T. H.; Tuttle, T. A.; Lowdermilk, W. H.; Milam, D.; Rainer, F. Op. cit., 377-390.

[8] DeShazer, L. G.; Newnam, B. E.; Leung, K. M. The role of coating defects in laser-induced damage to thin films. Glass, A. J.; Guenther, A. H., ed. Proceedings of the 5th annual symposium on optical materials for high power lasers; 1973 May 15-16; Boulder, CO. Nat. Bur. Stand. (U.S.) Spec. Publ. 387; 1977 December. 114-123.

[9] Wiggins, T. A.; Walker, T. W.; Guenther, A. H. A novel technique for investigating impurity initiated short pulse laser damage in thin films. Bennett, H. E.; Glass, A. J.; Guenther, A. H.; Newnam, B. E., ed. Proceedings of the 12th annual symposium on optical materials for high power lasers; 1980 September 30-1 October; Boulder, CO. Nat. Bur. Stand. (U.S.) Spec. Publ. 620; 1981 October. 277-286.

[10] Porteus, J. O.; Decker, D. L.; Seitel, S. C.; Soileau, M. J. Dependence of metal mirror damage thresholds on wavelength, material, pulse length, and preparation method. Op. cit., 201-209.

[11] Qualification testing was performed at the Hughes Aircraft Company, 2000 E. El Segundo Blvd., El Segundo, CA 90245.

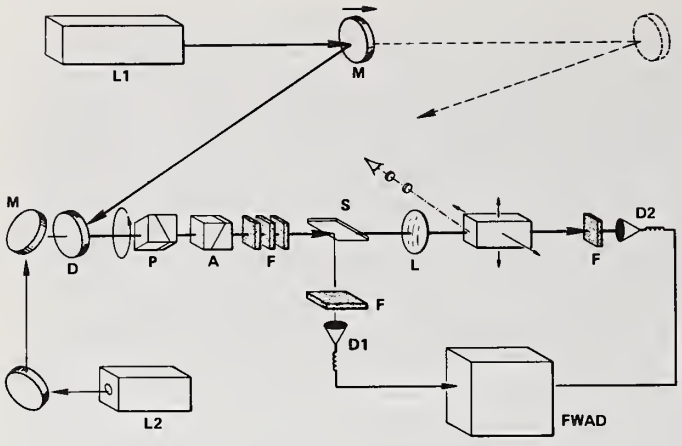

Figure 1. Short Pulse Laser Damage Facility.

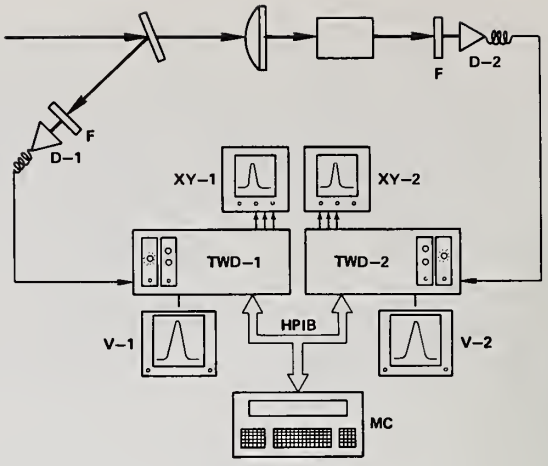

Figure 2. Fast Waveform Analysis Device.

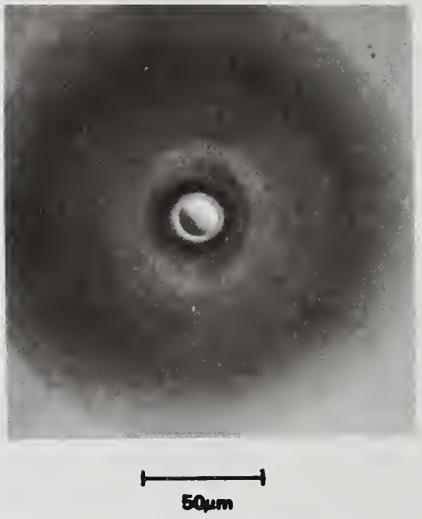

Figure 3. Typical uniform damage site.

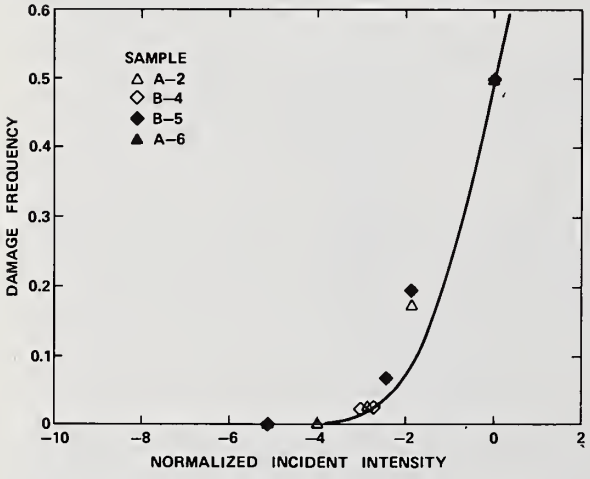

Figure 4. Damage frequency versus normalized intensity for samples exhibiting essentially uniform failure characteristics.

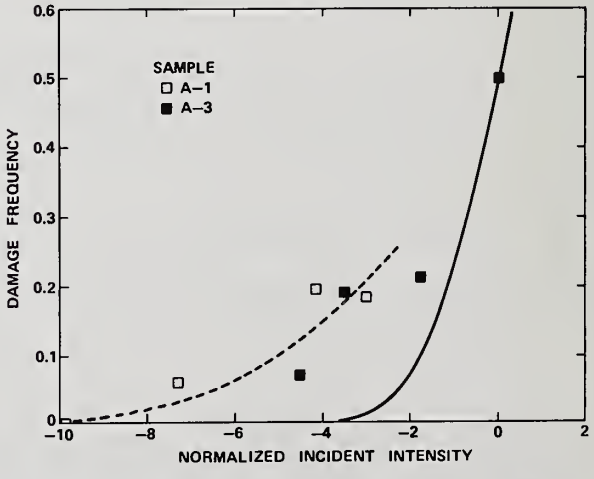

Figure 5. Damage frequency versus normalized intensity for samples exhibiting essentially selective failure characteristics.

The use of a 52 μm laser spot size was questioned. Was it an adequate size to sample over the defects? The speaker replied that the spot size was not intended to be large enough to sample over the defects but gave a preliminary indication of those coatings clearly plagued by defects. To characterize the defect distribution in the coating one should measure the threshold as a function of spot size. The questioner pointed out that if a large enough spot size were used a very definitive damage threshold would be obtained. The speaker agreed but pointed out that by using the small spot size it was possible to determine what the potential damage threshold of the coating is; whereas with large spot size measurements, one can only learn what the present performance is. The object of the technique described in the paper was to develop a product improvement approach, not a life testing or "where is it going to fail?" approach.

The cleaning procedure used was before each test to flush the samples with clean isopropyl alcohol and dry with a single drag wipe of a Kodak lens tissue. There were a few sites which failed at scratches which may have been produced by this cleaning procedure, but these were excluded from the data.

A Review of 1064-nm Damage Tests of Electron-Beam Deposited Ta_2O_5/SiO_2 Antireflection Coatings

D. Milam, F. Rainer, W. H. Lowdermilk and J. Swain*

Lawrence Livermore National Laboratories
P.O. Box 5508, L-470
Livermore, California 94550

and

C. K. Carniglia and Trudy Tuttle Hart

Optical Coating Laboratory, Inc.
P.O. Box 1599
Santa Rosa, California 95402

Damage tests of Ta_2O_5/SiO_2 antireflection films deposited under a variety of conditions showed that thresholds of films deposited at 175 C were greater than thresholds of films deposited at either 250 C or 325 C. Deposition at high rate and low oxygen pressure produced highly absorptive films with low thresholds. Thresholds did not correlate with film reflectivity or net stress in the films, and correlated with film absorption only when the film absorption was greater than 10^4 ppm. Baking the films for four hours at 400 C reduced film absorption, altered net film stress, and produced an increase in the average damage threshold.

Key words: tantalum oxide, silicon dioxide, antireflection films, laser damage, net stress, film absorption, variations in film deposition parameters.

1. Introduction

This study was conducted to determine the influence of deposition parameters on laser damage thresholds of silica/tantala antireflection (AR) coatings, and to determine what, if any, correlation exists between damage threshold and 1) the substrate material and the method of substrate polishing, 2) the net film stress, 3) the average absorption of the film, and 4) the reflectivity of the film.

2. Samples

The samples were four-layer silica/tantala AR films deposited by electron-beam evaporaton. An undercoat[1] layer of silica with an optical thickness of a halfwave at 1064-nm was deposited between the AR film and the substrate.

Three sets of coatings were produced. The first set (A) of coatings was deposited in separate runs under each of eighteen different deposition conditions corresponding to the unique combinations of three deposition temperatures (175 C, 250 C and 325 C), three values of oxygen pressure during the deposition of the tantala layers (0.5×10^{-4}, 1.0×10^{-4} and 2.0×10^{-4} Torr) and two rates of deposition (1.5 Å/sec and 5 Å/sec). In each run, coatings were deposited on two fused silica substrates to be used for damage samples, and on thin fused silica substrates to be used in measurements of coating stress and absorption. These eighteen runs were then repeated to provide information on the reproducibility of the results. These repeat samples constitute the second set (B) of coatings.

The third set (C) of samples was fabricated after damage tests of coatings in sets A and B indicated that the optimum deposition parameters were a substrate temperature of 175 C, an oxygen pressure of 1×10^{-4} Torr, and a rate of 1.5 Å/sec. Using these deposition parameters, three additional coating runs were made. In each of these runs, coatings were deposited onto two conventionally polished fused silica substrates, two conventionally polished BK-7 glass substrates, and two bowl-feed polished BK-7 substrates.

Substrates were made of Suprasil II fused silica (a product of Amersil, Inc.) or PH-3 quality BK-7 glass. Bowl-feed polishing was done by Optical Coating Laboratory, Inc. In the bowl-feed

*Work performed under the auspices of the U.S. Department of Energy by Lawrence Livermore National Laboratory under Contract No. W-7405-ENG-48.

process, the slurry is recirculated and breaks into successively finer particles.[2] Details of the process are proprietary and may vary among vendors. Conventional polishing was done by Zygo, Inc., using standard fresh-feed procedures specified by LLNL for high power laser components.

3. Data and Discussion

Laser-damage thresholds were measured[3] with 1-ns, 1064-nm pulses focused to provide an approximately Gaussian beam which was 2.5 mm in diameter at the sample surface. Each test site on a sample was irradiated once. The sites were examined and photographed before and after irradiation, using a Nomarski microscope at a magnification of 100 X. Damage was defined to be any permanent alteration of the surface that was detectable by the Nomarski inspection.

For each shot, we recorded the beam profile and the pulse energy, and computed the peak on-axis fluence. Threshold was defined to be midway between the lowest fluence that caused damage and the highest fluence that caused no damage.

Damage thresholds for samples in sets A and B are shown in Table 1. Films deposited at 175 C had thresholds that were generally greater than thresholds of films deposited at 250 C or 325 C. The films with the lowest thresholds were those deposited at the greatest rate (5 Å/sec) and lowest oxygen pressure (0.5×10^{-4} Torr).

Table 1.

Damage Thresholds (1-ns, 1064-nm) of Ta_2O_5/SiO_2 AR coatings with $\lambda/2$ SiO_2 undercoats deposited onto bowl-feed polished fused silica at three substrate temperatures, three oxygen pressures, and two deposition rates.

Deposition Rate (Å/s)	O_2 Pressure $\times 10^{-4}$ Torr	Substrate Temperature of 175 C		Substrate Temperature of 250 C		Substrate Temperature of 325 C	
		Sample*	Threshold (J/cm^2)	Sample	Threshold (J/cm^2)	Sample	Threshold (J/cm^2)
1.5	0.5	A-1a	13.0 ± 3.0	A-4a	7.1 ± 0.7	A-7a	6.6 ± 0.7
	"	A-1b	9.6 ± 1.0	A-4b	6.6 ± 1.0	A-7b	6.8 ± 1.0
	"	B-1	9.0 ± 1.4	B-4	5.7 ± 1.3	B-7	3.5 ± 0.4
"	1.0	A-2a	18.7 ± 1.9	A-5a	6.9 ± 0.7	A-8a	4.7 ± 0.5
	"	A-2b	14.9 ± 1.5	A-5b	8.0 ± 0.8	A-8b	8.1 ± 0.8
	"	B-2	10.3 ± 1.0	B-5	6.1 ± 1.4	B-8	6.3 ± 0.7
"	2.0	A-3a	12.9 ± 1.4	A-6a	6.7 ± 0.7	A-9a	6.6 ± 0.7
	"	A-3b	9.5 ± 1.5	A-6b	11.0 ± 1.1	A-9b	- -
	"	B-3	11.1 ± 1.2	B-6	7.3 ± 0.9	B-9	5.8 ± 0.9
5.0	0.5	A-10a	7.1 ± 0.8	A-13a	2.2 ± 0.3	A-16a	1.8 ± 0.6
	"	A-10b	6.8 ± 0.9	A-13b	3.0 ± 0.4	A-16b	- -
	"	B-10	4.9 ± 1.3	B-13	6.0 ± 0.6	B-16	3.9 ± 0.5
"	1.0	A-11a	6.7 ± 1.0	A-14a	5.3 ± 0.5	A-17a	5.4 ± 0.7
	"	A-11b	6.9 ± 0.7	A-14a	8.0 ± 0.8	A-17b	5.5 ± 0.6
	"	B-11	9.0 ± 1.0	B-13	6.9 ± 0.9	B-17	5.9 ± 0.8
"	2.0	A-12a	11.3 ± 1.1	A-15a	9.5 ± 1.4	A-18a	6.5 ± 0.6
	"	A-12b	9.3 ± 1.2	A-15b	8.5 ± 0.8	A-18b	6.4 ± 0.6
	"	B-12	5.5 ± 1.0	B-15	5.1 ± 0.5	B-18	5.5 ± 0.8

*Samples are designated by a symbol which indicates the coating set (A or B), the particular coating run (1 through 18), and an additional designator (a or b) to distinguish two parts made in a single coating run.

Thresholds for samples in set C are given in Table 2 and summarized in Table 3. For both fused silica and BK-7 substrates, thresholds were greatest for films deposited on bowl-feed-polished surfaces.[4]

Table 2

Damage thresholds (1-ns, 1064-nm) of Ta_2O_5/SiO_2 AR coatings with $\lambda/2$ SiO_2 undercoats deposited on three types of substrates at T = 175 C, Rate = 1.5 Å/sec, and O_2 pressure = 1.0 x 10^{-4} torr. Eighteen coatings were made in three separate runs.

Sample*	Substrate Material	Substrate Polish	Damage Threshold (J/cm^2)
C1-a	fused silica	conventional	9.2 ± 0.9
C1-b	"	"	6.8 ± 1.3
C1-c	BK-7	"	5.5 ± 0.9
C1-d	"	"	8.5 ± 1.2
C1-e	"	bowl feed	6.3 ± 0.6
C1-f	"	"	9.0 ± 1.0
C2-a	fused silica	conventional	5.8 ± 1.0
C2-b	"	"	3.7 ± 0.6
C2-c	BK-7	"	7.0 ± 0.8
C2-d	"	"	5.8 ± 0.6
C2-e	"	bowl feed	10.2 ± 1.0
C2-f	"	"	13.1 ± 1.3
C3-a	fused silica	conventional	9.4 ± 1.0
C3-b	"	"	11.4 ± 1.2
C3-c	BK-7	"	6.0 ± 0.8
C3-d	"	"	7.7 ± 0.8
C3-e	"	bowl feed	7.7 ± 0.8
C3-f	"	"	11.3 ± 1.2

*Sample designation indicates the coating run (C1, C2 or C3) and the particular substrate (a-f).

Table 3.

Summary of damage threshold data (1-ns, 1064-nm) for Ta_2O_5/SiO_2 AR coatings with $\lambda/2$ SiO_2 undercoats deposited on four types of surfaces. (T = 175 C, rate = 1.5 Å/sec, O_2 pressure = 1 x 10^{-4} Torr)

Material	Polish	Number of Samples	Median Threshold (J/cm^2)	Range of Observed Thresholds (J/cm^2)
fused silica	bowl-feed	3	14.9	10.3 - 18.7
BK-7	"	6	9.6	6.3 - 13.1
fused silica	conventional	6	8.0	3.7 - 11.4
BK-7	"	6	6.5	5.5 - 8.5

The absorption and net stress of the films in sets A and B were determined by measurements made on thin witness samples that were coated in each run. Film absorption was measured by laser calorimetry.[5] Net stress was determined by using a Fizeau interferometer to measure stress-induced deformation[6] of the witness. Measured values of stress and absorption are given in Table 4.

Absorption was largest for films deposited at the higher rate and at low oxygen pressure, which suggests that the absorption was due to incomplete oxidation of the film materials. Net stress was greater in films deposited at 175 C than in films deposited at either 250 C or 325 C, but not strongly dependent on either deposition rate or oxygen pressure.

Table 4.

Coating absorption and net coating stress measured from witness samples coated in the eighteen coating runs comprising set A.

Deposition Rate (Å/sec)	Substrate Temperature (C)	O_2 Pressure ($\times 10^{-4}$) Torr	Absorption (ppm) Set A	Absorption (ppm) Set B	Net Stress (KPSI) Set A	Net Stress (KPSI) Set B
1.5	175	0.5	100	67	50	46
"	"	1.0	365	166	49	48
"	"	2.0	91	79	34	44
"	250	0.5	573	88	48	45
"	"	1.0	54	41	48	45
"	"	2.0	27	46	37	41
"	325	0.5	308	1770	37	47
"	"	1.0	38	22	38	40
"	"	2.0	26	29	-	46
5.0	175	0.5	2770	547	53	61
"	"	1.0	1730	1030	53	62
"	"	2.0	2180	1390	53	57
"	250	0.5	9450	4620	-	52
"	"	1.0	294	898	47	47
"	"	2.0	2240	46	49	48
"	325	0.5	23000	2300	26	25
"	"	1.0	39	44	39	-
"	"	2.0	27	692	49	44

Table 5.

Damage thresholds (1-ns, 1064-nm), net stress and absorption for fourteen Ta_2O_5/SiO_2 AR coatings measured before and after the coatings were baked in air for four hours at 400 C.

Sample*	Rate (Å/sec)	Deposition Temp (C)	O_2 Pressure ($\times 10^{-4}$ Torr)	Thresholds (J/cm^2) pre-bake	Thresholds (J/cm^2) baked	Net Stress*(KPSI) pre-bake	Net Stress*(KPSI) baked	Absorption (ppm) pre-bake	Absorption (ppm) baked
A-1a	1.5	175	0.5	13.0±3.0	17.4±2.0	50	-12	100	16
A-3a	"	"	2.0	12.9±1.4	20.1±2.0	34	- 1	91	20
A-4a	"	250	0.5	7.1±0.7	4.7±0.5	48	-16	573	22
A-5a	"	"	1.0	6.9±0.7	7.6±0.8	48	-13	54	22
A-6a	"	"	2.0	6.7±0.7	12.7±1.8	37	- 1	27	25
A-7a	"	325	0.5	6.6±0.7	6.8±0.7	37	-14	308	23
A-8a	"	"	1.0	4.7±0.5	5.0±0.8	38	-15	38	30
A-10a	5.0	175	0.5	7.1±0.8	8.4±0.8	53	-17	2770	43
A-11a	"	"	1.0	6.7±1.0	9.0±1.0	53	-16	1730	31
A-12a	"	"	2.0	11.3±1.1	13.0±1.3	53	-10	2180	12
A-14a	"	250	1.0	5.3±0.5	3.9±0.7	47	-20	294	41
A-15a	"	"	2.0	9.5±1.4	4.9±1.2	49	-18	2240	30
A-17a	"	325	1.0	5.4±0.7	5.6±0.6	39	-14	39	26
A-18a	"	"	2.0	6.5±0.6	6.1±0.8	49	-13	27	11

* By convention, a positive value indicates compressive stress and a negative value indicates tensile stress.

After these initial tests, we baked a subset of the films in air for four hours at 400 C and remeasured the damage threshold, absorption, and stress. Values measured before and after baking are shown in Table 5. As a result of the bake, stress was reduced in magnitude and converted from compressive to tensile. Absorption was greatly reduced in some films and thresholds were, on the average, slightly increased. However, inspecton of the data in Table 5 indicates slight, if any, correlation between thresholds and either net stress or film absorption in either baked or unbaked films.

Finally, a Beckman DK2A two-beam spectrophotometer was used to measure the reflectance of each film in sets A and B. Reflectance values ranged from 0.01 to 0.18 percent except for one film with large absorption whose reflectance was 0.33 percent. This demonstrates that, low reflectance can be obtained in films deposited under a variety of deposition conditions; however, measurement of reflectance does not identify films with high damage thresholds.

4. Conclusions

Thresholds of silica/tantala antireflection films deposited by electron-beam evaporation on bowl-feed polished silica substrates were greatest when the films were deposited at low temperature (175 C) at low rate (1.5 Å/sec), and in the presence of adequate oxygen (1×10^{-4} Torr). Thresholds did not correlate with the measured net stress or the film reflectance, and correlated with film absorption only when the film absorption was greater than 10^4 ppm. Baking films for four hours at 400 C reduced film absorption, altered film stress, and produced some increase in the average damage threshold.

We are grateful to S. E. Peluso and G. Murphy for assistance in maintaining and operating the laser damage facility, to F. Robinson and W. P. Klapp, who deposited the coatings, to G. W. Dodds for making calorimetric measurements of film absorption, and to T. Janssen for assistance in preparation of the manuscript.

5. References

[1] Apfel, J. H.; Enemark, E. A.; Milam, D.; Smith, W. L.; and Weber, M. J., The Effects of Barrier Layers and Surface Smoothness on 150-ps, 1.064-μm Laser Damage of AR-Coatings on Glass; Laser-Induced Damage to Optical Materials: 1977, proceedings of the 1977 Boulder Damage Conference, NBS Spec. Publ. 509, p. 255-260 (1977).

[2] Dietz, R. W.; and Bennett, J. M., Bowl-feed Technique for Producing Supersmooth Optical Surfaces. Appl. Opt.(5): 881-882; 1966.

[3] Lowdermilk, W. H.; and Milam, D., Laser-Induced Surface and Coating Damage. IEEE J. Quant. Elect. QE-17: 1888-1903; 1981.

[4] Lowdermilk, W. H.; Milam, D.; and Rainer, F., Damage to Coatings and Surfaces by 1.06-μm Pulses; Laser-Induced Damage to Optical Materials: 1979, proceedings of the 1979 Boulder Damage Conference, NBS Spec. Publ. 568, p. 391-403 (1980).

[5] Allen, T. H.; Apfel, J. H.; and Carniglia, C. K., A 1.06-μm Laser Absorption Calorimeter for Optical Coatings; Laser-Induced Damage to Optical Materials: 1978, proceedings of the 1978 Boulder Damage Conference, NBS Spec. Publ. 541, p. 33-36 (1978).

[6] Ledger, A. M.; and Batista, R. C., Intrinsic and Thermal Stress Modeling for Thin-Film Multilayers; Laser-Induced Damage to Optical Materials: 1977, proceedings of the 1977 Boulder Damage Conference, NBS Spec. Publ. 509, p. 230-244 (1977).

A question of spot size was raised. The spot size, the speaker said, was 2-3 mm. The damage he reported occurred at the substrate interface and was in the form of small pits extending all the way to the substrate. They look like the stress fractures drawn by Duthler in 1973 or 1974. The coatings were deposited by electron beam deposition. The coatings were baked. The average threshold increased, but some thresholds went down.

Preparation of Thin Amorphous Films by E-Beam Evaporation from Multiple Sources

E. N. Farabaugh, D. M. Sanders, M. E. Wilke, S. A. Hurwitz, and W. K. Haller
National Bureau of Standards
Washington, D.C. 20234

E-beam codeposition was used to produce thin films in the system ZrO_2-SiO_2. Bk-7 glass, heated to 325 °C was used as substrate material for these depositions. The films, thus produced were studied by X-ray Diffraction and Scanning Electron Microscopy Techniques. These studies yielded information on the dependence of film crystallinity on composition and substrate temperature. Particular attention was paid to the compositional range in which the structure of the film changes from polycrystalline to amorphous. The change in film structure is easily determined from the change in the XRD patterns. Different film structures were observed using SEM methods.

Key words: amorphous; co-evaporation; glassy; thin films.

1. Introduction

Antireflection multilayers currently used in high energy laser applications are composed of alternating 1/4 wave optical thicknesses of high and low refractive index. For the 1060 NM wavelength, the low index material is normally SiO_2 and the high index layer TiO_2. Under usual deposition conditions, the SiO_2 layer appears to be amorphous, while the TiO_2 layer has a columnar microstructure which can be observed using transmission electron microscopy (TEM)[1][1]. A similar microstructure is found for many future candidates for the high index member of the optical stack, including the oxides of Ta, and Nb [1]. Such features can contribute to surface roughness [2-4] with potential optical loss from absorption and scattering. In addition, they may serve as paths for diffusion and subsequent sorption of water vapor [5].

Recently, there have been indications that this morphology might increase susceptibility to high energy laser damage. W. T. Pawlewicz et al [1], for instance, concluded that TiO_2 films produced by reactive dc-biased rf-sputtering demonstrated increased resistance to high energy laser damage with decreasing grain size. In fact, films which appeared amorphous using both X-ray diffraction and TEM techniques showed the highest damage thresholds of all. These results do not conclusively prove that completely glassy antireflection coatings are superior because the variation in sputtering process variables necessary to produce amorphous structures may have also changed other parameters such as adhesion to the substrate and to adjacent layers. It was therefore desirable to explore an alternate technique for varying film morphology to determine if glassy interference coatings do indeed exhibit superior optical properties.

The approach chosen, co-evaporation, is an old one, at least from resistively heated boat sources and was originally used to study preferential condensation of compounds from indium and arsenic vapors [6,7]. It was later employed to deposit vapors from metals with widely differing vapor pressure [8]. This technique has also found use in the production of gradient index optical coatings [9]. In the current application, a second component, SiO_2, was co-deposited with the normally high refractive index polycrystalline host with the aim of producing a mixed film with high refractive index, lacking polycrystalline morphology. The second component was chosen for its proven ability to easily form glasses during melt solidification. Because of rapid quenching rates experienced during physical vapor deposition, it was expected that less of this component would be necessary compared to the bulk case. Since the film formation process is similar to single source evaporation, the adhesion of the coatings in the co-evaporated films are also expected to be similar and a comparision of optical properties, including high energy laser damage thresholds, with film disorder should demonstrate if amorphous optical coatings are inherently better. This paper is an initial study to determine the effect of adding this second component on the morphology of the resulting films as determined by X-ray diffraction and scanning electron microscopy. The optical properties of these coatings will be the subject of subsequent investigations.

2. Thin Film Preparation

The facility used to produce the coatings investigated in this paper is described in more

[1] Numbers in brackets indicate the literature referenced at the end of the paper.

detail in reference 10. The stainless steel deposition chamber currently contains a triple electron beam evaporation crucible module which allows simultaneous evaporation from up to three sources. Each source is individually controlled by a quartz crystal monitor which is shielded from the vapors originating from the other sources. The BK7 glass substrates used in this study were heated using a quartz lamp. The steady state substrate temperature was related to the lamp temperature using a thermocouple embeded in the surface of a witness substrate using spongy platinum. This calibration was carried out with the E-beam crucibles at their deposition temperatures. Depositions were made with filament voltages at 10 KV. The deposition vacuums were 7-9 x 10^{-9} Pa with no attempt to maintain stoichiometry by backfilling with oxygen. The deposition rates were approximately 5 Å/sec for the overall film with the individual source rates adjusted to yield the desired film composition. Film thicknesses were 4500 Å for X-ray and SEM analysis. ZrO_2 was chosen as host compositions with SiO_2 as the glass-forming additive, as stated earlier.

3. Film Characterization

X-ray diffraction was used to evaluate the extent of disorder of films which were all deposited to 4500 Å thickness. The diffractometer employed $Cu_{K\alpha}$ radiation selected by a graphite single crystal monochromator.

Scanning Electron Micrographs of film fragments coated with gold-paladium to minimize charging were recorded at 35,000X. These fragments were obtained by drawing a diamond stylus over the deposited films. The micrographs are typical of those seen in a large sampling.

Because of the high deposition voltage (spitting) and low oxygen pressures used to deposit the coatings in this study, good optical quality was not expected. For this reason, extensive optical characterization of these particular films was not pursued with the exception of the preliminary waveguide measurements presented by A. Feldman and E. N. Farabaugh in these proceedings.

4. Experimental Results

Figure 1 shows a comparison of X-ray diffraction patterns for the starting source material and a pure ZrO_2 film deposited on BK-7 glass substrate at 325 °C. While there is only monoclinic phase present in the source material, the pattern for the ZrO_2 film indicates the presence of an additional phase which may have either a tetragonal or cubic structure. The relative peak heights indicate some degree of preferred orientation compared to published powder diffraction patterns. X-ray diffraction patterns of the remaining source material after heating by the E-beam showed a pattern identical to the original source material despite discoloration due to reduction.

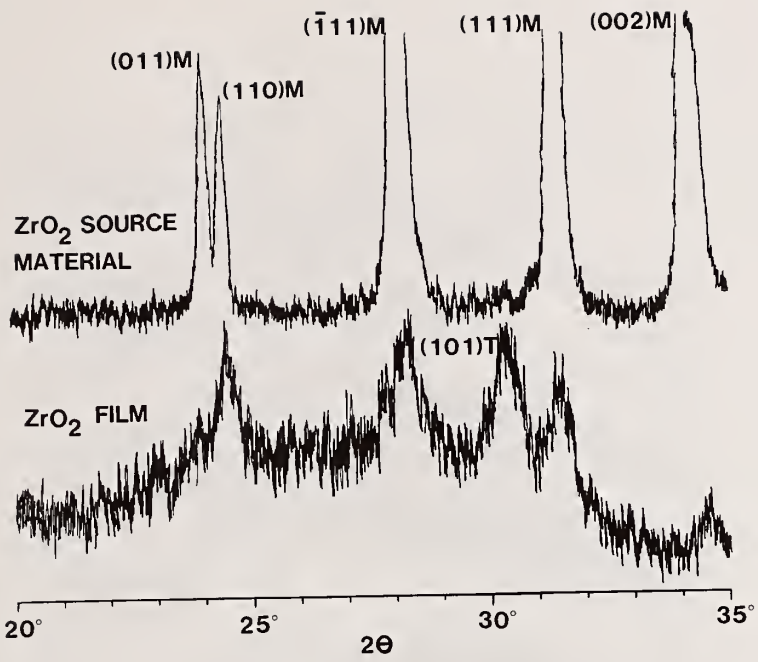

Figure. 1. X-ray diffraction patterns of pure ZrO_2 source material and a 4500 Å thick film deposited on BK-7 glass substrates at 325 °C.

Figure 2 presents the effect of substrate temperature on the nature of crystallinity of pure ZrO_2. As the substrate temperature is varied from 325 °C to 25 °C, the monoclinic peaks decrease in favor of a single tetragonal peak. The presence of this remaining peak, even at this low substrate temperature proves the strong tendency of this material to remain polycrystalline.

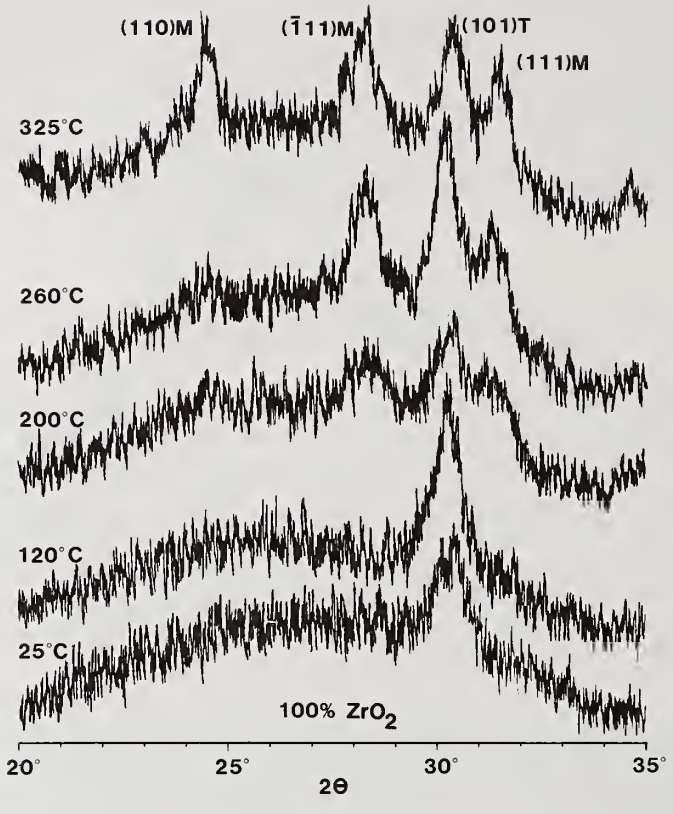

Figure 2. X-ray diffraction patterns of 4500 Å ZrO_2 films deposited on substrate at indicated temperatures (°C).

The effect of adding various concentrations of SiO_2 to the host ZrO_2 film is shown in figure 3. The substrate temperature was 325 °C. The reported concentration is computed from the relative rates of deposition of the constituents assuming a sticking coefficient for both components of unity. At 10% SiO_2, the X-ray diffraction pattern is roughly identical to the effect of deposition of pure ZrO_2 on a cold substrate. In other words, the combination of monoclinic and tetragonal phases has been converted to the tetragonal phase by the addition of a relatively small amount of additive. With additional SiO_2, the tetragonal peak diminishes and eventually disappears with 25% SiO_2. The resulting mixture film is free of crystalline structure which can be detected using a simple X-ray powder diffractometer.

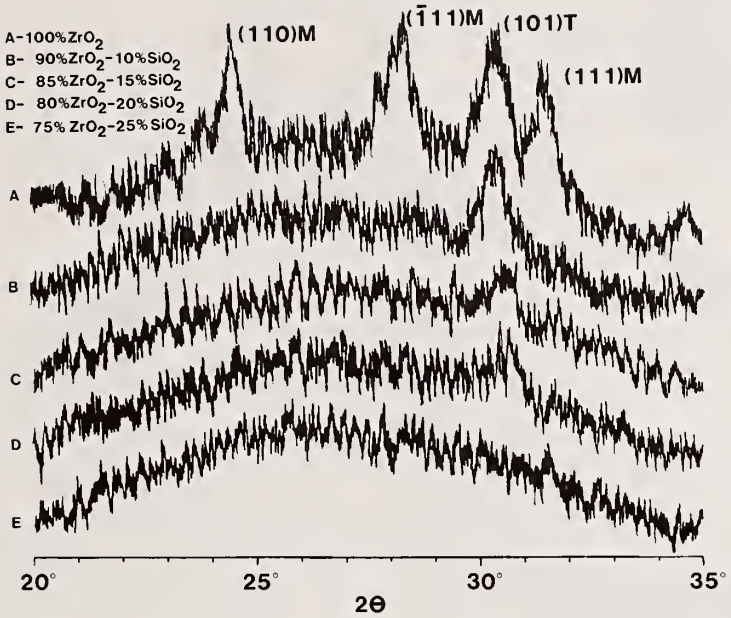

Figure 3. Effect of adding various concentrations of SiO_2 to host ZrO_2 film, all deposited at 325 °C. The concentrations are based on relative deposition rates as discussed in the text. (25% by rate = 19 mol % SiO_2)

Figure 4 shows a comparision of the microstructural changes which are observed with the addition of 25% SiO_2 using a SEM. The pure ZrO_2 film is seen to have a columnar structure, while no such features could be found in mixed ZrO_2-SiO_2 film even when a large number of fragments were examined.

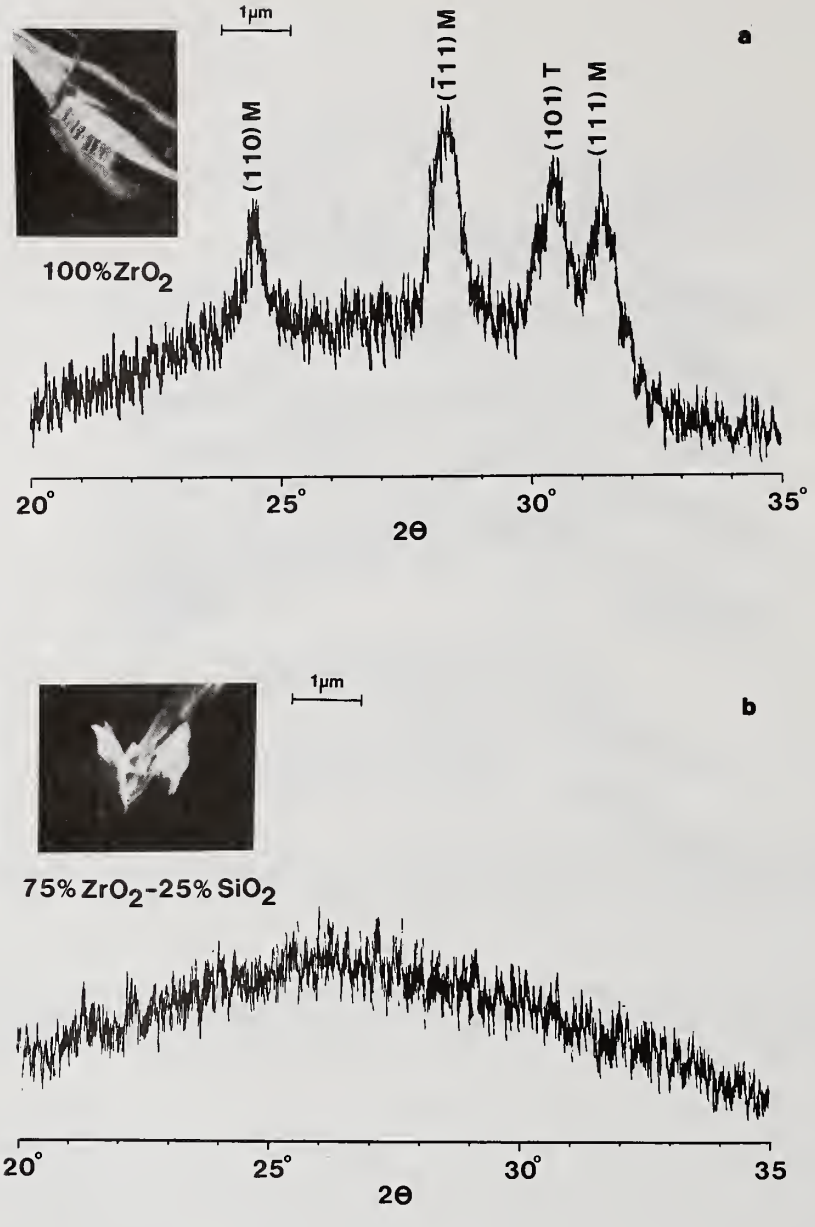

Figure 4. SEM micrographs of: (a) pure ZrO_2 and (b) mixed 25% SiO_2 by rate (19 mol %) SiO_2-ZrO_2 film with associated X-ray diffraction patterns. (35,000X magnification)

5. Discussion of Results

From considerations of crystallography of bulk ZrO_2, it is possible to draw certain conclusions. It is known that in the bulk form, the monoclinic phase of ZrO_2 is stable for grain sizes over 300 Å and the tetragonal for smaller sizes [11]. Using this information, we can conclude that much of the observed behavior in the thin film system is due to changes in grain size.

In the source material, for instance, we can conclude that the material is composed almost exclusively of grains which are greater than 300 Å. Upon deposition of pure ZrO_2 at 325 °C, a distribution of grain sizes can be found with a significant number being smaller than 300 Å and having a tetragonal crystal structure. As the substrate temperature is diminished, the distribution of grain sizes is shifted so that at room temperature all of the grains appear to be smaller than 300 Å.

With the addition of 10% SiO_2 at 325 °C, we observe a similar effect to depositing pure ZrO_2 at room temperature. The SiO_2 appears to inhibit grain growth during deposition. With additional additions of SiO_2, this grain growth is inhibited still further until there is no observable structure using either the X-ray diffraction or SEM techniques.

It is therefore concluded that codeposition can be a powerful technique for the control of microstructure of optical coatings. This should prove particularly valuable for coatings having either very high index of refraction such as ZrO_2, TiO_2, and Ta_2O_5 and very low refractive index such as MgF_2 and $Na_3(AlF_6)$. Since the microstructure caused by crystallinity may degrade optical properties of these materials, it is hoped that a new class of dense, but amorphous optical coating materials having lower scattering and absorption and higher resistance to high energy laser damage will emerge. This optimism will of course depend on demonstrated superior optical properties.

We wish to acknowledge financial assistance from the following sources: The Office of Naval Research, Contract No. N00014-79F-0030 and Lawrence Livermore Laboratory, Contract No. SANL716019.

6. References

[1] Pawlewicz, W. T.; Busch, R.; Hays, D. D.; Martin, P. M.; and Laegreid, N. Reactively sputtered optical coatings for use at 1064 NM in Laser Induced Damage in Optical Materials: 1979 Ed. H. E. Bennett, A. J. Glass, A. H. Guenther, and B. E. Newnam, NBS Special Pub. 568.

[2] Pearson, J. M. Electron microscopy of multilayer thin films. Thin Solid Films, Vol. 6; 349-358; 1970.

[3] Guenther, K. H. Nodular defects in dielectric multilayers and thick single layers. Appl. Opt., Vol. 20; 1034-1038; 1981.

[4] Guenther, K. H. and Pulker, H. K. Electron microscopic investigations of cross sections of optical thin films. Appl. Opt., Vol. 15; 2992-2994; 1976.

[5] Pulker, H. K. and Jung, E. Correlation between film structure and sorption behavior of vapor deposited ZnS, cryolite and MgF_2 films. Thin Solid Films, Vol. 9; 57-66; 1971.

[6] Guenther, K. G. Z. Naturforsch, Vol. 13a; 1081; 1958.

[7] Guenther, K. G. in The Use of Thin Films in Physical Investigations, J. C. Anderson, ed. Academic Press, Inc., New York, NY; 213; 1966.

[8] Belser, R. B. J. Appl. Phys., Vol. 31; 562; 1960.

[9] Jacobsson, R. Inhomogeneous and coevaporated homogeneous films for optical applications, Physics of Thin Films, Vol. 8, ed. G. Hass, M. H. Francombe, and R. W. Hoffman; 51-98.

[10] Sanders, D. M; Farabaugh, E. N.; Hurst, W. S.; and Haller, W. K. Summary abstract: an advanced multichamber system for preparation of amorphous thin films by coevaporation and their subsequent characterization by AES, ESCA, SIMS and ISS methods. J. Vac. Sci. Technol. Vol. 18; 1308-1309; 1981.

[11] Garvie, R. C. Zirconium dioxide and some of its binary systems in high temperature oxides. Part II Oxides of Rare Earths, Titanium, Zirconium Hafnium, Niobium and Tantalum, ed. A. M. Alper Academic Press, New York, NY; 1970; 117.

Improved Si-Based Coating Materials for High Power Infrared Lasers*

W.T. Pawlewicz and P.M. Martin

Pacific Northwest Laboratory+
Richland, Washington 99352

Data are presented to demonstrate that alloying of Si with H during thin film coating deposition reduces coating absorption at important infrared laser wavelengths such as 1.06, 1.315 and 2.7 μm by more than an order of magnitude compared to pure Si coatings. These results contradict earlier beliefs that the presence of H in Si was undesirable because of its association with H_2O. It appears that absorption values approaching state-of-the-art for near-infrared coatings can now be obtained for a material with many attractive physical properties such as very high refractive index, outstanding hardness and scratch-resistance, glassy structure, non-hygroscopicity and general environmental stability and durability. In particular, an absorption coefficient of 3 cm^{-1} has been obtained at a wavelength of 2.7 μm for a $Si_{1-x}H_x$ alloy with $x = 0.12$. The $Si_{1-x}H_x$ coatings are made by reactive sputtering, and cannot be made by conventional evaporative techniques. Controlled deposition of coatings with specific compositions and optical properties is briefly described, and optical property-composition relationships are presented for the alloy mixing interval $0 < x < 0.4$. The same sputtering system is used to deposit the low index material SiO_2 by simple exchange of H_2 for O_2 in the sputtering gas, making possible straightforward multilayer coating fabrication. Reflectance spectra for $Si_{1-x}H_x/SiO_2$ all-dielectric mirrors and dielectric-enhanced Au and Al mirrors are presented.

Key words: absorption; coatings; composition; glassy structure; mirror fabrication; reactive sputtering; refractive index; $Si_{1-x}H_x$ alloys

1. Introduction

Silicon is a particularly exciting infrared optical coating material because many of its physical properties are far superior to those of the halide and chalcogenide coating materials frequently used. Superior properties include glassy or amorphous structure (resulting in low scatter), very high refractive index (requiring fewer and thinner dielectric layers), hardness (scratch-resistance) and non-hygroscopicity (particularly important near infrared water absorption bands). In addition, starting material is available in high purity form, and complementary low-index coating materials such as SiO_2 are readily made.

---

* Work supported by the Materials Sciences Division of the Office of Basic Energy Sciences, U.S. Department of Energy.

+ Operated by Battelle Memorial Institute for the U.S. Department of Energy under Contract Number DE-AC06-76RLO-1830.

In the past few years, silicon has received much attention in efforts to develop coating materials for infrared chemical lasers. Significantly, multilayer coating designs using Si as a high-index layer have been found to exhibit stable reflectivities in both laboratory and simulated-space environments while fluoride, sulfide and selenide coatings deteriorate rapidly [1]. Unfortunately, coating materials with high refractive indices, such as silicon, to date have tended to exhibit higher absorption and hence lower damage threshold [2]. For example, evaporated silicon coatings typically show an absorption of 40 to 50 cm^{-1} at 2.8 μm wavelength while sulfides and selenides are found to absorb in the 1 to 2 cm^{-1} range.

The purpose of this paper is to report data accumulated during the past year which demonstrates that the absorption of Si coatings at important infrared wavelengths such as 1.06, 1.315 and 2.7 μm can be reduced by more than an order of magnitude by alloying of the Si with H during deposition. In particular, an absorption coefficient of 3 cm^{-1} was obtained at 2.7 μm for a $Si_{1-x}H_x$ alloy with $x = 0.12$. Thus absorption values approaching state-of-the-art for fluorides, sulfides and selenides appear possible for Si without significantly compromising its many superior physical properties. The beneficial effects of H reported here are particularly significant because previous work [1,2,3] on silicon coatings suggested the presence of H in Si was undesirable because of its association with H_2O.

The $Si_{1-x}H_x$ coatings are made by reactive sputtering, and cannot be made by conventional evaporative techniques. Controlled deposition of coatings with specific H contents in the mixing interval $0 < x < 0.4$ is described briefly here, and quantitative relationships between optical properties (real and imaginary parts of the refractive index) and composition are presented. Use of the same sputtering system to deposit the low index material SiO_2 by simple exchange of H_2 for O_2 in the sputtering gas is also described, and examples of successfully fabricated multilayer $Si_{1-x}H_x$/SiO_2 all-dielectric mirrors and dielectric-enhanced Au and Al mirrors are presented.

2. Experiment

2.1 Deposition Apparatus

$Si_{1-x}H_x$ and SiO_2 coatings were made in rf diode sputtering systems of the type shown schematically in Figure 1. The systems were mounted on conventional mechanical and diffusion pumps. The target or source was 99.999%-pure vacuum-cast Si bonded to an rf electrode.

The argon and oxygen sputtering gases were bottled with minimum purity of 99.999%. Hydrogen gas was generated on demand by electrolysis and purified by diffusion through a palladium membrane to better than the 99.9999% level. All sputtering gases were passed through a gas purifier to further reduce H_2O, O_2 and trace amount of organics before introduction to the sputtering chamber. A variable orifice was placed between the liquid nitrogen cold trap and diffusion pump to decrease contamination in the chamber due to residual H_2O, O_2 and N_2. With the variable orifice, the diffusion pump could be throttled to obtain the desired gas pressure in the chamber, while still maintaining unthrottled cryopumping of contaminants by the cold trap. The sputtering gases and the residual H_2O level in the deposition chamber were further reduced by getter sputtering of Si onto a shutter for approximately 60 minutes before commencing deposition on the substrates. A residual gas

analyzer was occasionally used to examine the purity of chamber gases during deposition.

2.2 Optical Measurements

Refractive index and semi-quantitative absorption coefficient measurements were made over the wavelength range from 0.2 to 3 μm with a dual-beam, double-monochromator spectrophotometer. Refractive index values were deduced using established methods [4]. Absorption coefficients were deduced from the difference between coated substrate transmission at half-wavelength points and the transmission of the bare substrate. Reflectance measurements were made with a spectrophotometer accessory and aluminum reference mirrors calibrated against NBS standards. Fused silica substrates were used for measurement of refractive index and rough measurement of absorption coefficient.

Reliable quantitative absorption measurements were made at a wavelength of 2.7 μm by HF laser calorimetry. CaF_2 substrates were used for this work.

2.3 $Si_{1-x}H_x$ Composition Measurements

$Si_{1-x}H_x$ composition was determined by infrared spectrophotometric measurement of the integrated areas under the absorption peaks due to Si-H bond stretching vibrational modes at 2000, 2090 and 2150 cm^{-1}. Germanium substrates were used for these measurements in a dual-beam spectrophotometer. Infrared data were calibrated against H content measurements made by vacuum fusion (gas release) techniques. Details have been published elsewhere [5].

2.4 $Si_{1-x}H_x$ Composition Control

Primary control of the H content of $Si_{1-x}H_x$ coatings was accomplished through the deposition rate and the H_2 partial pressure in the sputtering gas [6,7]. Low H contents are obtained at high deposition rates and low H_2 partial pressures. High H contents are obtained at low deposition rates and high H_2 partial pressures. Composition diagrams, similar to conventional phase diagrams, have been established to allow prediction of the H content that will result for a given set of values for deposition rate and H_2 partial pressure [6]. Use of these diagrams allows rapid and systematic variation of H content from 0 to 40 atom % for the type of experiments reported here.

$Si_{1-x}H_x$ cannot be made by conventional evaporative techniques. Molecular H_2 will not react with Si. A plasma or gas discharge is necessary to produce atomic H which will react with Si to form an alloy.

3. Results

3.1 Absorption Dependence on H Content

Alloying of Si with hydrogen produces remarkable changes in the optical properties of the coatings [8]. A change in the spectral dependence of the absorption coefficient is readily observed by eye for $Si_{1-x}H_x$ as x is varied over the interval from 0 to 0.4. For example, if a group of 1 μm-thick coatings is made in a series of deposition experiments in which x is varied from

0 to 0.4, the appearance of the coatings is seen to change from gray metallic for x = 0, to transparent red for x ≃ 0.2, to transparent yellow for x ≃ 0.35. All of the coatings have extremely smooth surfaces and extremely fine microstructural features (less than 50 Å) due to the intrinsic propensity for Si to form in a glassy or amorphous phase when deposited at substrate temperatures below 500°C. The potential utility of these coatings for optical applications was reported at this symposium two years ago [8].

The change in coating absorption with H alloying can be estimated from spectrophotometric measurements at wavelengths in the visible or near infrared to show the explicit functional dependence of the absorption coefficient on hydrogen content. Figure 2 shows the absorption coefficient as a function of H content at a wavelength of 1.06 μm. For non-hydrogenated Si a coefficient of approximately 7300 cm^{-1} is indicated by a least squares fit to the data points. Note that alloying with H results in an exponential drop in absorption coefficient. For a H content of 36 atom %, the least squares fit indicates an absorption coefficient of 87 cm^{-1}, a factor 80 lower than for pure Si. It should be cautioned that spectrophotometer measurement of absorption frequently does not yield reliable quantitative numbers. However, regardless of the exact absorption coefficient values, Figure 1 clearly demonstrates a very large decrease in coating absorption when H is added to the coatings.

Figure 3 shows similar spectrophotometer results for absorption coefficient as a function of H content at a wavelength of 1.315 μm. For pure Si, the absorption is 3200 cm^{-1}. Absorption again decreases exponentially with H content, reaching a value of 67 cm^{-1} for 36 atom %. This value is a factor of 48 lower than for pure Si.

Similar dependences of absorption coefficient on H content are observed for any wavelength between 0.5 and 2 μm, although at longer wavelengths absorption measurement by spectrophotometer becomes increasingly impractical because of diminishing absorption. At 2.7 μm, HF calorimetry was used to check the influence of H alloying. To date only two coatings (one pure Si and one hydrogenated) have been tested, but the results agree well with the spectrophotometer measurements at shorter wavelengths. Figure 4 shows absorption coefficient as a function of H content at 2.7 μm wavelength. For the pure Si coating, a value of 41 cm^{-1} was obtained. This value agrees well with all absorption values reported for Si coatings made by evaporation and sputter deposition techniques during the last few years. The reported values range from 17 to 80 cm^{-1}. For the 12 atom % H coating, the absorption coefficient was measured to be 3.1 cm^{-1}, a factor of 13 lower than for the pure Si coating made on the same type of substrate, with the same calorimeter, by the same investigators. Note that 3.1 cm^{-1} is 5 to 6 times lower than the lowest absorption value previously reported for silicon coatings.

3.2 Refractive Index Dependence on H Content

The decrease in the absorption of Si coatings with H alloying is well known to the solar photovoltaic community which has studied extensively the optical properties of amorphous $Si_{1-x}H_x$ for wavelengths in the visible region or those shorter than the optical band edge of crystalline Si (1.1 μm). The initial shift in the optical band edge to shorter wavelengths with increasing H content is due to removal of gap states as H completes dangling bonds associated with imcomplete Si

tetrahedral units [9]. At higher H contents the band edge continues to shift with an increase in the number of Si-H bonds, which are stronger than Si-Si bonds. The decrease in the absorption at longer infrared wavelengths, such as that seen in Figures 2, 3 and 4, is probably also due to gap state removal. Gap state removal decreases the number of defect states to which transitions can occur from the valence band.

The reduction in absorption with increasing H content, however, requires that some compromise be made on refractive index. Figure 5 shows the dependence of refractive index on H content over the region between 0 and 40 atom %. The index values here were measured at a wavelength of 2 μm. The refractive index is seen to decrease from a pure Si value of 3.6, first slowly and later more rapidly, to values as low as 2.0 for H content near 40 atom %. The decrease in the refractive index is due to a decrease in polarizability associated with the formation of stronger Si-H bonds, rather than Si-Si bonds, as H is added. Note, however, that even for 20 atom % H the index is still above 3.0, and that 30 atom % can be added before the index reaches 2.5. Thus the tradeoff between the real and imaginary parts of the index is not very severe, and low absorption appears to be possible for $Si_{1-x}H_x$ coatings with refractive index greater than other high-index infrared coating materials such as ZnS, ZnSe, As_2S_3 or As_2Se_3.

3.3 $Si_{1-x}H_x/SiO_2$ Multilayer Fabrication

One of the attractive features of preparing $Si_{1-x}H_x$ by sputtering from a pure Si source and separately introducing the H_2 as a gas is that the H_2 can be readily valved off and O_2 introduced in its place to reactively sputter the low index material SiO_2. In fact, a simple manifold and valving arrangement for Ar, O_2 and H_2, such as that shown in Figure 1, makes fabrication of $Si_{1-x}H_x/SiO_2$ multilayer stacks very straightforward. Completion of one layer and initiation of another is accomplished by closing one valve and opening the other while continuously sputtering from the Si target. This process is easily automatable for precise control of layer thickness.

Figure 6 is the reflectance spectrum for a typical all-dielectric high reflector made by reactive sputtering of $Si_{1-x}H_x$ and SiO_2 on a fused silica substrate for use near the Iodine laser wavelength. Here $x = 0.08$. Note that, because of the very high refractive index contrast obtained with the $Si_{1-x}H_x/SiO_2$ system, only nine layers are required for 99.9% calculated reflectivity and a broad, square reflection peak.

The reflectance spectra for other $Si_{1-x}H_x/SiO_2$ all-dielectric high reflectors are shown in Figures 7 and 8. Here again $x = 0.08$. The mirror of Figure 7 covers the wavelength region of the HF and DF chemical lasers (2.8 to 3.8 μm). The mirror of Figure 8 is tuned for use at the DF laser wavelength (3.8 μm). Again note that in both cases only nine layers are required for a 99.9% calculated reflectivity and a broad, square reflection peak.

Figures 9 and 10 are reflectance spectra for dielectric-enhanced metal reflectors tuned for use at 2.7 μm. The mirror of Figure 9 was made by sputtering two pairs of $SiO_2/Si_{1-x}H_x$ ($x = 0.12$) onto an Al-coated Mo substrate. The mirror of Figure 10 was made with one pair of $SiO_2/Si_{1-x}H_x$ ($x = 0.12$) on a Au-coated Mo substrate. As with the all-dielectric reflectors, the high refractive index contrast of the $Si_{1-x}H_x/SiO_2$ system requires fewer and thinner dielectric pairs for a given reflectivity.

4. Summary

A record low absorption coefficient of 3 cm^{-1} was obtained by HF-laser calorimetry for a sputtered Si coating to which H was added deliberately during deposition. Absorption in this $Si_{1-x}H_x$ ($x = 0.12$) coating was a factor of 13 lower than that obtained for a pure Si coating made with the same equipment on the same substrates. These calorimetry results agree well with semi-quantitative spectrophotometric absorption data at several infrared wavelengths which indicate an exponential decrease in coating absorption with H content for $Si_{1-x}H_x$ over the range $0 < x < 0.4$. These results contradict earlier suggestions that H in Si coatings was harmful at 2.7 μm wavelength because it indicated the presence of H_2O. Some decrease in refractive index occurs when Si is alloyed with H, however the index is still larger than 3.0 for $x = 0.2$. Synthesis of these $Si_{1-x}H_x$ coatings is controllable and reproducible, making possible useful multilayer coatings such as all-dielectric reflectors and dielectric-enhanced reflectors when the $Si_{1-x}H_x$ is used with reactively sputtered SiO_2. Both materials can be deposited from a single Si source by simple exchange of O_2 and H_2 in the sputtering atmosphere.

The authors gratefully acknowledge Major Ron Lusk of the Air Force Weapons Laboratory, Kirtland AFB, NM for his interest and efforts in testing these new coatings and, in particular, for arranging and coordinating the laser calorimetry measurements at the University of Dayton Research Institute. The authors also thank Darrell Hays and Ira Mann of Pacific Northwest Laboratory for computer data reduction and for coating deposition, respectively.

5. References

[1] Donovan, T.M.; Holmes, S.J.; Fogdall, L.B. Enhanced Reflectance Mirrors for Space-Borne HF Laser Applications. Proceedings of the SPIE meeting on High Power Lasers and Applications; 1981 February 11-13; Los Angeles, CA. Volume 270. 24-29.

[2] Donovan, T.M.; Porteus, J.O.; Seitel, S.C.; Kratz, P. Multithreshold HF/DF Pulsed Laser Damage Measurements on Evaporated and Sputtered Silicon Films. Bennett, H.E.; Glass, A.J.; Guenther, A.H.; Newnam, B.E., ed. Laser Induced Damage in Optical Materials:1980, Nat. Bur. Stand. (U.S.) Spec. Publ. 620; 1981 July. 305-312.

[3] Donovan, T.M.; Temple, P.A.; Wu, S-C; Tombrello, T.A. The Relative Importance of Interface and Volume Absorption by Water in Evaporated Films. Bennett, H.E.; Glass, A.J.; Guenther, A.H.; Newnam, B.E., ed. Laser Induced Damage in Optical Materials: 1979, Nat. Bur. Stand. (U.S.) Spec. Publ. 568; 1980 July. 237-246.

[4] Manifacier, J.C.; Gasiot, J.; Fillard, J.P. A Simple Method for the Determination of the Optical Constants n, k and the Thickness of a Weakly Absorbing Thin Film. Journal of Physics E:Scientific Instruments 9:1002-1004; 1976.

[5] Martin, P.M.; Pawlewicz, W.T. Property-Composition Relationships in Sputter-Deposited a-Si:H Alloys, Solar Energy Materials 2(2): 143-157; 1979/1980.

[6] Pawlewicz, W.T.; Martin, P.M. Bonding and Composition Diagrams for Sputter Deposited a-Si:H, Solid State Communications 39(2): 337-339; 1981.

[7] Martin, P.M.; Pawlewicz, W.T. Influence of Sputtering Conditions on H Content and Si-H Bonding in a-Si:H Alloys, Journal of Non-Crystalline Solids 45(1): 15-27; 1981.

[8] Pawlewicz, W.T.; Busch, R.; Hays, D.D.; Martin, P.M.; Laegreid, N. Reactively Sputtered Optical Coatings for Use at 1064 nm. Bennett, H.E.; Glass, A.J.; Guenther, A.H.; Newnam, B.E., ed. Laser Induced Damage in Optical Materials: 1979, Nat. Bur. Stand. (U.S.) Spec. Publ. 568; 1980 July. 359-375.

[9] Moustakas, T.D. Sputtered Hydrogenated Amorphous Silicon. Journal of Electronic Materials 8(3): 391-435; 1979.

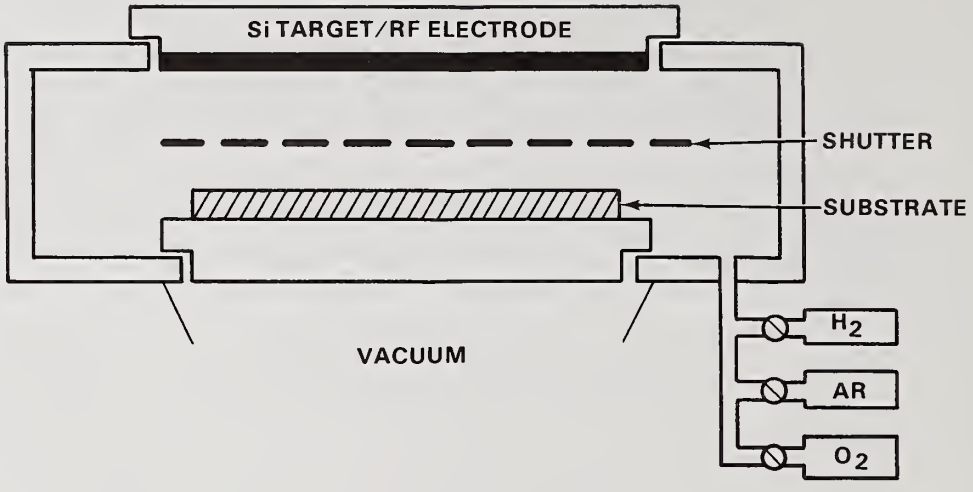

Figure 1. Rf diode sputtering system used for reactive synthesis of $Si_{1-x}H_x$ and SiO_2.

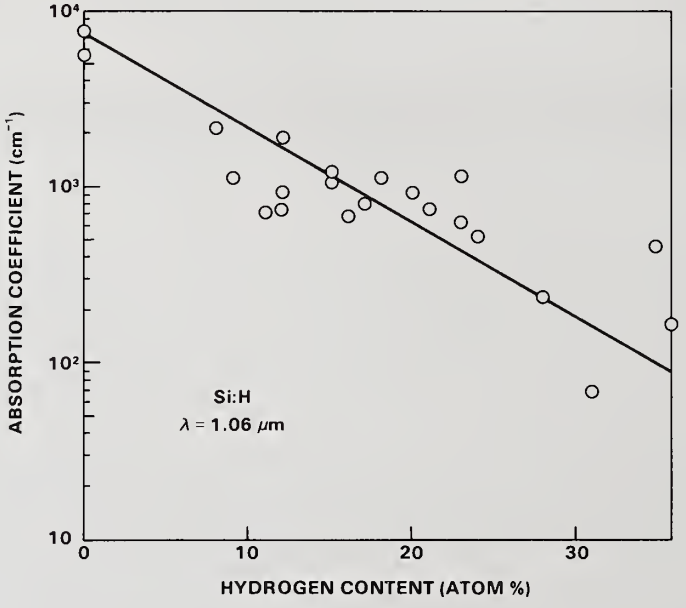

Figure 2. Exponential decrease in absorption coefficient at 1.06 μm wavelength with the H content of $Si_{1-x}H_x$ coatings. (Spectrophotometer measurements).

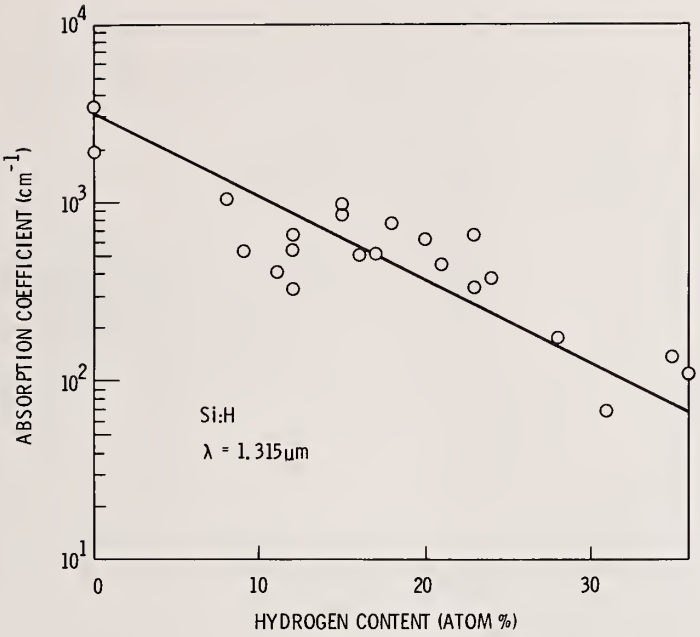

Figure 3. Exponential decrease in absorption coefficient at 1.315 μm wavelength with the H content of $Si_{1-x}H_x$ coatings. (Spectrophotometer measurements).

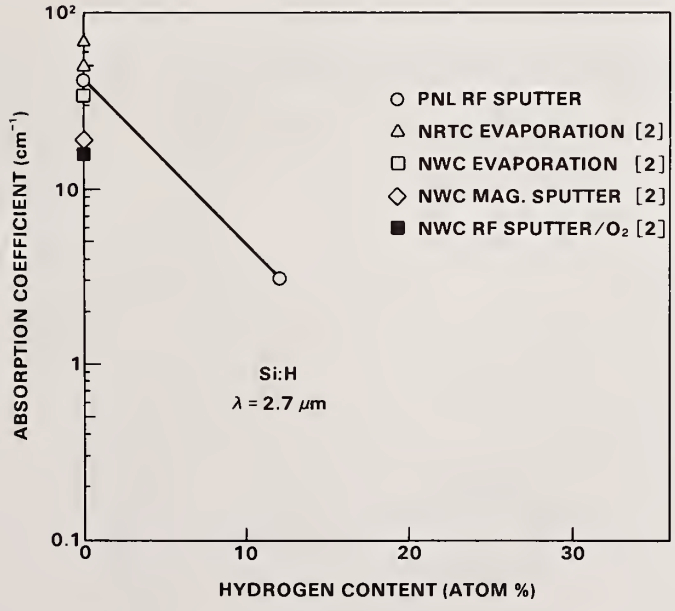

Figure 4. Record low absorption coefficient at 2.7 μm wavelength for Si coatings obtained by reactively alloying Si with 12 atom % H. (HF Calorimetry measurements).

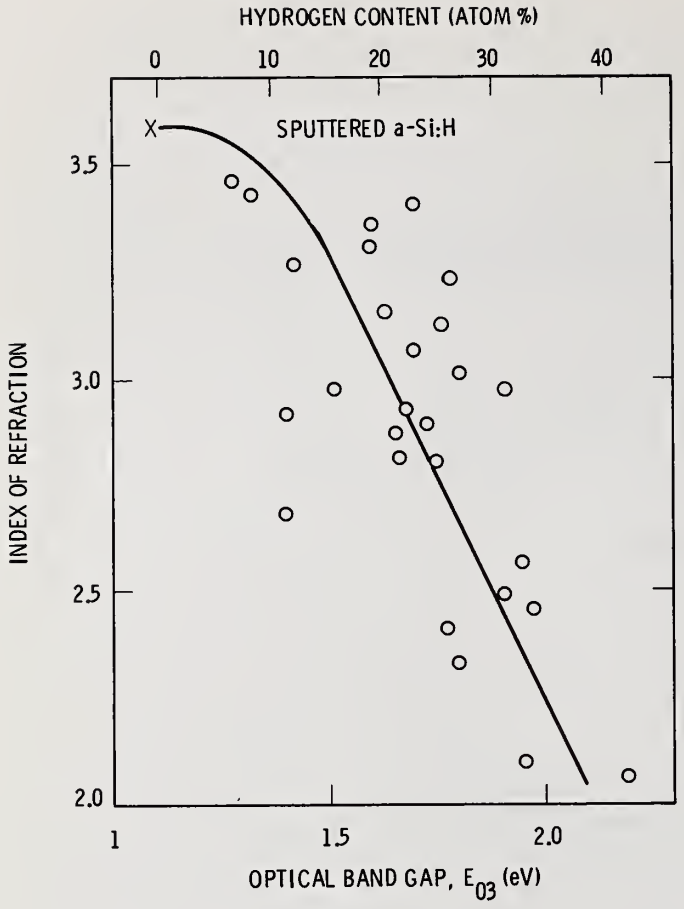

Figure 5. Refractive index and optical band gap for $Si_{1-x}H_x$ coatings with $0 < x < 0.4$.

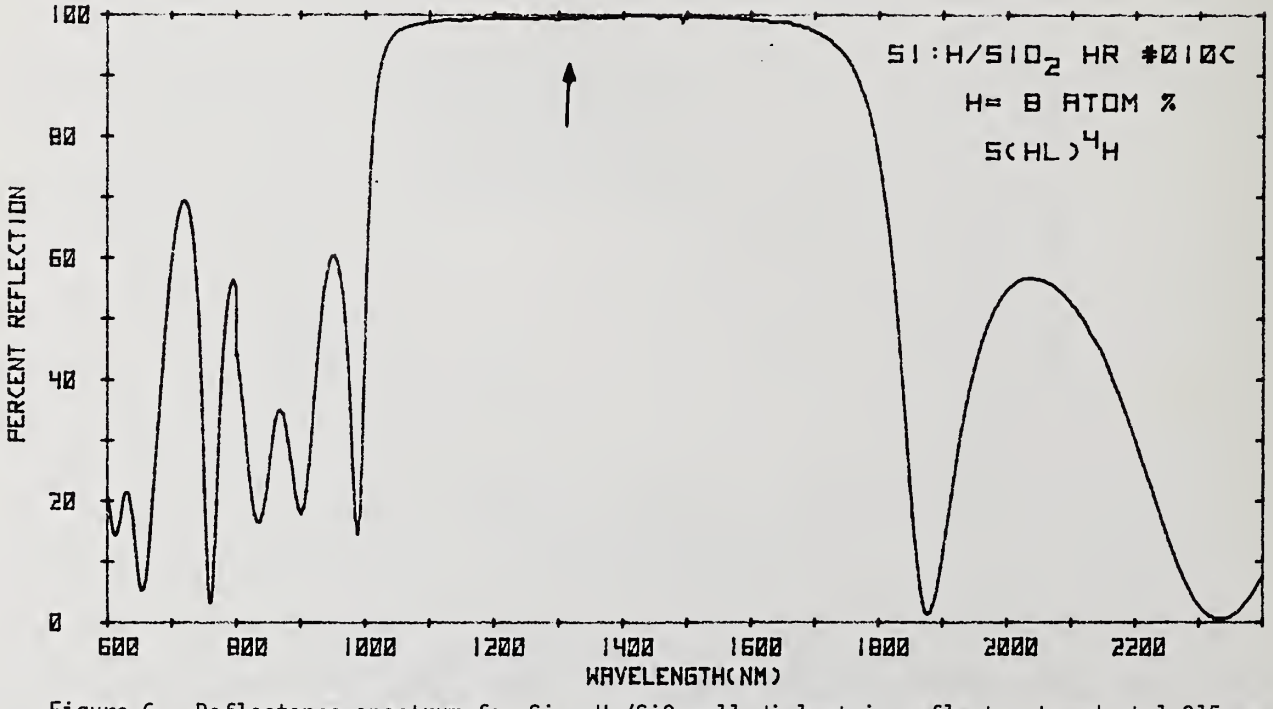

Figure 6. Reflectance spectrum for $Si_{1-x}H_x/SiO_2$ all-dielectric reflector tuned at 1.315 μm.

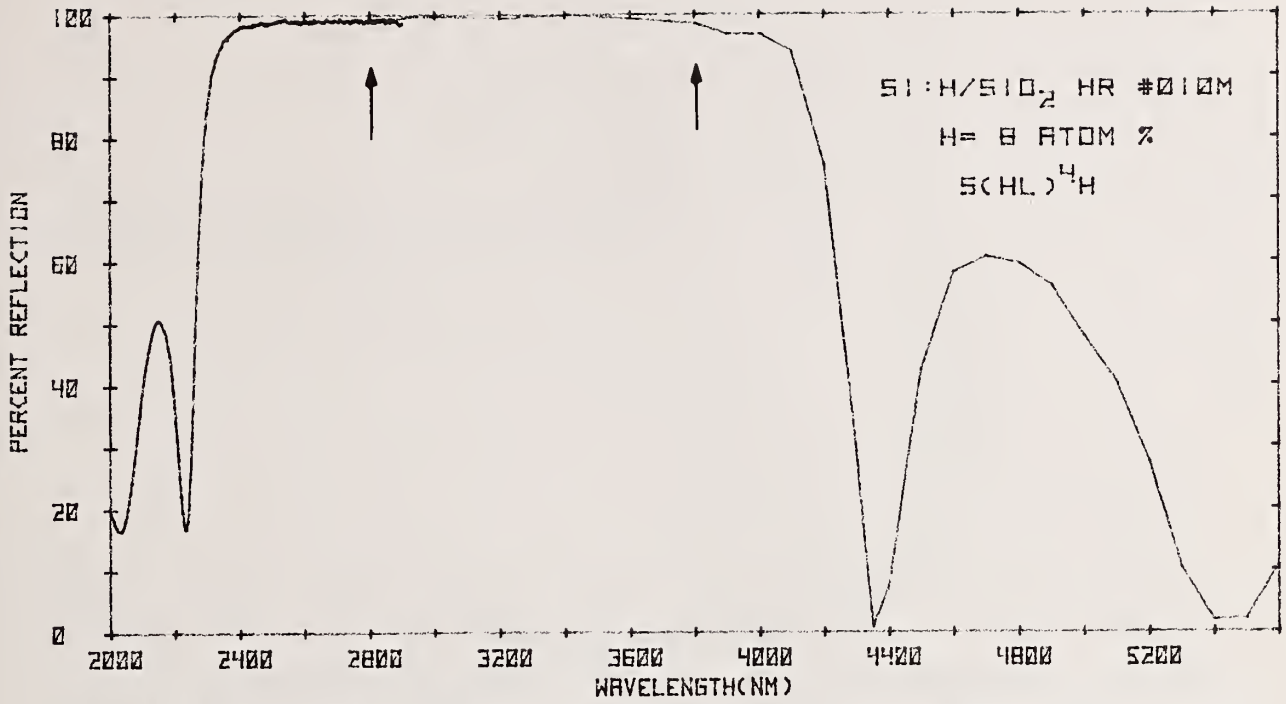

Figure 7. Reflectance spectrum for $Si_{1-x}H_x/SiO_2$ all-dielectric reflector tuned at 2.7 and 3.8 μm.

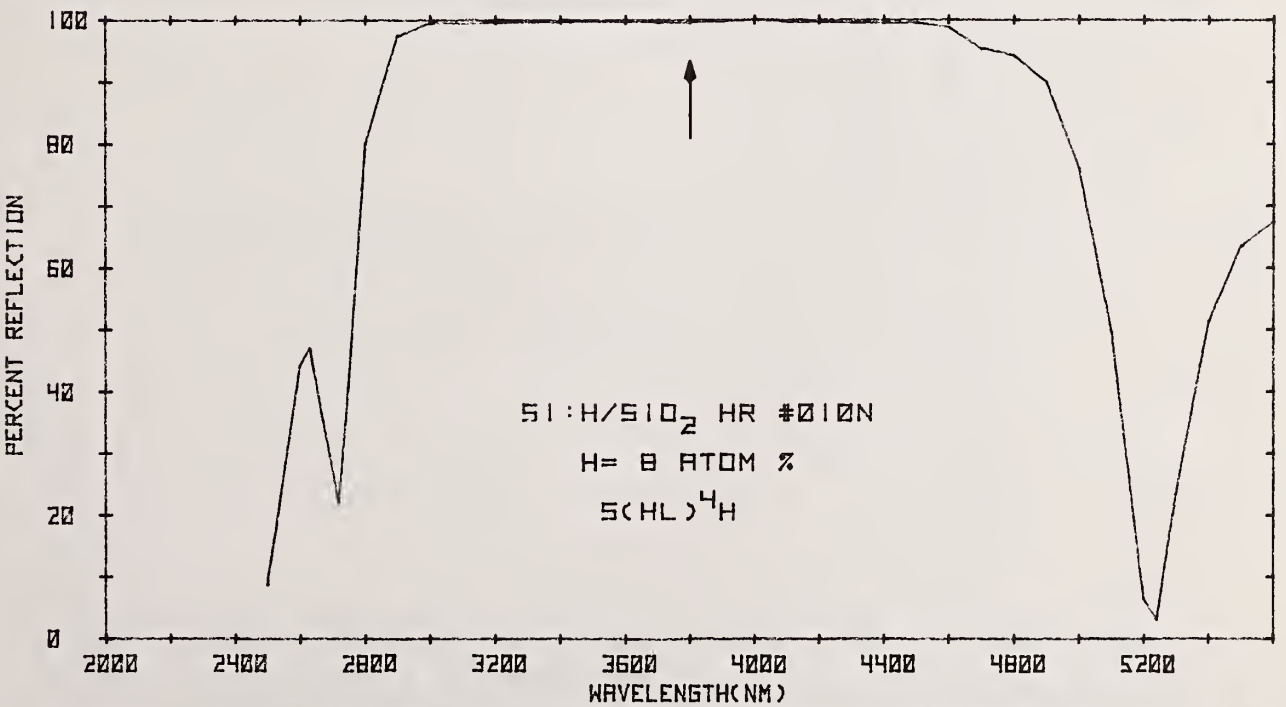

Figure 8. Reflectance spectrum for $Si_{1-x}H_x/SiO_2$ all-dielectric reflector tuned at 3.8 μm.

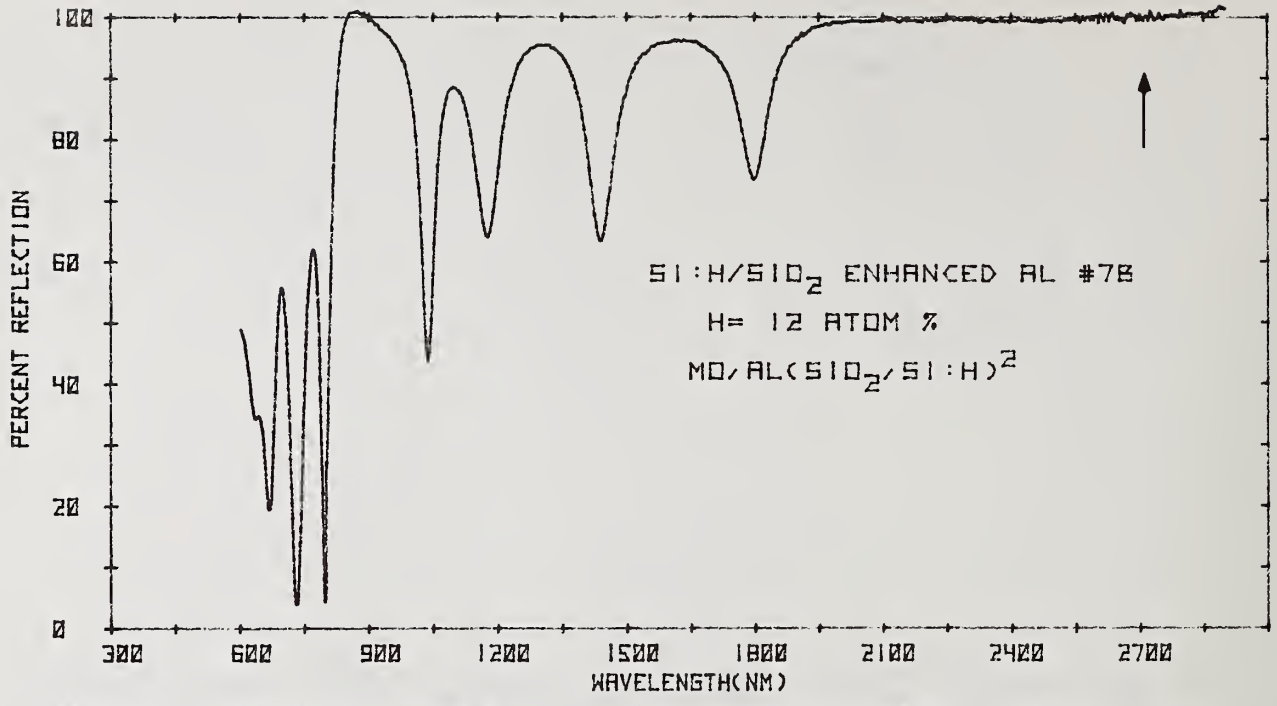

Figure 9. Reflectance spectrum for $Si_{1-x}H_x/SiO_2$ enhanced Al reflector tuned at 2.7 μm.

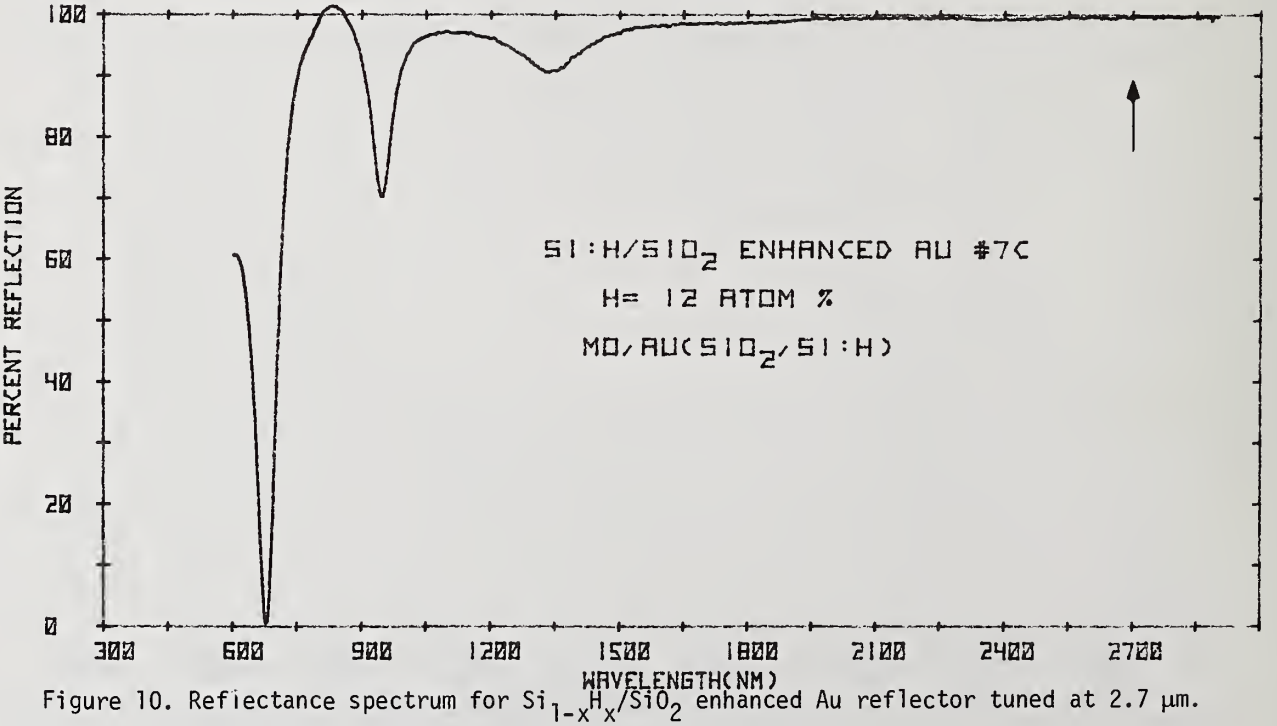

Figure 10. Reflectance spectrum for $Si_{1-x}H_x/SiO_2$ enhanced Au reflector tuned at 2.7 μm.

The question was asked whether outdiffusion of hydrogen when the hydrogenated silicon films were heated by a laser beam would be important. The speaker replied that the films needed to be heated to about 200°C before significant outdiffusion occurred. He did not know how important the effect would be in laser applications. The hydrogen content was determined from infrared spectrophotometry using the silicon hydride stretching modes at about 5 μm wavelengths. The sepctrophotometric data is calibrated using two techniques, gas evolution and resonant nuclear reaction. The question of thickness uniformity was raised. The speaker reported that in their diode sputtering system using a 6" target they routinely get ±1 percent over a 4" diameter area. For their 9" diameter target they get ±1 percent over a 7" diameter area. They are presently building a system with a 16" target, and they expect to get ±1 percent uniformity over a 14" diameter area.

Hydrogenated Amorphous Silicon Films: Preparation, Characterization, Absorption, and Laser-Damage Resistance*

T. M. Donovan, E. J. Ashley, J. B. Franck, and J. O. Porteus

Michelson Laboratory, Physics Division
Naval Weapons Center, China Lake, California 93555

Evaporated Si films in combination with oxide materials such as SiO_x form promising multilayer mirror coatings for chemical laser applications. However, high infrared absorption and relatively low damage threshold of the Si films presently limit the effectiveness of these multilayer designs.

Lower absorption values and higher damage thresholds have been obtained with sputtered Si films; this improvement apparently results from better film morphology and lower contamination levels in the sputtered films. Other work has shown that hydrogenation of as-deposited Si films can effectively passivate large numbers of bonding-type defects, and this results in further marked reductions in the infrared absorption.

In this paper, we discuss the preparation and absorption optimization of hydrogenated Si films and the formation of SiO_2, Si/SiO_2, and SiH/SiO_2 coatings by reactive sputtering. The morphology and composition of optimally prepared films will be described, and the results of absorption and chemical laser damage measurements are discussed.

Key words: amorphous silicon; electron microscopy; hydrogenated amorphous silicon; laser damage; optical absorption; optical coatings; silicon dioxide; silicon monoxide; water contamination.

1. Introduction

Silicon films have been of interest for some time as the high index component of multilayer, enhanced reflectance mirrors for use in the 2- to 4-micron wavelength region. In combination with low index oxide materials, they form highly reflective, physically and radiation hard, environmentally stable coatings [1][1].

Previously [2], we showed that sputtered Si films can be optically superior to evaporated Si films, i.e., they can be prepared with lower water content, lower absorption, and higher damage threshold than evaporated Si when similar purity Si is used as starting material.

In this paper, we report the results of continued work with sputtered Si films using (1) bias-assisted sputtering to further reduce the H_2O content of the films and improve the film morphology and (2) reactive sputtering in hydrogen-argon gas mixtures to passivate bonding defects and further reduce the film absorption. Also, we have formed SiO_2 directly by sputtering in oxygen-argon gas mixtures and formed multilayer structures of (Si/SiO_2) and (SiH/SiO_2) by the simple procedure of varying the sputter-gas mixture from $Ar + O_2$ to pure Ar or $Ar + H_2$. Preliminary small spot, pulsed, HF damage measurements indicate that improvements in damage resistance over conventional evaporated coatings may be possible using sputtered multilayer films.

2. Bias Deposition

Bias-assisted sputtering was accomplished using the dc magnetron source and 6N Si target material described previously [2]. A stainless steel grid was added 0.5 in. below the substrate, and -100 V were applied either directly to the grid or to the substrate itself. A schematic diagram of the magnetron source and the substrate-grid arrangement is shown in figure 1.

The hydrogen (H_2O) content and distribution and film morphology were determined, as before, by the resonant nuclear reaction technique [3] and transmission electron microscopy (TEM) [4], respectively.

---

*Work supported by Navy Independent Research Funds.

[1]Numbers in brackets indicate the literature references at the end of the paper.

Figure 2 shows a quantitative plot of the hydrogen content and distribution in a film deposited with -100 V dc bias applied to the stainless steel grid. The weight fraction of hydrogen (H_2O) in the film (40 ppm) is less than in evaporated films [2] and is similar to the results reported previously for magnetron films, with one significant difference: a large film-substrate interface component (reported in both evaporated and sputtered films [2]) is absent in the bias sputtered material. A more dramatic effect of bias sputtering is the marked structural change observed by TEM. Without bias, an island-defect morphology is observed in thin layers ($\leq$ 300 Å) that have been deposited and removed from NaCl substrates. The islands, which are 100-300 Å in diameter, are thought [5] to result from incomplete coalescence of the growing Si film and to lead to a columnar type, porous film morphology. With bias applied, evidence for this microstructure is strongly reduced, as shown in figure 3(b).

The above observations are consistent with the idea [6] that low energy Ar ions, extracted in this case from the plasma by the application of a negative voltage, can be effective in (1) desorbing low mass, weakly bound H_2O (OH^-) molecules (ions) and (2) enhancing the surface mobility of the condensing Si atoms. The latter effect could be accomplished by simple momentum transfer between the Ar ions and the Si atoms, by the reduction of surface contaminants, or by a combination of these two effects. In any case, judging from the TEM photographs, the coalescence process is enhanced by the bias conditions, leading to a denser, more homogeneous film morphology.

3. Reactive Sputtering

3.1. Optical Properties

The optical properties of sputtered Si films are changed significantly by the addition of reactive gases such as hydrogen or oxygen to the Ar sputter gas. With hydrogen, bonding defects or dangling bonds are passivated and this, in turn, results in a blue-shift of the absorption edge, a reduction of defect-related absorption in the 1- to 3-micron region (with a corresponding increase in SiH vibrational absorption), and a reduction of the index of refraction [7]. Values of absorption between 1 and 10 cm^{-1} at 2 microns have been reported for films deposited by the rf decomposition of silane [8]. With the addition of oxygen to the sputter gas, SiO_2 is formed, making possible multilayer (Si/SiO_2) formation by the simple periodic addition of oxygen to the sputter gas.

The effect on the optical absorption in the 1- to 3-micron region by adding hydrogen to argon in an rf diode sputter configuration is shown in figure 4. The solid line shows the absorption for pure sputtered Si (amorphous Si (α-Si)). These data are in agreement with that presented for magnetron sputtered α-Si [2]. By the addition of 2 x 10^{-4} torr hydrogen to 8 x 10^{-3} torr Ar, with 500 watts rf power applied to a 6-in. target, the data shown by the dashed (---) line was obtained (the absorption edge has shifted to a shorter wavelength). It was found that 4 to 8 x 10^{-4} torr was the optimum quantity of hydrogen required to minimize the absorption in the 1- to 3-micron region. This data is shown by the dash/dot curve (-·-) in figure 4. At the HF laser wavelength, sputtered Si has less absorption than evaporated Si. This absorption is further reduced by the addition of hydrogen to the sputter gas. The calorimetric results for evaporated and sputtered α-Si are summarized in table 1.

Table 1. HF laser calorimetric absorption of Si coatings[a]

Deposition method	B(cm^{-1})
Evaporated	$\geq$ 40
Sputtered, dc	18 ± 3
Sputtered, rf	17.5

[a]Laser calorimetry measurements were performed by Paul Kraatz of the Northrop Research Center, Palos Verdes, Calif.

3.2. First Thresholds

Small spot, pulsed multithreshold damage measurements at both HF and DF laser wavelengths were reported earlier for evaporated Si and SiO_x films [9], as well as other single-layer materials. Also, the HF/DF damage thresholds and absorption for magnetron sputtered and evaporated Si have been compared [2]. It was found that the HF thresholds are lower than DF thresholds, a result attributed to the presence of H_2O in the coatings and the strong OH^- absorption band at the HF wavelength [9]. While the effect is somewhat reduced in multilayer coated mirrors, the HF threshold is lower than the DF threshold in $(Si/SiO_x)^n$-coated mirrors.

Consistent with earlier [2] measurements on magnetron sputtered Si, we find that the first (or lowest) threshold of diode sputtered (rf) Si is about twice that of evaporated Si. It is interesting to note that in the case of sputtered Si in which dangling bonds have been passivated by hydrogen, the threshold is higher than for evaporated Si, but only about 80% of the value for pure sputtered Si; this is the case even though the absorption of α-SiH is lower than α-Si.

The slightly lower threshold of α-SiH relative to α-Si could be due to a relative instability of hydrogenated Si (α-SiH) which is actually a mixture containing about 15% (in this case) bonded hydrogen. The damage results for evaporated and sputtered Si are summarized in table 2, along with the results for silicon oxides and multilayers, which are discussed below.

Table 2. Small spot, pulsed HF laser first thresholds of Si coatings

	Evaporated, J/cm^2	Sputtered, J/cm^2
	Components	
Si	20 ± 5	55 ± 15
SiH	---	43 ± 12
SiO_x	200 ± 10	---
SiO_2	---	121 ± 12
	Design	
$(Si/SiO_x)^4AgMo$	70 ± 2	---
$(Si/SiO_2)^1Si$	---	98 ± 12
$(SiH/SiO_2)^1Si$	---	114 ± 48

Reactively sputtered SiO_2, as seen in table 2, has a lower first threshold than evaporated SiO_x, but a higher threshold than that reported [9] for SiO_2 formed by evaporation. Infrared transmission measurements indicate that reactively sputtered SiO_2 has a lower H_2O content than evaporated SiO_2 and an index of refraction close to bulk fused silica.

Multilayer Si/SiO_2 and SiH/SiO_2 coatings have higher first thresholds than state-of-the-art evaporated Si/SiO_x coatings. The difference in substrates and number of quarter-wave pairs should be noted; measurements made with similar designs will be required to verify these preliminary results.

In spite of the small but interesting differences in SiH and Si, these results for sputtered films are encouraging and suggest that further effort in the development of sputtered multilayer coatings would be worthwhile.

4. Conclusion

Sputtered Si films have continued to show promise as a coating material for the 2- to 4-micron region. Bias sputtering is useful in minimizing interface contamination and promoting the growth of high density, homogeneous layers. Reactive deposition in oxygen leads to stoichiometric, low water content, low index oxides that work well in multilayer combination with Si. Hydrogenation, while leading to a lower absorption form of Si (at least in the 1- to 3-micron region), does not appear to yield as stable a form of Si under pulsed HF laser irradiation as pure sputtered Si. This could result from the relative instability of SiH molecules. Based on these preliminary results and on results presented elsewhere at this conference [10], further work should be devoted to the development of multilayer structures using sputtering deposition.

5. References

[1] Donovan, T. M.; Fogdall, L. B.; Holmes, S. J. Enhanced reflectance mirrors for space-borne HF laser applications. SPIE 270: 24-29; 1981.

[2] Donovan, T. M.; Porteus, J. O.; Seitel, S. C.; Kraatz, P. Multithreshold HF/DF pulsed laser damage measurements on evaporated and sputtered silicon films. Bennett, H. E.; Glass, A. J.; Guenther, A. H.; Newnam, B. E., ed. Proceedings of the 12th annual symposium on optical materials for high power lasers; 1980 September 30-October 1; Boulder, CO. Nat. Bur. Stand. (U.S.) Spec. Publ. 620; 1981 October. 305-312.

[3] Donovan, T. M.; Temple, P. A.; Wu, Shiu-Chin; Tombrello, T. A. The relative importance of interfacial and volume absorption by water in various evaporated films. Bennett, H. E.; Glass, A. J.; Guenther, A. H.; Newnam, B. E., ed. Proceedings of the 11th annual symposium on optical materials for high power lasers; 1979 October 30-31; Boulder, CO. Nat. Bur. Stand. (U.S.) Spec. Publ. 568; 1980 July. 237-246.

[4] Transmission electron micrographs were supplied by J. H. Dancy, Naval Weapons Center.

[5] Knights, J. C. Structural studies of hydrogenated amorphous silicon. Solar Cells 2: 409; 1980.

[6] Ross, R. C.; Messier, R. Bombardment effects in a-SiH sputtered films. Proceedings of conference on tetrahedrally bonded amorphous semiconductors; 1981 March 12-14; Carefree, AZ. American Institute of Physics Proceedings No. 73; 1981. 53-57.

[7] Brodsky, M. H.; Cardona, Manuel; Cuomo, J. J. Infrared and Raman spectra of the silicon-hydrogen bonds in amorphous silicon prepared by glow discharge and sputtering. Phys. Rev. B16: 3556-3571; 1977. See also several papers on the optical properties of a-SiH presented at the amorphous and liquid semiconductor conference; 1981; Grenoble, France (published in J. de Physique).

[8] Jackson, W. B.; Amer, N. M. Direct measurement of the absorption tail of a-SiH in the range 2.1 eV > hν > 0.6 eV. Proceedings of conference on tetrahedrally bonded amorphous semiconductors; 1981 March 12-14; Carefree, AZ. American Institute of Physics Proceedings No. 73; 1981. 263-267.

[9] Porteus, J. O.; Donovan, T. M.; Jernigan, J. L.; Faith, W. N. Multithreshold evaluation of 100-nsec pulsed laser damage to coating materials at 2.7- and 3.8-μm wavelengths. Glass, A. J.; Guenther, A. H., ed. Proceedings of the 10th annual symposium on optical materials for high power lasers; 1978 September 12-14; Boulder, CO. Nat. Bur. Stand. (U.S.) Spec. Publ. 541; 1978 December. 202-211.

[10] Pawlewicz, W. T.; Martin, P. M. Improved Si-based coating materials for high power infrared lasers; this conference.

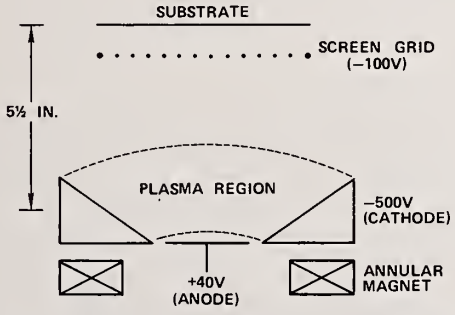

Figure 1. Schematic diagram of dc magnetron source (Varian s-gun) showing substrate-grid arrangement.

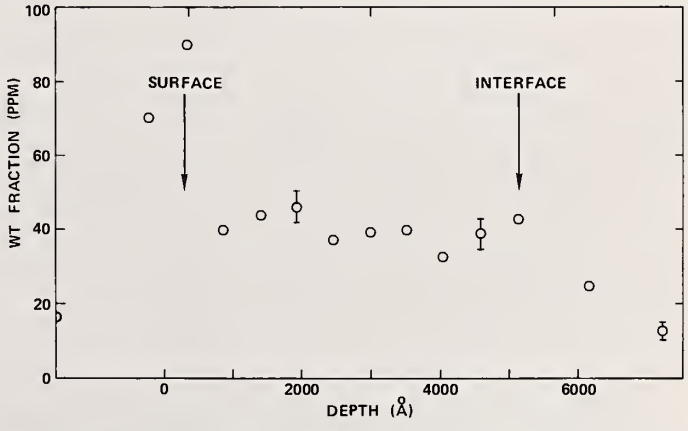

Figure 2. Resonant nuclear reaction analysis profile of hydrogen in a bias-deposited Si film. Note the absence of a film-substrate interface contamination layer.

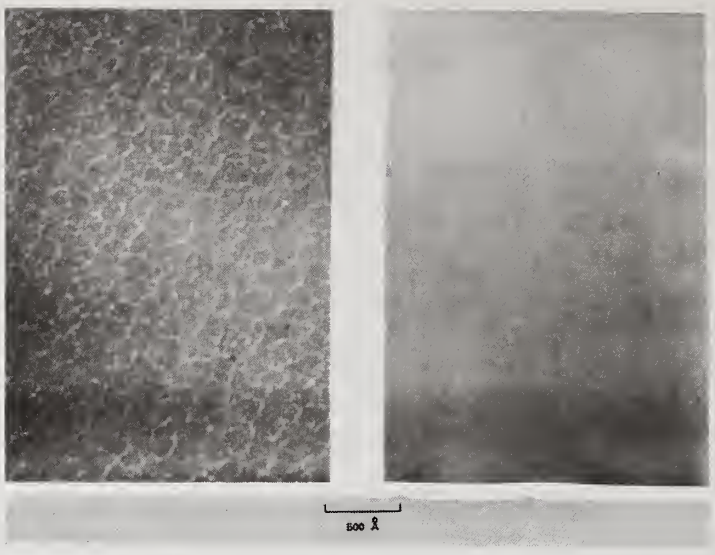

(a) (b)

Figure 3. (a) TEM of magnetron-sputtered Si. Note island-defect morphology. (b) TEM of bias-deposited Si. Note homogeneous morphology, fewer defects, and higher film density.

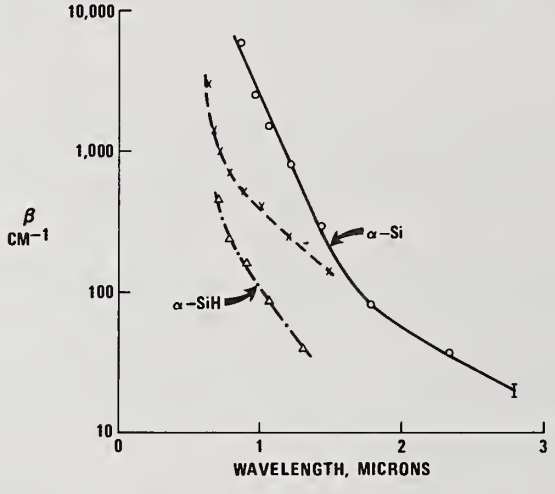

Figure 4. Spectral absorption of rf diode-sputtered Si films. Data for pure sputtered α-Si are represented by circles; hydrogenated α-Si with optimum hydrogen for minimizing absorption in the 1- to 3-micron wavelength region are represented by triangles (absorption in this film was below the limit of our spectral measurement at wavelengths higher than 1.5 microns).

The opinion was expressed by one of the members of the audience that in scaling the process to large sizes, film thickness uniformity was more easily achieved by diode sputtering than by conventional evaporation. The speaker reported that in his films the uniformity achieved using either diode sputtering or magnetron sputtering was about 5 percent. That value could be improved with additional effort. The thickness of the layers deposited was about 1 μm. The infrared scatter observed from these films was low although a detailed study of scattering had not been made.

Optical Properties of Hydrogenated Amorphous Carbon (a-C:H) - a Hard Coating for IR-Optical Elements

A. Bubenzer and B. Dischler
Fraunhofer-Institut für Angewandte Festkörperphysik
Eckerstr. 4, D-7800 Freiburg

and

A. Nyaiesh

University of Sussex, School of Engineering and Applied Sciences
Falmer, Brighton, Sussex BN1 9QT, England

Hydrogenated amorphous carbon films a-C:H were deposited on glass and germanium substrates. The films are transparent in the IR and are extremely hard (Mohs's hardness of about 8). The a-C:H coatings were prepared according to the method of Holland in an RF excited discharge sustained by various hydrocarbon gases.

Thickness, density, refractive index (at 0.3 μm and 2 - 10 μm) and relative hydrogen content were determined. Variations in IR-refractive index and relative hydrogen content could be correlated with deposition conditions. With a refractive index of approximately 2 a-C:H is an ideal AR-coating for germanium (n = 4). Laser calorimetric measurements of optical absorption at 10.6 μm give a loss as low as 4% for a 1.3 μm thick coating on germanium ($\lambda/4$ for n = 2 at 10.6 μm). Preliminary damage tests with a CO_2 laser (600 W, cw) were performed.

Key words: amorphous hydrogenated carbon; AR coating; germanium; hard coating; infrared; laser calorimetry; plasma deposition.

Introduction

During the last years an increasing attention has been drawn to a special form of carbon which in the form of thin films has been named: I-carbon, diamond like carbon, hard carbon or a-C. The material shows strong analogies to the well known amorphous silicon: a-Si [1,2]. Therefore we consider the name a-C to be the most adequate one. First of all the short range order in both amorphous materials is similar. Considering the physical properties of a-C (e.g. the exceptional hardness of 8 on the Mohs's scale[3]) there is strong evidence that a-C has a distorted "diamond like structure", like a-Si. This means each carbon atom has a tetrahedral or nearly tetrahedral coordination. Apparently due to this relatively disordered amorphous structure a-C like a-Si can incorporate high concentrations of hydrogen (up to 25% [4]). Thus the name a-C:H is more precise. Both materials can only be produced in the form of thin films up to several μm thickness.

There is one important exception to the analogy however: The thermodynamically stable form of carbon at normal pressure is graphite and not diamond. A graphite like structure does not exist for silicon. Due to these two totally different carbon modifications a-C:H thin films can differ significantly in their properties. Depending on the preparation conditions the material is either on the graphite side (electrically conducting, optically opaque) or on the diamond side (electrically insulating, optically transparent). The most valuable inheritance from the diamond side is the exceptional hardness of a-C:H thin films which can be as high as Mohs's hardness 8 (diamond:10).

One important application of a-C:H films are coatings for germanium optical elements. Due to its refractive index n = 2 a-C:H is an ideal antireflection, as well as protective coating for germanium with refractive index n = 4 [5] . With regard to this application the optical properties of a-C:H are of particular interest.

Preparation

There is a number of methods to produce a-C:H thin films, most of them rely on accelerating ionized C or C-H particles towards the substrate surface [3-20] . This paper is concerned only with a-C:H thin films prepared by deposition in an RF excited hydrocarbon plasma [6] . If the appropriate deposition parameters are chosen, homogeneous, large area coatings with high electrical resistivity, optical transparency and high mechanical hardness can be deposited by means of this method. Figure 1

shows the outline of the coating apparatus. A hydrocarbon gas is leaked into a glow discharge chamber with one RF electrode grounded and the other which is capacitively coupled to a RF source (MHz range) serving as the substrate carrier. In the discharge region the hydrocarbons are ionized and the positively charged C, C-H and H particles are accelerated towards the substrate under the negative cathode self bias [21,22] with respect to the plasma and thereby form a carbon film. The deposition time for a 1.3 μm thick coating (i.e. a $\lambda/4$ coating for 10.6 μm) is on the order of 30 minutes. Deposition conditions in the system are highly reproducable.

Optical Properties as a function of deposition parameters

Properties of a-C:H thin films largely depend on the kinetic energy with which ions hit the substrate surface. This energy is predominantly determined by the quotient negative bias voltage U_B divided by gas pressure P. In figure 2 this dependence of film properties on U_B/P is demonstrated in 3 examples:

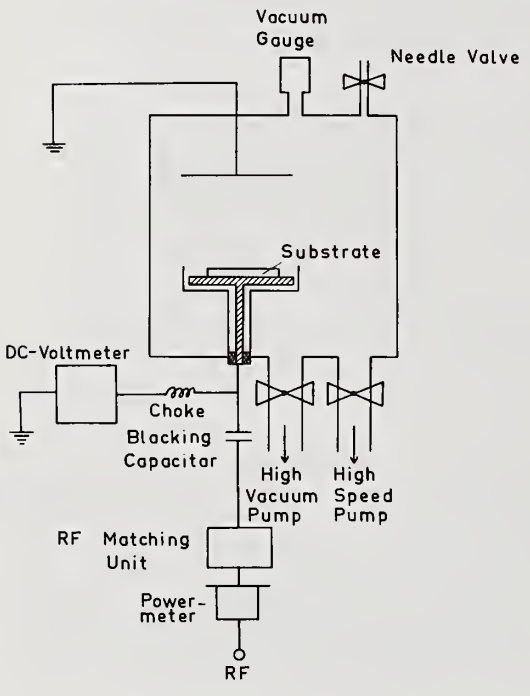

Figure 1. RF coating apparatus.

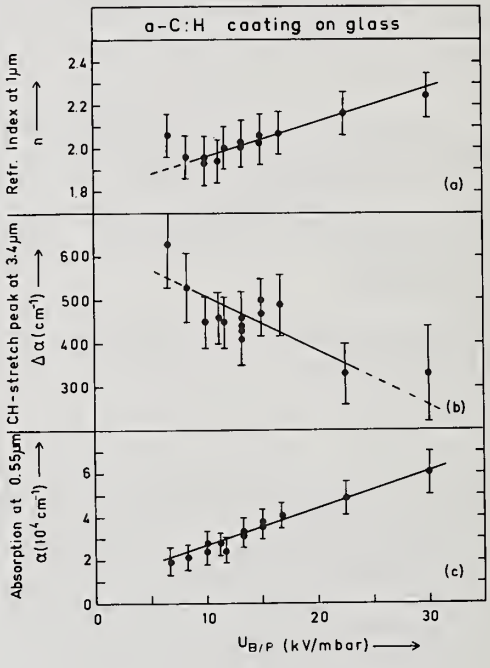

Figure 2. Dependence of a-C:H thin film properties on deposition parameters U_B/P = negative self bias/gas pressure.
(a) refractive index at 1 μm; (b) C-H stretch vibration peak at 3.4 μm; (c) absorption at 550 nm showing the shift of the short wavelength optical absorption edge.

The refractive index n at 1 μm (fig. 2(a)) was determined from thin film interference observed in transmission and reflection. Observed values of n vary from 1.86 to 2.24 approaching the diamond value of 2.4 for high ionic energies. For application as antireflection coating for germanium, n can thus be exactly tuned to a value of 2 by means of the proper deposition parameters U_B and P. Within experimental accuracy the dispersion between 1 and 10 μm is negligible in a-C:H.

a-C:H thin films can contain upto 25% of hydrogen, therefore the 3.4 μm C-H stretch vibration is a prominent feature of the optical absorption spectrum. As shown in figure 2(b) the strength of this vibrational band i.e. the relative hydrogen content decreases with increasing U_B/P. - A situation similar to that in a-Si:H.

Finally the optical absorption edge changes with U_B/P (fig. 2(c)): Films produced under increasing U_B/P change their color from yellow to black. This means, the short wavelength optical absorption edge is shifting to longer wavelength with increasing U_B/P. A similar shift of the absorption edge has been reported for a-Si:H [1,2]. Whether this effect like in a-Si:H is due to varying hydrogen content and thus a changing number of dangling bonds is unknown.

Infrared transmission of a-C:H

The applicational value of a-C:H as protective and antireflection coating for IR optical elements - particularly germanium - largely depends on its IR transmission spectrum. Figure 3 shows the transmission,(1-reflection) and loss spectrum of a 1 mm germanium disk coated with a-C:H on each side to give zero reflection at approximately 10.6 µm (fig. 3 curve 1).

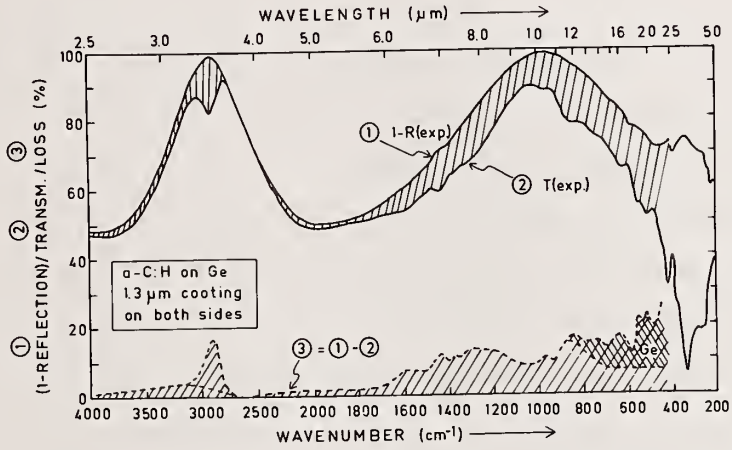

Figure 3. Transmission,(1-reflection) and loss spectrum of a germanium disk with an a-C:H $\lambda/4$ coating for 10.6 µm on each side.

As could be shown by a separate more precise measurement, the reflection around 10.6 µm is indeed less than 1%, this means the refractive index is very well tuned to the right value of 2.

Curve 2 of figure 3 gives the optical transmission which is lower than the (1-reflection) value due to the losses plotted in curve 3 of figure 3. The losses at 3.4 µm are due to the C-H stretch vibration mentioned above. The losses above 12 µm are mainly due to the germanium substrate. The origin of the losses between 6 and 12 µm is still an open question. But there seem to be basically two possible mechanisms: The first is C-C one phonon lattice vibrations. Although these are not infrared active in the closely related diamond structure according to the symmetry selection rules, they may became infrared active in a-C:H, where the symmetry is significantly lower. The second possibility is absorption by C-H deformation bands. From comparison of the structure in the loss spectrum with lattice phonon frequencies in diamond and with infrared spectra of organic polymers the latter mechanism appears to be more likely.

An independent and precise value of the losses at 10.6 µm of the sample in figure 3 was obtained from measurements with a CO_2 laser calorimeter. The actual loss in the two coatings including resonant interference effects is 8%. The value corrected for thin film interference is 6.4% [23]. The loss in the coated germanium sample can be fully attributed to the two coatings, since the loss within the 1 mm thick germanium substrate at 10.6 µm is on the order of 0.2%.

Damage tests

a-C:H coatings on germanium were tested with a CO_2 laser. Damage of the 1 mm germanium disk with a 0.8 µm coating occurred at 600 W with 1 cm^2 beam after 1 s irradiation, due to melting of the germanium substrate caused by thermal runaway. Another result of the damage test is the fact that the a-C:H coating surrounding the molten damage spot is undamaged and still sticks to the germanium. This

means the coating was resistant to the thermal shock of the molten germanium (900 centigrade).

Summary

We produced hydrogenated amorphous carbon coatings a-C:H which were extremely hard and optically transparent. They can be routinely deposited in a RF plasma from hydrocarbon gases.

We found that the refractive index increases with the quotient negative self bias divided by gas pressure U_B/P approaching the value for diamond.

The short wavelength absorption edge shifts to longer wavelengths with increasing U_B/P and hydrogen content decreases; the analogous behaviour has been previously reported for a-Si:H.

Finally a-C:H was shown to be applicable as protective (very hard and chemically resistent) as well as anti reflection coating for germanium.

References

[1] M.H. Brodsky, R.S. Title, K. Weiser and G.D. Petit, Phys. Rev. B1 (1970) 2632.

[2] Eva C. Freeman and William Paul, Phys. Rev. B20 (1979) 716.

[3] G. Brandt, IAF Freiburg, private communication.

[4] S.M. Ojha, H. Norström and D. McCulluch, Thin Solid Films, 60 (1979) 213.

[5] L. Holland and S.M. Ojha, Thin Solid Films, 58 (1979) 107.

[6] L. Holland, Brit. Pat. No. 15 82 231 (Appl. 1976)

[7] S.M. Ojha and L. Holland, Thin Solid Films, 40 (1977) L31.

[8] S.M. Ojha and L. Holland, Proc. 7th Int. Vacuum Congr. and 3rd Int. Conf. on Solid Surfaces, Vienna (1977), Berger, Vienna (1977) p. 1667.

[9] B. Meyerson and F.W. Smith, J. Non-Cryst. Solids, 35-36 (1980) 435.

[10] B. Meyerson and F.W. Smith, Solid State Commun., 34 (1980) 531.

[11] L. Holland and S.M. Ojha, Thin Solid Films, 38 (1976) L17.

[12] L. Holland and S.M. Ojha, Thin Solid Films, 48 (1978) L21.

[13] R.J. Gambino and J.A. Thompson, Solid State Commun., 34 (1980) 15.

[14] K. Enke, Thin Solid Films 80 (1981) 227.

[15] K. Enke, H. Dimigen and H. Hübsch, Appl. Phys. Lett., 36 (1980) 291.

[16] L.P. Andersson, S. Berg, H. Norström, R. Olaison and S. Towta, Thin Solid Films, 63 (1979) 155.

[17] L.P. Andersson and S. Berg, Vacuum, 28 (1978) 449.

[18] C. Weissmantel, G. Reisse, H.-J. Erler, F. Henny, K. Bewilogua, U. Ebersbach and C. Schürer, Thin Solid Films 63 (1979) 315.

[19] C. Weissmantel, Thin Solid Films, 58 (1979) 101.

[20] S. Aisenberg and R. Chabot, J. Appl. Phys. 42 (1971) 2953.

[21] J.W. Coburn and Eric Kay, J. Appl. Phys., 43 (1972) 4965.

[22] J.L. Vossen, J. Electrochem. Soc., 126 (1979) 319.

[23] H.E. Bennet and D.K. Burge, J. Opt. Soc. Am. 70 (1980) 268.

The speaker was asked if a sooty-like graphite coating was formed on the walls of his chamber. He replied, "No, there was a potential drop between the plasma and the anode which forms a polymer-like coating but no graphite coating." The suggestion was made that the hydrogen carbon mixture might result in a polymer coating rather than a pure carbon coating. The speaker replied that the resultant coating was hard and transparent with good adhesion, whether it was polymeric or not was probably unimportant from an applications point of view. He had not yet checked the reactivity of the film to solvents or the possible barrier properties of the films to block impurities from migrating to the substrate. They had not tried to deposit on alkali halides yet. They made a brief but unsuccessful effort to deposit films on BaF_2.

Studies of Diamond-Like Carbon Coatings for Protection of Optical Components

M.L. Stein* and S. Aisenberg*

Gulf + Western Applied Science Laboratories
335 Bear Hill Road
Waltham, Massachusetts 02154

B. Bendow

The BDM Corporation
1801 Randolph Road, S.E.
Albuquerque, New Mexico 87117

Ion-deposited diamond-like carbon is a promising candidate for thin protective coatings for optical components. Our recent studies have been directed to ascertaining several key properties of the coating, and verifying its protective nature.

Tests performed on coated discs of CaF_2 indicated improved resistance to environmental attack by acids, bases, and solvents. Hermeticity was corroberated by comparing the effects of HF-acid on coated and uncoated surfaces. The tenacity to substrates such as glass and CaF_2 was demonstrated by the difficulty to remove the coating with standard techniques, such as exposure to HF and water. Also, a marked decrease in abrasion was found (by measuring forward optical scatter) for the coated portion of a disc.

Optical measurements performed on these coated discs indicated that the coating neither significantly decreased transmission as measured from 2 to 6 microns, nor induced visible scatter. High resolution scanning and transmission electron micrograph studies indicate that the films are partly amorphous with a partial ordering of carbon atoms; while Raman studies indicated both graphite as well as microcrystalline diamond-type behavior. ESCA studies indicated a C to CaF_2 gradient throughout the coating indicative of ion implantation. Thickness determinations were made by substrate dissolution and surface profile measurements.

Key words: Diamond-like carbon film; ion deposition; protective optical coating; thin films.

1. Introduction

Ion deposition of carbon films has been considered as a potential coating technique for optical components for several years. This interest is due to several properties which are potentially desirable. These include low optical loss from visible to extended infrared wavelengths, chemical stability, and resistance to attack by oxidizing agents. The films have also demonstrated durability and scratch resistance with good adhesion to substrates. Consequently, the material seems desirable as a potential candidate for coating softer materials which can readily be damaged. One such material that we have studied and are reporting on in this paper is Calcium Flouride. This material possesses a very high laser damage threshold and low absorption throughout a significant portion of the infrared spectrum, but is relatively soft and can suffer from chemical and moisture attack as well.

While ion deposited carbon films have demonstrated these properties on several substrates, difficulty has been reported in achieving a good film deposition on the halide substrates. The purpose of this present effort is to evaluate several critical aspects and properties of diamond-like carbon films deposited on these substrates. As our research progressed, we noted initially that the adhesion of the diamond-like carbon films were relatively poor when bound to Calcium Flouride substrates. As a result, several techniques were developed to overcome this problem.

2. Ion Deposition Process

Our basic process and equipment for ion beam deposition has been described in a number of publications and patents[1][2][3]. This process and properties have been confirmed by Spencer & Schmidt[4]. Modifications to the process for Calcium Flouride substrates will be briefly

described here.

Since the quality of the adhesion to the substrate was somewhat poor, several attempts were made to improve adhesion. Standard techniques such as heating of the substrate or Argon ion bombardment prior to deposition proved to be advantageous. However, tenacious bonds as observed for materials such as silicon were not apparent. Consequently, it was felt that some degree of implantation into the crystalline substrate could achieve higher bond strength, since alloys between Carbon and Calcium Flouride are not readily formed.

Using the ion beam deposition technique at our facility, we were able to selectively control the incoming ion energy on the substrate. As a result, the specific dosage level could be maintained while increasing the depth of penetration of incoming ions. For this current work, the ion beam source has been extended along one dimension from the original cyclindrical beam of the basic design. This extended slit design allows better coating uniformity. It is clear that the extended beam source allows scanning of larger areas in one pass. This eliminates the necessity of rastering the ion beam across the specimen and consequently results in better uniformity. Also, since several species of ion can be extracted from the slit, it was found that a diffused argon ion beam overlaying the carbon deposition was beneficial in producing a hard film, as illustrated in figure 1. In order to achieve reasonable adhesion, implantation energies of several kilovolts were used which resulted in implantation of carbon ions to several hundred angstroms within the Calcium Flouride crystal. This is consistant with theoretical ion stopping distances based on a refinement of the Lindhard-Scharff-Schoitt formulation using an experimentally deduced value of electron stopping constant (5).

As a result of these improvements to the carbon ion beam deposition process, several unique benefits were possible over other deposition techniques. These include high surface mobility and high nucleation energies. The ability of using charged ions permits control of beam dosage as well as direction. The uniformity of the beam across the slit surface can be controlled to within one percent. Lower pressure deposition in the region of the sample results in high purity films with less inclusion of background gases. Implantation and compositional profiling into the substrate are possible besides coating. The precision of the ion beam also allows mask patterns and structures to be defined on optical surfaces.

3. Composition

Ion deposited carbon films formed with this new source have demonstrated several unique properties over previous films. Owing to the enhanced degree of implantation, a more complex, thicker structure has been defined beyond the basic coating thickness. Referring to figure 2, we can see the surface modification which occurred after coating a Calcium Flouride window. To start the process, the initial surface contamination layer was removed by Argon ion sputtering. The implantation energies vary from 2 to 10 kilovolts. Analyses of these samples have indicated a decrease of carbon as one looks deeper into the Calcium Flouride. The apparent thickness of the modified zone is approximately 600 angstroms. A profile after various periods of ion milling appears in figures 3 and 4. The total depth of penetration is estimated at 600 angstroms throughout the 20 minute ion milling profile. As is evident, the material still contains a significant portion of carbon, 67.8%, which had decreased from 79.3% on the sample surface as received. Relative percentages of Calcium and Flourine has increased proportionately.

Figure 5 shows Raman spectra taken on films of similar thickness deposited on polycrystalline silicon revealing structures indicative of both graphite and diamond. This is anticipated since it has been found that higher energy ion deposition can cause graphitization of the diamond lattice. Consequently, using energies greater than 50 or 60 volts can result in some degree of graphitization of the diamond. Future studies will be directed towards determining the degree of implantation needed to achieve the desired mechanical properties.

4. Optical Characteristics

Previous measurements on the optical properties of ion deposited carbon films have shown the films to be transparent spectrally from 0.35 microns to 50 microns. The IR spectrum of Calcium Flouride was established as a reference from 1.0 to 15 microns as illustrated in figure 6. The

other side of the reference sample was coated with a 600 angstrom thick carbon film. A scan of the coated and uncoated surfaces for two samples revealed no detectable IR activity within the precision of the instrument over the 1 to 8 micron window for Calcium Flouride. As a consequence of finding no detectable attenuation due to the coating, it was determined to use laser calorimetry for resolution of absorption. With the help of the Naval Weapons Center in China Lake, the following information presented in table 1 has been generated. By comparing coated and uncoated samples, total absorption for a 600 angstrom ion beam deposited film resulted in an extinction coefficient of approximately $150cm^{-1}$. For a coating of this thickness, the attenuation coefficient may be acceptable for some applications. Due to the flatness of the IR spectrum, it is assumed that the attenuation is due to free electron as well as atomic absorption.

5. Mechanical Properties

One of the desirable aspects of the carbon films is the reported hardness of this material. A true hardness number for carbon on CaF_2 is difficult to obtain because of the relative softness of the substrate and thinness of the film. Nonetheless, relative abrasion resistance of the material has been demonstrated using a falling sand test. This test was performed by pouring two kilograms of abrasive sand from a controlled height according to the ASTM D698 test method. This was done for coated and uncoated surfaces of the Calcium Flouride disc. The discs were then illuminated with a diffused laser beam, the pattern of which was photographed. Comparisons of the scattered intensities revealed that the coated side appeared to have a much smaller damage zone, approximately half the diameter of the uncoated side as illustrated in figure 7. Mechanical adhesion performed by a pull test showed a bond strength to Calcium Flouride to be greater than 6000 kPa. Evidently, the material does form a good tenacious bond to this substrate, and the bond is limited by the strength of the substrate.

6. Chemical and Barrier Properties

One of the other principle advantages of the film is its resistance to chemical attack. The film has been found to be stable in concentrated acids, as well as organic solvents. A typical technique used for removal of thin films is to expose the substrate to an etching vapor or by soaking it in a solution which will dissolve the substrate (6). Removal of the carbon films has been very difficult, sometimes requiring over an hour in hydrofluoric acid to be able to remove a small edge of the film. The barrier nature was confirmed by depositing the carbon over an aluminum film as illustrated in figure 8. Half of the aluminum film, 2000 angstroms thick, was coated with our Diamond-Like Carbon. This was then exposed to hydrofluoric acid and photographed through a microscope. As is evident, most of the uncoated aluminum was etched away, while no attack was apparent on the carbon coated aluminum.

7. Conclusions

As a result of this study we have found that using an ion beam deposition technique can be advantageous for deposition of thin carbon films. In particular, configuration of the ion source to include a ribbon beam with good uniformity as well as multi-component composition and the ability to achieve reasonable implantation depths has proved advantageous. In answering the basic questions of this study, the attenuation of the film has been shown to be low for some applications, however, some degree of graphitization does occur in the carbon film. Consequently, reducing the duration of the implantation period is expected to reduce the resulting attenuation. Since no infrared spectral activity has been observed, the absence of major hydrocarbon absorption is assumed. The film adhesion on Calcium Flouride has been enhanced to a useable level, making it a viable material as a protective agent for other materials and coatings. Also, the film has been demonstrated to have significant abrasion resistance indicating a two-fold decrease in damage area on Calcium Flouride for 600 angstrom thickness. Based on these findings, we are considering investigating films of greater thicknesses to determine optimal abrasion resistance protection.

In summary, the Diamond-Like Carbon Film has shown several useful properties predicted in connection with high power laser optical elements. These include low IR absorption, abrasion resistance, chemical inertness, barrier properties, and good adhesion. Based on these results, our future work should be directed towards further development of the ion beam process while

researching the composition and structure of the carbon films. We would anticipate finding a relationship between coating performance and deposition parameters such as ion type, ion energy, and dosage.

---

*This work was partially supported by RADC (AFSC).

We would like to acknowledge the following for their assistance in analyzing the materials studied: P. Temple - Naval Weapons Center, S. Mitra - University of Rhode Island, P. Banerjee - University of Rhode Island, R. Braun - Rome Air Development Center, J. Comer - Rome Air Development Center, and A. Gleubouic - Rome Air Development Center.

8. References

(1) Aisenberg, S., Chabot, R.: Ion-Beam Deposition of Thin Films of Diamond-Like Carbon, J. Appl. Phys. 42,2953, (1971).

(2) U.S. Patent No. 3,904,505, September 9, 1975, Apparatus for Film Deposition, by S. Aisenberg.

(3) U.S. Patent No. 3,961,103, June 1, 1976, Film Deposition, by S. Aisenberg.

(4) Spencer, E.G., Schmidt, P.H., Joy, P.C., and Sansalone, F.J.: Ion Beam Deposited Polycrystalline Diamondlike Films, Appl. Phys. Letters, 29,118, (1976).

(5) Wilson, R.G., and Brewer, G.R.: Ion Beams, (R.E. Krieger Publishing Company, NY, 1979).

(6) Stein, M.L., Aisenberg, S., and Stevens, J.M.: Ion Plasma Deposition of Hermetic Coatings for Optical Fiber. Presented at the 82nd Annual Meeting of the American Ceramic Society. April, 1980.

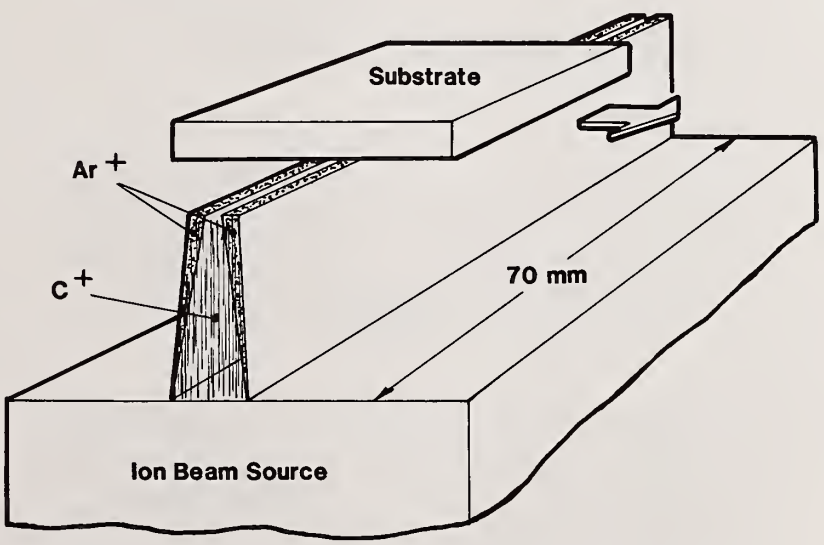

Figure 1 Strip type ion beam deposition process

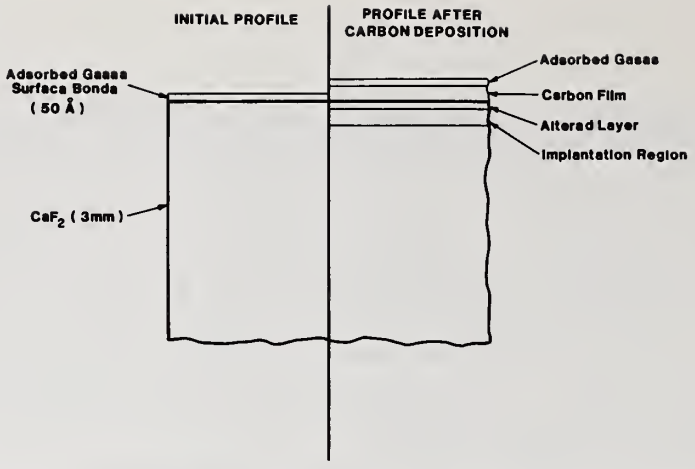

Figure 2 Surface modification and coating of CaF_2 window

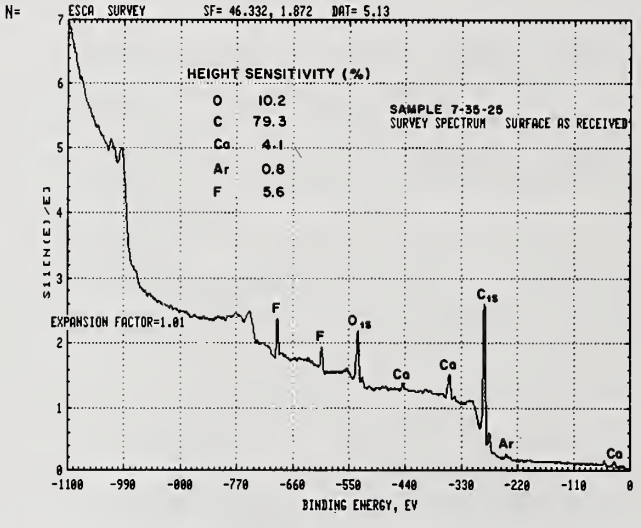

Figure 3 ESCA Survey Spectrum - Carbon on CaF_2 as received

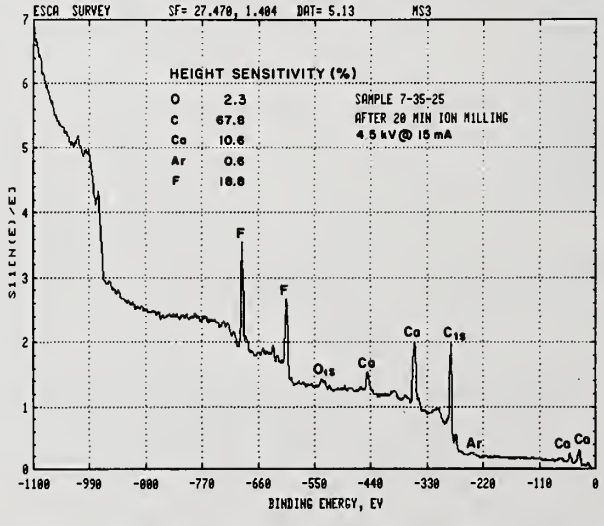

Figure 4 ESCA Survey Spectrum - Carbon on CaF_2 after 20 minutes ion milling

Sample	Wavelength (Microns)	Total Absorption
Uncoated	2.9	2.9×10^{-4}
Coated	2.9	10.3×10^{-4}
Uncoated	3.8	2.2×10^{-4}
Coated	3.8	7.8×10^{-4}

Uncoated: 3 mm 1/10 wavelength CaF_2

Coated: With 600Å Ion Beam Deposited Carbon

Table 1 Comparitive IR absorption for a half coated CaF_2 disc - Sample #7-28-4. Note that the coating has an absorption only 3.6 times greater than that of the uncoated surface.

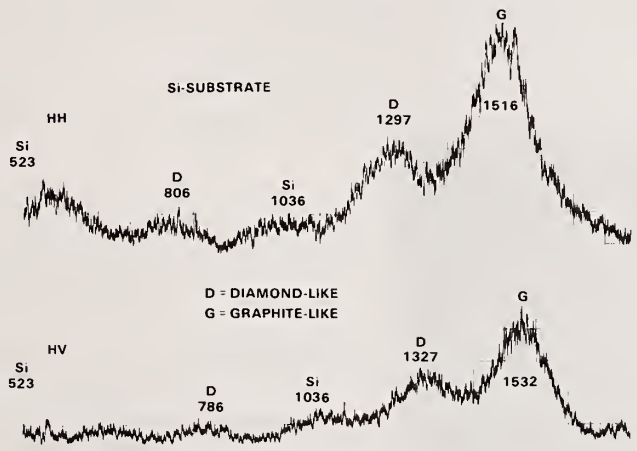

Figure 5 Raman spectra of Diamond-Like Carbon

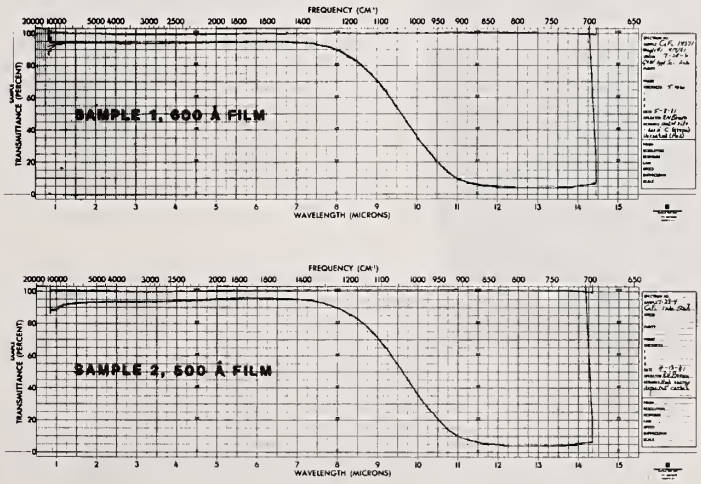

Figure 6 Absence of IR absorption bands in Ion Plasma Deposited Carbon Films on CaF_2 windows (coated transmission spectra overlays uncoated spectra - the two traces match showing no observable absorption). Two samples are shown.

COATED SIDE UNCOATED SIDE

- Abrasion for 2kg sand per ASTM D698
- Laser illumination at 0.6 micrometers

Figure 7 Relative laser scatter after abrasion on a CaF_2 disc half coated with 600 angstroms of carbon

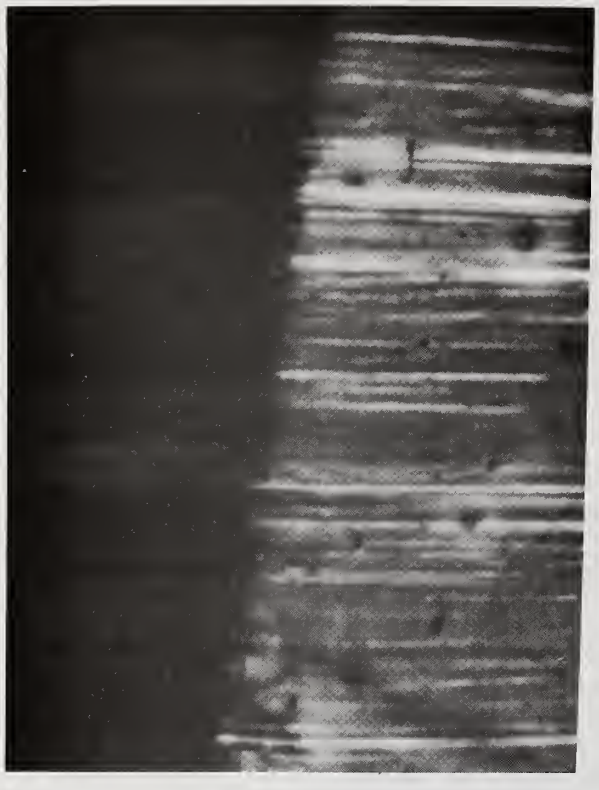

COATED UNCOATED

Substrate: Microscopy slide coated with 2000Å of Al (by evaporation).

Diamond-Like Carbon Film: Left half of slide coated with 400Å of ion deposited Carbon

Etchant: 1% HF solution @ 23°C for 100 seconds.

Figure 8 Photomicrograph (in transmission showing removal of uncoated Al, and protection of Aluminum with Diamond-Like Carbon coating.

THE DEPOSITION OF DIAMONDLIKE CARBON THIN FILMS ON CaF_2*

Thomas J. Moravec
Honeywell Corporate Technology Center
10701 Lyndale Ave. So.
Bloomington, MN 55420

As part of an AFML program, deposition conditions were studied to produce diamondlike carbon thin films on CaF_2. Halide materials are difficult to deposit diamondlike carbon coatings onto because of the moderate or large coefficient of thermal expansion of the halides which causes thermal induced separation of the coating. In addition, the adhesion of the carbon films to CaF_2 is poor. Several pretreatments were attempted to improve adhesion without much success. We describe a simple thermal technique that resulted in carbon films adhering most of the time to CaF_2 mechanical test bars and optical discs. The problem of adherence, however, has not been solved for this film-substrate system.

Key words: Diamondlike carbon; Carbon; Thin Film; CaF_2; Hard Coating; Laser Calorimetry; Plasma Deposition.

1. Introduction

This paper presents some of the results of a study to determine if diamondlike carbon thin films can be developed into protective coatings for CaF_2. These films are frequently referred to as i-Carbon (i-C) meaning that some ion process is involved in their production [1].[1] We have produced i-C films on metals, insulator, and semiconductors by radio frequency (rf) plasma decomposition of the alkane gases and low energy carbon ion beam deposition by the techniques described previously [1,2]. In this study the films reported on were produced by the first method, i.e. rf plasma decomposition of the alkane gases. We will discuss first the deposition of i-C films on CaF_2 and then measurements of the mechanical properties and laser calorimeter absorption of these films on CaF_2.

2. Experimental Techniques

All samples were coated in a capacitively coupled parallel plate electrode rf reactor system by decomposition of hydrocarbon gas. Electrode diameter was 15 inches, rf power typically 500 watts and deposition pressure 4.5×10^{-2} torr. An argon plasma etch was done prior to deposition without breaking vacuum to improve adhesion.

---

* This work supported by AFML Contract F33601-81-C-0098

1. Figures in brackets indicate the literature references at the end of this paper.

Adhesion to CaF_2 and all alkali and alkaline earth halides is poor probably due to the thermal mismatch between the i-C film and substrate. Thus, coating of CaF_2 is not straightforward. We succeeded some of the time in obtaining adherent coatings by keeping the deposition process slow enough to allow for little thermal heating of the surface. This was accomplished by interrupting the deposition every five minutes to allow for the surface to cool before proceeding. Coatings of 700-1000Å thick were produced in typically 45 minutes with this technique. An Argon plasma etch was done previous to deposition without breaking vacuum to improve adhesion. An oxygen plasma etch was tried without much success.

3. Mechanical Properties

Two sets of bar CaF_2 samples (5cm x 1cm x 5cm) were coated for testing by standard 4-point bend strength test. This was done to see if the i-C coatings increased the surface fracture strength of CaF_2. The testing was done at AFML. Table 1 presents the data, which were kindly supplied by Dr. Alan Hopkins, AFML. Note that there is a slight increase in ultimate strength exhibited by the coated samples, but the standard deviation is large.

4. Optical Absorption

One sample of a 1.52 inch diameter CaF_2 disc coated with 1200Å i-C film was measured by standard laser absorption calorimetry at AFML at three wavelengths. The data, supplied by Dr. Alan Hopkins, AFML, are as follows:

β_c (1.3 μm) = 446.3 cm^{-1}
β_c (2.9 μm) = 428.8 cm^{-1}
β_c (3.8 μm) = 121.5 cm^{-1}

5. Summary

i-C films were deposited on CaF_2 mechanical test specimens and optical discs. The coated specimens exhibited a slight increase in fracture strength, but this is probably not significant. Laser absorption calorimetry measurements of one coated sample showed infrared absorption to be too high to be used for high power applications with coatings made by present state-of-the-art techniques. In addition, it is very difficult to obtain adherent i-C coatings on CaF_2 with present techniques. Although these coatings are being used for other optical applications [3], more research is necessary before i-C films will be able to be used for high powered applications.

6. References

[1] T.J. Moravec and T.W. Orent, J. Vac. Sci. Technol. 18, 226 (1981).

[2] T.J. Moravec, Thin Solid Films 70, L9 (1980).

[3] T.J. Moravec and J.C. Lee, J. Vac. Sci. Technol., (to be published 1982).

TABLE 1

4-Pt. BEND STRENGTH, i-C FILMS ON CaF_2

Group 1. Gas: Methane, Thickness 700Å

Specimen Number		Ultimate Strength MPa	ksi
1		95.2	13.8
2		119.8	17.4
3		59.8	8.7
4		68.5	9.9
5		59.7	8.7
6		113.8	16.5
7		74.0	10.7
8		87.1	12.6
9		107.4	15.6
10		109.3	15.9
11		69.6	10.1
12		74.0	10.7
13		37.9	5.5
14		38.9	5.6
	$\bar{x}$	79.7	11.6
	s	26.6	3.9

Group 2. Gas: Ethane, Thickness 1000Å

Specimen Number		Ultimate Strength MPa	ksi
16		87.2	12.6
17		77.7	11.3
18		99.0	14.4
19		76.7	11.1
20		43.6	6.3
21		83.0	12.0
22		41.1	6.0
23		69.5	10.1
24		107.2	15.5
	$\bar{x}$	76.1	11.0
	s	22.3	3.2

Uncoated Controls (25 Specimens)

	Ultimate Strength MPa	ksi
$\bar{x}$	74.1	10.9
s	24.1	3.5

It was pointed out by a member of the audience that there are significant differences between the ion beam deposition technique and the rf plasma technique reported in the paper. The differences are that in the ion beam technique (1) the energy is much higher, (2) the pressure is much lower so that the mean free path is much longer, and (3) there is the ability to do some implantation into the substrate while deposition is occurring so that the adhesion is much better than is found with the plasma deposition technique. The questioner reported that his results were in agreement with those reported in the paper on poor adhesion to CaF_2 when he used the rf technique, but he found no difficulties when the ion beam method was used. The questioner also felt that the ion beam method produced lower stress films than the rf technique and since it is a low-temperature process one does not have to worry about the thermal delamination problem.

A second questioner asked if the film could be made conductive. The speaker replied that that was possible, there was a group in New York City which was doping the film to produce semiconductors. In response to a third question the speaker reported that methane, ethane, and butane were not equivalent. The hydrogen content and pressure regimes where the best properties were obtained varied with starting gas.

Relationship Between Coating Defects and the Limiting Flux Density a Cooled Laser Mirror Can Withstand

J. R. Palmer

TRW
One Space Park, Redondo Beach, California 90277

and

H. E. Bennett

Michelson Laboratory, Physics Division
Naval Weapons Center, China Lake, California 93555

The flux density which a cooled laser mirror can handle without catastrophic damage is predicted to be limited in typical situations by absorbing defects on the optical surface rather than by mirror reflectance. In this case, failure is predicted to occur either through coating damage in the vicinity of the defect or by burnthrough of the cooled faceplate following vapor barrier formation at the coolant-faceplate interface. Expressions are developed which predict the limiting defect size for a given flux density as a function of (1) thickness and composition of the faceplate, (2) transport properties and fluid mechanics of the liquid coolant, and (3) conditions generating a hydrodynamic crisis at the liquid coolant stagnation boundary beneath the defect. This parametric analysis can be used to optimize faceplate thickness as a function of mirror material, coolant flow, coating damage threshold, heat exchanger design, and the expected maximum size and absorption of multilayer film coating defects. According to this analysis, for thin faceplates the optimum faceplate thickness may be determined by the coating process rather than by average heat transfer considerations.

Key words: coating defects; cooled laser mirrors; defect damage; hot-face design; limiting flux density; mirror damage; vapor-barrier-induced burnthrough.

Introduction

Cooled laser mirrors used in high flux applications typically have a thin metal faceplate backed by a cooling structure through which water or some other liquid flows. Although uncoated molybdenum faceplates are sometimes used, it is more common to coat the faceplate with a metal or multilayer dielectric film to reduce the energy from the incident beam absorbed by the mirror surface. In designing such a mirror, it is usual to calculate the fraction of the incident beam energy absorbed by the mirror surface, the heat transfer through the thin metal faceplate or "hot face," and the heat removed by the coolant. If an absorbing defect exists on the mirror surface, however, a local hot spot will develop which may result in catastrophic damage to the mirror. Either the temperature of the surface may rise high enough to cause film damage, producing a larger or more highly absorbing area and resulting in a runaway situation, or enough heat may be transmitted through the thin hot face to the coolant in a localized area to cause localized boiling. A vapor barrier will then develop, the cooling system will no longer be effective in that localized region, and the hot face will burn through with catastrophic results.

The problem of film damage caused by localized defects was discussed previously [1].[1] The solution involves the integral of one minus the error function of x or ierfc(x). A look-up table was provided to evaluate this function in the earlier paper. In this paper, a set of polynomial expressions has been derived using the Forward Doolittle Matrix technique [2] to give a usable curve fit for most applications.

The vapor barrier burnthrough problem was not discussed previously. The solution to this problem at first glance appears to be a straightforward heat transfer problem. However, the heat can only be transported from the channel wall to the cooling fluid through the sublaminar boundary at the

[1]Numbers in brackets indicate the literature references at the end of the paper.

wall, and the short times which typically result when localized heating occurs significantly complicate this problem. A graphical approach is used in this paper to attack this question. The conclusion drawn from this analysis is that the hot-face thickness should be evaluated in terms of the coating used and the defect sizes anticipated. A hot face too thin will cause localized heating to quickly occur at the coolant channel wall, resulting in vapor barrier formation and rapid burnout. A hot face that is too thick will cause the steady-state gradient across it to be too high, making the allowable defect size at the film surface unrealistically low. A design tradeoff is thus required; the analysis in this paper may help to make it.

Symbols used in this paper are given below. English rather than metric units are used as is common in heat transfer calculations.

x,y spatial coordinates in plane of surface

z spatial coordinate normal to surface. Positive direction is into surface.

R radius in spherical coordinates, so $x^2 + y^2 + z^2 = R^2$.

J Bessel function

a defect radius in feet

$T_{o\Delta}$ temperature at point (0,0,z) in °F

q heat supplied in BTU/hr/ft^2

α thermal diffusivity of hot face in ft^2/hr, where $\alpha = K/\rho c_p$

K thermal conductivity of hot face in BTU/hr/ft/°F

ρ density of hot face in lbs/ft^3

c_p specific heat of hot face at constant pressure in BTU/lb/°F

τ time interval in hours

Z thickness of hot face in feet

$$\text{ierfc}(x) = \int_x^\infty [1 - \text{erf}(\xi)]d\xi$$

$$\text{erf}(x) = \frac{1}{\sqrt{\pi}} e^{-x^2}$$

D_T temperature at point (0,0,z) in hot face; also represented by depth L below front face

L total thickness of hot face

f flux absorbed by surface

k thermal conductivity of cooling fluid in BTU/hr/ft/°F

A area through which heat flows in ft^2

ℓ thickness of stagnation layer in feet

h_c equivalent film coefficient for heat transfer in BTU/hr/ft^2/°F

q_k heat conducted through coolant boundary layer in BTU/hr/ft^2

T_{hot} temperature at coolant face

T_{cold} temperature of coolant

P pressure

V velocity of water flow in ft/sec

$R_e = \frac{VD\rho}{\mu}$ Reynolds number

P_R Prandtl number

n_μ Nusselt number

μ viscosity of fluid

T_W temperature of face in contact with coolant, °F

T_S cooling fluid saturation temperature, °F

T_B temperature of bulk coolant, °F

Surface Heating from Localized Defects

For a homogeneous isotropic solid, assuming that the conductivity is independent of temperature in a semi-infinite medium due to a constant heat supply over a circular area [1-3],

$$\frac{\partial^2 T_{o\Delta}}{\partial R^2} + \frac{1}{R}\frac{\partial T_{o\Delta}}{R} + \frac{\partial^2 T_{o\Delta}}{\partial z^2} = 0 \tag{1}$$

for a circular area, $0 \leq R < a$ in the plane $z = 0$. Equation (1) is satisfied by $\exp[-(\lambda|z|)]J_o(\lambda R)$ for any λ, so that

$$T_{o\Delta} = \int_o^\infty e^{-\lambda|z|} J_o(\lambda R) f(\lambda) d \quad . \tag{2}$$

Using the Fourier-Bessel relationship and Neumann's integral theorém [4,5], one may use the well-known integral involving Bessel functions so that

$$\int_o^\infty J_o(\lambda R) J_1(\lambda a) d = \begin{cases} 0 & R > a \\ 1/2(a) & R = a \\ 1/a & R < a \end{cases} \quad . \tag{3}$$

In application, then, for heat supplied at a constant rate per unit area per unit time over a circular radius a in the plane $z = 0$,

$$-2K\left[\frac{\partial T_{o\Delta}}{\partial z}\right]_{z=+0} = \begin{cases} \phi & 0 < R < a \\ 0 & R > a \end{cases} \quad . \tag{4}$$

From eq (2),

$$T_{o\Delta} = \frac{Qa}{2K}\int_o^\infty e^{-\lambda|z|} J_o(\lambda R) J_1(\lambda a)\frac{d\lambda}{\lambda} \quad . \tag{5}$$

Carlslaw and Jaeger [6] show that for a constant heat supply at the rate of q per unit time per unit area for $\tau > 0$, $z = 0$ over the circle $(x^2 + y^2) < a^2$, the increase in temperature at the point whose cylindrical coordinates are (R,θ,z) may be found from

$$T_{o\Delta} = \frac{aq}{2K}\int_o^\infty J_o(\lambda R) J_1(\lambda a) \left\{ e^{-\lambda z}\,\mathrm{erfc}\left[\frac{z}{2\sqrt{\alpha\tau}} - \lambda(\sqrt{\alpha\tau})\right] \right. \tag{6}$$

$$\left. - e^{\lambda z}\left[\mathrm{erfc}\,\frac{z}{2\sqrt{\alpha\tau}} + \lambda(\sqrt{\alpha\tau})\right]\right\}\frac{d\lambda}{\lambda}$$

which generalizes the result of eq (5). Therefore, the increase in temperature at the point (0,0,z) is, in cylindrical coordinates,

$$T_{o\Delta} = \frac{2q\sqrt{\alpha\tau}}{K}\left\{ \mathrm{ierfc}\,\frac{z}{2\sqrt{\alpha\tau}} - \mathrm{ierfc}\,\frac{\sqrt{z^2 + a^2}}{2\sqrt{\alpha\tau}} \right\} \quad . \tag{7}$$

In order to simplify the use of the ierfc(x) integral, a set of polynomial expressions have been derived to provide a usable curve fit for engineering applications. These polynomial expressions were derived using the Forward Doolittle Matrix technique [7] and are given in table 1.

Table 1. Polynomial expressions for ierfc(x)

x interval	2ierfc
0 to 0.299	$1.1284 - 1.998(x) + 1.11(x^2)$
0.30 to 0.5499	$1.1150743 - 1.90863(x) + 0.9543(x^2)$
0.55 to 0.9999	$1.012 - 1.5524(x) + 0.64346(x^2)$
1.0 to 1.599	$0.6271 - 0.76914(x) + 0.241964(x^2)$
1.6 to 2.0	$0.21573 - 0.21165(x) + 0.0525(x^2)$

Then,

$$\Delta_T = \frac{q\sqrt{\alpha\tau}}{K}\left\{2\text{ierfc}\ \frac{z}{2\sqrt{\alpha\tau}} - 2\text{ierfc}\ \frac{(z^2 + a^2)^{0.5}}{2\sqrt{\alpha\tau}}\right\} \quad . \tag{8}$$

It should be noted that in any substance, the time required for any point to reach a given temperature is proportional to the square of the distance from the point where the heat load is introduced [1,8]. The time required for a given point to attain a given temperature increase thus varies inversely as the thermal diffusivity. The temperature gradient at any point will be

$$\frac{\partial T_{o\Delta}}{\partial x} = \frac{\Delta_T}{\sqrt{\pi\alpha\tau}}\, e^{-x^2/4\alpha\tau} \quad , \tag{9}$$

so that

$$T_{o\Delta} = \Delta_T \ \text{erf}\ \frac{x}{2\sqrt{\alpha\tau}} \tag{10}$$

for one dimension. In order to satisfy the boundary of $x^2 + y^2 < a^2$, which also satisfies the value for the Bessel integral shown in eq (3), in three dimensions, the mean square distance of the heat from the source at time τ is

$$R^2 = 6\alpha\tau = (2\sqrt{\alpha\tau}\,\frac{x}{L})^2 + (2\sqrt{\alpha\tau}\,\frac{y}{L})^2 + (2\sqrt{\alpha\tau}\,\frac{z}{L})^2 \quad . \tag{11}$$

From the Fourier modulus, L = volume/area = $\pi R^2 L/\pi R^2$, giving L = L = Z, where L = total depth of the hot face. Then

$$6\alpha\tau - (2\sqrt{\alpha\tau}\,\frac{z}{\mathit{L}})^2 = 2(2\sqrt{\alpha\tau}\,\frac{x}{L})^2 \quad , \tag{12}$$

where x and y are the same length viewed through an angle of 45 degrees. Thus,

$$x \text{ or } y = \left[\frac{6\alpha\tau - (2\sqrt{\alpha\tau})^2}{2}\right]^{0.5}(z)(2\sqrt{\alpha\tau})^{-1} \quad . \tag{13}$$

Since the value of a^2 must be greater than $2x^2$,

$$a^2 > \left\{\left[\frac{6\alpha\tau - (2\sqrt{\alpha\tau})^2}{2}\right]^{0.5}(z)(2\sqrt{\alpha\tau})^{-1}\right\}^{2.0}(2.0) \quad , \tag{14}$$

which reduces to $a^2 > z^2/2$.

For the surface of the heat exchanger which surrounds the defect, for a constant heat load per unit area [9],

$$f = -K\,\frac{\partial T_{o\Delta}}{\partial x} \quad , \tag{15}$$

which satisfies

$$\alpha \frac{\partial^2 f}{\partial x^2} = \frac{\partial f}{\partial \tau} \quad , \quad x > 0, \ \tau > 0 \tag{16}$$

so that

$$f = q_o \ \text{erfc} \ \frac{x}{2\sqrt{\alpha\tau}} \tag{17}$$

and

$$\Delta_T = \frac{q_o}{K} \int_x^\infty \text{erfc} \ \frac{x}{2\sqrt{\alpha\tau}} \, dx \quad . \tag{18}$$

Therefore, if $q \neq q_o$,

$$\Delta_T = \frac{q\sqrt{\alpha\tau}}{K} \, 2\text{ierfc} \ \frac{x}{2\sqrt{\alpha\tau}} \quad . \tag{19}$$

Equation (19) is obviously one dimensional in the x direction. Essentially, eq (8) provides the value of temperature rise as a function of time and material with a reduced reflectivity, i.e., greater absorptivity, at a defect of radius a.

Equation (19) provides the value of temperature rise for the surrounding surface which has the required high reflectivity. It may be noted that the temperature rise will be a direct function of the thermal diffusivity of the material. The diffusivity varies considerably even for different metals, as can be seen from table 2 [10,11].

Table 2. Diffusivity of various metals

Metal, pure	Diffusivity, ft^2/hr
copper	4.39
silver	6.589
gold	4.547
nickel	0.878
molybdenum	1.856
tungsten	2.430
aluminum	3.262

Consequently, the allowable defect size for any given heat exchanger will depend upon the material used in the hot face. It also depends on the allowable temperature rise which for dielectric-film-coated surfaces is conservatively estimated at 200°C [12,13].

There is yet another restraint placed upon the selection of material. The cooling heat transfer on the obverse side of defect — or hot face — would appear, at first blush, to be very straightforward, and in many instances such is the case. However, for the present problem, the heat transfer in the channel is not that straightforward. Because of the small time intervals to failure that are most often involved with CW lasers, the bulk flowing fluid provides a virtual adiabatic threshold in the z direction. It is this adiabatic threshold that complicates the overall theory.

The basis of this conclusion is founded on the basic premise that heat may only be transported to the bulk fluid from the channel wall by conduction through the sublaminar boundary at the wall. The film coefficient resulting from flow through the channel only enhances this conduction. The basic expression for conduction through the stagnation boundary (which assumes that the fluid velocity at the wall is zero from conservation of momentum) is [14-16]

$$q_k = -kA \frac{dT}{dz} \tag{20}$$

Equation (20) is the steady-state solution for thermal conductivity which becomes the well-known heat transfer equation for steady-state conduction, where dT/dz is now the temperature gradient through the stagnation layer boundary. But

$$q_k = \frac{k}{\ell}(A)(T_{hot} - T_{cold}) \quad . \tag{21}$$

One will note that the value of (k/ℓ) is an equivalent film coefficient for heat transfer, i.e.,

$$h_c = \frac{k}{\ell} \qquad (BTU/hr/ft^2/°F) \quad , \tag{22}$$

so that when one talks about a film coefficient for a flowing fluid, one is really expressing the enhanced conduction brought about by the fluid. The conventional expression for this enhancement is found from

$$q_k = h_c(A)(T_{hot} - T_{cold}) \quad . \tag{23}$$

Various investigators have determined a value of h_c based upon the dimensionless parameters of Reynolds number and Prandtl number with respect to a Nusselt number. For example, one of the most common expressions for a fully developed turbulent profile in a circular duct at a constant temperature was expressed by Dittus and Boelter [17]:

$$\eta_\mu = \frac{h_c D}{k} = 0.023\left[\frac{VD_\ell}{\mu}\right]^{0.8}[P_R]^{0.333} \quad . \tag{24}$$

Sider and Tate [18] developed a similar expression which is modified by the ratio of the bulk fluid viscosity to the viscosity of the material at the wall, i.e.,

$$\eta_\mu = \frac{h_c D}{k} = 0.023\left[\frac{VD_\ell}{\mu}\right]^{0.8}[P_R]^{0.333}\left[\frac{\mu_\beta}{\mu_\omega}\right]^{0.14} \quad . \tag{25}$$

In a similar fashion, Petukhov [19] developed a correlation based on a friction correlation developed by Idel'Chik [20]:

$$\eta_\mu = \frac{h_c D}{k} = \frac{R_{eb}P_{Rb}^{0.4}(f/8)}{1.07 + 12.7(P_R^{2/3} - 1.0)(f/8)} \quad , \tag{26}$$

where

$$f = [1.82 \log R_e - 1.64]^{-2.0} \quad . \tag{27}$$

Some form close to that of eqs (24-26) is generally used for predicting the enhanced conduction across the stagnation boundary.

For the present problem, the film coefficient provides the basis for the steady-state gradient across the hot face, i.e., from the reflecting surface to the inside channel wall. However, this is the established average steady-state gradient. For a small spot changing temperature in a very short time τ, very little water motion has occurred and, hence, the average film coefficient is virtually unaffected. Only the localized spot is affected. Little heat is carried to the surroundings by diffusion since the differences in thermal diffusivity of the hot-face materials and the cooling fluids are large.

For example, pure copper has a thermal diffusivity of 4.42 ft^2/hr as compared to water (at 100°F) of $5.88(10^{-3})$ ft^2/hr. This is a difference of over 700:1. The respective conductivities are almost of the same order of difference. Essentially, then, the water will be a virtual insulator to the channel wall and will allow the channel wall, at the localized spot, to increase in temperature without producing a significant change in the bulk fluid flowing in the channel. The localized spot at the wall could thus experience localized boiling. One can argue, with reasonable certainty, that we are dealing with a semi-infinite plate which is insulated on the back side for the localized point. McAdams and his students [21] were able to demonstrate that, under the above conditions, liquid velocity and subcooling have virtually no effect on the boiling curve of a liquid at the wall. Subcooled boiling can then occur at the localized defect. Because of the subcooled conditions, the vapor barrier and subsequent bubbles generated at the localized spot will be torn from the wall and

reabsorbed into the bulk fluid [22,23] as long as the bulk fluid is below the saturation point. No changes in the temperature of the bulk fluid will be recorded even when boiling is going forward at a localized spot. In addition, there will be no evidence of two-phase flow because the vapor bubbles and entrained air will be reabsorbed into the subcooled fluid prior to its exit [24-26].

There are, however, techniques for evaluating the points of boiling as a function of the referenced film coefficient, temperature of the bulk fluid, velocity of the bulk fluid, and the pressure in the system. A graph of the cooling fluid can be generated using the values derived from the curves which are generated for fully developed boiling, incipient boiling point, the threshold for thermal dynamic crisis (burnout), and for heat transfer before boiling. This is the technique suggested by Rohsenow and Bergles [27,28]. For subcooled boiling, the heat transfer before boiling is taken from [28]

$$\frac{q}{A} = h_c[(T_W - T_S) + (T_S - T_B)] \quad , \tag{28}$$

where T_S, the cooling fluid saturation temperature (°F), should be found as a function of the average pressure, i.e., one-half of the pressure drop through the heat exchanger. This assumes that the exit is into a plenum at a normal pressure of 1 atmosphere. If this assumption is not correct, the average pressure must be adjusted accordingly.

Equation (28) is similar to eq (20). The incipient boiling point is found from [28]

$$\left(\frac{q}{A}\right)_i = 15.60(P)^{1.156}[T_W - T_S]^{2.30/P^{0.0234}} \quad . \tag{29}$$

There are a number of investigators who have suggested correlations for a fully developed boiling curve. Jens and Lottes [29] have suggested

$$q'' = [(T_W - T_S)(e^{P/900})/60]^4 \times 10^6 \quad . \tag{30}$$

Weatherhead [30] has suggested

$$q'' = [(T_W - T_S)/(90 - 0.127T_S)]^4 \times 10^6 \quad . \tag{31}$$

More recently, Thom et al. [31] and Ginoux [32] have developed a very good correlation,

$$q'' = [(T_W - T_S)(e^{P/1260})/72]^{2.0} \times 10^6 \quad , \tag{32}$$

which is in good agreement with flow surface boiling data provided by Brown [33].

Several investigators have developed correlations for the hydrodynamic crisis point — or burnout — as a function of subcooled forced convection. One of the better studies of this problem has been outlined by Hewitt [34,35] and Bergles [36,37].

McAdams et al. [21,38] developed an expression for burnout based on velocity:

$$\frac{q}{A} = 4 \times 10^5 V^{1/3} + 4.8 \times 10^3 (T_S - T_B)V^{1/3} \quad . \tag{33}$$

Gambill [39], however, has developed an additive correlation which considers bubble growth at the wall and the film coefficient velocity relationship. His expression is $q_{critical} = q_{b,crit} + q_{c,crit}$, where

$$q_{b,crit} = 0.145(hfg)\rho_V \left[\frac{bg_o g_1(\rho_L - \rho_V)}{\rho_V^2}\right]^{0.25} \left\{1 + \left[\left(\frac{\rho_L}{\rho_V}\right)^{0.923} \left(\frac{c_p \Delta T}{25(hfg)}\right)\right]\right\} . \tag{34}$$

$$q_{c,crit} = h_c[T_{W,crit} - T_B] \tag{35}$$

$$T_{W,crit} = 102 \ln P - 97 \left(\frac{P}{P + 15}\right) - \frac{V}{2.22} + 32 \quad . \tag{36}$$

In eqs (33-35) consideration of L/D ratio has not been indicated. Bergles [40] and Tong [41,23] have shown that burnout becomes an important factor in terms of the length to diameter ratio of the channel. Tong has suggested, for example, an empirical correlation for water only:

$$q''_{crit} = [2.3 \times 10^5 + 0.094G][3 + 0.01(T_S - T_W)][0.435 + 1.25\, e^{-9.3\times10^{-3}L/D_e}][1.7 - 1.4\, e^{-a}] \ . \tag{37}$$

$$a = 0.532 \left(\frac{\rho_L}{\rho_V}\right)^{1/3} \left(\frac{h_S - h_i}{hfg}\right)^{3/4} \quad .$$

The asymptotic curve between the incipient boiling point and the burnout point along the fully developed boiling curve is found from

$$\mathring{q} = \left[1 + \frac{q_1}{q_2}\left(1 - \frac{q_3}{q_2}\right)^2\right]^{0.5} q_2 \quad . \tag{38}$$

An example of the graphical construction of these expressions is shown in figure 1. This represents the recommended procedure for construction of a curve for forced-convection surface boiling as shown by Rohsenow [28]. By constructing such a graph, it is possible to evaluate the maximum defect size that can be allowed using eq (7) when Z is the thickness of the hot face. In this manner, one may establish the necessary boundary in terms of the coolant fluid.

Essentially, then, when designing the hot face, the thickness must be a function of the maximum defect that will not allow the metallic reflecting surface to go above a critical value, conservatively estimated as 200°C, and will not allow the corresponding defect spot at the channel wall to climb too far along the asymptotic curve shown in eq (38). Both constraints will depend upon hot-face construction material, thickness, optical coating material, fluid cooling on the back surface, and system pressure.

The procedure used to determine incipient boiling caused by the presence of a defect may then be summarized as follows.

(1) Calculate the steady-state gradient through the hot face if no defects are present.

(2) Determine the pressure drop in the coolant.

(3) From (1) and (2) calculate h_c to use for defect calculations (assume that to a good approximation the heat transfer at the defect site is the same as at other points on the hot face).

(4) Use semifinite thickness calculation [39] to obtain approximate surface temperature and also temperature at the hot-face/coolant wall. No influence on the boundary layer properties caused by the defect is assumed, so that a quasi-adiabatic model is being employed.

(5) If the surface temperature exceeds a safe value, perhaps 200°C, or if the interface temperature goes above boiling, the possibility of burnout exists.

Example

In order to illustrate the proposed technique, a working example will be given.

Problem: A laser mirror (flat) will be subjected to a normal absorptivity of $2.537(10^5)$ BTU/hr-ft^2 for 100 sec. Cooling water flows at a rate of $4.46(10^{-4})$ ft^3/sec-channel. Under standard conditions, the water must transfer a Q = $12.844(10^3)$ BTU/hr. The area available for transferring Q will equal 0.09214 ft^2. The water enters at a temperature of 80°F and 100 psig. The pressure drop is 88 psig. The coolant flow channel is 0.12 x 0.015 in. in cross-sectional dimension. The mirror hot face is constructed of nickel. The reflecting surface has a dielectric coating to maximize reflectivity at the appropriate wavelength. The hot-face thickness is 0.0466 in.

What will be: (1) the steady-state gradient, (2) the pressure drop for a flow length of 7.5 in., (3) the film coefficient for the steady-state condition, and (4) maximum allowable defect with respect

to maintaining the reflective surface below 300°F and the cooling channel wall below the burnout point.

The hydraulic diameter of each channel is found from

$$D_H = 4\left[\frac{0.12(0.015)}{2(0.12) + 2(0.015)}\right] (12)^{-1} \tag{39}$$

$$= 2.22(10^{-3}) \text{ ft} \quad .$$

The cross-sectional area of the channel is

$$A = \frac{112(0.015)}{144}$$

$$= 1.25(10^{-5}) \text{ ft}^2 \quad .$$

The pressure drop will be found from [40,41]

$$\Delta\rho_{\text{lb/in.}^2} = \frac{[(f\frac{L}{D}) + \Sigma k_L]V^2\rho}{144(64.4)} \quad , \tag{40}$$

where

$L = 0.625$ ft; $D = 2.22(10^{-3})$ ft; Σk_L = entrance and exit losses = 1.5; $\rho = 62.15$ lb/ft^3;

$$f = [(1.8 \log \text{Re}) - 1.64]^{-2.0} \qquad [23,28,42] \tag{41}$$

$$\mu = 5.46(10^{-4}) \text{ lb/ft-sec} \qquad [28,42]$$

The Reynolds number is found from [43]

$$R_e = \frac{VD\rho}{\mu} \tag{42}$$

$$V = \frac{4.46(10^{-4}) \text{ ft}^3/\text{sec}}{1.25(10^{-5}) \text{ ft}^2}$$

$$= 35.65 \text{ ft/sec} \quad .$$

The film coefficient is found from eqs (24)-(26). Using eq (24),

$$h_c = 2.3(10^{-2})\left[\frac{0.356}{2.22(10^{-3})}\right][9008]^{0.8}[5.735]^{0.333} \quad , \tag{43}$$

where [20,44]

$$k = 0.356 \text{ BTU/hr-ft-°F} \quad ; \quad PR = 5.735 \quad .$$

The water must transfer $12.844(10^3)$ BTU/hr. The temperature rise in the cooling water will be

$$\Delta To_F = \frac{12.844(10^3)\ \frac{BTU}{hr}}{(4.46 \times 10^{-4}\ \frac{ft^3}{sec\text{-}ch})(21\ ch)(62.15\ \frac{lb}{ft^3})(\sim 1.0\ \frac{BTU}{lb\text{-}°F})(3600\ \frac{sec}{hr})}$$

$$= 6.13°F \quad .$$

The average water temperature of the cooling water will be

$$To_{F(mean)} = \frac{(84 + 6.13) + 84}{2}$$

$$= 87.07°F \quad (303.9°K) \quad .$$

The temperature differential across the stagnant boundary layer will be

$$Q = h_c(A)To_F \tag{44}$$

$$A = [2(0.015) + 2(0.12)] \times 2.34 \times 21 \times 144^{-1}$$

$$= 0.09214\ ft^2 \quad ,$$

so that

$$To_F = \frac{12.844(10^3)\ \frac{BTU}{hr}}{9624\ \frac{BTU}{hr\text{-}ft^2 °F}\ (0.09214\ ft^2)}$$

$$= 15.47°F \quad .$$

The temperature at the wall of the cooling channel will be

$$T_W = 90.14 + 15.47$$

$$= 105.6°F \quad (314.2°K) \quad .$$

The temperature at the surface is found from eq (20):

$$Q = \frac{k}{L}(A)\Delta\ To_F$$

$$A = 0.04095\ ft^2 \quad .$$

$$k = 34.5\ BTU/hr\text{-}ft^2 °F$$

$$L = 0.0466/12 = 3.883(10^{-3})\ ft \quad .$$

Then

$$To_F = \frac{12.844(10^3)\ \frac{BTU}{hr}\ (3.883)(10^{-3})\ ft}{34.5\ \frac{BTU}{hr\text{-}ft°F}\ (0.040905\ ft^2)}$$

$$= 35.34 \quad .$$

Reflecting surface temperature (steady state) will be

$$T_S = 105.6 + 35.34$$

$$= 140.9°F \quad (333.9°K) \quad .$$

If the hot face was twice as thick, the steady-state temperature at the surface (no defect present) would be

$$T_S = 176.3°F \quad (353.5°K) \quad .$$

The minimum defect radius that may be evaluated is found from eq (13).

$$a^2 > 0.5(Z)^2$$

$$Z = 3.883(10^{-3})\ ft$$

$$Z^2 = 1.5054(10^{-5})$$

$$a^2 > 7.5272(10^{-6})\ ft^2 \quad .$$

The minimum defect radius that can be evaluated will be 0.033 in. using this technique. For the purpose of this example, a defect size having a radius of 0.0932 in. will be evaluated.

The rise in surface temperature and wall temperature will be evaluated for

$$\left.\begin{array}{l} 3.17125(10^5)\ \frac{BTU}{hr\text{-}ft^2} \\ 6.34250(10^5)\ " \\ 9.51375(10^5)\ " \\ 1.2685(10^6)\ " \end{array}\right\} = q$$

τ = 100 sec
2.778(10^{-2}) hr

$K = 34.5\ \frac{BTU}{hr\text{-}ft°F}$

a = 0.0932 in.
7.767(10^{-3}) ft

α = 0.878 ft^2/hr .

Surface temperature for q = 3.17125(10^5) BTU/hr-ft^2 is T_S = 333.9 + 38.55 = 372.5°K; channel wall temperature [from eq (7)] is T_C = 314.2 + 23.83 = 338°K.

Surface temperature for q = 6.3425(10^5) BTU/hr-ft^2 is T_S = 333.9 + 77.1 = 411.0°K; channel wall temperature is T_C = 314.2 + 47.7 = 361.9°K.

Surface temperature for $q = 9.51375(10^5)$ BTU/hr-ft^2 is $T_S = 333.9 + 115.7 = 449.6°K$; channel wall temperature is $T_C = 314.2 + 71.5 = 385.7°K$.

Surface temperature for $q = 1.2685(10^6)$ BTU/hr-ft^2 is $T_S = 333.9 = 488.1°K$; channel wall temperature is $T_C = 314.2 + 95.3 = 409.5°K$.

It should be noted that the surface temperature approaches the maximum temperature of the dielectric coating early on. Figure 2 represents a numerical analysis of the same problem. This problem was modeled using a System Improved Numerical Differential Analyzer (SINDA) program. Figure 3 represents a plot of the data from eq (7).

The next phase of the problem is to determine the various points where the cooling water will fail at the channel wall.

For the heat transfer before boiling curve, we will use eq (28); minimum pressure will be 88.7 psia. Then, $q/A = 5634\ (T_W - 319) + (319 - T_B)$; $T_B = 90°F$ for $T_W = 322, 329, 339$.

Note. T_S @ 88.7 psia = 319 [10]: $q/A = 1.307(10^6)$ 322°F; $= 1.347(10^6)$ 329°F; $= 1.403(10^6)$ 339°F. The incipient boiling curve will be developed from eq (29): $q/A = 5(10^5)$ 329°F; $= 2.464(10^6)$ 339°F. The fully developed boiling curve will be developed from eq (30): $(q/A)^1 = 1.8311(10^4)$ 339°F; $= 9.2702(10^4)$ 349°F.

The critical burnout is established from McAdams [eq (33)]:

$$(q/A)_{CR} = 4(10^5)(35.65)^{1/3} + 4.8(10^3)(319\text{-}90)(35.65)^{1/3}$$

$$= 4.906(10^6) \text{ BTU/hr-ft}^2 \quad .$$

Checking the McAdams value with the Gambill correlation, using eqs (34)-(36),

$$q''_{b,crit} = 0.145(895 \text{ BTU/lb})(0.2035 \text{ lb/ft}^3)\ldots$$

$$\times \left[\frac{(4.04\text{x}10^{-3} \text{ lb}_f/\text{ft})(32.2 \text{ ft/sec}^2)(32.17 \text{ lb}_m\text{-ft/sec}^2\text{-lb}_f)(56.45 \text{ lb/ft}^3)}{(0.2035 \text{ lb/ft}^3)^2}\right]^{0.25}$$

$$\times \left[1 + \left(\frac{56.657}{0.2035}\right)^{0.923} \frac{103 \text{ BTU/lb-°F x } 229°F\Delta_T}{25(895 \text{ BTU/lb})}\right]$$

$$= 26.41 \text{ BTU/ft}^3[8.691 \text{ ft/sec}]2.903$$

$$= 666.242 \text{ BTU/sec-ft}^2 \quad .$$

$$q''_{B_{CR}} = 2.3985(10^6) \text{ BTU/hr}$$

$$T_{W_{CR}} = 102 \ln 88.7 - 97\left[\frac{88.7}{88.7 + 15}\right] - \frac{35.65}{2.22} + 32$$

$$= 390.5°F$$

$$q''_{C_{CR}} = 9624[390.5 - 90]$$

$$= 2.892(10^6)$$

$$q_{CR} = 2.3985(10^6) + 2.97(10^6)$$

$$= 5.29(10^6) \text{ burnout BTU/hr-ft}^2$$

Figure 1 is the graphical representation of the above equations. It should be noted that the channel wall does not achieve the necessary temperature for burnout. Additionally, it appears to be outside the boiling region. However, if the wall thickness were reduced by half, it is more than possible the water channel could have achieved temperatures sufficient to put the laminar boundary in the boiling regime.

References

[1] Carslaw; H. S.; Jaeger, J. C. Conduction of heat in solids, 2nd ed. London: Oxford University Press; 1959. 256.

[2] Jakob, M. Heat transfer, Vol. I. New York, NY: John Wiley and Sons; 1949. 339 ff.

[3] Ozisik, M. N. Heat conduction. New York, NY: John Wiley and Sons; 1980. 89 ff.

[4] Carslaw, H. S.; Jaeger, J. C. Conduction of heat in solids, 2nd ed. London: Oxford University Press; 1959. 218.

[5] Cushing, J. T. Applied analytical mathematics for physical scientists. New York, NY: John Wiley and Sons; 1975.

[6] Carslaw, H. S.; Jaeger, J. C. Conduction of heat in solids, 2nd ed. London: Oxford University Press; 1959. 264.

[7] Stanley, L. T. Practical statistics for petroleum engineers. Tulsa, OK: Petroleum Publishing; 1973.

[8] Carslaw; H. S.; Jaeger, J. C. Conduction of heat in solids, 2nd ed. London: Oxford University Press; 1959. 59.

[9] Ibid. 75.

[10] Ranznejevic, K. Handbook of thermodynamic tables and charts. New York, NY: McGraw-Hill; 1976. 24 ff.

[11] Eckert, E.R.G.; Drake, R. M. Heat and mass transfer, 2nd ed. New York, NY: McGraw-Hill; 1959. 498.

[12] Bennett, H. E. Insensitivity of the catastrophic damage threshold of laser optics to dust and other surface defects. Bennett, H. E.; Glass, A. J.; Guenther, A. H.; Newnam, B. E., ed. Proceedings of the 12th annual symposium on optical materials for high power lasers; 1980 September 30-October 1; Boulder, CO. Nat. Bur. Stand. (U.S.) Spec. Publ. 620; 1981 October. 256-263.

[13] Estimated maximum annealing temperature for most coatings.

[14] Kreith, F. Principles of heat transfer, 2nd ed. Scranton, PA: International Textbook Co.; 1966.

[15] McAdams, W. H. Heat transmission, 3rd ed. New York, NY: McGraw-Hill; 1954. 11.

[16] Gebhart, B. Heat transfer, 2nd ed. New York, NY: McGraw-Hill; 1971.

[17] Dittus, F. W.; Boelter, L. M. Heat transfer in automobile radiators of the tubular type, Vol. 2. Berkeley, CA: University of California Berkeley Publ. Eng; 1930. 443-461.

[18] Sieder, E. N.; Tate, C. E. Heat transfer and pressure drop in tubes. Ind. Eng. Chem. 28; 1429; 1936.

[19] Petukhov, B. S. Heat transfer and friction in turbulent pipe flow with variable properties, in Advances in heat transfer, Vol. 6. New York, NY: Academic Press; 1970. 503.

[20] Idel'Chik, I. E. Handbook of hydraulic resistance, Russian translation. Jerusalem, Israel: Israeli Program for Scientific Translations; 1960. 53.

[21] McAdams, W. H.; Kennel, W. E.; Mindon, C. S.; Carl, R.; Picornel, P. M.; Dew, J. E. Heat transfer to water with surface boiling. Ind. Eng. Chem. 41; 1945-1953; 1949.

[22] O'Connor, G. E.; Russell, T.W.F. Heat transfer in tubular fluid - fluid systems, in Advances in chemical engineering, Vol. 10. New York, NY; Academic Press; 1978.

[23] Tong, L. S. Boiling heat transfer and two phase flow. New York, NY: John Wiley and Sons; 1965. Passim.

[24] Zuber, N. On the stability of boiling heat transfer. Trans. ASME 80; pg; 1958.
Note: This paper provides an excellent explanation of bubble formation and suppression of heat transfer to a point of burnout.

[25] Bromley, L. A.; Leroy, N. R.; Robbers, J. A. Heat transfer in forced convective film boiling. Ind. Eng. Chem. 45; 1953.

[26] Chen, J. C. Correlation for boiling heat transfer to saturated fluids in convective flow. Ind. Eng. Chem. 5; 1966.
Note: There is some very good discussion of pool boiling and boiling with forced convection for the reader in:

Rohsenow, W. M. A method of correlating heat transfer data for surface boiling of liquids. Trans. ASME; Paper No. 31 - A110; Aug. 1952.

Mikic, B. B.; Rohsenow, W. M. A new correlation of pool boiling data including the effect of heating surface characteristics. J. Heat Transfer; May 1969.

[27] Bergles, A. E.; Rohsenow, W. M. The determination of forced convection surface boiling heat transfer. AIChE-ASME 6th national heat transfer conference; 1963; Boston, MA. Paper 63-HT-22.

[28] Rohsenow, W. M. Boiling, in Handbook of heat transfer. New York, NY: McGraw-Hill; 1973. 13-36.

[29] Jens, W. H.; Lottes, P. A. Analysis of heat transfer burnout, pressure drop, and density data for high pressure water. Argonne Nat. Lab. Rept. AN6-4627; 1951.

[30] Weatherhead, R. J. Nucleate boiling characteristics and the critical heat flux occurrence in subcooled axial-flow water system. Argonne Nat. Lab. Rept. AN6-6675; 1962.

[31] Thom, J.R.S.; et al. Boiling in sub-cooled water during flow up heated tubes or annuli. Proc. Inst. Mech. Eng. 180; 1965.

[32] Ginoux, J. J. Two-phase flows and heat transfer. New York, NY: McGraw-Hill; 1978.

[33] Brown, W. Study of flow surface boiling. Doctoral dissertation; M.I.T.; 1967.

[34] Hewitt, G. F.; Hall-Taylor, N. W. Annular two phase flow. Oxford, England: Pergamon Press; 1970.

[35] Hewitt, G. F. Introduction to two-phase heat transfer, in Two-phase flows and heat transfer. New York, NY: McGraw-Hill; 1978.

[36] Bergles, A. E. Survey and evaluation of techniques to augment convective heat transfer, in Prog. heat mass transfer. Oxford, England: Pergamon Press; 1969.

[37] Bergles, A. E. Burnout in boiling heat transfer, part II: subcooled and low quality forced - convection systems. Nucl. Safety; 18; 1977.

[38] McAdams, W. H. Heat transmission, 3rd ed. New York, NY: McGraw-Hill; 1954.

[39] Gambill, W. R. Generalized prediction of burnout heat flux for flowing subcooled, wetting liquids. AIChE-ASMA 5th national heat transfer conference; 1962; Houston, TX.

[40] Bergles, A. E. Forced convection surface boiling heat transfer and burnout in tubes of small diameter. Doctoral dissertation; M.I.T.; 1962.

[41] Tong, L. S.; et al. Studies in an open lattice core. USAEC Rept. WCAP-3736; 1964.

[42] Olson, R. M. Engineering fluid mechanics, 2nd ed. Scranton, PA: International Textbook Co.; 1967.

[43] Denn, M. M. Process fluid mechanics. Englewood Cliffs, NJ: Prentice-Hall; 1980.

[44] Yaws, C. L. Physical properties. New York, NY: McGraw-Hill; 1977.

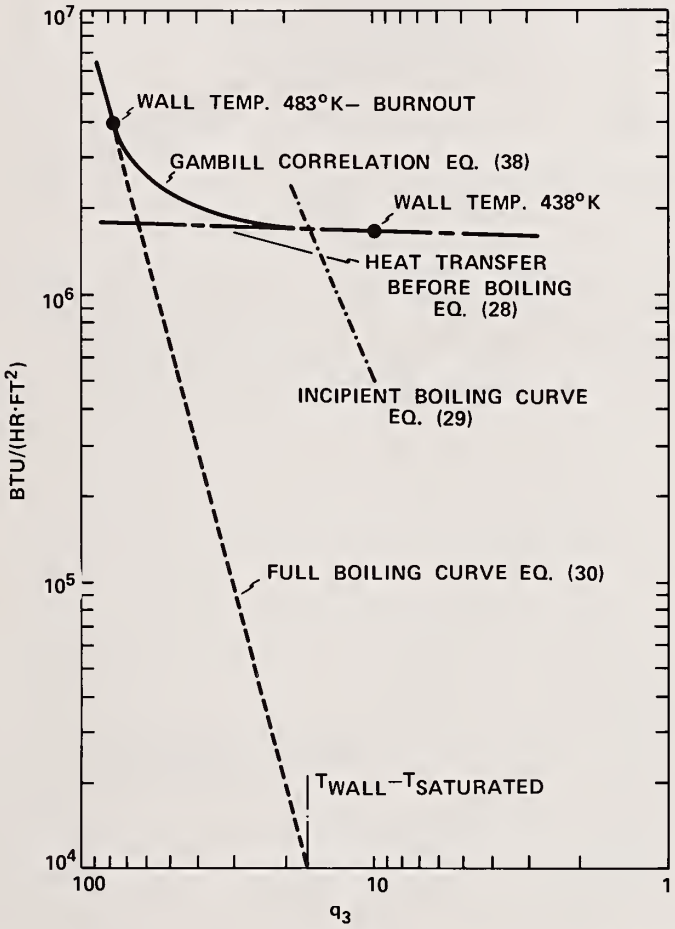

Figure 1. Full boiling curve, incipient boiling curve, and wall temperature as a function of absorbed flux. The curves were constructed following the procedure outlined by Rohsenow.

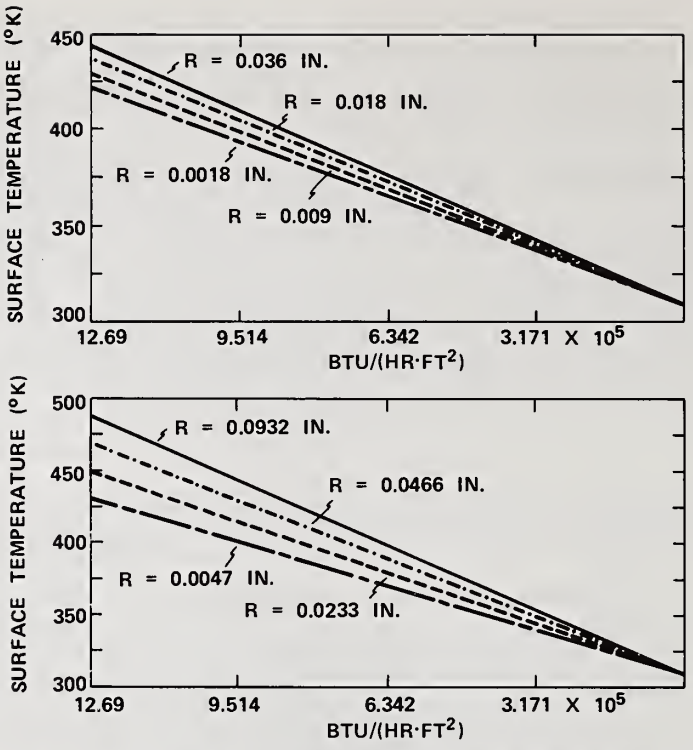

Figure 2. Surface temperature of defects as a function of absorbed flux. The HEX top layer thickness was assumed to be 0.018 in. for the upper graph and 0.0466 in. for the lower graph. The R values refer to the radii of the defects, assumed circular.

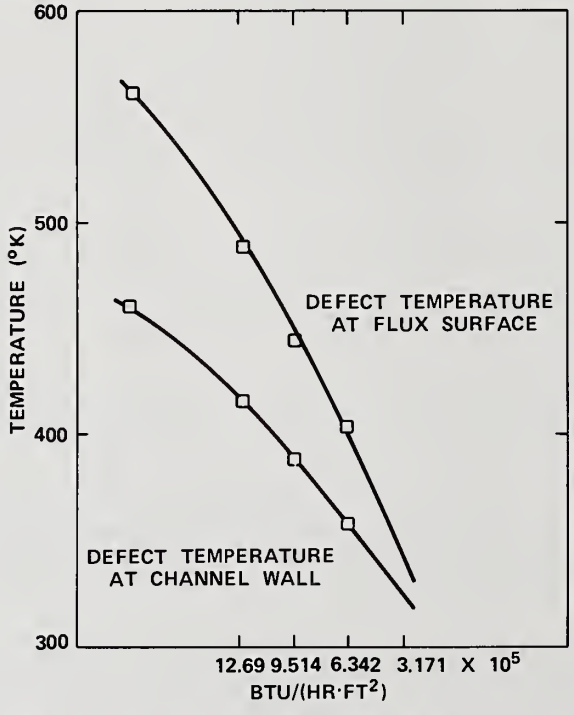

Figure 3. Surface temperature of an 0.0932-in.-diameter defect on a mirror with hot-face thickness of 0.0466 in. as a function of absorbed flux. The temperature beneath the defect at the hot face-coolant interface is also shown.

The possibility of using a heat pipe was suggested. The speaker replied that it has limited uses but cannot sustain the power levels which are often required in modern laser systems.

A Predictive Tool for Evaluating the Effect of Multiple Defects on the Performance of Cooled Laser Mirrors

J. R. Palmer

TRW
One Space Park, Redondo Beach, California 90277

and

H. E. Bennett

Michelson Laboratory, Physics Division
Naval Weapons Center, China Lake, California 93555

A technique is suggested for evaluating the distance two defects on the surface of a fluid-cooled laser mirror must be separated before they can be considered independently. The basic ingredient of the correlation is taken from a technique suggested by Max Jakob for steady-state conduction with heat generation in a circumferential fin. Using this technique with concomitant Bessel functions of zero order and first kind, a distribution of temperatures in a circumferential fin at various radii may be evaluated for cylindrical heat generators acting in concert.

Key words: catastrophic mirror damage; cooled laser mirrors; hot-face design; laser mirror burnthrough; limiting flux density; multiple coating defects.

Introduction

The objective of this paper is to provide a predictive technique by which multiple defects within the sphere of influence of one another may be evaluated. The technique to be described is, functionally, a corollary to the solution provided by the authors in dealing with a single defect on a fluid-cooled laser mirror optical surface [1].[1]

The basic concept is a variant suggested by Max Jakob [2,3] dealing with steady-state conduction. The basic concept has been expanded upon by Kern and Kraus [4] in using the modified Bessel differential equation to solve the temperature profile of a radial fin of rectangular profile.

The nature of the present problem is such that a defect becomes a heat generator. The heat load from the defect radiates radially along the "hot-face" surface. The inability of the hot-face material to conduct away the heat load requires that the heat be stored and allows the defect to increase in temperature. The amount of heat stored and thus the increase in temperature of the defect area are evaluated using the solution previously suggested [1]:

$$D_T = \frac{q\sqrt{\alpha\tau}}{K}\left[2\text{ierfc}\ \frac{z}{2\sqrt{\alpha\tau}} - 2\text{ierfc}\ \frac{(z^2 + a^2)^{0.5}}{2\sqrt{\alpha\tau}}\right] . \qquad (1)$$

From eq (1) the temperature of a single defect on the optical surface and the resultant localized temperature of the cooling fluid channel wall are determined.

Symbols used in this paper are as follows:

- x,y Cartesian coordinates in plane of surface
- r,θ polar coordinates in plane of surface
- k thermal conductivity of hot face
- q absorbed flux density
- h film coefficient of convection

[1]Numbers in brackets indicate the literature references at the end of the paper.

I_o, K_o modified Bessel functions

α thermal diffusivity

τ time since irradiation began

a radius of defect

$\text{ierfc}(x)$ $\int_o^\infty [1 - \text{erf}(\xi)]d\xi$

$\text{erf}(x)$ $\frac{1}{\sqrt{\pi}} e^{-x^2}$

D_T temperature increase of defect

T temperature

Sphere of Influence of a Defect

This paper deals with the sphere of influence of the defect which is defined as the radial distance required to reduce the D_T of eq (1) to zero. The most appropriate analog for our problem appears to be that of a radial fin. A generalized differential equation can be developed for any radial fin of arbitrary profile function [5-7]. The profile is confined by two symmetrical curves, $y = f_2(r)$ and $y = -f_2(r)$, where the difference in heat conducted into the differential element at r and that leaving the element r + dr is

$$dq = k \frac{d}{dr} [(2\pi r)2f_2(r) \frac{d\theta}{dr}]dr \quad . \tag{2}$$

This is the equation for a time-invariant, steady-state system which can be equated to heat leaving dr by convection. For a film coefficient of convection h,

$$dq = 2h(2\pi r dr)\theta \quad . \tag{3}$$

The heat balance, then, is

$$h\theta r = k[f_2(r)r \frac{d^2\theta}{dr^2} + f(r) \frac{d\theta}{dr} + r \frac{df_2(r)}{dr} \frac{d\theta}{dr}] \quad . \tag{4}$$

This is rearranged to the generalized differential equation of

$$0 = f_2(r) \frac{d^2\theta}{dr^2} + \frac{f_2(r)}{r} \frac{d\theta}{dr} + \frac{df_2(r)}{dr} \frac{d\theta}{dr} - \frac{h}{k}\theta \quad . \tag{5}$$

For a fin of rectangular profile, the profile function is

$$f_2(r) = \frac{\delta_0}{2} \quad . \tag{6}$$

Substituting eq (6) and its derivative (zero) into eq (5),

$$r^2 \frac{d^2\theta}{dr^2} + r \frac{d\theta}{dr} - m^2r^2\theta = 0 \quad . \tag{7}$$

This is Bessel's modified differential equation with the general solution of

$$\theta = C_1 I_o(Mr) + C_2 K_o(Mr) \quad , \tag{8}$$

where

$$M = [\frac{h}{k\delta_o}]^{0.5} \quad .$$

For our condition, $h = k/R_e$ of conduction only, so that

$$M = \left[\frac{k/R_e}{kS_o}\right]^{0.5} .$$

For the boundary conditions,

$$r = r_o \quad \text{at} \quad \theta = \theta_o$$

$$r = r_e \quad \text{at} \quad 0 = \frac{d\theta}{dr}$$

$$\theta_o = C_1 I_o(M_{Ro}) + C_2 K_o(M_{Ro})$$

$$0 = C_1 I_1(M_{Re}) - C_2 K_1(M_{Re})$$

when C_1 and C_2 are evaluated and substituted into eq (8), becomes

$$t(R) - t_2 = (t_1 - t_2)\,\frac{K_1(M_{Re})I_o(MR) + I_1(M_{Re})K_o(MR)}{I_o(M_{Ro})K_1(M_{Re}) + I_1(M_{Re})K_o(M_{Ro})} \quad . \tag{9}$$

The heat flow through the rest of the fin, i.e., the outer radius of the defect, from the general relationship,

$$qo = -2\pi k\, Ro\, So \left.\frac{d\theta}{dR}\right|_{R = Ro} \quad . \tag{10}$$

Differentiating eq (10) and evaluating $R = R_o$ with substitution into the general heat flow relationship,

$$qo = 2\pi Rok\, So\, M\theta \left[\frac{I_1(M_{Re})K_1(M_{Ro}) - K_1(M_{Re})I_1(M_{Ro})}{I_o(M_{Ro})K_1(M_{Re}) + I(M_{Re})K_o(M_{Ro})}\right] , \tag{11}$$

where qo represents the product of the flux density and the defect area.

The fin effectiveness is found from

$$N = \frac{2Ro}{M(Re^2 - Ro^2)} \left[\frac{I_1(M_{Re})K_1(M_{Ro}) - K_1(M_{Re})I_1(M_{Ro})}{I_o(M_{Ro})K_1(M_{Re}) + I_1(M_{Re})K_o(M_{Ro})}\right] . \tag{12}$$

Equation (12) becomes important to perform the necessary iteration.

Example

The use of the expressions can best be exemplified by using the example from our previous paper [1].

Question: (1) What is the sphere of influence of a 0.0932-in.-radius defect, i.e., when the temperature reduces to that of the steady-state gradient?

(2) What is the sphere of influence of a 0.0466-in.-radius defect?

The flux density is $12.69(10^5$/BTU/hr-ft^2; incident flux has a duration of 100 sec; thermal conductivity of hot-face materials is 34.5 BTU/hr-ft-°F; thermal diffusivity is 0.878 ft^2/hr.

From eq (1),

$$D_T = \frac{12.69(10^5)\ \frac{BTU}{hr\text{-}ft^2}\ [0.878\ \frac{ft^2}{hr}\ (0.0278\ hr)]^{0.5}}{34.5\ \frac{BTU}{hr\text{-}ft\text{-}°F}}$$

$$\times \left\{ 2ierfc\ \frac{0}{2[0.878(0.0278)]^{0.5}} - 2ierfc\ \frac{7.7667(10^{-3})}{2[0.878(0.0278)]^{0.5}} \right\} .$$

$$= 5744.38[2ierfc\ 0.0 - 2ierfc\ 0.024866] \quad .$$

For the interval of x, 0 to 0.299,

$$2ierfc(x) = 1.1284 - 1.998(x) + 1.11(x^2) \quad . \tag{13}$$

Then,

$2ierfc(0) = 1.1284$ $\qquad$ $2ierfc(0.024866) = 1.0793$

$D_T = 5744.38(0.0491)$ $\qquad$ $D_T = 282°F$ or $156.69°K$

The steady-state temperature is 150°F or 339°K. The surface temperature at the defect will be

$T = 150 + 282$ $\qquad$ $T = 432°F$

$$qo = 12.69(10^5)\ \frac{BTU}{hr\text{-}ft^2}\ [7.7667(10^{-3})ft]^2\pi \qquad qo = 240.48\ \frac{BTU}{hr} \quad .$$

By iterating eq (12), we find Re = 1.925(Ro). Checking the output:

$$1.925(Ro) = 0.01495\ ft \text{ or } 0.179\ in.$$

$$Ro = 7.7667(10^{-3})\ ft$$

$$So = 3.883(10^{-3})\ ft \text{ (hot-face thickness)}$$

$$M = \left[\frac{34.5/0.01495}{34.5(3.883)10^{-3}} \right]^{0.5}$$

$$= \frac{131.25}{ft}$$

$$M_{Re} = 0.01495(131.25)$$

$$= 1.962$$

$$M_{Ro} = 7.7667(10^{-3})(131.25)$$

$$= 1.02 \quad .$$

For M_{Ro},	For M_{Re},
$I_o = 1.27751$	$I_o = 2.21713$
$I_1 = 0.57926$	$I_1 = 1.53225$
$K_o = 0.40919$	$K_o = 0.11964$
$K_1 = 0.58189$	$K_1 = 0.14744$

Then,

$$\frac{1.53225(0.58189) - 0.4744(0.57926)}{1.27751(0.14744 + 1.53225(0.40919)} = \frac{0.8062}{0.81534}$$

$$0.9888 = \left[\frac{I_1(M_{Re})K_1(M_{Ro}) - K_1(M_{Re})I_1(M_{Ro})}{I_o(M_{Ro})K_1(M_{Re}) + I_1(M_{Re})K_o(M_{Ro})}\right] .$$

In accordance with eq (11),

$$240.48 = 2\pi R_o S_o M\theta_o [0.9888]k$$

$$= 2\pi(7.7667)10^{-3}\text{ft}\ (3.883)\ 10^{-3}\text{ft}\ \frac{131.25}{\text{ft}}$$

$$\times\ 282°F_{DT}\ (34.5\ \frac{\text{BTU}}{\text{hr-ft-}°F_{DT}})$$

$$240.48\ \frac{\text{BTU}}{\text{hr}} = 239.7\ \frac{\text{BTU}}{\text{hr}} .$$

Reasonable agreement, 99.7%.

The sphere of influence of a 0.0932-in. defect will be 1.925 radii, say 2.0. This suggests that two defects of the same magnitude should not be any closer together than 4.0 radii.

For the case of the 0.0466-in. defect,

$$2\text{ierfc}\left[\frac{3.883(10^{-3})}{2(0.878 \times 0.0278)^{0.5}}\right] = 2\text{ierfc}\ 0.0124$$

$$2\text{ierfc}\ 0.0124 = 1.1038\ \ (\text{from eq (13)})$$

$$D_{T_{°F}} = 5744.38°F[1.1284 - 1.1038]$$

$$= 141.3$$

$$qo = 12.69(10^5)\ \frac{\text{BTU}}{\text{hr-ft}^2}\ [3.883(10^{-3})\text{ft}]^2\pi$$

$$= 60.11\ \frac{\text{BTU}}{\text{hr}} .$$

Iterating eq (12), where N = 0.8723, we find $R_e = 1.75(R_o)$.

Check

$$60.11 \frac{BTU}{hr} = 2(3.883)10^{-3}(3.883)10^{-3}(194.68)$$

$$\times 141.3°F_{DT}(0.68)34.5 \frac{BTU}{hr\text{-}ft\text{-}°F_{DT}}$$

$$= 61.14 \frac{BTU}{hr} \quad .$$

Reasonable agreement, 98.32%.

In similar fashion, for cylindrical problems, the Bessel equations may be reduced in complexity by using the asymptotic expansion of the Bessel functions [8]. For very small fractions of time,

$$\frac{T - T_\infty}{T_o - T_\infty} = \frac{a^{0.5}}{R^{0.5}} \operatorname{erfc} \frac{R-a}{2\sqrt{\alpha\tau}} + \frac{R-a(\alpha\tau)^{0.5}}{4a^{0.5}R^{1.5}} \operatorname{erfc} \frac{R-a}{2\sqrt{\alpha\tau}}$$

$$+ \frac{(9a^2 - 2aR - 7R^2)\alpha\tau}{32a^{1.5}R^{2.5}} i^2\operatorname{erfc} \frac{R-a}{2\sqrt{\alpha\tau}}$$

$$+ \ldots \qquad (14)$$

For large fractions of time,

$$\frac{T - T_\infty}{T_o - T_\infty} = \frac{a^{0.5}}{R^{0.5}} \operatorname{erfc} \frac{R-a}{2\sqrt{\alpha\tau}} \quad , \qquad (15)$$

where

$$T_o - T_\infty = \frac{q\sqrt{\alpha\tau}}{K} \left\{ 2i\operatorname{erfc} \frac{z}{2\sqrt{\alpha\tau}} - 2i\operatorname{erfc} \frac{(z^2 + a^2)^{0.5}}{2\sqrt{\alpha\tau}} \right\} \quad ,$$

which follows from eq (1): a = radius of defect, as indicated before; R = radius greater than a.

Using the Forward Doolittle Matrix technique, polynomial expressions given in table 1 are derived for a curve fit of the erfc(x) function [1].

Table 1. Polynomial expressions for erfc(x)

Interval of x	erfc(x)
0 to 0.299	$1.0 - 1.1408(x) + 0.1377(x^2)$
0.30 to 0.549	$1.0167 - 1.26584(x) + 0.38269(x^2)$
0.55 to 0.99	$1.0394 - 1.35775(x) + 0.47606(x^2)$
1.0 to 1.59	$0.84562 - 0.98479(x) + 0.29598(x^2)$
1.60 to 2.09	$0.359744 - 0.34066(x) + 0.081586\ (x^2)$
2.1 to 3.0	$0.045659 - 0.032871(x) + 0.005892(x^2)$

Also, reference [8] has a table of erfc(x) functions in its Appendix.

The sphere of influence for the .0466-in.-radius sphere can then be found from eqs (1) and (14). From eq (1) for a single defect, the temperature increase is 281°F. From eq (14), the gradient radius is 0.00777 ft for a radius of a + a; 0.0155 ft for a radius of a + 2a; 0.0233 ft for a radius

of a + 3a; and 0.0311 ft for a radius of a + 4a. For this example, a defect one-half the size should not be any closer to the larger defect than 2.87 radii of the larger defect. The use of eq (9) will provide the temperature distribution along the fin from the radius of the defect to the point where the temperature is the same as the steady-state gradient.

Conclusion

By using the boundary of a steady-state gradient, the sphere of influence for a given defect may be determined from the modified Bessel equation for a circumferential fin. The use of this technique, in conjunction with the expressions for evaluating the maximum temperature increase of the defect, will permit evaluation of maximum defect size, defect temperature, defect sphere of influence, and the interrelationship of surrounding defects that may act in concert.

Each defect must be addressed independently. That is, each defect of a different size must be evaluated based upon the flux density, the time of incident energy, the reflectivity of the defect, the thermal diffusivity, thickness, and thermal conductivity of the hot-face material.

In the case of the example used in this paper, the largest defect had a temperature increase of 282°F for a defect size of .0932-in. radius, $12.69(10^5)$ BTU/hr-ft^2 incident flux, 34.5 BTU/hr-ft°F conductivity, 0.878 ft^2/hr diffusivity, and 0.0466-in.-thick hot face. The sphere of influence, then, is calculated to be 2.0 radii. For a defect one-half the size of the larger, the temperature increase is 141°F, and the sphere of influence is 1.75 radii. From this information one would suggest that two defects of the .0932-in. radius should not approach closer than 4.0 radii. For a defect one-half the larger should not approach closer than 2.87 radii of the larger defect.

From the technique suggested, one will be able to parametrically determine the characteristics that will optimize a particular cooled laser mirror heat exchanger design or determine the criticality of defects in an optical surface for an extant system.

There is the further suggestion that in addition to the normal scratch and dig specification for optical coatings, one will be able to specify the relative size and number of defects per unit area — or spatial distance — which will be acceptable for an optical thin film coated surface.

References

[1] Palmer, J. R.; Bennett, H. E. Relationship between coating defects and the limiting flux density a cooled laser mirror can withstand. This meeting.

[2] Jakob, M. Trans. ASME 65; 593; 1943.

[3] Jakob, M. Heat transfer, Vol. I. New York, NY: John Wiley and Sons; 1953. 181 ff.

[4] Kern, D. Q.; Kraus, A. D. Extended surface heat transfer. New York, NY: McGraw-Hill; 1972.

[5] Gardner, K. A. Efficiency of extended surfaces. Trans. ASME 67; 1945.

[6] Harper, W. P.; Brown, D. R. Mathematical equations for heat conduction in the fins of air-cooled engines. NACA Rept. 158; 1922.

[7] Schneider, P. J. Conduction heat transfer. Cambridge, MA: Addison-Wesley; 1955.

[8] Carslaw, H. S.; Jaeger, J. C. Conduction of heat in solids, 2nd ed. Oxford, England: Oxford University Press; 1959. 336.

PRELIMINARY EXPERIMENTAL RESULTS OF SPOT SIZE SCALING IN LASER INDUCED DAMAGE TO OPTICAL COATINGS

Alan F. Stewart
and
Arthur H. Guenther

Air Force Weapons Laboratory
Kirtland Air Force Base, New Mexico 87117

The laser damage threshold of various thin film coatings has been assessed using 1.06 μm radiation at a pulse length of 6ns FWHM. Samples of conventional coatings of several materials have been tested as a function of film thickness and spot size. Beam diameters employed range from approximately 9μm and larger.

From these preliminary data, previously observed scaling has been verified, i.e., thinner films are more damage resistant, while smaller spot sizes yield higher damage thresholds, as expected. The samples employed in these tests were conventional coatings of ThF_4, ZrO_2 and HfO_2 as well as specially prepared "low defect" coatings of Cerac and RAP grown ThF_4. These "low defect" coatings are initial efforts and unfortunately showed no advantage over conventional coatings in terms of damage threshold.

Key words: Laser damage, thin films, spot size dependence, film thickness dependence, impurity damage, scaling.

1. Introduction

One of the most perplexing observations in laser-induced damage to surfaces and coatings is a spot size effect where smaller beam diameters afford a higher damage threshold.[1,2,3,4] This effect was first reported at this conference eight years ago by DeShazer, Newnam and Leung.[1] That investigation and others which followed attempted to correlate the dependence of damage threshold with spot size by a calculated defect density in dielectric thin films. Recent experiments by Soileau, et al[5], VanStryland, et al[6], and Manenkov, et al[7] have shown that a similar spot size dependence exists for damage occuring in the bulk of an optical material. However, this recent work on bulk damage necessitated the use of beam diameters up to a factor of 10 smaller than those used in previous surface damage studies. The technique employed for measuring these small beam diameters, while not new, has benefitted from a considerable refinement.

This preliminary report will describe our successful effort to extend the state-of-the-art in small spot size measurements to damage experiments in dielectric thin films. The scope of the present study includes data obtained using a 1.06 μm laser having a 6ns FWHM pulse duration and specimen thin films of ZrO_2, HfO_2, and ThF_4. In addition to λ/2 films of the aforementioned materials, specially prepared "low defect" λ/2, λ/4 and λ/8 films of ThF_4, including some RAP[8] grown material have also been measured. Future work will include data taken at the harmonics of the Nd:YAG laser and with different pulse durations. These further and more comprehensive studies should greatly aid in unraveling the salient details of the damage mechanism for these classes of optical media, whether it be statistical, thermal, a combination or whatever. We feel the variation of spot size, frequency and pulse length (and perhaps sample temperature) will adequately cover the appropriate parameter space. Based upon these observations, one should then be able to propose an experiment based in large measure on material characteristics to verify or at least distinguish between competing mechanisms.

2. Experimental

The experiment was conducted with a Nd:YAG laser and beam diagnostics as depicted in figure 1. The laser is capable of producing output energies of up to 2 joules in a pulse duration of 6 nsec FWHM. The beam mode is TEMooq with single longitudinal mode operation obtained through the use of a passive q-switch. Representative temporal and spatial profiles appear in figures 2 and 3. These profiles were obtained from the vacuum biplanar[a] photodiode and an optical multichannel analyzer (OMA) as shown in figure 1 and described in reference 9. Only for the largest spot size (141μ) was it possible to use the OMA[b] for real time monitoring of the beam spatial profile at an equivalent focal plane[9]. Magnification of the smaller spot sizes and reimaging at the vidicon target was not possible with requisite diffraction limited performance.

The measurement of the spatial profile of beam radii as small as 4.4 microns was performed using a pinhole scan. A photodiode was placed behind a 1 micron diameter pinhole and the assembly was translated across the beam waist on a stage with 0.2 micron resolution.[4-6] Beam scans were performed at various positions along the beam path to determine accurately the position of the beam waist. A truly representative plot of data obtained in this way appears in figure 4 for the smallest spot size measured. Beam scans and damage experiments were conducted in the same holder to insure the measured intensity distribution corresponded exactly to that incident on the front surface of the sample.

The occurence of damage was determined by observation under a Normarski microscope[c] at magnifications up to 1000X. An indexing system was developed to allow precise translation into the field of view of the microscope each exposed site. Visual observation of spark formation proved to be a dependable indicator at the smallest spot size for these pulse lengths. This is because the intensities involved were often within a factor of 10 of that required for air breakdown. Any damage which ocurred would initiate an air plasma. This effect exhibits high correlation with the morphology of damage sites.

a. ITT Biplanar vacuum photodiode Model F4000 with S1 photodiode
b. Princeton Applied Research OMA system with 1252E detector head
c. Carl Zeiss Axiomat

3. Results

Our preliminary data, summarized in table 1 serves to verify to some extent the previously observed scaling of damage threshold with both spot size and film thickness. From data taken using spot sizes ranging from 4.4 μ to 141.4 μ (1/e radius in intensity) the measured threshold increases with decreasing spot size by a factor ranging from 3 to 35 depending on the material, film thickness, and deposition process. Figure 5 shows the variation in measured damage threshold with spot size for the seven samples studied. Figure 6 shows only the data obtained on the standard $\lambda/2$ ThF_4 film. For comparison purposes, least squares fitted curves for 1/ spot size and 1/ (spot size)^2 functional dependence are presented. We prefer not to discuss possible scaling relations at this time, but rather when the total project is completed[10].

Figures 7a and b show the effect of film thickness on the damage threshold with data derived using two spot sizes. As in Walker, et al[9], thicker films damage more easily. Plotted are damage thresholds in terms of the incident energy densities. Thresholds are also plotted in terms of the films internal energy densities. The internal energy density is the product of the incident energy density and the square of the ratio of the calculated standing wave field in the film to the incident field.

In a comparison of figures 7a and b, the relative relationships between damage thresholds observed using a large spot size are maintained in the small spot size data even though the thresholds are all much higher. This indicates that small spot sizes can be used to make relative measurements and possibly can be calibrated against a known standard.

There has been a great deal of discussion about the proper method of defining the damage threshold of surfaces or thin films. Uncertainty arises because there are usually no sharply defined thresholds in data obtained in experiments on thin films (save at picosecond exposure times where damage is primarily deterministic--with longer pulse durations in the several nanosecond regime experiments are strongly influenced by statistics while at very long exposure times the damage failure mechanism is principally thermal and finally thermo-mechanical). Data obtained using the largest spot size on one film appears in figure 8. Typically, there is a large overlap region where shots of the same energy resulted in either damage or nondamage from one site to the next. The definition of the damage threshold used in this experiment is to take the average value of the incident flux in this overlap region as given by[11]

$$\frac{\text{Ethreshold}}{\text{Area}} = \frac{1}{2} \frac{(\text{Emax no damage} + \text{Emin damage})}{\text{Area}}$$

The determination of the threshold using this definition is indicated on the data plot in figure 8.

The morphology of the damage sites changes drastically in going from large to small irradiation spot sizes. With a large diameter beam (a few hundred microns), one encounters a field of isolated pits surrounded by halos as in figure 9. The pits are typically 1-3 microns in diameter. Each site is centered on the peak intensity point in the beam as best can be determined. However, with smaller diameter beams, (~ a few microns), damage sites at threshold contain no pits but appear as though a circular portion of the film corresponding roughly to the beam diameter is about to

detach. This may be the more "intrinsic" film threshold level albeit not at all equal to the intrinsic bulk level[4]. Well above threshold it appears that the film has evaporated in the crater which is still less than 20μ in diameter. This type morphology may be a remnant of the air breakdown plasma. It is shown in figure 10. At extreme fluence levels, conchoidal fractures appear where portions of the substrate have also vaporized. These observations are typical for most samples measured with the smallest beam diameters, save ZrO_2 which still showed a small pit with halo morphology typical of the large diameter sites.

The statistics of the damage threshold measurement also change with spot size as seen in figure 11. The spread is the ratio of the width of the overlap region divided by twice the average value in the overlap region. The range of the spread is from 0 to 1. As opposed to earlier studies the spread is seen to increase as the spot size decreases.[1-3] This behavior is compatible with a defect or impurity-dominated damage threshold where the probability of missing a damaging defect increases with decreasing spot size.

The results of these preliminary experiments are summarized in table 1. Damage thresholds determined in this study using beam diameters of a few hundred microns compare favorably with previous studies. The magnitude of increase in damage threshold (~2x) between data taken with the 141 micron and 32 micron spot sizes also compares reasonably well to previous spot size studies.[1-3] The primary source of error in these experiments is uncertainty in determining the absolute intensities used. The absolute error in the damage thresholds reported here is due to uncertainty in laser spot size measurement, temporal profile measurement, the determination of the absolute energy of each pulse, and in the microscopic determination of the occurrence of damage.

4. Discussion

The appearance of an overlap region in the data has been attributed entirely to film inhomogeneities, defects, or impurities. In damage testing at Livermore, a high energy system is used with large (several mm) beam diameters. Only rarely is any overlap observed and this provides some justification for the small number (~5) of shots used to determine a film threshold. This is in marked contrast to the data obtained in this preliminary study. The overlap regions are large with beam diameters of a few hundred microns and get larger as the beam diameter decreases. At least 70 sites were sampled in each experiment with the number increasing to over 200 for the small spot data. As the spread increased with decreasing spot size it was necessary to increase the number of shots to block in the overlap region with reasonable confidence. Damage testing is almost always done using beams equal to or larger than the largest beam diameter used in this study. Therefore, it is difficult to determine exactly what the overlap region means since comparison with other data usually involves changes in not only spot size but pulse duration and wavelength as well. Under almost identical conditions, Walker, et al, using a spot size of 220μm reported overlap regions up to 80 percent narrower than those reported here with the largest spot size[9].

It appears that spot size is the primary determining factor in the width of the overlap region. This data is compatible with a model including a wide range of defects in the film each with a macroscopic distribution. With smaller beam diameters, a smaller number of defects are irradiated with each shot and hence the measured damage threshold increases. The distribution of

defects throughout the film, their sizes and composition will definitely affect the shape of a threshold versus spot size plot such as figure 5. As the spot size becomes very small, DeShazer, et al reasoned that it would be possible to measure the "intrinsic" threshold by irradiating an area of the film containing no defects. However, the present data (or the way it is interpreted) does not support such a model since there is no indication that with smaller spot sizes the damage threshold levels off at some "intrinsic" value. In fact, the measured thresholds ($\sim$ 50GW/cm^2) at the smallest spot size are larger than the bulk damage thresholds of various alkalai halides[5]. If we are to measure an "intrinsic" threshold for these thin films then it seems that still smaller beam diameters must be used. This is some indication that the density of defects in the films tested is much higher than we had hoped. A high defect density is clearly evident in the data set for ZrO_2 where the plot of damage threshold versus spot size is essentially level except at the smallest beam diameter (figure 5).

5. Conclusions

The preliminary data presented here does serve to demonstrate again that a spot size effect does exist in damage experiments on thin film coatings. The magnitude of the observed effect is proportionately greater than in earlier studies because of the smaller spot sizes used in this work. Future efforts will involve an intensive study of the statistics of this effect and also work with other pulse durations and wavelengths. By sampling equal surface areas with both large and small diameter beams we will attempt to prove that a true spot size effect exists and hopefully ascertain the appropriate scaling relations. We may find that the spot size effect is purely a matter of probability and that no generally applicable scaling relations can be derived or as noted. Stay tuned (same time next year).

[1] L. G. DeShazer, B. E. Newnam, and K. M. Leung, Appl. Phys. Lett. 23, 607 (1973).

[2] V. Wang, C. R. Guiliano, and B. Garcia, NBS Special Pub. #435, 216 (1975).

[3] I. V. Aleshin, A. M. Bonch-Bruevich, V. I. Zinchenko, Ya. A. Imas, and V. L. Komolov, Sov. Phys. Tech. Phys. 18, 1648 (1974).

[4] E.S. Bliss and D. Milam, NBS Special Pub No. ,108 (1972); E. S. Bliss, D. Milam, and R. A. Bradbury, Appl Optics, 677 (1973)

[5] M. J. Soileau, M. Bass, and P. H. Klein, NBS Special Pub #568, 497 (1979). M. J. Soileau, J. B. Franck, and T. C. Veatch, NBS Special Pub #620, 385 (1980).

[6] E. W. VanStryland, M. J. Soileau, Arthur L. Smirl, and William E. Williams, NBS Special Pub #620, 375 (1980).

[7] A. A. Manenkov and V. S. Nechitailo, Sov. J. Quantum Electronics 10, 347 (980).

[8] RAP ThF_4 was ~ 20% $ThOF_2$.

[9] T.W. Walker, A. H. Guenther, and C. G. Fry, NBS Special Pub. #568; 405, 1980 T. W. Walker, A. H. Guenther, and P. E. Nielsen, IEEE J. Quant Elect, QE-17, p 2041-2065 (1981)

[10] J.R. Bettis, R.A.House, III, and A. H. Guenther, NBS Special Pub. No. 462, 338 (1976)

[11] Richard A. House II, AFWL-TR-76-62, p. 42 (1976).

Table 1. Damage Threshold (J/cm^2) /Spread *

VS

Beam Spot Size

Spot Size (1/e radius)	4.4μm	10.6μm	32.7μm	141.4μm
ThF_4, Cerac Low Defect λ/8	908.8 0.675	193 0.49	NA NA	58 0.31
ThF_4, Cerac Low Defect λ/4	903.1 0.69	187 0.69	NA NA	49.6 0.15
ThF_4, RAP Low Defect λ/4	550.8 0.65	182.2 0.73	NA NA	29.6 0.13
ThF_4, Cerac Low Defect λ/2	490.2 0.57	117 0.76	NA NA	14 0.43
ThF_4, Cerac λ/2	527 0.60	109 0.66	56.8 0.39	18.1 0.50
HFO_2 λ/2	479.9 0.70	59.3 0.75	49.2 0.47	17.6 0.23
ZrO_2 λ/2	165.1 0.64	40.6 0.52	48.3 0.42	22.9 0.27

* Threshold measurements are ± 20% accuracy

Spread is defined as $\left(\frac{\text{E max. no damage - E min. damage}}{\text{E max. no damage + E min. damage}}\right)$

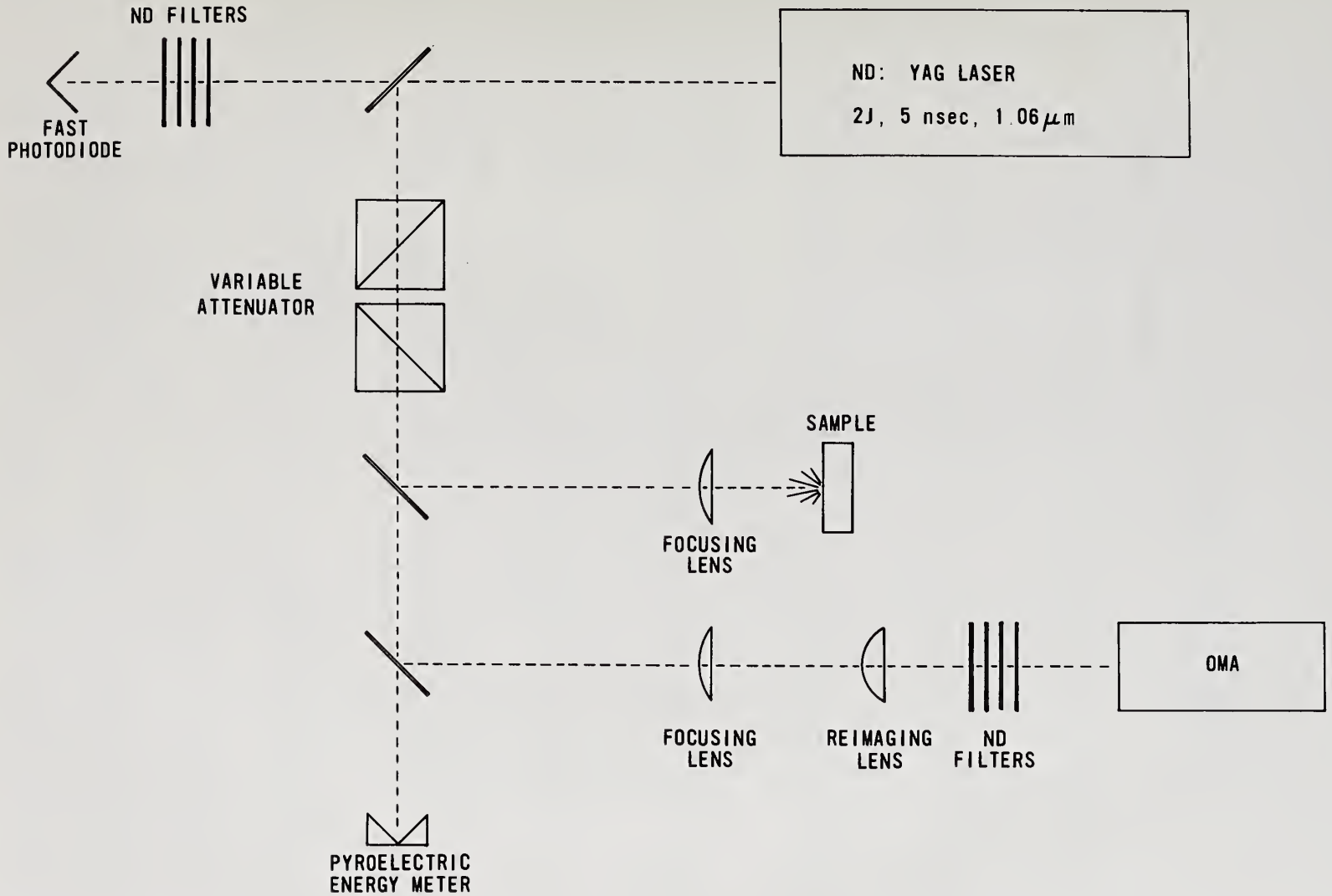

Figure 1: Experimental Arrangement

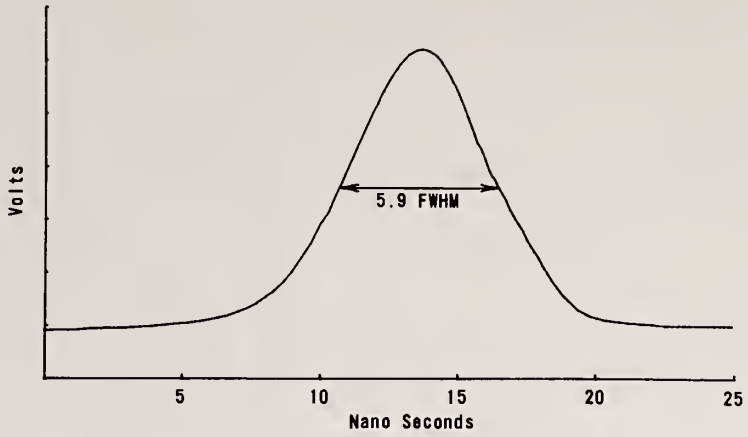

Figure 2. 1.06 μm pulse waveform from fast photodiode

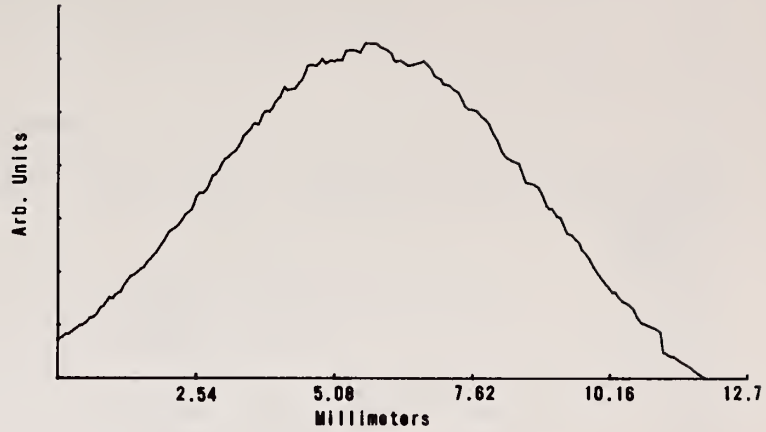

Figure 3. Unfocused beam profile at lens position from OMA.

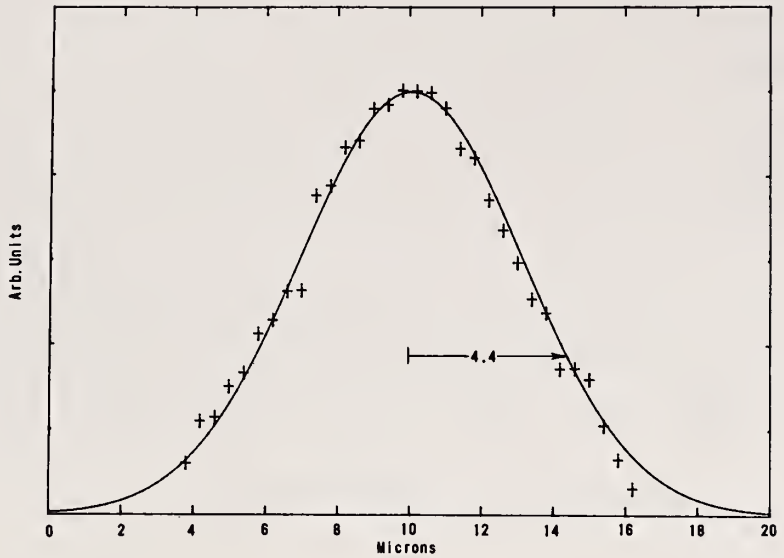

Figure 4. Beam profile at smallest spot size

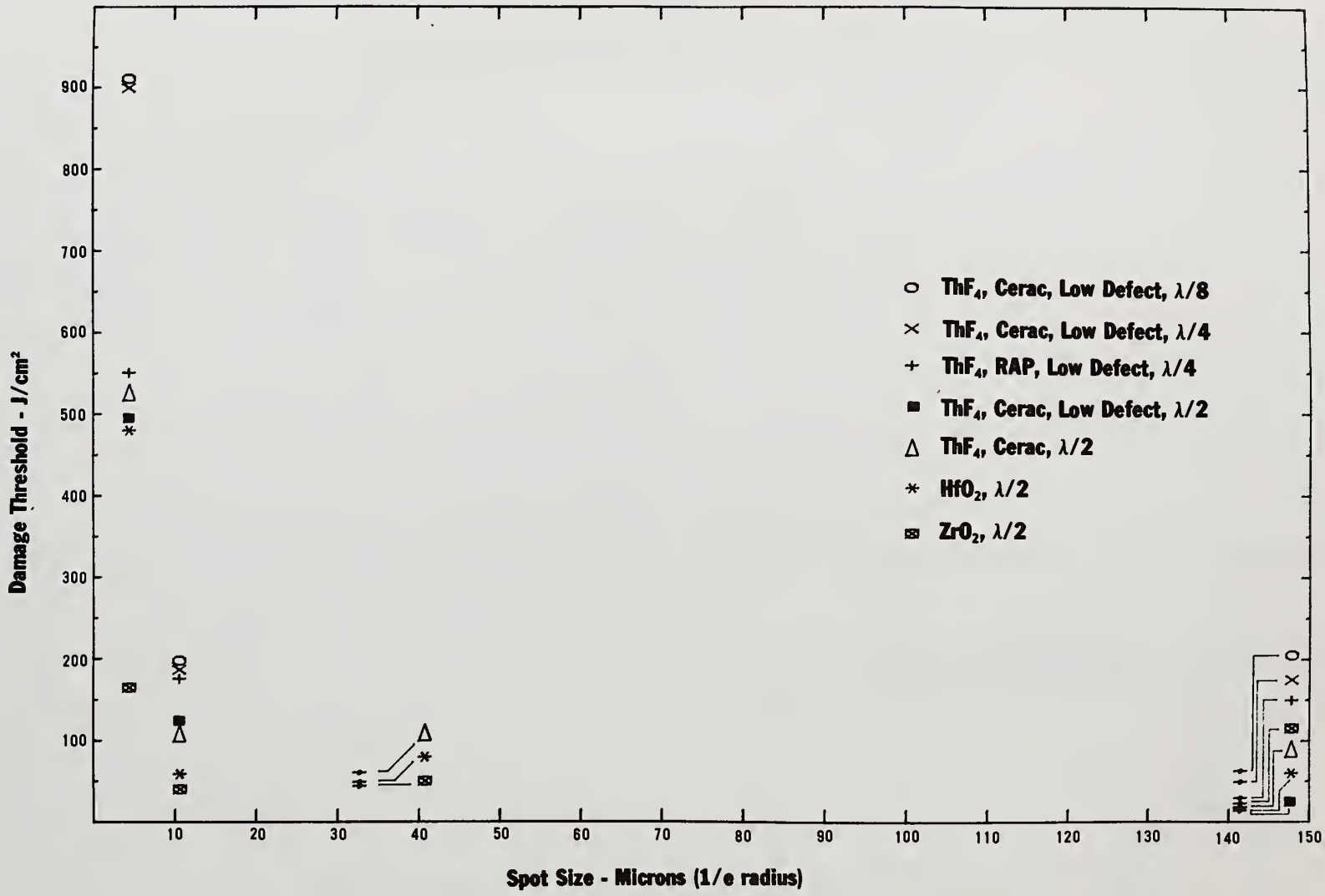

Figure 5. Damage threshold versus spot size for the seven samples tested.

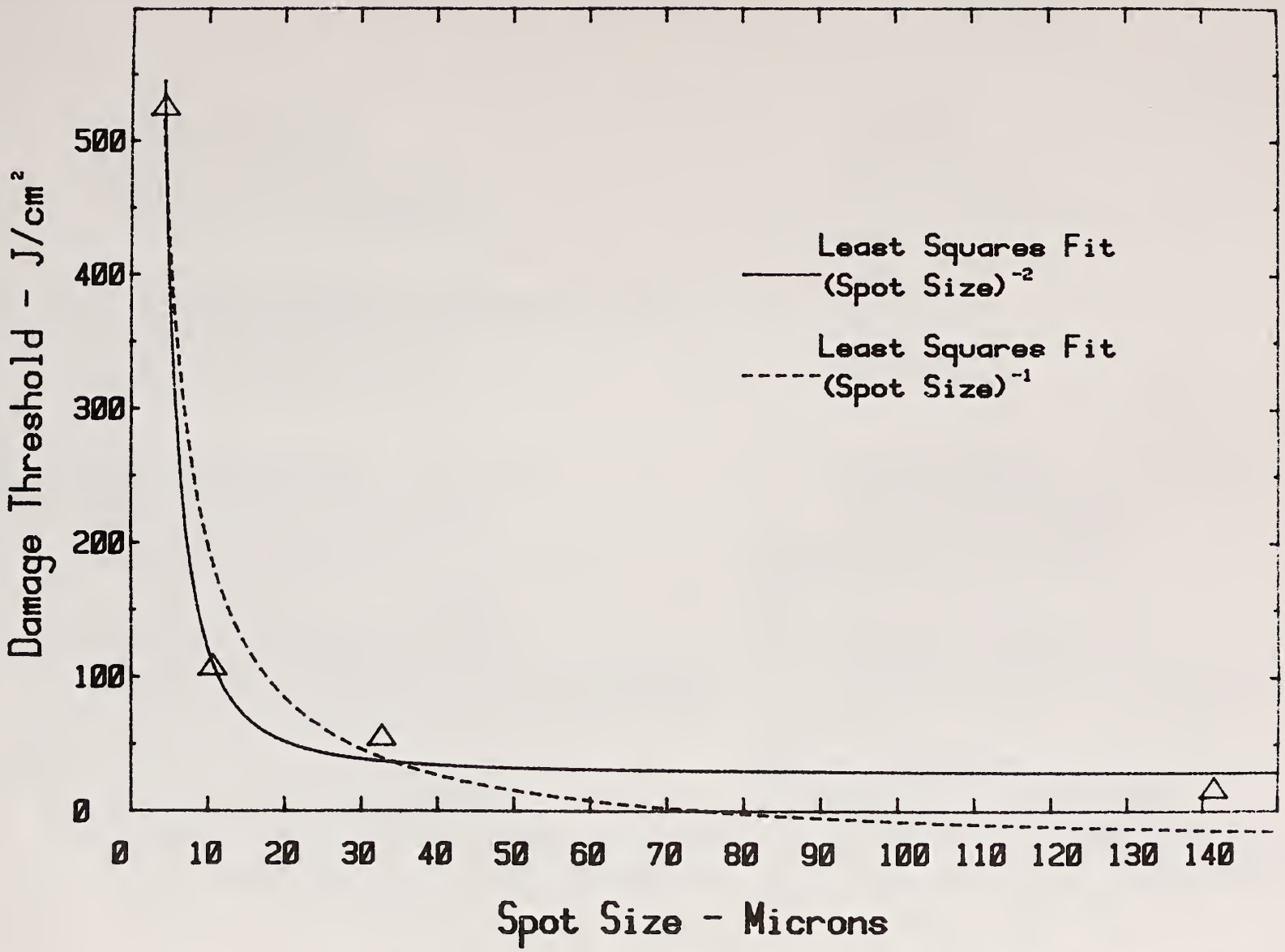

Figure 6. Damage threshold vs spot size - ThF_4, Cerac, $\lambda/2$ - compared with two possible theoretical fits.

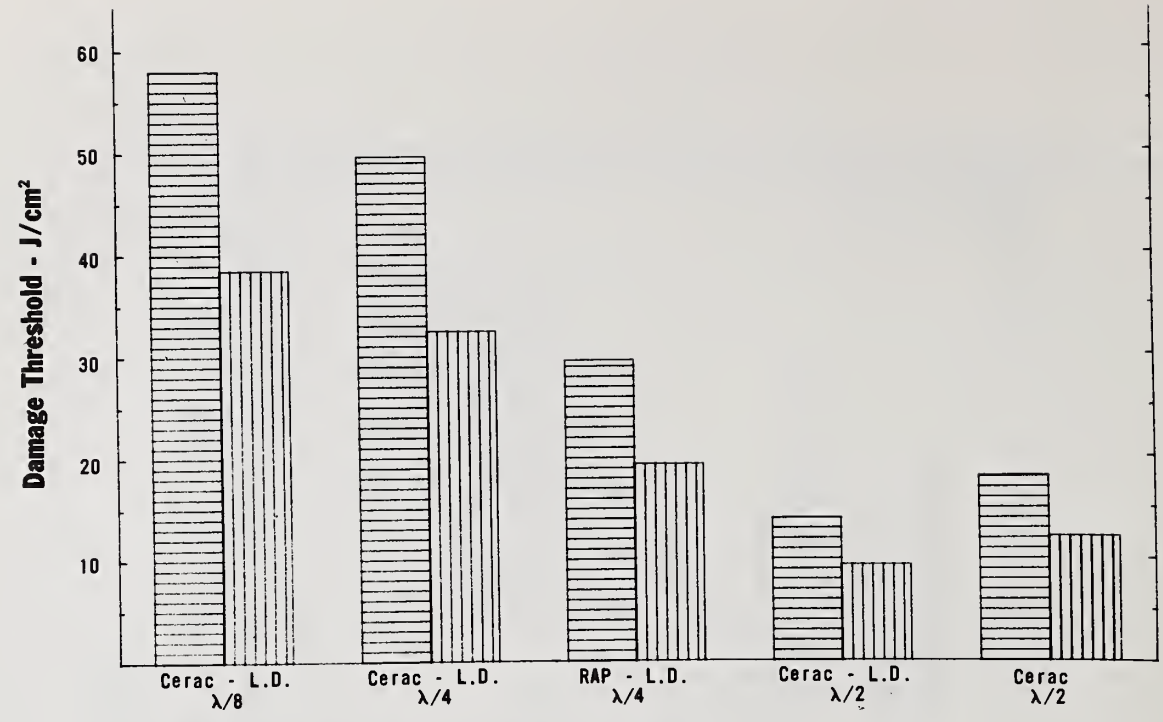

a) Data obtained with a 141.4 μm spot size

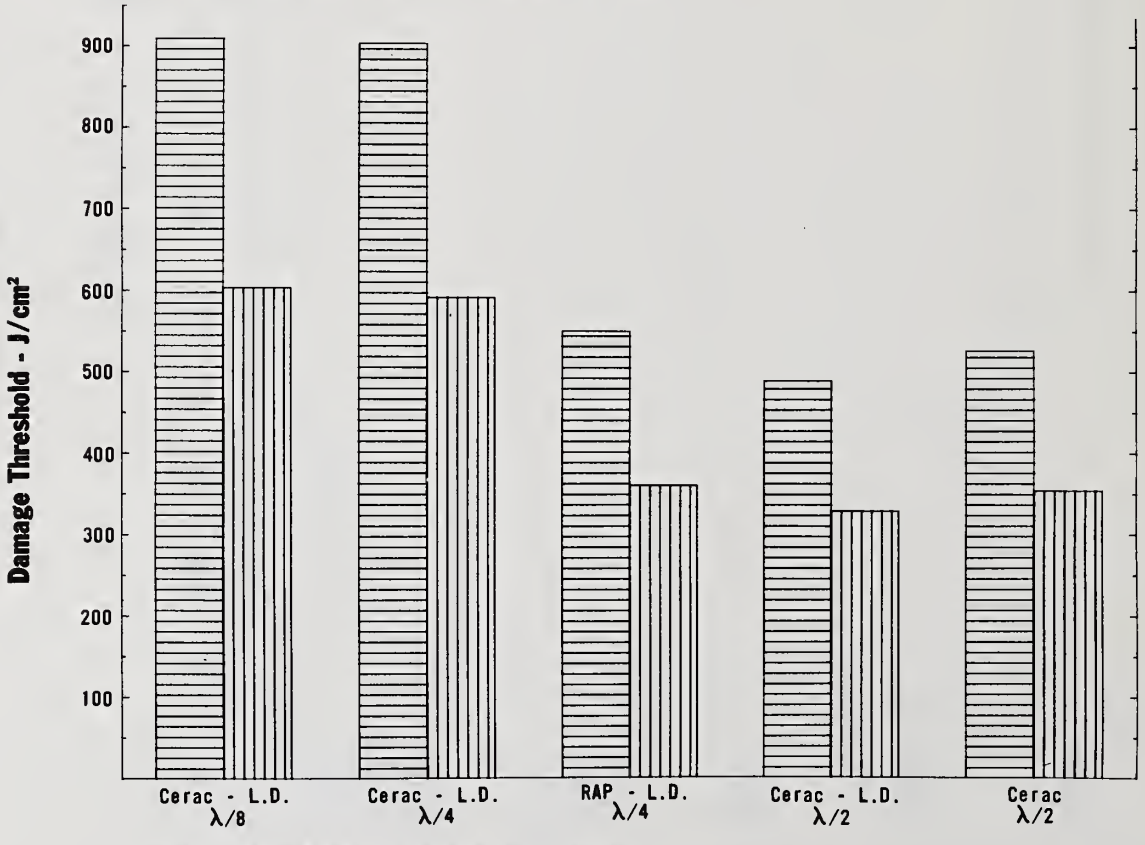

b) Data obtained with a 4.4μm spot size

Figure 7. Film thickness dependence of the damage threshold. Horizontal stripes indicate thresholds in terms of incident energy densities. Vertical stripes indicate thresholds in terms of internal energy densities calculated from the standing wave electric fields in the coating.

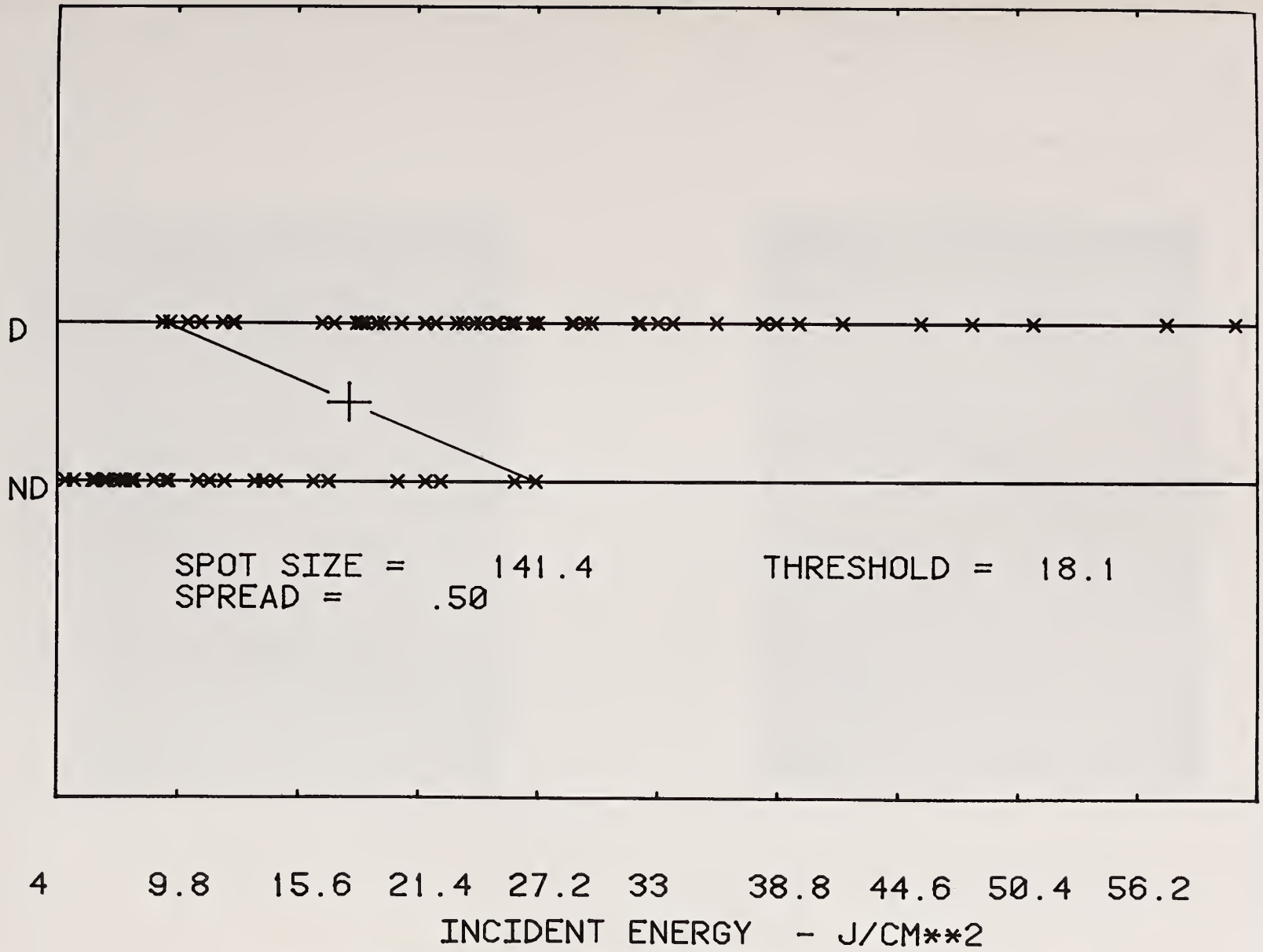

Figure 8. Representative data set obtained with a 141.4 μm spot size on ThF_4, Cerac, λ/2. Diagonal line with cross indicates the method of defining damage threshold used in this study.

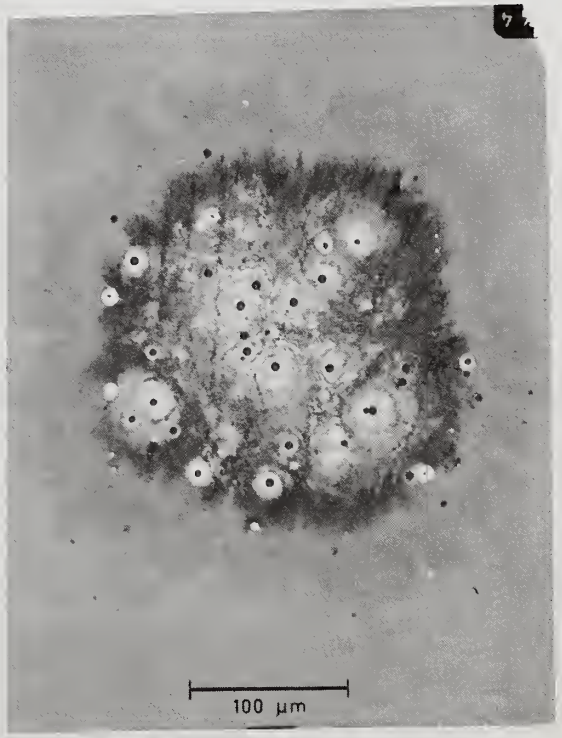

Figure 9. Damage site morphology observed with the largest spot size on HfO_2, $\lambda/2$.

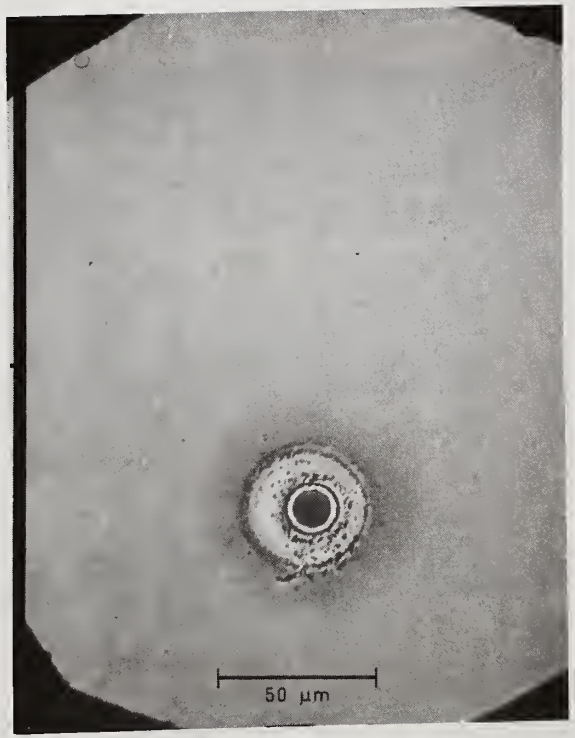

Figure 10. Damage site morphology observed with the 4.4 µm spot size on HfO_2, $\lambda/2$.

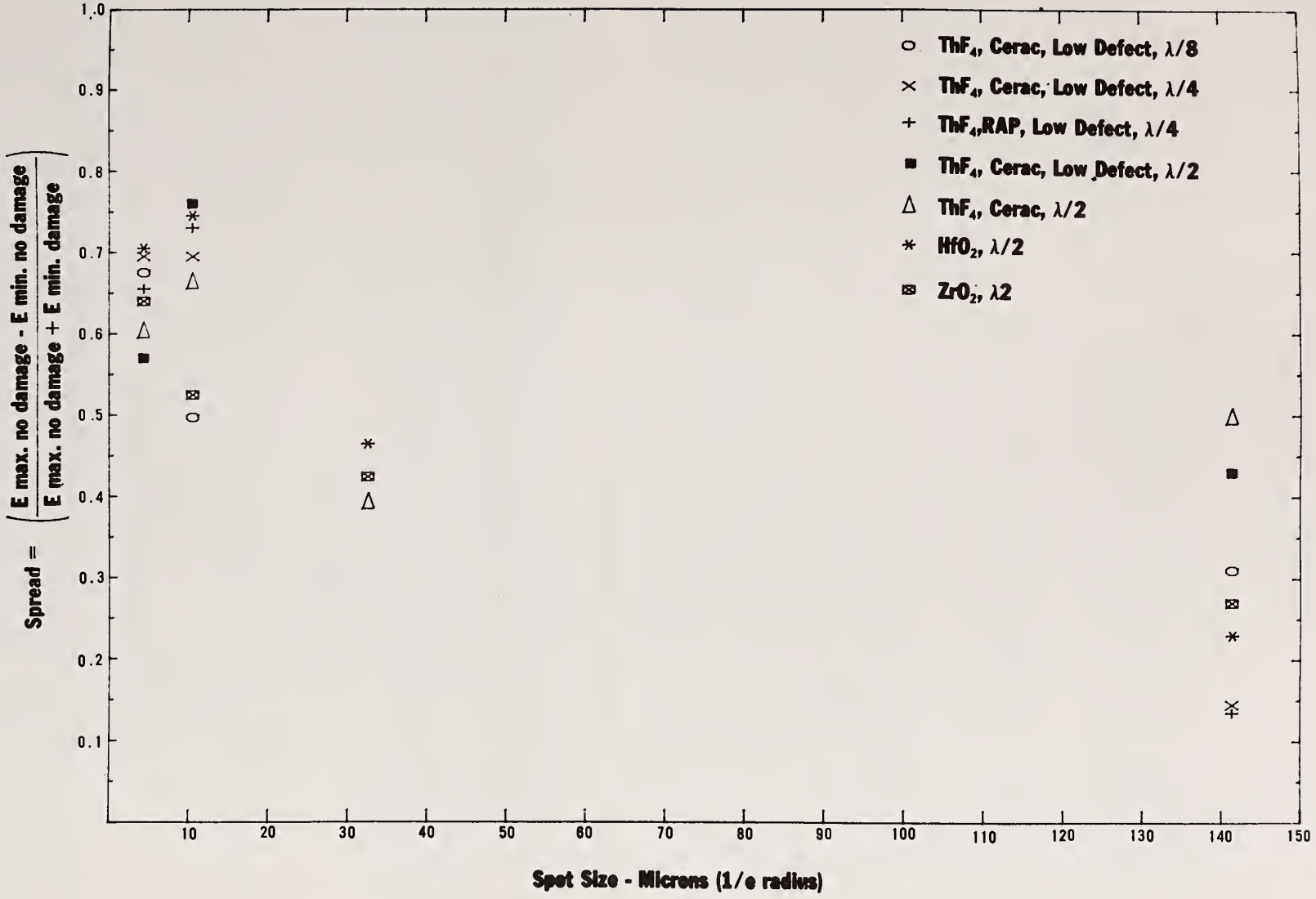

Figure 11. Damage statistics (spread) vs spot size for the seven samples tested.

Recent Progress in the Studies of Laser-Induced Intrinsic Damage of Transparent Solids: Deterrent Lack Effect of Seed Electrons in Avalanche Ionization Process

A. S. Epifanov, S. V. Garnov, G. V. Gomelauri, A. A. Manenkov, and A. M. Prokhorov

Lebedev Physical Institute of the USSR Academy of Sciences
Moscow, USSR

Peculiarities of laser-induced damage in transparent dielectrics caused by electron avalanche in the case of deterrent lack of seed electrons are discussed. Statistical models of the avalanche process initiated by multiphoton ionization of host atoms or impurities are described. Based on the breakdown probability expressions derived, the damage threshold dependence upon the temperature and the focal spot size are discussed. The theoretical results are found to be in good qualitative agreement with the experimental data for the laser-induced damage in alkali-halide crystals.

Key words: avalanche ionization; breakdown probability; seed electrons; spot-size dependence; temperature dependence.

1. Introduction

Avalanche ionization was recently investigated in detail both theoretically and experimentally as one of the basic mechanisms of intrinsic laser-induced damage [1-3]. The theoretical dependence obtained for the damage threshold of a series of crystals were experimentally confirmed. However, some experimental data, in particular, independence of the laser-induced breakdown threshold at 10.6 μm of temperature [2] and the peculiar behavior of the latter at the 3 μm wavelength [4] were not elucidated in the framework of the developed theory (Fig. 1). This theory assumed that the seed electrons needed for the avalanche initiation are always present in sufficient quantity in the interaction region. These data and some other experimental facts such as a strong spot-size dependence of damage thresholds observed for NaCl and KCl at 10.6 μm and 3 μm irradiation [5, 11] (Fig. 2), which also cannot be explained by the available avalanche ionization theory, have stimulated investigations of the influence of a number of initial electrons on the development of avalanche ionization. In this paper, some results of experimental and theoretical investigations recently performed in this direction in the Lebedev Physical Institute are reported.

2. Statistical Approach to the Theory of Avalanche Breakdown

The lack of seed electrons in the interaction region is shown in the theoretical analysis [6] to make the breakdown probabilistic and leads to increase of the damage threshold and its peculiar dependence on the size of an irradiated region and on the sample temperature.

This statistical approach to the avalanche breakdown theory can be described briefly as follows. A sequence of laser-induced impact ionizations by some electrons is assumed to be a Poissonian process, i.e., the probability of the K ionization acts, which produced an electron during the time t is given by:

$$P_k(t) = \frac{(t/\tau)^k}{k!} \exp(-t/\tau) \tag{1}$$

where $\tau = \gamma^{-1}$, γ is the avalanche rate parameter. A statistical analysis of the avalanche process [6] gives the following formula for the damage probability in a homogeneous laser field:

$$G_n^{\ell}(t) = 1 - \frac{\Gamma(n)}{\Gamma(\ell) \cdot \Gamma(n-\ell)} \cdot B_{1-\xi}(\ell, n-\ell) \tag{2}$$

Here ℓ is the initial number of the seed electrons in the interaction volume V, $n=N_{cr}V$, N_{cr} is the critical concentration of electrons ($N_{cr} \approx 10^{17}$ to 10^{18}cm^{-3}), $\xi = 1 - \exp(-t/\tau)$, $B_x(a,b)$ and $\Gamma(y)$ are the incomplete B and Γ - functions.

At $\ell = 1$ this formula reduces to the equation:

$$P = G_n^1(t) = [1-\exp(-t/\tau)]^{n-1} \tag{3}$$

If the damage probability P is chosen to be equal to 1/2 this formula gives:

$$t/\tau = \ln(n/\ln 2) \tag{4}$$

which is practically coincident with the usual laser damage criterion [1]:

$$\gamma \cdot t = \ln(n/\ell) \tag{5}$$

This means that even one initial electron in the interaction volume is enough to produce the avalanche breakdown. The analysis also shows that the variation of the breakdown probability in the reasonable range P = 0.1 to 0.9, in this case ($N_0 V \gg 1$), does not sufficiently change the damage critical field. Therefore, a statistical character of the avalanche damage can take place only in the opposite case ($N_0 V < 1$), when the seed electrons appear in the interaction volume as a result of some additional process. In order to elucidate the peculiarities of the damage in this case, we have considered the avalanche ionization initiated by the multiphoton ionization of impurities or host atoms in a dielectric. Assuming that the statistical appearance of electrons caused by the multiphotoionization can be described by the Poissonian law similar to that of the avalanche impact ionization process [1] and, considering both processes act simultaneously, the following relationship for the combined probability of production of n electrons at the time t are obtained, if initially there are no electrons in the interaction region:

$$S_n(t) = \int_0^t dt^1 \cdot S_{n-1}(t^1)\left(\frac{n-1}{\tau} + \frac{1}{\tau_1}\right)\left[\exp\left(-\frac{n(t-t^1)}{\tau}\right)\exp\left(-\frac{t-t^1}{\tau_1}\right)\right] \tag{6}$$

Here τ_1 is the characteristic time for the multiphoton ionization. The breakdown probability which is due to the electron avalanche process is given by:

$$G_n = \sum_{k=n}^{\infty} S_k(t) \simeq \frac{\Gamma(\alpha,\ n\cdot\exp(-t/\tau))}{\Gamma(\alpha)} \tag{7}$$

where $\alpha = \tau/\tau_1$. Together with the known relationships for τ and τ_1 as the functions of laser field intensity I ($\tau \propto$ exp (const/I) [2]; $\tau_1 \propto I^{-m}$). Equation 7 is considered at certain damage probability P as the equation for determining the damage threshold I_{cr}.

The calculations show that the damage threshold and its temperature and size are strongly dependent on the avalanche and multiphoton rates, i.e., for the parameter $\alpha = \tau/\tau_1$ they are principally different at $\alpha > 1$ and $\alpha < 1$. In the region of $\alpha > 1$, the damage threshold corresponds to the normal avalanche process. It does not depend on the value of α and is determined by the known relationships [1]. The case $\alpha < 1$ corresponds to the strongly deterred avalanche because of a lack of seed electrons. The breakdown probability in this case is given by:

$$G_n = 1 - \exp(-t/\tau_1) \tag{8}$$

and is determined by the probability of the appearance of the first free electron created by the multiphoton ionization. The critical field in this case is a falling function of α.

We have analyzed the temperature and size dependence of the damage threshold in the case of the deterred avalanche [6] and the results are summarized in the following sections.

3. Temperature Dependence of Avalanche Breakdown Threshold

It is known [1-3], that in the temperature dependence of the damage threshold I_d for the ordinary, i.e., nondeterrent by the lack of seed electrons, the avalanche mechanism is principally dependent on the relationship between the laser field frequency Ω , and the electron phonon collision frequency $\nu_{e\text{-}ph}$: $I_d \propto 1/T$ when $\Omega > \nu_{e\text{-}ph}$, and $I_d \propto T$ when $\Omega < \nu_{e\text{-}ph}$. For the deterrent avalanche breakdown, as determined from the above consideration, the damage threshold should not depend on the temperature.

A complicated situation can be expected. For the same crystal in some temperature range $T < T'$, the electron avalanche process can be normal, whereas at $T > T'$ it becomes deterred because not enough electrons can be generated in the interaction region under the given conditions (due to material parameter change with temperature or decrease in the damage threshold intensity). Such a situation is expected to be realized, for instance, in NaCl at $\lambda \approx 3$ μm.

The calculated temperature dependence of the damage threshold corresponding to this case (NaCl, $\lambda = 3$ μm) at various breakdown probabilities P are presented in Figure 3. (In these calculations, the 6-photon ionization has been assumed as a source of the seed electrons.) The dash curve of this figure corresponds to the nondeterred avalanche, whereas the upper line demonstrates a case where in the whole temperature range the avalanche process is deterred by the lack of seed electrons. On the intermediate curves, the temperature ranges are clearly seen where the avalanche process is deterred. It is important to point out that, along with the temperature independence, the scattering of the damage threshold (the difference of the thresholds corresponding to the various damage probabilities) takes place, indicating the statistical character of the avalanche process in this case.

4. Size Dependence of the Damage Threshold

The ordinary theory of the electron avalanche breakdown in solids, corresponding to the case of a sufficient number of seed electrons in the interaction region, does not predict any dependence of the damage threshold on the irradiation size, except for very small sizes (perhaps ~ 1 μm), when diffusional escape of electrons is important [2]. But, for the deterred avalanche mechanism where the damage threshold is determined by the appearance of the first electron, the size dependence is expected to be definitely important.

Indeed, if the first electron is generated by the K-photon ionization process, the rate of which is obviously given by

$$1/\tau_1 \propto V \cdot I^k$$

From Equation 8, at a fixed damage probability, it follows that

$$I_{c\tau} \propto V^{-1/k} \tag{9}$$

In the above consideration, the laser intensity distribution is assumed to be constant across the whole interaction volume V. In addition, impurities or defects, if they serve as the seed electron supply, are assumed to have high enough concentration and the same ionization rate (τ_1^{-1}).

A further development [8] of this simplified analysis, taking into consideratin both the spatial distribution of the laser radiation intensity and the variation of photoionization rates of impurities, has given the following relationship for the avalanche breakdown probability

$$P = 1 - \exp\left\{\sum_i \rho i \cdot \int_V [\exp(-t/\tau_i)-1]dV\right\} \tag{10}$$

Where ρi and τ_i^{-1} are the concentration and the rate constant, respectively, the impurity of i-type in the interaction volume V, defined as a region in which the laser radiation intensity $I(r,Z)$, exceeds the critical value I_a for the ordinary avalanche process. This relationship has been used to analyze the size dependence of the damage threshold for several particular cases of the multiphoton ionization rates ($\tau_i^{-1}(I) \propto I^K$) for the focused Gaussian-shaped laser beam.

Assuming in Equation 9 P = constant, the following expressions have been obtained for the spot size dependence at "long" and "short" laser pulses (i.e., at different relationships between the laser pulse width t_p and the ionization rate τ_i^{-1}):

At $t_p/\tau_i \gg 1$, for arbitrary K:

$$b^4\left[\frac{1}{3}\left(\frac{I_m}{I_a}+5\right)\left(\frac{I_m}{I_a}-1\right)^{1/2} - 2\,\mathrm{arctg}\left(\frac{I_m}{I_a}-1\right)^{1/2}\right] = \text{const} \tag{11}$$

here I_m is maximum on-axis beam intensity,

b is the minimum beam waist.

At $tp/\tau_i \ll 1$, $I_m \gg I_a$

$$b^4 \cdot \left(\frac{I_m}{I_a}\right)^{3/2} = \text{const} \tag{12}$$

for the one-photon ionization process, (K=1),

and

$$b^4 \left[\frac{3\pi}{8} \left(\frac{I_m}{I_a}\right)^2 - \frac{1}{4} \left(\frac{I_m}{I_a}\right)^{3/2} - \frac{1}{2} \left(\frac{I_m}{I_a}\right)^{1/2} \right] = \text{const} \tag{13}$$

for K=2,

and

$$b^4 \left[\frac{\pi}{8} \left(\frac{I_m}{I_a}\right)^3 + \frac{1}{4} \left(\frac{I_m}{I_a}\right)^{5/2} - \frac{1}{6} \left(\frac{I_m}{I_a}\right)^{3/2} - \frac{1}{3} \left(\frac{I_m}{I_a}\right)^{1/2} \right] = \text{const} \tag{14}$$

for K=3

5. Discussion and Conclusions

The above results indicate that the study of statistical peculiarities of the laser produced damage, including the investigation of the damage threshold statistics (i.e., measurement of the threshold value scattering) and the temperature and spot size dependence, can give valuable information on the damage mechanism. Particularly, the study of the spot-size dependence in some cases can indicate a source of the seed electrons excitation. Note that in the case where $t/\tau i \gg 1$ the spot-size dependence (Equation 10) is similar to that of the inclusion-caused damage [7]. The temperature dependence of the damage threshold is expected to be a very informative tool to elucidate the damage mechanism. A resemblance of the temperature dependence observed for NaCl at λ = 2.94 μm to the theoretically calculated shapes shown in Figure 3 supports the statistical avalanche breakdown model reported in this paper and indicates the deterrent seed electrons lack in this case.

The direct observations of the seed electron effect on the damage threshold, which can be made by means of an external UV-irradiation of the interaction region, are very desirable. The experiments of such a type done recently in our laboratory [9,10] have shown that in NaCl the laser damage threshold at 1.06 μm is not affected by the synchronous UV-irradiation of the sample, whereas the 10.6 μm laser damage threshold is reduced by the UV-irradiation. These results can be explained by assuming that 1.06 μm laser radiation produces ionization of the impurity atoms in the sample investigated easier than at 10.6 μm radiation. This results in the deterrent lack of seed electrons at 10.6 μm.

The obtained results of the theoretical analysis of avalanche ionization without seed electrons explain the anomalies observed in the laser-induced damage of high-laser damage resistant materials where an intrinsic mechanism of damage is realized and proves the essential role of the seed electrons in the development of avalanche breakdown.

References

1. Epifanov, A. S., Manenkov, A. A., and Prokhorov, A. M., "Theory of Avalanche Ionization in Transparent Dielectrics Induced by Electromagnetic Field," Zh.Eksp.Teor.Fiz., vol. 70, pp. 728-737, (1976) /Sov. Phys. JETP, vol. 43, p. 377 (1976)/.
2. Gorshkov, B. G., Danileiko, Yu.K., Epifanov, A. S., Lobachev, V. A., Manenkov, A. A., and Sidorin, A. V., "Laser-Induced Breakdown of Alkali Halide Crystals." Zh.Eksp.Teor.Fiz., vol. 72, pp. 1171-1181, (1977)/Sov.Fiz. JETP, vol. 45, p. 612 (1977)/.
3. Manenkov, A. A., "New Results on Avalanche Ionization as a Laser Damage Mechanism in Transparent Solids." Nat. Bur. Stand. (U.S.) Spec. Publ. 509, 1977, p. 455.
4. Gomelauri, G. V. and Manenkov, A. A., "Investigation of Laser-Induced Damage to Crystals at λ = 2.76 μm ($CaF_2:Er^{3+}$-laser)." Kvant.Elektr., vol. 6, pp. 45-48, (1979).
5. Soleau, M. J., Bass, M., Klein, P. H., "Frequency and Focal Volume Dependence of Laser-Induced Breakdown in Wide Band Gap Insulators." Nat.Bur.Stand.(U.S.) Spec. Publ. 568, 1979, p. 497.
6. Gomelauri, G. V., Epifanov, A. S., Manenkov, A. A., Prokhorov, A. M., "Statistical Peculiarities of Avalanche Ionization of Wide Band Gap Dielectrics by Laser Radiation in the Case of Lack of 'Seed' Electrons." Zh.Eksp.Teor.Fiz., vol. 79, pp. 2356-2363 (1980).
7. Fradin, D. W., and Bua, D. P., "Laser-Induced Damage in ZnSe." Appl. Phys. Lett., vol. 24, pp. 555-557 (1974).
8. Epifanov, A. S., and Garnov, S. V., "Statistical Approach to Theory of Electron Avalanche Ionization in Solids," IEEE J. Quantum Electron., vol. QE-17, pp. 2023-2026, October 1981.
9. Gorshkov, B. G., Epifanov, A. S., Manenkov, A. A., and Panov, A. A., "Breakdown of the Optical Materials in Crossed Beams at the Various Frequencies: Techniques and Experiment." Izvestiya Acad. Nauk. ser Fiz., vol. 44, p. 2062, 1980.
10. Gorshkov, B. G., Danileiko, Yu. K., Epifanov, A. S., Manenkov, A. A., Prokhorov, A. M., and Sidorin, A. V., "Effect of UV-Irradiation on Breakdown in Alkali-Halide Crystals by CO_2-Laser Radiation," Kvant. Electro., vol. 8, pp. 155-156 (1981).
11. Soileau, M. J. and Bass, M., "Optical Breakdown in NaCl and KCl from 0.53 to 10.6 μm." Appl. Phys. Lett. 35(5), 1 Sep 1979.

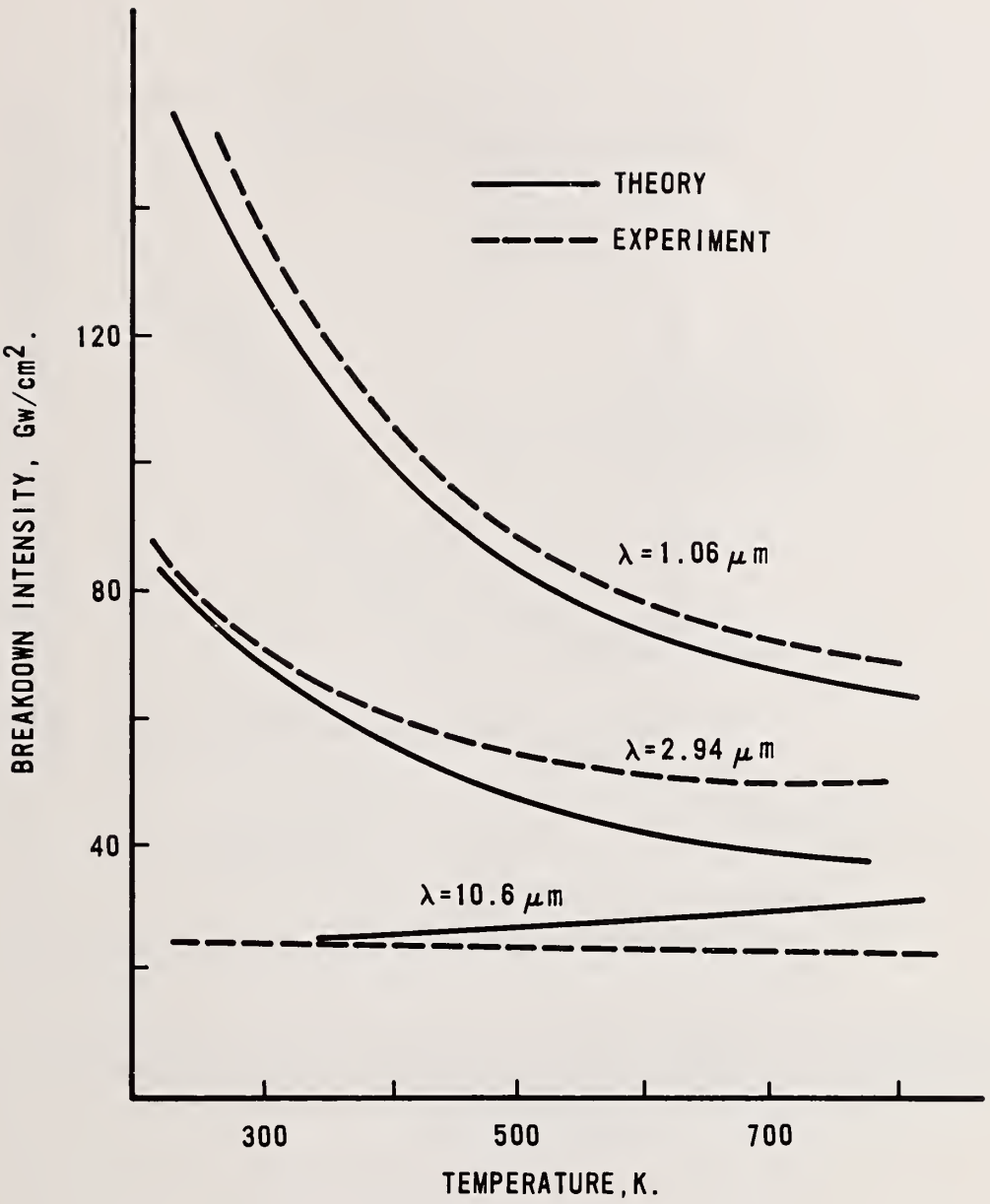

Figure 1. Temperature dependence of damage threshold for NaCl at various laser wavelengths.

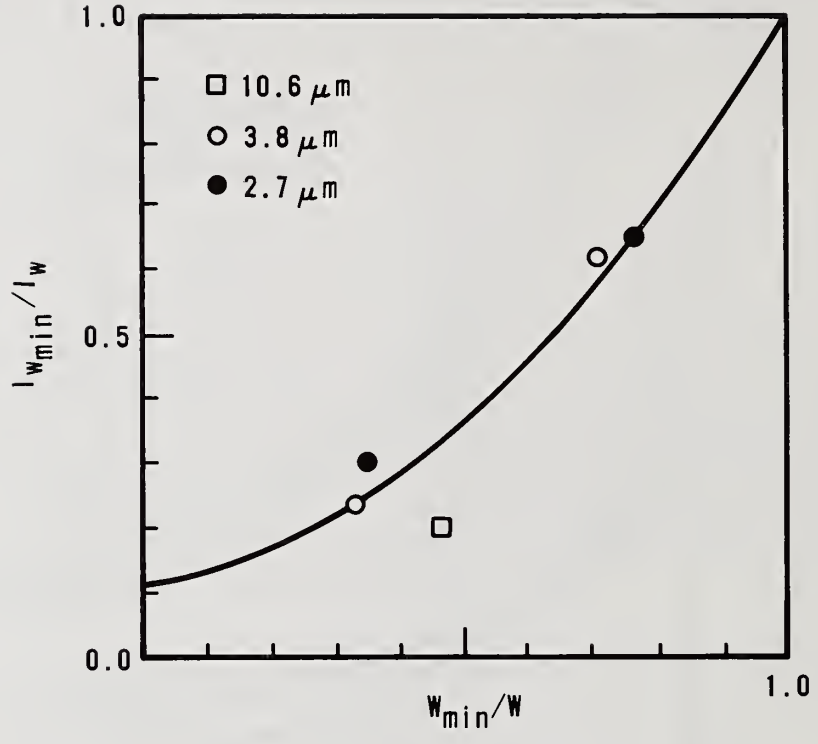

$$I_W/I_{W_{min}} = 0.8824\ (W_{min}/W)^2 + 0.1187$$

W is the focal spot radius ($1/e^2$ of intensity), W_{min} = 9.55 μm

Figure 2. Measured spot radius dependence of breakdown intensity in NaCl at 10.6, 3.8, and 2.7 μm (after M. J. Soileau and Michael Bass [14]).

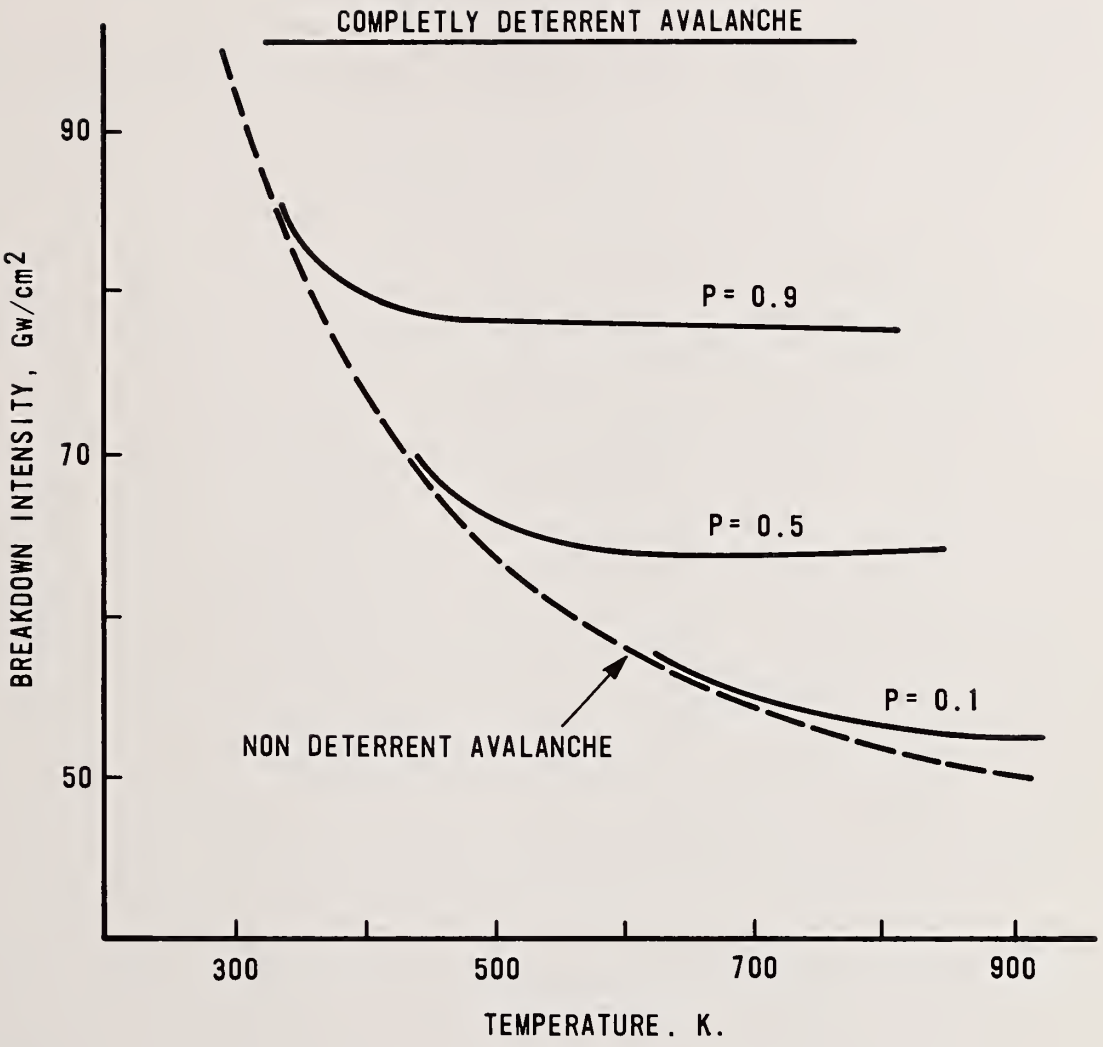

Figure 3. Calculated temperature dependence of damage threshold for NaCl, λ = 2.94 μm at various avalanche breakdown probability P.

Is there experimental data supporting the prediction that there should be a different spot size dependence depending on whether a single photon or multiphoton process is involved? The speaker replied that in their work on the damage of NaCl at a wavelength of 10 μm they observed the influence of ultraviolet irradiation of the sample on the damage threshold. They also performed a similar experiment at 1 μm but observed no influence of ultraviolet irradiation in this case. They explain this result by noting that at higher frequencies the initial electrons can be produced more easily by multiphoton processes than at lower frequencies. They thus have some experimental support for their theoretical statistical approach to the theory of avalanche ionization. In response to another question, the speaker pointed out that ordinary avalanche theory predicts an increase in laser damage with increasing temperature. However, if no initial electron is present and can only be supplied by a muiltiphoton process or other process which is temperature independent, there should be no temperature dependence of the breakdown field.

Quantum Theory of Multiphoton Free Carrier Absorption At High Intensities in Compound Semiconductors

B. Jensen

Department of Physics
Boston University
Boston, Massachusetts
02215

Multiphoton absorption and emission, accompanied by scattering of free carriers in an intense radiation field, is treated by an extension of the theory of one photon free carrier absorption in polar semiconductors. The rate equation for m photon absorption, where m is a positive integer, is obtained from the equation of motion of the quantum density matrix. It is shown to be proportional to the mth power of the radiation intensity. The effect of the field on the electron during scattering is taken into account by using the exact wavefunctions of an electron in an intense radiation field in the calculation of the transition matrix elements. An expression for the average Joule heating per electron is found. A comparison with earlier treatments is given.
Key words: Compound semiconductor; free-carrier absorption; multiphoton absorption.

Free carrier absorption in semiconductors refers to optical absorption in which the electron makes a transition from an initial state to a final state in the same band. At low intensities it is sufficient to treat the interaction of an electron with the radiation field, and with the phonon field of the lattice or the coulomb field of an impurity atom, as the absorption or emission of a single photon accompanied by scattering by a scattering mechanism. The scattering mechanism is required for conservation of momentum, as the interaction with the photon provides the electron with energy, but with negligable momentum transfer. At high intensities, the possibility of multiphoton absorption must be considered. One must also take into account the effect of the field on the electrons. One does this by using the exact wavefuncions of an electron in the field in calculating the transition matrix elements, rather than the Bloch functions appropriate to the low intensity case. These effects have been discussed by many authors.[1]-[14]

A theoretical calculation of the absorption coefficient α can be made from the rate equation for the time rate of change of the photon occupation number using the methods of time dependent perturbation theory.[15]-[17] Alternatively, the optical conductivity σ can be found from a calculation of the Joule heating of the electrons in the field which is based on the solution of the equation of motion of the quantum density matrix.[18]-[19] The two quantities are related by the expression

$$n\alpha = 4\pi\sigma/c = (w/c)\, e_2 \qquad (1)$$

where n is the real part of the complex refractive index, and e_2 the imaginary part of the complex dielectric constant, and where $n\alpha$ has been calculated using second order time dependent perturbation theory and σ has been derived using the quantum density matrix equation of motion which leads to a generalized Boltzmann equation. In the latter case, it can be shown that the generalized Boltzmann equation reduces to the usual Boltzmann equation at low frequencies in the case of an elastic scat-

tering mechanism.

The following relation can be derived between the time rate of change of the photon occupation number dn_q/dt, expressed in terms of the sum over electron scattering rates for photon absorption and emission accompanied by phonon absorption or emission, and the solution of the generalized Boltzmann equation.[19]

$$dn_q/dt = s\,\delta n_q = s\ tr\{\hat{N}_q F\} = (i/\hbar)\ tr\{\hat{N}_q [g, H^{er}]\} \tag{2}$$

$$p = F + g = \sum_m [g^{2m-1} + F^{2m}] \tag{3}$$

$$F^{2m}_{\alpha}\ H^{er 2m}\ ,\ g^{2m-1}\ \alpha\ H^{er 2m-1} \qquad m = 1,2,3,\ldots \tag{4}$$

In (2), $s\,\delta n_q$ denotes the Fourier-Laplace transform of the time rate of change of the photon number operator $\hat{N}_q$, p is the deviation from equilibrium of the quantum density matrix R which satisfies the quantum density matrix equation of motion

$$dp/dt = [H,R] = [H_0 + H' + H^{er}\ ,\ R] \tag{5}$$

and the trace is taken in the Hilbert space generated by eigenvectors of H_0, the Hamiltonian of the nointeracting system, in the occupation number representation.

$$H_0 = H^0(\text{electrons}) + H^0(\text{phonons}) + H^0(\text{photons}) \tag{6}$$

H^{er} is the interaction of the electron system with the vector potential $\vec{A}$ of the radiation field

$$H^{er} = -\ (e/mc)\ \vec{A}.\vec{P} \tag{7}$$

and $\vec{P}$ in (7) is the total momentum of the electron system, which is the sum over the individual electron momenta. H' is the interaction of the electron and phonon subsystems, and g and F, the off diagonal and diagonal parts of p, respectively, satisfy equations arising from taking the Laplace transform of (5) which can be written as

$$[H_0 + H',\ R] - i\hbar s\ p = [R,\ H^{er}] \tag{8}$$

Using (3) and equating terms of a given order in H^{er}, and noting that H^{er} and H' (involving absorption or emission of a photon or phonon) are off diagonal in the number representation, one has

$$[H_0 + H', g^{2m+1}] - i\hbar s\, g^{2m+1} = [F^{2m}, H^{er}], \qquad m = 0,1,2, \tag{9}$$

$$- i\hbar s\, F_N^{2m} = [g^{2m-1}, H^{er}]_N, \qquad m = 1,2... \tag{10}$$

where

$$F_N = (N|F|N), \qquad F_{N'N} = (N'|F|N) = 0$$

$$g_{N'N} = (N'|g|N), \qquad g_N = (N|g|N) = 0$$

$$H_0|N) = E_N|N) \tag{11}$$

denote diagonal and off diagonal elements of p taken between eigenstates of H_0 and E_N is the energy eigenvalue corresponding to $|N)$. The photon occupation number operator $\hat{N}_q$ is diagonal in the representation $|N)$, where $q = nw/c$ is the photon wave vector. In (10), $F_N^{2m} = F_N^{2mq}$ is the diagonal part of p and

$$s\, tr\{\hat{N}_q F^{2mq}\} = (i/\hbar)\, tr\{\hat{N}_q [g^{(2m-1)q}, H^{er^q}]\}$$

$$= (i/\hbar) \sum_{N'N} (N_q - N_q')\, g_{NN'}^{(2m-1)q}\, H_{N'N}^{er^q} \tag{12}$$

On solving (9) for $g^{(2m-1)q}$ and inserting the result in (12), one obtains the rate equation for m photon absorption. This is shown in detail in Ref. (19) for $m = 1$. The expansion of $g^{(1)}$ to second order in H' (ie: to lowest order in the scattering rate), gives the generalized Boltzmann equation. Insertion of this into (12) and calculation of the resulting trace gives the same solution for intraband free carrier absorption as that calculated using second order time dependent perturbation theory.[17] The latter is identical to what one obtains on using the electron distribution function found from the solution of the generalized Boltzmann equation to calculate the current $\vec{J}$ the taking the trace $\langle \vec{J}.\vec{E} \rangle_q / \hbar w$ to obtain the Joule heating per photon or dn_q/dt.

The method described above for $m = 1$ gives the result for low intensities when only one photon processes are important. At high intensities, when multiphoton processes must be considered, one can repeat the process for $m = 2,3,4$, to obtain the photon rate of change due to m photon absorption and emission. This is shown in detail in Ref. (20). An expression for the rate equation for m photon absorption is derived from (12) in terms of the interaction of the corresponding Fourier components $\vec{J}^{(m)}$ and $\vec{E}^{(m)}$. An expression for the Joule heating corresponding to m photon absorption, which is proportional to the m^{th} power of the radiation intensity, is given in terms of an associated conductivity. The effect of the intense radiation field on the electronic wavefunctions and scattering matrix element involved in the calculation of the electron distribution function is taken into account by using Houston wave functions[13][21] rather than the Kane[22] wavefunctions of

the low intensity theory. A comparison of results obtained as described above with previous results is given and the conditions under which these coincide are discussed.

References

[1] A. V. Vinogradov in "Multiphoton Processes" J. H. Eberly & P. Lambropoulos, Editors. Wiley (1978) pp 403.

[2] A. V. Vinogradov, Sov. Phys. JETP 43, 521 (1976).

[3] N. M. Kroll, K. M. Watson, Phys. Rev. A 8, 804 (1973).

[4] L. V. Keldysh, Sov. Phys. JETP 20, 1307 (1975).

[5] L. V. Keldysh, Sov. Phys. JETP 6, 763 (1958); Sov. Phys. JETP 34, 788 (1958); Sov. Phys. JETP 21, 1135 (1965).

[6] F. B. Bunkin, A. E. Kazakov, M. V. Fedorov, Sov. Phys. Uspekhi 15, 416 (1973); Sov. Phys. JETP 22, 844 (1966).

[7] N. Bloembergen, Y. R. Shen, Phys. Rev. 133, 37 (1964).

[8] H. H. Nickle, J. Math. Phys. 7, 1497 (1966).

[9] A. Vaidyanathan, T. W. Walker, A. H. Guenther, IEEE Journal of Quantum Electronics 16, 89 (1980); Phys. Rev. B 20, 3526 (1979).

[10] A. Schmid, P. Kelly in "Laser Induced Damage in Optical Materials: 1977" NBS Special Publication 509 (pp 465).

[11] A. A. Manenkov in "Laser Induced Damage in Optical Materials: 1977" NBS Special Publication 509 (pp 455).

[12] V. P. Silin, Sov. Phys. JETP 20, 1510 (1965); Sov. Phys. JETP 11, 1277 (1960), Sov. Phys. JETP 14, 617 (1962).

[13] W. V. Houston, Phys. Rev. 57, 184 (1940).

[14] A. V. Vinogradov, Sov. Phys. JETP 41, 540 (1976).

[15] W. P. Dumke, Phys. Rev. 124 1813 (1961).

[16] E. Haga, H. J. Kimura, J. Phys. Soc. Japan 18, 777 (1963); 19, 471, 658, 1596 (1964).

[17] B. Jensen, Ann. Phys. 80, 284 (1973).

[18] B. Jensen, Phys. Stat. Sol. 86, 291 (1978); J. Appl. Phys. 50, 5800 (1979).

[19] B. Jensen, Ann. Phys. 95, 229 (1975).

[20] B. Jensen, Phys. Rev. B 24, (1981) (In Press)

[21] W. Franz in "Tunneling Phenomena in Solids" Eds. E. Burstein, S. Lundquist, Plenum, New York (1969).

[22] E. O. Kane, J. Phys. Chem. Solids 1, 249 (1957).

*Research supported by the Department of Energy under contract # DE-AC02-79ER]0444.A000

Comment on "Intense-field Effects in Solids"

A. Vaidyanathan
Universal Energy Systems
Dayton OH 45432

A. H. Guenther
Air Force Weapons Laboratory
Kirtland AFB NM 87117

Recent theoretical work by Jones and Reiss predict that the effective energy gap of a crystalline solid in the presence of electromagnetic radiation increases with radiation intensity. Thus, at sufficiently great intensities higher order multiphoton processes could become more probable than lower order processes. It is shown that, although this behavior contradicts the well-known perturbative results in the low intensity region, it appears to be confirmed by the experimental data on GaP at 0.694 μm, due to Pyshkin et al. Theoretical and experimental results regarding the intensities needed for the observation of this phenomenon are compared, and its implications for nonlinear optics are discussed.

Key words: Conduction bands; gallium phosphides' conduction electrons; electric fields; band structure; multi-photon; nonlinear optics; semiconductors.

Introduction

Recently Jones and Reiss[1] reported the results of a theoretical investigation of the effects of intense electromagnetic radiation on multiphoton processes in solids. An interesting prediction of their theory is that at sufficiently high intensities there can be a reversal in interaction behavior as a function of photon multiplicity, i.e., a higher order process can become more probable than a lower order process. This result is in contradiction with the well known perturbative results in the low intensity domain[2]. It is not clear whether the above result is an artifact of the model employed, or whether any intrinsic physical significance can be attributed to it. In this note we point out that there exists in the literature at least one experimental result, which seems to lend support to the Jones and Reiss prediction. Some implications of their theory to nonlinear optics are discussed.

Comparison of theory and experiment

Jones and Reiss studied the multiphoton transition rates in crystalline solids by employing the S-matrix formalism. They assumed that the conduction electron wavefunction was a Volkov function[3], which is the exact solution of the Schrodinger's equation for a free electron in a plane-wave electromagnetic field. An interesting consequence of this theory was that the conduction electron energy E_c increased with increasing radiation intensity, as

$$E_c(A) = E_c(0) + \frac{e^2 A_o^2}{4m_c} \tag{1}$$

where A_o is the amplitude of the vector potential and m_c is the effective mass of the conduction electron. The energy of the valence electron remained the same as the field-free value. Hence, the photon energy needed to effect an interband electronic transition increased with increasing intensity. For example, it is conceivable that a two-photon transition energetically allowed at low intensities could not take place at high intensities, where now a three-photon process would be required due to an increase in the band gap. This result is similar to that of Keldysh[4] where the effective band-gap ($\tilde{E}_g$) in the presence of electromagnetic radiation can be much larger than the ordinary band-gap (E_g). There Keldysh showed that

$$\tilde{E}_g = \frac{2}{\pi} E_g \frac{\sqrt{1+\gamma^2}}{\gamma} E\left(\frac{1}{\sqrt{1+\gamma^2}}\right) \tag{2}$$

where E is the complete elliptic integral of the second kind, and γ is the adiabaticity parameter:

$$\gamma = \frac{\omega \sqrt{\mu^* E_g}}{eE_o} \tag{3}.$$

In Eq. (3) μ^* is the reduced effective mass of the valence and conduction bands, while E_o is the electric field amplitude. In the limit $\gamma >> 1$, which corresponds to multiphoton transition, the Keldysh result for the increase in the band gap coincides with that of Jones and Reiss, if the valence band effective mass is very much larger than the conduction band effective mass.

If the band-gap energy does indeed increase with increasing radiation intensity, it will be very important in many nonlinear optics areas. However, to our knowledge there has not been any discussion of this subject in the literature. In the following, a comparison of the above theoretical predictions with the results of an experiment that seems to support these theories will be made, even though the experimental results were interpreted differently.

Pyshkin et al.[5], in their experimental investigation of multiphoton absorption in GaP at 77.3K using a continuously increasing intensity Q-switched ruby laser, found that the generated carrier density initially increased as I, then at sufficiently high intensities varied as I^3 and at still higher intensities varied as I^4. This behavior was interpreted as being the result of distinct two-, three-, and four-photon absorptions respectively. The authors explained their observation in terms of the band structure of GaP. The two-, three- and four-photon transitions were interpreted as taking place in the neighborhood of the symmetry points Γ and L as shown in Figure 1. These authors suggested that the oscillator strength between the states near L_3^v and L_3^c was much larger than between the states near Γ_{15}^v and Γ_{15}^c, which in turn was larger than the momentum matrix element connecting states close to Γ_{15}^v and Γ_1^c. This accounted for the observed reversal of dominance in terms of photon multiplicity. However, it is difficult to visualize the momentum matrix elements varying in a sufficiently strong manner as functions of energy and wave vector to reverse the usual trend, where the multiphoton transition probabilities decrease drastically with increasing order of the process. For example, Pantell et al.[2] have both calculated and measured

the three-photon and two-photon absorption cross-sections of many crystalline solids and found the ratio to be approximately 10^{-32}. The four-photon absorption cross-section was considerably smaller by another factor of 10^{-38}.

Another explanation of the noted behavior, which suggests itself from the Jones and Reiss work, would be to consider an increase in the effective band gap with increasing radiation intensity. Initially two-photon absorption is observed due to transitions in the vicinity of $\Gamma_{15}^{v} \rightarrow \Gamma_{1}^{c}$ (E_g = 2.9 eV $\neq$ hν.79 eV). For sufficiently high intensities it is possible that $E_g(\Gamma_{15}^{v} - \Gamma_{1}^{c}) > 3.58$ eV, preventing two-photon absorption at the ruby wavelength. If, however, E_g is still less than or equal to 5.37 eV, three-photons of ruby laser could be absorbed simultaneously. At even higher intensities four photon absorption might become the dominant mechanism. Eq. (1) predicts that in GaP at 0.694 μm, the intensities needed for the order of the multiphoton transition to change from two to three and from three to four are respectively 1.92×10^{31} and 7.69×10^{31} photons/cm^2-sec. The predictions of the Keldysh formula are four times larger, while the experimental results are much lower being 1.77×10^{26} and 2.81×10^{26} photons/cm^2-sec respectively. This discrepancy between the theoretical predictions and experimental data is not surprising, because of the numerous approximations made in the theoretical models and the several factors which seriously influence the experimental measurement of multiphoton processes.

The theoretical model of Jones and Reiss assumes that the valence electron wavefunction in the presence of the intense electromagnetic radiation is the same as the field-free Bloch function, while the conduction electron wavefunction is significantly perturbed by the radiation, resulting in a Volkov wavefunction. Keldysh, however, assumes that both valence and conduction electron wavefunctions are Volkov functions. Since the Volkov wavefunction is strictly correct only for a free electron in a plane-wave electromagnetic field, its use for the description of the crystalline electrons is suspect. In addition, the theoretical models employ the electric dipole approximation and omit the term proportional to the square of the vector potential in the interaction Hamiltonian. More importantly, they usually assume simple analytical expressions for the electronic energy bands neglecting the effects of excitons and impurities. The validity of these aproximations in GaP at the intensities considered here is not clear. On the other hand, the experimental data are seriously influenced by the presence of excitons and impurities, the temperature of the sample, spatial and temporal fluctuations, polarization of the laser, etc. As a consequence, even in the case of two-photon absorption, the experimental data for the same material at a given wavelength may vary by as much as four orders of magnitude[6-8], and the absolute numerical agreement between theory and experiment only useful as an indication of trends or approaches to agreement. These large discrepancies point to the need for improved calculations that treat more rigorously the effect of the radiation on the crystalline electron wavefunction, as well as the effects of impurities and

excitons on the absorption process. Such calculations should also employ more realistic energy band structures such as those obtained from empirical pseudopotential matter, orthogonalized plane-wave matter, augmented plane-wave matter, etc. On the experimental side the laser and crystal parameters which affect the multiphoton absorption processes should be systematically studied and controlled, i.e., one needs ideal experiments to benchmark the various theoretical estimates or barring that, parametric trends which would point the way toward appropriate theoretical description. It will be a long time before we have in hand an experimental measurement yielding a very high degree of absolute accuracy in the measurement of a multiphoton absorption coefficient due not only to the changes introduced by the passage of the intense laser beam in the sample (particularly in the focal region on such a generally short temporal basis), but as well because of the lack of an intrinsic material.

Conclusion

There seems to be at least qualitative agreement between theory and experiment, that at sufficiently high intensities, there is a reversal of dominance as a function of photon multiplicity which could be explained by the Jones-Reiss mechanism.

If the increase in the effective band gap with increasing intensity is a true physical phenomenon, then it should be taken into account in all theoretical and experimental studies of high power laser-matter interaction. For example, in multiphoton absorption (MPA) experiments, the increased band gap could significantly decrease the absorption at high intensities. This could explain, in part, the large disparities among the reported experimental values of the MPA coefficients of a given solid at a given laser frequency[6]. Also at high intensities the dynamic Franz-Keldysh effect could result in a 'blue shift' of the absorption spectrum, opposite to the well known red shift resulting from the static Franz-Keldysh effect[9]. Further experimental and theoretical work in this area is definitely in order.

Acknowledgement

This research was supported in part by Contract No. F33615-79-C-5129 of the Materials Laboratory, Air Force Wright Aeronautical Laboratories, Wright Patterson Air Force Base, OH 45433. The first author (A.V.) was a National Research Council Postdoctoral Resident Research Associate at the Air Force Weapons Laboratory, Kirtland Air Force Base, New Mexico 87117 when this research was initiated.

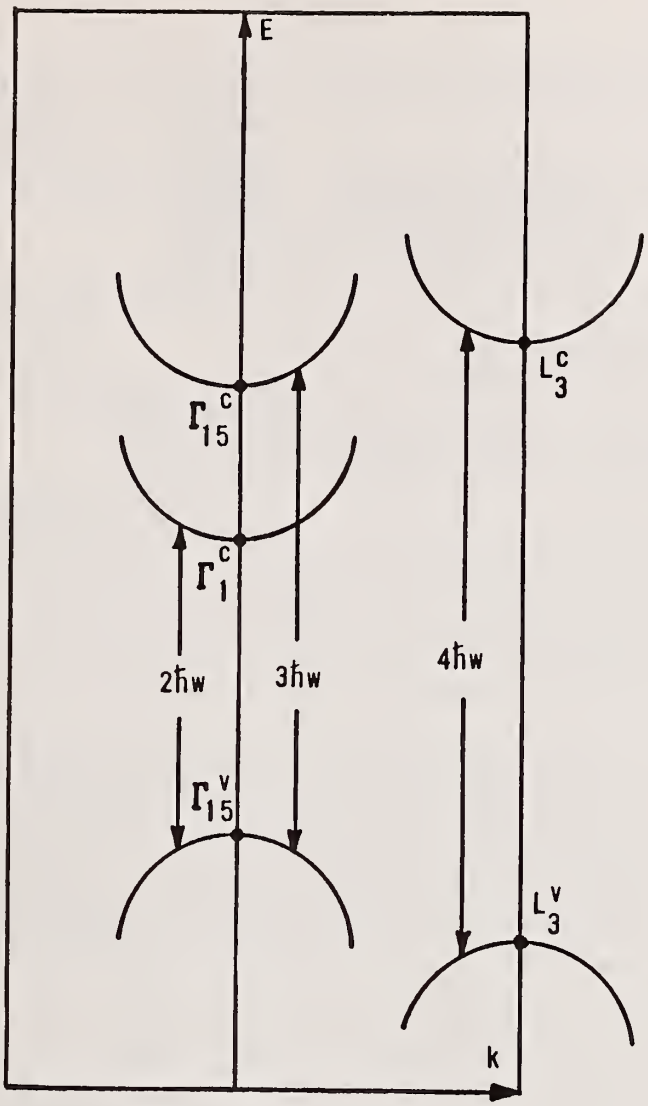

Figure 1. Schematic of the band structure of GaP, showing the direct interband transitions resulting from the simultaneous absorption of two, three and four photons of ruby light ($\hbar\omega$ = 1.79 eV).

References

1. H. D. Jones and H. R. Reiss, Phys. Rev. B 16, 2466 (1977).

2. See, for example, R. Loudon, Proc. Phys. Soc. 80, 952 (1962), and the references therein; R. Pantell, F. Pradere, J. Hanus, M. Schott and H. Puthoff, J. Chem Phys. 46, 3507 (1967).

3. D. M. Volkov, Z. Phys. 94, 250 (1935).

4. L. V. Keldysh, Zh. Eksp, Teor. Fiz. 47, 1945 (1964) (Sov. Phys. JETP 20, 1307 (1965)).

5. S. L. Pyshkin, N. A. Ferdman, S. I. Radautsan, V. A. Kovarskii, and E. V. Vitiu, Optoelectronics 2, 245 (1970).

6. See, for example, A. Vaidyanathan, T. W. Walker, A. H. Guenther, S. S. Mitra, and L. M. Narducci, Phys. Rev. B 21, 743 (1980), and the references therein. Also A. Vaidyanathan, A. H. Guenther, and S. S. Mitra, Phys. Rev. B 22, 6480 (1980).

7. B. Bosacchi, J. S. Bessey, and F. C. Jain, J. Appl. Phys. 49, 4609 (1978).

8. A. F. Gibson, C. B. Hatch P. N. D. Maggs, D. R. Tilley, and A. C. Walker, J. Phys. C 9, 3259 (1976).

9. W. Franz, Z. Naturforsch 13a, 484 (1958); L. V. Keldysh, Zh. Eksp. Teor. Fiz. 34, 1138 (1958) (Sov Phys. JETP 34, 788 (1958)).

Based on the model presented, wouldn't one expect that as the band gap increases from the two-photon process the joint density of states for that process would decrease and one should see a decrease in absorption coefficient as the power goes up until the threshold for two-photon absorption is reached? The speaker replied that the absorption coefficient is indeed predicted to decrease with increasing intensity. The questioner then suggested that experiments indicate that the total absorption goes up, not down, with increasing intensity and suggested that the discrepancy may be caused by the generation of free carriers.

It was also asked how the coefficients could be functions of intensity since they are themselves coefficients in a Taylor expansion of the absorption as a function of intensity. Wouldn't it be better to say that higher order terms appear? The speaker replied that the intensity dependence of the coefficients occurs because the energy gap increases, not because of higher order multiphoton processes. If the energy gap were constant, the coefficient would be constant.

The use of a low power probe laser was suggested to check the energy gap shift. The speaker did not think the effect would be detectable with a probe laser. It was also suggested that similar theoretical work, but on gases, had been done by Cohen and Tenuchi on resonant absorption. The speaker was not familiar with this work. It was also suggested that the experimental work cited in this theoretical paper be looked at closely since probably as laser pulse built up one would go from two-photon to three-photon absorption. A temporally square wave pulse is difficult to achieve.

Effects of Higher Order Nonlinearities on Second Order Frequency Mixing

by

Donald J. Harter
Institute of Optics
University of Rochester
Rochester, New York 14627

and

David C. Brown*
Laboratory for Laser Energetics
University of Rochester
Rochester, New York 14623

The theory which has been developed to study the effects of higher order nonlinearities in second-order frequency mixing can be applied to the case of up-conversion of high powered lasers. We have considered the effect of the intensity dependence of the refractive index upon phase-matching for second-order frequency mixing. We have also considered the effects of second-order generation on higher-order nonlinearities which have to be considered in the design of other components of high power lasers. This includes the effect of second-order frequency generation on small-scale self-focusing and on the whole beam phase profile.

Key Words: nonlinear optics; phase-matching; second order frequency mixing; self-focusing

*On assignment from Standard Oil of Ohio Research Laboratories, Warrensville, Ohio.

The theory describing second-order frequency conversion has been known for some time (1) and has been generalized here to include higher-order nonlinearities. We start with Maxwell's equations to obtain the Helmholtz equation given by;

$$\frac{\partial^2 \tilde{\underline{E}}_j}{\partial z^2} + \frac{\omega_j^2}{c^2}\,\tilde{\underline{E}}_j = \frac{4\pi\omega_j^2}{c^2}\,\tilde{\underline{P}}_j \tag{1}$$

The induced polarization at frequency ω_1 is;

$$\begin{aligned}\tilde{P}_1 = {} & \frac{1}{2}\,\hat{a}_1 \cdot \chi^{(1)}(\omega_1,\omega_1)\varepsilon_1 e^{-i\omega_1 t} + \frac{1}{2}\,\hat{a}_1\,\chi^{(2)}(\omega_1,-\omega_2,\omega_3);\ \hat{a}_2^*\,\hat{a}_3\varepsilon_3\varepsilon_2^* e^{-i\omega_1 t} \\ & + \frac{3}{8}\,\hat{a}_1 \cdot \chi^{(3)}(\omega_1,\omega_1,-\omega_1,\omega_1);\hat{a}_1^*\,\hat{a}_1\,\hat{a}_1|\varepsilon_1|^2\varepsilon_1 e^{-i\omega_1 t} \\ & + \frac{3}{4}\,\hat{a}_1 \cdot \chi^{(3)}(\omega_1,-\omega_2,\omega_2,\omega_1);\hat{a}_2\,\hat{a}_2^*\,\hat{a}_1|\varepsilon_2|^2\varepsilon_1 e^{-i\omega_1 t} \\ & + \frac{3}{4}\,\hat{a}_1 \cdot \chi^{(3)}(\omega_1,-\omega_3,\omega_3,\omega_1);\hat{a}_3\,\hat{a}_3^*\,\hat{a}_1|\varepsilon_3|^2\varepsilon_1\, e^{-i\omega_1 t},\end{aligned} \tag{2}$$

where

$$\omega_3 = \omega_1 + \omega_2\ ,$$

and the total electric field is,

$$\underline{E} = \frac{1}{2}\left(\hat{a}_1(z)\,\varepsilon_1 e^{-i\omega_1 t} + \hat{a}_2(z)\,\varepsilon_2\, e^{-i\omega_2 t} + a_3(z)\,\varepsilon_3\, e^{-i\omega_3 t}\right) + \text{c.c.} \tag{3}$$

In the equation for the polarization eq (2) $\chi^{(1)}$ is the linear susceptibility which describes linear absorption and dispersion. The second-order susceptibility $\chi^{(2)}$ is responsible for frequency mixing while the third-order susceptibility $\chi^{(3)}$ involves the intensity dependence of the dispersion and two-photon absorption in this example. The first of the third-order terms in equation 2, $\chi^{(3)}(\omega_1,\omega_1,-\omega_1,\omega_1)$ describes self-phase modulation while $\chi^{(3)}(\omega_1,\omega_3,-\omega_3,\omega_1)$ and $\chi^{(3)}(\omega_1,\omega_2,-\omega_2\omega_1)$ are terms which describe phase-modulation due to the intensity of the waves at different frequencies. The induced polarization at frequencies ω_1,ω_2 and ω_3 can be applied in the Helmholtz equation to obtain coupled amplitude and phase equations for the electric fields. Since the general equations are quite lengthy[1] the equations for a simpler example will be written. Thus the coupled amplitude and the phase equations for second-harmonic generation where absorption is neglible are;

$$\frac{d\rho_1}{dz} = \pi k_1 \eta_1^2 \rho_1 \rho_3 \sin\theta \quad , \tag{4a}$$

$$\frac{d\rho_3}{dz} = -\pi k_3 \eta_3^2 \rho_1^2 \sin\theta \quad , \tag{4b}$$

$$\frac{d\theta}{dz} = \Delta k + \pi\Big\{2k_1\eta_1^1 - k_3\eta_3^1 + \left(2k_1\eta_1^2\rho_3 - k_3\eta_3^2\frac{\rho_1^2}{\rho_3}\right)\cos\theta$$

$$+ \frac{3}{4}\left(\rho_1^2(k_1\eta_{11}^3 - 4k_2\eta_{31}^3) + \rho_3^2(4k_1\eta_{13}^3 - k_2\eta_{33}^3)\right)\Big\}, \tag{4c}$$

where $\Delta k = k_3 - 2k_1$ and the amplitude and phase are defined by,

$$1/2\;\hat{a}_1(z)\,\varepsilon_j = \tilde{\rho}_j(z,\omega_j)\,e^{i(k_j z + \phi_j)} \tag{5}$$

and where θ is the phase variation between the fields defined by;

$$\theta = 2\phi_1 - \phi_3 + (k_3 - 2k_1)z \quad , \tag{6}$$

and where

$$k_i = \omega_1/c \quad ,$$

and the η's are the real parts of the susceptibilities where;

$$\hat{a}_j \cdot \chi^{(1)}(\omega_j,\omega_j) = i\alpha_j^1 + \eta_j^1 \quad , \tag{7a}$$

$$\hat{a}_j \cdot \chi^{(2)}(\omega_j, \omega_k, \pm\omega_\ell);\ \hat{a}_k\ \hat{a}_l(*) = i\,\alpha_j^2 + \eta_j^2 \quad , \tag{7b}$$

$$a_j \cdot \chi^{(3)}(\omega_j, \omega_k, -\omega_k, \omega_j); \hat{a}_k\ \hat{a}_k^*\ \hat{a}_j = i\,\alpha_{jk}^3 + \eta_{jk}^3 \quad . \tag{7c}$$

It is apparent from equations 4 (a-c) that if the relative phases of the waves is $\pi/2$ for maximum coupling at the beginning of the process, then as the amplitudes of the waves change with conversion, the relative phase will change as is described in equation 4c and will become less than optimum. Because of details in the analysis, equations 4 (a-c) can be solved only if the values of the η's are known. In spite of the loss of phase-matching due to the intensity dependence of the refractive index, it may be possible to obtain complete conversion by varying Δk in equation 4c but this cannot be determined without knowing the values of the η's. The variation of the phase front caused by propagating through the nonlinear medium can be obtained by integrating equation 4 (c) across the intensity profile of the beam.

Small-Scale Self-Focusing

The growth of off-axis waves at the same frequency as the strong pump wave has been described previously as non-degenerate four-wave [2] mixing and as the process leading to small-scale self-focusing [3]. The phase-matching geometry is illustrated in figure 1. It should be noted that off-axis weak waves can be phase-matched to collinear strong pump waves at the same frequency since the refractive index for weak waves in the presence of a strong pump wave is greater than the refractive index for the strong pump wave [2]. For an electric field with weak waves at frequency (ω_1):

$$\vec{E} = \tfrac{1}{2}\left((\hat{a}_1\varepsilon_1 + \hat{a}_1'(\Delta\varepsilon_{11} + \Delta\varepsilon_{12}))e^{-i\omega_1 t} + \hat{a}_2\varepsilon_2 e^{-i\omega_2 t} + \hat{a}_3\varepsilon_3 e^{-i\omega_3 t} + \text{c.c.}\right) \quad . \tag{8}$$

the induced polarization for the weak off-axis wave, $\Delta\varepsilon_{11}$, is:

$$\begin{aligned} P(\omega_1) = {} & 1/2\hat{a}_1' \cdot \chi^1(\omega_1;\omega_1)\Delta\varepsilon_{11}e^{-i\omega_1 t} + 1/2\hat{a}_1' \cdot \chi^2(\omega_1;-\omega_2,\omega_3);\hat{a}_2^*\hat{a}_3\varepsilon_2^*\varepsilon_3\ e^{-i\omega_1 t} \\ & + 3/4\hat{a}_1' \cdot \chi^3(\omega_1;\ \omega_1,-\omega_1,\omega_1)\vdots\hat{a}_1\hat{a}_1^*\hat{a}_1'|\varepsilon_1|^2\Delta\varepsilon_{11}e^{-i\omega_1 t} \\ & + 3/8\hat{a}_1' \cdot \chi^3(\omega_1;\omega_1,-\omega_1,\omega_1)\vdots\hat{a}_1\hat{a}_1\hat{a}_1'^*\varepsilon_1^2\Delta\varepsilon_{12}^*e^{-i\omega_1 t} \\ & + 3/4\hat{a}_1' \cdot \chi^3(\omega_1;-\omega_2,\omega_2,\omega_1)\vdots\hat{a}_2\hat{a}_2\hat{a}_1'|\varepsilon_2|^2\Delta\varepsilon_{11}e^{-i\omega_1 t} \\ & + 3/4\hat{a}_1' \cdot \chi^3(\omega_1;-\omega_3,\omega_3,\omega_1)\vdots\hat{a}_3\hat{a}_3\hat{a}_1'|\varepsilon_3|^2\Delta\varepsilon_{11}e^{-i\omega_1 t} + \text{c.c.} \end{aligned} \tag{9}$$

This polarization can be applied to the Helmholtz equation along with a similar equation for $\Delta\varepsilon_{12}$ and the polarization at ω_2 and ω_3 to obtain coupled wave equations for the amplitudes $\Delta\rho_{11}$, $\Delta\rho_{12}$ for these weak waves. The general equations are again quite lengthy and simplifications will be made for our example.[2] Absorption is ignored, phase-matching of both the second-harmonic and

four-wave mixing is assumed perfect and the initial values of the amplitude of the weak waves are equal. These assumptions are not unreasonable as will be seen in what follows. Thus, the coupled amplitude equations for the electronic field $\Delta\varepsilon_{11}$ and $\Delta\varepsilon_{12}$ can be solved analytically to give:

$$\Delta\rho_{11}(z)=\Delta\rho_{11}(0)\exp(\kappa_t z) \tag{10a}$$

where

$$\kappa_t = 3/4(\eta_1^2\rho_3 + \eta_{11}^3\rho_1^2 \sin\gamma)/\cos\psi \tag{10b}$$

The first term in equation 10b is the weak wave gain for second-harmonic generation and the second term is the growth of weak off-axis waves, by means of degenerate four-wave mixing. If in equation 10b the second-harmonic gain is ignored, the gain term is the same as the gain predicted by the Bespalov-Talanov [3] theory for small-scale filament growth. Thus the gain for phase-matched degenerate four-wave mixing is the same as that predicted for the gain of small-scale self-focusing without second-harmonic generation. The gain of small-scale self-focusing is substantially greater due to weak-wave gain for second-harmonic generation. The direct coupling of second harmonic generation to off-axis waves is illustrated in figure 2. Figure 2a illustrates phase-matched second-harmonic generation. Figure 2b illustrates phase-matched degenerate four-wave mixing for off-axis weak waves. From figure 2a and b, it follows that the wave in figure 2c are phase-matched.

Conclusion

In this report, the effects of higher order terms on second-order frequency conversion is applied to the case of up-conversion of high-powered lasers. It is shown that:

The optimum phase-matching is a function of intensity and that the conversion efficiency may be lowered at higher intensities. However, complete analysis depends on the knowledge of the values of the self-induced intensity variation of the refractive index for each frequency present and the intensity variation of the refractive index at one frequency due to the intensity at another frequency.

The change in the phase front from traversing the non-linear medium can be obtained by integrating equation 4c with respect to z and as a function of the beam intensity profile.

The gain for self-focusing consists of two terms, one which is similar to the gain without second-order frequency mixing and the other is the weak signal gain of the second-order frequency process. The gain for self-focusing is much greater in this nonlinear medium than in a media with the same third-order nonlinear susceptibilities. However, knowledge of the values of the nonlinear susceptibilities is necessary to analyize the competition between second-order frequncy generation and self-focusing.

References

[1] D.J. Harter, and D.C. Brown, IEEE J. Quantum Electron (to be published).

[2] J.A. Armstrong, N. Bloembergen, J. Ducuing, and P.S. Pershan, Phys. Rev. 127, 1918 (1962).

[3] R.Y. Chiao, P.L. Kelley, E. Garmire, Phys. Rev. Lett. 17, 1158 (1966).

[4] V.I. Bespalov and V.I. Talanov, JETP Lett. 3, 307 (1966).

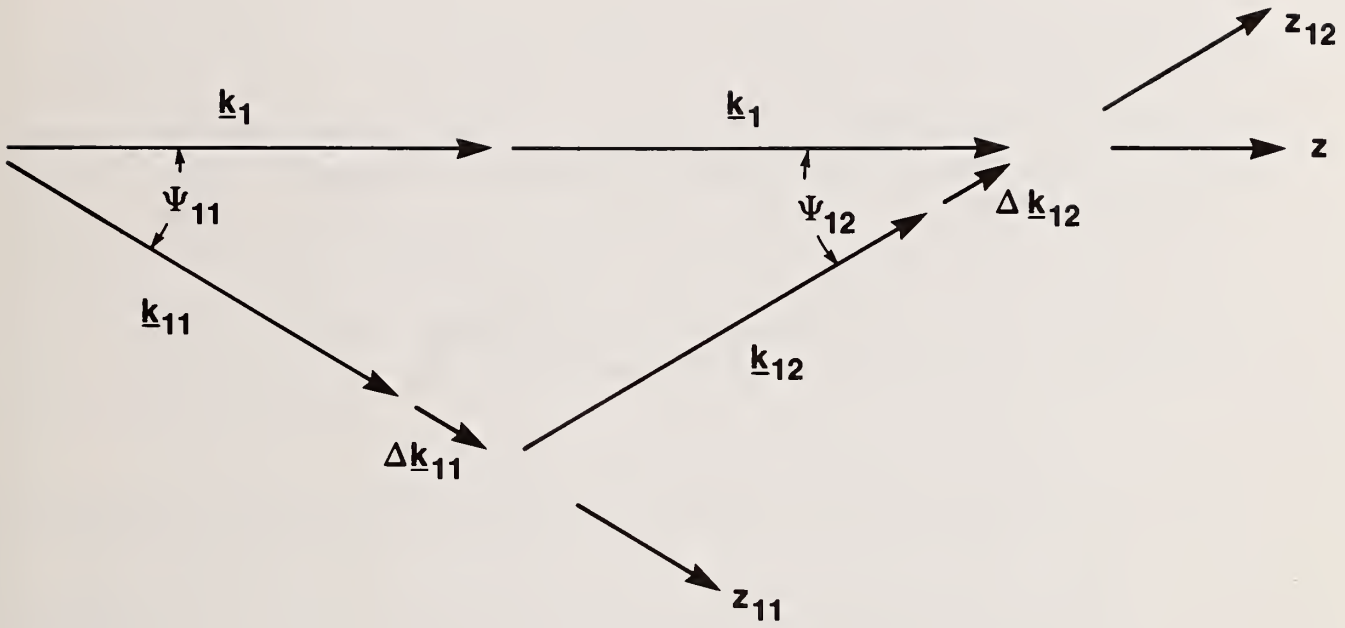

S255

Figure 1

Phase-matching conditions are shown for the four-wave mixing of two weak-fields, $\Delta\varepsilon_{11}$ and $\Delta\varepsilon_{12}$, with the pump field ε_1. The wave vectors are $\underline{k}_{11}$, $\underline{k}_{12}$, and $\underline{k}_1$ and the directions of propagation for the fields are z_{11}, z_{12}, and z_1 respectively.

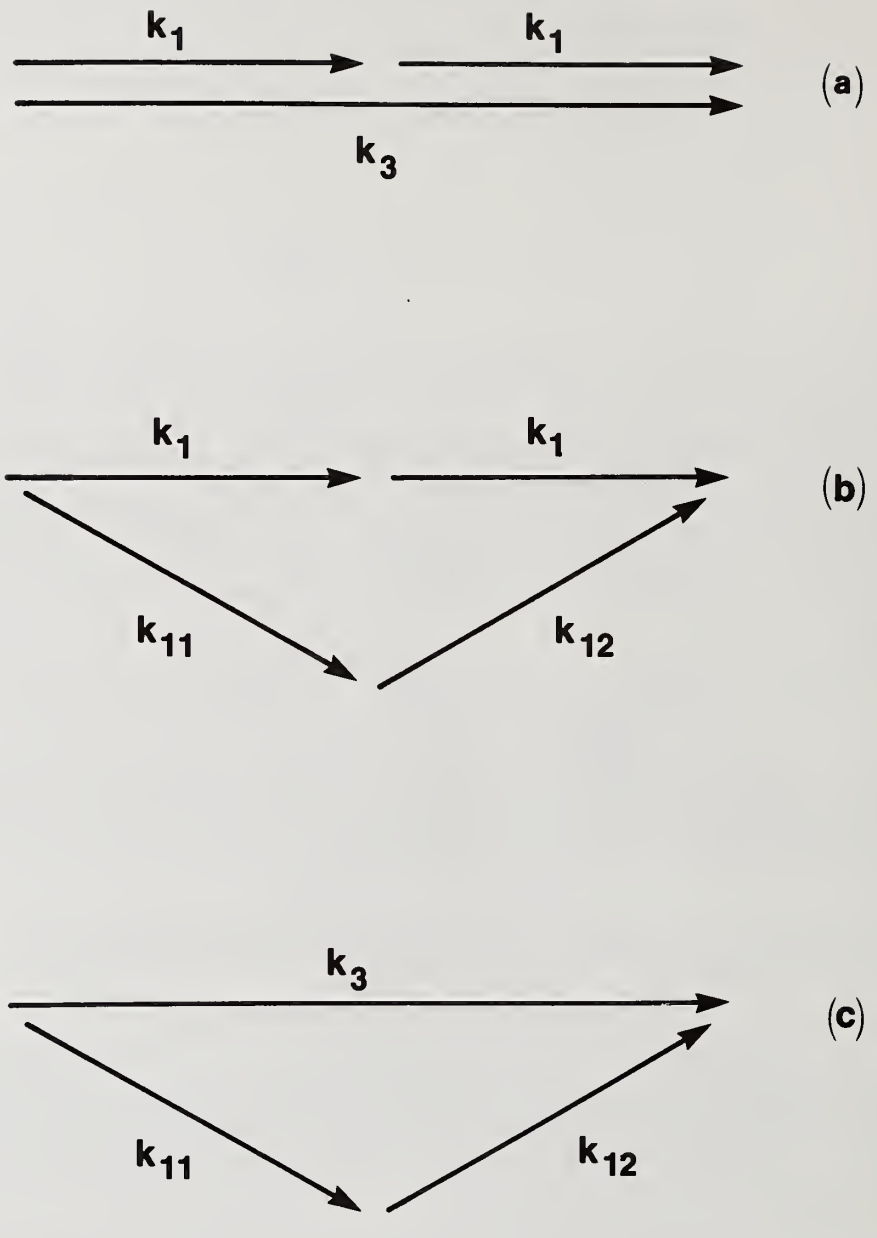

Figure 2

A series of simultaneous phase-matched second-harmonic and four-wave mixing processes are present in colinear, strong-field, second-harmonic generation (a). The strong field, ε_1, is coupled to off-axis weak-fields, $\Delta\varepsilon_{11}$ and $\Delta\varepsilon_{12}$, all with the same frequency, ω_1, (b). From (a) and (b) it follows that these weak fields are also phase-matched with the strong field ε_3(c).

THE USE OF SELF-FOCUSING IN THE PREVENTION OF LASER-INDUCED DAMAGE

M. J. Soileau, William E. Williams,
Eric W. Van Stryland, and Stephen F. Brown

Center for Applied Quantum Electronics
Department of Physics, North Texas State University
Denton, Texas 76203

Laser-induced breakdown in thin foils and gasses have been used to limit transmission at high laser powers in order to prevent damage to sensitive optical components in complex laser systems. In this paper we report results of using self-focusing in liquids to produce laser-induced breakdown and phase aberrations which in turn limit the transmitted power. Optical self-action in CS_2 and other liquids was used to make a power limiting device with psec response time. This device has linear response near unity transmission for input power below P_c, which is of the order of the critical power for self-focusing, and limits the transmitted power to a nearly constant value for input power greater than P_c. The onset of nonlinear transmission was adjusted by mixing various liquids to adjust n_2. Experimental results using linearly and circularly polarized, 40 psec (FWHM) pulses at 1.06 μm are presented.

Key words: self-focusing; laser-induced breakdown; nonlinear absorption; nonlinear refraction; Kerr liquids.

1. Introduction

Laser-induced breakdown and self-focusing are usually associated with catroscophic damage to optical components. In this paper we describe a technique by which these phenomena can be used in the prevention of laser-induced damage. The basic concept is to use intensity dependent refraction (self-focusing) and intensity dependent absorption (associated with laser-induced breakdown) to make a passive optical device which has high transmission for low input power but low transmission for high input power. Such a device can be considered an optical power limiter or a nonlinear optical switch. Our results show that a device with psec response time can be made. Possible uses of this device include the protection of detectors used to study pre-lasing in large oscillator-amplifier laser systems and to optically isolate sensitive oscillator components from back propagating high power beams from amplifier sections.

2. Passive, Nonlinear Power Limiter Concept

Figure 1 is a schematic of the device which we call a nonlinear power limiter (NPL). The solid lines trace the input beam for low input power. The beam is focused by lens L_1 into a material with high nonlinear refractive index, n_2. For low input powers the light is imaged by lens L_2 through a

pinhole onto detector D_4. As the input power is increased to approximately P_2, the critical power for self-focusing, [1] the beam undergoes severe phase abberations, (i.e., nonlinear refraction), and consequently the waist from lens L_1 is no longer in the proper location to be reimaged by L_2 onto detector D_4. The high power situation is shown schematically by the dotted lines.

The NPL shown in figure 1 has been previously demonstrated using nsec pulses at 1.06 μm with CS_2 as the nonlinear medium [2] and is similar to the arrangement used by Bjorkholm et al. [3] to make a passive bystable device. In this work we demonstrated the power limiting feature of this concept for psec pulses at 1.06 μm. Various nonlinear media were investigated including CS_2, nitrobenzene and mixtures of these liquids in ethanol. The laser source used in this work was a mode-locked Nd:YAG laser operated at 1.06 μm with Gaussian spatial and temporal profiles. The single pulse energy was variable up to approximately 10 mJ. The temporal puslewidth was variable from 40 psec to 300 psec, however, all data presented in this paper corresponds to pulsewidths of 40 psec (FWHM). The laser system and associated diagnostic equipment is described in greater detail in Ref. [4].

Figure 2 shows the power limiting capability of the NPL using CS_2 as the nonlinear medium and linearly polarized light. Note that the output of the device (D_4) is effectively clamped, even for the maximum input of approximately 4×10^6 W. The "step-function" like transmission for low input power is the region of linear response. The linear response for low input power and the onset of the nonlinear response are shown more clearly in figure 3 in which the horizontal scale (input power) has been expanded. Note that the device transmission is linear for input power lower than approximately 26 kW and is clamped for higher input powers. CS_2 is highly transparent at 1.06 μm so with the exception of Fresnel reflection losses (which can be avoided with antireflection coating) the device transmitts all the incident power until the cutoff power is reached.

3. Power Limiting Mechanisms

The mechanisms for the limiting action shown in figures 2 and 3 were investigated by measurement of the threshold for nonlinear transmission (P_c) as a function of n_2 (nonlinear refractive index), the f/no. of lens L_1 and of the polarization of the incident laser radiation. These masurements were conducted with and without the limiting aperature in front of detector D_4. The results of these measurements indicate that the mechanisms which limit the transmission of the NPL are intensity dependent refraction (self-focusing) and intensity dependent absorption associated with laser-induced breakdown (initiated by self-focusing).

Analysis of the data shown in figure 3 and two additional experiments under identical conditions indicate that the critical power for the onset of nonlinear transmission (P_c) is 26 ± 3 kW for CS_2. The data points shown in figure 3 and the other plots in this paper are the averages of the reading on detector D_4 for 5 laser shots. P_c was determined by monitoring the ratio the reading on D_4 to the input power. The standard deviation of this ratio for a group of 5 shots was relatively small for powers significantly above or below P_c. The standard deviation of this ratio increased by as much as an order of magnitude at P_c. Thus, monitoring the standard deviation in the ratio of the reading on detector D_4 to the input power was a sensitive and reliable method of determining P_c.

Marburger [1] has solved the nonlinear wave equation for the case of a focused Gaussian beam. The least critical power for a self-trapped mode is $P_{c1} = 3.72\ P_1$ where

$$P_1 = \frac{c\lambda^2}{32\pi^2 n_2}$$ and where n_2 = nonlinear index of refraction, λ = laser wavelength, c = speed of light

The beam will self-focus for powers greater than a critical power P_2 which is slightly higher than P_{c1} but is taken to be equal to P_{c1} for Gaussian beams [1]. Assuming that our measured value of P_c corresponds to P_2 we then calculate n_2 for CS_2 at 1.06 μm to be $1.5 \pm 0.3 \times 10^{-11}$ esu. The $\pm 0.3 \times 10^{-11}$ esu total uncertainty includes the ±15% absolute uncertainty in the power measurement and the ±13% relative uncertainty in P_c. The total uncertainty is calculated assuming the absolute errors in power measurement and relative error in determining P_c are uncorrelated. This value of n_2 is in excellent agreement with the value of $1.3 \pm 0.3 \times 10^{-11}$ esu for CS_2 at 1.06 μm deduced from direct interferometric measurements by Witte et al. [5] at 1.32 μm using 700 psec pulses.

The measurements by Witte et al. [5] are the only known direct measurement of n_2 in CS_2 at optical frequencies. Moran et al. [6] inferred a value of $1.10 \pm 0.33 \times 10^{-11}$ esu for CS_2 at 1.06 μm by comparing their direct measurement of n_2 for ED-2 glass with independent measurements of n_2 for ED-2 glass by Bliss et al. [7] and relative measurements of n_2 for ED-2 glass and CS_2 by Owyoung [8]. Shen [9] and Owyoung [8] used the d.c. Kerr constant for CS_2 to calculate n_2 for CS_2 at 0.67 μm and 0.694 μm. When extrapolated to 1.06 μm Shen and Owyoung's values give n_2 at 1.06 μm of 2×10^{-11} esu and 2.55×10^{-11} esu respectively.

The n_2 value for CS_2 at 1.06 μm deduced from the measurements of P_c in this work and the n_2 values determined by direct interferometric measurements have overlapping error bars and are therefore in reasonable agreement. However, there are several tests for self-focusing which do not depend on knowing the absolute value of n_2 and are independent of absolute errors in the input power measurements. In the paragraphs that follow we describe the results of several of these tests which confirm that self-focusing was the primary mechanism for the limiting action shown in Figs. 2 and 3.

Self-focusing theory [1] predicts that $P_2 \sim 1/n_2$. Prior work [10] has shown that one can vary n_2 by mixing CS_2 with ethanol (which has a very low n_2). A 50-50 mixture of CS_2 and ethanol has an n_2 equal to approximately one-half that of neat CS_2. Therefore for self-focusing in a 50-50 mixture one would expect that the onset of the power limiting would occur at a power approximately twice as high as required for neat CS_2. The data shown in figure 4 for this mixture indicates that the onset of limiting occurs at approximately 58 ± 7 kW which is in good agreement with the predictions of self-focusing theory. Note that this result means that one can adjust the output of the NPL by simply mixing a high n_2 material with a low n_2 material to adjust P_2 to the desired level.

The data shown in Figs. 2 to 4 were taken using a 37 mm focal length lens (L_1) used at f/7.9 to focus the light into the nonlinear medium. A critical test for self-focusing is to vary the focal length of L_1. The onset of self-focusing is dependent on the power rather than the input intensity and thus the onset of nonlinear transmission will be independent of the focal length of L_1 if self-focusing is the critical mechanism. Figure 5 is a plot of D_4 versus input power with the 37 mm focal lengths lens replaced by a 75 mm focal length lens (used at f/16). The cutoff power is approximately the same as that shown in figure 3 (26 ± 3 kW). An intensity dependent process would have required a factor of four increase in input power and one can see from figures 3 and 5 that the critical power is independent of the focal lengths of lens L_1 within the experimental uncertainty.

The relatively large n_2 values for materials such as CS_2 and nitrobenzene are due to the orientational dependence of the linear refractive index of these molecules. Thus, the self-focusing observed in these materials is due to optically induced ordering of the molecules, i.e., the AC Kerr effect. Therefore, self-focusing in these materials should be critically dependent on the polarization of the incident light. Figure 6 is a plot of D_4 versus P for circularly polarized light. P_c, the cutoff power for linear polarized light, is approximately 26 ± 3 kW while that for circularly polarized light, P_{cc} is approximately 47 ± 4 kW. Figure 7 is a plot of D_4 versus P for the 50-50 mixture of CS_2 and ethanol using circularly polarized light. For this case P_{cc} = 125 ± 10 kW as compared to 58 ± 7 kW for linear polarization and the same mixture. Similar measurements in neat nitrobenzene yielded P_c = 72 ± 7 kW and P_{cc} = 133 ± 13 for linear and circular polarization respectively. The average ratio of P_{cc} to P_c for the various measurements was 1.9 ± 0.2. This compares favorably with the value of 2.0 found by Close et al. [11] and Wang [12] for the ratio of the critical power for self-focusing in CS_2 using completely different techniques and nanosecond ruby laser pulses (λ = 0.694 μm). However, theoretical calculations by Shen [9] predicts that the ratio of n_2 for circular polarization to the n_2 for linear polarization should be 4 for self-focusing which is due to molecular reorientation. The approximate factor of 2 difference between the measured ratio in this work and Refs. 11 and 12 and the theoretical value is not understood at this time. Feldman et al. [13] measured a ratio of approximately 1.1 to 1.3 for various solids for which electrostriction and electronic self-focusing are thought to be important. Hellwarth [14] and Wang [12] have pointed out that the circular to linear polarization ratio should be related to the ratios of the various components of $\chi^{(3)}$, the third-order optical susceptibility. While there is considerable debate in the literature as to what the exact ratio of n_2 for circular and linear polarization should be there is agreement that n_2 for circular polarization is less than that for linear polarization.

The dependence of P_c on n_2, the beam polarization and the focal length of lens L_1 are all consistent with the idea that the observed nonlinear transmission is due to the onset of self-focusing. Additionally we observed bright "streamers" of flashes (due to laser-induced breakdown) for input power substantially above P_c which suggests self-trapping or a moving self-focus position. These "streamers" are evidence that self-focusing is the mechanism for the self-limiting action of the NPL, however, they also suggest that the observed limiting behavior may be due to the nonlinear absorption in the laser induced plasma (initiated by self-focusing). The effects of laser-induced breakdown were investigated by removing the pinhole in front of the detector (D_4 in fig. 1) so that all the light transmitted through the cell was intercepted by the detector. The results are shown in figure 8.

The results shown in figure 8 indicate that nonlinear absorption is taking place, however, the onset of the nonlinear absorption is associated with the same input power as observed in figure 3. The test previously described for self-focusing were repeated without the pinhole in place and the onset of nonlinear behavior varied as predicted by self-focusing theory. We conclude that the observed clamping of the output of the NPL is due to both nonlinear refraction and nonlinear absorption and that both mechanisms are associated with self-focusing.

The above results indicate that P_c, the critical power for the onset of nonlinear transmission, has the polarization, focal length and n_2 dependence consistent with self-focusing. These experiments were repeated with neat ethanol and $CC\ell_4$ substituted for the high n_2 material. Figures 9 and 10 are the results for ethanol using the 75 mm focal length lens for L_1 for linear and circular polarization respectively. Figure 11 is a similar plot for $CC\ell_4$ for linear polarization. Table 1 summarizes the resulting P_c's for this material and the other materials tested. The ratio of P_c for the 37 mm and 75

mm focal length lenses is 4.1 ± 0.4 whereas the square of the focal lengths of the lenses is 4.11. Therefore, the onset of nonlinear behavior is intensity dependent instead of power dependent as in the Kerr liquids. The data in table 1 indicate that the critical power for linear (P_c) and circular (P_{cc}) polarization are approximately equal for ethanol and $CC\ell_4$. The lack of polarization dependence of P_c and the dependence of P_c on the focal length of lens L_1 confirms that the nonlinear transmission in ethanol and $CC\ell_4$ is due to nonlinear absorption in the laser - induced plasma which accompanies dielectric breakdown in these materials. From table 1 we see that the ratios of P_c for CS_2 to P_c for ethanol and $CC\ell_4$ are approximately 0.020 and 0.063 respectively. Hellwarth et al. [15] determined that the ratio of the n_2 for CS_2 to that of $CC\ell_4$ is 56 ± 6 at 0.694 μm, indicating that P_c ($CC\ell_4$) = 56 P_c (CS_2). This implies that P_c ($CC\ell_4$) due to self-focusing should be approximately 1460 kW, which is more than a factor of 3.5 greater than the value required to induce breakdown in this material. The ratio of the optical Kerr constant for ethanol to that of CS_2 is 0.0064 [9] which implies that P_c (ethanol) due to self-focusing should be approximately 4060 kW, a factor of 3.1 greater than that required to induce breakdown. Thus, one would expect that self-focusing was not a factor in the observed nonlinear transmission of these two materials.

4. Pulsewidth Dependence of the NPL

The molecular reorientational relaxation time for CS_2 is approximately 2.1 psec [16] and therefore much shorter than the pulsewidth used in this work. P_c and P_{cc} for CS_2 are expected to be independent of pulsewidth for pulsewidths substantially longer than 2 psec. P_c for similar measurements in Ref. 10 at 1.06 μm with 9 nsec pulses was 14 ± 1 kW. More recent measurements [17] using the same laser system as in Ref. 10 resulted in P_c = 20 ± 3 kW which is in reasonable agreement with the 40 psec data reported here. The large discrepancy in the nsec data ia probably due to errors in power measurements in the earlier work (Ref. 10) due to unresolved partial mode-locking of the Q-switched pulse or a calibration error.

The ratio of P_c (nitrobenzene) to P_c (CS_2) from table 1 is 2.8 ± 0.4 and the corresponding ratio of P_{cc}'s is 2.7 ± 0.4. The ratio predicted by the optical Kerr constant [9] for these materials is 1.23 and the measured ratio for P_c for nsec pulses [10] is 1.8 ± 0.3. Since the molecular relaxation time for nitrobenzene is 44 psec [18] (the same order as the laser pulsewidth in this work) the contribution of molecular reorientation to the n_2 of nitrobenzene should be diminished. The ratio of n_2 for CS_2 to n_2^e, the nonlinear index of nitrobenzene due to electronic self-focusing, is 2.74. We conclude that the P_c and P_{cc} measured for nitrobenzene is primarily due to electronic self-focusing. Thus while P_c and P_{cc} for CS_2 are expected to be much smaller for subpicosecond pulses than the values reported here, the corresponding values for nitrobenzene are expected to be independent of pulsewidth for pulsewidths from 40 psec to the order of 10^{-14} sec. Limiting charactertistics for nitrobenzene for circular polarization and the 37 mm focal length lens are shown in Figs. 12 and 13.

5. Summary

We have demonstrated a device that can be used as a power limiter for the prevention of laser-induced damage. The mechanisms which limit the transmission of this device are intensity dependent refraction (self-focusing) and intensity dependent absorption associated with laser-induced breakdown (initiated by self-focusing). This device, which we call a nonlinear optical switch, has been shown to work for 1.06 μm pulses of 40 psec duration. The ultimate response time for this device is deter-

mined by the response time of the nonlinear medium, e.g., 2 psec for CS_2. A medium in which the dominant nonlinear refraction is electronic is expected to have a response time on the order of 10^{-14} seconds. The advantage of this power limiting technique include rapid response and recovery, completely passive operation, relatively low "turn off" power P_c (26 kW for CS_2) at 1.06 μm and P_c can be adjusted by varying n_2.

This work was supported by North Texas State University faculty research funds, The Robert A. Welch Foundation, the National Science Foundation, and the Office of Naval Research.

TABLE 1

Material	L_1 Focal Length P_c	Linear Polarization P_c in kW	Circular Polarization P_{cc} in kW
CS_2	37 mm	26 ± 3	50 ± 7
CS_2	75 mm	26 ± 3	43 ± 3
CS_2:Ethanol	37 mm	58 ± 7	125 ± 10
Nitrogenzene	37 mm	72 ± 7	133 ± 13
Ethanol	37 mm	350 ± 30	380 ± 20
Ethanol	75 mm	1300 ± 200	1700 ± 20
$CC\ell_4$	37 mm	410 ± 40	466 ± 40

Table 1. P_c and P_{cc} for various materials and focal lengths of lens L_1. Note that the average ratio of P_{cc} to P_c is 1.9 ± 0.2 for CS_2 and the Kerr liquids and 1.2 ± 0.1 for the ethanol and $CC\ell_4$. P_c and P_{cc} is independent of L_1 focal length for the Kerr liquids and scale as the ratio of the focal length squared for ethanol and $CC\ell_4$.

6. References

[1] J. H. Marburger, Progress of Quantum Electronics, J. H. Sanders and S. Stenholm, editors (Pergamon Press, 1977), pp. 35-110.

[2] M. J. Soileau, "Passive Intensity Limiter Based on Nonlinear Optics", Oct. 1980 Annual Meeting of the Optical Society of America, Chicago, IL, Abstract published in J. Opt. Soc. Am. 20 (8), 1051 (1980).

[3] J. E. Bjorkholm, P. W. Smith, and W. J. Tomlinson, "Optical Bistability Based on Self-focusing", Opt. Lett. 6, 345-347 (1981).

[4] E. W. Van Stryland, M. J. Soileau, Arthur L. Smirl, and William E. Williams, "Pulsewidth and Focal Volume Dependence of Laser-Induced Breakdown", Phys. Rev. B 23, 2144-2151 (1981).

[5] K. J. Witte, M. Galanti and R. Volk, "n_2-Measurements at 1.32 μm of Some Organic Compounds Usable as Solvents in a Saturable Absorber for an Atomic Iodine Laser", Opt. Comm, 34, 278-282 (1980).

[6] Michael J. Moran, Chiao-Yao She, and Robert L. Carman, "Interferometric Measurments of the Nonlinear Refractive-Index Coefficient Relative to CS_2 in Laser-System-Related Materials", IEEE J. Quan. Elect. QE-11, 259-263 (1975).

[7] E. S. Bliss, D. R. Speck and W. W. Simmons, "Direct Interferometric Measurements of the Nonlinear Index Coefficient n_2 in Laser Materials," Appl. Phys. Lett., Vol. 25, pp. 728-730 (1974).

[8] A. Owyoung, "Ellipse Rotation Studies in Host Materials," IEEE J. Quantum Electron. QE-9, 1064-1069, 1973.

[9] Y. R. Shen, "Electrostriction, Optical Kerr Effect and Self-Focusing of Laser Beams", Phys. Lett. 20, 378-380 (1966).

[10] M. J. Soileau, J. B. Franck, and T. C. Veatch, "On Self-Focusing and Spot Size Dependence of Laser-Induced Breakdown", in Laser-Induced Damage in Optical Materials, NBS Spec. Pub. No. 620, pp. 375-384 (1980).

[11] D. H. Close, C. R. Giuliano, R. W. Hellwarth, L. D. Hess, F. J. McClung, and W. G. Wagner, IEEE J. Quant. Electron. QE-2, 553 (1966).

[12] Charles C. Wang, "Nonlinear Susceptbibility Constant and Self-focusing of Optical Beams in Liquids", Phys. Rev. 152, 149-156 (1966).

[13] Albert Feldman, Deane Horowitz, and Roy M. Waxler, "Relative Contribution of Kerr Effect and Electrostriction to Self-Focusing", in Laser-Induced Damage in Optical Materials, NBS Spec. Pub. 372, pp. 92-99, 1972.

[14] R. W. Hellwarth, "Third-Order Optical Susceptibilities of Liquids and Solids", in Progress in Quantum Electornics, Vol. 5, pp. 1-68, Pergamon Press, NY, 1977.

[15] R. W. Hellwarth, Adelbert Owyoung, and Nicholas George, "Origin of the Nonlinear Refractive Index of Liquid $CC\ell_4$," Phys. Rev. A, 4, 2342-2347 (1971).

[16] E. P. Ippen and C. V. Shank, "Picosecond Response of a High-Repetition-Rate CS_2 Optical Kerr Gate", Appl. Phys. Letts. 26, 92-93 (1975).

[17] S. C. Seitel, M. J. Soileau, J. B. Frank, and D. G. Hargrove, 1980, unpublished.

[18] J. Etchepare, G. Grillion, R. Muller, and A. Orszag, "Kinetics of Optical Kerr Effect Induced by Picosecond Pulses", Opt. Cumm. 34, 269-272, (1980).

Figure Captions

Figure 1. Nonlinear Optical Switch (NPL) Concept. Lens L_1 was a single element lens of "best form" design. The input beam radius (to the $1/e^2$ points of irradiance) was 2.35 mm and the focal length of lens L_1 was 37 mm. L_1 was located so as to produce a focal spot in the middle of the nonlinear cell. L_2 was an 80 mm focal length microscope objective placed approximately 68 mm behind the 12 mm thick cell. This arrangement produced a focal spot of approximately 100 μm diameter which matched the 100 μm diameter aperature located 525 mm behind lens L_2.

Figure 2. Intensity Limiter Response. This is a plot of the results of measurements using CS_2 as the nonlinear medium (NL)in figure 1. The laser source was a Nd:YAG laser operating at 1.06 μm with puslewidth of 40 psec. The region of linear (the nearly vertical line on the extreme left of this graph) response is shown in more detail in figure 3.

Figure 3. The Onset of Nonlinear Transmission. This plot is for the same material (CS_2) and laser source as used for the data in figure 2. Here the horizontal scale has been expanded to show the region of linear response and the onset of nonlineaer transmission (P_c = 26 ± 3 kW). Each data point is an average of 5 shots. P_c was determined by monitoring the standard deviation in reading of detector D_4 in the raw data.

Figure 4. P_c for a 50-50 mixture of CS_2 and ethanol. These data are for linearly polarized light and a 50-50 mixture of CS_2 and ethanol. P_c = 58 ± 7 kW was determined from the increase in the standard deviation in the readings of detector D_4.

Figure 5. Nonlinear power limiter with the focal length of L_1 equal to 75 mm. The nonlinear medium was neat CS_2 and the incident radiation was linearly polarized. For this case P_c = 26 ± 3 kW as in the case where the L_1 focal length was 37 mm.

Figure 6. Nonlinear power limiter with circularly polarized light. These data are for CS_2 with circularly polarized light. L_1 focal length was 37 mm. The cutoff power was determined to be 47 ± 4 kW.

Figure 7. CS_2 - Ethanol, Circular Polarization. The focal length of L_1 was equal to 37 mm. In this case P_{cc} = 125 ± 10 kW.

Figure 8. Linear Polarization, CS_2, 37 mm, f.ℓ. for L_1. The aperature in front of D_4 was removed and the reading on D_4 was measured as a function of input power. Note that the change in slope occurs at P_c = 26 kW as in figure 3. The change in slope is due to nonlinear absorption in the laser-induced breakdown that results from the self-focusing.

Figure 9. Linear Polarization, Ethanol, 75 mm f.ℓ. for L_1.

Figure 10. Circular Polarization, Ethanol, 75 mm f.ℓ. for L_1.

Figure 11. Linear Polarization, $CCℓ_4$, 37 mm f.ℓ. for L_1. Note that nonlinear transmission begins at P_c = 410 kW but the transmission is not clamped as was the case for the Kerr liquids.

Figure 12. Circular polarization, nitrobenzene, 37 mm f.ℓ. for L.

Figure 13. Circular polarization, nitrobenzene, 37 mm f.ℓ. for L, expanded scale.

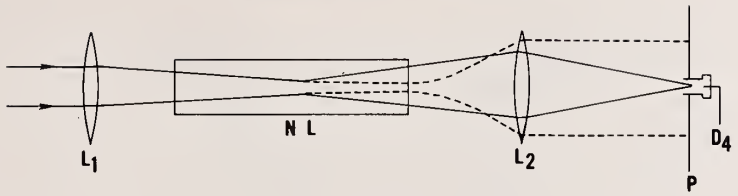

Figure 1

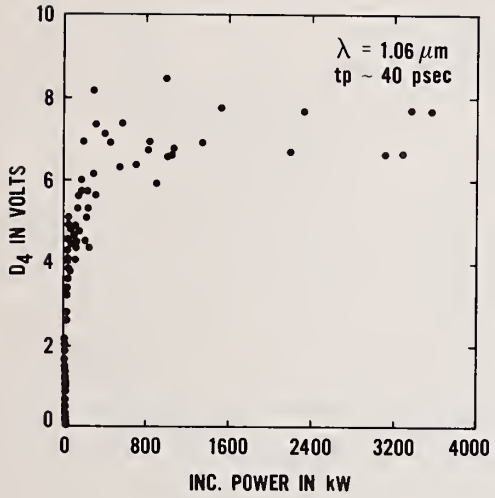

Figure 2

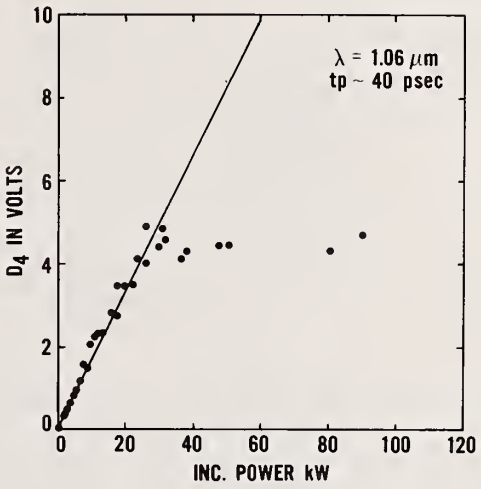

Figure 3

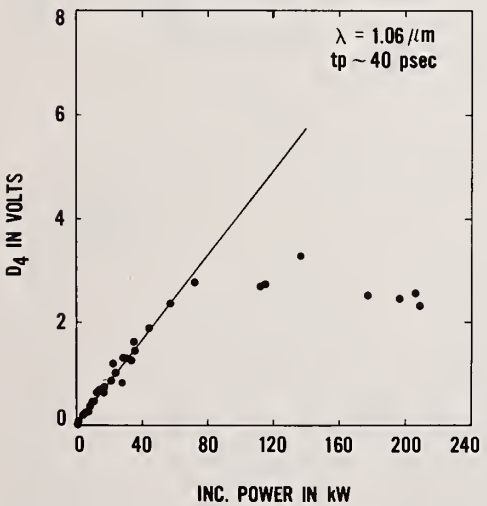

Figure 4

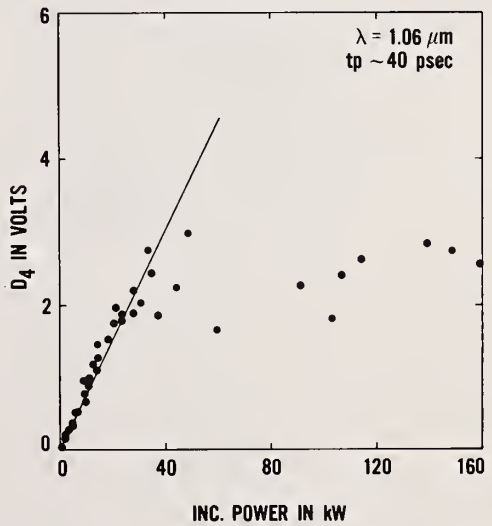

Figure 5

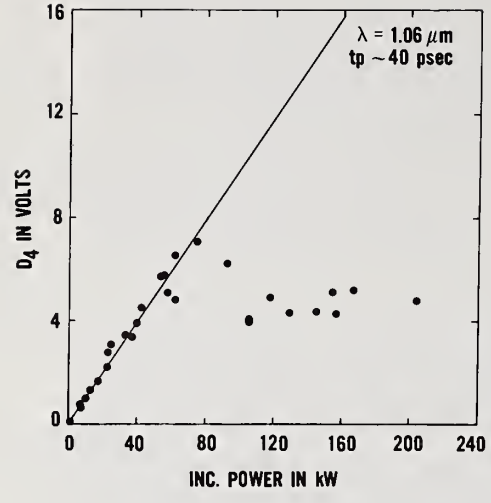

Figure 6

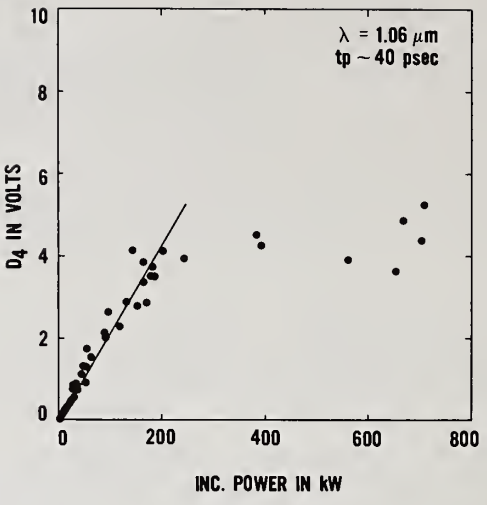

Figure 7

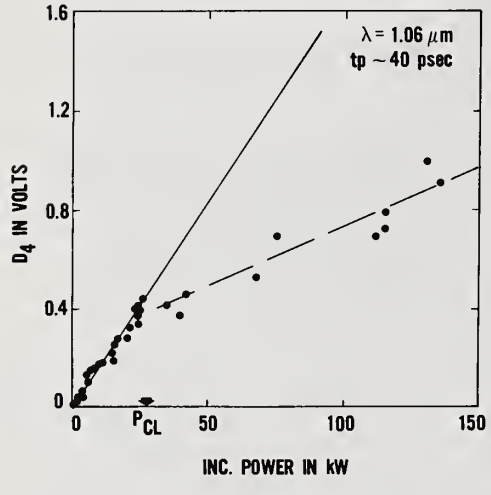

Figure 8

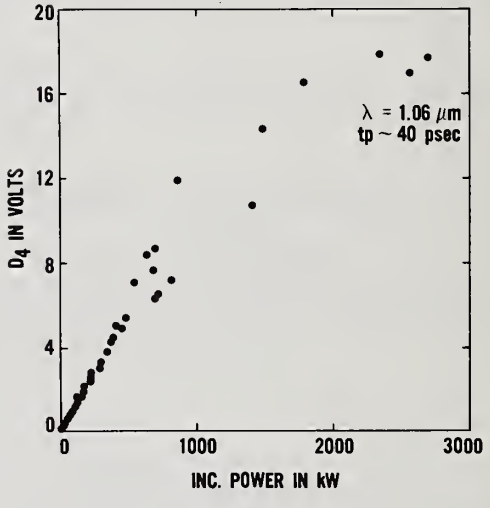

Figure 9

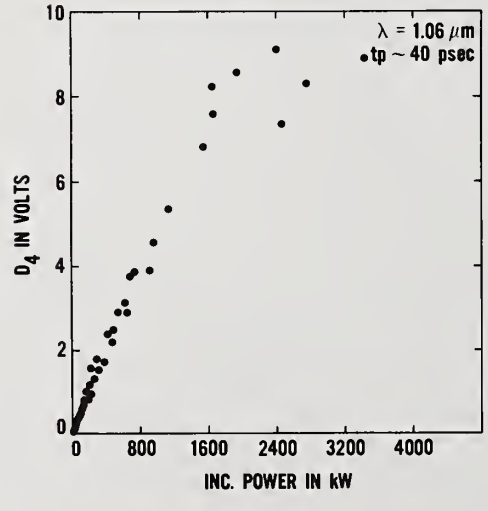

Figure 10

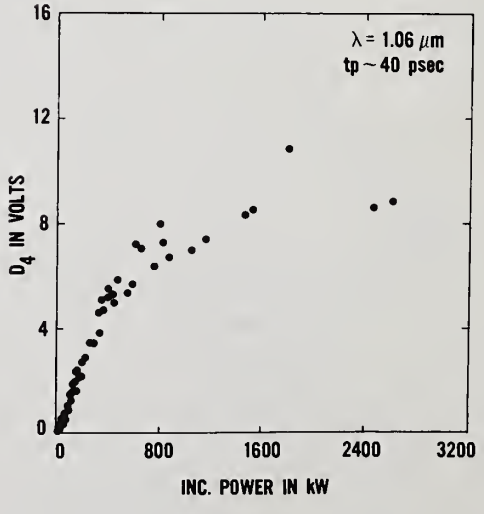

Figure 11

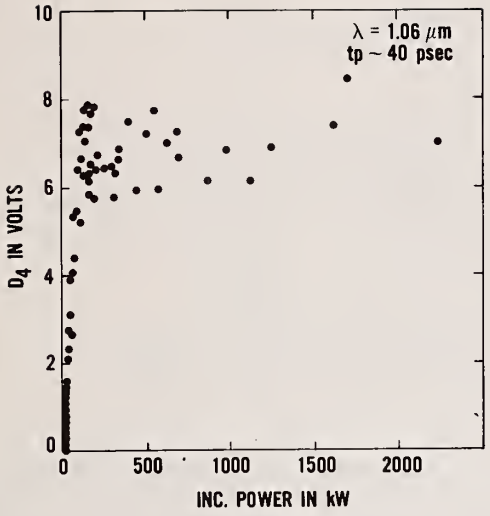

Figure 12

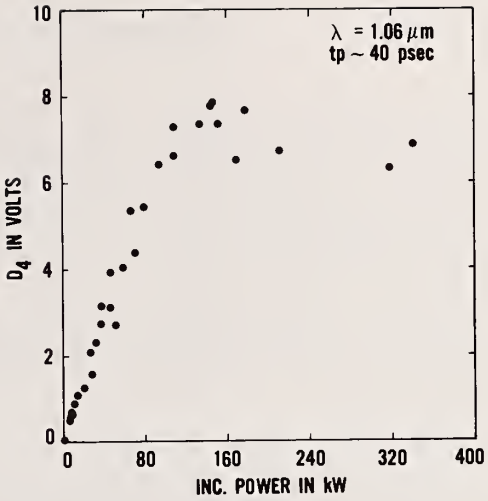

Figure 13

It was pointed out that with large beams the self focusing was not power dependent but is intensity dependent. The analysis given in the paper would have to be modified if one wanted to increase the total power. A device similar to that suggested in this paper was reported as an isolator by Tom Loree in 1974 and should be referred to. Another question was, "What is the spatial intensity of the output beam in the limiting self focusing mode?" The speaker replied that once nonlinear effects occur the output is completely distorted and will not pass the light through the pinhole to the detector.

Nonlinear Refractive Coefficient and Self-Focusing Damage in Glasses

Deng He Gan Fuxi
Shanghai Institute of Optics and Fine Mechanics,
Academia Sinica, Shanghai, P.R.C.

We have investigated some nonlinear optical effects in a series of optical glasses and laser glasses. Using different methods, we have measured the nonlinear refractive coefficient of these glasses. We have analyzed the possible mechanisms resulting in refractive index change in glass and calculated their nonlinear refractive coefficients. We have also discussed the dependence of laser-induced damage and thermo-optical blooming on nonlinear refractive coefficients.

Key words: Dispersion of nonlinear parameters; glass; inherent absorption wavelength; laser-induced birefringence; laser-induced damage; nonlinear refractive coefficient; self-focusing; self-induced polarization change; thermal blooming.

1. Introduction

For about twenty years, the development of high power laser systems has depended largely on investigation and improvement of laser glasses. Presently, the power density of the laser beam is so high that various nonlinear optical effects, such as self-focusing [1,2], self-induced polarization change [3,4] and laser-induced birefringence [5,6], etc., can take place in the glass medium that did not belong to the nonlinear materials in the past. These effects not only seriously influence the propagation characteristics of high-power laser beams in the medium, but also provide information about the nonlinear polarization mechanisms. In addition, these nonlinear optical effects provide various methods of measuring the nonlinear polarizability and nonlinear refractive coefficients.

Considering that glass is a very important optical material and is used widely in optical and laser technology, it is obviously significant to study and to master its various nonlinear optical properties. In this paper, some nonlinear optical effects in a series of optical glasses and laser glasses were systematically investigated. Using different effects or methods, the nonlinear refractive coefficients of these glasses were measured. The possible mechanisms resulting in a refractive index change in glass were theoretically analyzed, and these nonlinear changes were calculated. The influence of nonlinear refractive coefficients on laser-induced damage and optical thermal blooming are discussed. In addition, the dispersion of the optical Kerr-coefficients of these glasses was found in the experiment.

2. Measurement of Nonlinear Refractive Coefficients

Because a nonlinear refractive coefficient is a very important property of glass, several different methods were applied to measure it in a series of optical glasses and laser glasses.

2.1 Self-Focusing Damage

According to the theory of steady-state, self-focusing [7], the self-focusing damage threshold I_{max} and the self-focusing damage filament length L_{sf} are given by

$$I_{max} = \frac{P}{\pi r_o^2} \left(1 - \frac{P}{P_{cr}}\right)^{-1} \tag{1}$$

and

$$L_{sf} = \frac{R^2}{R_d} \left(\frac{P}{P_{cr}} - 1\right)^{1/2} \tag{2}$$

where P is the power of the laser beam, P_{cr} is the self-focusing critical power of the material, r_o, the radius of the focal spot without self-focusing, $R_d = kw_o^2$, k, the wave vector, w_o is the radius of the laser beam at the entrance to glass sample, and R, the curvature radius of laser beam at the same point. Using several lenses with different focal lengths to focus a TEM_{00} laser beam, the self-focusing damage thresholds and filament lengths in these glasses have been measured. In this way, the self-focusing critical power P_{cr} was determined. The experimental results are shown in Table 1.

Table 1. The self-focusing damage parameters of glasses

glass	n_o	E_d (10^2J/cm^2)	P_d (10^{10}W/cm^2)	P_{cr} (10^6W)
ZF-7	1.806	6.6	1.3	0.082
BaF-2	1.570	19.5	4.9	0.13
QK-3	1.487	14.3	2.9	0.4
N0312	1.522	14.5	2.9	0.3
N0812	1.535	9.5	1.9	0.33
N1012	1.517	16.2	3.2	0.33
P7701		17.2	3.7	0.33
N2120	1.578	26.5	5.3	0.38
N2420	1.543	18.0	3.8	0.40

E_d is damage energy threshold, P_d is damage power threshold

2.2 Self-Induced Polarization Change

While a high-power laser beam with elliptical polarization transmits through an isotropic medium, the main axis of the polarization ellipse will rotate. The rotation angle θ depends on the nonlinear property of the materials and the laser beam power:

$$\theta = \frac{48\pi^2\omega}{n_o^2 C^2} C_{1221} PL \cos 2\phi \qquad (3)$$

where ω is the frequency of the laser beam, C is the velocity of light in vacuum, L, n_o and C_{1221} are the length, refractive index and cubic nonlinear polarizability of glass, respectively. Figure 1 shows the optical arrangement of the experiment. The lens in Figure 1 is used to converge the laser beam in order to increase the power density of the beam. The self-induced polarization changes in a number of glasses were observed and the cubic nonlinear polarizability of these glasses at the wavelength of 1.06 μm were measured. The experimental results are shown in Figure 2a, Figure 2b and Table 2.

Table 2. The experimental results of SIPC in glasses at 1.06 μm wavelength

glass	$n_{1.06}$	θ (at 500MW/cm^2)	C_{1221} (10^{-15} esu)
ZF-7	1.775	7°31'	11.77
ZF-2	1.651	5°13'	7.26
BaF-2	1.557	3°24'	4.12
N0312	1.512	2°18'	2.62
N1012	1.508	2°10'	2.45
N2120	1.574	2°11'	2.72
N2420	1.530	2°03'	2.44

2.3 Laser-Induced Birefringence

High-power laser beams can also make another weak probe beam demonstrate birefringence in glass. In general, the effect in glass is quite small, but the laser beam power is so high that this laser-induced birefringence of various glasses applied in a high-power laser system is not negligible. Using a weak light at 1.06 μm as the probe beam, the laser-induced birefringence in some glasses was investigated, and the optical Kerr-coefficients n_k of these glasses were measured. Figure 3 is the experimental apparatus for a laser-induced birefringence measurement. The experimental results are shown in Table 3.

Table 3. Optical Kerr-coefficient of some glasses at the wavelength of 1.06 μm

glass	ZF-7	BaF-2	N0300	N2400
n_k (10^{-13} esu)	5.7±0.5	2.0±0.1	1.4±0.1	0.77±0.1

Three nonlinear parameters of P_{cr}, C_{1221} and n_k were measured using the above methods. Therefore, the nonlinear refractive coefficients of these glasses were determined from these parameters by the following equations:

For SF method,

$$n_2 = C\lambda_o^2 / \left(64\pi^2 P_{er}\right) \tag{4}$$

For SIPC method,

$$n_2 = \frac{36\pi}{n_o} C_{1221} \tag{5}$$

For LIB method,

$$n_2 = \frac{3}{2} nk \tag{6}$$

All the results are shown in Table 4.

Table 4. The nonlinear refractive coefficients of glasses measured by various methods

glass	$n_2(10^{-13}$esu)		
	SF	SIPC	LIB
ZF-7	6.4	7.5	8.3
ZF-2		5.0	
BaF-2	4.1	3.0	3.0
QK-3	1.3		
N03	1.9	2.0	2.0
N08	1.6	1.8	2.0
N10	1.6	1.8	2.0
N21	1.3	2.0	
N24	1.2	1.6	1.2

3. The Possible Mechanisms of Nonlinear Refractive Coefficient

The mechanisms resulting in refractive index nonlinear change in glass were theoretically analyzed [8]. The changes, both in density and polarizability of glass, lead to a refractive index change. The possible mechanisms are as follows:

3.1 Thermal Effect

As the glass medium absorbs laser energy and causes a temperature field, both the density and polarizability will change, and these changes depend on the laser beam intensity. Because glass is a thermal insulator, the heating process was treated as adiabatic for the laser pulse with a millisecond duration or less. In the simple case, the nonlinear refractive coefficient $n_2(T)$ caused by a thermal effect is expressed as

$$n_2(T) = (dn/dT) \cdot \alpha \cdot t/\rho \cdot C_p \tag{7}$$

where t is the laser pulse duration, α, C_p and ρ is the optical absorption coefficient, specific heat and density of glass, respectively. (dn/dT) is the temperature coefficient of a refractive index.

3.2 Electro-Striction Effect

Under the action of an intense laser electric field, the Brillouin scattering generates an electro-striction, which gives rise to the variation in density change. Thus, the nonlinear change of a refractive index is caused. According to steady electro-striction theory, the nonlinear refractive coefficient $n_2(S)$ caused by this effect can be expressed as

$$n_2(S) = \frac{no}{4\pi E}\left[\frac{(1+\mu)(1-2\mu)}{(1-\mu)}\right] \cdot \left(\rho \cdot \frac{dn}{d\rho}\right)^2 \tag{8}$$

where E and μ is Young's modulus and Poisson's ratio of glass, respectively, $(\rho\ dn/d\rho)^2$ is the acousto-optic coupling coefficient.

3.3 Nonlinear Polarization Effect

Under the action of a laser field, the distortion of the electron clouds around the nucleus and the movement of the nuclei will lead to the nonlinear polarization in glass. We consider the nonlinear refractive index as a refractive index increment due to the inherent frequency in the ultra-violet region generating a Stock's displacement and shifting to a longer wavelength as the intensity of the laser beam increases. Thus, the nonlinear refractive coefficient $n_2(E)$ is directly proportional with the square of intrinsic ultra-violet absorption wavelength λ_s^2 [9].

For oxide glasses,

$$n_2(E) = -39 \cdot 10^{-14} + 29 \cdot 10^{-4} \cdot \lambda_s^2 \tag{9a}$$

For fluorophosphate and fluoride glasses,

$$n_2(E) = -11 \cdot 10^{-14} + 12 \cdot 10^{-4} \cdot \lambda_s^2 \tag{9b}$$

All these nonlinear refractive coefficients of glass were calculated and compared with the experimental results. Table 5, shows that the nonlinear refractive coefficients for nanosecond laser pulses are mainly caused by a nonlinear polarization effect, but for millisecond laser pulses, it is mainly caused by thermal effect. Table 6 shows that the calculated values of $n_{2(E)}$ are consistent with the experimental values of n_2 measured by nanosecond laser pulses.

4. Some Nonlinear Optical Effects in Glass

The nonlinear refractive coefficient n_2 is a very important nonlinear property of glass. Many nonlinear optical phenomena in glass under the action of an intense laser beam are concerned with it.

Table 5. The nonlinear refractive coefficient of glass N03 under the action of different pulse durations

nonlinear effects	response time	$n_2(cm^2/W)$		
		ms pulse	μs pulse	ns pulse
thermal effect	10^{-6}-10^{-7}	6×10^{-12}	6×10^{-15}	
electro-striction effect	10^{-7}-10^{-8}	1.06×10^{-16}	1.06×10^{-16}	1.06×10^{-16}
nonlinear polarization effect	10^{-15}-10^{-16}	0.92×10^{-15}	0.92×10^{-15}	0.92×10^{-15}

4.1 Laser-Induced Damage

Table 6. The comparison between calculated and experimental values of n_2

glass	cal. values (10^{-13} esu)			exp. val. of n_2 (10^{-13} esu)
	$n_2(T)$	$n_2(S)$	$n_2(E)$	
ZF-7	1.05	1.09	9.0	6.4±1.1
BaF-2	0.37	0.22	3.6	4.1±0.4
QK-3	0.17	0.21	1.2	1.3±0.4
N0312	0.32	0.19	1.7	1.9±0.4
N0812	0.12	0.17	1.9	1.6±0.5
N1012	0.29	0.17	1.7	1.6±0.5
N2120	0.04	0.28	1.5	1.3±0.3
N2420			1.4	1.2

The laser-induced damage in a number of glasses under the action of a nonosecond laser pulse and a millisecond laser pulse were observed. From the experiments, it was found that the damage under the action of a millisecond laser pulse mainly depends on $n_2(T)$ caused by thermal effect, and the damage under the action of a nanosecond laser pulse mainly depends on $n_2(E)$ caused by a nonlinear polarization effect. This dependence is shown in Figure 4. Usually, the glasses with smaller nonlinear refractive coefficients n_2 possess higher damage thresholds, but they are not completely consistent, because the laser-induced damage of materials also depends on other physical properties besides the nonlinear refractive coefficient n_2.

4.2 Thermal Blooming

An intense millisecond laser pulse will make the divergence angle of another weak probe beam increase. The thermal bloomings of a number of glasses under the action of a 5-millisecond intense laser pulse were investigated. From the experiments, it was found that the increment of divergent angle $\Delta\theta$ depends on $n_2(T)$ caused by the thermal effect. This dependence is shown in Figure 5, where E_A is the portion of a laser energy absorbed by glass.

4.3 Dispersion of Laser-Induced Birefringence

The probe beam at 0.53 μm was applied to measure the laser-induced birefringence in place of the probe beam at 1.06 μm. From the experimental results (Table 7), it was found that the optical Kerr-coefficients n_k at 0.53 μm are larger than those at 1.06 μm, that is, the optical Kerr-coefficients in these glasses have obvious dispersion. This dispersion is an important problem in both a technological application and theoretical studies of nonlinear polarization mechanisms in glass.

Table 7. The optical Kerr-coefficients of several glasses

glass	$n_k(10^{-13}$ esu)		$n_2(10^{-13}$ esu)	
	1.06 μm	0.53 μm	1.06 μm	0.53 μm
ZF-7	5.7±0.5	11.4±0.9	8.3±0.8	17.1±1.4
BaF-2	2.0±0.1	5.3±1.0	3.0±0.2	8.0±1.6
N0300	1.4±0.1	2.5±0.5	2.0±0.1	3.8±0.7
N2400	0.77±0.1		1.2±0.1	

References

1. W. L. Smith, J. H. Bechtel, N. Boembergen, Phys. Rev., 12B (2), 706 (1975).
2. Deng He, Zhang Meizhen, Laser Journal (Chinese), 6 (1), 13 (1979).
3. A. Owyoung et al, Phys. Rev., 5B, 628 (1972).
4. Zhang Meizhen, Deng He, Li Chenfu, Laser Journal (Chinese), 8 (4), 22 (1981).
5. B. Lacour, J. P. Pochalle, IEEE J.Q.E., QE8 (5), 456 (1972).
6. Deng He, Zhang Meizhen, Li Chengfu, Laser Journal (Chinese), 8, (1981).
7. S. A. Akhmanov et al., Uspekhi Fizicheshikh Nauk, 93 (1), 19 (1967).
8. Can Fuxi, Lin Fengying, Acta Optics Sinica (Chinese), 1 (1), 75 (1981).
9. Gan Fuxi et al., Laser Journal (Chinese), 6 (4), 12 (1979).

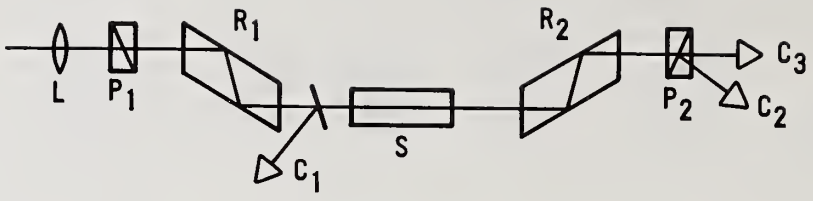

Figure 1. The optical arrangement for SIPC measurements L--lens; P_1, P_2--polarimeters; S--sample; R_1, R_2— Fresnel rhomb; C_1, C_2, C_3--detectors.

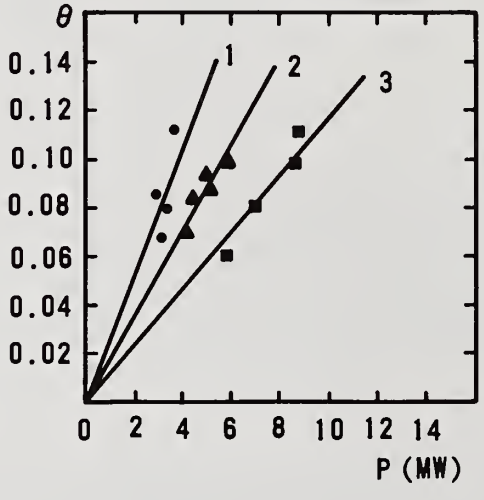

Figure 2a. The dependence of SPIC rotation angle on laser power.
1--ZF-7; 2--ZF-2; 3—BaF-2.

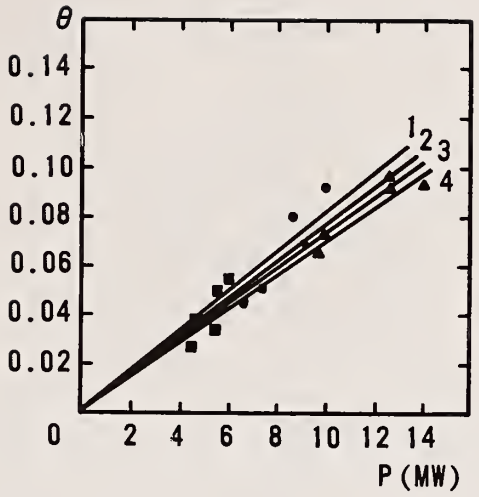

Figure 2b. The dependence of SIPC rotation angle on laser power

1--NO312; 2--N2120;
3--N1012; N2420.

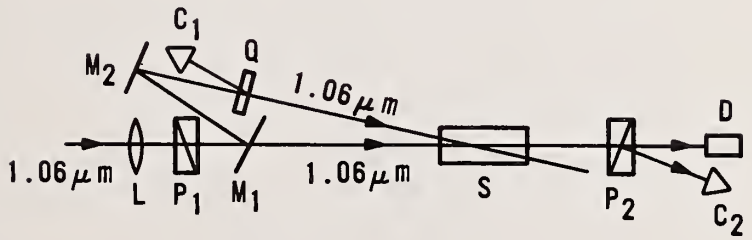

Figure 3. Experimental arrangement for LIB measurement at 1.06 μm wavelength,

L--lens; P_1, P_2--polarimeters;
M_1--beam splitter; S--sample;
M_2--directing mirror;
C_1, C_2, D--detectors;
Q--rotation plate.

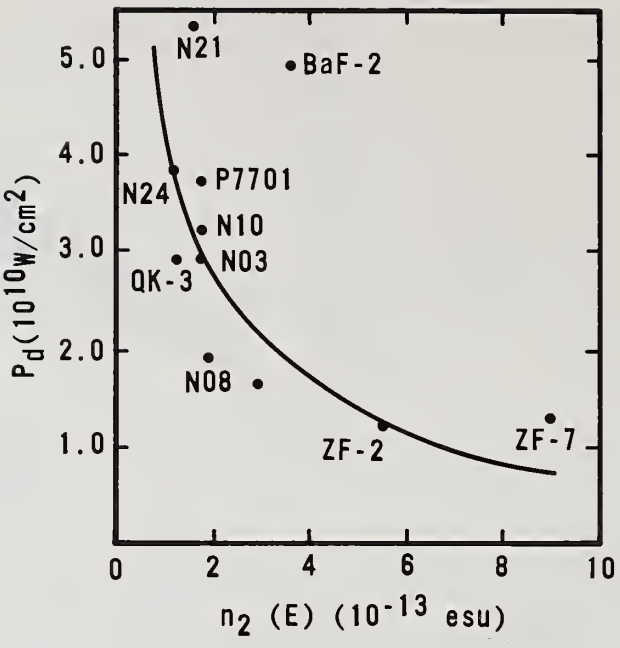

Figure 4. The dependence of laser-induced damage threshold on $n_2(E)$.

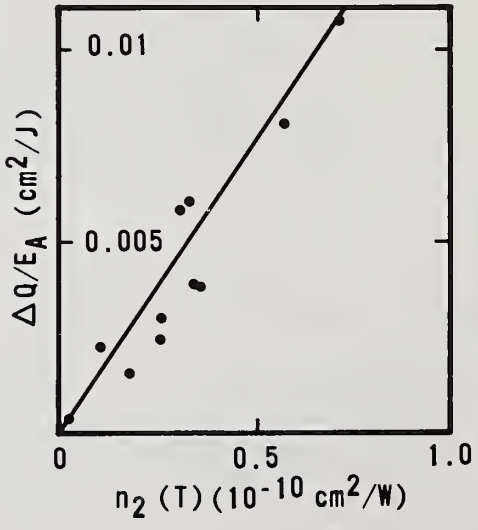

Figure 5. The dependence of thermal blooming effect on $n_2(T)$.

What laser was used to make the measurements reported at 0.53 μm? The speaker replied that they used both a gas laser and a second harmonic laser.

Nonlinear Absorption and Self-Defocusing of Intense IR-Laser Radiation in Semiconductors Due to Generation of Free Carriers

Yu. K. Danileiko, T. P. Lebedeva, A. A. Manenkov and A. V. Sidorin

P. N. Lebedev Physical Institute of the USSR Academy of Sciences
Moscow, USSR

Results of experimental studies of the interaction of high power CO_2 (λ = 10.6 μm), CaF Er^{3+} (λ = 2.76 μm) and YAG Er^{3+} (λ = 2.96 μm) lasers with undoped Ge and Si are presented. The experiments included photoconductivity, microwave absorption and laser beam transmission measurements at various intensities up to the level of laser damage. For both the Ge and Si samples, nonequilibrium carrier generation has been observed with both CO_2 and Er-laser excitation.

It is shown that the carrier generation in Ge is due to two-photon ionization at the Er-laser wavelength, whereas none of the considered mechanisms (impact, multiphoton and thermal ionizations), explain the anomalous dependence of carrier density upon CO_2-laser excitation intensity.

Nonequilibrium carrier generation results in nonlinear absorption and self-defocusing, which in turn lead to the intensity saturation of high power laser beams. Analysis of these effects for prefocused beams is presented. It is shown, in particular, that the absence of bulk damage in Ge under CO_2 and Er-laser radiation is attributed to these effects even at very high incident intensities. It is pointed out that these effects play an important role in the application of Ge as a material for use in high power IR lasers.

Key words: high power laser interaction with semiconductors; nonequilibrium carrier generation; photoconductivity; nonlinear absorption; self-defocusing; laser-produced damage; high-power laser materials; Ge; Si.

1. Introduction

Investigation of the interaction of intense IR laser radiation with wide-gap semiconductors is of great interest for both the physics of semiconductors, and the use of these materials as elements of laser optics (windows, modulators, phase conjugators, etc). In the framework of a general program of the interaction of high-power laser radiation with transparent solids carried out by our laboratory, we have recently studied the interaction of IR-laser radiation at 3 μm and 10 μm wavelength with Ge, Si and GaAs materials widely used in laser optics.

This paper presents results of investigations involving Ge and Si. Particular attention will be paid to the interaction of 10.6 μm pulsed CO_2-laser radiation with Ge in connection with the "anomalous" effect of nonequilibrium carrier generation which we observed in 1977 [1,2]. The anomaly of this effect manifests itself in the unusual dependence of the concentration of nonequilibrium carriers on laser intensity, which is not explained by the known photoexcitation mechanisms. Note that in recently published work [3,4] by Lax and his collaborators, carrier generation in p-Ge exposed to CO_2-laser radiation was attributed to 7-photon ionization, but our results for pure Ge are not accounted for by such a process.

Generation of nonequilibrium carriers has a considerable effect on the character of high power IR-radiation propagation in a semiconductor, causing, in particular, intensity saturation due to nonlinear absorption and self-defocusing. These effects may be rather important when employing semiconductor materials in high power laser systems. In this connection we have investigated in detail the effect of carrier generation in Ge exposed to 10.6 μm CO_2-laser radiation, applying different techniques, such as d.c. photoconductivity, and microwave and laser radiation absorption measurements. In addition, a series of experiments have been carried out using the $CaF_2 \cdot Er^{3+}$ and YAG$\cdot Er^{3+}$-lasers, operating in the 3 μm wavelength region, as the excitation sources. The results of these experiments are presented and possible mechanisms of nonequilibrium carrier generation in Ge and Si, and the effects of nonlinear absorption and self-defocusing due to this generation are discussed.

2. Experimental

In our experiments we have investigated pure dislocation-free Ge and Si single crystals with impurity concentration not exceeding $10^{12} cm^{-3}$.

Single-mode CO_2, $CaF_2 \cdot Er^{3+}$ and YAG$\cdot Er^{3+}$-lasers, whose characteristics are presented in Table 1, were used in the experiments.

a. Investigation of Photoconductivity

Figure 1 shows a schematic of the experimental arrangement used for the laser induced photoconductivity measurements. The excitation geometry is also shown. Input and output surfaces of the samples were carefully polished and etched just before the experiment.

For correct measurement of the sample photoconductivity, σ, and for determination from it of the nonequilibrium carrier concentration, N, we excited the entire sample bulk uniformly. Calibration of the recording system was carried out by use of known replacement resistors. The relationship between conductivity and carrier concentration was determined by measuring the temperature dependence $\sigma(T)$ in the range, 15-100°C.

The resolution time of the recording system was $\sim$ 1 ns, allowing us to investigate in detail the kinetics of photoconductivity with pulsed laser excitation.

The shapes of the photoconductivity signals were revealed to be essentially different at relatively low and high input intensities, I_i, of the exciting laser radiation. For instance, with excitation by CO_2-laser radiation at $I_i \lesssim 0.1$ MW/cm^2, the observed signal corresponds to that of the laser pulse (Fig. 2a), whereas with $I_i > 0.1$ MW/cm^2 it corresponds to the "positive photoconductivity," and its shape greatly differs from that of the laser pulse (Fig. 2b). After the laser pulse the conductivity relaxes to its equilibrium value with the characteristic time $\tau \simeq$ 100 μs (at T=300°K), which corresponds to the electron recombination time in pure Ge. We interpret the character of these signals as a result of two effects: reduction in the carrier mobility, due to their heating by laser radiation, and generation of nonequilibrium carriers.

By measuring the photoconductivity signal amplitude at various excitation intensities in the range of I_i = 1-20 MW/cm^2, where the process of nonequilibrium carrier generation predominates, we determined the dependence of their concentration on the input intensity. Figure 3 shows this dependence approximated by the relationship $N \sim I_i^{\gamma}$ with $\gamma \simeq 1.7$. The maximum concentration of nonequilibrium carriers attained in these experiments amounted to about 2×10^{16}cm^{-3}. Investigation of the dependence $N(I_i)$ at higher input intensities of the exciting CO_2-laser radiation was limited by the appearance of laser produced plasma on the sample surface. Higher excitation levels can be achieved by focusing the incident beam into large enough samples, but this hampers quantitative calibration of the observed signals due to the complex geometry of the excitation region and the necessity to consider carrier diffusion and the effects of nonlinear absorption and self-defocusing. This was confirmed by experiments on microwave and infrared probing, as described in the two following sections.

b. Investigation of Microwave Absorption by Nonequilibrium Carriers

Figure 4 shows a schematic of a 3-cm spectrometer used for investigating microwave absorption by nonequilibrium carriers, as well as the geometry of sample excitation in collimated and focused beams. For correct measurements of carrier concentration and its kinetics, we used the simple theory of microwave absorption in semiconductors [5]. According to this theory the microwave power absorbed by a unit volume of a semiconductor sample is given by:

$$P_a = \sigma E_i^2 \qquad (1)$$

where σ is the conductivity related to the dielectric susceptibility, $\varepsilon = \varepsilon' + i\varepsilon''$, of the free electron gas by

$$4\pi\sigma/\nu = -\varepsilon'' = 4\pi Ne^2/m \left(\omega^2 + \nu^2\right)$$

$$\varepsilon'/\varepsilon'' = -\omega/\nu$$

$E_i = E_0/E_{e++}$ is the microwave field inside the sample whose effective dielectric susceptibility is $E_{eff} = 1 + \alpha\,(E-1)$. Here α is the depolarizating factor, depending on a sample shape, $E = E_0 + E' + E''$, E_0 is the lattice part of the dielectric susceptibility, E_0 is the external microwave field of frequency ω, ν is the collision frequency, and M is the electron effective mass.

We have analyzed in detail microwave-absorption signals observed for Ge excited by the CO_2- and $CaF_2.Er^{3+}$-lasers at room and liquid nitrogen temperatures. The absorption amplitudes were calibrated by means of comparison of laser produced signals with those arising from the thermal generation of carriers, as the samples were heated up to 100°C. The results of these microwave experiments are as follows:

(1) At both 10.6 μm and 2.76 μm, the generation of nonequilibrium carriers has a strongly pronounced intensity threshold, which at room temperature is about 1 MW/cm^2 and 0.3 MW/cm^2, respectively. Above this threshold, the dependence of carrier concentration on the CO_2-laser intensity is approximately linear in the range of $N \lesssim 10^{14}$cm^{-3}, and it becomes stronger but does not exceed $N \sim I_i^{17}$ for $N > 10^{14}$cm^{-3}.

This is in agreement with the d.c. photoconductivity measurements described above.

At 10.6 μm, the efficiency of carrier generation (slope of $N(I_i)$) at T=300° K was found to be twice as much as at T=77°K. At 2.76 μm, the dependence $N(I_i)$ is quadratic in the range of 0.3 to 2 MW/cm^2, as is seen from Figure 5.

(2) Microwave probing of a 5-cm-long sample has shown that for collimated CO_2-laser beam excitation, up to an incident intensity of 20 MW/cm^2, the nonequilibrium carrier concentration is homogeneous over all the sample length along the beam, whereas with focused beam excitation, a sharp asymmetry of the concentration distribution is observed in respect to the focus, which decreases sharply behind the focus in the direction of beam propagation.

We attribute such an asymmetry to nonlinear absorption and self-defocusing of the exciting radiation by nonequilibrium carriers. These results were confirmed in direct experiments on transmission of high power exciting and weak probing CO_2-laser beams.

c. Transmission of CO_2-Laser Radiation in Ge

Figure 6 shows a schematic of an arrangement for transmission experiments. The exciting beam from a powerful multimode laser with a pulse duration of 200 ns was crossed inside the Ge sample with a 60 ns probing beam from a single-mode laser at angles of ∿10° and 90° . The time delay of these pulses was varied up to 1 ms. The intensity of the probing beam was small enough ($I_p \sim 1$ KW/cm^2) to avoid any effect on the carrier generation process or on the saturation of intervalence transitions. Both the dependence $I_p(\Delta t)$ at fixed intensity I_i of the high power exciting radiation, and the dependence of the output intensity I_{out} on the input intensity I_i for both thin (0.3 cm long) and thick (8 cm long) samples were investigated. These experiments have shown that for collimated beam excitation of high enough incident intensity (I_i = 20 MW/cm^2), the transmitted energy, for both the exciting and probing beams, does not decrease at zero delay even for the 8cm-long sample, whereas at $\Delta t \geq 200$ns delay, i.e., after the exciting pulse passage, attenuation of the probing beam is considerable (the absorption coefficient was measured to be K_p = 11.2 cm^{-1}). Keeping in mind that the hole absorption cross-section in Ge at 10.6 μm is much larger than the electron absorption cross-section ($\sigma_h = 6 \cdot 10^{-16}$cm^2, $\sigma_e = 3 \cdot 10^{-17}$cm^2 [6], we may conclude that at Δt 200 ns, absorption is mainly associated with the nonequilibrium holes, whose concentration under these excitation conditions is $N = K_p \sigma_h = 2 \times 10^{16}$cm^{-3}. This value coincides with the concentration of nonequilibrium electrons measured by photoconductivity, under the same excitation conditions. This directly proves that electron-hole pairs are generated in pure Ge under CO_2-laser irradiation. The fact that there is no attenuation of the exciting and probing beams at zero delay indicates that the hole transitions are saturated at rather low intensities. Our measurements have shown that the hole transition saturation intensity $I_s < 1$ MW/cm^2.

Transmission of the exciting radiation of a single-mode CO_2-laser was investigated for a tightly focused beam. Figure 7 shows the beam propagation geometry and results obtained for the output power attenuation, as a function of the input power of the beam. It is seen that nonlinear attenuation takes place, which becomes noticeable at the incident power of about 1 KW, which corresponds to the intensity of I_f = 2GW/cm^2 in the linear focus inside the sample. The attenuation increases by an order of magnitude at input intensity of about 1 MW/cm^2, after which a tendency to saturation is observed. We attribute such nonlinear attenuation to the absorption by nonequilibrium electrons, since, as was mentioned above, nonequilibrium holes do not make a noticeable contribution to 10.6 μm absorption, at high intensities, due to saturation of intervalence transitions.

An interesting result has been obtained from IR-microscopic studies of the Ge sample exposed to high power laser irradiation. No traces of damage were seen in the focal region inside the Ge sample, even at maximum input powers of CO_2-laser greater than 1 MW. At such powers, the intensity

in the linear focus inside the sample would have reached very high levels, $I_f \simeq 2 \cdot 10^{12}$ W/cm^2, which would lead to damage.*

As will be shown below, the nonlinear transmission and absence of laser produced damage in Ge are associated with nonlinear absorption and self-defocusing which lead to the intensity saturation at the focus.

d. Investigation of Si

Experiments similar to those for Ge were also carried out for Si. The results of these experiments can be summarized as follows. Using microwave diagnostics, we have observed the generation of nonequilibrium carriers in Si under excitation by both CO_2-laser and Er^{3+}-lasers only at such high intensities (~ 1 GW/cm^2) that bulk damage of the samples occurred in the focal region. A cut-off of the transmitted beam pulse was observed in this case, which we attribute to the nonequilibrium carrier generation at the instant of damage. As nonequilibrium carriers in Si occurred only under conditions of sample damage, we did not investigate in detail the characteristics of the process of their generation as has been done for Ge.

3. Discussion

Let us discuss the possible mechanisms of generation of nonequilibrium carriers in Ge and the effects of nonlinear absorption and self-defocusing caused by them.

As the experimental results convincingly prove, in pure Ge, electron-hole pairs are generated on exposure to both 10.6 μm and 3 μm radiation with concentrations at high intensities (~ 1 GW/cm^2) exceeding 10^{17}cm^{-3}. This generation is evidently due to intrinsic ionization processes rather than impurity ionization. In principle, all the ionization processes, such as thermal, multiphoton and impact ionizations can play a role.

Simple consideration shows that for pulsed radiation ($\tau \leq 200$m ns) the mechanism of thermal ionization, associated with the direct heating of a crystal, results in carrier generation with concentrations several orders of magnitude less than that observed.

Multiphoton ionization must also be considered. As was shown, two-photon absorption is undoubtedly an efficient mechanism of carrier generation in Ge for 3 μm-excitation. The results of the excitation intensity dependence measurements of nonequilibrium carrier concentration, with 2.76 μm CaF_2:Er-laser radiation, obtained at room temperature (see Fig. 5), are well explained by this mechanism with the two-photon absorption coefficient $\beta = 7.4 \times 10^{-2}$ cm/MW.

As far as 10 μm excitation is concerned, at least seven photons are needed to excite direct transitions in Ge at room temperature. This process must lead to a strong dependence of carrier concentration on the intensity ($N \sim I^7$). The experiments indicate, however, a far weaker dependence ($N \sim I^{\gamma}$, with $\gamma \lesssim 1.7$) through all the intensity range investigated. Therefore, the role of multiphoton ionization in carrier generation in Ge with 10.6 μm excitation is improbable in our experiments.

In this connection we would like to note the recently published results by Lax and his collaborators [3,4] on the investigation of photoconductivity and the nonlinear absorption of CO_2-laser radiation at 9.6 μm and 10.6 μm, in doped n- and p-type Ge. Their experimental data are essentially different from our data, though obtained in similar excitation conditions. In particular, the discrepancies in photoconductivity and nonlinear absorption data are marked: concenrations of nonequilibrium carriers ($\sim 10^{13}$cm^{-3}) and incident intensities (20 MW/cm^2) at which nonlinear absorption occurs, three orders of magnitude less than those observed in our experiments were reported by these authors. They account for their results by seven-photon absorption. Such an interpretation does not agree with their own and our data on intensity dependence of photoconductivity, however. In [3] $N \sim I_j$, and we have observed $N \sim I_j^{\gamma}$, with $\gamma \simeq 1.7$. The reasons for such a pronounced discrepancy of experimental data and interpretation remain unclear.

Thus, we must consider impact ionization as the primary process of nonequilibrium carrier generation in Ge by CO_2-laser radiation. The theory of this process in laser fields is well developed for the model of single parabolic conduction bands [8], and predicts a rapid exponential growth

*Note for comparison that the damage threshold of GaAs, the most resistant semiconductor material for CO_2-laser radiation, is equal to 50 GW/cm^2 [7].

of carrier concentration with the field. Though our experiments indicate a weak dependence $N(I_i)$, we do not rule out the role of impact ionization in carrier generation in Ge. We suppose that the complex band structure of Ge, and intervalley transitions, may be responsible for the observed, anomalously weak dependence $N(I_i)$. Of course, only a detailed theoretical analysis of such processes is capable of confirming this expectation.

Consider now the role of nonlinear absorption and self-defocusing in propagation of high power laser radiation in Ge. As indicated by the known relationship for the absorption coefficient and dielectric susceptibility of the electron gas,

$$K_e = \sigma_e N_e = 3 \cdot 10^{-17} N_e \text{cm}^{-1}, \quad \varepsilon_e' = -4\pi e^2 N_e / m \left(\omega^2 + \nu^2\right) \simeq 10^{-18} N_e,$$

these effects must be essential at nonequilibrium carrier concentrations $N_e \sim 10^{16}\text{cm}^{-3}$. That is in agreement with our experimental data for CO_2-laser radiation transmission: such concentrations were attained at the intensities $I_i > 20$ MW/cm^2.

Of particular interest is the case of focused beam propagation, where, under our experimental conditions, intensity in the linear focus must be as high as $I_f \simeq 10^{12}$ W/cm^2. If we extrapolate the dependence $N \sim I_i^{1.7}$, obtained with collimated beams, to the focused beam case, then very high concentrations of nonequilibrium carriers exceeding 10^{22}cm^{-3} would occur in the focal region. But such concentrations must lead to strong absorption and self-defocusing, which would limit the intensity in the focus. Thus, a self-consistent regime for both the intensity and carrier concentration saturation is realized in the focal region.

A theoretical analysis of self-defocusing in germanium is quite difficult because of the integrating character of the nonlinearity, due to the fact that the nonequilibrium carrier recombination time greatly exceeds the excitation pulse duration of both the CO_2- and Er-lasers used in our experiments. For this reason, this paper presents an analysis based on the assumption of fast-response nonlinearity which simplifies the problem, while preserving the main characteristics of the self-defocusing process. We have analyzed such a regime by solving the well-known parabolic equation describing the propagation of an electromagnetic field in a nonlinear refractive medium

$$2ik \frac{\partial E}{\partial Z} + \Delta_r E + k^2 \frac{\delta\varepsilon(|E|^2)}{\varepsilon_o} = 0 \qquad (2)$$

Here k is the wave number, and $E = E_o + \delta E\,(|E|^2)$ is the dielectric susceptibility of the medium. Three different forms of nonlinear susceptibility $\delta\varepsilon$ have been considered: $\delta\varepsilon \sim (I_i - I_o)$, $\delta\varepsilon = \varepsilon_2 |E|^2 \sim I_i$ and $\delta\varepsilon \sim I_i^{\gamma}$ with $\gamma = 1.7$, where I_i is the incident intensity of the electromagnetic field, and I_o is the threshold intensity of carrier generation. All three cases correspond to different parts of the dependence $N(I_i)$ observed for Ge excited by CO_2 laser radiation. An analytical solution of Equation 2 with the cubic nonlinearity of E ($\delta E = E_2|E|^2$) for focused beams with Gaussian incident intensity profiles, in the so called aberrationless approximation, has shown that a strong enough negative nonlinearity $(E_2|E_o|^2/E_o > 1/(Ka_o)^2$, where a_o is the incident beam radius leads to intensity saturation in the focal region. The maximum intensity reached in this saturation regime is independent of the incident intensity, with the corresponding maximum change of dielectric susceptibility given by the relationship:

$$\delta\varepsilon_{max}/\varepsilon_o = \varepsilon_2 |E|^2_{max}/\varepsilon_o = (a_o/F)^2 \qquad (3)$$

where F is the focal length of the focusing lens. We see that δE_{max} is proportional to the focusing angle squared.

A more exact analysis of the problem has been carried out by the numerical solution of Equation 2 using a computer. This solution for the cubic nonlinearity case has shown that the saturated intensity in the focal region is given by:

$$\delta\varepsilon_{max}/\varepsilon_o = \varepsilon^2 |E|^2_{max}/\varepsilon_o \simeq 5(a_o/F)^2 \qquad (4)$$

i.e., it differs from Equation 3 by the factor of 5. Both the radial and axial intensity distributions are essentially distorted. The radial distribution deviates from the Gaussian shape and becomes flat-topped, while the focal beam radius increases with incident intensity, and the on-axis beam distribution broadens strongly and is shifted behind the geometric focus. These results are shown in Figures 8 and 9, where the results of the numerical calculation for a medium with cubic negative nonlinearity are presented for various input intensities.

Calculations carried out for other types of negative nonlinearity, corresponding to different dependencies of nonequilibrium carrier generation in Ge, have shown that the shape of the nonlinearity does not change the general picture of self-defocusing, and only slightly affects the maximum value $\delta\varepsilon_{max}/\varepsilon_0$ in the focal region.

We used these results for analysis of the experimental data on propagation of high power CO_2- and Er-laser radiation in Ge. It follows from this analysis that with excitation by CO_2-laser in a focused beam geometry with $a_0/F = 0.13$, the maximum concentration of the generated nonequilibrium carriers, and the maximum intensity in the focus, are as high as $N_{e\ max} \simeq 10^{18} cm^{-3}$, and $I_{f\ max}$ 3×10^8 W/cm^2, respectively. The intensity saturation at the focus accounts for the absence of bulk damage in Ge crystals for both CO_2- and Er-laser irradiation.

4. Conclusions

Investigation of the interaction of high power CO_2- and Er-laser radiation with Ge and Si has shown that nonequilibrium carriers are generated in both crystals, but the characteristics of this process and generation mechanisms are essentially different for the two crystals. The threshold for carrier generation in Ge is rather low ($I_{th} \simeq 1$ MW/cm^2), whereas in Si the carriers occur only at the sample damage threshold (~ 5 GW/cm^2). Generation of carriers in Ge by Er-laser radiation at 2.76 μm and 2.94 μm is shown to be produced by two-photon ionization, while at 10.6 μm, carrier generation is not accounted for by any of the possible ionization processes (thermal, multiphoton and impact ionizations) in the framework of usual conceptions.

At high excitation intensities, generation of nonequilibrium carriers in Ge is shown to cause nonlinear absorption and self-defocusing which leads to the intensity saturation of the propagating beam.

These effects account for the absence of bulk damage in Ge under CO_2- and Er-laser irradiation and are expected to play an important role in other phenomena such as four-wave mixing and phase conjugation, which are important for many practical applications.

References

1. Yu. K. Danileiko, A. S. Epifanov, T. P. Lebedeva, A. A. Manenkov, V. A. Miljaev, and A. V. Sidorin. "Nonequilibrium Carrier Excitation in Germanium and Silicon Produced by CO_2 Laser Radiation." Doklady of the USSR Acad. of Sciences 232, No 6, 1296 (1977).
2. Yu. K. Danileiko, A. A. Manenkov, and A. V. Sidorin. "Photoconductivity of Germanium Excited by Pulsed CO_2 Laser Radiation." Phys. and Techn. of Semiconductors 12, 1938 (1978).
3. S. Y. Yuen, R. L. Aggarwal, N. Lee and B. Lax. "Nonlinear Absorption of CO_2 Laser Radiation by Nonequilibrium Carriers in Germanium." Opt. Commun. 28, No 2, 237 (1979).
4. S. Y. Yuen, R. L. Aggarwal and B. Lax. "Saturation of Transmitted Intensity of CO_2 Laser Pulses in Germanium." J. Appl. Phys. 51 (2), 1146 (1980).
5. B. V. Zubov, A. A. Manenkov, V. A. Milyaev, G. N. Mikhailova, T. M. Murina, V. A. Sanina, A. S. Seferov. Solid State Physics (Soviet Journal) 18, 706 (1976).
6. C. R. Phipps, Jr. and S. J. Tomas. Opt. Lett. 1, 97 (1977).
7. Yu. K. Danileiko, A. A. Manenkov, and A. V. Sidorin. "Laser Induced Damage in Semiconductors." Laser Induced Damage in Optical Materials, NBS Spec. Publ. 541 (1978), pp. 305-307.
8. A. S. Epifanov, A. A. Manenkov and A. M. Prokhorov. "Theory of Avalanche Ionization in Transparent Dielectrics in Electromagnetic Field." JETP 70, 728 (1976).

Table 1. Laser Characteristics

Laser	Wavelength (μm)	Pulse width (ns)
TEA CO_2	10.6	60 + 100 (single-mode) 150 (multimode)
$CaF_2.ER^{3+}$	2.76	100
$YAG.ER^{3+}$	2.94	10^5 *)

*)A spiked pulse with the spike width 1.5 μm.

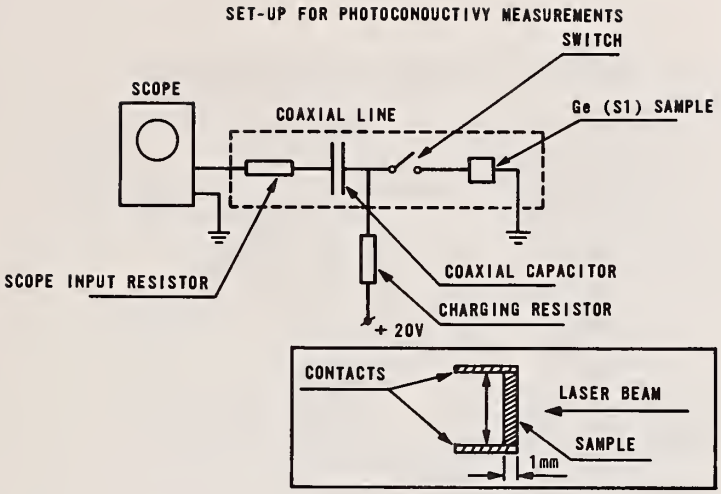

Figure 1. Schematic of the experimental arrangement for laser induced photoconductivity measurement in semi-conductors. The laser excitation geometry is shown in the insert.

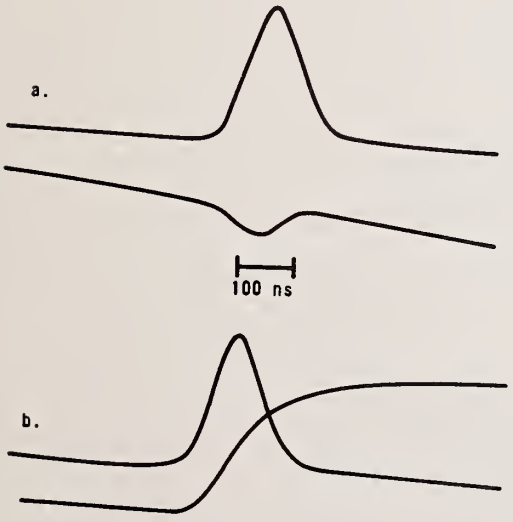

Figure 2. Typical photoconductivity signals (bottom traces) observed in Ge at room temperature, under CO_2 laser excitation at different incident intensities I_i: a) low ($I_i \simeq 0.1$ MW/cm^2); b) high ($I_i \simeq 20$ MW/cm^2). Top traces are the laser pulse shapes.

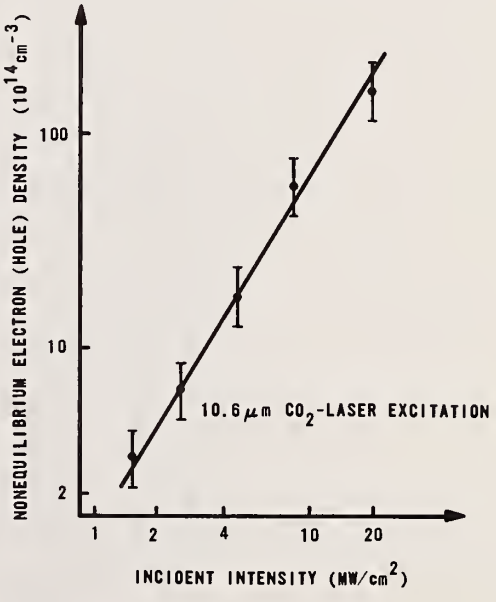

Figure 3. Nonequilibrium electron (hole) density in a pure Ge sample at room temperature versus incident intensity of the exciting CO_2 laser. Experimental data have been obtained from d.c. photoconductivity measurements.

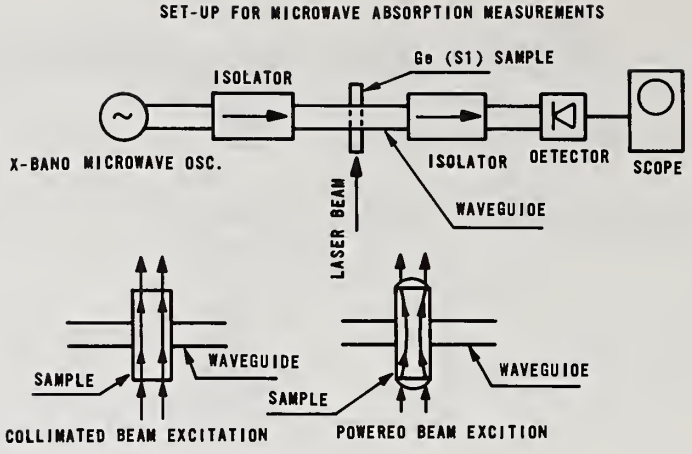

Figure 4. Setup for microwave absorption measurements in semiconductors. Sample excitation geometry for collimated and focused laser beams is also shown.

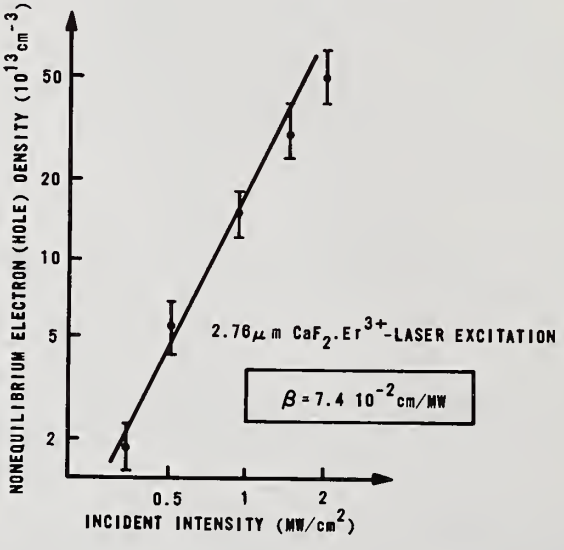

Figure 5. Nonequilibrium electron (hole) density in a pure Ge sample at room temperature versus incident intensity of the exciting $CaF_2.Er^{3+}$ laser. Experimental data have been obtained from microwave absorption measurements. Also shown is the two-photon absorption coefficient β determined from the solid line slope of the carrier density versus incident intensity dependence.

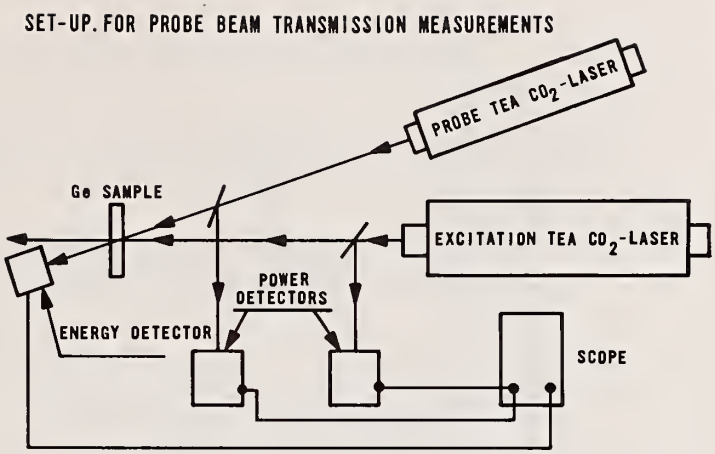

Figure 6. Setup for probe beam transmission measurement.

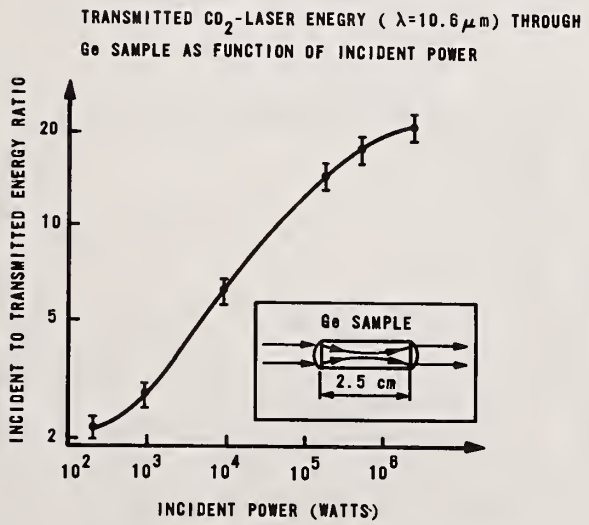

Figure 7. Transmitted CO_2 laser energy (λ = 1.06 μm) through a Ge sample versus incident power. Also shown in Ge sample excitation energy.

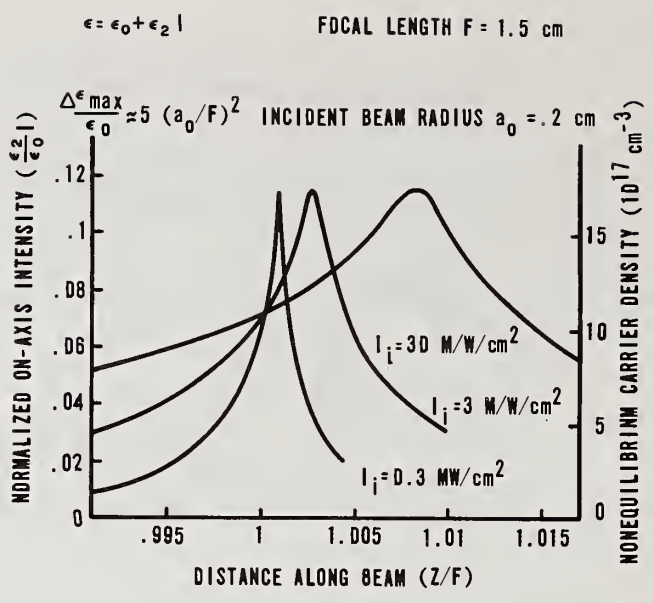

Figure 8. Axial intensity distribution of a focused laser beam in a semiconductor for various incident intensities. Nonequilibrium carrier density corresponding to the intensity dependent dielectric susceptibility indicated on the right vertical axis has been calculated for Ge. Maximum intensity saturation, axial intensity profile broadening, and shift are due to self-defocusing produced by nonequilibrium carriers.

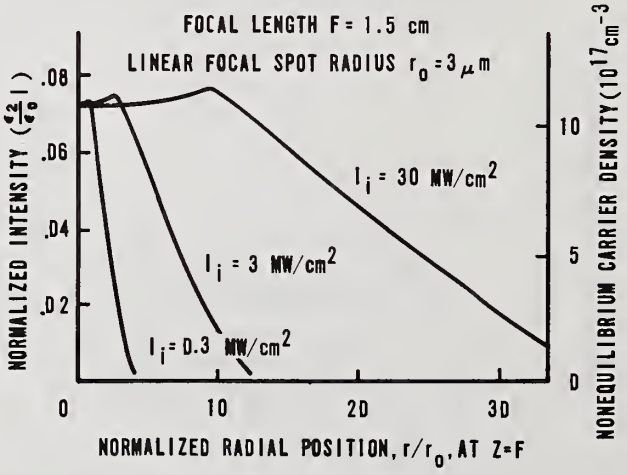

Figure 9. Intensity distribution of the focused laser beam in a semiconductor for various incident intensities. Nonequilibrium carrier density corresponding to the intensity-dependent dielectric susceptibility is indicated on the right vertical axis corresponding to Ge. Maximum intensity saturation and beam radial profile broadening are due to self-defocusing caused by nonequilibrium carriers.

Two-and Three-Photon Absorption in Semiconductors with Subsequent Absorption by Photogenerated Carriers

E. W. Van Stryland, M. A. Woodall,
W. E. Williams, and M. J. Soileau

Center for Applied Quantum Electronics
North Texas State University
Denton, Texas 76203

A careful examination of two-photon absorption in CdTe and three-photon absorption in CdS and ZnSe was made by studying the transmission of picosecond pulses at 1.06 μm and the photoacoustic signal generated in the sample by the absorption of light. We found that in order to separate the direct nonlinear absorption from the subsequent absorption by the photogenerated carriers, careful analysis of the data over a wide range of irradiance levels was necessary. The nonlinear absorption coefficients for these three materials were determined, as well as an overall excess carrier absorption cross section. In addition, for CdTe we used two different temporal pulsewidths to verify our analysis. The photoacoustic data had a 1 to 1 correspondence with the transmission data indicating that this more sensitive technique should be useful for measuring nonlinear absorption spectra in solids with a variety of less powerful lasers. In addition for samples such as BK7 glass, which showed no nonlinear transmission even when surface damage occured, the photoacoustic signal showed abrupt large increases when damage occured. No nonlinear absorption was observed in two types of CVD ZnS prior to damage.

Key Words: nonlinear absorption, photoacoustic, two-photon, three-photon, CdTe, CdS, ZnSe

1. Introduction

Over the past several years there has developed an increased interest in the nonlinear optical properties of semiconductors for use as active elements in integrated optics. Additionally there has been considerable controversy over the initiation process of laser induced damage, multiphoton absorption being a prime candidate for supplying the electrons to start an avalanche [1,2]. As such, the magnitude of 2, 3 and higher order multiphoton absorption processes are of interest. Additionally since selection rules for nonlinear absorption are different than for linear absorption new information on band structure constants are obtained [3,4].

We observed two-photon absorption (2PA) in CdTe by monitoring the transmission and photoacoustic signals using single picosecond 1.06 μm laser pulses [5]. A wide range of irradiance levels was used up to the point at which front surface damage occured. At such high light levels 2PA induced carrier

absorption was the dominant loss mechanism. Even at a relatively low irradiance these excess carriers significantly affected the absorption. We performed these measurements using two different pulsewidths to verify the effects of photogenerated carrier absorption.

Three photon absorption (3PA) in CdS and ZnSe was observed in a similar manner. Again induced carrier absorption was dominant at irradiance levels near those required to produce damage. Nonlinear absorption larger than predicted by 3PA plus induced carrier absorption at high irradiance levels was observed in both samples. No nonlinear absorption was observed in CVD ZnS, either heat treated (Cleartran*) or non-heat treated, or in BK7 glass. A large increase in the photoacoustic signal was observed when the BK7 glass surface damaged. Such a large increase upon damage was not observed in CdTe, CdS, or ZnSe.

2. Theory

The change in light irradiance I of a laser pulse as a function of depth z in a sample which exhibits n-photon absorption is given by

$$\frac{dI}{dz} = -[\alpha I + \beta_n I^n] - \sigma_{ex} N_{ex} I \tag{1}$$

where α is the linear absorption coefficient, and β_n, n = 2, 3, ... is the multiphoton absorption coefficient [6]. (Lower order multiphoton absorption events are neglected whenever $(n - 1)\, h\omega < E_{gap}$ the band gap energy). σ_{ex} is the "mean" linear absorption cross section for multiphoton excited electrons and holes with N_{ex} (the number of multiphoton excited carriers) determined by

$$\frac{dN_{ex}}{dt} = \frac{\beta_n I^n}{nh\omega} \tag{2}$$

Recombination and diffusion during the picosecond pulses are neglected. N_{ex} is assumed negligible prior to the laser pulse. Neglecting the excited state absorption ($\sigma_{ex} = 0$) eq. (1) gives

$$I(L,r,t) = \frac{I(0,r,t)(1 - R)^2 e^{-\alpha L}}{[I + \frac{\beta_2}{\alpha} I(0,r,t)(1 - R)(1 - e^{-\alpha L})]} \qquad \text{for } n = 2 \tag{3}$$

and

$$I(L,r,t) = \frac{I(0,r,t,)(1 - R)^2 e^{-\alpha L}}{[I + \frac{\beta_3}{\alpha} I^2 (0,r,t)(1 - R)^2(1 - e^{-2\alpha L})]^{1/2}} \qquad \text{for } n = 3 \tag{4}$$

where R is the surface reflectivity and I(0,r,t) is the irradiance incident on the front surface of the sample. The effects of rear surface reflections, which can be significant for high index

*Cleartran is a trade name for CVS ZnS used by CVC Inc. Woburn, MA, to describe material which has been made "water clear" by a proprietary heat treatment process.

materials, have been neglected. These effects are discussed in Ref. 8. From eqs. 3 and 4 and similar equations for higher order multiphoton absorption processes it is clear that

$$\frac{1}{T^{n-1}} = T^{1-n} = [1+\frac{\beta_n}{\alpha} I^{n-1}(0,r,t)(1-R)^{n-1}(1-e^{-(n-1)\alpha L})]x\left(\frac{e^{\alpha L}}{(1-R)^2}\right)^{n-1} \quad (5)$$

where T is the transmission through the sample. Thus a plot of T^{1-n} as a function of I^{n-1} yields a straignt line whose intercept determines the linear absorption coefficient α, and whose slope determines the nonlinear absorption coefficient β_n. Integrals over the measured Gaussian spatial and temporal profiles give a negative curvature to these lines. We take the incident irradiance to be $I(0,r,t) = I_0 e^{-(r/r_0)^2} e^{-(t/t_0)^2}$ where r_0 and t_0 are the half width at the e^{-1} height for the spatial and temporal profiles respectively. For n = 2 and 3 the spatial integral can be performed yielding for two photon absorption

$$\frac{1}{T} = \frac{I_0\sqrt{\pi}\beta_2(e^{\alpha L}-1)}{2\alpha(1-R)} \int_0^\infty dx \ell n[1+\frac{\beta_2}{\alpha} I_0(1-R)(1-e^{-\alpha L}) e^{-x^2}]^{-1} \quad (6)$$

and for three-photon absorption

$$\frac{1}{T^2} = \frac{I_0^2 \pi \beta_3(e^{2\alpha L}-1)}{\alpha(1-R)^2}\left\{\int_0^1 \frac{dx}{x\sqrt{\ell n \frac{1}{x}}} \ell n(\sqrt{\delta}\, x + \sqrt{1+\delta x^2})\right\}^{-2} \quad (7)$$

where $\delta = \beta_3 I_0^2(1-R)^2(1-e^{-2\alpha L})/\alpha$.

The increased sensitivity of the photoacoustic (PA) method over transmission has made PA (optoacoustic) spectroscopy extremely useful for the determination of small linear absorptivities (down to 10^{-6} cm^{-1}) [9,10,11]. The increased sensitivity is due to the ability of PA spectroscopy to directly measure the absorbed energy, rather than measure a small change in the large transmitted energy. A similar advantage is incurred for nonlinear absorption measurements, however, the total linear absorption then appears as a background [5,7]. In order to observe the nonlinear absorption it must be comparable to the linear absorption. This restriction limits the applicability to low loss samples, which means that pure materials are needed since the photon energy is below the band-gap energy for multiphoton absorbing samples.

Calculating the energy absorved, E_{abs}, in the sample, which is directly proportional to the PA signal, [10] yields (neglecting rear surface reflections)

$$\frac{E_{abs}}{E_{inc}} = 1 - R \doteq \frac{T}{1-R} \quad (8)$$

where E_{inc} is the energy incident on the sample. Equation 8, of course assumes the fluorescence efficiency is small, as was the case for the semiconductors studied. This equality allows us to predict from the transmission measurements what is expected for the PA measurements. For low total absorption, (i.e. $(\alpha + \beta_2 I)\, L \ll 1$ or $(\alpha + \beta_3 I^2)L \ll 1$ etc.).

$$\frac{1}{T^{n-1}} = [1 + (n - 1)\,\alpha L + (n - 1)\,\frac{\beta_n I_o^{n-1}}{n\sqrt{n}}\,(1 - R)^{n-1}L]/(1-R)^{2(n-1)} \qquad (9)$$

and

$$\frac{E_{abs}}{E_{inc}} = (1 - R)L[\alpha + \frac{\beta_n I_o^{n-1}}{n\sqrt{n}}\,(1 - R)^{n-1}] \qquad (10)$$

showing more explicitly the increased sensitivity of the photoacoustic technique. The term including β_n for the PA method is compared to a term involving α, which can be very small, rather than being compared to unity.

The effects of the absorption of carriers created by nonlinear absorption can be included by numerically solving eqs. 1 and 2 using Gaussian temporal shaped pulses, and then integrating the result over the Gaussian spatial profile. The carrier density is taken to be zero prior to the pulse.

3. Experiment

The laser source used in these experiments was a microprocessor-controlled, mode-locked, Gaussian-mode Nd:YAG laser producing single pulses of up to 10 mJ per pulse at 1.06 μm as shown in figure 1. The pulsewidth was variable between ~30 and 200 psec (FWHM) by choosing various etalons for the output coupler. The temporal waveform was Gaussian as determined by measuring the second harmonic autocorrelation function, accepting only pulses having a fixed ratio R. R is the ratio of the square of the energy in the fundamental to the energy produced at the second harmonic in a doubling crystal. R is measured by the "t_p monitor" in figure 1. This ratio is directly proportional to the pulsewidth as was verified by measuring the second order autocorrelation functions for the various etalons [11,6]. Thus the ratio R served as a single shot pulsewidth monitor. Data was accepted only for pulses having a pulsewidth within ~15% of the stated value as determined by the ratio R. The spatial profile was determined to be Gaussian by performing pinhole beam scans and by observing the irradiance distribution on a vidicon tube. The energy incident and transmitted was monitored with linear photodiode peak and hold detectors directly calibrated against a GenTec Ed-100 pyroelectric detector which was in turn checked against a thermopile calorimeter. The irradiance was calculated from the energy, beam profile, and pulsewidth. Absolute irradiances are estimtated to be correct within ~35% while relative intensity readings are within ~10%.

Since there is a possibility that the spatial beam profile changes within the sample due to self-focusing or defocusing, we checked the transmitted intensity profiles on a vidicon. Although these were not quantitative measurements, no substantial deviation from the expected broadening due to nonlinear absorption was observed.

The acoustic transducers were 4 mm diameter by 4 mm thick lead zirconate titanate cylinders pressed against the sample surface with a thin coat of vacuum grease [10,12]. The acoustic signal was amplified and fed to a gated detector. The gate was set to sample the peak height of one of the first acoustic spikes caused by bulk absorption. The signal peak voltage has been shown to be directly proportional to the energy absorbed by the sample [10]. The signal produced by light scattered directly

onto the transducer was in several cases small compared to the signals of interest. In some cases the scattered signal could not be ignored and gave the appearance of an anamalously large linear absorption. In other cases such as in ZnSe this signal occured long enough prior to the bulk absorption signal that it had substantially decayed.

These experiments were specifically designed to allow simultaneous measurement of transmission and optoacoustic signals so that an absolute calibration and direct comparison was possible. Therefore many of the possible advantages of the optoacoustic method were not used.

4. Results

We present nonlinear absorption data at 1.06 μm in CdTe, CdS, and ZnSe. No nonlinear absorption was observed in CVD ZnS either in its heat treated form (Cleartran) or as deposited. No nonlinear transmission was observed in BK7 glass, but when optical damage occured a very large increase in the photoacoustic signal was observed with only a very slight decrease in transmission.

Figure 2 shows a plot of inverse transmission versus irradiance for relatively low irradiance, 40 psec (FWHM) pulses incident on a 0.30 cm thick polycrystalline CdTe sample. The straight line is a fit using eq. 6 ignoring free carrier absorption. The fit corresponds to β_2 = 35 cm/GW. Bechtel and Smith [6] used a similar technique on single crystal CdTe to obtain a value of 25 cm/GW. We saw no differences in the nonlinear absorption coefficient with slightly thinner single crystal samples. At higher irradiance levels, as shown in figure 3, we see that the data deviates significantly from the solid line which neglects photogenerated carrier absorption. If these excess carriers are included by numerically solving eqs. 1 and 2 and integrating over space and time the dotted line is obtained using a free carrier cross section, σ_{ex}, equal to 2 x 10^{-16} cm^2 (β_2 remains 35 cm/GW). Figure 4 shows that further deviation from simple two-photon absorption theory (solid line) is seen as the irradiance is increased up to the level where permanent optical damage of the front surface occurs. In fact, the optical absorption from the excess carriers dominates the total absorption near damage. The surface damage is not limited by nonlinear absorption but by surface defects as described in Ref. 14. Figure 4 shows an extension of the dotted line of figure 3. There is only a small deviation from the theory at high irradiance levels. At the highest irradiances less than 10% of the incident light is transmitted. This is seen in figure 5 which is a replot of figure 4 now with transmission as the vertical axis. A comparison of figures 4 and 5, for low transmission T, shows that a plot of T^{-1} is more sensitive to the parameters β_2 and σ_{ex} than a similar plot of T. The reasons for the observed deviations are unclear but the theory is certainly oversimplified. The fact that such a good fit is obtained up to 2 GW/cm^2 where the surface damages and where the carrier density is calculated in this model to be 10^{19} $1/cm^3$ is really quite remarkable.

The fits obtained are unfortunately not unique. The method used was to fit the very lowest irradiance ignoring excess carriers to obtain β_2, and then to include photogenerated carrier absorption to fit higher irradiance data. For example, if we use the data of figure 3, ignore carriers and fit this data to obtain β_2, we find β_2 = 50 cm/GW. As shown in figure 6 this fit appears to be quite good over this limited irradiance range. If, however, we now try to add in the effects of photogenerated carriers to explain the higher irradiance data we cannot obtain nearly as good an overall fit. This observation may explain some of the disagreement in reported values for two-photon absorpton coefficients. If a limited range of irradiance is used and excess carrier absorption is not carefully included, different coefficients can be obtained using different pulsewidth lasers. Indeed one might also "observe" a pulsewidth dependence of the nonlinear absorption coefficient as has been reported,

[13] and explained using the above arguement [14]. In order to verify that the deviation from simple two-photon absorption theory was due primarily to subsequent photogenerated carrier absorption we repeated the experiment using 150 psec (FWHM) pulses. This data is shown in figure 7. Again the solid line is two-photon absorption only. The dotted line includes subsequent excess carrier absorption where again β_2 = 35 cm/GW and σ_{ex} = 2 x 10^{-16} cm^2. A comparison with figure 4 shows that for longer pulses more carriers are created and transmission decreases more rapidly. This is expected since for a given irradiance the energy per pulse is larger. The theory includes these effects (dotted line) and again the fit is quite good. This data confirms the previous analysis and shows that near damage the excess carrier absorption dominates the nonlinear absorption even for picosecond pulses. We estimate that the value of β_2 is within 20% and σ_{ex} is within 50%.

We obtain similar results for the three-photon absorbers CdS and ZnSe. Data for CdS is shown in figure 8 for low I and figure 9 for high I. Data for ZnSe is shown in figure 10. Here for three-photon absorption the inverse of the square of the transmission is plotted versus the square of the irradiance as indicated by eq. 7. The increased scatter for the ZnSe data is because three separate sets of data are shown. The apparatus was dissassembled and reassembled between two of the runs. To determine the three-photon absorption coefficient for CdS and ZnSe we used the technique previously discussed for determining two-photon absorption coefficients, namely fitting the low irradiance levels ignoring excess carriers and then including carrier absorption to account for the high irradiance data. For both CdS and ZnSe, however, it was found that the irradiance range over which there was an observable transmission change and a negligible excess carrier contribution to the absorption was extremely limited if not nonexistent. (See Fig. 8) We therefore iterated the procedure using progressively smaller three-photon absorption coefficients and larger free carrier cross sections to obtain a fit over the largest low irradiance range. No combination of these constants could fit the data at the highest irradiance. As was observed with CdTe, the absorption is larger at high irradiance levels than our simple model predicts except that in CdS and ZnSe the deviations are considerably greater. One possible explanation for the deviation is the onset of avalanche breakdown. Additionally very weak second harmonic at 0.53 μm was observed in both ZnSe and CdS [13]. The efficiency was much less than a percent and doesn't account for the observed differences. The constants obtained are, for CdS, β_3 = 0.06 cm^3/GW^2 and σ_{ex} = 1.5 x 10^{-17} cm^2. The estimated errors here are much larger (within a factor of 2 for β_3 and for σ_{ex}) because the nonlinearity is higher order and the separation between the pure three-photon absorption and subsequent carrier absorption is not nearly as clean as for CdTe. For ZnSe we obtained β_3 = 0.01 cm^3/GW^2 and σ_{ex} = 1 x 10^{-17} cm^2. Here β_3 and σ_{ex} are known only within an order of magnitude. A pulsewidth dependent study of the nonlinear transmission is in progress to verify this separation.

In the case of CdS a similar transmission experiment on a 0.1 cm thick CdS sample using 7 psec pulses from a mode-locked Nd:glass laser has previously been reported [16]. If the data of Ref. 17 is replotted as in our figure 9 and the irradiance is scaled down by a factor of ~2.8, that data nearly reproduces our data. The difference in sample thicknesses and the shorter pulsewidths used accounts for only part of the irradiance difference. That data was taken using a mode-locked Nd:glass laser and it was not stated whether the laser was operating in a single transverse mode. Glass lasers are notoriously difficult to operate $TEM_{0,0}$ when mode-locked. Spatial beam inhomogenesities could easily account for a factor of three difference in calculated intensities.

An example of the photoacoustic data is shown in figure 11 for ZnSe. Figure 12 shows what is expected for the photoacoustic data as calculated from the transmission data using eq. 8. The ver-

tical axis of figure 11 was scaled to match that of figure 12. There is a quite good one-to-one correspondence of the data as we reported earlier for two-photon absorption [5]. Data at low irradiances was very noisy both using PA spectroscopy and as calculated from transmission. The deviation at the very highest intensities is probably due to the onset of surface damage. A small pitting of the entrance surface was observed at an incident irradiance of 20 GW/cm^2 (400 GW^2/cm^4 in Fig. 11 and 12). If the light were predominantly scattered, the absorption as measured by the transducer could be reduced more than the transmission. The photoacoustic (optoacoustic) technique, thus yields the same information as the transmission experiment when calibrated. It's increased sensitivity when using lower irradiance and higher repetition rate laser systems should prove valuable in the future for the measurement of nonlinear absorption.

5. Conclusion

The results for two-photon absorption in CdTe indicate that great care must be taken in analyzing nonlinear absorption data. Any direct absorption process in a semiconductor will be accompanied by another higher order absorption process; namely photogenerated carrier absorption. We presented a method to separate the contributions of direct nonlinear absorption from the subsequent multiphoton generated carrier absorption. This method necessitates having data over a wide range of irradiances. Taking data using different laser pulsewidths confirmed the separation to be correct. This separation was shown to be more difficult for higher order nonlinearities by observing three-photon absorption in CdS and ZnSe. In addition, a significant deviation from the simple theory presented at the highest irradiance levels was observed for these materials. A possible explanation is the onset of avalanche breakdown.

All the data indicates that to unambiguously separate the contributions of direct nonlinear absorption from subsequent excess carrier absorption one must use both the shortest possible pulses and the lowest possible irradiance where a signal can still be observed. The photoacoustic technique, used in conjunction with higher repetition rate short pulsed lasers, offers the best possibility of achieving both criteria. In particular we are currently investigating the PA techniques for observing nonlinear absorption of visible light from synchronously pumped mode-locked dye lasers which offer high repetition rate ultrashort pulses.

The authors gratefully acknowledge the support of the Office of Naval Research, the National Science Foundation, The Robert A. Welch Foundation, and the North Texas State Faculty Research Fund.

6. References

[1] See for example, N. Bloembergen, IEEE, J.Q.E. QE-10, 375 (1974), D. W. Fradin, Laser Focus 41, 45 [1974].

[2] E. W. Van Stryland, M. J. Soileau, A. L. Smirl, and William E. Williams, Phys. Rev. B1 23, 1 (1981).

[3] "Two-Photon Spectroscopy" by J. M. Worlock in Laser Handbook V2, 1323-1369, North Holland, 1972.

[4] C. R. Pidgeon, B. S. Wherrett, A. M. Johnston, J. Dempsey, and A. Miller, Phys. Rev. Letters 42, 1785 (19779).

[5] E. W. Van Stryland and M. A. Woodall, NBS Special Publication No. 620, 50, 1980.

[6] J. H. Bechtel and W. L. Smith, Phys. Rev. B13, 3515, 1976.

[7] M. Bass, E. W. Van Stryland, and A. F. Stewart, Appl. Phys. Lett. 34, 142, 1979.

[8] Y. A. Pao, "Opto-acoustic Spectroscopy and Detection", Academic Press 1977.

[9] A. Rosencwaig, "Photoacoustics and Photoacoustic Spectroscopy", Chemical Analysis, Vol. 57, John Wiley, 1980.

[10] C. K. N. Patel and A. C. Tam, Rev. Mod. Phys. 53, 517 (1981).

[11] W. H. Glenn and M. J. Brienza, Appl. Phys. Lett. 10, 221 (1967).

[12] A. Hordvik, and H. Schlossberg, Appl. Opt. 16, 101, 1977.

[13] M. J. Soileau, William E. Williams, E. W. Van Stryland, and M. A. Woodall, submitted for publication in Applied Optics, 1982.

[14] A. F. Stewart and M. Bass, Appl. Phys. Lett. 37, 1040 (1980).

[15] C. R. Pidgeon, A. M. Johnston and J. Dempsey, Proceedings of the 4th International Conference on Physics of Narrow gap Semiconductors, Linz, September 1981.

[16] A. Penzkofer and W. Falkenstein, Optics. Comm. 16, 247 (1976).

Figure Captions

Figure 1. Experimental apparatus for monitoring the transmission and the photoacoustic signal in nonlinearly absorbing samples.

Figure 2. Inverse transmission of 40 psec (FWHM) 1.06 μm pulses as a function of incident irradiance on CdTe. The x's are data and the solid line is a theoretical curve for two-photon absorption with β_2 = 35 cm/GW.

Figure 3. Inverse transmission of 40 psec (FWHM) 1.06 μm pulses as a function of incident irradiance on CdTe. The x's are data and the solid line is a theoretical curve for two-photon absorption with β_2 = 35 cm/GW. The dashed line is a theoretical fit including the effects of excess carrier absorption with $\sigma_{ex} = 2 \times 10^{-16}$ cm^2.

Figure 4. Inverse transmission of 40 psec (FWHM) 1.06 μm pulses as a function of incident irradiance on CdTe. The x's are data and the solid line is a theoretical curve for two-photon absorption with β_2 = 35 cm/GW. The dashed line is a theoretical fit including the effects of excess carrier absorption with $\sigma_{ex} = 2 \times 10^{-16}$ cm^2.

Figure 5. This graph is a replot of figure 4 but with the vertical axis replaced by the transmission.

Figure 6. This graph shows the same data as in figure 2. The solid line is a fit with β_2 = 50 cm/GW where excess carriers are ignored.

Figure 7. Inverse transmission of ~150 psec (FWHM) 1.06 μm pulses as a function of incident irradiance on CdTe. The x's are the data and the solid line is a theoretical curve for two-photon absorption with β_2 = 35 cm/GW. The dashed line is a theoretical fit including the effects of excess carrier absorption with $\sigma_{ex} = 2 \times 10^{-6}$ cm^2.

Figure 8. The inverse of the square of the transmission of 40 psec (FWHM) 1.06 μm pulse as a function of the square of the irradiance on CdS. The x's are data and the solid line is a theoretical curve for a three-photon absorption coefficient of $\beta_3 = 0.06$ cm^3/GW^2. The dashed line is a theoretical fit including the effects of excess carrier absorption with $\sigma_{ex} = 1.5 \times 10^{-17}$ cm^2.

Figure 9. The inverse of the square of the transmission of 40 psec (FWHM) 1.06 μm pulse as a function of the square of the irradiance on CdS. The x's are data and the solid line is a theoretical curve for a three-photon absorption coefficient of $\beta_3 = 0.06$ cm^3/GW^2. The dashed line is a theoretical fit including the effects of excess carrier absorption with $\sigma_{ex} = 1.5 \times 10^{-17}$ cm^2.

Figure 10. The inverse of the square of the transmission of 40 psec (FWHM) 1.06 μm pulses as a function of the square of the irradiance on ZnSe.

Figure 11. The ratio of the photoacoustic signal in volts to the incident energy in Joules as a function of the square of the incident irradiance of 40 psec (FWHM) 1.06 μm pulses on ZnSe.

Figure 12. The vertical axis is what is expected for figure 11 as calculated from the transmission data shown in figure 10. See the discussion in the text.

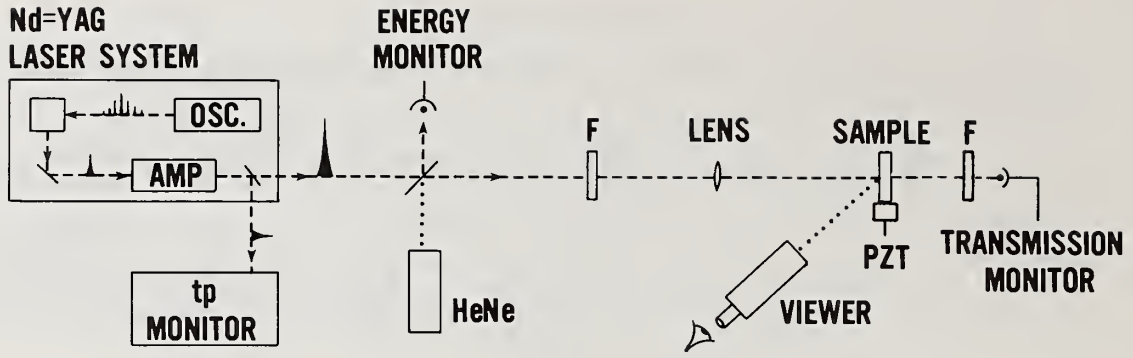

Figure 1

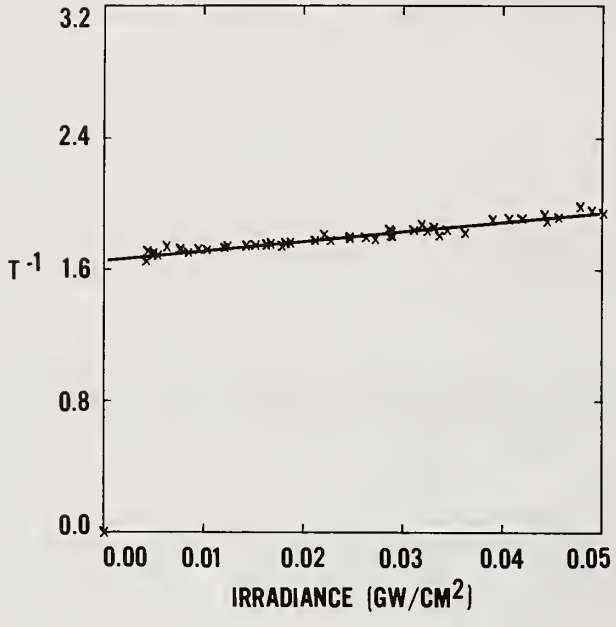

Figure 2

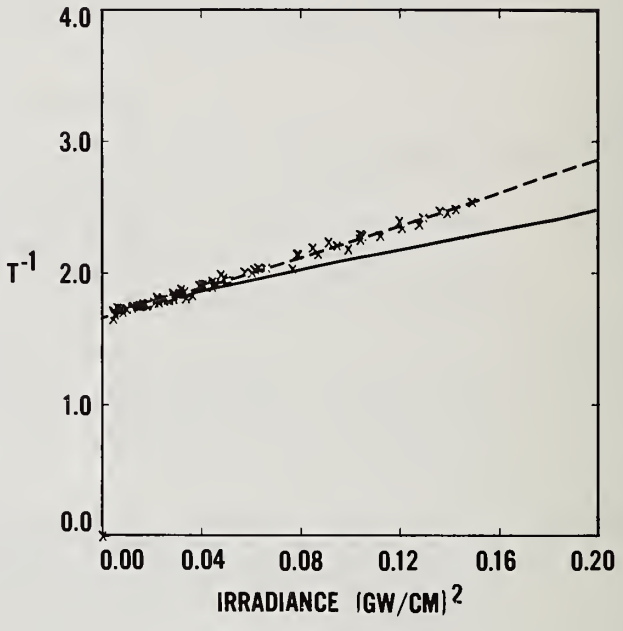

Figure 3

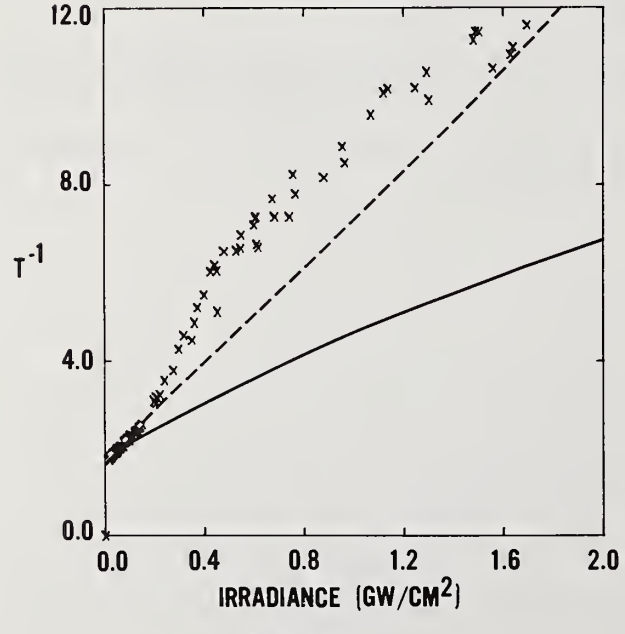

Figure 4

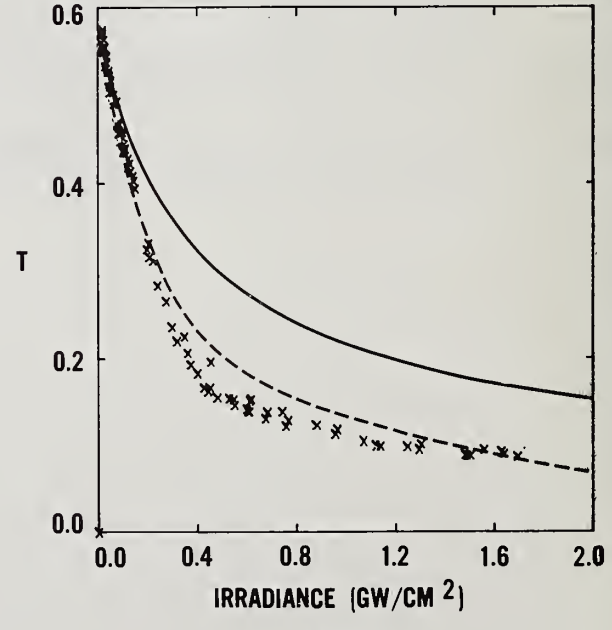

Figure 5

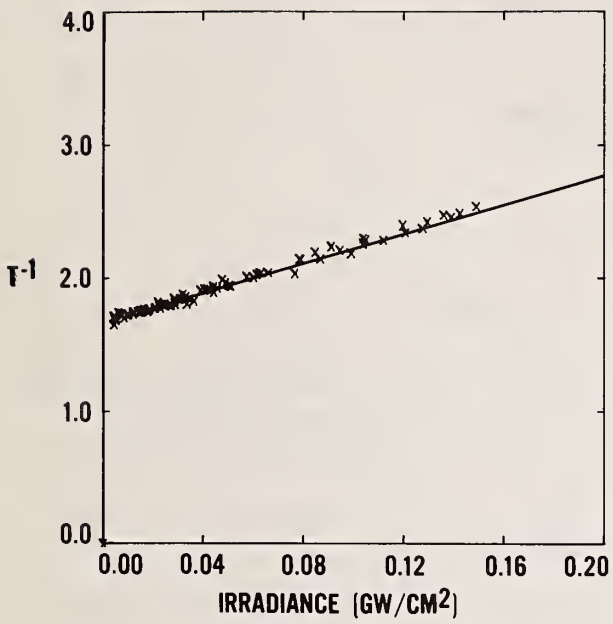

Figure 6

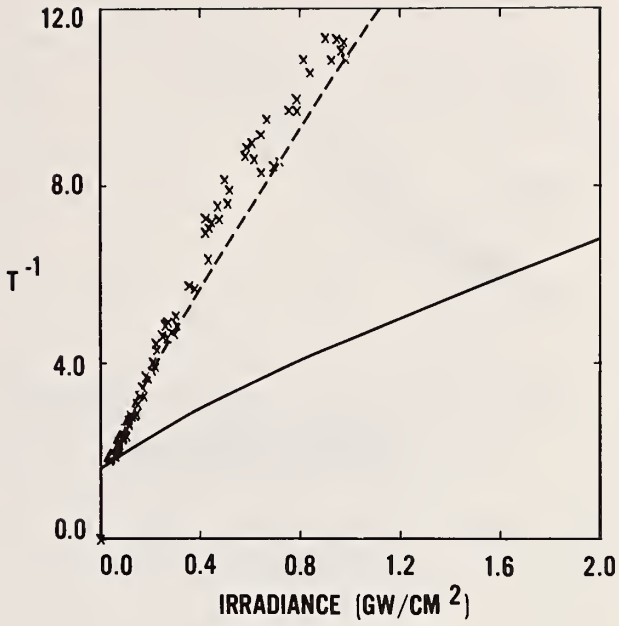

Figure 7

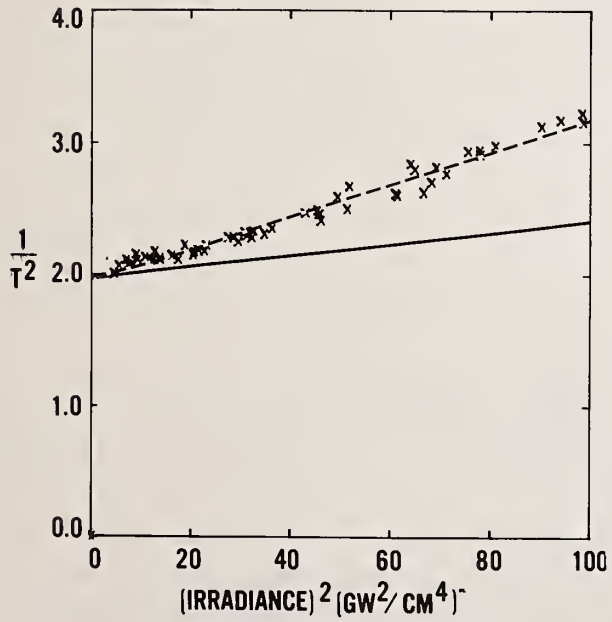

Figure 8

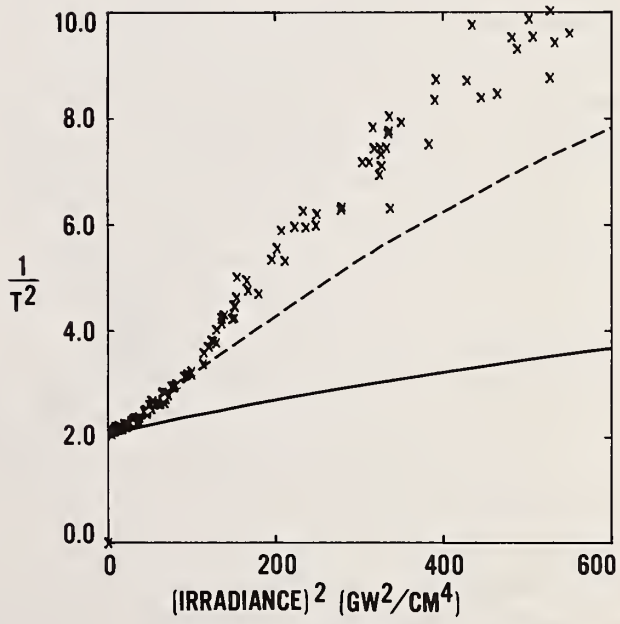

Figure 9

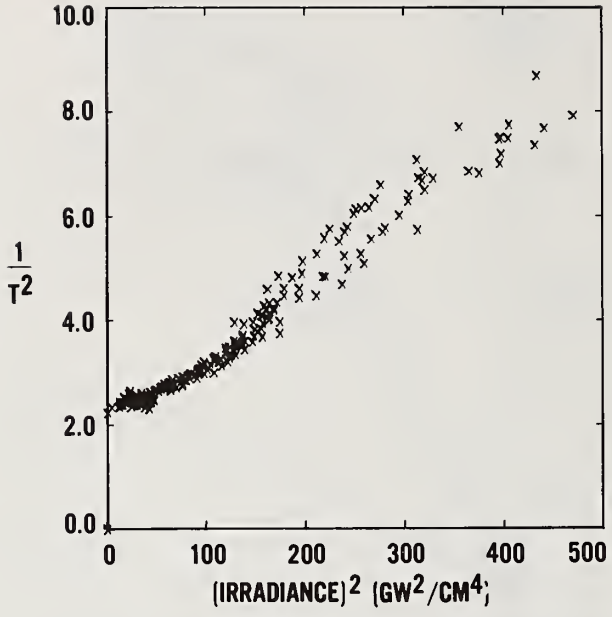

Figure 10

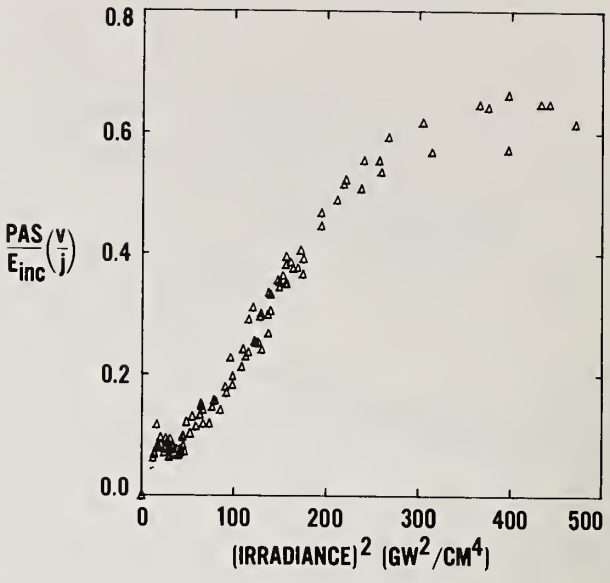

Figure 11

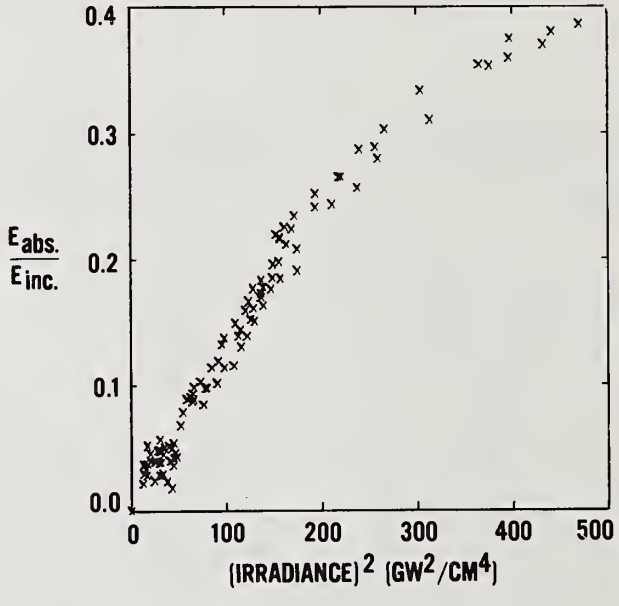

Figure 12

In response to a question, the author pointed out that the index of refraction does change as a function of intensity, probably because of the influence of free carriers. The theory as presented, however, is not sophisticated and includes both holes and electrons, both hot and over a range of temperatures. He expects about $10^{14}/cm^3$ free carriers for the semiconductors tested, but the actual values were not measured. Also, a recent paper by Bloembergen suggests that thermalization can occur between electrons and phonons in 40 ps, the pulse length used. The author pointed out that Bloembergen's paper was controversial, and his predictions were not included in this paper.

Simple Theory of Microwave Absorption in Alkali Halides

M. Sparks, D.F. King, and D.L. Mills*

Scientific Research Center, 1640 Fifth Street, Suite 216, Santa Monica, California 90401

The intrinsic microwave absorption coefficient β of alkali halides is well explained by lifetime-broadened two-phonon difference processes, in contrast to energy-conserving two- and three-phonon processes as previously thought. A simple closed-form expression for β with no adjustable parameters gives excellent agreement with the magnitude, frequency dependence, and temperature dependence of β in NaCl, KBr, and KI. As ω increases from $\omega<\omega_c/3$ to $\omega=\omega_c+\gamma_{293}$, the frequency and temperature dependence of β at 293 K (or 1000 K) change from the low-frequency limit $\beta\sim T^{\ell}\omega^2$ to $\beta\sim T^{h}\omega^{2+}$, where $2.0 \le \ell \le 2.6$ (or $2.2 \le \ell \le 4.0$) and $1.1 \le h \le 1.2$ (or $0.57 \le h \le 1.6$) for the three materials. Here $\omega_c = 20$ cm^{-1} for NaCl is the frequency difference between the transverse-acoustical and transverse-optical phonon modes at the Brillouin zone edge and γ is the combined phonon inverse lifetime at 293 K. The temperature dependence of the phonon frequencies and other parameters must be included in order to explain the temperature dependence of the experimental results. The present lifetime-broadened results agree with previous energy-conservation results (apart from smoothing) and with experimental results in the region $\omega>\omega_c+\gamma$. Previous energy-conserving results disagree with the T and ω dependence and magnitude of the experimental results in the region $\omega<\omega_c$.

Key words: Alkali halides; microwave absorption; multiple-photon absorption.

1. Introduction

Recent advances in the development of high-power microwave sources, motivated by plasma-fusion studies, have renewed interest in the microwave absorption of materials. The heating of windows in microwave systems is a major problem, for example. There have been many theoretical and experimental studies [1-21] of infrared absorption at frequencies both less than and greater than the fundamental reststrahlen absorption frequency. In 1912, Rubens and Hertz [1] measured the absorption of sodium chloride, potassium chloride, and calcium fluoride at 300 μm (33 cm^{-1}) and found that the absorption coefficient β was linear in the temperature T. Based on Ewald's [2] suggestion in 1922 that the absorption may be caused by anharmonic interactions between the radiation and thermal lattice vibrations, the linear temperature dependence of β at frequencies not too far below the fundamental frequency is now well understood as two-phonon difference absorption. [3,4,5,6]

As a result of their measurements of the microwave absorption of alkali halides at temperatures from 15 K to room temperature and wavelengths from 0.3 to 1 mm, Stolen and Dransfeld [3] suggested that the well-known two-phonon difference absorption (with absorption coefficient $\beta\sim T$) became negligible at frequencies below a critical frequency ω_c and that three-phonon absorption (with $\beta\sim T^2$) became dominant at $\omega < \omega_c$. They envisioned that ω_c was the frequency difference between an optical phonon mode and an acoustic phonon mode at a Brillouin-zone boundary, and that transitions between the closer spaced (lower frequency-difference) acoustic modes were not allowed.

Stolen and Dransfeld also suggested that lifetime-broadened two-phonon difference processes could contribute to the absorption at frequencies lower than ω_c. However, they neglected lifetime broadening, based on the argument that the absorption coefficient at frequencies removed from the center frequency of a group of transitions is much smaller than the absorption at the center frequency. This view that two- and three-phonon processes without lifetime broadening determined the intrinsic microwave absorption of alkali halides has been generally accepted. However, there has

not been a detailed comparison between experiment and theory for the amplitude, temperature dependence, and frequency dependence of the microwave absorption coefficient to test this view.

Recently, Mills [4] showed that the rough argument of Stolen and Dransfeld was not sufficient to show that lifetime-broadened two-phonon processes were negligible. He calculated the absorption coefficient for these processes and showed explicitly that they were non-negligible and that both the lifetime-broadened two-phonon difference processes and the three-phonon difference processes gave $\beta \sim T^2$ in the high-temperature long-wavelength limit for the alkali halides.

Eldridge and coworkers [11-13] included lifetime broadening by a formal smearing of β, which was sufficient for their purpose--to show that lifetime broadening removed fine structure in β in the infrared region. However, the smearing method fails in the microwave region, giving incorrect magnitude, frequency dependence, and temperature dependence of β, as discussed in section 3.

In the present paper, Mills' results for the lifetime-broadened two-phonon difference process are refined by using more accurate approximations and including the temperature dependence of the phonon frequencies and other parameters. The theory is also extended to include the corresponding results for energy-conserving two-phonon difference processes. The results which differ from Mills' results, particularly in the temperature dependence of β, are in excellent agreement with experimental results for the magnitude, temperature-dependence, and frequency-dependence of the microwave absorption coefficient for the alkali halides with no adjusted parameters. The transition from the lifetime-broadened two-phonon difference-band results to the previous energy-conserving two-phonon difference-band results is shown to occur at a frequency near the critical frequency ω_c.

In the limit of infinite phonon lifetimes, the present theory is formally the same as previous theories of two-phonon absorption, except that the temperature dependences of the phonon frequencies and other parameters are included in the present theory. The numerical results from the present and previous computations in the region $\omega > \omega_c$ differ slightly because the temperature dependence of the parameters is included in the present theory, the methods of evaluating the Brillouin-zone summations (in eq (8) below) are different, and the explicit inclusion of phonon lifetime effects here is different from the tacit and explicit inclusion in other computations. The effects of including phonon lifetimes are much less important in the region $\omega > \omega_c$ than in the region $\omega < \omega_c$. The results of the present and previous computations in the region $\omega < \omega_c$ are, of course, quite different in general.

Detailed numerical computations [11-14] of two- and three-phonon absorption in alkali halides have been performed for the infrared region (from 0 to 500 cm^{-1} for sodium chloride, for example). Unfortunately, these results generally cannot be extended to the microwave region, and the microwave results usually cannot be obtained from the extreme ends of the infrared curves. Phonon-lifetime broadening has been neglected in most cases, except as discussed in section 3.

Three types of two-phonon difference-band processes are important. As illustrated in figure 1, the first is the usual two-phonon difference-band process in which energy and wavevector are conserved. This E (energy-conserving) process is important at infrared frequencies. The second process D is the annihilation of a phonon, accompanied by the annihilation of a phonon i on branch i and the creation of a second phonon j on a different branch j. This D (different-branch) process is important in the microwave region for such crystals as sodium chloride with the rocksalt structure for which every ion is at a site of inversion symmetry. The third process S is the same as D, except that the annihilated phonon i and the created phonon i are on the same branch i. This S (same branch) process is important in the microwave region for such crystals as gallium arsenide with the zincblende structure, for which each ion is not at a site of inversion symmetry. The energy-conserving process in which phonons i and j are on two different but closely spaced acoustical branches, with microwave frequency $\omega = \omega_j - \omega_i$ (not shown on fig. 1), contributes to the microwave absorption in zincblende-structure crystals, but not in rocksalt-structure crystals.

The absorption coefficients for the E and D processes are derived from a single simple model in section 2. We believe that the model contains the essential physical effects of two-phonon difference-band absorption in the microwave and infrared regions. The agreement between theory and experiment is extremely good, especially in view of the model's simplicity.

The critical frequency ω_c is not the usual "gap" corresponding to the region of no phonon modes between the acoustical modes and optical modes of such widegap materials as potassium iodide. Rather, ω_c is the frequency difference between the optically active phonon modes at high density-of-states regions of the Brillouin zone. The strongest, lowest-frequency transitions govern the choice of ω_c. In potassium iodide, for example, there are strong transitions [12] at ω slightly greater than 40 cm^{-1} from the regions near L_3 to L_3' (transverse acoustic to transverse optic, at the Brillouin-zone boundary along the (111) axis, with ω = 42 cm^{-1}), Σ_4 (acoustic) to Σ_4 (optic) (three-quarters of the way between Γ and K along (110), with ω = 42 cm^{-1}), and W_1 to W_2' (at the W boundary, with ω = 46 cm^{-1}). Such lower-frequency transitions as Σ_1 (LA)-Σ_4 (TO), with ω = 30 cm^{-1} and Σ_1 (LA)-Σ_4 (TA), with ω = 12 cm^{-1}, are much weaker than the three transitions above with ω = 42, 44, and 46 cm^{-1}. Thus we chose ω_c = 42 cm^{-1}. This choice is reasonable, as seen in figure 1 of reference 12 which shows a sharp drop in Γ as ω decreases through the value ω = 42 cm^{-1}.

Similar examination of the phonon dispersion relations in other alkali halides indicates that taking ω_c as the frequency difference between the transverse-acoustic and transverse-optic frequencies at the Brillouin-zone boundary along the (111) direction is a reasonable choice. Values of ω_c for the materials considered are listed in table 1.

A complete analysis using a state-of-the-art eleven-parameter phonon-dispersion model and numerical computation of the Brillouin-zone summation by Subbaswamy, Mills, Sparks, and King [22] is currently underway. The accuracy of the results may not be significantly greater than the accuracy of the present results obtained from the simple model because the lifetimes of the phonon modes (all of which are used in the numerical computation) are not well known. Nevertheless, it is anticipated that the complete analysis will support the results of the present simple model, which can then be used with greater confidence for developing intuition, scaling, and obtaining values of β without elaborate numerical computation.

The relations between the absorption coefficient β, the imaginary part κ of the index of refraction $n_r + i\kappa$, the imaginary part ε_I of the dielectric constant $\varepsilon_r + i\varepsilon_I$, the loss tangent $\tan\delta = \varepsilon_I/\varepsilon_r$, and the conductivity σ are as follows:

$$\beta = 2\,(\omega/c)\kappa = (4\pi/\lambda)\kappa = 4\pi\kappa\omega(cm^{-1}) \tag{1}$$

$$\beta = (\omega/c\ \varepsilon_r^{1/2})\ \varepsilon_I, \qquad \text{for } \varepsilon_I << \varepsilon_r \tag{2}$$

$$\beta = (\varepsilon_r^{1/2}\ \omega/c)\ \tan\delta \cong k_{med}\ \tan\delta, \qquad \text{for } \varepsilon_I << \varepsilon_r \tag{3}$$

$$\beta = (4\pi/n_r c)\sigma \tag{4}$$

where ω is the frequency of the driving electromagnetic field, c is the velocity of light, and $k_{med} = n_r k_{vac} = 2\pi n_r/\lambda_{vac} = n_r\omega/c$ is the wavelength in the dielectric medium. The relative frequency dependences of these parameters from eq (1) through (4) are as follows:

$$\Gamma \sim \tan\delta \sim \kappa \sim \varepsilon_1 \sim \beta/\omega \sim \sigma/\omega. \tag{5}$$

Some authors use γ, defined as

$$\gamma \equiv (\omega_f/\omega)\Gamma \qquad \text{or} \qquad 2(\omega_f/\omega)\Gamma \tag{6}$$

rather than Γ, and some authors [13] use $2\Gamma_{ES} = \Gamma$.

The contents of the paper are as follows: 1. Introduction; 2. Model and Calculation; 3. Discussion of Results; and Acknowledgments.

2. Model and Calculation

The fundamental reststrahlen transverse-optical phonon, which is driven by the electromagnetic field, behaves as a harmonic oscillator. Thus, the energy absorption is determined by the loss factor (relaxation frequency Γ) of the fundamental reststrahlen transverse-optical phonon. Since this oscillator is driven far off resonance (microwave frequencies very much less than the oscillator frequency ω_f), it is essential to treat the frequency dependence of Γ. The dominant contribution to Γ in the microwave region is the process marked D in figure 1 and discussed in section 1.

For materials with the rocksalt or zincblende structure, it is not difficult to show that if the contribution from the second-order dipole moment is ignored, the value of the absorption coefficient is given by

$$\beta = \frac{(\varepsilon_0 - \varepsilon_\infty)}{c\varepsilon_0^{1/2}} \frac{\omega_f^3 \omega\Gamma}{(\omega^2 - \omega_f^2)^2 + (\omega_f\Gamma)^2} \tag{7a}$$

$$\cong (\varepsilon_0 - \varepsilon_\infty)\, \omega\Gamma/c\varepsilon_0^{1/2}\omega_f, \qquad \text{for } \omega << \omega_f. \tag{7b}$$

where ε_0 and ε_∞ are the real parts of the dielectric constant for $\omega << \omega_f$ and $\omega_f << \omega << \omega_{\text{electronic}}$, respectively.

The golden-rule expression for the rate of change of the number of transverse-optical phonons n_f is

$$dn_f/dt = \sum_{n_i, \underset{\sim}{k}_i} \sum_{n_j, \underset{\sim}{k}_j} (TP_+ - TP_-) \tag{8}$$

where n_i and n_j are phonon branches, $\underset{\sim}{k}_i$ and $\underset{\sim}{k}_j$ are phonon wavevectors, and $TP_\pm$ are the transition probabilities for n_f to increase by one (+) or decrease by one (-). That is,

$$TP_\pm = (2\pi/\hbar)|\langle n_f \pm 1|H|n_f\rangle|^2 \delta(E), \tag{9}$$

where the argument of the energy-conservation δ function is

$$E = \hbar\omega - \hbar\omega_{ji}, \qquad \omega_{ji} \equiv \omega_j - \omega_i, \tag{10}$$

and H is the anharmonic-lattice-potential Hamiltonian. Equation 8 is reduced to the form in which n_f relaxes to its thermal-equilibrium value $\bar{n}_f$ by a standard procedure [23] $dn_f/dt = -\Gamma(n_f - \bar{n}_f)$,

where Γ is the relaxation frequency given by the expression

$$\Gamma = (36N_B V_S/\pi\hbar) \int_0^{k_{BZ}} dk\, k^2 V_{fij}{}^2 \delta(E)\, (\bar{n}_i - \bar{n}_j) \tag{11}$$

The integral in eq (11) can be approximated and evaluated in a way that gives both the standard results in the energy conservation limit of case E and the new results for the lifetime-broadened case D. The transverse-acoustical phonon frequency is approximated by

$$\begin{aligned} \omega_i &= \omega_m(k/k_{BZ}), && \text{for } \omega > \omega_c \\ &= \omega_m, && \text{for } \omega < \omega_c \end{aligned} \tag{12}$$

where ω_m is the value at the zone boundary along the (111) direction. The transverse-optical frequency is approximated by

$$\begin{aligned} \omega_j &= \omega_f - (k/k_{BZ})(\omega_f - \omega_m - \omega_c), && \text{for } \omega > \omega_c \\ &= \omega_m + \omega && \text{for } \omega < \omega_c \end{aligned} \tag{13}$$

The value of k corresponding to energy conservation (that is, for $\omega = \omega_{ji}$) is

$$\begin{aligned} k_0 &= k_{BZ}\, (\omega_f - \omega)/(\omega_f - \omega_c) && \text{for } \omega > \omega_c \\ &= k_{BZ} && \text{for } \omega < \omega_c. \end{aligned} \tag{14}$$

The second equality, for $\omega < \omega_c$, does not come from the energy conservation condition, but it is defined for later convenience.

Using $\omega_j = \omega_m + \omega$, rather than $\omega_j = \omega_m + \omega_c$, for the case of $\omega < \omega_c$ is dictated by the results of a complete diagrammatic treatment of Γ, which shows that a good approximation is to replace both phonons by Lorentzian distributions and retain the energy-conserving delta functions. Thus, depending upon the relative widths of the two distributions, the actual frequency will be closer to either $\omega_m + \omega$ for a narrower ω_i distribution or $\omega_m + \omega_c - \omega$ for a narrower ω_j distribution. Since the lower branch ω_i tends to the narrower, we use $\omega_m + \omega$. In any case, there is little difference between the two for crystals for which $\omega_c \ll \omega_m$ ($\omega_c = 20$ cm^{-1} and $\omega_m = 115$ cm^{-1} for sodium chloride, for example).

The occupation number factor $\bar{n}_j - \bar{n}_i$ in eq (11) is

$$\tilde{n} \equiv n_i - n_j = n(\omega_i) - n(\omega_i + \omega)\,. \tag{15}$$

The lifetime broadening of the phonon modes is taken into account formally by replacing the δ function $\delta(E)$ in eq (11) by a normalized Lorentzian function

$$\delta(E) \to L(E) \equiv \frac{\gamma/\pi\hbar}{(\omega_{ji} - \omega)^2 + \gamma^2}\,, \tag{16}$$

where γ is the combined relaxation frequency of the phonon modes i and j, $(\gamma_i + \gamma_j)$. Substituting

eq (16) into eq (11), using the approximations in eqs (13) and (14), and changing the variable of integration yields [23]

$$\Gamma = \int_{\omega_c}^{\omega_f} d\omega_{ji}\, g(k,\omega)\, \frac{\gamma/\pi\hbar v_l}{(\omega_{ji} - \omega)^2 + \gamma^2} \,. \tag{17}$$

where $g(k,\omega) = 36 N_B V_S k^2 V_{fij}^2\, \tilde{n}/\pi\hbar$.

For $\omega \gtrsim \omega_c + \gamma$ and $\gamma << \omega_f$, the narrow Lorentzian in eq (16) picks out the value of the integrand $g(k,\omega)$ at $\omega = \omega_{ji}$ (that is, $k = k_{BZ}(\omega_f - \omega)/(\omega_f - \omega_c)$), which gives the energy-conserving result $\Gamma = \Gamma_E$. For $\omega = \omega_c$, half the Lorentzian lies outside the range of integration ω_c to ω_f; thus $\Gamma = \Gamma_E/2$ at $\omega = \omega_c$. For $\omega < \omega_c$, the tail of the Lorentzian function extends into the integration region and Γ decreases as ω decreases. In evaluating the integral of eq (16), the approximation $g(k,\omega) = \langle g(k,\omega)\rangle = 1.5\, g(k_0,\omega)$ is used. This is a good approximation in the microwave region ($\omega \leqslant 30$ cm^{-1}), as can be verified by numerical integration of the exact and approximate expressions. the maximum error, which occurs at the peak near $\omega = 70$ cm^{-1} (outside of the microwave range), is a factor of ~ 1.5. Using the above approximation, eq (16) gives the central result [23]

$$\Gamma \cong [1.5 g(k_0,\omega) k_{BZ} \gamma/\pi h(\omega_f - \omega_c)] \int_{\omega_c}^{\omega_f} d\omega_{ji} [(\omega_{ji} - \omega)^2 + \gamma^2]^{-1}$$

$$= (2/\pi)\, \Gamma_0 \left(\tan^{-1} \frac{\omega_f - \omega}{\gamma} - \tan^{-1} \frac{\omega_c - \omega}{\gamma} \right) \tag{18a}$$

$$\cong \Gamma_0 = \Gamma_E/2, \qquad \text{for} \quad \omega = \omega_c \tag{18b}$$

$$\cong \Gamma_E, \qquad \text{for} \quad \omega_f - \omega >> \gamma, \quad \omega - \omega_c >> \gamma \tag{18c}$$

where

$$\Gamma_0 = \frac{1.5 g\,(k_0)}{2h v_l} = \left(\frac{27 N_B V_{fij}^2 V_s K_0^2 n}{\pi h^2 v_l} \right)_{k = k_0} \tag{19a}$$

$$= \Gamma_\infty \tilde{n} \left(\frac{k_0}{k_{BZ}} \right)^2 \left(\frac{\omega_m^3}{\omega_i \omega_j (\omega_f - \omega_c)} \right) \sin^2 \pi k_0/2k_{BZ} \tag{19b}$$

with

$$\Gamma_\infty = \pi N_B h \phi_3^2/6 M_r M_< M_> \omega_f\, \omega_m^3 . \tag{19c}$$

The values of the parameters used in the calculations are listed in table 1. Studies by Eldridge and coworkers [11,12,13] were an important source of comparison data, and their parameter values were used whenever possible. Values of the phonon frequencies ω_c, ω_m and ω_f were determined from the dispersion relations tabulated in reference 11 and scaled to room temperature, where necessary.

Values of γ and its temperature dependence are difficult to estimate accurately because there is a paucity of experimental data and the value of γ is an average over all phonons contributing to β. Fortunately, the room-temperature values of β are somewhat insensitive to changes in γ from the values used in the calculations [23]. For values of γ much smaller than ω_c, Γ reduces to the energy-conservation value g in eq (17) because a very narrow Lorentzian is a representation of the delta function. From these considerations and the discussion of the values of γ below, the errors in β resulting from the uncertainties in the values of γ are not expected to exceed a factor of two in general.

The value $\gamma = 18\ cm^{-1}$ used in the present calculations for sodium chloride was chosen as a compromise between the following values: $\gamma = 2\gamma_i = 4\gamma_{iES} = 12\ cm^{-1}$, where γ_i is the relaxation frequency of one of the two phonons, from Eldridge and Staal [13] (with one factor of two coming from the two phonons and one factor of two coming from the different definition of their relaxation frequency mentioned at the end of section 1); $\gamma = 2\gamma_i = 20\ cm^{-1}$ as a typical value from estimates based on thermal conductivity data [24]; and $\gamma = 2\gamma_i = 40\ cm^{-1}$ as a typical value from quality factors $Q = \omega_{res}/\gamma \cong 8$ from neutron scattering in alkali halides [25-27].

In order to be consistent from one material to another, the values of γ for lithium fluoride, potassium bromide, and potassium iodide in table 1 were obtained by scaling from the sodium chloride value of $\gamma = 18\ cm^{-1}$, assuming constant quality factors. For example,

$$\gamma_{LiF} = \gamma_{NaCl} \frac{[\omega_m + (\omega_m + \omega_c)]_{LiF}}{[\omega_m + (\omega_m + \omega_c)]_{NaCl}} = 37\ cm. \qquad (20)$$

This value $\gamma = 37\ cm^{-1}$, although possibly somewhat low, is reasonable in view of the following neutron-scattering values [26]: $\gamma = 2\ (44.3) = 88.6\ cm^{-1}$ $(Q = 6.9)$ for Γ'_{15} (TO); $\gamma = 2\ (15) = 30\ cm^{-1}$ $(Q = 13.1)$ for Σ_3 (TA); and $\gamma = 2\ (57) = 113\ cm^{-1}$ $(Q = 11.2)$ for Σ_1 (LO). Although using the smaller value $\gamma = 20\ cm^{-1}$ improves the agreement with experiment, as seen in figure 13, unadjusted values of γ are used for all materials.

The resulting value $\gamma = 11.4\ cm^{-1}$ from eq (20) for potassium bromide is reasonable, though perhaps somewhat low, in view of the following neutron scattering results [25]: $\gamma = 2\ (12) = 24\ cm^{-1}$ $(Q = 7.8)$ for L_1 (LA), and $\gamma = 2\ (12) = 24\ cm^{-1}$ $(Q = 9.2)$ for Γ'_{15} (TO). The resulting value $\gamma = 10\ cm^{-1}$ for potassium iodide is reasonable in view of the neutron scattering result [27] $\gamma = 2\ (4.2) = 8.4\ cm^{-1}$ $(Q = 24$ for Γ'_{15} (TO) and the corresponding experimental value $\gamma = 2\ (3.4) = 7\ cm^{-1}$ $(Q = 29)$.

3. Discussion of Results

Figures 2 through 8 display values of β calculated using eqs (18a) and (7a), along with experimental data from several sources. The materials, lithium fluoride, sodium chloride, potassium bromide, and potassium iodide, were selected to give a large amount and a wide range of experimental results and a large range of values of ω_c, including one material, potassium iodide, with an actual wide gap. The agreement between theory and experiment is excellent, especially in view of the model's simplicity and the fact that no parameters were adjusted. The only cases in which a factor of two or less agreement is not achieved are for sodium chloride and potassium bromide at $\omega = 0.28\ cm^{-1}$. It is not surprising that the experimental values of β are greater than the theoretical values when the intrinsic value is small because it is likely that extrinsic absorption processes also contribute to β.

The absorption coefficient is quadratic in the frequency, $\beta \sim \omega^2$, for $\omega \leq \omega_c/3$, as seen in figure 2 (with $\beta \sim \Gamma\omega$ for $\omega << \omega_f$) and in figures 3, 4, and 5. At greater frequencies, $\omega > \omega_c/3$, β increases more rapidly than the quadratic, low-frequency behavior. At still greater frequencies, the frequency dependence of β becomes more complex, being determined by the frequency dependence of Γ illustrated in figure 2. The three-phonon contribution to Γ, calculated by Eldridge and Staal [13] is seen to be negligible at microwave frequencies $\omega < \omega_c$.

In calculating the temperature dependence of β, simple linear temperature scaling was used on the parameters a_{nn}, B, ϕ_3, ω_f and ω_m. Values of the parameters and their temperature derivatives are listed in table 1. At low temperatures ($T \leq \hbar\omega_f/2k_B$, roughly) the flattening of the parameters with decreasing temperature should be taken into account. Since ω_c is the difference between the two phonon branches on which ω_f and ω_m are located, this parameter was kept constant. If we assume that the neutron scattering linewidths correspond to phonon inverse lifetimes, some γ_i's appear to be relatively temperature independent. However, the γ_i's are expected to be proportional to T theoretically. It is possible that the temperature independence is an artifact of the experiments.

In view of the uncertainty in the frequency dependence of γ, two curves are thus displayed for each value of ω--a solid curve for $\gamma = \gamma_{293}$, and a dashed curve for $\gamma = \gamma(T)$, where γ was scaled linearly between the room temperature value γ_{293} and $\gamma = 0$ at absolute zero. Apart from a few exceptions, such as potassium bromide at $\omega = 11.1\ cm^{-1}$ and $T < 150$ K in figure 7 and potassium iodide at $\omega = 20\ cm^{-1}$ in figure 8, the experimental data fit the curves with $\gamma = \gamma_{293}$ better than the curves with $\gamma \sim T$. In many cases, such as $T > 293$ K and $\omega \geq \omega_c$, the differences between the two cases become much less pronounced, so that distinguishing between the two is difficult.

This simple treatment of the implicit temperature dependences gives excellent agreement with experimental results, as seen in figures 6, 7, and 8. Values of the local power-law exponent m, which is the exponent in the expression $\beta \sim T^m$ for the tangent to the $\beta(T)$ curve are listed in table 2 for T = 293 K and 1000 K. The slope of the curve of log β as a function of log T is also equal to m. Room-temperature (or 1000 K) values of m at the low frequency, $\omega = 1.18\ cm^{-1}$ range from m = 2.0 to 2.6 (or m = 2.2 to 4.0) for the three materials. As the frequency is increased to the energy conservation range, the slope decreases, reaching the values m = 1.1 to 1.2 (or 0.6 to 1.6) at $\omega = \omega_c + \gamma_{293}$. Values of m at the intermediate frequencies $\omega_c/2$ and ω_c are included in the table. The slope m increases as the temperature increases above 293 K, as seen in table 2 and in figures 6, 7, and 8.

Including the temperature dependence of the parameters (listed above), in addition to the explicit temperature factor T in $\bar{n}_j - \bar{n}_i$ in eq (15), greatly improves the agreement between the theoretical and experimental temperature dependences of β in the microwave region $\omega < \omega_c$ [23]. It was also necessary to include the temperature dependence of the parameters to explain the temperature dependence of the infrared multiphonon absorption [28].

As the temperature or frequency decreases, the intrinsic absorption decreases. At sufficiently small intrinsic absorption, any extrinsic absorption becomes observable. The good agreement between experiment and the intrinsic-absorption theory in figures 3 through 8 suggests that the absorption in these figures is intrinsic, except for the value $\beta \cong 10^{-3} cm^{-1}$ at $\omega = 0.28\ cm^{-1}$ observed for both sodium chloride and potassium chloride.

Next, consider the difficulties encountered in formally extending previous infrared theories to the microwave region. Phonon lifetimes were taken into account in reference 13 by first calculating the relaxation frequency (Γ in eq (11)) in the absence of phonon-lifetime effects and then smearing out the resulting $\Gamma(\omega)$ curves over a frequency range corresponding to the phonon inverse lifetime. Although this procedures does illustrate that the fine structure in $\Gamma(\omega)$ in the infrared region is removed by finite phonon lifetimes, it yields incorrect results in the microwave region. For example, the smearing-out procedure gives nonzero Γ at $\omega = 0$, which is known to be incorrect by quite general arguments. The corresponding frequency dependence $\beta \sim \omega$ at low frequencies is also incorrect. The correct low-frequency dependence is $\beta \sim \omega^2$. Furthermore, the temperature dependence obtained by the smearing-out procedure -- $\beta \sim T$, roughly, in the microwave region--is incorrect.

Another example of the difficulties in extending calculations that were made for the infrared region to the microwave region is that numerical computations of β in the absence of explicit lifetime broadening introduce a lifetime-broadening type of effect by bin-size effects or by the representation used for the energy-conservation δ-function. In general this tacit inclusion of lifetime broadening gives incorrect results. For instance, using a square-wave representation of the δ-function does not account properly for the wings of the broadened phonon states. Also, the values of lifetimes included in this manner are generally incorrect.

Finally, consider the agreement between experiment and previous theories. Based on three-phonon absorption for $\omega < \omega_c$ and two-phonon absorption for $\omega > \omega_c$, Stolen and Dransfeld [3] predicted that $\beta \sim T^2$ should hold at high temperatures for $\omega < \omega_c$ and that β should drop sharply at $\omega = \omega_c$ as the frequency decreases. Both predictions disagree with experimental results. The temperature dependence is not $\beta \sim T^2$ for $\omega < \omega_c$, as discussed above. There is no decrease in β at ω_c as ω decreases corresponding to the transition from two-phonon to three-phonon absorption, as seen in figures 3 through 5.

There are many examples in figures 2 through 8 of this poor agreement between experiments and the previous theories. For example, the temperature dependence $\beta \sim T^{4.0}$ for potassium bromide at $\omega = 1.18$ cm^{-1} at the high-temperature end of the curve in figure 7 disagrees with both $\beta \sim T$ and $\beta \sim T^2$ from previous theories. For sodium chloride, Eldridge and Staal [13] found that the two-phonon absorption dominated the three-phonon absorption at all microwave frequencies. The resulting temperature dependence, $\beta \sim T$, is not in good agreement with the experimental results shown in figure 6 at high temperatures--$\beta \sim T^{1.2}$ at $\omega = 31.8$ cm^{-1}, $\beta \sim T^{1.4}$ for $\omega = 9.8$ cm^{-1}, and $\beta \sim T^{2.0}$ for $\omega = 5.38$, 3.24, and 1.18 cm^{-1}. In addition, the amplitudes from the previous theories did not agree with the experimental values. The other temperature exponents in table 2 also disagree with the previously predicted $\beta \sim T$ or $\beta \sim T^2$.

4. Acknowledgment

Support by the Office of Naval Research, with technical administration by the Naval Research Laboratory, is gratefully acknowledged.

Table 1. Values of Material Parameters

	NaCℓ	KBr	KI
$a_{nn}(10^{-8}$ cm)	2.815	3.293	3.526
$da_{nn}/dT(10^{-12}$cm/K)	1.09	1.23	1.34
$B(10^{12}$ergs/cm^3)	0.244	0.154	0.118
$dB/dT(10^{8}$ergs/cm^3-K)	-0.58	-0.44	-0.41
ε_0 (dimensionless)	5.90	4.78	5.09
ε_∞ (dimensionless)	2.33	2.33	2.65
$\gamma(cm^{-1})$ at 293 K	18	11.4	10.1
$M_<$ $(10^{-23}g)$	3.82	6.49	6.49
$M_>$ $(10^{-23}g)$	5.89	13.3	21.1
M_r $(10^{-23}g)$	2.32	4.36	4.96
ϕ_3 $(10^{12}$ergs/cm^3)	-5.93	-3.75	-3.85
$d\phi_3/dT$ $(10^{9}$ergs/cm^3-K)	2.4	3.2	3.4
ω_c (cm^{-1})	20	30	42
ω_m (cm^{-1})	115	64	49
ω_f (cm^{-1})	164	105	101
$d\omega/dT$ $(10^{-3}$cm/K)	-4.1	-3.3	-3.0

Table 2. Temperature Dependence of β. The values of m are the power-law exponents in the expression $\beta \sim T^m$.

Material, T \ m,ω, or γ		m at 1.18 cm^{-1}	m at $\omega_c/2$	m at ω_c	m at $\omega_c+\gamma_{293}$	ω_c (cm^{-1})	γ_{293} (cm^{-1})
NaCℓ	293K	2.0	1.8	1.4	1.2	20	18
	1000K	2.3	2.2	1.9	1.6		
KBr	293K	2.6	2.2	1.5	1.2	30	11.4
	1000K	4.0	2.8	2.0	1.5		
KI	293K	2.3	2.2	1.3	1.1	42	10.1
	1000K	2.2	1.5	0.8	0.6		

References

[1] Rubens, H. and Hertz, G., Berlin, Ber. 14, 256 (1912).

[2] Ewald, P.D., Naturwiss 10, 1057 (1922).

[3] Stolen, R. and Dransfeld, K., Phys. Rev. 139, 1295 (1965).

[4] Mills, D.L., "Two-Phonon Difference Processes and Microwave Absorption in Dielectrics," to be published, Solid State Communication.

[5] Genzel, L., Happ, H. and Weber, R., Z. Physik 154, 13 (1959).

[6] Bilz, H. and Genzel, L., Z. Physik 169, 53 (1962).

[7] Mitskevich, V.V., Soviet Phys.--Solid State 3, 2211 (1962); 4 1222 (1963).

[8] Dotsch, H. and Happ, H., Z. Physik 177, 360 (1964).

[9] Owens, J.C., Phys. Rev., 181, 1228 (1969).

[10] Berg, J.I. and Bell, E.E., Phys. Rev. B 4, 3572 (1971).

[11] Eldridge, J.E. and Howard, R., Phys. Rev. B 7, 4652 (1973).

[12] Eldridge, J.E. and Kembry, K.A., Phys. Rev. B 8, 746 (1973).

[13] Eldridge, J.E. and Staal, P.R., Phys. Rev. B 16, 4608 (1977).

[14] Berg, J.I. and Bell, E.E., Phys. Rev. B 16, 3834 (1977).

[15] Cowley, R.A., Adv. Phys. 12, 421 (1963).

[16] Cowley, E.R. and Cowley, R.A., Proc. R. Soc. Lond. A 287, 259 (1965).

[17] Cowley, E.R., J. Phys. C 5, 1345 (1972).

[18] Sparks, M. and Sham, L.J., Solid State Commun. 11, 1451 (1972).

[19] Duthler, C.J. and Sparks, M., Phys. Rev. B 9, 830 (1974).

[20] Duthler, C.J., Phys. Rev. B 14, 4606(1976).

[21] Spitzer, W.G., in Semiconductors and Semimetals, Vol. 3, edited by R.K. Willardson and A.C. Beer (Academic Press, New York, 1967), pp. 17-69.

[22] Subbaswamy, K.R., Mills, D.L., Sparks, M., and King, D.F., 1981 unpublished.

[23] Sparks, M., King, D.F. and Mills, D.L., 1981 unpublished.

[24] Sparks, M., and Sham, L.J., Phys. Rev. Lett. 31, 714 (1973).

[25] This value of γ_i = 10 cm^{-1} may be inferred from the table on page 225 of C. Kittel, Introduction to Solid State Physics, Fourth Edition (John Wiley and Sons, Inc., New York, 1981), as shown by Mills.

[26] Woods, A.D.B., Brokhouse, B.N., and Cowley, R.A., Phys. Rev. 131, 1025 (1963).

[27] Dolling, G., Cowley, R.A., Schittehelm, and Thorson, I.M., Phys. Rev., 147, 577.

[28] Jones, G.O., Martin, D.H., Manov, P.A., and Perry, C.H., Proc. Roy Soc. A. 261, 10 (1961).

[29] Sparks, M., and Sham, L.J., Phys. Rev. Lett. 31, 714 (1973).

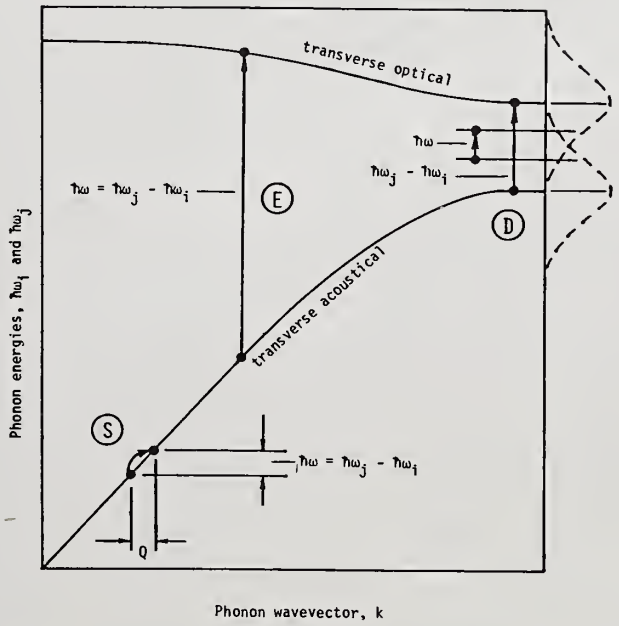

Fig. 1 Schematic representation of three important two-phonon absorption processes: E, energy-conserving; D, $\omega < \omega_j - \omega_i$ with phonons i and j on different branches; S, $\omega < \omega_j - \omega_i$ with phonons i and j on the same branch.

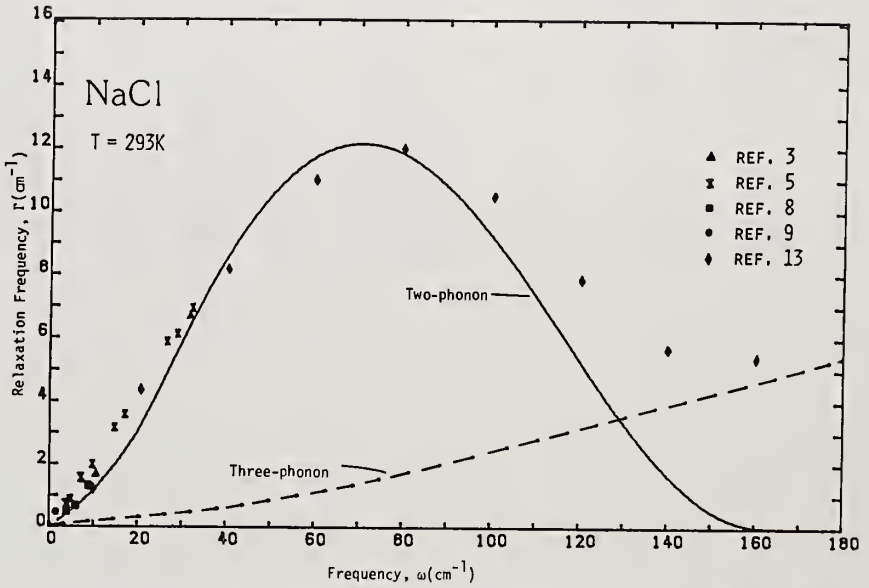

Fig. 2 Calculated frequency dependence of the relaxation frequency Γ for the two-phonon mode (solid line), compared with experimental data and the previously calculated three-phonon contribution.

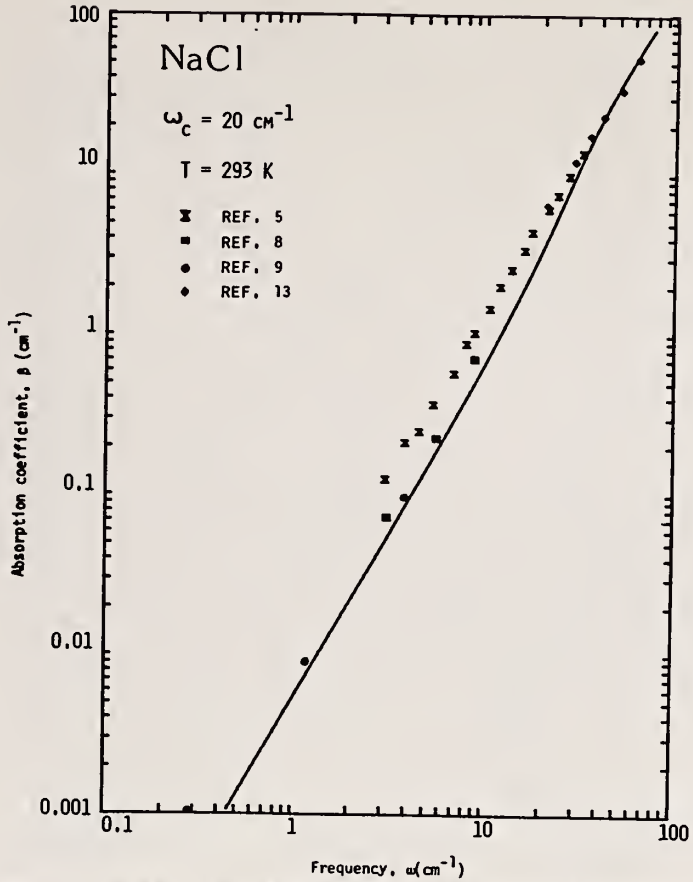

Fig. 3 Calculated frequency dependence of the absorption coefficient, compared with experimental data for sodium chloride at T = 293 K.

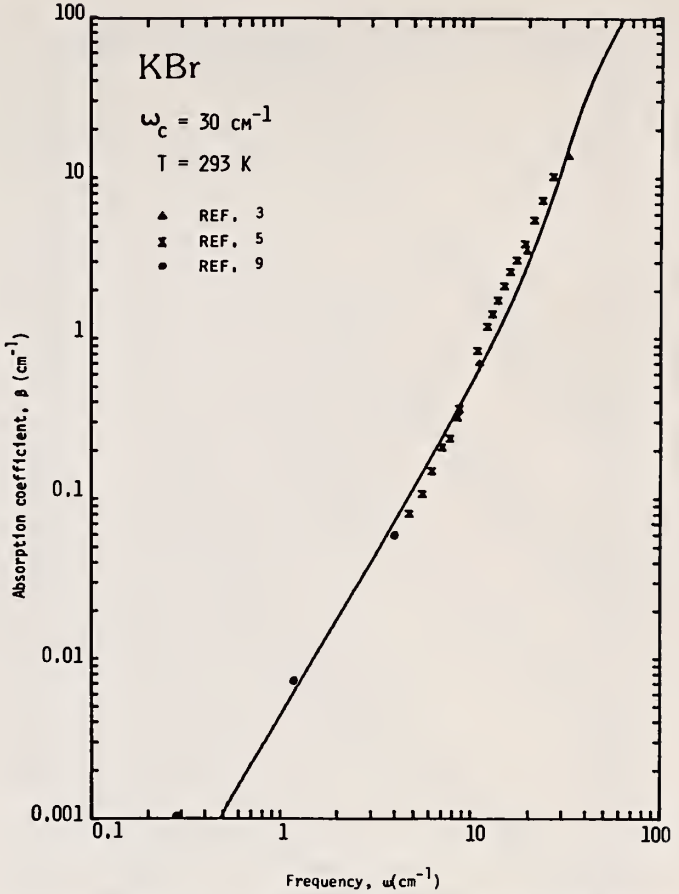

Fig. 4 Calculated frequency dependence of the absorption coefficient, compared with experimental data for potassium bromide at T = 293 K.

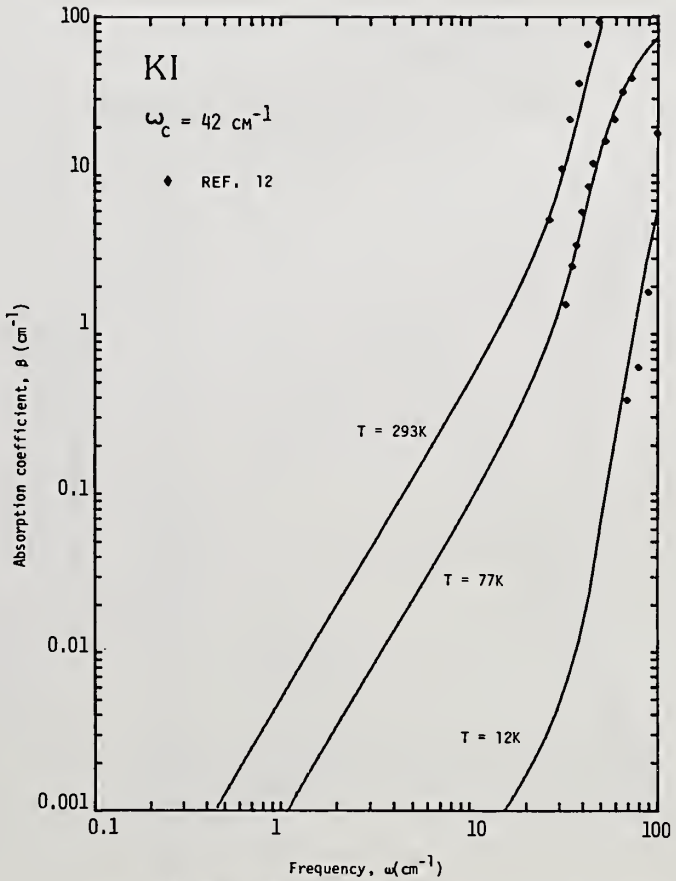

Fig. 5 Calculated frequency dependence of the absorption coefficient, compared with experimental data for potassium iodide at T = 293 K, 77 K and 12 K.

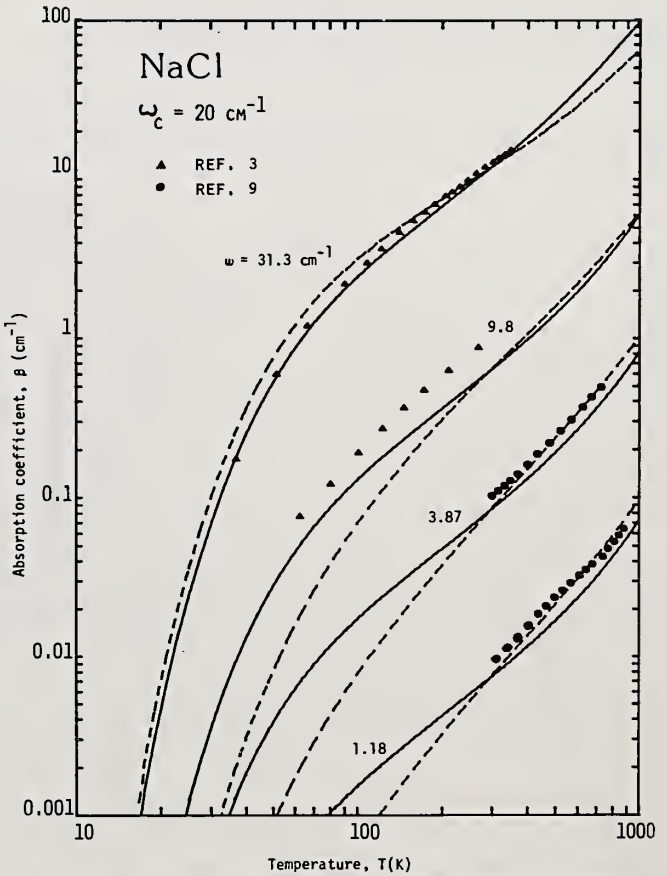

Fig. 6 - Calculated temperature dependence of the absorption coefficient, compared with experimental data for sodium chloride for the frequencies ω = 1.18, 3.87, 9.8 and 31.3 cm^{-1}. Solid lines are for constant combined phonon relaxation frequency γ, and dashed lines are for $\gamma \sim T$.

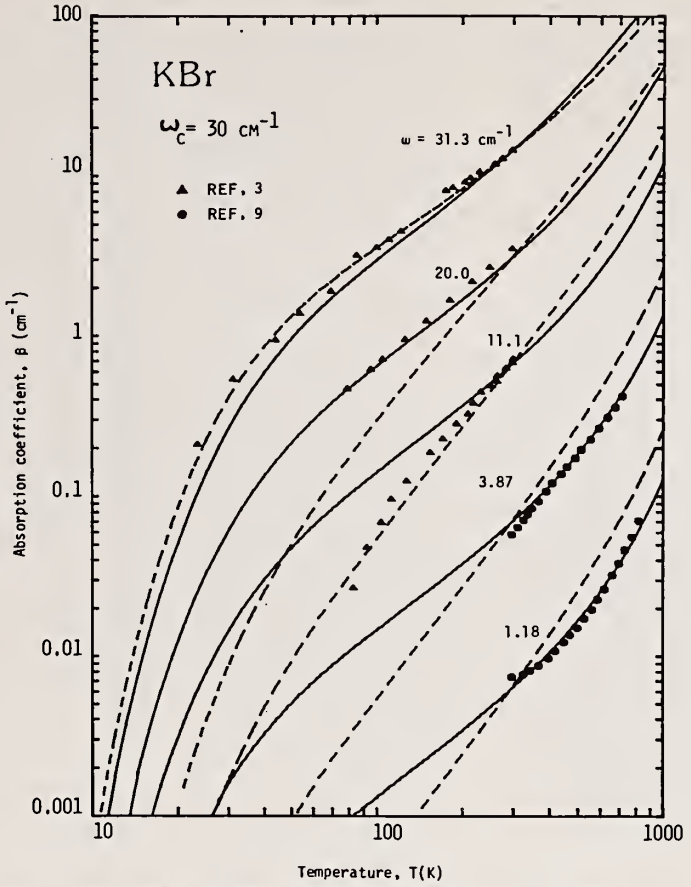

Fig. 7 - Calculated temperature dependence of the absorption coefficient, compared with experimental data for potassium bromide for the frequencies ω = 1.18, 3.87, 11.1, 20.0 and 31.3 cm^{-1}. Solid lines are for constant combined phonon relaxation frequency γ, and dashed lines are for $\gamma \sim T$.

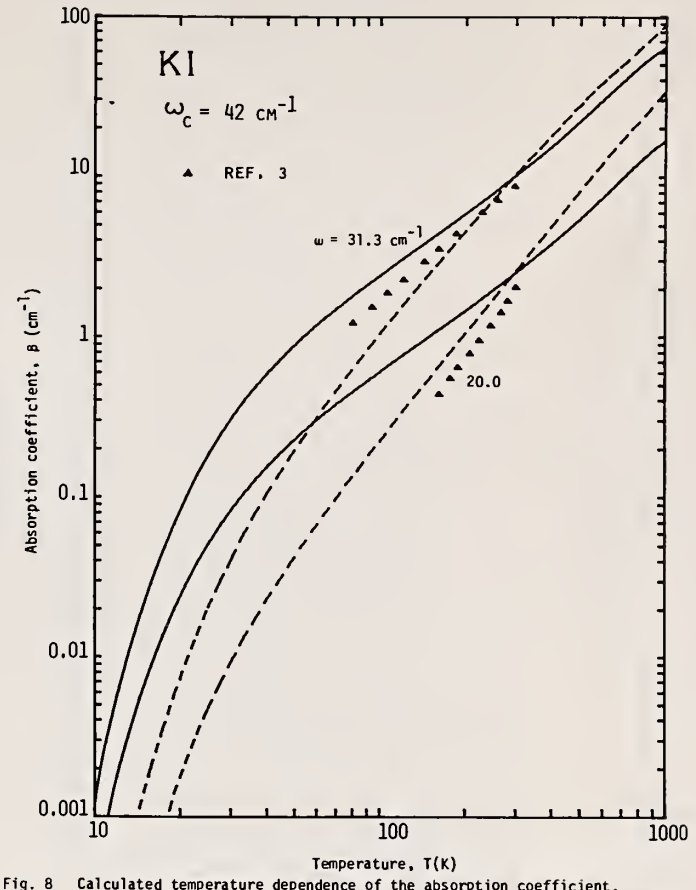

Fig. 8 Calculated temperature dependence of the absorption coefficient, compared with experimental data for potassium iodide for the frequencies ω = 20.0 and 31.3 cm^{-1}. Solid lines are for constant combined phonon relaxation frequency γ, and dashed lines are for $\gamma \sim T$.

The prediction in the last viewgraph that impurity effects were becoming noticeable at high temperature but not low temperature was questioned. The speaker responded that in this case the intrinsic absorption coefficient went to lower and lower values so that ultimately the extrinsic process became dominant. In response to another question, the speaker pointed out that although the experiments reported were at 20-50 Torr, it was because there was not enough power to achieve breakdown at atmospheric pressure. The primary interest in the phenomenon is, however, at atmospheric pressure.

Increased Breakdown Thresholds in Air by Admixing an Electronegative Gas*

Howard C. Volkin†

University of Dayton Research Institute
Air Force Weapons Laboratory
Kirtland Air Force Base, NM 87117

The intrinsic breakdown by large area laser beams of gases containing the attaching species SF_6 mixed with clean dry Air has been analyzed in detail. The results show that SF_6 is equally effective in inhibiting avalanche breakdown of these gases for near infrared pulses longer than 100 nanoseconds as for DC fields. The breakdown intensities were obtained for various pulse durations at 10.6 μm by numerically solving the Boltzmann equation for the energy distribution $n(\epsilon)$ of electrons in the generated plasma. Published electron collision cross sections considered the best available for our application were used. The calculated breakdown intensity for very long pulses of constant intensity in air at 1 atm and 300K is $I^* = 2.7 \times 10^9$ w/cm^2, which agrees within experimental uncertainty with the measured value. At any given intensity, the power absorbed by the plasma and the power losses in the various electron collision processes (elastic, inelastic excitation of vibrational and electronic levels, ionization, and attachment) are evaluated in our calculations. Discrete photon effects in power absorption and photoelectric processes are expected to be small for wavelengths larger than 1 μm, so the frequency scaling (I^*/ω^2) of classical field theory should hold for our results over the near infrared region.

Key Words: attaching species; avalanche ionization; breakdown threshold; electron attachment; electronegative gas; gas breakdown; laser beam; laser-induced breakdown; laser-produced plasmas; plasma production.

1. Introduction

Laser-induced breakdown of gases is important in a number of applications: (1) limiting the beam intensity that can be propagated through the atmosphere or within a gas laser device, (2) coupling an intense laser pulse to a material surface through plasma produced near the solid-gas interface, and (3) the design of laser-controlled gas switches and plasma radiation sources. In some cases fast controlled generation of plasma is utilized, but in others breakdown is an undesirable occurrence, leading to damage of an optical component or to degradation of the beam quality. Certain gas mixtures are known to possess significantly better insulation properties than air under strong DC electric fields. Among the best of these are SF_6/N_2 mixtures [1]. We have made a theoretical study to determine if SF_6/Air and SF_6/N_2 mixtures have correspondingly superior resistance to avalanche breakdown under intense laser irradiation.

2. Theory

Our calculation of intrinsic breakdown intensities is based on numerically solving the Boltzmann equation for the energy distribution function of the unbound electrons in the generated plasma. To a given beam intensity and gas mixture with specified populations of the various molecular states, there corresponds a unique quasiequilibrium distribution $F(\epsilon)$ normalized to unit integral over all electron energy ϵ. The mean rate per unbound electron of ionization α_s and of attachment β_s for each molecular species s are obtained by averaging the appropriate electron collision cross sections over $F(\epsilon)$. We assume the electron loss rate due to diffusion out of the beam volume is negligible, as is the case for large beam diameters. Then the net electron growth rate per electron is $\gamma = \alpha - \beta$, where $\alpha = \Sigma_s \alpha_s$ and $\beta = \Sigma_s \beta_s$ are the total ionization and attachment rates, respectively.

We employ the time-dependent Boltzmann equation formalism of Rockwood et al [2,3]. The equation used is that given by Rockwood [4], except for the power input term and additional collision terms describing two-body (dissociative) and three-body attachment. The power input term must be converted

---

*This work is supported by the Air Force Weapons Laboratory, Kirtland AFB, NM 87117 under Contract F29601-79-C-0027.
†Present address: Rockwell International, Rocketdyne Division, Kirtland AFB, NM 87185

from the form for DC fields to one based upon the absorption of energy by free electrons from optical fields. We use two expressions for this purpose. The one given by classical field theory is familiar from microwave breakdown theory. A quantum version [5,6], which takes account of the discrete photon energy in the absorption and emission of radiation by the electrons, is based on a low-frequency approximation for the coefficients of the dominant free-free radiative processes, namely single-photon inverse bremsstrahlung absorption and stimulated bremsstrahlung emission. For reliable results the quantized-field expression must be used for photon energies exceeding about 1.0 ev. The electron collision terms appearing in our Boltzmann equation description are those due to the following processes: elastic scattering with molecular neutrals and ions; inelastic excitation, including vibrational, electronic, and ionizing; superelastic collisions with excited molecules; and both two- and three-body attachment. The calculation of the electron distribution function models the detailed collisional kinetics occurring in the gas. Measured electron collision cross sections are used and no adjustable physical parameters enter into the results.

The time-dependent Boltzmann equation governs the time evolution of the number density $n(\epsilon,t)d\epsilon$ of electrons with energy between ϵ and $\epsilon + d\epsilon$. The power input term P in the equation is such that $P(\epsilon,t)d\epsilon$ is the rate of change of electron density in the energy interval $(\epsilon,\epsilon+d\epsilon)$ due to the collisional absorption of radiant energy by the electrons. From classical field theory P has the form

$$P_{cl} = -\frac{\partial J_f}{\partial \epsilon},$$

$$J_f = -\frac{2}{3}\epsilon^{3/2} Q_J \frac{\partial}{\partial \epsilon}(\epsilon^{-1/2} n),$$

$$Q_J(\epsilon) = INa_c, \quad I = \frac{c\epsilon}{4\pi} E^2,$$

$$a_c(\epsilon) = \frac{4\pi e^2}{mc\epsilon N}\left(\frac{\nu_m}{\omega^2 + \nu_m^2}\right)$$

$$\nu_m(\epsilon) = Nv(\epsilon) \sum_s \psi_s \sigma_{ms}(\epsilon).$$

Here e and m are the electron charge and mass; c, ω and E are the speed, frequency, and root-mean-square electric field, respectively, of the light; ψ_s is the molecular fraction of species s in the gas mixture of total number density N; and $v(\epsilon) = (2\epsilon/m)^{1/2}$. For an electron at energy ϵ, $\sigma_{ms}(\epsilon)$ is the cross section for momentum transfer in elastic collisions with molecules s, and $\nu_m(\epsilon)$ is the momentum transfer collision frequency. When the rate at which ν_m varies with ϵ can be neglected, the light absorption coefficient and the energy absorption rate of an electron in a beam of intensity I given by the classical theory become equal to a_c and Q_J respectively. The quantity J_f can be viewed as a flux of electrons along the energy axis driven by the radiation field. We take the dielectric constant in the medium ε to be unity. Note that ε enters in these expressions only in relating the beam intensity I to E. When written in terms of E, both Q_j and J_f become independent of ε.

In the quantized-field theory, the expression for P appropriate to the fields of interest here is determined by the rates at which electrons leave and enter an interval $(\epsilon,\epsilon,+d\epsilon)$ by the free-free radiative processes of single-photon inverse bremsstrahlung absorption and stimulated bremsstrahlung emission, whose coefficients for an electron of energy ϵ are denoted by $a(\epsilon)$ and $b(\epsilon)$, respectively:

$$P_{qm} = N(I/\hbar\omega)\left\{-[a(\epsilon)+b(\epsilon)]n(\epsilon) + a(\epsilon-\hbar\omega)n(\epsilon-\hbar\omega) + b(\epsilon+\hbar\omega)n(\epsilon+\hbar\omega)\right\}.$$

The principle of detailed balance relates the absorption and emission coefficients as

$$b(\epsilon+\hbar\omega) = [\epsilon/(\epsilon+\hbar\omega)]^{1/2}\, a(\epsilon).$$

For the relatively low photon energies $\hbar\omega$ of optical fields, the low frequency approximation

$$a(\epsilon) = \frac{2}{3}\, a_c(\epsilon + \tfrac{1}{2}\hbar\omega) \left(\frac{\epsilon+\hbar\omega}{\hbar\omega}\right) \left(\frac{\epsilon+\frac{1}{2}\hbar\omega}{\epsilon+\hbar\omega}\right)^{1/2}$$

is sufficiently accurate.

By finite differencing the energy axis into M intervals or bins of width $\Delta\epsilon$, the Boltzmann equation is converted into a set of M-coupled first-order differential equations, which in matrix notation has the form

$$\dot{n}(t) = Cn(t),$$

where n(t) is the M-dimensional vector whose kth component $n_k(t)$ is the number density at time t of electrons with energy values in the kth bin $(\epsilon_k \pm \frac{1}{2}\Delta\epsilon)$. Summing all components of the vector n(t) gives the total number density of electrons $n_0(t)$. The elements of the M x M matrix C are the transfer rates of electrons between the bins due to the electromagnetic field and the various collision processes and are calculated from the power input and collision terms. A finite difference approximation of Equation 1 using the small time step h gives the implicit algorithm

$$n(t+h) = (I-hC)^{-1}n(t)$$

used in the numerical solution. Starting from some initial energy distribution n° at t=0, the distribution n(t) under constant laser intensity approaches the quasiequilibrium form

$$n(t) = n_q e^{\gamma t},\ t>t_q \qquad (1)$$

very rapidly at ordinary gas densities (in a time t_q set by the momentum transfer collision frequency), where the components of the vector n_q and the electron growth rate γ are independent of time. In any particular case, the computation is completed when a convergence test indicates that the distribution has attained the form (1). If the M-dimensional vector n_q is normalized to unit magnitude, the kth component of the normalized vector corresponds to the value $F(\epsilon_k)\Delta\epsilon$ from the normalized quasiequilibrium distribution F(ε) at the energy of the kth bin. Note that upon reaching quasiequilibrium, the total density $n_0(t)$ also increases as $\exp(\gamma t)$.

It is the calculation of γ that is the central problem in analyzing the avalanche growth of electron density. Since collisional ionization of molecules from the ground state occurs only at electron energies above the ionization threshold, typically 12 ev or more, the rate γ is very sensitive to details in the high-energy tail of the distribution function. Hence the energy range $\epsilon_M = M\Delta\epsilon$ covered in a computation must be sufficiently large that $F(\epsilon_M)$ is relatively small, generally at least five orders of magnitude below the maximum value of F(ε). However, the computation involves storing two arrays having M^2 elements so that the computer memory capacity sets an upper limit to the value of M that can be used. Generally the interval $\Delta\epsilon$ should be small enough to resolve the structure of the low-energy resonances present in some of the vibrational excitation and in the three-body attachment data for O_2 that we have used. As the beam intensity I increases in a given gas mixture, the electron distribution shifts toward higher energies and requires a larger energy range to reach an adequate fall off. Fortunately, a larger energy interval $\Delta\epsilon$ can be used with increasing I because the contribution from the low-energy region becomes relatively smaller.

In the calculations we ignore (1) the time variation of the populations in the various molecular states and (2) the electron-electron interactions between free electrons. These effects do not influence the growth rate of electron density significantly so long as the total electron density n_0

is small compared to the density of each molecular species in the gas. In this regime the Boltzmann equation is linear and eq (1) describes the growth of electron density due to avalanche ionization under constant laser intensity. We neglect the small time interval in which quasiequilibrium is attained and extend eq (1) down to the initial time t=0, where it is understood that the quasiequilibrium distribution n_q has a total density $n_0(0)$ equal to that of the distribution n° of initiating electrons.

In the overall transition from essentially neutral gas to hot plasma, eq (1) applies to the formative growth stage, in which the total number density $n_0(t)$ of unbound electrons increases exponentially with time. During this stage, the total density grows from some small initiating value $n_0(0)$ to a "breakdown" value $n_0(\tau_p)$ that defines the state of breakdown and the cascade time τ_p required to reach it. The value of $[n_0(\tau_p)/n_0(0)]$ is somewhat arbitrary, but because the density growth is exponential, τ_p is not very sensitive to this choice. The value is commonly taken to be exp (40) and then $\tau_p = (40/\gamma)$. For a laser pulse of duration τ_p, the breakdown intensity I_{BD} is that which produces the net ionization rate $\gamma = (40/\tau_p)$. The value of I_{BD} for very long pulses ($\tau_p > 10^{-7}$ sec) is denoted by I* and corresponds to the limit of very small γ.

3. Results

In order to assess the effect of SF_6 admixed to Air, we calculated the ionization rate over a range of intensities in various SF_6/Air mixtures. Clean dry air is represented by the molecular mixture N_2/O_2:0.789/0.211. In air mixtures the molecular fractions of N_2 and O_2 have the same ratio as in air. Recently published electron collision cross sections were used [1,7,8]. All computations were done with an energy mesh of M=600, approximately the maximum allowable using the Cray-1 computer system with our computer program ACNOMAD.

Our calculations ignored superelastic collisions and employed for the most part the classical model of power absorption. To check the frequency scaling law (I_{BD}/ω^2) of the classical theory, several corresponding scaled cases computed with the quantum and classical models were compared at 10.6, 2.6, and 1.06 μm. In pure air the collision rates were essentially the same at 10.6 μm, within 5% at 2.6 μm, and within 25% at 1.06 μm and the differences appeared to lessen with increasing intensity. Greater differences in the rates were found for a few processes involving O_2, namely excitation of the first and second vibrational levels and three-body attachment, whose low energy cross sections have pronounced narrow resonances (∿0.03ev in width). However, the resonance contributions are calculated less accurately than the other processes, because even at the lower intensities the smallest energy interval giving an adequate energy range was $\Delta\epsilon$=0.04ev. Our results show that the Oxygen resonances contribute relatively little at intensities beyond 1.0×10^{10} w/cm^2. However in pure air three-body attachment (whose effective cross section consists entirely of narrow resonances lying below 1.05 ev) plays a significant role at the lower intensities (longer pulse lengths) where the mean electron energies do not exceed a few electron volts. It comprises 25% of the total attachment rate at 2.7×10^9 w/cm^2 ($\langle\epsilon\rangle$=1.8ev) and is down to 10% at 6.0×10^9 w/cm^2 ($\langle\epsilon\rangle$= 3.2ev). Besides photon absorption another quantum effect arises from photoelectric processes, namely photoionization from excited electronic states and photodetachment of negative ions. These are expected to be small for wavelengths larger than 1 μm. Hence the classical frequency scaling should extend our results with reasonable accuracy over the near infrared region.

Calculated breakdown intensities at 10.6 μm as a function of laser pulse duration τ_p are shown for various SF_6/Air mixtures in figure 1. All results refer to 1 atm and 300K. For long pulses, the calculated value in Air is $I^* = 2.7\times10^9$ w/cm^2, which agrees within experimental uncertainty with the measured value 3×10^9 w/cm^2. The corresponding intensity for pure SF_6 is 2.9×10^{10} and for the mixture SF_6/Air:0.3/0.7 is 1.9×10^{10}. This shows that the breakdown resistance of gases can be appreciably improved by admixing suitable electronegative species. As a function of SF_6 fraction F, the breakdown intensity of admixed air exceeds that of admixed N_2 because O_2 also attaches. But for 0.2 < F < 1, the difference does not exceed 4.5%. In this range of F values, our calculated breakdown intensities for long pulses I_F^* follow very closely the empirical relationship

$$(I_F^*/\omega^2) = (I_1^*/\omega^2)(F)^p,$$

where p is equal to 0.34. The equivalent functional form for the breakdown electric field is $(E_F^*/\omega) = (E_1^*/\omega)(F)^m$, where $m = \frac{1}{2}p$. In the DC case, both measured and calculated breakdown fields obey the corresponding scaling relation (usually written in terms of E_F^*/N) with m = 0.18[1].

Figures 2 and 3 show for pure Air and for a 30% SF_6 admixture, respectively, the collision rate per unbound electron of the following energy loss processes: ionization, attachment, vibrational and electronic inelastic excitation as a function of intensity I. As explained in section 2, to

maintain the precision of the calculation with increasing values of the intensity, particularly with respect to the ionization rate, it is necessary to increase the interval size $\Delta\epsilon$ of the energy mesh. The calculated collision rate of a process is not sensitive to small changes of $\Delta\epsilon$ when its cross section varies relatively slowly with energy. However, resonance structure in the cross section causes a sensitivity to the interval size when $\Delta\epsilon$ is not very small relative to the resonance widths. We have already discussed the difficulty of calculating three-body attachment by O_2 for this reason. But the contribution of the three-body attachment is never large and is in fact negligible except at low intensities in pure Air. In the Air mixtures attachment is dominated by SF_6, whose various attachment processes have cross sections with broad energy peaks (wider than 1 ev) except for the large narrow capture resonance at zero energy. In our calculations the attachment rate of SF_6 shows some sensitivity to $\Delta\epsilon$ and generally becomes smaller for a larger $\Delta\epsilon$. Figure 3 shows the behavior in the mixture of the attachment rate β with varying intensity and indicates the reduced absolute accuracy at higher intensities by the broken-line portion of the curve.

Generally the energy range $M\Delta\epsilon$ of a calculation was considered adequate if the distribution function at the last interval n_{qM} was less than 10^{-5} of the peak value, although at the high intentensities it was not possible to maintain this criterion. Our procedure was to keep the value of $\Delta\epsilon$ constant as the intensity I was increased until the falloff of $F(\epsilon)$ approached the limit of acceptability. At this higher intensity larger $\Delta\epsilon$ were tried over a range of values in which the calculated collision rates did not change appreciably compared to those from the old value of $\Delta\epsilon$. A new value of $\Delta\epsilon$ was then chosen on the basis of adequate falloff of n_{qM}. The values of $\Delta\epsilon$ went from 0.05ev at the very low intensities to 0.4 ev at the very high intensities. At a given intensity the electron distribution $F(\epsilon)$ associated with the SF_6 fraction F has a somewhat more rapid falloff the larger F is. The accuracy of the calculation is considered good for $I < 10^{11}$ w/cm^2.

In a given mixture, as I increases the ionization rate α increases monotonically, since the mean electron energy increases with I and at the mean energies of interest the total ionization cross sections are all increasing functions of energy. At any given intensity, α does not depend strongly on F but tends to have a slow increase with increasing F, viz the average increase in α from F = 0 to F = 1 is about 10% for $I \lesssim 10^{11}$ w/cm^2 and within the accuracy of our calculations becomes larger for higher intensities. This increase is due entirely to the larger ionization cross section of SF_6 relative to N_2 and O_2, since at intensities beyond about 8×10^{10}w/cm^2 the mean electron energy decreases as F increases. The slope $d\alpha/dI$ is fairly uniform throughout our parameter space. It is about 1 cm^2/j near 1.0×10^{10} w/cm^2 and peaks at about 3 cm^2/j around 6×10^{10} w/cm^2. The tangent to the α curves in figures 2 and 3 corresponds to $d(\log\alpha)/d(\log I)$, of course, and falls off appreciably with increasing I as α becomes large. As can be seen in figures 1 and 2, the attachment rate in a given mixture varies slowly with I compared to the ionization rate and has a maximum value (occurring between 10^{10} and 10^{11} w/cm^2 for the mixtures analyzed here). Of course, β increases monotonically with F at any given intensity.

The detailed behavior of α and β obtained from our calculations accounts for the properties of admixed SF_6 in inhibiting air breakdown exhibited in figure 1. In a mixture with SF_6 fraction F, the long-pulse breakdown intensity I_F^* corresponds to the intensity at which $\alpha=\beta$ and equals the limiting value of I as τ_p becomes large on the associated I-τ_p curve in Figure 1. In a given mixture, for intensities $I < I_F^*$ the electron growth rate $\gamma = \alpha-\beta < 0$ but as I increases the increase in α is very rapid compared to that of β. For any intensity in the range $(1.0\text{-}4.0)\times10^{10}$ w/cm^2, where the values of I_F^* lie, the rate at which β increases with F lessens as F becomes larger. This explains the relatively decreasing effect of SF_6 as F increases, which becomes particularly noticeable when F>0.5. In the intensity range containing all the I_F^* values, the variation of α with I can be reasonably approximated for all mixtures F by a single curve. A rougher approximation is to replace each β-I curve by its mean-value line parallel to the I-axis. Then the β curves are represented by a family of parallel lines, and any set of these lines corresponding to equal increments of F has decreasing distances between consecutive lines as F increases. The approximation to I_F^* is given by the value of I at which the α curve intersects the β line for F and is seen to have the qualitative behavior found in figure 1.

As the intensity increases beyond I_F^*, the rapid increase of α compared to β causes γ to go from zero to an appreciable value, say $\gamma_a = 4\times10^8$, within a short distance from I_F^*. This region corresponds to the relatively flat asymptotic portions of the curves in figure 1, since τ_p goes from very large values to $\tau_{pa} = 10^{-7}$ in a small interval of intensities. The intersection of the α and β curves occurs at ever larger values of $\alpha=\beta$ as F increases, so that the difference $(\alpha-\beta)$ attains the value γ_a in shorter intensity intervals. This accounts for the increasing flatness of the asymptotic portions as F increases. It is within the range of pulselengths up to 100 ns, where the value of α exceeds but is still close to β that SF_6 exerts its greatest effect in increasing the breakdown intensity of the mixtures relative to that of pure Air.

With further increase of intensity in a given mixture, α will increase to where it has become very large compared to β and $\gamma \approx \alpha$. At this point the influence of the SF_6 in the mixture due to its attachment property is small. The breakdown curve for the mixture now lies close to the curve for pure Air, since the value of α is about equal in the two gases. In fact, as the intensity continues to increase, the two curves will cross over since the larger ionization cross section of SF_6 ultimately causes γ to become larger in the mixture at equal intensities. We see from figure 1 that at the lower intensities (longer τ_p) a mixture rich in SF_6 ($F \approx 1$) is little more effective than one significantly lower in SF_6 (say $F=0.3$) in elevating I_{BD} over that of pure Air. However, a richer mixture performs relatively much better at higher intensities (shorter τ_p), although with smaller increase of $[I_{BD}/I_{BD}\ (F=0)]$ than can be obtained at the low intensities, and thereby extends the intensity range over which some improvement over pure Air can be obtained. This is due to the fall off in $d(\log\alpha)/\ d(\log I)$ with increasing I. The larger β curve for $F \approx 1$ intersects the α curve at a higher I and consequently runs over a larger interval of $\log\ (I/I_F^*)$ before the $\log(\alpha/\beta)$ becomes sufficiently small that the breakdown curve for the mixture F approaches close to the curve for pure air.

Figures 4 and 5 show for Air and a 30% SF_6 mixture, respectively, the energy loss rates per electron in vibrational and electronic excitation, ionization, and attachment. Also shown is P_{in}, the power absorption per electron from the field, and $\delta = \gamma < \epsilon >$, which is the excess of P_{in} over the total energy loss rate per electron and represents the power expended in bringing secondary electrons from ionization into the distribution $F(\epsilon)$. The power input $P_{in}(I)$ is the average power absorption over the distribution $F(\epsilon)$ at intensity I. We see from the figures that P_{in} varies nearly linearly with I except at very high intensities where the variation rate falls off. When ν_m changes negligibly over the range of electron energies, the power absorption is equal to Q_J and is independent of ϵ. Then $P_{in}=Q_J$ and the dependence on I is precisely linear. In the region of small intensities where the net ionization rate is relatively low, almost all the power absorption goes into energy loss processes other than ionization. This is the energy-loss dominated regime. Breakdown requires relatively long pulses ($\tau_p > 10^{-7}$ s) in this limit. For a given τ_p, γ increases rapidly with increasing intensity above I_F^* until the breakdown threshold I_{BD} is reached, where γ becomes large enough to attain the breakdown state in the time τ_p. In the loss dominated regime the breakdown intensity is nearly constant (the flat portion of the curves in figure 1).

At the other extreme of very high intensities (very short τ_p for breakdown), the mean electron energy is high, γ is large, and approximately all the absorbed power goes into the net ionization loss rate: $P_{in} \approx (R_{ion} + \delta)$. This is the "loss-free" regime. To a good approximation $R_{ion}=\gamma\phi$, where ϕ is some average ionization potential of the mixture, and we can characterize the loss-free condition by

$$P_{in} = \gamma(\phi + <\epsilon>).$$

To the extent that the dependence of $<\epsilon>$ on I can be ignored in this equation, as when $<\epsilon>$ is less than ϕ, the intensity dependence of γ is the same as that of P_{in}, i.e., linear. Since the pulse-length τ_p for breakdown at the intensity I_{BD} is defined by a relation $\tau_p\gamma(I_{BD})=$constant, we now have that I_{BD} is inversely proportional to τ_p. Hence in the loss-free regime, for a given gas mix and pressure, the breakdown threshold corresponds to a constant pulse energy fluence $I_{BD}\tau_p$. At the very high intensities, δ becomes larger the R_{ion} or equivalently $<\epsilon>$ exceeds ϕ. Then the present formalism predicts the rate of increase of γ with I becomes less than linear and increasing energy fluence is required for breakdown. However, at these intensities other effects, such as multiphoton free-free processes, start to be important and must be incorporated for a complete theory.

Our results demonstrate that for pulses greater than 100 ns, an order of magnitude increase over the breakdown intensity threshold in Air is readily obtained by admixing SF_6.

4. Acknowledgements

The author is grateful to A. V. Phelps who provided the cross section data for N_2 and O_2 and generous assistance in their interpretation and likewise to L. E. Kline for the SF_6 data. Thanks are also due to B. J. Pierce for helpful discussions and interest in this work, to R. B. W. Kwong and A. F. Baca for their expert help in implementing the computer programming, and to A. E. Greene for detailed advice concerning the computer program NOMAD from which our program was developed.

REFERENCES

[1] Kline, L. E.; Davies, D. K.; Chen, C. L.; Chantry, P. J. Dielectric properties for SF_6 and SF_6 mixtures predicted from basic data. J. Appl. Phys. 50 (11):6789-6796; 1979 November.

[2] Rockwood, S. D.; Brau, J. E.; Canavan, G. H.; Proctor, W. A. Time-Dependent Calculations of Carbon Monoxide Laser Kinetics. IEEE J. Quantum Electron. QE-9(1):120-129; 1973 January.

[3] Rockwood, S. D.; Greene, A. E. Numerical Solutions of the Boltzmann Transport Equation. Computer Physics Communications, 19(3); 377-393; 1980 July.

[4] Rockwood, S. D. Elastic and Inelastic Cross Sections for Electron-Hg Scattering from Hg Transport Data. Phys. Rev. 8A (5):2348-2358; 1973 November.

[5] Phelps, A. V. Theory of Growth of Ionization During Laser Breakdown. Kelley, P. L.; Lax, B. Tannewald, P. E., eds. Physics of Quantum Electronics Conference Proceedings; 1965 June; New York, NY:McGraw-Hill; 1966. 538-547.

[6] Kroll, N.; Watson, K. M. Theoretical Study of Ionization of Air by Intense Laser Pulses. Phys. Rev. 5A(4):1883-1905; 1972 April.

[7] Tachibana, K.; Phelps, A. V. Excitation of the $C^3\pi_u$ state of N_2 by low energy electrons. J. Chem. Phys. 71(8):3544-3546; 1979 October 15.

[8] Lawton, S. A.; Phelps, A. V. Excitation of the $b\,^1\Sigma_g^+$ state of O_2 by low energy electrons. J. Chem. Phys.69(3):1055-1068; 1978 August 1.

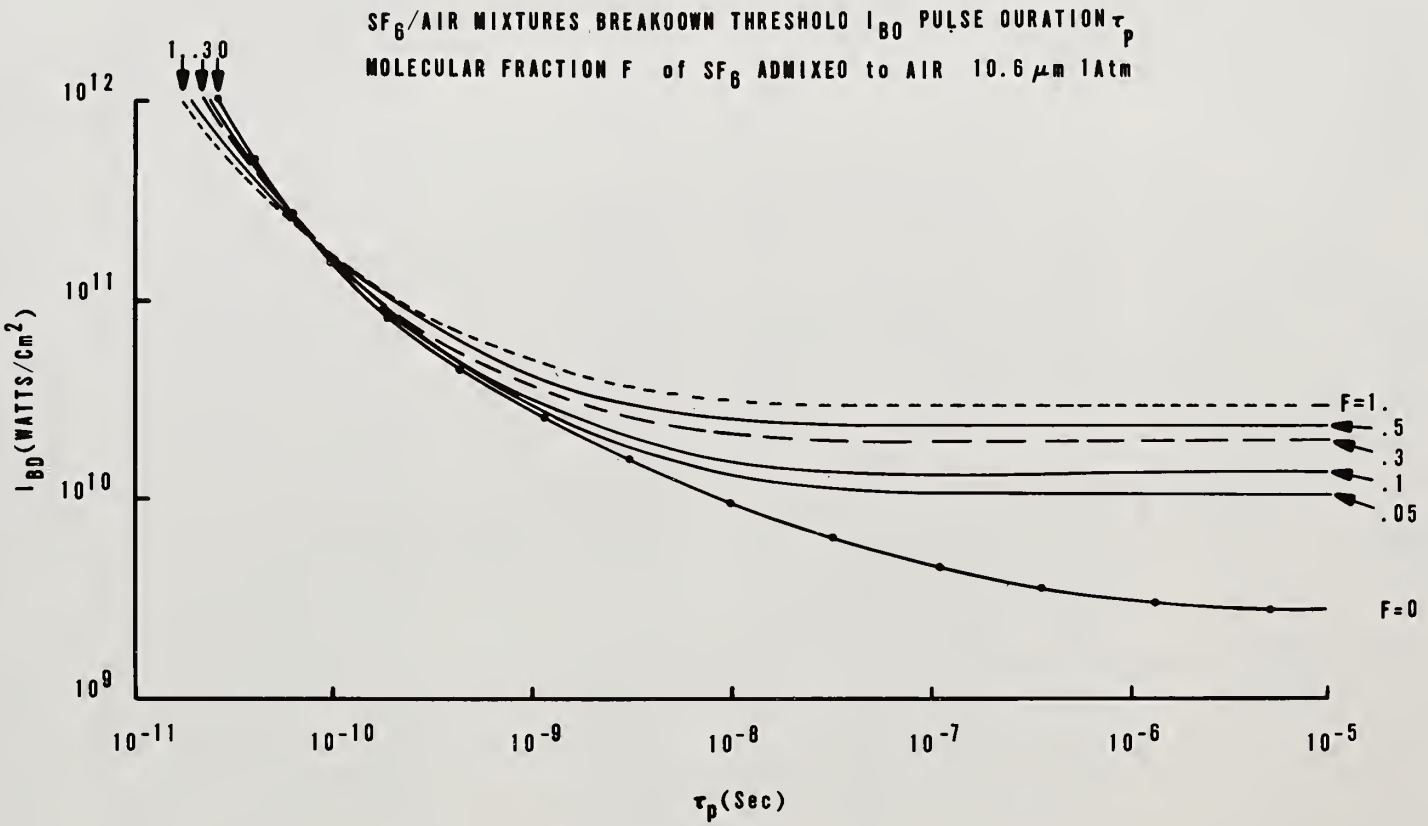

Figure 1. Calculated breakdown threshold intensity I_{BD} as a function of laser pulse duration τ_p for various SF_6/Air mixtures.

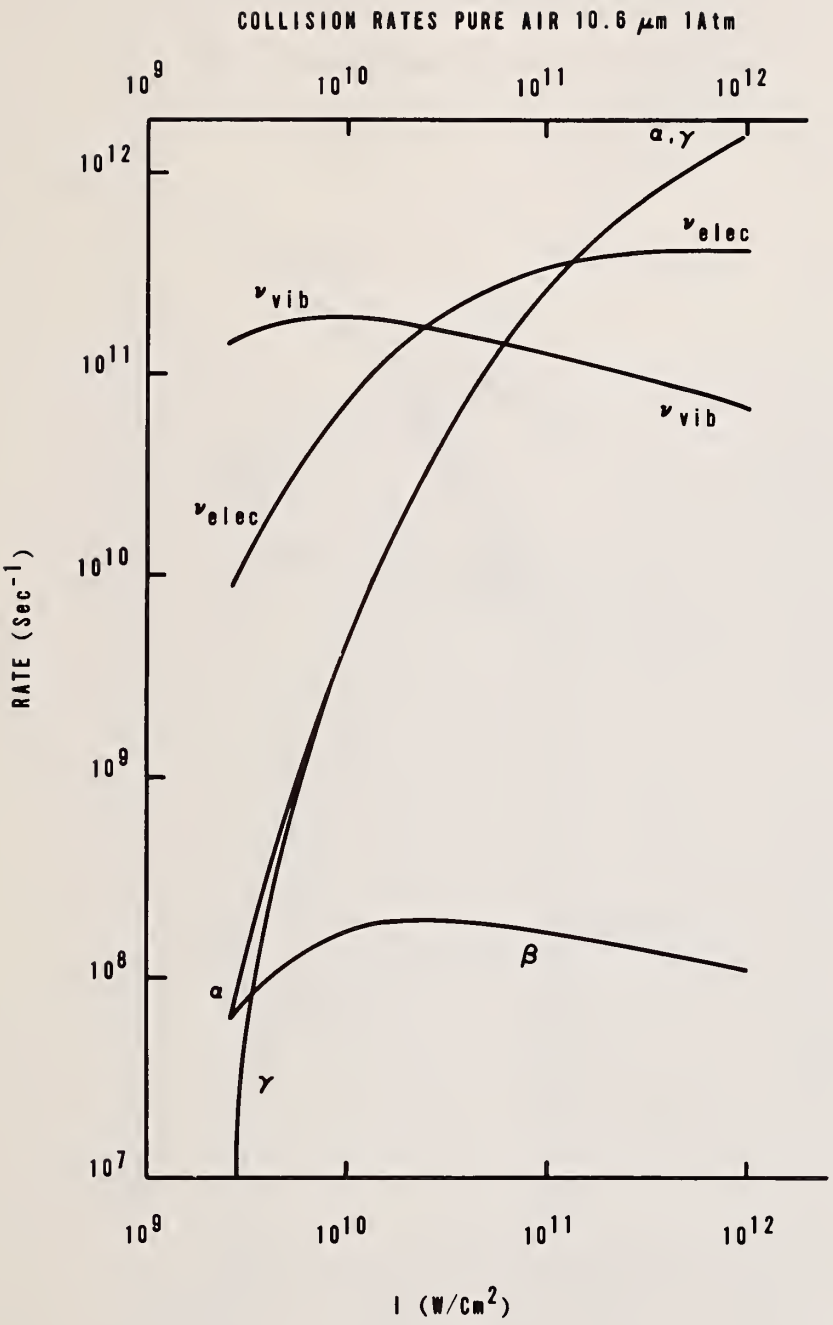

Figure 2. For pure Air calculated collision rate of ionization α, attachment β, vibrational excitation ν_{vib}, electronic excitation ν_{elec} and electron growth rate $\gamma = \alpha - \beta$.

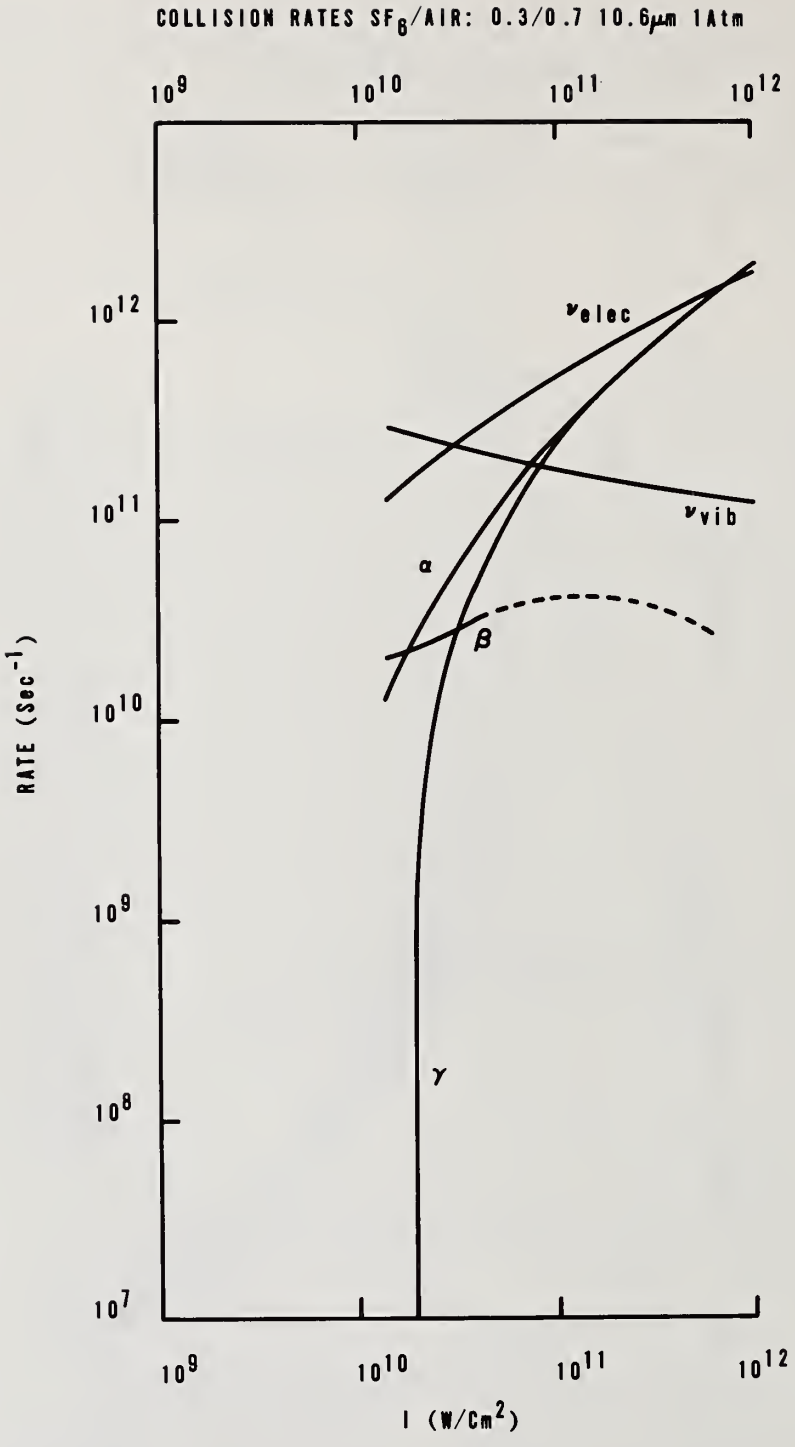

Figure 3. For SF_6/Air mixture with SF_6 molecular fraction F = 0.3, calculated collision rates as in figure 2.

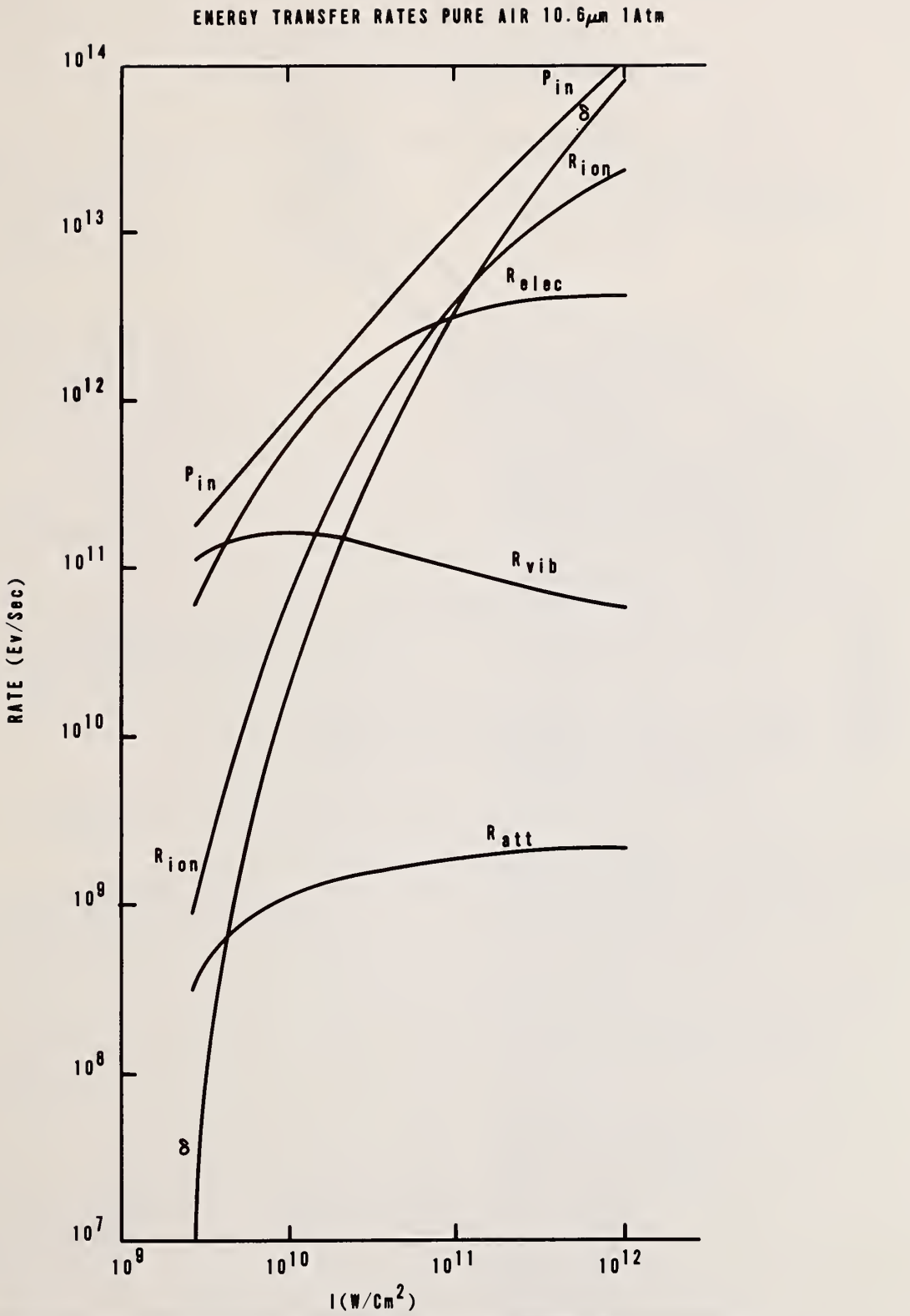

Figure 4. For pure Air calculated energy loss rate in ionization R_{ion}, attachment R_{att}, vibrational excitation R_{vib}, electronic excitation R_{elec}; energy gain rate by absorption P_{in}; and energy expenditure rate δ in bringing secondaries into the quasiequilibrium distribution.

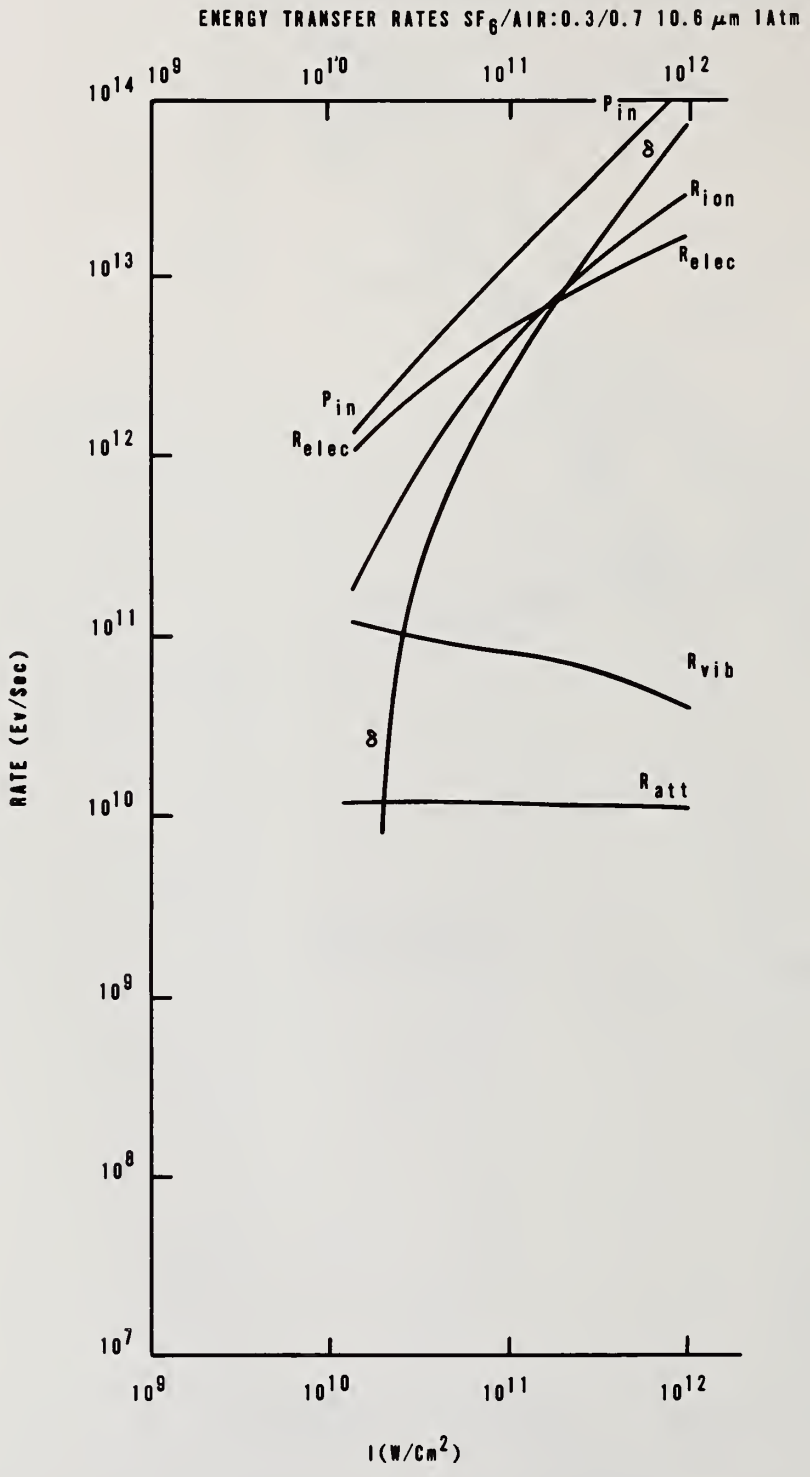

Figure 5. For SF_6/Air mixture with SF_6 molecular fraction F = 0.3, calculated energy transfer rates as in figure 4.

APPENDIX I

List of Attendees

Boulder Damage Symposium
November 17-18, 1981

Joseph Abate
Laboratory for Laser Energetics
University of Rochester
250 East River Road
Rochester, New York 14623
(716) 275-5181

Sol Aisenberg
Applied Science Laboratories
Gulf & Western Research
335 Bear Hill Road
Waltham, Massachusetts 02154
(617) 890-5100

S. Amimoto
Aerospace Corporation
P. O. Box 92957
Los Angeles, CA 90009
(213) 648-7660

Robert J. Andrews
Univ. of Dayton Research Institute
Kettering Laboratories, Rm. 165
300 College Park Avenue
Dayton, OH 45469
(513) 229-3221

R. Russel Austin
OCLI
Box 1599
Santa Rosa, CA 95402
545-6440

E. Douglas Baird (L-792)
Lawrence Livermore National Laboratory
P. O. Box 808
Livermore, CA 94550
(415) 422-7633

William P. Barnes, Jr.
ITEK Corporation
10 Maguire Road
Lexington, MA 02123
(617) 276-2246

Michael Bass
Univ. of Southern California
Center for Laser Studies
University Park DRB 17
Los Angeles, CA 90007
(213) 743-7994

Jod Batteh
Science Applications Inc.
6600 Powers Ferry Road, Suite 220
Atlanta, GA 30339

Pat Beauchamp
Optical Coating Lab, Inc.
2789 Northpoint Parkway
Santa Rosa, CA 95401
(707) 525-7649

Dr. Michael F. Becker
University of Texas at Austin
Electrical Engineering Department
133 Engineering Science Building
Austin, TX 78712
(512) 471-3628

Bernard Bendow
The BDM Corporation
1801 Randolph Road, SE
Albuquerque, NM 87106
(505) 848-5000

Harold E. Bennett
Michelson Laboratory
Naval Weapons Center, Code 38101
China Lake, CA 93555
(714) 939-2869 or 939-2970

Jay Bernard
Aerpospace Corp.
P. O. Box 92957
Los Angeles, CA 90009
(213) 648-5798

Steven L. Bernasek
Princeton University
Department of Chemistry
Princeton NJ 08544
(609) 452-4986

Dr V. W. Biricik
Northrup Research and Technology Center
One Research Park
Palos Verdes Peninsula, CA 90274
(213) 377-4811 X306

Chris Bjork
Mail Stop 533
Los Alamos National Laboratory
Los Alamos NM 87545

Lynn Bonsall
Rockwell International
Rocketdyne Division
6633 Canoga Avenue
Canoga Park, CA 91304
(213) 700-4900

Gordon Boultbee
Optical Coating Laboratory, Inc.
P.O. Box 1599
Santa Rosa, CA 95402
(707) 545-6440

Theodore Broberg
Honeywell Inc.
2600 Ridgeway Park MN17-1622
Minneapolis, MN 55413
(612) 378-5974

D. C. Brown
Institute of Optics
University of Rochester
Rochester, NY 14627
(716) 275-2471

Achim Bubenzer
Fraunhofer Institut
fur Angewandte Festkorperphysik
Eckerstr. 4, D-78 Freiburg
WEST GERMANY
0761 2714 298

Dennis Burge
Naval Weapons Center, Code 3816
China Lake, CA 93555
(714) 939-2869

Dr Charles A. Burke
Balzers Corporation
211 Second Avenue
Waltham, MA 02254
(617) 890-4200

Charles K. Carniglia
Optical Coating Laboratory, Inc.
2789 Griffen Ave.
Santa Rosa, CA 95402
(707) 545-6440

Stephen Congdon
Airtron Division of Litton Industries
200 E. Hanover Avenue
Morris Plains, NJ 07950
(201) 539-5500

Michael Costelle
TRW, Mail Stop 01-1030
One Space Park
Redondo Beach, CA 90278
(213) 536-3035

Don Dalton
United Technology Research Center
P.O. Drawer 4181
West Palm Beach, FL 33402

Jim Darnell
Ball Aerospace
P. O. Box 1062
Boulder, CO 80306
(303) 441-4118

Donald L. Decker
Code 3816
Naval Weapons Center
China Lake, CA 93555
(619) 939-3247

Marilyn DeLuca
Ferranti Electric Inc.
87 Modular Avenue
Kommac, NY 11725

John A. Detrio
University of Dayton
Research Institute
300 College Park
Dayton, OH 45469
(513) 229-3527

Andrew Devlin
Ferranti Ltd
Dunsinane Avenue
Dundee DD1 3PN
Scotland
UNITED KINGDOM
0382 89321

T. M. Donovan
Code 3812
Naval Weapons Center
China Lake, CA 93555
(619) 446-2115

Kai Druehl
University of New Mexico
Inst. for Modern Optics
700 Yale NE
Albuquerque NM 87131
277-4300

Richard Dyer
W. J. Schafer Associates
10 Lakeside Office Park
Wakefield, MA 01880
(617) 246-0450

David F. Edwards
MS564
Los Alamos National Laboratory
Los Alamos, NM 87545
(505) 667-7102

Osama El-Bayoumi
U.S. Air Force
RADC/ESM
Hanscom AFB, MA 01731
(617) 861-5832

Edward A. Enemark
Optical Coating Lab., Inc.
P. O. Box 1599
Santa Rosa, CA 95402
(707) 545-6440

Donald J. Evans
Air Force Wright Aeronautical Labs
AFWAL/MLPO
Wright Patterson AFB, OH 45433
(513) 255-4474

Fuad Faizullov
Lebedev Physical Institute
Academy of Sciences USSR
53 Leninsky Prospect
Moscow
USSR

Albert Feldman
National Bureau of Standards
A257 Materials Bldg.
Washington, DC 20234
(301) 921-2817

Nils C. Fernelius
Research Institute, University of Dayton
300 College Park Avenue
Dayton, OH 45469
(513) 254-2641

Joseph F. Figueira, AP-5
Los Alamos National Laboratory
P.O. Box 1663, MS/535
Los Alamos, NM 87545
(505) 662-5271

Lawrence B. Fogdall
Boeing Aerospace
Mail Stop 2R-00, P.O. Box 3999
Seattle, WA 98124
(206) 773-2455

Stephen R. Foltyn
Los Alamos National Laboratory
MS-J 566, CHM-5
Los Alamos, NM 87545
(505) 667-1123

Venelsoa D. Foster
Optical Coating Lab., Inc.
2789 Northpoint Parkway
Santa Rosa, CA 95401
(707) 525-7652

Jerome B. Franck
Naval Weapons Center
China Lake, CA 93552
(714) 939-2470

Douglas L. Franzen
724.02
National Bureau of Standards
325 Broadway
Boulder, CO 80303
(303) 497-3346

Daniel Friart
CEA Limeil, BP 27
94190 Villeneuve - St. Georges
FRANCE
569.96.60

Dr. E. Joseph Friebele
DARPA/DSO
1400 Wilson Blvd.
Arlington, VA 22209
(202) 694-1346

Ann T. Glassman
Air Force Avionics Lab., AFWAL/AARI-1
Wright-Patterson AFB, OH 45433
(513) 255-5292

Mark Goldstein
Martin Marietta
Aerospace Corp.
Denver, CO 80201

George A. Graves
University of Dayton
Research Institute, KL 162
300 College Park
Dayton, OH 45469
(513) 229-2517

David L. Griscom
DARPA/DSO
1400 Wilson Blvd.
Arlington, VA 22209
(202) 694-1346

Arthur H. Guenther
AFWL/ALO
Kirtland AFB, NM 87117
(505) 844-9856

Galen J. Hansen
Utah State University
Physics Dept. UMC 41
Logan, UT 84321
(801) 750-2846

Wilford N. Hansen
Physics Dept.
Utah State Univ.
Logan, UT 84321
(801) 750-2852

Richard J. Harris
University of Dayton
Research Institute
300 College Park Ave.
Dayton, OH 45464
(513) 254-2641

Donald J. Harter
Institute of Optics
University of Rochester
Rochester, NY 14627
(716) 275-2471

Deng He
Shanghai Institute of Optics
and Fine Mechanics,
Academia Sinica
Shanghai
CHINA

Lowell M. Hobrock
Bldg 5/B107
Hughes Aircraft Company
Centinela & Teale Street
Culver City, CA 90230

Stuart A. Hoenig
Dept. of Electrical Eng.
University of Arizona
Tucson, AZ 85721
(602) 626-1617

Robert Hofland, Jr.
Aerospace Corp.
P. O. Box 92957
Los Angeles, CA 90009
(213) 648-6115

Samuel J. Holmes
Northrop Research & Technology Center
One Research Park
Palos Verdes Peninusla, CA 90274
(213) 377-4811 X314

Alan K. Hopkins
AFWAL/Materials Lab
Wright-Patterson AFB, OH 45433
(513) 255-4474

John M. Hublin
Bldg. 130/Rm 143
2350 E. El Segundo Blvd.
El Segundo, CA 90245

Dr. Thomas Hynes
U.S. Army
Arsenal Street
Watertown, MA 02172

Stephen D. Jacobs
Laboratory for Laser Energetics
University of Rochester
250 East River Road
Rochester, NY 14623
(716) 275-4837

A. Jacquemmoz
Section Lasers
Centre Universitaire-Bont 503
91 405 Orsay Cedex
FRANCE

B. Jensen
Boston University
Department of Physics
111 Cummington Street
Boston, Mass. 02215
(617) 353-2610

Eric G. Johnson
724.02
National Bureau of Standards
325 Broadway
Boulder, CO 80303

George Johnston
Rockwell International
Rocketdyne Division
AFWL/ARAO
Albuquerque, NM 87106
(505) 843-9780

L. John Jolin
Los Alamos National Laboratory
AP-2 MS J566
Los Alamos, NM 87545
(505) 667-7314

Kenneth Jungling
Univ. of New Mexico, EECE
Albuquerque, NM 87131
277-3317

Robert A. Kamper
724.00
National Bureau of Standards
325 Broadway
Boulder, CO 80303

Thomas A. Kardos
Broomer Laboratories, Inc.
3 Beech St.
Islip, NY 11751
(516) 277-0500

Kenneth A. Kaufman, 01/1080
TRW DSSG
One Space Park
Redondo Beach, CA 90278
(213) 535-1740

John Kern
TRW
One Space Park
Redondo Beach, CA 90278
(213) 535-1792

Christopher Klein
The Aerospace Corporation
MY 980
P.O. Box 92957
Los Angeles, CA 90009
(213) 648-6226

Bengt Kleman
Radians Innova AB
Box 219, S-18252
Djvrsholm
SWEDEN
08-7559125

A. Klugman
Northrop Research & Technology
One Research Park
Palos Verdes Peninsula, CA 90274
(213) 377-4811 X466

Walter L. Knecht
AFWAL/MLPO
Wright Patterson AFB, OH 45433
(513) 255-4474

Kent Kogler
IIT Research Institute
10 West 35th Street
Chicago IL
(513) 256-7700

William Koldewyn
Ball Aerospace Systems Division
Boulder, CO 80306

Nicholas Koumvakalis
Center for Laser Studies, USC
Denney Research Bldg, Rm. 17
Los Angeles, CA 90089-1112
(213) 743-5024

Munson A. Kwok
The Aerospace Corporation
P.O. Box 92957, 130-139
Los Angeles, CA 90009
(213) 648-5441

Mike Lang
Ball Aerospace Systems Div.
P.O. Box 1062
Boulder, CO 80306
(303) 441-4000

Chun-Sheu Lee
USC Center for Laser Studies
DRB Rm 5, USC
Los Angeles, CA 90007
(213) 743-6790

R. Lenfant
Laboratories De Marcoussis
Center De Recherches De LA C.G.E.
Route de Nozay
91 460 Marcoussis
FRANCE
449 11 49

Daniel H. Leslie
Optical Sciences Division
Naval Research Laboratory
Washington, DC 20375
(202) 767-3005

J. R. Lifsitz
MIT/Lincoln Laboratory
244 Wood St.
Lexington, MA 02168
(617) 862-5500

W. Howard Lowdermilk
Lawrence Livermore
National Laboratory
P.O. Box 5508, L-470
Livermore, CA 94550
(415) 422-5498

Michael Lunt
Technical Optics
Second Avenue,
Onchan, Isle of Man
UNITED KINGDOM
0624 4443

Amy G. Lusk
USAF, AFWL/ARAO
Kirtland AFB, NM 87117
(505) 844-1776

Major Ronald L. Lusk
AFWL/ARAO
Kirtland AFB, NM 87117
(505) 844-1776

H. Angus Macleod
Optical Sciences Center
University of Arizona
Tucson, AZ 85721
(602) 3025

Alexander A. Manenkov
Lebedev Physics Inst.
Academy of Sciences, USSR
Leninsky Prospect, 53
Moscow
USSR

Jay Marmo
TRW, Bldg 01/1051
One Space Park
Redondo Beach, CA 90277
(213) 535-2753

C. Denton Marrs
Naval Weapons Center
Physics Division
Code 3817
China Lake, CA 93555
(714) 939-2470

John K. McIver
Univ. of New Mexico
Inst. for Modern Optics
Albuquerque, NM 87131
(505) 277-5909

Ted McMinn
McDonnelll Douglas Astronautics Co.
5311-K Forest Creek Dr.Hazelwood, MO 63042
(314) 232-9097

Russell Mellon
Ball Aerospace Systems Division
Boulder, CO 80306

Larry D. Merkle
Univ. of Southern California
Center for Laser Studies
DRB 17, University Park
Los Angeles, CA 90089-1112
(213) 743-4379

David Milam
Lawrence Livermore
National Laboratory
PO Box 5508, L-490
Livermore, CA 94550
(415) 422-5499

Dr. Perry A Miles
Raytheon Company
Hartwell Road
Bedford, MA 01730
(617) 274-7100 X3553

Kent Moncur
KMS Fusion, Inc.
PO Box 1567
3621 S. State Rd.
Ann Arbor, MI 48106-1567
(313) 769-8500, X381

Thomas J. Moravec
Honeywell Inc.
10701 Lyndale Ave. S
Bloomington, MN 55420
(612) 887-4309

Dennis Morelli
Optical Coating Laboratory, Inc.
2789 Northpoint Parkway
Santa Rosa, CA 95401-7397
(707) 525-7011

Richard N. Mostrom
Honeywell Ceramics Center
5121 Winnetka Ave. North
New Hope, MN 55428
(612) 536-3200

Jacques Mouchart
Laboratories de Marcoussis
Centre de Recherches
de la Compagnie Generale d'Electricite
Route de Nozay
91460 Marcoussis
FRANCE

James Munroe
Los Alamos National Laboratory
P.O. Box 1663, MS J564
Los Alamos, NM 87545

Fred Myland
Martin Marietta
Aerospace Corp.
Denver, CO 80201

George Nado
Texas Instruments
Box 226015
Mail Stop 3177
Dallas, TX 75266

Yoshiharu Namba
University of New Mexico
Albuquerque, NM 87131
(505) 277-5625

Roy D. Nelson
Ball Aerospace Systems Division
P.O. Box 1062
Boulder, CO 80306
(303) 441-4000

Brian E. Newnam
Los Alamos National Laboratory
Group CHM-6, MS-J564
Los Alamos, NM 87545
(505) 667-7979 or-7102

Davis B. Nichols
Boeing Aerospace Co.
Mail Stop 88-46
PO Box 3999
Seattle, WA 98124
(206) 773-8938

James Nicol
Physical Systems Research Section
Arthur D. Little, Inc.
Acorn Park
Cambridge, MA 02140
(617) 864-5770 X3071

Frederic S. Nyland
Martin Marietta
830 B 13th St.
Boulder, CO 80302
(303) 977-0816

E. John O'Grady
Eastman Kodak Company
Kodak Apparatus Division
800 Lee Road
Rochester, NY 14650
(716) 722-0387

F. D. Orazio
VTI Inc.
4126 Linden Avenue
Dayton, OH 45432
(513) 254-6201

Henry J. B. Orr
Ferranti Ltd.
Dundee Optical Facility
Dunsinane Ave.
Dundee DD2 3PN
SCOTLAND
0382 89311

James R. Palmer
Doc Jim Enterprises
1250 N. Lynwood Dr.
Anaheim, CA 92807
(714) 779-0589

James L. Parham
US Army Missile Command
ATTN: DRSMI-RLM
Redstone Arsenal, AL 35898
(205) 876-4933

Walter T. Pawlewicz
Battelle Northwest Lab.
P. O. Box 999
Richland, WA 99352
(509) 373-2537

David Payne
P.M.S. Optics
1855 So. 57th Ct
Boulder, CO
(303) 443-7100

Allen B. Petersen
Spectra Physics
1250 W. Middlefield Road
Mountain View, CA 94042
(415) 961-2550 X2064

Ronald E. Peterson
Honeywell Inc.
2600 Ridgway Parkway
P.O. Box 312
Minneapolis, MN 55440
(612) 378-4543

Major Bruce J. Pierce
USAF - AFWL/ARAO
Kirtland AFB, NM 87117
(505) 844-1776

Timothy Pittner
Laboratory for Laser Energetics
University of Rochester
250 East River Road
Rochester, NY 14623

Robert D. Poirier
Perkin Elmer Corp
77 Danbury Rd MS420
Wilton, CT 06897
(203) 834-4934

James O. Porteus
Naval Weapons Center
Code 3817
China Lake, CA 93555
(714) 939-3827

Tim Pottenger
University of Dayton
Research Inst. KL 102
300 College Park
Dayton, OH 45469
(513) 229-3221

Richard S. Quimby
Univ. Southern California
Center for Laser Studies
University Park
Los Angeles, CA 90007
(213) 743-5024

Frank Rainer
Lawerence Livermore
National Laboratory
P. O. Box 5508, L-490
Livermore, CA 94550
(415) 422-4376

Max E. Reed
Los Alamos National Laboratory,
MS S601
Los Alamos, NM 87545

Stanley J. Refermat
Eastman Kodak Company
Kodak Apparatus Division
901 Elmgrove Road
Rochester, NY 14650
(716) 724-5426

Dick Reynolds
U.S. Army Missile Command
Redstone Arsenal
Huntsville, AL 35898

J. Earl Rudisill
Laser Power Optics
11211-U Sorrento Valley Rd
San Diego, CA 92121
(714) 455-0751

Lt. Thomas Rueff
Air Force Wright Aeronautical
Flight Dynamnic Laboratory
AFWAL/FDL/FISL
Wright Patterson AFB, OH 45433

Lt. Col. Theodore T. Saito
FJSRL/NH
USAF Academy, CO 80840
(303) 472-3122

Aaron Sanders
724.02
National Bureau of Standards
325 Broadway
Boulder, CO 80303
(303) 497-5341

David Sanders
B328, Bld 223
National Bureau of Standards
Washington, DC 20234
(301) 921-2817

Paul Schall
The Aerospace Corporation
P.O. Box 92597
Los Angeles, CA 90009
(213) 648-7502

Ansgar Schmid
Physics Dept.
Washington State Univ.
Pullman, WA 98164
(509) 335-4672/9531

Marija S. Scholl
Rockwell Intl, Rocketdyne Div.
6633 Canoga Avenue, MS-FA42
Canoga Park, CA 91304
(213) 700-4900

Dennis Schre
Westinghouse Electric Corp.
1310 Beulah Road
Pittsburgh, PA 15235

Dave A. Segawa
Hoya Optics USA, Inc.
3400 Edison Way
Fremont, CA 94538

Steven C. Seitel
Michelson Lab.
Code 3817, Naval Weapons Center
China Lake, CA 93555
(714) 939-3049

R. R. Shannon
Optical Science Center
Univ. of Arizona
Tucson, AZ 85721
(602) 626-3345

C. Y. She
Physics Dept.
Colorado State Univ.
Fort Collins, CO 80523
(303) 491-6262

Keith Shillito
AFWL
Kirtland AFB, NM 87117
(505) 844-1776

R. M. Silva
VTI Inc.
4126 Linden Avenue
Dayton, OH 45432
(513) 254-6201

Meyer Silver
TRW
One Space Park
Redondo Beach, CA 90266
(213) 535-6709

Robert A. Simms
Litton Industries
1215 S. 52nd St.
Tempe, AZ 85281
(602) 968-4471

James H. Simpson
The Singer Co.-Kearfott Div.
1150 McBride Avenue, MC 03A76
Little Falls, N.J 07424
(201) 256-4000 X2133

James R. Sites
Physics Departmnet
Colorado State Univ.
Fort Collins, CO 80523
(303) 491-5850

David H. Sliney
U.S. Army Environmental
Hygiene Agency
Aberdeen Proving Ground MD 21010
(301) 671-3932 or 3468

M. J. Smith
Avco Everett Research Lab.
2385 Revere Beach Parkway
Everett, MA 02149
(617) 381-4697

M. J. Soileau
North Texas State University
Physics Department
P.O. Box 5368
Denton, TX 76203
(817) 565-3263

Marshall Sparks
Scientific Research Center
1640 Fifth Street, Suite 216
Santa Monica, CA 90401
(213) 394-0219

Fred W. Spong
Storage Technology Corp. MSGG
2270 S. 88th St.
Louisville CO
(303) 673-5917

James L. Stanford
Naval Weapons Center, Code 3818
China Lake, CA 93555
(619) 939-2443

James L. Stapp
United States Air Force,
AFWL/ARLO
Kirtland AFB, NM 87117
(505) 844-1704

Bob Steele
Allied Corp, E.O.P.D.
P.B. Box 4901
Warren, NJ 07060

Martin Stein
G&W Applied Science Laboratories
335 Bear Hill Road
Waltham, Mass. 02154
(617) 890-5100

Donald F. Stevison
Materials Lab.
AFWAL/MLPJ
Wright Patterson AFB, OH 45433
(513) 255-2210

Alan F. Stewart
AFWL/ARAO
Kirtland AFB
Albuquerque, NM 87117
(505) 844-7368

James E. Swain
Lawrence Livermore Lab
P.O. Box 5508, L470
Livermore, CA 94550
(415) 422-5402

Raymond L. Taylor
Research & Laser Technology Inc.
36 Commerce Way
Woburn, MA 01801
(617) 938-1524

Paul A. Temple
Naval Weapons Center, Code 3816
China Lake, CA 93555
(714) 939-3247

James H. Tillotson
Rocketdyne/Rockwell International
6633 Canoga Avenue
Canoga Park, CA 91304
(213) 700-4942

Bruce Tirri
Perkin-Elmer Corp, MS420
77 Danbury Rd.
Wilton, CT 06856
(203) 775-4794

N. Tzoar
Physics Dept.
City College
Convent Ave & 138th St.
New York, NY 10031
(212) 690-6923

A. Vaidayanathan
Universal Energy Systems
Air Force Materials Lab
AFWAL/MLPJ
Wright Patterson AFB, OH 45433
(513) 255-6671

Eric W. VanStryland
Physics Department
North Texas State University
Denton, TX 76203
(817) 788-2626

Howard C. Volkin
Rockwell International
Rocketdyne Division
P.O. Box 5670 KAFB
Kirtland AFB, NM 87185
(505) 846-2441

Marc von Gunten
Spectra-Physics
1250 West Middlefield
Mountain View, CA 94042
(415) 961-2550 X3008

Harshadrai Vora
Honeywell Corporate Technology
Center
10701 Lyndale Ave. S.
Bloomington, MN 55420
(612) 887-4412

Rodger M. Walser
University of Texas
437 ENS
Austin, TX 78712
(512) 471-5733

James D. Weigner
Honeywell Ceramics Center
5121 Winnetka Ave. N.
New Hope, MN 55428
(612) 536-3161

Jeremy Weston
British Aerospace P.L.C
Dynamics Group, Laser
Systems Dept., F.P.C.67
Filton, Bristol BS12 7QW
UNITED KINGDOM
(272) 693831 Ext 1012

Garry D. Williams
Crystal Technology
1035 East Meadow Circle
Palo Alto, CA 94303
(415) 856-7916

William E. Williams
North Texas State Univ.
Center for Applied Quantum Electronics/Physics
Dept.
Denton, TX 76203
(817) 788-2626

Charles B. Willingham
Raytheon Company/Research Division
131 Spring St.
Lexington, MA 02173
(617) 863-5300 X3062

Jim Willis
Lawrence Livermore Lab
P. O. Box 808, L-461
Livermore, CA
(415) 422-1051

Harry V. Winsor, USAF
Air Force Office of Scientific Research
Bolling AFB, DC 20332
(202) 767-4931

Roger M. Wood
The General Electric Company Limited
Hirst Research Centre
East Lane, Wembley, Middlesex HA7 9PP
UNITED KINGDOM
01-904-1262 Ext. 205

☆ U.S. GOVERNMENT PRINTING OFFICE : 1983 O—380-997 (5196)

NBS-114A (REV. 2-8C)

U.S. DEPT. OF COMM. BIBLIOGRAPHIC DATA SHEET (See instructions)	1. PUBLICATION OR REPORT NO. NBS SP 638	2. Performing Organ. Report No.	3. Publication Date September 1983

4. TITLE AND SUBTITLE

Laser Induced Damage in Optical Materials: 1981

5. AUTHOR(S) Editors: Harold E. Bennett (NWC), Arthur H. Guenther (AFWL), David Milam (LLNL), and Brian E. Newnam (LANL)

6. PERFORMING ORGANIZATION (If joint or other than NBS, see instructions)

NATIONAL BUREAU OF STANDARDS
DEPARTMENT OF COMMERCE
WASHINGTON, D.C. 20234

7. Contract/Grant No.

8. Type of Report & Period Covered
Final

9. SPONSORING ORGANIZATION NAME AND COMPLETE ADDRESS (Street, City, State, ZIP)

National Bureau of Standards
American Society for Testing and Materials
Office of Naval Research
Department of Energy
Defense Advanced Research Project Agency
Air Force Office of Scientific Research

10. SUPPLEMENTARY NOTES

Library of Congress Catalog Card Number: 83-600570

☐ Document describes a computer program; SF-185, FIPS Software Summary, is attached.

11. ABSTRACT (A 200-word or less factual summary of most significant information. If document includes a significant bibliography or literature survey, mention it here)

The Thirteenth Annual Symposium on Optical Materials for High Power Lasers (Boulder Damage Symposium) was held at the National Bureau of Standards in Boulder, Colorado, Nov. 17-18, 1981. The Symposium was held under the auspices of ASTM Committee F-1, Subcommittee on Laser Standards, with the joint sponsorship of NBS, the Defense Advanced Research Project Agency, the Department of Energy, the Office of Naval Research, and the Air Force Office of Scientific Research. Approximately 200 scientists attended the Symposium, including representatives of the United Kingdom, France, Japan, West Germany, the Peoples Republic of China, Sweden, and the USSR. The Symposium was divided into sessions concerning Materials and Measurements, Mirrors and Surfaces, Thin Films, and finally Fundamental Mechanisms. As in previous years, the emphasis of the papers presented at the Symposium was directed toward new frontiers and new developments. Particular emphasis was given to materials for high power apparatus. The wavelength range of prime interest was from 10.6 μm to the uv region. Highlights included surface characterization, thin film-substrate boundaries, and advances in fundamental laser-matter threshold interactions and mechanisms. The scaling of damage thresholds with pulse duration, focal area, and wavelength was discussed in detail. Harold E. Bennett of the Naval Weapons Center, Arthur H. Guenther of the Air Force Weapons Laboratory, David Milam of the Lawrence Livermore National Laboratory, and Brian E. Newnam of the Los Alamos National Laboratory were co-chairmen of the Symposium. The Fourteenth Annual Symposium is scheduled for Nov. 15-17, 1982, at the National Bureau of Standards, Boulder, Colorado.

12. KEY WORDS (Six to twelve entries; alphabetical order; capitalize only proper names; and separate key words by semicolons)

laser damage; laser interaction; optical components; optical fabrication; optical materials and properties; thin film coatings.

13. AVAILABILITY

☒ Unlimited

☐ For Official Distribution. Do Not Release to NTIS

☒ Order From Superintendent of Documents, U.S. Government Printing Office, Washington, D.C. 20402.

☐ Order From National Technical Information Service (NTIS), Springfield, VA. 22161

14. NO. OF PRINTED PAGES
651

15. Price
$12.00

NBS TECHNICAL PUBLICATIONS

PERIODICALS

JOURNAL OF RESEARCH—The Journal of Research of the National Bureau of Standards reports NBS research and development in those disciplines of the physical and engineering sciences in which the Bureau is active. These include physics, chemistry, engineering, mathematics, and computer sciences. Papers cover a broad range of subjects, with major emphasis on measurement methodology and the basic technology underlying standardization. Also included from time to time are survey articles on topics closely related to the Bureau's technical and scientific programs. As a special service to subscribers each issue contains complete citations to all recent Bureau publications in both NBS and non-NBS media. Issued six times a year. Annual subscription: domestic $18; foreign $22.50. Single copy, $5.50 domestic; $6.90 foreign.

NONPERIODICALS

Monographs—Major contributions to the technical literature on various subjects related to the Bureau's scientific and technical activities.

Handbooks—Recommended codes of engineering and industrial practice (including safety codes) developed in cooperation with interested industries, professional organizations, and regulatory bodies.

Special Publications—Include proceedings of conferences sponsored by NBS, NBS annual reports, and other special publications appropriate to this grouping such as wall charts, pocket cards, and bibliographies.

Applied Mathematics Series—Mathematical tables, manuals, and studies of special interest to physicists, engineers, chemists, biologists, mathematicians, computer programmers, and others engaged in scientific and technical work.

National Standard Reference Data Series—Provides quantitative data on the physical and chemical properties of materials, compiled from the world's literature and critically evaluated. Developed under a worldwide program coordinated by NBS under the authority of the National Standard Data Act (Public Law 90-396).

NOTE: The principal publication outlet for the foregoing data is the Journal of Physical and Chemical Reference Data (JPCRD) published quarterly for NBS by the American Chemical Society (ACS) and the American Institute of Physics (AIP). Subscriptions, reprints, and supplements available from ACS, 1155 Sixteenth St., NW, Washington, DC 20056.

Building Science Series—Disseminates technical information developed at the Bureau on building materials, components, systems, and whole structures. The series presents research results, test methods, and performance criteria related to the structural and environmental functions and the durability and safety characteristics of building elements and systems.

Technical Notes—Studies or reports which are complete in themselves but restrictive in their treatment of a subject. Analogous to monographs but not so comprehensive in scope or definitive in treatment of the subject area. Often serve as a vehicle for final reports of work performed at NBS under the sponsorship of other government agencies.

Voluntary Product Standards—Developed under procedures published by the Department of Commerce in Part 10, Title 15, of the Code of Federal Regulations. The standards establish nationally recognized requirements for products, and provide all concerned interests with a basis for common understanding of the characteristics of the products. NBS administers this program as a supplement to the activities of the private sector standardizing organizations.

Consumer Information Series—Practical information, based on NBS research and experience, covering areas of interest to the consumer. Easily understandable language and illustrations provide useful background knowledge for shopping in today's technological marketplace.

Order the **above** *NBS publications from: Superintendent of Documents, Government Printing Office, Washington, DC 20402.*

Order the **following** *NBS publications—FIPS and NBSIR's—from the National Technical Information Service, Springfield, VA 22161.*

Federal Information Processing Standards Publications (FIPS PUB)—Publications in this series collectively constitute the Federal Information Processing Standards Register. The Register serves as the official source of information in the Federal Government regarding standards issued by NBS pursuant to the Federal Property and Administrative Services Act of 1949 as amended, Public Law 89-306 (79 Stat. 1127), and as implemented by Executive Order 11717 (38 FR 12315, dated May 11, 1973) and Part 6 of Title 15 CFR (Code of Federal Regulations).

NBS Interagency Reports (NBSIR)—A special series of interim or final reports on work performed by NBS for outside sponsors (both government and non-government). In general, initial distribution is handled by the sponsor; public distribution is by the National Technical Information Service , Springfield, VA 22161, in paper copy or microfiche form.

U.S. Department of Commerce
National Bureau of Standards

Washington, D.C. 20234
Official Business
Penalty for Private Use $300

POSTAGE AND FEES PAID
U.S. DEPARTMENT OF COMMERCE
COM-215

SPECIAL FOURTH-CLASS RATE
BOOK